



Kumamoto University

INTERNATIONAL ENGINEERING SYMPOSIUM 2011 (IES 2011)

**100th Anniversary Memorial Hall &
Faculty of Engineering (Building No.2),
Kumamoto University**

March 3-5, 2011



Organized by

**Graduate School of Science & Technology
Kumamoto University, Japan**

PROCEEDINGS OF
**INTERNATIONAL ENGINEERING
SYMPOSIUM 2011**
(IES 2011)

Venue

100th Anniversary Memorial Hall & Faculty of Engineering (Building No.2)
Kumamoto University

Date

March 3-5, 2011

Convener

Shuichi TORII

Professor, Dept of Mechanical System Engineering
& Deputy Director, Center for Globalization

Organized by

**Graduate School of Science & Technology
Kumamoto University
Kumamoto City, Japan**

PREFACE

The International Engineering Symposium (IES2011) at Kumamoto University (KU) is intended to provide a common platform for bringing together researchers from universities and research organizations for expanding academic collaborations. The researchers from abroad have been invited to visit Kumamoto University and get familiar with its educational and research activities. The event focuses on the current research and development of the participating countries on topics of mutual interest, with special emphasis on "Science & Technology". The emerging technologies and scientific advancements are discussed during the symposium. Presentations feature new and innovative technologies in the relevant fields.

This proceedings volume contains the technical papers presented at the symposium. The topics include a wide spectrum of themes covering all major disciplines of science and engineering. The efforts by faculty, staff and students of Kumamoto University in organizing this event are greatly appreciated.

I sincerely hope that all the readers will find the contents of this proceedings volume useful and productive. We look forward to more intense academic collaborations and research interactions in the coming days, to achieve the common goal of technological advancement for global peace and prosperity.

Torii Shuichi
Convener

IES2011 Program Schedule

Venue: **100th Anniversary memorial Hall (March 3)**
Faculty of Engineering, Building No.2 (March 4)

March 3, 2011 (Thursday)

9:30 – 10:00	Registration
10:00 – 10:30	Welcome address & Introduction to KU
10:30 – 11:00	Keynote Lectures (<i>K1</i>)
11:00 – 11:30	Break
11:30 - 12:45	Keynote Lectures (<i>K2</i>)
12:45 – 14:00	Lunch Break
14:00 – 15:00	Campus Tour
15:00 – 17:00	Laboratory Visits
17:00 – 17:30	Free Time
17:30 – 19:00	Welcome Reception

March 4, 2011 (Friday)

9:30 – 11:00	Technical Sessions (<i>M1,C1,C4,E1</i>)
11:00 – 11:30	Break
11:30 - 12:45	Technical Sessions (<i>M2,C2,C5,E2</i>)
12:45 – 14:00	Lunch Break
14:00 – 15:30	Technical Sessions (<i>M3,C3,C6,S1</i>)
15:30 – 16:00	Break
16:00 – 17:00	Technical Sessions (<i>M4,A1,C7</i>)
17:00 – 17:30	Free time
17:30 – 19:00	Symposium Dinner

March 5 2011 (Saturday)

9:00 – 17:00	Field visits
--------------	--------------

Notations:

- K Keynote Lectures*
M Technical Sessions (Mechanical Engineering & Related Fields)
C Technical Sessions (Civil Engineering, Earth Sciences & Related Fields)
A Technical Sessions (Architecture)
E Technical Sessions (Electrical, Electronics, Computer Engineering & Related Fields)
S Technical Sessions (Biology, Chemistry & Chemical Engineering)

Contents

Keynote Lectures

- K1 Bioethanol Processing Control by Real-Time Sensor System
Carlos K. Suzuki
- K2-1 Nanofluid Research at the University of Hong Kong
L W Wang
- K2-2 A Sustainable Building Material from Biological Sources
A Mukherjee, V Achal and M S Reddy
- K2-3 Correlation between correlation between petrographical and engineering properties of Ilkal granites, Karnataka
D Venkat Reddy, H G Santosh and K Priyanka

Mechanical Engineering & Related Fields

- M1-1 Vibration and responses characteristics of lateral cantilever shaft vibration of a vertical-axis ocean current turbine
I K A P Utama and R Hantoro
- M1-2 Foot pressure mapping system for a biped robot
Cheng-Hsin Chuang, Yi-Rong Liou and Ming-Yuan Shieh
- M1-3 Fuzzy logic controller to regulate the pH and EC for irrigation system in greenhouse
Duy Anh Nguyen, Hoang Nguyen, Thanh Tung Tran, Quoc Dat Le & Tan Tien Nguyen
- M1-4 Static characteristics of a journal bearing with engineered slip/no-slip surfaces
Raghunandana K and John V Corda
- M1-5 Single and multilayer polyvinylidene fluoride piezo film for force sensing
Navin Karanth P, Vijay Desai and S M Kulkarni
- M1-6 A comparative study of size effect on entropy generation in micro-channels
Shu-Min Tu, Shuichi Torii and Yang-Cheng Shih
- M2-1 Effect of B₂O₃ addition on the mechanical property of Mg-RE alloy
Takeyuki Yagi, Sayuri Yoshimoto, Hiromoto Kitahara and Shinji Ando
- M2-2 Vibration and cylinder chamber pressure characteristics of a reciprocating compressor: effects of a change on a discharge valve seat profile
Bambang Daryanto Wonoyudo and Ardi Nugroho
- M2-3 Dynamic modeling and experimental verification of polyvinylidene fluoride actuator for a valve-less micropump
Navin Karanth P, Vijay Desai and S M Kulkarni

- M2-4 Characterization of polyvinylidene fluoride piezo film for fluid pressure sensor application
Navin Karanth P, Vijay Desai and S M Kulkarni
- M2-5 Computational modelling of compression process in a dual fuel compression ignition engine
Krishna Murthy, Madhwesh N and Shrinivasa Rao B R
- M3-1 Development of combustor for mixed combustion biomass with waste oil
Masato Urashima and Shuichi Torii
- M3-2 Design and analysis of air flow control mechanism of automotive HVAC module using CAE tools
Daljeet singh
- M3-3 Numerical analysis of flow through abrasive water suspension jet: the effect of abrasive grain size and jet diameter ratio on wall shear
Deepak D, N Yagnesh Sharma and Anjaiah D
- M3-4 Unmanned aerial vehicle for coastal zone management
Pruthviraj U, Sohan S, Ashwin L N and Shritheja U
- M3-5 Experimental study on convective heat transfer of Al₂O₃ nanofluid dispersed in ethylene glycol
Hajime Yoshino and Shuichi Torii
- M4-1 Thermal fluid flow transport characteristics in confined channels with two dimensional dual jet impingement
Caner Senkal and Shuichi Torii
- M4-2 Thermal hydraulics in macro channel using venturi effect of outer air
Giichi Nakamura and Shuichi Torii
- M4-3 Investigation of combustion furnace fuelled by compost
Shota Watanabe and Shuichi Torii
- M4-4 High-sensitivity concentration sensor based on fiber bragg grating
Raikar U S, Lalasangi A S, Akki J F, Radhakrishnan P, Manohar K.G and Srinivas T

Civil Engineering, Earth Sciences & Related Fields

- C1-1 Studies on the influence of infill on dynamic characteristics of reinforced concrete frames
Chethan K, R Ramesh Babu, Katta Venkataramana and Akanshu Sharma
- C1-2 Vulnerability analysis in seismic design of structures
Balaji K V G D, Gopala Raju S S S V and Praveena Gorla
- C1-3 Response control of MDOF space frame structure using multiple tuned mass dampers
Kiran K Shetty, Krishnamoorthy and Gopinath Nayak

- C1-4 Static and dynamic analyses of laminated composite plates using higher order refined computational models
S Shantharam Patil
- C1-5 Stress analysis of antisymmetric angle ply sandwich plates- analytical evaluation of refined higher order shear deformation theories
K Swaminathan and Govind R Sangwai
- C2-1 Conservation of civil engineering heritage in Japan
K Nagamura, I Kobayashi and K Venkataramana
- C2-2 The alternative building materials and technologies for individual housing in coastal Karnataka, India
Rajendra Kalbavi Rao, Sudeep Kumar Shetty and John Kenet D'Souza
- C2-3 Slim – GAL for shape optimization of structures
Babu Narayan K.S, Devraj Manai and Arun Prabha K S
- C2-4 Performance appraisal of RC beams using welded wire fabrics as lateral reinforcement in seismic zones
H C Chinnagiri Gowda, K S Babu Narayan and Katta Venkataramana
- C2-5 Ground response at Kandla port region during the 2001 Bhuj earthquake – a case study
L Govindaraju and Santoshkumar Patil
- C3-1 Weibull analysis of acoustic emission hits behaviour for evaluation of deteriorated concrete due to freezing and thawing
Ni Nyoman Kencanawati and Mitsuhiro Shigeishi
- C3-2 Characteristics of normal strength concrete with and without chemical admixtures at elevated temperatures
Subhash C Yaragal, Sharanabasappa A Warad, K S Babu Narayan and Katta Venkataramana
- C3-3 Properties of self-compacting mortars containing steel fibre with cementitious blends of fly ash, ground granulated furnace slag and silica fume
S.Bhavanishankar, H D Devadas and M C Nataraja
- C3-4 Study of properties of high strength concrete - partial substitution by marine sand
Ravindranatha, Udaya Shankar H N and Muhsin Shafeeq V
- C3-5 An experimental study on influence of bamboo fibre on strength and ductility of concrete
Gopinandan Dey
- C4-1 Upflow anaerobic wastewater treatment using PVA/PEG beads as biomass carriers
Khanh Do Phuong, Quan Lai Minh, Hiroaki Fujii and Kenji Furukawa
- C4-2 Study on domestic wastewater treatment with two-step feed processes (A2O2)
Tan Phong Nguyen and Thanh Hung Nguyen

- C4-3 Reject water treatment by improvement of whole cell anammox entrapment using polyvinyl alcohol/alginate gel
Lai Minh Quan, Do Phuong Khanh, Daisuke Hira, Takao Fujii and Kenji Furukawa
- C4-4 Effect of paper mill effluents on the river water chemistry: a case study of river Godavari at Rajahmundry
K Balakrishna, G P Gurumurthy, A M Shiller and G Mugeraya
- C4-5 Community response to transportation noises in Vietnam
Thu Lan Nguyen, Quang Nguyen Huy, Takashi Yano, Tsuyoshi Nishimura, Tetsumi Sato and Takashi Morihara
- C4-6 Rain water harvesting-conservation and rescue
Ditimonri Baruah
- C5-1 Traffic management proposals for Udupi city.
Raviraj H Mulangi, A U Ravi Shankar and Varghese George
- C5-2 Development of concrete armoured protected breakwater structure
Manu, Subba Rao and Kiran G Shirlal
- C5-3 Comprehensive physical model study on wave transmission at plate structure
Kiran G Shirlal, Subba Rao and Roobin V Verghese
- C5-4 Microfabric and mineralogical studies using SEM and XRD on the lithomargic clay stabilized with cement and quarry dust
Purushotham G. Sarvade and Sitaram Nayak
- C6-1 Analysis of longitudinal and transverse profiles in Seetha-Swarna and Gangolli rivers of coastal Karnataka, India
Udaya Shankara H N
- C6-2 Hydrogeological characterization of Swarna watershed of coastal Karnataka, India using GIS approach
Prakash Rao B and Mohandas Chadaga
- C6-3 Evaluation of morphometric characteristics by using GIS in Kollur watershed of coastal Karnataka, India
Mohandas Chadaga, Udayashankar H N, Prakash Rao B and Bhat Gangadhar H
- C6-4 Preliminary liquefaction potential analysis of Vijayawada region
K Rajesh Chandra, Akhila Manne and Neelima Satyam D
- C7-1 Hydrogeochemical studies of groundwater along coastal region of mulki-udipi, Karnataka state, india
Radhakrishnan K, Shenoy K Narayana and Lokesh K N
- C7-2 Evaluation of reference evapotranspiration methods at a sub-humid location in Karnataka state, india
Boregowda S B, Lakshman Nandagiri and Gicy M Kovoor

- C7-3 Development of digital terrain modelling using cartosat-1 satellite imagery
(a case study of Manipal city of Udupi district, Karnataka State)
K N Lokesh , B Naveenchandra, Usha and H Gangadhara Bhat
- C7-4 Computing of Udyavara fluvial systems-a river of western ghats, India: a pragmatic inference of runoff to hydrological cycle
B S Maddodi, H N Udaya Shankara and B R Raghavan
- C8-1 Rain water harvesting – a handy tool to preserve water
Rajendra Kalbavi Rao, Sathyaranjan Rao, Raviprasad Upadhyaya
- C8-2 Flexure, shear and torsion interaction: Design aids for optimization
Babu Narayan K S, Prithivi Hegde and Sadanand Shetty
- C8-3 Simplified solutions for shape searching
Babu Narayan K S, Shamir R and Satish B
- C8-4 Strength retention studies on normal concrete and self compacting concrete subjected to elevated temperatures
Babu Narayan K S, Vinay Kumar G, Subhash C Yaragal and Katta Venkataramana

Architecture

- A1-1 A field study on the moderating effect of sound absorption on the noisy sound environment in nursery school classrooms
Munehide Saito, Kazuaki Sakoda and Keiji Kawai
- A2-1 Study on soundproofing windows
Quang Nguyen Huy, Yuya Nishimura, Takashima Yusuke and Takashi Yano
- A2-3 Advanced construction systems For urban housing
N K Garg
- A2-4 Living the common styles---tracing common paradigms between Indo-Japanese architecture
Nisha Soares and Ajai Chandran C K
- A2-5 Beyond activism
Ajai Chandran C K and Priti Pai

Electrical, Electronics, Computer Engineering & Related Fields

- E1-1 Bandwidth enhancement of circularly polarized square slot antenna with separated L-probes
Ronald Joseph, Shuhei Nakao and Takeshi Fukusako
- E1-2 Confirmed message delivery to mobile agents: A theoretical model
Kumkum Garg and Rama Sushil

- E1-3 Design and implementation of genetic algorithm as the PID controller parameter optimization method for networked control system
Aditya Tejo Widagdo, Katjuk Astrowulan and Imam Arifin
- E1-4 Improving modern port competitiveness by using data mining to obtain strategic decision
Dhanika Budhi A, Mahendrawathi E R and Rully Soelaiman
- E1-5 Intelligent clustering of spatial data for spatial classification using data mining
Ahamed Shafeeq B M and Govardhan Hegde
- E2-1 Reliability of fault tolerant routing algorithm for torus embedded hypercube interconnection network
N Gopalakrishna Kini, M Sathish Kumar and Mruthyunjaya H S
- E2-2 An intelligent cashew kernels classification using color features
Narendra V G and Hareesha K S
- E2-3 Enterprise knowledge grid provisioning for resource sharing
Praveen Desai and U Dinesh Acharya

Biology, Chemistry and Chemical Engineering

- S1-1 Tissue culture studies on different explants of rice (*oryza sativa l.*) varieties cultivated by ethnic communities of Jharkhand state, India
H P Sharma, Kanak and Meena Misra
- S1-2 Evaluation of feeding strategies for enhanced cell-associated tannase production by *serratia ficaria* DTC
Prasanna D Belur and Dinesh C Goudar
- S1-3 Studies on chitosan incorporated nanocomposite polymer membranes
K Karuppasamy, C Vijil Vani, S Balakumar and X Sahaya Shajan
- S1-4 Alumina supported nanoruthenium efficient catalyzed N-oxidation of tertiary amines by using H_2O_2
P Veerakumar, S Balakumar and S Rajagopal

KEYNOTE LECTURES

Bioethanol Processing Control by Real-Time Sensor System

Carlos K. Suzuki

*Faculty of Mechanical & Mechatronics Engineering,
UNICAMP - The State University of Campinas,
13083-970 Campinas, SP, Brazil
email: suzuki@fem.unicamp.br*

Abstract

Presently, more than fifty percent of the Brazilian gasoline demand has been substituted by sugarcane based ethanol. Its cost is highly competitive, even though without subsidies. Such a use of sugarcane ethanol is being adopted by other almost one hundred countries around the world due to its advantage in terms of social and environmental sustainability. Recent studies conducted by Brazilian Bioethanol Science and Technology Laboratory (CTBE) indicate that the use of 7% of the total area currently used for agriculture in Brazil, if dedicated to cultivate sugarcane, it becomes possible to produce enough amount of bioethanol (1st generation processing) to displace almost 10% of worldwide gasoline use in 2025.

On the other hand, analysis of the current production process has shown several flaws identified in 15 sub-processes stages, such as sugarcane milling, evaporation, fermentation, distillation, rectification, etc, involving considerable losses to attain more than 10% of total production. These represent economical loss of billions of dollars.

In the present project, a networking of various institutions in Brazil and abroad (Japan and Sweden) has demonstrated the importance of Engineering solutions through the development of various optoelectronic sensor systems for online determination of sugar and ethanol concentrations. Sensors were based on optical fibre reflectometry and spectrometry, wavelength analysis of signal modulation, and analysis of electromagnetic properties by interdigitated electrodes. Signal response data have been treated by intelligent algorithms based on artificial neural networks, in order to provide fast and accurate results. The results show that the present technology fulfills the needs of bioethanol and sugar production units, especially the medium and large scale plants.

Other countries around the world, especially Asian countries present huge potential for biofuel production. Certainly, the present symposium will be an important forum to discuss and to establish exchange and cooperation activities on this theme and other strategic issues.

Nanofluid Research at the University of Hong Kong

L. Q. "Rick" Wang

*Department of Mechanical Engineering,
The University of Hong Kong
Pokfulam Road, Hong Kong
email: lqwang@hku.hk*

Abstract

Unlike the past century that was blessed with ever-abundant cheap oil, this century energy has been rated as the single most important issue facing humanity. A global-scale energy crisis looms ahead. Nanotechnology will figure centrally in providing technological solutions. Nanofluid technology, one of the enabling technologies of the nanotech revolution, holds the promise of significantly enhancing the thermal properties of fluids and thus providing high quality heat-transfer fluids of the future that are vital for solving the terawatt challenge facing us.

Nanofluids, fluid suspensions of nanometer-sized (<100nm) structures, are research challenges of rare potential but daunting difficulty. The potential comes from both scientific and practical opportunities in many fields. The difficulty reflects the issues related to multiscales. Nanofluids involve at least four relevant scales: the molecular scale, the microscale, the macroscale and the megascale. The molecular scale is characterized by the mean free path between molecular collisions, the microscale by the smallest scale at which the law of continuum mechanics apply, the macroscale by the smallest scale at which a set of averaged properties of concern can be defined and the megascale by the length scale corresponding to the domain of interest. By their very nature, research and engineering practice in nanofluids are to enhance fluid macroscale and megascale properties through manipulating microscale physics (structures, properties and activities). Therefore, interest should focus on addressing questions like: (i) how to effectively manipulate at microscale, (ii) what are the interplays among physics at different scales, and (iii) how to optimize microscale physics for the optimal megascale performance. In this talk, we summarize our work on addressing these key issues with powerful microfluidic technology, thermal-wave theory and constructal theory.

A Sustainable Building Material from Biological Sources

A. Mukherjee¹

V. Achal²

M. S. Reddy³

1 Director, Thapar University, Patiala, Punjab, India, email : director@thapar.edu

2 Research Scholar, Department of Biotechnology and Environmental Sciences, Thapar University, Patiala, Punjab, India, email: varenyam@gmail.com

3 Head, Department of Biotechnology & Environmental Sciences, Thapar University, Patiala, Punjab, India, e-mail:msreddy@thapar.edu

Abstract: Manufacturing of building materials such as cement, steel and bricks needs high energy input. Carbon emission by these industries mandates a paradigm shift in the present building technology. Nature, on the other hand, builds with local materials, at normal temperature and atmospheric condition. Anthills and coral reefs hold significant clues towards a sustainable building technology for human habitat. *Natural construction* requires dramatically lower energy; they are reversible; thus they are totally recyclable. They also have the enviable property of self healing. Although adoption of all these attributes into human construction is a distant dream there are some early signs of bio-inspired materials that enhance human building materials. This paper describes a novel strategy to produce a cement-like binder using a microbe, *Sporosarcina pasteurii*. The nutrient for sustaining the microbe is recycled industrial pollutant such as corn steep liquor. Thus, the process is highly economical and sustainable.

Keywords: *Sporosarcina pasteurii*, biomineralization, calcite, industrial by-products, permeability, corrosion.

Introduction

Modern building technology requires very high energy input in manufacturing of building materials, their transportation, processing and placement at site. In emerging economies like India where new structures are being built at an accelerated pace. CO₂ emission by the construction industry is as high as 22% at present. This consumption is likely to multiply in near future. Moreover, many performances enhancing building materials such as polymers and mineral agents are toxic and hazardous.

Nature, on the other hand, builds and heals structures with local materials without any requirement of high temperature or pressure. The calcification and polymerization happen at ambient condition. Anthills and coral reefs hold significant clues towards a sustainable building technology for human habitat.

Microbial mineral precipitation (biodeposition) technologies have already been used for consolidation of sand columns (Achal, et al. 2009a, 2009b, for repair of limestone monuments (Dick, et al. 2006), and to a small extent for remediation of cracks in concrete (Bang, et al. 2001). However, for successful commercialization of the technique economical alternatives of the medium ingredients that cost as high as 60% of the total costs must be developed. Researchers have hitherto used standard nutrient media like nutrient medium or yeast extract medium to grow the bacteria. Process economics reveal that the use of inexpensive, high protein containing industrial byproducts such as corn steep liquor (CSL) or lactose mother liquor (LML) not only reduce the overall production cost but also eliminate an environmental pollutant (Achal, et al 2009a).

The present paper investigates use of industry byproducts such as corn steep liquor (CSL) and lactose mother liquor

(LML) as the sole source of nutrients for calcite production. To improve the performance of *S. pasteurii*, UV induced mutants are developed and compared with the wild types. The effect of biomineratization on water and chloride impermeability of concrete has been reported.

2 Materials and methods

2.1. Microorganism and media

Sporosarcina pasteurii (previously known as *Bacillus pasteurii*) MTCC 1761 (Bp W), procured from Institute of Microbial Technology, Chandigarh, India was used in this study. The culture was routinely maintained on Nutrient agar (pH 8.0) medium. Lactose Mother Liquor (LML) and Corn Steep Liquor (CSL) were collected from the dairy industry (Cepham Milk Specialties Pvt. Ltd., Derrabassi, Punjab, India) and corn wet milling industry (Bharat Starch Industries Ltd, Yamunanagar, Haryana, India) respectively and analyzed for its physico-chemical properties (Tab. 1). Microbiological urease production, calcite precipitation, permeability and corrosion analysis tests were carried out in the following three media (per liter); CSL-urea medium (1.5% CSL with a C:N ratio of 6:1, 5 g NaCl, 2% urea and 25mM CaCl₂), LML-urea medium (10% LML with a C:N ratio of 8:1, 5 g NaCl, 2% urea and 25mM CaCl₂) and NB-urea medium (8 g nutrient broth, 5 g NaCl, 2% urea and 25mM CaCl₂). The pH of the media was adjusted to 6.5 with 1N HCl prior to autoclaving without urea and CaCl₂. Filter-sterilized urea and CaCl₂ was added later.

2.2 Mutagenesis

The phenotypic mutants of *S. pasteurii* (Bp W) were developed by UV irradiation. *S. pasteurii* was grown overnight in nutrient broth containing 2% urea solution at 37°C under shaking condition. The cells were washed twice with 0.5M phosphate buffer (pH 8.0) and resuspended in 1 ml of the same buffer. The cells were diluted in phosphate buffer to obtain $\approx 4 \times 10^7$ cfu/ml and exposed to UV inside the UV chamber using Philips 20 W germicidal

lamp at a distance of 17 cm for different time interval (5, 10, 15, 20 and 30 min). The survival percentages were estimated for each treatment. One of the best mutants, designated as Bp M-3, was chosen based on urease producing ability for further studies.

2.3 Urease activity

Urease activity was determined for bacterial cells in all three media by measuring the amount of ammonia released from urea according to the phenol-hypochlorite assay method at different time intervals. Ammonium chloride (50-1000 µM) was used as the standard. One unit of urease is defined as the amount of enzyme hydrolyzing one µmole urea per min.

2.4 Sand consolidation and microbial cementation

Microbiological sand plugging was performed to study calcite precipitation as described by Achal et al (2009a) for Bp W and Bp M-3. The sand columns were divided into three layers (upper, middle and lower layer) and each layer was individually ground and sieved through a 45 µm diameter mesh prior to calcite estimation. Precipitated calcite from each layer was measured by EDTA titration method (American Public Health Association 1989).

2.5 SEM-EDX analysis

The morphology and chemical constituents of bacteria and sand consolidated column was analysed with a Scanning Electron Microscope (SEM) fitted with an Energy Dispersive X-ray (EDX) analyzer. Samples were completely dried at room temperature, then examined on a Zeiss EVO50 SEM at accelerating voltages ranging from 15 to 35 kV. A Bruker-AXS, QuanTax 200 XRD for elemental analysis was used. Samples were gold coated with a sputter coating Emitech K575 prior to examination. Consolidated sand cores of the microbial sand column were cut open prior to examination.

2.6 Water Impermeability Test

For conducting the water impermeability test concrete cubes of dimension 150 mm (M20 grade) were prepared with grown culture of Bp W and Bp M-3 in different media and all specimens were cured in corresponding medium at room temperature. Ordinary Portland cement, fine aggregate (medium-sized natural/river sand) and crushed stone coarse aggregate with maximum size of 20 mm was used in concrete. The ratio of cement: sand: coarse aggregate was 1:1.54:2.86. The water-cement ratio was 0.47. Control samples (without bacterial cells) were also prepared in similar manner. After air drying, specimens were firmly secured in position in the impermeability test apparatus (AIMIL India Ltd, Delhi) and analyzed as per German standard DIN 1048. Atmospheric pressures of 1, 3 and 7 bar were applied sequentially 24 hours each. After the regime the samples were removed and split in to two halves using a wedge and compression testing machine. The penetration depth of water into the concrete was measured and marked with paint. Resistance to penetration is a measure of impermeability of concrete.

2.7 Rapid Chloride Permeability Test (RCPT)

Cylindrical concrete samples (diameter 100 mm, height 50 mm) were prepared with Bp W and Bp M-3 cells in different media, cast and cured in respective media for 28 days by regularly replenishing the media. The resistance to chloride ion penetration in terms of total charge passed in coulombs through concrete specimens was measured as per ASTM C 1202 (2005) using PROOVE'it instrument (Denmark). After 28 days of curing, the concrete specimens were subjected to RCPT test by impressing 60 V. The concrete specimens were placed in between two compartments of a diffusion cell containing 3% NaCl solution in one compartment and 0.3 M NaOH solution in the other. The processor records the current passed through the specimens every 5 min and at the end chloride permeability was calculated in Coulombs.

2.8 Corrosion analysis

Concrete slab specimens (M20 grade) of 200 mm diameter and 100 mm height were cast with one 25-mm diameter reinforcing bar steel at the center. A standard reinforcing bar of 300 mm length and 25 mm nominal diameter of Fe 415 grade was used (Fig. 1).

To simulate the condition of a corroded reinforcement in concrete, the process of corrosion was accelerated by impressing anodic current of 100mA to all the samples. The specimens were kept immersed in 3.5% NaCl solution for 24 hours to ensure full saturation of the test specimen. A cotton gauge was wound around the slab for uniform distribution of the NaCl solution. A stainless steel (SS) mesh rolled over the cotton gauge and was used as cathode. The concrete slab was exposed to the NaCl solution drip. A constant current was impressed for 7 days on all the specimens. The crack widths were measured after 2 days, 4 days and 7 days.

3 Results and discussion

3.1 Mutagenesis

A few bacterial colonies were randomly selected after UV mutagenesis and transferred onto Urea Agar base medium (HiMedia, India) to check the production of urease based on the intensity of pink color. One of the best mutants, designated as Bp M-3, based on urease production ability was selected and compared with wild type strain (Bp W). This strain was deposited with the Institute of Microbial Technology Chandigarh, India, and was assigned an accession number of MTCC 5428 under International Budapest Treaty and a patent was filed.

3.2 Urease activity

Fig. 2 presents the urease activity of Bp W and Bp M-3 in different media. There was a consistency in the growth curves for both the strains and for all the media. Initially, the activity had an increasing trend. It peaked at 120 hrs in all the media. After 120 hrs, urease production was decreased monotonically. The activity was comparable in all the media. However, CSL-U had higher activity than even the standard laboratory nutrient NB-U. LML-U

was also not far behind NB-U. Thus, industry byproducts such as CSL-U and LML-U can replace NB-U in bioremediation process. This is a particularly comforting observation not only because industry byproducts would be far economical alternative in comparison to the laboratory nutrients but also a pollutant effluent could be recycled in large quantities.

Comparison of Figs. 2a and 2b reveals that the mutant Bp-M3 had significantly higher urease activity than the wild Bp-W at all times regardless of the media. At the peak level (120 hr) the difference was around 20%. This demonstrates that the mutant is significantly more efficient than the wild variety. Therefore, we conclude that Bp-M3 with CSL-U is the best combination. However, locally available industry byproducts should always be attempted as nutrient.

3.3 Microbial cementation

The control column (without *S. pasteurii*) collapsed on removal of the plastic tube. All sand columns with bacterial cells were found to be tightly packed regardless of media (Fig. 3). The calcite content was measured at three levels of the column. It ranged between 30% (at top level) and 7% at the bottom. From Fig. 4a it is clear that the industry byproducts have performed very well in comparison to the laboratory grade media. In CSL the deposition is maximum, followed by NB and LML.

When one compares Figs. 4a and 4b it is evident that mutant Bp M-3 precipitated significantly higher amount of calcite compared to its wild type. This corroborates with the observation in case of urease production. Thus, one should use Bp M-3 with LML as media for best results.

The scanning electron microscope image (Fig. 5) clearly shows the rod like forms of the bacterium and extra cellular deposition of calcium carbonate. To further characterize the deposition, energy dissipative x-ray spectrum was plotted (Fig. 6). It clearly shows calcite form of the crystal both in wild and mutated varieties.

3.4 Extracellular polymeric substances and biofilm production

A significant difference between Bp M-3 and its wild type was found in terms of EPS and biofilm production. The mutant Bp M-3 was able to produce higher amount of EPS (37 nmol/ml) compared to Bp W in CSL-urea medium (Fig. 7). The mutant Bp M-3 also showed higher monoxenic biofilm (355 cfu/mm²) compared to other mutants including the wild type. Dick, et al (2006) showed that the production of EPS and biofilm were not significant among the bacterial isolates used to remediate the degraded lime stones. The structure of biofilm is clearly influenced by a number of biological factors such as twitching motility, growth rate, cell signaling, and EPS production. The biofilm structure appears to be largely determined by the production of slime-like matrix of EPS, which provides the structural support for the biofilm. In our study, however, we found significant differences in the ability of the UV induced bacterial isolates as compared to the wild type to produce EPS and form biofilms. We postulate that the higher EPS production by the mutants is responsible for larger calcite precipitation. Thus, EPS and biofilm could be a very suitable indicator for ability of calcite precipitation.

3.5 Water Impermeability Evaluation

The resistance to water is measured as penetration depth at the top and the sides of the concrete cubes (Tab 2). The penetration at the sides is higher than that at the top. This is due to better compaction and closing of pours at the top. Bacterial intervention has dramatically reduced the depth of penetration regardless of the type of bacteria or the media. This demonstrates the profound effect the proposed process has on the permeability of concrete. This can be extremely beneficial in remediating porous or deteriorated concrete.

The bacterial intervention was far more effective on top than on the sides. Understandably, calcite precipitates better on the top surface due to gravity. Consistent with previous tests LML showed better performance than the other media and Bp M-3 mutant was better than Bp W.

However, bacterial intervention with any strain or media is more significant than none at all. The reduction of water penetration leads us to think that bacterial intervention should also reduce ingress of chlorides in concrete. The next section presents results of chloride penetration test.

3.6 Rapid Chloride Permeability Test

Permeability of concrete depends on the pore structure of concrete, while electrical conductivity or resistivity of concrete is determined by both pore structure and the chemistry of the pore solution. The ASTM C1202-05 (ASTM, 2005) rapid chloride ion penetration test (RCPT) results of cylindrical concrete samples are shown in Tab. 3. These are average results of RCPT experiments. The permeability class type was "moderate" for control concrete specimens whereas when specimens were treated with bacterial cells in NB-U and CSL the class changed to "low". For control samples, the average charge passed was 3177 Coulombs, whereas for samples prepared with bacterial cells it was 1054 and 1303Coulombs respectively. Thus, bacterial intervention dramatically reduces the chloride permeability of concrete.

One significant difference from the previous experiments was relatively higher charge passed in CSL than NB. Presence of various ions such as Ca, Mg, P, Na, K, Zn etc. in CSL might attribute to its higher chloride ion permeability.

4 Conclusions

In the present study, a search for a low energy binder in concrete is reported. The binder should reduce the quantity of cement used in conventional concrete and yet offer environmental protection. The study has demonstrated an improved the strain of *S. pasteurii* by mutagenesis. The mutant (Bp M-3) showed increased urease

activity and calcite precipitation. The importance of being able to use a low-cost nutrient such as corn steep liquor or lactose mother liquor is reflected in its contribution to the cost of the urease and calcite products. The results obtained in this work demonstrate that these industrial byproducts can be used as a better and inexpensive growth media for bacterial cells. The efficacy of the proposed method in reducing water and chloride ion permeability is established. Although this study establishes the efficacy of the bacterial concrete more detailed study would be necessary by carefully calculating the energy input of each alternative for a definite recommendation on proportioning the bacterial and conventional cementitious binders.

Acknowledgements

The research reported here is funded partially by the Atomic Energy Regulatory Board, India and the Department of Science and Technology, India

References

- [1] Achal, V; Mukherjee, A; Basu, P.C; Reddy, M.S. (2009a) Lactose mother liquor as an alternative nutrient source for microbial concrete production by *Sporosarcina pasteurii*. *J. Ind. Microbiol. Biotechnology*, Vol.36, pp 433-438.
- [2] Achal, V; Mukherjee, A; Basu, P.C; Reddy, M.S. (2009b) Strain improvement of *Sporosarcina pasteurii* for enhanced urease and calcite production. *J. Ind. Microbiol. Biotechnology*, Vol.36, pp 981-988.
- [3] Bang, S.S; Galinat, J.K; Ramakrishnan, V. (2001) Calcite precipitation induced by polyurethane-immobilized *Bacillus pasteurii*. *Enzyme and Microbial Technology*, Vol.28, pp 404-409.
- [4] Dick, J; De Windt, W; De Graef, B; Saveyn, H; Van der Meeren, P; De Belie, N; Verstraete, W. (2006) Bio-deposition of a calcium carbonate layer on degraded limestone by *Bacillus* species. *Biodegradation*, Vol.17, pp 357-367.

International Engineering Symposium, March 3-5, 2011 Kumamoto Univ., Japan
Tables and Figures

Table 1: Physico-chemical characteristics of the LML and CSL (Achal, Mukherjee, Basu and Reddy 2009a)

LML		CSL	
Component	Measure	Component	Measure
pH	6.20	pH	3.86
Solid (%)	5.50	Solids (%)	46-50
Lactose (%)	15.40	Carbohydrate (%)	5.80
Proteins (%)	8.00	Proteins (%)	24
Fats (%)	2.00	Fats (%)	1.00
Ash (%)	0.53	Minerals (%)	8.80
Calcium (mg/l)	353	Arginine (%)	0.4
Phosphorus (mg/l)	35	Cystine (%)	0.5
Potassium (mg/l)	186	Glycine (%)	1.1
Sodium (mg/l)	44	Isoleucine (%)	0.9
Chloride (mg/l)	90	Inositol (mg/100g)	602
Sulphur (mg/l)	15	Choline (mg/100g)	351

Table 2: Water penetration in concrete prepared with *S. pasteurii* cells in different media

Sample	Top penetration (mm)	Side penetration (mm)
Control	32.67±2.52a	40.00±3.00a
Bp W (CSL-U)	11.00±2.00e	25.33±3.06e
Bp W (NB-U)	12.33±2.08d	27.33±3.51d
Bp W (LML-U)	14.57±3.12b	31.68±3.88b
Bp M-3 (CSL-U)	8.22±1.79f	17.47±2.33f
Bp M-3 (NB-U)	10.83±2.64e	24.74±3.25ef
Bp M-3(LML-U)	13.62±4.07c	29.12±4.11c

Table 3: Permeability class distribution based on RCPT report of different concrete specimens

Treatment	Charge passed (Coulomb)			Mean charge passed (Coulomb)	Permeability (ASTM C 1202)
	1	2	3		
Control	2890	3245	3396	3177	Mode-rate
Bp W (NB-U)	1125	952	1085	1054	Low
Bp W (CSL-U)	1266	1293	1351	1303.3	Low

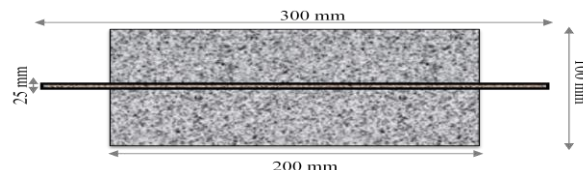


Figure 1: A schematic representation of reinforced concrete slab specimen

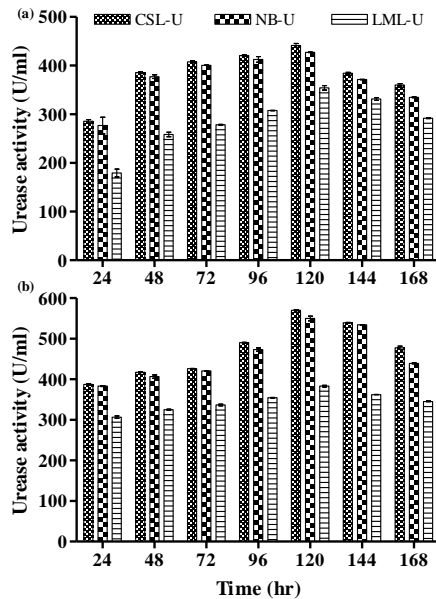


Figure 2: Urease activity of (a) *S. pasteurii* (Bp W) and (b) Bp M-3. Error bars show standard deviation ($n = 3$).



Figure 3: Microbial Sand Column

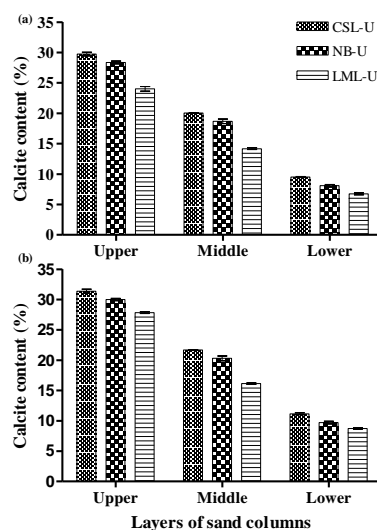


Figure 4: Calcite content in different layers of sand columns consolidated with (a) *S. pasteurii* (Bp W) and (b) Bp M-3. Error bars show standard deviation ($n = 3$).

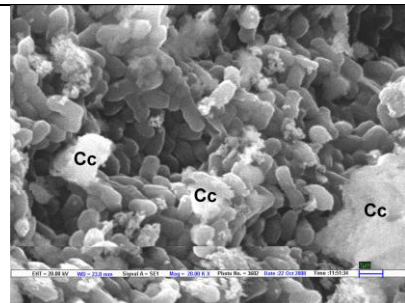


Figure 5: Microbiologically-Induced Calcite Precipitation in Sand Consolidation (Cc – Calcite crystals)

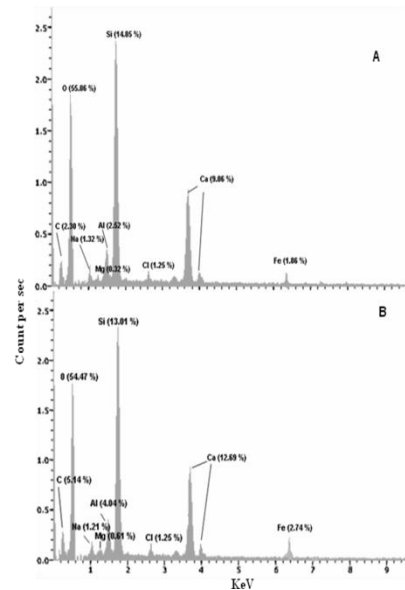


Figure 6: Energy Dispersive X-ray Spectrum of the Microbial Precipitation with A) *S. pasteurii* (Bp W) and B) Bp M-3 in Sand.

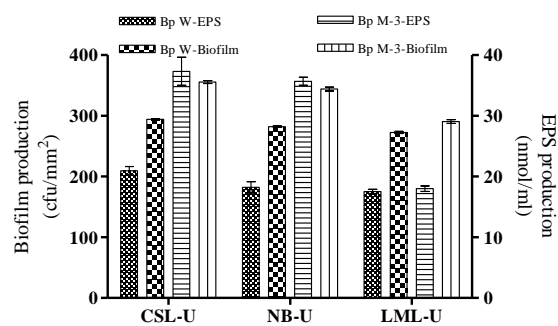


Figure 7: Extracellular Polymeric Substances (EPS) and Biofilm Production by *S. pasteurii* (Bp W) and Bp M-3

Correlation between Petrographical and Engineering Properties of Ilkal Granites, Karnataka

D. VENKAT REDDY, H. G. SANTOSH and K.PRIYANKA

*Department of Civil Engineering
National Institute of Technology Karnataka
Surathkal, Karnataka, India-575025*

Email: dvr1952@gmail.com, santoshg.hir@gmail.com,

Abstract: Granitic rocks show a variety of engineering properties that may affect quarrying operations, slope stability, mining and the use of rock as a structural as well as architectural material. In present investigation, correlation analysis is carried out for experimental results to study the influence of mineralogical and textural characteristics on physical and strength properties using SPSS software. A variety of granitic rock samples from different parts of Ilkal were subjected to study petrographical and then same samples were tested to determine the specific gravity, bulk and dry density, water absorption, porosity, *P*-wave velocity, rebound hardness, point load strength index, uniaxial compressive strength and tensile strength. The study revealed that a petrographical characteristic like grain size, mineral composition and the bonding between each mineral of granitic rocks plays a major role in contributing the strength of the granitic rock and also a significant or fairly good correlation exists between above mentioned engineering properties (physical and strength properties).

Keywords: Volcanic rocks, Strength properties, correlation

Introduction:

Granite stones for engineering applications have to satisfy not only the aesthetic needs but also the technical characteristics for optimal usage of natural resources in civil engineering. So it is necessary to analyze the properties and inter-relationship between petrographical, physical and strength properties. Reddy. D. V (2002) explained clearly about requirements for decorative and dimensional building stones. Many authors have developed a number of petrographical techniques to study the mineral composition and textural characteristics like grain sizes and mineral composition of granitic rocks using optical microscopy (Willard and McWilliams, 1969; Irfan and Dearman, 1978) and several authors have studied the effect of grain size on the strength properties of the rock. In general strength of rocks is greater in finer grained rocks. Onodera and Asoka Kumara (1980) reported that, strength is decreased significantly as the grain size is increased in

volcanic rocks. The relationships between the petrographical characteristics, physical and strength properties of granitic rocks have been studied by different authors (Merriam et al., 1970; Tugrul, I.H. Zarif, 1999; Asoka Kumara, 1980). Reddy. D. V (2002) clearly explained requirements for decorative and dimensional building stones.

The purpose of this study is to quantify the relationship between the petrographical characteristics, physical and strength properties of pink granitic rocks of Ilkal, Karnataka, which have been widely used in structural and architectural purpose.

Rock samples were collected from different quarries of Ilkal area. Thin section of specimen were subjected to petrographical examination and then tested for physical and strength properties. The physical properties analyzed includes, specific gravity, bulk and dry density, water absorption, porosity, *P*-wave velocity, rebound hammer, point load strength index, uniaxial compressive strength and tensile strength.

Finally, petrographical characteristics, physical and strength properties of the granite specimens from 7 different quarries (Fig: 2) were correlated by statistical linear regression analyses using SPSS software.

Study Area:

The study area lies in the Bagalkot district of Karnataka state. It is bounded by $15^{\circ} 58'$ and $15^{\circ} 97'$ North latitude and $76^{\circ} 08'$ and $76^{\circ} 13'$ East longitudes in survey of India (SOI) Toposheet No. 57 A/1, covering the places like Ilkal, Hunugund, Gudur and Balkundi of Bagalkot district.

Petrographic Examination:

The mineralogical and textural characteristics of the samples were studied by using microscope. The thin sections were examined under a CDIC microscope to find grain size of rock studied. The location of each rock sample collected is shown in the Figure 2. All rocks tested were fresh, and exhibited a porphyritic texture, coarse grained to fine grained phenocrysts of feldspar arranged with larger axis parallel to the direction of foliation. The crystals of potash feldspar are tabular and prismatic in nature. The associated minerals with this granite are biotite, mica and hornblend as small elongated blebs of blue fluorite aligned along the cleavages. Orthoclase (K_f), plagioclase (P) and quartz (Q) were the main mineral present in all examined samples. The point-count method was used to determine mineral composition (Hutchinson, 1974). The grain size of orthoclase, plagioclase, quartz, mica and other minerals were measured and distinguished for each thin section (fig: 4.a-4.d) by CDIC microscope. Grain size and percentage of minerals determined are consolidated in Table 1 and 2 respectively. (CDIC-Central Differential Interface Contrast)

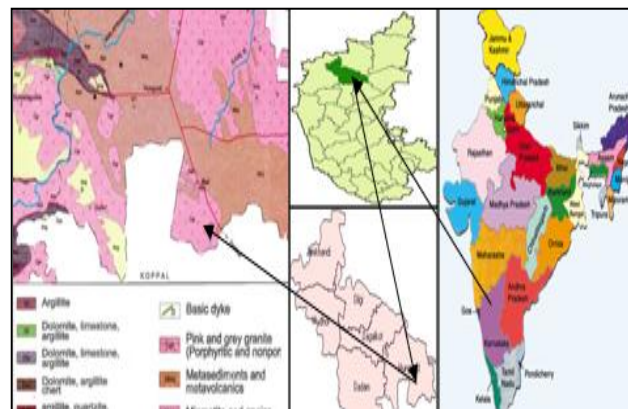


Fig 1: Geological map of study area

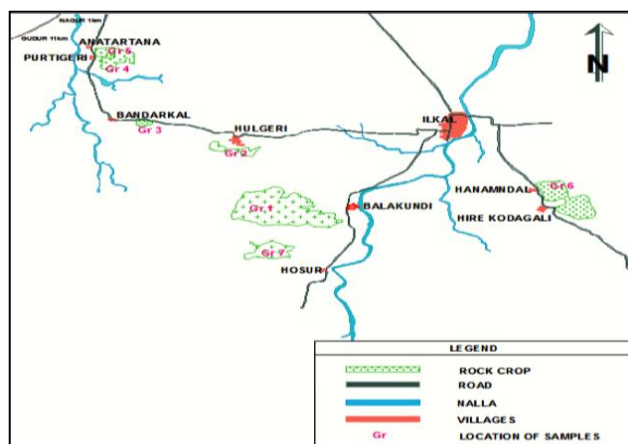


Fig: 2 Location of map rock tested

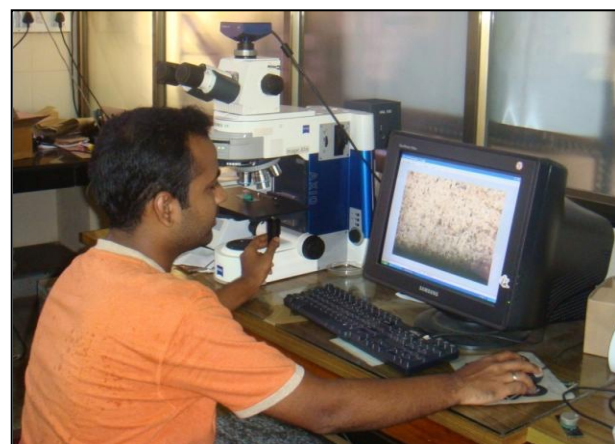


Fig: 3 CDIC microscope

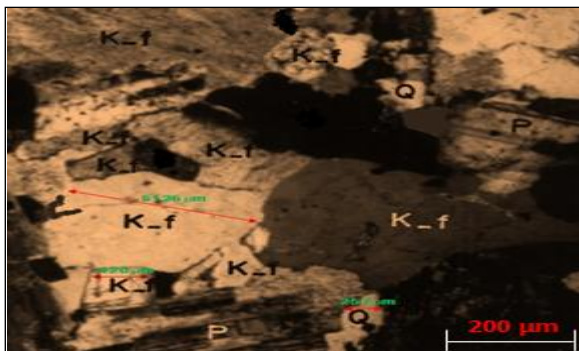


Fig: 4.a Photomicrography of GEM quarry sample



Fig: 4.b Photomicrography of Bandarkal quarry sample

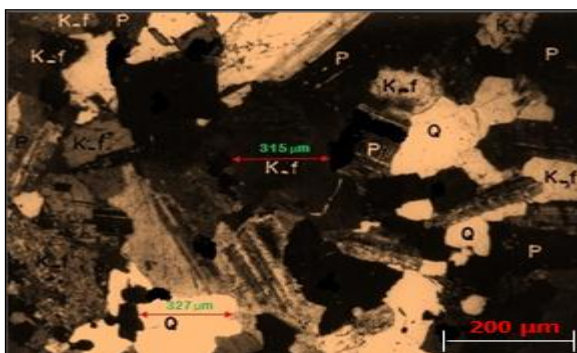


Fig: 4.c Photomicrography of Purthigeri quarry sample

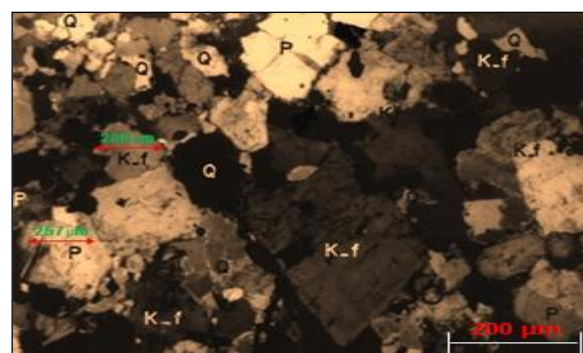


Fig: 4.d Photomicrography of SR quarry sample

Table: 1 Grain size of the rocks tested

Quarry name	Sample No.	K_f (mm)	P (mm)	Q (mm)	M (mm)
GEM	Gr 1	0.62-8.20	0.40-3.70	0.80-4.85	0.85-1.50
Hulgeri	Gr2	0.50-5.98	0.45-3.76	0.50-4.18	0.82-3.70
Bandarkal	Gr3	0.41-5.12	0.47-2.80	0.40-4.57	-
Purthigeri	Gr4	0.25-3.76	0.25-2.45	0.80-2.82	0.54-2.50
Antartana	Gr5	0.40-4.50	0.18-2.76	0.50-3.80	-
S.R	Gr6	0.25-3.12	0.17-2.80	0.70-2.85	0.90-1.24
Hosur	Gr7	0.59-7.16	0.39-3.20	1.10-4.25	0.82-2.30

Table: 2 Percentage of mineral composition of the rocks tested

Sample No.	K_f %	P %	Q %	M %	B %	H %	A %	SUM %
Gr 1	60	06	25	3.5	2.0	1.5	2.0	100
Gr2	52	12	28	3.0	2.5	1.0	1.5	100
Gr3	45	16	30	4.5	1.0	2.0	1.5	100
Gr4	42	10	38	3.5	4.0	2.0	0.5	100
Gr5	50	08	34	2.0	3.5	1.5	1.0	100
Gr6	40	12	42	1.5	2.0	1.5	1.0	100
Gr7	55	10	28	2.0	3.0	1.5	0.5	100

Where, K_f- Orthoclase; P- Plagioclase; Q- Quartz; M- Mica; B-Biotite; H-Hornblend; A-Altered mineral.
K2-3-3

Physical Properties:

The physical properties of the granitic rocks were determined by a variety of laboratory tests. The specimens were prepared and tested generally in accordance with the procedures given in IS codes. Bulk density and water absorption were determined. Water absorption is a useful property in evaluating the durability of different rocks as building material specific gravity, bulk and dry density and water absorption of the granitic rocks are given in Table 4 and 5.

Strength Properties:

Strength properties on the core samples included the point load strength index, the uniaxial compressive strength (UCS) and the tensile strength. The results are given in Table 5. The uniaxial compressive strength of the granitic rock samples was determined using an uniaxial compression testing machine. Determination of tensile strength was done by the Brazilian test. All tests were carried out in accordance with ISRM suggested methods.

Table: 3 Bulk density and Dry density of granitic rocks

Sample No.	Bulk Density (kN/m ³)			Dry Density(kN/m ³)		
	Min	Max	Avg	Min	Max	Avg
Gr 1	25.66	26.09	25.87	25.03	25.98	25.50
Gr 2	25.82	26.12	25.97	25.38	26.02	25.70
Gr 3	25.93	26.25	26.09	25.78	26.12	25.95
Gr 4	26.90	27.40	27.15	26.29	27.35	26.82
Gr 5	26.50	27.00	26.75	26.18	26.85	26.51
Gr 6	27.18	28.85	28.01	27.04	28.15	27.59
Gr 7	25.12	25.85	25.48	24.95	25.42	25.18

Table: 4 Water absorption, Porosity, P-wave velocity and Rebound hammer value of granitic rocks

Sample No.	Water absorption (%)	Porosity (%)	P-wave Velocity Vp (m/sec)			Rebound Hammer Value R		
			Min	Max	Avg	Min	Max	Avg
Gr 1	0.195	0.240	3945.40	4585.64	4265.32	58	64	61
Gr 2	0.135	0.184	4150.40	4980.85	4565.62	63	65	64
Gr 3	0.155	0.182	4682.11	5082.22	4882.16	60	68	64
Gr 4	0.140	0.124	5312.36	5825.28	5568.82	64	72	68
Gr 5	0.131	0.150	4805.40	5590.38	5197.89	64	66	65
Gr 6	0.122	0.112	5809.38	6150.36	5979.80	69	75	72
Gr 7	0.153	0.238	4150.24	4720.60	4435.82	59	63	61

Statistical Analysis on Experimental Results:

The statistical analysis technique used to correlate petrographical characteristics, physical and strength properties of the granite sample collected from different

quarries of study area and linear regression analysis was carried out by using SPSS statistical package program. Some petrographical physical and mechanical properties of the granitic rocks were plotted against each other in order to predict and estimate one property from another.

Table: 5 Point load strength index, Uniaxial Compressive strength and Tensile strength of granitic rocks

Sample No.	Point load Strength Index I_s (MPa)			Uniaxial Compressive Strength σ_c (MPa)			Tensile Strength σ_t (MPa)		
	Min	Max	Avg	Min	Max	Avg	Min	Max	Avg
Gr 1	7.31	8.02	7.66	109.00	117.42	113.21	12.15	12.44	12.29
Gr 2	7.81	8.51	8.16	119.72	124.36	122.04	11.81	13.80	12.80
Gr 3	8.12	8.58	8.35	120.24	128.35	124.29	12.96	13.38	13.17
Gr 4	8.34	9.02	8.68	127.12	135.20	131.16	13.52	14.16	13.84
Gr 5	7.71	8.10	7.90	114.15	124.72	119.43	12.64	13.86	13.25
Gr 6	8.82	9.37	9.09	136.82	137.50	137.16	14.54	14.27	14.40
Gr 7	7.3	7.95	7.63	112.52	119.74	116.13	12.23	13.65	12.94

Correlations between the Petrographical Characteristics and the Engineering Properties:

In order to determine the influence of the petrographical characteristics on the engineering properties, the ratio of quartz to feldspar and grain size were correlated with the engineering properties using regression analyses.

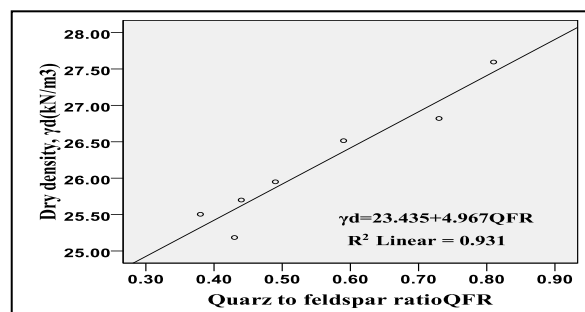
The quartz content has an influence on dry bulk density. Quartz grains fills spaces between the other grains because of which dry unit weight increases as the quartz to feldspar ratio (QFR) increases. From regression analysis (Fig: 5.a) it is found that, the relationship between dry density and quartz to feldspar ratio is significant ($R^2=0.931$) and also a similar relation exists between QFR and UCS (Fig: 5.b). From these figure it's clear that, the QFR is directly related to dry density and UCS

Figures 6.a, 6.b and 6.c show the reduction in compressive strength with increase in the grain size of the minerals because, as grain size is large, compactness or bonding between mineral grains is less hence, resulting in low compressive strength. The correlation between the UCS and the size of orthoclase mineral (Fig: 6.a) of the granite rocks is more significant ($R^2=0.815$) than other minerals like plagioclase and quartz

(Fig: 6.b & 6.c) because, orthoclase mineral has more micro fissures and cleavages.

Relationship between maximum grain size (orthoclase, plagioclase and quartz) and uniaxial compressive strength is shown in figure 7.a. Size of the mineral grain is important factor for strength of granitic rocks. This figure represents the fact that, the smaller the grain size higher will be the compressive strength.

Similarly, Figure 7.b shows the relation between percentage of main minerals (orthoclase, plagioclase and quartz) and uniaxial compressive strength. In this figure, presence of quartz mineral is important in contributing strength of granitic rocks, because, quartz mineral has less or no cleavages and microfissures compared to orthoclase and plagioclase minerals.

**Fig: 5.a Relationship between QFR & Dry density**

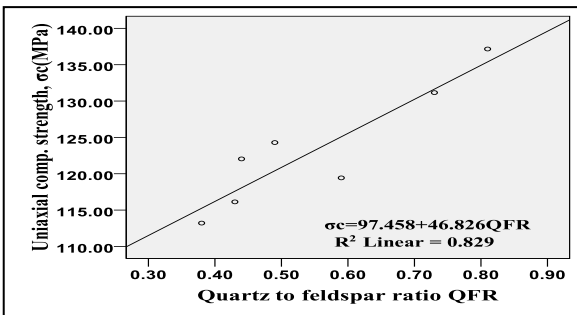


Fig: 5.b Relationship between QFR & UCS

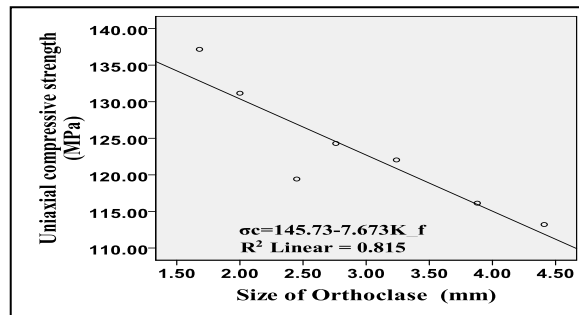


Fig: 6.a Relationship between UCS & size of orthoclase

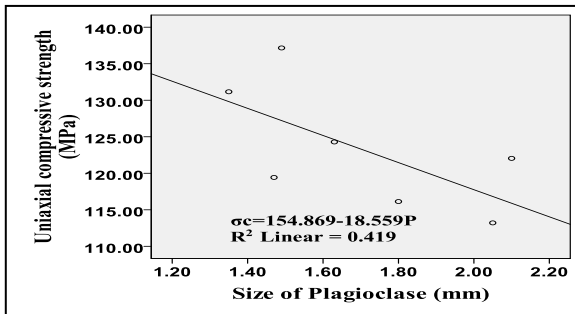


Fig: 6.b Relationship between UCS & size of plagioclase

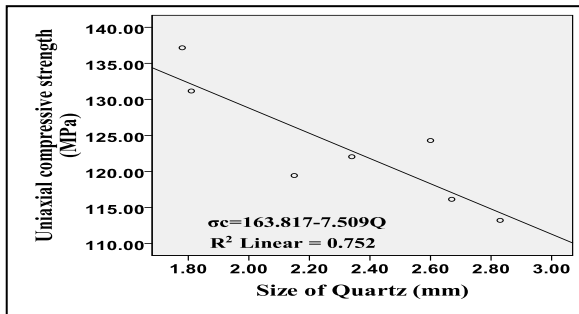


Fig: 6.c Relationship between UCS & size of quartz

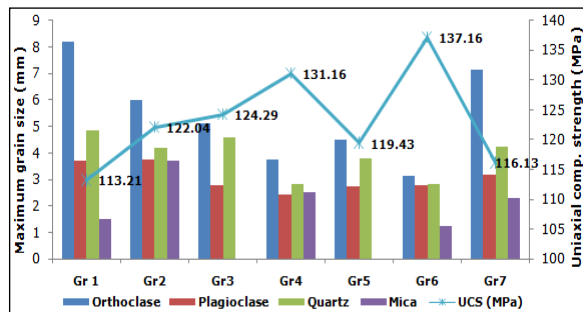


Fig: 7.a Relationship between the maximum grain size and UCS

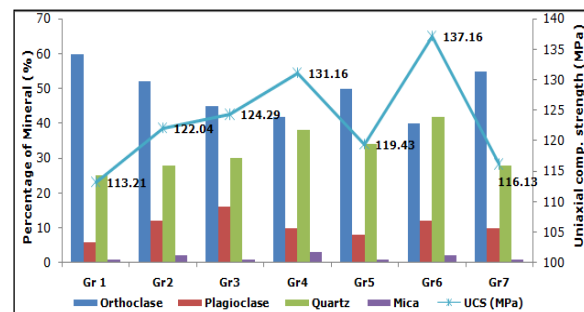


Fig: 7.b Relationship between the percentage of main minerals and UCS

Correlation between Physical and Strength Properties:

There is a linear relationship between the porosity and dry density. The dry density increases as the porosity increases. There is also a similar relationship between the porosity and P -wave velocity (Fig. 8.a and 8.b).

There are statistically significant correlations between uniaxial compressive strength and both bulk density and P -wave velocity (Fig. 9.a and 9.b). The uniaxial compressive

strength increases as the bulk density and P -wave velocity increase.

Point load and rebound hammer tests are most commonly used, principally because they can be used on a greater variety of rock types with better predictability of strength (Johnson and De.Graff, 1988).

Figure 10.a illustrates the variation of rebound hammer values (R) with UCS of the granitic rocks. As seen in this figure a linear correlation exists between the R and the

UCS. The point load strength index has been widely used to estimate the uniaxial compressive strength of rocks in the field and laboratory (Deere and Miller, 1966; Bieniawski, 1975; Ghosh and Srivastava, 1991) correlation between the point load

strength index and the compressive strength for the granitic rocks (Fig. 10.b) is significant ($R^2=0.98$) Similarly correlation between the tensile strength and UCS ($R^2=0.88$) for the granitic rocks is also significant (Fig: 10.c).

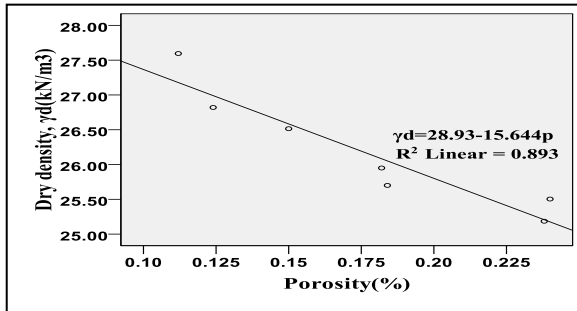


Fig: 8.a Relationship between Porosity & Dry density

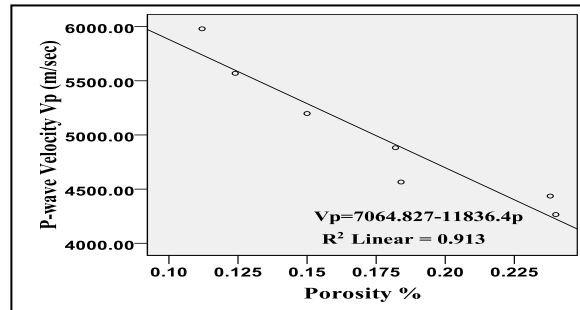


Fig: 8.b Relationship between Porosity & P-wave velocity

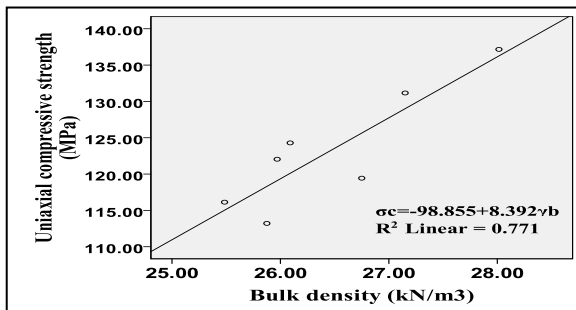


Fig: 9.a Relationship between Bulk density & UCS

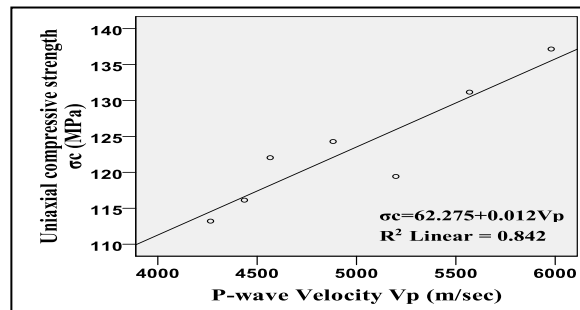


Fig: 9.b Relationship between P-wave velocity & UCS

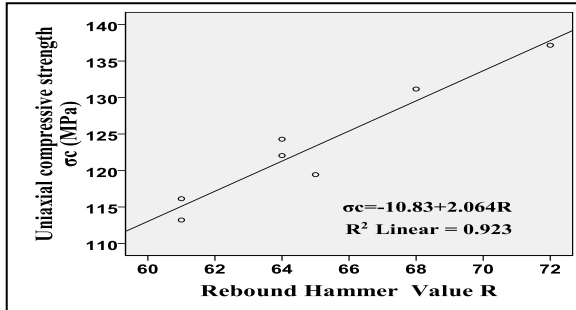


Fig: 10.a Relationship between Rebound hammer value & UCS

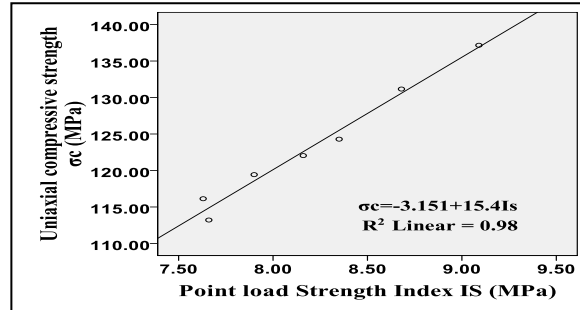


Fig: 10.b Relationship between Point load strength index & UCS

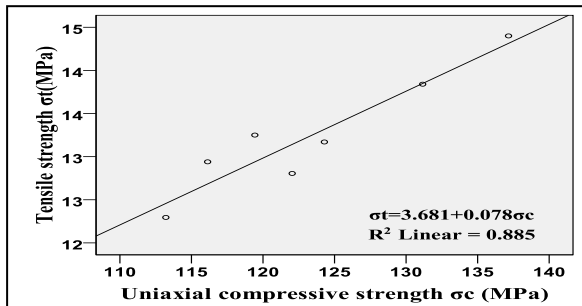


Fig: 10.c Relationship between UCS & Tensile strength

Conclusions:

Linear regression analysis was carried out between petrographical and engineering properties to find interrelationship among these properties of granitic rocks which were collected from different quarries of Ilkal area. From this study following conclusions can be drawn:

- 1) The impact of petrographical properties is more on engineering properties of study area granitic rocks.
- 2) Grain size of the mineral is the most important parameter affecting the engineering properties. Strength increases as grain size decreases. Among three important minerals (K_f, P & Q) grain size of the orthoclase mineral plays the significant role in reducing the strength because, experimental study showed that orthoclase mineral has more cleavages and micro fissures.
- 3) Mineralogical composition of quartz and feldspar play important role on the engineering properties. A significant linear relationship exists between mineral composition and strength properties.
- 4) Interrelationship between petrographical and strength properties are more significant

compared to the relation between petrographical and physical properties.

5) The significant empirical relation obtained by regression analysis gives more accurate results to find the strength properties from physical properties, when used with samples of granitic rocks that have the similar mineralogical structure as those reported in this study.

References:

- [1] Bieniawski, Z.T., 1975. Point load in geotechnical practice. *Engineering Geology* 9, 1-11.
- [2] Ghosh, D.K., Srivastava, M., 1991. Point load strength: an index for classification of rock material. *Int Assoc. Bull. Eng. Geol.* 44, 27-33.
- [3] Hutchinson, C.S., 1974. *Laboratory Handbook of Petrographic Techniques*. Wiley, New York.
- [4] International Society for Rock Mechanics, 1981. *Rock Characterization, Testing and Monitoring*. In Brown, E.T. (Ed.), *ISRM Suggested Methods*. Pergamon, Oxford.
- [5] Irfan, T.Y., Dearman, W.R., 1978. The engineering petrography of weathered granite in Cornwall, England. *Q. J. Eng. Geol.* 11, 233-244.
- [6] Johnson, R.B., De Graff, V.J., 1988. *Principles of Engineering Geology*. Wiley, New York.
- [7] Merriam, R., Rieke, H.H., Kim, Y.C., 1970. Tensile strength related to mineralogy and texture of some granitic rocks. *Eng. Geol.* 4, 155-160.
- [8] Onodera, T.F., Asoka Kumara, H.M., 1980. Relation between texture and mechanical properties of crystalline rocks. *Bull. Int. Assoc. Eng. Geol.* 22, 173-177.
- [9] Reddy, D.V. (1995). "Engineering Geology for Civil Engineering." Oxford & IBH publisher, New Delhi.
- [10] Reddy, D.V. (2002). "Requirements for Decorative and Dimensional building Stone- A critical Analysis." Stone -2002 Fifth International granite and stone fair, Bangalore. pp. 98-109.b
- [11] Tugrul, A., I.H. Zarif, I.H.,(1998). "Correlation of mineralogical and textural characteristics with engineering properties of selected granitic rocks from Turkey." *Engineering Geology* 51 (1999) 303-317.
- [12] Willard, R.J., McWilliams, J.R., 1969. Microstructural techniques in the study of physical properties of rocks. *Int. J. Rock Mech. Min. Sci.* 6, 1-12.

**MECHANICAL ENGINEERING
&
RELATED FIELDS**

Vibration and Responses Characteristics of Lateral Cantilever Shaft Vibration of a Vertical-Axis Ocean Current Turbine

I.K.A.P. UTAMA¹ and R. HANTORO²

- ¹ *Departement of Naval Architecture and Shipbuilding Engineering, Institut Teknologi Sepuluh Nopember (ITS), Surabaya 60111, Indonesia Email : kutama@na.its.ac.id*
- ² *Faculty of Marine Technology, Institut Teknologi Sepuluh Nopember (ITS), Surabaya 60111, Indonesia, Email : hantoro@ep.its.ac.id*
-

Abstract: An investigation into the characteristics of force responses has been carried out on the lateral shaft vibration of a passive variable-pitch of vertical-axis ocean current turbine (VAOCT). The work was carried out numerically using CFD approach and experimentally using tank test. A shaft type cantilever was modeled using finite element mesh and simulated using lumped mass matrix in order to obtain its vibration characteristics and responses. Variations of incoming fluid velocity and the corresponding rotation were used to identify the pattern of lateral displacement responses. The repeated pattern of periodic displacement responses due to the functions of force acting on the foils was identified and correlation of critical azimuth position of the foils and displacement responses was presented. Experimental investigation was carried out to validate the simulation results at a node in x- and y-directions of the finite element model. Periodic pattern responses resulted from simulation and experiment at the validated node demonstrates a suitable average error and in general.

Keywords: cantilever, finite-element, lateral vibration, pitch, vertical-axis

INTRODUCTION

Research on the effect of fluctuations of the force on the output power generated by energy conversion system from renewable energy sources (wind, ocean currents) has become a serious concern among researchers, Kiho, et al (1996) and Robert (1978). In the case of ocean current turbine system, the force of the fluid causes structure to rotate and change its orientation to the incoming fluid flow. Force fluctuations which follow the turbine during rotation was strongly influenced by foil's position to the incoming flow and become potency of vibrations on the turbine shaft. The use of fixed-pitch not allowed foil to change its relative position to the arm.

This paper discussed the characteristics of lateral vibration on the main shaft of vertical-axis ocean current turbine with the use of passive variable-pitch foil. A

cantilever type of shaft was used and modeled using finite element method. Simulation was carried out using lumped mass matrix to obtain the natural frequencies, mode shapes and deflection of vibration response. Fourier force function used in the simulation was taken from force fluctuations data obtained at previous CFD simulation by Hantoro, et al (2009a). Experiment was conducted as validation of the simulation results at a node of the finite element model.

VIBRATIONS SIMULATION USING FINITE ELEMENT AND LUMPED MASS MATRIX

For dynamic response analysis, a linearized finite element model was employed to establish a control scheme for rotor systems, Firoozian and Stanway (1988). The finite element method was also applied to a complex rotor system to evaluate its vibration response due to fluid

forces, Diewald and Nordmann (1989), and gyroscopic moments, Sakata, et al (1989). Although early dynamic models of rotor systems were formulated either analytically, Rouch (1989) or using transfer matrix approach, Dimentberg (1961), the potential of the powerful finite element technique was recognized at a very early stage, Black (1974). In general, a structure is analyzed as a system of continuous or discrete systems (lumped system). A uniform structures like rod can be more appropriate if treated as a continuous system. Finite element method in fact can be called a combination of two methods, namely the continuous and discrete elements in the level of general coordinates.

In this study, the vertical axis turbine is modelled as a system consisting of the shaft which is divided into 10 elements. Three foils as producer of excitation force rests at two points on the shaft (node-3 and node-10), as shown in Fig. 1. With the total length of 1400 mm, each element has length of 140 mm. Magnetic probe sensor (eddy currents) is placed at node-1 in the x- and y-direction with a distance of 140 mm from the bearing in order to obtain displacement data. Parameters of Cantilever shaft turbine used in simulation and experiment are:

Table 1 Material Specifications

- shaft material	: SS304
- mod. elasticity (E)	: 200 GPa
- shear modulus (G)	: 86 GPa
- shaft dimension	: Length 400mm, Diameter 4.5mm
- density	: 8000 kg/m ³

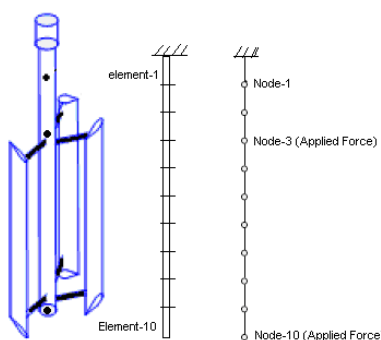


Fig. 1 Finite element model of vertical-axis turbine

The element stiffness matrix can be developed using basic strength of materials techniques to analyze the forces required to displace each degree of freedom a unit value in the positive direction. Using the degrees of freedom of element stiffness matrix results in the following element stiffness matrix:

$$K_{e,i} = E_i I_i \begin{bmatrix} \frac{12}{l_i^3} & \frac{6}{l_i^2} & \frac{-12}{l_i^3} & \frac{6}{l_i^2} \\ \frac{6}{l_i^2} & \frac{4}{l_i} & \frac{-6}{l_i^2} & \frac{2}{l_i} \\ \frac{-12}{l_i^3} & \frac{-6}{l_i^2} & \frac{12}{l_i^3} & \frac{-6}{l_i^2} \\ \frac{6}{l_i^2} & \frac{2}{l_i} & \frac{-6}{l_i^2} & \frac{4}{l_i} \end{bmatrix} \quad (1)$$

For cantilever beam with two element model with one end not allowed to move, it is necessary to eliminate the degree of freedom. Elimination made to the rows and columns which correspond to the constrained global degrees of freedom, reducing the global stiffness matrix to a 4x4 matrix, resulting as in Eqn.2 .

$$K_g = \begin{bmatrix} \left(\frac{12E_1I_1}{l_1^3} + \frac{12E_2I_2}{l_2^3}\right) & \left(\frac{-6E_1I_1}{l_1^2} + \frac{6E_2I_2}{l_2^2}\right) & \frac{-12E_2I_2}{l_2^3} & \frac{6E_2I_2}{l_1^2} \\ \left(\frac{-6E_1I_2}{l_1^2} + \frac{6E_2I_2}{l_2^2}\right) & \left(\frac{4E_1I_1}{l_1^2} + \frac{4E_2I_2}{l_2^2}\right) & \frac{-6E_2I_2}{l_2^2} & \frac{2E_2I_2}{l_2} \\ \frac{-12E_2I_2}{l_2^3} & \frac{-6E_2I_2}{l_2^2} & \frac{12E_2I_2}{l_2^3} & \frac{-6E_2I_2}{l_2^2} \\ \frac{6E_2I_2}{l_2^2} & \frac{2E_2I_2}{l_2} & \frac{-6E_2I_2}{l_2^2} & \frac{4E_2I_2}{l_2} \end{bmatrix} \quad (2)$$

The same method can be performed on the number of element more than two with considering of the computing capability to perform high-order matrix operations. The parameters of mass and inertial mass matrix element connecting rods in the inertial load point to point and given the acceleration in the diagonal matrix. Eqn.3 shows the lumped mass matrix (LM), including translation and rotation,

$$m_s = \begin{bmatrix} \left(\frac{ml}{2}\right) & 0 & 0 & 0 \\ 0 & \left(\frac{ml^3}{24} + \frac{mll_y}{2A}\right) & 0 & 0 \\ 0 & 0 & \left(\frac{ml}{2}\right) & 0 \\ 0 & 0 & 0 & \left(\frac{ml^3}{24} + \frac{mll_y}{2A}\right) \end{bmatrix} \quad (3)$$

With the acquisition of \mathbf{m}_g and \mathbf{k}_g then the eigenvalue problem for homogeneous equations of motion can be written,

$$m_g \ddot{\mathbf{z}} + k_g \mathbf{z} = [0] \quad (4)$$

Fourier-force function are used to obtain the vibration response with respect to time and the external forces acting on the shaft. It is obtained by making Eqn.4 becomes,

$$[m_g k_g] [\bar{\mathbf{z}}] = [\bar{\mathbf{F}}] \quad (5)$$

and all nodes in the deviation of \mathbf{z} is,

$$[\bar{\mathbf{z}}] = [m_g k_g]^{-1} [\bar{\mathbf{F}}] \quad (6)$$

CFD simulation performed on previous research by Hantoro, et al (2009b) have resulted the pattern of force fluctuations in variations of flow velocity and rotation speed of turbine. Variations that are performed in this study are as follows:

Table 2 Towing Tank Variations Test

Variation	U (m/s)	RPM
Var-1	0.8	37
Var-2	0.9	41
Var-3	1	45

Force fluctuation patterns appear in a full rotation at all variations classified in two directions as defined in Fig.2. Simulation of lateral vibration on the main shaft for every variation was performed in two directions, namely in x- and y-direction. Force in x-direction is the force acting on a rotating turbine in the same direction with the incoming fluid flow, while the y-direction is for the force that is perpendicular to the incoming fluid flow.

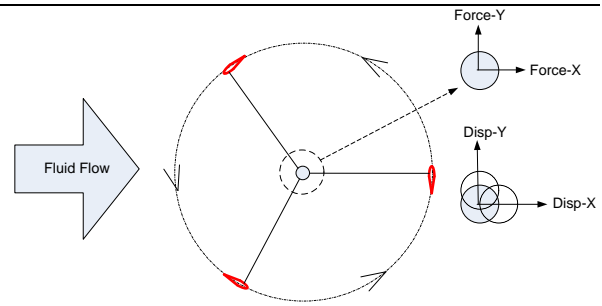
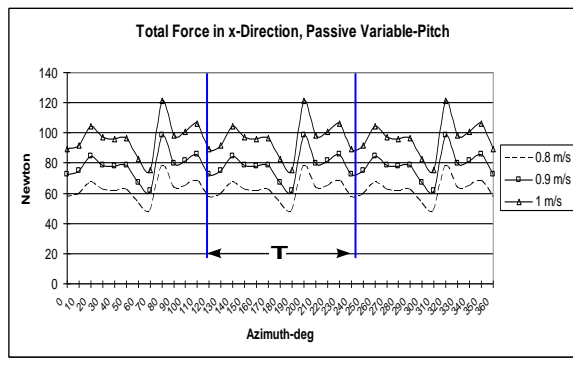
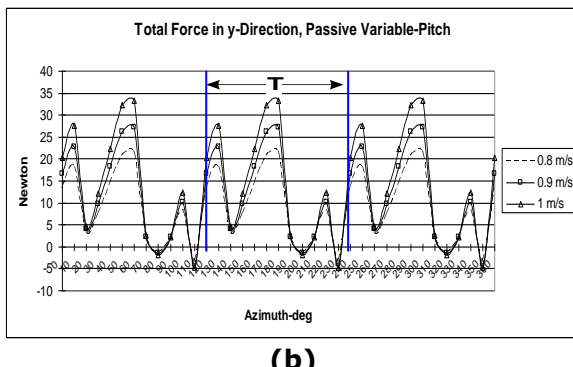


Fig.2 Definition of the lateral direction of the force and the vibration on the main shaft of turbine

The resulted force fluctuations of turbine for all variations which are acting on the shaft provides periodic pattern as shown in Fig. 3.



(a)



(b)

Fig. 3 Fluctuation pattern of the force at all variation, (a) x-direction, (b) y-direction

Fourier force function modeling performed by taking a period (T) of fluctuation patterns. Results of modeling achieve agreement to fit after the 6th-order iterations. Plots of Fourier force function fluctuations performed with Matlab provides good agreement compared with

the results of CFD data simulation. Fig. 4 shows an example of the suitability at Var-1 variation.

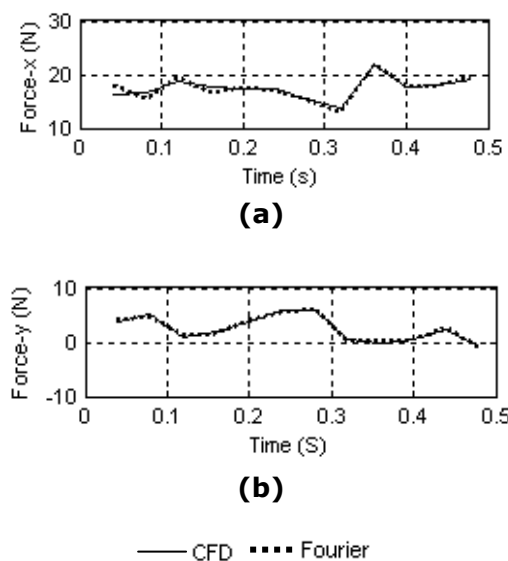


Fig. 4 The suitability of the force fluctuation pattern at Var-1 variation, (a) x-direction (b) y- direction

Natural frequencies and mode shape

The natural frequency (ω_n) was obtained by solving the roots of the determinant of the equations of motion using,

$$[m_g k_g][z] = [0] \quad (9)$$

$$\omega_n = \det[m_g k_g] \quad (10)$$

Coupling between elements gives the degrees of freedom two times the number of elements, resulting 10 varieties of lateral natural frequency as shown in Fig.5 and Table 3.

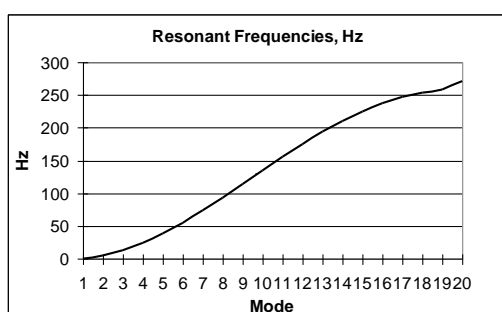


Fig.5 Natural Frequency of turbine shaft

Table 3. Natural Frequency of Turbine Shaft

Mode	ω_n (Hz)	Mode	ω_n (Hz)
1	0.8	6	54.7
2	4.6	7	73.3
3	12.6	8	93.3
4	23.9	9	114.1
5	38.1	10	135.1

The first three of 10 mode shapes that occurred is shown in Fig.6.

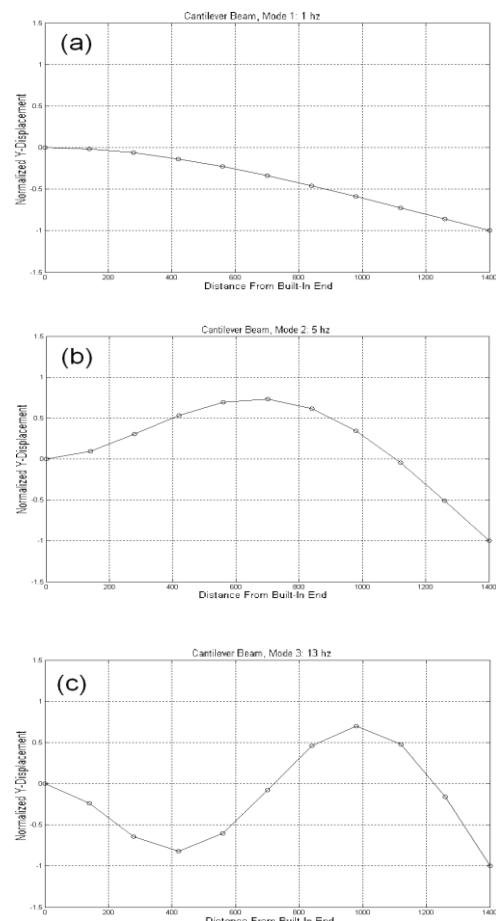


Fig. 6. First three mode shapes of main turbine shaft

Modes are associated with structural resonances. The majority of structures can be made to resonate. That is, under the proper conditions, a structure can be made to vibrate with excessive, sustained motion. Resonant vibration is caused by an interaction between the inertial and elastic properties of the materials within a structure. Furthermore, resonant vibration is the cause of, or at least a contributing

factor to, many of the vibration related problems that occur in structures and operating turbine.

TESTING OF VIBRATION DISPLACEMENT

Experiments included the manufacture and testing of the work piece was carried out at the towing tank facility at Hydrodynamics Laboratory, Faculty of Marine Technology ITS, with specifications:

- length 50 m
- width 3 m
- depth 2 m.



Fig.7 Towing tank facility at FTK ITS

The foil chord was set at 100 mm, with span of 1000 mm giving aspect ratio of 10, and 500 mm arm to the shaft. The turbine was designed with three foils. The NACA 0018 profile was chosen as the foil section with data from Sheldahl and Klimas (1981). This foil is commonly used for Darrieus turbines because it has relatively high thickness to chord ratio hence gives it good strength in bending. The radial arms of the turbine were made from high strength aluminium. Turbine shaft uses cantilever type with one end fixed by the bearing and the other end free (overhanging) as shown in Fig.8.

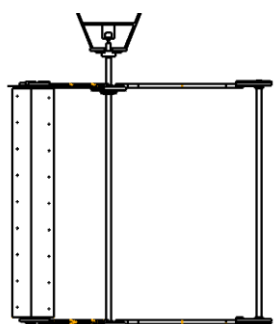


Fig.8 Vertical-axis turbine with three straight foils

Data collection was conducted with the same variation as mention in Table 1. The use of passive variable-pitch was allowed foil to change its relative position to the arm, as shown in Fig.9. The position of passive variable-pitch gives the freedom to move within the interval -10° to 10° , as shown in Fig.9.

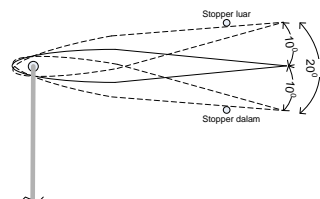


Fig.9 Fixed-pitch and passive variable-pitch position at foil

Changes in pitch angle position with 3 (three) freedom identified conditions, namely in the middle position between the two stoppers, the position of sticking/stuck stopper outside, and the position of sticking/stuck in the stopper. Identification of such position and the turbine rpm are obtained by video recording from a mounted camera and taken during the testing.

Magnetic probe sensor (eddy currents) was placed at node-1 in the x and y-direction with a distance of 140 mm from the bearing in order to obtain displacement data (Fig. 10). Data collection was performed after towing tank carriage speed has stable with time sampling of 0.01 second.

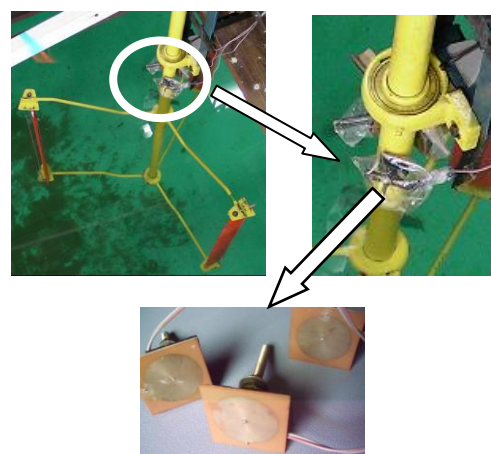


Fig.10 Installation of Eddy current sensors to the turbine shaft

RESULTS AND DISCUSSION

Resulted displacement from simulation at all nodes at the same time indicating the possibility of mode shape occurrence. Fig.11 and 12 show sample of the displacement resulted at all nodes in x and y-direction for all variations at $t_{i=1}$ and $t_{i=10}$. Similar mode of displacement at all node was presented for all variations in x- and y-direction, and these modes recognized have close agreement to the 1th mode shape resulted from simulation (Fig. 6(a)).

Changes in inter-elements in the node-9 to give significant difference when compared to the other nodes. This indicates that the use of the cantilever shaft for vertical-axis ocean current turbine give potential problems on the tip of shaft. It is obvious due to half of the force received on turbine concentrated at cantilever tip.

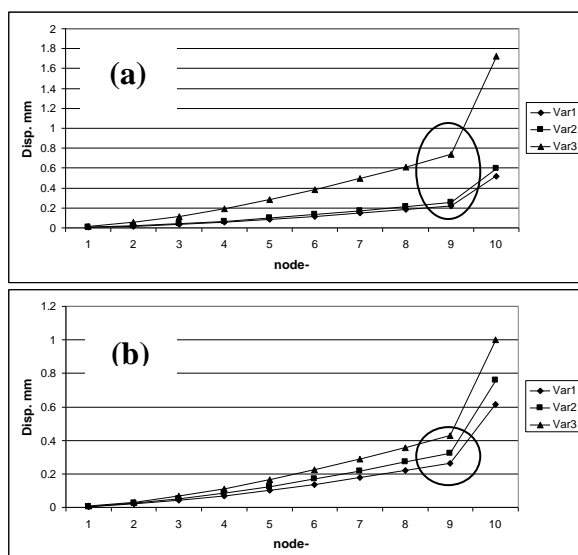


Fig.11 Displacement in x-direction at all nodes for all variations at (a) $t_{i=1}$, (b) $t_{i=10}$

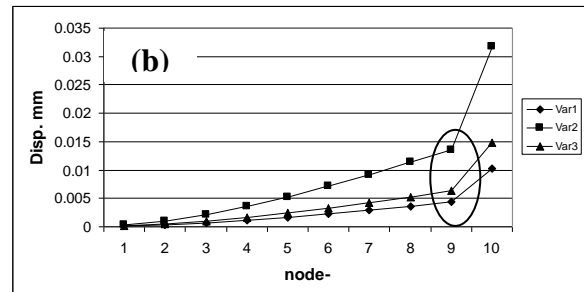


Fig.12 Displacement in y-direction at all nodes for all variations at (a) $t_{i=1}$, (b) $t_{i=10}$

Vibration response generated in the simulation and testing in all variations and directions give a periodic pattern follows the force pattern on the turbine shaft (Fig. 13, 14 and 15). Displacement resulted at node-1 from the test provide lower values compared with simulation.

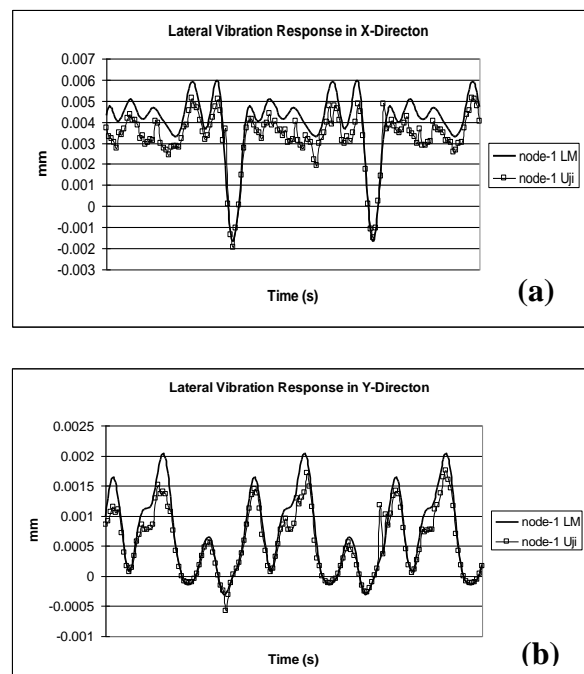
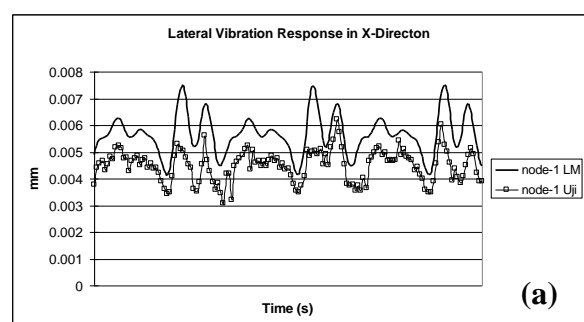
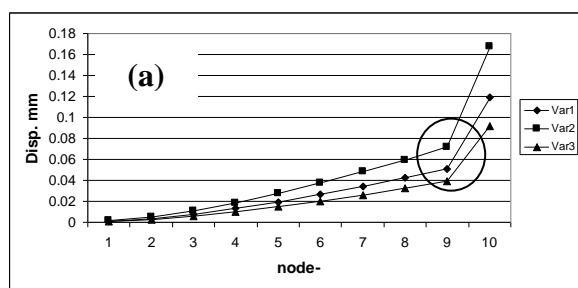


Fig.13 Responses at node-1 at Var-1, (a) x-direction, (b) y-direction



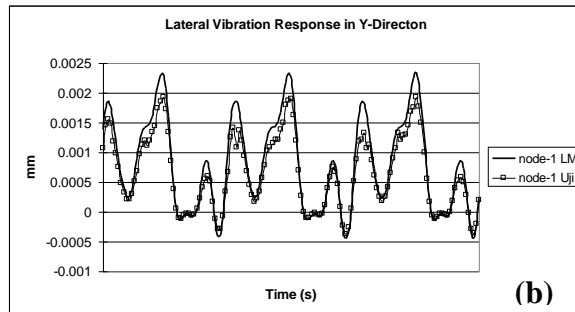


Fig.14 Responses at node-1 at Var-2, (a) x-direction, (b) y-direction

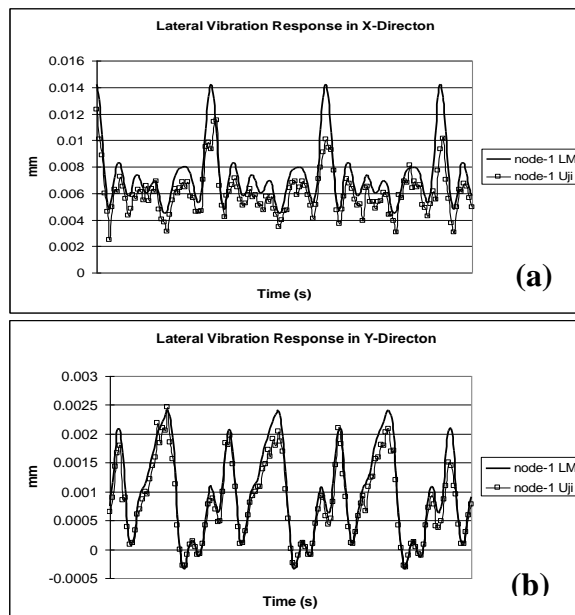


Fig.15 Responses at node-1 at Var-3, (a) x-direction, (b) y-direction

Responses of displacement appears in x-direction are consistent in positive value. According to the definition of the direction of displacement which has been described previously, the position displacement is always in the region of x+. Displacement at this area generated by the excitation force resulted form interaction between the incoming fluid and foils according to the position at the azimuth as the turbine rotates. This indicates that turbine shaft always experience lateral bending along its rotation.

The highest deflection occurs at each variation according to the azimuth position (0° - 360°) of the turbine shown in Table 4. The increase in turbine rotation speed is generally deliver enhanced value of the lateral deviation in x- and y-direction. However, the maximum deviation is not

always occur at the same azimuth position despite the azimuth angle intervals are repeated consistently in value close or equal to 120° .

Table 4. Position of azimuth of the highest displacement

U (m/s)	Direction	Azimuth (degree)
0.8	x	$87^{\circ}, 109^{\circ}, 221^{\circ}, 243^{\circ}$
	y	$57^{\circ}, 191^{\circ}, 328^{\circ}$
0.9	x	$84^{\circ}, 206^{\circ}, 325^{\circ}$
	y	$60^{\circ}, 181^{\circ}, 300^{\circ}$
1	x	$112^{\circ}, 221^{\circ}, 325^{\circ}$
	y	$60^{\circ}, 169^{\circ}, 279^{\circ}$

Different direction of vibration response in y-direction showing strong influence of lift force generated by fixed-pitch foil as force producer for vertical-axis ocean current turbine. Real displacement obtained using simple Pythagoras formula for displacement in x and y-direction. The average error between the simulation and measurement at each of variation are given in Table 5.

Table 5. Average Error For All Variations

U(m/s)	Ave. Error (%) x-direction	Ave. Error (%) y-direction
0.8	25%	25%
0.9	26%	26%
1	23%	23%

CONCLUSIONS

Simulation and experimental test of lateral vibration of fixed-pitch vertical-axis ocean current turbine have been performed. Some conclusions are drawn :

- Finite element method and lumped mass matrix are used to perform vibration response. The present of similar mode of response displacement at all recognition nodes have close agreement to the 1th mode shape resulted from simulation.
- Resulted displacement from simulation at all nodes at the same time indicating the present of critical part at node-9. Potential problems on the tip of shaft obviously due to half of the force of turbine received concentrated at cantilever tip.

International Engineering Symposium, March 3-5, 2011 Kumamoto Univ., Japan

- The use of eddy currents sensor for displacement measurement has given consistent response pattern compared to simulation results with the maximum displacement error of 25% at Var-2 ($U=0.9$ m/s) and the minimum of 23% at Var-3 ($U=1$ m/s) in x- and y-direction.

ACKNOWLEDGEMENTS

- The authors expressed their gratitude to DP2M Dikti and LPPM ITS for funding the research under research scheme known as Postgraduate Research Grand (HPTP) of the year 2009 and 2010.
- The authors also thanks to technicians at the ITS towing tank for their helps in the experimental work.

REFERENCES

- [1] Black H., (1974) Journal of Engineering for Industry, "A linearized model using transfer matrix to study the forced whirling of centrifugal pumps rotor systems".
- [2] Dimentberg F., (1961), Flexural Vibrations of Rotating Shafts. London: Butterworth.
- [3] Diewald W. and Nordmann R., (1989) ASME Journal of Vibration and Acoustics, Stress, and Reliability in Design 111, 370-378, "Dynamic analysis of centrifugal pump rotors with fluid-mechanical interactions".
- [4] Firoozian R. and Stanway R., (1988) Journal of Vibration and Acoustics, Stress, and Reliability in Design 110, 521-527. "Modeling and control of turbomachinery vibrations".
- [5] Hantoro. R., Utama. I.K.A.P., Erwandi (2009a), "Unsteady Load Analysis on a Vertical Axis Ocean Current Turbine", The 11th International Conference On QIR (Quality In Research), 3-6 August 2009, Indonesia University.
- [6] Hantoro. R., Utama. I.K.A.P., Erwandi , Sulisetyono A. (2009b), "Unsteady load and fluid-structure interaction of vertical-axis ocean current turbine", Journal of Mechanical Engineering , Petra University Surabaya, Vol.11, No.1, April 2009, ISSN 1410-9867.
- [7] Kiho S., Shiono M. and Suzuki K., (1996), "The power generation from tidal currents by Darrieus turbine, WRFC 1996".
- [8] Rouch K. E., Mcmaines T. H., Stephenson R. W. And Ermerick M. F., (1989) 4th International ANSYS Conference and Exhibition, Part 2, 5.23-5.39. "Modeling of complex rotor systems by combining rotor and substructure models".
- [9] Sakata M., Kimura K., Park S. K. and Ohnabe H., (1989), Journal of Sound and Vibration 131, 417-430. "Vibration of bladed flexible rotor due to gyroscopic moments".
- [10] Reuter Robert C., Worstell Mark H. (1978), "Torque ripple in a vertical axis wind turbine, Sandia Report SAND78-0577", Unlimited Release • UC-60, Printed April 1978.
- [11] Sheldahl, R., Klimas, P. (1981), "Aerodynamic characteristics of seven symmetrical airfoil sections through 180-degree angle of attack for use in aerodynamic analysis of vertical axis wind turbines". Technical Report SAND80-2114, Sandia National Laboratories, March 1981.

Foot Pressure Mapping System for a Biped Robot

Cheng-Hsin Chuang¹ Yi-Rong Liou² and Ming-Yuan Shieh³

- ¹ Department of Mechanical Engineering, Southern Taiwan University, Tainan, Taiwan.
e-mail:chchuang@mail.stut.edu.tw
- ² Department of Mechanical Engineering, Southern Taiwan University, Tainan, Taiwan.
e-mail:brad_0502@yahoo.com.tw
- ³ Department of Electrical Engineering, Southern Taiwan University, Tainan, Taiwan. e-mail:myshieh@mail.stut.edu.tw
-

Abstract: Controlling the balance of motion in a context involving a biped robot navigating a rugged surface or a step is a difficult task. In the present study, a 3×5 flexible tactile sensor array was developed to assist in improving the acuity of a foot pressure map of a biped robot. We introduced an innovative concept involving structural electrodes upon a piezoelectric film in order to detect variations in pressure, which is unlike piezoresistive-type and capacitive-type pressure sensors used in conventional pressure mapping systems. The tactile sensor consisted of a polymer piezoelectric film, PVDF, between two patterned flexible print circuit substrates (FPC). Additionally, a silicon rubber microstructure was attached to the FPC and covered by a PDMS layer. Experimental results showed that the output signal of the sensor exhibited a linear behavior within 0.2N ~ 9N while its sensitivity was approximately 41.96 mV/N. According to the characteristic of the tactile sensor, we designed the readout module for an in-situ display of the pressure magnitudes and distribution within 3 by 5 taxels. Furthermore, the zero moment point (ZMP) also can be calculated by this program. Consequently, our tactile sensor module can provide the pressure map and ZMP information to in-situ feedback control the balance of moment for a biped robot.

Keywords: Tactile Sensor, Piezoelectric, Microstructures, Biped Robot

I. INTRODUCTION

Walking is the most common mode in which people move from one place to another and it is relatively easy for a human to maintain balance whether they are walking on a rugged surface, a sloping surface, or a stairway; this is due to feedback from the tactile perception of one's feet. Feet are a connection between the rest of the body and the environment, such that they provide a great deal of information about the current state of what is underfoot, helping us maintain dynamic balance of motion. However, it is currently a difficult task for the most advanced biped robot because the robot cannot adjust its center of gravity to maintain balance without sensing the reaction force from the feet. Although the foot pressure mapping system has been available for medical applications or shoe design, a real-time and low-cost flexible

sensor for the feedback of foot pressure is lacking in the context of robotic motion control. In order to maintain a satisfactory dynamical postural stability for a humanoid robot, the concept of zero moment point (ZMP) [1] is commonly used to reduce the overturning moment, which is the point with respect to the dynamic reaction force at the contact of the foot with the ground without producing any moment. Therefore, the magnitude and distribution patterns of foot pressure under dynamic variations are crucial for the calculation of ZMP.

Early foot pressure measuring employed ink for the imprinting of pressure distributions of the foot. Welton, E. A. [2] also used this method to imprint foot pressure and transferred the pattern into normal force value in 1992. So far, foot pressure measuring systems can be divided into: the force plate system [3], and the placed sensors system [4]. For the force plate system, the main structure is a flat platform with a sensory array and

usually is fixed on the surface or placed on the ground to measure the contact force between the foot and the ground. Although the force plate system possesses high resolution, only a single step can be measured due to the limited area and stationary nature of the process. On the other hand, (or foot for that matter) a placed sensor system describes embedding a sensor on the bottom of the foot for continuous measurement of the reaction force in motion. Therefore, a portable placed sensor system is more likely to fulfill requirements for foot pressure measurements for the motion balance control of a biped robot. Two kinds of sensors have been utilized for the placed sensor system: Force Sensing Resistors (FSR)[5] and F-Scan [6].The FSR is a single-point pressure measurement device based on piezoresistive effects and manufactured by Interlink Electronics Inc. Though FSR is simple and user-friendly, the point size cannot satisfy the minimum resolution requirement for a foot pressure mapping system. In addition, the output signal depends on the resistance change of conductive rubber in response to pressure, which usually exhibits non-linear characteristics in the sensing range. Hence, additional calibration is needed [7]. F-Scan is a multi-sensory pressure measurement device based on piezoresistive effects and is manufactured by Tekscan Inc. The F-Scan system has demonstrated in-shoe pressure monitoring for clinical purposes; however, there are considerable kinks which need to be dealt with. For example, when applying 500kPa force on the F-Scan for 15 minutes, the output value has been shown to decline 19% on margin [8]. In contrast to piezoelectric-type pressure sensors based on polymer piezoelectric material, polyvinylidene fluoride (PVDF) has exhibited characteristics of flexible mechanics, an output voltage of good linearity for dynamic loading, and a low-hysteresis effect with repeatability of exercise pressure [9-12]. In the present study, we introduced the concept of a structural electrode [13] in order to increase the sensitivity of the piezoelectric tactile sensor and to reduce issues related to cross-talk. Furthermore, we used micromachining technology (MEMS) to fabricate a 3 by 5 tactile sensor array for foot pressure mapping. In addition to the

tactile sensor array, a read-out circuit module and a program of pressure mapping and zero moment point calculation were also integrated with the tactile sensor, so that the robot can receive real-time feedback from this foot pressure mapping system so as to control its balance of motion.

II. TACTILE SENSOR WITH STRUCTURAL ELECTRODE ARRAY

The flexible 3×5 tactile sensor array consists of two patterned flexible printed circuits (FPC) sandwiching a polymer piezoelectric film (PVDF) and 15 microstructures made of silicone rubber attached to the FPC surface and packaged with PDMS material, as shown in Fig. 1. By adding the microstructure to the electrode patterned on the FPC, the sensitivity of the piezoelectric-type tactile sensor can be improved; this is the so called the structural electrode which replaces the thin-film electrode in the traditional piezoelectric sensor [14]. Contrary to what occurs with a thin-film electrode, the effect of stress concentration can be generated in the piezoelectric material while the contact force is transferred through the microstructures instead of through the uniform contact on the piezoelectric material. The induced charge of the piezoelectric material is increased due to the stress concentrated underneath the microstructures.

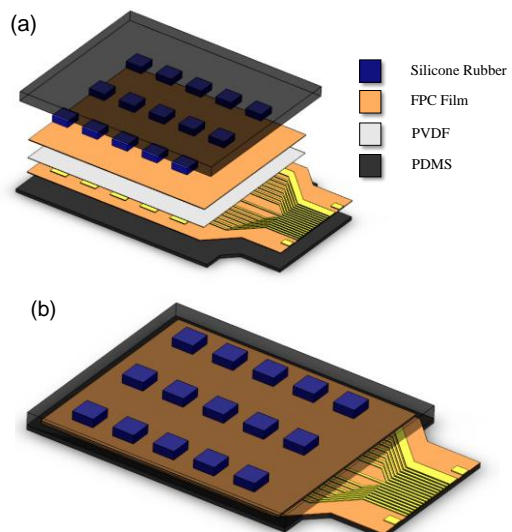


Fig. 1: The illustration shows the structure of a 3×5 flexible tactile sensor array, and its dimensions in length, width, and height: 53mm, 48mm, and 4mm, respectively. (a) The structure of sensor is separated layer by layer. (b) The finished sensor after packaging by PDMS material.

III. NUMERICAL SIMULATION

A. 3D Model of the tactile sensor with a single structural electrode

When the contact force is acting on the surface of the tactile sensor, the inner microstructure and outside packaging layer respond, in the force transfer, to the sensor material (PVDF). Therefore, in order to enhance the stress concentration underneath the microstructure, we utilized a numerical method to evaluate the effect of Young's Modulus ratio between the microstructure material and the packaging layer on the sensor output. A 3D model of the tactile sensor with single structural electrode was established and calculated based on commercial finite element software, ABAQUS. All dimensions and material properties of the simulation model are laid out in Fig. 2 and Table 1, respectively. In the simulations, the external force of 1N was set to load on the tactile sensor top surface within a 10×10 mm² square, and the bottom surface was set as a fixed-end boundary condition. The mesh was established by 8-node hexahedral elements and the total element number was around 100,000 - decided by convergence test.

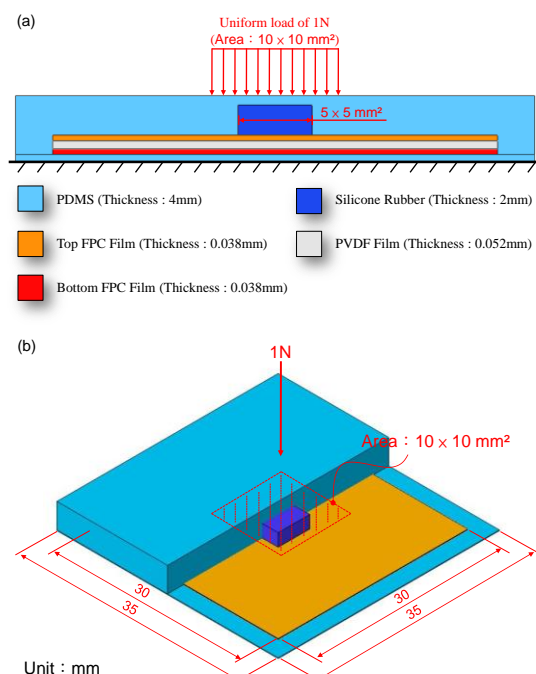


Fig. 2: The 3D simulation model of the tactile sensor with a single structural electrode: (a) the cross section and thickness of each layer (b) the domain of model and loading conditions

TABLE 1: MATERIAL PROPERTIES FOR NUMERICAL SIMULATION

	PVDF	Silicon Rubber	FPC Film	PDMS
Density (kg/m ³)	1780	1570	1353	1083
Young's modulus (MPa)	3000	5.45	2500	0.5~10
Poisson's ratio	0.35	0.45	0.34	0.45
Dielectric constant (Farad/m)	11×10^{-10}			
d_{211}, d_{233} (m/Volt)	23×10^{-12}			
d_{222} (m/Volt)	-33×10^{-12}			

B. Simulation results

The contour of electric potential at the piezoelectric film as 1N loaded on the tactile sensor is illustrated in Fig. 3(a) and a cross-sectional profile of electric potential is plotted in Fig. 3 (b). The results indicate that there is a plateau region of electrical potential corresponding to the concentration stress underneath the silicone rubber microstructure; therefore, although the applied loading is uniform, the resulting stress level is enhanced due to the microstructure. Furthermore, a peak value of electrical potential occurred at the edge of the microstructure due to the edge effect and the deformation of the PVDF film. In general, the cross-talk effect needs to be avoided as we wish to exactly identify the image of the contact area when an object or a force contacts a tactile sensor. Cross-talk refers to zero contact at the taxel but it still maintaining the ability to gather the output signal due to the influence of other neighboring taxels. As shown in Fig. 3(b), we still can gather the electric potential outside the loading area as indicated by the influence range; therefore, cross-talk effect has to take into account the spacing between two microstructures or the isolation of the ground electrode in the sensor backside. In spite of the sensitivity enhancement due to the microstructure, we also can improve the sensitivity by altering the package material. As shown in Fig. 4, when the Young's Modulus ratio between microstructure material and package material increased, the output voltages also increased. That is, a combination of a harder microstructure and a softer package layer creates higher sensitivity because most of the contact force can be

transferred by a stiffer microstructure instead of compliant package material.

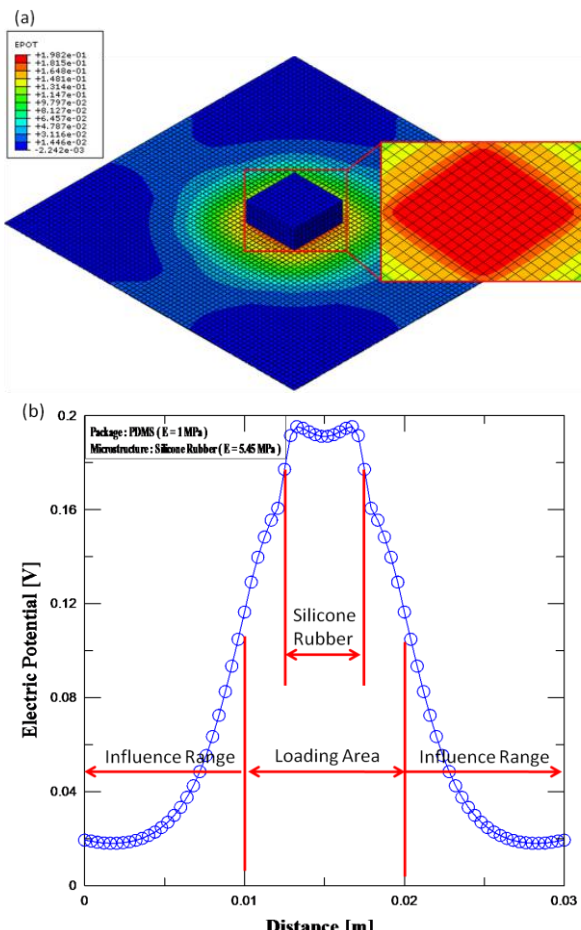


Fig. 3: Simulation results of tactile sensor with a single silicone rubber microstructure ($E=5.45\text{ MPa}$) and packaged by PDMS ($E=1\text{ MPa}$) as applied 1N; (a) the contour of electric potential at PVDF film (b) the cross-sectional profile of electric potential at PVDF film

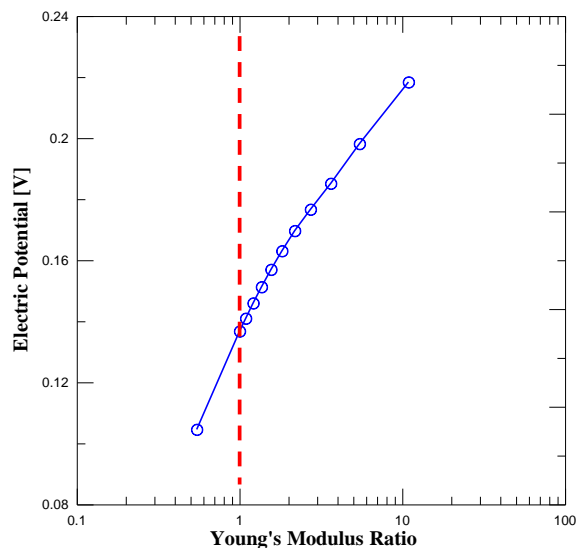


Fig. 4: The simulation results of output voltages versus the ratios of Young's Modulus between the inside microstructure material and the outside package material

IV. SENSOR FABRICATION

The fabrication process of a flexible tactile sensor array is shown in Fig. 5 and the details are described as follows:

- A commercial flexible printed circuit spun coating a positive photoresist S1813, then a photo mask with a design of distributed electrodes was used to pattern the photoresist by standard photolithography, as referred to in Figs. 5(a) and (b).
- The patterned photoresist was then used as an etching mask for the wet etching of a metal layer on the FPC. First, the FPC was steeped in a ferric chloride solution and oscillated by ultrasonic for 9 min. It was then taken out of the patterned FPC for cleaning with D.I. water and dried using a N_2 gun. Then, the distributed electrode on the FPC can be completed after being removed from the residual photoresist by acetone, as shown in Figs. 5(c) and (d).
- The Ag layers on both sides of a commercial PVDF film (Measurement Specialties Inc.) were removed by acetone and cleaned by D.I. water and N_2 gun, as referred to in Figs. 5(e) and (f).
- After top and bottom FPCs have been patterned, a stripped PVDF film was sandwiched by two FPCs with adhesive, as shown in the Fig. 5(g).
- The microstructures were fabricated using a molding technique. The master was made of PMMA fabricated using precision machining. Each microstructure was made of silicone rubber, as indicated in Figs. 5(h) and (i).
- 15 microstructures were placed upon the electrodes of a laminated FPC and then packaged in PDMS material in a full size PMMA mold. The tactile sensor can be completed after PDMS solidification at 85°C for 30 min, as referred to in Figs. 5(j) and (k). The specifications of the finished tactile sensor are listed in Table 2 and shown in Fig. 6.

TABLE 2: THE SPECIFICATIONS OF TACTILE SENSOR

Materials	Length (mm)	Width (mm)	Thickness (mm)
Microstructure (Silicone rubber)	5	5	2
Package layer (PDMS)	52.9	47.4	4
PVDF film	50.9	45.4	52×10^{-3}
FPC	50.9	45.4	50×10^{-3}

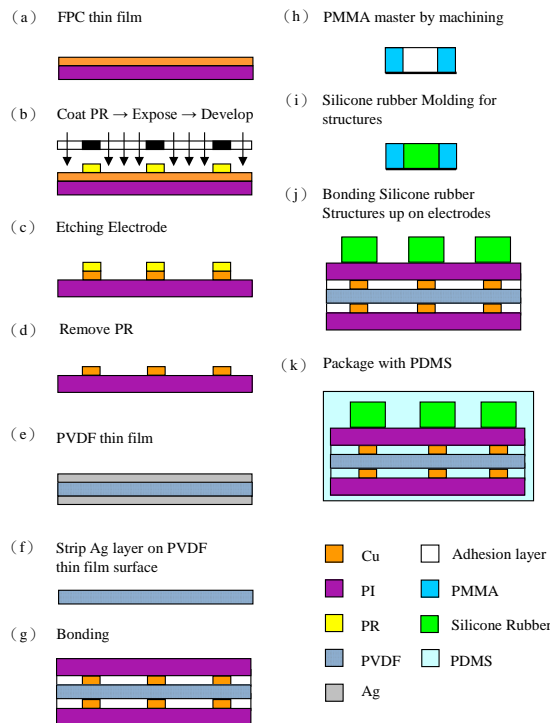


Fig. 5: The fabrication processes of 3×5 tactile sensor array



Fig. 6: Photograph of 3×5 array of tactile sensor

V. EXPERIMENTAL RESULTS AND DISCUSSIONS

A. Characterization of tactile sensor

As regards a piezoelectric tactile sensor, it is difficult to measure a static force due to the notion that induced charges by a static force could dissipate rapidly. Therefore, a dynamic test system was built to obtain the output characteristics of a tactile sensor, as shown in Fig. 7. The dynamic test bed utilized a shaker (Data Physics Corp.) driven by a function generator (Agilent33220A) with a sinusoidal voltage of 2 Hz. Additionally, a force sensor (PCB209C02, PCB Piezotronics, Inc.) was mounted in front of the shaker shaft for force calibration and

its signal outputted to the oscilloscope via channel 1 (CH1) for real-time monitoring. Thus, a periodic and calibrated force can be generated and vertically acted upon a single sensing element (taxel) of the tactile sensor. The output signal of a tactile sensor passed through a charge amplifier (B&K NEXUS2690A) to the oscilloscopes channel 2 (CH2) for signal acquisition. In the experiments, we didn't amplify the output signal from the tactile sensor rather a low-pass filter with a cutoff frequency of 60 Hz was employed for noise reduction from city power. By using a 3-axis stage, the shaker shaft can exactly act on the taxel where we wired out. Moreover, the applied force can be tuned by the input voltage from a function generator. As Fig. 8 shows, the relationship between the applied force and the output voltages of a single taxel has good linearity from 0.2 N to 9 N. In addition, its sensitivity is about 41.96 mV/N calculated by curve fitting. As far as we are able to tell, our tactile sensor has a higher sensitivity and lower detectable threshold force than the conventional thin-film electrode PVDF tactile sensor demonstrated by Yu et al. [14]. In Yu's work, the sensitivity and the threshold force are 0.2 mV/N and 0.7 N, respectively. Consequently, the concept of a structural electrode and soft package material could not only improve the sensitivity but also lower the minimum detectable force of a piezoelectric tactile sensor.

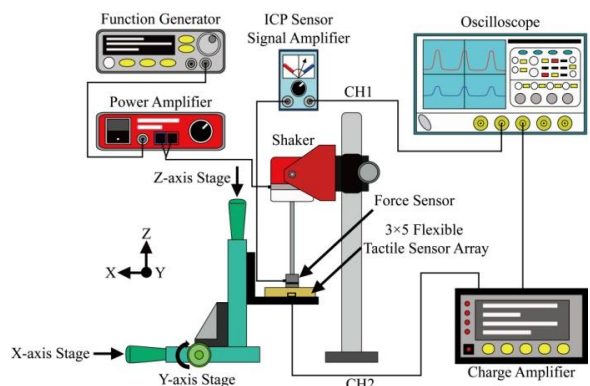


Fig. 7: The experimental setup for a characterization measurement of the sensor. (a) The illustration of characterization measurement set-up (b) Photograph of characterization measurement device.

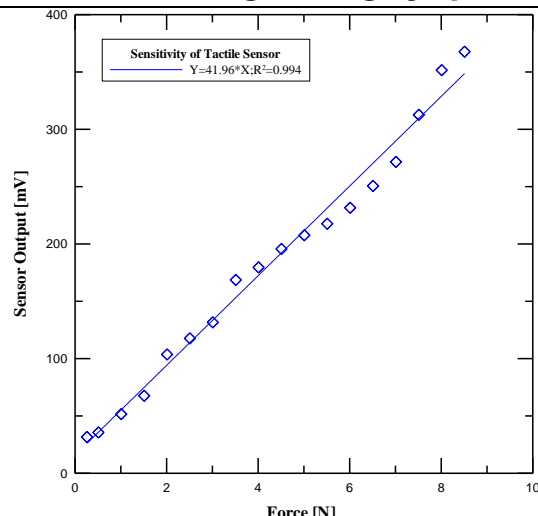


Fig.8: The characteristic of sensor shows that the linearity between 0.2 to 9 N and its sensitivity is about 41.96 mV/N.

B. Foot pressure mapping system

The foot pressure mapping system comprises three parts: two 3×5 tactile sensor arrays of flexible tactile sensors, a readout circuit module for acquisition of the sensor outputs and transmitting signals to computer, and the signal processing program for calculating the zero moment point and displaying a real-time pressure map on the computer screen. Two tactile sensors were attached on the each foot of a biped robot, and the control box was placed on the head of robot and connected to the sensor and computer by a parallel interface and USB, respectively, as shown in Fig. 9. The readout circuit module included 30 CMOS OP amplifiers for each taxel, two 16-channel multiplexers connected with a 60 Hz notch filter and power amplifier, and a microcontroller (LM3S811, Texas Instruments Inc.) for A/D conversion and signals IO between the sensor and computer, as shown in Fig. 10; As indicated in Fig. 10, the tactile sensor was first connected to a CMOS OP for magnifying the current signal in order to compensate for the low voltage output of the piezoelectric sensor which easily loses its signal through transduction. Furthermore, the noise also can be effectively reduced due to the OP having high input impedance and low output impedance for the impedance match between a piezoelectric sensor and the circuitry in the control box.

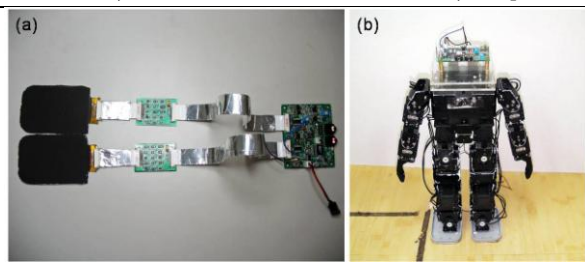


Fig. 9: (a) The photograph is of a read-out circuit module integrated with a tactile sensor; (b) two 3×5 tactile sensors were installed at the bottom of each biped-robot foot.

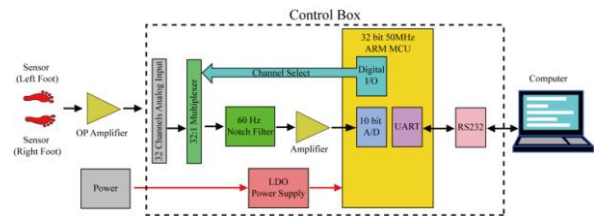


Fig. 10: The architecture of readout circuit module

As regards the biped robot walking, the foot mapping system will scan and transfer the output signals of a tactile sensor array to the connected computer via USB. Then, these signals will be processed by a computer program for a real-time display of the pressure map and the calculation of the zero moment point. The location of zero moment point can be denoted as ZMP (\bar{X} , \bar{Y}), where \bar{X} and \bar{Y} are the coordinates

with respect to the origin point at the bottom left of the sensors array as shown in Fig. 11. The calculations of the coordinates \bar{X} and \bar{Y} can be expressed as follows:

$$\bar{X} = \frac{\sum x_i \cdot \omega_i}{\sum \omega_i} \text{ and } \bar{Y} = \frac{\sum y_i \cdot \omega_i}{\sum \omega_i} \quad (1)$$

where x_i and y_i are the x-axis coordinate and y-axis coordinate of i^{th} sensor, and ω_i is the pressure value of the i^{th} sensor. Therefore, when the computer program receives the sensor output of each taxel, the pressure map can be displayed on the screen as well as the location of ZMP. In this program, the refresh rate of each frame of pressure display is 0.8 ms and the maximum incidences of the recorded ZMP trajectory is 20 times in a cycle.

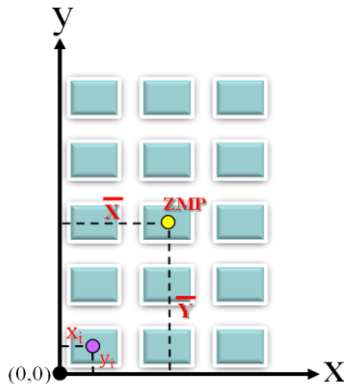


Fig. 11: The location of zero moment point, ZMP (X, Y), with respect to the origin point at the left bottom of the 3×5 sensor array

In order to easily recognize the distribution and magnitude of foot pressure, we divided the pressure into 7 levels, as shown in Fig. 12. The bigger concentric circle indicates a higher pressure measured at this point, but the real pressure value of each taxel also can be seen in the same frame at the bottom. For example, the foot pressure maps of a real walking test for a biped robot can be seen in Fig. 13. Two foot pressure maps represent the left and right foot, respectively, and the location of ZMP is also indicated in the foot maps as a white spot. Hence, the trajectory of ZMP also can be traced in this walking test.

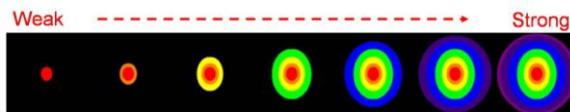


Fig. 12: Seven different levels for the magnitude of foot pressure displayed in the computer screen.

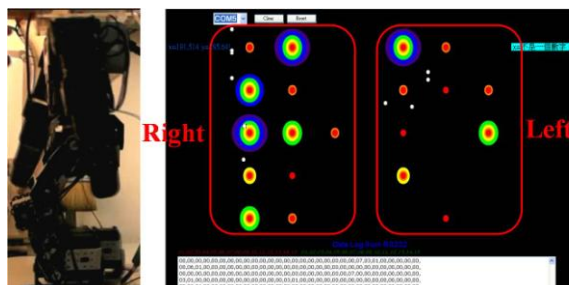


Fig. 13: Two foot pressure maps of a walking test for a biped robot, the pressure of each taxel can be seen either in a symbolic display or the real value at the bottom

In the simulation results shown in Fig. 3, the cross-talk effect of the tactile sensor needs to be avoided for the identification of the contact area. Thus, a proper spacing

between two structural electrodes was designed for reducing the cross-talk effect. A knocking test was performed to demonstrate that there is no cross-talk effect in our foot mapping system, as illustrated in Fig. 14. The sensor was knocked by a pen and the pressure magnitude and distribution can be observed on the computer screen; only the knocked point in the 3×5 taxels showed the pressure signal on the screen while the untouched taxels didn't exhibit any signal, as shown in Fig. 14(b). In addition, the knocking test was consistent for different taxels as indicated in Figs. 14(c) and (d): Consequently, the foot mapping system can actually feedback the reaction force of an uneven surface or obstacle in the walking path of a biped robot

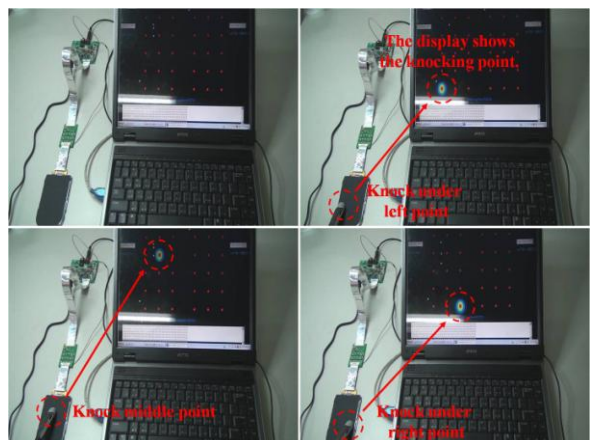


Fig. 14: The knocking test of 3×5 tactile sensor, single knocking on the surface of tactile sensor by a pen. The pressure mapping results corresponding to the knocking test, showed the magnitude and distribution of the pressure on the computer screen. (a) knocking test setup; (b) knock at left point; (c) knock at middle point; (d) knock at right point.

VI. CONCLUSION

This study has successfully developed a 3×5 flexible tactile sensor array and applied it to a biped robot with regards to foot pressure mapping. The novel tactile sensor introduced the concept of a structural electrode for sensitivity enhancement and the reduction of the cross-talk effect. By choosing a soft material for a packaging layer, sensitivity can be improved by 41.96 mV/N, which is better than the conventional piezoelectric tactile sensor. The foot pressure mapping system is not only a real-time display of the dynamic pressure distribution and magnitude but also provides the trajectory of the zero moment point while walking. In

the future, the system will integrate with motion control for the biped robot, thus allowing a robot to adjust its posture in order to maintain balance during motion.

VII. ACKNOWLEDGEMENT

The project was able to be conducted successfully due to the much appreciated financial support of the Nation Science Council of Taiwan (NSC 98-2221-E-218-023), and Optoelectronics Research Center at Southern Taiwan University for the MEMS fabrication facilities.

References

- [1] Abhinav Ashok Kalamdani, "Development and characterization of a high-spatial-temporal-resolution foot-sole-pressure measurement system," CMU-RI-TR-06-38, 2006, pp. 9-11.
- [2] elton, E.A, "The Harris and Beath footprint: interpretation and clinical value," Foot Ankle, 1992, vol. 13, pp. 268-462.
- [3] B.A. MacWilliams, P.F. Armstrong, "Clinical applications of plantar pressure measurement in pediatric orthopedics," Pediatric Gait, 2000, PP. 143-150.
- [4] H. Zhu, N. Maalej, J.G. Webster, W.J. Tompkins, P. Bach-y-Rita, J.J. Wertsch, "An umbilical data-acquisition system for measuring pressures between the foot and shoe," IEEE Trans. Biomed. Eng., 1990, vol. 37, pp. 908-911.
- [5] Interlink Electronics, Inc. <http://www.interlinkelec.com/>, 2010.
- [6] Tekscan, Inc. <http://www.tekscan.com/>, 2010.
- [7] S.W. Yip, T.E. Prieto, "A system for force distribution measurement beneath the fee," Biomedical Engineering Conference, 1996, pp. 32-34.
- [8] Woodbum J and Helliwell PS "Observations on the F-Scan in shoe pressure measuring system," Clin. Biomech., 1996, 11 301-304.
- [9] Cheng-Hsin Chuang, Chen-Tai Lu, Te-Hua Fang, "Slippage and Direction Sensing Based on a Flexible Tactile Sensor with Structural Electrodes," IEEE SENSORS 2009, 2009, pp. 958-962.
- [10] Mohammad Ameen Qasaimeh, Saeed Sokhanvar, Javad Dargahi, Mojtaba Kahrizi, Journal of Microelectromechanical Systems, 2009, 195-207.
- [11] Seiichi Teshigawara, Masatoshi Ishikawa, Makoto Shimojo, SICE Annual Conference, 2008, 900-903.
- [12] Naoki Saito, Toshiyuki Satoh and Hideharu Okano, "Grasping Force Control in consideration of Translational and Rotational Slippage by a Flexible Sensor," IEEE Industrial Electronics, IECON 32nd Annual Conference, 2006, pp. 3892-3897.
- [13] Cheng-Hsin Chuang, Wen-Bin Dong, Wen-Bin Lo, "Flexible Piezoelectric Tactile Sensor with Structural" IEEE 3rd International Conference on Sensing Technology, 2008, pp. 504-507.
- [14] K-H Yu, M-J Yoon, T-K Kwon and S-C Lee, "Distributed flexible tactile sensor system", International Journal of Applied Electromagnetics and Mechanics 18 (2003) 53-65.

Fuzzy Logic Controller to regulate the pH and EC for irrigation system in Greenhouse

**DUY ANH NGUYEN¹ HOANG NGUYEN² THANH TUNG TRAN³ QUOC DAT LE⁴
and TAN TIEN NGUYEN⁵**

*1,2,3,4,5 Hi-Tech Mechatronics Lab., Faculty of Mechanical Eng., Mechatronics Eng.
Dept., Ho Chi Minh City University of Technology, 268 Ly Thuong Kiet, Dist. 10, Ho
Chi Minh City, Vietnam, e-mail : duyanhkmu@yahoo.com*

Abstract: In this paper, specific fuzzy controller is design for regulation of pH and EC. System modelling and control was base on McAvoy model, and simulated with SIMULINK Matlab. The system control pH and EC concentration simultaneously. The model has two reagent flows (Acid and Base) for pH control, integrated with another reagent flow (KCl) for controlling EC. The model of pH control process is highly considered because of the distinct nonlinear of pH and delay time for mixing and transmitting. The simulation results obtained demonstrate that Fuzzy Logic theory can create a good controller for this difficult control problem and controller model has ability to be applied because of the small errors in simulation result. And the experiment results show that the Fuzzy Logic Controller designed in this paper is suitable for fact system.

Keywords: Fuzzy, pH control, EC, irrigation system, pH neutralization process.

Introduction

In Greenhouse system, besides the conditions about temperature, CO₂ concentration and light, pH and EC concentration are important conditions which affect the good quality and the productivity of crops.

pH is well known difficult process control due to its serious nonlinearity and considerable delay time. For nonlinear system, controlling with conventional controllers such as PI, PID controllers, is difficult. Fuzzy Logic Controllers provide reasonable and effective alternatives to classical controllers naturally. Fuzzy controllers are efficient nonlinear controllers and good robustness. By using a linguistic approach, Fuzzy set theory can be integrated into control theory using rules of the form, If {condition} Then {action}. Recent applications of Fuzzy Logic Controllers are on over various field of automatic control which are surveyed in Segeno (1985) and Lee (1990).

Various controller and model designed for this tough control problem. The models used to research the pH process control are base on the model of McAvoy et al [4]. For that model, many control algorithms were applied to create different controllers.

Yong and Rao designed a sliding-mode controller for pH process combining the variable structures and the Smith prediction method [3]. Fuzzy logic controller is designed for pH neutralization process in [2], [5]. Proudfoot et al introduced a Self-tuning PI controller which easily find the suitable fixed parameter values for the PI controller [5]. Maulik Parekh et al described a new technique of in-line control of pH neutralization based on fuzzy logic [6].

In this paper, based on McAvoy model, we design a controller which can regulate both pH and EC to the desired value with acceptable error by using Fuzzy logic control algorithm.

Control pH and EC

pH control is a common issue in many industrial process. Control pH and EC is an important problem for irrigation system in Greenhouse. Method to control pH and EC variations is using the regulating of the input liquid flow. The control objective is to maintain the pH and EC value in the effluent flow as close to desired value as possible. This influent liquid flows through the pipe system, where it is mixed with amount of three concentrated reagents to

adjust its pH and EC. The influent is water, HCl and NaOH are used for pH regulating, KCl is used to control EC. The reagents are more concentrated than effluent because they are added to effluent as little as possible.

Electrical Conductivity (EC) is a measure of ability of water to conduct an electric current and depends on: concentration of ions (higher concentration, higher EC), temperature of the solution (higher temperature, higher EC), specific nature of the ions (higher specific ability and higher valence, higher EC). The determination of the electric conductivity is a rapid and convenient means estimating the concentration of ions in solution. Since each ion has its own specific ability to conduct current, EC is only an estimate of the total ion concentration [7].

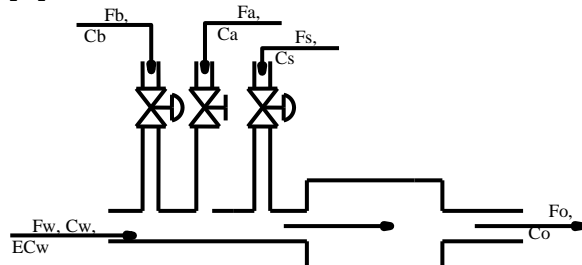


Fig.1 pH and EC control

The conductivity of a water sample can be calculated by using following approximated function [7]:

$$EC = \sum (C_i \times F_i) \quad (1)$$

where:

EC: electrical conductivity, $\mu\text{S}/\text{cm}$

C_i : concentration of ionic specie in solution, mg/L

F_i : conductivity factor for ionic specie i.

As shown in Figure 1, the pH and EC are controlled in the pipes system – the influent is pumped through pipes system, and the reagents are added into the pipes, where the influent and reagents are mixed to adjust pH and EC value. The effluent is also pumped out of the system.

System model

The model in this paper is based on the model that proposed by McAvoy et al (1972). Under ideal conditions, such as perfect mixing, no polluting elements in the pipes system, neglect the effect of

temperature on pH and EC. The mixing dynamics are as follow:

$$V \frac{dX_a}{dt} = F_a(t - T_a) \cdot C_a - [F_w + F_a(t - T_a) + F_b(t - T_b)] X_a \quad (2)$$

$$V \frac{dX_b}{dt} = F_b(t - T_b) \cdot C_b - [F_w + F_a(t - T_a) + F_b(t - T_b)] X_b \quad (3)$$

$$V \frac{dX_w}{dt} = F_w \cdot C_w - [F_w + F_a(t - T_a) + F_b(t - T_b)] X_w \quad (4)$$

$$\begin{aligned} V \frac{dEC}{dt} = & F_w \cdot EC_w + F_a(t - T_a) \cdot C_a \cdot K_{Cl^-} + F_b(t - T_b) \cdot C_b \cdot K_{Na^+} \\ & + F_s(t - T_s) \cdot C_s \cdot K_{K^+} + F_s(t - T_s) \cdot C_s \cdot K_{Cl^-} \\ & - [F_w + F_a(t - T_a) + F_b(t - T_b) + F_s(t - T_s)] EC \end{aligned} \quad (5)$$

where :

C_a , C_b , C_s , C_w : concentration of acid titration, base titration, salt KCl titration and water (influent) stream (mol/L).

X_a , X_b : concentration of non-reacting acid and base solution in pipe (mol/L)

X_w : concentration of non-reacting chemical elements in pipe (mol/L)

F_a , F_b , F_s , F_w : flow rate of acid titration, base titration, salt titration and influent stream (L/s)

$F_o = F_a + F_b + F_w + F_s$: flow rate of effluent stream (L/s)

EC_w : EC concentration of influent (cS/cm)

EC: EC concentration of effluent (cS/cm)

K_{Na^+} , K_{K^+} , K_{Cl^-} : conductivity factor of Na^+ , K^+ , Cl^- ($\mu\text{S}/\text{cm}$ per mg/L)

V: volume of the pipe from the conjunction of pipes to pH meter (L)

T_a , T_b , T_s : delay time because of transmitting signal and mixing substances (s).

The concentrations of reagents are constant and we control the pH and EC of effluent by varying the reagents flow. The concentrations are the excess concentrations. This means that we measure the excess concentration of hydrogen ions in effluent. The H^+ excess concentration can convert into pH by using following formula:

$$pH = -\lg \left[\sqrt{0.25C^2 + 10^{-14}} + 0.5C \right] \quad (6)$$

Design of Fuzzy Logic Controller

Fuzzy Logic Controller (FLC)

Fuzzy Logic Controllers (FLCs) allow for simpler human like approach to control system design and do not need the mathematical model as in the case of conventional control design methods.

A typical fuzzy logic controller has three basic parts: input signal fuzzification, a fuzzy engine that handles rule interface and defuzzification that create continuous signal for actuators such as control valve.

Fig.2 show a typical of fuzzy logic controller. The fuzzification block transform the continuous input signal into linguistic fuzzy variables such as Negative Big, Negative Medium, Negative Small, Positive Small, Positive Medium. The fuzzy engine carries out rule inference where human experience can injected through linguistic rules. The defuzzification block converts the inferred control action back to a continuous signal that interpolates between simultaneously fired rules.

The knowledge of Fuzzy logic control has two components: database and rule base. Database gives the necessary definitions which are used to define linguistic variables and fuzzy data manipulation in the fuzzy logic control. The rule base describes the control goal and the way to control by means of a set of linguistic control rules.

The most common method is used for defuzzification is the "Center of Area" method, that generates the the center of gravity of the final fuzzy space. It produce a result that is sensitive to all the rules. It is given by:

$$U = \frac{\sum_{i=1}^m C_i \mu_i}{\sum_{i=1}^m \mu_i} \quad (7)$$

Where:

C_i is the value corresponding to the center of the output fuzzy set.

μ_i is the membership value of the output fuzzy set.

U is the clear value of the output variables.

Two clearly features of fuzzy logic control are (i) that human experience can be integrated and (ii) that fuzzy logic provides a non-linear relationship induced by membership functions, rules and

defuzzification. Because of these feature, fuzzy logic is prefer for process control where popular control technologies is not suitable and human experience exist. There are many fields that fuzzy logic control can be applied such as: temperature, pH, EC, nutrients or toxic substances. Most of them only use error (e) and change of error (Δe) for the controller inputs.

Design of Fuzzy Logic Controller

Selection of Fuzzy logic controller

The input variables used for the FLC: Error $e(t)$ and Change in error $\Delta e(t)$.

Error $e(t)$: the difference between the measured value of pH and the desired pH.

Change in error $\Delta e(t)$: difference between the present instant $e(t)$ and the error at the previous instant $e(t-1)$.

$$\Delta e(t) = e(t) - e(t-1) \quad (8)$$

The output variable is "Change in output $\Delta u(t)$ ". The systems have two valves to control the reagents flow so there are two output variables: control1 for acid and control2 for base. The output control is given by:

$$u(t) = u(t-1) + \Delta u(t) \quad (9)$$

Selection of linguistic variables

The fuzzy input variables (Error, Change in error) and output variables (Change in output) are divided into seven linguistic (fuzzy) variables.

Error $e_{\text{pH}}(t)$: Negative Big (NB), Negative Medium (NM), Negative Small (NS), Zero (ZR), Positive Small (PS), Positive Medium (PM), Positive Big (PB).

Change in output $\Delta u(t)$: Close Fast (CF), Close Medium (CM), Close Slow (CS), State (ST), Open Slow (OS), Open Medium (OM), Open Fast (OF).

Determination of the value range of variables, and knowledge base

For pH control

Error $e(t)$ range: -2 pH to 2 pH.

Change in error $\Delta e(t)$ range: -2 pH to pH.

Change in output $\Delta u(t)$ range: -0.02 L/s to +0.02 L/s.

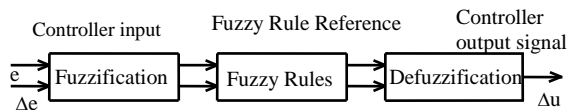


Fig.2 A typical fuzzy logic controller

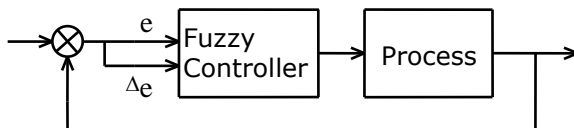


Fig.3 Fuzzy pH & EC control system

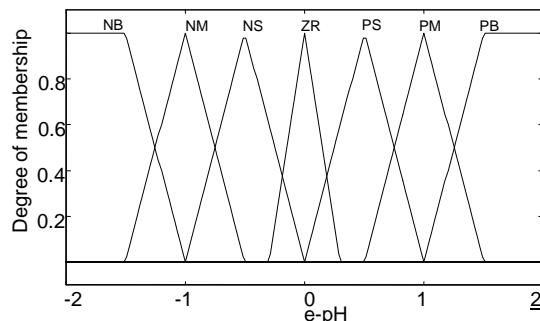


Fig.4(a) Membership functions for Error e_pH

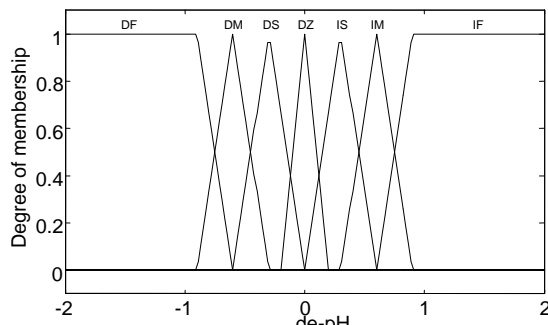


Fig.4(b) Membership functions for Change in error de_pH

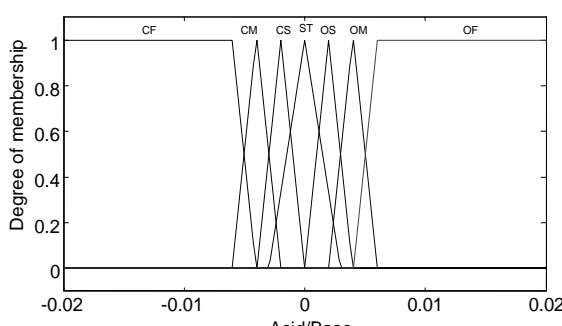


Fig.4(c) Membership functions for Change in output Control 1, 2

For EC control

Error e(t) range: - 1 EC to 1 EC.

Change in error $\Delta e(t)$ range: -1 EC to 1 EC.

Change in output $\Delta u(t)$ range: -0.02 L/s to +0.02 L/s.

Knowledge Base

For pH control

The membership functions for input and output variables are given in Figs. 4(a) to 4(c).

The rule of FLC is given in Table 1,2.

For EC control

The membership functions for input and output variables are given in Figs. 5(a) to 5(c). The rule of FLC is given in Table 3.

Table 1 Rule Base of the FLC for Control1 (Acid)

Control1 (Acid)		Error pH						
Change in error $\Delta e_{pH}(t)$	DF	NB	NM	NS	ZR	PS	PM	PB
	DM	CF	CF	CF	CM	CS	ST	OS
	DS	CF	CF	CM	CS	ST	OS	OM
	ZR	CF	CM	CS	ST	OS	OM	OF
	IS	CM	CS	ST	OS	OM	OF	OF
	IM	CS	ST	OS	OM	OF	OF	OF
	IF	ST	OS	OM	OF	OF	OF	OF

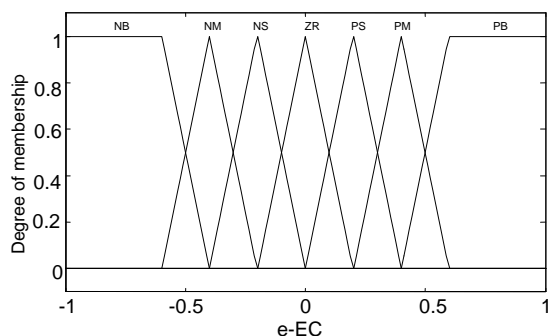


Fig.5(a) Membership functions for Error e_{EC}

Table 2 Rule Base of the FLC for Control2 (Base)

Control2 (Base)		Error pH						
Change in error $\Delta e_{pH}(t)$	DF	OF	OF	OF	OF	OM	OS	ST
	DM	OF	OF	OF	OM	OS	ST	CS
	DS	OF	OF	OM	OS	ST	CS	CM
	ZR	OF	OM	OS	ST	CS	CM	CF
	IS	OM	OS	ST	CS	CM	CF	CF
	IM	OS	ST	CS	CM	CF	CF	CF
	IF	ST	CS	CM	CF	CF	CF	CF

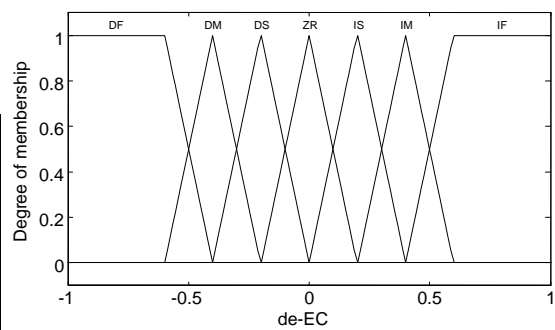


Fig.5(b) Membership functions for Change in Error de_{EC}

Table 3 Rule Base of the FLC for Control3 (KCl)

Control3 (Salt)		Error pH						
Change in error $\Delta e_{pH}(t)$	DF	OF	OF	OF	OF	OM	OS	ST
	DM	OF	OF	OF	OM	OS	ST	CS
	DS	OF	OF	OM	OS	ST	CS	CM
	ZR	OF	OM	OS	ST	CS	CM	CF
	IS	OM	OS	ST	CS	CM	CF	CF
	IM	OS	ST	CS	CM	CF	CF	CF
	IF	ST	CS	CM	CF	CF	CF	CF

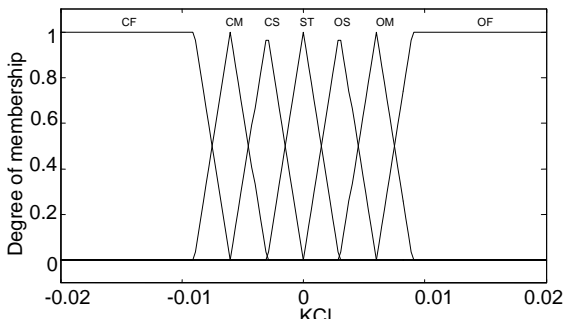


Fig.5(c) Membership functions for Change in output control3

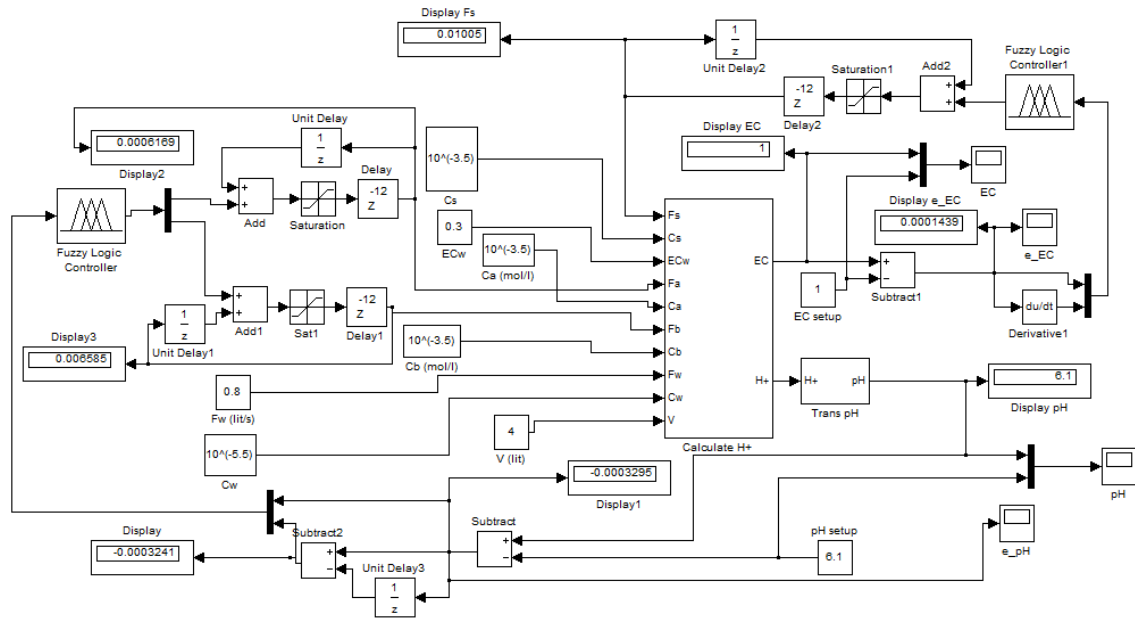


Fig.6 Simulink system model

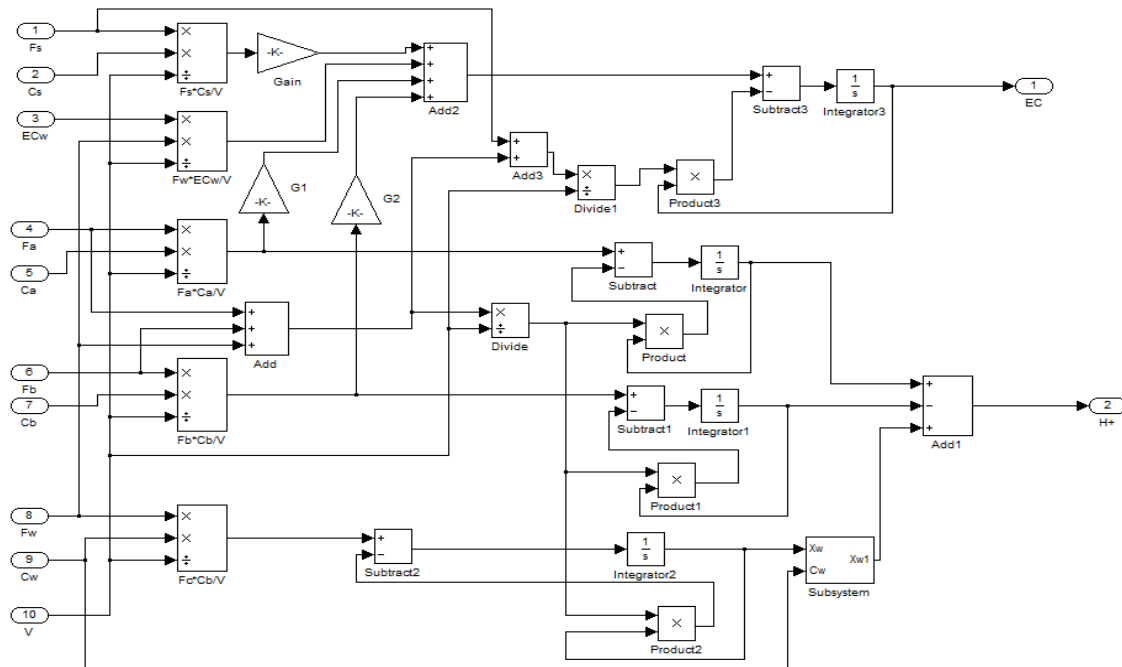


Fig.7 Process sub-module for model

RESULT AND DISCUSSION

Simulation

SIMULINK is a useful program for simulating the FLC, and give the best result in modelling the pH/ EC process.

Fig.6, 7 are show the simulation model of process. The parameters of the pH and EC control process described in equations (2) to (5) are given as $C_a = 10^{-3.5}$ mol/l, $C_b = 10^{-3.5}$ mol/l, $C_w = 10^{-5.5}$ mol/l, $C_s = 10^{-3.5}$ mol/l, $F_w = 0.8$ l/s, $EC_w=0.3$ mS/cm, $T = T_a = T_b = T_s = 12s$, $K_{Na^+} = 2.1$ mS/cm for every g/l , $K_{K^+} = 1.84$ ms/cm, $K_{Cl^-} = 2.14$ cS/cm. This parameters are similar to the parameters of system in experiment.

Fig.8, 9 show that Fuzzy logic controller does manage to maintain the pH and EC around the desired value at the small level. The steady-state error is quite small and the system gets steady-state error before the 100th second.

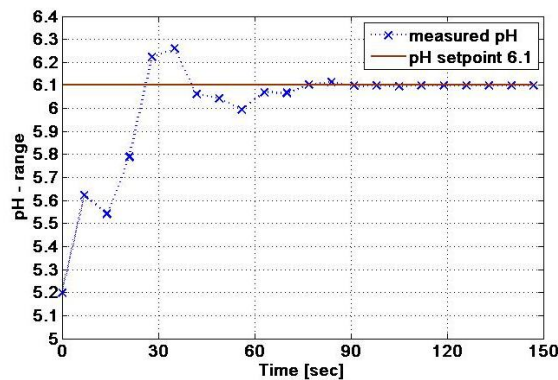


Fig.8 pH control curve of set point 6.1 with EC set point 1.0

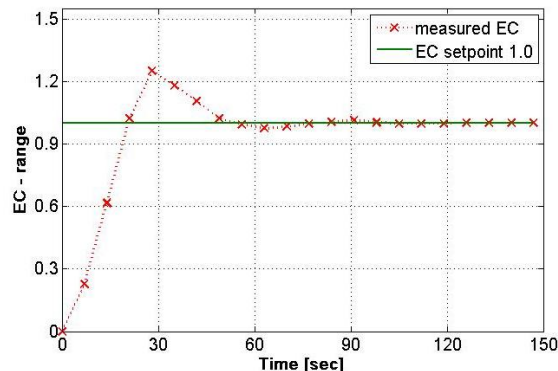


Fig.9 EC control curve of set point 1.0 with pH set point 6.1

Experiment

In experiment, test conducting grown in Da Lat city, the center of vegetable production in southern Vietnam. Test plant is spinach. We used DSPIC 30F4011 for the Fuzzy Logic Controller. The actual data shows the parameters of system in Simulink Matlab and experiment are the same.

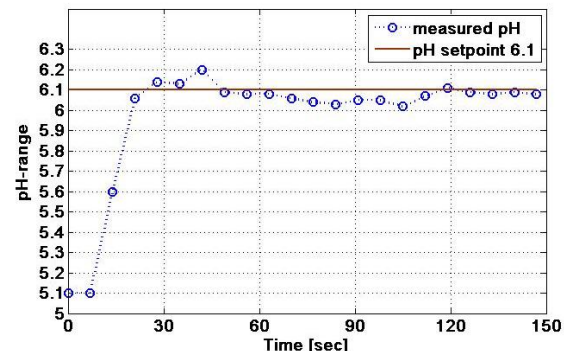


Fig.10 pH control curve of setpoint 6.1 with EC setpoint 1.0

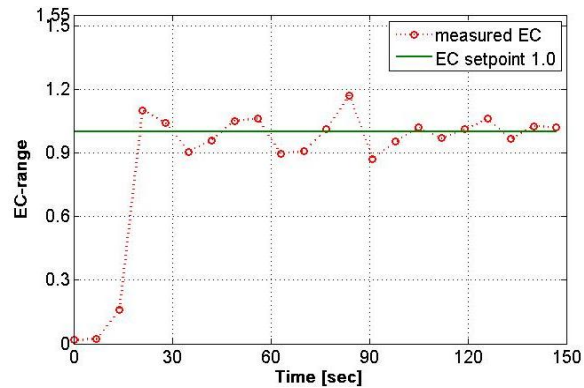


Fig.11 EC control curve of set point 1.0 with pH set point 6.1

From Fig.10,11 are show that the results from experiment of the system get steady-state error around the 120th second, that mean later than the time that the system does in Simulink. However, pH and EC are maintained around the desired value at the acceptable level. Measured the pH of the soil before using the control system and after use are different. Before is 5.1 and after is 5.8.

CONCLUSION

The main goal of this research model is to create a controller that control both pH and EC value around the desired value with the acceptable error. Simulation result by SIMULINK show that this is achieved with the building of Fuzzy Logic Controller. The result in experiment show that Fuzzy Logic Controller proposed in this paper for the pH and EC regulation case has proved to be robust and gives very good result.

More adjusting should be done with Fuzzy algorithm to get better result in pH and EC process. Research on integrated fuzzy controller tuning all three PID parameters should be admired. Using

Neural Networks, Genetic Algorithms is another method to improve the controller.

References

- [1] C. G. Proudfoot, B. A. Gawthrop, M. A., D. Phil.,and O. L. R. Jacobs, M. A., Ph.D., "Self-tuing PI control of a pH neutralisation process", IEEE proceedings, vol. 130, Pt.D, No.5, 1983.
- [2] D. P. Kwok and p. Wang, "Enchanced fuzzy control of pH neutralization process", Industrial Electronics, Control, and Instrumentation, vol. 1, pp.15-19, 1993.
- [3] G. E. Yong and S. Rao, "Robust slidding-mode control of Nonlinear process with Uncertainty and Delay", J.of Dynamics systems measurement and control, vol. 109, pp. 203-208,1987.
- [4] McAvoy, T. J., E. Hsu, and S. Lowenthal, "Dynamics of pH in controlled stirred tank reactor" Ind. Eng. Chem. Process Des. Dev., vol. 11, pp. 68-70, 1972.
- [5] Muthu, R. El Kanzi, E., "Fuzzy logic control of a neutralization process", ICECS2003, vol.3, pp.1066, 2003.
- [6] Parekh, M. Deisa, M. Hua Li Rhinehart, R.R., "In-line control of nonlinear pH neutralization based on Fuzzy logic", IEEE Transactions on components, Packaging, and Manufacturing Technology, Par A, vol.17, no.2, 1994
- [7] www.rrcap.unep.org/male/manual/national/12chapter12.pdf Young

Static Characteristics of a Journal Bearing with Engineered Slip/no-slip Surfaces

RAGHUNANDANA K¹

and

JOHN V CORDA²

1 Department of Mechanical & Mfg. Engg, Manipal Institute of Technology, Manipal, Manipal University, Manipal – 576 104, India. e-mail:bhatraghu@yahoo.com

2 Department of Mechanical & Mfg. Engineering, MIT Manipal – 576 104, India. email:corda.john@gmail.com

Abstract: The no-slip boundary condition is part of the foundation of the traditional lubrication theory. It has been found by recent experimental research that for certain engineered surfaces no-slip boundary condition is not valid. In the present study the effect of an engineered slip/no-slip surface on journal bearing performance is examined. Numerical Analysis is carried out by solving the modified Reynolds equation satisfying the boundary conditions using successive over relaxation scheme in a finite difference grid which gives the steady state pressure. These pressure values are used to evaluate the dimensionless steady-state load bearing capacity, attitude angle and friction force. It is found that the cautious application of slip to a journal bearing's surface can lead to improved bearing performance.

Keywords: Lubrication, Journal Bearing, Slip, Load carrying capacity, Friction force.

Introduction

The basic principle of fluid film lubrication in the Reynolds equation is that there is no slip of the liquid lubricant against the two, bounding, solid surfaces. This 'no - slip' boundary condition assumption enables the velocity gradient within the fluid film to be determined and hence the Reynolds continuity equation to be derived.

In recent years, however, experimental evidence has begun to emerge that some simple, Newtonian liquids can slip against solid surfaces. Such slip occurs when the solid surface is very smooth and the liquid is only 'weakly bonded' to the solid, which in practical terms means that the liquid does not wet the solid surface. This evidence has been based on the measurements done by Zhu Y et al (2002) on the influence of non-wetting velocity gradients in fluids on viscous shear forces.

Spikes (2003) derived the extended Reynolds equation for half wetted bearings and analyzed the influence of the wall slip on the hydrodynamic properties of the fluid film bearings. It is proposed that the fluid slips against the stationary smooth bearing surface and adheres to the moving

rough surface. The half wetted bearings have limitations in macro scale contacts due to the difficulty in producing very smooth non-wetted surfaces for the slip to occur. Indeed Spikes (2003) addressed the possibility of a quarter-wetted bearing with one of the contacting surfaces partially wetted at the inlet zone.

Fortier A. E. et. Al. (2004) exploited the slip phenomenon based on the choice of the pattern of the slip/no-slip surface regions with an emphasis on increased load support.

Using the limiting shear stress model Wu and Ma (2005) found that the performance of a hydrodynamic lubrication journal bearing with wall slip is controlled by the limiting shear stresses of the two lubricated surfaces, especially by the smaller limiting shear stress.

Chengwei Wu (2008) used the finite element analysis and the quadratic programming algorithm to study the performance of the journal bearing with a slip zone on the sleeve surface. Analysis indicated that the location and size of the slip zone greatly affect the journal performance.

In the present study, the exploitation of the slip phenomenon to improve the

performance of journal bearings is examined by means of a numerical analysis. By constructing an engineered heterogeneous bearing surface, on which slip occurs in certain regions and is absent in others, the flow pattern in the liquid lubricating film can be altered. It is believed that the judicious choice of a pattern of slip/no-slip regions will lead to improved bearing characteristics, such as load support and friction.

Analysis

The journal bearing configuration is as shown in Fig. 1. The shaft and the sleeve have a clearance denoted as c . The operational eccentricity of the shaft and the sleeve, as measured along the line of centers, is denoted by e . The thickness of the lubricant film is a function of the bearing clearance, eccentricity and circumferential location and is given as

$$h(\theta) = c + e \cos(\theta) \quad (1)$$

The θ axis originates and ends at the line of centers where the film thickness is a maximum. Minimum film thickness occurs at θ equal to π .

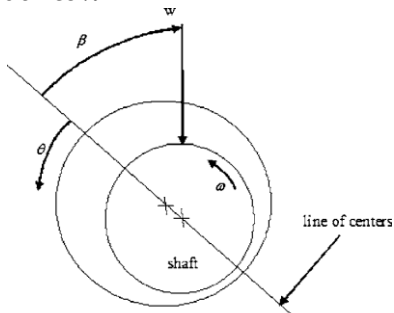


Fig. 1 Journal Bearing Configuration

Fig. 2(a) illustrates the film thickness distribution. Surface 1 corresponds to the surface of the shaft and is moving at a speed ωR . Surface 2 is the stationary surface and represents the bearing sleeve. The slip/no-slip pattern is applied on surface 2 and is as shown in Fig. 2(b). Region I is the region in which slip is imposed, while region II is the no-slip region. This configuration is chosen to force fluid entering the slip region to exit through the no-slip region.

The slip velocity in region I is proportional to the surface shear stress, resulting in the boundary conditions

$$\text{At } z = 0, \quad u_\theta = u_s, \quad u_y = 0$$

At $z = h$, $u_\theta = -\alpha \mu \frac{\partial u_\theta}{\partial z}$, $u_y = -\alpha \mu \frac{\partial u_y}{\partial z}$
where α is the slip coefficient.

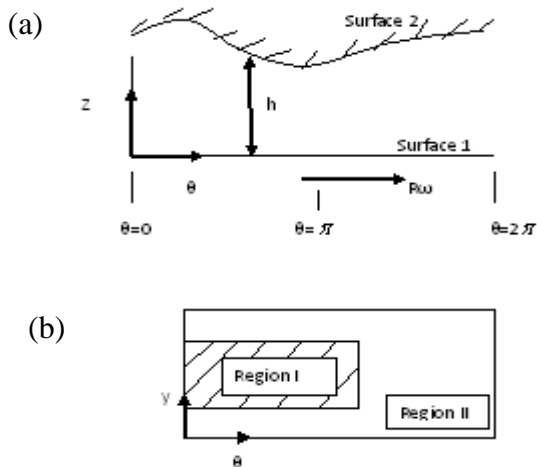


Fig. 2 Film thickness distribution (a) slip/no-slip pattern (b)

With the basic assumptions, we have the Navier-Stokes equation in the form

$$\frac{\partial^2 u_x}{\partial z^2} = \frac{1}{\mu} \frac{\partial p}{\partial x} \quad (2) \quad \frac{\partial^2 u_y}{\partial z^2} = \frac{1}{\mu} \frac{\partial p}{\partial y} \quad (3)$$

Integrating these equations twice and applying the boundary conditions we have the velocity components

$$u_x = \frac{z^2}{2\mu} \frac{\partial p}{\partial x} - \frac{hz}{2\mu} \frac{\partial p}{\partial x} \left(\frac{h+2\alpha\mu}{\alpha\mu+h} \right) - \left(\frac{u_s z}{\alpha\mu+h} \right) + u_s \quad (4)$$

$$u_y = \frac{z^2}{2\mu} \frac{\partial p}{\partial y} - \frac{h}{2\mu} \frac{\partial p}{\partial y} \left(\frac{h+2\alpha\mu}{\alpha\mu+h} \right) z \quad (5)$$

On the basis of continuity of flow and assuming no supply of lubricant in the z direction for the journal bearing we have

$$\frac{\partial q_x}{\partial x} + \frac{\partial q_y}{\partial y} = 0 \quad (6)$$

$$\text{where } q_x = \int_0^h u_x dz \text{ and } q_y = \int_0^h u_y dz \quad (7)$$

Integrating u_x and u_y under the limits we have

$$q_x = \frac{-h^3}{12\mu} \frac{\partial p}{\partial x} \left(1 + \frac{3\alpha\mu}{h+\alpha\mu} \right) + \frac{u_s h}{2} \left(1 + \frac{\alpha\mu}{h+\alpha\mu} \right) \quad (8)$$

$$q_y = \frac{-h^3}{12\mu} \frac{\partial p}{\partial y} \left(1 + \frac{3\alpha\mu}{h+\alpha\mu} \right) \quad (9)$$

Substituting these flow values in the continuity equation, the governing equation for a liquid lubricant film in the journal bearing, taking account of slip, the modified Reynolds equation is deduced as follows:

$$\begin{aligned} & \frac{1}{R^2} \frac{\partial}{\partial \theta} \left[\frac{h^3}{12\mu} \frac{\partial p}{\partial \theta} \left(1 + \frac{3\alpha\mu}{h+\alpha\mu} \right) \right] + \\ & \frac{\partial}{\partial y} \left[\frac{h^3}{12\mu} \frac{\partial p}{\partial y} \left(1 + \frac{3\alpha\mu}{h+\alpha\mu} \right) \right] = \\ & \frac{\partial}{\partial \theta} \left[\frac{\omega h}{2} \left(1 + \frac{\alpha\mu}{h+\alpha\mu} \right) \right] \end{aligned} \quad (10)$$

In the dimensionless form it is represented as:

$$\begin{aligned} & \frac{\partial}{\partial \theta} \left\{ H^3 \frac{\partial p}{\partial \theta} \left(1 + \frac{3A}{(H+A)} \right) \right\} + \\ & \left(\frac{D}{L} \right)^2 \frac{\partial}{\partial Y} \left\{ H^3 \frac{\partial p}{\partial Y} \left(1 + \frac{3A}{(H+A)} \right) \right\} \\ & = 6 \frac{\partial}{\partial \theta} \left\{ H \left(1 + \frac{A}{(H+A)} \right) \right\} \end{aligned} \quad (11)$$

On substitution of $A = 0$ in the above equation, we arrive at the standard Reynolds equation which does not consider the slip. The dimensionless Reynolds equation (11) is solved numerically using finite difference method based on the Reynolds boundary condition using the successive over relaxation technique.

Table 1 shows the results obtained and verified with the slip coefficient value of $A = 0$ as calculated by Pinkus (1961) which is the standard Reynolds equation. The results are in good agreement.

The load capacity is evaluated by integration of the pressure profile as:

$$\begin{Bmatrix} F_x \\ F_y \end{Bmatrix} = \begin{Bmatrix} W \\ 0 \end{Bmatrix} = -2 \int_0^{0.5} \int_0^{2\pi} P \begin{Bmatrix} \cos \theta \\ \sin \theta \end{Bmatrix} d\theta dY \quad (12)$$

	Eccentricity ratio	Present	Pinkus(5)
Sommerfeld Number	0.2	0.630986	0.632
	0.5	0.178579	0.179
	0.8	0.04456	0.0448
Frictional force	0.2	12.6669	12.9
	0.5	4.234294	4.31
	0.8	1.686238	1.71
Attitude angle	0.2	74.06338	74
	0.5	56.80425	56
	0.8	36.25673	36

Table 1: Values of Sommerfeld number, frictional force and attitude angle for different values of eccentricity ratio for a conventional bearing.

The dimensionless friction force in the θ direction is found by integrating the shear stress over the surface area.

$$F = \int_0^{2\pi R} \int_{-L/2}^{L/2} \tau_x dy dx \quad (13) \text{ where } \tau_x = \frac{\partial u_x}{\partial z}$$

Once the values of friction force and load are evaluated coefficient of friction is found

$$f = \frac{F}{W} = f(R/c)$$

Results

Computations have been made for a range of journal bearing configurations and operating conditions.

Fig. 3 shows the pressure distribution for a bearing with a length to width ratio $L/D = 1$, eccentricity ratio $\epsilon = 0.8$ for a conventional bearing and a bearing with a dimensionless slip coefficient of 10 and slip applied in region I. It is observed that the bearing with a dimensionless slip coefficient is flattened due to slip.

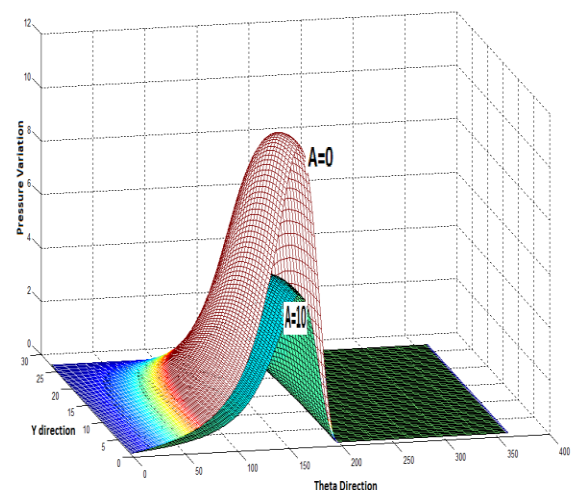


Fig.3:Pressure distribution for $L/D=1$ and $E=0.8$

Table 2 show that there is a decrease in the load carrying capacity when a bearing with slip ($A > 0$) is compared to a conventional bearing ($A = 0$). This gradual decrease is seen for a few values of A and then it is observed that there is a marginal increase in the load carrying capacity even when the slip is considered. This increase is seen only up to a value of $A=12$ and then load carrying capacity remains constant irrespective of the value of A . The same trend is shown graphically in fig. 4.

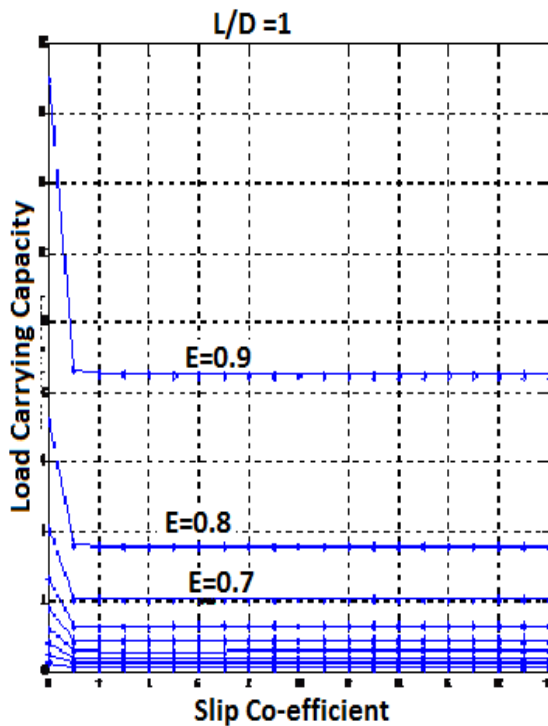


Fig.4: Effect of slip coefficient on load carrying capacity

A	Load	A	Load
0	2.632132	6	1.299652
1	1.322767	7	1.301249
2	1.294991	8	1.302594
3	1.293772	9	1.30373
4	1.295648	10	1.304699
5	1.297768	11	1.305531

Table 2: Load carrying capacity for different slip co-efficients

Fig. 5 ,6 and 7 shows the variation of Sommerfeld number with eccentricity ratio for different values of L/D ratios starting from 0.5 to 2.0 for dimensionless slip coefficient of $A = 0$, $A=2$ and $A = 15$ respectively. It is observed that there is an increase in Sommerfeld number from $A=0$

to $A=2$ which indicates a decrease in the load carrying capacity. From $A=2$ to $A=15$ there is a decrease in the Sommerfeld number and conversely an increase in the load carrying capacity.

It is also seen that for a particular value of slip co-efficient(say $A=0$) the bearing with $L/D=0.5$ (short bearing) has a higher Sommerfeld number indicating a lower load carrying capacity when compared to the bearings with higher L/D ratio.

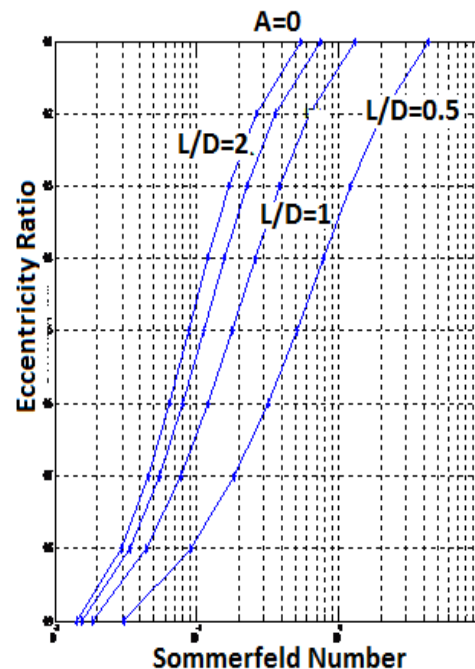


Fig.5:Eccentricity Ratio Vs. Sommerfeld Number for $A = 0$

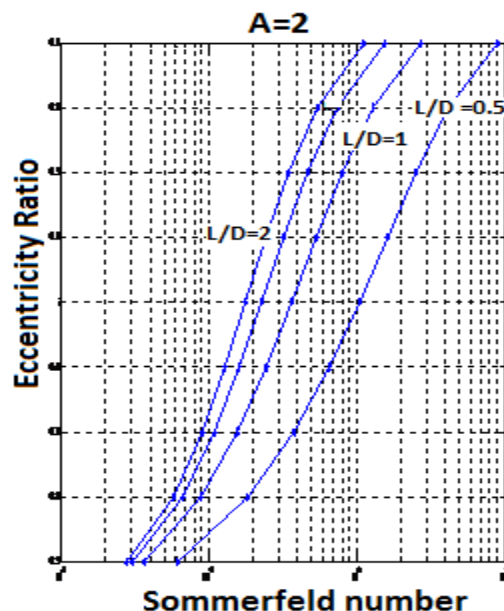


Fig.6:Eccentricity Ratio Vs. Sommerfeld Number for $A = 2$.

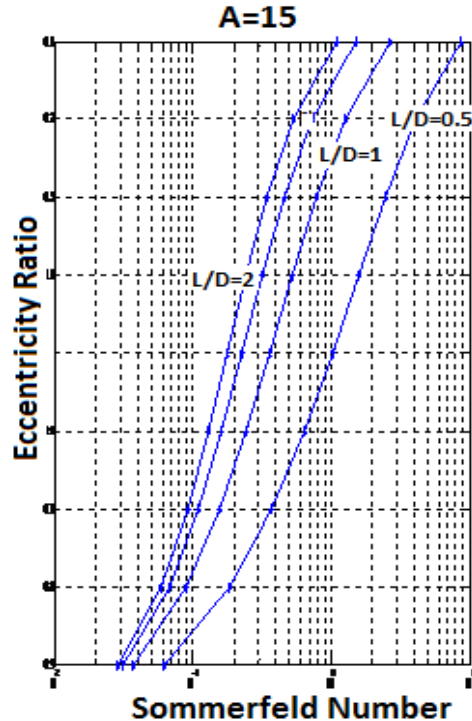


Fig. 7: Eccentricity Ratio Vs. Sommerfeld Number for $A = 15$.

Fig. 8 shows the relation between the Sommerfeld number and the friction co-efficient. The L/D ratio is maintained at 1 and the values of slip co-efficient considered are $A=0$ and $A=10$. The values are plotted on a log-log scale. It is seen that in the bearing with no slip ($A=0$) there is consistently a higher friction co-efficient for the same Sommerfeld number.

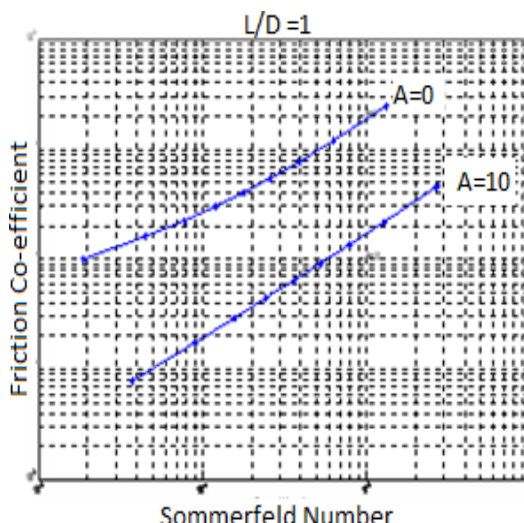


Fig. 8: Friction coefficient Vs Sommerfeld Number for $L/D = 1$, $A = 0$ and 10 .

Fig. 9 and 10 shows the relationship between friction co-efficient and Sommerfeld number for different values of L/D ratio ranging from 0.5 to 2.0. Two values of slip co-efficient $A=0$ (no slip) and $A=15$ is considered. The tendency show that L/D ratio has a much smaller effect on the co-efficient of friction for bearing with no slip than the bearing with slip.

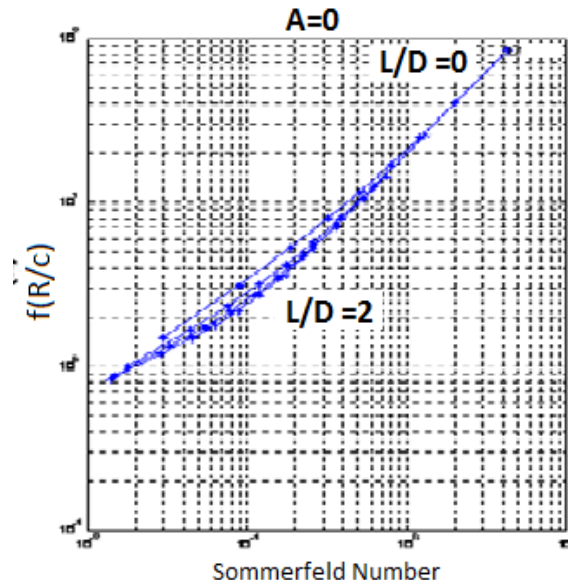


Fig. 9: Friction coefficient Vs Sommerfeld Number for various L/D ratio and $A = 0$

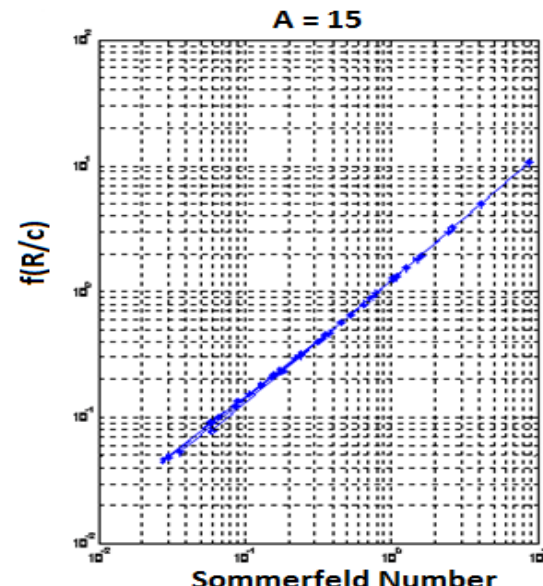


Fig. 10: Friction coefficient Vs Sommerfeld Number for various L/D ratio and $A = 15$

Fig. 11 shows the relationship between attitude angle and the slip co-efficient for

different values of L/D ratio. The eccentricity ratio is taken as $\epsilon=0.6$ and the

slip co-efficient is varied from A=0 to A=20. It is observed that there is an increase in the attitude angle from A=0 to A=2 after which it follows a decreasing trend from A=2 to A=12 and then it remains constant.

Also it is observed that the attitude angle is the lowest for a short bearing ($L/D=0.5$) and the value increases as L/D increases.

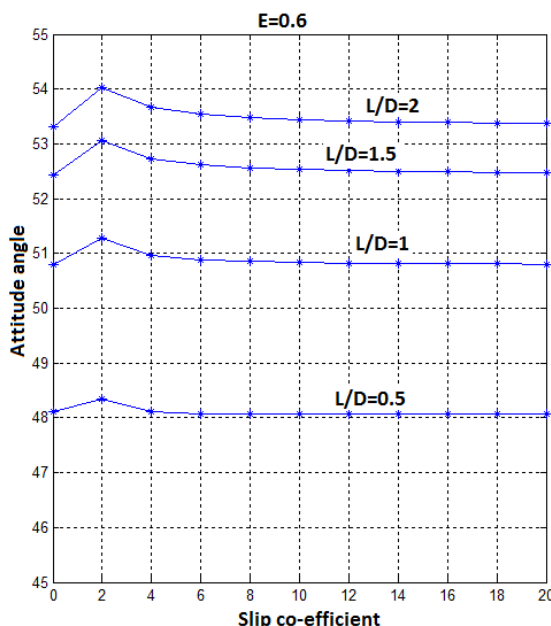


Fig. 11 Attitude angle Vs Slip co-efficient for different values of L/D ratio.

Conclusions

The performance of a hydrodynamic lubrication journal bearing with wall slip usually gives rise to a low friction drag, but also decreases the hydrodynamic pressure. If the bearing surface exhibits a perfect slip property, it was found that the fluid load support was only half of that without slip.

A journal bearing with a slip zone on the sleeve surface carries less load but has a low friction drag. The effect of the enhancement of such a slip wedge on the journal bearing performance is much greater at a small eccentricity ratio than at large eccentricity ratio. Under very low load and very smooth sliding microscale contact applications as those in microelectromechanical systems (MEMS) and hard disc drives.

Nomenclature

A = dimensionless slip co-efficient, α_w/c
c = clearance
D = bearing diameter
F = dimensionless friction force
f = friction coefficient
H = dimensionless film thickness, h/c
h = film thickness
p = pressure
R = bearing radius
S = Sommerfeld number
τ_x = dimensionless shear stress in the circumferential direction
u_s = shaft surface speed, ωR
u_x = x component of velocity
u_y = y component of velocity
W = dimensionless load carrying capacity
Y = dimensionless y coordinate
y = axial coordinate
z = cross-film or radial coordinate
α = slip coefficient
β = attitude angle
ϵ = eccentricity ratio
θ = circumferential coordinate
μ = viscosity
ω = angular speed

Acknowledgements

The authors would like to thank Manipal University for providing financial support to carry out this research.

References

- [1] Chengwei Wu (2008), "Performance of hydrodynamic lubrication journal bearing with a slippage surface", Industrial Lubrication and Technology, Vol. 60, No. 6, pp 293 - 298 Jackets, ACI Structural Journal, Vol.103, No.1, pp 28-37.
- [2] Fortier, A. E. and Salant, R. F. (2004), "Numerical Analysis of a slider bearing with a heterogeneous slip/no-slip surface," STLE Tribology Transactions, Vol. 47, pp 328 – 334.
- [3] H. A. Spikes (2003), "The half-wetted bearing. Part 1: Extended Reynolds equation," Proc. Of IMechE: Journal of Engineering Tribology, 217 J, pp 1 - 14.
- [4] H. A. Spikes (2003), "The half wetted bearing. Part 2: Potential application in Low load contacts," Proc. Of IMechE: Journal of Engineering Tribology, 217 J, pp 15 - 26.
- [5] Oscar Pinkus & Beno Sternlicht (1961), "Theory of Hydrodynamic Lubrication," McGraw-Hill Book Company.
- [6] Wu, C.W. and Ma, G.J. (2005), "Abnormal behaviour of a hydrodynamic lubrication journal bearing caused by wall slip", Tribology International, Vol. 38, pp 492 – 499.
- [7] Zhu, Y. And Granick, S (2002) Limits of hydrodynamic no - slip boundary condition. Phys. Rev. Lett., Vol. 88, pp 106102 1 – 4.

Single and Multilayer Polyvinylidene Fluoride Piezo Film for Force Sensing

Navin Karanth P, Vijay Desai and S M Kulkarni

Department Mechanical Engineering, National Institute of Technology Karnataka, Surathkal Srinivasanagar, Mangalore 575 025, Karnataka, India. email: navinkaranth@gmail.com

Abstract: In this study the response of a single and a multilayer polyvinylidene fluoride (PVDF) piezo film for force sensing is presented. Three configurations of the force sensor are proposed using PVDF film i.e as single layer and double layer with series and parallel connection. The three configuration of the force sensor is modeled using finite element method and are experimentally evaluated and compared. The response of the sensor is studied for a force variation of 1N to 10N applied by the shaker. The PVDF film force sensor exhibits high sensitivity and linearity. A good agreement is observed between the modeling predictions and the experimental findings. The response of the force sensor improved with double layer stacking. Double layer PVDF force sensor with parallel connection exhibited an improvement in response and resolution by 85% to 90%.

Keywords: Polyvinylidene fluoride (PVDF), multilayer stacking, force sensor

Introduction

The basic response of a mechanical system involves measurement of force like in machining process, automation and material handling. In these systems it is required to monitor the forces and control the system based on the response. Direct measurement of forces is useful in such control of the above mentioned mechanical systems.

Depending on the magnitude and variation in the force, different force sensors are used for sensing, Elbestawi M.A. (1999). When the magnitude of the force sensing is large combined with static or slowly varying force, load cells are used E. O. Doebelin, (1990). These are relatively accurate means of sensing force. The design of the load cell could be based on hydraulic or pneumatic principle. For measurement of small magnitude force with varying amplitudes a great variety of device designs, transduction methods are available. The main transduction methods include resistive, capacitive, conductive, optical, ultrasonic magnetoresistive, magnetoelastic and piezoelectric Mark (2000).

The magnitude of force, accuracy and sensitivity govern the type of sensor used. Strain gauges, capacitive and piezoresistive sensors are sensors which require a power source for the transduction effect and their resolution is small. The optical techniques have high resolution compared to other methods but are expensive and have narrow dynamic range Yantao Shen et al. (2004). The piezoelectric sensors are used for force sensing because the charge generated by a piezoelectric is almost linearly proportional to the force exerted on its surface. The piezoelectric materials such as quartz, tourmaline, Rochelle salt, ammonium dihydrogen phosphate (ADP), lithium sulfate, barium titanate, and lead zirconate titanate (PZT) are being used for force sensing since long. Piezoelectric ceramics and crystals typically suffer from low fracture toughness B. K. Atkinson (1979) and W.S Oates et.al. (2004) where as polymer family on the other hand exhibits much less mechanical problems, as the polymer is much more ductile than any ceramic system Y. Wang (2007). Piezoelectric polymer polyvinylidene fluoride has low modulus, high sensitivity, low quality factor, high electromechanical coupling coefficient and compliance and also

exhibits ease of use Barsky et al. (1989) which are ideal requirements of a material for force sensing.

In this paper the response of a single layer PVDF film force sensor is modeled in finite element analysis and compared with experimental measurement. Further an attempt is made to improve the response of the sensor by considering stacking of the PVDF film. Two numbers of PVDF film are stacked to make a double layer force sensor. Two configurations of the double layer force sensor are considered i.e series and parallel connection. The finite element analysis of both the configurations of the double layer force sensor is accomplished and the voltage response of the double layer force sensor is compared with experimental findings.

Sensor

The cross section of the proposed single layer force sensor (SLFS) using PVDF is shown in Fig. 1. The sensor consists of commercially available PVDF film supplied by M/s Measurement Specialties Inc, Hampton, VA. In the sensor the PVDF film is rectangular shaped of size 12mm by 30mm and thickness 28- μ m. The film is screen-printed with silver electrode for lead connections. In order to shield the film it is covered with a polyester film layer on both sides. A pair of leads is drawn out for response of the film as shown in the Fig. 1.

In the double layer force sensor (DLFS) two single layer force sensor are stacked in series and parallel connections. Fig. 2 shows the schematic representation of proposed three configurations of the sensor for force measurement. The finite element modeling of the proposed sensor configurations is explained in ensuing section.

Modeling of the Sensor

Sensor configurations shown in Fig. 2 are modeled using a commercial finite element modeling (FEM) software package ANSYS® version 10.0. The details of the elements used for different materials and their properties used in the modeling the sensor are given in Table 1. The generated mesh of

the sensor is shown in Fig. 3. The force applied and boundary conditions for the FEA model are shown in Fig. 4. Analysis is performed with the force varying from 1N to 10N and the PVDF output voltage for single layer force sensor is determined. Further, to study the improvement in the response of the force sensor the modeling and analysis of the two configurations of the double layer force sensor are performed. The sensor response from the finite element model for all three configurations is compared with the experimental measurement and presented in the later section.

Experimental setup

An experimental setup is developed to investigate the performance of the PVDF force sensor. Fig. 5 shows the block diagram of the experimental setup while Fig. 6 shows the photograph of the setup. A sinusoidal force at a frequency of 10Hz is applied to the single layer PVDF force sensor by a brass probe using a electrodynamic shaker (V203, PA25E-CE, Ling Dynamic Systems). The shaker is actuated using a function generator NI 5412 and a power amplifier (Techron 5507). The excitation force is monitored by a force transducer (Kistler 9712B50) placed between shaker and probe. The amplitude of the shaker is adjusted such that the force recorded from the transducer varies between 1N to 10N. It is taken care to ensure that load is applied uniformly on the force sensor by inserting a slip gauge between the probe and the sensor. The output response generated by the PVDF force sensor is directed to the charger amplifier (M68D3). To record and analyse the output of the PVDF force sensor and the force transducer a data acquisition system, NI PXI-4496 on PXI 1031 chassis operated by LabVIEW® software (Version 8.6) is used. Peak output voltage from both PVDF films and the force transducer are recorded. The experiments are repeated for double layer force sensor with series and parallel connection configurations as mentioned earlier (Fig.2). Results obtained from finite element analysis and experiment are compared in the following section.

Results and Discussion

The response of the proposed PVDF force sensors are studied using finite element analysis and measured experimentally. Fig. 7 shows the response of single layer PVDF force sensor determined by FEM and experiment. The linear variation of the sensor output for corresponding force is demonstrated. It can be observed that the experimental results are comparable with the finite element predictions for the single layer force sensor. The variation in the response between the experiment and FEM prediction is around 6 to 8%. The results obtained are in line with similar work done on single layer by Dargahi et. al. (2004). To improve the response and resolution of the force sensor, double layer configurations are considered. Fig. 8 shows the FEM and experimental results for the response of the double layer PVDF force sensor with series connection. The linearity of the sensor response is maintained with a small improvement in the response, as observed from the graph. The response of the force sensor further improved with double layer PVDF force sensor with parallel connection as shown in Fig. 9. Comparison of experimental results for three configurations of the sensor is shown in Fig. 10. In this figure it can be clearly ascertained that double layer PVDF force sensor with parallel connection is a better configuration compared to others. The improvement of the response and resolution is about 85 to 90% compared to single layer PVDF force sensor.

Conclusion

In this paper, three configuration of the PVDF force sensor is studied. ANSYS® modeling of single layer and double layer force sensor with series and parallel connection is analysed and verified experimentally. It is observed that FEM predictions and experiment results match with a variation of 6 to 8%. Linearity in the response of the single layer PVDF force

sensor is observed and the response is improved by 85 to 90% with double layer PVDF force sensor with parallel connection.

References

- [1] Barsky, M. F., D. K. Lindner and R.O. Claus, (1989), Robot gripper control system using PVDF Piezoelectric Sensors, IEEE Transactions on ultrasonics, ferroelectrics and frequency control, Vol. 36. No.1 P.129-134.
- [2] B.K. Atkinson, (1979) A fracture mechanics study of subcritical tensile cracking of quartz in wet environments, Pure Appl. Geophys. 117 1011-1024.
- [3] Elbestawi M.A. et.al, (1999), Measurement, Instrumentation, and Sensors, Handbook CRCnetBASE.
- [4] E. O. Doebelin, (1990) Measurement Systems, Application and Design, 4th ed., New York: McGraw-Hill.
- [5] Javad Dargahi and Siamak Najarian, (2004), Theoretical and experimental analysis of a piezoelectric tactile sensor for use in endoscopic surgery, Sensor Review, 24, 1, pg 74-83
- [6] Mark H. Lee, (2000), The International Journal of Robotic research, Vol. 19, No.7, pp. 636-643.
- [7] W.S Oates, C.S. Lynch, D.C. Lupascu, A.B. Kounga Njiwa, E. Aulbach, J. Rödel, (2004), Subcritical crack growth in lead zirconate titanate, J. Am. Ceram. Soc. 87 1362-1364.
- [8] Yantao Shen, Ning Xi, U.C. Wejinya and Wen J. Li, (2004), High sensitivity 2-D force sensor for assembly of surface MEMS devices, Proceedings of 2004 IEEE/RSJ International Conference on Intelligent Robots and Systems, Sept. 28- Oct. 2 2004, Sendai, Japan
- [9] Y. Wang, K. Ren, Q.M. (2007), Zhang, Direct piezoelectric response of piezopolymer polyvinylidene fluoride under high mechanical strain and stress, Appl. Phys. Lett. 91 222905.

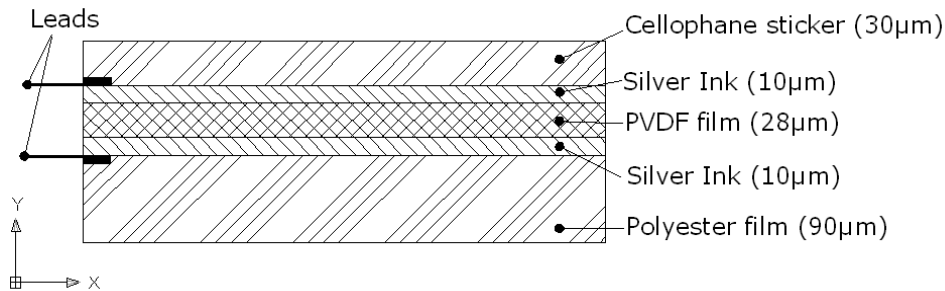


Fig. 1 Schematic cross section of the single layer PVDF force sensor

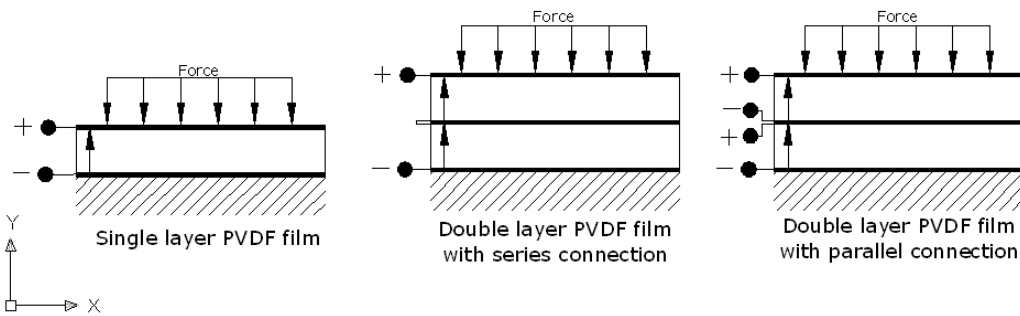


Fig.2 Schematic representation of three configuration of the proposed force sensor

Table 1 Elements for different material and their properties used in FE modeling

Material	Element type	Young's Modulus E GPa	Poisson's Ratio
Cellotape	Solid 95	1.5	0.36
Silver Ink	Solid 95	7.8	0.32
PVDF	Solid 226	2.0	0.29
Polyester	Solid 95	3.34	0.38

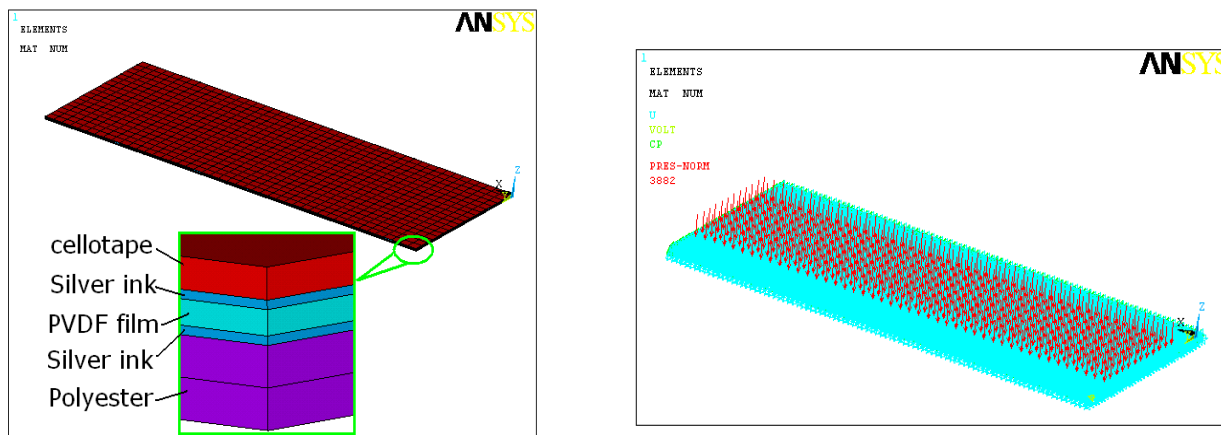


Fig. 3 Generated mesh of the sensor including all layers

Fig. 4 Force applied and boundary conditions

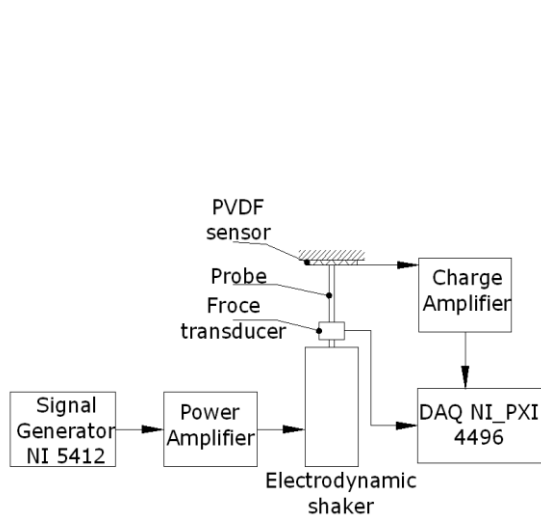


Fig.5 Block diagram of the experimental setup

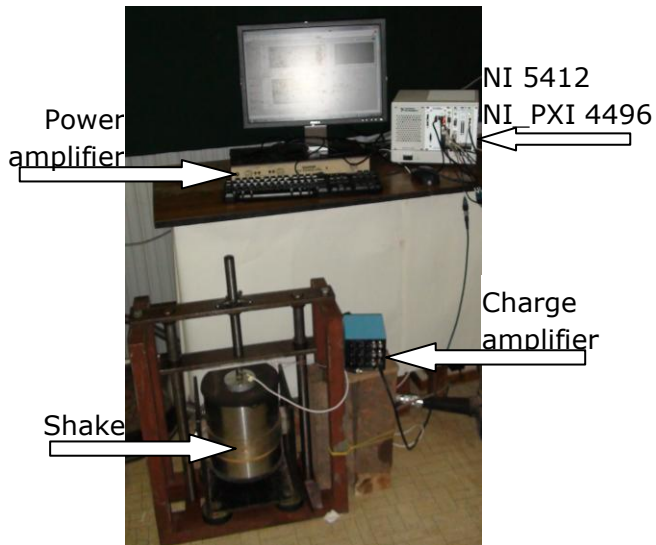


Fig.6 Photograph of the experimental setup

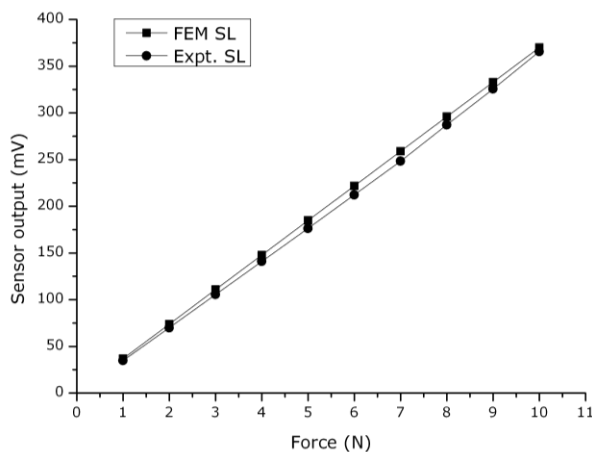


Fig. 7 FEM and experiment results for single layer PVDF force sensor

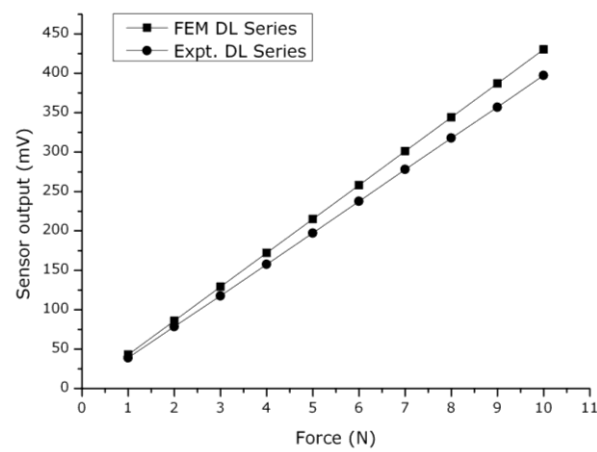


Fig. 8 FEM and experiment results for double layer PVDF force sensor with series connection

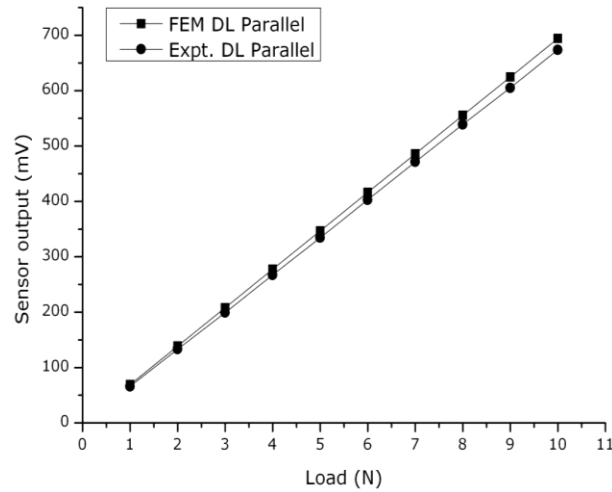


Fig. 9 FEM and experiment results for double layer PVDF force sensor with parallel connection

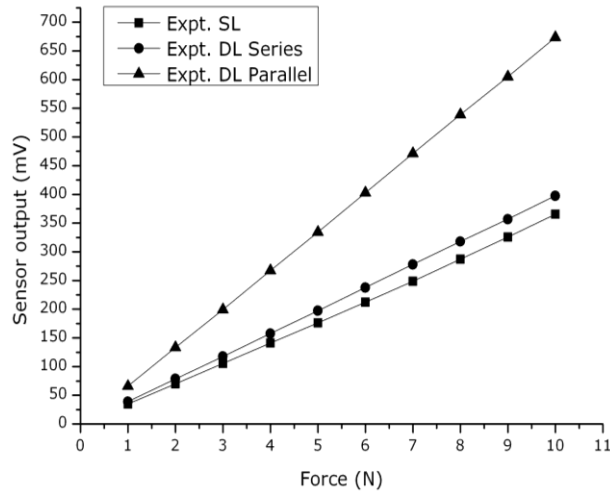


Fig. 10 Experiment results comparison for three configurations of the sensor

A comparative study of size effect on entropy generation in micro-channels

Shu-Min Tu¹

Shuichi Torii²

Yang-Cheng Shih³

1 Department of Mechanical System Engineering, Kumamoto University, Kurokami, 2-39-1, Kumamoto 860-8555, Japan. e-mail: 099d9211@st.kumamoto-u.ac.jp

2 Department of Mechanical System Engineering, Kumamoto University, Kurokami, 2-39-1, Kumamoto 860-8555, Japan. e-mail: torii@mech.kumamoto-u.ac.jp

3 Department of Energy and Refrigerating Air-Conditioning Engineering
National Taipei University of Technology, Taiwan. e-mail:f10958@ntut.edu.tw

Abstract: The analysis of entropy generation mechanism is utilized to optimize the second-law performance of these energy conversion devices in micro-scale. In micro-channel, the length-to-diameter ratio is considerably large, the effect of the viscous dissipation rise in fluid temperature due to the conversion of kinetic motion of the fluid to thermal energy is particular significance in fluid flow and heat transfer. The objective of the present study is to optimize heat transfer in X-shaped micro-channels via both first and second laws of thermodynamics. As the working fluid, water is injected to micro-channel at different mass flow rate. Over a wide range of flow condition, $1.06 < Re < 514$, have been discussed. Through the evaluations of the overall entropy generation in the whole flow domain, the results show that: (1) The entropy generation increased with increasing the mass flow rate and decreasing the channel diameter. It is clear that the size of the channel plays an important role in the X-shaped micro-channels.

Keywords: X-shaped micro-channels, entropy generation, mixing performance

Introduction

Fluid transport in micro-channels plays a vital role in a wide variety of micro-scale engineering applications such as micro-pumps, micro-valves, and micro-sensors. Especially the application of micro-channels in electronic cooling is becoming important due to the irreversibility and entropy generation during the thermal transporting process. In the past design work of thermal system, the efficient utilization of energy has been treated as an essential consideration except the analysis from the view point of thermodynamic first-law. Nowadays, the second-law of thermodynamic, irreversibility and entropy generation in the flow field have been adopted as a gauge for evaluating the optimization of thermal system. Entropy generation minimization is a method of modelling of real devices that owe their thermodynamic imperfection to heat transfer and velocity distribution. Entropy generation is associated with thermodynamic

irreversibility, which is present in all types of heat transfer processes. Therefore, it makes good engineering sense to focus on the irreversibility of heat transfer and fluid flow processes, and try to understand the function of entropy generation mechanism.

A number of investigations of the micro-channel mixer internal flow have been widely carried out before. To discuss the entropy generation method (EMG), Bejan [1-4], one of the first researchers to study the second-law on the optimal mechanism design, presented the second-law aspect of heat transfer using different examples of fundamental forced convection problems. He studies the thermodynamic optimization of geometry in engineering flow systems [1]. The paper illustrated by simple examples: the optimization of dimensions, spacing, and the distribution of heat transfer surface to the two heat exchangers of a power plant. The results show that, the entropy generation rate accounted for the irreversibility due to discharging the ram-air stream in to the atmosphere. The

optimized geometric features were relatively insensitive to this additional effect, emphasizing the robustness of the thermodynamic optimum.

The objective of the present study is to optimize heat transfer in X-shaped micro-channels via both first and second laws of thermodynamics. Fluid flow transport phenomenon in X-shaped micro-channels consists of converging, mixing and diverging flows. A 2-D modeling approach is adopted to examine the complex flow on the X-typed micro mixer. Our goal is to design a mixer by studying the effects of channel sizing. Since mixing in passive mixer occurs primarily by diffusion, reducing the entropy generation is generally beneficial for faster mixing.

Experimental methods

Numerical Simulation

The micro mixer designs were modelled and simulated by using the CFD FLUENT software (ANSYS, Inc.). To minimize effects of meshing on mixing, the mesh density was increased by grid-independent until (as show in Fig.1). Six different structured grid systems, wherein the number of grids ranges from 7190 to 57408, were tested for each micro-channel. Finally, from the results of the grid-independent test, 42536 were selected (relative error in velocity equal to 0.006%) as the optimal number of grids.

Mathematical Formulation

The analysis was carried out for a steady-state, continuum, incompressible, two-dimensional flow, no-slip boundary condition, laminar and a fully developed convection with constant fluid properties. According to Shohel M. and Roydon A. [7], the volumetric rate of entropy generation in Cartesian coordinates is:

$$S_G = \frac{k}{T_0^2} \left[\left(\frac{\partial T}{\partial x} \right)^2 + \left(\frac{\partial T}{\partial y} \right)^2 \right] + \frac{\mu}{T_0} \left[2 \left\{ \left(\frac{\partial u}{\partial x} \right)^2 + \left(\frac{\partial v}{\partial y} \right)^2 \right\} + \left(\frac{\partial u}{\partial y} + \frac{\partial v}{\partial x} \right)^2 \right] \quad (1)$$

The above form of entropy generation shows that the irreversibility is due to two effects, conductivity (k) and viscosity (μ).

Entropy generation rate (S_G) is positive and finite as long as temperature and

velocity gradients are present in the medium. Simplified assuming the flow is hydro-dynamically developed ($\partial v / \partial x = 0$) and thermally developing ($\partial T / \partial x \neq 0$) or developed ($\partial T / \partial x = 0$), references by Bejan [4] and White [8]. In such case Eq. (1) can be reduced into:

$$S_G = \frac{k}{T_0^2} \left[\left(\frac{\partial T}{\partial x} \right)^2 + \left(\frac{\partial T}{\partial y} \right)^2 \right] + \frac{\mu}{T_0} \left[\left(\frac{\partial u}{\partial y} \right)^2 \right] \quad (2)$$

The dimensionless form of entropy generation rate is termed as entropy generation number. Entropy generation rate (S_G) is the ratio between the volumetric entropy generation rate (S_{gen}''') and a characteristics transfer rate (S_0'''). The characteristics transfer rate for the present problem can be estimated from the following equation:

$$S_0''' = \frac{k(\Delta T)^2}{L^2 T_0^2} \quad (3)$$

In the above equation, L is the length of channel (m). Eq (2) can be simplified for the present problem in the following form:

$$\begin{aligned} N_s''' &= \frac{S_{gen}'''}{S_0'''} = \frac{1}{Pe^2} \left[\frac{\partial \Theta}{\partial X} \right]^2 + \left[\frac{\partial \Theta}{\partial Y} \right]^2 + \frac{Br}{\Omega} \left[\frac{\partial U}{\partial Y} \right]^2 \\ &= N_c + N_Y + N_F \end{aligned} \quad (4)$$

In the above equation, Pe is the Peclet number, which determines the relative importance between convection and diffusion. Br is the Brinkman number, which determines the relative importance between dissipation effects and fluid conduction effects. Ω is the dimensionless temperature difference, which is equal to $\Delta T / T_0$. On the right-hand side of Eq. (4), the first term (N_c) represents the entropy generation by heat transfer due to axial conduction, second term (N_Y) accounts for entropy generation due to the heat transfer in normal direction to the axis and the last term (N_F) is the fluid friction contribution to entropy generation. According to Bejan [4], the irreversibility distribution ratio (Φ) is equal to the ratio of entropy generation due to fluid friction (N_F) to heat transfer ($N_c + N_Y$). Heat transfer dominates over fluid friction irreversibility for $0 \leq \Phi < 1$ and fluid friction dominates when $\Phi > 1$. For $\Phi = 1$,

both the heat transfer and fluid friction have the same contribution for generating entropy. As an alternative irreversibility distribution parameter, Paoletti et. [9] define Bejan number (Be) which is the ratio of entropy generation to the total entropy generation. Mathematically Bejan number is:

$$Be = \frac{N_c + N_Y}{N_s} = \frac{1}{1 + \Phi} \quad (5)$$

Bejan number ranges from 0 to 1. Accordingly, $Be = 1$ is the limit at which the heat transfer irreversibility dominates, $Be = 0$ is the opposite limit at which the irreversibility is dominated by fluid friction effects, and $Be = 1/2$ is the case in which the heat transfer and fluid friction entropy generation rates are equal.

The governing equations include continuity, momentum, and energy equations, which obey the principle of conservation that can be expressed in the following general form,

$$\frac{\partial}{\partial t}(\rho\phi) + \nabla \cdot (\rho\vec{V}\phi - \Gamma_{\phi,\text{eff}} \nabla\phi) = S_\phi \quad (6)$$

ρ is the density, ϕ is the dependent variable, \vec{V} is the velocity vector, $\Gamma_{\phi,\text{eff}}$ is the effective diffusion coefficient, and S_ϕ is the source term. The diffusion-convection term of Eq. (6) is discretized by the second-order upwind scheme and the implicit method is used to discretize the transient term. After Eq. (6) is discretized, the general discretized equation can be written as (7),

$$a_p\phi_p = \sum a_{nb}\phi_{nb} + b \quad (7)$$

where a_p and a_{nb} are discretized coefficient, and b is the discretized source term. In Eq. (7), subscript p represents the grid point under consideration and nb indicates the neighbors of grid point p . By employing the iterative scheme of a point implicit (Gauss-Seidel) linear equation solver in conjunction with an algebraic multi-grid (AMG) method, the pressure and velocity, fields can be solved from Eq. (7). During the iterative procedure, the SIMPLEC (Semi-Implicit Method for Pressure - Linked Equations - Consistent) algorithm was employed to solve the pressure-velocity coupling equations. The boundary condition of both outlets pressure was set to be 0 Pa. The solutions are considered to

have attained the convergence when the value of the relative residual is at most 10^{-6} .

Apparatus Setup

The present study selected X-shaped channels having the different channel sizing ranging from 0.7 to 1.3 mm are shown in Fig. 2.

In Fig. 2, L is the mixing area equals to 40 mm, B is the total length of the X-shaped micro-channel equals to 80 mm, θ is the converging and diverging angle equals to 90° . The two inlets were driven at flow rates ranging from 0.00141 Kg/s ($Re = 1.321$) to 0.70522 Kg/s ($Re = 661.201$), The Reynolds number in (8) is valid for the common channel, whereas the X-shaped micro-channels have two inlet and both the inlet channels are characterized by half the Reynolds number.

$$Re = \frac{\rho v d}{\mu} \quad (8)$$

Two series of simulation were conducted: One supplied the same mass flow rate in both Inlet 1 and Inlet 2 but increasing it in each case (Case 1, Case 2, Case 4 and Case 7), and the other supplied the different mass flow rate to Inlet 1 and Inlet 2 (Case 3, Case 5 and Case 6) for understanding the mixing preference (As Tab.2).

Results and Discussion

The simulation results of the entropy generation in each case are shown in Fig. 3 (a) and (b) (EG_h and EG_f represent the entropy generation caused by heat transfer and fluid friction). In Fig.3 (a), the EG_h increased with the increasing mass flow rate and decreasing the channel diameter. In Case 4, 6, and 7, it is obviously, channel size 0.7, 0.8, and 0.9 mm are the top three within all experiments, for the others, the EG_h are all almost the same, therefore the sizing effect is an important effect to the entropy generation. In Case 5, the inlet 1 is fifty times over than inlet 2, in this condition, the mixing efficiency gets worse. Hence the entropy generation in this case is smaller than Case 3 and 4. In Fig.3 (b), at the term of EG_f , the entropy generation increased with the increasing total mass flow rate. After increasing the mass flow rate to 0.36 Kg/s (Case 5), we can easily

understand the difference among all the designs.

Fig. 4 represents the relationship between pressure drop to Reynolds number and Fig. 5 represents the velocity to mass flow rate of Inlet 1 in case1, 2, 4 and 7. As Shakhawat Hossain [8] declared that at a very low Reynolds number, micro mixers can be classified into two categories: active and passive. Active micro mixers use additional structures or external sources to stir the fluids. Passive micro mixers do not require external energy: the mixing process relies entirely on molecular diffusion. Therefore, in this case, it was the biggest channel size that had the slowest flow velocity and got the best performance of mixture requiring the shortest distance in the mixing area.

In case 4, with higher mass flow rate in both inlets, the entropy generation increases remarkably. As shown in Fig. 6, EG_h occurs highly in the entire mixing area. By the results of temperature distribute, in this case, all the models cannot mix to the average temperature (Fig.7), the mixing mechanism becomes dominated by convection rather than diffusion.

In case 5, by supplying different mass flow rates to Inlet 1 (0.007 Kg/s) and Inlet 2 (0.352 Kg/s), as shown in Fig.8. With channel size = 0.7 mm (Fig. 8 (a)), there is a vortex formed in the converging area, the mass flow rate in Inlet 2 is 50 times than Inlet 1, caused the mix overflow in the end of the Inlet 1, the Inlet 1 is almost blocked by Inlet 2. With channel size = 1.3 mm (Fig. 8 (b)), though the Reynolds number are almost the same, the pressure drop in 0.7 mm (302.8 Pascal) is 6 time lower than 1.3mm (50.7 Pascal), hence the Inlet 1 can pass through to the mixing area. For the all experiments data as show in Fig.9, the entropy generation decreases with the increasing in channel size. Only in channel size = 0.7 mm, there is a vortex formed in the end of Inlet 1, so the EG_h is rather higher than the others.

In case 6, (Inlet 1 = 0.070 Kg/s and Inlet 2 = 0.352 Kg/s) with higher mass flow rate input in this case, the transition form early from laminar to turbulent flow in channel size 0.7 mm. Many investigations had focused on the early transition form in micro-channels. Mehendale et al. [9] noted that for the early transition form laminar to turbulent

flow in micro-scale tubes, the properties of the liquid change markedly as the fluid flows along the channel so that Reynolds number at the channel exit could be twice that at the inlet. Therefore, the early transition to turbulence might be partially attributed to the variation in Reynolds number. With supplying different mass flow rate in case 3, 5 and 6, by increasing channel size, the pressure difference between Inlet 1 and Inlet 2 get lower, (as shown in Fig.10) consequently, in case 6, the smaller channel size acquires better performance of mixture. However, in case 5, the pressure difference between Inlet 1 and Inlet 2 is higher than case 6, but the difference is the mass flow rate, it is too high, Inlet 1 is blocked by Inlet 2 resulting in a bad mixing preference.

In case 7, with channel size 0.7 mm, the flow is unsteady (Fig. 11). On micro channel, in order to let the fluid passes through the channel more fluently, the entrance has to add more pressure to resist the friction of the wall. With the greater aspect ratio, greater velocity gradient, and greater shear stress, the effect of the pressure becomes more conspicuously. Therefore, the instability occurs when low pressure drops and high velocity inlet in model 1, acquires the best mixing performance.

In this paper, all kind of channel sizes have the irreversibility distribution ratio approximate to 0 and Bejan number approximate to 1, represented the $EG_h \gg EG_f$ (the entropy generation cause by heat transfer irreversibility is much larger than that of the fluid friction irreversibility). Moreover, in case 5, the differences of the mass flow rate input in inlet 1 and inlet 2 is too high, hence the worst coordinated, rather higher irreversibility distribution ratio, and lower Bejan number.

Conclusions

The developing convection and entropy generation in different channel size are investigated in this paper with numerical method. The studied Reynolds number is ranging from 1.06 to 514, mass flow rate ranging from 0.0014 to 0.7 kg/s. Several important conclusions are as follows: (1) The EG_h increased with increasing the mass flow rate and decreasing the channel diameter. (2) In case 7, the unsteady flow occurs during low pressure drops and high

velocity in channel size 0.7 mm, hence the best mixing performance. (3) In this paper, all kind of channel sizes have the irreversibility distribution ratio approximate to 0 and Bejan number approximate to 1, represented the $EG_h >> EG_f$. (4) There is no difference in changing the channel geometry in heat transfer, the effect factor of the mixing preference only depends on the mass flow rate. These results are the important first step in the quest to devise methods for the production of better micro mixer design and the reduction of entropy generation in order to enhance the thermodynamic efficiency of thermal systems. Further studies should be conducted on the PIV (Particle Image Velocimetry) measurement to compare with the simulation results.

References

- [1] A. Bejan, Entropy Generation Minimization, CRC Press, Boca Raton, 1995.
- [2] A. Bejan, Entropy Generation Through Heat and Fluid Flow, Wiley, New York, 1982.
- [3] A. Bejan, A Study of Entropy Generation in Fundamental Convective Heat Transfer, ASME J. Heat Transfer 101 (1979) 718-725
- [4] A. Bejan, Method of Entropy Generation minimization, or Modeling and Optimization based on Combined Heat Transfer and Thermodynamics, Rev Cen Therm (1996) 35, 637-646
- [5] J.Koo, C. Kleinstreuer, Viscous Dissipation Effects in Microtubes and Microchannels, Heat and Mass Transfer 47 (2004) 3159-3169
- [6] Ridha Ben Mansour, Nicolas Galanis, and Cong Tam Ngyyen, Dissipation and Entropy Generation in Fully Developed Forced and Mixed Laminar Convection, Thermal Sciences, 45 (2006) 998-1007
- [7] Shohel Mahmud and Roydon Andrew Fraser, Flow, Thermal, and Entropy Generation Characteristics Inside a Porous Channel with Viscous Dissipation, Thermal Sciences 44 (2005) 21-32
- [8] Guillermo Ibanez, Sergio Cuevas, Mariano Lopez de Haro, Minimization of Entropy Generation by Asymmetric Convective Cooling, Heat and Mass Transfer 46 (2003) 1321-1328
- [9] S. Sugiyama, K. Shimaoka, and O. Tabata, Surface Micromachined Micro-Diaphragm Pressure Sensors, in Proc. 6th Int. Conf. Solid-State Sensors and Actuators (Transducer'91), pp.188-191, 1991.
- [10] Mehendale, S.S., Jacobi, A.M., Shah, R.K., Heat Exchangers at Micro- and Meso-scales. In: Proceedings of the International Conference on Compact Heat Exchangers and Enhanced Technology for the Process Industries, Banff, Canada, 1999. pp. 55-74

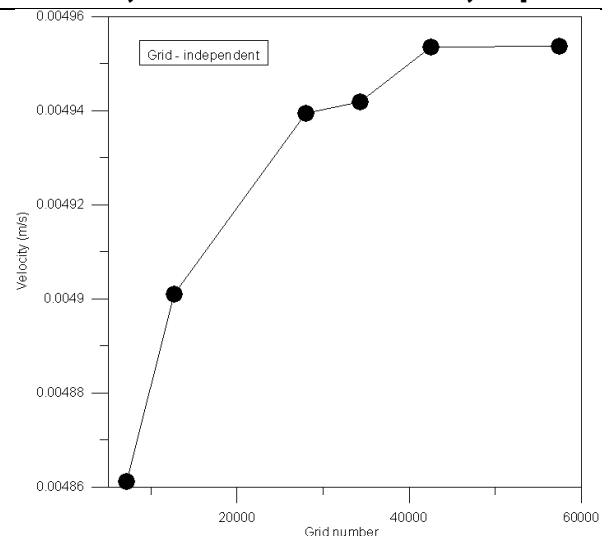


Fig 1. Grid-independent until

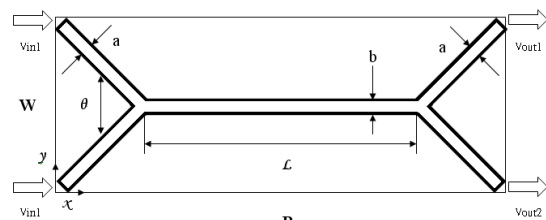
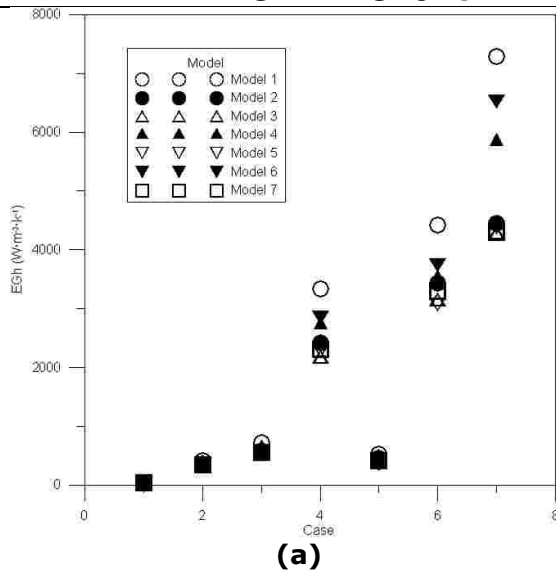


Fig 2. X-shaped micro-channels

Table 1. Mass flow rate in each case (Kg/s)

	Inlet 1	Inlet 2	Total
Case 1	0.000705	0.000705	0.001410
Case 2	0.007052	0.007052	0.014104
Case 3	0.007052	0.070522	0.077575
Case 4	0.070522	0.070522	0.141045
Case 5	0.007052	0.352614	0.359666
Case 6	0.070522	0.352614	0.423137
Case 7	0.352614	0.352614	0.705228



(a)

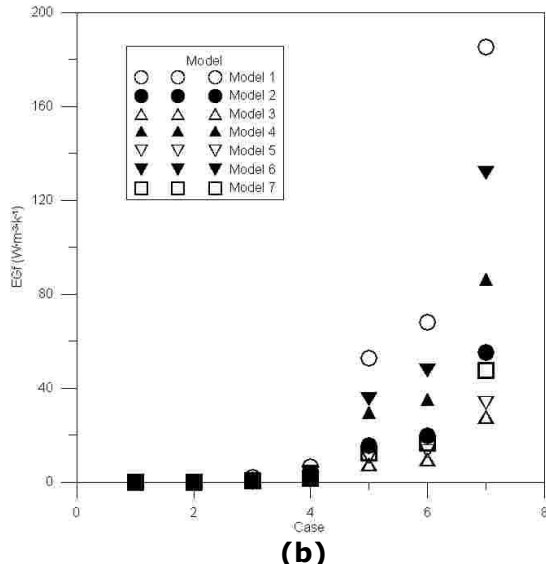


Fig 3. Entropy generation in each case

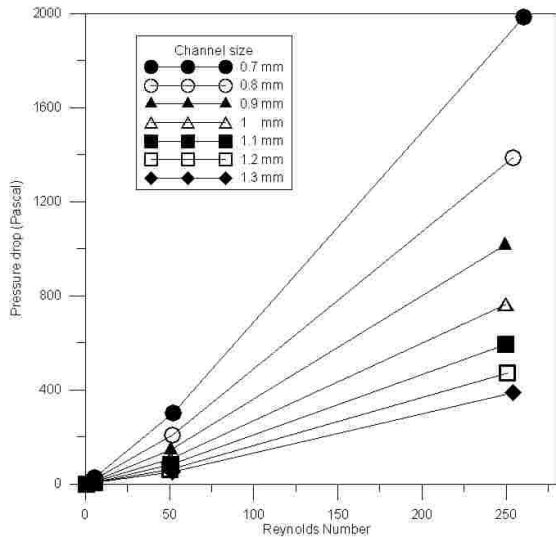


Fig 4. Reynolds Number to Pressure drop

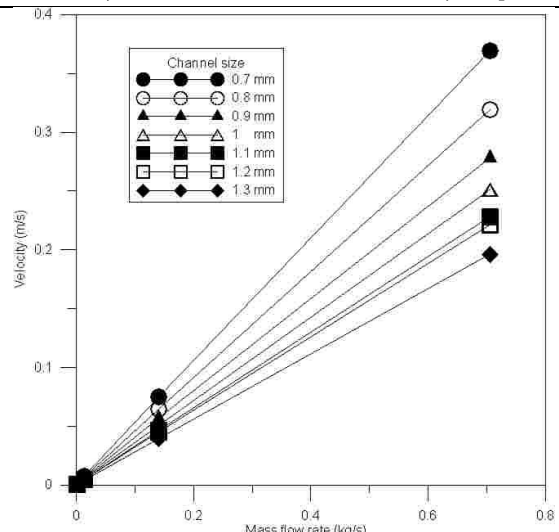
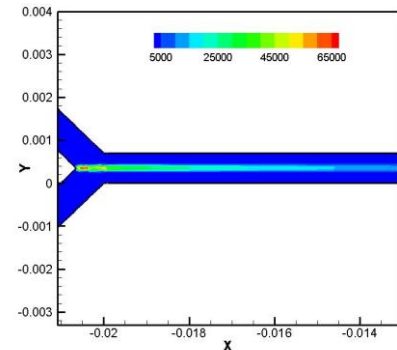


Fig 5. Velocity to mass flow rate



(a)

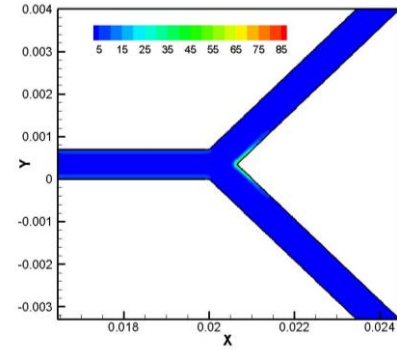


Fig 6. Entropy generation in Case 4 0.7 mm

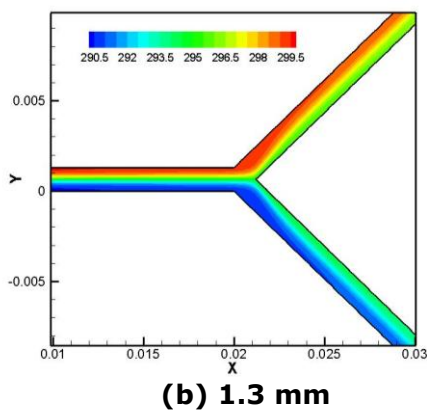
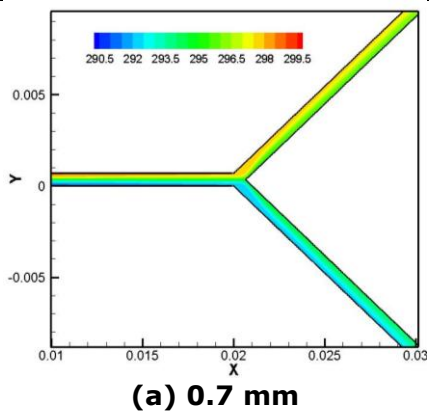


Fig 7. Heat transfer Case 4

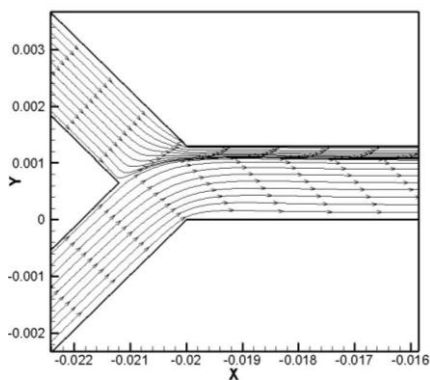
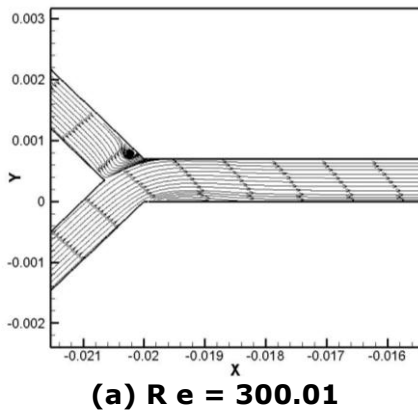


Fig 8. The mixing preference in case 5

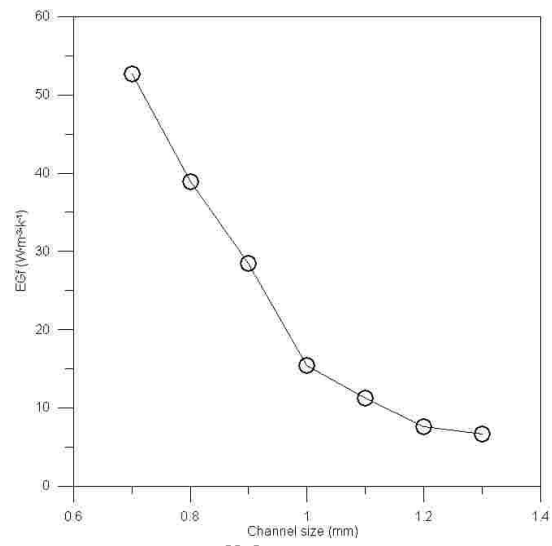
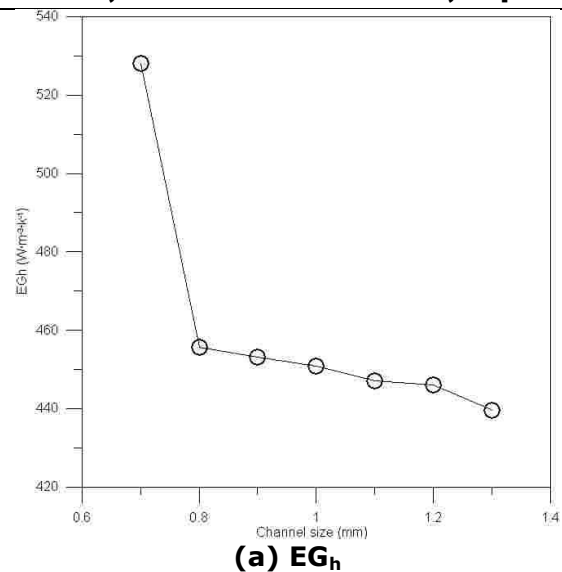


Fig 9. Entropy generation in case 4

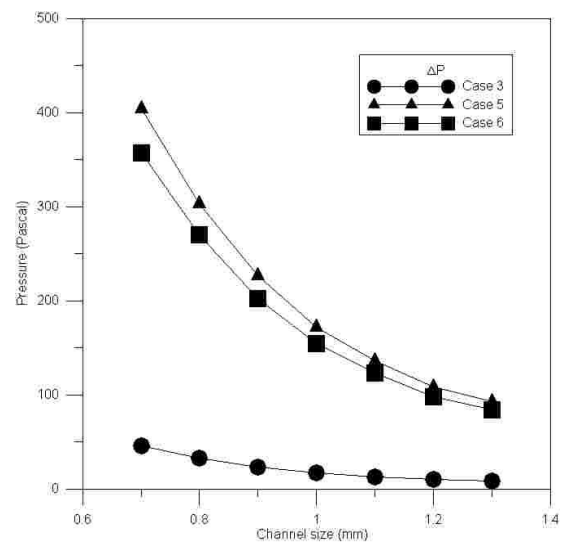
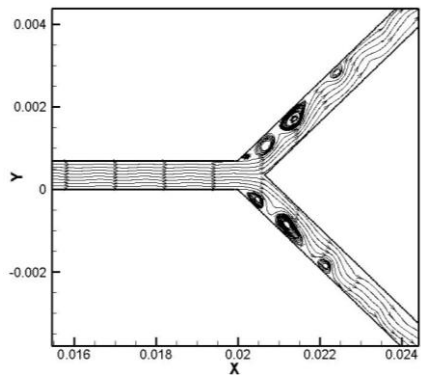
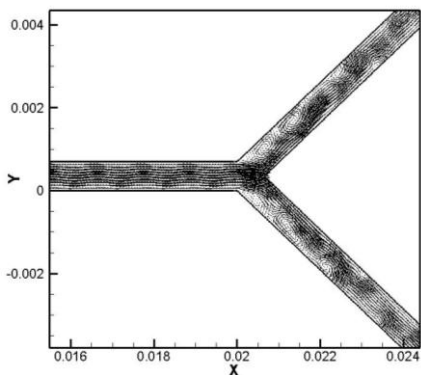


Fig 10. Pressure difference between inlet1 and inlet2



(a) Stream line



(b) Velocity contour

Fig 11. Flow pattern in model 1

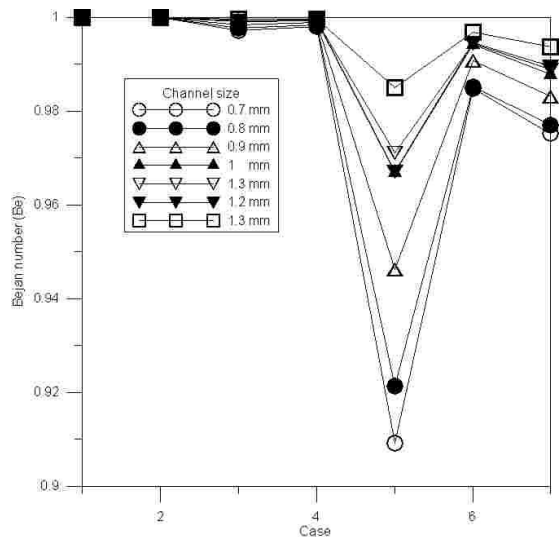


Fig 12. Bejan number

Effect of B_2O_3 addition on the mechanical property of Mg-RE alloy

Takeyuki Yagi¹, Sayuri Yoshimoto², Hiromoto Kitahara³ and Shinji Ando³

- 1 Faculty of Engineering, Kumamoto University, Kurokami, 2-39-1, Kumamoto 860-8555, Japan. e-mail:71t2742@st.kumamoto-u.co.jp
 - 2 Faculty of Engineering, Kumamoto University, Kurokami, 2-39-1, Kumamoto 860-8555, Japan. (Present Address : Nihon Light Metal Co. Ltd.)
 - 3 Department of Materials Science and Engineering, Kumamoto University, Kurokami, 2-39-1, Kumamoto 860-8555, Japan. e-mail:shinji@msre.kumamoto-u.co.jp
-

Abstract: In recent years, to reduce energy consumption of automotive, research and development of magnesium alloys have been greatly. However, applications of magnesium alloys are limited because of poor mechanical properties at higher temperatures. For development of high strength magnesium alloys, a combination method of melt stirring and in-situ synthesizes of reinforcement have been developed. In this study, B_2O_3 powder was added into Mg-RE (rare earth metal) alloy melts and stirred in 20 minutes with argon atmosphere. Grain sizes of Mg-RE alloy were decreased by B_2O_3 addition. This result shows that B_2O_3 have good grain refinement effects to magnesium alloys. However, micro-Vickers hardness of Mg-RE alloy did not improved by B_2O_3 addition. To improve the microstructure of the alloy, hot extrusion at 473K was applied. After the extrusion, tensile strength of the Mg-RE- B_2O_3 alloy was increased more than Mg-RE alloy.

Keywords: *Mg-RE, Rare earth, boride, tensile strength, microstructure refinement, extrusion*

Introduction

In recent years, to reduce energy consumption of automotive, research and development of magnesium alloys have been greatly promoted. Generally, applications of magnesium alloys are limited because of poor mechanical properties at higher temperatures. To improve high temperature properties of magnesium alloys, Mg-RE (rare earths) alloys have been investigated by Lü et al. (2000). On the other hand, magnesium matrix composites are also investigated. For example, Mg_2Si / Mg composite alloys were developed by hot forging of magnesium and SiO_2 powders compact (Du et al. (2003), Muramatsu et al. (2003)) and by hot extrude of AZ31 and Si powders compact (Tsuzuki et al. (2003)). In these methods, reinforce particles, Mg_2Si , have been in-situ solid-state synthesized from the mixed Mg and Si powders. Lu et al. (2002) reported that Mg-Al alloys with Ti_3B_4 and MgB_2 as reinforcements were developed by mechanical alloying method. In these

solid-state synthesizes, reinforce particles can be produced from cheap materials, however processing cost is high. Casting process is the conventional method for production of alloy matrix composites because of easy treatment and high cost performance. Sasaki et al. (2003) have tried to develop $Al_{18}B_4O_{33}$ whisker / Mg composite by compo-casting method.

In this study, a combination method of in-situ synthesizes of reinforcement and compo-casting method have been developed to produce high performance magnesium alloys with low cost. As reinforcement material, B_2O_3 powder was employed. Melting point of B_2O_3 is 723K and it can reduce to boron in molten magnesium. Therefore, it is expected that intermetallic compounds, namely boride, as reinforcement would be synthesized from the reduced boron and magnesium or other alloy elements. In this paper, alloying effect of B_2O_3 for microstructures and mechanical properties of Mg-RE was investigated.

Experimental method

Pure Mg (99.9%), RE ingot (mish-metal, 51.76%Ce, 26.05%La, 17.23%Nd, 4.89%Pr) and B_2O_3 powder (particle size is 200 μm to 400 μm) were employed. Figure 1 shows the experimental equipment used in this study. Considering reactivity of molten magnesium, a mild steel crucible and stainless steel shaft and stirring blade were used. To avoid oxidation on surface of melt with air, argon gas was poured inside furnace. Magnesium and RE ingots were put into the crucible, and they heated to 1013K. After melting the ingots, B_2O_3 powder was added into the molten metal and stirred in 20 min. The molten metal was cast into a metal mold after the stirring process.

Microstructures of the specimens were observed by optical microscopy and scanning electron microscopy (SEM). Mechanical properties of specimen were evaluated by micro-Vickers hardness and tensile test.

Results and discussion

Figure 2 shows microstructures of as cast Mg-6RE and Mg-6RE-xB₂O₃ alloys. Microstructure of Mg-6RE system became fine by B₂O₃ addition. Figure 3 shows relationship between B₂O₃ contents and dendrite arm spacing (DAS). As shown in the figure, DAS decreased with increasing B₂O₃ addition. DAS of Mg-6RE-6 B₂O₃ was a half of the Mg-6RE without B₂O₃. This result indicates that B₂O₃ has high potential to refine microstructure.

To investigate effect of B₂O₃ on Mg-6RE alloy, amount of area fraction of intermetallic compound vs content of B₂O₃ was measured and the result is shown in Fig. 4. The fraction of compound increased by applying B₂O₃, and the value of Mg-6RE-6B₂O₃ was about three times as much as Mg-6RE. This result indicates that applied B₂O₃ powder would form some kind of compound such as boride.

Figure 5 shows results of XRD analysis of Mg-6RE and Mg-6RE-6B₂O₃ alloys. While Mg₁₂RE type intermetallic compound was formed in both alloys, peaks of REB₄ and REB₆ could be confirmed in Fig. 5(b). As expected, borides of RE were formed in Mg-RE alloy by addition of B₂O₃.

Micro-Vickers hardness of as cast sample is shown in Fig. 6. The hardness of Mg-6RE was slightly increased by B₂O₃

addition in spite of increasing compounds and decreasing DAS. To improve mechanical property of Mg-RE-B₂O₃ alloy, extrusion process was attempted to apply.

Figure 7 shows microstructures of as extruded Mg-RE alloys. Extrusion temperature was 473K and extrusion ratio R was 10. Independent to content of B₂O₃, microstructures of all samples became finer than as cast, showed in Fig. 2. DAS of as extrusion were also showed in Fig. 3. DAS was decreased by extrusion, however, the difference of DAS between Mg-RE and Mg-RE-B₂O₃ was very small. As showed in Fig. 4, amount of compound after extrusion was also increased to about 30%. The hardness also increased by extrusion, as showed in Fig. 5, however, the increment of Mg-RE-B₂O₃ is larger than that of Mg-RE. Reason of the increment would be a formation of borides in Mg-RE-B₂O₃.

Tensile test specimens with 3mm in diameter and 15mm in gage length were machined from the as extruded Mg-6RE and Mg-6RE-3B₂O₃ alloys. Tensile test was carried at room temperature and cross-head speed of 1mm/min. Obtained tensile properties were plotted in Fig. 8. 0.2% proof strength and tensile strength of extruded Mg-6RE-3B₂O₃ alloy was about 280MPa and 320MPa, respectively. From this result, we can conclude that B₂O₃ addition is effective process for improving mechanical properties of Mg-RE alloy.

Conclusions

To develop high performance magnesium alloy, a combination method of in-situ synthesizes of reinforcement and compo-casting method with Mg-6RE and B₂O₃ powders. Microstructure and mechanical properties of the Mg-RE-B₂O₃ alloy were investigated. The results are summarized below.

- The microstructure became fine and the DAS was decreased by addition of B₂O₃ in as cast sample.
- The amount of compound increased with increasing content of B₂O₃.
- REB₄ and REB₆ type borides were formed by addition of B₂O₃.
- The 0.2% proof stress and tensile strength of extruded Mg-6RE alloy improved by addition of 3%B₂O₃.

References

- [1] Du, W. et al. (2003), In-situ solid-state synthesis of Mg₂Si/MgO/Mg composites, Materials Science Forum Vols.419-422, pp.783-788.
- [2] Lu, L. et. al. (2002), Structure and properties of Mg-Al-Ti-B alloys synthesized via mechanical alloying, Materials Science and Engineering, A334, pp.163-172.
- [3] Lü, Y et al. (2000), Effects of rare earths on the microstructure, propeties and fracture behavior of Mg-Al alloys, Materials Science and Engineering A278, pp.66-76.
- [4] Muramatsu, H. et al. (2003), Tribological property of Mg composites via powder metallurgy process, Materials Science Forum Vols.419-422, pp.801-804.
- [5] SASAKI, G. et al. (2003), Mechanical properties and microstructure of Al₁₈B₄O₃₃/Magnesium Alloy composites prepared by compo-casting, Materials Science Forum Vols.419-422, pp.777-782.
- [6] Tsuzuki, R. (2003), Effect of extrusion conditions on properties of hot extruded Mg composite with Mg₂Si dispersions via solid-stare synthesis, Materials Science Forum Vols.419-422, pp.789-794.

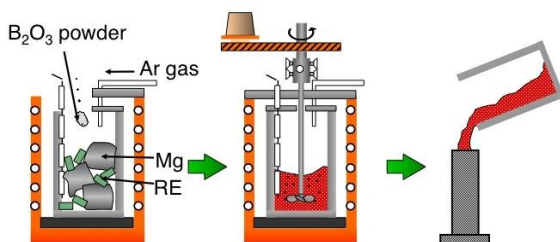


Fig.1 Specimen preparation method.

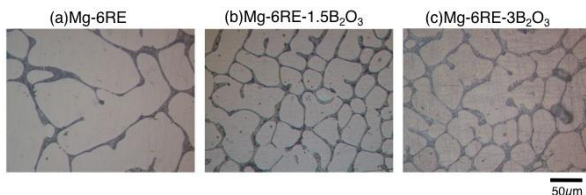


Fig. 2 Optical microphotographs of cast (a) Mg-6RE, (b) Mg-6RE-1.5B₂O₃ and (c) Mg-6RE-3B₂O₃.

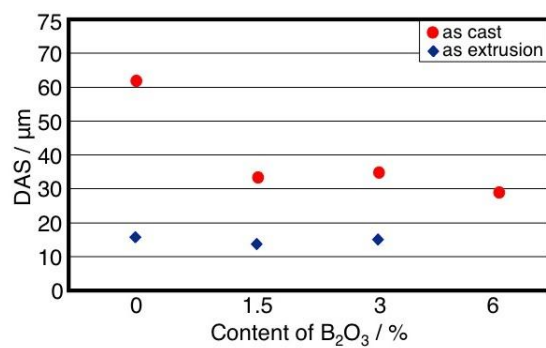


Fig.3 Relationship between dendrite arm spacing (DAS) and content of B₂O₃.

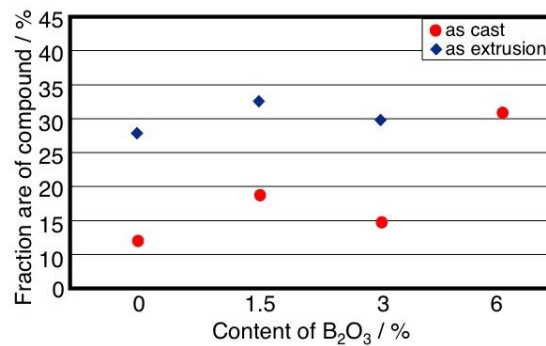


Fig.4 Relationship between amount of compound and content of B₂O₃.

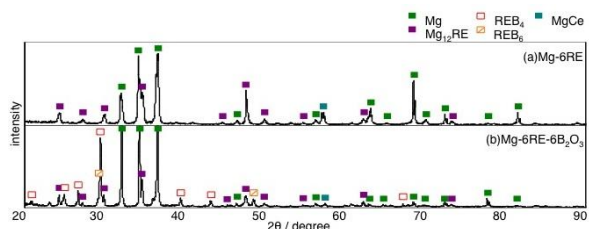


Fig.5 XRD patterns of cast (a)Mg-6RE, (b)Mg-6RE-6B₂O₃ .

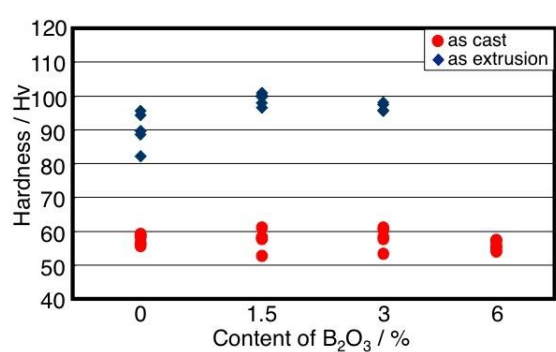


Fig. 6 Relationship between micro-Vickers hardness and content of B₂O₃.

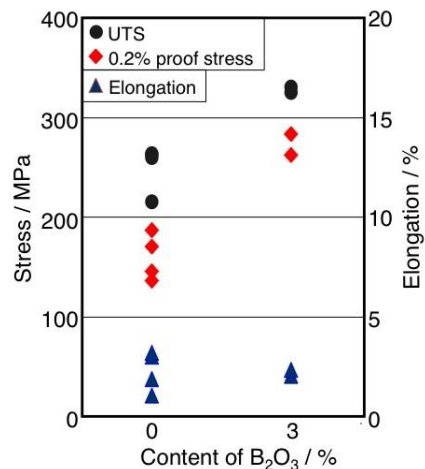


Fig.8 Relationship between tensile properties and content of B₂O₃ as extruded samples.

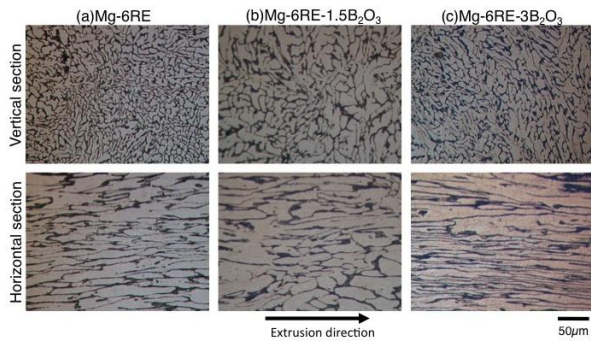


Fig. 7 Optical microphotographs of as extruded samples

Vibration and Cylinder Chamber Pressure Characteristics of a Reciprocating Compressor: Effects of a Change on a Discharge Valve Seat Profile

BAMBANG DARYANTO WONOYUDO¹ and ARDI NUGROHO²

1 Department of Mechanical Engineering, Institut Teknologi Sepuluh Nopember (ITS), Surabaya 60111, Indonesia. e-mail: bambang@me.its.ac.id

2 PT. PJB-PLN (State Electric Company), Surabaya 60231, Indonesia. e-mail: ardi_nugroho@ptpj.com

Abstract: Failures that happen on a reciprocating compressor can be minimized by having a proper valve design. In this paper a single-stage, single-acting air compressor performance is analyzed based upon its vibration signals and cylinder pressure diagrams. The performance is investigated due to a change in valve design, where the change is materialized by modifying a geometric profile of a discharge valve seat. Experimental results show that reducing flow area of a discharge port will increase a pressure for opening a discharge valve, increase valve losses, and increase an overall vibration level. Adding a chamfer on a discharge seat profile will not affect a pressure diagram, but yields a better overall vibration level. While an increase of a working load causes a longer time to reach a pressure to open the valve.

Keywords: reciprocating compressor, valve seat, vibration, cylinder pressure

Introduction

Reciprocating compressors are amply utilized in industries for many applications, either as auxiliary equipment or as main units. Therefore it is in the best interest that reciprocating compressors are in good conditions and reliable. One of the methods to sustain a good operating condition of a compressor is to monitor the resulted vibration and the ensuing performance.

In industrial applications failures on reciprocating compressors are often caused by valve malfunction. Hence, a compressor valve has become a subject of many investigations or studies: experimentally or analytically, research or trouble shooting, theoretically or practically. A proper design of a valve would increase its useful life and brought dependable compressor performance (Woollatt, 2003). An increase in compressor reliability due to valve and piston designs on an oil, gas and petro-chemical industry was shown

by Wilson (2007). Another study of a valve design was done by Brun et al. (2006) who developed a compressor valve equipped with a controllable electromagnetic damper that worked based on valve velocity. While a compressor performance analysis for smaller discharge and suction ports, due to leakage on piston rings and valves was conducted by Diab and Howard (2005). On-line monitoring was reported by Schirmer, Fernandes and De Chaux (2004), where the measurement data were displayed in a P-V diagram that became a basis for a compressor performance analysis. The effect of valve losses (detected from a P-V diagram) on a valve lifetime was presented as a computer simulation by Howes and Long (2001), where the computer simulation was intended as a reference in designing an optimum compressor valve. A vibration signature in an operation cycle of a reciprocating compressor might be studied in a technical note published by Spectra Quest (2007). While a research on

vibration and noise characteristics on an intermediate plate of a discharge port of a reciprocating compressor, with varied loads, was done by Erol and Gurdogan (2000).

The objective of an experimental research on a reciprocating compressor, upon which this article is written, is intended to present the vibration and pressure characteristics if there is a geometry change in a valve seat of a discharge port. The investigation was conducted at different level of a working load (1 bar to 7 bars). The result is intended to be a reference in designing a valve seat profile, in order to increase durability and performance of a reciprocating compressor.

Methodology

Data measurement is taken from a single-stage, single-acting reciprocating compressor, of 630 rpm and 2 HP, where working fluid is air. Variables to be measured are vibration acceleration of a cylinder head and a pressure of a cylinder chamber. For a particular shaft velocity both variables are taken simultaneously, and are plotted against a crank angle. The same measurement time is triggered by used of a tachometer. Measurement data are recorded by a data logger, which in turn are downloaded to a digital computer, so that a cylinder pressure and a vibration profile graphs can be displayed.

A hole is drilled in the cylinder head to place a pressure transducer. On the cylinder head is also placed an accelerometer with magnetic base to measure the ensuing vibration. Measurements of data are taken for a different discharge valve seat design, as shown by Figure 3, to be used in the reciprocating compressor.

Data and Analysis

Valve Seat – Normal Profile

The normal profile refers to the valve seat profile / design as supplied by the OEM. The valve seat has a uniform cen-

tral hole of a 14-mm diameter and an 8-mm thickness (Figure 3 a).

Figures 4 and 5 show the P-θ graphic and the time waveform (of acceleration) of a reciprocating compressor using a normal discharge valve seat, for working pressures of 1 bar to 7 bars. The time waveform indicates that the vibration level due to an opening-closing of a discharge valve is higher than an opening-closing of a suction valve. A discharge valve starts to open several degrees before TDC and starts to close when the expansion cycle is complete (several degrees after TDC). The higher the compression pressure, the opening process of the discharge valve moves to the right (comes later). The movement to the right is also detected for another design of a discharge valve. The pushing force of a discharge valve increases with the addition of a working pressure, while the pushing force of a suction valve is relatively the same. The increase of the pushing force moves the moving parts with higher acceleration, and thus strikes the guard with higher impact.

Valve Seat – Modified Design 1

The discharge valve seat of modified 1 has a uniform central hole of smaller diameter (7 mm) than a normal one. In Figure 6, the P-θ graphic indicates the raise in a pressure level compared to a normal design. Reducing the diameter of a passage (up to 50% in this experiment) causes a decrease in the effective flow area, while the required force to displace the moving part remains the same. Therefore, the compression pressure has to be increased to move the moving part. Due to the late movement of the moving part, the opening of discharge valve is also late. The high compression pressure causes an increase in valve losses. The valve losses represent unusable power which happens during an expansion cycle. Compared to the normal design, vibration waveform shows the increase of a vibration signal, from opening to closing of a discharge valve (Figure 7).

Valve Seat – Modified Design 2

The difference from a normal one is that (approximately) a half of a discharge valve seat modified 2 has a torus central hole of decreasing diameter. P-θ diagram of Figure 8 shows almost the same character as a diagram of a normal profile. Although there is reduction on the volume, a chamfer on a valve hole brings a better fluid flow characteristic. Recorded vibration indicates that there is an improvement on a vibration level, compared to the normal design. An experiment result indicates that there is a smoothing in the flow, which will decrease the vibration level (Figure 9).

Valve Seat – Modified Design 3

In a discharge valve seat modified 3, (approximately) a half of a valve seat has a chamfered central hole of increasing diameter. P-θ diagram of Figure 10 shows almost the same character as a diagram of a normal profile. In general, there is a slight improvement on a vibration level compared to the normal design (Figure 11).

Effect of Different Design of Discharge Valve Seat

Compared to the normal discharge valve seat (the one supplied by OEM), reducing a diameter of a central (uniform) hole does not give an improvement on the pressure and vibration characteristics. An addition of a chamfer on the inside diameter of a discharge valve seat does not change much the P-θ diagram, but gives an improvement on the vibration signal.

Figures 12 and 13 show typical examples (taken for a 5-bar load) of the effects of a different design of the inside hole profile of the discharge valve seat. And, Table 1 shows overall vibration acceleration recorded on the cylinder head, for different working pressures during the experiment.

The vibration level affects the compressor durability, particularly in correlation with the fluttering effect of the opening and closing of the valve.

Fluttering action indicates repeated impacts on seat and guard components, when moving parts still have high acceleration.

Figure 14 shows a typical example of a P-V diagram (taken for a 5-bar pressure), for a normal, modified-2, and modified-3 profile of a discharge valve seat. We can see that the P-V diagram (indicates the useful work) is almost the same, while a chamfer on the central hole gives an improvement on vibration.

Conclusion

Analyses on the pressure and vibration signals of varied discharge valve seat profiles of a reciprocating compressor give several findings, as follows:

- Reducing a flow area (a modified-1 profile) will raise an opening pressure of a discharge valve, delay time to open and to close a discharge valve, increase valve losses, and add an ensuing vibration level.
- Adding a chamfer on the central hole of a discharge valve seat, either as a decreasing torus (a modified-2 profile) or an increasing torus (a modified-3 profile), shows relatively the same pressure graph and gives an improvement on a vibration level.
- Increasing a compressor load will cause a delay on the discharge valve opening (because it takes longer time to reach an opening pressure), and in general will raise a vibration level.

The experiment results are intended to be referred by those who are interested in knowing operation characteristics of a reciprocating compressor, if there is a change in a compressor's discharge valve.

Acknowledgement

The PT. PLN-PJB (State Electric Company) provided financial support and the Department of Mechanical Engineering - ITS provided necessary equipment to carry out this research.

References

- [1] Basaraba, Bruce M., and Archer, J.A., *Rotating Equipment Handbook: Machinery Reliability &*

- Condition Monitoring*, IPT Publishing and Training Ltd, Edmonton, Canada, 2000
- [2] Bloch, Heinz P., and Hoefner, J.J., *Reciprocating Compressors Operation & Maintenance*, Gulf Publishing Company, Houston, 1996
- [3] Brun, Klaus, Gernertz, R.S., Smolik, M.O., and Platt Jr., J.P. (2006), "Semi-Active Compressor Valve Development and Testing", *Pipeline & Gas Journal*, pp. 40-42
- [4] Diab, Sary, and Howard, B. (2005), "Reciprocating Compressors Management Systems Provide Solid Return on Investment", Technical Paper, GE Energy
- [5] Erol, Haluk, and Gurdogan, A. (2000), "The Noise and Vibration Characteristics of a Reciprocating Compressor : Effects of Size and Profile of Discharge Port", Proceedings of 15th International Compressor Engineering Conference, Purdue University, pp. 677-683
- [6] Hanlon, Paul C., editor, *Compressor Handbook*, McGraw-Hill, New York, 2001
- [7] Howes, Brian, and Long, B. (2001), "Using Simulation of Reciprocating Compressor Valve Dynamics to Improve Economic Performance", Technical Paper, Beta Machinery Analysis, Calgary, Canada
- [8] Schirmer, Alberto G.F., Fernandes, N.F., and De Caux, J.E. (2004), "On-line Monitoring of Reciprocating Compressors", Paper presented at NPRA Maintenance Conference, San Antonio, USA
- [9] Spectra Quest, "Vibration Signatures of Reciprocating Compressors", Technical Note, Spectra Quest Inc., 2007, www.spectraquest.com
- [10] Wilson, Robin S. (2007), "Compressor Optimisation", Paper presented at Conference CO 2007, Aberdeen, Scotland
- [11] Woollatt, D., "Reciprocating Compressor Valve Design: Optimizing Valve Life and Reliability", Dresser Rand, New York, 2003, www.dresser-rand.com



Fig.1: Reciprocating Compressor

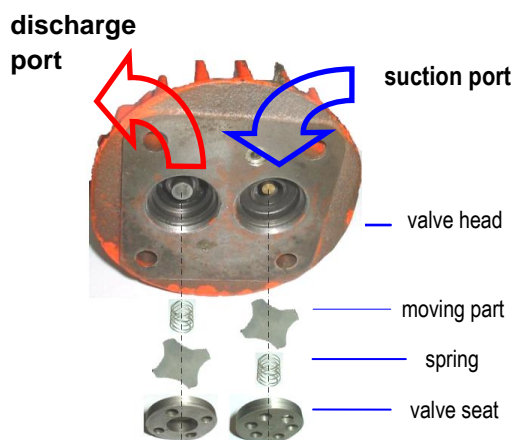


Fig.2: Valve and Its Component

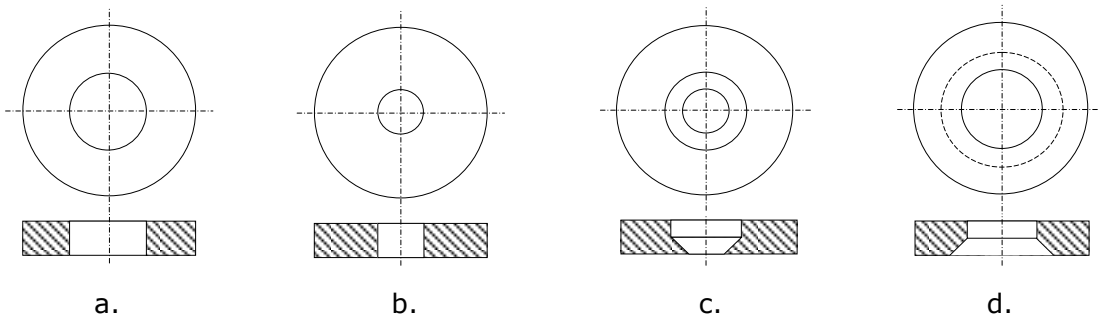


Fig.3: Valve Seat: a. normal, b. modified 1, c. modified 2, d. modified 3

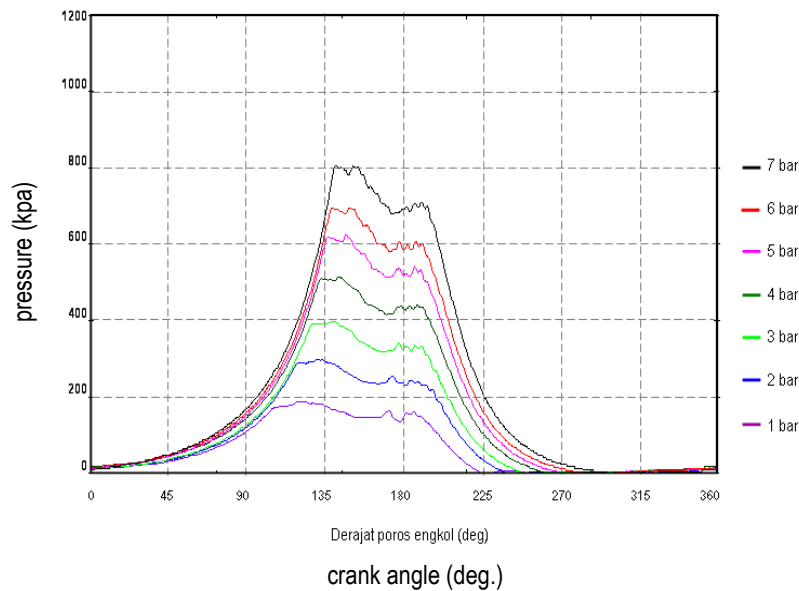


Fig.4: P-θ Diagram of Normal Valve

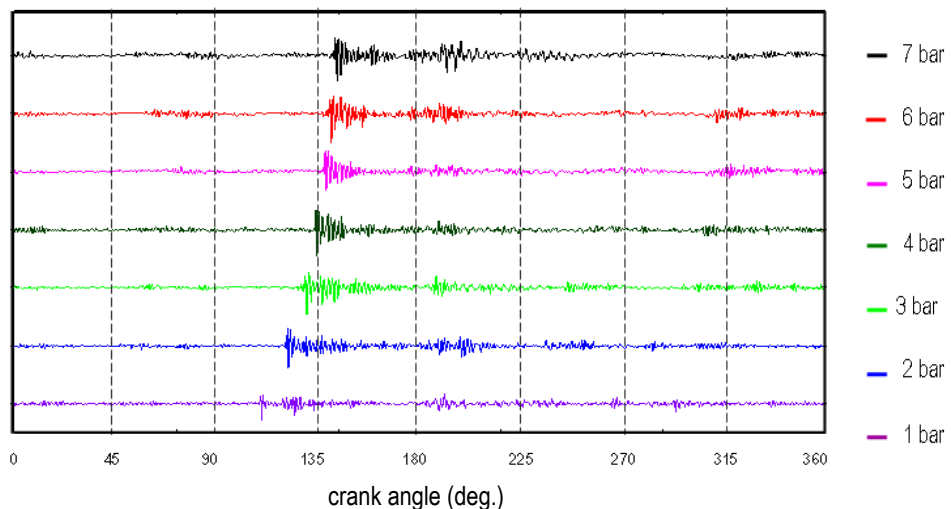


Fig.5: Waveform of Normal Valve

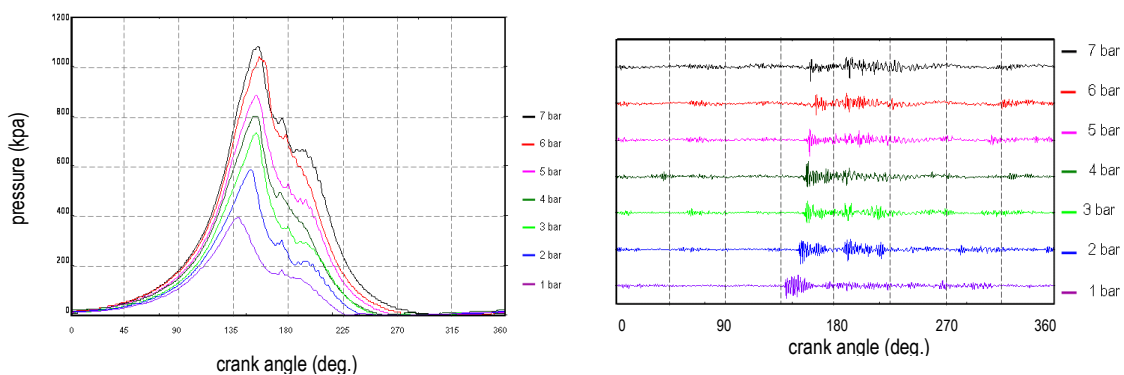


Fig.6: P-θ Diagram of Valve Mod. 1

Fig.7: Waveform of Valve Mod. 1

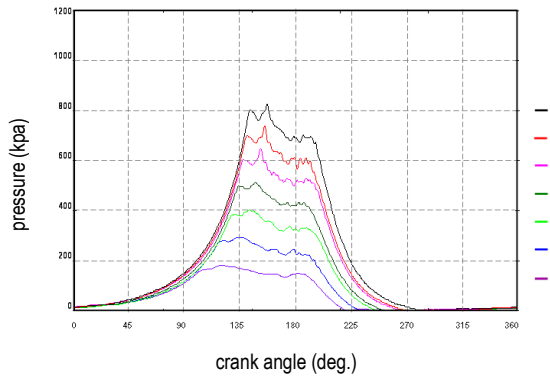


Fig.8: P-θ Diagram of Valve Mod. 2

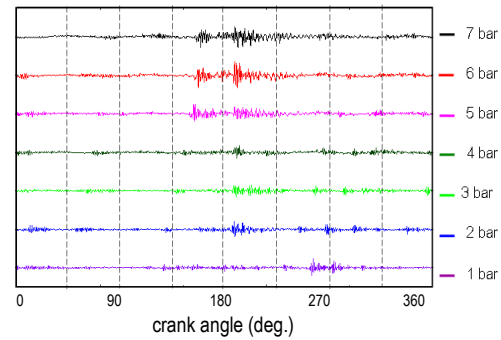


Fig.9: Waveform of Valve Mod. 2

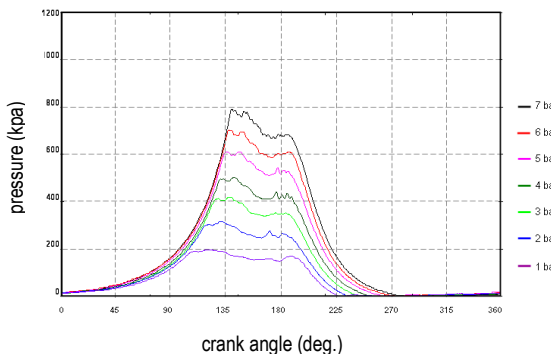


Fig.10: P-θ Diagram of Valve Mod. 3

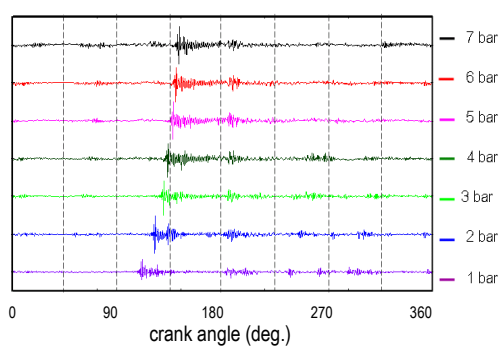


Fig.11: Waveform of Valve Mod. 3

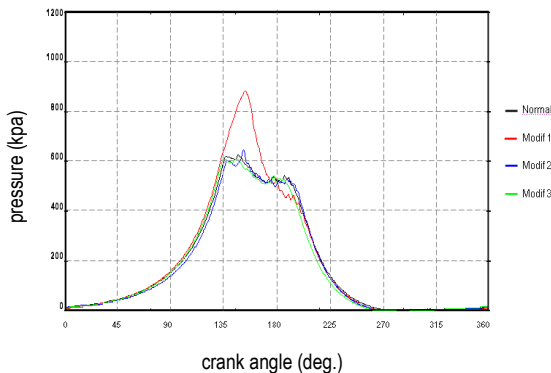


Fig.12: P-θ Diagram of Different Design of Discharge Valve Seat

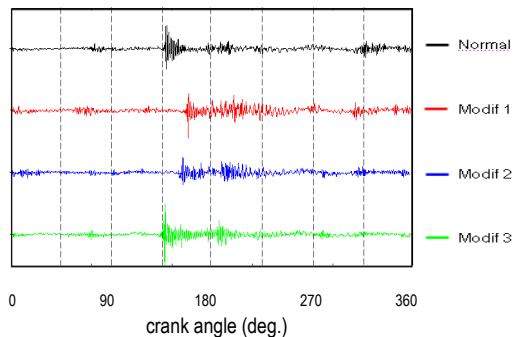


Fig.13: Waveform of Different Design of Discharge Valve Seat

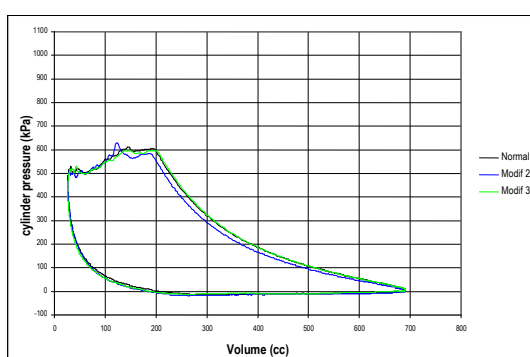


Fig.14: P-V Diagram

Table 1: Overall Acceleration [g]

press. (kpa)	nor- mal	mod. 1	mod. 2	mod. 3
100	0.267	0.406	0.255	0.287
200	0.299	0.399	0.252	0.305
300	0.334	0.376	0.251	0.317
400	0.370	0.384	0.263	0.349
500	0.375	0.389	0.313	0.356
600	0.390	0.393	0.358	0.360
700	0.419	0.416	0.376	0.372

Dynamic Modeling and Experimental verification of Polyvinylidene Fluoride actuator for a valve-less Micropump

Navin Karanth P, Vijay Desai and S M Kulkarni

Department Mechanical Engineering, National Institute of Technology Karnataka, Surathkal Srinivasanagar, Mangalore 575 025, Karnataka, India. email: navinkaranth@gmail.com

Abstract: Micropumps find application in several Micro-Mechanical and Micro-Fluidic systems where a minute, precise quantity of fluid needs to be pumped. The majority micro pumps reported for such applications are of positive displacement type where the actuating member is a diaphragm. The performance characteristics of a micropump may be attributed to its ability to have high flow rate and output pressure over a cycle. These performance characteristics mainly depend on volumetric displacement of the pump which in turn depends on the central deflection of the diaphragm of the pump. In the present work polyvinylidene fluoride actuator for valve-less micropump is modeled using ANSYS Multiphysics Version 10.0®, to determine the natural frequency through diaphragm modal analysis. Dynamic analysis is performed to estimate the central deflection of the diaphragm. The same is verified experimentally and the variations between the experimental and finite element results are found to be within 8 %. The effect of the film thickness on the central deflection of the diaphragm for different actuating voltages are also studied and compared. It is observed that central deflection depends on the thickness of actuator film.

Keywords: Polyvinylediene fluoride (PVDF), micropump, modal analysis.

Introduction

Micropumps have become quite popular due to their increasing demand in several medical and Technical applications Adam T. Woolley et al. (1996) like drug delivery systems, Micro-total Analysis Systems and Lab-on-chip systems. These systems require a device to deliver minute and accurate measure of the fluid at different intervals which is performed by a Micropump D J Laser et al. (2004).

Earlier micropumps had active valves which were either difficult to fabricate or reduce the life of the micropump. These active valves gave way to passive valves which were found to be easier to fabricate and had longer life Van Lintel (1998). The valve-less category of micropumps have been proposed and studied exhaustively E.

Stemme et al. (1993); A Olsson et al. (1995); A Olsson et al., (1996); A Olsson et al.(1997). In these pumps the conventional valves are replaced by diffuser-nozzles that offered differential resistance to flow. These micropumps, despite their back flow losses, are more popular mainly due to their ease in fabrication processes A Olsson, et. al., (1996), A Olsson, et. al., (1997). Diffuser-nozzles due to their planar structures, can be easily and economically fabricated using common techniques.

The research literature on micropumps extensively focuses on Lead Zirconate Titanate (PZT) as the actuator for pump diaphragm. This is mainly due to its high piezoelectric coefficient Peter Woias (2005); Shifeng Li (2003); A. Ullmann (1998); A. Ullmann et al. (2001); A. Ullmann et.al. (2002). However, the brittle nature and

large Young's Modulus, which allows low strain values, could be problems for designers besides the the fabrication of the PZT actuator P. Navin Karanth et al. (2010). Polymer based Polyvinylidene Flouride (PVDF) could be promising substitute for PZT to bring in increased reliability and service life to the pump, furthermore, design and manufacturing could also be simplified with PVDF actuation P. Navin Karanth et al. (2010). The lower Young's modulus of these films facilitates large strains and hence large displacements/deflections could be achieved. Reliability and service life with such PVDF film actuation are also expected to be more on account of above properties. Literature on the performance of such micro pumps is scarcely available, hence in this paper, a study of PVDF actuation in valve-less micro pump is envisaged.

In the present work, dynamic modeling and experimental verification of the PVDF as an actuator for valve-less micropump is attempted. The proposed actuator consists of a circular steel diaphragm with PVDF film glued to it. As the pump performance greatly depends on the deflection of the diaphragm, pump actuator is modeled in the finite element method (FEM) based software, ANSYS®. Analysis of the diaphragm is performed to estimate the central deflections. The finite element results are compared with deflections obtained experimentally. The deflections for different thicknesses of PVDF actuator are studied

Principle of actuation in micropump

The pump configuration considered for modeling of the actuator is shown in Fig.1. The diffuser-nozzle elements at the inlet and outlet ports of the pumping chamber act as valves. The pump operates in two modes, the supply mode and the pump mode. The pump operation is shown schematically in Fig.2. The volume of fluid flowing in the diffuser direction is higher than the volume of fluid flowing in the nozzle direction as depicted in the Fig.2.

During the supply mode, the cavity volume of the pumping chamber increases and a large quantity of fluid enters the chamber through the inlet port acting as a diffuser element, than the outlet port acting as a nozzle element. During the pump mode the cavity volume of the pumping chamber decreases and a large amount of fluid flow out of the chamber through the outlet port, which acts as a diffuser than through the inlet port, which acts as a nozzle. The two combined modes result in one complete pump cycle, where a net volume of fluid is transported from inlet to outlet port of the pump Anders Olsson et al. (1995).

The effect of the PVDF film thickness and driving voltage on deflection of diaphragm is studied. PVDF films having thicknesses of 0.028, 0.052 and 0.110 mm are considered for the analysis and actuated by six different driving voltages (90V - 140V in steps of 10V). The experimental deflections are measured for the above mentioned thicknesses of PVDF and driving voltages and the results are compared.

Modeling of PVDF actuator

The PVDF film and the metal diaphragm are modeled using a commercial finite element modeling (FEM) software package ANSYS® version 10.0 for the configuration shown in Fig.3. The dimensions of the metal diaphragm and the PVDF film are shown in Table 1. Details of the elements and materials used for modeling the actuator of the micro pump are given in Table 2. The generated mesh for the metal diaphragm and the PVDF film actuator is shown in Fig.4. The loading and boundary conditions on the finite element model for the actuator is shown in Fig.5. The model is subjected to dynamic analysis to estimate the central deflection of the diaphragm. To perform the dynamic analysis, initially the natural frequency of the PVDF actuated diaphragm is evaluated by performing modal analysis. The central deflection of the diaphragm is estimated through harmonic analysis by actuating the PVDF at driving voltages of

90V to 140V in steps of 10V and frequency of excitation at first mode natural frequency. The analysis is performed for PVDF films of different thicknesses.

Experiments

A steel diaphragm is diced for the dimensions tabulated in Table 1. The PVDF film is attached to the diaphragm with leads as shown in the Fig.6. An analog voltage input signal with maximum voltage level up to ± 400 V is used. A power source and a single stage common emitter (CE) amplifier with capacitive coupling is designed and implemented. The sinusoidal signal from the signal generator is sent to the single stage common emitter amplifier that drives the PVDF film attached to the diaphragm. The central deflection of the steel diaphragm is acquired by using a laser displacement sensor having a resolution of 1 micron. The output voltage of the laser displacement sensor is acquired using data acquisition hardware NI 4472 run by data acquisition software LabVIEW version 8.5. The experimental setup to determine the central deflection of the diaphragm with PVDF film actuation is shown in the Fig.7. The value of central deflection of the diaphragm will be highest when it is actuated at its resonance frequency. The PVDF actuator is excited at the resonance frequency obtained from ANSYS results to determine the maximum central deflection of the metal diaphragm. Further the experiments are conducted to study the variation in central deflection due to actuation voltages from 90V to 140V in steps of 10V. The results of the experiment and the analysis are compared in the next section.

Results and Discussion

The central deflection of the metal diaphragm with PVDF film actuation obtained from ANSYS and experiments, for thicknesses of 0.028, 0.052 and 0.110 mm and voltages varying from 90 to 140 V are tabulated in Table 3. The corresponding resonance frequencies for actuation of the diaphragm actuator are also listed in the

Table 3. The results obtained from theoretical and experiments are comparable and the variation in the results is within 6 to 8%. It can be observed from the data in Table 3 that the central deflection is proportional to the input voltage and thickness of the PVDF film. A high input voltage and a thicker PVDF film can produce a large central deflection and hence give better performance of the pump. Fig. 8 shows the variation in central deflection and input voltage for different thickness of the PVDF film.

Conclusion

In this work, proposition of using PVDF as an actuator in a micro pump is explored. Modeling of pump diaphragm deflection for PVDF film actuation is studied. The PVDF actuated pump diaphragm is fabricated and tested. The experimental results are within 8% of the theoretical estimates of deflections. It can be inferred from the results that central deflection of the diaphragm increases with increase in driving voltage and PVDF film thickness.

References

- [1] A Olsson, G. Stemme, E. Stemme, 1995, A valve-less planar fluid pump with two pump chambers, Sensors and Actuators A, 46-47, 549-556.
- [2] A Olsson, P. Enoksson, G Stemme, E. Stemme, 1997, Micromachined Flat-Walled Valve-less Diffuser Pumps, Journal Microelectromechanical Systems, Vol. 6, No. 2, 161-166.
- [3] A. Olsson, P. Enoksson, G. Stemme and E. Stemme, 1996, A valve-less planar pump isotropically etched in silicon, J. Micromech. Microeng., 6, 87-91.
- [4] A. Ullmann I. Fono, 2002, The Piezoelectric Valve-Less Pump- Improved Dynamic Model, [5] Journal of Micro-electromechanical Systems, 11, 6, 656-664.
- [6] A. Ullmann, 1998,The piezoelectric valve-less pump-performance enhancement analysis, Sensors and Actuators A, 69 97-105.
- [7] A. Ullmann, I Fono, Y. Taitel, 2001, A Piezoelectric Valve-Less Pump-Dynamic Model, J. Fluids Eng., 93, 92-98.
- [8] E. Stemme, G. Stemme, 1993, A valveless diffuser/nozzle-based fluid pump, Sensors and Actuators A, 39, 159-167.
- [9] P. Navin. Karanth, V. Desai, S.M. Kulkarni, 2010, Modeling of single and multilayer polyvinylidene fluoride film for micro pump actuation, Microsystem Technologies,116, 4, 641-646.

- [10] Peter Woias, 2005, Micropumps—past, progress and future prospects, Sensors and Actuators B 105 28-38.
- [11] Shifeng Li, Shaochen Chen, 2003, Analytical analysis of a circular PZT actuator for valveless micropumps, Sensors and Actuators A 104 151-161.
- [12] Van Lintel, 1988, A Piezoelectric Micropump Based on Micromachining of Silicon. Sensors and Actuators, International Search Report, 2-15, 153-167.

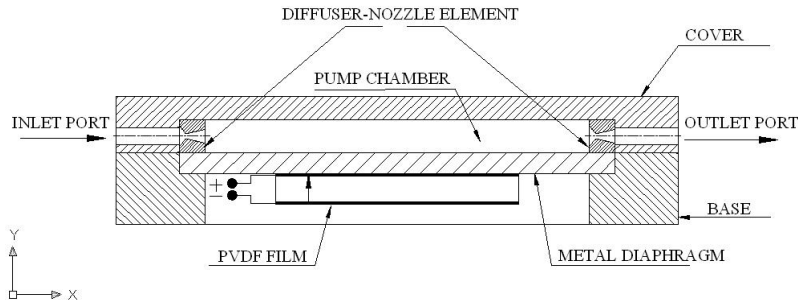


Fig.1 Configuration of the micro pump

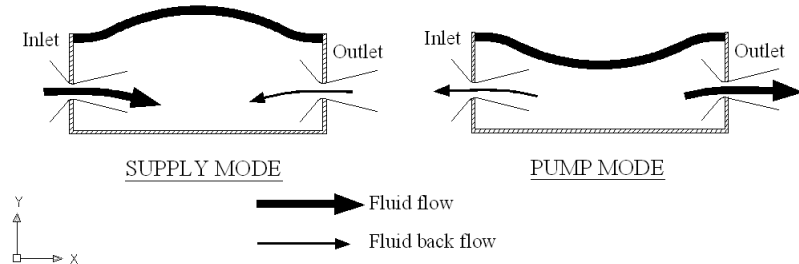


Fig.2 Operation of the micro pump

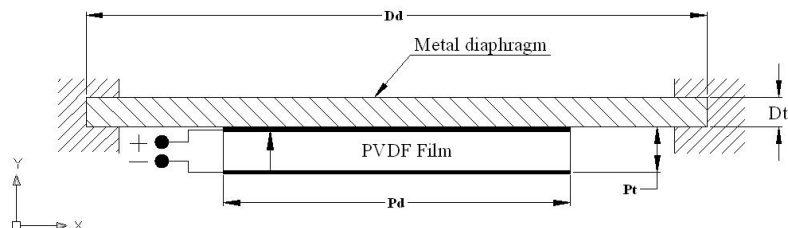


Fig.3 Actuator for the micro pump

Table 1 Actuator parameters

Metal diaphragm diameter D _d	20 mm
---	-------

Metal diaphragm thickness D_t	0.102mm
PVDF film diameter P_d	16 mm
PVDF film thickness P_t	0.028, 0.052, 0.110 mm

Table 2 Elements used in modeling actuator

Part	Material	Element type	Young's Modulus E GPa	Poisson's Ratio
Metal diaphragm	Aluminium	Solid 95	73	0.33
Actuator	PVDF	Solid 226	3.0 *	0.18*

* As per the specification of the supplier

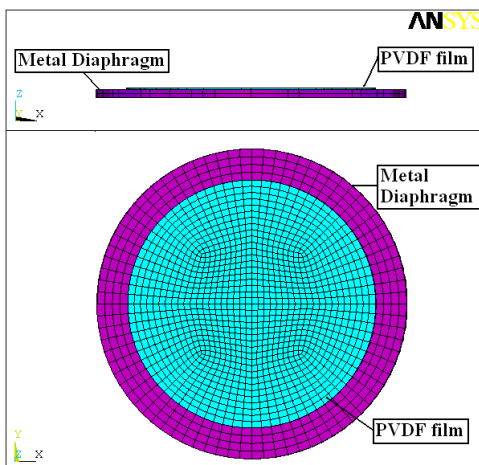


Fig.4 Generated mesh of the diaphragm and the PVDF film

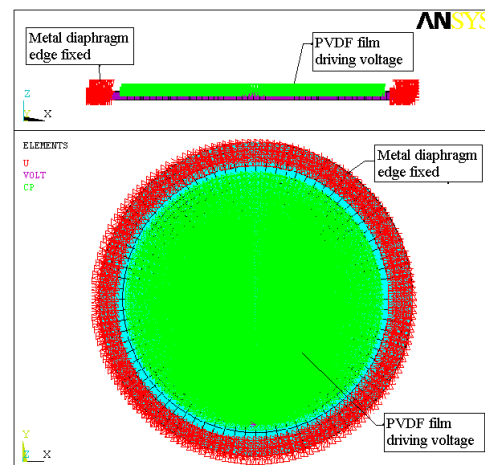


Fig.5 Loading and boundary conditions

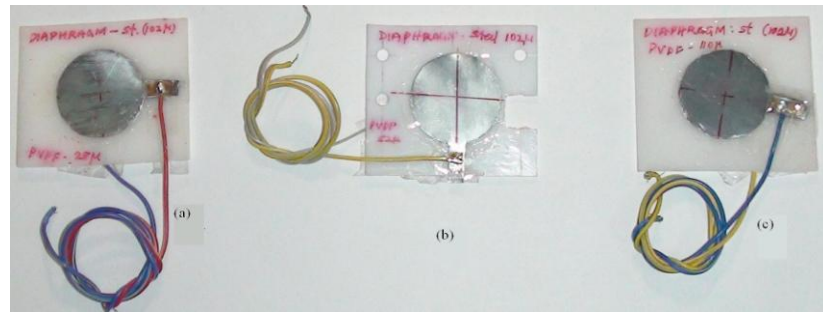


Fig.6 Steel diaphragms attached with PVDF film of different thickness a) 28 microns b) 50 microns c) 110 microns

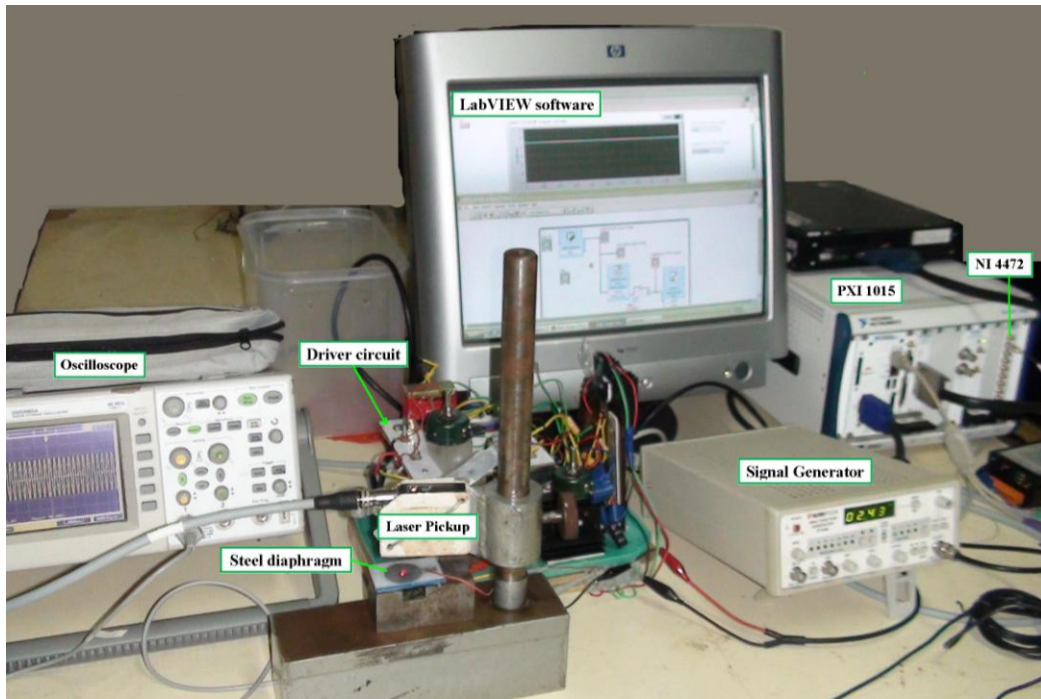


Fig.7 Experimental setup for the diaphragm actuator

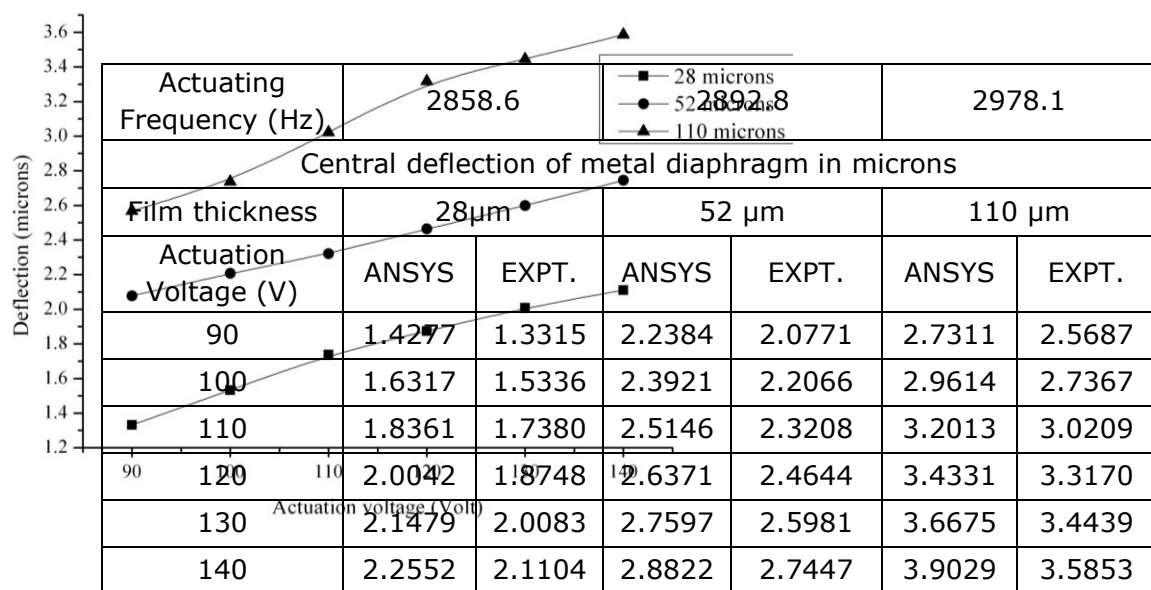


Fig.8 Variation in central deflection with change in PVDF film thickness for different actuation voltage

Table 3 Comparison of theoretical and experimental central deflection values

Characterization of Polyvinylidene Fluoride Piezo Film for fluid pressure sensor application

Navin Karanth P, Vijay Desai and S M Kulkarni

Department Mechanical Engineering, National Institute of Technology Karnataka, Surathkal Srinivasanagar, Mangalore 575 025, Karnataka, India. email: navinkaranth@gmail.com

Abstract : A novel pressure sensor for fluid pressure application is developed using piezoelectric polyvinylidene fluoride (PVDF) film as the sensing element. The sensor is designed for measuring liquid or air pressure. The objective of this work is to develop a low cost pressure sensor that provides pressure as the measurable information of the process that can be used as a processing variable in mechatronic system. The PVDF film pressure sensor is developed by mounting the film on a copper diaphragm enclosed in a capsule. In the present study the behavior of pressure sensor is investigated in measurement of pneumatic pressure. A pneumatic circuit is rigged up to ensure a specific pressure on the sensor. Single and double layer configurations of the sensing element are considered. The response of the sensor is comparable with commercially available pressure sensor. The PVDF film pressure sensor exhibits high sensitivity and linearity. A good agreement among the modeling predictions and the experimental findings is observed. The response of the pressure sensor improved with double layer stacking. Double layer PVDF pressure sensor with parallel connection exhibited an improvement in response and resolution by 5 times compared to single layer pressure sensor.

Keywords: Polyvinylidene fluoride (PVDF), pressure sensor

Introduction

Pressure sensor plays a vital role in providing measurable information of the process for a wide range of industrial and medical applications. In aeronautical industry pressure measurement is important in developing and understanding of the aerodynamic behavior of planes and ground vehicles M. Zagnoni et. al. (2005). In medical application, these sensors are used in medical equipment like endoscopes to provide information to doctors regarding the magnitude of pressure exerted on internal organs or tissue J. Dargahi et. al. (1998). In automotive applications, pressure sensor provide information regarding fuel injection pressure, fuel system leak pressure etc William J Fleming (2008).

The pressure measurement is generally done by measuring the deformation of the

sensing element. Pressure sensing elements currently used are largely diaphragms, capsules, bellows and tubes. In the pressure sensor having diaphragm as the sensing element the deformation of the diaphragm is converted into pressure readout by different transduction effects such as capacitive, piezoresistive and piezoelectric. Kevin H et. al. (1999). The capacitive and piezoresistive pressure sensors provide wider range for pressure sensing but suffer from non linearity beyond some values of pressure Kevin H et. al. (1999) and William P Eaton (1997). The piezoelectric sensors are used for pressure sensing because the charge generated by a piezoelectric is almost linearly proportional to the deflection of the diaphragm due to pressure. The piezoelectric materials such as quartz, tourmaline, Rochelle salt, ammonium dihydrogen phosphate (ADP), lithium sulfate, barium titanate, and lead zirconate

titanate (PZT) are being used for pressure sensing. Piezoelectric ceramics and crystals typically suffer from low fracture toughness B. K. Atkinson (1979) and W.S Oates et.al. (2004) where as polymer family on the other hand exhibit much less mechanical problems, as they are ductile compared to ceramics Y. Wang (2007). Piezoelectric polymer polyvinylidene fluoride (PVDF) has low modulus, high sensitivity, low quality factor, high electromechanical coupling coefficient, compliance and ease of use Barsky et al. (1989) which makes it a suitable material for sensor. A.V. Shirinov et. al. (2008) developed a low cost pressure sensor using PVDF as the diaphragm for sensing pressure in pneumatic application.

In the present work response of a single layer PVDF film pressure sensor is modeled in finite element analysis and compared with experimental measurements. Response of the PVDF pressure sensor is compared with the commercially available pre-calibrated pressure sensor ASCX. Further an attempt is made to improve the response of the proposed sensor by considering the stacking of the PVDF film. Two PVDF films are stacked to make a double layer pressure sensor. Two configuration of the double layer pressure sensor is considered where in responses of layers are in series and in the second case, parallel. Based on the earlier study on force sensing, by same authors, it is expected that double layer sensor with parallel configuration gives better response than double layer senor with series configuration. Theoretical response of the sensor is estimated through finite element analysis of parallel configuration is compared with response obtained in experimental findings.

Pressure Sensor

The cross section of the proposed single layer pressure sensor (SLPS) using PVDF is shown in Fig. 1. The sensor consists of pressure chamber cup, sealing cap, copper

diaphragm, flexible pipe and commercially available PVDF film supplied by M/s Measurement Specialties Inc, Hampton, VA. The sensor consists of a circular PVDF film of diameter 8mm and thickness 28- μm . The film has pre-fabricated silver electrodes for tapping out response. The pressure chamber cup and sealing cap are fabricated using nylon material. The PVDF film is glued on the copper diaphragm with an adhesive tape of conducting material form sensing element. Photograph of the full assembly of the sensor is shown in Fig. 2. A pair of leads is drawn out of assembly for response of the sensor.

In the proposed double layer pressure sensor (DLPS) two PVDF films are stacked in parallel connections on the copper diaphragm. Fig. 3 shows the schematic representation of proposed single layer and double layer configurations of the sensor for pressure measurement. The finite element modeling of the proposed sensor configurations for theoretically estimating the sensor response is explained in ensuing section.

Modeling of Pressure Sensor

Sensor in its two configurations shown in Fig. 3 is modeled using a commercial finite element modeling (FEM) software package ANSYS® version 10.0. The details of the elements used for different parts and their material properties are given in Table 1. The generated mesh of the sensor is shown in Fig. 4. The pressure applied and boundary conditions for the FEA model are shown in Fig. 5. Analysis is performed with the pressure varying from 180kPa to 620kPa and the PVDF output voltage for single layer pressure sensor is determined. Further, to study the improvement in the response of the pressure sensor the modeling and analysis of the double layer pressure sensor is also performed. The sensor response from the finite element model for single and double layer configurations is compared with the

experimental measurement and presented in the later section.

Experiment setup

The PVDF pressure sensor is tested in pneumatic environment. An experimental setup is developed to investigate the performance of the single layer PVDF pressure sensor. A commercially available pressure sensor ASCX150DN from Honeywell International Inc. Illinois is used as a standard sensor to compare the output of the PVDF pressure sensor. The pneumatic circuit diagram of the experimental setup used for testing the pressure sensor is shown in the Fig. 6. The photograph of the setup is shown in Fig. 7. The pneumatic circuit is rigged in such a way as to ensure uniform pressure on the sensor for all the pressure values tested. The sensor is tested for pressure values starting from 180kPa to 620kPa in steps of 40kPa set by a control unit in the pneumatic circuit. The output response generated by the PVDF pressure sensor is directed to a charger amplifier (M68D3). To record and analyse the output of the PVDF pressure sensor a data acquisition system, NI PXI-4442 on PXI 1042 chassis operated by LabVIEW® software (Version 8.6) is used. The master pressure sensor ASCZ response is also recorded using data acquisition system NI PCI 6229 on PXI 1042 chassis. Peak output voltages from both the pressure sensors are recorded. The experiments are repeated for double layer pressure sensor as mentioned earlier (Fig. 3) and the responses are recorded. Results obtained from experimentation are presented in the following section and are also compared with its theoretical responses.

Results and Discussion

The response of the proposed single and double layer PVDF pressure sensors are obtained using finite element analysis and are measured experimentally. Fig. 8 shows the response of single layer PVDF pressure sensor determined through FEM and

experiment. The linear variation of the sensor output for corresponding pressure input could be observed with experimental results comparing well against finite element estimates. The variation in the responses of experiment and FEM estimation is not very significant around 4 to 7%. The results obtained are in line with earlier work done on single layer by A.V. Shirinov et. al. (2008). The comparison of the response of the single layer PVDF pressure sensor with the standard pressure sensor is shown in Fig. 10 where it can be observed that the responses of the PVDF pressure sensor are comparable with standard pressure sensor. To improve the response and resolution of the pressure sensor double layer PVDF pressure sensor is considered. Fig 9 shows the FEM and experimental results for the response of the double layer PVDF pressure sensor with parallel connection. It could be observed from the figure that the linearity of the sensor is maintained with improvement in the response. The variation in the response between the experiment and FEM predication is around 6 to 11%. Comparison of experimental results for single layer and double layer PVDF pressure sensor is shown in Fig. 11. The improvement of the response and resolution is about 4 to 5 folds compared to single layer PVDF pressure sensor.

Conclusion

In this paper, PVDF as a pressure sensor is studied. The single layer and double layer pressure sensor is analysed using ANSYS® and the finite element results are verified experimentally. It is observed that FEM predictions and experiment results match with a variation of 4 to 11%. The response of the single layer PVDF sensor is comparable with a commercially available sensor. Linearity in the response of the single layer PVDF pressure sensor is observed and the response is improved by 4 to 5 time with double layer PVDF pressure sensor with parallel connection.

References

- [1] A.V. Shirinov, W.K. Schomburg, (2008), Pressure sensor from a PVDF film, Sensors and Actuators A 142 pp. 48–55.
- [2] M. Zagnoni, A. Gofarelli, S. Callegari, A. Talamelli, V. Bonora, E. Sangiorgi and M. Tartagni, (2005) A noninvasive capacitive sensor strip for aerodynamic pressure measurement, Sensors and Actuators A:Physical, vol. 123-124, , pp. 240-248.
- [3] J. Dargahi, M. Parameswaran and S. Payandeh, (1998), A Micromachined Piezoelectric Tactile Sensor for use in Endoscopic Graspers," presented at Intl. Conference on Intelligent Robots and Systems, Victoria, B.C., Canada,
- [4] William J. Fleming,(2008), New Automotive sensors, IEEE sensors journal, vol. 8, no. 11, pp.1900-1921
- [5] Kevin H. and L Chau, (1999)), Pressure sensors, Measurement, Instrumentation, and Sensors, Handbook CRCnetBASE.
- [6] William P. Eaton and James H. Smith, (1997) Micromachined Pressure Sensors: Review and Recent Developments, from the Center for High Technology Materials, the University of New Mexico, Albuquerque,
- [7] B.K. Atkinson, (1979) A fracture mechanics study of subcritical tensile cracking of quartz in wet environments, Pure Appl. Geophys. 117 1011–1024.
- [8] Yantao Shen, Ning Xi, U.C. Wejinya and Wen J. Li, (2004), High sensitivity 2-D force sensor for assembly of surface MEMS devices, Proceedings of 2004 IEEE/RSJ International conference on Intelligent Robots and Systems, Sept. 28- Oct. 2 2004, Sendai, Japan
- [9] Y. Wang, K. Ren, Q.M. (2007), Zhang, Direct piezoelectric response of piezopolymer polyvinylidene fluoride under high mechanical strain and stress, Appl. Phys. Lett. 91 222905.

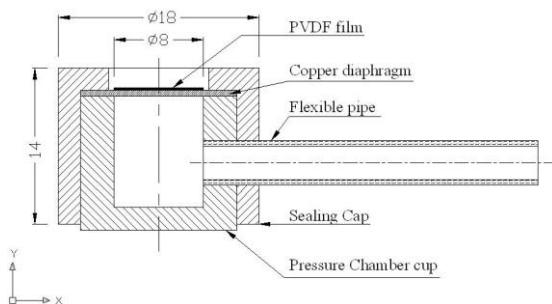


Fig. 1 Schematic cross section of the single layer PVDF pressure sensor



Fig. 2 Single layer PVDF pressure sensor

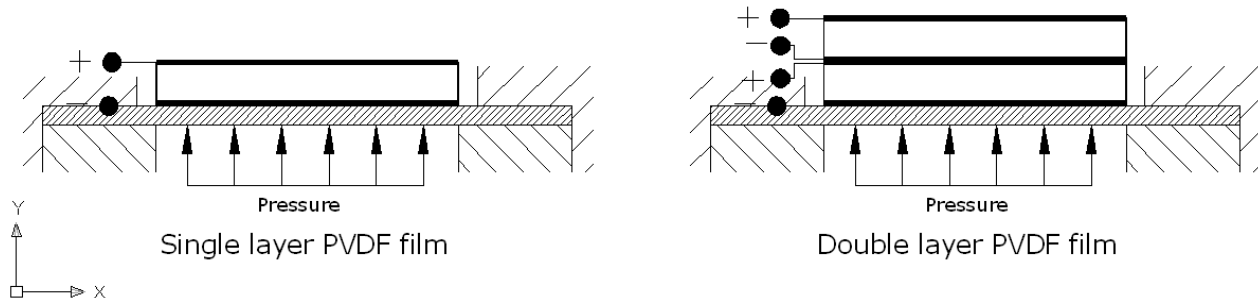


Fig.3 Schematic representation of single and double layer configuration of the proposed pressure sensor

Table 1 Elements for different material and their properties used in FE modeling

Part	Element type	Young's Modulus E GPa	Poisson's Ratio
Cellophane sticker	Solid 95	1.5	0.36
Silver Ink	Solid 95	7.8	0.32
PVDF film	Solid 226	2.0	0.29
Conductive tape	Solid 95	5.2	0.42
Copper diaphragm	Solid 95	118	0.3

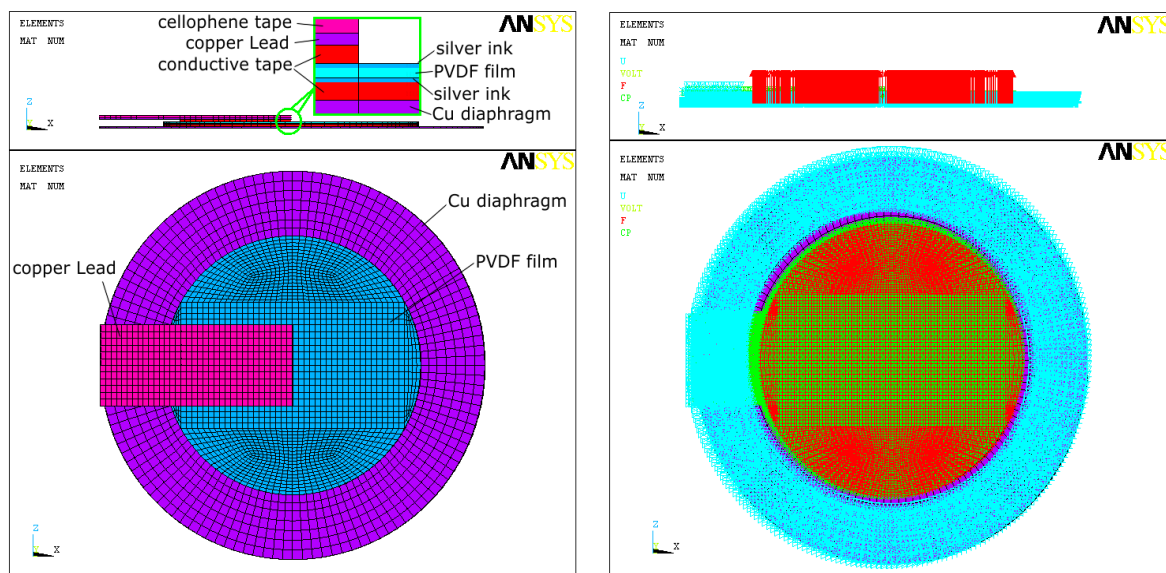


Fig. 4 Generated mesh of the sensor including all layers

Fig. 5 Pressure applied and boundary conditions

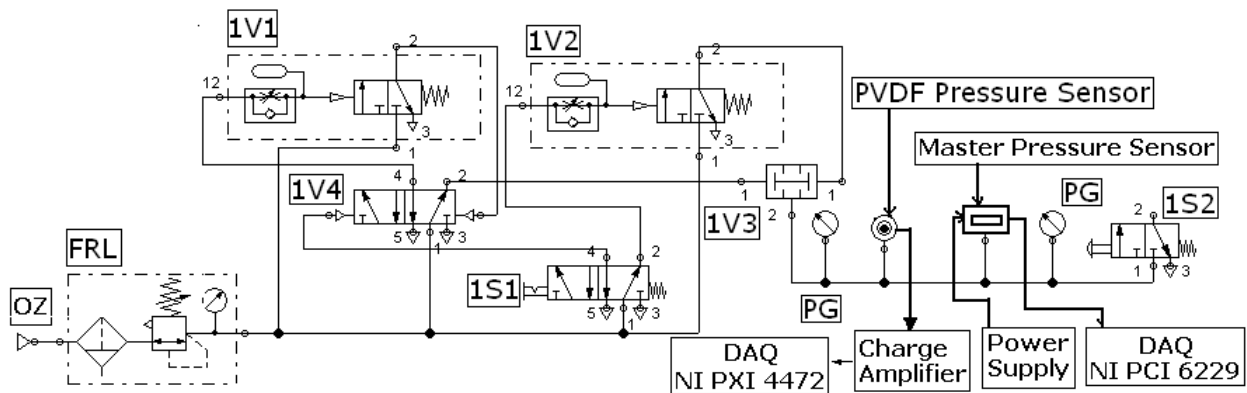


Fig. 6 Pneumatic circuit diagram of the experimental setup

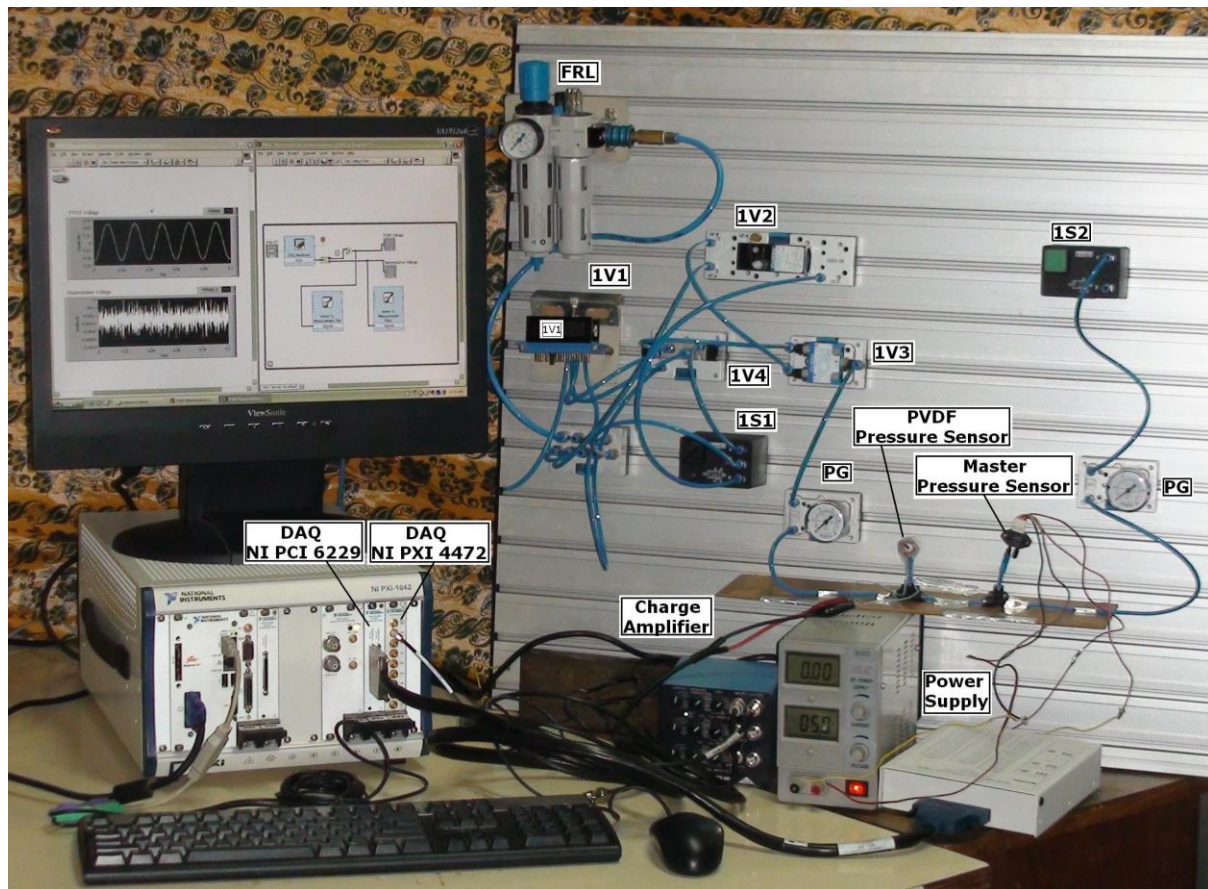


Fig. 7 Photograph of the experimental setup

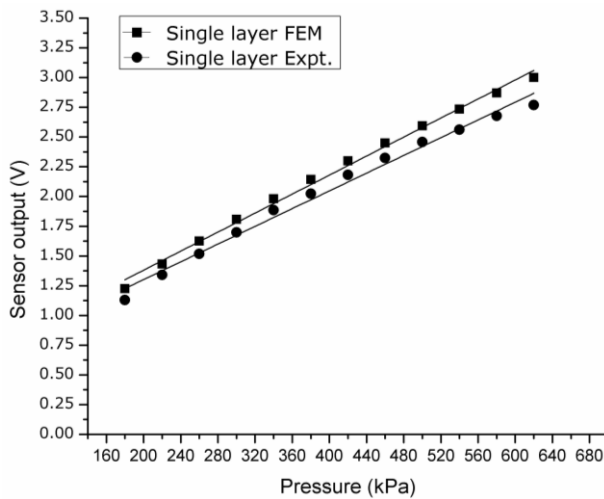


Fig. 8 FEM and experiment results for single layer PVDF pressure sensor

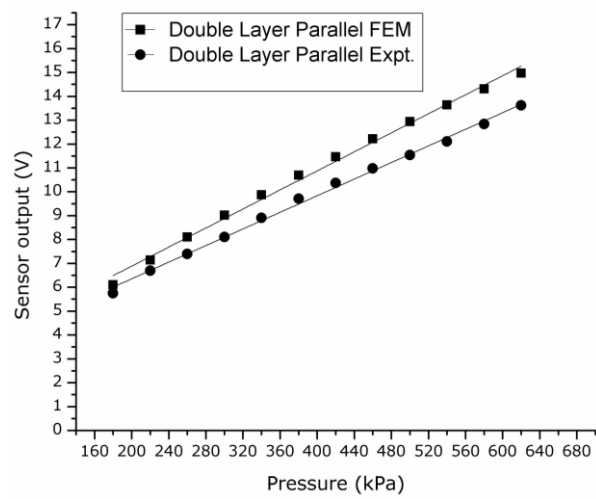


Fig. 9 FEM and experiment results for double layer PVDF force sensor with parallel connection

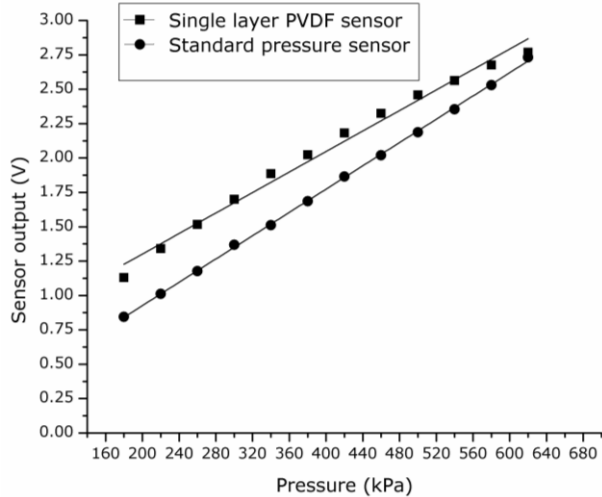


Fig. 10 Experiment result comparison for single layer PVDF pressure sensor and standard pressure sensor

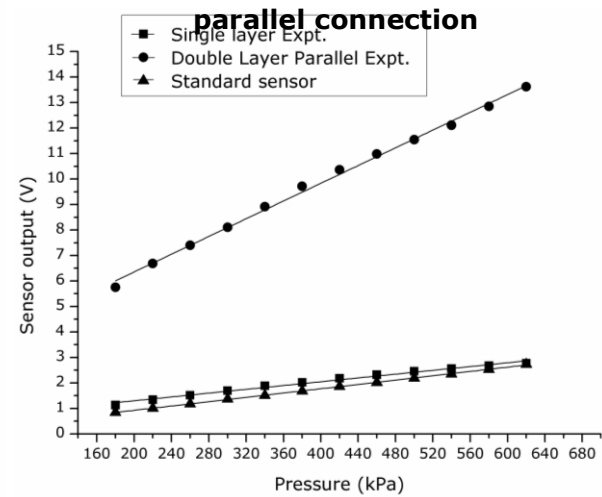


Fig. 11 Experiment results comparison for all configurations of PVDF pressure sensor with standard sensor

Computational Modelling of Compression Process in a Dual Fuel Compression Ignition Engine

KRISHNA MURTHY¹ MADHWESH. N² SHRINIVASA RAO. B.R³

*1 &2 Department of Mechanical & Manufacturing Engineering, Manipal Institute of Technology Manipal, Karnataka state, 576104 India.
e-mail: krishnamurthy2k4@rediffmail.com*

3 Department of Mechanical Engineering, NMAM Institute of Technology, Nitte, Karnataka State, India. 574110.

Abstract: This paper presents a computational method for the analysis of compression process using different heat transfer correlations for a 4 stroke LPG- Diesel dual fuel compression ignition engine and these results form the basic input for the combustion process. Variable heat exchange between the air+ gaseous fuel+ residual gas mixture and the cylinder wall during the compression process will affect the work requirement for the compression process as well as thermal load variation in the cylinder wall. A computer program was formulated in MATLAB 7.01 for compression cycle computation of index of compression, pressure, temperature, heat transfer and work required. Results show that average compression index for the compression process is 1.35 which is very close to the value suggested by Hardenberg & Hase. It has been observed that computed values of temperature and pressure match with the experimental values.

Keywords: Dual fuel engine, index of compression, LPG, heat transfer correlations.

Introduction

Dual fuel engines are modified diesel engines wherein primary fuel usually gaseous fuel is inducted along with the air and compressed. A small quantity of liquid (usually diesel fuel or any other liquid fuel having properties close to Diesel) called as pilot fuel is injected nearly at the top dead center. The pilot fuel self ignites due to the high temperature obtained during compression. Flame initiated at multiple spots, due to pilot fuel propagates through the gaseous air mixture thus causing it to burn. The combustion process in a dual fuel engine is a complex combination of features of both diesel and spark ignition engines. The induction of a gaseous fuel with air in the cylinder modifies greatly the mixture formation and further combustion process in a dual fuel engine: Andrei M (2006), Liu, Z.et al. (1997),.

Compression of cylinder charge follows the intake stroke as the piston moves from bottom dead center to top dead center.

Compression causes the cylinder charge to reach high temperature which is necessary for the self ignition of pilot fuel injected into the cylinder near to the top dead center. There is variable heat exchange between the air+inducted liquefied petroleum gas (LPG) + residual gases and the cylinder wall during compression process. At the beginning of the compression stroke the temperature of the inside walls of the cylinder is considerably higher than the temperature of the intake mixture, hence heat transfer takes place from the wall to the mixture. This results in higher index of compression above the adiabatic index during starting. As the compression proceeds, at some point it equals to the adiabatic index of the mixture. At this point there is no heat transfer between the walls and cylinder mixture because temperature of the charge is equal to the mean temperature of walls. Once the temperature of the charge crosses the wall mean temperature index of compression start decreasing below adiabatic index of the mixture.

During this period heat transfer takes place from the gas to the cylinder walls.

If the whole process of compression is divided into small parts and each part is considered as a polytropic process with its own value of polytropic exponent then it is possible to evaluate the index of compression for each interval. The index of compression mainly depends on various factors like heat transfer rate, crankshaft revolution, cylinder dimension, compression ratio, cooling rate of the cylinder, heat load on cylinder, and wear of the cylinder and piston rings: Andrei Makartchouk (2007).

Thermodynamic Analysis of working substance

For the present analysis a Single zone model is used to simulate the compression process starting from bottom dead center up to the end of delay period. When the piston is at the BDC the cylinder content consists of residual gases and inducted LPG+ air. It is assumed that the residual gasses +LPG+ air mixture behaves like an ideal gas. The LPG considered as Propane with the chemical formula C₃H₈ and Diesel as C_{14.5}H_{24.9}. The Stoichiometric fuel -air ratio (F/A)_{st} of a fuel mixture made up of two hydrocarbon fuel components C_{x1}H_{y1} and C_{x2}H_{y2} mixed in proportions A₁: A₂ is

$$\left(\frac{F}{A}\right)_{st} = \left(\frac{a}{a+b}\right)\left(\frac{F}{A}\right)_{st1} + \left(\frac{b}{a+b}\right)\left(\frac{F}{A}\right)_{st2} \quad (1)$$

Where st1 and st2 are the Stoichiometric fuel air ratios of Diesel and LPG separately:Liu, Z. et.al (1997).

$$a = \left(\frac{x_1 + y_1}{4}\right) A_1 \text{ and } b = \left(\frac{x_2 + y_2}{4}\right) A_2 \quad (2)$$

where x₁ = 14.5, y₁ = 24.9, x₂ = 3, y₂ = 8,

As the combustion take place in dual fuel engine with relative fuel - air ratio less than one, it is assumed that the products of combustion consists of CO₂, H₂O, N₂, O₂ with no CO and H₂ on product side. Composition of products of combustion is required to determine mass fraction of residual gases which is further used to determine the mixture gas constant. Specific heat variation for the above six products of combustion as well as air and LPG can be obtained using the equation;

$$\frac{Cp}{R} = a_1 + a_2 T + a_3 T^2 + a_4 T^3 + a_5 T^4 \quad (3)$$

where coefficients a₁ to a₅ are sourced from Colin R. Ferguson. The surfaces surrounding the cylinder charge namely cylinder head, piston crown and cylinder liner are assumed to be at a mean temperature of 506K, 503K and 550K respectively: Mc. Aulay et al (1965). The residual gases are assumed to be at a temperature of 500K and mixing takes place with the fresh air fuel mixture adiabatically.

Computational procedure

To start with the computation mean temperature (T_i) of air+LPG + residual gas is obtained by considering adiabatic mixing process which forms initial temperature for iteration. The displacement (X) of the piston at any crank angle is known from the engine kinematics and can be found out as follows

$$X_i = r + CRL - r * \cos \theta_i - [(CRL)^2 - r^2 \sin^2 \theta_i]^{1/2} \quad (4)$$

The volume at any crank angle related to the displacement can be written as

$$Vi = VC + AP * Xi \quad (5)$$

Crank angle is increased by a specified value depending upon the accuracy required. In the present case it is increased by 1° so that j = i + 1 again X_j and V_j are calculated. Now we can write

$$T_j = T_i * \left(\frac{Vi}{Vi}\right)^{n-1} \quad (6)$$

$$P_j = P_i \left(\frac{Vi}{Vi}\right)^n \quad (7)$$

$$dT1 = T_j - T_i \quad (8)$$

Now it is possible to find the average temperature (Tavg) and average pressure (Pavg) for the interval as well as weighted mean wall temperature for all the exposed surfaces (Twm).

$$Twm = \frac{AP * (T_h + T_p) + \pi * D(C + X)T_i}{2 * AP + \pi * D(C + X)} \quad (9)$$

where X = (X_j + X_i) * 0.5

Work done during the interval can be calculated by the relation

$$Wi-j = Pavg(Vj - Vi) \quad (10)$$

The Heat transfer Analysis during compression

Actual measurement of heat loss/gain for the compression process in an engine is very difficult. An indirect method using an engine heat transfer formulation therefore has been used wherein instantaneous heat transfer rates during the cycle is estimated using an engine heat transfer formulation. Several heat transfer formulae have been suggested in literature to estimate the heat transfer rates: Abdul Sharief et al (2007), Z.Liu et al. (1997), B.S. Samaga et al. (1976). It has been shown elsewhere that almost all of them agree qualitatively, though they differ in magnitude of calculated heat transfer. In the present work Eichelberg, Woshni, Annand and recently introduced Sharief correlations are used separately to study the heat exchange rates during compression process.

Sharief correlation is given by

$$havg = 20.42 * Tavg^{-0.22} * Pavg^{0.6} Vj^{0.6} D^{-0.4} \quad (11)$$

where $Vj = C * (A \text{ piston} / A \text{ port})$

Eichelberg's formulation can be written as

$$havg = 2.440667 * (Tavg * Pavg)^{1/2} * C^{1/3} \quad (12)$$

where $C = 2 * L * N / 60$

Once the heat transfer and work transfer are calculated for a given crank angle interval, using first law of thermodynamics, it is possible to calculate the change in internal energy. By knowing the mass of the mixture and Cv for the mixture we can calculate the increase in temperature 'deltT2'. If the 'deltT1' is equal to 'deltT2' then the initially assumed index of compression is correct. An iterative technique can be used by suitably changing the value of index 'n' so that deltT1 is very close to deltT2, within any specified accuracy.

Experimental set up

A single cylinder four stroke variable compression ratio, compression ignition engine which develops 5.2 kW at 1500 rpm was retrofitted with additional equipments and instrumentations. It is provided with temperature sensors and pressure sensors for combustion gas pressure and fuel injection pressure

measurement and an encoder for crank angle record. The LPG cylinder is connected to the inlet manifold through a rubber hose provided with a control valve. The signals from these sensors are interfaced with a computer to display P-θ, P-V diagrams. The engine can be run on neat diesel as well as dual fuel with LPG as inducted fuel and Diesel as pilot fuel. LPG flow rate can be adjusted using a gas flow meter which was calibrated in kg/hr.

Results and discussions

The pressure transducer along with the crank angle decoder gives the pressure variation for different crank angles for the entire cycle starting from suction till the exhaust. However, for the present analysis pressure variation with respect to crank angle for compression process is considered. Experimentally obtained P-θ curves follow the computed curve as shown in the fig-1. Computation was performed only up to the end of delay period. In the present analysis compression process was carried out up to 340°C, where the combustion assumed to start.

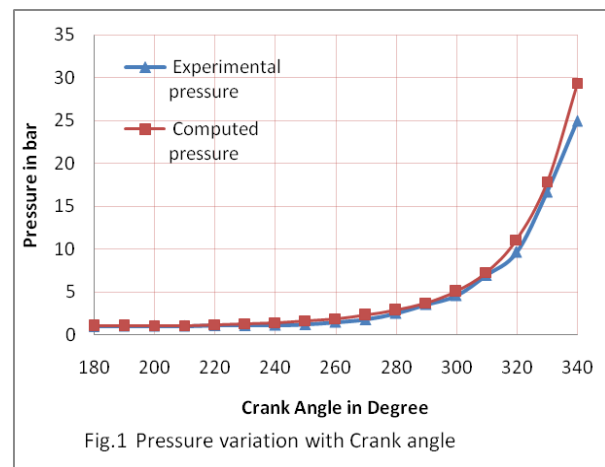


Fig-2 shows variation of polytropic index with gas concentration at full load. In the experimental analysis LPG flow rate was varied from 0.2kg/hr up to 0.8 kg/hr. Corresponding gas concentration in the inlet mixture can be obtained on mass basis. It was found that Polytropic index of compression do not vary significantly with load but decreases with increase in LPG flow rate.

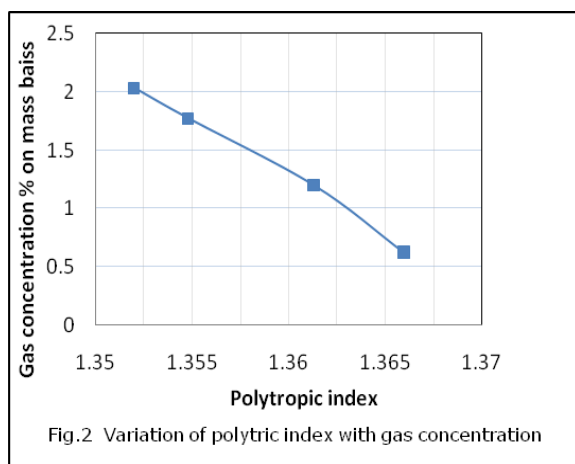


Fig.3 shows the variation of adiabatic index of compression with crank angle. As the compression proceeds it decreases both for normal diesel engine as well as for dual fuel engine. For dual fuel engine adiabatic index of compression is less than that for normal diesel engine. During the start of compression rate of decrease in C_p and C_v are less as compared to the change near to the end. Hence change in adiabatic index is more prominent nearly at the end compression.

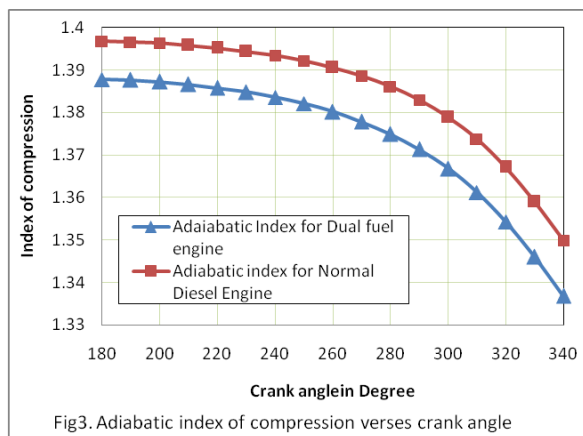
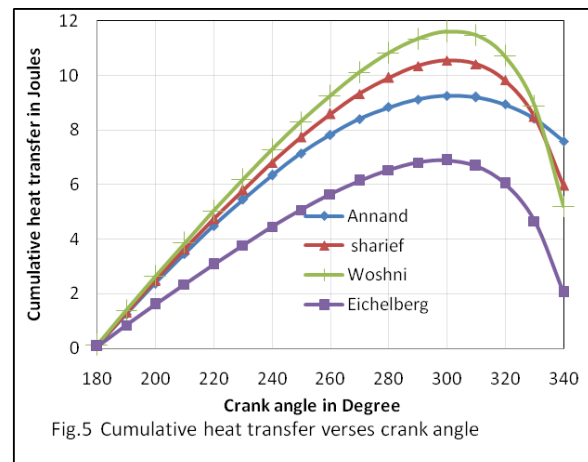
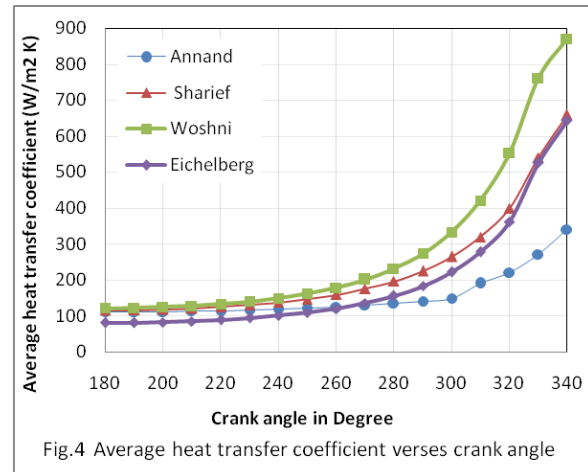


Fig.4 shows heat transfer coefficient variation with crank angle using different correlations. Sharief and Eichelberg equations give fairly good results as compared to Annand and Woshni equations. Anand equation predicts almost uniform heat transfer coefficient for the compression process and in case of Woshni equation variation is substantial nearly at the end of compression.

Fig.5 shows the variation of cumulative heat transfer with crank angle based on

different heat transfer correlations. It is clear that except Eichelberg equation all other three equations give almost same net heat transfer at the end of compression process.



Conclusions

Thus the final conclusion from the experiments and computation are;

1. The polytropic index of compression obtained is around 1.35 which is close to the value 1.36 suggested by Hardenberg & Hase.
2. At full load as the LPG flow rate increases gas concentration increases and index of compression decreases.
3. In all the correlations heat transfer direction changes from gas to the wall at about 50-55° before the top dead center during compression.

4. Predicted cumulative heat transfer at the end of compression process is much less in case of Eichelberg equation as compared to other equations.
5. Cumulative work of compression at the end is almost the same irrespective of heat transfer correlations used.

Nomenclature

- r - Crank radius (m)
CRL - Connecting rod length (m)
VC - Clearance volume (m^3)
AP - Cross section area of the piston (m^2)
D - Bore diameter (m)
L - Stroke length (m)
N - Engine speed (rpm)
C - Clearance height (m)
T - Temperature (K)
 Θ - Crank angle (deg)
n - Polytropic index of compression
 V_j - Intake jet velocity (m/s)
 C_p - Specific heat at constant pressure (kJ/kg K)
 C_v - Specific heat at constant volume (kJ/kg K)
h - Heat transfer coefficient in (W/m^2K)
R - Gas constant (kJ/kg K)

Subscript

- h - Cylinder head
l - Cylinder liner
p - Piston head
st - Stoichiometric

References

1. Abdul Sharief, A.J.Antony 'Study of Heat Transfer Correlation in Compression Ignition Engine' International Conference & Exhibition on Total Engineering, Analysis & Manufacturing Technologies" Team Tech- 2007, at IISc Bangalore, Karnataka India, October 2007
2. Andrei Makartchouk, 'Diesel Engineering Engineering' Markel Dekker Inc. New York- Basel.
3. B.S. Samaga and B.S Murthy, 'Some studies on Distribution of Heat losses in a S I Engine cycle' Journal of Institute of Engineers (India) Vol 56, May 1976.
4. Colin R. Ferguson – Internal combustion engines- Applied thermal sciences, 2nd Edition john Wiley & Sons. Inc
5. Liu, Z. and Karim, G.A., 'Simulation of Combustion Processes in Gas- Fueled Diesel Engines' Proceeding of Institution of Mechanical Engineers Vol. 211, Part A, 1997.
6. Mc. Aulay, K.J. et al, 'Development and Evaluation of the Simulation of the Compression Ignition Engine.' SAE Paper 650451, 1965
7. Prakash, G., Ramesh, A, and Anwar Basha Shaik, 'An Approach for Estimation of Ignition Delay in a Dual fuel Engine' SAE paper 1999-01-0232 p399.
8. Shrinivasa Rao B.R, Samaga B.S., Mohanan P (2005). Combustion Studies on a LPG-Diesel Dual Fuel Engine. *Proceedings of the 19th National Conference on I.C. Engine and Combustion*, Chidambaram. pp.125 -130
9. Taylor and Taylor, 'The Internal Combustion Engines.'
10. W J D Annand. 'Heat transfer in the cylinder of the reciprocating internal combustion engines' Proceedings of the Institute of Mechanical engineers, London, Vol- 177, 1963 p973.

Development of Combustor for Mixed Combustion Biomass with Waste Oil

MASATO URASHIMA ¹

SHUICHI TORII ²

¹ Department of Mechanical System Engineering, Kumamoto University, Kurokami,
2-39-1, Kumamoto 860-8555, Japan. e-mail:092d8511@st.kumamoto-u.ac.jp

² Department of Mechanical System Engineering, Kumamoto University, Kurokami,
2-39-1, Kumamoto 860-8555, Japan. e-mail:torii@mech.kumamoto-u.ac.jp

Abstract: In general, biomass is a renewable energy source because the energy that it contains comes from the sun. One of sources of biomass is municipal solid waste. The final goal of the study is to develop the combustor for the micro gas-turbine using the biomass as a fuel. Here, it is very important to remove big ashes in the gas because its affects the strength of the turbine blade. The aim of the present study is to observe the combustion phenomena relevant to a mixture of waste fluid and waste oil. Emphasis is placed on the ash size which is produced from the combustion chamber developed here.

Keywords: Mixed Combustion, Ash remove

INTRODUCTION

Biomass is a renewable energy source because the energy that it contains comes from the sun. Through the process of photosynthesis, chlorophyll in plants captures the sun's energy by converting carbon dioxide from the air and water from the ground into carbohydrates, complex compounds composed of carbon, hydrogen, and oxygen. When these carbohydrates are burned, they turn back into carbon dioxide, a greenhouse gas, and water and release the sun's energy they contain. This is because when biomass crops are grown, a nearly equivalent amount of carbon dioxide is captured through photosynthesis.

One of sources of biomass is called municipal solid waste. Trash that comes from plant or animal products are also biomass. Food scraps, lawn clippings, and leaves are all examples of biomass trash. Municipal solid waste can be a source of energy by either burning it in waste-to-energy plants, or by capturing biogas.

Waste oil includes used crankcase oils from automobiles and trucks, used industrial lubricating oils (such as metal working oils), and other used industrial oils (such as heat transfer fluids). When discarded, these oils become waste oils due to a breakdown of physical properties and contamination. The different types of waste oils may be burned as mixtures or

as single fuels where supplies allow. Waste, or used, oil can be burned in a variety of combustion systems. The aim of the present study is to develop the combustor for a micro gas turbine by using biomass such as pig excrement with waste oil. And removing large ashes (10 μm in diameter) from exhaust gas is necessary. As the first step, the experimental study is performed on the optimum conditions so as to remove ashes, to attain stable continuous combustion, and to measure emission gas.

EXPERIMENTAL APPRATUS

The experimental apparatus consists of the combustion chamber and the fuel injection device. Fig. 1 shows the combustion chamber which is the shape of the cyclonic separator capable to remove large particle, i.e., combustion ashes contained in combustion gas. The combustion gases which are injected from the inlet port of combustion chamber, flow along the inner side-wall of the chamber and exit from outlet port. While it passes along chamber, big particles are separated by difference of centrifugal force from combustion gas. And thermo couples are set in shown point in Fig. 1.

Fig. 2 depicts the fuel injection device which consists of two tanks and injection nozzle. Two tanks include biomass and waste oil, respectively, and are pushed at high pressure air. At the same time a

mixture of biomass, waste oil and air is injected through the nozzle. Note that this nozzle has special construction nature that causes spiral injection flow.

Fig. 3 illustrates a joint part between the combustion chamber and the fuel injection device. Here, a left-side of the figure is the fuel injection nozzle and the opposite one is combustion chamber's inlet port. The mixture of biomass and waste oil are injected from the injection nozzle and is ignited by the ignition which is installed in the joint part. Note that the joint part is made of a quartz-glass pipe for observation. In order to measure the combustion gas temperature, K-type thermocouples are employed near here.

The fuel injected from the nozzle are ignited by a burner at joint part, and combustion starts and it is maintained also inside the chamber. Therefore, while it passes along the chamber, ashy separation and combustion occur simultaneously.

Notice that the tank and nozzle are maintained at 353K using heater in case of pyrolysis oil. This is because pyrolysis's viscosity used here as the fuel is too high to flow at room temperature [2]. In order to catch combustion ashes, paper seat is attached in outlet of chamber. The combustion gas are injected from outlet to paper seat, and the ash are adhered. The size of ash are measured by microscope. In the present study, pig excrement are used as biomass, and heavy oil A or pyrolysis oil are used as waste oil.

In order to catch combustion ashes, paper seat is attached in outlet of chamber. The combustion gas are injected from outlet to paper seat, and the ash are adhered. The size of ash are measured by microscope.

An uncertainty analysis [3] yields the following results: the uncertainty interval for the flow rates of waste liquid and waste oil is estimated to be 2.5% and the corresponding value of the flame temperature is 2.0%. The average relative uncertainty in flame temperature is in the range of 3.0%.

RESULTS AND DISCUSSION

Fig. 4 and Fig. 5 show time history of combustion gas temperature in the chamber about mixed combustion of heavy oil A with pig excrement. From Fig. 4 Fig.5, in the case of heavy oil and pig excrement,

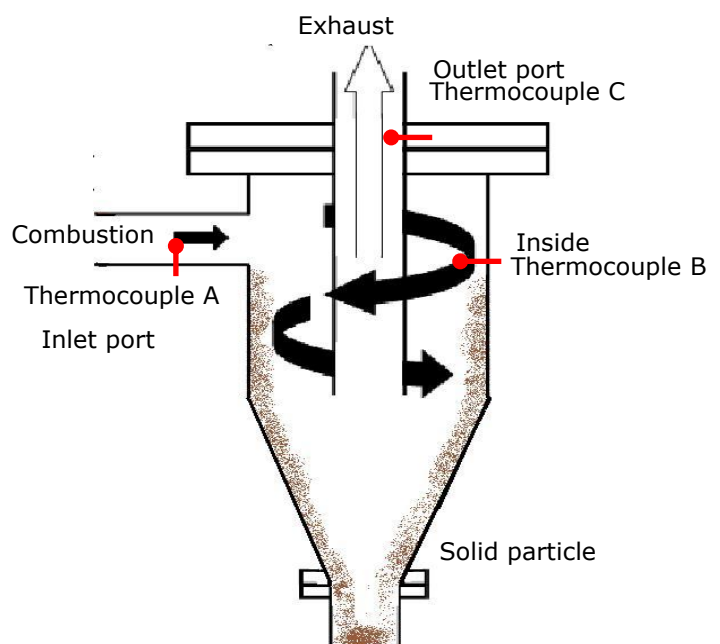


Fig.1 Schematic of the chamber

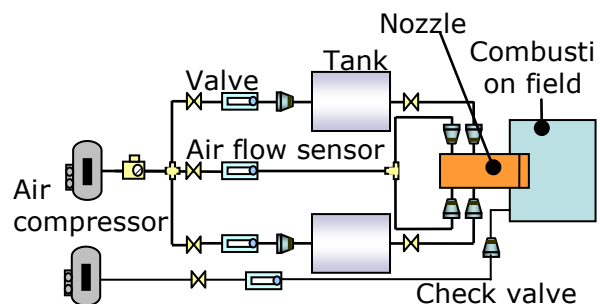


Fig.2 Mimetic diagram of fuel injection device

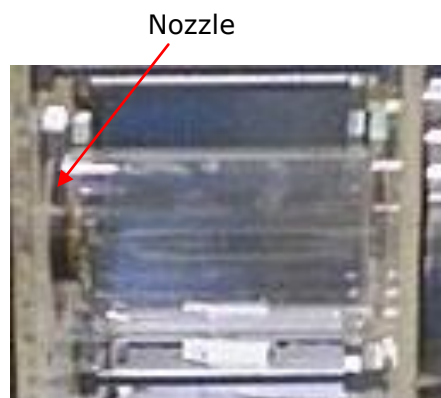


Fig.3 Joint of experimental apparatus

the combustion continue long time, and the outlet temperature were increasing while burning and reach to over 450 [K]. And these combustion continue until tank become empty.

On the other hand, Fig. 6 show time history of combustion gas temperature about mixed combustion of pyrolysis oil with pig excrement. However, in this case, combustion time are not long.

The ash size distribution at the exit of the combustion chamber, at 190 of air-to-oil ratio, is depicted in Fig. 7 in the form of the particle size versus the number of particle. Based on this distribution, the largest ash sizes are summarized in Fig. 8 and Fig.9 for the ratio of air and oil. Here, Pyrolysis oil and swine urine are used as waste oil and waste liquid, respectively. One observes that a larger ash particle size over 10 μm is substantially removed from the exhaust gas and the maximum ash size is attenuated with an increase in the air-to-oil ratio because the perfect combustion is attained in the combustion chamber at higher air-to-oil ratio.

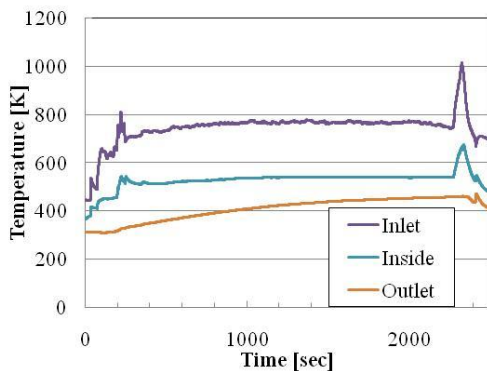


Fig.4 Time history of temperature heavy oil A with pig excrement (a)

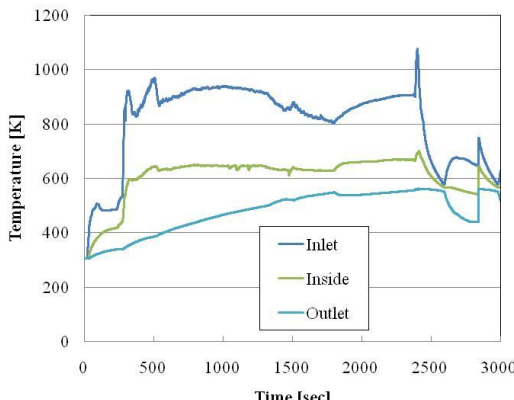


Fig.5 Time history of temperature heavy oil A with pig excrement (b)

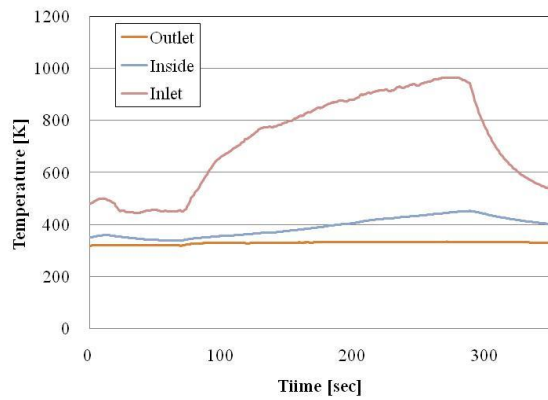


Fig.6 Time history of temperature Pyrolysis oil with pig excrement

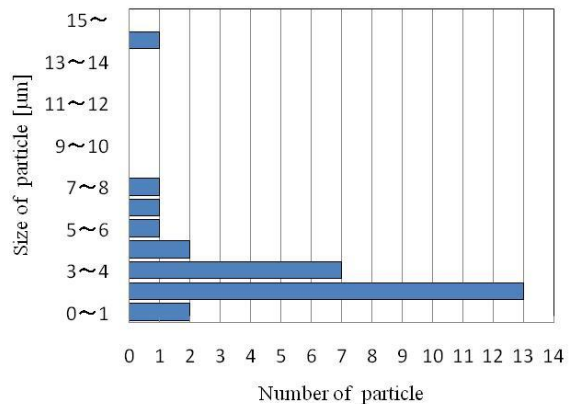


Fig.7 Ash particle size distribution

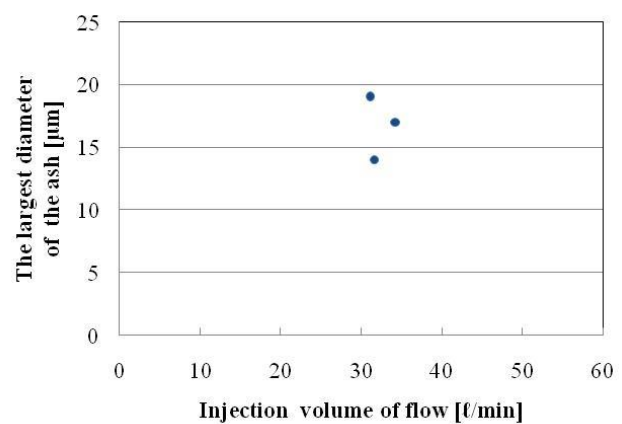


Fig.8 Maximum ash particle sizes in the case of heavy oil A with pig excrement

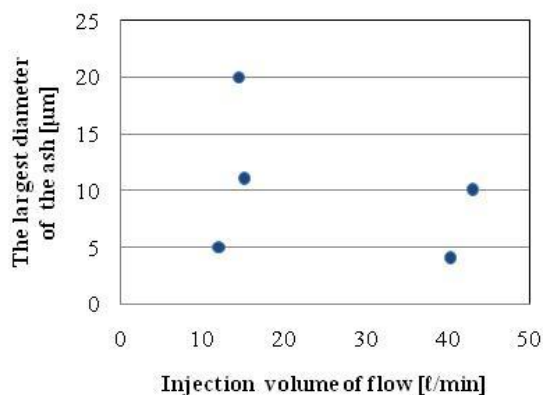


Fig.9 Maximum ash particle sizes in the case of pyrolysis oil with pig excrement

Conclusions

The following conclusions are deduced from the experimental results:

- The combustor of this study can continue mixed combustion for the purpose in the case of heavy oil A with pig excrement.
- The chamber of this study can remove large ash, and some case are enough to apply.

References

- [1] Hideaki Tatibana, Misao Shioya, Keiji Wakai, Masaaki Fukushima, Technical development and future expectation of the pyrolysis for municipal post-use plastics (Journal of the japan institute of energy, 2007).
- [2] Akira Ogawa, Ensishinbunriki(1980)
- [3] Kline, S.J. and McClintock, F.A., 1953, Describing Uncertainties in Single-Sample Experiments, Mechanical Engineering, 75

Design and Analysis of Air flow Control Mechanism of Automotive HVAC module using CAE tools

DALJEET SINGH

Department of Mechanical Engineering, Thapar University, Patiala-147004, Punjab, India. e-mail:daljeet.singh@thapar.edu

Abstract: With the automotive air-conditioning industry aiming at higher levels of quality, cost effectiveness and a short time to market, the need for simulation is at an all time high. In this paper, the use of CAD tools and the multibody dynamics approach is proposed in the design, simulation and analysis of the airflow control mechanisms of an automotive HVAC module for opening various doors/dampers used for passenger comfort. Various steps involved in the design and analysis have been explained in detail. The movements of various parts have been analyzed using the animation in HyperView 8.0. The other important outputs include the displacement and torque graphs plotted with the use of HyperGraph 8.0. The results from the analysis have been used for comparison between the benchmark data and the new design. The new design has been improved after this study.

Keywords: HVAC, Kinematics Analysis, Mechanism Design, Air Flow Control

1. INTRODUCTION

An automotive air-conditioning system has an HVAC module mounted on the firewall of the vehicle. The HVAC module consists of various parts like heater, evaporator, blower, doors/dampers, levers, cams, etc. All these parts are placed in plastic cases, and the final assembly is mounted in the vehicle. The air blown by the blower passes through the evaporator and/or the heater located inside the HVAC module and is thus cooled and/or heated up accordingly. There are openings provided in the cases for airflow in various modes. Five different modes are face, foot, bi-level (face/foot), defrost and foot/defrost. The HVAC module has a mechanism consisting of various links and a cam responsible for controlling the air flow going through

these modes to the passenger cabin. The calculation of displacement and torque for these modes is a major challenge while designing the kinematics mechanism for an HVAC module. The torque required to operate the cam should not be very high, as this would lead to passenger discomfort

while using the various knobs on the control panel in the vehicle. In this paper, an approach for achieving these objectives has been discussed. Benchmarking has been done with an existing vehicle, which is referred to as "Vehicle A" here, and the results have been compared with those of the new design ("Vehicle B"). The desired output levels have been achieved with suitable modifications. The HVAC module parts considered for the analysis are as follows, as shown in Fig. 1.

- Cam
- Levers
- Foot damper
- Face damper
- Defrost/demist damper

Altair HyperMesh [1] software has been used for discretization of the domain, Motionview and Hyperview for building the model and viewing the animation respectively. Hypergraph has been used for plotting the graphs.

2. PROCESS METHODOLOGY

In this section, the HVAC mechanism design methodology required to prepare the problem for kinematics analysis followed by the details of the kinematics analysis is described.

2.1 Problem Setup for the Kinematics Analysis

Some of the details of the background information needed for the kinematics analysis, conducted for the HVAC module of a benchmark vehicle A using Altair HyperWorks 8.0 software is briefly summarized now.

The complete design and analysis cycle requires: (1) design of internal parts of HVAC module such as dampers, plastic cases, etc. (2) CFD analysis for damper angle design, and (3) kinematics design of HVAC mechanism. The following are the major steps for the design and analysis of the HVAC mechanism.

1. The layout design of all the internal HVAC parts is done. This is based on the packaging space available in the vehicle, and the A/C system selection based on the heat load calculations.
2. Based upon this, the location, layout and design of dampers are finalized.
3. The customer data for air flow distribution is studied. This data and the CAD parts (HVAC cases and dampers) are given for CFD analysis, which provides the damper angles for proper air flow in various modes.
4. Based on the CFD input, the damper angles are finalized and the other parts like levers, cam, rods, etc. are designed.
5. HyperWorks is used for calculation of displacement and torque values required to operate the kinematics parts, and the results are compared with the benchmark data for the validation of design.
6. In order to fine-tune the model, modifications are done, and the rapid prototype (RPT) is made and validated, by checking the actual air flow distribution on RPT.

2.1.1 Cam Design

In the design of the kinematics mechanism, cam design is a very important and crucial step. A procedure to do so for one of the modes is discussed here. In the beginning, a skeleton diagram is drawn, which is based on the CFD results. This diagram is a plot between the damper/door angles and the cam rotation angles, for the various modes. The diagrams for the foot and the face modes for a vehicle A, are shown in fig.2 and fig.3, respectively.

The steps for making the face profile in the cam are described below:

1. Join O to S.
2. Rotate OS by 36 deg (23 deg + 13 deg), to the new position OS'.
3. From S', draw arc at 23 deg (position S").
4. Join S" to E.
5. Now, we get S'S"E.
6. Rotate S'S"E by 34 deg(70 deg - 36 deg).
7. Join E' to E by arc (the last idle portion) and get the complete segment S'"E'E.
8. Rotate the complete segment, made above by 70 deg., and bring to start position, to get the final profile.

The profile made above is cut in the cam of the kinematics mechanism. The pins, which are fixed inside the levers (shown in fig.1), move along the surface of these grooves inside the cam. The lever is further fixed to the door/damper, and thus the rotation of the cam rotates the doors with the help of the intermediate levers in the mechanism.

2.2 Kinematics Analysis

The details of the kinematics analysis done for the HVAC mechanism are discussed in this section. The following inputs are used to create the model in MotionView 8.0,

- CAD model of the assembly
- Material properties
- Inertial properties of the various parts in the mechanism

- Information on the motion of the cam

The following steps are used to create the MV (MotionView) model, conduct the analysis and generate the results for the HVAC mechanism.

- Discretization of the CAD geometry in HyperMesh 8.0
- Creation of graphic H3D file for representing graphics and contacts in MV
- Pre-processing in MV
- Solution
- Post processing

The discretization of CAD geometry, creation of graphic H3D files, pre-processing and solution are briefly summarized below.

2.2.1 Discretization of CAD Geometry

The CAD parts in the assembly are imported in HM (HyperMesh) in the IGES (Initial Graphics Exchange Specification) format. The different parts are meshed in HM using triangular elements. A fine mesh is used for the contact surfaces (Fig. 5), which are placed in a different collector/group, and the rest of the surfaces are meshed coarse. The direction of the normal vectors of the elements used in contacts is of particular importance. The normal vectors of the surfaces coming in contact should face each other.

2.2.2 Creation of Graphic H3D files

In MotionView 8.0 [2], the tool for H3D file creation is used (see Fig. 6) to make the H3D files for different parts, which are later used to attach graphics to bodies during model build up.

2.2.3 Pre-Processing in MotionView 8.0

- Points and Bodies: Points are defined at the center of gravity (cg) locations and joint locations of various parts involved as shown in Fig. 7. Bodies are defined at cg locations using the mass and inertia properties extracted from the CAD software.

- Joints: Spherical (Ball) Joints are provided at the bearing locations where the dampers are supported. These locations are extracted from HyperMesh. Fixed joints are defined to attach the levers to the dampers. A revolute joint is provided at the cam centre to facilitate the rotation of the cam.
- Contacts: Contacts are defined between the cam slots and the portion of the lever pin outer surface as shown in Fig. 5. A suitable value of penalty (3000) and restitution coefficient (0.05) is given for the contacts. Friction is not taken into consideration, as it increases the complexity of the model and thus, the solver time. The level of correlation achieved is sufficient for the present study, as the values in the plots are matching those in the benchmark data.

- Motion: A rotational motion of 10 degrees per second is defined at the cam revolute joint, using the expression "10D*TIME".
- Outputs: Outputs are defined for the cam rotation, damper rotation and the torque required to operate the cam.

2.2.4 Solution

The solver (MotionSolve) is run for an end time of 7s, using the ABAM integrator type, and the outputs obtained are plotted using HyperGraph from the HyperWorks 8.0 suite. The workstation used for the analysis has 2047 MB RAM, and a CPU speed of 3400 MHz.

3. RESULTS AND DISCUSSION

The following outputs are obtained for the foot mode of HVAC kinematics of Vehicle A: (a) damper rotation as a function of cam rotation, and (b) torque as a function of cam rotation as shown in Fig. 8. The plot of damper rotation as a function of cam rotation in Fig. 8(a) shows that there is a gradual rotation of the damper because of the cam rotation. The value of

torque required is not very high as seen in Fig. 8(b). The spikes in the graph are due to inertial effects.

In a manner similar to above, MotionView analysis has been carried out for the mechanism of a new vehicle B. The CAD geometry which is used as an input for the analysis is shown Fig.10. Using the methodology described earlier, the analysis has been run and the outputs are obtained, as shown in Fig. 9. The plots shown in Fig. 6a reveal that for very little cam rotation, the damper rotation is large (see the left-hand side of the curve having a steep rise) which is undesirable. Also, as compared to the benchmark model, the torque observed is very high at the beginning and near the end of cam rotation in a cycle as shown in Fig. 6b. So, some modifications are needed in the design. After a few iterations, the configuration of the mechanism shown in Fig. 11 has been reached. In the modified design, to reduce the torque required, a two-link configuration has been used instead of the one-link arrangement used earlier.

The cam slots are also made smoother, i.e., without any sharp edges so that there is no obstruction to the movement of the pins inside those slots. As seen in Fig. 12b, the torque required to operate the cam is significantly less than the previous design. Some fine tuning has been done in the final prototype to take care of the higher torque shown by the spike at the end of the graph. The displacement plot (Fig. 12a) shows that the shape of the curve is closer to that of the benchmark design. The curve is obtained for 60 degree rotation of the cam, as the cam slot portion at the end is similar to that at the start.

4. CONCLUSIONS AND SUMMARY

A new method for design validation of HVAC mechanisms has been proposed in this paper. The kinematics analysis has been done for an existing design using Altair HyperWorks 8.0. The same is done for the mechanism of a new vehicle, and the results are compared with the benchmark data. Based on the analysis, the torque value in the new design was

found to be higher. It was also found that the single lever configuration used in the new design led to higher torque requirement. Since, the profile of the slots in the cam has sharp edges, some modifications have been made, considering these points; and the analysis has been redone. The torque value required is reduced significantly, and the displacement graph is also closer to the benchmark data, thus yielding the good design for the application, i.e. smoother rotations with low effort level to rotate levers from the control panel.

With the use of the above approach, (1) a proper design of kinematics of linkages/damper movement has been arrived with acceptable forces applied for various damper movements; (2) there is a significant cost saving as the number of physical prototypes required to be made is reduced.

ACKNOWLEDGEMENTS

I express my gratitude to Dr. R.K. Shah, Executive Adviser, R&D, Subros Ltd., Noida, for discerning valuable comments on this paper. I thank Mr. D.M. Mani, Head, R&D, for his support during the execution of the project. The background information for the problem set up for kinematics analysis has been provided by Mr. Sanjay Batra, Manager, R&D. The staff at Subros and Altair India has provided the much needed support for the completion of this work. I would also like to thank Dr. S.K. Mohapatra, Dean, Academic Affairs, and Dr. Ajay Batish, Head, Mechanical Engineering Department, Thapar University, Patiala, for their able guidance and much needed support.

REFERENCES

- [1] Altair HyperMesh, Version 8.0, Altair Engineering.
- [2] Altair MotionView, Version 8.0, Altair Engineering.

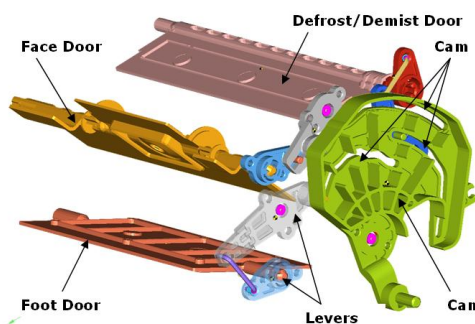


Fig. 1 HVAC mechanism for Vehicle A

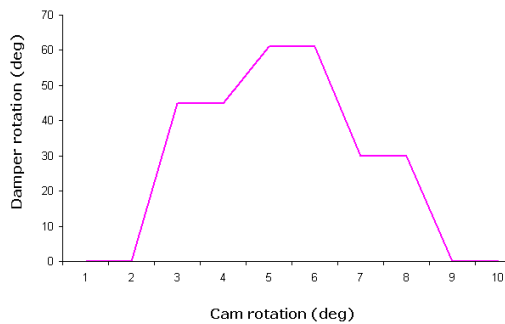


Fig. 2 Foot mode plot

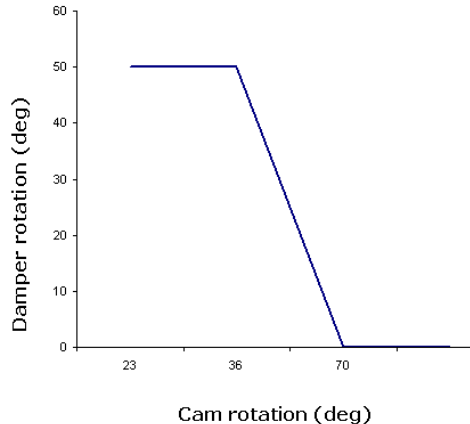


Fig. 3 Face mode plot

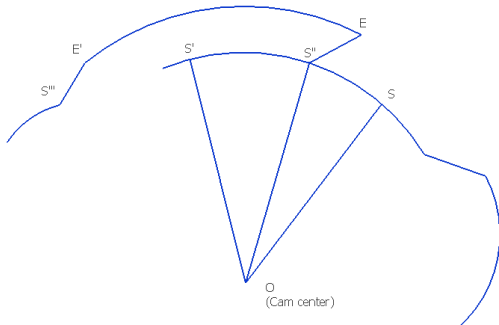


Fig. 4 Steps to make face profile in the cam

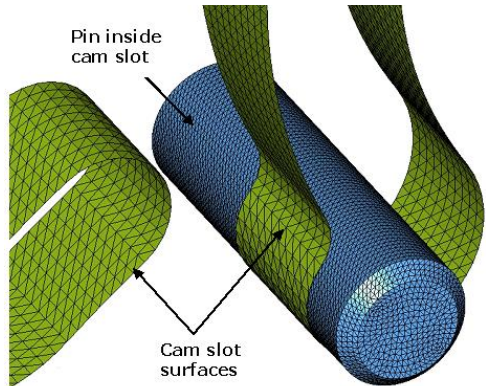


Fig. 5 Fine mesh used at contact locations

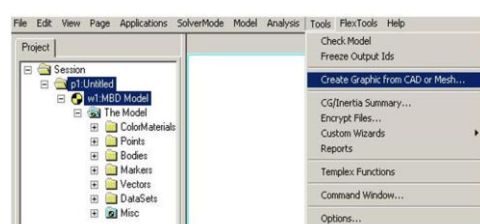


Fig. 6 Tool used for creating Graphic H3D file

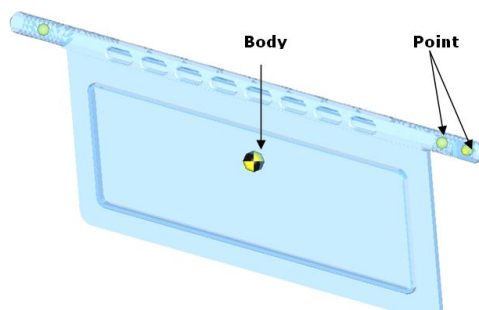


Fig. 7 Points and bodies created in MotionView

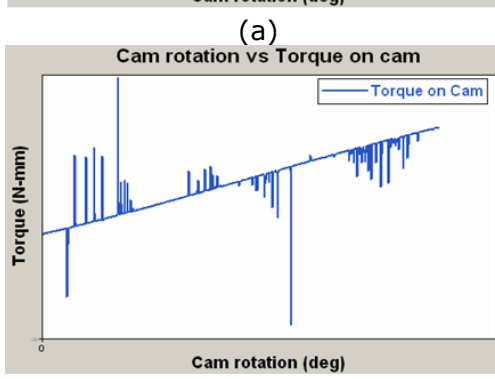
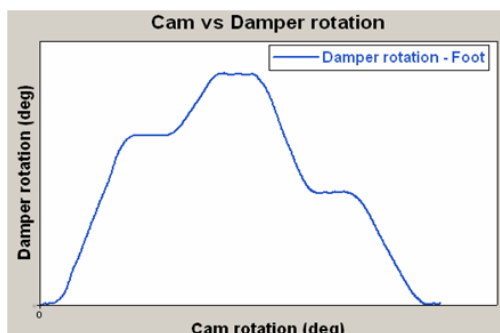


Fig. 8 Graphs of displacement and torque for Vehicle A

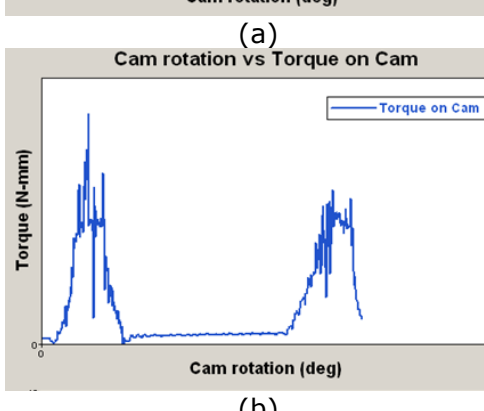
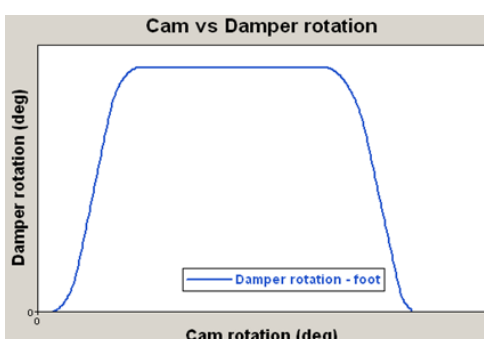


Fig. 9 Graphs of displacement and torque for Vehicle B

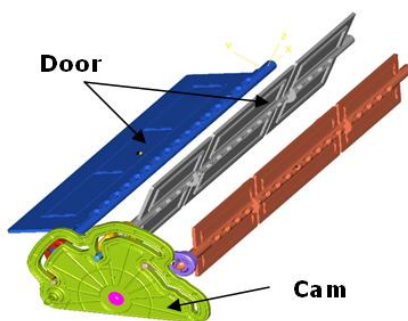


Fig. 10 HVAC mechanism of Vehicle B

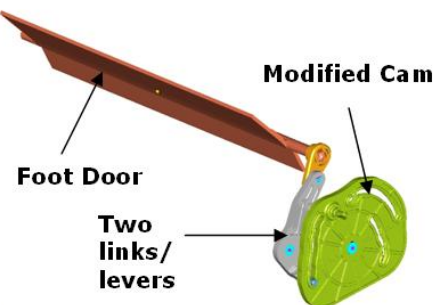


Fig. 11 Modified mechanism of Vehicle B

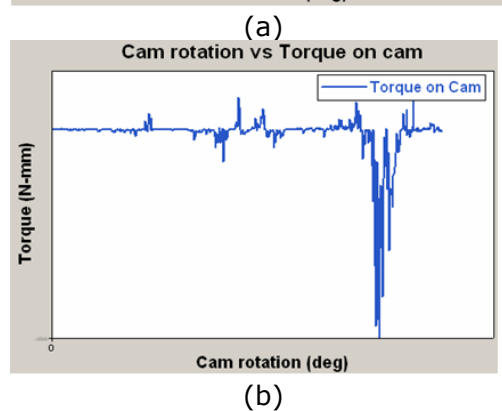
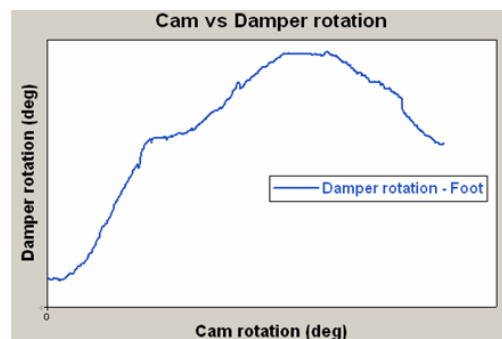


Fig. 12 Graphs obtained for the modified model of Vehicle B

Numerical Analysis of Flow through Abrasive Water Suspension Jet: The Effect of Abrasive Grain size and Jet Diameter Ratio on Wall Shear

Deepak D¹

N. Yagnesh Sharma²

and

Anjaiah D³

1 Dept of Mechanical and Manufacturing Engg, Manipal Institute of Technology, Manipal University, Manipal-576104, Karnataka, India. e-mail:nie.deepak@gmail.com

2 Dept of Mechanical and Manufacturing Engg, Manipal Institute of Technology, Manipal University, Manipal-576104, Karnataka, India. e-mail:nysharma@hotmail.com

3 Dept of Mechanical and Manufacturing Engg, Manipal Institute of Technology, Manipal University, Manipal-576104, Karnataka, India. e-mail:anjaiah.d@manipal.edu

Abstract: It is well known that the diameter of the nozzle as well as the particle size of the abrasive materials have significant effect on the erosion characteristics of the inside surface in the nozzle. Abrasive particles moving with the flow causes severe wall shear, thereby altering the nozzle diameter due to wear which in turn influences the exit flow velocity characteristics. This will reflect on the life of the nozzle for effective machining. In consideration of this aspect, in the present work, not only the effect of particle size on the wall shear is considered and analysed, but also the effect of diameter ratio of the nozzle itself on the wall shear is examined. It is found from the analysis that an increase in diameter ratio results in significant decrease in the wall shear stress. Also an increase in the abrasive particle size results in perceptible decrease in the wall shear stress.

Keywords: Abrasive Water Suspension Jet, Jet Diameter Ratio, Abrasives Grain size, Wall Shear

1 Introduction

Advances in engineering materials and product design require the development of non-traditional machining processes. Components with complex shapes that need to be produced from harder and difficult-to-machine materials can now be machined by a relatively recent non-traditional method called Abrasive Water Jet (AWJ) Machining which is developed over last two decades. Abrasive water suspension jet (AWSJ) is one of variants of Abrasive water jet machining where abrasives are premixed with a suspended liquid to form slurry. The slurry is pressurized and expelled through a nozzle in AWSJ process. Advantages of AWSJ over AWJ are higher power density, no jet expansion and efficient energy transfer to abrasive particles (D. Anjaiah et. al, 2003 and T. Nguyen et. al 2003). An AWSJ can effectively machine delicate materials because of the relatively small cutting forces and lesser heat dissipation. Through

computer numerical control attachment, it is possible to cut complex profiles with good surface quality and precision using AWSJ (M. Hashish, 1994).

The typical character of flow through the AWSJ, results in rapid wear of the nozzle and degrades the cutting performance. Nozzle replacement costs play a significant role in the economics of the process and improvements in its wear characteristics are critical for the growth of AWSJ technology (M.Nanduri et.al, 2002). A host of articles are available on both the experimental and numerical aspects of flow through the AWSJ nozzle (Z. Shangxian et. al, 2010, L.J.Graham et. al, 2003 and A.C. Phase et. al, 2008). Recently with the development of CFD general purpose code it has become possible to model and simulate the flow through the AWSJ nozzle.

In the present work, the diameter ratio of the nozzle and particle size of the abrasive material are taken in a parametric way to assess the effect of the same on the wall shear stress produced on the inside nozzle surface. It is to be understood that due to relatively high pressure used, in the order of 60 MPa, the jet velocity correspondingly is quite high. The abrasive particles moving with the flow cause severe wall shear thereby altering both the nozzle diameter and the exit flow velocity. This will reflect on the life of the nozzle for effective machining. In consideration of this aspect, in the present work not only the effect of particle size on the wall shear is considered and analysed but also the effect of diameter ratio of the nozzle itself on the wall shear is examined.

Nomenclature

d	Focus tube diameter
D	Diameter of jet
L	Lift force
E	External body force
V	Virtual mass force
K	Momentum exchange co-efficient
\dot{m}	Mass flow rate of mixture m^3/s
u	Velocity of jet m/s
ϕ	Volume fraction of the phase
ρ	Density of suspension mixture kg/m^3
d_p	Diameter of abrasive particles

Subscripts

p, q	phases
l	liquid phase
s	solid phase

2 Theoretical formulations

2.1 Problem statement and assumptions

The flow domain consists of a nozzle connected to the focus tube as shown in Fig 1. Abrasive water suspension mixture is supplied at the inlet of the nozzle. Based on experimental observation on liquid-solid (two-phase) flow in the jet, the following assumptions are made.

- (1) Water is a continuous medium and incompressible.
- (2) Flow is considered as two phase flow mixture in which water is the liquid phase and abrasives of equal diameter constitute

the solid phase, but well mixed with the liquid phase.

- (3) There is no mass transfer between the two phases.
- (4) Two-phase flow is steady and possesses turbulent flow characteristics.

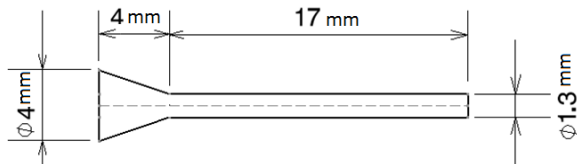


Fig.1: Geometry of the AWSJ nozzle

2.2 Numerical model

Numerical simulation was carried out using Eulerian multiphase model which is in built in the commercially available software. The governing partial differential equations, for mass and momentum are solved for the steady incompressible flow. The velocity-pressure coupling has been effected through the phase coupled SIMPLE algorithm (Semi Implicit Method For Pressure-Linked Equations) developed by Patankar s.v et.al (1972). First order upwind discretization scheme was chosen for the convective terms. Turbulence is modelled using standard k- ϵ turbulence model as the preferred model. The simulated results are more accurate for the high Reynolds number flow as occurs in the present study.

2.2.1 Continuity equation

The volume fraction of each phase is calculated from the continuity equation:

$$\frac{1}{\rho_{rq}} \left(\frac{\partial}{\partial t} (\alpha_q \rho_q) + \nabla \cdot (\alpha_q \rho_q \mathbf{v}_q) \right) = \sum_{p=1}^n (\mathbf{m}_{pq} - \mathbf{m}_{qp}) \quad (1)$$

2.2.2 Fluid-Solid momentum equation

Fluent uses a multi-fluid granular model to describe the flow behaviour of a fluid-solid mixture. The solid phase stresses are derived by making an analogy between the random particle motion arising from particle-particle collisions and the thermal motion of molecules in a fluid, taking into account of inelasticity of the granular phase. Intensity of the particle velocity fluctuations determines the stresses,

viscosity and pressure of the solid phase. The kinetic energy associated with the particle velocity fluctuations is represented

by granular temperature which is proportional to the mean square of the random motion of particles (Fluent).

The conservation of momentum equation for the solid phase is as follows.

$$\begin{aligned} \frac{\partial}{\partial t} (\alpha_s \rho_s v_s) + \nabla \cdot (\alpha_s \rho_s v_s v_s) = \\ - \alpha_s \nabla p - \nabla p_s + \nabla \cdot \tau_s + \alpha_s \rho_s g \\ + \sum_{l=1}^N (k_{ls} (v_l - v_s) + (m_{ls} v_{ls} - m_{sl} v_{sl})) \\ + (F_s + F_{lift,s} + F_{vm,s}) \end{aligned} \quad (2)$$

The conservation of momentum equation for the fluid phase is as follows.

$$\begin{aligned} \frac{\partial}{\partial t} (\alpha_q \rho_q v_q) + \nabla \cdot (\alpha_q \rho_q v_q v_q) = \\ - \alpha_q \nabla p + \nabla \cdot \tau_q + \alpha_q \rho_s g \\ + \sum_{p=1}^N (k_{pq} (v_p - v_q) + (m_{pq} v_{pq} - m_{qp} v_{qp})) \\ + (F_q + F_{lift,q} + F_{vm,q}) \end{aligned} \quad (3)$$

3 Method of solution

3.1 Numerical scheme

The particles were assumed to be spherical and uniformly distributed in the suspension mixture.

Conservation equations were solved for each control volume to yield the velocity and pressure fields. Convergence was effected when all the residuals fell below 1.0E-5 at all control volume in the computational domain.

Computational domain was modelled using the pre-processor routine called GAMBIT and meshing was also done using appropriate grid cells of suitable size available in the routine. Wall region in the flow domain were fine meshed using the

boundary layer mesh concepts for extracting high velocity gradients near the

boundary walls. According to the structure

of nozzle and jet characteristics, computational domain is built as axis-symmetric model. The solution domain consists of 8460 cells of Quad type.

The grid independence test was performed to check validity of the quality of mesh on the solution. The influence of further refinement did not change the result by more than 1.25 % which is taken here as the appropriate mesh quality for computation.



Fig.2 Mesh of the computational domain

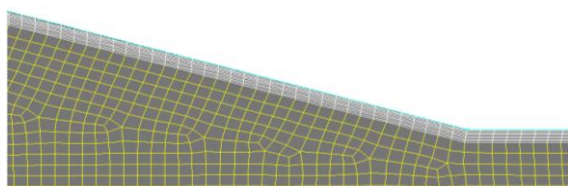


Fig.3 Closer view of the mesh near converging section

3.2 Boundary conditions and Operating parameters

Appropriate boundary conditions were impressed on the computational domain, as per the physics of the problem.

Inlet boundary condition was specified as velocity boundary condition. Average velocity of AWSJ at inlet was calculated using mass flux equation.

$$\dot{m}_{in} = 0.25 \rho \pi d^2 u \quad (4)$$

u is the inlet velocity of abrasive and water suspension mixture. The velocity distribution is considered as plug flow at inlet.

Pressure outlet boundary condition was applied at the outlet with static pressure of flow taken as zero, so that the computation would yield relative pressure differences for the entire domain of the flow.

Wall boundary conditions were used to bound fluid and solid regions. In viscous flow models, at the wall, velocity components were set to zero in accordance with the no-slip and impermeability conditions that exist there.

Center line of the nozzle is considered as axis of nozzle and hence symmetry boundary condition was applied at the axis.

In Numerical simulation, mixture of water and suspension liquid is treated as Phase I and abrasive as Phase II. The input parameters used in the analysis are as shown in the table 1 below.

Table 1. Input parameters
(G. Hu et.al, 2008)

Parameter	Set value
velocity of mixture	25.6m/s
Volume fraction	7%
Density - Phase I (Suspension Liquid)	998.2 kg/m ³
Density - Phase II (Garnet abrasive)	2300 kg/m ³
Viscosity - Phase I	0.001003kg/(m.s)
Viscosity - Phase II	1.7894e ⁻⁰⁵ kg/(m.s)
Size of abrasive	0.1mm
Slip of phases	no slip

4 Results and Discussion

4.1 Validation of the numerical model

To establish validation of the present model, the work of G.Hu et.al,(2008) was used to replicate the velocity distribution as obtained by them (Fig 4) with the existing numerical model adopted in this work (Fig 5).

The graph of the velocity distribution of one of the phases (Liquid phase) has been calibrated in the present work with that of the work cited in the literature as shown in Fig 4. It is clear that there is good agreement between the two models as regards to the velocity distribution.

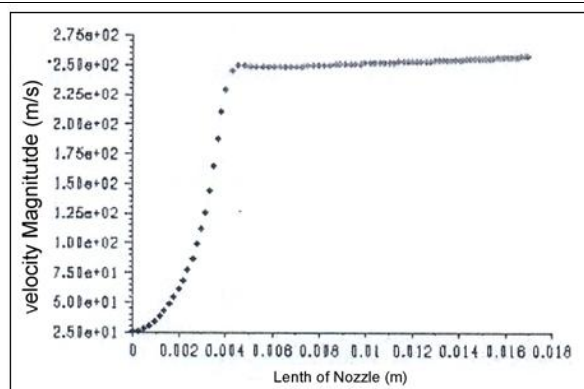


Fig 4. Plot of Velocity, G.Hu et.al,(2008).

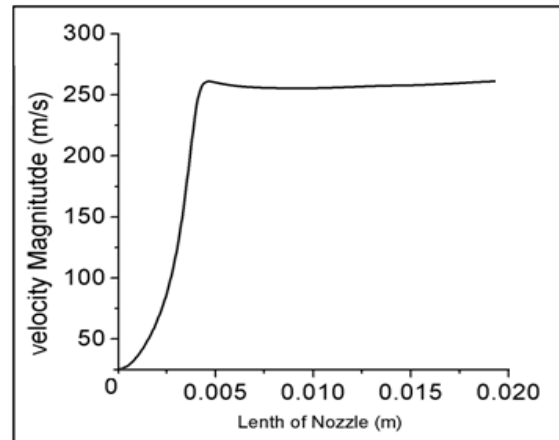


Fig 5. Plot of Velocity as per the present model

4.2 Effect of Diameter Ratio on wall shear stress:

The nozzle chosen for the analysis has entry diameter (D) of 4mm. The Focus diameter (d) is parametrically varied to get different diameter ratios to assess the impact of the diameter ratio on the wall shear stress in the nozzle. The diameter ratio is defined as the ratio of focus diameter to entry diameter.

It is clear from Fig. 6 that as the diameter ratio increases the wall shear stress shows significant decrease. This may be attributed to the fact that as the velocity of the jet decreases with increase in focus diameter of the nozzle, resulting in decrease in the velocity gradient near to the wall of the nozzle. This leads to lower wall shear stress.

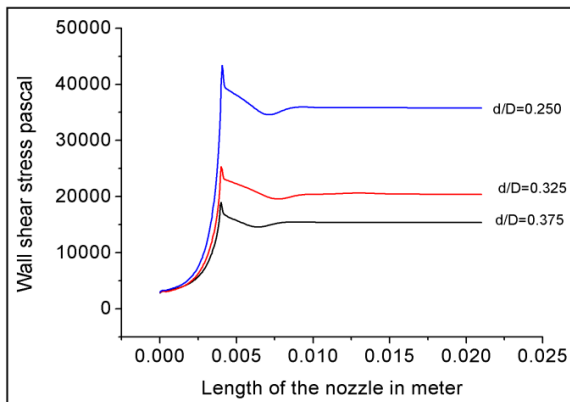


Fig 6. Wall shear stress along the nozzle length for different d/D ratio

Further, the Wall shear stress shows a peak near the point corresponding to the critical region where cross section changes from conical to straight length. This could be explained by the fact that a sudden velocity change caused due to a higher velocity gradient in the near wall region at the critical section, produces a peak in the wall shear stress at that region.

4.3 Effect of Particle Size on Wall Shear:

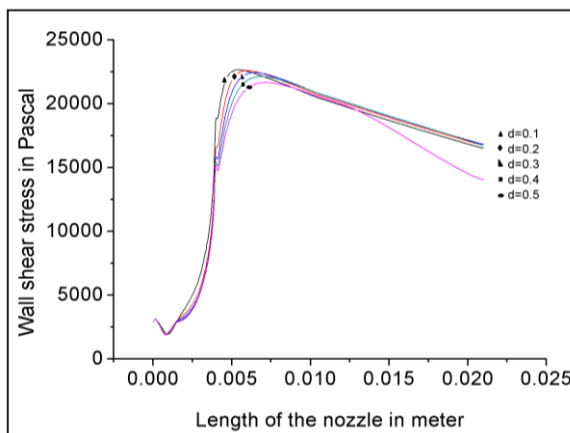


Fig 7. Wall shear stress along the nozzle length for abrasives of various diameters

It is observed from Fig. 7 that there is almost no variation in wall shear stress distribution except for the larger size particles corresponding to diameter from 0.4 to 0.5 mm. For the particles of finer diameter chosen, the inertial effect of mass particles on the throughflow is insignificant and hence do not contribute to any significant changes in the velocity

of the particle. Whereas for the coarser particles of size varying from 0.4 to 0.5 mm, a perceptible inertial effect on the particles can be foreseen from the Fig 7. The inertia of the particles cause lowering of the velocity of the flow field and hence contributing to a decreased wall shear stress.

5. Conclusions

The following conclusions are deduced from the numerical simulation:

- Increase in diameter ratio results in significant decrease in the wall shear stress.
- Increase in the abrasive particle size results in significant decrease in the wall shear stress.

Acknowledgement

The authors wish to gratefully acknowledge the financial support extended by the Manipal University for sponsoring the principal author to this symposium.

References

- [1] D.Anjaiah, A.M Chincholkar and B. Siddeswarappa, "Effect Of Process Parameters On The Material Removal Rate On Glass In Low Pressure Abrasive Slurry Jet Machining", in Proc. of National Conference on World class manufacturing, India, 2003, pp 20-24.
- [2] D.Anjaiah and A.M Chincholkar, "AWSJ Cutting Of Ceramics – An Experimental Study Of The Effect Of Process Parameters On The Surface Roughness Using DOE", in Proc. of 9th Pacific Rim International Conference on Water Jetting Technology, Nov 20-23, 2009.
- [3] D.Anjaiah, A.M Chincholkar and B. Siddeswarappa, "Effect of Liquid Environment On The Material Removal Rate On Glass In Low Pressure Abrasive Slurry Jet Machining," in Proc. of XIII National Conference of Indian Society of Mechanical Engineers, IIT, Roorkee, India, 2003.
- [4] D.Anjaiah and A.M.Chincholkar, "Cutting of Glass Using Low Pressure Abrasive Water Suspension Jet With The Addition Of Zycoprint Polymer", in Proc. of 19th International Conference on Water Jetting, BHR Group, UK, 2008, pp.105-119.
- [5] G.J. Brown, "Erosion Prediction In Slurry Pipeline Tee-Junctions", Applied mathematical modelling, vol. 26, 2002, pp.155-170.
- [6] Fluent user's guide, Volume I to IV

International Engineering Symposium, March 3-5, 2011 Kumamoto Univ., Japan

- [7]B.K.Gandhi, "Study Of The Parametric Dependence Of Erosion Wear For The Parallel Flow Of Solid -Liquid Mixtures", *Tribology International*, vol.32, 1999, pp.275-282.
- [8]L.J.Graham, D. Lester, and J. Wu, "Slurry Erosion In Complex Flows : Experiment and CFD", *Seventh International Conference On CFD In The Minerals And Process Industries*, CSIR, Melbourne, Australia, 2009,pp.1-6.
- [9]M.Hashish, "Observations Of Wear Of Abrasive Waterjet Nozzle Materials", *Journal of Tribology*, Vol-116, 1994, pp. 439-444
- [10] G. Hu, W. Zhu, T. Yu, and J. Yuan, "Numerical Simulation and Experimental Study of Liquid-solid Two-phase Flow in Nozzle of DIA Jet", *Proceedings of the IEEE International conference industrial informatics(INDIN 2008)*, Daejeon, Korea, July 13-16th 2008.
- [11] M. Nanduri, D.G. Taggart, and T.J. Kim, "The Effects Of System And Geometric Parameters On Abrasive Water Jet Nozzle Wear", *Wear*, vol. 42, 2002, pp. 615-623.
- [12] T. Nguyen, D.K. Shanmugam and J. Wang, "Effect Of Liquid Properties On The Stability Of An Abrasive Waterjet", *International Journal of Machine Tools and Manufacture*, Volume 48, Issue 10, pp 1138-1147, 2008.
- [13]A.C. Phase and C. Equation, "Numerical Simulation on Flow Field of Pre-mixed Abrasive Water Jet Nozzle", *IEEE-2008 Asia Simulation Conference-7th Intl. Conf. on Sys. Simulation and Scientific Computing*, 2008, pp. 247-251.
- [14]Patankar S.V. and D.B. Spalding, "A calculation procedure for heat, mass and momentum transfer in three-dimensional parabolic flows", *International Journal of Heat Mass Transfer*, 1972, vol. 15, p. 1787
- [15]Z. Shangxian, L. Yan, W. Quan, B. Discretization, and G. Space, "Track Calculation and Numerical Simulation on Particles in High Pressure Abrasive Water Jet Nozzle", *IEEE International Conference on Measuring Technology and Mechatronics Automation* 2010, pp. 1039-1042.

Unmanned Aerial Vehicle for Coastal Zone Management

PRUTHVIRAJ U¹ SOHAN S² ASHWIN L N³ and SHRITHEJA U⁴

- 1 Department of Applied Mechanics & Hydraulics, National Institute of Technology Karnataka, Surathkal, Mangalore 575025, India. email:pruthviju@gmail.com
 - 2 Department of Mechanical Engineering, National Institute of Technology Karnataka, Surathkal, Mangalore 575025, India. email: sohan.suvarna@gmail.com
 - 3 Department of Mechanical Engineering, National Institute of Technology Karnataka, Surathkal, Mangalore 575025, India. email:ashwin.nandagiri@gmail.com
 - 4 Department of Mechanical Engineering, National Institute of Technology Karnataka, Surathkal, Mangalore 575025, India. email: shriteja@gmail.com
-

Abstract: Data collection is an important part of coastal zone management. But collection of data in coastal zone is not an easy task. Extensive field measurements are very expensive. The beach is a transient feature and beach erosion should be fully considered when locating either residential development or commercial facilities in coastal areas. Planning of coastal development is critical because of the danger of occupying the low lying land along the coast. Primary requirement in this regard is the availability of constantly updated image for monitoring applications. Satellite images are costly and sometimes incoherent when it comes to clarity and detail. Here, an unmanned aerial vehicle (UAV) is best suited for the purpose. It is viable in terms of cost, ease of deployment and its effectiveness in areas of varying geographical terrain. In the present case, a complete UAV is developed – structural design, aerodynamic testing and load cell tests were performed to design and build an autonomous vehicle of this specific utility. The post-flight image processing work takes the obtained overhead images and processed them to retrieve data relevant to coastal zone management. Another main advantage is the availability and suitability of the image capturing vehicle at any point of time. Times of the day, season or cloud cover are not significant hindrances.

Keywords: Unmanned Aerial Vehicle, coastal zone management, GPS, image processing

Introduction

Data on coastal erosion trends are necessary and must be used properly if the development is to be accomplished with due regard to the changing beach with adequate safety and most economically from the standpoint of all concerned. Main concern are property loss as a result of storm damage and natural long term erosion, financial loss to coastal resort businesses as a result of the loss of the recreational qualities of the beach, the expenses on providing protective structures to prevent damage to coastal facilities or to attempt rehabilitation of damaged beaches. These economic losses could have been decreased considerably if coastal erosion data had been used in planning coastal development. Extensive field measurements are very expensive.

Aerial photographs are an ideal means of coastal surveying technique. The unmanned aerial vehicle (UAV) provides an ideal platform for this purpose. Since the use of UAV is far less expensive than manned aircraft, regular updating of images and aerial monitoring is possible.

UAV system

The Aerial Vehicle is dual controlled – from ground based remote control and by the control centre, which is a Paparazzi autopilot board. This autopilot is fed with relevant geographical co-ordinates of the required area and by synchronising it with the dynamic GPS data it receives on board, the flight follows a pre-determined flight-path. Unmanned Aerial Vehicle inspired by a paper plane design was built. Wind tunnel testing and CFD analyses of the

aerial vehicle were carried out. The aerial vehicle was found to be an efficient flier with good aerodynamic characteristic. This vehicle could be hand launched making it simple to deploy. A balsa wood fuselage and thermocol wings were used making it lightweight and portable as shown in Fig. 3. Using ANSYS Multiphysics software, numerical analyses of the airflows over the airfoils at different angles of attack have been made as shown in Fig. 2 and the data generated by computational means have been compared with the wind tunnel experiments and found to be in good accordance with the data available. It was powered by a brushless DC motor with lithium polymer batteries. UAV was equipped with an image sensor of 10 megapixel and a Autopilot board merged with Global Positioning System (GPS) unit.



Fig. 1 CAD model of the UAV

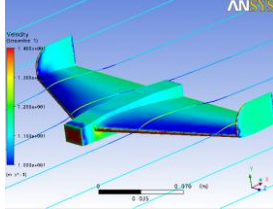


Fig. 2 Results of CFD analysis



Fig. 3 The UAV in flight



Fig. 4 A screenshot of ground station showing the flight-path

The Ground Control Station (GCS) comprises of a computer for display of real-time data such as video and GPS coordinates. Fig.4 shows a flight plan detail as a screenshot from the software interface. Using the GCS the flight path can be easily set up and the autonomous

vehicle can be made to fly along the predetermined path at a required altitude. The images obtained from the UAV as shown in Fig. 5 to Fig. 8 and have been processed to identify various characteristics such as water bodies, shorelines, fire, buildings etc as shown in Fig. 9 and Fig. 10.



Fig. 5 Image showing check dam, bridge across river



Fig. 6 Image showing bridge along National Highway

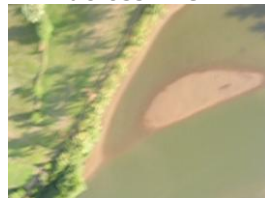


Fig. 7 River at low tide



Fig. 8 River at high tide

Image processing:

OpenCV and Matlab code is used to separate one from of a detected geographic entity from the background of the image. The program is written such that a user friendly GUI menu pops up which is used to identify the shoreline, buildings, roads, vegetation, water-bodies etc. This brings out the colour differences in the given image which is subjected to a de-correlation stretch. The decorrstretch function is used here to enhance the colour separation across correlated channels. The processed images of a large area can be done separately and stitched together along with latitude and longitude co-ordinate data obtained from the GPS unit in-built in the autopilot system. The images obtained from the UAV have been processed to identify various characteristics such as water bodies, shorelines, fire, buildings etc.



Fig. 9 Image showing check dam, bridge across river



Fig. 10 River boundary marked

Final image of water body is marked and obtained as a result of image processing. It may be noticed that the undulations caused by separating out the image based on the colour differences are approximated to get a final bordered image as shown below. This way, any water body can be detected and clearly marked out. Usage of Unmanned Aerial Vehicle used for aerial photographs in coastal zone has several advantages over other methods. This method is more economical than field survey and tremendous amount of detail is achieved when image is captured in frequent intervals, even within hours even though this technique has disadvantage like errors due to scale variations and error due to tilt.

Conclusions

Aerial photographs show the location of the beach, river and natural and cultural features adjacent to the beach that can be used as stable images to references beach location with great ground detailed. This study proposes new spatial data collection system to add a three dimensional view for coastal zone management. This system includes a fixed wing aerial vehicle equipped with digital video camera, GPS integrated autopilot board. It can be stated that the UAV is a very viable and cheap method of detailed overhead imagery. The processed data from such an image capturing system can be used for coastal zone management and in disaster management in crisis situations like floods and forest fires as well as for selective imagery like vegetation, water bodies. The auto-pilot navigation system enables the aircraft to fly between specific co-ordinates in even hard to reach geographical terrains.

Acknowledgements

The authors are very much thankful to the National Institute of Technology Karnataka, Surathkal for the financial support provided for the project. The authors are grateful to Dr. Prashanth T for his guidance in autonomous flying.

References

- [1] ANSYS 10 Multiphysics Reference Manual, 2009 Release
- [2] Anderson F David and Scott Eberhardt (2001) "Understanding Flight", McGraw-Hill publications
- [3] Chen M N et all (2001)A river ministering system using UAV and GIS, 22nd asian conference on remote sensing,
- [4] <http://www.paperang.com> (accessed on April 20 ,2009)
- [5] Kimon P Valavanis (2007), "Advances in Unmanned Aerial vehicles", Springer publications
- [6] Kosmatka John et al (2008)"Unmanned Aerial System (AUVSI UAS)", University of California at San Diego
- [7] Lloyd Dingle and Mike Tooley (2006), "Aircraft Engineering Principles", Elsevier Butterworth Heinemann Publications
- [8] Luiz Augusto Tavares de Vargas, Paulo Henriques Iscold Andrade de Oliveira (2006), Fast Aerodynamic Procedure for a Complete Aircraft Design Using the Know Airfoil Characteristics, Society of Automotive Engineers, Inc
- [9] MATLAB 2006b User Manual
- [10] Pope Alan and John J Harper (1966),"Low-speed Wind tunnel testing", John Wiley and Sons Inc. publication
- [11] Stafford B Donald (1971), An Aerial Photographic Technique for Beach Erosion Surveys in North Carolina Technical Memorandum No 36, U.S Army, Corps of Engineers

EXPERIMENTAL STUDY ON CONVECTIVE HEAT TRANSFER OF Al_2O_3 NANOFUID DISPERSED IN ETHYLENE GLYCOL

HAJIME YOSHINO ¹

and

SHUICHI TORII ²

¹ Department of Mechanical System Engineering, Kumamoto University, Kurokami, 2-39-1, Kumamoto 860-8555, Japan. e-mail: 077t3845@st.kumamoto-u.ac.jp

² Department of Mechanical System Engineering, Kumamoto University, Kurokami, 2-39-1, Kumamoto 860-8555, Japan. e-mail: torii@mech.kumamoto-u.ac.jp

Abstract: In general heat transfer fluids, such as water, oil and ethylene glycol mixture are used in several industrial field. But traditional heat transfer fluids are inherently poor heat transfer fluids. There is a strong need to develop advanced heat transfer fluids. The aim of the present study is to disclose the thermal fluid flow transport phenomenon of nanofuids in the heated horizontal circular tube. Al_2O_3 particles dispersed in ethylene glycol are used as the working fluid. It is found from the study that (1) the viscosity of nanofuids increase in accordance with an increase of the volume fraction of the nanoparticles, (2) heat transfer enhancement is caused by suspending nanoparticles.

Keywords: nanofuids, viscosity, Convective Heat Transfer

Introduction

The working fluids with low thermal conductivity such as water or ethylene glycol suppress development of compact and higher performance heat exchangers. A new way to enhance thermal conductivity of the fluid is to suspend small solid particles in a fluid. Fluid including nanoparticles is called nanofuid. The nanofuid is found to possess long time stability and large efficient thermal conductivity[1]. Heat transfer performance for the nanofuid is superior to that of the original pure fluid. This is because the suspended ultrafine particles cause a substantial enhancement of the thermal conductivity of the mixture and improve its capability of energy change. Among numerous studies, Xuan and Li[2] measured convective heat transfer coefficient of Cu/water nanofuids of 0.3% in volume fraction to 2.0% at constant heat flux, and reported a substantial heat transfer enhancement. The purpose of this study is to disclose the thermal fluid flow transport phenomenon of nanofuid by measuring the effective viscosity and the convective heat transfer performance.

Experimental Method

The experimental apparatus employed here is illustrated in Fig. 1. It consists of a closed flow loop, a heating unit, a cooling part, and a measuring and control unit. A straight stainless tube with 1000 mm in length, 3.96 mm in inner diameter, and 0.17 mm in thickness is employed as the test section and electrodes for the direct electric current heating are installed at both ends. The power supply is adjustable. The test tube is surrounded by a thick thermal insulation material to suppress heat loss along the test section. The six K-type thermocouples, which are welded on the outer surface of the test tube, are used to measure the local wall temperature along the heated surface of the tube, and the other thermocouples are inserted into the flow at the inlet and outlet of the test section to measure the bulk temperature of working fluid. The viscosity is generally one of important physical properties. In this study, capillary viscometer is employed to measure the viscosity of nanofuids. The testfluids are diluted by adding pure water. The ratio of Al_2O_3 / ethylene glycol nanofuid to pure water is 1 to 1.

Results and Discussion

Figure 2 depicts the viscosities for Al_2O_3 nanofluids, which are normalized by that of the pure water. The result show that the viscosity ratio of nanofluids increases in accordance with an increase of the volume fraction of the nanoparticles.

Heat transfer performance is illustrated in Fig. 3 in the form of Nusselt number (Nu) versus Reynolds number (Re) with Al_2O_3 nanofluid, as the parameter. The results show that nanofluids, containing only a small amount of nanoparticles, have substantially higher value of Nusselt number than the same liquids without nanoparticles. And the Nusselt number of nanofluids increase in accordance with an increase of the Reynolds number. For all test fluids, the Nusselt number increase drastically between $Re=1200$ and $Re=1400$.

Conclusions

The following conclusions are deduced from the experimental results:

- Heat transfer enhancement is caused by suspending nanoparticles.
- The viscosity of nanofluids increase in accordance with an increase of the volume fraction of the nanoparticles.

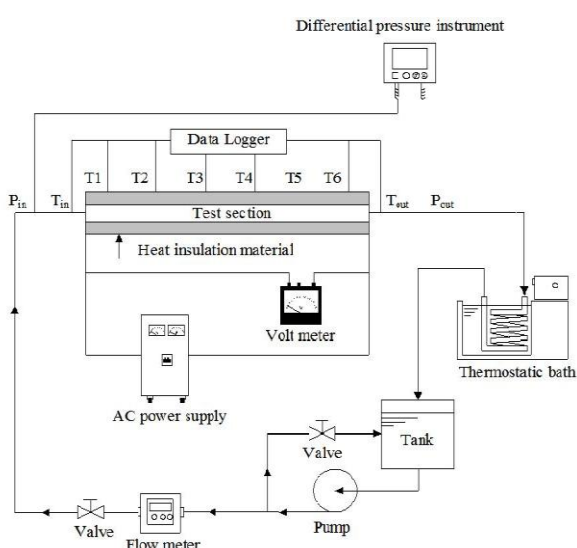


Fig.1 Experimental apparatus

References

- [1] Khanafer, K., Vafai, K. and Lightstone, M., International Journal of Heat and Mass Transfer, 46 (2003) 3639-3653.
- [2] Xuan, Y. and Li, Q., Journal of Heat Transfer, 125 (2003) 151-155.

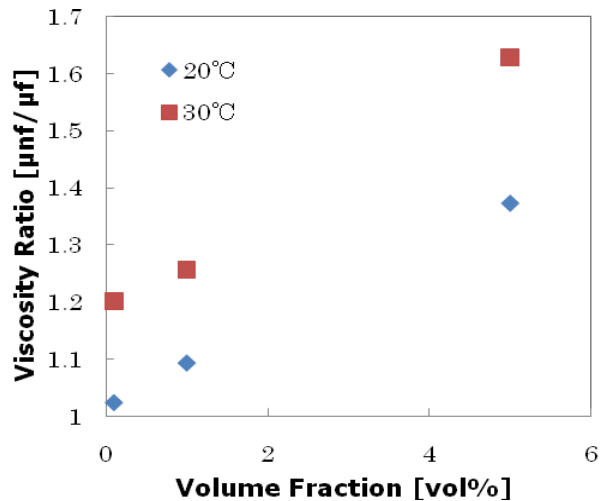


Fig.2 Viscosity ratio of nanofluid

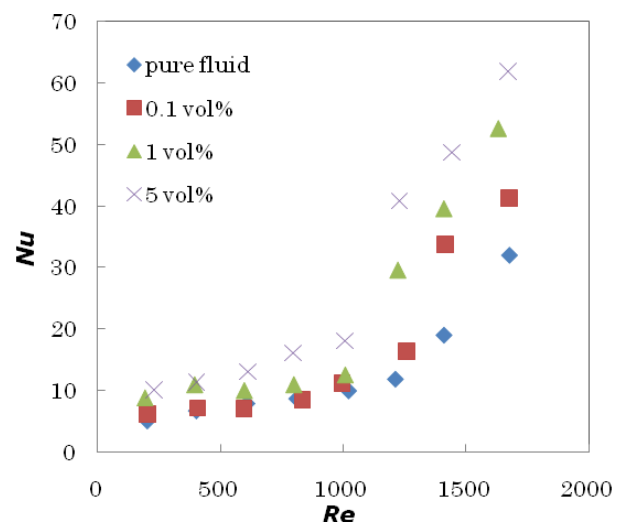


Fig.3 Relation between Nusselt number and Reynolds number for nanofluid and pure fluid

Thermal Fluid Flow Transport Characteristics in Confined Channels with Two Dimensional Dual Jet Impingement

Caner Senkal¹

Shuichi Torii²

1 Department of Mechanical System Engineering, Kumamoto University, Kurokami, 2-39-1, Kumamoto 860-8555, Japan. e-mail: 091d8565@st.kumamoto-u.ac.jp

2 Department of Mechanical System Engineering, Kumamoto University, Kurokami, 2-39-1, Kumamoto 860-8555, Japan. e-mail: torii@mech.kumamoto-u.ac.jp

Abstract: The flow and heat transfer characteristics of laminar dual circular jet impinging on a heating plate has been investigated numerically. The simulations have been carried out for Reynolds number ($250 \leq Re \leq 418$), the angle of inclination of the confined upper wall ($0 \leq \theta \leq 10^\circ$), circular jet to annular jet velocity ratio ($0 \leq VR \leq 2$) and jet to target plate distances between $2D$ and $8D$ where D is the outer diameter of dual jet. Heat transfer performance along the heated wall is amplified with an increase in the velocity ratio and the reynolds number. The heat transfer rate in the stagnation zone is attenuated by increasing the jet nozzle to impinging plate distance.

Keywords: impingement, dual jet, electronics cooling

Introduction

Impingement is a promising and reliable cooling method because of its high heat transfer rates. jet impingement cooling systems is used for vast various industrial applications such as annealing of metal, cooling of textile products, temperature distribution control at glass production, cooling gas turbine blades and film materials as well as thermal management of electronic components.

The experimental and numerical studies on impinging jets are mostly related to turbulent jets. although many industrial processes involve turbulent jet flow,laminar jets are appropriate way to cool down of objects in a limited volume such as microchip modules in microelectronics. Heat transfer rate of impinging jets are also strongly affected by confinement of the fluid flow. Chou and Hung[1] represents the effect of jet reynolds number, ratio of seperation distances and jet exit velocity profile on stagnation and local heat transfer characteristics in confined slot-jet

impingement systems.They also proposes a new nusselt number correlation to predict stagnation and local heat transfer characteristics on a isothermally heated surface.Seyedein et. al.[2] examined laminar impinging slot jets with inclined confinement surface numerically.They reported that inclination of the confinement surface accelerate the exhaust flow and it also effects heat transfer on isothermal impingement surface. Lin et. al.[3] conducted experimental study on heat transfer behaviours of a confined slot jet impingement.According to their study,the effect of jet seperation distance is not significant on stagnation, local and average nusselt number on the heated surface; while the heat transfer performance increases with increasing jet reynolds number.In their study also introduced a concept of effective cooling length to evaluate the average nusselt number on a finite-length target surface. Nozzle shape of impinging jet plays significant role on flow distribution and heat transfer on target surface. San et al[4] examined fluid flow and heat transfer

distribution of circular impinging air jet. They used four different diameters of jet nozzle (3,4,6 and 9 mm) to investigate recirculation and mixing effect on heat transfer while the jet reynolds number is in the range of 30,000-67,000 .They concluded that the jet hole diameter is a strong factor affecting the nusselt number.for the same reynolds number; smaller jet hole diameter causes lower value of the nusselt number but for a jet hole diameter greater than 6 mm, the influence of the jet hole diameter on the nusselt number tends to decrease.

Annular or circular jet flow is often used in many engineering applications to control heat transfer on a flat plate surface or in a two-dimensional channel. Himadri[5] performed numerical simulation to predict heat transfer characteristics of laminar annular jet and it is reported that heat transfer of annular jet is %20 less compared to the circular jet.Yang et al.[6] examined experimentally of annular jet characteristics with/without swirling induced motion and they concluded that swirling motion in the exit flow of annular jet causes non uniform heat transfer and wall pressure distribution on the impingement plate, however, if the seperation distance from jet nozzle to target impingement surface is increased, heat transfer and wall pressure distribution of swirling motion annular jet is more uniform than the reference annular jet without swirling.

Present study deals with the fluid flow and thermal fields in a two dimensional channel with inclined upper wall surface in which circular dual jet impinges on a constant heat flux bottom wall surface.a numerical method is employed to determine the velocity and temperature profiles.parameters used in numerical simulations are reynolds number,angle of inclined upper wall, circular jet to annular jet velocity ratio and nozzle to target plate distance.

Computational Scheme

The steady-state, two-dimensional, Navier-Stokes and energy equations in cylindrical coordinates are used in this study.The following assumptions are imposed in the formulation of the problem

based on the characteristics of the flow: it is an incompressible, laminar, steady flow with constant fluid properties; there is constant wall temperature, uniform inlet velocity and uniform inlet fluid temperature at the nozzle tip and negligible axial conduction (due to the high Peclet number).Buoyancy effects are neglected.The physical configuration of impinging jet and coordinates system are shown in Fig.1

Governing differential equations for mass,momentum and energy can be expressed as:

Continuity Equation:

$$\frac{1}{r} \frac{\partial}{\partial r} (\rho r V_r) + \frac{\partial}{\partial z} (\rho V_z) = 0 \quad (1)$$

r-momentum:

$$\begin{aligned} \rho(V_r \frac{\partial V_r}{\partial r} + V_z \frac{\partial V_r}{\partial z}) &= \\ -\frac{\partial p}{\partial r} + \mu \left[\frac{\partial}{\partial r} \frac{1}{r} \frac{\partial}{\partial r} (r V_r) + \frac{\partial^2 V_r}{\partial z^2} \right] &\quad (2) \end{aligned}$$

z-momentum:

$$\begin{aligned} \rho(V_r \frac{\partial V_z}{\partial r} + V_z \frac{\partial V_z}{\partial z}) &= \\ -\frac{\partial p}{\partial z} + \mu \left[\frac{1}{r} \frac{\partial}{\partial r} \left(r \frac{\partial V_z}{\partial r} \right) + \frac{\partial^2 V_z}{\partial z^2} \right] + \rho g_z &\quad (3) \end{aligned}$$

Energy equation:

$$\rho C_p \left(V_r \frac{\partial T}{\partial r} + V_z \frac{\partial T}{\partial z} \right) = k \left[\frac{1}{r} \frac{\partial}{\partial r} \left(r \frac{\partial T}{\partial r} \right) + \frac{\partial^2 T}{\partial z^2} \right] \quad (4)$$

Only half of the computational domain is taken into account because of the symmetry of the fluid flow.

Non-dimensional variables in this study are defined as:

$$V^* = \frac{V}{V_{inlet}} \quad (5)$$

$$T^* = \frac{T - T_{inlet}}{\frac{q'' D_i}{k}} \quad (6)$$

$$L^* = \frac{L}{D} \quad (7)$$

In the above equation, V_{inlet} , T_{inlet} , q'' and D_i represent inlet jet velocity, inlet jet temperature, constant heat flux on the heated wall and inner diameter of circular jet, respectively. The superscript in equation (5)-(6) and (7) represents non-dimensional variables. V^* , T^* , L^* are non-dimensional velocity, temperature and length.

The Boundary conditions in the two-dimensional channel are specified as:

at the channel wall ($z=H$):

$$V_r = V_z = 0, T = T_{surface}$$

at the upper inlet wall:

$$V_r = V_z = 0, \frac{\partial T}{\partial z} = 0$$

at the inlet, i.e., ($z=0$):

$$V_z = V_{inlet}, V_r = 0$$

at the centerline($r=0$):

$$\frac{\partial V_z}{\partial r} = 0, V_r = 0, \frac{\partial T}{\partial r} = 0$$

at the outlet($L=r$, $0 < z < H$):

$$\frac{\partial V_r}{\partial r} = 0, \frac{\partial V_z}{\partial r} = 0, \frac{\partial T}{\partial r} = 0$$

on the heated bottom wall ($z=H$):

$$q'' = 1000 \frac{W}{m^2}$$

Method of Solution

The governing equations are discretized by using the finite-volume method in staggered, uniform grids. SIMPLE algorithm[7] is used to obtain velocity and temperature fields. The outlet boundary is located far enough downstream for

conditions to be substantially developed so the distance of outlet to the symmetry line is set to $L_z=10$. Hybrid difference scheme is adopted for the discretized terms in the governing equations. The discretised equations are solved iteratively using the tridiagonal matrix algorithm line solver.

A systematic grid resolution study was performed. Three grid structures were considered: 16x80, 32x160 and 64x320 where the numbers are the number of grids in the r - and z -directions, respectively. The difference between the results obtained for the average Nusselt number with 16x80 and 32x160 is %11 while the difference between 32x160 and 64x320 is %2. Hence, all calculations are performed with 32x160 grids.

An under-relaxation factor of 0.3 for V_r and V_z , 0.2 for P and 0.5 for T is used for momentum and energy equations in all calculations. Iterations are continued until the residual source of the continuity equation reduced below 10^{-4} where no significant variations are observed at this residual level.

Results

Prandtl number is taken 0.71 in this study and air is chosen as working fluid. Once the flow and thermal fields are obtained, the local Nusselt number can be calculated with the following equation:

$$Nu_x = \frac{h_x D}{k} = \frac{1}{T^*} \quad (8)$$

where h_x represents the local heat transfer coefficient on the target surface. Figure 2a-d depicts the velocity vector over the r - z cross section in the channel at four different Reynolds numbers Re .

It is observed that recirculation zone appears in the vicinity of the annular jet and at the middle part of the computational domain and is extending towards outlet with the increase of Reynolds number. Temperature field of four different Reynolds number in the channel depicts at Figure 3a-d. A thermal boundary layer is developed along the heated impingement wall and the temperature gradient at each axial location is intensified with increasing the Reynolds number

The change in thermal boundary according to the velocity vector can be seen clearly in figure 3a-d. Figure 4 illustrates the local Nusselt number Nu as a function of the Reynolds number Re . One observe that with Re fixed, the Nusselt number have a primary peak in the vicinity of annular jet and Nusselt number tends to decrease until secondary peak. The reason of first peak of Nusselt number on the heated impinging plate is interaction of circular jet and annular jet on the impingement plate. Nusselt number tends to decrease monotonously towards lateral exit until meet with other recirculation zone. Heat transfer performance is induced over the heated wall with an increase in the reynolds number. The local heat transfer rate is illustrated in figure 5 in the same form as figure 4 with the velocity ratio VR as the parameter. The numerical results are obtained at $\text{Re}=250$ and $H=2$.

For the absence of inner nozzle injection, i.e, $\text{VR}=0$, the Nusselt number increases along the heated wall, achieves the maximum value near the location of the outer nozzle injection and after that, decreases monotonously in the downstream direction. A substantial reduction in the Nusselt number at the stagnation point is suppressed due to the presence of the inner nozzle injection. In particular, the peak of the Nusselt number at $\text{VR}=0.5$ yields at the stagnation point and near the outer nozzle. As the inner nozzle injection velocity increased, the peak value of the Nusselt number near the outer nozzle tends to move to the inner nozzle vicinity. This heat transfer behavior becomes clearer for the temperature distribution illustrated in figure 6. Figure 6 depicts the temperature and velocity distributions in the channel at different velocity ratios VR . The change in the velocity ratio gives an effect on the temperature and velocity distributions in the channel. In other words, heat transfer performance along the heated wall is controlled by the velocity ratio.

Figure 7, for $\text{Re}=250$ and $\text{VR}=1$, shows the effect of dimensionless nozzle to impingement plate distance H on the local Nusselt number in the channel. Nusselt number decreases monotonously until a

peak value around $r=1.2D$. After this peak value, Nusselt number tends to decrease monotonously towards to lateral exit. However, at the case of $H=2$, it is observed that it yields 2 peak Nusselt number value along the heated plate. An attenuation in the stagnation zone is supressed as the injection nozzle approaches the heated wall

Next is to study the effect of the inclination angle θ of a confined surface on the local Nusselt numbers in the channel. Figure 8 and fig.9 describes numerical results obtained for $\text{Re}=250$ and $\text{VR}=1$. The same profile appears near the stagnation point, while the streamwise variation of the local Nusselt number is affected by θ . That is, the heat transfer performance in the down stream region is induced with an increase in θ , i.e., for $\theta=10^\circ$.

Conclusion

Numerical simulation has been employed to investigate two-dimensional, incompressible thermal-fluid flow of a dual laminar jet with an inclined confinement surface. Consideration is given to the influences of the velocity ratio, the Reynolds number, the nozzle height. And the inclination angle of the upper plate on the flow pattern and the heat transfer performance in the channel. The results are summerized as follows:

- When a dual laminar jet is introduced into the two-dimensional channel, the flow pattern, isotherms, and heat transfer performance are affected by the velocity ratio, the nozzle height, and the reynolds number. Heat transfer performance along the heated wall is amplified with an increase in the velocity ratio and the reynolds number.
- A substantial reduction in the heat transfer rate, for $\text{VR}=0.0$, occurs in the stagnation zone, because the absence of the inner nozzle injections causes the recirculation in the corresponding region due.
- The heat transfer rate in the stagnation zone is attenuated by increasing the nozzle to impinging plate distance. In particular, the effect of the inclination angle in the

downstream region, especially at the vicinity of outlet, is major then other effects.

- The streamwise reduction in the heat transfer rate for $\theta=0.0^\circ$ is suppressed by the presence of the inclined confinement surface and its value is intensified by the inclination angle

References

- [1] Chou,Y. J., Hung Y.H.(1994): " Impingement Cooling of an Isothermally Heated Surface With a Confined Slot Jet". *Heat Transfer Division of the american society of mechanical engineers*. Vol 116., pp. 479-482.
- [2] Seyeddin,S. H.,Hasan,M.,Mujumdar, A. S.(1994):" Laminar flow and heat transfer from multiple impinging slot jets with an inclined confinement surface". *Int. J. Heat and Mass Transfer*. Vol. 37. No 13, pp. 1867-1875.
- [3] Lin,Z. H., Chou,Y. J., Hung, Y. H.(1997):" Heat transfer behaviors of a confined slot jet impingement" *Int. J. Heat and Mass Transfer*, Vol. 40, No. 5, pp. 1095-1107.
- [4] San,J.Y., Huang, C. H., Shu, M.H. (1997): "Impingement cooling of a confined circular air jet". *Int. J. Heat and Mass Transfer*. Vol. 40, No. 6, pp. 1355~1364.
- [5] Himadri, C.(2004):" Numerical investigations of heat transfer from impinging annular jet". *International Journal of Heat and Mass Transfer* 47 (2004) 3197-3201
- [6] Yang,H. Q.,Kim, T., Lu, T.J. Ichimiya, K.(2010):" Flow structure, wall pressure and heat transfer characteristics of impinging annular jet with/without steady swirling". *International Journal of Heat and Mass Transfer*, Volume 53, pp. 4092-41
- [7] SV Patankar, *Numerical heat transfer and fluid flow* Washington, DC, Hemisphere Publishing Corp., 1980. 210 p., 1980 - adsabs.harvard.edu

Figures

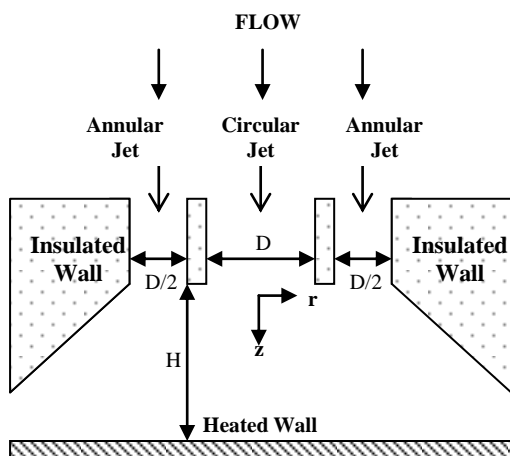
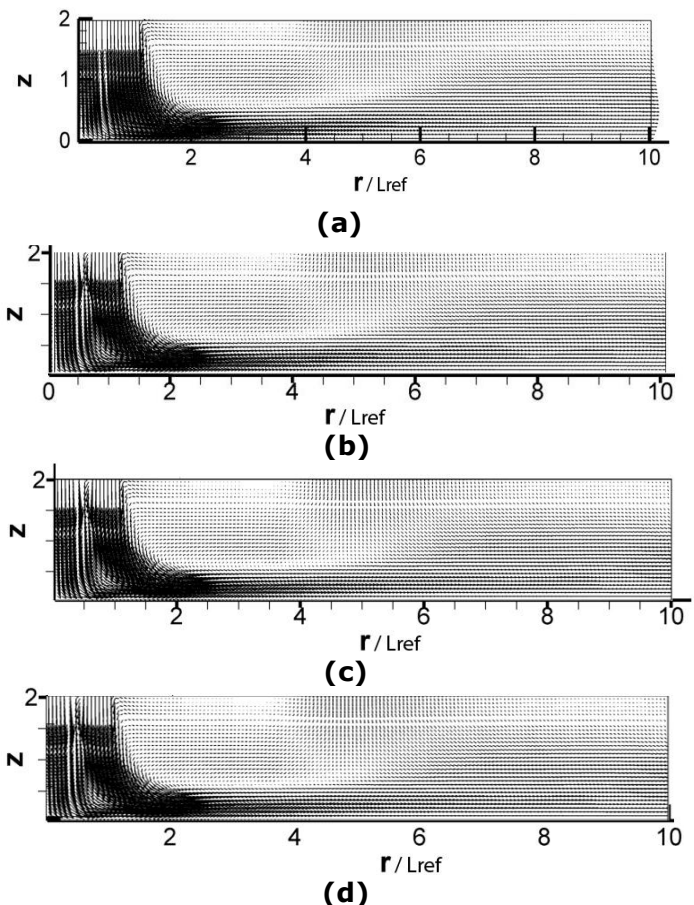
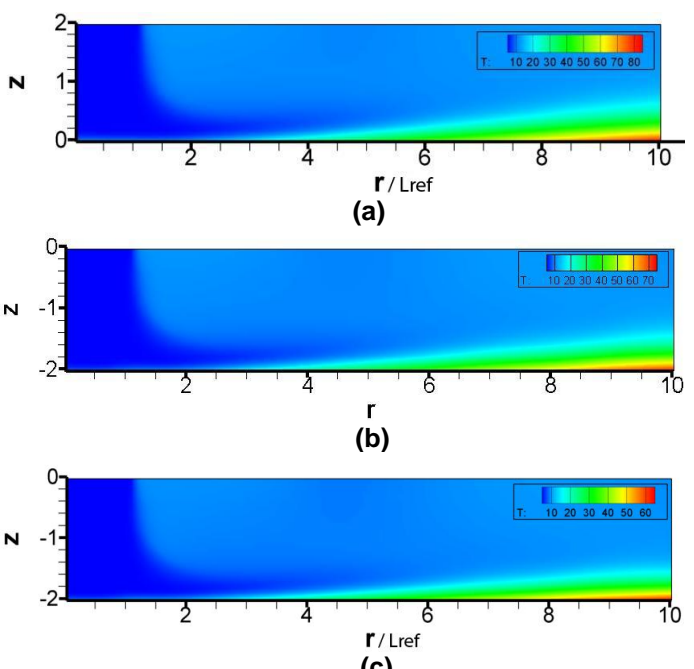


Fig.1 Diagram of Two Dimensional Channel Wall Impinged by Dual Jets With Coordinates



**Figure 2. Velocity Vector at H=2
VR=1, $\theta=0^\circ$ (a) Re=250, (b) Re=300,
(c)Re=350, (d) Re=418.**



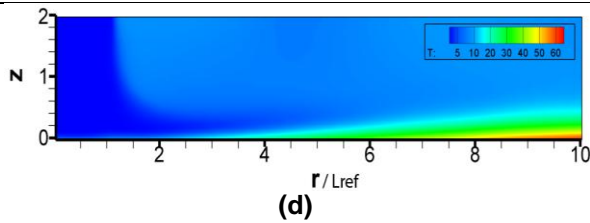


Figure 3. Temperature Distribution in the Channel at $H=2$, $VR=1$, $\theta=0^\circ$, (a) $Re=250$, (b) $Re=300$, (c) $Re=350$, (d) $Re=418$.

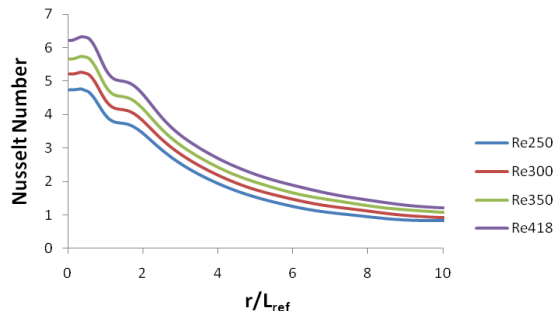


Figure 4. Effects of Reynolds Number on The Local Nusselt Number for $h=2$, $VR=1$, $\theta=0^\circ$.

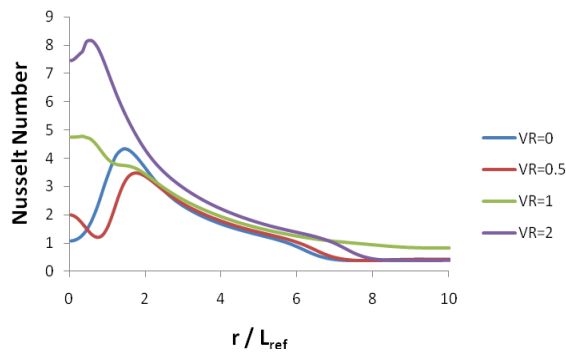


Figure 5. Effect of Velocity Ratio on The Local Nusselt Number for $H=2$, $Re=250$ and $\theta=0^\circ$.

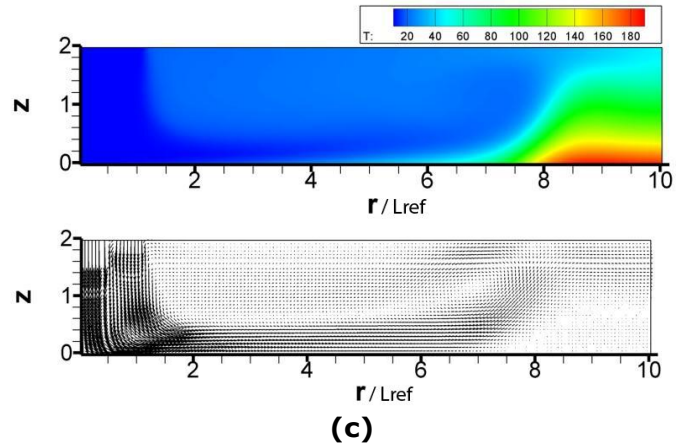
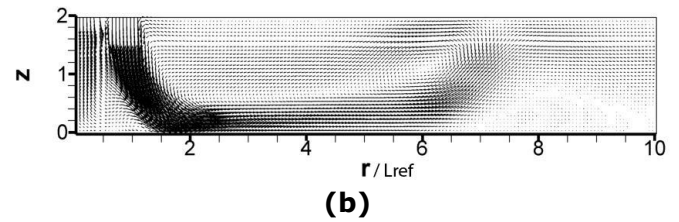
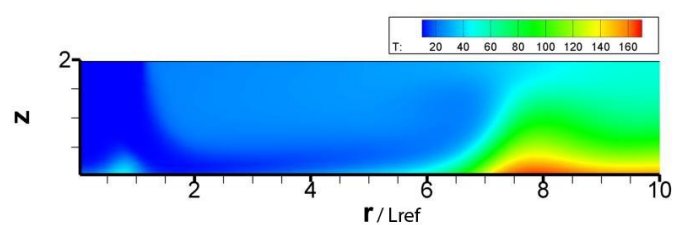
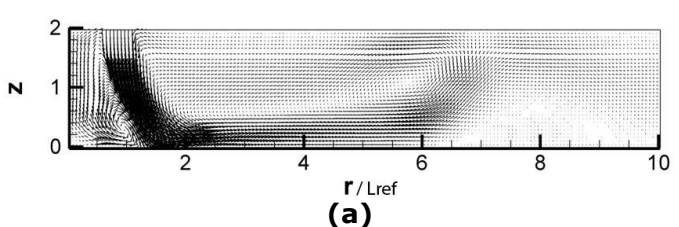
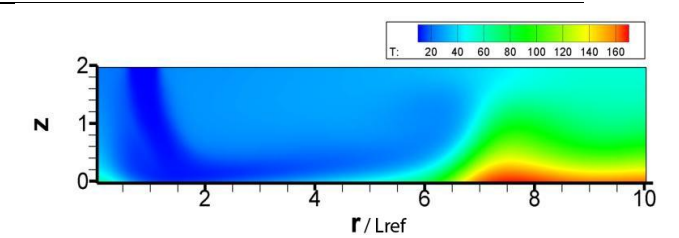


Figure 6. Temperature and Velocity Distributions $Re=250$, $H=2$ and $\theta=0^\circ$. (a) $VR=0.0$, (b) $VR=0.5$, (c) $VR=2$

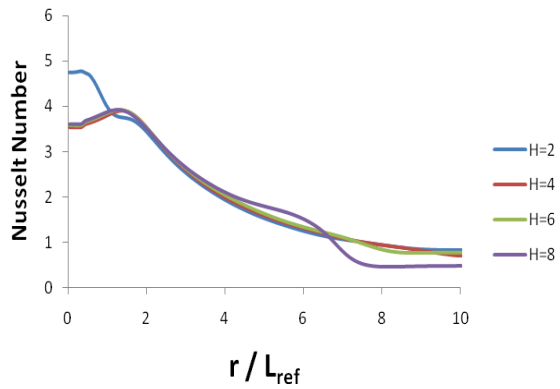


Figure 7. Effect of Nozzle to Impingement Plate Separation Distance on Local Nusselt Number for $\text{Re}=250$, $\text{VR}=1$ and $\theta=0^\circ$

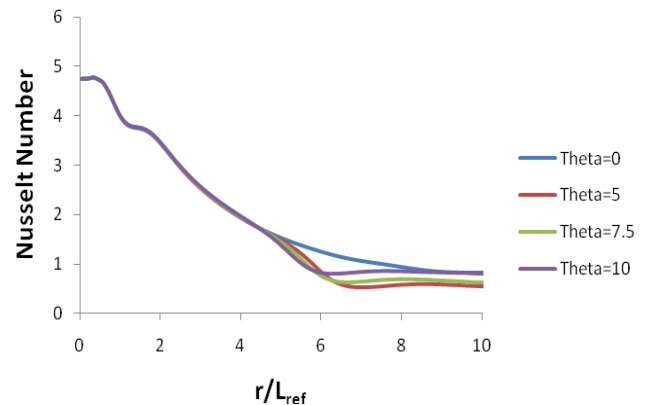


Figure 9. Effect of Inclination Angle of a Confinement Surface on The Local Nusselt Number for $\text{Re}=250$ and $\text{VR}=1$

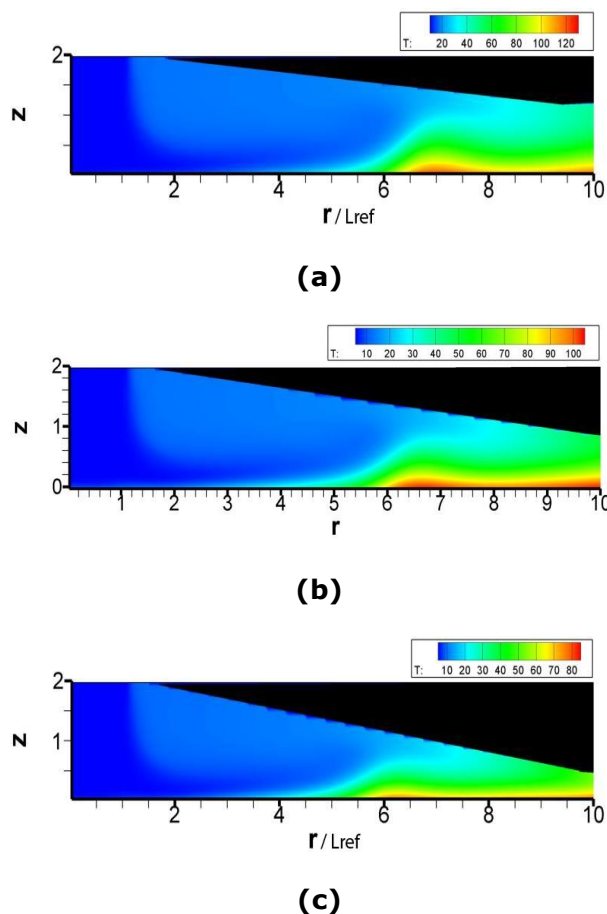


Figure 8. Temperature distributions in a two-dimensional channel with inclined upper wall at $\text{Re}=250$ and $\text{VR}=1$, (a) $\theta=5^\circ$, (b) $\theta=7.5^\circ$, (c) $\theta=10^\circ$

Thermal Hydraulics in Macro Channel using Venturi Effect of outer air

Giichi Nakamura¹ Shuichi Torii²

1 Department of Mechanical System Engineering, Kumamoto University, Kurokami, 2-39-1, Kumamoto 860-8555, Japan. e-mail: 060t3808@st.kumamot-u.ac.jp

2 Department of Mechanical System Engineering, Kumamoto University, Kurokami, 2-39-1, Kumamoto 860-8555, Japan. e-mail: torii@st.kumamoto-u.ac.jp

Abstract: The aim of this study is to utilize solar panels for a power source of a refrigerator on a car. Warming solar panels make efficiency of power generation worse. So we studied the cooling of the back of solar panels using venturi effect. In this study, the aluminum plate warmed by a silicon-rubber heater was used in place of a solar panel. There are two type of test section. One of the types doesn't have the cooling mechanism using venturi effect (Case1). Another type has the mechanism (Case2). Temperature of Case1 and Case2 are compared in the various reynolds number. If reynolds number is higher than 27000, temperatures of Case2 are higher than Case1.

Keywords: Solar Panel, Aluminum Plate, Air Flow, Venturi Effec

Introduction

In recent years, solar panel is expected to be one of things what solve the environmental problem. The aim of this study is to utilize solar panels for a power source of a refrigerator on a car. Warming solar panels make efficiency of power generation worse. So we studied the cooling of the back of solar panels using blow.

RINCIPLE OF COOLING

Figure.1 shows the outline of the solar panel. On the surface of the solar panel, two projections which have each one hole are made. The hole leads to back Then the space is made between back of the solar panel and the refrigerator. The two holes and the space are connected. When the head wind blows on the surface of the solar panel, the air pressure between the projections goes down by acceleration of the air current. This negative pressure between the projection and the atmospheric pressure in the front spoiler make the flow of air flow in the space in accordance with the Bernoulli's theorem. This air flow takes the heat of back of the solar panel through the holes of the projections.

EXPERIMENTAL METHOD

Figure.2 shows an outline of the experimental device.

Figure 3 shows front view of the test section of Case1. The shape of the PVC pipe in the test section is showed at Figure.4. The aluminum plate is used instead of solar panel. There is no space to draw in atmospheric air under the aluminium plate. Temperature of the aluminium plate of Case1 is measured.

Figure.5 shows test section of Case2 of the experimental apparatus. The shape of PVC pipe at test section is same as Case1. There is a space leading to the atmosphere and PVC pipe under the aluminium plate. The air is blown on the top surface of the aluminium plate in the test section through the PVC pipe. The electric power of the heater is 9.56 W. This is calculated by the radiation of the sun.

Temperature of the aluminium plate is measured by thermocouple at various Reynolds numbers in the PVC pipe.

Besides that, the flow of the air in the space is measured and visualized by smoke.

RESULT AND DISCUSSION

Figure.6 shows the temperatures of aluminium plates of Case1 and Case2 at various Reynolds numbers in PVC pipe. Temperature of Case1 is lower, if Reynolds number of PVC pipe is lower than about 5000. If Reynolds number is 5000 to 27000, both temperatures are same. If Reynolds is over 27000, temperature of Case2 is lower than Case1.

Figure 7 shows Reynolds numbers of blow in PVC pipe and space under the aluminium pipe. It shows two Reynolds numbers are proportional.

Conclusion

- The refrigerator using venturi effect at this study has good effect , if Reynolds number in PVC pipe is more higher than 27000.
- It is made sure that atmospheric air is drawn in the space under the plate by visualization using smoke.

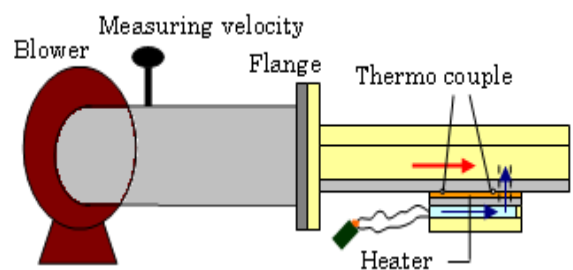


Figure.2 Experimental Apparatus

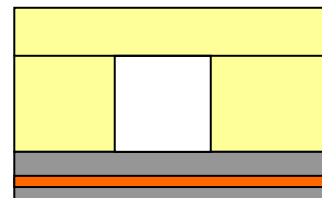


Figure.3 Front View of Case2

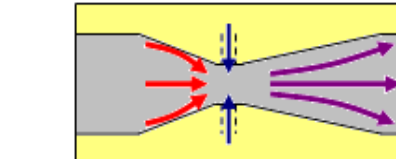
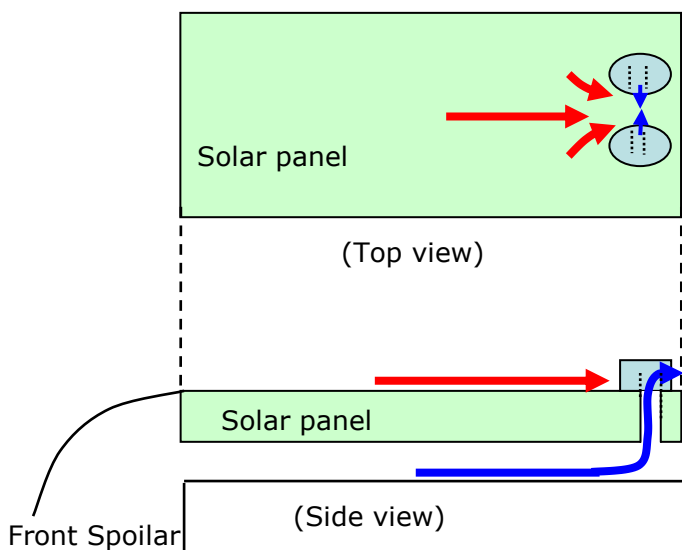


Figure.4 Top View of Both Case1 and Case2

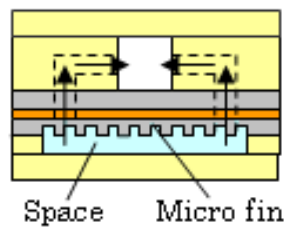


Figure.5 Front View of Case2

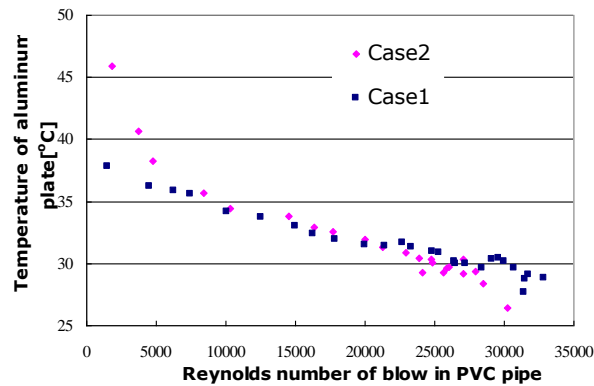


Figure.6 Relation of Reynolds Number and Temperature

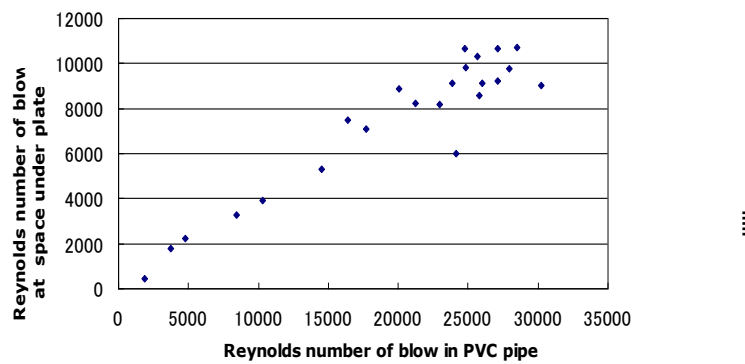


Figure.7 Relation of Reynolds numbers in Two Segment



Figure.8 Visualization of Flow under the Plate

Investigation of Combustion Furnace Fuelled by Compost

SHOTA WATANABE¹

SHUICHI TORII²

1 Department of Mechanical System Engineering, Kumamoto University, Kurokami,
2-39-1, Kumamoto 860-8555, Japan. e-mail:073t3847@st.kumamoto-u.ac.jp

2 Department of Mechanical System Engineering, Kumamoto University, Kurokami,
2-39-1, Kumamoto 860-8555, Japan. e-mail:torii@mech.kumamoto-u.ac.jp

Abstract: In Japan, The livestock waste is changed to the compost actively because of the law about livestock wastes and its production increases rapidly in recent years. But now the compost have been excess of supply. Therefore a new method to use the compost is required. Combustion system consists of four main components: combustion furnace, burner, blower, and compost feeder. The burner is used for preheating. Composts fed by the compost feeder are transformed to the combustion furnace with the air. Composts are burned in the furnace. It are results that when the burner is started and composts put into the furnace, the temperature rises to over 600°C smoothly. But after the burner is stopped, it falls rapidly and is not stability. From this, it can be said that it is necessary for stable combustion to more preheat.

Keywords: compost, combustion, furnace

Introduction

In Japan, the law about livestock wastes have been enforced in 1999. The livestock waste is changed to the compost actively because of the law and its production increases rapidly in recent years. The compost had been used as a fertilizer. But now, chemical fertilizer have taken the place of it. Therefore the compost is left too much because the use of it is a little. So a new method to use the large compost is required quickly. The authors propose the method which a mixture of the compost and the air is burned in the Compost Furnace and the heat from it is used in various scenes. The purpose of this investigation is to observe the condition of stable combustion and found out the relationship with fed compost rate and stable combustion temperature.

Experiment method

Fig. 1 shows the Compost Combustion Furnace system. It consists of four main components: combustion furnace, burner, blower, and compost feeder. The burner is used for preheating. Composts

fed by the compost feeder are transformed to the combustion furnace with the air from the blower. Composts are burned in the furnace. The combustion gas is discharged from the furnace chimney. The thermocouple measures the temperature in the furnace. The location of the thermocouple is top of the furnace, middle of the furnace, bottom of the furnace and the inside of the chimney. In this experimentation, the time of preheat is 30 min. Fed compost rate is changed variously (170 g/min, 240 g/min, 310 g/min, 380 g/min, 400 g/min, 550 g/min ,630 g/min, 740 g/min) 740 g/ min is maximum rate of Compost Feeder and 170 g/min is it's minimum rate. The temperature when the combustion is stable is found out in each situation.

Results and Discussion

Table 1 shows condition of combustion and stable combustion temperature in each situation. Fig. 2 shows compost before combustion and Fig. 3 shows compost after stable combustion. Fig. 4

shows the relationship with the fed compost rate and stable combustion temperature. The condition of combustion is stable in all situations. One of reasons of this fact is enough preheating. Fig. 2 and Fig.3 prove that the compost is completely burned. The stable temperature is between about 500 °C and about 700 °C. The stable combustion temperature rise as the fed compost rate is increased. From this, it can be said that maximum rate of Feeder makes highest temperature combustion possible.

Conclusions

The following conclusions are deduced from the experimental results:

- The combustion is stable over full range of Compost Feeder's feed.
- The stable combustion temperature rise as the fed compost rate is increased.

References

- [1] Ministry of Agriculture, Forestry and Fisheries of Japan, The law of livestock wastes, Website: http://www.maff.go.jp/j/chikusan/kankyo/taisaku/t_mondai/03_about/index.html

Table 1 Condition of combustion and temperature

Fed compost [g/min]	Condition of combustion	Temperature [°C]
170	stable	506
240	stable	485
310	stable	594
380	stable	534
400	stable	536
550	stable	594
630	stable	721
740	stable	720

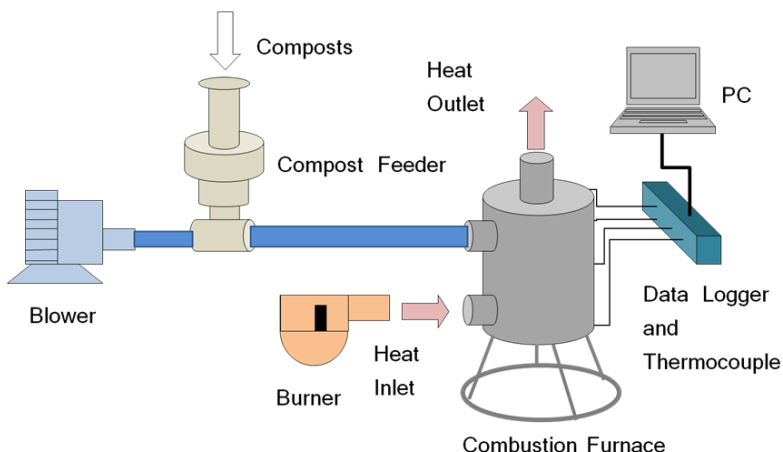


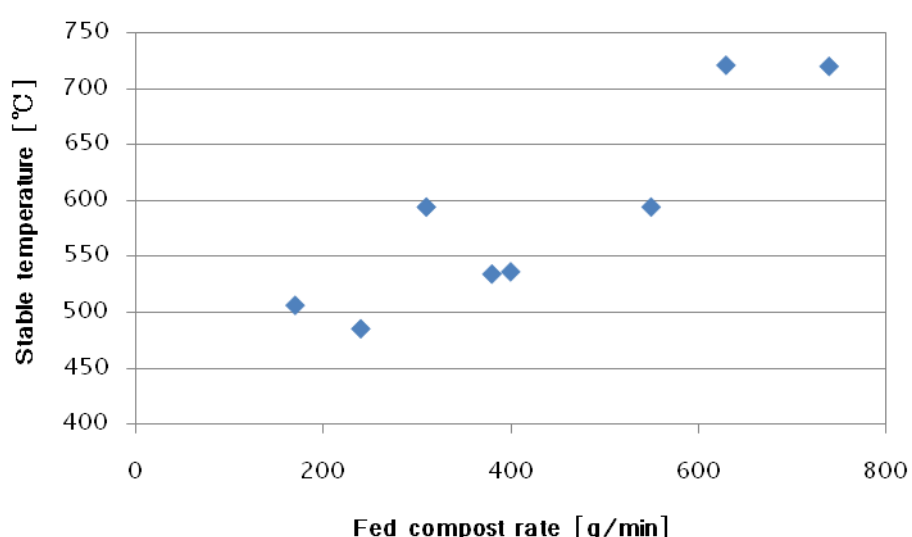
Fig. 1 Combustion system



Fig. 2 Compost (before combustion)



Fig. 3 Compost (after combustion)



**Fig. 4 The relationship
with the fed compost rate and
stable combustion temperature**

High-sensitivity Concentration Sensor Based on Fiber Bragg Grating

**RAIKAR U.S¹, LALASANGI A.S², AKKI J.F³, RADHAKRISHNAN P⁴, MANOHAR K.G⁵
AND SRINIVAS T⁶**

- 1 *Dept. of Physics, Karnatak University, Dharwad-580003, Karnataka, India.*
e-mail:usraykar_kud@yahoo.co.in
 - 2 *Dept. of Physics, Karnatak University, Dharwad-580003, Karnataka, India.*
e-mail:lalsangi_kud@yahoo.com
 - 3 *Dept. of Physics, Karnatak University, Dharwad-580003, Karnataka, India.*
e-mail:jyoti18779@gmail.com
 - 4 *International School of Photonics, Cochin University of Science & Technology, Cochin-682022, Kerala, India. e-mail: radhak@cusat.ac.in*
 - 5 *Laser & Plasma Technology Division, BARC, Mumbai-400085, India.*
e-mail:kmanohar@barc.gov.in
 - 6 *Electrical Communication Engineering Dept., Indian Institute of Science, Bengaluru-560012, Karnataka, India. e-mail:tsrinu@ece.iisce.ernet.in*
-

Abstract: Fiber Bragg grating (FBG) chemical sensors are one of the most exciting developments in the field of optical fiber sensors. In this paper we have proposed a simple and effective FBG chemical sensor for detecting the traces of Cadmium (Cd) in drinking water at ppm level.

For proper designing of FBG to act as a concentration sensor, the cladding region of the grating has been etched using HF solution. We have characterized the FBG concentration sensor sensitivity for different solutions of Cd concentrations varying from 0.01ppm to 0.04ppm by injecting broad band source and observed reflected spectrum using Optical Spectrum Analyser (OSA). Proper reagents have been used in the solutions for detection of the Cd species. The shift of Bragg wavelength is of the order of 0.07nm for 0.01 to 0.04ppm concentrations. The wavelength shifts with resolution of picometer range at lower concentration could be obtained. A comparative study has been done using sophisticated spectroscopic atomic absorption and emission spectrometer instruments. The spectral sensitivity enhancement was done by modifying grating surface with gold nano particles.

Keywords: *Fiber Bragg Grating (FBG), Cadmium, Chemical Sensor, aqueous gold nanoparticles, λ_B*

Introduction

After demonstration by Meltz et al. (1989), fiber Bragg grating (FBG) emerged as break through in both communication and sensing fields. The reasons for the popularity of FBG in sensing are many. Most important features of this are non interference of electromagnetic radiation, and freedom from recalibration Lee (2003). Fiber Bragg gratings, whose periodic variation in refractive index (RI) of the fiber core over several millimeters allows it to selectively reflect a particular wavelength (λ_B) of light due to the Bragg

light weight, small size, higher sensitivity, remote sensing over large distance with negligible signal degradation. The most important factor is that the measurand information is encoded in the resonance wavelength of the structure, an absolute parameter that brings up properties of immunity to optical power fluctuations, reflection. FBG are expected to offer a better performance than the conventional fiber sensors because sensing area is not distributed over long length of fiber but is localized in a shorter area Nobuaki et al. (1997). Hence, now a days FBGs are

widely used in sensing many parameters such as pressure Xinyong et al. (2005), acceleration Berkoff T et al. (1996), pressure Xu M G et al. (1993), strain, temperature Dong X et al. (2001), refractive index Iadicicco et al. (2003). Apart from all these, FBG chemical sensors are most exciting developments of fiber optic sensors. They are extensively used in industrial and biomedical applications.

Regular supply of drinking water to the growing population is really tough task. A number of measures like digging bore wells to get ground water are being taken on large scale. The accuracy in detection and determination of concentration of chemicals / contaminants (especially in ppm / ppb level) present in the ground water are very important to meet the drinking water standards of World Health Organization (WHO). If the concentration of dissolved chemicals in water crosses its limit, it may lead to harmful effects on human health. Out of many dissolved chemicals, Cadmium is an important one. A very large amount of cadmium is released into the environment every year (about 25,000 tons a year). About half of this is released into rivers through weathering of rocks and some cadmium is released into air, through forest fires and volcanoes. The rest of the cadmium is released through human activities, such as manufacturing, zinc ore processing etc. Contamination of drinking-water may occur as a result of the presence of cadmium as an impurity in the zinc galvanized pipes or cadmium-containing solders in fittings, water heaters, water coolers and taps. Short-term consumption (over days or weeks) of high levels of cadmium (Cd) through drinking water can cause nausea, vomiting, and diarrhea, while long-term (over years or decades) consumption may cause kidney dysfunction and osteoporosis Krajnc et al. (1987), Jarup et al. (1998). As per World Health Organization, the maximum permissible limit of Cd in water is 0.005ppm. So, precise measurement of Cd in drinking-water at low concentration is very important.

Many chemical concentration sensors and refractive index sensors (RI sensors) have been proposed previously based on FBGs,

fabricated using telecommunication fibers Wei Liang (2005), single mode depressed cladding fiber by Krestin et al. (2001), Ge doped silica fiber and hydrogen loaded silica fiber. This paper presents the design and development of FBG based concentration sensor. Concentration measurements have been carried out in non-isothermal conditions.

Sensor Design and Principle

FBG is periodic RI modulation in the core of a fiber as shown in Fig.1 with grating pitch is typically less than 100 μm . Normally the length of FBG is less than 20mm. The RI modulation is brought into core by exposing the fiber to a UV light through a phase mask (shown in Fig.1). When FBG is illuminated by broad band light source, a beam reflected from the partially reflecting planes formed by the periodic core index modulation interfere with each other. According to Bragg's law, only the wavelength that satisfies phase matching condition is reflected back to form back reflected peak with central wavelength defined by grating parameters Rao (1997), Andreas (1997). The phase matching condition is given by

$$\lambda_B = 2n_{\text{eff}}\Lambda \quad (1)$$

where,

λ_B is central wavelength known as Bragg wavelength

n_{eff} is effective RI of core

Λ is period of grating

The full width half maximum ($\Delta\lambda_B$) of reflected band of wavelengths is given by Russel et. al. (1993)

$$\Delta\lambda_B = \lambda_B S \sqrt{\left(\frac{\Delta n_{\text{eff}}}{2n_{\text{eff}}}\right)^2 + \left(\frac{1}{N}\right)^2} \quad (2)$$

Where

$S \sim 1$ for strong gratings (near 100% reflection)

$S \sim 0.5$ for weak gratings

N is number of grating planes

When n_{eff} or Λ changes the reflecting central wavelength changes correspondingly. FBG are intrinsically insensitive to surrounding medium RI (SRI) since the light coupling takes place only between well bound core modes that

are well screened from the influence of SRI by the cladding Zhou et al. (2004). However, if the cladding diameter is reduced along the grating region, n_{eff} is significantly affected by surrounding RI, resulting in a shift in Bragg wavelength.

Sensor Fabrication & Characterization

a) FBG Fabrication: Fabrication of a stable fiber Bragg grating is very important. External writing method was introduced by Meltz et al. (1989) using holographic technique. After this two more techniques were introduced, the phase mask technique by Hill et al., (1993) and the point-by-point technique by Malo et al. (1993). Out of three stable techniques, holographic technique and phase mask technique are widely used all over world, leaving point-by-point technique owing to its draw backs. For uniform grating fabrication phase mask technique has many advantages over holographic technique. We fabricated FBG using phase mask technique. Phase mask is diffractive element with one dimensional surface relief structure fabricated on high-quality fused silica flat surface transparent to UV writing beam Andreas (1997). The profile of the periodic gratings is chosen such that when an UV beam is incident on the phase mask, the zero order diffracted beam is suppressed and the diffracted plus and minus first orders are maximized. A near-field fringe pattern is produced by the interference of the plus and minus first-order diffracted beams. The period of the fringes is one-half that of the mask. The interference pattern photo imprints a RI modulation in the core of a photosensitive optical fiber placed very near to the phase mask (Fig. 1).

A single mode Ge-B co-doped photosensitive fiber (Newport F- SBG -15, with step index profile of NA 0.12 - 0.14, cladding diameter $125\pm1\mu m$, and operating wavelength 1550nm) is chosen to form the FBG gratings in the core region. Acrylate buffer coating surrounding cladding (about 5 to 6cm) where the grating to be written is stripped off and placed in-front of phase mask as shown in Fig.1. UV beam from KrF laser (248nm) is made to incident on the fiber through a phase mask. When a broad band light source (JDS Uniphase, 1530-1600nm,

17mW) is injected into one end of FBG, the wavelength that satisfies Bragg condition is reflected back and the reflected wavelength is collected using a 3dB coupler and characterized using OSA (Proximion software) as in Fig.2. The grating formation can be monitored using optical spectrum analyzer. The grating is formed in a very small time interval of 20 seconds. The advantage of Ge-B co-doped photosensitive fiber is that the exposure time for grating formation is remarkably reduced. The reflected spectrum of FBG is shown in Fig. 3, having a peak reflectance of 75%, a centered wavelength 1546.96nm (Bragg resonance wavelength), a band width (FWHM) of 0.2nm and peak power 30.16 μW .

b) Fabrication of chemical sensor using fabricated FBG:

As such FBG is insensitive to change in surrounding RI due to the presence of cladding. For FBG to act as concentration sensor, the cladding portion above the grating is to be removed allowing core mode to interact directly with surrounding medium. In the proposed sensor, the cladding region of the grating has been etched using 40% HF solution, for proper designing of FBG to act as a concentration sensor. During etching, the shift of Bragg wavelength is monitored at regular interval of time. A graph of shift in wavelength against time is shown in Fig.4. Now FBG is ready to act as concentration sensor.

Experimental setup and sensor test

A schematic diagram of the proposed FBG based concentration sensor the experimental set up is shown in Fig.2. Different solutions of cadmium in the range 0.01ppm - 0.04ppm are prepared by dissolving CdSO₄ (Aldrich) in distilled water (Aldrich). 4ml solutions are taken into different test tubes. To each Cd concentration solution, reagents N,N-dimethylformamide and thiourea are added in appropriate volumes and let it stand for 5 minutes to complete reaction to take place. Now, FBG is completely immersed in these solutions taken in special glasscells designed in the laboratory. In each case λ_B is recorded. Fig.5 shows the overlap of reflected spectra of FBG with solutions of different concentration. Before going to each

concentration the FBG region is cleaned with acetone. The graph of λ_B versus solution concentration is plotted (Fig.6) which is used to determine the concentration of Cd in drinking water.

Ground water samples (test samples) were collected from different places in the local geographic region. Grating spectra measurements for Bragg wavelength identification have been carried out by recording the reflected spectrum from the sensing grating for each water sample by adding proper reagents and hence Cd concentration in each water sample could be determined from the calibrated graph Fig.6. Allowing resolution in wavelength of the order pico meter range over the whole investigated range used for detection of Cd concentration.

Many workers have proposed and demonstrated the use of a noble metal layer coating on sensing region of fiber to enhance the chemical sensing sensitivity of the fiber Shu-Fang et al. (2003), Galina et al. (2007), Jaw-Luen et al. (2008). Optical properties like absorption and peak wavelength of noble nanoparticles are sensitive to the RI of the surrounding medium. In order to exploit this property for enhancing the chemical sensitivity of our designed FBG sensor, we proposed a simple and effective method to improve the spectral sensitivity of the sensor by modifying the grating surface by coating a layer of aqueous gold nanoparticles of size 4-12 nm. The aqueous Gold (Au) nanoparticles were procured from Nanobio Chemicals, India Pvt. Ltd. Grating region of the fiber was kept in the aqueous solution of Au nanoparticles for about 4 hours and then removed and then the liquid was allowed to drain out for two hours. The dried sensor kept in an oven for an hour at steady temperature of 80°C and allowed to cool. By doing so, a thin layer of Au nanoparticles on FBG is formed and sufficient spectral sensitivity could be achieved in detection of Cd in test samples.

Results and Discussion

The spectral response of change in wavelength with concentration is shown in Fig.5. It can be observed that as the concentration of surrounding medium increases the reflected spectrum shifts towards shorter wavelength. With the

increase in concentration of the solution surrounding the etched FBG, n_{eff} of core mode decreases resulting in shift of λ_B towards lower wavelength. Fig.6 represents the graph of Bragg wavelength λ_B versus concentration of Cd solutions. The shift in wavelength is linear with correlation factor of -0.91376. There is reduction in power of the reflected peaks with increasing concentration. This can be attributed to the etching induced multi-modal propagation conditions along the etched region Iadicicco et al. (2003). The overall shift of Bragg wavelength is 0.07nm for concentration of 0.01 to 0.04ppm. At lower concentration, the wavelength shifts of picometer resolution range could be obtained. We can determine the concentration of Cd in these samples using graph of λ_B versus concentration (Fig.6) by interpolating the graph. The concentration of Cd in collected water sample is found to be 0.001ppm. A comparative study has been done using atomic absorption spectrometer (AAS) and inductively coupled plasma spectrometer (ICP) and the results are found to be in agreement. The results are given in Table 1. Table 2 provides information on detection limits for Cd element by flame atomic absorption and ICP atomic emission.

Conclusions

We have fabricated and designed a highly sensitive etched FBG sensor using B-Ge co-doped fiber to detect the traces of Cd in drinking water. We have also observed the enhancement in sensitivity of chemical sensor by depositing Au nanoparticle layers on unclad portion of FBG. FBG sensors can be used for measuring the cadmium compounds in water with good sensitivity in the lower concentration range. The advantage of this type of sensor is its simplicity in construction and ease of use. We believe a better sensitivity of our designed sensor, can be achieved by optimization of some key parameters such as length of unclad fiber, RI profile of the core and optical design.

Acknowledgements

Authors are thankful to DAE-BRNS for providing grants. (No.2006/34/22-BRNS/2801).

International Engineering Symposium, March 3-5, 2011 Kumamoto Univ., Japan

References

- [1] Andreas O. (1997), Fiber Bragg Gratings, Rev. Sci. Instrum, Vol 68, No.1, pp 4309-4341.
- [2] Berkoff T. A. and Kersey A. D. (1996), Experimental Demonstration of Fiber Bragg Grating Accelerometer, IEEE Photonics Technology Letters, Vol. 8, No. 12 , pp 1677-1679.
- [3] Dong X., Liu Y., Liu Z., Dong X. (2001), Simultaneous Displacement and Temperature Measurement With Cantilever Based Fiber Bragg Grating Sensor, Optics Communication, Vol. 192, pp 213-217.
- [4] Friberg L., Nordberg G. F., Vouk V. B., eds. (1986), Handbook of The Toxicology of Metals, Elsevier, Amsterdam, Vol. II, pp 130-184.
- [5] Hill O. K., Malo B., Bilodeau F., Johnson D. C. and Albert J. (1993), Bragg Gratings Fabricated in Monomode Photosensitive Optical Fiber by UV Exposure Through a Phase Mask, Applied Physics Letters, Vol. 62, pp 1035-1037.
- [6] Galina Nemova and Raman Kashyap (2007), Novel Fiber Bragg Grating Assisted Plasmon-Polariton for Bio-medical Refractive Index Sensors, J. Material Science: Material Electronics, Vol. 18, No. 1, pp 327-330.
- [7] Iadicicco A., Cusano A., Persiano G.V., Cutolo A., Bernini R., Fiordano M. (2003), Refractive Index Measurements by Fiber Bragg Grating Sensor", IEEE Conference on Sensors, Vol. 1, pp 101-105.
- [8] Jarup L. et al. (1998), Health Effects of Cadmium Exposure — a Review of the Literature and a Risk Estimate. Scandinavian Journal of Work, Environment and Health, 24(Suppl. 1), pp 1-51.
- [9] Jaw-Luen T. and Jein-Neng W. (2008), Chemical Sensing Sensitivity of Long-Period Grating Enhanced by Colloidal Gold Nanoparticles, Sensors, Vol. 8, pp 171-184.
- [10] Krestin S. Wolfgang E., Rudolf M., Reinhardt W., Andrey A. (2001), A Fiber Bragg Grating Refractometer, Measurement Science and Technology Vol. 12, pp 757-764.
- [11] Lee B. (2003), Review of Present Status of Optical Fiber Sensors, Optical Fiber Technology, Vol.9, No.2, pp 57-79.
- [12] Malo B., Hill O. K., Bilodeau F., Johnson D. C. and Albert J. (1993), Point-by-Point Fabrication of Micro-Bragg Gratings in Photosensitive Fiber Using Single Excimer Pulse Refractive Index Modification Techniques, Electronics Letters, Vol. 29, pp 1668-1669.
- [13] Meltz G., Mooreyet W. W., Glenn W. H. (1989), Formation of Fiber Bragg Gratings in Optical Fibers by a Transverse Holographic Method, Optics Letters, Vol. 14, No. 15, pp 823-825.
- [14] Nobuaki et al. (1997), Under Water Acoustic Sensor With fiber Bragg Grating, Optical Review, Vol. 4, No. 6, pp 691-694.
- [15] Rao Y. J. (1997), In-Fiber Bragg Grating Sensors, Measurements Science and Technology, Vol. 8, pp 355-375.
- [16] Russel P. J., Archambault J. -L, Reekie L. (1993), Fiber Gratings, Physics World, Vol. 6, pp 41-46.
- [17] Shu-Fang C. and Lai-Kwan C. (2003), Colloidal Gold-Modified Optical Fiber for Chemical and Biochemical Sensing, Analys of Chemistry, Vol. 75, pp 16-21.
- [18] Wei L., Yanyi H., Yong X., Reginald K. L., Amnon Y. (2005), Highly Sensitive Fiber Bragg Grating Refractive Index Sensors, Applied Physics Letters, Vol. 86, pp 151122-1-3.
- [19] Xinyong D., Xiufeng Y., Chun-Liu Z., Lei D., Shum P., Ngi N. Q. (2005), A Novel Temperature Insensitive Fiber Bragg Grating Sensor for Displacement Measurement, Smart Material Structures, Vol. 14. PP N7-N10.
- [20] Xu M. G., Reekie L., Chow Y. T., Dakin J. P. (1993), Optical in Fiber Grating High Pressure Sensor, Electronics Letters Vol. 29, pp 398-399.
- [21] Zhou K., Chen X., Zhang L., Bennion I. (2004), High-Sensitivity Optical Chemosensor Based on Etched D-Fiber Bragg Gratings, Electronics Letters, Vol. 40, No. 4, pp 232-233.

Table 1 Concentration of Cd in test sample as measured using different methods

Chemical Species	FBG Sensor (ppm)	Atomic absorption Spectrometer (ppm)	Inductive coupled plasma (ppm)	WHO Standard (ppm)
Cadmium	0.001	0 *	<0.03 **	0.005

*measurements were made in USIC (University Scientific Instrument Center, Karnataka University Dharwad, India.)

**Measurements were made at Met – Chem Laboratories, Bangalore. (India Pvt. Ltd.)

Table 2 Detection limits for Cd

AAS (ng/mL)	ICP (ng/mL)
1 (0.001 ppm)	2 (0.002 ppm)

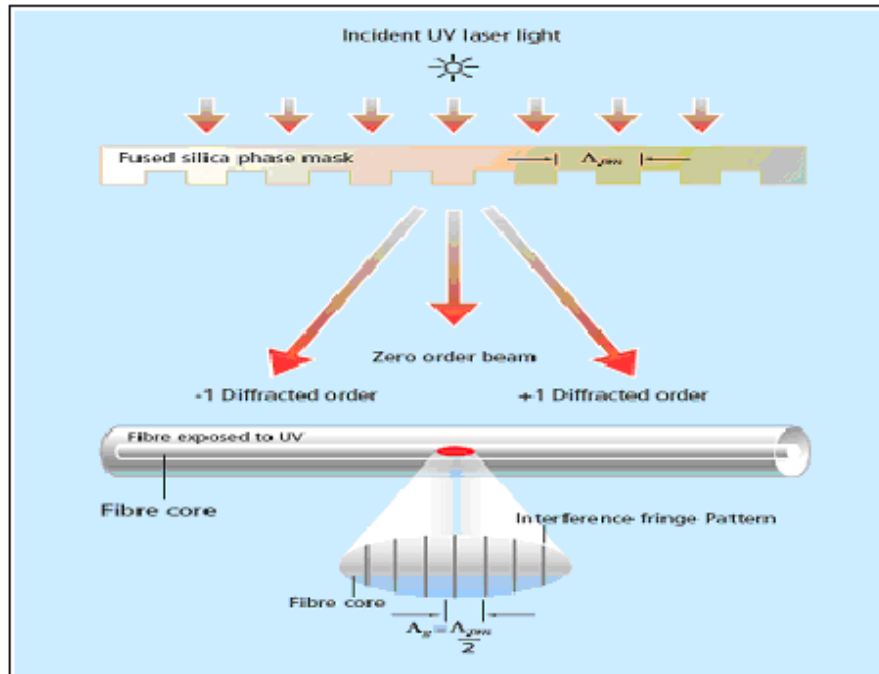


Fig.1 Fabrication of FBG using phase mask technique

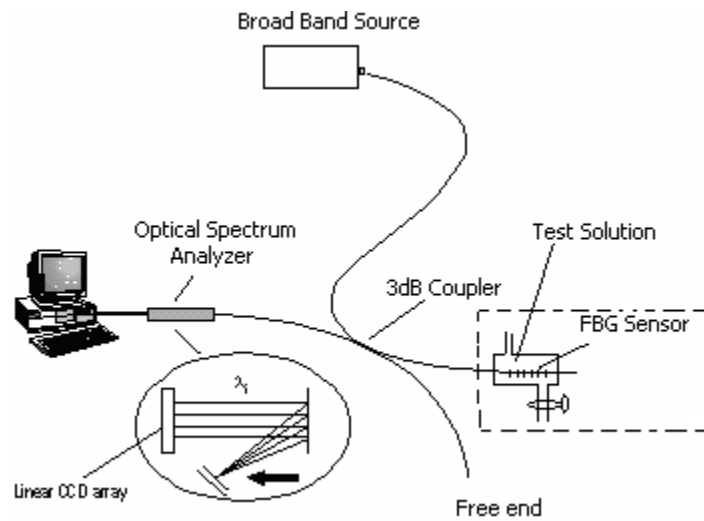


Fig.2 Experimental set up to observe

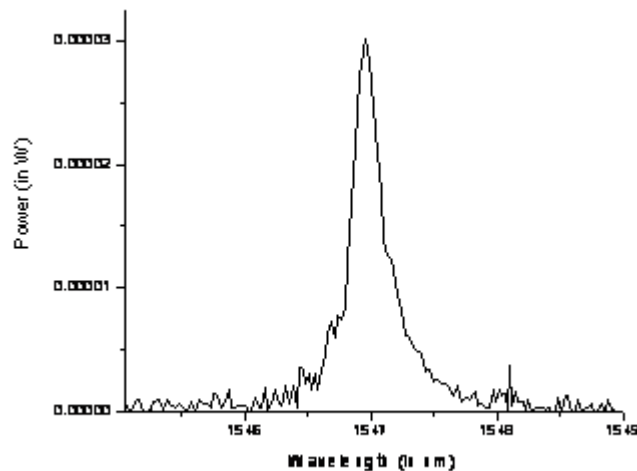


Fig.3 Reflected spectrum of FBG

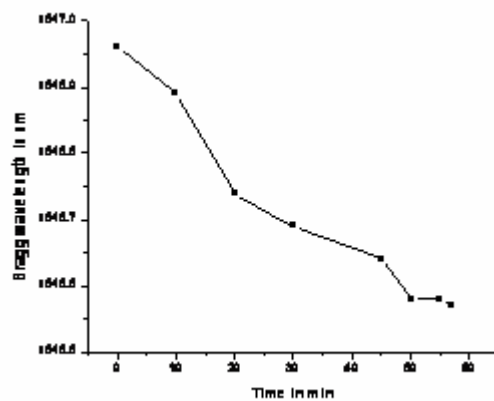


Fig.4 Bragg wavelength shift during etching

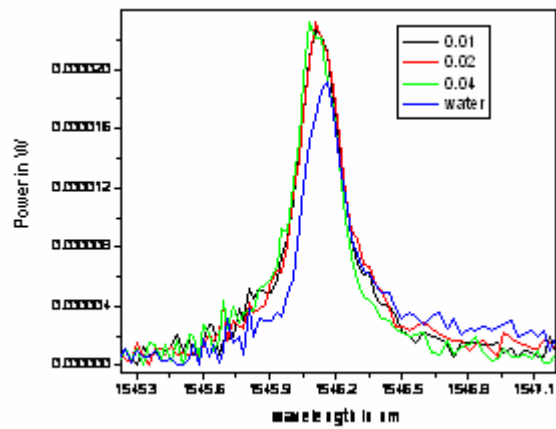


Fig.5 Reflected spectra of FBG for different concentrations of Cd solutions

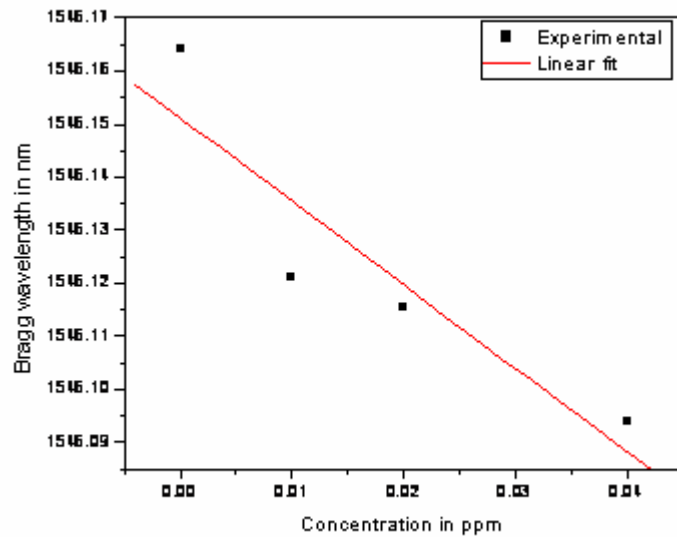


Fig.6 Bragg wavelength versus concentration of cadmium solution

**CIVIL ENGINEERING,
EARTH SCIENCES
&
RELATED FIELDS**

Studies on the Influence of Infill on Dynamic Characteristics of Reinforced Concrete Frames

**CHETHAN.K¹, R.RAMESH BABU², KATTA VENKATARAMANA³
and AKANSHU SHARMA⁴**

- 1 *Department of Civil Engineering, University Visvesvaraya College of Engineering, Bangalore University, Bangalore 560056, Karnataka, India. email: k_chethu@rediffmail.com*
- 2 *Earthquake Engineering and Vibration Research Centre, Central Power Research Institute, Bangalore 560080, Karnataka, India. email: rbabu@cpri.in*
- 3 *Department of Civil Engineering, National Institute of Technology Karnataka, Surathkal, Mangalore 575025, India. email: ven.nitk@gmail.com*
- 4 *Bhabha Atomic Research Centre, Trombay, Mumbai 400085, Maharashtra, India. email: akanshu@barc.gov.in*

Abstract: The basic investigation under dynamic loads starts with the estimation of the natural frequencies of the structure or system under consideration. This is an important parameter under dynamic analysis. Hence a detailed study has been carried out on the influence of masonry infill (MI) on fundamental natural frequency of RC frames. MI though considered as non-structural element largely affect the strength, stiffness and ductility of the framed structure during the application of lateral forces such as wind and earthquake loads. Experimental and Numerical studies are carried out on RC frames under different configurations of MI in addition to bare frames. The RC frames are designed and detailed as per the relevant Indian standard codes. A simple numerical method has been formulated to obtain the natural frequencies of RC frames with MI using FE analysis. Tri-axial shake table is used for the determination of natural frequencies experimentally. This is a part of the collaborative project between BARC, Mumbai and CPRI, Bangalore focusing on the Response evaluation of RC frames under dynamic loading. This paper consists of numerical formulation, FE analysis, Shake table tests and comparison of results.

Keywords: *RC frames, Natural frequency, Masonry infill(MI), Shake table*

Introduction

Masonry infill (MI) increases the initial stiffness of RC frames and hence attracts most of the lateral seismic forces on buildings, thereby reducing the demand on the RC frame members. However, behaviour of MI is difficult to predict because of significant variations in material properties and due to brittle failure modes. As a result, MI has often been treated as non-structural elements in buildings, and their effects are not included in the analysis and design procedure. This assumption of neglecting the effects of MI is a reasonable and justifiable for the structure under gravity loads. However, the same is not true for the structures with MI when subjected to lateral loads, especially seismic loads. Under seismic loads, the stiffness additions due to MI modify the behaviour of

structure significantly by altering its frequency. To design the structure for seismic loading, it is essential to estimate the natural frequency of the structure. Many national and international codes specify empirical formulae for estimating the natural frequencies or the time period of the frames with and without MI. Most of the formulae depend only on the height and base dimension of the structure without giving importance to the characteristics and location of MI. The concept of analysing the MI as equivalent diagonal strut has been suggested by many researchers which can be effectively used in the FE analysis to find the natural frequencies of the structures. In this direction an effort has been made to develop a simple and effective method for calculation of width of the equivalent diagonal strut which can be used to find

the natural frequencies of the structures with MI. The responses obtained from this method are compared with previous prominent methods mentioned in literature. Six numbers of 2D RC frames of one and two bays having one, two and three storeys are cast and tested with different configurations of MI. The RC frames are designed as per relevant Indian Standards codes. A tri-axial shake table of size 3m x 3m with six degrees of freedom at Earthquake Engineering and Vibration Research Centre (EVRC), Central Power Research Institute (CPRI), Bangalore, India is used to carryout the resonance search tests on the 2D RC frames with and without MI and the natural frequencies and damping are obtained. This is a part of the collaborative project between Bhabha Atomic Research Centre (BARC), Mumbai, India and CPRI, Bangalore focusing on the Response evaluation of RC frames under dynamic loading. Results obtained from experimental and numerical studies are compared and conclusions are drawn.

Background

A large number of RC and steel buildings are constructed with MI. MI are often used to fill the void between the vertical and horizontal members of the building frames with the assumption that these, will not take part in resisting any kind of load either axial or lateral; hence its significance in the analysis of frame is generally neglected. Moreover, non-availability of realistic and simple analytical models of MI and the complexity they introduce to analysis, generally keep them unaccounted. In fact an MI wall considerably enhances the strength and rigidity of the structure. Extensive researches are being carried out worldwide in the last five decades and many methods have been developed for the dynamic analysis of RC frames with MI incorporating one or more simplifying assumptions regarding its stiffness.

Paulay & Priestley (1992) caution that although MI may increase the overall lateral load capacity, it can result in altering structural response and attracting forces to different or undesired part of structures with asymmetric arrangements. The analytical modeling of MI frames is a complex issue, because these structures exhibit highly nonlinear inelastic behaviour,

resulting from the interaction of the MI panel and the surrounding frame (Singh and Das, 2006). Generally, the available modeling approaches for MI can be grouped into Micro models and Macro models. Micro models capture the behaviour of MI and its interaction with the frames in much detail, but these models are computationally expensive. On the other hand, macro models try to capture the gross behaviour of the MI, are approximate but computationally efficient (Singh and Das, 2006). Under macro models, Smith & Carter (1969) examined the behaviour of multi-story MI frame under lateral loading. The main objective of their study was to obtain reasonable information about stiffness and strength of horizontally loaded MI frames.

Construction of RC Frame

Six numbers of 2D RC frames of one and two bays having one, two and three storeys are cast. The RC frames are designed as IS 456-2000, IS 1893-2002 (Part 1) and detailed as per IS 13920-1993. The concrete grade is M25 and both mild steel (MS) and Tor steel are used for reinforcement. Commercially available bricks are used for construction of MI. The member details are shown in Table 1.

Numerical Modelling of MI

The presence of MI affects the distribution of lateral loads in the framed structure because of the increase of stiffness. The study of interaction of MI with frames has been attempted by using rigorous analysis like finite element analysis or theory of elasticity. But due to uncertainty and complexity in defining the interface conditions between MI and the frames, many approximate methods are being developed. One of the most common and popular approximations is, replacing the MI by equivalent diagonal strut whose thickness is equal to the thickness of the MI. The main problem in this approach is to find the effective width of the equivalent diagonal strut. Many researchers have suggested different method to find the width of equivalent diagonal strut. The width of strut depends on the length of contact between the wall and the columns, ' a_h ', and between the wall and beams, ' a_L ' as shown in Fig. 1.

Smith and Carter (1969) are the first to propose the formula to find the width of the equivalent diagonal strut on the basis of beam on an elastic foundation. Most of the methods proposed later are generally based on this work.

The column contact length, ' a_h ', is related with the relative stiffness of the MI to frame by the approximate equation

$$\alpha_h = \frac{\pi}{2\lambda_h} \quad \text{--- (1)}$$

and beam contact length ' a_L ' is taken approximately half of its span. The width 'w' of the strut is given by

$$w = \sqrt{\alpha_L^2 + \alpha_h^2} \quad \text{--- (2)}$$

' λ_h ' is an empirical parameter expressing the relative stiffness of the column to MI

$$\lambda_h = \sqrt[4]{\frac{E_m t \sin 2\theta}{4E_c I_c h}} \quad \text{--- (3)}$$

where;

E_m = Modulus of elasticity of MI

t = Thickness of MI

h = Height of MI

E_c = Modulus of elasticity of column

I_c = Moment of inertia of the column

θ = Slope of MI diagonal

Paulay and Priestley (1992) proposed a formula for finding the width of the equivalent diagonal strut 'w'

$$w = 0.25d \quad \text{--- (4)}$$

where, 'd' is the diagonal length of the MI. In this present study, a **new method is proposed** for calculating width of the equivalent diagonal strut based on the work of Smith and Carter.

$$\alpha_h = \frac{\pi}{2\lambda_h} \quad \text{--- (5)}$$

where, ' λ_h ' is an empirical parameter expressing the relative stiffness of the column to the MI and is given by,

$$\lambda_h = \sqrt[4]{\frac{E_m t \sin 2\theta}{4E_c I_c h}} \quad \text{--- (6)}$$

Assuming $a_L = a_h$, where a_L is a parameter for contact length of beam member with the MI, the width 'w' of the equivalent diagonal strut is given by

$$w = \sqrt{\alpha_L^2 + \alpha_h^2} \quad \text{--- (7)}$$

$$w = 1.414 a_h \quad \text{--- (8)}$$

Here the strut width is obtained by assuming the modulus of elasticity of the MI is constant and is equal to initial

modulus of elasticity. The thickness of the strut is kept as the thickness of the wall. It is found that proposed simplified method lead to a reasonably good estimate of the natural frequencies for the RC frames. A typical calculation is carried out to find the width of the equivalent diagonal strut using the above methods and the results are tabulated in Table 2.

Parameters to find the width of equivalent diagonal strut

- Breadth of Beam/Column, $b = 0.075$ m
- Depth of Beam/Column, $d = 0.1$ m
- Thickness of MI, $t = 0.075$
- Height of MI, $h = 0.8$ m
- Length of MI, $l = 1.1$ m
- Diagonal length of MI, $d = 1.36$ m
- Height of column, $h_{col} = 0.9$ m
- E_c of concrete = 2.5×10^7 kN/m²
- E_m of MI = 1.4×10^7 kN/m²
- Slope of MI diagonal $\theta = 0.629$ radians

These widths of equivalent diagonal strut are used for FE analysis of RC frames with different configurations of MI.

FE analysis of RC Frames

The RC frames are analysed using STAAD Pro software. The equivalent diagonal strut elements are assumed for modelling of MI. RC frames analysed with different configuration of MI are shown in Fig. 2. The geometry of models is developed as per dimensions. Appropriate material, boundary conditions and properties are assigned and modal analysis is carried out to find the natural frequency and mode shape of the frames. The natural frequencies obtained from modal analysis are compared with the shake table test results. Typical in-plane mode shape for two bays three storey frame is shown in Fig. 3.

Shake Table Tests on RC Frames

Shake table is a basic testing facility for development of earthquake resistant techniques. Shake table test results enhance further the understanding of the behaviour of structures and calibration of various numerical tools used for analysis. The shake table facility at EVRC, CPRI, Bangalore, India is used to carryout the resonance search tests on the RC frames with and without MI. Analysing the result, natural frequencies and damping of the RC frames are obtained.

Six 2D RC frames are cast and MI is constructed in these RC frames outside the laboratory and suitable arrangements are made to move the frames on to the shake table. Precautions are taken such that no structural damage occurs during transportation and placing of the frames on the shake table. The RC frames are mounted on the shake table as shown in Fig. 4. During Pre-testing, the frames are thoroughly checked for any cracks or damage after placing it on the shake table. At predetermined locations on the frames, accelerometers are mounted. In total 26 different configurations of MI including bare frames are tested. Resonance search tests are conducted along the in-plane direction as exploratory tests to determine the natural frequencies and damping at a very low acceleration level so that the MI and RC frames are not damaged. After each tests the frames are thoroughly checked for any damage or cracks. The frames are then removed from the shake table and the MI is removed at predetermined locations without damaging the RC frame. The specimens are again placed on the shake table and testing is continued.

Resonance Search Test

During this test, a sinusoidal input with continuously varying frequency at 1 octave/min is applied to the structure along the in-plane direction. The frequency is varied from 1-50 Hz. A Typical input time history is as shown in Fig. 5. A typical response time history is shown in Fig. 6. At natural frequency the transfer function (TF) of response to input motion generally exceeds 2, there is a phase shift between input and response motion and also there is a sudden dip in the coherence at that point. Table 3 gives the resonance search test parameters. The natural frequencies and damping are tabulated in Table 4.

Results

This work is carried out to find the influence of MI on the dynamic characteristics of RC frames. Here RC frames are cast and tested with different configurations of MI to find the natural frequencies and damping using shake table. A new numerical method is formulated for calculating the width of equivalent diagonal strut. This method is

compared with previous two prominent methods mentioned in literature. FE analysis is carried out assuming MI as equivalent diagonal strut and natural frequencies are obtained. These results are compared with the shake table test results as shown in Table 5.

Conclusions

Experimental and numerical studies are carried out on 2D RC frames under different configurations of MI in addition to bare frames. The RC frames are designed and detailed as per the relevant Indian standard codes. A simple numerical method has been formulated to obtain the natural frequencies of RC frames with MI in the FE analysis. Shake table is used for the determination of natural frequencies experimentally. The following are the major conclusions:

- The MI, although do not interfere in the vertical load resisting system for RC frames, they significantly affect lateral load-resisting system of the same.
- Smith and Carter method gives high value for the width of equivalent diagonal strut. Paulay and Priestley is the simplest of all the methods as its formulation is only 0.25 times the diagonal length of the MI but do not consider the characteristics of the MI. The proposed formulation is simple and effective method in finding the width of the equivalent diagonal strut, considering characteristics of the MI.
- The natural frequency of the structure with complete MI is significantly higher than the natural frequency of the bare framed structure. In most of the cases, the natural frequencies of the frames with complete MI are found to be around twice as that of the bare framed structures.
- By comparing the results of 2B3SF & 1B3SF, 2B2S2 & 1B2S1, 2B3S & 1B3S it can be said that the natural frequency does not depend on the number of bays, whether it is bare, complete MI or MI with similar type of openings in the subsequent bays.
- The reduction in the natural frequency is more, when the MI is removed in the lower floor as compared to the removal of MI in the upper floors as can be seen from the 2B3S5 & 2B3S and 2B3S3 & 2B3S4 tests. This is due to the

- contribution of MI towards the stiffness being more in the lower floors as compared to the upper floors.
- Similarly, there is an increase in the natural frequency when the MI is removed from the upper floors as observed from 1B3S2A & 1B3S and 1B2S1 & 1B2S. From this we can conclude that contribution of MI towards mass being more in the upper floors as compared to the lower floors.
 - The natural frequencies and damping values in 2D RC frames will be high in the presence of MI. Hence the role of MI in resisting the lateral forces like earthquake and wind is significant and has to be accounted during designing of the structures.
 - The prediction of natural frequencies using the proposed formulation in FE analysis matches reasonably well with the shake table test results.

Acknowledgements

The authors gratefully acknowledge the encouragement and support extended by UVCE, CPRI, NITK and BARC in bringing out this research paper.

References

- [1] Drydale R.G, Hamid A.A and Baker L.R, (1994), "Masonry Structures-Behaviour and Design", Prentice Hall, Englewood cliffs, New Jersey, USA
- [2] Indian Standard, IS 456-2000, "Plain and Reinforced Concrete-Code of Practice," BIS, New Delhi, India.
- [3] Indian Standard IS 1893-2002, "Criteria for earthquake resistant design of structures", Part 1: General Provisions and Buildings, Fifth Revision, BIS, New Delhi, India.
- [4] Indian Standard, IS 13920-1993, "Ductile Detailing of Reinforced Concrete Structures subjected to Seismic Forces" -Code of Practice, BIS, New Delhi, India.
- [5] Murty, C. V. R., and Jain, S. K., "Beneficial influence of masonry infills on seismic performance of RC frame buildings", Proceedings, 12th World Conference on Earthquake Engineering, New Zealand, Paper No. 1790, 2000
- [6] Paulay T and Priestley, M.J.N (1992), "Seismic Design of Concrete and Masonry Buildings", John Wiley & Sons Inc., New York, USA
- [7] Smith B.S and Carter C (1969), "A method of analysis for infilled frames", Proceedings of the Institute of Civil Engineers, Vol-44, 31-48
- [8] Yogendra Singh and Dipankar Das (2006), "Effect of URM Infills on Seismic Performance of RC Frame Buildings", 4th International Conference on Earthquake Engineering, Taipei Taiwan, Paper No. 064

Table 1 Details of RC frames

Description	RC Frame
No. of storeys	1, 2 & 3
No. of bays	1 & 2
Storey Height	0.9 m
Bay width	1.2 m
Beam and Column	75 mm x100 mm
Longitudinal Reinforcement	4-6 mm MS in beam, 4-8 mm Tor in column
Transverse Reinforcement	2L-3 mm MS @75mm c/c

Table 2 Width of Equivalent diagonal strut

Sl no.	Methods	Width (m)
1.	Smith and Carter	0.598
2.	Paulay and Priestley	0.340
3.	Proposed method	0.332

Table 3 Sine sweep test parameters

Type of vibration	:	Sinusoidal sweep
Axis of vibration	:	In-plane Direction
Frequency (range)	:	1 to 50 Hz
Acceleration (Peak)	:	0.1 g
Sweep rate (Logarithmic)	:	1 octave/minute
Number of Sweeps	:	One up sweep per axis

Table 4

Shake

Table test results of 2D RC frames

SL. No	Model	Natural Frequency (Hz)	Damping (%)
1	2B3SF	29.50	11.86
2	2B3S1	36.00	9.78
3	2B3S2	30.00	8.41
4	2B3S3	26.25	7.26
5	2B3S4	25.75	6.50
6	2B3S5	19.25	3.92
7	2B3S	14.00	1.96
8	2B2SF	42.00	9.78
9	2B2S1	35.00	7.02
10	2B2S2	15.00	4.26
11	2B2S3	15.50	1.98
12	2B2S	19.25	1.94
13	2B1SF	**	**
14	2B1S1	**	**
15	2B1S	39.75	1.80
16	1B3SF	29	6.96
17	1B3S1	34	4.72
18	1B3S2	20.75	2.04
19	1B3S1A	12.75	2.82
20	1B3S2A	11.25	2.12
21	1B3S	14.00	1.74
22	1B2SF	42.75	4.43
23	1B2S1	16.5	2.34
24	1B2S	20.00	1.89
25	1B1SF	**	**
26	1B1S	41.25	1.85

Note: Frequency range of operation for shake table test is only between 0-50 Hz.

** indicates that the natural frequency is out of the test range (> 50 Hz).

Table 5 Comparison of natural frequencies of 2D RC frames obtained from three methods for equivalent diagonal strut with shake table test results (Hz)

Model	Shake table	Smith & carter	Paulay & Priestley	Proposed Method
2B3SF	29.50	30.99	30.52	30.47
2B3S1	36.00	43.08	41.87	41.78
2B3S2	30.00	35.39	34.14	34.06
2B3S3	26.25	29.91	29.46	29.40
2B3S4	25.75	28.62	27.92	27.88
2B3S5	19.25	20.07	19.85	19.84
2B3S	14.00	14.13* Bare RC frame		
2B2SF	42.00	47.71	44.68	44.50
2B2S1	35.00	42.69	37.52	37.25
2B2S2	15.00	15.47	16.55	16.58
2B2S3	15.50	16.65	17.84	17.87
2B2S	19.25	21.25* Bare RC frame		
2B1SF	**	123.16	115.43	115
2B1S1	**	112.85	102.49	102
2B1S	39.75	41.42* Bare RC frame		
1B3SF	29	29.97	30.54	30.54
1B3S1	34	37.32	36.47	36.42
1B3S2	20.75	17.34	18.25	18.28
1B3S1A	12.75	11.58	12.54	12.57
1B3S2A	11.25	10.29	10.71	11.03

1B3S	14.00	14.31* Bare RC frame		
1B2SF	42.75	45.41	44.7	44.62
1B2S1	16.5	16.38	17.66	17.70
1B2S	20.00	22.42* Bare RC frame		
1B1SF	**	123.92	114.5	114
1B1S	41.25	43.14* Bare RC frame		

Note: Frequency range of operation for shake table test is only between 0-50 Hz.

** indicates that the natural frequency is out of the test range (> 50 Hz)

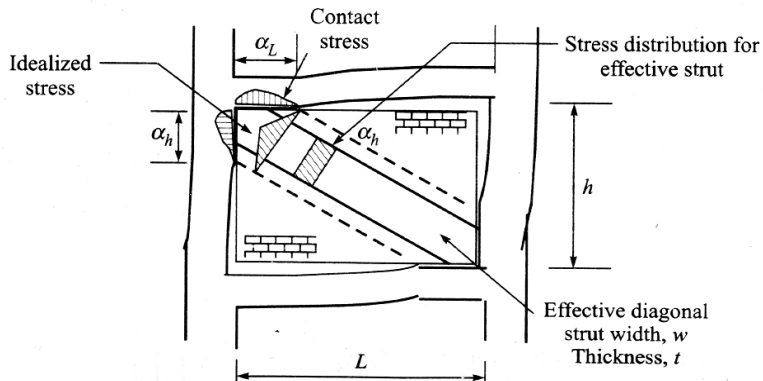


Fig. 1 Equivalent diagonal strut (Drysdale, et al. 1994)

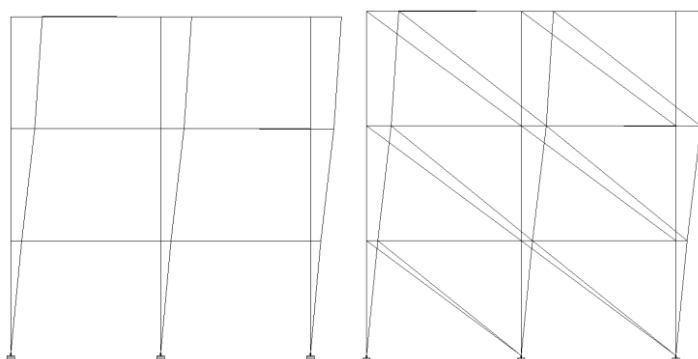


Fig 3 Typical in plane mode shapes for two bay three storey frame



Fig. 4 RC Frames placed on Shake table

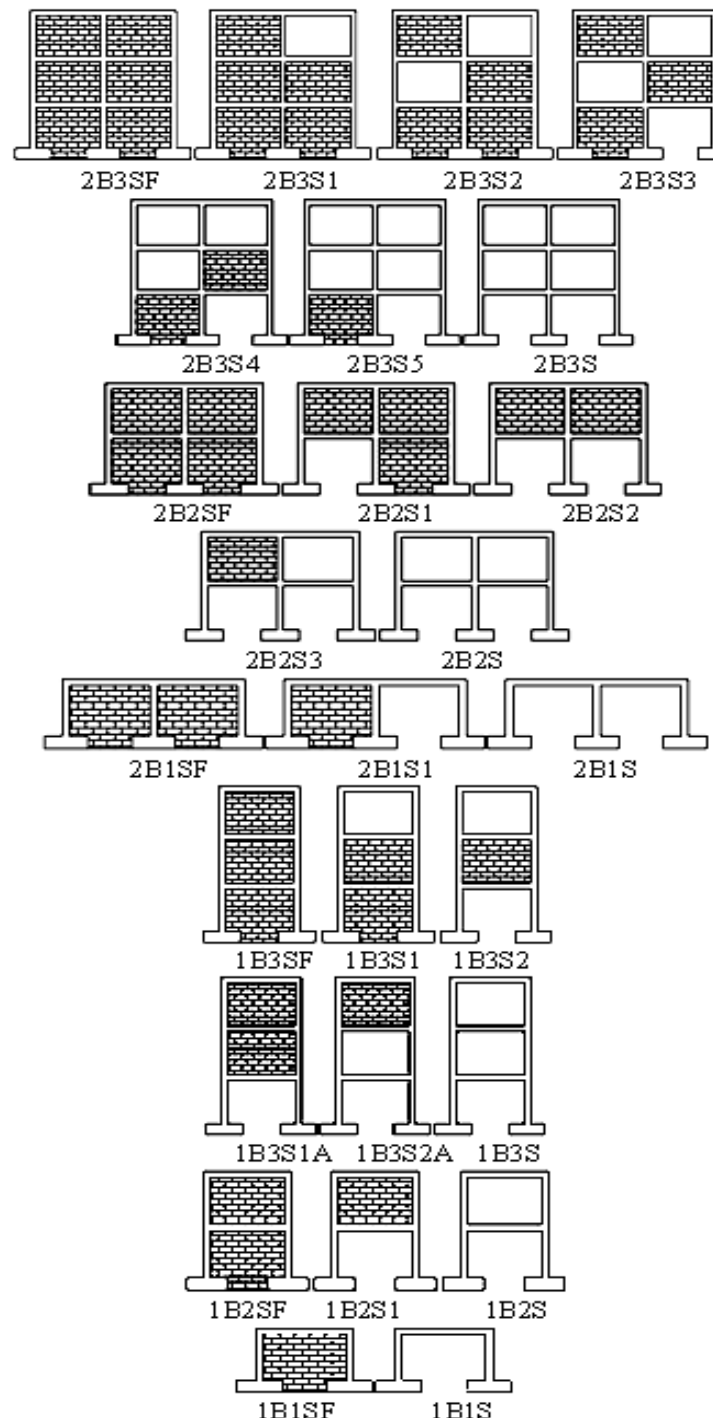


Fig 2 Different Configurations of MI in 2D RC frames

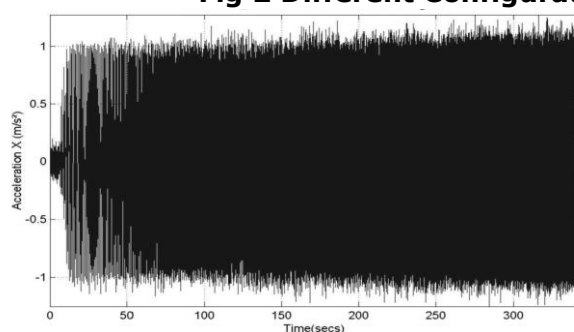


Fig 5 Typical Input time history

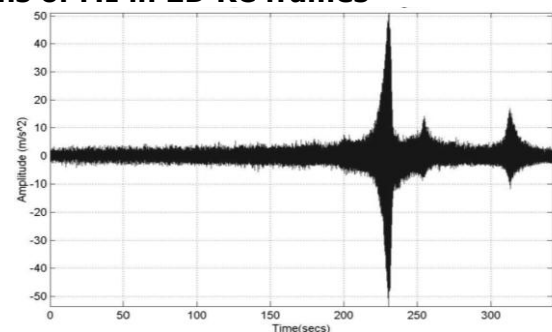


Fig 6 Typical Response time history

VULNERABILITY ANALYSIS IN SEISMIC DESIGN OF STRUCTURES

Balaji K.V.G.D.¹ Gopala Raju S.S.S.V.² Praveena Gorla⁴

1. Dept. of Civil Engg, GITAM University, India, balaji@gitam.edu
2. GITAM University, India, gopalaraju@gitam.edu
3. Dept. of Civil Engg., GITAM, pravee.smiley@gmail.com

ABSTRACT: The design philosophy adopted in Indian codes of earthquake resistant design is to resist the Design Based Earthquake (DBE) without significant structural damage and to withstand the Maximum Considered Earthquake (MCE) without collapse. The improved design philosophy proposed in this paper is to resist the Design Based Earthquake (DBE) with no structural damage, to resist the Maximum Considered Earthquake (MCE) with no or affordable structural damage, and to resist Mega Earthquake (ME) with no or localized collapse without entering into progressive collapse mode. A case study of a five storeyed residential building is taken to design as per the design philosophies given in Indian Standard Code and with the proposed improved design philosophy with Mega Earthquake. The impact of improved design philosophy on the structure along with increase in cost is presented.

Key words: *Earthquake resistant design, Progressive Collapse analysis, Design Based Earthquake, Maximum Considered Earthquake*

Introduction: After the occurrence of Latur earthquake (magnitude 6.2) on 29th September 1993 in a zone which is least susceptible for earthquakes, there is greater concern to develop earthquake resistant design for Structures even in the areas which are very less susceptible to earthquake prone. Further the collapse of structures in Bhuj earthquake (magnitude 7.9) on 26th January 2001 demands an insight into the existing design philosophy and to improve the design philosophy further to resist a mega earthquake without entering a progressive collapse mode to prevent loss of life (Ye Lieping (2010)) by mobilizing the potential strength of the structural system. Hence there is necessity to develop the methods for the design of multistory structures to resist maximum considered earthquake (MCE) with no or affordable structural damage and to resist a mega earthquake with no or localized collapse without entering into progressive collapse mode (Wang Yayong(2010)).

A multistoried structure in Zone-II a zone corresponding to least earthquake prone with an open ground floor intended for parking and five upper floors with four flats in each floor as shown in Fig.1 is taken for study. This is used for comparing the existing method of philosophy of design with the improved method of philosophy of design developed for the multistory structures. The earthquake load considered for MCE is taken as twice that of the DBE as recommended in Indian codes of practice IS 1893 - 2002 and the same has been implemented even in the improved design philosophy. The Mega Earthquake considered for the improved design philosophy is the maximum earthquake

Existing Design Philosophy: The requirement of steel in various columns as per the existing code of practice for design based earthquake and Maximum Considered Earthquake are found out and tabulated in Table 1. The load factors adopted while

calculating the quantities of steel in MCE are same as that of DBE. The strength of concrete and steel for design based earthquake are equal to their characteristic strengths which in present case will be 25MPa and 415MPa respectively. The strength of concrete and steel for Maximum Considered Earthquake are equal to their strengths without material safety factors (materials safety factors adopted for concrete and steel will be 1.5 and 1.15 respectively) which in present case will be 37.5 MPa and 477.25MPa respectively.

Proposed Design Philosophy (Static Analysis): The requirement of steel in various columns as per the proposed method of design for DBE and MCE and ME are found out and tabulated in Table 2. The load factors adopted while calculating the quantities of steel in MCE are same as that of DBE and equal to unity in ME. The strength of concrete and steel for design based earthquake are equal to their characteristic strengths (corresponding to 95% value) which in present case will be 25 MPa and 415 MPa respectively. The strength of concrete and steel proposed for Maximum Considered Earthquake are equal to their mean strengths (corresponding to 50% value) which in present case will be 33.75 MPa and 469MPa respectively. The strength of concrete and steel proposed for Mega Earthquake are corresponding to 5% value which in present case will be 37.5 MPa and 477.25 MPa respectively.

Proposed Design Philosophy (Progressive Collapse Analysis): The requirement of steel in various columns is calculated by removing one column at a time. The maximum amount of steel required for each column is identified and the same has been tabulated. The maximum requirement of steel in each column in progressive analysis for DBE, MCE and ME are found out and tabulated in Table 3. The load factors adopted while calculating the

quantities of steel in DBE, MCE and ME are as recommended in UFC 4-023-3 (2009). The strength of concrete and steel for design based earthquake are equal to their characteristic strengths (with out material safety factors and corresponding to 95% value) which in present case will be 37.5 MPa and 477.25 MPa respectively. The strength of concrete and steel proposed for Maximum Considered Earthquake are equal to their mean strengths (corresponding to 50% value) which in present case will be 50.63 MPa and 539.35 MPa respectively. The strength of concrete and steel proposed for Mega Earthquake are corresponding to 5% value which in present case will be 63.75 MPa and 601.45 MPa respectively.

Discussion of Results for Existing Design Philosophy: The requirement of steel estimated for the columns to resist maximum considered earthquake is higher when compared to the requirement of steel based on the Design Based Earthquake. The Ratio (ζ) steel required for MCE to the steel required for DBE varying from 1.1 to 2.7. This reveals that the columns with low ζ resist maximum considered earthquake and the columns with high ζ do not have the adequate resistance. The columns in the stilt and ground floors have relatively higher values of ζ indicating the requirement of enhanced local resistance

Discussion of Results for Proposed Design Philosophy (Static Analysis): The requirement of steel estimated for the columns to resist MCE is higher when compared to the requirement of steel based on the DBE. The Ratio (ζ) steel required for MCE to the steel required for DBE varying in the similar range of existing design philosophy. However, the ratio (ξ) i.e., steel required for ME to the steel required for MCE will be in the range of 1.1 to 1.3 for 30% of

columns in stilt floor and close to unity for all columns in the top most floor.

Discussion of Results for Proposed Design Philosophy (Progressive Collapse Analysis):

It can be observed from Table 3 that some of the members which are not critical in the static analysis become critical and requires additional attention. Thus progressive collapse analysis assists in identifying the members which become critical due to a loss of member which otherwise will not be critical.

Conclusions

Based on the procedure outlined in the paper, the following conclusions can be drawn based on the above analysis

- The behaviour of the structure as a whole and the members which need extra precaution can be identified at the design stage to resist unexpected mega earthquakes effectively.
- The additional resistance required for various members can be identified through progressive collapsed analysis to resist the gravity and earthquake loads without leading to major collapse of the structure.
- The study brings out the need for defining logically the Maximum Considered Earthquake (MCE) and Mega Earthquake and the resistance parameters for concrete and steel to be adopted in the analysis for MCE and ME.
- The vulnerability of large number of columns in ground and first storey corroborates the recommendation of UFC 4-023-03 for enhanced local resistance in flexure (clause 2-2.4.3) by a factor of 2.

- In place of over strength factors used in UFC 4-023-03 in the progressive collapse analysis strengths corresponding to 95%, 50% and 5% are suggested. This will be useful for existing grades of concrete and could be easily extended to grades of concrete being developed under different controlled conditions. This will also result in the development of design towards ensuring a desirable level of probability of survival.

The cost of the structure increases in the present case increased by about 4 %. However, the increase of cost depend on a variety of reasons such as number of columns, layout of columns and beams, symmetry maintained in the structure, height of the structure and the earthquake zone in which the structure is located.

Acknowledgements: The authors are grateful to the management and the authorities of GITAM University for the facilities provided to carry out this work.

References

- [1] IS 456: 2000, Indian Standard Code of Practice for Plain and Reinforced Concrete, Fourth Revision, Bureau of Indian Standards, New Delhi, July 2000.
- [2] IS 1893 (Part I) : 2002, Indian Standard code of practice on Criteria for Earthquake Resistant Design of Structures,, Fifth Revision, Bureau of Indian Standards, New Delhi, June 2002.
- [3] UFC 4-023-03:2009, Unified Facilities Criteria (UFC) for Design of Buildings to Resist Progressive Collapse, Department of Defence, United States of America, July 2009.
- [4] Wang Yayongi (2010), Revision of Seismic Design Codes Corresponding to Building Damages in the Objectives and Collapse Prevention for Building Structures in the "5.12" Wenchuan Earthquake, Journal of Earthquake Engineering and Engineering Vibration, Vol. 9, No. 2, pp. 147-155.
- [5] Ye Lieping et al (2010), Design Objectives and Collapse Prevention for Building Structures, Journal of Earthquake Engineering and Engineering Vibration, Vol. 9, No. 2, pp. 189-199

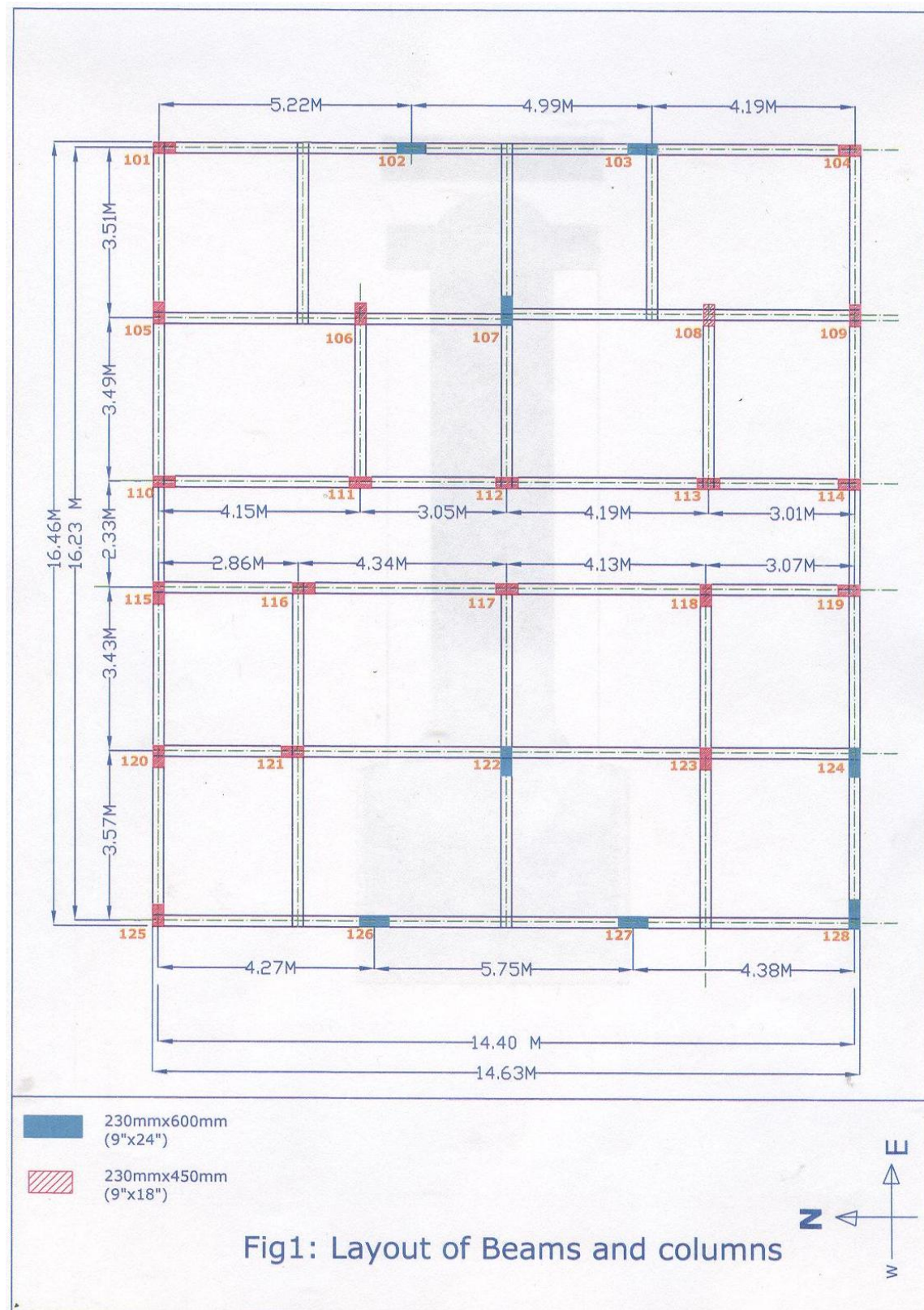


Table 1: Area of Steel Required for DBE and MCE in Existing Static Analysis

Col . No.	Stilt floor		Ground floor		1st floor		2nd floor		3rd floor		4th floor	
	DBE	MCE										
101	1738	2981	1746	2650	1503	2880	1417	2595	1123	1772	943	1059
102	764.33	1799	900	1999	875	1875	760	1726	544	1439	440	767
103	833.28	2523	1034	2646	1086	2533	1051	2595	858	1722	721	1029
104	975.01	2732	1209	2650	1105	2584	1099	2106	852	1443	683	820
105	1587	3047	1758	2642	1625	2892	1560	2530	1277	2203	1089	1429
106	1484	2714	1365	2718	1009	2537	931	2252	642	1543	402	616
107	1098	2841	1478	2919	1610	2825	1635	2630	1294	2737	418	836
108	1198	2897	1204	3028	1001	2865	843	2347	573	1409	410	639
109	973	2674	1408	2971	1330	2798	1189	2413	866	1696	595	912
110	1920	3064	2013	2529	1903	3166	1686	2654	1244	2358	711	1160
111	1844	2566	1950	2587	1753	2685	1685	2574	1306	2472	594	789
112	3229	3859	2539	4140	2511	2554	1817	2618	1061	2311	418	768
113	1516	2952	1558	2900	1334	2575	1327	2730	1084	2068	581	808
114	1715	3342	1847	3429	1776	3113	2532	2522	1094	2232	781	1304
115	2468	3177	2390	3016	2291	2733	1966	2858	1381	2573	967	1406
116	2565	3030	2582	3404	2013	2743	1560	3227	952	2058	603	828
117	2544	2977	2666	3385	2160	2787	1714	2669	1095	2221	593	918
118	1528	2620	1677	2756	1419	2582	1323	2780	1053	1976	814	1087
119	1454	3302	1507	3459	1423	3232	1261	2703	934	1896	684	1114
120	1698	2908	1843	2539	1757	2839	1567	2799	1163	2166	725	1036
121	2595	2779	2658	2717	2393	2582	2066	3247	1335	2723	436	686
122	1546	2780	1783	3134	1536	3043	1466	2699	1044	2444	269	680
123	1536	2746	1893	2781	1627	2562	1625	2906	1023	2113	432	756
124	1432	3127	1380	3032	1293	2608	1128	2265	872	1661	686	782
125	761	2165	978	2185	929	2126	815	1940	601	1595	354	687
126	760	2193	1016	2231	962	2175	846	2014	644	1535	361	702
127	1214	2791	1353	2518	1331	2861	1238	2503	992	1785	739	882
128	878	2365	1209	2628	1271	2572	1314	2437	1171	1947	1022	1274
Totals	42976	76586	45735	76965	41555	72755	38107	68902	26907	54151	16449	24500

Table 2 - Area of Steel Required for DBE, MCE and ME in Proposed Static Analysis

Col . No.	Stilt floor			Ground floor			1st floor			2nd floor			3rd floor			4th floor		
	DBE	MCE	ME	DBE	MCE	ME	DBE	MCE	ME	DBE	MCE	ME	DBE	MCE	ME	DBE	MCE	ME
101	1738	4075	3643	1746	3989	3229	1503	3466	2609	1417	2819	2677	1123	1889	1771	943	1119	934
102	764	1908	2437	900	2133	2580	875	1989	2389	760	1795	2092	544	1509	1704	440	800	919
103	833	3232	3193	1034	3376	3114	1086	3181	2829	1050	2749	2531	857	1801	2069	721	1069	1012
104	975	2898	2810	1209	3208	2957	1105	2813	2537	1099	2301	2535	852	1533	1638	683	858	803
105	1587	3529	2895	1758	3758	3053	1625	3678	2745	1560	3197	2771	1277	2336	2325	1089	1502	1394
106	1484	3030	4070	1365	2926	3872	1009	2719	3414	930	2357	2713	642	1616	1813	402	644	665
107	1098	3611	4318	1478	3873	4128	1610	3920	3740	1635	3766	3105	1294	2863	2846	418	866	954
108	1198	3138	2842	1204	3240	2742	1001	3058	2514	843	2499	2911	573	1486	1680	410	689	732
109	973	2870	2951	1408	3176	3077	1330	3032	2760	1189	2570	2984	866	1780	2028	595	946	985
110	1920	4007	3974	2013	4140	3477	1903	4045	2895	1685	3537	3115	1244	2478	2543	711	1199	1235
111	1844	4091	3404	1950	3935	2741	1753	4103	3187	1685	3908	2635	1306	2641	2618	594	818	756
112	3229	4140	3194	2539	4140	2576	2511	4031	3425	1817	4129	2845	1061	2491	2656	418	797	912
113	1516	3728	4140	1558	3779	4140	1334	3551	3531	1327	3068	2658	1084	2193	2505	581	852	877
114	1715	4140	4140	1847	4140	4140	1776	4140	3880	2532	3569	3081	1093	2348	2657	781	1375	1439
115	2468	4140	2882	2390	4051	2418	2291	4129	4140	1966	4006	3668	1381	2736	2784	966	1476	1449
116	2465	4140	4140	2582	4140	4140	2013	4140	3761	1560	3775	3099	951	2181	2384	602	855	877
117	2543	4140	3512	2666	4140	3781	2160	4140	3399	1714	3961	2792	1095	2387	2477	593	949	924
118	1528	3480	3653	1677	3929	3725	1419	3697	3375	1323	3170	2847	1053	2125	2374	814	1133	1144
119	1453	4030	4140	1507	4089	4140	1423	3804	4119	1261	3045	3340	932	2009	2269	684	1163	1234
120	1698	4016	3836	1843	4020	3505	1757	3814	2858	1567	3254	2728	1163	2262	2382	725	1068	1050
121	2595	4066	2903	2658	4140	2745	2393	4138	2623	2066	3969	2814	1335	2970	3005	436	728	747
122	1546	3430	4019	1783	3625	4039	1536	3646	3585	1466	3468	2772	1044	2568	2870	269	702	801
123	1536	3821	4140	1893	3865	4140	1627	3720	3641	1625	3605	2786	1023	2227	2583	432	802	896
124	1432	3312	4140	1379	3470	4099	1293	3026	3408	1128	2399	2558	872	1723	1862	686	822	694
125	761	2277	2623	978	2398	3034	929	2238	2618	815	2044	2286	601	1689	1871	354	722	822
126	760	2300	2941	1016	2340	2906	962	2289	2607	846	2110	2481	644	1596	1839	361	714	783
127	1214	3422	3763	1353	3432	3929	1331	3161	3344	1238	2688	2709	991	1874	2105	739	919	916
128	878	2527	2562	1209	2826	2916	1271	2793	2740	1314	2582	2937	1171	2051	2220	1022	1327	1264
Total	43753	97498	97264	46943	100278	95343	42826	96462	88673	39417	86341	78470	28073	59364	63879	17469	26913	27217

Table 3 - Area of Steel Required for DBE, MCE and ME in Proposed Progressive Collapse Analysis

Col. No.	Stilt floor			Ground floor			1st floor			2nd floor			3rd floor			4th floor		
	DBE	MCE	ME	DBE	MCE	ME	DBE	MCE	ME	DBE	MCE	ME	DBE	MCE	ME	DBE	MCE	ME
101	1738	4078	4140	1746	4140	3583	1503	3574	3493	1417	3281	2698	1123	2340	1885	943	2153	1656
102	764	2437	2635	900	3959	4456	875	2277	2530	760	2114	2303	543	1655	1779	440	1255	1307
103	833	3120	3898	1034	4301	25937	1086	2973	3111	1050	2566	2653	857	2066	1911	721	1670	1396
104	975	3341	2898	1209	3395	3280	1105	3083	3073	1099	2443	2394	852	1752	1703	683	1821	1656
105	1587	4133	3048	1758	4117	2983	1625	3147	2846	1560	3868	3474	1277	2959	2670	1089	2460	2047
106	1484	2958	4050	1365	4140	4140	1009	3169	3342	930	2702	2809	642	1882	1879	402	828	828
107	1098	3829	4127	1478	4745	4241	1610	3455	3200	1635	3362	3197	1294	2621	2617	418	1242	1214
108	1198	3068	3550	1204	4098	4140	1001	3266	3002	843	2787	2958	573	1842	1907	410	1026	938
109	973	3518	3236	1408	4140	3082	1330	3822	2872	1189	3168	3164	866	2338	2274	595	1717	1462
110	2468	4140	4140	2390	4140	4140	2291	4140	4140	1966	4140	3511	1381	2936	2825	966	2272	2056
111	2465	4140	4140	2582	4140	4140	2013	4217	4140	1560	3626	3396	951	2179	2207	602	1447	1312
112	2543	4140	4140	2666	4140	4140	2160	4140	4128	1714	3924	3909	1095	2428	2217	593	7557	1225
113	1528	4140	3597	1677	4020	4140	1419	3615	3947	1323	3066	2936	1053	2193	2326	814	1722	1622
114	1453	4002	4140	1507	4140	4140	1423	3896	3970	1261	3175	3271	932	2345	2376	684	1970	1786
115	1920	4046	3643	2013	4140	3521	1903	4140	3329	1685	3941	2941	1244	3489	2649	711	2451	2154
116	1844	4140	3814	1950	4140	4140	1753	4140	4140	1685	4103	3795	1306	2925	2737	594	1651	1428
117	3229	4140	4140	2539	4140	4140	2511	4140	4140	1817	4140	4140	1061	2753	2523	418	1794	1522
118	1516	4140	4140	1558	4140	4140	1334	4140	3479	1327	4140	2843	1084	3265	2548	581	1929	1788
119	1715	4140	3833	1847	4140	3749	1776	4140	3248	2532	4064	4140	1093	2847	2916	781	2373	2203
120	1698	4029	3553	1843	4140	3790	1757	4140	3260	1567	3658	3279	1163	2675	2414	725	1800	1506
121	2595	4140	3985	2658	4140	4140	2393	4140	4140	2066	4140	3914	1335	2662	2601	436	1358	1184
122	1546	3276	4439	1783	4297	4449	1536	3190	3090	1466	3019	3155	1044	2329	2632	269	1104	1104
123	1536	4140	4140	1893	3217	4109	1627	3823	3626	1625	3458	3300	1023	2285	2380	432	1716	1503
124	878	3025	2945	1209	3952	3335	1271	4085	3597	1314	3385	2973	1171	2707	2311	1022	2628	1730
125	1432	4140	4140	1379	3726	4140	1293	4140	3001	1128	3346	2523	872	2581	1986	686	2176	1551
126	761	3265	3246	978	3955	3334	929	2588	2518	815	2374	2320	601	1908	1839	354	1104	1104
127	760	3257	4054	1016	3950	3988	962	2609	2838	846	2407	2582	644	1900	1970	361	1156	1104
128	1214	4140	4140	1353	3952	3335	1331	4085	3597	1238	3385	2974	992	2707	2311	739	2628	1923
Total	43753	105062	105951	46943	113644	130852	42826	102274	95797	39417	93782	87552	28072	68569	64393	17469	55008	42309

Response Control of MDOF Space Frame Structure Using Multiple Tuned Mass Dampers

KIRAN K. SHETTY¹

KRISHNAMOORTHY²

GOPINATH NAYAK³

¹ Department of Civil Engineering, Manipal Institute of Technology, Manipal University, Manipal 576104, India. e-mail: kiran_manoor@yahoo.com

² Department of Civil Engineering, Manipal Institute of Technology, Manipal University, Manipal 576104, India. e-mail: moorthy.mit@manipal.edu

³ Department of Civil Engineering, Manipal Institute of Technology, Manipal University, Manipal 576104, India. e-mail: palligopi@rediff.com

Abstract: Dynamic response of a multi-storey asymmetrical space frame structures having six degrees of freedom (three translations along x, y, z-axes and three rotations about these axes) at each node, with multiple tuned mass dampers (MTMD) on its top is obtained. Each tuned mass damper (TMD) is modeled using a two-noded element having two translational degrees of freedom at each node. MTMD with uniformly distributed frequencies are considered for this purpose. The effectiveness of MTMD in suppressing the structural response is determined by comparing the response of corresponding structure without MTMD. It is found that the MTMD can be used effectively to suppress the translational and rotational responses of the asymmetrical structures.

Keywords: Vibration control, MTMD, six degrees of freedom at each node, asymmetrical space frame structures

Introduction

The concept of vibration control has been accepted and is nowadays frequently applied to civil engineering problems. One of the simplest and the most reliable control measures at present is the tuned mass damper (TMD) which is composed of a mass, a spring and a damper. The natural frequency of the damper is tuned to a frequency near the natural frequency of the main structure. The vibration of the main structure causes the damper to vibrate in resonance. Because the light mass of the damper vibrates much more violently than the heavy mass of the main structure, the vibration energy dissipated through the damping in the tuned mass damper is more pronounced than the dissipation through the damping in the main structure. The main disadvantage of a single TMD is the sensitivity to the error in the natural frequency of the structure and/or that in the damping ratio of the TMD. Either mis-tuning or off-optimum damping can reduce significantly the effectiveness of a TMD. To remedy such a drawback, more than one tuned mass

damper with different dynamic characteristics have been proposed. Multiple tuned mass dampers with distributed natural frequencies were proposed by Xu and Igusa (1992, 1994) and also studied by Yamaguchi and Harnpornchai (1993), Jangid and Datta (1994), Abe and Igusa (1995), Park and Reed (2001) and Chunxiang (2000, 2003). It was shown that MTMD is more effective for vibration control as compared to single TMD. Almost all of these studies considered the controlled structure as a single degree of freedom (SDOF) system with its fundamental modal properties to design the TMD and MTMD. However, a real building usually possesses a large number of degrees of freedom and is actually asymmetric to some degree even with a nominally symmetric plan. It will undergo lateral as well as torsional vibrations simultaneously under purely translational excitations. Thus, the simplified SDOF system, which ignores the structural lateral-torsional coupling and TMD effect on different modes, could overestimate the control effectiveness of TMD (Jangid and Datta (1997)).

Consequently, the controllers have to be designed through taking into account the effect of transverse-torsional coupled vibration modes in such cases. Examination of the TMD and MTMD for structures, which possess transverse-torsional coupled vibration modes has already been performed by Jangid and dutta (1997), Chunxiang and Weilan (2006), Lin et al. (1999), Singh et al. (2002) and Pansare and Jangid (2003).

Jangid and dutta (1997), Pansare and Jangid (2003) and Chunxiang and Weilan (2006) have studied the response control of two degrees of freedom (one translation and one rotation) torsional systems by a cluster of MTMD. Lin et al. (1999) studied the response reduction of a multi-storey torsional building (with two translations and one rotation at each floor) system with one and two tuned mass dampers. Singh et al. (2002) studied the response control of a multi-storey tensional building (with two translations and one rotation at each floor) system with four tuned mass dampers, placed along two orthogonal directions in pairs.

The formulation of mathematical model of the structure is the most critical step in any seismic analysis, because how well the computed response agrees with the actual response of a structure during an earthquake depends primarily on the quality of the structural idealization. The quality of the structural idealization can be improved by more realistic idealizations of buildings that consider beam flexure, all translations along x, y, z-axes and all rotations about these axes. In the present paper, the effectiveness of MTMD in controlling the response of a asymmetrical multi-storey space frame structures having six degrees of freedom (three translations along x, y, z-axes and three rotations about these axes) at each node are investigated. The total degrees of freedom of the controlled structure (with MTMD) in this idealization are $(6 \times N) + (2 \times n)$, where N is the number of nodes and n is total number of MTMD.

Analysis

The structure is divided into number of elements consisting of beams and columns. The beams and columns are modeled

using two noded frame elements with six degrees of freedom at each node i.e., three translations along x, y and z-axes and three rotations about these axes. For each element, the stiffness matrix, consistent mass matrix, and transformation matrix are obtained. The mass matrix and the stiffness matrix of each element from local direction are transformed to global direction as proposed by Paz (2001). The mass matrix and the stiffness matrix of each element are assembled by direct stiffness method to get the overall mass matrix, M, and overall stiffness matrix, K, for the entire structure. Knowing the overall mass matrix, M, and overall stiffness matrix, K, the frequencies for the structure is obtained using simultaneous iteration method. The damping matrix for structure is obtained using Rayleigh's equation, $C = \alpha M + \beta K$, where α and β are the constants. These constants can be determined easily if the damping ratio for each mode is known. The overall dynamic equation of equilibrium for the entire structure can be expressed in matrix notations as

$$M\ddot{u} + C\dot{u} + Ku = f(t) \quad (1)$$

where M, C and K are the overall mass, damping, and stiffness matrices of size $6N \times 6N$, where N is the number of nodes.

\ddot{u} , \dot{u} , u are the relative acceleration, velocity and displacement vectors with respect to ground and $f(t)$ is the nodal load vector. $u = u_1, v_1, w_1, \theta_{x1}, \theta_{y1}, \theta_{z1}, u_2, v_2, w_2, \theta_{x2}, \theta_{y2}, \theta_{z2}, \dots, u_N, v_N, w_N, \theta_{xN}, \theta_{yN}, \theta_{zN}$.

The nodal load vector due to earthquake is obtained using the equation

$$f(t) = -M I \ddot{u}_g(t) \quad (2)$$

Where M is the overall mass matrix, I is the influence vector of size $6N \times 1$, and $\ddot{u}_g(t)$ is the ground acceleration. The resulting equation of dynamic equilibrium is solved using Newmarks method to obtain the displacements and acceleration at the nodes as explained in Chopra (1995). Owing to its unconditional stability, the constant average acceleration scheme (with $\beta = 1/4$ and $\gamma = 1/2$) is adopted.

Modeling of multiple tuned mass dampers

Each tuned mass damper (TMD) is modeled using a two-noded element with two translational degrees of freedom (x and z direction) at each node. The natural frequencies of the MTMD are uniformly distributed around their average natural frequency. The natural frequency ω_j (i.e. $\omega_j = \sqrt{k_j/m_j}$) of the jth TMD is expressed as

$$\omega_j = \omega_T \left[1 + \left(j - \frac{n+1}{2} \right) \frac{\beta}{n-1} \right] \quad (3)$$

and

$$\omega_T = \sum_{j=1}^n \omega_j / n \quad (4)$$

$$\beta = \frac{\omega_n - \omega_1}{\omega_T} \quad (5)$$

Where n is the total number of MTMD, ω_T is the average frequency of all the MTMD and β is the frequency range parameter of the MTMD.

As suggest by Xu and Igusa (1992), the manufacturing of MTMD with uniform stiffness is simpler than those with varying stiffnesses. In this study, the distribution of natural frequencies of the MTMD is achieved by keeping the stiffness constant (i.e., with $k_1 = k_2 = \dots = k_n = k_T$), but allowing the mass of each TMD to vary. The mass and the damping constant of the jth TMD are expressed as

$$m_j = \frac{k_T}{\omega_j^2} \quad (6)$$

$$c_j = 2m_j \xi_T \omega_j \quad (7)$$

where ξ_T is the damping ratio which is kept constant for all the MTMD.

The ratio of total mass of MTMD to the total mass of the structure is defined as the mass ratio i.e.

$$\mu = \frac{\sum_{j=1}^n m_j}{m_s} = \frac{m_T}{m_s} \quad (8)$$

The constant stiffness required for each TMD can be evaluated as

$$k_T = \frac{\mu m_s}{\sum_{j=1}^n 1/\omega_j^2} \quad (9)$$

The average frequency of MTMD corresponds only to the lateral mode of vibration. In case of an asymmetrical building the translations in x and z directions have different dominant modes. Keeping these in view, two different tuning frequency ratios are considered in the study, namely;

$$f_1 = \frac{\omega_T}{\omega_{s1}} \quad (10)$$

and

$$f_2 = \frac{\omega_T}{\omega_{s2}} \quad (11)$$

where ω_{s1} and ω_{s2} are the natural frequency of lateral vibration of the structure corresponding to the dominant mode in x and z direction respectively.

The natural frequency, stiffness, damping and mass parameters of the dampers in x-direction are denoted by ω_{jx} , k_{Tx} , c_{jx} and m_{jx} . Similar parameters for the dampers along the z-direction are denoted by ω_{jz} , k_{Tz} , c_{jz} and m_{jz} . It is to be noted that the stiffness and damping parameters of the jth TMD in x and z directions are different where as mass parameter of the jth TMD in x and z directions are same ($m_{jx} = m_{jz} = m_j$).

The stiffness, damping and mass matrices of each TMD is expressed as

$$k_{TMD} = \begin{pmatrix} k_{Tx} & 0 & -k_{Tx} & 0 \\ 0 & k_{Tz} & 0 & -k_{Tz} \\ -k_{Tx} & 0 & k_{Tx} & 0 \\ 0 & -k_{Tz} & 0 & k_{Tz} \end{pmatrix} \quad (12)$$

$$c_{TMD} = \begin{pmatrix} c_{jx} & 0 & -c_{jx} & 0 \\ 0 & c_{jz} & 0 & -c_{jz} \\ -c_{jx} & 0 & c_{jx} & 0 \\ 0 & -c_{jz} & 0 & c_{jz} \end{pmatrix} \quad (13)$$

$$m_{TMD} = \begin{pmatrix} 0 & 0 & 0 & 0 \\ 0 & 0 & 0 & 0 \\ 0 & 0 & m_j & 0 \\ 0 & 0 & 0 & m_j \end{pmatrix} \quad (14)$$

The stiffness, damping and mass matrices of each TMD are added to the overall stiffness matrix, overall damping matrix and overall mass matrix of the structure at corresponding global degrees of freedom.

Dynamic response of a multi-storey asymmetrical space frame structure with and without MTMD

The material and geometric properties of the controlled (with MTMD) asymmetrical four storey space frame structure considered for the study are shown in Fig. 1. The natural frequency of lateral vibration of the structure corresponding to the dominant mode in x and z direction are $\omega_{s1} = 8.737$ rad/sec and $\omega_{s2} = 8.376$ rad/sec respectively. The structure is subjected to bi-directional (x and z directions) harmonic ground excitation equal to $a_0 \sin(\omega t)$ (where a_0 is equal to 20% of acceleration due to gravity and ω is the excitation frequency). The damping ratio of structure is taken as 2% of critical for all modes, damping ratio of MTMD is taken as 1% of critical, mass ratio is taken as 1%, the total number of MTMD is taken as 8, the frequency range parameter of the MTMD is taken as 0.2 and tuning frequency ratio ($f = f_1 = f_2$) is taken as unity. Fig. 2 shows the variation of translational and rotational response of the structure against the frequency ratio 1 (ω/ω_{s1}) and frequency ratio 2 (ω/ω_{s2}) for a structure with and without MTMD. The response of the uncontrolled structure is sharply peaked and the peak is centered around the fundamental natural frequency of the uncontrolled structure. This peak is due to resonating effect. Further, it can also be seen from the Fig. 2 that there is a significant reduction in the peak value of the horizontal displacements and rotations of the structure due to MTMD. Hence the MTMD can be used effectively to suppress the translational and rotational responses of the structure. It is also found that, in the frequency range, $0.8 > \omega/\omega_s > 1.3$, the response curves of structure with and without MTMD is almost same; this indicates that MTMD are effective only near the fundamental natural frequency of structure. Thus the effectiveness of MTMD is dependent on the frequency characteristics of ground motion.

Conclusions

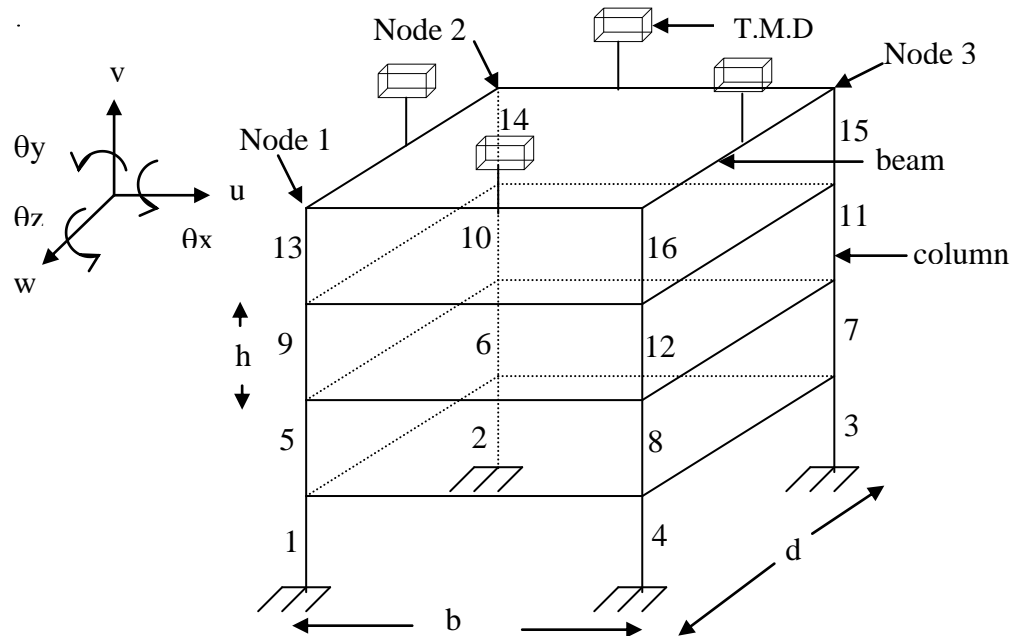
The performance of MTMD for controlling the dynamic response of a multi-storey asymmetrical space frame structures having six degrees of freedom at each node is investigated. The responses of the structure with MTMD are compared with those of the same structure without MTMD. It is found that MTMD can be used effectively to suppress the translational and rotational responses of the asymmetrical structure. It is also found that the effectiveness of MTMD is dependent on the frequency characteristics of ground motion.

References

- [1] Abe, M. and Igusa, T. (1995), Tuned Mass Dampers for Structures with Closed Spaced Natural Frequencies, *Earthquake Engineering and Structural Dynamics*, Vol. 24, pp 247-261.
- [2] Chopra, A.K., *Dynamics of Structures*, Prentice-Hall, Englewood Cliffs, N.J. 1995.
- [3] Chunxiang, Li. (2000), Performance of Multiple Tuned Mass Dampers for Attenuating Undesirable Oscillations of Structures Under the Ground Acceleration, *Earthquake Engineering and Structural Dynamics*, Vol. 29, No. 9, pp. 1405-1421.
- [4] Chunxiang, Li. and Weilian, Qu. (2006), Optimum Properties of Multiple Tuned Mass Dampers for Reduction of Translational and Torsional Response of Structures Subjected to Ground Acceleration, *Engineering Structures*, Vol. 28, pp. 472-494.
- [5] Chunxiang, Li. and Yanxia, Liu. (2003), Optimum Multiple Tuned Mass Dampers for Structures Under the Ground Acceleration Based on the Uniform Distribution of System Parameters, *Earthquake Engineering and Structural Dynamics*, Vol. 32, pp. 671-690.
- [6] Igusa, T. and Xu, K. (1994), Vibration Control Using Multiple Tuned Mass Dampers, *Journal of Sound and Vibration*, Vol. 175, No. 4, pp. 491-503.
- [7] Jangid, R.S. and Datta, T.K.(1994), "Dynamic Characteristics of Structure with Multiple Tuned Mass Dampers", *Proceedings of 10th Symposium on Earthquake Engineering*, University of Roorkee, India, pp. 259-267.
- [8] Jangid, R.S. and Datta, T.K. (1997), Performance of Multiple Tuned Mass Dampers for Torsionally Coupled System, *Earthquake Engineering and Structural Dynamics*, Vol. 26, pp. 307-317.
- [9] Lin, C.C., Ueng, J.M. and Huang, T.C. (1999), Seismic Response Reduction of Irregular Buildings Using Passive Tuned Mass Dampers, *Engineering Structures*, Vol. 21, pp. 513-524.
- [10] Pansare, A.P. and Jangid, R.S. (2003), Tuned Mass Dampers for Torsionally Coupled Systems, *Wind structures*, Vol. 6, No. 1, pp. 23-40.
- [11] Park, J. and Reed, D. (2001), Analysis of Uniformly and Linearly Distributed Mass Dampers Under Harmonic and Earthquake Excitation, *Engineering Structures*, Vol. 23, pp. 802-814.
- [12] Paz ,M. *Structural Dynamics*, CBS Publishers, Delhi, 2001.
- [13] Singh, M.P., Singh, S. and Moreschi, L.M. (2002), Tuned Mass Dampers for Response Control of

International Engineering Symposium, March 3-5, 2011 Kumamoto Univ., Japan

- Torsional Buildings, Earthquake Engineering and Structural Dynamics, Vol. 31, pp. 749-769.
 [14] Xu, K. and Igusa, T. (1992), Dynamic Characteristics of Multiple Substructures with Closely Spaced Frequencies, Earthquake Engineering and Structural Dynamics, Vol. 21, pp. 1059-1070.
 [15] Yamaguchi, H. and Harnporntchai, N. (1993), Fundamental Characteristics of Multiple Tuned Mass Dampers for Suppressing Harmonically Forced Oscillations, Earthquake Engineering and Structural Dynamics, Vol. 22, No. 1, pp. 51-62.



Time period of the structure (sec)	Mass on each beam ($\text{kN}\cdot\text{sec}^2/\text{m}^2$)	b (m)	d (m)	h (m)	Size of beam (m)	Size of column 1,5,9,13, 2,6,10,14, (m)	Size of column 4,8,12,16 3,7,11,15 (m)	Modulus of elasticity (kN/m^2)
0.75	2.9	6	6	3.3	0.3×0.6	0.6×0.6	0.4×0.4	2.24×10^7

Fig. 1 (a) Four-storey space frame structure with MTMD on its top.

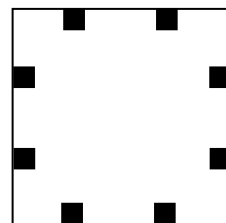


Fig. 1 (b) The placement of MTMD on the top of the structure

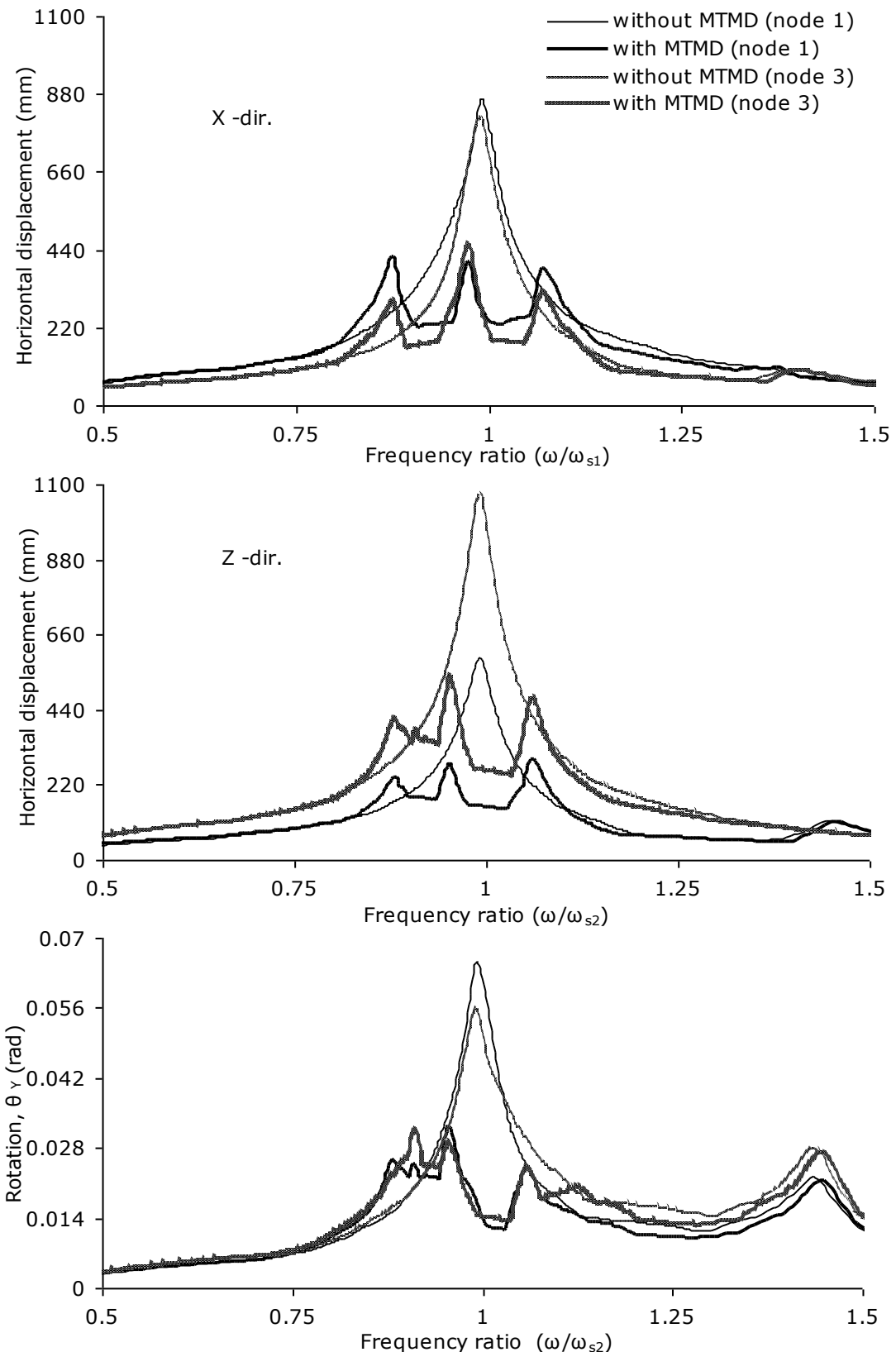


Fig. 2 Variation of translational and rotational response of the structure against frequency ratio

Static and Dynamic Analyses of Laminated Composite Plates Using Higher Order Refined Computational Models

S. SHANTHARAM PATIL

*Faculty of Architecture, Manipal Institute of Technology, Manipal University,
Manipal 576104, India. Email:spatilss@yahoo.com*

Abstract: Present study is to assess the accuracy of the few computational models based on various shear deformation theories in predicting the static and dynamic behaviour of antisymmetric angle-ply laminated composite plates. Five two-dimensional analytical models available in the literature are used for the present evaluation. The equations of equilibrium are obtained using Principle of Minimum Potential Energy (PMPE) and the equations of motion using Hamilton's principle. Solutions are obtained in closed-form using Navier's solution technique. The solutions of the static analysis are obtained by solving the boundary value problem and the natural frequencies are obtained by solving the eigenvalue problem. The accuracy of the solutions obtained from the different models are established by comparing the results with the solutions wherever available in the literature.

Keywords: *Composite laminates, higher order theories, computational models, analytical solutions, flexural, shear deformation.*

Introduction

Fibre-reinforced laminated composite plates and shells are increasingly used as structural elements in the aeronautical, aerospace and automobile industry as well as in other fields of modern technology. This is mainly due to the high strength-to-weight and stiffness-to-weight ratios of composite material as well as their ability to be tailored to meet the design requirement. To use them efficiently a good understanding of their structural and dynamical behaviour and also an accurate knowledge of the deformation characteristics, stress distribution and natural frequencies under various load conditions are needed. The Classical Laminate Plate Theory of Reissner and Stavsky (1961) which ignores the effect of transverse shear deformation becomes inadequate for the analysis of multilayer composites. The First Order Shear Deformation Theories of Whitney and Pagano (1970) based on Reissner (1945) and Mindlin (1951) assume linear in-plane stresses and displacements, respectively, through the laminate thickness. The

Classical Laminate Plate Theory (CLPT) and the First Order Shear Deformation Theory (FSDT) are the simplest equivalent single layer theories and they adequately describe the kinematic behaviour of most laminates. In order to overcome the limitations of FSDTs, Higher Order Shear Deformation Theories (HSHTs) were developed. Higher order theories can represent the kinematics better, may not require shear correction factors and can yield more accurate prediction of stress distributions. Owing to these reasons, an increasing number of higher order theories for laminated composite plates and shells has been published over the past two decades. Results were reported in the literature using analytical and numerical methods. Hildebrand et al. (1949) were the first to introduce this approach to derive improved theories of plates and shells. Reddy (1984, 1990) derived a set of variationally consistent equilibrium equations for the kinematic models originally proposed by Levinson (1980) and Murthy (1981). Using the theory of Reddy, Senthilnathan et al. (1987) presented a simplified higher order theory

by introducing a further reduction in the functional degrees of freedom by splitting up transverse displacement into bending and shear contributions. Using the higher-order theory of Reddy (1984) free vibration analysis of isotropic, orthotropic and laminated plates was carried out by Reddy and Phan (1985). A complete review of various shear deformation theories for the analysis of multilayer composite plates and shells is available in the review articles by Noor and Burton (1989, 1990). Rohwer (1992) presented a comparative study of various higher order shear deformation theories. A selective review of the various analytical and numerical methods used for the stress analysis of laminated composite and sandwich plates was presented by Kant and Swaminathan (2001). Analytical formulations, solutions and comparison of numerical results for the buckling, free vibration, stress analyses of cross ply composite and sandwich plates based on the higher order refined theories already reported in the literature by Kant (1982), Pandya and Kant (1987, 1988) and Kant and Manjunatha (1988) were presented by Kant and Swaminathan (2001, 2002). Theoretical formulations and solutions for the static and dynamic analyses of antisymmetric angle ply laminated composite and sandwich plates was presented by Swaminathan and Patil (2007, 2008). In this paper, analytical formulations developed and solutions obtained is presented for the stress and free vibration analyses of antisymmetric angle-ply laminated composite plates using two higher order refined computational models. Plates with varying slenderness ratios, fibre orientations, number of layers, degree of anisotropy, edge ratios and material property relations are studied. A set of computer programs in C-language using all the models is developed to solve the boundary value problem for the stress analysis and eigenvalue problem for the free vibration analysis. Extensive numerical results are obtained and presented for static and free vibration analysis. Solutions obtained using these models are also compared with the results available in the literature and then benchmark results with real properties using all the models are

presented for the antisymmetric angle-ply composite plates.

Displacement models

For the purpose of evaluation, the following two higher order displacement models are considered. Analytical formulations and solutions for the static and dynamic analyses of antisymmetric angle-ply laminated composite plates are obtained in this investigation and results obtained using these two models (Model-1 and Model-2) are referred to as *present* in all the tables.

Model -1 (Kant and Manjunatha, 1988)

$$\begin{aligned} u(x, y, z, t) &= u_o(x, y, t) + z\theta_x(x, y, t) + z^2u_o^*(x, y, t) + z^3\theta_x^*(x, y, t) \\ v(x, y, z, t) &= v_o(x, y, t) + z\theta_y(x, y, t) + z^2v_o^*(x, y, t) + z^3\theta_y^*(x, y, t) \\ w(x, y, z, t) &= w_o(x, y, t) + z\theta_z(x, y, t) + z^2w_o^*(x, y, t) + z^3\theta_z^*(x, y, t) \end{aligned} \quad (1)$$

Model -2 (Pandya and Kant, 1988)

$$\begin{aligned} u(x, y, z, t) &= u_o(x, y, t) + z\theta_x(x, y, t) + z^2u_o^*(x, y, t) + z^3\theta_x^*(x, y, t) \\ v(x, y, z, t) &= v_o(x, y, t) + z\theta_y(x, y, t) + z^2v_o^*(x, y, t) + z^3\theta_y^*(x, y, t) \\ w(x, y, z, t) &= w_o(x, y, t) \end{aligned} \quad (2)$$

In addition to the above, the following higher order models and the first order model developed by other investigators are also considered for the evaluation. Analytical formulations developed and numerical results generated independently using these models are also being presented here with a view to have all the results on a common platform.

Model -3 (Reddy, 1984)

$$\begin{aligned} u(x, y, z, t) &= u_o(x, y, t) + z\left[\theta_x(x, y, t) - \frac{4}{3}\left(\frac{z}{h}\right)^2\left\{\theta_x(x, y, t) + \frac{\partial w_o}{\partial x}\right\}\right] \\ v(x, y, z, t) &= v_o(x, y, t) + z\left[\theta_y(x, y, t) - \frac{4}{3}\left(\frac{z}{h}\right)^2\left\{\theta_y(x, y, t) + \frac{\partial w_o}{\partial y}\right\}\right] \\ w(x, y, z, t) &= w_o(x, y, t) \end{aligned} \quad (3)$$

Model - 4 (Senthilnathan et al. 1987)

$$\begin{aligned} u(x, y, z, t) &= u_o(x, y, t) - z\frac{\partial w_o^b}{\partial x} - \frac{4z^3}{3h^2}\frac{\partial w_o^s}{\partial x} \\ v(x, y, z, t) &= v_o(x, y, t) - z\frac{\partial w_o^b}{\partial y} - \frac{4z^3}{3h^2}\frac{\partial w_o^s}{\partial y} \\ w(x, y, z, t) &= w_o^b(x, y, t) + w_o^s(x, y, t) \end{aligned} \quad (4)$$

Model - 5 (Whitney and Pagano, 1970)

$$\begin{aligned} u(x, y, z, t) &= u_o(x, y, t) + z\theta_x(x, y, t) \\ v(x, y, z, t) &= v_o(x, y, t) + z\theta_y(x, y, t) \\ w(x, y, z, t) &= w_o(x, y, t) \end{aligned} \quad (5)$$

Where the terms u , v and w are the displacements of a general point (x, y, z) in the laminate domain in the x , y and z directions respectively. The parameters u_o , v_o , are the in-plane displacements w_o , w_o^b and w_o^s are the transverse displacement, it's bending and shear components respectively of a point (x, y) on the middle plane. The functions θ_x , θ_y are rotations of the normal to the middle plane about y and x axes respectively. The parameters u_o^* , v_o^* , w_o^* , θ_x^* , θ_y^* , θ_z^* and θ_z are the higher -order terms in the Taylor's series expansion and they represent higher-order transverse cross sectional deformation modes.

Numerical result and discussions

To study the accuracy of prediction of the static and dynamic response using the various higher order displacement models, the numerical examples solved are described and discussed. For all the problems a simply supported plate is considered for comparison. Sinusoidal transverse loading is considered for the stress analysis. The equations of equilibrium are obtained using the Principle of Minimum Potential Energy (PMPE) and the equation of motion using Hamilton's principle. Results are obtained in closed-form using Navier's solution technique for the above geometry and loading and the accuracy of the solution is established by comparing the results with the solutions wherever available in the literature.

A. Static analysis

Example 1. A simply supported two and four layered ($n=2,4$) square antisymmetric angle-ply ($\theta/\!-\theta/\dots$) composite plates under sinusoidal transverse load is considered. The layers are of equal thickness. The numerical values of maximum transverse deflection \bar{w} for the two and four layered square composite plates are given in Table 1. The following material properties Ren (1990) were used in obtaining numerical results.

$$E_1 = 40 \times 10^6 \text{ psi (276 GPa)}$$

$$E_2 = E_3 = 1 \times 10^6 \text{ psi (6.895 GPa)}$$

$$G_{12} = G_{13} = 0.5 \times 10^6 \text{ psi (3.45 GPa)}$$

$$G_{23} = 0.6 \times 10^6 \text{ psi (4.12 GPa)}$$

$$\nu_{12} = \nu_{23} = \nu_{13} = 0.25$$

The results are compared with the values already reported in the literature (Ren, 1990). In the case of a thick plates (a/h ratio 4 and 10) with different fibre orientations considered, the transverse displacement values predicted by Model-2 is very much closer to the values reported by Ren. All other models show large difference in displacement values. For a/h ratio equal to 4 and fibre orientation equal to 15° , the transverse deflection \bar{w} values predicted by Model-1, Model-2, Model-3, Model-4 and Model-5 are 4.88%, 2.62%, 11.22%, 27.86%, and 3.36% lower for a two layered square plate and 3.39%, 1.39%, 8.79%, 26.59% and 8.18% lower for a four layered square plate as compared to the values obtained by Ren. For thin ($a/h=100$) square plate, all the models give almost the same results and they are in very good agreement with those given by Ren. The results clearly indicates that the percentage difference in values with respect to Ren in predicting transverse displacement is lesser in case of Model-2 and more in case of Model-4.

Example 2. To study the effect of degree of anisotropy a simply supported four layered antisymmetric angle-ply ($30^\circ/-30^\circ/30^\circ/-30^\circ$) rectangular composite plate ($b=3a$) with layers of equal thickness for various values of E_1/E_2 ratios under sinusoidal transverse load is considered. The side-to-thickness a/h ratio considered equal to 4. The following material properties were used in obtaining numerical results

$$E_1/E_2 = 3, 20, 40, \quad E_2 = E_3, \quad G_{23} = 0.5E_2$$

$$\nu_{12} = \nu_{23} = \nu_{13} = 0.25, \quad G_{12} = G_{13} = 0.6E_2$$

The non-dimensionalized maximum values of transverse displacement \bar{w} , in-plane stresses $\bar{\sigma}_x$, $\bar{\sigma}_y$ and $\bar{\tau}_{xy}$ for various values of E_1/E_2 ratios are given in Table 2. At lower range of E_1/E_2 ratio there is no much deviation in the values obtained using all the models. For E_1/E_2 ratio equal to 3, the value of \bar{w} predicted by Model-2, Model-3, Model-4 and Model-5 are respectively 1.51%, 1.26%, 1.26%, and 1.16% higher as compared to Model-1, the values of $\bar{\sigma}_x$ predicted by Model-2, Model-3, Model-4 and Model-5 are respectively 1.38%, 1.91%, 1.86% and 6.25% lower as compared to Model-1 and

the values $\bar{\tau}_{xy}$ predicted by Model-2, Model-3, Model-4 and Model-5 are respectively 2.06%, 2.83%, 2.39% and 1.54% higher as compared to Model-1. At higher range of E_1/E_2 ratio the transverse deflection values computed using Model-1 and Model-2 are very much closer but a considerable difference exists between these two and other models. For E_1/E_2 ratio equal to 40, the value of \bar{w} predicted by Model-2, Model-3, Model-4 and Model-5 are respectively 1.14% higher, 4.09%, 4.09% and 5.39% lower as compared to Model-1, the values of $\bar{\sigma}_x$ predicted by Model-2, Model-3, Model-4 and Model-5 are respectively 22.06%, 1.23%, 1.30% higher and 31.06% lower as compared to Model-1 and the values $\bar{\tau}_{xy}$ predicted by Model-2, Model-3, Model-4 and Model-5 are respectively 0.19%, 43.06%, 42.30% higher and 2.36% lower as compared to Model-1. The result clearly shows that for all values of E_1/E_2 ratios considered, the non-dimensionalized transverse deflection \bar{w} decreases with the increase in degree of anisotropy. For all E_1/E_2 ratios considered, the values of in-plane stresses $\bar{\sigma}_x$ and $\bar{\sigma}_y$ computed using Model-1, Model-2, Model-3 and Model-4 increases, as increase in degree of anisotropy, where as little deviation exists in the values predicted by Model-5.

B. Dynamic analysis

Example 3. The orthotropic material properties of individual layers in all the square laminates considered are

$$E_1/E_2 = 40, E_2 = E_3, G_{23} = 0.5E_2$$

$$G_{12} = G_{13} = 0.6E_2, \nu_{12} = \nu_{13} = \nu_{23} = 0.25$$

The variation of natural frequencies with respect to side-to-thickness ratio a/h for a two and eight layered composite plate is presented in Table 3 and Table 4. The results are compared with the values already reported in the literature (Reddy and Phan, 1985). In the case two layered thick plates (a/h ratios 2, 4, 5 and 10) the values predicted by Model-1 and Model-2 are very much closer whereas Model-3, Model-4 and Model-5 very much overpredicts these values. For thick plates with a/h ratio equal to 2, the values predicted by Model-2, Model-3, Model-4 and Model-5 are respectively 0.49% lower, 17.84%, 18.83% and 3.53% higher as

compared to Model-1. For a eight layered plate with a / h ratio equal to 4, the values predicted by Model-2, Model-3, Model-4 and Model-5 are respectively 0.06% lower, 2.27%, 2.27% and 0.88% higher as compared to Model-1. The difference between the models tends to reduce for thin and relatively thin plates. As the number of layers increases the percentage difference in values obtained using above theories decreases significantly. It is seen that the non-dimensionalized fundamental frequency increases with increase in the number of layers.

Example 4. The variation of non-dimensionalized natural frequencies with respect to side-to-thickness ratio a/h for different E_1/E_2 ratio in a four layered antisymmetric angle-ply ($45^\circ/-45^\circ/45^\circ/-45^\circ$) square laminate with layers of equal thickness are given in Table 5. In case of four layered thick composite plate with a/h ratio equal to 2 and E_1/E_2 ratio equal to 3 the values predicted by Model-2, Model-3, Model-4 and Model-5 are respectively 0.80% lower, 0.10%, 0.10% and 0.04% higher as compared to Model-1, whereas at E_1/E_2 ratio equal to 40 the values predicted by Model-2, Model-3, Model-4 and Model-5 are respectively 0.21% lower, 9.69%, 9.69% and 4.58% higher as compared to Model-1. At higher range of E_1/E_2 ratio equal to 20-40, the values obtained using Model-1 and Model-2 are very much closer but a considerable difference exists between these two and other models. The results clearly shows that non-dimensionalized fundamental frequency increases as E_1/E_2 ratio and a/h ratio increases. The percentage difference in values in above theories increases with the increase in the degree of anisotropy. As the number of layer increases, the percentage difference in values obtained using the above theories decreases significantly.

Conclusions

Analytical solutions to the static and dynamic analyses of simply supported antisymmetric angle-ply laminated composite plates based on two higher order refined computational models which takes in to account the effects of both transverse shear and transverse normal deformations are presented. Comparative

International Engineering Symposium, March 3-5, 2011 Kumamoto Univ., Japan

study on the static and dynamic response of various shear deformation theories applied to multilayer composite plates is done. Exact solutions already available in the literature are used for comparison. Some sample results are detailed for the comparison. The results of all the models compared include the transverse displacement, in-plane stresses and natural frequencies. From the extensive numerical results presented in this paper it is concluded that for the laminated composite plates, Model-1 and Model-2 considered in the present investigation predicts the transverse displacements, in-plane stresses and natural frequency values with reasonable accuracy compared to other models.

Acknowledgements

All India Council for Technical Education, Government of India provided financial support to carry out this research.

References

- [1] Hildebrand et al. (1949), Note on the Foundations of the Theory of Small Displacements of Orthotropic Shells, NACA TN-1833.
- [2] Kant, T. (1982), Numerical Analysis of Thick Plates, Computer Methods in Applied Mechanics and Engineering, Vol. 31, pp. 1-18.
- [3] Kant, T. and Manjunatha, B. S. (1988), An Unsymmetric FRC Lamineate C⁰ Finite Element Model with 12 Degrees of Freedom per node, Engineering Computation, Vol. 5(3), pp. 300-308.
- [4] Kant, T. and Swaminathan, K. (2001), Estimation of Transverse/Interlaminar Stresses in Laminated Composites-A Selective Review and Survey of Current Developments, Composite Structures, Vol. 49(1), pp. 65-75.
- [5] Kant, T. and Swaminathan, K. (2001), Free Vibration of Isotropic, Orthotropic and Multilayered Plates based on Higher Order Refined Theories, Journal of Sound and Vibration, Vol. 241(2), pp. 319-327.
- [6] Kant, T. and Swaminathan, K. (2001), Analytical Solutions for Free Vibration of Laminated Composite and Sandwich Plates based on a Higher Order Refined Theory, Composite Structures, Vol. 53(1), pp. 73-85.
- [7] Kant, T. and Swaminathan, K. (2002), Analytical Solutions for Static Analysis of Laminated Composite and Sandwich Plates based on a Higher Order Refined Theory, Composite Structures, Vol. 56(4), pp. 329-344.
- [8] Levinson, M. (1980), An Accurate Simple Theory of the Statics and Dynamics of Elastic Plates, Mechanics Research Communications, Vol. 7, pp. 343-350.
- [9] Mindlin, R. D. (1951), Influence of Rotary Inertia and Shear on Flexural Motions of Isotropic Elastic Plates, ASME Journal of Applied Mechanics, Vol. 18, pp. 31-38.
- [10] Murthy, M.V.V. (1981), An Improved Transverse Shear Deformation Theory for Laminated Anisotropic Plates, NASA Technical Paper, No. 1903.
- [11] Noor, K. and Burton, W. S. (1989), Assessment of Shear Deformation Theories for Multilayered Composite Plates, Applied Mechanics Reviews, Vol. 42(1), pp. 1-13.
- [12] Noor, K. and Burton, W. S. (1990), Assessment of Computational Models for Multilayered Composite Shells, Applied Mechanics Reviews, Vol. 43(4), pp. 67-97.
- [13] Pandya, B. N. and Kant, T. (1987), A Consistent Refined Theory for Flexure of a Symmetric Laminate, Mechanics Research Communications, Vol. 14, pp. 107-113.
- [14] Pandya, B. N. and Kant, T. (1988), A Refined Higher Order Generally Orthotropic C⁰ Plate Bending Element, Computers and Structures, Vol. 28, pp. 119-133.
- [15] Pandya, B. N. and Kant, T. (1988), Finite Element Stress Analysis of Laminated Composites using Higher Order Displacement Model, Composite Science and Technology, Vol. 32, pp. 137-155.
- [16] Reddy, J. N. (1984), A Simple Higher Order Theory for Laminated Composite Plates, ASME Journal of Applied Mechanics, Vol. 51, pp. 745-752.
- [17] Reddy, J. N. (1990), A Review of Refined Theories of Laminated Composite Plates, The Shock and Vibration Digest, Vol. 22, pp. 3-17.
- [18] Reddy, J. N. and Phan, N. D. (1985), Stability and Vibration of Isotropic, Orthotropic and Laminated Plates according to Higher Order Shear Deformation Theory, Journal of Sound and Vibration, Vol. 98(2), pp. 157-170.
- [19] Reissner, E. (1945), The Effect of Transverse Shear Deformation on the Bending of Elastic Plates, ASME Journal of Applied Mechanics, Vol. 12(2), pp. 69-77.
- [20] Reissner, E. and Stavsky, Y. (1961), Bending and Stretching of Certain Types of Heterogeneous Aelotropic Elastic Plates, ASME Journal of Applied Mechanics, Vol. 28, pp. 402-408.
- [21] Ren, J. G. (1990), Bending, Vibration and Buckling of Laminated Plates, In: Cheremisinoff NP, Handbook of Ceramics and Composites, New York: Marcel Dekkar, Vol. 1, pp. 413-450.
- [22] Rower, K. (1992), Application of Higher Order Theories to the Bending Analysis of Layered Composite Plates, International Journal of Solids and Structures, Vol. 29(1), pp. 105-119.
- [23] Senthilnathan et al. (1987), Buckling of Shear Deformable Plates, AIAA Journal, Vol. 25(9), pp. 1268-1271.
- [24] Swaminathan, K. and Patil, S. S. (2007), Higher Order Refined Computational Model with 12 Degrees of Freedom for the Stress Analysis of Antisymmetric Angle Ply Plates - Analytical Solutions, Composite Structures, Vol. 80(4), pp. 595-608.
- [25] Swaminathan, K. and Patil, S. S. (2008), Analytical Solutions using a Higher Order Refined Computational Model with 12 Degrees of Freedom for the Free Vibration Analysis of Antisymmetric Angle Ply Plates, Composite Structures, Vol. 82(2), pp. 209-216.
- [26] Swaminathan, K. and Patil, S. S. (2008), Higher Order Refined Computational Models for the Free Vibration Analysis of Antisymmetric Angle Ply Plates, Journal of Reinforced Plastics and Composites, Vol. 27(5), pp. 541-553.
- [27] Whitney, J. M. and Pagano, N. J. (1970), Shear Deformation in Heterogeneous Anisotropic Plates, ASME Journal of Applied Mechanics, Vol. 37(4), pp. 1031-1036.

Table 1. Non-dimensionalized transverse deflection \bar{w} in a simply supported anti-symmetric angle-ply ($\theta/\theta\ldots$) square laminate under sinusoidal transverse load.

θ	a/h	Models	\bar{w}	
			$n = 2$	$n = 4$
15°	4	Ren ^{\$}	1.4989	1.3050
		Model - 1	1.4258	1.2608
		Model - 2	1.4596	1.2869
		Model - 3	1.3307	1.1903
		Model - 4	1.0813	0.9580
		Model - 5	1.4485	1.1982
	10	Ren ^{\$}	0.6476	0.4505
		Model - 1	0.6296	0.4423
		Model - 2	0.6374	0.4446
		Model - 3	0.6213	0.4329
		Model - 4	0.5672	0.3785
		Model - 5	0.6361	0.4289
	100	Ren ^{\$}	0.4680	0.2668
		Model - 1	0.4621	0.2662
		Model - 2	0.4679	0.2667
		Model - 3	0.4678	0.2666
		Model - 4	0.4672	0.2660
		Model - 5	0.4679	0.2666

^{\$}Ren, J. G. (1990), Bending, vibration and buckling of laminated plates, In: Cheremisinoff NP, editor. Handbook of Ceramics and Composites, New York: Marcel Dekker, Vol.(1), pp. 413-450.

Table 2. Non-dimensionalized transverse deflection and in-plane stresses in a simply supported four layered antisymmetric angle-ply ($30^\circ/-30^\circ_2$) rectangular ($b=3a$) laminate under sinusoidal transverse load. ($a/h = 4$)

E_1 / E_2	Models	\bar{w}	$\bar{\sigma}_x$	$\bar{\sigma}_y$	$\bar{\tau}_{xy}$
3	Model - 1	5.6563	0.5441	0.1500	-0.1167
	Model - 2	5.7415	0.5366	0.1338	-0.1191
	Model - 3	5.7276	0.5337	0.1327	-0.1200
	Model - 4	5.7274	0.5340	0.1325	-0.1195
	Model - 5	5.7218	0.5101	0.1268	-0.1149
20	Model - 1	2.2739	0.6116	0.2012	-0.1063
	Model - 2	2.3020	0.6733	0.2109	-0.1074
	Model - 3	2.2241	0.6046	0.1880	-0.1293
	Model - 4	2.2240	0.6052	0.1880	-0.1285
	Model - 5	2.1935	0.4869	0.1511	-0.1043
40	Model - 1	1.8199	0.6986	0.2352	-0.1059
	Model - 2	1.8406	0.8527	0.2760	-0.1061
	Model - 3	1.7454	0.7072	0.2272	-0.1515
	Model - 4	1.7454	0.7077	0.2274	-0.1507
	Model - 5	1.7217	0.4816	0.1545	-0.1034

Table 3. Non-dimensionalized fundamental frequencies $\bar{\omega} = (\omega b^2 / h) \sqrt{\rho / E_2}$ for a simply supported two layered antisymmetric angle-ply ($45^\circ/-45^\circ$) square laminated plate.

a/h	Model-1	Model-2	Model-3\$	Model-4\$	Model-5\$
2	5.3325	5.3062	6.2837	6.3367	5.5205
4	8.8426	8.8096	9.7593	9.7593	9.1681
5	10.0350	9.9996	10.8401	10.8401	10.3352
10	12.9115	12.8678	13.2630	13.2630	13.0439
12.5	13.4690	13.4233	13.7040	13.7040	13.5500
20	14.1705	14.1220	14.2463	14.2463	14.1790
25	14.3500	14.3008	14.3827	14.3827	14.3385
50	14.6012	14.5509	14.5723	14.5723	14.5608
100	14.6668	14.6159	14.6214	14.6214	14.6182

\$Results using these theory are computed independently and are found to be the same as reported in Literature.(Reddy and Phan, 1985).

Table 4. Non-dimensionalized fundamental frequencies $\bar{\omega} = (\omega b^2 / h) \sqrt{\rho / E_2}$ for a simply supported eight layered antisymmetric angle-ply ($45^\circ/-45^\circ$)₄ square laminated plate.

a/h	Model-1	Model-2	Model-3\$	Model-4\$	Model-5\$
2	5.9234	5.9227	6.2837	6.3140	5.8484
4	10.7473	10.7401	10.9905	10.9905	10.8425
5	12.7523	12.7429	12.9719	12.9719	12.8925
10	19.1258	19.1150	19.2659	19.2659	19.2894
12.5	20.7784	20.7688	20.8884	20.8884	20.9165
20	23.1829	23.1764	23.2388	23.2388	23.2591
25	23.8713	23.8659	23.9091	23.9091	23.9241
50	24.8959	24.8925	24.9046	24.9046	24.9093
100	25.1741	25.1714	25.1744	25.1744	25.1759

\$Results using these theory are computed independently and are found to be the same as reported in Literature.(Reddy and Phan, 1985).

Table 5. Non-dimensionalized fundamental frequencies $\bar{\omega} = (\omega b^2 / h) \sqrt{\rho / E_2}$ for a simply supported four layered antisymmetric angle-ply (45°/-45°/ 45°/-45°) square laminated plate.

E_1/E_2	Models	a/h					
		2	4	10	20	50	100
3	Model -1	4.6498	6.4597	7.6339	7.8724	7.9442	7.9545
	Model -2	4.6125	6.4292	7.6201	7.8631	7.9365	7.9475
	Model -3	4.6546	6.4554	7.6267	7.8649	7.9366	7.9472
	Model -4	4.6546	6.4554	7.6267	7.8649	7.9366	7.9471
	Model -5	4.6519	6.4626	7.6293	7.8657	7.9368	7.9470
10	Model -1	5.2061	8.3447	11.4116	12.2294	12.4952	12.5351
	Model -2	5.1838	8.3170	11.3924	12.2152	12.4828	12.5229
	Model -3	5.3887	8.5119	11.4674	12.2380	12.4866	12.5238
	Model -4	5.3887	8.5119	11.4674	12.2380	12.4866	12.5235
	Model -5	5.3765	8.5633	11.4939	12.2463	12.4881	12.5242
20	Model -1	5.4140	9.3306	14.4735	16.2570	16.8949	16.9927
	Model -2	5.3985	9.3095	14.4553	16.2436	16.8837	16.9821
	Model -3	5.7431	9.6855	14.6609	16.3146	16.8964	16.9848
	Model -4	5.7431	9.6855	14.6609	16.3146	16.8964	16.9850
	Model -5	5.6542	9.7575	14.7292	16.3394	16.9008	16.9861
30	Model -1	5.5079	9.7966	16.4543	19.2323	20.3134	20.4839
	Model -2	5.4951	9.7795	16.4376	19.2198	20.3035	20.4746
	Model -3	5.9481	10.2785	16.7750	19.3499	20.3277	20.4807
	Model -4	5.4981	10.2785	16.7750	19.3499	20.3277	20.4805
	Model -5	5.7640	10.3391	16.8825	19.3944	20.3361	20.4829
40	Model -1	5.5674	10.0731	17.8773	21.6229	23.1949	23.4499
	Model -2	5.5559	10.0585	17.8618	21.6112	23.1858	23.4409
	Model -3	6.1067	10.6507	18.3221	21.8063	23.2236	23.4507
	Model -4	6.1067	10.6507	18.3221	21.8063	23.2236	23.4507
	Model -5	5.8227	10.6838	18.4633	21.8722	23.2367	23.4509

Stress Analysis of Antisymmetric Angle Ply Sandwich Plates- Analytical Evaluation of Refined Higher Order Shear Deformation Theories

K. SWAMINATHAN¹ and GOVIND R. SANGWAI²

¹ Dept. of Civil Engineering, National Institute of Technology Karnataka, Surathkal, Mangalore – 575025, Karnataka, India. e-mail: swami7192@yahoo.co.in

² Dept. of Applied Mechanics, Government Polytechnic, Osmanpura, Aurangabad - 431005, Maharashtra State, India. e-mail: gr.sangwai@gmail.com

Abstract: In this paper two refined higher order computational models with 9 DOF and 12 DOF are considered. Analytical formulation developed and solutions obtained for the first time using these models for the stress analysis of antisymmetric angle ply sandwich plate. In addition, higher order model proposed by Reddy and the first order model already reported in the literature are also considered for the evaluation. A simply supported plate with SS-2 boundary conditions is considered for the analysis. The equations of equilibrium are obtained using Principle of Minimum Potential Energy (PMPE). Solutions are obtained in closed form using Navier's technique. In-plane stresses are computed using the three dimensional constitutive relationships and the transverse stresses by post processing technique. Extensive numerical results using all the models are compared with 3D elasticity solutions already available in the literature to decide the accuracy of model. After establishing accuracy of the solution method benchmark results and comparison of solutions are presented for multilayer sandwich plates. It is observed that ESL models with twelve DOF are accurate, efficient and simple.

Key words: Higher Order Shear Deformation Theories, Analytical Solutions, Composite Plates, Sandwich Plates, Navier's technique

Introduction:

The high values of specific moduli and strength of fibre reinforced composite materials make them attractive for aerospace structural components such as plates and shells. Laminated composite plates are very weak in interlaminar strength. Transverse stresses play a vital role in the failure of laminated composite plates. Developing accurate and efficient methods for analysis of composite structures have consistently been an important area of research. Equivalent Single Layer (ESL) theories and Layerwise Theories (LT) are proposed by various researchers for analysis of composite plates and shells. ESL theories are computationally simple and economical as compared to LT and 3D elasticity solutions. Many researchers developed two dimensional computational models based on Classical Laminate Plate Theory (CLPT), First Order Shear Deformation Theories (FSDTs) and Higher Order Shear

Deformation Theories (HSDTs). A complete review of literature is found in the articles presented by many authors [Reddy (1993), Kant and Swaminathan (2000), Noor and Burton (1989), Noor et al. (1996), Reddy and Robbins (1994), Zhang and Yang (2009)]. Almost all researchers agree on the usefulness and accuracy of ESL computational models based on HSDT's in predicting global responses but have mixed opinion about its accuracy in predicting the local responses [Matsunaga (2002)]. This observation of researchers is based on the results obtained by them using computational models with fewer Degrees-of-Freedom (DOF). To ascertain the accuracy of the computational models with higher degrees-of-freedom, two refined higher order computational models with 9 DOF and 12 DOF are considered in the present investigation. Analytical formulation developed and solutions obtained for the first time using these models are presented. In addition, higher

order model proposed by Reddy and the first order model developed by other investigators and available in the literature are also considered for the evaluation. A simply supported plate subjected to sinusoidal transverse load with SS-2 boundary conditions is considered for the analysis. The equations of equilibrium are obtained using Principle of Minimum Potential Energy (PMPE). Solutions are obtained in closed form using Navier's technique. In-plane stresses are computed using the three dimensional constitutive relationships and the transverse stresses by integrating the elasticity equilibrium equations as post processing. Extensive numerical results for the inplane and transverse stresses using all the models are presented and the accuracy of each model in predicting the stresses is judged by comparing the results with 3D elasticity solutions already available in the literature. After establishing accuracy of the solution method benchmark results and comparison of solutions are presented for multilayer sandwich plates.

Theoretical Formulation

A rectangular laminated plate with planar dimensions a and b and total thickness ' h ' is considered. The structural coordinate system is taken such that xy plane coincides with the middle plane of the plate and z axis perpendicular to middle plane as shown in Figure1. The laminated plate is composed of perfectly bonded orthotropic laminae. For the purpose of evaluation, the following higher order displacement models are considered.

Model - 1 [Kant and Manjunatha (1988)]

$$\begin{aligned} u(x, y, z) &= u_o(x, y) + z\theta_x(x, y) + z^2u_o^*(x, y) + z^3\theta_x^*(x, y) \\ v(x, y, z) &= v_o(x, y) + z\theta_y(x, y) + z^2v_o^*(x, y) + z^3\theta_y^*(x, y) \\ w(x, y, z) &= w_o(x, y) + z\theta_z(x, y) + z^2w_o^*(x, y) + z^3\theta_z^*(x, y) \end{aligned} \quad (1)$$

Model - 2 [Pandya and Kant (1988)]

$$\begin{aligned} u(x, y, z) &= u_o(x, y) + z\theta_x(x, y) + z^2u_o^*(x, y) + z^3\theta_x^*(x, y) \\ v(x, y, z) &= v_o(x, y) + z\theta_y(x, y) + z^2v_o^*(x, y) + z^3\theta_y^*(x, y) \\ w(x, y, z) &= w_o(x, y) \end{aligned} \quad (2)$$

In addition to the above, the higher-order theory proposed by Reddy and the first-order theory developed by other investigators and reported in the literature for the analysis of antisymmetric laminates

are also considered for the evaluation. Though the above two models were already reported earlier in the literature and numerical results were presented using finite element formulations, analytical solutions to obtain transverse stresses for antisymmetric angle ply composite plates and sandwich plates with angle-ply face sheets are obtained for the first time in this investigation and so the results obtained using the above two models are referred to as present in all the tables and figures. In addition to the above, the following higher order model and the first order model developed by other investigators are also considered for the evaluation. Analytical formulations developed and numerical results generated independently using these models are also being presented here with a view to have all the results on a common platform.

Model - 3 [Reddy J. N. (1984)]

$$\begin{aligned} u(x, y, z) &= u_o(x, y) + z\left[\theta_x(x, y) - \frac{4}{3}\left(\frac{z}{h}\right)^2\left\{\theta_x(x, y) + \frac{\partial w_o}{\partial x}\right\}\right] \\ v(x, y, z) &= v_o(x, y) + z\left[\theta_y(x, y) - \frac{4}{3}\left(\frac{z}{h}\right)^2\left\{\theta_y(x, y) + \frac{\partial w_o}{\partial y}\right\}\right] \\ w(x, y, z) &= w_o(x, y) \end{aligned} \quad (3)$$

Model - 4 [Whitney and Pagano (1970)]

$$\begin{aligned} u(x, y, z) &= u_o(x, y) + z\theta_x(x, y) \\ v(x, y, z) &= v_o(x, y) + z\theta_y(x, y) \\ w(x, y, z) &= w_o(x, y) \end{aligned} \quad (4)$$

The parameters u_o , v_o are the in-plane displacements and w_o is the transverse displacement of a point (x, y) on the middle plane. The functions θ_x , θ_y and θ_z are rotations of the normal to the middle plane about y and x axes respectively. The parameters u_o^* , v_o^* , w_o^* , θ_x^* , θ_y^* and θ_z^* are the higher-order terms in the Taylor's series expansion and they represent higher-order transverse cross sectional deformation modes.

Strain-Displacement Relations:

The relationship between the strains at any point within a laminate and the corresponding deformations are functions of the assumed displacement fields.

$$\begin{aligned}\varepsilon_x &= \frac{\partial u}{\partial x}; \quad \varepsilon_y = \frac{\partial v}{\partial y}; \quad \gamma_{xy} = \frac{\partial u}{\partial y} + \frac{\partial v}{\partial x} \\ \varepsilon_z &= \frac{\partial w}{\partial z}; \quad \gamma_{yz} = \frac{\partial v}{\partial z} + \frac{\partial w}{\partial y}; \quad \gamma_{xz} = \frac{\partial u}{\partial z} + \frac{\partial w}{\partial x}\end{aligned}\quad (5)$$

Stress Strain Expressions

The strain expressions corresponding to displacement model given by Eqns. (1-4) in the form of derivatives of displacement were established using equations (5). The three-dimensional stress-strain relations for L^{th} lamina with reference to laminate axes are defined by considering lamina in a composite or sandwich laminate as a homogeneous and orthotropic material with three orthogonal planes of material symmetry.

$$[\sigma]^L = Q_{ij} [\varepsilon]^L \quad (6)$$

Where

$[\sigma]^L = (\sigma_x, \sigma_y, \sigma_z, \tau_{xy}, \tau_{yz}, \tau_{xz})$ are the stresses and $[\varepsilon]^L = (\varepsilon_x, \varepsilon_y, \varepsilon_z, \gamma_{xy}, \gamma_{yz}, \gamma_{xz})$ are the strains with respect to the laminate axes. Q_{ij} s are the transformed elastic constants or the stiffness matrix with respect to the laminate axes x,y and z.

Equations of Equilibrium And Natural Boundary Conditions:

The equations of equilibrium and boundary conditions for the stress analysis are obtained using the principle of minimum potential energy (PMPE).

$$\delta \Pi = \delta (U - W_s - W_{ex} - W_{ey}) = 0 \quad (7)$$

where U is the strain energy of the plate, W_s represents the work done by surface tractions, W_{ex} and W_{ey} represents the work done by edge stresses on typical edges $x = \text{constant}$ and $y = \text{constant}$ respectively.

Analytical Solution

Here the exact solutions for the antisymmetric angle-ply plates are obtained assuming that the plate is simply supported with SS-2 boundary conditions by allowing the tangential displacement and restricting the normal displacement at supports. To satisfy these boundary conditions the generalized displacement fields are expanded in double Fourier Series. A set of simultaneous equations is then solved to obtain the values of Fourier

amplitudes and these values are used to calculate the generalized displacements and its derivatives. The values of the generalized displacement and their derivatives are then substituted in the strain-displacement relations equation to obtain the values of strains. The complete three-dimensional Hooke's law is used to compute the in-plane stresses and the transverse stresses are then calculated by integrating the 3D elasticity equilibrium equations. In the following sections the mathematical expressions obtained for the computation of transverse shear stresses (τ_{xz} , τ_{yz}) and transverse normal stress (σ_z) are presented.

Transverse Stresses (τ_{xz} , τ_{yz} , σ_z):

The evaluation of transverse stresses from the stress-strain constitutive relations leads to discontinuity at the interface of two adjacent layers (laminae) of a laminate and thus violates the equilibrium conditions. The three-dimensional analysis becomes very complex due to the thickness variation of constitutive laws and continuity requirements of transverse stresses and displacements across the interfaces. Thus, elasticity equilibrium equations are used to derive expressions for the transverse stresses in the L^{th} lamina of a multilayered laminate. The Equilibrium Equations without the body forces are given by,

$$\begin{aligned}\frac{\partial \sigma_x}{\partial x} + \frac{\partial \tau_{xy}}{\partial y} + \frac{\partial \tau_{xz}}{\partial z} &= 0; \\ \frac{\partial \tau_{xy}}{\partial x} + \frac{\partial \sigma_y}{\partial y} + \frac{\partial \tau_{yz}}{\partial z} &= 0; \\ \frac{\partial \tau_{xz}}{\partial x} + \frac{\partial \tau_{yz}}{\partial y} + \frac{\partial \sigma_z}{\partial z} &= 0\end{aligned}\quad (8)$$

From the above set of equations, we get

$$\begin{aligned}\tau_{xz}^{(I)} &= - \int_{z_l}^z \left(\frac{\partial \sigma_x^{(L)}}{\partial x} + \frac{\partial \sigma_{xy}^{(L)}}{\partial y} \right) dz + C_1^{(L)}(x, y) \\ \tau_{yz}^{(I)} &= - \int_{z_l}^z \left(\frac{\partial \sigma_{xy}^{(L)}}{\partial x} + \frac{\partial \sigma_{yz}^{(L)}}{\partial y} \right) dz + C_2^{(L)}(x, y)\end{aligned}$$

$$\sigma_{zz}^{(l)} = - \int_{z_l}^z \left(\frac{\partial \sigma_{xz}^{(L)}}{\partial x} + \frac{\partial \sigma_{yz}^{(L)}}{\partial y} \right) dz + C_3^{(L)}(x, y) \quad (9)$$

The above equilibrium equations are valid for any layer (L) for $-h/2 \leq z \leq Z_{L+1}$

Where $C_1^{(L)}$, $C_2^{(L)}$ and $C_3^{(L)}$ are the constants of integration for any layer (L) corresponding to τ_{xz} , τ_{yz} and σ_z which are evaluated using the following conditions viz., the bounding plane criteria and the continuity of stress τ_{xz} , τ_{yz} and σ_z at layer interface between two layers

From the bounding plane criteria we obtain

$$\begin{aligned} \tau_{xz}\left(x, y, -\frac{h}{2}\right) &= 0 \\ \tau_{yz}\left(x, y, -\frac{h}{2}\right) &= 0 \\ \sigma_z\left(x, y, -\frac{h}{2}\right) &= 0 \end{aligned} \quad (10)$$

Continuity of stress at layer interfaces gives the following conditions

$$\tau_{xz}^L(x, y, z_{L+1}) = \tau_{xz}^{L+1}(x, y, z_{L+1}) ;$$

$$\tau_{yz}^L(x, y, z_{L+1}) = \tau_{yz}^{L+1}(x, y, z_{L+1}) \quad (11)$$

$$\sigma_z^L(x, y, z_{L+1}) = \sigma_z^{L+1}(x, y, z_{L+1}) \quad (12)$$

After integration of the above three equations given in equation (9) for the bounding plane criteria and interlayer continuity criteria given in equation (10-12), the constants associated with integration C_1 , C_2 and C_3 of any layer (L) corresponding to τ_{xz} , τ_{yz} and σ_z are computed. By using equation (9) the transverse stresses at any Lth layer are computed.

4. Numerical Results and Discussions:

In this section, the numerical examples solved are described and discussed. A simply supported plate with SS-2 boundary conditions subjected to sinusoidal transverse loading is considered for the analysis. Plates with different aspect ratios, number of layers, fibre orientation and material properties are

studied. The following set of data is used in obtaining numerical results.

Material 1

$$E_1 = 25 \times 10^6 \text{ psi (175 GPa)}$$

$$E_2 = E_3 = 1 \times 10^6 \text{ psi (7GPa)}$$

$$G_{12} = G_{13} = 0.5E_2 ; \quad G_{23} = 0.2 E_2$$

$$\nu_{12} = \nu_{23} = \nu_{13} = 0.25$$

Material 2

Face sheets (Graphite Epoxy T300 / 934)

$$E_1 = 19 \times 10^6 \text{ psi (131 GPa)}$$

$$E_2 = E_3 = 1.5 \times 10^6 \text{ psi (10.34GPa)}$$

$$G_{12} = G_{23} = 1.0 \times 10^6 \text{ psi (6.895GPa)}$$

$$G_{13} = 0.9 \times 10^6 \text{ psi (6.205GPa)}$$

$$\nu_{12} = \nu_{13} = 0.22 \text{ and } \nu_{23} = 0.49$$

Core (Isotropic)

$$E_1 = E_2 = E_3 = 2G = 1000 \text{ psi (6.90} \times 10^{-3} \text{ GPa)}$$

$$G_1 = G_2 = G_3 = 500 \text{ psi (3.45} \times 10^{-3} \text{ GPa)}$$

$$\nu_{12} = \nu_{23} = \nu_{13} = 0$$

$$E_1 = 19 \times 10^6$$

Results reported in tables and plots are obtained using the following non-dimensional form.

$$\begin{aligned} \bar{w} &= w \left(\frac{100h^3 E_2}{p_0 a^4} \right) & \bar{\sigma}_x &= \sigma_x \left(\frac{h^2}{p_0 a^2} \right) \\ \bar{\sigma}_y &= \sigma_y \left(\frac{h^2}{p_0 a^2} \right) & \bar{\tau}_{xy} &= \tau_{xy} \left(\frac{h^2}{p_0 a^2} \right) \\ \bar{\tau}_{xz} &= \tau_{xz} \left(\frac{h}{p_0 a} \right) & \bar{\tau}_{yz} &= \tau_{yz} \left(\frac{h}{p_0 a} \right) \\ \bar{\sigma}_z &= \sigma_z \left(\frac{h^2}{p_0 a^2} \right) \end{aligned} \quad (16)$$

Numerical Results:

Example 1: A simply supported two layered antisymmetric angle ply (15/-15) square composite plate under sinusoidal transverse load is considered. The layers are of equal thickness. Material Set 1 is used. The nondimensionalized maximum inplane stresses ($\bar{\sigma}_x$, $\bar{\sigma}_y$, $\bar{\tau}_{xy}$) and transverse stresses ($\bar{\tau}_{xz}$, $\bar{\tau}_{yz}$) for plates with varying a/h ratios and fibre orientation (15/-15) are given in Table 1. The solutions using 3D elasticity theory [Savioia and Reddy (1992)] and other shear deformation theories considered in present study are used for comparison. In the case of thick plates (a/h ratio 4 and

10), it has been found that for all the fibre orientations considered the inplane and transverse stress values obtained using the present model 1 and 2 are very much closer to 3D elasticity solutions. For plate with a/h ratio equal to 4 and fibre orientation equal to 15° the values of $\bar{\tau}_{xz}(a/2,0)$ predicted by the models Model 1, Model 2, Model 3 and Model 4 and RSDT [He and Zhang. (1996)] are respectively 11.534%, 14.86%, 52.43%, 36.97% and 22.94% higher as compared to 3D elasticity solutions. Similarly for the same plate the values of $\bar{\tau}_{yz}(0,a/2)$ predicted by the present and other models are respectively 2.75%, 4.76%, 16.54%, 17.51% and 7.26% higher as compared to the solutions reported using 3D elasticity theory. Similar patterns in the percentage difference between the models can be observed in all other stress values also for all the fibre orientations considered. For thin plates ($a/h=100$) all the models shows more or less same values of stress. Figures 2 show through the thickness variation of nondimensionalized transverse stress $\bar{\tau}_{xz}$ for all Models 1 to Model 4 at $(a/2,0)$ for plates with a/h ratio 4 and fibre orientation equal to 15° .

Table 2 gives stress values for a simply supported two layered antisymmetric angle ply (30/-30) rectangular composite plate under sinusoidal transverse load. Model-1 and 2 gives accurate values as compared to other models.

Example 2: To study the performance of present model and other models in predicting the flexural behaviour of antisymmetric angle ply sandwich plates a five layered square sandwich plates ($\theta/\theta/\text{core } / \theta/\theta$) with isotropic core and antisymmetric angle ply face sheets with varying a/h ratios and ply angles are considered. The ratio of the thickness of the core t_c to the thickness of the face sheets t_f considered equal to 10. Material Set 2 is used. Here the results of transverse shear and normal stresses are only reported in Table 3. The through the thickness variation of nondimensionalized transverse shear stresses $\bar{\tau}_{xz}$ and $\bar{\tau}_{yz}$ at locations $(0,a/2)$ for plates with a/h ratios 4 for all Models 1 to Model 4 are shown in figures 3-4.

Conclusions:

Analytical formulations and solution method for the computation of transverse stresses using a higher order computational model with 12, 9 and 5 DOF along with FSDT are presented. The computation of transverse stresses is done by integrating the three-dimensional equations of equilibrium in the thickness direction. From the numerical results and discussions presented it is shown that for all the parameters considered in this study, the present models with 9 and 12 DOF based on ESL theory could predict the transverse stresses in antisymmetric angle ply plates very accurately and the results obtained are in very good agreement with 3D elasticity solution already reported in the literature. Computational models based on ESL theories with higher degrees of freedom (9 DOF and 12 DOF) could predict the local response and variation of stresses through the thickness of plate accurately as contrast to the observations made by some researchers against the use of ESL models (based on theories with 5 DOF). Model with 12 DOF can be used to predict the local response accurately and precisely for antisymmetric angle ply sandwich plate as it considers quadratic variation of stress in z - direction.

References:

- [1] Hiroyuki Matsunaga (2002), Assessment Of A Global Higher-Order Deformation Theory For Laminated Composite And Sandwich Plates, COMPOSITE STRUCTURES, V. 56 pp. 279–291.
- [2] Ji-Fan He and Zhi-Zhou Zhang. (1996), Bending Analysis Of Antisymmetric Angle-Ply Laminated Plates Including Transverse Shear Effects, COMPOSITE STRUCTURES, V. 34, pp. 437-444.
- [3] Kant T. and Manjunatha B. S. (1988), An Unsymmetric Frc Laminate C0 Finite Element Model With 12 Degrees Of Freedom Per Node, ENG COMPU, V. 5 pp. 300–308.
- [4] Kant T. and Swaminathan K. (2000), Estimation of Transverse/Interlaminar Stresses In Laminated Composites- A Selective Review And Survey Of Current Developments, COMPOSITE STRUCTURES 2000;49:65-75.
- [5] Noor A. K. and Burton W. S. (1989), Assessment Of Shear Deformation Theories For Multilayered Composite Plates, APPLIED MECHANICS REVIEWS, V. 42, pp. 1-13.
- [6] Noor A. K., Burton W. S. and Bert C. W. (1996), Computational Models For Sandwich Panels and Shells, APPLIED MECHANICS REVIEWS, V. 49 pp. 155-199.
- [7] Pandya B. N. and Kant T. (1988), Finite Element Stress Analysis Of Laminated Composites Using Higher Order Displacement Model, COMPOS SCI. TECHNOL, V. 32 pp. 137-55.
- [8] Reddy J. N. (1984), A Simple Higher-Order

- Theory For Laminated Composite Plates, J APPL MECH, V. 51 pp. 745–52.
- [9] Reddy J. N. and Robbins Jr. D. H. (1994), Theories and Computational Models For Composite Laminates, APPLIED MECHANICS REVIEWS, V. 47, pp. 147–169.
- [10] Reddy J.N.(1993), An Evaluation of Equivalent-Single-Layer and Layerwise Theories of Composite Laminates. COMPOSITE STRUCTURES, V. 25, pp. 21–35.
- [11] Savoia M. and Reddy J. N. (1992), A Variational Approach To Three-Dimensional Elasticity Solutions Of Laminated Composite Plates, J. APPL. MECH, V. 59 pp.166-175.
- [12] Whitney J. M. and Pagano N. J. (1970), Shear Deformation In Heterogeneous Anisotropic Plates. J APPL MECH, V. 37 pp. 1031–1036.
- [13] Zhang Y. X. and Yang C. H. (2009), Recent Developments In Finite Element Analysis For Laminated Composite Plates, COMPOSITE STRUCTURES, V. 88, pp. 147–157.

Table 1 Non-dimensionalised maximum in-plane and transverse stresses in a two layered (15/-15) simply supported antisymmetric angle ply square laminate under sinusoidal transverse load (Material Set 1)

a/h	Theory	$\bar{\sigma}_x(a/2,a/2)$	$\bar{\sigma}_y(a/2,a/2)$	$\bar{\tau}_{xy}(a/2,a/2)$	$\bar{\tau}_{xz}(a/2,0)$	$\bar{\tau}_{yz}(a/2,0)$	$\bar{\tau}_{xz}(0,a/2)$
4	3D-Elasticity[11]	0.6645	0.1135	0.1489	0.0841	0.0960	0.3145
	Present(Model-1)	0.6557	0.1206	0.1443	0.0938	0.0855	0.2987
	Present(Model-2)	0.6859	0.1088	0.1455	0.0966	0.0923	0.3122
	Model-3*	0.7023	0.1064	0.1633	0.1282	0.0899	0.3060
	Model-4*	0.4969	0.0868	0.1090	0.1152	0.0968	0.3283
	RSDT [2] ^{\$}	0.5884	0.0980	0.1305	0.1034	0.0929	0.3186
10	3D-Elasticity[11]	0.5633	0.0806	0.1244	0.0991	0.0814	0.3421
	Present(Model-1)	0.5601	0.0813	0.1237	0.1011	0.0791	0.3399
	Present(Model-2)	0.5681	0.0798	0.1242	0.1025	0.0802	0.3415
	Model-3*	0.5680	0.0792	0.1264	0.1079	0.0800	0.3396
	Model-4*	0.5330	0.0759	0.1171	0.1058	0.0810	0.3445
	RSDT [2] ^{\$}	0.5514	0.0778	0.1216	0.1039	0.0807	0.3427

* Results using these models are generated independently for the first time.

3D-Elasticity[11] Savoia M. and Reddy J. N. (1992)

^{\$} RSDT - Refined Shear Deformation Theory [2] [He and Zhang. (1996)].

Table 2 Non-dimensionalised maximum in-plane and transverse stresses in a two layered (30/-30) simply supported antisymmetric angle ply rectangular laminate (b=3a) under sinusoidal transverse load (Material Set 1)

a/h	Theory	$\bar{\sigma}_x(a/2,a/2)$	$\bar{\sigma}_y(a/2,a/2)$	$\bar{\tau}_{xy}(a/2,a/2)$	$\bar{\tau}_{xz}(a/2,0)$	$\bar{\tau}_{xz}(0,a/2)$	$\bar{\tau}_{yz}(0,a/2)$
4	3D-Elasticity [11]	0.9282	0.3000	0.4260	0.1029	0.3885	0.1427
	Present (Model-1)	0.9067	0.2994	0.4113	0.1141	0.3806	0.1496
	Present (Model-2)	0.9879	0.3152	0.4152	0.1163	0.3891	0.1516
	Model-3*	0.9720	0.3087	0.4642	0.1389	0.3905	0.1592
	Model-4*	0.8114	0.2549	0.3734	0.1323	0.3890	0.1534
	RSDT [2] ^{\$}	0.8514	0.2689	0.3906	0.1225	0.3956	0.1532

* Results using these models are generated independently for the first time.

3D-Elasticity[11] Savoia M. and Reddy J. N. (1992)

^{\$} RSDT - Refined Shear Deformation Theory [2] [He and Zhang. (1996)].

Table 3. Non-dimensionalised maximum in-plane and transverse stresses in five layered ($\theta / -\theta / \text{core} / \theta / -\theta$) simply supported anti-symmetric angle-ply square sandwich plate under sinusoidal transverse load for material set 2 and $t_c/t_f = 10$.

θ	a/h	Theory	$\bar{\sigma}_x(a/2,a/2)$	$\bar{\sigma}_y(a/2,a/2)$	$\bar{\tau}_{xy}(0,0)$	$\bar{\tau}_{xz}(0,a/2)$	$\bar{\tau}_{yz}(a/2,0)$	$\bar{\sigma}_z(a/2,a/2)$
15	4	Model-1	4.9568	1.1452	1.1412	0.3546	0.1880	0.1035
		Model-2	4.6401	1.0312	1.1543	0.3361	0.1759	0.1139
		Model-3*	1.9865	0.5801	0.6595	0.2028	0.1634	0.2010
		Model-4*	0.6437	0.2256	0.2751	0.2246	0.1220	0.0750
	10	Model-1	1.3692	0.5310	0.4857	0.1872	0.1510	0.0186
		Model-2	1.2718	0.4182	0.4857	0.1864	0.1533	0.0195
		Model-3*	0.8530	0.3005	0.3570	0.2060	0.1376	0.0331
		Model-4*	0.8298	0.1662	0.2122	0.2542	0.0924	0.0120
30	4	Model-1	3.6538	1.9380	1.8181	0.2794	0.2225	0.1043
		Model-2	3.2416	1.5436	1.8200	0.2655	0.2087	0.1149
		Model-3*	1.4210	0.7587	0.9119	0.1683	0.1661	0.2021
		Model-4*	0.4680	0.2590	0.3386	0.1995	0.1473	0.0750
	10	Model-1	1.0131	0.6202	0.6345	0.1771	0.1584	0.0100
		Model-2	0.8975	0.5037	0.6306	0.1793	0.1607	0.0100
		Model-3*	0.6141	0.3448	0.4407	0.1914	0.1531	0.0332
		Model-4*	0.5464	0.2414	0.3083	0.2114	0.1355	0.0120

* Results using these models are generated independently for the first time.

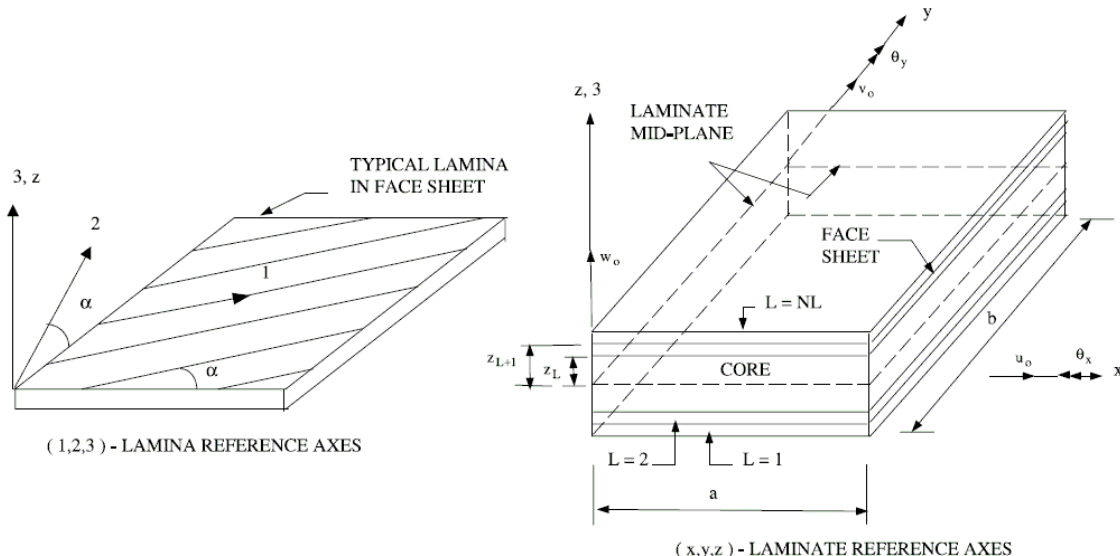


Fig. 1: Geometry of a sandwich plate with positive set of lamina/laminate reference axes, displacement components and fibre orientation

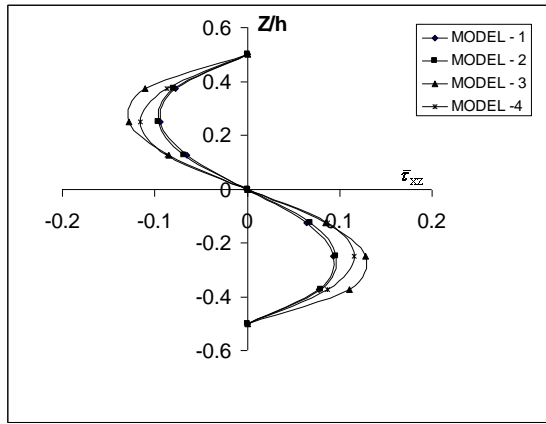


Fig. 2: Through thickness variation of $\bar{\tau}_{xz}$ for two layered square composite plate (15, -15) and $a/h = 4$ at $(a/2, 0)$ under sinusoidal loading for material set 1

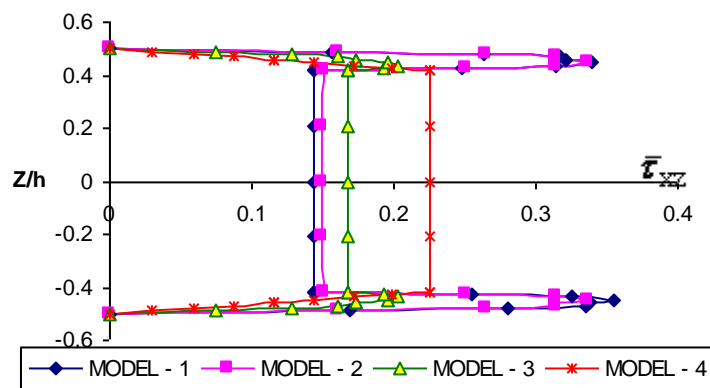


Fig. 3: Through thickness variation of $\bar{\tau}_{xz}$ for five layered square sandwich plate (15/ -15/ core/ 15/-15) and $a/h = 4$ at $(0, a/2)$ under sinusoidal loading for material set2

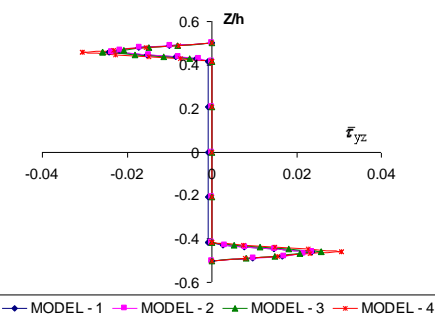


Fig. 4: Through thickness variation of $\bar{\tau}_{yz}$ for five layered square sandwich plate (15, -15, core, 15,-15) and $a/h = 10$ at $(0, a/2)$ under sinusoidal loading for material set 2

CONSERVATION OF CIVIL ENGINEERING HERITAGE IN JAPAN

K.Nagamura¹ I.Kobayashi² and K.Venkataramana³

¹ Dept. of Civil & Environmental Engineering, Kumamoto University, JAPAN
Email :108d9403@st.kumamoto-u.ac.jp

² Dept. of Civil & Environmental Engineering, Kumamoto University, JAPAN

³ Center for Globalization, Kumamoto University, JAPAN (on leave from NITK, India)

Abstract: There are many Civil Engineering Heritages in Japan which need to be protected and preserved. Although some Civil Engineering Heritages have speciality or permanent value in civil engineering history, many of them have been broken down. Sometimes, even if they are saved from demolition, there are many cases where they have not been reused effectively. In this paper, we outline the measures and the policies related to the preservation of cultural heritage and on the Law for the Protection of Cultural Properties. Then, we describe the current state of preservation and management of civil engineering in Japan. Finally, we try to propose the possible conservation steps for these heritages.

Keywords: civil engineering heritage, cultural property, conservation,

1. Introduction

In recent years, Japan has been at the center of "the heritage boom", for example, World Heritage, Industrial Heritage etc.

There are various kinds of treatment of heritages. One is legally preserving under the "Law for the Protection of Cultural Properties". Another is certification by related organization. And some local residents and specialists call it heritage due to the historical values. Civil Engineering Heritage is also historical Engineering Works of general interest, such as bridges, dams, tunnels, levees, locks, and so on. Meanwhile, many of

them have been broken down, because of urban-development or defective function of the structure. Even if they have been fortunately able to avoid tearing down, there are far too many cases where these structures have not been reused effectively.

2. Protection for Heritage in Japan

2.1 Categories of Cultural Properties

In Japan, there is a legal system about preservation of cultural properties. Since 1950, the Cultural Properties are protected by establishment of the law, called the "Law for the Protection of Cultural

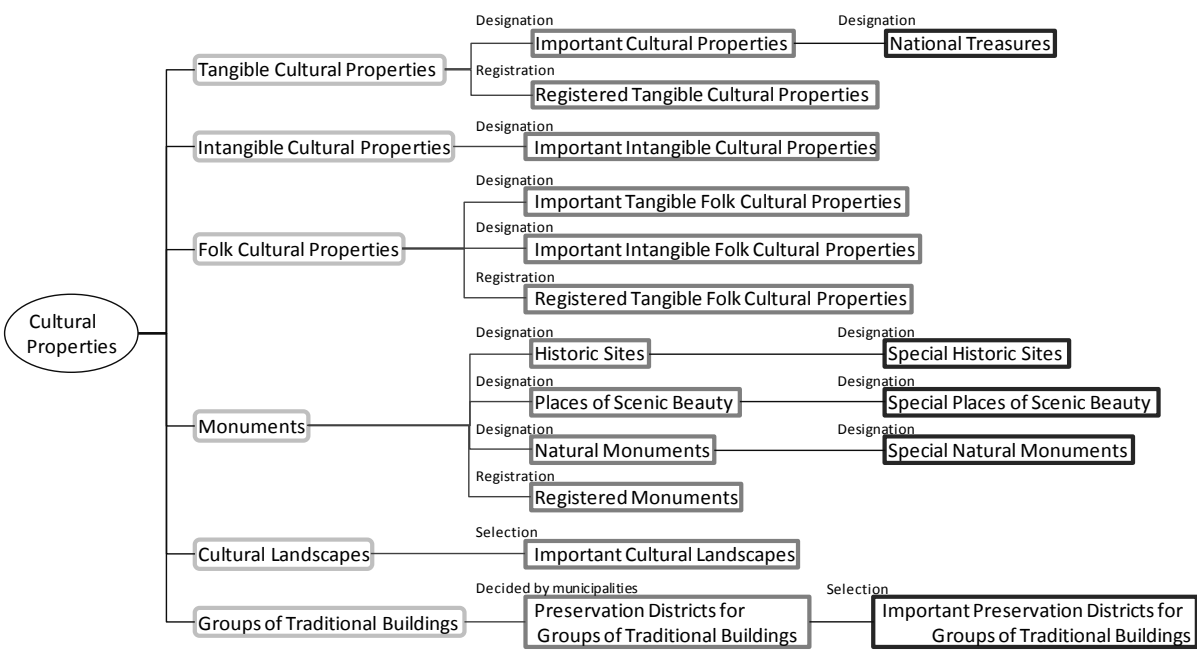


Fig. 1 Schematic Diagram of Cultural Properties in Japan[1]

International Engineering Symposium, March 3-5, 2011 Kumamoto Univ., Japan

Properties." This law is a unified legal framework which covers "Tangible Cultural Properties" such as structures, works of fine arts and crafts, "Intangible Cultural Properties" such as drama, music, craft techniques, natural landscape, and so on^{[1][2]}. (Fig.1)

Cultural Properties for civil engineering include "Tangible Cultural Properties" such as "Important Cultural Properties" and "Registered Tangible Cultural Properties", "Monuments" such as "Historic Sites", "Places of Scenic Beauty", and "Important Cultural Landscapes".

The categories of Cultural Properties are outlined, with bridges as example, below.

Important Cultural Properties - Tsuuujyun-kyo bridge (Photo 1)

For "Tangible Cultural Properties" which are important at national level, the government subsidizes the investigation, regular maintenance, protection, and publication. The owners of the properties are obliged to refrain from certain acts, such as random repairs, and the owners need to get prior permission from the government for any activity.

Tsuuujyun-kyo bridge is designated as a nationally "Important Cultural Property", and is huge masonry aqueduct which is part of irrigation system. The bridge was constructed about 150 years ago. The users have been continued to remove sediment and repair any water leak. So the bridge has been supplying water even today.

Registered Tangible Cultural Properties - Kounogawa bridge (Photo 2)

"Registered Cultural Properties" is the system for the preservation of structures other than those designated by the national or local governments. This system is governed by loose regulation, and gives the owners tax incentive.

Several concrete arch bridges were built

before World War 2, for the old Japanese National Railways, for the Miyanoharu railway line. The existing seven bridges were registered just after establishment of this system. After the line went out of use, the management of the railway site was transferred to the local government. Today, two bridges among them have been opened as part of a walking trail.

Historic Sites - Lake Biwa Canal (Photo 3)

National "Historic Sites" are important items of Ancient sites which possess a high historical and scientific value. They are designated or registered under similar regulation with "Tangible Cultural Properties".

The Lake Biwa Canal was built in the Meiji period, about 120 years ago. Water in the canal is taken from Lake Biwa, passes through Kyoto city, and discharges into Uji river. Among them, the part which was built in the first period has been designated among Historic Sites. At that time, the canal was also working as waterway for hydroelectricity, water supply, and so on. Today the canal is managed by Kyoto City Waterworks Bureau.

Places of Scenic Beauty - Kintaikyo bridge (Photo 4)

National "Places of Scenic Beauty" are important items which possess a high artistic or scenic value. They are designated or registered under similar regulation with "Tangible Cultural Properties" just as "Historic Sites".

Kintaikyo bridge was built in 1673, which is a five-span wooden bridge. The bridge had been destroyed by flood and replaced over and over again till today. And the structure and the location of bridge pier has changed at modern times. So the bridge has never been acknowledged as "Tangible Cultural Properties". However, the bridge is very much talked about as a



Photo1 Tsuuujyun-kyo bridge



Photo2 Kounogawa bridge

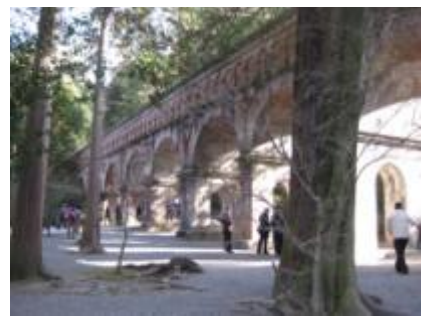


Photo3 Lake Biwa Canal



Photo4 Kintaikyo bridge



Photo5 Chinka-bashi bridge
(Photo by: Shimanto-gawa zaidan)

famous ancient bridge, because the technique of timber-work is wonderful, and the scenery at all the four seasons is extremely beautiful with cherry blossom and maple, etc.

Important Cultural Landscapes – Chinka-bashi bridge spanning Shimanto-gawa river (Photo 5)

The definition of "Cultural Landscapes" is "Landscapes that have evolved in association with the modes of life or livelihoods of the people and the geocultural features of the region, which are indispensable to the understanding of the lifestyle and/or livelihoods of the people of Japan." Specially important items have been selected as "Important Cultural Landscapes". If selected, they would be preserved under regulations on alterations to current state.

Shimanto-gawa river has been hailed as the last limpid stream in Japan, and has been selected as an Important Cultural Landscape. 47 bridges of Chinka-bashi bridges spanning Shimanto-gawa river have been selected for preservation.

Thus, there are a wide variety of Cultural Properties, even if they are the same class of structures.

2.2 Transition of the system for the protection of Cultural Properties

The system for the protection of cultural properties in Japan has been expanded responding to the social conditions of the time. (Table.1)

In Meiji period, the "Law for the Preservation of Ancient Artifacts (1871)" and the "Ancient Temples and Shrines Preservation Law" were established, because there was fear that the ancient artifacts had been scattered and lost, or ancient temples and shrines had been destroyed due to the anti-Buddhist

movement and Europeanism after the Meiji Restoration. Against a backdrop of destroying monuments because of modernizing influence related to development and industrialization between the end of the Meiji and Taisho period, the "Historical Sites, Places of Scenic Beauty, and Natural Monuments Preservation Law" was established in 1919. In the early Showa period, the feudal lords had abandoned their historical treasures because of economic slump, and the castles which had been left since the Meiji period needed repair. Therefore it was necessary to protect the structures other than Temples and Shrines. So the "National Treasures Preservation Law" was established in 1929.

After the World War 2, the destruction by fire of the mural paintings in the golden hall of Horyuji Temple led to the establishment of the existing law, the "Law for the Protection of Cultural Properties" in 1950. This Law has been unified the legal framework for the protection of cultural properties, which involves Structures, Works of fine arts and crafts, Monument which has been protected since the Meiji period, and added intangible cultural products as objects to be protected^[2].

And the existing law was improved as changes occurred in society. Some examples of Civil Engineering Heritages are as follows. At the first law revision in 1954, the local governments could designate and take protection measures for cultural properties based on the revised law. When the change of lifestyle in urban and rural areas turned historic landscapes of villages and towns, the system of "Preservation Districts for Groups of Traditional Buildings" were established in

International Engineering Symposium, March 3-5, 2011 Kumamoto Univ., Japan

Table.1 Transition of the system for the protection for Cultural Properties

Year	Main Events and Activities
1871	Law for the Preservation of Ancient Artifacts
1897	Ancient Temples and Shrines Preservation Law
1919	Historical Site, Places of Scenic Beauty, and Natural Monuments Preservation Law
1929	National Treasures Preservation Law
1950	Enactment of the Law for the Protection of Cultural Properties
1954	Amendments <i>Expansion of system for Buried Cultural Properties</i>
1975	Amendments <i>Establishment of system of Preservation Districts for Groups of Traditional Buildings</i>
1990	Start of the national investigation for Heritage of Modernization
1996	Amendments <i>Establishment of system of Registered Cultural Properties</i>
2004	Amendments <i>Establishment of system for protection of Cultural Landscapes</i>

1975. The system had used know-how of facade retention for historical townscape as a reference. This has been designed to preserve building facade. With this law revision, the system for protection of Conservation Techniques for Cultural Properties was also established. The conservation methodology for cultural properties in Japan has been institutionalized at this time. The repair technique for wooden building based on many years of experience, has been applied even today.

In 1980s, the destruction of cultural properties by development and change of lifestyle had affected the Heritage of Modernization. Responding to these situations, Agency for Cultural Affairs launched the national investigation, and established the system of Registered Cultural Properties in 1996. This system has a loose regulation, therefore, it is expected to promote effective use of the cultural properties.

Furthermore, in accordance with the movement of preservation of landscapes with environmental conservation activities spread across the country since 1980s, the "Landscape Law" was established in 2004. This led to amendments to the "Law for the Cultural Properties". "Cultural Landscapes" were added as the new definition of cultural properties. This has established the today's system for the protection of cultural properties in Japan.

In accordance with including Heritage of Modernization, and establishment of the system of Registered Cultural Properties, Civil Engineering Heritages which have been preserved as cultural properties have increased considerably. However, in the cultural properties field, there is no established measure for the protection of Civil Engineering Heritage, and we don't have much experience. There is need to preserve function of civil engineering facilities, and treat some modern materials which include concrete, steel, brick, etc.

3. Context of Civil Engineering in Japan

3.1 Situation of Civil Engineering field

Concrete is a standard construction material in Japan, which is considered as a maintenance-free material. In high economic growth in 1960s and 70s, many structures had been constructed using Standard Specification for Concrete Structures which had been based on this concept, and they have performed well till today. The long-term behavior of concrete had been suspected from 1984, and it is urgent that the maintenance system is in-place quickly. After various discussions, the full-scale maintenance system for concrete structures was established in 2001.

Steel is also a standard construction material in Japan. The anticorrosion engineering for steel had been well-established. In addition to this, the technical manual for maintenance against deterioration was updated in 1996, and now, maintenance techniques are being widely discussed.

Thus, not only in the field of the cultural properties but also the civil engineering in Japan in general, the maintenance of existing structures has not been completely satisfactory and sufficient.

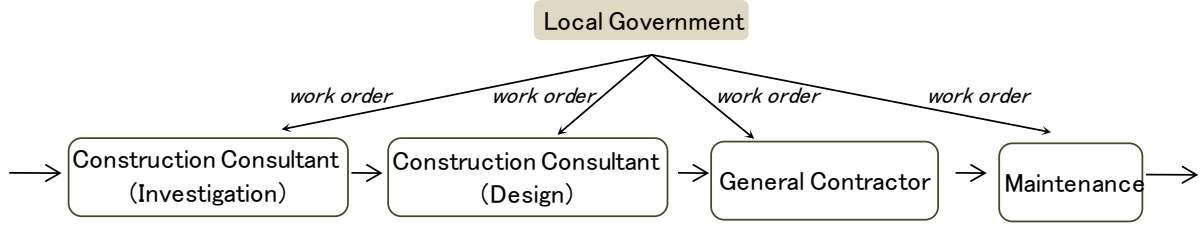


Fig.2 Work order system for Infrastructure by local government

3.2 Situation of Civil Engineering government

In Japan, many infrastructures are constructed, owned and managed by public body such as the national or local governments. The repair works for maintenance are entrusted to professionals. For ensuring fairness, the work order is divided into survey, design and construction. Each work is undertaken by different enterprise.(Fig.2) This system is used mainly for new constructions. This system also applies to the maintenance works. The public body decides the total project cost based on the survey, design, and the construction within the cost ranges.

Civil engineering field has excelled in new construction, and system is well-established in Japan. However, most of the technology for the treatment of existing structures has not been effectively developed.

4. Present situation of conservation of Civil Engineering heritages in Japan

4.1 Situation of preservation and use of Civil Engineering Heritages

2,800 Civil Engineering Heritages all over the country have been ranked and listed by the Japan Society of Civil Engineers. They also established the recommendation system of Civil Engineering Heritages since 2000. This will help to appeal to society or civil engineer, to effectively use for regional development, and save those

heritages. As the system has headed in the right direction, some people have offered familiar Civil Engineering Heritages by themselves. Additionally, since 2007, the Ministry of Economy, Trade and Industry has selected the heritage of industrial modernization across Japan as "33 Heritage Constellations of Industrial Modernization." The aim of this certification program is to encourage community members to effectively use their local heritage for regional development. Those heritages have often included some Civil Engineering Heritages.

Following examples show these Civil Engineering Heritages.

Misumi West Port^[3] (Photo 6)

Misumi West Port is said to be one of the three major harbor constructions in Meiji period in Japan. The Dutch engineer, Mulder designed this port. This is westernized stone-built port. While it has been repaired with mortar in patches, it has retained the original form as well. This port has been designated as a nationally "Important Cultural Property" in 2002.

Momosuke bridge^[4] (Photo 7)

Momosuke bridge was constructed in 1922. The bridge lost its function due to damage to the storm cable by disasters. It was decided to restore the bridge in 1990, around the same time as starting the national investigation of the Heritages of Modernization. The restoration work attracted attention as progressive approach for the Heritages of



Photo6 Misumi West Port



Photo7 Momosuke bridge

International Engineering Symposium, March 3-5, 2011 Kumamoto Univ., Japan

Modernization. In 1994, the year after the completion of the work, the bridge was designated as a nationally Important Cultural Property.

Gohonmatsu Dam at Nunobiki Water Source^[5] (Photo 8)

Gohonmatsu Dam at Nunobiki Water Source is one of the waterworks facility which was constructed in 1900. This is the oldest gravity dam of stone masonry. After this dam was registered as "Registered Tangible Cultural Properties" in 1998, there had been strengthening work for the dam since 2001. The dam had been reinforced by concrete, and landscaped by stone pitching work on the surface. In 2006, the year after the completion of the work, the dam was also designated as a nationally Important Cultural Property.

Sogi Hydroelectric Plant Remains^[6] (Photo 9)

This brick building for hydroelectric plant was constructed in 1910. The electric generation plant had been shut down in 1965, and had been submerged because new dam was built downstream. The building remains have a full view during summer due to drawdown. Following the momentum for effective reuse as the industrial heritages, the plant was restored in 2004, and registered as national "Registered Tangible Cultural Properties" in 2006.

Katsunuma Wine Cave and Ohikage Tunnel (Photo 10)

Katsunuma Wine Cave and Ohikage Tunnel had been built in 1903. These are brick railway tunnels. As the rail cars were becoming larger, it was decided to construct the new tunnel. But these two tunnels had not been in use since 1997. After that, the local government has used one of them as wine cave (since 2005), another as walking trail (since 2007). Thus, these tunnels were effectively used as local attraction resources or wine industrial

development. These are selected among "33 Heritage Constellations of Industrial Modernization" in 2007.

4.2 Unused or demolished situation of Civil Engineering Heritages

While there is increase of some cases that Civil Engineering Heritages are preserved and effectively reused, a lot of heritages have still remained neglected or demolished.

As examples of neglected heritage, there are five bridges of the seven concrete arch bridges which are at the old Japanese National Railways, for the Miyanoharu Line. Although "Registered Tangible Cultural Properties", these bridges are not being used and not even people are allowed to go there(Photo11). The old rail facility of Usui Pass has been closed off except the walking trail zone for safety reason in the tunnels(Photo12). These two cases are old rail facilities which have been managed by the local governments. It is not necessarily the case that Civil Engineering Heritages which were managed by the local government have been a success. (If these facilities are diverted as road infrastructures, these would have been managed by Construction Division as civil engineering facilities.) These have been also managed by Planning Division, or tentatively abandoned to Administrator of Property Division. In the latter two situations, there is no idea to effectively reuse and those heritages have remained neglected until the local government or residents gather momentum of reuse. It is hard not to feel that those heritages will be forgotten in the future.

If some Civil Engineering Heritage is in the danger of demolition, Japan Society of Civil Engineers has often requested for its preservation by the owner. In the last ten years, since establishment of the recommendation system of Civil



Photo8 Gohonmatsu Dam



Photo9 Sogi Hydroelectric Plant



Photo10 Ohikage Tunnel



Photo 11 The old rail bridges



Photo 12 The old rail Tunnel

Engineering Heritages, there were seven preservation requests, six of them requested to the local government.

Thus, it shows that it is difficult to preserve and effectively reuse by the local governments.

5. Civil engineering management by local government

5.1 Political context of local government

The Cultural Properties Protection Division of local government follows mainly the procedure for Protection of all Cultural Properties.

In addition, as the candidates for Cultural

Properties have increased, with the addition of Heritage of Modernization and Cultural Landscape, some of infrastructures which are owned by local governments have been now designated as Cultural Properties. It seems that this case is easier to preserve as Cultural Properties than when the owner is individual or a private company. However actually, there are some difficult problems because they belong to the same organization, and have to preserve their cultural properties as part of other's duties.

One of the difficult problems is the relationship between the Cultural Properties Protection Division and the Construction Division. If the area of civil engineering works has ancient sites, the sites cannot be developed without proper investigation of the site. The work has to stop until the investigation of ancient site is finished, and the investigation cost is borne by the construction firm by convention^[7].

The government's vertical administrative structure is another difficult problem. In Japan, the local administration had been nominal, and many local governments had subcontracted works for national government for a long time. Also, the national ministries and agencies do not have proper coordination among themselves^[8]. Then each Division of the local government had dealt with the administratively delegated work in accordance with the national laws (Fig.4). There was a system of delegating the national-policy administrative works to the

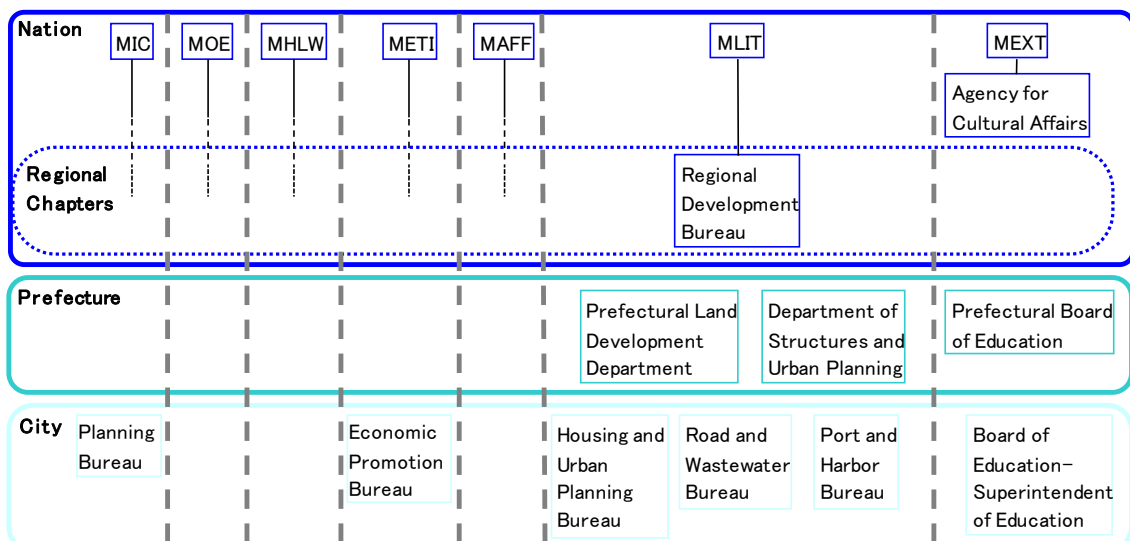


Fig.4 The government's vertical administrative structure

local governments. This system was abolished in 2000, and the decentralization of power was promoted as a result of reform. It's hard to say that this has changed the way of the administrative working condition yet^[9].

The Construction Division arranges for the minimum protection with the Cultural Properties Protection Division if the infrastructure has been designated as a Cultural Property. This is limited to the prohibition of activity or regulations on alterations to current state.

Thus, even if Civil Engineering Heritage has been the legal Cultural Properties, it is difficult to say that there is smooth policy coordination about the protection between the Construction Division and the Cultural Properties Protection Division. In the light of these things, and partly due to administration's problem, the non-legal Civil Engineering Heritages are often not used effectively, or are demolished.

5.2 Proposition for effective management of Civil Engineering Heritage by local government

Under the complicated system of their organization, the local government officers are often helpless. It is difficult for them to expand their tasks devotedly and aggressively to preserve non-legal Civil Engineering Heritage on their own.

In a organization where they can implement all government administration, the local government may be able to leverage Civil Engineering Heritages effectively with multiple perspectives. However, if the management has to direct them to each division, we cannot expect much results. Therefore we propose the following ways for protection of Civil Engineering Heritage:

i) Consider the conservation of the Civil Engineering Heritage more specifically, and put them in the statutory form.

ii) Confirm all divisions who have been involved in the Civil Engineering Heritage, and put each role in the statutory.

First group will decide what to conserve, for example, facade, member, facility, material, and other specific things. They need to share the data and the repair method. Second group consists of the management division of the Civil Engineering Heritage and they should prepare the conservation document with

the help of experts and the Cultural Properties Protection Division, and save them for future use. It's preferable that the Cultural Properties Protection Division observes protection for these heritages even if they are non-legal heritages, and fully cooperates with the investigation and publicity.

6. Concluding Remarks

There are a lot of problems for conservation of Civil Engineering Heritage technically and procedurally. Since late 1980s, however, technical experience for their repair has been increasing in Japan. These visionary projects have been big projects, or under the sponsorship of experts. We expect that the local government establish the system for conservation of Civil Engineering Heritages by building multi-organization partnerships.

Until now, we have emphasized on evaluating Civil Engineering Heritage technically or academically. Through such efforts, we are moving on to the next stage of effective conservation.

References

- [1] Cultural Properties Department, Agency for Cultural Affairs, JAPAN (2007), Cultural Properties for Future Generations, Website: http://www.bunka.go.jp/bunkazai/pamphlet/pdf/pamphlet_en_03.pdf
- [2] NAKAMURA, K. (2007), Exposition of system for the Protection of Cultural Properties, Tokyo : Gyosei, pp.1, 14-20. (in Japanese)
- [3] HOSHINO, Y. and KITAGAWA, D. (2004), "Historical Research for Planning and Construction of MISUMI Port", J. of Historical Studies in Civil Engineering(JSCE-2004), Vol.24, pp.95-108.
- [4] Nagiso town ed.(1994), Report of restoration work for Momosuke bridge. (in Japanese)
- [5] Committee for Historical Engineering Works JSCE ed. (2010), Conservation of Historical Engineering Works, Tokyo : Kajima-publishing, pp.234-238
- [6] MARUTA,Y. et al.(2008), "Preservation works for the ruins of Old SOGI Power Station by reusing the bricks made 100years ago", Proc. of the 28th Annual Conference of Historical Studies in Civil Engineering(JSCE-2008) Vol.28, pp.43-52.
- [7] WAKATSUKI, K. (2003), "Protection of Buried Cultural Assets and Excavation Research Expense Paid by Caused Person Policy", J. of the study of modern society and culture, No.26, pp.17-33
- [8] IMAGAWA, A. eds.(2007), Local government in decentralized era, Tokyo : Sanseido, pp.22-23. (in Japanese)
- [9] ISOZAKI,H et al.(2007), HORN BOOK Local government, Tokyo : Hokujyushuppan, p.184. (in Japanese)

The Alternative Building Materials and Technologies for Individual Housing in Coastal Karnataka, India.

RAJENDRA KALBAVI RAO¹ SUDEEP KUMAR SHETTY²and JOHN KENET D'SOUZA³

- 1 Project Director D. K. Nirmithi Kendra, National Institute of Technology Karnataka, Surathkal, Mangalore, India. 575025 email: dknirmithi@yahoo.com
 - 2 Rachana consultants, Consulting Engineers and Architects, 1st floor, Venkataramana Arcade, Bhavanti Street, Mangalore, India. 575001. email- sudeepshetty2009@yahoo.com
 - 3 Consulting Engineer, 1st Floor, Krishna Complex, MG Road, Kodailball, Mangalore, India. 575003. email- keneshma@rediffmail.com.
-

Abstract: The various research organizations in the country and world wide are in continuous investigation to develop different alternative materials and technologies. In the development of alternative materials, it is always emphasized to use locally available materials like mud, fibre, powder, stone etc. or a mixture of them to produce a different product to be used in modern day construction. This paper likes to give an insight into the various types of technologies developed by these Organizations and implemented right from the basic materials like building blocks to finished roofing elements in coastal Karnataka, India. It also discusses how these techniques are implemented and put to use for the benefit of the common man. It also enlightens the cost effectiveness and the energy efficiency that could be achieved in using these alternative materials and technologies in the region.

Keywords: Alternative, technologies, investigation, locally available, elements.

Introduction

World hates change, yet, it is the only thing that has brought progress- Charles Kettering.

'Normal is boring' is the common saying. Man needs change in every aspect of life, for which construction is no exception. He needs change, needs different designs, needs variety, needs choices and other options before he decides. The various research Organizations in the country and world wide are in continuous investigation to develop different alternative materials and technologies. These vary from basic materials like stone and sand to finishing materials like paints and coatings. As science and technology advances, it is becoming challenging work to the scientists to give an improvised, fault free and performance oriented products and technologies to suit the general public. List of building materials to choose from has become very exhaustive and expensive

results in the urge to develop newer and different materials to suit local condition and to suit the varying human requirements.

Costal Karnataka

The cities in costal Karnataka are situated attached to Arabian Sea. Mangalore is located at 12°-52'N latitude and 74°-49'E longitude. The average rainfall is 3875 mm between Junes to September every year. The ambient temperature varies minimum from 17°C to a maximum 37°C. The maximum average humidity is 93% in July and average minimum humidity is 56% in January. There are only 2 seasons, namely rainy season and summer season. Generally days are warm through out the year. Sloped roof with Mangalore tiles are commonly used, before invention over concrete. Bricks, cement, steel, aluminium, plastic products, paints, polished stone, ceramic products, etc. are the commonly

used materials of construction today. Modern day house construction involves in construction of framed structure with lintels and chajjas and RCC for roof slabs. Those who can afford will have air conditioned rooms and others will keep large openings for ventilation and comfort inside the house.

Why Alternative building Materials and technologies

Selection of materials and technologies for the building construction should satisfy the felt needs of the user as well as the development needs of the society, without causing any adverse impact on environment. The first energy crisis of 1973 was perhaps the trigger, which lead to the concept of Alternative Building Technology. Technologies of the Developed West often could not meet these requirements and many thinkers argued in favour of a middle path and this approach is the genesis of the Alternative Technology movement. With the development of science and technology alternative materials and technology is available, right from the basic materials like cement to building blocks, from foundations to finishing items. Few of them are explained below.

Building Blocks

Naturally occurring laterite stone blocks are commonly used in coastal areas. Fig.1. The concrete blocks have spearheaded the construction industry with varying sizes form brick to laterite. The investment is very low and it can be produced throughout the year as compared to the brick industry. (Fig.2)

Burnt Clay Hollow Blocks:-

These are burnt high clay blocks made by a process of extrusion. The wall thickness of the hollow block is often as low as 15 to 20 mm. They come in various sizes from laterite block to brick.

Stabilized Mud Blocks

Soils when compacted using external energy, the density of the soil reaches a maximum value at the optimum moisture content (OMC). The value of OMC and the maximum density depends on the energy input during compaction. The compressive strength of the soil, in the dry state,

depends on the density. Thus the process of mechanical compaction can lead to densification and strengthening of the soil. Addition of stabilized additives like Cement, lime or bitumen further improves the densification during saturation. These blocks can be produced locally with manually operated machines with suitable mould sizes. (Fig 3)

Stone Blocks using recycled wastes

The BIS specification IS: 12440 give the details of this technique. It is a very simple technology involving using odd sized stones, which are shaped by a layer of concrete surrounding the stone. Steel moulds resting on level ground can be used to place the odd shaped stone in the centre of the mould. Lean concrete is now poured in the space between the stone and the mould. Block sizes matching to laterite or concrete blocks are commonly used. Compressive strength in the range of 5.0 to 7.0 MPa can be easily achieved.

Masonry construction techniques

English bond is the most common mode of construction in India. When Concrete blocks are used, the blocks have to be kept in 'Stretcher bond' leading to a wall thickness of 100,150 or 200mm and a course height of 200mm as shown again in Fig.2. When stabilized mud blocks of size 230x190x100mm are used, either a header bond with wall thickness of 230mm or a stretcher bond of 190mm wall thickness can be used. The concept of rat-trap bond was popularized by Ar.Laurie Baker in Kerala in the seventies. This involves keeping bricks on edge creating a gap in the thickness of the wall. About 25% of the bricks can be saved by this process. The cavity created within the wall offers thermal comfort inside the house. (Fig 4&5)

Arches, Corbels and Reinforced brick lintels

Masonry arches are the age old construction techniques can still today replace concrete lintels. Arches can be circular, segmental or even flat. (Fig 6 & 7) These are also used in the masonry foundations between the corners to save on earthwork excavation and materials. Corbels (Fig 8) and arches give aesthetic look to the structure while carrying the

desired load. Reinforced brick lintels are the one used or small openings up to 1.8m with and nominal reinforcement of 3-8 mm in CM 1:3 and bricks laid on edges with the same mortar.

Ferro Cement Elements

Ferro cement is a special form of reinforced concrete. It is a composite material consisting of cement-sand mortar (matrix) reinforced with layers of small diameter wire meshes. It differs from conventional reinforced concrete primarily by the manner in which the reinforcement is arranged within the brittle matrix. The success of ferro cement in various terrestrial applications can be attributed to ready availability of materials locally, need of low level technology for its production, better utilization of available human resources and architectural flexibility. Ferro cement products are so versatile that they have reached common man's kitchen to drawing room furniture to commercial structures. It is all geared to replace timber in all the areas of construction. (Fig 9)

Alternative Roofing Systems:-

Due to invent of extensive research done by various institutions various technological options are available for implementation. The research for an alternative roof must be based on a simultaneous satisfaction of several objectives.

1. Withstand imposed dead and live loads.
2. Prevent leakage during rainy season
3. Provide a secure enclosure
4. To be cost effective
5. Provide a durable comfort in the interior
6. Give aesthetics to the structure

Roofs can be

- i) Pre fabricated roof
- ii) Partially prefabricated roof
- iii) Cast in-situ roof

Few of the technologies commonly used in coastal Karnataka are explained below.

a) Filler Slab Roofs:-

Filler slab roofs are basically solid reinforced concrete slabs with partial replacement of the concrete in the tension zone by a filler material. The filler material could be cheaper and lighter. A number of filler materials can be thought of a) Brick or brick panel, b) Mangalore tile, c)

Stabilized mud block d) Hollow concrete block, e) Hollow clay tile block etc. Size and shape of the filler material are governed by the factors like slab thickness, code guidelines on spacing of reinforcement bars, desired ceiling finish etc and has to be carefully selected. This is a cast in situ system and is widely accepted and is most suitable for tropical Climate and for buildings in coastal region. The laying of this roof is in line with conventional technique. The form work is done at desired height and shape, the filler material is placed and the reinforcement is tied and the concrete is laid. This method also satisfies all the requirements of the code and the needs of the common man. Layout of filler material (Hollow clay block roofing block) along with the reinforcements before the pouring of the concrete and the ceiling (with regular Mangalore tile) after completion are shown in figure. (Fig 10, 11 & 12)

b) The Concept of Composite Beam and Panel Roofs:

This system is similar to the traditional wooden rafters and wooden planks used as attic in the olden days. Now we are using concrete beams and planks made of materials like brick, ferro cement, stabilized mud blocks etc are used. The roofing system consists of panels and beams cast separately and assembled such that the system behaves like a T-beam. The beams can be fully pre cast or partially pre cast beams. These types of roofing systems can be broadly grouped into two categories viz: Flat panel roof and curved panel or jack-arch roof, based on the shape/geometry of the panel. Since the panels and beams are cast separately and then assembled, there should be proper shear connection between them to achieve composite action for the system to behave as an integral structural unit. The flexibility of composite beam and panel roofs arises out of the fact that the materials for the beams and the panels could be of two different materials and the composite action between them could be achieved by proper shear connectors. Both the beams and the panels can be precast and then assembled into a roofing system. In case of precast beams, the beams are partially cast and hence they require some props while assembling the roofing system.

These roofs can be laid flat or with gentle slope. Fig 13

c) Masonry Domes and Vaults:

Romans rediscovered the use of the arch, and the vault. However, they often used semicircular barrel vaults built out of concrete. The vaulted constructions spread to Europe and one can see vaults in Roman architecture of England. The vault construction was no longer confined to mosques in this region. The superiority of the brick masonry vault over the conventional construction using timber palaces, granaries, ammunition stores were some of the important structures where the vaulted construction was readily accepted. A thin layer of nominally reinforced concrete over and above the unreinforced masonry can vastly enhance the performance of masonry roofs. Fig 14. Use of modern materials like glass fiber reinforced plastic as externally attached reinforcement can also provide additional flexibility and strength.

d) Mangalore tiles over ferro cement rafters and reapers.

Mangalore tiles over wooden supporting structure are accepted and adopted technology since centuries. It is most suitable roof for the coastal region in the tropical country like India. Timber of good quality is not available as per requirement and above that it is expensive material. Concrete and ferrocement can be a suitable substitute alternative replacement for implementing Mangalore tile roofing system. The size and the shape can match the timber and the member can be designed as per requirement on IS codes. The wall plate, the rafters and the reapers are manufactured to design in a factory and shifted and erected at site. These structures are unlike wood are fire resistant, termite resistance, anti fungal, low maintenance and it has a long life then compared to timber structures. It is a look-a-like structure and one cannot make out the difference between the conventional and alternative method once erected. Fig 15.

Energy efficient and eco friendly:

Considerable amount of energy is spent in the manufacturing processes and transportation of various building materials.

Conservation of energy becomes important in the context of limiting of green house gases emission into the atmosphere and reducing costs of materials. A comparison of energy in different types of masonry has been studied. Energy in different types of alternative roofing systems has been discussed and compared with the energy of conventional reinforced concrete (RC) slab roof. It is found that total embodied energy of load bearing masonry buildings can be reduced by 50% when energy efficient/alternative building materials are used. Table1.

Conclusion

Opening up of the Indian market has given the common man to look for the latest and the best suited material and technique for his suited budget and needs. Table 2 shows the cost benefit in using these technologies. With internet available at nook and corner of the state, every man is well informed and has access to knowledge super highway. Recently lot of materials and techniques are coming to the market and the common man is confused to use, adopt, judge and implement the right technology. We Engineers with all the technical back ground and experience should have the updated knowledge to use the appropriate technology at right place at correct time with proper technical design, supervision and implementation. Thus the efforts of the scientists and researchers will have a value addition and a dream come true for the common man. Fig1. The only shortfall is the information which reaches the common man gradually and all the building materials and technologies are time tested over the years, it takes its own time to prove its credibility and durability requirements.

References:

- [1] A.J.Joseph Increasing the service life of low-cost buildings, Building Materials for Low-Income Housing, Oxord & IBH Publishing Co.Pvt.Ltd. New Delhi. P 335-340.
- [2] Harrison S. W, Sinhat B. F, A study of alternative building materials and technologies for housing in Bangalore, India Construction and Building Materials Vol. 9, No. 4, January 1995, pp. 21 I-211.
- [3] Jagadish K. S, venkatarama Reddy K. S, Nanjunda Rao, Alternative Building Materials and Technologies.2008.New Age International Publishers. New Delhi.

International Engineering Symposium, March 3-5, 2011 Kumamoto Univ., Japan

- [4] Jamal M. Khatib, Sustainability of construction materials. Woodhead publishing Limited.New Delhi. P 85,86 & 116.
- [5] Venkatarama Reddy B. V, Sustainable building technologies, Current Science, Vol. 87, NO. 7, 10 OCTOBER 2004, pp 899-907.
- [6] Venkatarama Reddy B. V, and Jagadish K.S., Embodied energy of common and alternative building materials and technologies, Energy and Buildings 35 (2003) 129-137.
- [7] Venkatarama Reddy B.V., Jagadish K.S. / Energy and Buildings 35 (2003) 129-137, Energy and Buildings 35 (2003) 129-137, Embodied energy of common and alternative building materials and technologies .
- [8] Ross Spiegel, Dru Meadows, Green Building Materials, John wiley & sons, Inc. Professional/Trade Division,605 Third Avenue, New York,N.Y.10158-0012.P 9,27-30.
- [9] S.Q.Jamal and A.S.Sheikh, The use and Performance of soil stabilized blocks in flood affected rural areas, Building Materials for Low-Income
- Housing, Oxord & IBH Publishing Co.Pvt.Ltd. New Delhi.P 302-309.
- [10] **Internet reference:**
- 1) <http://ezinearticles.com/?AlternativeBuilding-Materials & nid=353963>
 - 2) <http://lauriebaker.net/work/work/alternative-building-materials-timeless-mud.html>
 - 3) <http://mangalore.webs.com/>
 - 4) <http://sciencedirect.com>
<http://www.build-smarter.com>
 - 5) <http://en.wikipedia.org/wiki/Mangalore>

Acknowledgement:

The authors are extremely grateful to Dr. K.S. Babunaryan, Dr. Katta Venkataramana, Dr. M.C. Narashnman and the department of Civil Engineering who have guided during the implementation of these technologies. Thanks are due to the DK District administration and the Staff of D.K. Nirmithi Kendra who are the back bone in execution of these works. The efforts of Mr. Dilip Kumar, Mr.Rajanna.H. and Mr. Vandana Pinto in preparing this paper are also acknowledged.

Table 1.

Energy in different roofs/floor systems			
	Number Type of roof/floor	Energy/m ² of plan area (MJ)	Equivalent of RC solid slab energy (%)
1	RC slab	73.0	100
2	SMB filler slab roof	59.0	80.8
3	Composite brick panel roof	56.0	76.7
4	Burnt clay brick masonry vault roof	57.5	78.8
5	SMB masonry vault roof	41.8	57.3
6	Mangalore tile roof	22.7	31.1
7	Ferro concrete roof	15.8	21.6
8	RC ribbed slab roof	49.1	67.3

Table 2. Cost savings of Innovative technologies over conventional options

No	Innovative Technologies	Conventional Options	% of saving
1	230mm thick wall	330mm brick walls	5
3	Rat trap bond walls	English/Flemish bond	25
4	Hollow blocks walls	Hollow blocks walls	20
5	Tiles over RCC rafters	Tiles over timber rafters	25
6	Brick panel with joists	RCC	20-25
7	Ferro cement shell roofing	RCC	40
8	Filler slab roofing	RCC	22
9	Jack arch brick roofing	RCC	15
10	Precast blocks over inverted T-beams	RCC	25
11	Corbelling for lintels	RCC lintels	40
12	Brick arch for lintels	RCC lintels	30
13	Hollow clay block	walls & corners	20
14	Hollow roofing block	RCC slabs	15-25
15	Precast ferro cement shelves	Timber/concrete	35-45



Fig 1 The residence of Mr. Kenet D'souza(Co author) constructed using Laterite stone blocks and alternative building technologies

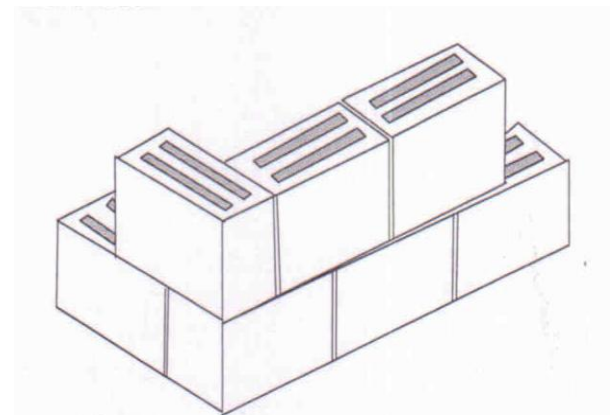


Fig 2 Hollow concrete block laid with stretcher bond for wall construction



Fig 3 Stabilized Mud block under production.

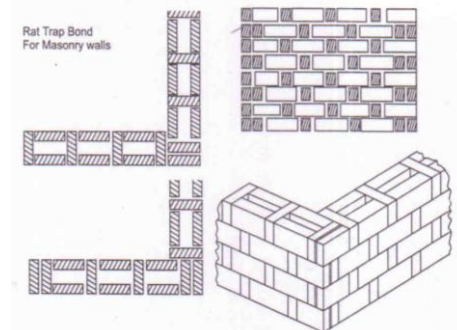


Fig 4 Layout for rat-trap bond construction



Fig 5. Brick wall constructed with rat-trap bond technique.



Fig 6. Brick arches in place of lintels and beams



Fig 7. Flat arch with brick masonry to avoid lintels.



Fig 8. Large corbels can replace lintels, arches and beams.

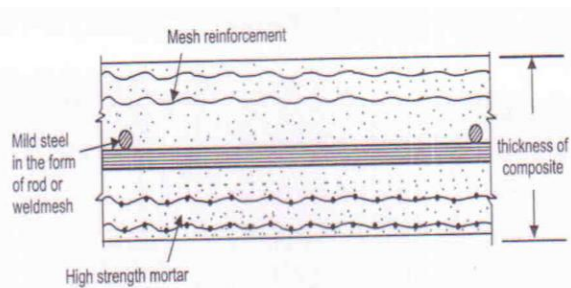


Fig 9 Cross section of a Ferro cement member



Fig 10 Hollow clay block Filler slab before pouring of concrete.



Fig 11 Filler slab ceiling after completion



Fig 12 Filler slab ceiling using Mangalore tiles after completion.



Fig 13. Ceiling view of a brick panel roof.



Fig 14 View of a circular brick vault



Fig 15. Mangalore tiles supported on Ferro cement rafters and reepers.

SLIM – GAL FOR SHAPE OPTIMIZATION OF STRUCTURES

BABU NARAYAN K.S¹, DEVRAJ MANAI² and ARUN PRABHA K.S³

- 1 *Civil Engineering Department, National Institute of Technology Karnataka, Surathkal, Mangalore 575025, India, e-mail: shrilalisuta@gmail.com*
- 2 *Shankar Industries, Kavoor, Mangalore-575 006, Karnataka, India*
- 3 *Skycell Towers & Infrastructure Pvt.Ltd, Gandhinagar, Mangalore-575 003, Karnataka, India*
-

Abstract: Structural Optimization has been & continues to be an active area of research offering scope and need to handle a wide & varied range of problems. Genetic Algorithms (GA) recently have been, with great success employed to solve structural engineering problems either in conjunction with traditional methods or as alternatives.

Sizing, shape and topology design of trusses is an interesting exercise that has attracted the attention of researchers. However design problems have not been kept free of conceptual designs, defeating the possibility of evolution of more efficient & innovative designs, the reason being the complexity of the problem on hand.

This paper presents GA based methodology of arriving at the best configuration & member sizing employing simultaneous mode of failure approach for problem formulation of the multi-objective type to yield a structure that satisfies functional & structural requirements optimally.

Keywords: Lattice, Fitness, Selection, Chord, Deflection.

Introduction

Structures are built with an intended end use for a specified utility period. The functional requirement is to serve the purpose and the structural requirement constitutes stability, strength, safety, serviceability and durability. Satisfaction of these requirements at affordable costs is the goal of structural optimization. Economy is wise spending and cost effectiveness is "maximum effect with minimum efforts".

Realization of cost effective structures heavily relies on factors like progress made in material sciences, knowledge of behavior of materials and structural systems, analytical tools for assessment of strength, safety and serviceability, construction practices and construction economy. True innovation is proper synthesis of these factors.

The mode of transmission of force is a function of configuration. The technical success of optimization depends on how efficiently the load flow is accomplished. Decision-making that leads to final geometry represents the highest level of Structural Engineering.

Planning, analysis, design, detailing, execution, operation and maintenance of engineering systems involve decision making at several stages. The decision making process should lead to utilization of least resources and realization of maximum benefits. Operations Research is the branch of mathematics that deals with the application of scientific methods in decision-making process. Available literature on application of optimization techniques for shape optimization of structures has been gathered and presented in this paper and shape optimization of lattice girders by GA has been illustrated.

Literature review

Tzonis and Lefaiure (1975) credit Galileo Galilei as the initiator of shape optimization, for it was Galileo who made the famous proposition that "it would be a fine thing if one could discover the proper shape to give to an object in order to make it equally resistant at every point". Much work has been done on optimal structures since then and the search is still on, as there is no single way to address the wide and varied range of problems encountered in Structural Engineering.

The fact that there exists a unique geometry for the structure of absolute minimum weight under a specific loading arrangement was first suggested by Michell (1904). He demonstrated that optimal structures are built up of orthogonal nets of pin-jointed members shaped like slip-lines.

Richards and Chan (1966) have reviewed and confirmed Michell's theory. Though Michell's gives an inverse design method, it cannot include many design considerations and hence finds little application. Nevertheless Michell's work is regarded as the beginning of shape optimization because it was recognized for the first time that shape should be a fundamental variable in designing an efficient structure.

A method of design that finds best shape without investigating all possible shapes was first attempted by Dorn et al. (1964) employing linear programming technique. The results were in the range from the interesting to the unexpected. As objective functions and constraints in structural optimization generally are non-linear, it was accepted that clumsy linearization to include them in linear programming was of no much help.

Application of Dynamic Programming, a method of non-linear programming technique was suggested by Bellman (1957) and applied to pin-jointed frameworks by Porter-Golf (1968). Failure to adequately include design considerations makes this technique generate solutions that are not always

optimal. Palmer (1968) has used dynamic programming for limit design of beams, to include asymmetry, alternative loading conditions and use of real members instead of artificial and has demonstrated the benefit of shape optimization over usage of conventional standard geometry.

Geometric programming as a mathematical aid in engineering design was proposed by Zener (1961) and Templeman (1970) showed its utility in Structural Engineering problems. Though the technique depends on the form of objective function and constraints and degree of difficulty, it can be of use coupled with other methods to find either complete solutions or approximate ones.

An approach called Reanalysis with Sub-optimization has been attempted by Tom Lassen (1993) for shape optimization of large three-dimensional frameworks. The method assumes that large frame works are assemblages of small groups of limited number of members and only one active constraint for one member of the group that is critical considered for sub-optimization. Sequential Quadratic Programming Technique is employed for sub-optimization. Though there is no sound theoretical basis for the assumptions, experience with the technique has indicated that it is robust and consistent, offering optimum solutions at low computational costs.

Zimmerman et al. (1993) have suggested application of stochastic optimization models for identification of geometry and failure modes for structures where loads and resistances are to be treated as random variables. An attempt to address axial-force moment interaction as a function of geometry, integrating rigid plastic model with mathematical programming has been made.

Calatrava (1981) presents detached explanation of the subject of shape optimization by defining Profiling-as selection of geometry contour and Differentiating-as dividing the structure to several separate members each performing different functions using materials best suiting members assigned

function. He has demonstrated by mathematical programming that three dimensional space frames can be folded first to two dimensions and then into one. Calling this program a super 3D compass, he tries to explain generation of best geometry by movement of the joints in space.

Genetic Algorithms (GAs) are efficient and broadly applicable global search procedures based on a stochastic approach which rely on the survival of the fittest strategy. In recent years GAs have been used in structural optimization by many researchers [Goldberg and Samtani, (1986); Rajeev and Krishnamoorthy (1992); Rajan (1995); Rajeev and Krishnamoorthy (1997)]. All these studies have demonstrated that GAs can be utilized as a powerful decision making tool for optimization. Since GAs do not need gradient information they offer a very general search approach. GAs do not require explicit relationship between the objective function and the constraints. The value of the objective function for a set of design variables is adjusted to reflect any violation of the constraints by using penalty function approach.

Critical review of the available literature shows the complexity of the problem of the shape optimization of structures. It also reveals the need and scope for the same. The availability of the state-of-art computational gadgetry can offer tremendous thrust to this potentially wide and interesting area of research in Structural Engineering.

Genetic algorithms in structural optimization

GAs are efficient and broadly applicable global search procedures based on stochastic approach relying on the survival of the fittest strategy. Because GAs do not require gradient information they offer a very general approach of handling unsmooth or even randomly ordered data. The advantages of applying GAs for optimization of structures are the open format of constraint statements and non requirement of explicit relationship between the objective functions and constraints. The value of the objective function for a set of design variables is

adjusted to reflect any violation of constraints by using penalty function approach.

GAs operate on a population of design variable sets with each design variable set defining a potential solution is called a string. Each string is made up of a series of characters typically binary numbers, representing values of performance as defined by the objective functions and constraints.

GAs basically consist of a series of three processes. i) coding and decoding of design. ii) evaluation of fitness of each solution string. iii) application of genetic operations to evolve the next generation. The fitness of each string is evaluated by performing some type of system analysis or computation of objective function. If solution violates constraints, value of objective function is penalized. The evolution process involves reproduction operations on the Darwinian random selection and survival of the fittest strategy. Cross over operations create variations in solutions consisting parts selected from parent strings. Mutation operation introduces random changes to retain diversity in a population.

Traditional GAs are designed to work on maximization problems whereas most structural engineering problems involve minimization. Hence necessary transformations have to be done for the problem at hand to apply GAs.

Configuration optimization of parallel chord lattice girder using GA

General

Parallel chord lattices are extensively used in buildings, bridges, towers, hangers and gantries. If for instance, a cantilevered parallel chord lattice for a roof is considered and if the cells are assumed to be equal in length, for a given span and loading condition, the weight of the girder essentially depends on the depth and number of cells. A large depth and quite many cells results in reduced forces in members but the number of members themselves will be large necessitating more material consumption. At the same time too small a depth and too few cells

though leads to few members results in large member forces and hence overall weight determination of the right depth and number of cells such that the weight is the least, satisfying constraints like material stresses and deflection, is an interesting optimization problem that can be formulated and solved by GA.

Problem Description

A cantilevered parallel chord lattice girder is to be configured such that the weight is the minimum for the particulars as under. Span = 10m

All inclusive service load = 4 kN/m

Depth range permissible = 1m to 4m.

Number of cells = 3 to 11

Yield strength of steel = 250 N/mm²

Maximum deflection permissible = L/250.

Approach to Minimum Weight Design

To avoid lengthy and cumbersome process of section selection it has been assumed that all members are circular tubes with wall thickness of 5% of central diameter. Simultaneous mode of failure has been considered as the right approach to minimum weight design, wherein member dimensions have been worked out based on member forces and corresponding permissible stresses. Permissible stress in tension has been assigned as 150 N/mm² and in compression has been taken based on the popular straight line formula

$$112.5 - 0.492 \times (l/r) \text{ N/mm}^2$$

where l/r is the slenderness ratio for the member in question.

In order to eliminate too stiff a configuration, deflection has been limited to less than maximum permissible (span/250) but more than say 90% of permissible (span/275).

GA Search Details

Number of cells and depth are taken as design variables and are coded with string length 10 each. The total number of generations considered is 200. The population size is 20.

Cross over probability is 0.75.

Mutation probability is 0.005

Optimal control parameters have been chosen to guarantee good performance. Objective function to be maximized has been taken as $1/(\text{Weight} * (1 + \text{CVF}))$ where

CVF is constraint violation function which is computed as $\text{CVF} = \sum 10 * C_j$ where $C_j = G_j(X)$ if $G_j(X) \geq 0$ and 0 otherwise and $G_j(X)$ is the magnitude of violation.

Results and discussions

The application of genetic algorithms in structural optimization has been presented. The problem formulation of configuration optimization of cantilevered parallel chord lattice girder using genetic algorithms with problem statistics has been detailed in the preceding section. The problem formulated has been run and the results obtained are presented in figure 1(a) to figure 1(d). Figure 1(a) gives the improvement in the fitness as the generations evolve. Figure 1(b) shows the reduction in weight which is the merit function being minimized with evolution. Figure 1(c) clearly demonstrates the adherence of the fittest to constraints on stiffness. The best configuration evolved is shown in figure 1(d).

Results obtained very clearly demonstrate the utility of the methodology suggested in shape optimization of structures. The multi-objective problem of minimum weight design avoiding too stiff a configuration has been accomplished. It is prudent to mention here that to solve problem on hand with traditional gradient search method like sequential unconstrained minimization technique, one should begin the search from a starting feasible point. For the multi-objective problem even at the expense of a very large objective function, getting a feasible starting point is very difficult and at times may be impossible. In this context, the utility of GA attains great significance.

Conclusions

Structural optimization is a very interesting exercise. Consideration of shape as a design variable is important. Arriving at the best shape topology and member sizes is an exercise that needs tremendous amount of computational efforts. Traditional gradient search methods may not be of much use or may pose difficulties in selection of starting feasible point for search. GAs can best be used to handle such situations and the solutions obtained may be adopted as starting points in traditional search methods for future refinement.

International Engineering Symposium, March 3-5, 2011 Kumamoto Univ., Japan

References

- [1] Tzonis and Lefaire, "The Mechanical v/s Divine Body: The Rise of Modern Design Theory", Journal of the Society of Architectural Historians, 1975, Vol. 3.
- [2] Michell A.G.M, "The Limits of Economy of Materials in frame structures", Phil. Mag, 1904, S6, 8(November), No. 47, Pp. 589-597.
- [3] Richards D.M & Chan H.S.Y, "Developments in Theory of Michell Optimum Structures", AGARD report 543, 1966.
- [4] Dorn W. S et al, "Automatic Design of Optimal structures", Journal of Mechanics, 1964, Vol. 3, Pp. 25-52.
- [5] Bellman R., "Dynamic Programming", Princeton university Press, 1957.
- [6] Porter-Goff R.F.D, "Shape as a Structural Design Parameter", PhD thesis, Leicester University, 1968.
- [7] Palmer A.C, "Optimum Structure Design by Dynamic Programming", Journal of Structural engineering, ASCE, 1968, Pp. 1887-1907.
- [8] Zener C, "A Mathematical Aid in Optimizing Engineering Designs", Proc. of National Academy of Sciences, USA, 1961, Vol. 47, No.4.
- [9] Templeman A.B, "Structure Design for Minimum Cost Using the Method of Geometric Programming", Proc. of Institution of Civil Engineers, London, 1970, Vol. 46, pp. 459-472.
- [10] Tom Lassen, "Optimum Design of Three Dimensional Frame Work Structures", Journal of Structural Engineering, ASCE, 1993, Vol.119, No.3, pp. 713-727.
- [11] Zimmerman et al, "Stochastic Optimization Models for Structural Reliability Analysis", Journal of Structural Engineering, ASCE, 1993, Vol.119, No.1, Pp. 223-239.
- [12] Santiago Calatrava Valls, " Zur faltbarkeit Von Fachwerken", PhD Dissertation, Zurich: TCH, 1981.
- [13] Goldberg, D. E. and Samtani, M. P., "Engineering Optimization via Genetic Algorithms", Proc. of 9th Conf. on Electronic Computation, ASCE, New York, N. Y., 1986, 471-482.
- [14] Rajeev, S. and Krishnamoorthy, C. S., "Descrete Optimization of structures using genetic algorithms", J. of Computing in Civil Engrg., ASCE, 1992, 118 (5), 1233-1250.
- [15] Rajan, S. D., "Sizing, shape and topology design optimization of trusses using genetic algorithms", J. of Struct. Engrg. ASCE, 1995, Vol 121 (10), 1480-1487.
- [16] Rajeev, S. and Krishnamoorthy, C. S., "Genetic algorithms-based methodologies for design optimization of trusses", J. of Struct. Engrg., ASCE, 1997, 123 (3), 350-358.

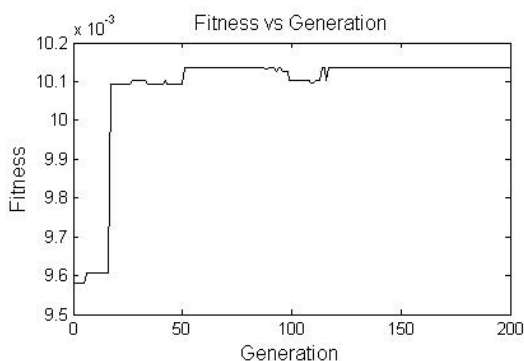


Fig. 1(a) Plot of Fitness

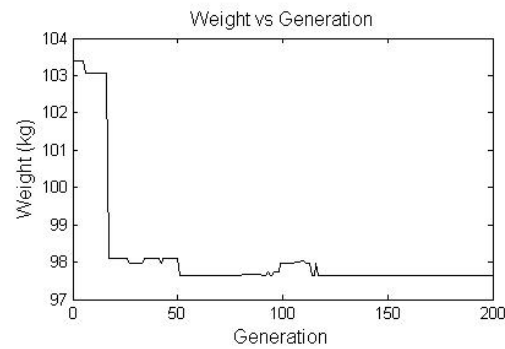


Fig. 1(b) Plot of Weight

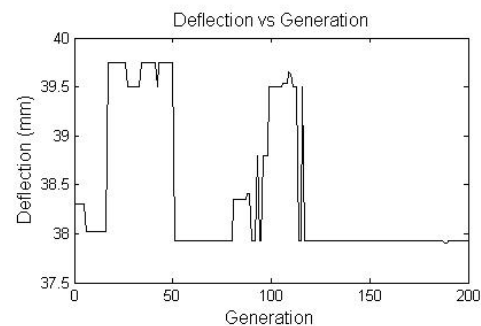


Fig. 1(c) Plot of Deflection

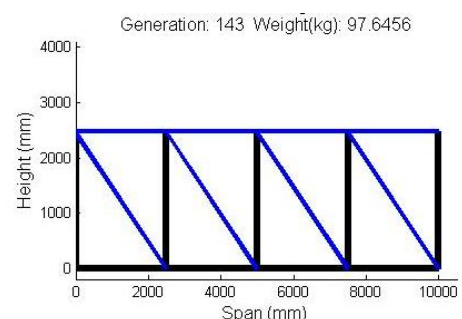


Fig. 1(d) Best Truss Configuration

PERFORMANCE APPRAISAL OF RC BEAMS USING WELDED WIRE FABRICS AS LATERAL REINFORCEMENT IN SEISMIC ZONES

H C Chinnagiri Gowda¹ K S Babu Narayan² and Katta Venkataramana³

1. *Department of Civil Engineering, Government Polytechnic, Bantwal 575211, DK district, India. email: chinnagiri_hc@yahoo.co.in*
 2. & 3 *Department of Civil Engineering, National Institute of Technology Karnataka, Surathkal, Mangalore 575025, India. email: shrilalisuta@rediffmail.com*
-

ABSTRACT: Ductility is the key to design earthquake resistant structures. More rigid the structure or the element, more it attracts inertia forces. Structures and elements of infinite rigidity are out of question. Codes of practice also advocate design philosophies wherein effects of small earthquakes are to be absorbed with little or no damage, medium with damage to such extents that rehabilitation is possible and large earthquake effects to be catered without collapse. To absorb the tremendous energies that are input to structures and elements unless ductility is ensured, performance levels proposed by codes and standard practices cannot be attained. Lateral ties hold longitudinal reinforcement of R.C. elements in place and also confine the concrete. The basis of the present work is the usage of welded wire fabrics as lateral reinforcement in RC beams. A series of beams were tested with lateral ties and welded wire fabric at discrete locations and welded wire fabric alone throughout the beam with different mesh opening sizes. This paper presents the encouraging results with marginal increase in strength and considerable improvement in ductility in addition to reduced crack widths as observed for specimens having welded wire fabric with smaller mesh openings as lateral reinforcement by confining concrete.

Key Words: *Ductility, Welded wire fabric, Cracking Pattern, Discrete locations*

INTRODUCTION

Experimental and analytical research has been done in the past to investigate confinement of concrete by reinforcement in the form of ties. It has become clear that transverse reinforcement plays an important role in confining the concrete. It is reasonable to expect that concrete confinement will be increased if concrete is in a cage. Welded Wire Fabric (WWF) appears to satisfy this requirement. Tests on reinforced concrete elements have indicated that strength and ductility of concrete in compression are significantly improved when confined by reinforcement. Concrete under high axial compression develops transverse strains. In the presence of reinforcement the core concrete applies pressure on the reinforcement, which in turn applies

reactive pressure on concrete. This improves its ability to sustain higher stresses.

Sundara Raja Iyengar, et al. (1970) have studied "Stress-Strain characteristics of concrete confined in Steel binders". Circular spirals, square spirals and stirrups have been compared for effectiveness of confinements. It has been reported that confinement is effective only when the pitch, which is less than least lateral dimension of the specimen. Among the three types of stirrups are the least effective circular spirals are the most.

Crack arrest mechanism of WWF in tension members, studied by Lee, et al. (1987), indicates better crack control is provided by WWF than by conventional reinforcement. Also such crack control is

achievable only for certain critical values of spacing of transverse wires. The mathematical models predict width and spacing of cracks in good agreements with test results. Analytical stress-strain model developed by J.B.Mander, et al. (1988) for concrete subjected to uniaxial compressive loading and confined by transverse reinforcement, demonstrates that transverse steel enhances the member strength and ductility. Confining steel of different shapes with or without supplementary cross ties for uniaxial compressive loading has been studied. A.A. Maghsoudi and Y. Sharifi (2009) have conducted experiments on beams to study effect of variation of compressive reinforcement on flexural ductility. For heavily steel reinforced HSC beams, the displacement ductility for singly reinforced beams have been found to be too close to doubly reinforced beams. Improvement of strength and ductility of reinforced concrete beams by placing helixes with different diameter as variable parameter in the compression zone has been investigated and reported by Ross Jeffry, and Muhammad N.S. Hadi (2010). Available literature indicates that research in this area is organized at times and scattered more often. A number of studies have been conducted in the area of concrete confinement with WWF. Benefits of concrete confinement by WWF can be exploited only after appreciation of behavior qualitatively and quantitatively. The present work is an attempt in this direction.

EXPERIMENTAL INVESTIGATIONS

Two span continuous beams with concentrated loads at center of span have been investigated for strength, ductility and cracking characteristics. Conventional beams have been compared with specimen were in confinement has been provided with WWF. Effects of mesh opening size on characteristics and performance appraisal of confinement in discrete (plastic hinges) locations have also been studied. Quantification of strength, ductility enhancement and response reduction factors have been presented.

Materials

Materials used in beam specimens were tested as per relevant codal provisions. The locally available river sand has been used as fine aggregate. Coarse aggregate, 20mm and down size granite metal has been used. High yield strength deformed bars Fe415 has been used for main reinforcement. The steel was tested for yield stress, and the result obtained was 478MPa, which is more than the specified value. Mild steel bars of yield stress 250MPa, designated as Fe250, have been used for shear reinforcement.

Concrete Mix

Design mix of M20 grade concrete as per IS: 10262-1982 is produced and used to cast beam specimens. The proportion of cement, fine aggregate and coarse aggregate were obtained as 1: 1.9: 3.8 and 0.55 water cement ratio is maintained throughout the work.

Test specimens

Twenty-one beams of seven series have been investigated. Three specimens in each series were cast and their designations are shown in Table 1. One series was the conventional RCC beam, other series with welded wire fabric as lateral reinforcement at discrete locations (at plastic hinge zones) with lateral ties and throughout without lateral ties. All the beams were reinforced with 2 bars of 12mm diameter in tension zone and 2 bars of 12mm diameter in compression zone. The shear reinforcement is of 6mm diameter 2 legged vertical stirrups at 200mm c/c throughout the length. The beams were loaded with point loads at the mid span A and C (Fig.1). After 28days days control cubes were tested for their strength and the results have been used to calculate theoretical strength of beams. The beams were water cured for 28days and prepared for testing.

Test Setup

The test specimens are mounted on 500kN capacity loading frame. Deflection and strain measuring devises are fixed to measure the deflections and strains at

span A and C and at support B (Fig.2). The specimens have been tested till failure and deflections and strains were recorded. During the test initial cracking load, ultimate load, crack width and crack propagations have been observed and recorded at regular intervals of loading.

RESULTS AND DISCUSSIONS

Load-displacement, moment-curvature behavior of conventional beam and confined beams with and without lateral ties have been compared. Beams confined with WWF at discrete locations and throughout with different mesh opening sizes as lateral reinforcement with and without lateral ties have been studied vis-a-vis conventional beam. Tables 2 to 5 show the results of all the series of beams. The load-deflection behavior is shown in Figure 3. The moment-curvature behavior of the beams at the mid-spans (A and C) as well as at mid-support (B) is shown in Figures 4.

Load-displacement characteristics

Theoretical strength and test strength

The effect of confining pressure provided by WWF wrap is to induce a triaxial state of stress in the concrete, which thus exhibits superior behavior in both strength and ductility than concrete under uniaxial compression. Almost all codes recommend Mander's (1988) model to evaluate the effective strength of confined concrete. The Mander's equation is given by

Ultimate load

The test ultimate load is more than theoretical ultimate load in all specimens. The increase in ultimate load is 40% for beams with WWF throughout and 15% for beams confined at discrete zones with 25.4mm square mesh over conventional beam. This is due to the presence of WWF closer spacing welded wire. Test results of all the series have been computed without considering the effect of WWF and recorded in Table 2 and 3. Theoretical strength of confined beams and unconfined beams have been computed with effective concrete strength

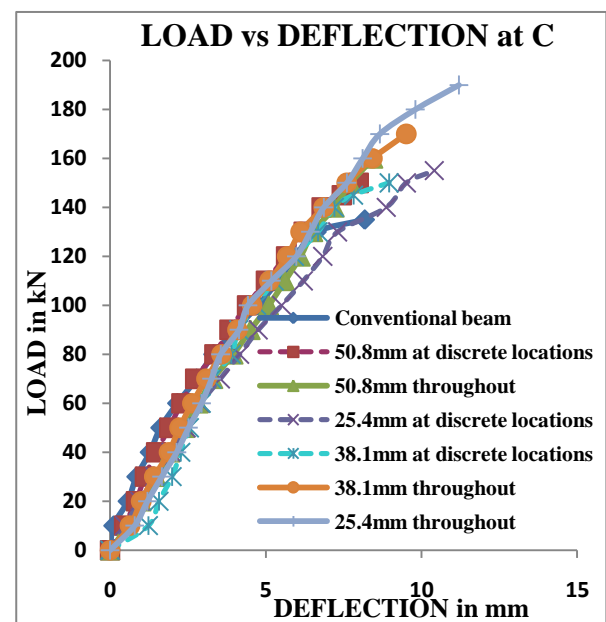
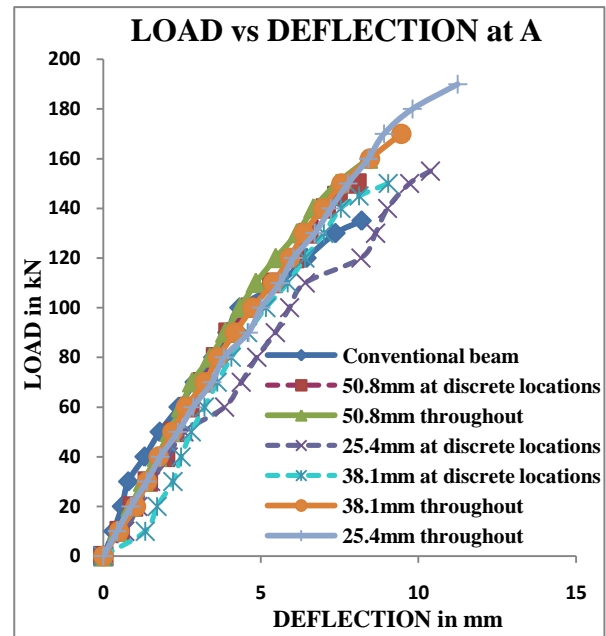


Figure 3. Load-Displacement characteristics at span A and B of conventional beam, beams confined at discrete locations with ties and throughout without ties by square mesh

considering confinement effect by Mander's equation and reported (Table 4). As seen from the results no much difference in ultimate load and ultimate moment between beams without wire mesh and effective concrete strength. Whereas without mesh and mesh with effective concrete strength of beams with

closer mesh observed to be 5% more load resisting capacity and 6.5% in beams with lateral ties and mesh at discrete locations. Moment resisting capacity in beams confined with closer mesh at discrete locations and throughout 6.5% more. Also, it is observed that, test load more in beams with closer wire mesh 30% and 7% throughout and at discrete locations respectively. Moment resisting capacity has been improved by 29% and 7% in beams confined by closer mesh throughout and at discrete zones over theoretical moment resisting capacity.

Moment-Curvature Characteristics

Cracking moment

In all the beams, observed cracking moments at support section are found to be greater than those at the mid-span section, thereby conforming to bending moment constants. The cracking moment is improved by 11% and 33% in beams confined at discrete locations and throughout respectively over conventional beam.

Ultimate moment

In all the cases first plastic hinge has formed at support subsequently hinges have formed at load point. Increase in ultimate moment for WWF with 25.4mm square mesh opening is 40% where as for beam with WWF in plastic hinge zones is 15%. The beneficial effect of improvement in strength can easily be recognized. The curvature obtained for WWF throughout the beam is 20% more than for beam at discrete location, thereby accommodating larger deformation before failure.

Ductility The ductility factors have been calculated as the ratio of ultimate curvature to curvature at first yield.

The ductility enhancement of 34% for WWF with 25.4mm square mesh opening throughout the beam and 22% for beam with WWF at discrete location has been observed. This clearly indicates that inclusion of WWF vastly improves ductility.

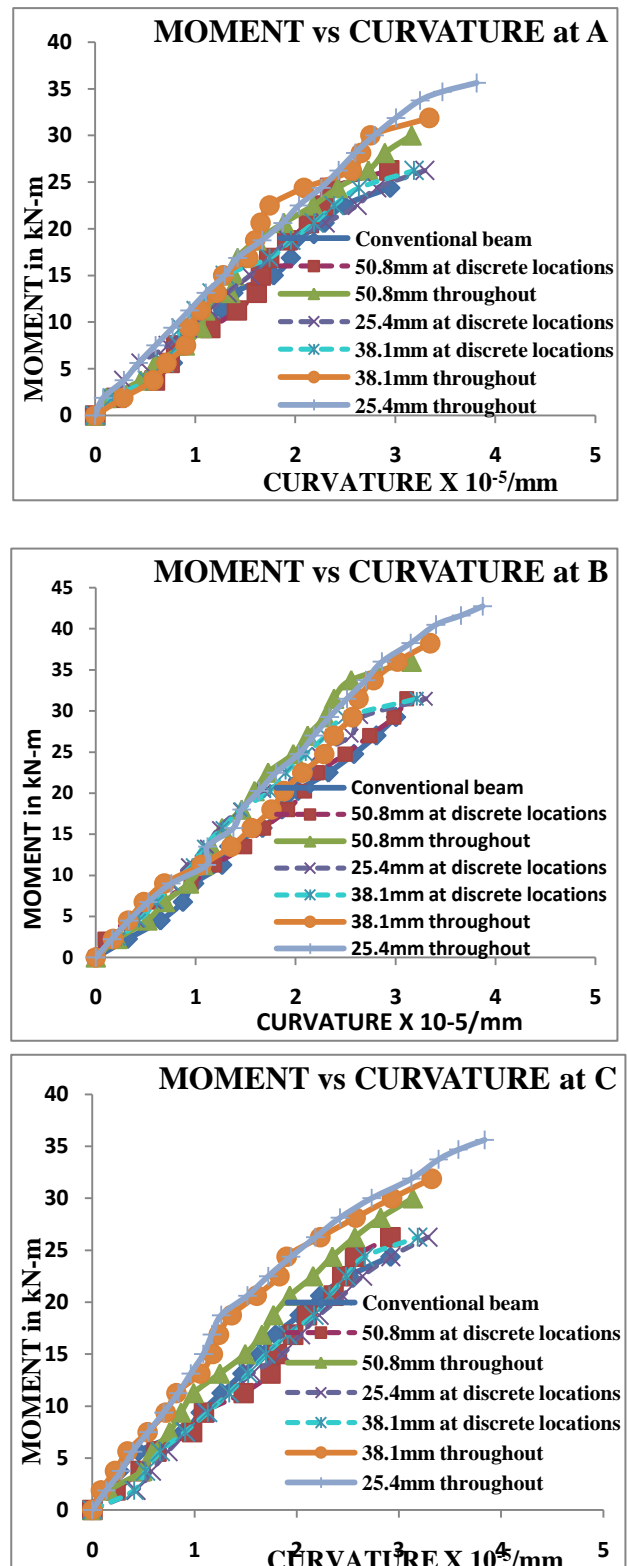


Figure 4. Moment-Curvature behavior at span A, B and C of conventional beam, beams confined at discrete locations with ties and throughout without ties by square mesh

Crack Width and Crack Pattern

The crack widths are measured with the help of crack measuring microscope. It is observed from the tests results that the beam with welded wire fabric as lateral reinforcement is effective in arresting the growth as well as propagation of cracks. This is due to the dissipation of part of the energy in destroying the bond between the WWF, thus the energy available for developing crack surface is considerably reduced. Crack patterns, width and propagation observed during the tests indicate superiority of performance in all the beams with WWF as lateral reinforcement both at discrete locations and throughout compared with conventional beam. Initial crack width observed in conventional beam is 0.2mm, whereas, it is 0.12mm in beams confined with WWF to an extent of 40% less. The maximum crack width in case of conventional beam was 0.96mm, whereas in beams with WWF as lateral reinforcement, maximum crack width was 0.52mm. The beams with WWF as lateral reinforcement both at discrete locations and throughout exhibit more number of minute cracks, which are discontinuous and more evenly distributed. The Figure 5 shows the crack patterns of beams with and without WWF throughout and at discrete locations. Welded wire fabric as lateral reinforcement aiming at the arrest of cracks resulted in a reduction of crack width in the range of 45%. This reduction in crack width is attributed to the presence of WWF as confining reinforcement. Also, it has been observed that the cracks are narrow and distributed in beams with welded wire mesh and deep, wider and isolated in conventional beams (Fig.5). Hence beams with welded wire mesh exhibited better crack arrest mechanism than conventional beams. At the ultimate load stage, the cracks in tension zone of conventional beam opened up considerably.

Response Reduction Factor (R)

As per IS 1893(Part 1): 2002 Response Reduction Factor (R) is the factor by which the actual base shear force, that would be generated if the structure were to remain

elastic during its response to Design Basis Earthquake shaking, shall be reduced to obtain the design lateral force. This characteristic represents the structures ductility, damping as well as the past seismic performance of structure with various structural framing systems. It is achieved by applying those base shears for linear design that are reduced by a factor $1/R$ from those that would be obtained from fully elastic response. Experiments and performance of structure during earthquake have shown that the structure designed for reduced force level performs adequately, if properly detailed. The value of R increases with the increase of structural ductility and its energy dissipation capacity and degree of redundancy. The factor R is assigned to different types of building structures generally on the basis of empirical or semi-empirical judgment, experience with building performance in past earthquakes, on analytical and experimental studies and on calibration with force levels in codes.

The response reduction factor may be same as ductility factor (μ) in the case of structures, with a very long period with respect to the period of the predominant frequency content of earthquake ground motion. Response reduction factor may be equal to $R = \sqrt{2\mu - 1}$. Which is applicable only, if the structure is subjected to relatively very short acceleration pulse and the input energy for linear elastic structure is the same as that for the inelastic structure. Response reduction factor is calculated from the equation $R = \sqrt{2\mu - 1}$ for all series of beams at span (A and C) and support (B) and tabulated in Table 5.

Ductility ratio is calculated from the moment-curvature characteristic plot $\Psi_u / \Psi_y = \mu$

Where Ψ_u = ultimate curvature

Ψ_y = yield curvature

And the curvature is calculated from strain profiles $(\varepsilon_t + \varepsilon_b)/d \times 10^{-5} / \text{mm}$

Where ε_t = strain at top, ε_b = strain at bottom

From the computations of ductility ratio and response reduction factor for beams of various series, it can be seen that ductility ratio and response reduction factor are more for beams confined with closer mesh spacing throughout.

CONCLUSIONS

In the light of results obtained and observations made during the present investigation, the following conclusions have been drawn. Quantification of strength and ductility enhancement, and response reduction factor are listed below.

- It is evident that strength enhancement to the tune of 40 % can be accomplished by concrete confinement in beams if such confinement is throughout the element. Confinement at discrete locations like plastic hinge zones also leads to strength gains of 15%.
- Enhancement in ductility is 22% and 34% for partial and full confinement respectively. The narrow difference suggests even partial confinement leads to substantial ductility gains.
- Response reduction factors quantified for beams indicate full confinement (3.05) is superior to partial (2.53) for exploitation of potential benefits.

REFERENCES

- [1] A.A. Maghsoudi and Y. Sharifi (2009) " Ductility of high strength concrete heavily steel reinforced members" *Journal of Scientia Iranica*, 16 (4) pp 297-309.
- [2] Chinnagirigowda H.C. (2010), PhD Thesis, Dept. of Civil Engg.,NITK-Surathkal. INDIA. *Usage potential of Welded Wire fabrics as Lateral Reinforcement in R.C. Frames and Elements in Seismic Zones*.
- [3] J.B.Mander, M.J.N.Priestly, and R.Park(1988) "Theoretical stress-strain model for confined concrete" *Journal of Structural Engineering*, ASCE No.8, 1084-1826.
- [4] Iyengar, K.T., Desayi, P and Reddy .K. (1970). "Stress-Strain characteristics of concrete confined in Steel binders" *Magazine of Concrete Research*, London, England, 22(72), 173-184.
- [5] Sami W and Tabsh S.W (2007) "Stress-strain model for high-strength concrete confined by Welded Wire Fabric. *Journal of materials in civil engineering*, ASCE, Vol.19: No.4 286-294.
- [6] Razvi,S.R, and Saatcioglu. M (1989) "Confinement of reinforced concrete columns with welded wire fabrics" *ACI Structural Journal*, 85 (5), 615-623.
- [7] Ross Jeffry, and Muhammad N.S. Hadi (2010) "The effect of confinement shapes on reinforced HSC beams" *International Journal of Computer and Information Science and Engineering* 4:2, 110-117.

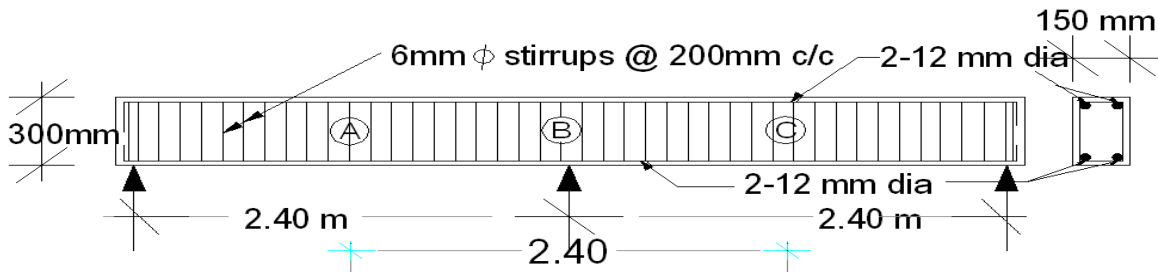


Fig. 1 Longitudinal section of test beam



Fig.2 Test Setup.

Table 1. Designations of Experimental Beam Specimens.

Specimen details		Designation
Beams with lateral ties Conventional		Series 1
Beams with lateral ties and 25.4mm Square mesh at discrete zones		Series 2
Beams with lateral ties and 38.1mm Square mesh at discrete zones		Series 3
Beams with lateral ties and 50.8mm Square mesh at discrete zones		Series 4
Beams without lateral ties and 25.4mm Square mesh throughout		Series 5
Beams without lateral ties and 38.1mm Square mesh throughout		Series 6
Beams with no lateral ties and 50.8mm Square mesh throughout		Series 7

Table 2. Comparison of Theoretical and Test Cracking Load and Cracking Moment

Beam Designation	Cube Strength in N/mm ²	Theoretical Cracking Load in kN		Test Cracking load in kN	Theoretical Cracking Moment in kN-m	Test Cracking Moment in kN-m	
		Span	Support			Span	Support
Series 1	33.8	24.42	20.35	45	5.66	8.44	10.13
Series 2	34.2	24.56	20.47	50	5.66	9.38	11.25
Series 3	29.3	22.73	18.95	50	5.66	9.38	11.25
Series 4	36.3	25.30	21.09	50	5.66	9.38	11.25
Series 5	35.6	25.06	20.88	50	5.66	9.38	11.25
Series 6	34.2	24.56	20.47	55	5.66	10.31	12.38
Series 7	43.5	27.70	23.08	60	5.66	11.25	13.5

Table 3. Test Strength of Beam without Considering the Effect of Welded Wire Fabric

Beam Designation	Cube Strength in N/mm ²	Neutral Axis depth in mm	Ultimate Moment (M_u) in kN-m	Ultimate Load (M_u) in kN	Total Load in kN	Test Load in kN	Percentage Variation
Series 1	33.80	35.543	27.16	67.91	135.82	135	-0.60
Series 2	34.20	35.127	27.19	67.96	135.93	150	10.35
Series 3	29.30	41.002	26.87	67.17	134.34	160	19.10
Series 4	36.30	33.095	27.30	68.24	136.48	155	13.57
Series 5	35.60	33.746	27.26	68.15	136.30	150	10.05
Series 6	34.20	35.127	27.19	67.96	135.93	170	25.07
Series 7	43.50	27.617	27.59	68.98	137.96	190	37.72

Table 4. Theoretical Strength of Beam with Effective Concrete Strength Considering the Confinement

Beam Designation	Without Wire Mesh			With Wire Mesh			Mesh+eff Concrete strength in kN	Test load in kN	M_u in kN-m
	M_u in kN-m	W_u in kN	Total load in kN	M_u in kN-m	W_u in kN	Total load in kN			
Series 1	27.16	67.91	135.82	27.16	67.91	135.816	135.817	135	27.0
Series 2	27.19	67.96	135.93	28.07	70.16	140.329	140.330	150	30.0
Series 3	26.87	67.17	134.34	27.73	69.31	138.629	138.630	160	32.0
Series 4	27.30	68.24	136.48	29.07	72.67	145.336	145.337	155	31.0
Series 5	27.26	68.15	136.30	28.59	71.47	142.935	142.936	150	30.0
Series 6	27.19	67.96	135.93	28.50	71.26	142.521	142.522	170	34.0
Series 7	27.59	68.98	137.96	29.41	73.52	147.031	147.032	190	38.0



Fig.5 Crack pattern of tested beams.

Table 5. Ductility Ratios and Response Reduction Factor

Beam Series	Ductility Ratio(μ)			Response Reduction Factor (R)			Average
	A	B	C	A	B	C	
Series 1	3.20	3.07	3.28	2.33	2.27	2.36	2.32
Series 2	3.63	2.09	2.98	2.50	1.78	2.23	2.17
Series 3	2.98	2.95	3.17	2.23	2.22	2.31	2.25
Series 4	2.87	2.98	2.99	2.18	2.23	2.23	2.21
Series 5	3.71	3.31	2.82	2.53	2.37	2.15	2.35
Series 6	3.67	2.48	4.05	2.52	1.99	2.66	2.39
Series 7	4.06	5.16	3.52	2.67	3.05	2.46	2.73

GROUND RESPONSE AT KANDLA PORT REGION DURING THE 2001 BHUJ EARTHQUAKE – A CASE STUDY

L.GOVINDARAJU¹ and SANTOSHKUMAR PATIL²

*1 Department of Civil Engineering, Bangalore University, Bangalore, India.
e-mail:lgr_civil@yahoo.com*

*2 Department of Civil Engineering, Bangalore University, Bangalore, India.
e-mail:santosh.ctpl@gmail.com*

Abstract: This paper presents a case study on the evaluation of ground response at Kandla port area. In this region no strong motion records are available and therefore synthetic earthquakes are developed taking in to account the site conditions. Dynamic ground response analyses have been carried out to estimate the site amplifications and to develop ground surface response spectra. The potential for liquefaction of sandy soils and cyclic failure of clayey soils in the region have been evaluated. Further, analyses have been carried out to estimate the post liquefaction settlement of soil deposits. The results of the study revealed the liquefaction of the deep sandy soil strata below the clay layer and excessive settlement of the ground in the port area. These findings are in close agreement with the field observations after the 2001 Bhuj earthquake.

Keywords: Amplification, Cyclic failure, Liquefaction, Synthetic earthquakes, Response spectra

Introduction

It has been well recognized that earthquake ground surface amplification and response spectra are affected by earthquake source conditions, source-to-site wave propagation path and site conditions. The site conditions include the rock properties beneath the site, the local soil conditions at the site above bedrock to ground surface and the topography of the site. The local soil conditions play a dominant role on the ground surface response parameters. It was demonstrated by dramatic differences in ground motions in different parts of Mexico City in the 1985 Mexico earthquake. Very significant amplifications of peak ground accelerations (PGA) for soil depths of 30m to 40m were observed. However, much smaller amplifications for soil depths exceeding about 50m were noticed. At locations of the City where higher PGA values were noticed, the heaviest earthquake damages were observed (Isam G Jardaneh, 2004). This paper sets out to demonstrate a case

study of damages to many structures in Kandla Port area in Gujarat state due to ground motion parameters at the surface and liquefaction induced ground settlements.

The earthquake

The Bhuj earthquake that struck the Kutch region in Gujarat with a magnitude of $M_w=7.7$ at 8.46 A.M. (IST) on January 26, 2001 was one of the most damaging earthquake in India in the last 50 years. The epicenter of the earthquake was located at 23.4° N, 70.28° E and at a depth of about 25 km. This quake has caused significant damage to life and property in a large area. Earthquake Spectra (EERI, 2002) can be referred for the detailed information about the earthquake and the associated damages.

Kandla Port Region

Gujarat state has 41 ports. These include one major port (Kandla), 11 intermediate ports (including Navlakhi and Adani) and 29 minor ports. Kandla

and Navlakhi ports are located at 50 km from the Bhuj earthquake epicenter and the port of Adani is about 90 km away. Fig. 1 shows the location of these ports and epicenter of the earthquake. Kandla Port is ranked as the sixth major port in India and plays a major role in Indian international trade. It is well connected with other major cities and industrial centres by national highway and railway systems. The Port of Kandla covers an area of 1.163 km² and extends over 7.5 km of coastline.

Damage to the port was confined to a few buildings, warehouses, and cargo berths. The most extensive damage occurred to five dry cargo berths built prior to 1955. After the earthquake, most of the 2300 hollow reinforced concrete (RC) piles supporting these berths exhibited cracks close to the pile caps. Two oil jetties were seriously damaged and one partially damaged. Three warehouses with heavy roof structures were damaged. As a result of soil liquefaction and permanent ground deformation, the six-story Port and Customs Office tower tilted, the ground floor of the two-story building adjacent to the tower collapsed, a small nearby building settled, and the RC columns of the berthing jetty for port craft cracked at their deck joints due to bending. The open ground in the port settled uniformly, was littered with a few sand boils, and slightly deformed laterally along some unsupported waterfront sections (EERI, 2002).

Characteristics of Site conditions

The Port of Kandla is built on natural ground comprising recent unconsolidated deposits of interbedded clays, silts and sands. The vertical profile of the region slopes downwards in the easterly direction towards the coast line at about 12.5 m per kilometer. The water table is about 1.2 m to 3.0 m below the ground. Geotechnical characteristics of the ground at Kandla Port area are presented in EERI (2002). The typical borehole profiles in Kandla Port area are presented in Fig. 2 to 5.

Fig.2 Soil Profile near Port and Custom Office Tower close to Berths I-V

(site-1)The soil profile suggests that the upper soil layers consist of 5 to 10 m thick deposits of soft silty clay underlain by sand and hard clay minerals. The lower soil layers consist of yellowish-brown fine and coarse sand, reddish-brown hard silty clay with gypsum, and yellowish-brown dense clayey sand. The upper soil layers have liquid and plastic limits representative of highly plastic clays and have in-situ water content in the range of 42 % to 47%. The soft silty clay has liquid limit in the range of 62 to 68% and plastic limit between 26 to 28 % with undrained shear strength of 10 kPa (measured from vane shear tests). However, hard clayey soil has liquid limit in the range of 54% to 77% and plastic limit between 39% and 64% with undrained strength of 100 kPa. The in-situ water content of hard clay varies from 18% to 27%. The Standard Penetration Test (SPT) 'N' values (after correction) for upper sandy layers is less than 15 while the underlying deep sandy layers have SPT values of less than 50. The insitu moisture content of these sandy layers varies from 10% to 12.5%. The blow counts ($N = 15$ to 50) of the sandy layers with fines content between 1% and 32% indicate that the soils are potentially liquefiable under strong and sustained shaking (for details, see Dash et al., 2009).

Ground response studies

The ground response studies enable to compute acceleration time histories at the top of each of the soil layers as well as on the ground surface, amplification rating and response spectra at each site. The methodology adopted in the present study involves (a) Selection of Peak Ground Acceleration (PGA) at bed rock level to represent the seismic hazard (b) Development of synthetic ground motions so as to match the target code-specified response spectrum of the site (c) Ground response analysis for different sites in the study area.

a)Selection of peak ground acceleration (PGA)

Based on structural response records (SRR) a maximum acceleration of 0.33g at the ground surface has been estimated in the Port of Kandla (for

details see EERI, 2002). Hence in this study the same value of PGA has been considered for the seismic response analysis.

b)Development of synthetic earthquake motion

Presently, there are no records of strong ground motion in the study area and therefore there is a need for the development of synthetic earthquakes for the region. The usual practice is to generate synthetic earthquake motion based on the knowledge of earthquake source mechanisms, path effects and recorded motion at the point of interest. This approach is of great importance, especially in the regions where ground motion records of engineering interest are totally absent.

In this study a wavelet-based method has been used for the generation of spectrum-compatible time-history of earthquake. The wavelet-based procedure uses the decomposition of recorded accelerogram in to desired number of time-histories with non-overlapping frequency contents, and then each of the time-history has been suitably scaled for matching the response spectrum of the revised accelerogram with the specified design spectrum suggested by the code of practice. RSPMatch2005 is one such wavelet-based method developed by Lilhanand and Tseng (1987, 1988). The original computer code was written by Abrahamson (1993) and subsequently updated by Jonathan Hancock et al.(2006).

Synthetic earthquakes for Kandla Port region have been developed using RSPMatch2005. As a basic step, the methodology requires the use of strong motion records available from historical earthquakes. While selecting a suitable strong motion, several important factors are considered. These include similar magnitude, peak ground acceleration close to the target value, similar fault distance and similar site conditions (Kramer, 1996).Based on these factors, three earthquakes of magnitude (M_w) in the range of 6.5 to 7.7 recorded at soft soil sites as per IS: 1893-2002 were

selected from the earthquake data base. Table 1 illustrates three earthquake records and their characteristics obtained from the database compiled by the Pacific Earthquake Engineering Research Center (PEER), University of California at Berkeley. Fig. 6 (a) to 6 (c) shows the time history of selected strong motions.

The response spectrum of selected earthquake motions before and after matching the target spectra are shown in Fig. 7 to 9. Figs. 10 (a) to 10 (c) show the spectral matched time history of accelerations. The peak accelerations (a_{max}) of spectral matched records have been indicated in these Fig. for respective strong motions. These accelerations correspond to ground surface motions. Therefore, in order to conduct site response analysis, the ground motions from the surface were deconvoluted at respective soil site and the required input motions at the bottom of soil profiles were obtained. These input motions were then utilized to evaluate the amplification and response spectra at the ground surface for various soil sites.

Site response analysis

One dimensional seismic site response analysis has been carried out based on equivalent linear approach using the computer program SHAKE2000. The input parameter for the model such as shear wave velocity of each soil layer has been obtained from the empirical relation between SPT 'N' value and shear wave velocity as proposed by Japanese Road Association (Shannon Hsien-Heng Lee, 1992). To account for soil behaviour under irregular cyclic loading, the dynamic properties of soils such as modulus reduction and damping versus shear strain curves proposed by Vucetic and Dobry (1991) are used based on plasticity characteristics of respective soil layers in soil profiles 1 to 4.

The results of the site response analysis using spectrum compatible time histories developed from three strong motion records are presented below.

Amplification of ground motion parameters

The maximum amplification of ground motion parameters considering three spectrum compatible input motions for soil site-1 at 5% damping is shown in Fig. 11. As observed from this Fig., a maximum amplification ratio (A) of 4.73 can be noticed corresponding to the frequency (f) of 1.06 Hz. Similarly, amplification ratios of 5.26, 3.61 and 5.16 can be noticed at frequencies of 1.17, 2.34 and 1.99 for site-2, site-3 and site-4 locations respectively.

Response Spectra

Fig. 12 shows the variation of spectral acceleration (S_a) with period (T) corresponding to 5% damping for site-1 based on three earthquake excitations. Also shown in this Fig. the variation of average spectral acceleration based on three events. A maximum spectral acceleration of 1.28g at a period of 0.84s can be observed at this site-1. Similarly, maximum spectral accelerations of 1.43, 1.86 and 1.93 can be noticed at site-2, site-3 and site-4. The higher values of spectral accelerations at site-3 and site-4 indicate the magnification of accelerations due to unconsolidated very soft sediments at these sites when compared to site-1 and site-2.

Liquefaction of sandy soils and cyclic failure of clayey soils

In the present study, the potential for liquefaction of sandy soils has been evaluated based on the method recommended by Idriss and Boulanger (2004). Further, cyclic failure in clays has been evaluated based on the new procedure proposed by (Boulanger and Idriss, 2005). The proposed methods are semi-empirical in nature. The method is based on two essential components: (a) Back-analyzing past case histories; (b) Use of plasticity index (PI) to represent the soil behaviour in to "sand-like" ($PI < 7$) and "clay-like" ($PI > 7$). Soils exhibiting "sand-like" behaviour have been evaluated using SPT methodology and that the term "liquefaction" is reserved for these types of soils. Further, soils exhibiting "clay-like" behaviour have been evaluated using the

procedures appropriate for clays, and the term "cyclic failure" is used to describe the failure in these types of soils.

The results of the analysis for the liquefaction potential and cyclic failure with depth at different sites are presented in Fig. 13 to Fig.16. It is evident from these results that most of the clay stratum except the top 2 to 3m undergoes cyclic failure resulting in ground deformation and cracking. This might have developed uniform settlement and littering with sand boils at open ground in the Port area. Furthermore, the sand stratum ranging from depths of 8m to 22 m is likely to have experienced liquefaction resulting in settlement and flow failure.

Settlement of ground at port area

In this study, two kinds of analysis have been carried out to estimate the total settlement of the soil deposits in the Port of Kandla. The first analysis (Method-1) is based on the approach suggested by Tokimatsu and Seed (1987). The method provides an estimate of post liquefaction volumetric strain in saturated sands from cyclic stress ratio 'CSR_{M=7.5}' and standard penetration resistance '(N₁)₆₀'. The settlement of each layer is given by the product of the volumetric strain in each layer and the layer thickness. The second analysis (Method-2) is based on the approach suggested by Ishihara and Yoshimine (1992). This approach provides an estimate of post liquefaction volumetric strain as a function of either the factor of safety against liquefaction or the maximum cyclic shear strain and the relative density or SPT resistance. Table 2 illustrates the settlement analysis for each site in the Port area. Both methods yield almost similar values of total settlement at respective sites in the port area. These results are in close agreement with the observed settlements at several locations soon after the earthquake.

Conclusions

Dynamic ground response analysis of soil deposits for the Port of Kandla is carried out. Spectrum compatible time

International Engineering Symposium, March 3-5, 2011 Kumamoto Univ., Japan

histories of accelerations based on the available peak ground acceleration at the surface were developed and deconvoluted. One dimensional site response analysis was carried out using deconvoluted ground motions. From the results of the study the following conclusions are drawn.

- The soft deposits in port of Kandla have tendency to increase the amplification of ground motion parameters in the range of 3.61 to 5.26.
- The maximum spectral acceleration at four locations in the region varies in the range of 1.28g to 1.93g.
- A greater depth of soft clay stratum except the top 2 to 3m undergoes cyclic failure resulting in ground deformation and cracking.
- Furthermore, the sand stratum between the depths of about 8m to 22 m is likely to have experienced liquefaction resulting in settlement of many structures in the Port area.

References

- [1]Abrahamson, N. A. (1992), Non-stationary spectral matching, Seismological Research Letters, 63(1), 30.
- [2] Boulanger, R.W. and Idriss, I.M. (2005), New criteria for distinguishing between silts and clays that are susceptible to liquefaction versus cyclic failure". Proceedings, Technologies to Enhance Dam Safety and the Environment, 25th Annual United States Society on Dams Conference, USSD, Denver, Co, 357-366.
- [3]Dash S R, Govindaraju L, Bhattacharya S. (2009), A case study of damages of the Kandla Port and Customs Office tower supported on a mat-pile foundation in liquefied soils under the 2001 Bhuj earthquake. Soil Dynamics and Earthquake Engineering, Volume 29(2), 333-346.
- [4]EERI (2002), Bhuj, India Earthquake Reconnaissance Report, Supplement A to volume No. 18, Earthquake Spectra, Journal of Earthquake Engineering Research Institute.
- [5] Idriss, I.M. and Boulanger, R.W, (2004), "Semi-empirical procedures for evaluating liquefaction potential during earthquakes", Proceedings, 11th International Conference on Soil Dynamics and Earthquake Engineering, Vol.1, 32-56.
- [6]IS 1893 - Part 1 (2002), Criteria for earthquake resistant design of structures, Bureau of Indian Standards, New Delhi, India.
- [7]Isam G Jardaneh (2004), Evaluation of ground response due to earthquakes-case study, Journal of Applied sciences, 4(3), 364-368.

[8]Ishihara K and Yoshimine M (1992), Evaluation of settlement in sand deposits following liquefaction during earthquakes. Soils and Foundations, 32 (1), 173-188.

[9]Jonathan Hancock, Jennie Watson-Lamprey, Norman A. Abrahamson, Julian J. Bommer, Alexandros Markatis, Emma Mccoy and Rishmila Mendis (2006), An improved method of matching response spectra of recorded earthquake ground motion using wavelets, Journal of Earthquake Engineering, Vol. 10, Special Issue 1, 67-89.

[10] Kramer, S.L. (1996), Geotechnical Earthquake Engineering, Pearson Education Inc.

[11]Lilhanand, K. and Tseng, W. S. (1987), Generation of synthetic time histories compatible with multiple-damping design response spectra, Transactions of the 9th International Conference on Structural Mechanics in Reactor Technology, Lausanne, K1, 105-110.

[12]Lilhanand, K. and Tseng, W. S. (1988), Development and application of realistic earthquake of the 9th World Conference on Earthquake Engineering, Tokyo Japan, II, 819-824.

[13]Shannon Hsien-Heng Lee (1992) Analysis of the multicollinearity of regression equations of shear wave velocities. Soils and Foundations, 32: 205 – 214.

[14]Tokimatsu, K. and Seed, H.B. (1987), Evaluation of settlements in sand due to earthquake shaking, Journal of Geotechnical Engineering, ASCE, Vol.23, No.4, 56-74

[15]Vucetic, M. and Dobry, R. (1991) , Effect of soil plasticity on cyclic response. Journal of Geotechnical Engineering, ASCE, Vol. 117, 1: 89-107.

Table 1 Characteristics of selected earthquake records

	Date	Magnitude (Mw)	PGA (g)
Imperial Valley	15/8/79	6.5	0.359
Northridge	17/1/94	6.7	0.325
Kocaeli	17/8/99	7.4	0.349

Table 2 Settlement analysis

Site	Total Settlement (m)	
	Method-1	Method-2
Site-1	0.311	0.373
Site-2	0.23	0.27
Site-3	0.124	0.153
Site-4	No Liquefaction	No Liquefaction

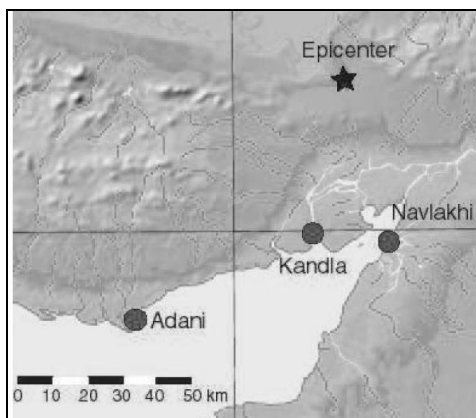


Fig.1 Location of Kandla Port (EERI, 2002)

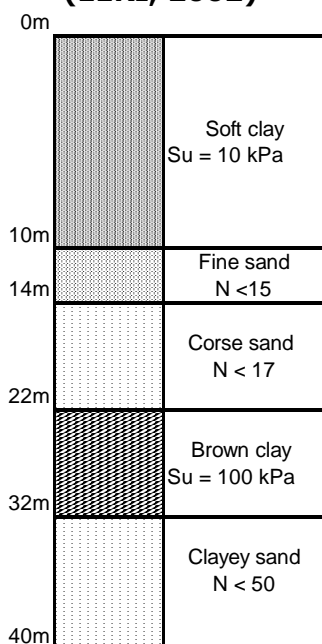


Fig.2 Soil Profile near Port and Custom Office Tower close to Berths I-V (site-1)

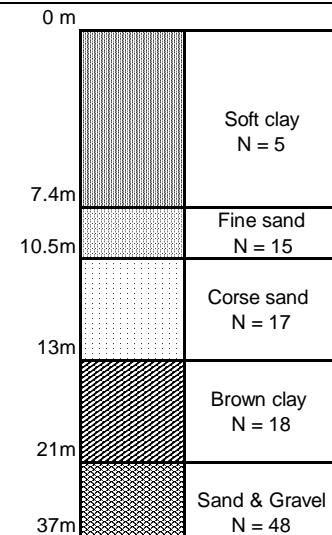


Fig.3 Soil Profile near transit shed and parking place of Berth-III (site-2)

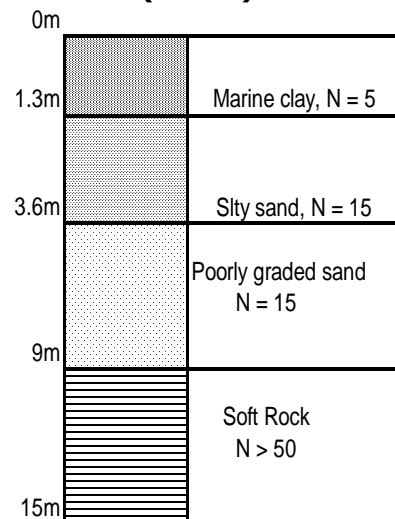


Fig.4 Soil Profile near pile supported wharf situated in the south side of the Port (site-3)

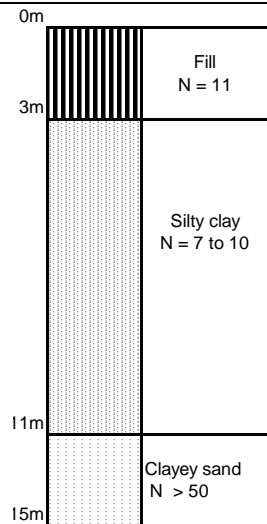
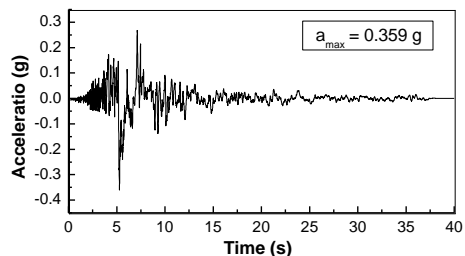
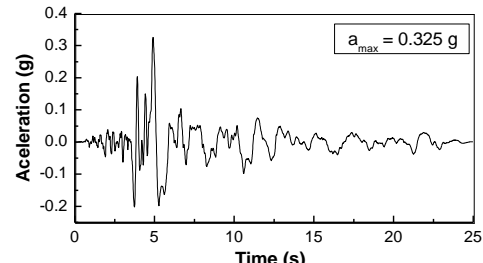


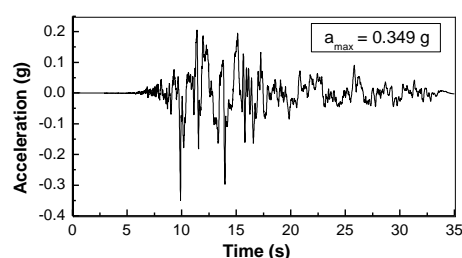
Fig.5 Soil Profile pile near pile supported wharf around kandla Port (site-4)



(a) Acceleration time history of Imperial Valley earthquake



(b) Acceleration time history of Northridge earthquake



(c) Acceleration time history of Kocaeli earthquake

Fig. 6 (a) to (c) Time history of selected strong motion records

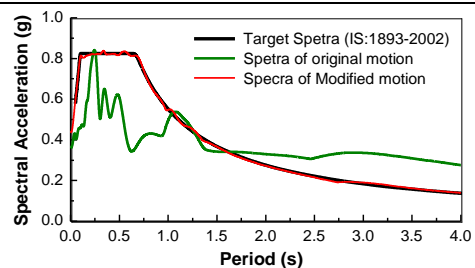


Fig.7 Comparison of target and response spectrum of Imperial Valley earthquake time history

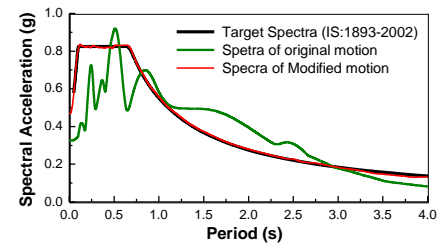


Fig.8 Comparison of target and response spectrum of Northridge earthquake time history

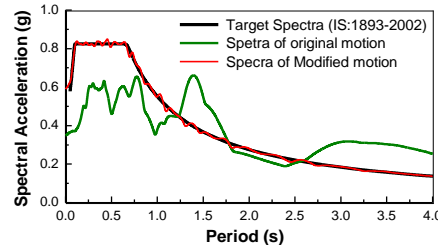
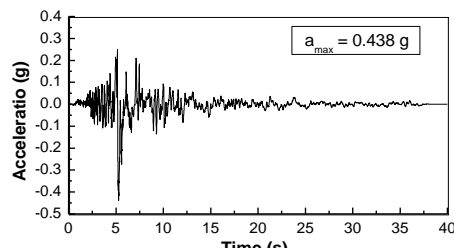
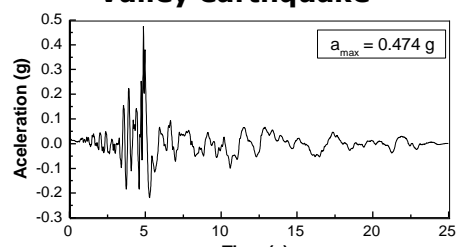


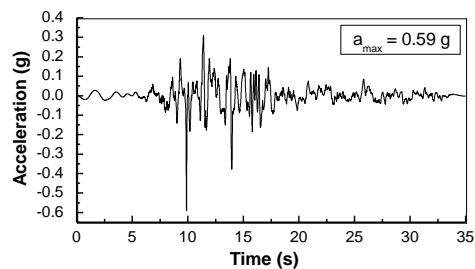
Fig.9 Comparison of target and response spectrum of Kocaeli earthquake time history



(a) Spectrum compatible acceleration time history of Imperial Valley earthquake



(b) Spectrum compatible acceleration time history of Northridge earthquake



(c) Spectrum compatible acceleration time history of Kocaeli earthquake

Fig.10 (a) to (c) Spectral matched time history of accelerations for three earthquakes

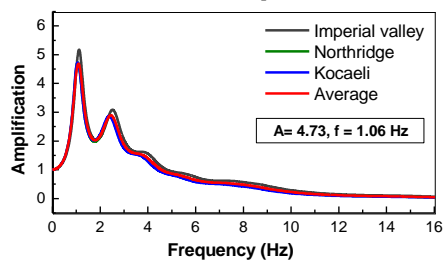


Fig. 11 Amplification at site-1

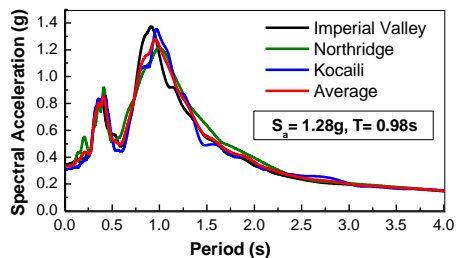


Fig.12 Spectral accelerations at ground surface for site-1

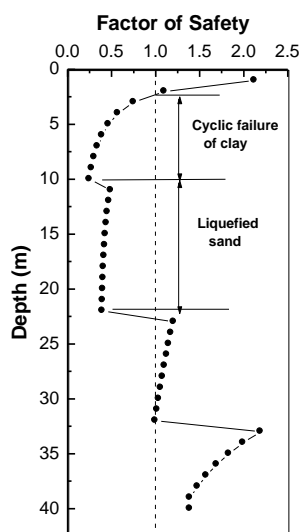


Fig.13 Zone of occurrence of liquefaction and cyclic failure at site-1

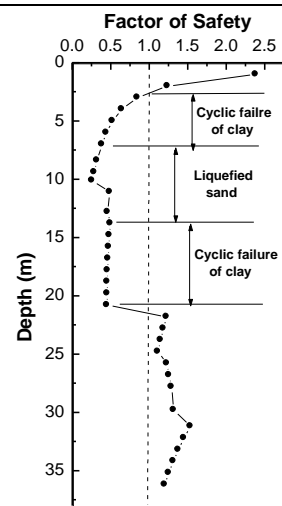


Fig.14 Zone of occurrence of liquefaction and cyclic failure at site-2

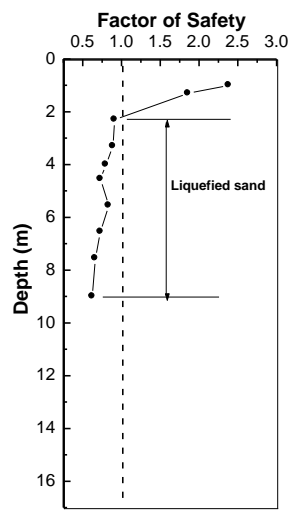


Fig.15 Zone of occurrence of liquefaction and cyclic failure at site-3

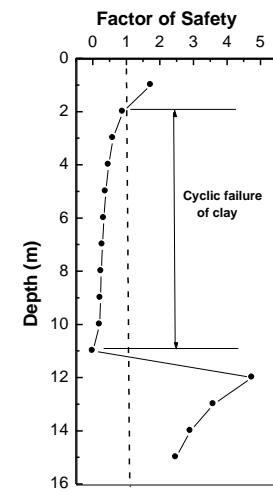


Fig.16 Zone of occurrence of cyclic failure at site-4

Weibull Analysis of Acoustic Emission Hits Behaviour for Evaluation of Deteriorated Concrete due to Freezing and Thawing

NI NYOMAN KENCANAWATI^{1,2} and MITSUHIRO SHIGEISHI¹

- ¹ Graduate School Science and Technology, Kumamoto University, Kurokami, 2-39-1, Kumamoto 860-8555, Japan. e-mail:087d9412@st.kumamoto-u.ac.jp, shigeishi@civil.kumamoto-u.ac.jp
² Department of Civil Engineering, Mataram University, Jl. Majapahit No.62 Mataram, West Nusa Tenggara, 83125, Indonesia
-

Abstract: Acoustic Emission (AE) is a non destructive testing technique which is able to evaluate the damage on material such as concrete. In this research, Weibull analysis of AE hits distribution is proposed to evaluate the deterioration on concrete sample due to freezing and thawing. Concrete samples were experienced to zero and 90 freezing-thawing cycles with the temperature range between +10°C and -20 °C. Concrete compressive strength was also measured to study the deterioration level of the damaged concrete. The results of Weibull analysis of AE hits distribution shows the good agreement with the compressive strength, indicating that concrete is heavily deteriorated and much lower reliability compared to that of sound (zero freezing-thawing cycle) concrete. Furthermore, Weibull analysis of AE hits distribution can be utilized as a parameter to show the reliability of deteriorated concrete.

Keywords: AE, Weibull analysis, deteriorated concrete, freezing-thawing

Introduction

Acoustic emission (AE) is phenomenon of rapid released energy due to fracture, crack or damage in a material, as it can produce elastic waves, which propagate inside a material and are detected by AE sensor usually attached at the surface of a material such as concrete (Ohtsu, 2008). AE technique is an effective non destructive testing on material such as concrete. This method is often applied to evaluate the concrete deterioration (Suzuki et. all, 2009 and Kencanawati and Shigeishi, 2010). In this research AE technique is employed to study about deteriorated concrete due to freezing and thawing.

Freezing and thawing is a natural phenomenon which enables to decrease concrete durability. The mechanism of frost damage on concrete material can be explained as follow. When concrete is exposed to moisture, water moves through

the concrete in pores. When the temperature drops below freezing, the water turns to ice. Ice occupies 9 percent more volume than water. The expanding ice forces the water through the capillaries as it freezes. The repeated freezing and thawing can damage concrete and deterioration is increased. In addition, unfrozen water is attracted to the ice crystals during periods of freezing. This causes the slow growth of the crystals (ice accretion), which in turn increases the internal stresses developed (Newman and Choo, 2003).

AE activities of both sound and freeze-thawed concrete were measured during compression load test. Furthermore, a Weibull analysis of AE event distribution was applied to evaluate the reliability of deteriorated damaged concrete. Then the results were compared to the other effect of freeze-thawing such as compressive strength of concrete and AE hits generation behavior.

Acoustic Emission Parameter Analysis

AE is a phenomenon of a rapid released energy due to a fracture, crack or damage in a material which produces elastic waves that propagate inside a material. These waves are detectable by an AE sensor usually attached to the material surface (Ohtsu, 2008). AE parameters have been applied to evaluate the deteriorated concrete due to carbonation (Kencanawati and Shigeishi, 2010). AE parameter used in this research is AE hits which is briefly explained below.

AE hits

AE hit is defined as a signal that exceeds a threshold level and can cause the system to accumulate the data (Shiotani, 2008). It is frequently applied to show AE activity with a counted number over a period or rate of time. Fig.1 shows one waveform corresponds to one AE hit.

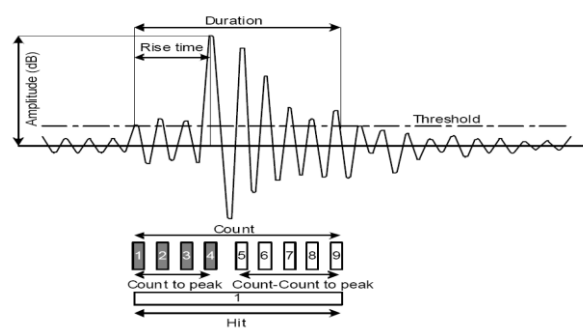


Fig.1 AE hits definition (Shiotani, 2008)

Weibull Distribution Analysis

Weibull distribution is a probability modeling of failure in a material or in a product (Rinne and Alghuwainem, 2003). The failure rate is described using equation (1). We propose this function be applied to AE activity behavior.

$$F(x) = 1 - e^{-\left(\frac{x}{\alpha}\right)^m} \quad (1)$$

where, x is stress level (%), $F(x)$ is cumulative number of AE hits at the x stress level, m is Weibull shape parameter, and α is Weibull scale parameter.

Taking twice logarithms on both sides, the equation (1) becomes,

$$\log \left[\log n \left(\frac{1}{1-F(x)} \right) \right] = m \log x - m \log \alpha \quad (2)$$

and m becomes the slope of the line which indicates class of failure. Generally, when m parameter becomes lower than one, means infant mortality occurs, m parameter equals to 1 means random failures, and m parameter is higher than 1 indicates wear out failures.

We propose this function to be correlated to AE concrete behavior according to the stress level during loading test as explained by Fig. 2. If the scale of two graphs are converted into Weibull distribution graph, the m value lower than 1 is obtained on graph A, indicating high AE generation occurs at a low stress level. In contrast, in case B, the m parameter is greater than 1, indicating low initial AE generation leading to fracture occurrence near maximum stress level.

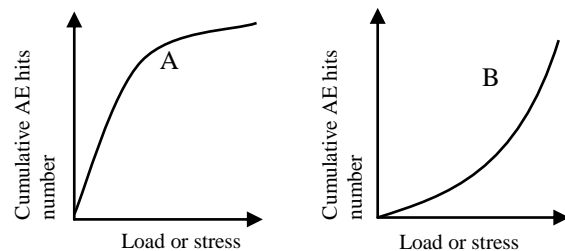


Fig.2 Two cases of AE generation behaviour

Experiment

Material

Aggregate properties used in this research and mixture proportion of the concrete are shown in Table 1 and Table 2 respectively. Ordinary Portland was used and the maximum size of coarse aggregate was 20 mm. The water-to-cement ratio by weight was kept as 50%. Specimens were cylindrical 100 mm in diameter and 200 mm in height.

Table 1 Aggregate properties

Properties	Aggregate	
	Coarse	Fine
Density (g/cm ³)	2.95	2.565
Absorption ratio(%)	0.59	3.25
Finess modulus	6.52	2.28

Table 2 Concrete mixture proportion

W/C (%)	s/a (%)	Weight per unit volume (kg/m ³)				AE-WR agent
		W	C	S	G	
55	46	175	318	818	1106	1272

W/C: water-to-cement ratio; s/a: volume of fine aggregate to total aggregate; W: water; C: cement; S: sand; G: gravel; AE: air entraining; and WR: water reducing.

Method of Testing

Freezing and thawing exposure

After curing time of 28 days, concrete specimens were put into freezing-thawing case to be exposed by freezing and thawing cycle. Concrete samples were exposed to Concrete samples were experienced to 90 freezing-thawing cycles with the temperature range between +10°C and -20 °C. During exposure, concrete specimens were immersed in non-freezing solution. Concrete specimens without exposure to freezing-thawing cycle were also prepared to compare the properties of freeze-thawed concrete.

Compression testing

AE measurement was performed during uni-axial compression test of concrete specimens. The setup for concrete testing is illustrated in Fig.3. Two wide-band UT 1000 type AE sensors were attached to the concrete sample surfaces. AE signals were amplified by 40 dB. Threshold level was set at 40 dB. AE measurement was based on Mistras system from PAC. Concrete samples were loaded from zero until failure.

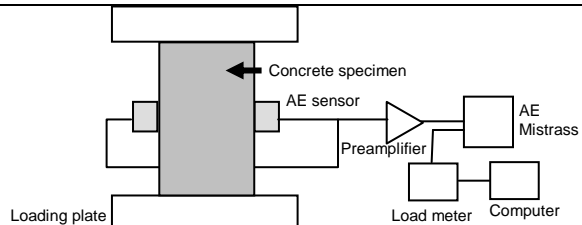


Fig.3 Compression test and AE measurement

Results and Discussion

Compressive Strength

The average value of concrete compressive strength for deteriorated concrete due to freezing-thawing is shown in Table 3. As comparison, the average compressive strength of sound concrete is also shown. It is clearly understood that the compressive strength of concrete has experienced degradation after being exposed by 90 cycle freezing-thawing process. The compressive strength has been deteriorated around 50.3%. It was observed that freezing and thawing cycles damage the cement paste, meanwhile aggregate is left undamaged. The ice formation is initiated in pores and water is forced out. If the water flow is limited, hydraulic pressure is generated within the solid matrix. This pressure damages the cement paste and the repeated process make it weakens. Thus, concrete experiences decreasing of compressive strength.

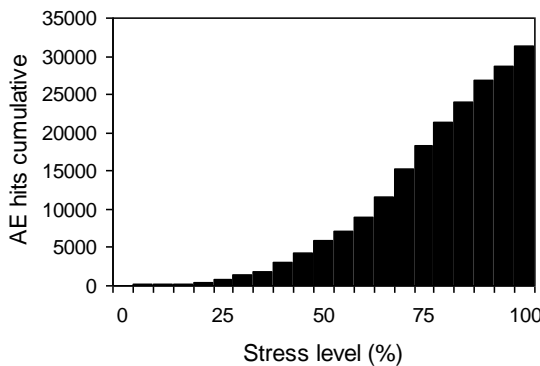
Table 3 Concrete compressive strength

Concrete Specimen	Compressive strength (MPa)
Freeze-thawed	24.7
Sound	49.2

AE hits

Fig.4 shows the relationship between AE hits and stress level during compression loading from deteriorated and sound concrete. In sound concrete, AE hits increases rapidly only around 75% of final stress level. It is generally observed in a new concrete sample. Otherwise, in

deteriorated concrete, AE activity was observed earlier around 30% of stress level and then increases significantly until final stress. Detection of AE activity since lower stress level indicates that concrete has experienced deterioration due to freezing and thawing cycles.



(a) Deteriorated concrete

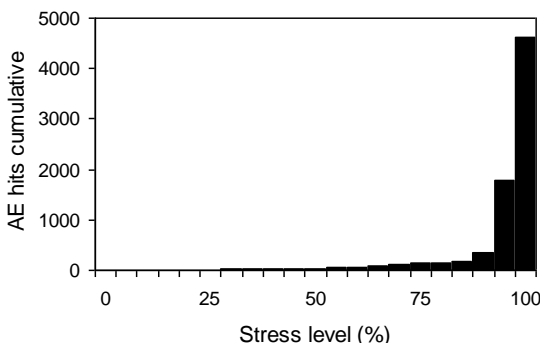


Fig.4 Relationship between AE hits and stress level

Weibull analysis

Fig.5 illustrates Weibull distribution of AE hits behavior according to stress level for both deteriorated and sound concrete. Sound concrete sample has m parameter of 7.0935. Meanwhile, the deteriorated concrete sample shows decreasing of m parameter which is 4.1066. This value is lower 42.1% than that of sound concrete. It can be concluded that the reliability of concrete is decreasing after being exposed by 90 cycles freezing-thawing process.

Furthermore, the result of Weibull analysis of AE activity according to the stress level under compression load shows good

agreement with compressive strength and AE hits behavior. All indicate that the compressive strength, failure process and reliability of freeze-thawed concrete have been deteriorated. It also suggests that the evaluation of reliability of concrete during compression loading can be done successfully using Weibull analysis of AE activity behavior according to stress level under compression load.

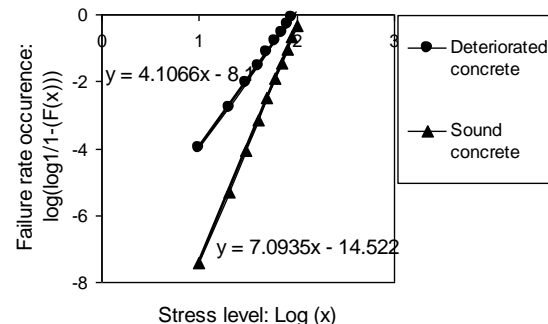


Fig.5 Weibull analysis of AE hits according to stress level

Conclusions

This research studies about damaged concrete using AE technique. The deterioration is due to freezing-thawing. 90-cycle freezing-thawing with the temperature range between +10°C and -20°C was exposed to the concrete. A Weibull analysis is proposed to be applied to AE activity behaviour according to stress level under compression load. The aim is to evaluate the reliability of deteriorated concrete. The sound concrete was also prepared to evaluate the damage level of concrete.

Compressive strength of concrete decreased from 49.2 MPa to 24.7 MPa after exposed by 90 freezing-thawing cycles. In addition, the detection of AE activity since lower stress level (around 30%) indicates that concrete has experienced significant deterioration due to freezing and thawing cycles. According to Weibull analysis the reliability of damaged concrete is 42% lower than that of sound concrete.

The results of Weibull analysis of AE activity according to the stress level show good agreement with compressive

International Engineering Symposium, March 3-5, 2011 Kumamoto Univ., Japan

strength and AE hits behaviour indicating that concrete has much deteriorated due to freezing and thawing. The ice formation in pores forces water out. Then hydraulic pressure is generated within the solid matrix which damages the cement paste and the repeated process make it weakens. Thus, concrete experiences degradation.

Furthermore, it also suggests that the proposed technique of the reliability evaluation of damaged concrete can be done successfully using Weibull analysis of AE activity behaviour according to stress level under compression loading.

References

[1] Newman, J. and Choo, B.S, Advanced Concrete Technology: Concrete Properties, Elsevier, London, 2003. 8/4 pp.

- [2] Ohtsu, M., Sensors and instrument, Acoustic emission testing basic research-applications in civil engineering, Springer Berlin, 2008, 19-40 pp.
- [3] Kencanawati, N.N, and Shigeishi, M., Acoustic Emission Sources of Breakdown Failure due to Pulsed-Electric Discharge in Concrete, *J. Constr Build Mater*(2010), doi:10.1016/j.conbuildmat.2010.10.013 (article in press).
- [4] Kencanawati, N.N., and Shigeishi, M., Acoustic Emission Weibull Analysis for Evaluation of Deteriorated Concrete due to Carbonation, (2010), Proceeding of International Student Conference on Advanced Science and Technology, Kumamoto, Japan, December 5-6. pp. 10-1.
- [5] Shiotani, T., Parameter Analysis, Acoustic emission testing basic research-applications in civil engineering, Springer Berlin, 2008, 41-51 pp.
- [6] Suzuki, T., Komono, G., and Ohtsu, M., Damage Mechanics of Carbonated Concrete by AE Rate Process Analysis, Graduate School Science and Technology, Kumamoto University, 2010.
- [7] Rinne, H. and Alghuwainem, S.M, Weibull Distribution, A Handbook, CRC Press , Boca Raton, 2009.

Characteristics of Normal Strength Concrete with and without Chemical Admixtures at Elevated Temperatures

SUBHASH C YARAGAL, SHARANABASAPPA A WARAD , K S BABU NARAYAN and KATTA VENKATARAMANA

Department of Civil Engineering, National Institute of Technology Karnataka, Surathkal, Mangalore 575025, India, e-mail: subhashyaragal@yahoo.com

Abstract: Fire is one of the most destructive powers to which a building structure can be subjected. Behavior of concrete when exposed to fire in cases like nuclear plants, cooling towers or any accidental fire in industrial buildings, is a serious concern, on the strength retention property of concrete. This work reports strength retention studies on compressive and split tensile strength of normal concrete with and without the chemical admixture (Reobuild 918, BASF make) at elevated temperatures. Concrete cubes of size 100 mm have been cast as per prior mix design for M30 grade of concrete, 28 days water cured and tested by destructive method for strength before exposure. Later these specimen were subjected to elevated temperatures of 200°C, 400°C, 600°C and 800°C with a retention period of 2 hours and were allowed cool within the furnace to reach ambient temperature. Later their appearance, colour and cracks were observed and also weight losses were determined. Further, destructive tests were conducted to estimate residual compressive and residual split tensile strengths and prediction equations are proposed to ascertain splitting tensile strengths from compressive strengths.

Keywords: *Normal strength concrete, Elevated Temperatures, Residual strength, Chemical Admixture*

Introduction

Every concrete structure should continue to perform its intended function like maintaining its required strength and serviceability during the specified or expected service life, even after the exposure to adverse conditions like elevated temperatures, aggressive environmental conditions etc.

The advantage of concrete structures is that it is non-combustible, it neither burns nor supports combustion. The behavior of concrete in fire is very complicated because not only reinforced cement concrete is a composite material with components having different thermal characteristic, it also has properties that depend on moisture and porosity. Exposure of concrete to fire in cases like nuclear plants, cooling towers or any

accidental fire in buildings, warrants information on post fire strength retention property of concrete.

When exposed to high temperatures, the chemical composition and physical structure of the concrete change considerably. The dehydration such as the release of chemically bound water from the calcium silicate hydrate (CSH) becomes significant above about 110°C. The dehydration of the hydrated calcium silicate and the thermal expansion of the aggregate increase internal stresses and from 300 °C micro cracks are induced through the material. Calcium hydroxide [Ca(OH)₂], which is one of the most important compounds in cement paste, dissociates at around 530°C resulting in the shrinkage of concrete. The fire is generally extinguished by water and CaO turns into [Ca(OH)₂] causing cracking and crumbling of concrete. Therefore, the

effects of high temperatures observed are colour change, surface cracking and high temperatures around 500°C . CSH gel, which is the strength giving compound of cement paste, decomposes further above 600°C . As a result, severe micro structural changes are induced and concrete loses its strength significantly and thus affecting durability.

Design Mix Details

Economical mix proportions have been obtained from trial mixes, for normal strength concrete (NSC) and concrete with superplasticizer (CWP) i.e. Reo-build918 BASF make, from trial mixes to obtain slump value in the range of 75-100 mm. Typical properties of superplasticizer (Reobuild-918 BASF make) and mix proportion incorporated in this study have been tabulated in following Tables 1 and 2 respectively.

Experimental Setup

From economic mix proportions, 100mm cubes were cast as listed in Table 3 for NSC and CWP. Cubes were arranged in electric furnace with clearance on all sides. The temperatures build up of furnace with time, for a different elevated temperature was observed. It is noticed that temperature build up rate is about $20^{\circ}\text{C}/\text{min}$ upto 400°C , and $7^{\circ}\text{C}/\text{min}$ for temperature rise above 400°C .

After exposing the specimen to target temperature and retaining it for 2 hours, specimen were allowed to cool within electric furnace till it reaches room temperature. Later study on physical appearance, colour change, spalling and cracking was done. Finally specimen were tested for destructive test to obtain residual compressive and split tensile strengths as per IS 516-1959 (reaffirmed 1999) and BS 1881-Part 117 respectively.

Results and discussions

After exposure to elevated temperatures there was no significant distortion of the specimen is observed but, however, for the specimen which were kept at 600°C and 800°C , a small amount of deterioration

of concrete at the edges and corners was occurred (smudged corners and edges).

At 200°C , the concrete colour change was not noticeable. When temperatures were in the range of $400^{\circ}\text{C} - 600^{\circ}\text{C}$ concrete colour slightly changed to dust colour or brownish/ yellowish grey. Beyond 600°C temperature, concrete colour change observed is straw yellow to pinkish yellow/pinkish red as also observed by Jianzhuang Xiao and H. Falkner (2006).

Crack density was hardly noticed at specimen exposure temperatures of 200°C and 400°C , but cracks observed for exposure conditions of 600°C and were more pronounced at 800°C .

In both cases of NSC and CWP, about 70% of total weight loss occurred at exposure condition of 200°C , mainly because of loss of moisture content. Remaining 30 % of total weight loss occurred gradually as temperature increased from 200°C to 800°C . And it was also observed in Fig 1. that percentage loss of weight in case of NSC was higher compared to CWP because of higher water content. NSC had water content of 194 Kg/m^3 , while CWP had 160 Kg/m^3 of water content

From destructive testing the residual strengths as factor/co-efficient for both NSC and CWP were tabulated as shown in Table 4.

In both cases of NSC and CWP it was observed that at elevated temperature of 200°C the residual compressive strength was higher than that of compressive strength at room temperature. This is mainly because moisture content in concrete creates vapour pressure contributing to additional strength of concrete known as autoclaving effect. And gradually reduces for further increase in temperature as shown in Fig 2, which is also compared with results of other investigators.

From Fig 3 an Fig 4 it is seen that the residual split tensile strength (Factor/Co-efficient) is less than that of residual compressive strength (Factor/Co-efficient) at elevated temperatures, in case of both conventional concrete and concrete with superplasticizers. This is because as

concrete is weak in tension and at elevated temperatures is further prone to decreased tension capacity of concrete by inducing crack as also observed by Leyla Tanacan et al (2009), shown in fig 5.

For the known values of residual compressive and residual split tensile strengths, graphs have been plotted to obtain relation between the same by fitting best fit line as shown in Fig 6 and Fig 7.

From Fig 6 and Fig 7 for best fit line, power equations are obtained as given in Equation 1 and 2 below having R^2 value 0.962 and 0.985 for NSC and CWP respectively.

$$Y = 0.146X^{0.825} \text{ ----- For NSC} \quad (1)$$

$$Y = 0.206X^{0.716} \text{ ----- For CWP} \quad (2)$$

Where,

Y= Residual split tensile strength in MPa

X= Residual Compressive strength in Mpa

From these prediction equations, computed values of residual split tensile strength were in the range of $\pm 9.05\%$ and $\pm 4.48\%$ from destructive test results of NSC and CWP respectively.

Further, comparison was made between Equation 1 and 2 to find, percentage difference between residual split tensile strengths for various residual compressive strength for both NSC and CWP and are tabulated in Table 5.

From Table 5 it is noticed that percentage difference between prediction Equation 1 and 2 varies $\pm 5.95\%$. Hence any of the two prediction equations can be used to determine the residual split tensile either for NSC or CWP, from compressive strengths.

Conclusions

The following conclusions are deduced from the experimental results:

- It is observed that there is major percentage loss in weight by about 70% at early elevated temperature around 200°C , and there is gradual decrease of percentage loss in weight at further increment of temperature both in case of NSC and CWP.

- The total percentage weight loss of the specimen increases as the exposure temperature increases.
- Percentage loss of weight in NSC was found to be slightly higher than in CWP, this is attributed to the higher water content in NSC.
- The residual coefficient of compressive strength decreases with increase in temperature except at early elevated temperature around 200°C due to autoclaving effect, for both NSC and CWP.
- The residual coefficient of split tensile strength decreases with increase in temperature for both NSC and CWP. There was no such increase of residual coefficient for split tensile at early elevated temperature than its room temperature strength as in case of compressive strength. This is due to concrete is weak in tension and it is further prone to cracking at elevated temperature.
- The residual coefficient of compressive strength and residual coefficient of split tensile strength for both NSC and CWP reduced gradually upto elevated temperature of 400°C and above 400°C the drop of residual coefficients were higher. This is mainly due to many irreversible reactions taking place in the microstructure of concrete like disintegration of CSH gel.
- The residual coefficient of split tensile strength and residual coefficient of compressive strength for NSC is found to be slightly higher than CWP, which is mainly attributed to the higher density of concrete and also availability of lower water content in case of CWP.

References

- [1] Arioiz O. (2007). "Effects of elevated temperatures on properties of concrete", Fire Safety Journal 42, 516-522.
- [2] Jianzhuang Xiao, Meng Xie, Ch. Zhang (2006), "Residual compressive behaviour of pre-heated high-performance concrete with blast-furnace-slag", Fire Safety Journal 41 ,91-98
- [3] K. Sakr, E. EL-Hakim (2005), "Effect of high temperature or fire on heavy weight concrete properties", Cement and Concrete Research 35, 590 - 596.
- [4] Leyla Tanaçan, Halit Yas_a Ersoy, Ümit Arpacioğlu, (2009) "Effect of high temperature and cooling conditions on aerated concrete properties", Construction and building materials, 23, 1240-1248
- [5] Metin Husem (2006), "The effects of high temperature on compressive and flexural strengths of

International Engineering Symposium, March 3-5, 2011 Kumamoto Univ., Japan

ordinary and high-performance concrete", Fire Safety Journal 41, 155-163.

[6] Saava A., Manita P., Sideris K.K. (2005), "Influence of elevated temperatures on the mechanical properties of blended cement concretes prepared with limestone and siliceous aggregates", Cement & Concrete Composites 27, 239-248.

[7] Y. Xu, Y.L. Wong, C.S. Poon, M. Anson (2003), "Influence of PFA on cracking of concrete and cement paste after exposure to high temperatures", Cement and Concrete Research 33, 2009 - 2016.

Table 1 Properties of Reo-Build 918 BASF make

Aspect -Dark brown free flowing liquid
Relative Density - 1.18 ± 0.02 at 25°C
pH > 6
Chloride ion content < 0.2%
Optimum dosage - 500ml to 1500ml per 100Kg of cementitious material
Workability - Ensures workability for 3 hours at $+25^\circ\text{C}$

Table 2 Mix proportions of concrete (NSC and CWP)

Designation	Proportion
M30 (NSC)	w/c : C :FA: CA 0.45:1:1.198:2.923
M30 (CWP)	w/c : C : FA : CA 0.45:1:1.845:3.580

30 %10mm and 70% 20mm were used out of total CA.

Table 3 Number of specimen cast

Exposure Temperature ($^\circ\text{C}$)	For direct compression		For split tensile test	
	NSC	CWP	NSC	CWP
27	3	3	3	3
200	3	3	3	3
400	3	3	3	3
600	3	3	3	3
800	3	3	3	3
Total	15	15	15	15

Table 4 Residual strengths for NSC and CWP

Exposure Temperature ($^\circ\text{C}$)	Residual strengths (Factor/Co-efficient)			
	Compression		Split tensile	
	NSC	CWP	NSC	CWP
27	1.00	1.00	1.00	1.00
200	1.06	1.10	0.88	0.83
400	0.95	0.87	0.67	0.67
600	0.51	0.48	0.44	0.42
800	0.39	0.27	0.36	0.31

Table 5 Comparison between Eqⁿ 1 and 2

Residual compressive strength (MPa)	Residual split tensile strength from prediction (MPa)		Percentage difference (%)
	Eq ⁿ 1 (NSC)	Eq ⁿ 2 (CWP)	
20	1.73	1.76	1.76
25	2.08	2.06	-0.66
30	2.42	2.35	-2.68
35	2.74	2.63	-4.42
40	3.06	2.89	-5.95

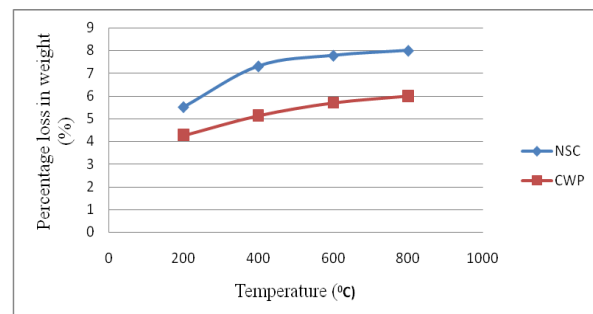


Fig. 1 percentage loss in weight V/s temperature for NSC and CWP

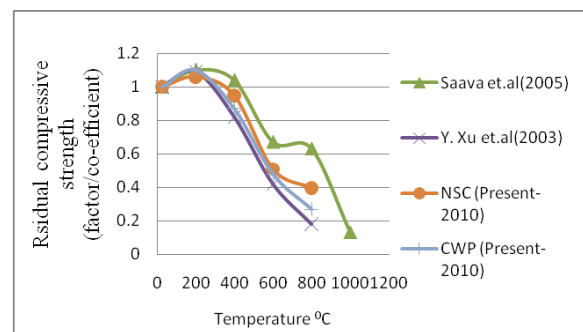


Fig. 2 Comparison of residual compressive strength (factor/co-efficient) V/s temperature from data of other investigators

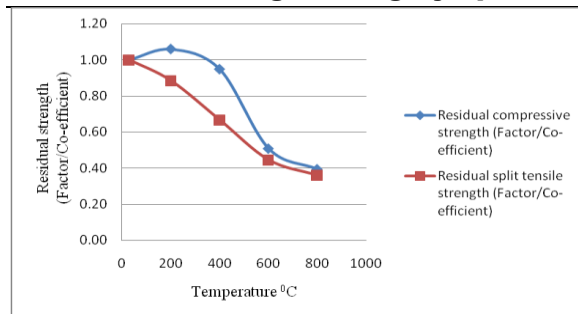


Fig. 3 Residual strengths (Factor/co-efficient) V/s temperature for NSC

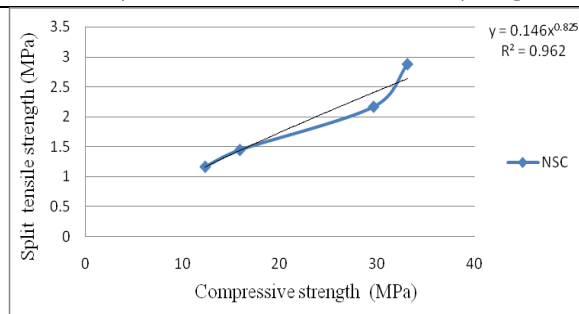


Fig. 6 Residual compressive strength V/s residual split tensile strength for NSC

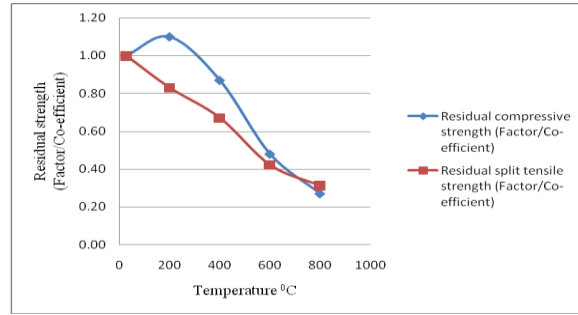


Fig. 4 Residual strengths (Factor/co-efficient) V/s temperature for CWP

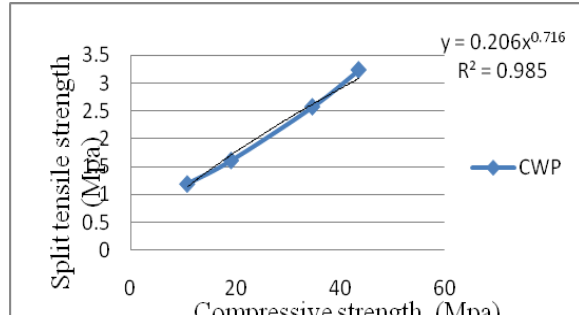


Fig. 7 Residual compressive strength V/s residual split tensile strength for CWP

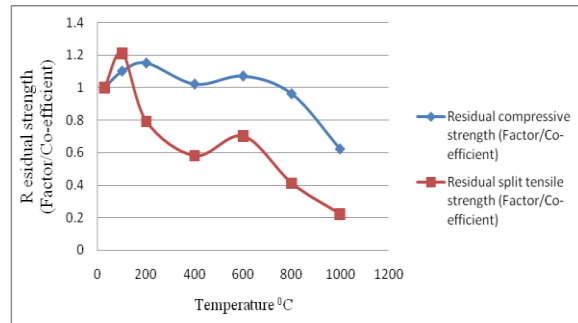


Fig. 5 Residual strengths (Factor/co-efficient) V/s temperature as observed by Leyla Tanacan et al (2009)

Properties of Self-compacting Mortars containing Steel Fibre with Cementitious Blends of Fly Ash, Ground Granulated Furnace Slag and Silica Fume

S.Bhavanishankar¹ H.D. Devadas² M.C.Nataraja³

1 Department of Civil Engineering, Bangalore University, Bangalore 560056, India.
e-mail: sbhavanishankar@gmail.com

2 Department of Civil Engineering, Bangalore University, Bangalore 560056

3 Department of Civil Engineering, SJCE, Mysore, VTU, Belgaum, India.

Abstract: The relation between the flow properties and the formulation is actually one of the main issues for the design of Self- compacting concrete [SCC]. As an integral part of SCC, Self compacting mortars [SCM] may serve as a basis for the design of concrete since the rheological properties of SCC is often difficult due to the need of complex equipments. In this study the properties of SCM with steel fiber and different combinations of Fly ash [FA], Ground Granulated Blast furnace Slag [GGBFS] and Silica fume [SF] with Port land cement were used. With the frame work of this experimental study a total of 12 SCMs were prepared having a constant water-binder ratio of 0.50 and total cementitious material of 600 kg/m³. Then the fresh properties of the mortars were tested for mini- slump flow diameter and mini-V- funnel flow time. The results of flexure and compressive strength are presented.

Keywords: *Self-compacting mortar, strength, steel fiber, cementitious blends*

Introduction

Self compacting concrete(SCC) is considered as a category of high performance concrete that has excellent deformability in the fresh state and high resistance to segregation, and can be placed and compacted under its self weight without applying vibration, assuring complete filling of formworks even when access is hindered by narrow gaps between reinforcement bars. To produce SCC the major work involves designing an appropriate mix proportions and evaluating the properties of the concrete. SCC shows high fluidity, self compacting ability and segregation resistance, all of which contributing to reduce the risk of honeycombing of concrete. Moreover, the fresh SCC must be stable to ensure the homogeneity of the mechanical strength of the structure.

The stability of SCC can be enhanced by incorporating fine materials such as flyash (FA), Ground Granulated Blast Furnace Slag (GGBFS) and Silica fume (SF). The

use of such powder may provide greater cohesiveness by improving the grain size distribution and particle packing [Sonebi M et al .1999]. Alternatively, a viscosity modifying admixture (VMA) along with a superplasticizer (SP) may be used to impart high fluidity accompanied by the adequate viscosity [Fujiwara H et al. 1996]. Using of chemical admixture, may however increase the material cost such that savings in labour cost might offset the increased cost. But the use of mineral admixture not only reduces material cost but also improved the fresh and hardened properties of SCC [Gesogln M et al. 2007]. Also SCC rheology can be optimized if the matrix part of the concrete is designed properly. Self-Compacting mortar (SCM) may serve as a basis for the design of concrete and properties of SEMs highlight the workability of SCCs. According to Domone and Jin [Domone PL et al.1999] mortar are being tested for the following reasons.(i) SCC has a lower coarse aggregate content than the traditionally vibrated concrete(TVC) (typically 31-35%

by volume) and therefore the properties of mortar are dominant.(ii) Assessing the properties of the mortar is an integral part of many SCC mix design processes and therefore knowledge of the properties of mortar itself is useful.(iii)The combination of powder material is also used to control the hardened properties, such as strength.(iv)Testing mortar is more convenient than testing concrete.

Objective

Utilization of mineral admixture will invariably increase over the next decade to provide greater sustainability in construction, and there will therefore be pressures to maximize their effectiveness with regard to cost, environmental impact, durability and performance. The objective of this paper is to investigate the combined effect of mineral admixtures used as partial replacement of port land cement (PC) and also the influence of steel fibre on the performance of SCMs. For this a total of 12 SCMs were prepared in which the binder was composed of the combination of PC, FA, GGBFS and SF at varying replacement levels.

Experimental program

Materials

The materials used to produce the SCMs in this investigation are Portland cement 43 grade, a class F FA, GGBFS and SF, fine aggregate and superplasticizer. The properties of mineral admixtures and cement are given in Table 1. The physical properties of the fine aggregate are presented in Table 2. The steel fibre of 35 mm length and density 7.80 g/cm³ is used. Super plasticizer with a specific gravity of 1.143 was used to achieve the desired workability in all mortar mixes.

Mix proportions

Twelve mortar mixes each with and without steel fibre were designed having water/binder ratio of 0.50 and a total binder content of 600 kg/m³. The reference mortar mix (M1) was made of only with PC as the binder while the other mixes incorporated with combination of (PC+FA, PC+GGBFS, PC+SF and PC+FA+GGBFS+SF) cementitious blends in which portion of the PC was replaced with the mineral admixtures. In all the

mixes, 30% of cement was replaced by different combinations of admixtures. Similarly the mixes containing steel fibres also have same type of replacement of cement with mineral admixtures. The mix proportions are summarised in the Table 3(a) & Table 3(b), in which the mixes are designated according to type and amount of cementitious material used.

Casting, Curing, Testing

In the preparation of SCMs, the mixing process was kept same to maintain the same homogeneity and uniformity in all mixes. First cement and mineral admixtures are intimately mixed together, and then fine aggregate was mixed with thoroughly mixed powder using a standard mixer, described by ASTM. Then three quarters of the mixing water was added to the grout and mixed for an additional minute. Thereafter SP with remaining water was added and mortar was mixed for an additional three minutes. The mortar was designed to give a slump flow diameter of 24-26 mm, which was achieved by using the SP at varying amount. In this study the quantity of steel fibre is fixed at 1% by weight of the binding material. Trial mixes were produced for each mixes till the desired slump is achieved.

For each mix, nine cubes of 150 mm and prisms of 40×40×160 mm side were produced. Specimens were cast in steel moulds. After demoulding, the cubes and prisms were placed in water for curing. The cubes were used to determine the compressive strength and the prisms were used to determine the flexural strength. Testing was conducted at 7, 14 & 28 days.

Test methods

Tests carried out on fresh mortar involved mini slump flow, mini V- funnel flow time. The slump flow diameter and V-funnel flow time were measured according to the procedure recommended by EFNARC committee. Figure 9 - 11 demonstrate the mini slump flow and mini V-funnel flow tests respectively.

The hardened mortar specimens were also tested for compressive strength and flexural strength. The testing was conducted at 7, 14, and 28 days. The average of three test specimens was computed for each property.

Results and discussions

Fresh properties of SCM

The test results for slump flow diameter, V-funnel flow time are presented in Table 4(a) & (b) for various SCMs. All the mortar mixes were designed to give slump flow diameter of 25 ± 1 cm which was obtained by adjusting the dosage of SP used. Therefore all the mixes had slump flow diameter generally conforming to EFNARC recommendations. From the results of mini slump flow test in Table 4(a) & (b), it was observed that using of FA, GGBFS and SF blends slightly increased the flow diameter of the mixes, whereas the mixes containing the combinations of (PC+FA or PC+GGBFS or PC+SF) shows a reduction in the flow diameter. Thus the use of two or more mineral admixtures in combination appeared to be very influential on properties of SCMs. The same trend is also observed in case of mortar containing steel fibre.

The result of V-funnel flow time of the SCMs is tabulated in Table 4(a) & (b). The reference mortar (M1) had a flow time of 7.49s which reduced to 5.36s, 5.72s, 4.45s when 30% FA, 30% GGBFS, and 30% SF was incorporated in mixes M2, M3 and M4 respectively. The same trend of reduced V-funnel flow is observed in SCMs containing steel fibres. The combined use of mineral admixtures has increased slightly the flow time compared to the mixes M2, M3 and M4. However all the mixes fulfilled the limitations of EFNARC recommendations in terms of V-funnel flow time in spite of containing different combinations of mineral admixtures.

Compressive strength

The compressive strength development of various SCMs is presented in Fig. 1 and Fig. 2. It was observed that the compressive strength of mortar containing 30% FA is lower than the strength of mortars containing 30% of GGBFS and 30% SF. This trend is also seen in SCMs containing fibres. The compressive strength of control mix M1 at 7 days was measured to be 41.84 MPa which increased to 68.11 MPa at 28 days. The mix M2, which contains 30% FA, shows less strength development in 7 days and also at 28 days. This is consistent with the previous studies which have shown that FA does not contribute

notably to the early strength development of cementitious system. In case of mortar mix M3 which contains 30% of GGBFS a remarkable increase was observed in the strength gain at 7 days and also at 28 days. But in case of mortar mix M4 which contains 30% SF the early strength at 7 days was less but the strength after 28 days was almost equal to that of M3 mix strength at 28 days. In case of mortar mixes containing FA, GGBFS and SF (M5-M9) with different combinations as shown in Fig. 3 and Fig. 4 a slight decrease in strength was observed. On the other hand the mixes M10-M12 which contain FA, GGBFS and SF, the rate of gain of strength in the early age is less, but the gain of strength in these mixes is more as they age.

Flexural strength

The flexural strength development of various SCMs is presented in Fig. 5 and Fig. 6 and the percent difference in the flexural strengths of SCMs (with and without fibres) made with different combinations of mineral admixtures with respect to that of reference mix are demonstrated in Fig. 7 and Fig. 8.

Conclusions

Based on the test results presented in this paper, following conclusion can be drawn:

- For the targeted spread value, the dosages of SP used in mineral modified mortars changed with the mineral additives types and their combinations in different proportions. The use of SF in mortar significantly increased the dosage of SP because of its extremely high surface area for the constant water/binder ratio.
- Maximum compressive strength was observed for 30% GGBFS and 30% SF replacement ratio of cement. This increase in strength can be attributed to the improved aggregate-matrix bond resulting from the formation of less porous transition zone in the mortar. The compressive tests revealed that the mortars containing the combinations of FA, GGBFS and SF have shown the strength gain. Same trend is also observed in mortar containing the steel fibres
- The incorporation of steel fibres considerably improved both flexural

and compressive strengths. This improvement may be attributed to enhanced compatibility of the mix and compatibility of steel and mortar from the viewpoint of interfacial strength gain.

References

- [1] ASTM C 348 2002 Standard test method for flexural strength of hydraulic cement mortar, Annual book of ASTM Standards.
- [2] Domone PL, Jin J (1999) Properties of mortar for self compacting concrete. In proceedings of the first international RILEM symposium on Self compacting concrete. Stockholm, Sweden, PP 109-120
- [3] Erhan Guneyisi, Mehmet Gesoglu (2008) Properties of Self compacting mortars with binary and ternary Cementitious blends of flyash and metakaolin, Materials and structures (2008) 41:1519-1531
- [4] EFNARC 2005, Specification and guidelines for self compacting concrete.
- [5] Fujiwara H, Nagataki S, Otsuki H (1996) Study on reducing Unit powder content of high fluidity concrete by controlling powder particle size distribution. Concrete Library io JSCE 28:117-128
- [6] Gesoglu M, Ozbay.E (2007) The effect of mineral admixture on fresh and hardened properties of Self compacting concretes. Mater Struct 40:923-937
- [7] IS 8112:1989, Specification for 43 grade OPC
- [8] IS 383: 1970, Specification for Coarse and fine aggregate from natural sources for concrete (second revision)
- [9] Sonebi M, Bartos PJM (1999) Hardened SCC and its bond with reinforcement. In: proceedings of the first international RILEM symposium on Self compacting concrete. Stockholm, Sweden, PP 275-289

Table 1 Chemical composition and physical properties of cement and mineral admixtures

Analysis	PC	FA	GGBFS	SF
CaO%	62.58	4.24	38.80	0.20
SiO ₂ %	20.25	56.2	34.80	95.00
Al ₂ O ₃ %	5.31	20.17	12.20	0.25
Fe ₂ O ₃ %	4.04	6.69	1.20	0.15
MgO%	2.82	1.92	7.20	0.40
SO ₃ %	2.73	0.49	0.08	---
K ₂ O%	0.92	1.89	0.39	0.32
Na ₂ O%	0.22	0.58	0.34	0.20
Specific gravity	3.15	2.25	2.56	2.20

Table 2 Physical properties of fine aggregate

Properties	
Fineness modulus	2.723
Bulk density	1.274
Specific gravity	2.55

Table 3(a) Mix Proportion Details of SCM's without Fibres

SL NO	SAMPLE NOTATION	PORTRAL D CEMENT (%)	FLY ASH (%)	GGBFS (%)	SILICA FUME (%)	WATER BINDER RATIO	SUPER PLASTICISER (L/M ³)	SUPER PLASTICISER (%)
1	M1(PC)	100	0	0	0	0.5	8.400	1.40
2	M2	70	30	0	0	0.5	5.035	0.84
3	M3	70	0	30	0	0.5	6.294	1.05
4	M4	70	0	0	30	0.5	26.014	4.34
5	M5	70	25	5	0	0.5	5.455	0.91
6	M6	70	25	0	5	0.5	8.811	1.47
7	M7	70	20	10	0	0.5	5.874	0.98
8	M8	70	20	0	10	0.5	11.329	1.89
9	M9	70	20	5	5	0.5	7.972	1.33
10	M10	70	15	10	5	0.5	9.231	1.54
11	M11	70	15	5	10	0.5	11.329	1.89
12	M12	70	10	10	10	0.5	12.168	2.03

Table 3(b) Mix Proportion Details of SCM's with Fibres

SL NO	SAMPLE	PORLTAND CEMENT (%)	FLY ASH (%)	GGBF (%)	SILICA FUME (%)	WATER BINDER RATIO	SUPER PLASTICISER (L/M ³)	SUPER PLASTICISER (%)
1	MF1(P)	100	0	0	0	0.5	9.600	1.60
2	MF2	70	30	0	0	0.5	5.455	0.91
3	MF3	70	0	30	0	0.5	7.552	1.26
4	MF4	70	0	0	30	0.5	26.014	4.34
5	MF5	70	25	5	0	0.5	5.874	0.98
6	MF6	70	25	0	5	0.5	11.329	1.89
7	MF7	70	20	10	0	0.5	5.874	0.98
8	MF8	70	20	0	10	0.5	12.168	2.03
9	MF9	70	20	5	5	0.5	12.168	2.03
10	MF10	70	15	10	5	0.5	11.329	1.89
11	MF11	70	15	5	10	0.5	11.748	1.96
12	MF12	70	10	10	10	0.5	13.007	2.17

**Table 4 Slump Value and Mini V-funnel Value of SCM's
(a) without fibres and (b) with fibres**

(a)

SI no	Sample	Mini slump	V- Funnel
		Value in mm	value in sec
1	M1	24.3	7.49
2	M2	24.2	5.36
3	M3	23.9	5.72
4	M4	25.6	4.45
5	M5	24.7	7.13
6	M6	24.5	6.21
7	M7	26.3	6.68
8	M8	25.3	5.94
9	M9	24.4	7.37
10	M10	24.1	8.16
11	M11	25.9	4.85
12	M12	25.5	6.74

SI no	Sample	Mini slump	V- Funnel
		Value in mm	value in sec
1	MF1	25.1	8.11
2	MF2	23.8	5.40
3	MF3	24.7	5.36
4	MF4	24.2	5.18
5	MF5	24	6.48
6	MF6	25.2	7.73
7	MF7	24.8	8.02
8	MF8	24.6	7.52
9	MF9	25.4	9.46
10	MF10	24.6	6.28
11	MF11	25.7	6.93
12	MF12	25.3	6.45

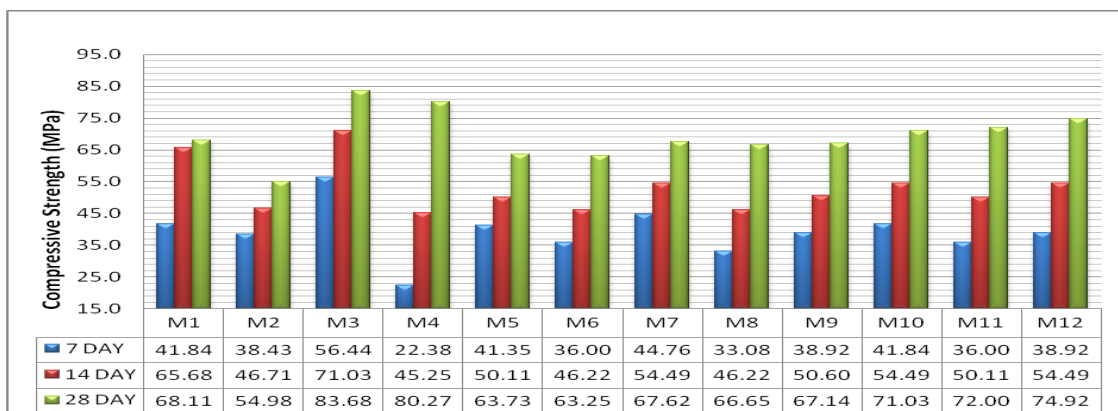


Fig. 1 Compressive Strength of SCM's without Fibres @ 7, 14 & 28 Days

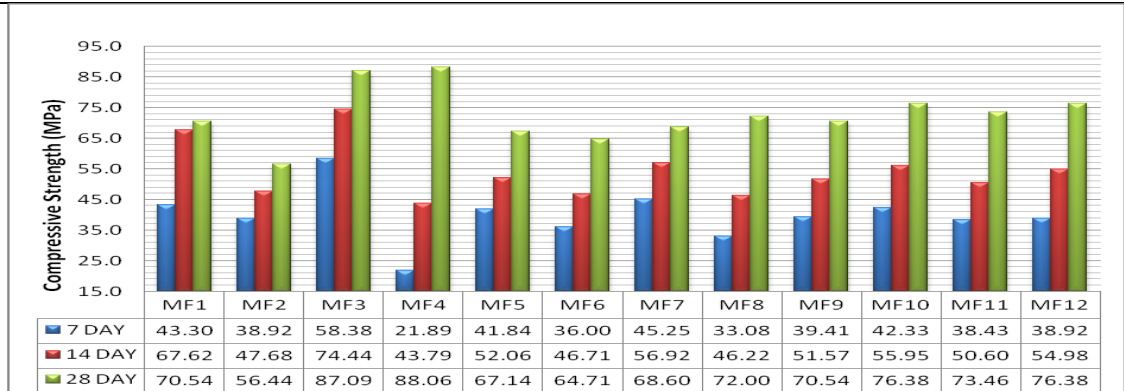


Fig. 2 Compressive Strength of SCM's with Fibres @ 7, 14 & 28 Days

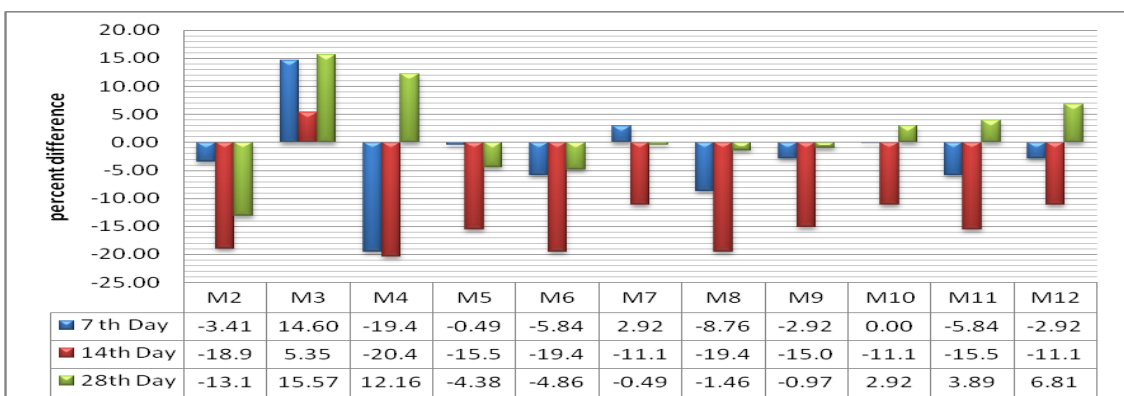


Fig. 3 Percent Difference in Compressive Strength of SCM's without Fibres compared with Compressive Strength of CONTROL-PC without Fibres

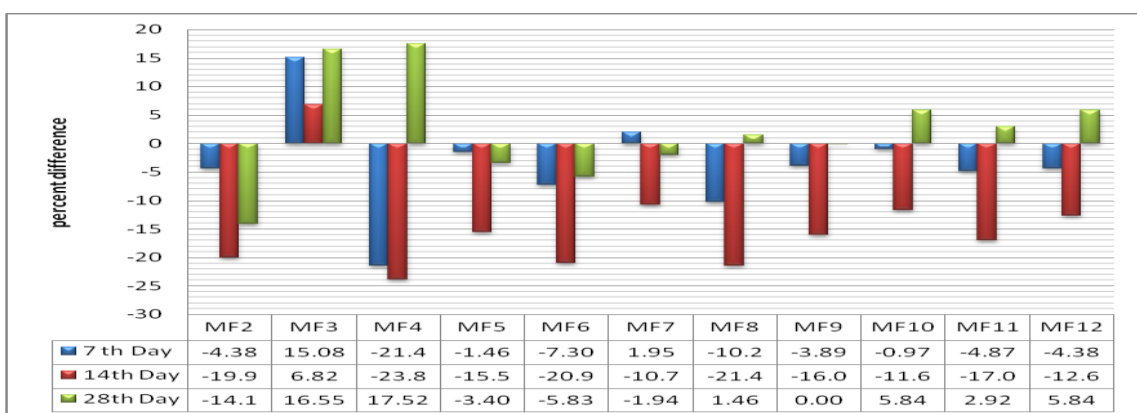


Fig. 4 Percent Difference in Compressive Strength of SCM's with Fibres compared with Compressive Strength of CONTROL-PC with Fibre

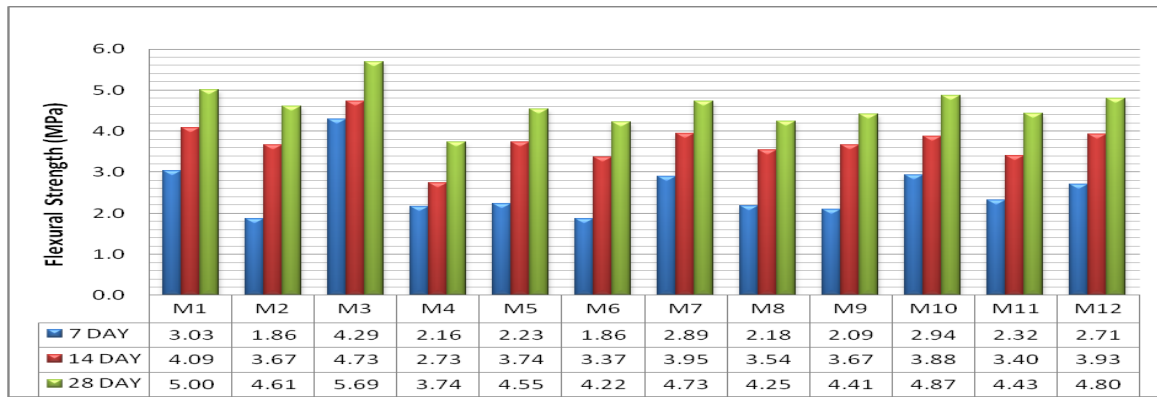


Fig. 5 Flexural Strength of SCM's without Fibres @ 7, 14 & 28 Days

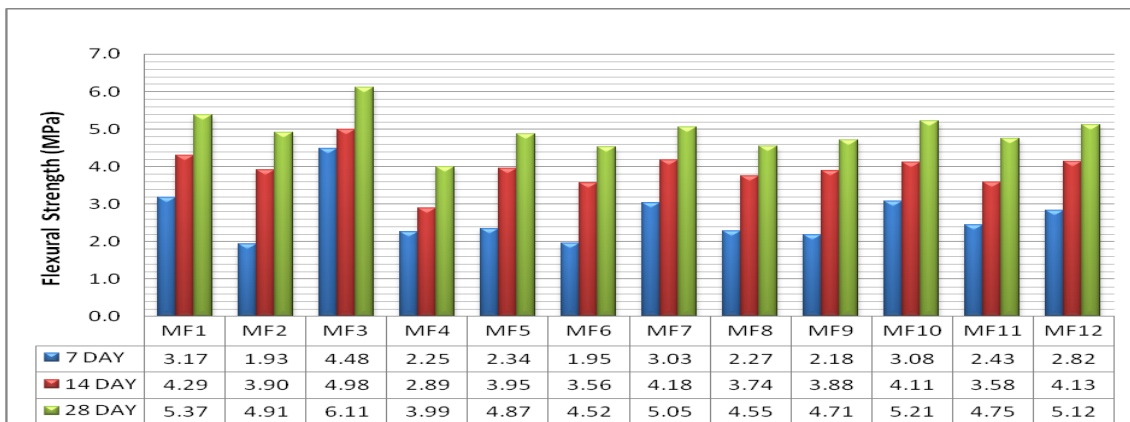


Fig. 6 Flexural Strength of SCM's with Fibres @ 7, 14 & 28 Days

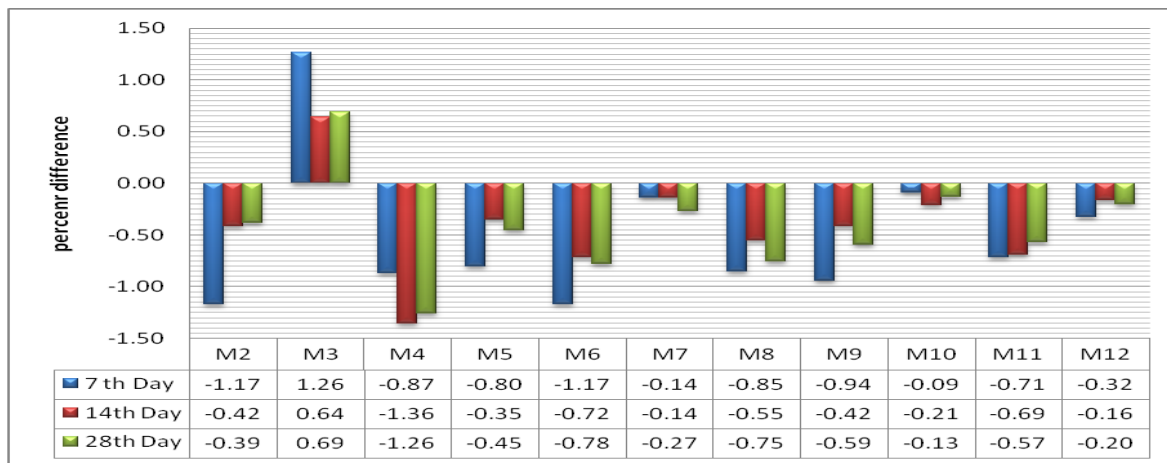


Fig. 7 Percent Difference in Flexural Strength of SCM's without Fibres compared with Flexural Strength of CONTROL-PC without Fibres

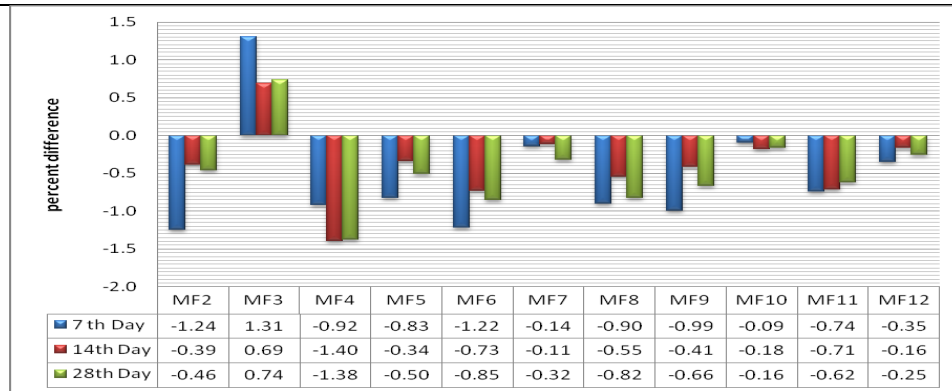


Fig. 8 Percent Difference in Flexural Strength of SCM's with Fibres compared with Flexural Strength of CONTROL-PC with Fibres



Fig. 9 Mini Slump flow test for fresh mortar



Fig. 10 Slump flow spread



Fig. 11 Mini V-Funnel test for fresh mortar

Study of Properties of High Strength Concrete - Partial Substitution by Marine Sand

Ravindranatha¹

Udaya Shankar H.N.²

Muhsin Shafeeq V³

1 Department of Civil Engineering, Manipal Institute of Technology, Manipal University, Manipal, 576104, India. e-mail:ravi.nath@manipal.edu

2 Department of Civil Engineering, Manipal Institute of Technology, Manipal University, Manipal, 576104, India. email:udaya.shankar@manipal.edu

3 Department of Civil Engineering, Manipal Institute of Technology, Manipal University, 576104, India.e-mail:vmuhsin@gmail.com

Abstract: As some constraints make the availability and use of river sand less attractive, a substitute product for concrete industry needs to be found. This paper presents the feasibility of the usage of marine sand from Malpe beach, along west coast of Karnataka, as partial substitute for natural sand in concrete. Tests were conducted on cubes and beams of M40 concrete made of marine sand and the results were compared with the 100 percent natural sand concrete. On fresh concrete the tests related to workability measures and strength were carried out. Durability tests on concrete like resistance to sea water, and capillary action were carried out. It is found that the compressive, flexural strength and Durability Studies of concrete made of 30% marine sand as partial substitute are more or less equal to the conventional concrete.

Keywords: marine sand, tests on concrete, M40 concrete

INTRODUCTION

India has taken a major initiative on developing the infrastructures to develop the requirements of globalization. In the construction of buildings and other structures concrete plays the rightful role. River sand, which is one of the constituents used in the production of conventional concrete, has become scarce. In the backdrop of such a bleak atmosphere, there is a large demand for alternative materials. Suggestions for various river sand alternatives, such as marine sand, offshore sand, dune sand, quarry dust and washed soil have also been made[1,2]. Chandrasekharthy's results do not indicate any adverse effects on strength or absorption for concrete made with beach sand [1]. Although offshore sand is reportedly used in many countries such as UK, Continental Europe, India and Singapore, most of the documentation regarding its use was found mainly regarding UK practice [4].

STATEMENT OF THE PROBLEM

The concrete construction industry is not sustainable, due to various reasons. First, it consumes huge quantities of virgin materials. Secondly, the principal binder in concrete is Portland cement, the production of which is not only highly energy intensive but also a significant contributor to greenhouse gas emissions that are implicated in global warming and climate change. Thirdly, many concrete structures suffer from lack of durability which has an adverse effect on the resource productivity of the industry[3]. The study reported here is on marine sand, which was being considered as an alternative for river sand, with respect to availability, ease of extraction and cost. For countries like Taiwan, China and India, this technology can play an important role in meeting the huge demand for infrastructure .

OBJECTIVES AND STRATEGY

The main objective of the investigation is an attempt to compare the properties of fresh concrete, strength and durability properties of hardened concrete, Capillary action and studies relating to the concrete mixes produced with four different proportions of marine sand as partial substitute to fine aggregate. Investigations are carried out on M40 grade of concrete using ACC OPC 43 Grade Cement, with a water-cement ratio of 0.43. Secondly to measure the relevant properties of marine sand and also various physical properties such as specific gravity, water absorption rate etc. This study may help us to understand the limits and uses of marine sand in making concrete for suitable development, harmony without compromising with the performance characteristics of concrete including workability, strength and durability.

RESEARCH PLAN

The physical properties of ingredient materials i.e. cement, fine aggregate (river sand and marine sand) and coarse aggregates were determined. On fresh concrete the tests related to workability measures such as Slump, Compaction factor and Vee-Bee tests and on hardened concrete tests related to strength such as Compression, Split Tensile and Flexural tests were conducted. All the above tests are conducted in accordance with BIS specifications. Durability related tests on concrete like Sea water attack, Capillary action test etc. were also conducted.

The following properties were determined using the respective BIS procedures:

- The physical properties of Cement, Coarse aggregate and Fine aggregate (river sand and marine sand) used for the study.
- Chloride content of the Marine sand used.
- Fresh concrete properties such as slump, compaction factor and vee-bee tests.
- Hardened concrete properties such as compressive strength, split tensile strength, and flexural strength.
- The effect of seawater attack on concrete by direct immersion in sea water.

- Capillary measurement on concrete cylinders.

The marine sand used for the study was obtained from the shores of the Malpe Beach, which is little away from Malpe Harbour, a natural port, about 6km to the west of Udupi, Karnataka.

MATERIALS

Cement: Tests on OPC-43 grade cement is carried out in accordance with IS: 12269-1987 .

Fine Aggregate: The specific gravity and sieve analysis of both fine aggregates (river sand and sea sand) was carried out in accordance with BIS specifications and was used throughout in preparing the required mix of concrete. The sieve analysis was carried out to determine the grading zone and fineness modulus. The Chloride test was also done on marine sand, to determine, whether the Chloride content is well within specified limits.

Coarse Aggregate: To determine the fineness modulus the sieve analysis was done on crushed coarse aggregates of 20 mm and down size and its specific gravity was found in accordance with BIS specifications. The results of this test were in accordance to the specifications .

Water: Water used for concrete making and curing is conformed to drinking water standards.

Results:

Workability of Concrete:

All the five mixes, i.e. concrete mixes made with marine sand as partial substitutes in the order 10%, 20%, 30% and 40% were easily workable(Table 4). However the workability performance of control mix concrete is better than marine sand substitute concretes.

Compressive Strength:

Compressive strength of the cement concrete made with partial substitution of marine sand is less than the concrete made with ordinary river sand. But the change in compressive strength is small compared to the control mix; The

reduction in strength is seen minimal in 30% mix. The decrease in strength of 30% concrete with respect to control mix concrete for 56,90,180 days are found to be 0.75%, 2.32%, 1.64%, 2.47% and 1.53% respectively.(Table-6)

- The percentage loss in weight at 90 days is calculated to be 0.304%, 0.318%, 0.331%, 0.342% for 10%, 20%, 30% and 40% mixes respectively.(Table 8)

Flexural Strength

- The flexural strengths of cements concretes with marine sand substitutes are marginally lower than conventional concrete at early and later ages.
- The variation of flexural strength with respect to the 30% mix which is found to be a better choice for 3,7,28,56,90 days are found to be 4.52%, 5.56%, 4.41%, 0.11% and 0.92% respectively.(Table-5)
- Eventhough some increase in strengths are found in some cases , they are omitted from the study view since they cannot be explained based on any theory.

Split Tensile Strength:

- The initial Split tensile strength of the marine sand concretes are lower compared to the control mix but it gradually attains strength in the final stages.
- The variation of split tensile strength with respect to the 30% mix for 3,7,28,56,90 days are found to be 4.23%, 5.48%, 6.53%, 1.75%, 3.08% of control mix respectively.
- Comparing the later strengths for 120,150 and 180 days the 30 % mix when compared with the control mix was 3.02%, 0.39%, 3.35%. (table 7)

Resistance of Concrete to Sea water attack:

- There is an appreciable loss of weight in all four types of concretes resulting in the deterioration of concrete. It is initiated at about 28 days of aging.
- The percentage loss in weight is found to be increasing at an alarming pace for all four types of concretes and is almost double the rate at 90 days.

Conclusions:

- Concrete produced using 30%marine sand is giving optimum results from strength consideration.
- Concrete using adopted marine sand can be used for ordinary works.
- Resistance to sea water attack decreases as we increase percentage of marine sand.

Recommendations for further research:

- The property of cement pastes with marine sands should be studied for improving the setting time.
- Mix design specifications IS: 10262 – 1982 is more inclined towards conventional cement concretes. In this regard more study is required to generate new curves for the selection of water-cement ratio in order to design the mixes for cement concretes with marine sand substitutes for fine aggregates.
- The effect of the absorption coefficients, stiffness, and specific gravity of aggregates on the performance of concrete. A concrete model has to be developed involving all these factors on selecting the amount of coarse aggregates to be used in various applications.
- Strength properties should be studied beyond 180 days to at least for 2 years period.
- Alternatives to fine aggregates should be explored and the effect of manufactured sand on the four types of cement concretes should be studied.

Acknowledgements

Manipal University has provided financial support to carry out this research and to attend the conference.

References

- [1] ChandraKeerthy, S.R.De S. F et al (1994), "Suitability of sea sand as a fine aggregate for concrete Production", Transactions of the Institution of Engineers,,Sri Lanka,Vol.1, pp. 93-114.
- [2] Dias W.P.S.,Seneviratne G.A.P.S.N.,Nanayakkara S.M.S. (2008),"Offshore sand for reinforced concrete", Construction and Building Materials,22,Science Direct,pp1377-1384
- [3] M.S. Shetty, (2004)" A brief survey of advancement made in concrete technology", Proceedings of international conf. on advancement in concrete and construction, , Hyderabad, pp 99-124.
- [4] National practices and regulations in the extraction of marine sand and gravel, Ch. 3 in Sandpit.Book.
<http://sandpit.wldelft.nl/reportpage/reportpage.htm>

Sl No.	Mix designation	Type Of Cement Concrete
1	A40	100% River sand
2	B40	10% Marine Sand + 90% River Sand
3	C40	20% Marine Sand + 80% River Sand
4	D40	30% Marine Sand + 70% River Sand
5	E40	40% Marine Sand + 60% River Sand

Table 1: Mix Design Parameters

Sl.No.	Particulars	Parameters
1	Grade of concrete	M40
2	Type and shape of aggregate	Granite and angular
3	Maximum size of aggregate, mm	20
4	Characteristic compressive strength at 28 days, MPa	40
5	Degree of workability	Corresponding to a CF of 0.85
6	Exposure condition	Moderate
7	Degree of quality control	Very Good
8	Target mean strength, MPa	50.89
9	Water /cement ratio	0.41

Table 2: Designation of Mixes

Mix	Mix proportion		
	C : Fa	: Ca	: W/C
A40	1	: 1.14	: 2.57 : 0 .41

Sl.No.	Type of Concrete	Slump (mm)	Compaction Factor
1	A40	33	0.87
2	B40	33	0.86
3	C40	29	0.86
4	D40	27	0.85
5	E40	25	0.84

Table 3: Mix proportions

Table4: Workability tests

Table5: Average Flexure strength

Type of concr ete	Flexural Strength, MPa							
	3 days	7 days	28 days	56 days	90 days	120 days	150 days	180 days
A40	6.63	8.09	8.39	9.04	9.82	9.93	10.04	10.11
B40	5.81	7.79	8.14	8.67	9.71	9.89	9.95	10.06
C40	5.49	8.24	8.43	8.74	9.69	9.86	9.92	10.04
D40	6.33	8.54	8.76	9.03	9.73	9.88	9.98	10.08
E40	6.25	8.39	8.51	8.77	9.66	9.82	9.88	10.04

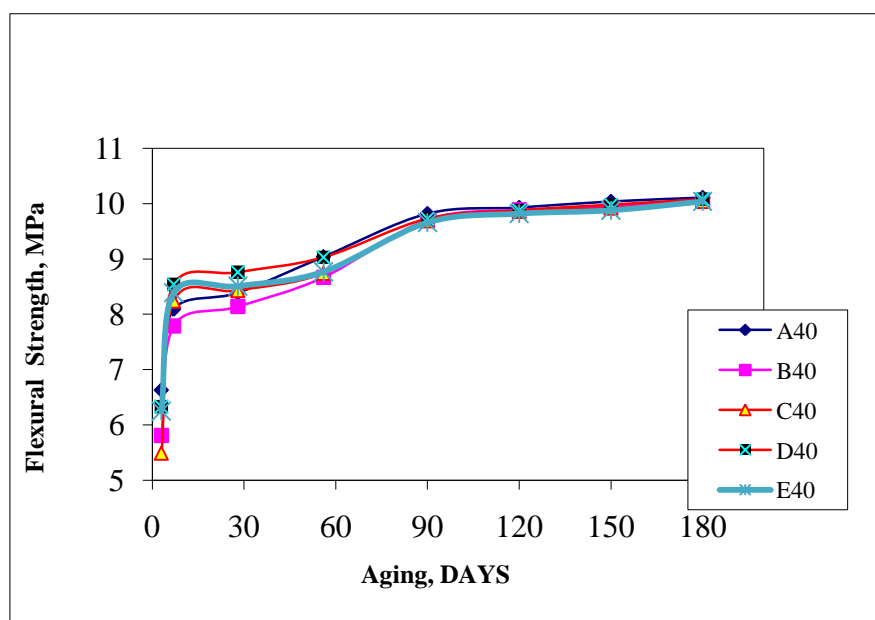


Fig.1 variation of Flexural Strength

Table 6: Average Cube compressive strength

Type of concrete	Compressive Strength, MPa							
	3 days	7 days	28 days	56 days	90 days	120 days	150 days	180 days
A40	34.42	44.31	50.67	51.49	52.33	54.56	56.88	58.77
B40	32.89	43.99	48.34	49.14	49.98	51.86	55.11	56.87
C40	32.44	41.56	47.14	48.83	49.56	50.88	54.53	55.69
D40	33.47	43.28	49.84	50.22	51.53	54.53	56.80	58.72
E40	33.18	42.66	48.86	49.57	50.93	52.63	55.88	57.08

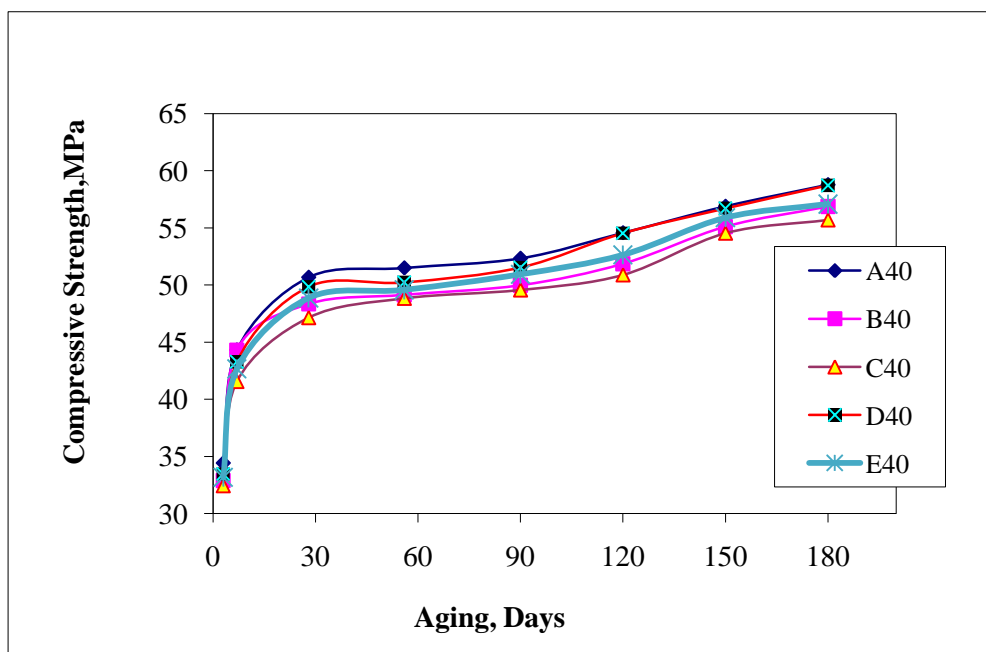


Fig.2 Variation of Compressive Strength

Table 7: Average Splitting Tensile Strength

Type of concrete	Splitting Tensile Strength, MPa							
	3 days	7 days	28 days	56 days	90 days	120 days	150 days	180 days
A40	2.84	3.47	4.29	4.58	4.87	4.96	5.14	5.38
B40	2.48	2.97	3.41	4.1	4.68	4.76	5.11	5.14
C40	2.52	3.13	3.62	4.38	4.66	4.74	5.00	5.13
D40	2.72	3.28	4.01	4.50	4.72	4.81	5.12	5.20
E40	2.47	3.19	3.72	4.43	4.70	4.78	5.11	5.18

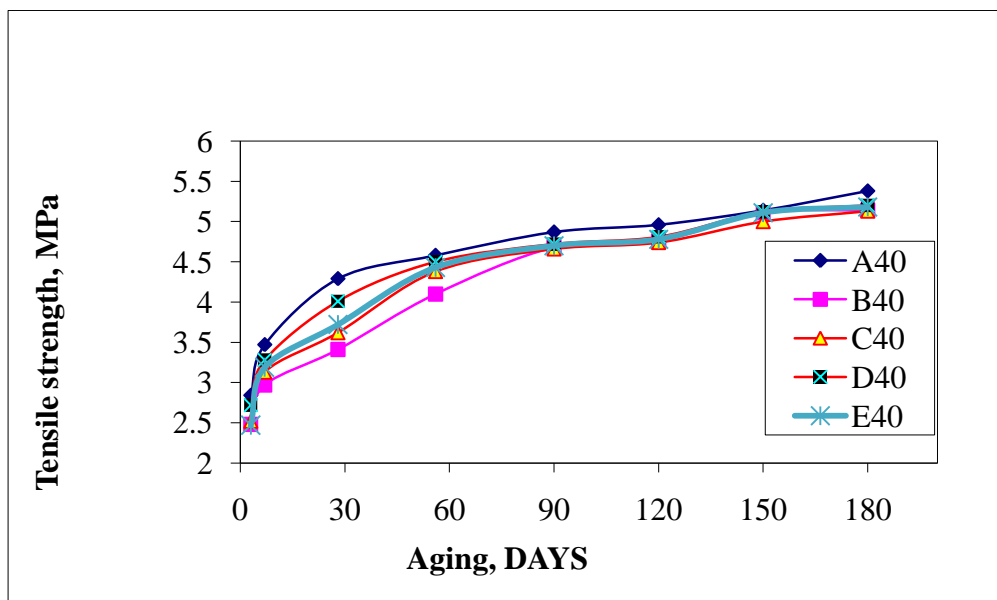


Fig.3 Variation of Split Tensile Strength

Particulars	28 Days		56 Days		90 Days	
	% Loss in Wt	Comp. Strength Mpa	% Loss in Wt	Comp. Strength Mpa	% Loss in Wt	Comp. Strength Mpa
A40	0.107	47.83	0.193	51.89	0.291	53.81
B40	0.113	48.63	0.208	48.66	0.304	50.39
C40	0.128	47.76	0.216	48.09	0.318	49.72
D40	0.147	49.55	0.227	49.73	0.331	53.73
E40	0.159	48.89	0.235	49.18	0.342	51.64

Table 8: Resistance of concrete to Sea Water Attack

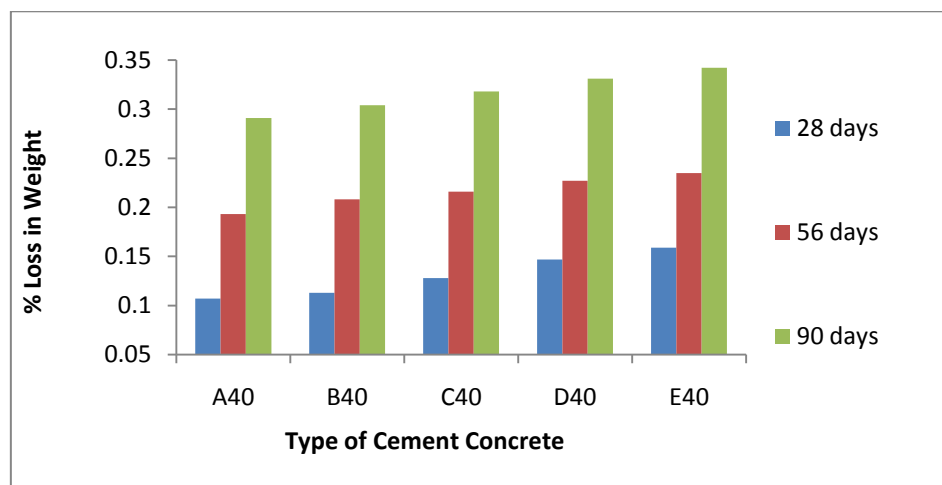


Fig.4 Resistance to sea water Attack

An Experimental Study on Influence of Bamboo Fibre on Strength and Ductility of Concrete

GOPINANDAN DEY

*Department of Civil Engineering, National Institute of Technology Agartala,
Agartala, Tripura-799055, India. email:gopinita@ymail.com*

Abstract: Concrete exhibits only a few micro-cracks during loading and the energy is absorbed predominantly elastically and thus failure occurs explosively. To avoid the brittleness of the concrete various types of commercially available fibres are used in the concrete which produce more micro-cracks and increase ductility.

For sustainable development and to have low cost construction materials it is required to use non-polluting and locally available material. The study was made to investigate the feasibility of use of bamboo fibre separately or in hybrid forms in concrete alongwith polypropylene and steel fibre to increase the ductility of concrete. The experimental findings indicate that introduction of bamboo fibre in the concrete mix increases both strength and ductility.

Keywords: Ductility, Fibre reinforced concrete, Bamboo fibre, Sustainable development.

Introduction

Ductility is an essential attribute in the design philosophy of reinforced concrete as it provides sufficient warning of impending failure. Ductility upto certain extent may be achieved by providing reinforcement in the form of laterals but it was found that the stirrup reinforcement provided beyond the requirement for resisting the shear failure will only provide confinement, so achieving required ductility by providing the laterals alone may not be possible (Sudhakar et al. 2009).

Low tensile strain capacity and poor fracture toughness make concrete a brittle material. It was reported that using fibre in concrete raises ductility (Balendra et al, 2001; Eswari et al, 2008; Ravichandran et al, 2009; Hameed et al. 2009). The mechanical properties of brittle matrix vary with the geometrical, mechanical and physical properties of fibres (Hameed et al, 2009) as well as fibre volume. Additions of randomly distributed discrete fibres in the concrete matrix enhance its ductile performance. In general, tensile strain in the neighbourhood of fibres improves significantly, when fibres are added to concrete. This, in turn, improves the

cracking behaviour, ductility and energy absorption capacity of the composite. This type of concrete is known as Fibre Reinforced Concrete (FRC).

FRC and its Beneficial Effect

Fibre Reinforced Concrete (FRC) overcomes characteristics of brittleness and rigidity of cement concrete and enhances alround performance. When cement based matrix is reinforced with the fibres it delays the growth of cracks and increases toughness by transmitting the stress across a cracked section so that a much larger deformation is possible beyond the peak stress as compared with concrete products made without fibres (Neville and Brooks, 2003). Impact and abrasion resistance of FRC is more than the plain concrete. It also increases static and dynamic tensile strength, energy absorbing qualities and better fatigue strength.

Considering the advantages, slowly the use of FRC gaining popularity but all these fibres are industrial product, which consume a large amount of power for production, resulting environmental degradation. If these fibres can be substituted with organic fibres it will lead

towards sustainable development. The main impediment for the application of the organic fibre in structural composites is the lack of adequate information about the constituents of the composites and about their durability.

Bamboo as an Engineering Material

For sustainable development there is an intense on-going search for non-polluting materials and manufacturing processes, which require less energy. In the recent past attention of researchers and industries has turned to materials such as vegetable fibres including bamboo, wood, wastes from industry and mining for engineering applications. In the last half century, advanced materials such as synthetic polymers, new alloy metals and carbon fibres were developed and these were introduced in places where locally produced materials exist in abundance. Lack of reliable technical information about the local materials makes the consumers use mainly industrialized materials for which the information is freely available (Ghavami K., 2005).

Mechanical properties such as tensile strength, compressive strength, shear strength, flexural strength and modulus of elasticity are important for load carrying structural composite products. The high lignin content of bamboo contributes to its structural rigidity. Its modulus of elasticity is about one twentieth of steel and tensile strength about 370 MPa. The ratio of tensile strength to specific weight of bamboo is six times greater than that of steel (Ghavami K., 2005). Bamboo has a remarkable economical advantage, as it reaches its maximum mechanical resistance in just few years. Moreover, it exists in abundance in tropical and subtropical regions of the globe (Ghavami K., 1995). Therefore the material attracts the attention of the researchers to use it for structural application. In Asian and South American countries, the natives have used bamboo intensively for centuries. In India the use of bamboo was limited to the construction of some scaffolding and simple dwellings.

Using the material selection method developed at Cambridge University, the structural advantage of bamboo, over

other engineering materials was studied in terms of modulus of elasticity, E, and density, ρ , as shown in Fig. 1. In this figure the line presenting the equation $C = E^{1/2}/\rho$ applies to the properties of bamboo. Materials, which are situated above the line, have better performance than bamboo, and those, which have a worse performance, are below the line. It is seen that steel, concrete and aluminium are located far below the line. (Ashby M.F., 1992; Wegst U.G.K. et al, 1993; Ghavami K., 2005)

Selection of Bamboo Species

An investigation was made by taking interview of the local people who often use the bamboo for various engineering and non engineering application. As per their opinion it is perceived that *Bambusa Tulda* (*Mritinga*) has higher tensile and bending strength comparing to other locally available variety. Therefore for the present work *Bambusa Tulda* (*Mritinga*) has been selected. The Tensile Strength of this particular variety of bamboo as reported by Prof. N.K. Naik, Indian Institute of Technology Bombay is 207 MPa.

Few tests were also conducted to verify the results. The tensile strength tests were carried out with the help of HEICO Universal Testing Machine of 600 kN. The corresponding strain and modulus of elasticity were measured using Micron Data acquisition system and electrical strain gauge having gauge length 50 mm. Apart from this water absorption and dimensional stability tests of bamboo were also performed. The corresponding results have been shown in Fig. 2 and Fig. 3. The average tensile strength of 6 (six) samples as obtained by test is 407 MPa.

Test Program

To ensure adequate ductility to the concrete structure FRC is a viable alternative. If the organic fibre can be used instead of industrialised product there will be manifold benefit. In the present study it is proposed to use bamboo fibre as a substitute of polypropylene and steel fibre or as an additional fibre which are used to improve the ductile behaviour by many researchers.

Initially all the major ingredients of concrete, polypropylene fibre and high range water reducing admixture (Conplast® SP 430) were collected. Steel fibre was supplied by Bakul Castings Pvt. Ltd. Approximately 4(four) year old bamboo culms (*Mritinga - Bambusa Tulda*) were procured in raw form from local market (Agartala) and fibres were prepared in certain aspect ratio. Bamboo fibres were dried in open air for a period of nearly 2 (two) months.

Plain concrete mould and concrete mould with fibre reinforcement in 0.5% volume proportion and using three types of fibres viz steel fibre, polypropylene fibre and bamboo fibre were casted for individual fibre as well as hybrid fibre. The test moulds are 150 mm x 150 mm x 150 mm cube, 150 mm x 300 mm cylinder and 100 mm x 100 mm x 500 mm prism. Prior to starting the concreting the properties of main ingredients of concrete were tested. The fineness modulus of coarse aggregate found to be 5.79 and that of fine aggregate is 1.65. The cement used in this project is 43-grade Ordinary Portland Cement (OPC) conforming to IS 8112-1989. The quantities of the ingredients of concrete for 1 Cum concrete were calculated as per IS: 10262-2009 for plain concrete of M50 which has been tabulated in Table 1.

For the present study mainly 0.50% volume proportions of fibres have been fixed. The details of each type of fibre have been given in Table 2. Six types of FRC samples were prepared having individual fibre content 0.50% for steel fibre, polypropylene fibre and bamboo fibre and also making hybrid of two fibres for the same volume proportion of fibre. One sample of plain concrete was prepared. The ingredients were mixed and concrete were prepared in a tilting type concrete mixture machine. After pouring the concrete, slump tests were conducted for checking the workability of the concrete. Demoulding was done on the next day and all the moulds were cured in the curing tank in the standard manner for a period of 28 days and on completion of 28 days moulds were taken out from the curing tank for necessary tests.

Test Result and discussion

Three types of fibres were used separately in three trial mixes using 0. 5% (by volume of concrete) fibre and with the same proportion of ingredients one plain concrete sample was prepared. The test result of these three types of FRC were compared with plain concrete . It is observed from Fig. 4 and Fig. 5 that addition of steel fibre increases the compressive strength by 14%-19% and increases flexural strength by 13%, addition of polypropylene fibre increases the strength by 1% to 6% and but decreases the flexural strength by 3%. For bamboo fibre 3% to 7% enhanced compressive strength and 12% more flexural strength are observed. From Fig.6 it is seen that descending part of the stress-strain diagrams for all the FRC are flatter than their plain counterpart which represent the increased ductility of concrete.

Moreover from Fig. 7 to Fig. 10 it is observed that the demolished test specimens of FRC possess much more finely ramified cracks compared to plain concrete specimen which represent more energy absorption i.e. higher ductility.

For a total volume proportion of 0. 5% (by volume of concrete) three types of fibres were used in the hybrid form using equal proportion of 2(two) fibres in three trial mixes and keeping the quantities of other ingradeients same as plain concrete of M50 grade and accordingly the samples were prepared. The test result of these three types of Hybrid Fibre Reinforced Concrete(HFRC) were compared with plain concrete. It is observed from Fig. 11 and Fig.12 that addition of steel-polypropylene hybrid fibre increases the compressive strength by 1%-8% and increases flexural strength by 8%, addition of bamboo-polypropylene hybrid fibre increases the compressive strength by 12% to 14% and flxural strength by 7%. For bamboo-steel hybrid fibre 3% to 11% enhanced compressive strength, 13% more flexural strength are observed and refering Fig. 13 it is found that descending part of the stress-strain diagrams for all the FRC are flatter than their plain counterpart which represent the increased ductility of concrete.

International Engineering Symposium, March 3-5, 2011 Kumamoto Univ., Japan

Comparing the results of all these three types of HFRC with the plain concrete it can be said that bamboo fibre can be used as fibre reinforcement to enhance the mechanical behavior of the concrete.

From Table 3 it is observed that maximum deflection can be accommodated by FRC with polypropylene fibre which is 79% more than control concrete followed by steel-polypropylene hybrid fibre and bamboo- polypropylene hybrid fibre which are 62% and 54% more than the plain concrete respectively. Therefore it can be inferred that polypropylene has a bearing on ductility though there are some reduction in strength with the use of polypropylene.

Conclusions

The experimental study has been made introducing bamboo fibre separately as well as in the hybrid forms alongwith other fibres viz. polypropylene (PP) and steel fibre in concrete in the proportion of total 0.5% by volume of concrete. A comparative study has been made with bamboo fibre reinforced concrete (BFRC) with polypropylene and steel fibre reinforced concrete as well as hybrid fibre reinforced concrete. From the experimental results obtained so far in this study the following conclusion can be made:

- For individual fibre content, steel fibre performs better than bamboo and polypropylene (PP) fibre in terms of compressive and flexural strength followed by bamboo and polypropylene (PP).
- In case of hybrid fibre reinforced concrete (HFRC) bamboo-polypropylene fibre has a good combination for compressive strength and bamboo-steel fibre combination shows better performance in terms of flexural strength.
- The presence of polypropylene fibre either alone or in combination with steel or bamboo fibre allows a larger amount of deflection. Therefore for strength and ductility point of view instead of single type

of fibre hybrid fibre either steel-polypropylene or bamboo-polypropylene fibres can be used.

- As this project is mainly to study the feasibility of the bamboo fibre in FRC, so, it can be concluded that bamboo fibre can be used with advantage in FRC taking due consideration regarding durability aspect.

Further outlook

Influence of bamboo fibre for different volume percentage will be studied alongwith their durability aspect. A numerical model will be established to verify the experimental results.

Acknowledgements

All India Council for Technical Education (AICTE), Government of India provided financial support to carry out this research.

References

- [1] Ashby M.F., Materials selection in mechanical design. Oxford: Pergamon Press; 1992.
- [2] Balendra R.V., Zhou F.P., Nadeem A., Leung A.Y.T. (2002) "Influence of steel fibres on strength and ductility of normal and lightweight high strength concrete". Building and Environment 37, 1361-1367.
- [3] Eswari S., Raghunath P.N., Suguna K. (2008), "Ductility Performance of hybrid fibre reinforced concrete". American Journal of Applied Sciences, 5 (9): 1257-1262.
- [4] Ghavami K. (1995) "Ultimate load behaviour of bamboo reinforced lightweight concrete beams". J. Cement Concrete Compos; 17(4):281-8.
- [5] Ghavami K. (2005) "Bamboo as reinforcement in structural concrete elements". Cement & Concrete Composites 27, 637-649.
- [6] Hameed R., Turatsinze A., Duprat F. and Sellier A.(2009), "Metallic Fiber Reinforced Concrete: Effect of Fiber Aspect Ratio on the Flexural Properties" ARPN Journal of Engineering and Applied Sciences Vol. 4, NO. 5.
- [7] IS: 516 – 1959, Methods of tests for strength of concrete.
- [8] IS: 2386 (Part I to VI) – 1963, Methods of test for aggregates for concrete.
- [9] Neville A.M. and Brooks J.J.(2003) "Concrete Technology" Pearson Education (Singapore) Pte.Ltd.
- [10] Ravichandran A., Suguna K., and Ragunath P.N. (2009) "Strength Modeling of High-Strength Concrete with Hybrid Fibre Reinforcement" American Journal of Applied Sciences 6 (2): 219-223.
- [11] Sudhakar M. , Seshu D.R and Rao A. K.(2009) "A Study of Confined Steel Fiber Reinforced Concrete in the Plastic Hinging Regions of RC Beams" Asian Journal of Civil Engineering (Building and Housing) Vol. 10, No. 2, pages 215-219.
- [12] Wegst U.G.K., Shercliff H.R., Ashby M.F., "The structure and properties of bamboo as an engineering material", University of Cambridge, UK, 1993.

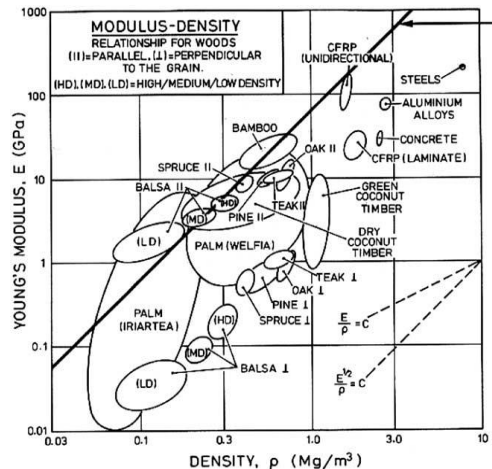


Fig.1 Performance of bamboo and other materials, in relation to their E and ρ , [Ghavami K.,2005]

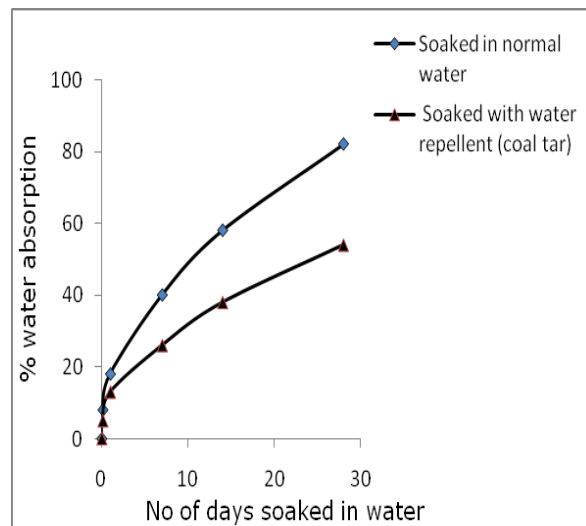


Fig.2 Water absorption of Bamboo

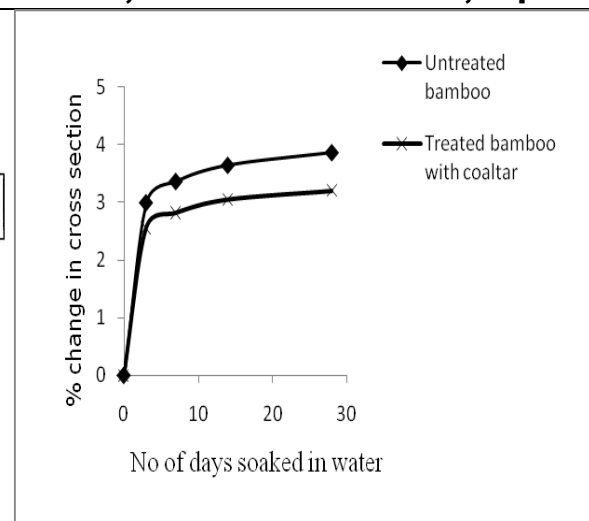


Fig.3 Dimensional stability of Bamboo

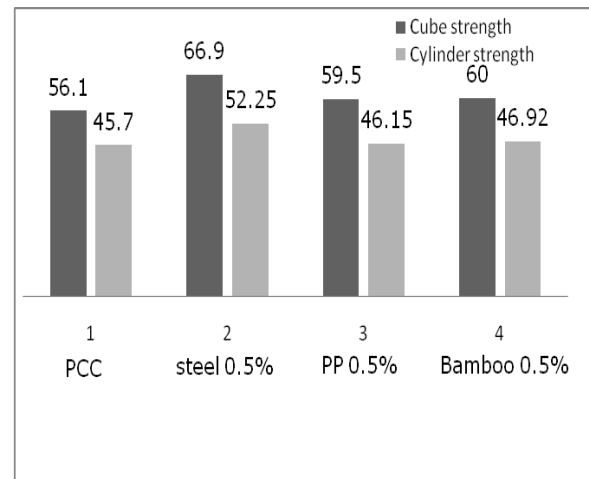


Fig.4 Comparison of Compressive strength (in MPa) for PCC and FRC for 0.5% fibre

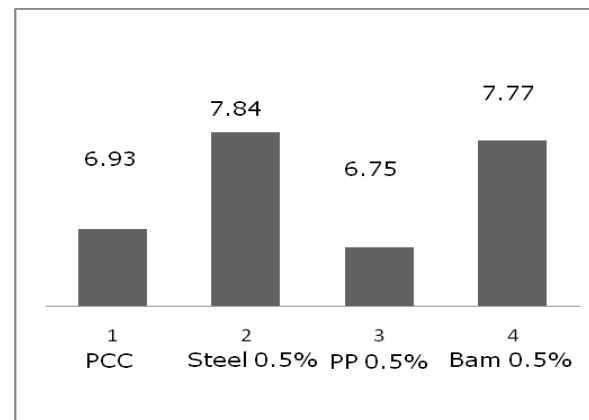


Fig.5 Comparison of Flexural strength (in MPa) for PCC and FRC for 0.5% fibre

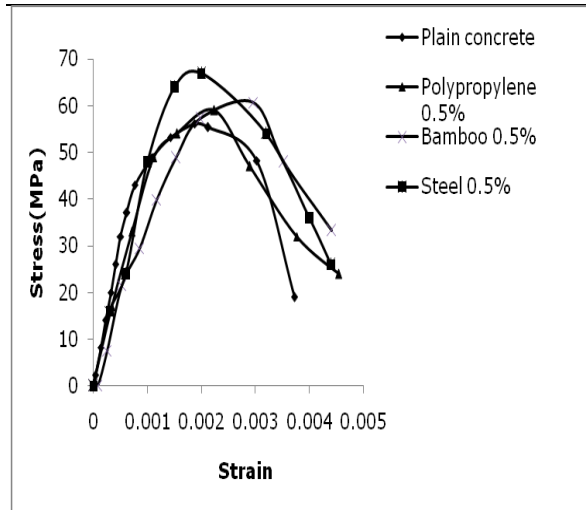


Fig.6 Stress- strain relationship of PCC and FRC with 0.5% fibre



Fig.7 Demolished specimen of PCC

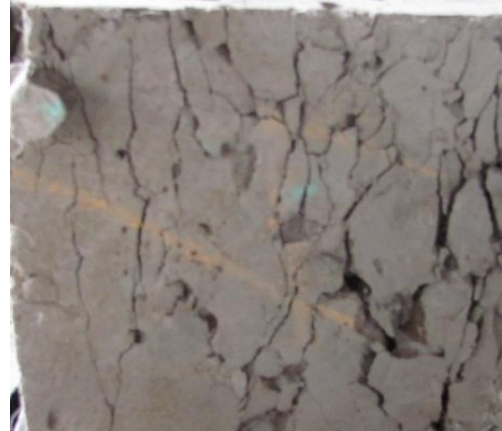


Fig.9 Demolished specimen of FRC with steel fibre



Fig.10 Demolished specimen of FRC with polypropylene fibre.



Fig.8 Demolished specimen of FRC with bamboo fibre

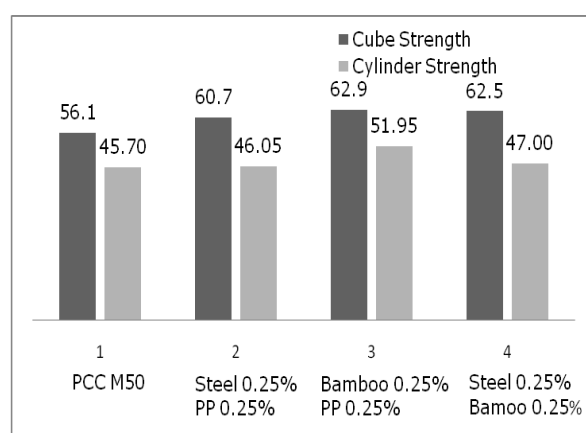


Fig.11 Comparison of Compressive strength (in MPa) for PCC and FRC for 0.5% hybrid fibre

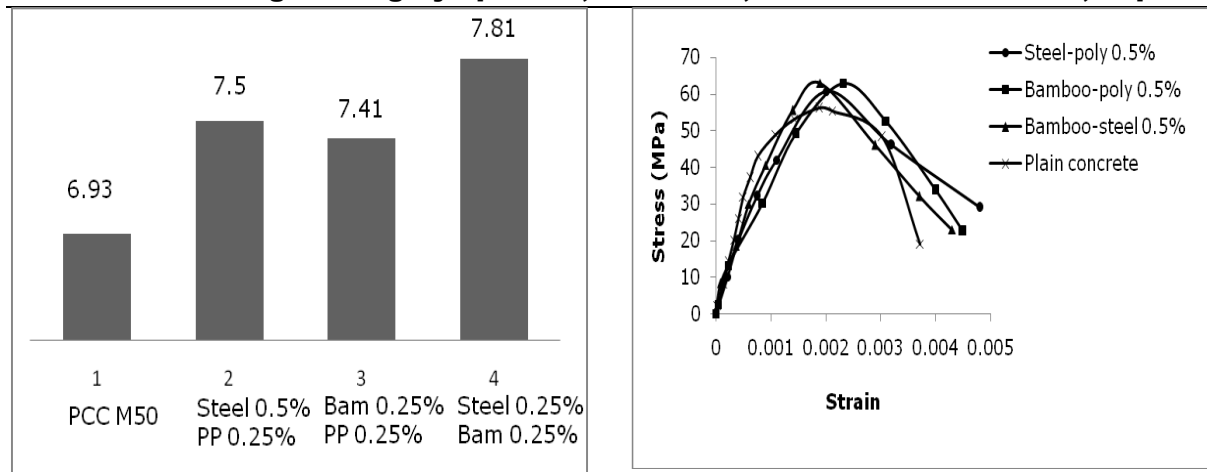


Fig.12 Comparison of Flexural strength (in MPa) for PCC and FRC for 0.5% hybrid fibre

Fig.13 Stress- strain relationship of PCC and FRC with 0.5% hybrid fibre

Table 1 Quantities of ingredients of 1 Cum concrete

Coarse Aggregate (kg)	Fine Aggregate (kg)	Cement (kg)	Water (kg)	Superplasticizer (kg)
1327.00	472.00	420.00	160.00	3.35

Table 2 Details of the fibres

SL. No	Fibre properties	Fibre details		
		Polypropylene	Steel	Bamboo
1	Length (mm)	12	36	40
2	Shape	Straight	corrugated	Straight
3	Size/Dia (mm)	0.03	1.00	0.80
4	Aspect Ratio	400	36	50
5	Tensile strength	551	532	407
6	Modulus of Elasticity (MPa)	3450	2×10^5	0.24×10^5

Table 3 Flexural strength and ultimate deflection of PCC and FRC

Sl. No	Type of concrete	Flexural strength (MPa)	Ultimate deflection (mm)	Increase of deflection over PCC
1	Plain concrete	6.93	0.48	--
2	FRC with 0.5% steel fibre	7.84	0.67	40%
3	FRC with 0.5% polypropylene fibre	6.75	0.86	79%
4	FRC with 0.5% bamboo fibre	7.77	0.66	37%
5	FRC with hybrid fibre containing 0.25% steel and 0.25% polypropylene	7.50	0.78	62%
6	FRC with hybrid fibre containing 0.25% bamboo and 0.25% polypropylene	7.41	0.74	54%
7	FRC with hybrid fibre containing 0.25% steel and 0.25% bamboo	7.81	0.70	46%

Upflow Anaerobic Wastewater Treatment using PVA/PEG Beads as Biomass Carriers

KHANH DO PHUONG¹, QUAN LAI MINH¹, HIROAKI FUJII², KENJI FURUKAWA¹

- 1 *Graduate School of Science and Technology, Kumamoto University, Kurokami, 2-39-1, Kumamoto 860-8555, Japan. e-mail: dophuongkhanh@gmail.com, lmquan_ceetia@yahoo.com, k-furu@gpo.kumamoto-u.ac.jp*
- 2 *Kuraray Co., Ltd., 7471 Tamashimaotoshima, Kurashiki, Okayama 713-8550, Japan. email: hiroaki_fujii@kuraray.co.jp*
-

Abstract: High rate anaerobic wastewater treatment process by upflow attached growth bioreactors was studied. The first experiment evaluated the performance of a modified UASB reactor using PVA beads to treat low-strength wastewater with load maximization. This reactor was firstly operated at 25°C and organic loading rate was achieved 27 kg COD/m³/d, resulting in reduction of HRT from 2 h to 0.39 h. Sequential tests with 10°C changes showed the highest effective loading rates were 21 kg COD/m³/day at 15°C, and 40 kg COD/m³/d at 35°C, respectively. In the second experiment, PVA gel beads and their competitor (PEG beads) were applied for two anaerobic upflow bioreactors operated at 30°C with same influent. More biogas and lower effluent COD concentrations were collected from the reactor supported by PVA beads. The obtained results showed potentials of this biomass carrier in high rate wastewater treatment.

Keywords: *high rate wastewater treatment, attached growth bioreactor, polyvinyl alcohol (PVA), polyethylene glycol (PEG), upflow anaerobic sludge blanket (UASB),*

Introduction

Upflow anaerobic sludge blanket (UASB) are widely accepted as a proven technology for the methanogenic treatment of organic wastewater. The main advance of this system is the high treatment capacity of wastewater, related to the good retention of anaerobic bacteria by formation of biofilm or granular sludge (*Lettinga et al., 1995* and *Speece et al., 1996*). The pioneer reactor in this study is Expanded Granular Sludge Bed (EGSB), a variant of UASB process. The study objective is to clear the acceptable organic loading rates (OLR) for low-strength wastewater treatment. To achieve this purpose, influent COD concentration was kept stable while hydraulic retention time (HRT) is reduced with all values less than 2 hours. As a result, OLR was increased step by step at low COD concentration of 400-450 mg/L. The biomass carrier provided by Kuraray Co., Ltd. (Japan) played a key role in successful operation of the bioreactor. After long-term operation

of EGSB process, polyvinyl alcohol (PVA) gel beads changed from white to black color, having high density, bigger size and good settling velocity.

Materials and Methods

First experiment

The experimental apparatus and process flow chart of the EGSB reactor is shown in Fig.1. The EGSB reactor was made of acrylic resin and had a total liquid volume of 3.9 L with a square cross-section of 36 cm², height of 110 cm. The influent was continuously provided to the EGSB reactor using a peristaltic pump. The reactor had a recirculation pump to adjust the level of bed expansion (recycle rate 1.5 L/h). The temperature was controlled by a water jacket. A sampling port was located at height of 95 cm above the reactor bottom. A gas solid separator and a capture tank with simple structure were designed for the collection of biogas. The PVA-gel beads provided by Kuraray Co., Ltd (Osaka, Japan) were used as biomass carrier. PVA-

gel beads had porous structure, round shape with diameter of 4 mm and a density of 1.03 g/cm³. Before used in the EGSB reactor, PVA-gel beads were cultivated in an anaerobic fluidized reactor to treat synthetic wastewater mainly composed of ethylene glycol. The beads introduced into the EGSB reactor contributing to about 1/4 of the reactor volume (0.8 L).

The synthetic wastewater characterized by COD), BOD concentrations of 420±30 mg/L and 220±10 mg/L was prepared using stock solution consisted of a peptone and bonito fish-meat (extract Ehrlrich) at 40 and 60 g/L, respectively, which were mixed with tap water at a volumetric ratio of 0.008:1. The tap water was of groundwater origins. A buffer solution consisting of NaHCO₃ was also added to a final concentration 80 mg/L (40 mg CaCO₃/L alkalinity addition). The pH values were within the neutral value (7.1-7.3) throughout the study. The EGSB reactor was operated at 25°C, then 15°C and 35°C with the same operational condition as summarized in Table 1.

The analysis parameters for water samples (pH, alkalinity, sCOD, BOD, volatile suspended solids), biogas (gas production, gaseous compounds), and granular sludge (settling velocity of PVA-gel beads, biomass attachment and microbial community) were examined in accordance with standard methods (APHA, 1995).

Second experiment

The synthetic wastewater characterized by COD concentrations of 300 mg/L. The substrate consisted of peptone and bonito fish-meat as well as mineral salts was mixed with tap water. Sodium bicarbonate was used as a buffer solution and the influent pH values were 7.0 to 7.2. The treatment system consisted of two upflow bioreactors which was supported by different biomass carriers (Fig.2), PVA-gel beads for the left and polyethylene glycol (PEG) beads for the right. The properties of blank PVA-PEG beads were described as Table 2. Temperature of these bioreactors was controlled at 30°C by thermometers. Biogas released from two reactors was collected by plastic bags (Fig.3).

The quality of water samples, biogas and

biomass carriers were examined with standard methods (APHA, 1995).

Results and Discussion

Load maximization of EGSB reactor in low-strength wastewater treatment

At first, EGSB reactor was operated at 25°C with the increase in organic loading rate. The COD removal efficiency decreased from 74% to 61% during this test (Fig.4). With extreme decrease in HRT, the organic removal rate declined to very low values. The operational stage before the breakdown was considered as a climax for effective treatment.

The similar trends were observed in the sequential tests with 10°C reduction and 10°C increase. The maximum loading rate of EGSB reactor was 20 kg COD/m³/d at 15°C, reached to 27 kg COD/m³/d at 25°C, and doubled at 35°C (Fig.5).

For more COD removal, the post-treatment by a swim-bed reactor operated at 25°C has been carried out. The aerobic reactor could remove 30% of initial COD, contributed to 95% of COD removal in total under volumetric loading rate of 6.5 to 27 kg COD/m³/d. This process is now under evaluation. In Furukawa's Laboratory, PVA-gel beads have been applied for several UASB processes: Conventional UASB, Anaerobic Fluidized Bed (AFB) and EGSB (Table 3). The granular development from the first to the last bioreactor showed the high application capability of PVA-gel as support media. These gel beads with porous structure were a good condition for thick biomass attachment on the surface and deep attachment at the core (Fig.6).

Comparisons between PVA-gel and PEG biomass carriers

In the second experiment, two upflow anaerobic bioreactors using PVA and polyethylene glycol (PEG) beads were operated at 30°C to treat low-strength wastewater. Compared to PVA-gel beads, PEGs are bigger, heavier, and having no porosity that makes difficulties for biomass attachment. Although the bioreactors operated in same condition, big difference in organic removal efficiency was observed. Fig.7 shows the performance of the two bioreactors. The differences were estimated by COD removal performance

and methane production. At higher organic loading rates, PVA-gel beads showed more effectiveness than PEG beads.

After the start-up process with seed sludge (45 days) and then operated without sludge, the differences in COD removal efficiency and biogas generation are enlarged nearly 20%. Furthermore, the color development of the gel beads due to attached biomass became visible from the second month of experiment. On a cultivated PVA-gel bead, the white-to-black state could be seen at both of inner and outer parts. The scanning electron microscope (SEM) taken on Day 100 (Fig.8) showed the strong biomass attachment at the core of PVA-gel. Whereas, the black was observed on the surface of a cultivated PEG bead but the pure white was kept inside. It presented to a cursory attachment due to non-porous structure. By SEM observation, the cores of blank PEG bead and cultivated PEG bead were similar (Fig.9), where no biomass attachment could be found. Otherwise, these experimental results demonstrated the appreciation of PVA-gel beads as biomass carrier in organic wastewater treatment.

Conclusions

The following conclusions are deduced from the experimental results:

In the first experiment, EGSB reactor showed a stable performance even under low temperature and extremely short hydraulic retention time. The superior of PVA-gel contributed to the good results. It was affirmed by the differences in treatment capabilities of the two upflow bioreactors using PVA and PEG gel beads as biomass carriers in the second experiment.

After three years in use with different types of UASB process, PVA gel biomass carrier has kept its good function. The beads presented higher competition than polyethylene glycol beads due to a porous structure.

Acknowledgements

We would like to thank Kuraray Co. Ltd for their PVA material supporting.

References

- [1] APHA, AWWA and WEF (1995), Standard Methods for the Examination of Water and Wastewater, 19th edition, American Public Health Association, Washington, D.C, USA.
- [2] Hoa T.T.H., Khanh L.N., Zhijun L., Fujii T., Rouse J.D. and Furukawa K. (2006), Nitrogen removal by immobilized anammox sludge using PVA gel as biocarrier, Japan Journal of Water Treatment Biology 42 (3) 139–149.
- [3] Kato, M.T., Field, J.A., Lettinga, G, The anaerobic treatment of low strength wastewaters in UASB and EGSB reactors (1997) Water Science and Technology, 36 (6-7), pp. 375-382.
- [4] Lettinga G., "Anaerobic digestion and wastewater treatment systems", *International Journal of General and Molecular Microbiology* 67 (1995), pp. 3-28.
- [5] Rouse J.D., Fujii T., Sugino H., Tran H., Furukawa K. (2005), PVA-gel beads as a biomass carrier for anaerobic oxidation of ammonium in a packed-bed reactor, Proceedings of 5th International Exhibition and Conference on Environmental Technology, Athens, Greece.
- [6] Speece R.E., "Anaerobic Biotechnology for Industrial Wastewaters", *Archae Press, Nashville, USA* (1996), p.3.
- [7] Wenjie, Z., Dunqiu, W., Yasunori, K., Taichi, Y., Li, Z., & Kenji, F. (2008), PVA-gel beads enhance granule formation in a UASB reactor. *Bioresource Technology*, 99(17), 8400-8405.
- [8] Zhang W., Xie Q., Rouse J.D., Qiao S., Furukawa K. (2009), Treatment of high-strength corn steep liquor using cultivated polyvinyl alcohol gel beads in an anaerobic fluidized-bed reactor, *Journal of Bioscience and Bioengineering* 107 (1) 49-53.

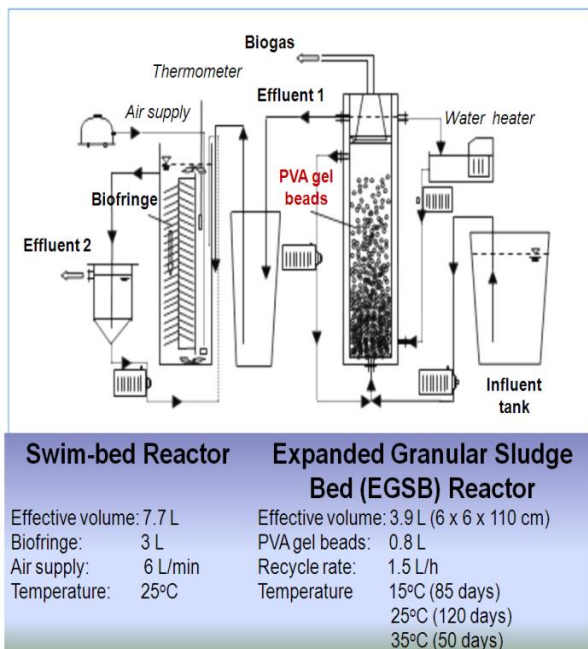


Fig.1 Schematic of treatment system

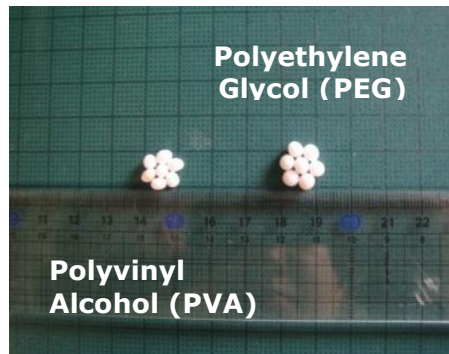


Fig.2 Blank PVA beads and blank PEG beads

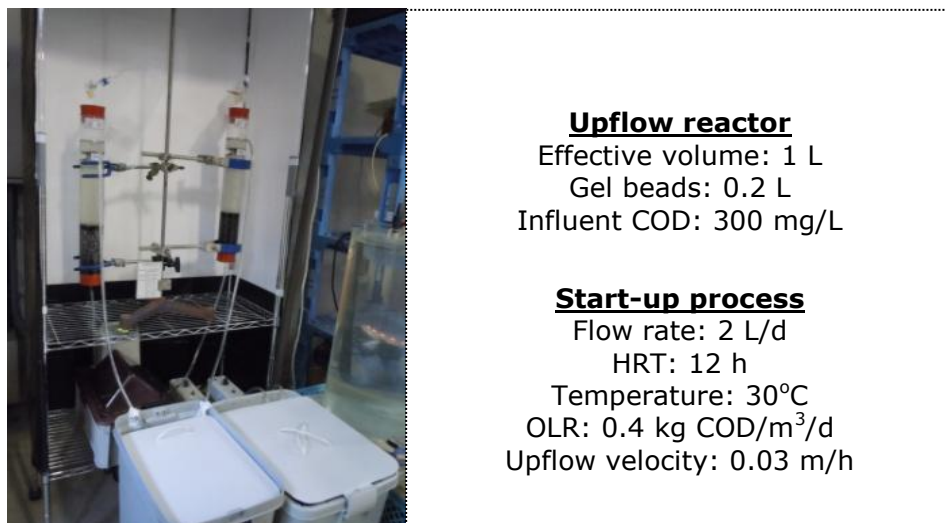


Fig.3 Upflow bioreactors with PVA and PEG biomass carriers

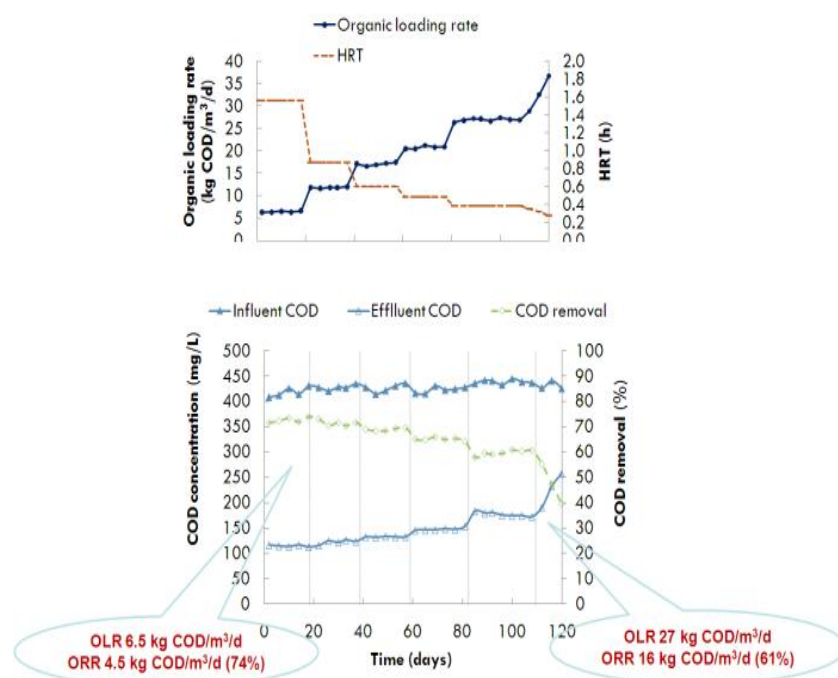


Fig.4 COD removal performance of EGSB reactor at 25°C

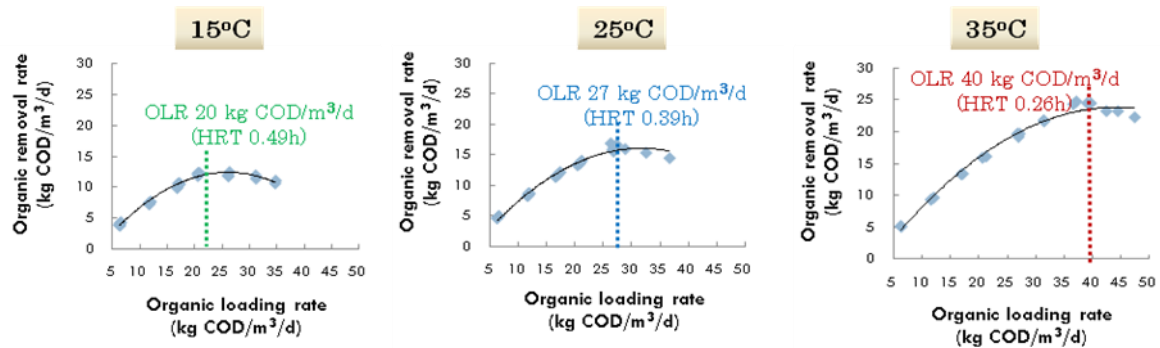


Fig.5 Maximum organic loading rates of EGSB reactor at different temperatures

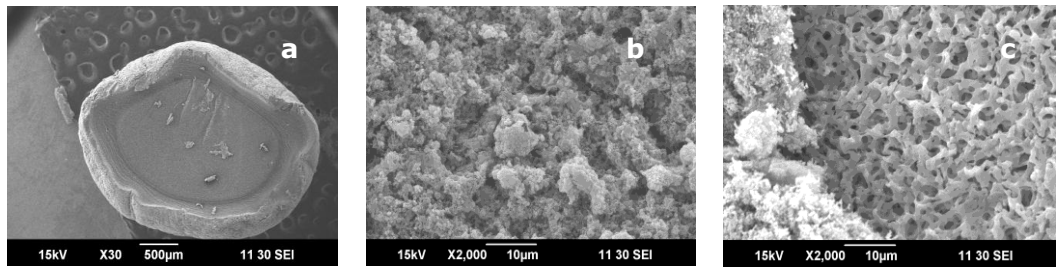


Fig.6 Scanning electron microscopic images of a cultivated PVA-gel bead: surface (a, b) and inner part (c)

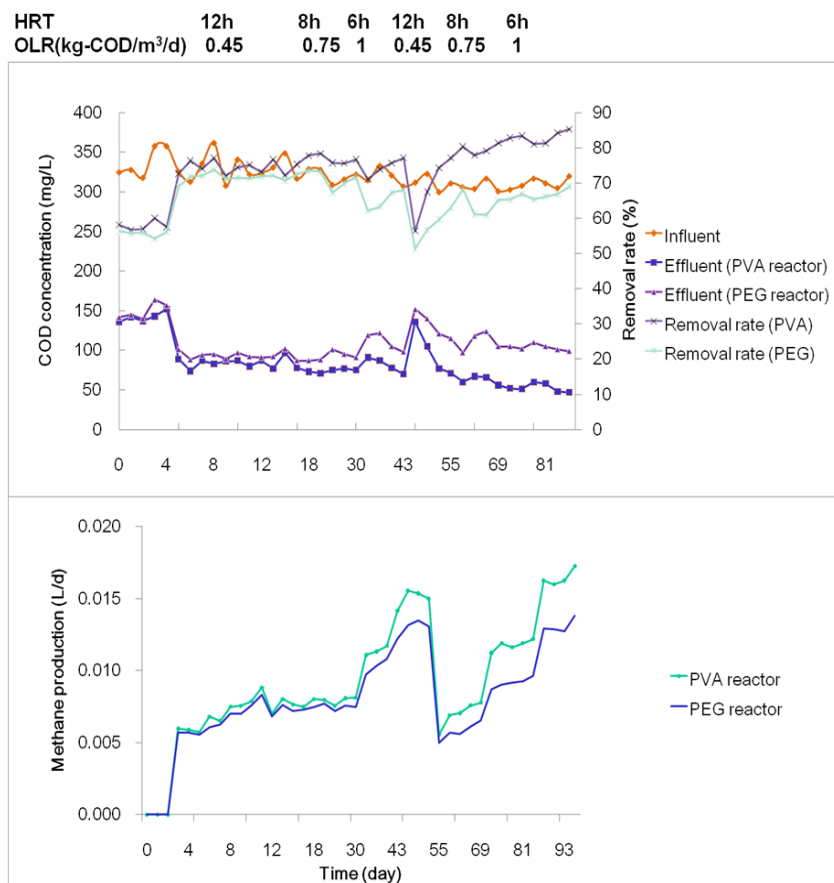


Fig.7 COD removal performance and methane production

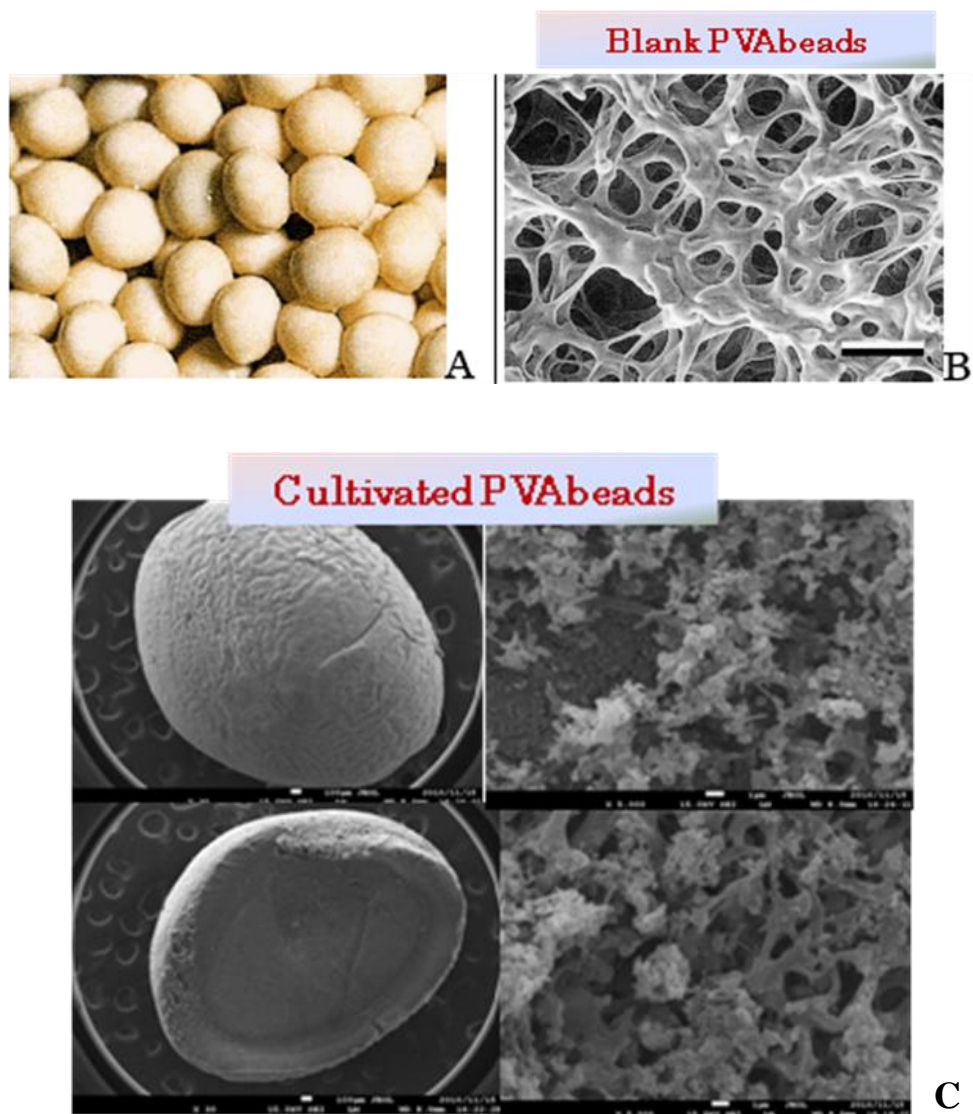


Fig.8 Magnified views of blank PVA-gel bead (A, B) and a cultivated bead on Day 100 (C)

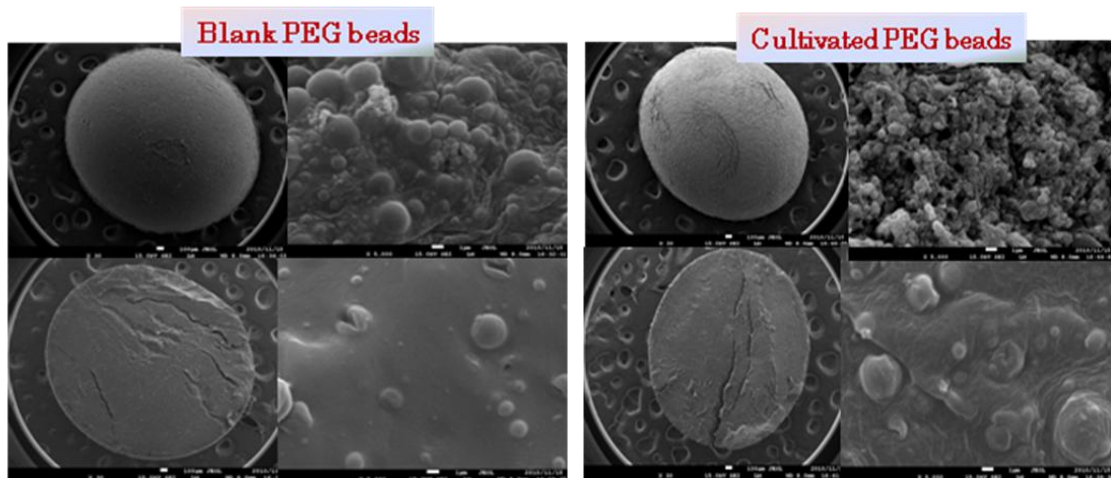


Fig.9 Magnified views of a blank PEG bead and a cultivated bead on Day 100

Table 1 Operational conditions of EGSB reactor

Run	HRT (h)	Flow rate (L/h)	Liquid upflow velocity (m/h)	Organic loading rate (kg-COD/m ³ /d)
I	1.56	2.5	2.2	6.5
II	0.87	4.5	2.8	11
III	0.60	6.5	3.3	17
IV	0.49	8.0	3.8	21
V	0.39	10	4.3	27

Table 2 Properties of blank PVA and PEG Beads

Biomass carrier	PVA bead	PEG bead
Structure	Porous	Non-porous
Density	1.04 g/cm ³	1.08 g/cm ³
Diameter	3 mm	4 mm

Table 3 PVA-gel beads as biomass carrier in different UASB processes

Parameter	UASB Reactor (Wenjie et al., 2008)	AFB Reactor (Zhang et al., 2009)	EGSB Reactor (this study)
	High-strength wastewater OLR 12 g/L	High-strength wastewater OLR 24 g/L	Low-strength wastewater OLR 6 g/L
Color	Black	Black	Black
Temperature (°C)	35	35	35
Biomass attachment (gVSS/gPVA)	0.93	0.83	0.89
Settling velocity (m/h)	200	168	191
Dominant bacteria	<i>Methanosarcina</i>	<i>Methanosaeta</i>	<i>Methanobacterium</i>

Study on Domestic Wastewater Treatment with Two-Step Feed Processes (A2O2)

Tan Phong Nguyen¹, Thanh Hung Nguyen²

1 Faculty of Environment, Ho Chi Minh City University of Technology, 268 Ly Thuong Kiet, District 10, Ho Chi Minh city, Vietnam. Email: ntphong@hcmut.edu.vn

2 Faculty of Engineering – Technology – Environment, An Giang University, 18 Ung Van Khiem, Dong Xuyen ward, Long Xuyen city, An Giang province, Vietnam.
Email : nthung@agu.edu.vn

Abstract: This paper presents a pilot-scale reactor study including anaerobic, aerobic, anoxic and aerobic in serial with two stepwise feeding into anaerobic and anoxic. Raw domestic wastewater with influent flow rates ranging 31 – 43 - 54 L/d was fed to the unit at residence time 8 – 10 – 14 h (COD loading rates of 0.5 – 0.8 – 1.0 kg COD/m³.d) and 3 ratio step feed into two tanks (6:4; 7:3; 8:2). The results of pilot with 9 conditions study evaluate removal efficiencies of total COD, completed nitrification, removal Total Kjendahl Nitrogen, total nitrogen removal through de-nitrification, and phosphorus removal. Moreover, the siltation of operational conditions evaluate by sludge settleability characteristics. The results obtained from this study shown that removal of COD, TKN, N-NH₄, T-P and SVI were 90.88%, 85.44%, 88.09%, 52.85%, and 118 ml/g, respectively at step feed 8: 2 and HRT 10h.

Keywords: Domestic wastewater, anaerobic, anoxic, aerobic, two-step feed.

Introduction

Preventing of the eutrophication in enclosed water system, biological nitrogen and phosphorus removal from wastewater has been extensively investigated and employed. Daigger et al. (1991), Wanner et al. (1992), Cooper et al. (1994). Recently, interest has been developed in use of biological, gather than chemical processes for phosphorus and nitrogen removal from wastewater. The removal nitrogen, phosphorus in wastewater treatment has been research many success. Various biological nutrient removal processes such as pre-denitrification process (A/O), Anaerobic/Anoxic/ Aerobic process (A2O), University of Cape Town (UCT), Sequencing Batch Reactor process (SBR), modified Bardenpho processes and Virginia Initiative Plant (VIP) were developed and widely applied. Wentzel et al. (1992), Ostgaard et al. (1997), William et al (1998), Guibing Zhu et al. (2007), Vaiopoulos et al. (2007). In this process, bacteria remove nitrate have function removal nitrogen and

phosphorus accumulation of microorganisms (PAOs) have function removal phosphorus influent.

From the basis result of the above process, the study intended application as technology anaerobic, aerobic, anoxic integrated with to two-step feed. This is a technology include 4 stage anaerobic, aerobic, anoxic and aerobic in series and step feed to plant by 2 steps in anaerobic and anoxic (Q1/Q2). This process is able to remove organic matter, nitrogen, phosphorus in domestic wastewater.

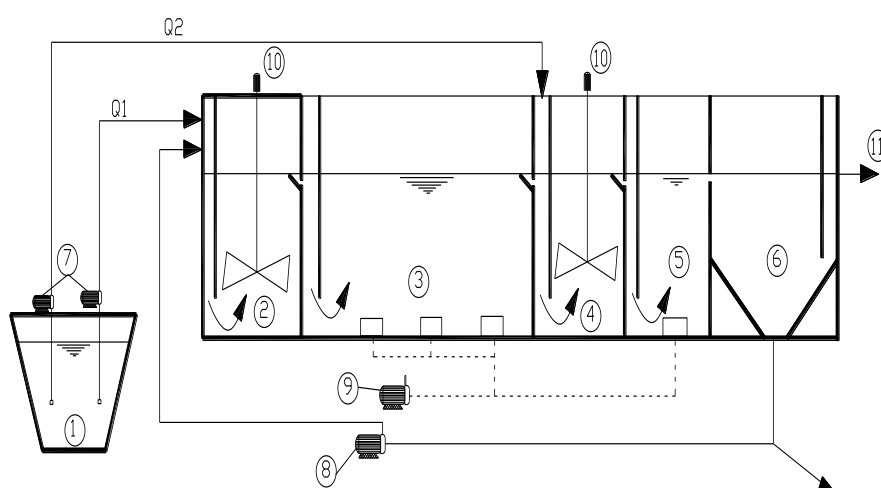
The objective of this work is to present the design and functionality of a novel pilot scale activated sludge system for biological removal of organic substrate, nitrogen and phosphorus by anaerobic, anoxic, aerobic integrated process with two-step feed.

Materials and methods

The experimental unit describe in this research is an activated sludge

prototype system for removal of COD, nitrogen and phosphorus (Fig. 1), which includes anaerobic, aerobic, anoxic and aerobic series with step feed Q1, Q2 in anaerobic and anoxic. The pilot reactor has total operational volume of 18L and consists of anaerobic tank of 3L, aerobic 1 tank of 9L, an anoxic to de-nitrification of 3 L and an aerobic 2 tank of 3L. Operational volumes and abbreviation names for the unit compartments describe in Table 1. The alternation of anaerobic and aerobic conditions is responsible for Phosphate Accumulating Organism (PAOs) growth, and thus, biological phosphorus removal, as PAOs gain the selective advantage over other. Wagner et al. (2002), Seviour et al.

(2003), Metcaft Eddy (2003). Finally, a secondary sedimentation tank is used for sludge separation and recycling into the anaerobic tank. A timer that switches on/off by a magnetic three-way valve controls sludge wastage and sludge recycle. The peristaltic pumps used to feed wastewater to reactor. In particular, the reactors connect with a piping system where the wastewater or mixed liquor suspended solids (MLSS) introduced at the bottom and withdraw from the top of each reactor. Aeration performs by the diffused aeration method. Air supplies for aeration tank by porous material. Anaerobic and anoxic tanks gently stirred.



1. Raw wastewater; 2. Anaerobic tank; 3. Aerobic 1 tank; 4. Anoxic tank; 5. Aerobic 2 tank; 6. Clarifier; 7. Peristaltic pumps; 8. Recycle pump; 9. Air pump; 10. Stirrer; 11. Effluent.

Figure 1 Schematic layout of the pilot scale system

Table 1 Operational volume for each tank of the pilot plant

Bioreactor	Operational conditions	Abbreviation	Operational volume (L)
Anaerobic	Anaerobic	Ana	3
Aerobic 1	Aeration/ Nitrification	Ae 1	9
Anoxic	De-nitrification	Ano	3
Aerobic 2	Aeration	Ae 2	3
Clarifier	Settling tank	Se	7

The pilot scale reactor feed with raw domestic wastewater from the combined sewer system of Hoang Anh Gia Lai Supper Apartment. Influent average concentrations of COD 336.06 ± 26.21

mg/l, TKN 42.82 ± 2.98 mg/l, and Total Phosphorous (TP) 8.53 ± 1 mg/l. In order to support the sufficiency nitrification condition, NaHCO_3 add to reactor to adjusting pH and alkalinity.

Influent wastewater rate (Q) was distributed to anaerobic with a flow rate of Q_1 , and to the second with a flow to anoxic of Q_2 , as shown in Fig. 1. During the experiments reported here, influent flow distribution to the anaerobic tank and anoxic zone was set to 60: 40, 70: 30, 80: 20%. Influent flow rate (Q) were increased from 31, 43, 54 litter/day in order to obtain a hydraulic residence time (HRT) from 14, 10 and 8h.

During the experimental period, the SRT control at 20 days using hydraulic control approach. The sludge returns ratio was set at 80 percent of influent flow rate control by a peristaltic pump.

Analytical methods

Samples taken regularly from each unit process were analyzed for the purpose

of monitoring the COD, SS, TN, TKN, NH_4^+ -N, NO_2 -N, NO_3 -N, TP, alkalinity, color, turbidity, mixed liquor suspended solids (MLSS), and mixed liquor volatile suspended solids (MLVSS), according to Standard Methods. APHA (1998). pH and DO were measured by using pH meter (HI 8314, Hanna) and DO meter (HI 9146, Hanna), respectively.

Result and discussion

Operational conditions for the pilot scale plant with SRT, sludge recycle rate are constant. The average MLSS (mixed liquor suspended solid) of the sludge blanket in pilot very from 2450 – 3120 mg/l. The water temperature in the unit process varied from 30-31°C.

Table 2 Operational conditions and influent concentration of wastewater in steady state experiments

Steady state run no.	Q (l/h) (Q1: Q2) (%Q)	HRT (h)	Influent Concentration (mg/l)			
			COD	TKN	N-NH₄⁺	T-P
1	1.3 (60: 40)	14	343.00	41.23	34.77	8.27
2	1.3 (70: 30)	14	329.00	47.80	40.62	8.82
3	1.3 (80: 20)	14	359.00	42.80	36.05	8.05
4	1.8 (60: 40)	10	325.00	42.47	34.67	9.05
5	1.8 (70: 30)	10	382.00	39.53	33.63	8.07
6	1.8 (80: 20)	10	308.00	42.44	37.18	9.00
7	2.25 (60: 40)	8	323.00	41.52	35.94	8.48
8	2.25 (70: 30)	8	293.00	43.12	37.64	8.72
9	2.25 (80: 20)	8	325.00	44.52	37.68	7.30

The results of all operational conditions show in Table 3. This table also present

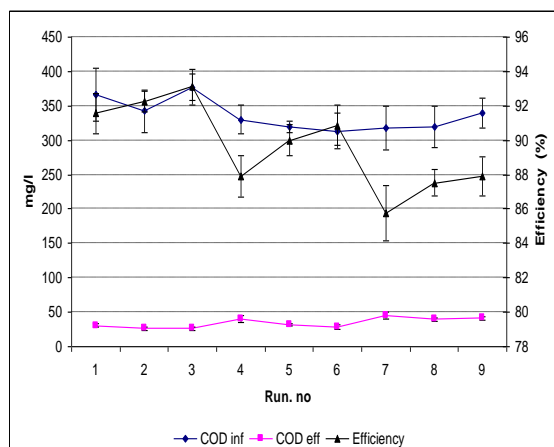
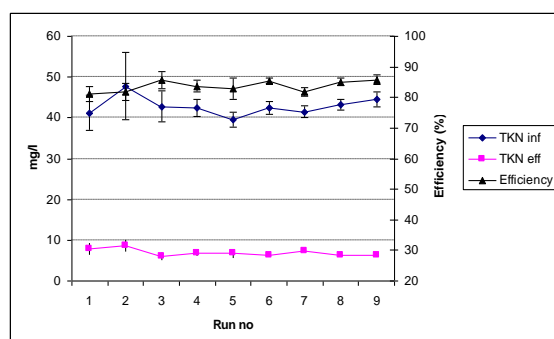
the removal (%) efficiency of COD, TKN, N-NH_4^+ , and T-P.

Table 3 Operational conditions and influent concentration of wastewater in steady state experiments

Steady state run no.	Effluent Concentration (mg/l)				Removal (%)			
	COD	TKN	N-NH ₄ ⁺	T.P	COD	TKN	N-NH ₄ ⁺	T-P
1	30.83	7.80	4.72	3.97	91.57	81.18	86.26	51.30
2	26.50	8.60	3.70	4.35	92.26	81.82	90.69	50.44
3	26.00	6.13	3.00	4.17	93.11	85.58	91.63	47.65
4	40.00	6.90	5.28	4.62	87.89	83.74	84.76	48.52
5	32.00	6.72	4.45	4.18	89.99	82.94	86.77	47.50
6	28.60	6.18	4.42	4.24	90.88	85.44	88.09	52.85
7	45.20	7.46	6.42	4.84	85.75	82.00	82.10	46.94
8	39.80	6.40	5.30	4.86	87.53	85.15	85.85	43.96
9	41.00	6.32	5.04	5.08	87.91	85.77	86.61	38.13

In table 2 operational conditions and loading rates for organic, nitrogen and phosphorus substrate for each run are presented. Although real wastewater does not provide a constant concentration of pollutants, loading rates of organic and nitrogen tend to

increase when increasing the influent flow rate, as expected. However, intense fluctuation in influent phosphorus concentration result to phosphorus loading rate fluctuations, which are not correlated to the step feed rate.


Figure 3 Removal performances of COD

Figure 4 Removal performance of TKN

Removal performances of COD by a pilot scale plant is shown in Figure 3. Results obtained by the pilot scale plant are summarized in Table 3. Average of 9 influent concentration of COD during this study were shown in table 2. The average effluent concentration of COD during 9 study from 26.00 ± 2.45 to 45.20 ± 4.44 mg/l which corresponded to a removal efficiency from 93.11 ± 0.60 to 87.53 ± 0.74 mg/l. Figure 3 shows the COD treatment effect were decreased by creasing of step feed rate and organics removal efficiency seems to decrease as hydraulic residence time decrease. Figure 4 shows removal ability of TKN. Removal TKN effect does not fluctuate high., 81.18 ± 2.38 - $85.77 \pm 1.49\%$.

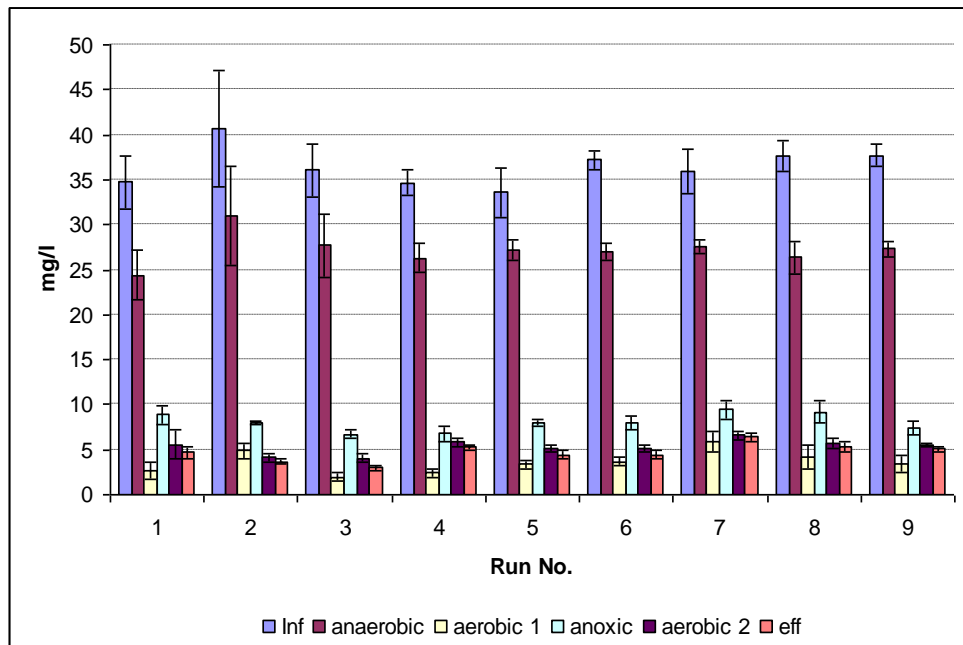


Figure 5 Removal performances of N- NH_4^+

Fig. 5, 6 shown that N- NO_3^- and N - NH_4^+ effluent was opposite. N- NO_3^- effluent was increased together with two step feed 60: 40; 70: 30; 80: 20%, respectively, but N - NH_4^+ effluent was opposite. To show, biodegradable soluble Chemical Oxygen Demand (bsCOD) in raw wastewater supply

electronic for de-nitrification. bsCOD take in anoxic high is decreased N- NH_4^+ effective of process because nitrification process was happen in aerobic 2. Hence, the pilot needs a reasonable ratio to be effective effluent. On fig 5, run no 2, 5, 8 (Q1: Q2: 70: 30%) is better each other.

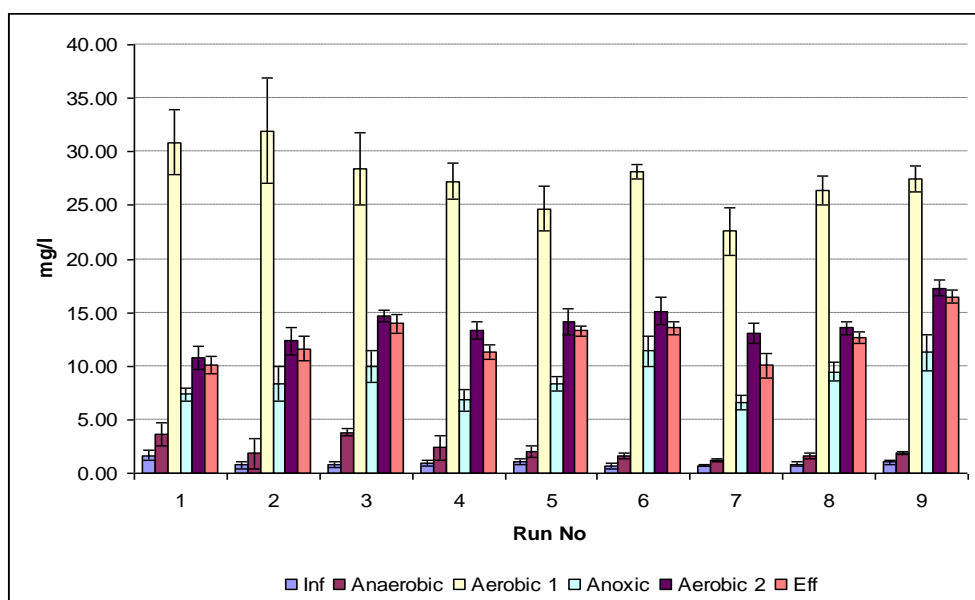


Figure 6 Removal performance of NO_3^-

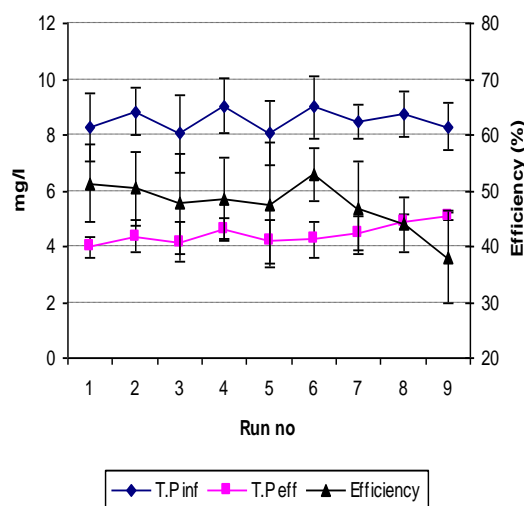


Figure 7 Removal performances of T-P

As shown in table 4 and figure 7, phosphorus removal efficiency is low because nitrate concentration in recycle flow which consume rbCOD of influent flow. In study 6, removal phosphorus is the highest, $52.85 \pm 4.79\%$.

When compared to the step feed with three feed. Vaipouou et al. (2007). and compared with two-step feed wastewater together with add glucose, Ouyang et al. (2001) the removal efficiencies of COD, nitrogen, T-P is lower. However, this study only uses two feed and not add glucose in system, with simple construction and low operation cost.

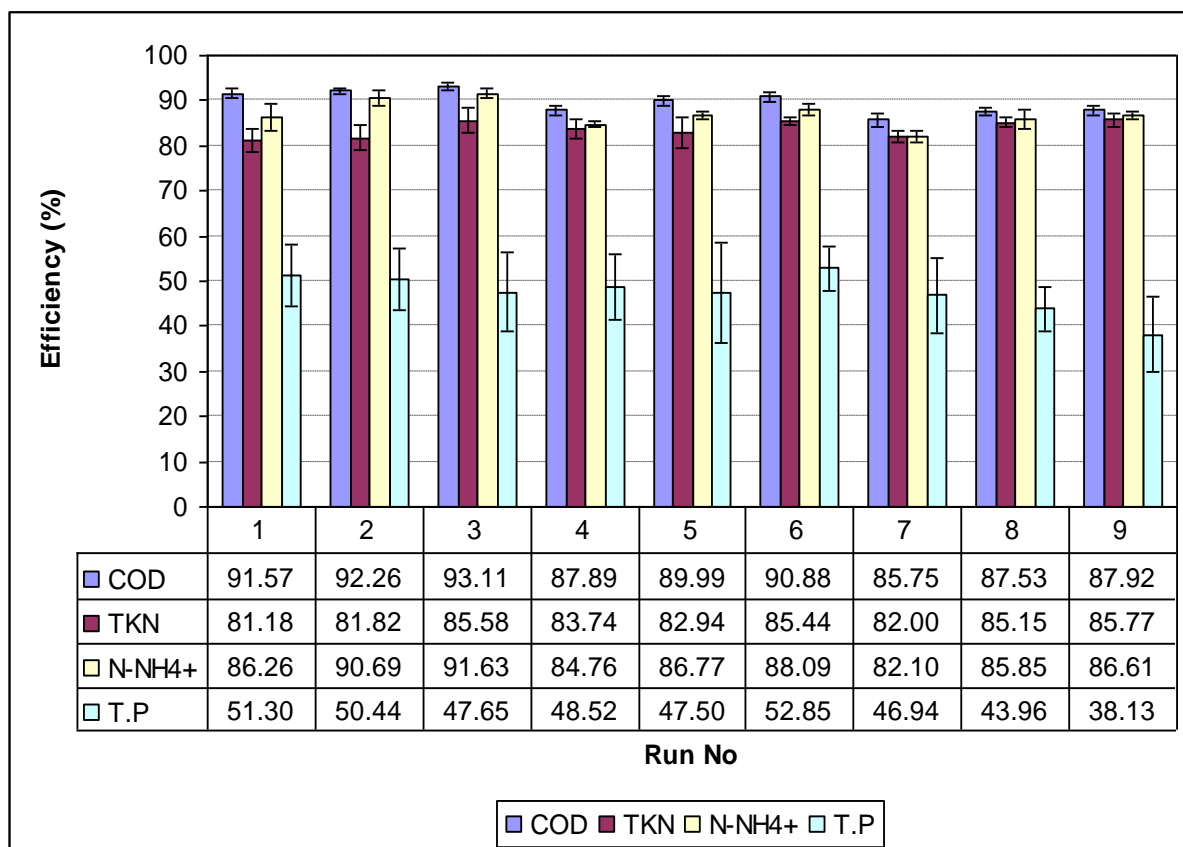


Figure 8 Removal of organic substrate in form COD, nitrogen in form of ammonium and TKN, and Tot P during the steady state runs.

The sludge in pilot is controlled to SRT 20 day and MLSS is between 2600 and 3200 mg/l. SVI was been test during experimental period, it is between 98 and 118 ml/g. These SVI values

compare with Vaiopouou et al. (2007), Jenkins et al. (1993) and show this pilot to enhanced sludge settle ability. Mean effluent MLSS concentration was less than 35 mg/l.

Fig.8 shows that the run, which led to the highest removal efficiency, was run no. 6, which COD, TKN, N-NH₄⁺, T.P removal efficiency were 90.88, 85.44, 88.09, 52.85%, respectively. Nitrate effluent was 13.56 mg/l at run no 6. However, nitrate effluent was the lowest during this study at run no 7, nitrate effluent is 10.6 mg/l. So run no 6 was the best run condition.

COD removal efficiency seems to decrease when hydraulic residence time decreases, HRT 8h is the lowest removal COD and at the highest removal, COD is 14 h. On the hand, nitrification, TKN and N-NO₃⁻ of effluents depend on influent rate and HRT. Influent rate 60: 40 is nitrification low and N-NO₃⁻ effluent low because de-nitrification in anoxic have many bsCOD. Otherwise, influent rate 80: 20% is nitrification of system high but N- NO₃⁻ of effluent high because bsCOD is not enough for de-nitrification in anoxic. TP change when the pilot change influent rate.

Conclusion

This present shows that the efficiency of this pilot scale reactor for removal COD, nitrogen, and phosphorous with HRT for domestic wastewater 10h. Effluent concentrations of the pollutions are below the National technical regulation on domestic wastewater of Viet Nam. Anaerobic, aerobic, anoxic integrated processes and two-step feed in this the present work has significant economical advantages compared to the UCT, A2O, because no internal recycle for de-nitrification is necessary.

Moreover, the sludge settle-ability characteristics is good (SVI < 120 ml/g) and enhanced clarification of the effluent. The high efficiency and economical of pilot is recorded when the pilot HRT is about 8h and two step feed is distributed 80% to anaerobic and 20% to anoxic condition.

Acknowledgement

The authors thank all staffs of environmental engineering laboratory, Ho Chi Minh City University of

Technology, Vietnam for technical support during this work.

Reference

- [1]. APHA, AWWA, WPCF. Standard methods for the examination of water and wastewater, Washington DC, USA, 1998, 2671 pp
- [2]. Cooper, P. et al (1994), Process options for phosphorus and nitrogen removal from wastewater. J. IWEM, Vol.8 (2), pp. 84 - 92.
- [3]. Ouyang, C.F. et al (2001), Optimization of enhanced biological wastewater treatment processes using step feed approach, Advanced in water and wastewater treatment technology (Molecular technology, Nutrient removal, Sludge reduction, Environmental Health), Elsevier, pp.295 – 304.
- [4]. Jenkins, D. et al., Manual on the Causes and Control of Activated Sludge Bulking and Floaming. Lewis Publisher, Washington DC, USA,1993, 193 pp
- [5]. Daigger, G.T. and Polson, S.R., Design and operation of biological phosphorus removal facilities, In: Phosphorus and Nitrogen Removal from Municipal Wastewater-Principles and Practice, Lewis Publishers, New York, 1991, pp.167-198.
- [6]. Vaiopouou, E et al, (2007), An activated sludge plant for integrated removal of carbon, nitrogen and phosphorus. Desalination, Vol. 211, pp. 192 – 199.
- [7]. Guibing Zhu et al, (2007), Development and experimental evaluation of a steady- state model for the step-feed biological nitrogen removal process. J. Chem. Eng, Vol. 15(3), pp 411 - 417.
- [8]. Guibing Zhu et al, (2007), Effect influent flow rate distribution on the performance of step- feed biological nitrogen removal process. Chemical Engineering Journal, Vol.131, pp 319 - 328.
- [9]. Ostgaard, K. et al,(1997), Anoxic biological phosphorus removal in a full scale UCT process. Wat. Sci. Technol, Vol. 31 (11), pp. 2719 – 2726.
- [10]. Wentzel, M.C. et al, (1992), Process and modeling of nitrification denitrification biological excess phosphorus removal systems- a review. Wat. Sci. Technol, Vol.26 (6), pp.59 - 82.
- [11]. Wagner, M. et al, (2002), Microbial community composition and function in wastewater treatment plants, Atonie vab Leeuwenhoek, Vol.81, pp. 650- 665.
- [12]. Metcalf & Eddy, Inc. Wastewater Engineering, treatment and reuse, 4th ed., McGraw- Hill, USA, 2003, 1819 pp
- [13]. Seviour, R.J. et al, (2003), The Microbiology of biological phosphorus removal in activated sludge systems. FEMS Microbiol. Rev, Vol. 27, pp. 99-127.
- [14]. Wanner, J. et al, (1992). New process design for biological nutrient removal. Water Sci. Tech, Vol. 25 (4/5), pp. 445- 448.

Reject Water Treatment by Improvement of Whole Cell Anammox Entrapment using Polyvinyl Alcohol/Alginate Gel

LAI MINH QUAN^{1,*}, DO PHUONG KHANH¹, DAISUKE HIRA¹, TAKAO FUJII² and KENJI FURUKAWA¹

¹ Graduate school of Science and Technology, Kumamoto University, 2-39-1 Kurokami, Kumamoto 860-8555, Japan

² Department of Applied Life Science, Faculty of Biotechnology and Life Science, Sojo University, 4-22-1 Ikeda, Kumamoto 860-0082, Japan

Abstract: Reject water treatment performance was investigated by whole cell anammox sludge entrapped polyvinyl alcohol/sodium alginate gel in the stirred tank reactor (STR). The whole experiment was conducted through Phase 1 and Phase 2 in which synthetic wastewater and modified reject water were used as feeding medium, respectively. The anammox reactor demonstrated stable and relatively high nitrogen removal rate of more than 8.0 kg-N m⁻³ d⁻¹ during the two both phases even under moderately low temperature of 25°C ± 0.5°C during the last 2 months of Phase 2. The bacterial community was identified by 16S rDNA analysis revealing the concurrent presence of KSU-1 and new kind anammox bacterium Kumadai-I after changing influent from synthetic wastewater to reject water. These results demonstrate the potential application of whole cell anammox entrapment by PVA/alginate gel for achieving stable and high-rate nitrogen removal from high ammonium with low C/N ratio contained wastewaters, such as reject water, digester liquor or landfill leachate.

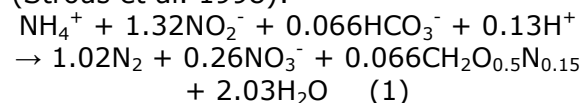
Keywords: anammox; PVA/alginate; reject water; whole cell entrapment

Introduction

The nitrogenous pollutants causing a eutrophication have attracted increasing attention recently. Conventionally, ammonium nitrogen removal from wastewater by biological processes involves well-known aerobic nitrification (ammonium NH₄⁺-N as the electron donor while oxygen as the electron acceptor) followed by anoxic denitrification (organic matter as carbon source and the electron donor and nitrate NO₃⁻-N as electron acceptor). Biological nitrogen removal is considered to be common because of its low cost and high efficiency compared to physical and chemical treatments (Van Dongen et al. 2001a, b). However, the application of conventional biological processes to wastewaters containing high ammonium and low carbon content, such as reject water, digester liquor or landfill leachate seems to be limited. Because the available biodegradable carbon in these wastewaters is insufficient for the heterotrophic denitrification, an external carbon sources such as acetate, glucose, ethanol and methanol must be added.

Recently, the new biological approach,

anaerobic ammonium oxidation – anammox, which bypasses the formation of NO₃⁻-N and converts NO₂⁻-N to dinitrogen (N₂) gas with NH₄⁺-N as the electron donor and NO₂⁻-N as the electron acceptor under anaerobic condition is recommended to remove ammonia from wastewater without addition of biodegradable carbon source. The stoichiometric conversion of NO₂⁻-N and NH₄⁺-N to N₂ gas with negligible production of cell material and nitrate is shown below (Strous et al. 1998):



However, the maintenance of a sufficient amount of anammox bacteria in the reactor, which is very important during the start-up, is not easy due to its extremely slow growth rate, low biomass yield and vulnerability to being washed out from the reactor by intensive N₂ gas bubble production. Because the anammox process produces large amounts of N₂ gas under high-rate nitrogen removal, gas bubbles become trapped in the anammox biomass, causing it to float.

Immobilization of microbial cells has received increasing interest in the field of wastewater treatment. It offers a promising potential for the improvement of bioprocess efficiency. Compared to free cell, immobilized cell has significant advantages as follow: (1) it can increase the biodegradation rate through a higher cell density; (2) the continuous process can be carried out under high loading rate without washing out of cell because it is easier to release gas bubble under mixing condition; (3) it is easy to separate liquid and solid phase in the reactor, leading to simple operation and maintenance.

A simple and economical technique of cell immobilization with PVA is PVA-boric acid method. Two potential problems with this technique, however, are the agglomeration of PVA gel beads and the toxicity of saturated boric acid to microorganisms. Another simple technique is freezing-thawing method, but it has some drawbacks such as: high energy cost for freezing at extremely low temperature of minus 20°C and negative effect of low temperature to microorganisms activity.

In this study, an improved immobilization technique using the complex of PVA and sodium alginate solution solidified by solution of NaNO₃ and CaCl₂ was applied. To our knowledge, it was the first time that continuous experiment of whole cell anammox entrapment using PVA/alginate gel has been investigated. The objectives of this study were to: (1) improve the whole cell entrapment technique using PVA/alginate gel; (2) evaluate sludge retaining capability of PVA gel bead and its characteristics; (3) investigate the start-up period and treatment capacity of immobilized anammox sludge through the continuous nitrogen removal experiment and (4) investigate the function of bacterial community on anammox performance.

Materials and methods

Seed anammox sludge

The enrichment of anammox sludge was carried out using 50 L of up flow fixed-bed reactor filled with a polyester non-woven fabric carrier at 36°C (Furukawa et al. 2005). The concentrated anammox sludge characteristics were 33.3 g-SS (suspended solid) L⁻¹ and 25.2 g-VSS (volatile suspended solids) L⁻¹, respectively.

Immobilization technique

PVA/sodium alginate was prepared with PVA-HC (100% saponification, Kuraray Co. Ltd, Osaka, Japan) at the concentration of 15% (w/v) and sodium alginate (Wako Pure Chemical Industries Ltd., Osaka, Japan) at the concentration of 2% (w/v). This mixture was heated by autoclave at 120°C for 20 minutes until dissolved. The mixture was then cooled to room temperature and 150 mL of concentrated anammox sludge was added slowly into the PVA solution to a final volumetric ratio of 1:1. The final concentration of PVA, sodium alginate and anammox sludge were 7.5% (w/v), 1% (w/v) and 1.67% (w/v), respectively. The mixture of PVA/sodium alginate and anammox sludge was dropped slowly into solidifying solution (50% w/v NaNO₃ and 2% w/v CaCl₂) by syringe to make spherical beads. PVA gel beads were then immersed in a solidifying solution for 12 h at room temperature to increase their mechanical strength ("harden" the beads).

Feeding media

A synthetic medium and reject water taken from Kumamoto East Wastewater Treatment Plant (Kumamoto, Japan) were used for Phase 1 and Phase 2, respectively. The synthetic medium was prepared according to Van de Graaf et al. (1996). The compositions of reject water contained (per liter): NH₄⁺-N, 0.8-0.85 g; NO₂⁻-N and NO₃⁻-N, not detectable; BOD₅, 0.1-0.2 g; SS, 0.02-0.1 g; pH, 7.6-9.1. Tap water was used for dilution; the concentrated NO₂⁻-N aqueous solution was artificially added to make the suitable NH₄⁺-N/NO₂⁻-N ratio for anammox of 1:1. The influent pH for anammox reactor was adjusted around 7.0 by adding 1N hydrochloric acid.

Reactor and experimental setup

The stirred tank reactor (STR) with a total volume of 1.2 L and reaction volume of 1.0 L was used in continuous experiments (Fig. 1).

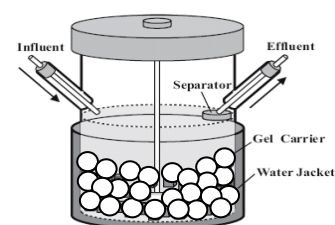


Fig. 1 Schematic of immobilized anammox reactor used for continuous treatment

300 mL of gel carriers containing anammox sludge concentration of 1.67% w/v were placed inside the reactor. The reactor temperature was maintained at 33°C, controlled thermostatically with a water jacket. The reactor pH was not controlled. The gel beads were stirred continuously at 100 rpm. Purging with nitrogen gas was used to keep the dissolved oxygen (DO) level in the influent below 0.5 mg L⁻¹.

Chemical analyses

Nitrite nitrogen (NO_2^- -N) and nitrate nitrogen (NO_3^- -N) were determined colorimetric method and UV cadmium reduction method, respectively. Ammonium was quantified based on the indophenol reaction with ortho-phenylphenol (OPP) (Kanda 1995). Absorbance, pH, and DO were measured using a spectrophotometer (U-1900, Hitachi High Technologies Corporation, Tokyo, Japan), a pH meter (F-55, Horiba Ltd, Kyoto, Japan) and a DO meter (D-55, Horiba Ltd), respectively.

Scanning electron microscope (SEM) observation of porous structures of PVA gel beads

A PVA gel was cut into 1-2 mm pieces and washed by 0.1M phosphate buffer (pH 7.4) twice for 5 min each. The PVA gel pieces were then fixed by 2.5% glutaraldehyde solution prepared with 0.1M phosphate buffer for 1-2 hours and washed by 0.1M phosphate buffer three times for 10 min each. The samples were then fixed by 1.0% OsO₄ solution prepared with 0.1M phosphate buffer and washed again by 0.1M phosphate buffer three times for 10 min each. Subsequently, the samples were dehydrated in serially graded ethanol solution at concentrations of 10, 30, 50, 70, 90 and 95% for 5-15 min each, and at a concentration of 99.5% twice for 30 min each. The samples were frozen in a freezer then dried by a freeze-drying device (JEOL JFD-300) and sputter-coated with gold for 100 s by an ion sputtering device (JEOL JFC-1100E). Finally, the samples were observed by SEM (JEOL JSM 6390LV).

DNA extraction and PCR amplification

The sludge sample was taken from the reactor on day 119 and day 200. The sludge sample was first ground with a pestle under liquid nitrogen. Meta-genomic DNA was extracted using an ISOIL kit (Wako, Osaka, Japan) according to the manufacturer's instructions. The amplification of 16S rRNA gene was performed with Phusion High-Fidelity DNA polymerase (FINNZYMES, Finland) using conversed eubacterial primers 6F (forward primer: 5'-GGAGAGTTAGATCTTGGCTCAG-3') (Tchelet 1999) and 1492r (reverse primer: 5'-GGTTACCTGTTACGACT-3') (Lane 1991). PCR was carried out according to the following thermocycling parameters: 30 s initial denaturation at 98°C, 25 cycles of 10 s each at 98°C, 20 s each at 51°C, 35 s each at 72°C, and 5 min final elongation at 72°C. The amplified products were purified using a Wizard SV Gel and PCR Clean-up System (Promega, USA).

Results and discussion

Anammox reactor operation

For the enrichment of anammox sludge, the synthetic medium was first used as the influent during Phase 1 of experiment. After successful achievement of high rate nitrogen removal, the influent wastewater was changed to modified reject water.

The STR was started-up fed with a nitrogen loading rate (NLR) of 0.2 kg-N m⁻³ d⁻¹ corresponding to 100 mg l⁻¹ T-N concentration. In phase 1 (from day 0 to day 119), the NLR was increased by adjusting the influent nitrogen concentration as well as the HRT. For the first 13 days, the NLR was increased by an increase in influent T-N concentration from 100 mg l⁻¹ to 200 mg l⁻¹ while the HRT was kept constant at 12 h. Immobilized anammox sludge quickly adapted to the increase in NLR and a maximum nitrogen removal rate (NRR) of 0.34 kg-N m⁻³ d⁻¹ was obtained. Consequently, the HRT was decreased to 8 h and T-N concentration was increased from 200 mg l⁻¹ to 400 mg l⁻¹ corresponding to maximum NLR of 1.2 kg-N m⁻³ d⁻¹. Anammox performance showed the satisfactory results with the maximum NRR of 1.0 kg-N m⁻³ d⁻¹. In this study, an ammonium removal rate of 0.5 kg NH₄-N m⁻³ d⁻¹ was considered as standard criteria for the start-up of anammox process which surpassed the

upper limit for nitrification/denitrification process, i.e. 0.3 – 0.5 kg NH₄-N m⁻³ d⁻¹ (Zhang et al. 2010a). Strous et al. (1997) reported that it took 115 and 84 days for starting up the fixed-bed and fluidized-bed reactor with NRR achieving at 1.1 and 1.8 kg-N m⁻³ d⁻¹, respectively. Zhang et al. (2010a) showed that the NRR reached 1.0 kg-N m⁻³ d⁻¹ after 56 days of operation in an up-flow reactor. Trigo et al. (2006) reported that the breakage of the granules due to an excess of agitation of 75 rpm was considered to be one of the reasons of the loss of system activity during the first 80 days, leading to the fail of quick start-up. Moreover, the activity still diminished in spite of diminishing the stirring speed in order to reduce the inhibition of shear stress on the biomass. In our study, the start-up with NRR reaching at 1.0 kg-N m⁻³ d⁻¹ was successfully achieved within 22 days and there was no breakage of PVA beads observed even under stirring speed of 100 rpm. These indicate that the start-up in this study, from our best knowledge, was the shortest compared to the others and PVA beads themselves should be considered to be the perfect granules and to protect anammox sludge against the effect of shear stress, showing that the whole cell entrapment of anammox sludge was ideal to start up a new reactor. The explanation for the quick start-up may be attributed to: (1) mild immobilization, (2) a high concentration of the initial anammox sludge of 5 g-MLSS l⁻¹ in this reactor, (3) high sludge retaining capability of whole cell entrapment technology indicated by the effluent SS as almost zero during these periods (data not shown).

After successful start-up, the NLR was increased rapidly by the means of increasing influent T-N concentration and decreasing HRT. From day 23 to the end of Phase 1 (day 119), the influent concentration of NH₄⁺-N and NO₂⁻-N was increased step wisely from 195 to 550 mg l⁻¹ and from 205 to 550 mg l⁻¹, respectively. The stable and high removal efficiencies of NH₄⁺-N and NO₂⁻-N was shown as 83% and 98%, respectively. The maximum NRR of 8.2 kg-N m⁻³ d⁻¹ was achieved at maximum NLR of 9.9 kg-N m⁻³ d⁻¹ while the average effluent NO₂⁻-N concentrations were always below 10 mg l⁻¹. The performance of anammox reactor during Phase 1

demonstrated that stable and relatively high-rate nitrogen removal was successfully established with synthetic wastewater as feeding medium.

From day 120, the reject water from Kumamoto East Wastewater Treatment Plant supplemented with NO₂⁻-N was fed to anammox reactor in order to investigate the treatability of reject water and the reactor performance with the presence of organic matter. The reactor was re-started fed with an influent T-N concentration of 330 mg l⁻¹ (5 times dilution of reject water) at HRT of 2.4h corresponding to NLR of 3.3 kg-N m⁻³ d⁻¹. During period 8 (Table 1), NLR was increased to 7.8 kg-N m⁻³ d⁻¹ with decrease in reject water dilution time, however, anammox bacteria showed the quick response to the change of NLR. At the end of this period (day 140), nitrogen removal efficiency of around 85% was obtained. Consequently, NLR was kept constant at 8.8 kg-N m⁻³ d⁻¹ during the next 28 days (period 9) to evaluate the stability of our immobilized anammox reactor. Stable anammox treatment with high nitrogen removal efficiency of 91% was obtained.

In period 10 (from day 169 to day 230), the reaction temperature was kept constant at moderately low of 25°C ± 0.2°C while NLRs were changed in the range of 8.4 – 10.2 kg-N m⁻³ d⁻¹ to investigate the treatment capacity of immobilized anammox sludge under low temperature and high nitrogen loading rate (the dilution time decreased to two). The same trend of nitrogen removal performance as seen in previous periods was observed except that effluent NO₂⁻-N concentration increased to 78 mg l⁻¹ on day 177 due to sudden decrease in temperature of 20°C. However, the treatment performance recovered quickly right after the temperature was increased to 25°C. At the end of this period, the maximum NRR of 8.5 kg-N m⁻³ d⁻¹ was successfully achieved. These results demonstrated that there was no negative effect of organic matter and moderately low temperature of 25°C on anammox activity. However, further studies should be required to make clear the effect of higher organic matter and lower temperature. The daily changes in nitrogen loading and removal rates during the whole experiment are shown in Fig. 2 and Fig. 3

Organic matter removal

The reject water used in this study was low C/N ratio with BOD_5 concentration of 100 – 210 mg l⁻¹. During steady-state period (day 169 to 230), the influent BOD_5 concentrations were measured as 60-70 mg l⁻¹ and the removal efficiencies were around 20% (data not shown). These relatively low organic matter removal efficiencies could be attributed to the presence of non-biodegradable or slowly biodegradable organic matter in the test reject water. In addition, self-decayed anammox sludge might contribute to the increase of organic carbon concentration in the reactor. However, negative effect of remaining organic matter on anammox reactor performance was not observed during Phase 2. This result might give the conclusion that anammox bacterial community can show the proper treatment capability under low organic matter concentration from reject water.

PVA gel beads characteristics

The PVA beads were ivory white color at the start of continuous experiment due to a small amount of entrapped anammox sludge. The variation in appearance was recorded using stereomicroscope after 200 days of operation (shown as below). On day 200, the PVA beads had become brownish red due to the growth of anammox bacteria on the outer layer of PVA beads.

Typical reported buoyant densities of granules are 1.03 to 1.08 g cm⁻³ (Andras et al. 1989). Reported settling velocities for granular sludge are in the range of 18 to 100 m h⁻¹ (Fukuzaki et al. 1991). In this study, the matured brownish red PVA beads had an average settling velocity of 141 m h⁻¹ (3.9 cm s⁻¹) based on the method of Ghangrekar et al. (2005), buoyant density of 1.10 g cm⁻³ and average diameter of 4 mm. An appropriate diameter of PVA beads and high settling velocity resulted in the complete retention of PVA gel beads (no wash-out of PVA gel beads) during the experiment. In addition, the PVA gel beads showed the excellent mechanical strength under mixing condition during whole experiment.

Stereomicroscopic and SEM observation of the porous structure of PVA gel beads

Fig. 3 shows the immobilized anammox sludge in PVA gel beads. Compared with

the original appearance of PVA beads, a large amount of anammox bacteria was grown on the outer and inner parts of the beads after 200 days of operation. The obvious different of amount of anammox sludge after long-term operation demonstrated that anammox sludge successfully retained in PVA gel beads and grew even near the core of beads. This resulted in the quick start-up and high nitrogen removal rate as mentioned above.

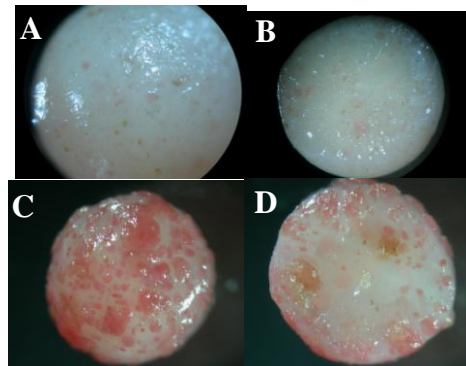


Fig. 4 Stereomicroscopic of surface and cross-section of PVA gel bead at the beginning of experiment (A, B) and on day 200 (C, D)

Scanning electron microscopic (SEM) was also carried out to observe the outer and inner structure of PVA gel beads. Many micropores, which play an important role on substrates diffusion into inner part of bead that gave an explanation of existence and growth of anammox bacteria near the core of bead, could be clearly seen.

Genomic characterization of the bacterial community

DNA extracted from the biomass sample of anammox reactor was amplified and thirty five and thirty four clones were obtained on day 119 and 200, respectively when cloning this amplified DNA fragment. The decomposition of sludge consortium was shown in Table 1.

On day 119, the anammox bacteria KSU-1 (Accession No. AB057453, Fujii et al. 2002) was identified as the dominant species, accounting for 94% (33/35) which is in agreement with previous research in our laboratory (Rouse et al. 2005). After switching influent medium to modified reject water, the new kind anammox bacteria Kumadai-I (Accession No. J.B.B 110 72-78 (2010)) and *Candidatus*

Brocadia anammoxidans (Accession No. AF375994) were detected, accounting for 26% (9/34); simultaneously, the anammox bacteria KSU-1 substantially decreased to 62% (21/34) in the consortium. However, the dominant bacterial species were still KSU-1.

It is very difficult to clearly explain the shift of bacterial communication, however, possible that they are due to the mode of enrichment, presence of organic matter, reaction temperature. The species of anammox bacteria were responsible for the adaptation of reactor to modified reject water under moderately low temperature. There appear to be two plausible explanations of our results obtained. One is that anammox bacteria in the freshwater (KSU1) were partly replaced by other organic matter-tolerant anammox strains (Kumadai-I). The other is that Kumadai-I originally existed in the inoculum and could survive and grow under existence of organic matter. Hence, it could be speculated that Kumadai-I might play an important role under existence of organic matter, while KSU-1 played a role on high-rate nitrogen removal. However, intensive studies on Kumadai-I should be investigated to make clear the mechanism of bacterial community shift.

Conclusions

The potential application of whole cell anammox entrapment by PVA/alginate gel on relatively high-rate nitrogen removal from synthetic and modified reject water was successfully achieved in this study. During phase 1 and phase 2, stable and high nitrogen removal rates of more than $8.0 \text{ kg-N m}^{-3} \text{ d}^{-1}$, which are the highest values compared to other anammox reactors using whole cell immobilization technique, were obtained. The matured brownish red PVA beads had good characteristics with the buoyant density of 1.10 g cm^{-3} , settling velocity of 141 m h^{-1} and diameter of 4 mm, leading to complete PVA beads retention during whole experiment. The switching from synthetic wastewater to modified reject water as influent led to the shift of bacterial community with the concurrent presence of new kind anammox bacteria Kumadai-I and KSU-1 in the consortium.

Acknowledgements

We would like to thank Kuraray Co. Ltd (Osaka, Japan) for their PVA material supply.

References

- [1] Andras E, Kennedy KJ, Richardson DA (1989) Test for characterizing settleability of anaerobic sludge. Environ Technol Lett **10**: 463 – 470
- [2] Fujii T, Sugino H, Rouse JD, Furukawa K (2002) Characterization of the microbial community in an anaerobic ammonium oxidizing biofilm cultured on a nonwoven biomass carrier. J Biosci Bioeng **94**: 412 – 418
- [3] Fukuzaki S, Nishio N, Nagai S (1991) The use of polyurethane foam for microbial retention in methanogenic fermentation of propionate. Appl Microbiol Biotechnol **34**: 408 – 413
- [4] Furukawa K, Rouse JD, Yoshida N, Hatanaka H (2003) Mass cultivation of anaerobic ammonium-oxidizing sludge using nonwoven biomass carrier. J Chem Eng Jpn **36**: 1163 – 1169
- [5] Furukawa K, Rouse JD, Bhatti Z, Imajo U, Ishida H (2005) Anaerobic oxidation of ammonium confirmed in continuous flow treatment using nonwoven biomass carrier. Japan J Water Treat Biol **38**: 87 – 94
- [6] Ghargrekar MM, Asolekar SR, Joshi SG (2005) Characteristics of sludge developed under different loading conditions during UASB reactor start-up and granulation. Water Res **39**: 1123 – 1133
- [7] Kanda J (1995) Determination of ammonium in sea water based on the indophenol reaction with o-Phenylphenol (OPP). Water Res **29**: 2746 – 2750
- [8] Lane J (1991) 16S/23S rRNA sequencing. In Nucleic acid techniques in Bacterial Systematics ed. Goodfellow, M. Chichester, UK, Wiley 115 – 148
- [9] Rouse JD, Fujii T, Sugino H, Tran H, Furukawa K (2005) PVA-gel beads as a biomass carrier for anaerobic oxidation of ammonium in a packed-bed reactor. CD-ROM, In: Proceedings of 5th International Exhibition and Conference on Environmental Technology, Heleco '05, Athens, Greece. http://library.tee.gr/digital/m2045/m2045_rose.pdf
- [10] Strous M, Van Gerven E, Zheng P, Gijs Kuenen J, Jetten MSM (1997) Ammonium removal from concentrated waste streams with the anaerobic ammonium oxidation (anammox) process in different reactor configurations. Water Res **31**: 1955 – 1962
- [11] Strous M, Heijnen JJ, Kuenen JG, Jetten MSM (1998) The sequencing batch reactor as a powerful tool for the study of slowly growing anaerobic ammonium-oxidizing microorganisms. Appl Microbiol Biotechnol **50**: 589 – 596

- [12] Tchelet R, Meckenstock R, Steinle P, Van der Meer J (1999) Population dynamics of an introduced bacterium degrading chlorinated benzenes in soil column and in sewage sludge. *Biodegradation* **10**: 113 – 125
- [13] Trigo C, Campos JL, Garrido GM, Mendez R (2006) Start-up of the Anammox process in a membrane bioreactor. *J Biotechnol* **126**: 475 - 487
- [14] Van Dongen LGJM, Jetten MSM, Van Loosdrecht MCM (2001a) The combined Sharon/Anammox process – A sustainable method for N-removal from sludge water. IWA Publishing, Alliance House, London, 2001a
- [15] Van Dongen LGJM, Jetten MSM., Van Loosdrecht MCM. (2001b) The Sharon-Anammox process for treatment of ammonium rich wastewater. *Water Sci Technol* **44**: 153 – 160
- [16] Van de Graaf AA., De Bruijn P, Robertson LA., Jetten MSM., Kuenen JG (1996) Autotrophic growth of anaerobic ammonium oxidizing microorganisms in a fluidized bed reactor. *Microbiology* **142**: 2187 – 2196
- [17] Zhang L, Yang J, Ma Y, Li Z, Fujii T, Zhang W, Nishiyama T, Furukawa K (2010a) Treatment capability of an up-flow anammox column reactor using polyethylene sponge strips as biomass carrier. *J Biosci Bioeng* **110**: 72 - 78
- [18] Zhang L, Yang J, Furukawa K (2010b) Stable and high-rate nitrogen removal from reject water by partial nitrification and subsequent anammox. *J Biosci Bioeng* **110**: 441 - 448

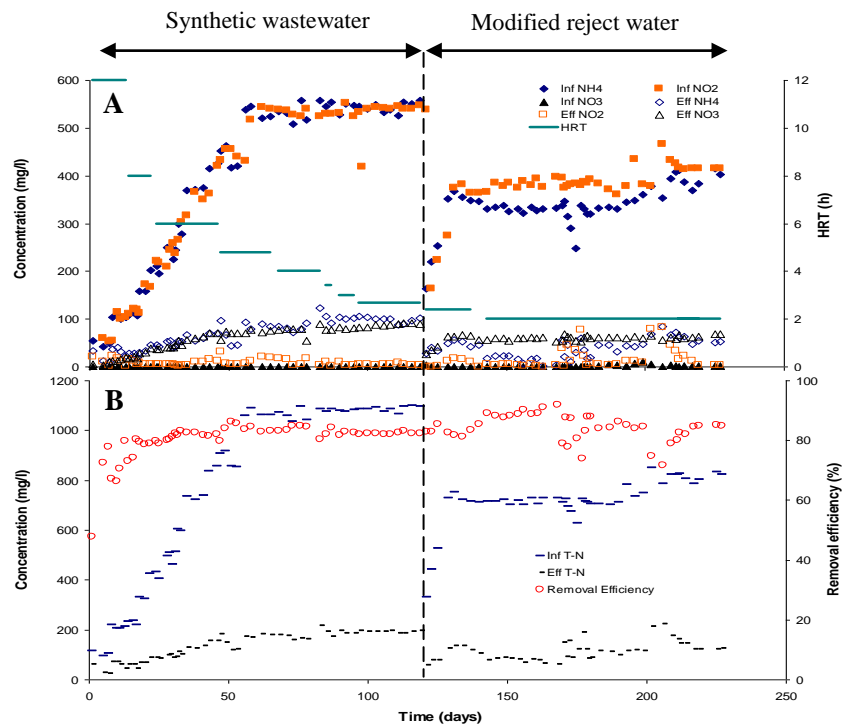


Fig. 2 Time courses of influent and effluent concentrations of nitrogenous compounds (A) and total nitrogen (B)

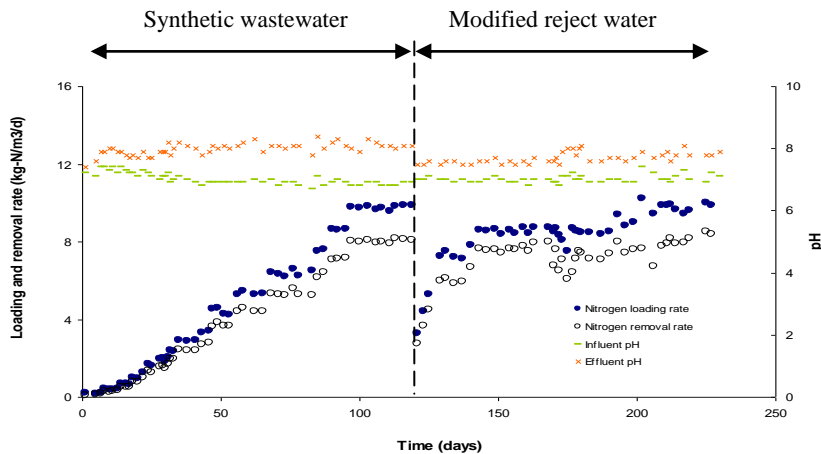


Fig. 3 Daily changes in nitrogen loading, removal rates, influent and effluent pH

Table 1 Results of bacterial community analysis during different phases in the anammox reactor

OUT	Taxon	Accession	Identity	Day 119 (SW)	Day 200 (MRW)
1	Planctomycete KSU-1	AB057453	100-99	33 (33/35)	21 (21/34)
	Kumadai-I	J.B.B 110 72-78 (2010)	100-99		
2	<i>Candidatus Brocadia anammoxidans</i>	AF375994	95-94	0 (0/35)	9 (9/34)

EFFECT OF PAPER MILL EFFLUENTS ON THE RIVER WATER CHEMISTRY: A CASE STUDY OF RIVER GODAVARI AT RAJAHMUNDRY

K Balakrishna¹, G P Gurumurthy¹, A M Shiller² and G Mugeraya³

¹ Department of Civil Engineering, Manipal Institute of Technology, Manipal University, Manipal 576104, India. E-mail: k.balakrishna@manipal.edu

² Department of Marine Science, University of Southern Mississippi, 1020 Balch Blvd., Stennis Space Center, Mississippi 39529-9904, USA

³ Department of Chemical Engineering, National Institute of Technology Karnataka, Surathkal, Mangalore 575025, India

Abstract: Bimonthly sampling was done from the river Godavari, the largest in peninsular India, over a period of two years to measure the major ion and heavy metal composition to elucidate the effect of paper mill effluents on the river chemistry. Six sampling stations are spaced in a stretch of 6 km. Major ions and silica variations in the river convey their dominant sources from rock assemblages comprising of Ca and Mg rich basalts and sodic plagioclase rich granitic gneiss. The magnification of major ion and heavy metal (As, Zn, Cd, Co, Ni, Cu, Mn and Pb) composition in two stations near the paper mill (station PM) and VIP ghat (station VIP) compared to the rest of the stations, clearly indicates the influence of paper mill effluents and anthropogenic activities on the river chemistry in these stations. Though the chemical composition is magnified in station PM, it is getting diminished downstream, because of the self-purification ability of the river. It could be due to fractionation of elements from dissolved to particulates involving processes like complexation and adsorption of metals on to the inorganic ferro-magnesium oxides.

Keywords: Paper mills, effluents, major ion, heavy metal, Godavari river, spatial variability

1. Introduction

Chemical weathering of rocks is the primary contributor of major ions (Na, K, Ca, Mg, HCO₃, Cl, NO₃, PO₄, SO₄), silica and trace metal concentrations to the river (Berner and Berner 1996). Atmospheric (sea salts transported into the river via rains) and anthropogenic sources like industrial and agricultural effluents, domestic sewage and saline soils are the other chief sources to the river.

Anthropogenic activities have dominated the major ion, organic carbon and trace metal chemistry of many European and North American rivers (Yang et al 1996; Flintrop et al 1996; Gaillardet et al 1999). Indian rivers are also affected by anthropogenic sources but reliable data on major ions, trace metals and organic carbon in the peninsular Indian rivers are few (Sarin et al 1989; Sarin et al

1992; Krishnaswami et al 1999; Singh et al 2005; Das et al. 2005). Balakrishna and Probst 2005 reported the sources and fluxes of organic carbon transport in the Godavari river to the adjacent Bay of Bengal, and Balakrishna et al., 2006 reported the spatial and temporal variability of dissolved organic carbon in the Godavari river at Rajahmundry. Recently, Jha et al 2009 reported the chemical weathering and associated carbon dioxide consumption of the Godavari river basin for the entire river catchment. Effect of paper mills and other industries located in the lower catchment of river Godavari on the river chemistry is not yet reported. Therefore, this study is attempted with 47 samples collected near the river mouth, as a prelude to more detailed studies in the entire Godavari river catchment planned in future projects.

The objectives of the study are:

- i) To identity the natural and anthropogenic sources of major ions and trace metals into the Godavari river at Rajahmundry
- ii) To understand the role of paper mill effluents and other anthropogenic sources on the chemistry of the Godavari river at Rajahmundry

Subramanian 1988; Gupta et al 1997; Sarin et al 2002; Balakrishna and Probst 2005).

2. Materials and Methods:

The river water samples were collected at five stations in the Godavari at Rajahmundry (Fig. 1). The sampling stations starting from the upstream end to the downstream are located in a six kilometer stretch.

1. Upstream of the paper mill (US)
2. Location immediately downstream of the effluent tanks of paper mill (PM)
3. Downstream of the paper mill (DS)
4. PushkarGhat (Place for holy dip and recreation; PG)
5. VIP Ghat (Bathing, washing and recreation; VIP)

Surface water samples are collected from the bow of a motorboat approximately from the centre of the river. Water samples are collected in pre-cleaned polypropylene (PP) bottles (that is kept soaked in quartz double-distilled water for at least two days) after thoroughly rinsing in the ambient water. Parameters like temperature, pH, conductivity, dissolved oxygen (DO) are measured on-site using a HACH make multiparameter apparatus. Alkalinity is measured on-site by alkalinity test kit (Merck make). Samples collected for major ions are processed within few hours of collection by filtering through 0.45 μ m pore size Millipore filters held in a polycarbonate Sartorius filter holder. Sodium and potassium are measured by a Flame Photometer (ELICO CL 22D), Ca and Mg by Flame Atomic Absorption Spectrophotometer (GBC 932 Plus), Cl, NO₃, SO₄ ions by Ion Chromatograph (Compact IC, Metrohm) and SiO₂ by UV Spectrophotometer. The precision of cations, anions and silica are based on several repeat measurements, which are within 5%. Dissolved trace metal measurements are made by ICP-MS at two laboratories, the first at the DST National Facility of National Geophysical Research Institute (NGRI), Hyderabad and the second at the Centre for Trace Analysis at University of Southern Mississippi, USA. The accuracy and precision of major ions, DOC and tracemetsals are based on

1.1 Study Area:

Godavari ranks 34th and 32nd in terms of catchment area and water discharge respectively, amongst the 60 largest rivers of the world (Balakrishna and Probst 2005, Gaillardet et al 1999). The Godavari basin (16-18° N and 75-83.3° E) covers an area of 313,147 km² in the central and southern part of the Indian sub-continent and discharges 105 km³ of water annually to the Bay of Bengal. Godavari originates in the Western Ghâts near Nashik in Maharashtra and extends for 1465 km before emptying into the Bay of Bengal. Around 50% of the Godavari basin is under agricultural cover, which uses abundant fertilizers and pesticides. The climate over the basin is primarily semi-arid (10-45°C) with annual rainfall of 1185 mm.

Rajahmundry, one of the largest cities of coastal Andhra Pradesh is situated in the left bank of Godavari, about 75 km upstream of the confluence of the river into the Bay of Bengal. The entire population of Rajahmundry is dependent on Godavari for drinking water. There are many industries located in Rajahmundry, of which Andhra Pradesh Paper Mills is prominent (Fig 1). The mill discharges the treated effluents into the tanks dug out on one of the islands in the centre of the river ~5 km upstream of Rajahmundry town. The discharges are observed to overflow into the river at all periods of the year. The Godavari waters are utilized for irrigating about 10 lakh acres in East Godavari and West Godavari districts of Andhra Pradesh, by means of Sir Arthur Cotton barrage located at Dowlaishwaram, about 10 km downstream of Rajahmundry. Godavari river basin includes major geological formations such as tertiary Deccan basalts (48%) Archean granites (39%) Precambrian and Gondwana sedimentary rocks (11%) and recent alluvial cover (2%) (Bikshamand

several repeat measurements, and are within 10%.

The discharge data for the year 2003-04 and 2004-05 is obtained from the

Irrigation Department of Government of Andhra Pradesh at Dowlaishwaram, ~10 km downstream of Rajahmundry.

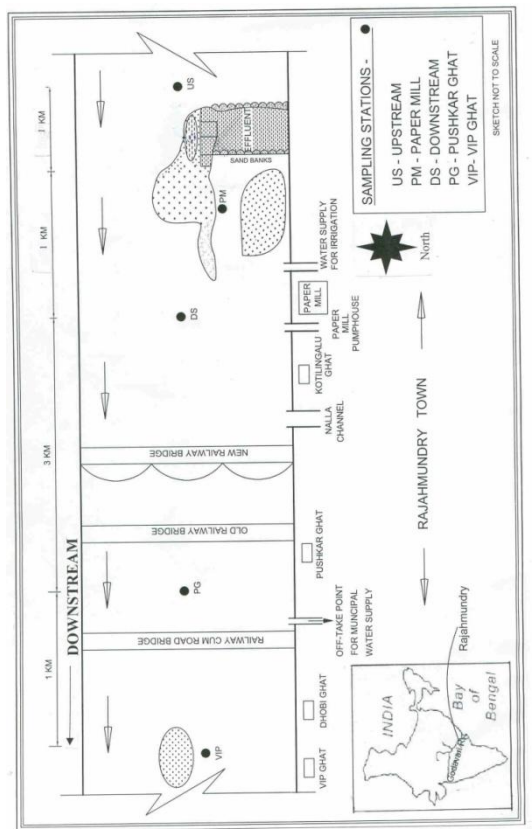


Figure 4 Location map of the sampling stations

Figure1: Study area showing sample locations

3. Results and discussion:

3.1 Physico-chemical parameters:

The physico-chemical and major ion data is presented in the Table 1. River surface temperature varies between 24.6°C and 39.3°C; the higher temperature is recorded in summer (May 2004), at station PM, while the lowest is in winter (Jan 2004) at station US. The pH of water samples collected at Rajahmundry varies from 6.9 to 9.3 with an average of 7.8; with higher values recorded at VIPGhat and lower values recorded at station paper mill (PM) and downstream of paper mills (DS) (Fig 2). Most of the sample shows neutral to alkaline nature, suggesting the presence of basic rock types in the catchment. The conductivity of the samples collected ranges from 99 to 279 μ S/cm with an average of 151 μ S/cm.

The conductivity measurements shows river water is diluted and draining igneous or metamorphic lithology. Conductivity ranges between 99 μ S/cm and 277 μ S/cm for the stations US, DS, PG and VIP, while in the station PM, conductivity ranges between 182 μ S/cm and 2860 μ S/cm (Fig.2). The high conductivity in PM is due to the abundant presence of major ions that are used in the paper manufacturing process and that are discharged with the effluents (Dara 1998). There is no significant variation seen in dissolved oxygen concentrations in the river spatially and temporally. The values range between 6 mg/l and 9 mg/l (Fig 2), which indicate oxidizing conditions in the river. This is an indication of lesser organicpollutants and degradable wastes in the river water during the study period.

The total dissolved solids (TDS) in samples ranges from 94 mg/l to 232 mg/l with an

average of 145mg/l ($n=39$). However, at station PM the total dissolved solids ranges from 318mg/l to 1879mg/l; with an average of 881 mg/l ($n=7$) which receives effluents from the paper mill located just upstream of the sampling station. The total cation (TZ^+) concentrations ranged between 1 meq/l and ~40 meq/l with the highest end member belonging to station PM. Among the cations, Ca is the dominant cation contributing ~40% of the total cations, followed by Mg, Na and K. Among the anions HCO_3^- is the dominant anion, followed by Cl and NO_3^- .

If we look in to the standard deviation of measured dissolved major ion chemical composition of river Godavari at Rajahmundry (Table 1), the station PM shows maximum deviation from the mean value, suggesting local addition of pollutants to the chemical composition over time. The major ion composition at station PM is increasing as the monsoon diminishes. Similar trend of variation was also observed for the dissolved metals.

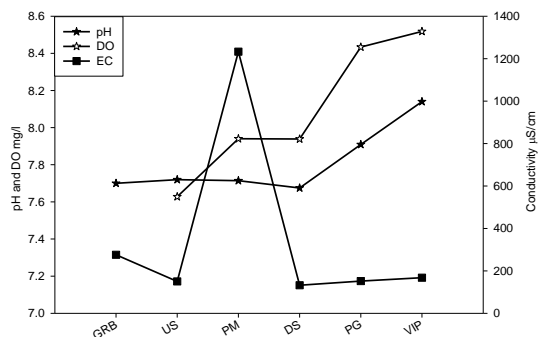


Figure 2. Variation of pH, conductivity and DO in the river Godavari at Rajahmundry different stations (GRB: Godavari river basin data from Jha et al 2009)

3.2 Major ion chemistry of Godavari at Rajahmundry:

The anions, cations and Si are plotted in ternary diagrams (Fig 3a and Fig 3b) to get an overview of the dominances of specific anions and cations in the samples and to derive the type of weathering prevailing in the catchment. In both these ternary plots, station PM stands separated from the rest, oriented more towards the $Cl+SO_4$ and $Na+K$ end members. Its source could be from the Na, Cl and

SO_4 -bearing compounds used in the processing of paper pulp (Dara 1998). Two stations at VIP ghat collected during January 2004 and January 2005 are separated from the rest, enriched in Mg and a relatively higher concentration of Cl. This sample is collected close to the riverbank, which is extensively used for bathing and washing clothes, with abundant use of Mg and Cl bearing detergents. In the remaining samples, plots fall between Si and HCO_3^- apex (Fig. 3a) with approximately 37% contributed by Si. The source of Si could be from the granite-gneiss-sandstone terrain in the lower catchment of the Godavari, which is also the largest contributor of Godavari's discharge at the Bay of Bengal. Pekka et al 2004 observed similar trends in world's rivers draining granitic, gneissic and sandstone lithologycatchment(data from Meybeck et al 1992). Carbonate weathering is also evident in the catchment as these plots show samples rich in Ca, Mg and HCO_3^- (Fig 3a, 3b). Das et al 2005; Ramam and Murty 1997 report presence of limestones, alkaline soils, augite pyroxene and calcic plagioclase rich basalts and carbonate patches in granitic gneiss in the catchment. The second most abundant anion after HCO_3^- is Cl (in eq units) as against SO_4 prevailing in Himalayan rivers (Singh et al 2005; Dalai et al 2002). This is an indication of the dry weather prevailing in the river catchment, leading to the enrichment of Cl over SO_4 and the continued contribution from atmosphere. Studies made in the catchments of Krishna and other west flowing rivers originating in Deccan traps have also found Cl as the second most abundant anion (Das et al 2005). The average Cl/Na ratio of studyarea in the lower reaches of Godavari, is 0.43. This value is lesser than the previously reported values for the same river basin (Chakrapani and Subramanian 1990) and it is similar to the findings of Jha et al 2009. The ratio suggests the prevailing weathering source of Na in the catchment. The average Cl/Na ratio for the station PM (0.91) is higher than other stations of the river. The higher ratio of Cl/Na in that particular station reveals discharge of chloride bearing pollutant from the paper mills. This study is attempted to quantify the percent contributions of major ions

individually from the atmosphere, weathering (Na, Ca, Mg, Cl, SO₄), and saline soils+anthropogenic sources (Na, Cl) using the rainfall data available for Deccan traps and Western Ghats (Parashar et al 1996; Das et al 2005). The correction applied to calculating the source contribution is explained in Das et al 2005; Jha et al 2009. Sources of Na from atmosphere ranges between 15-18% and anthropogenic sources between 20-29% for stations US, DS, PG and VIP. The highest contribution from anthropogenic sources is from station VIP (29%). This confirms the influence of unchecked human bathing and washing using detergents along the riverbank. This observation is further supported by relatively high pH (averaging 8.6 during dry seasons). pH>8.3 confirms the presence of carbonates in natural waters (Drever 1997). In the case of Godavari river at station VIP, the carbonates could have its source from the detergents. Station PM receives majority of Na from the sodium bearing compounds used in the manufacturing of paper, which are let out as effluents.

To elucidate the SO₄ component from anthropogenic sources, Cl+SO₄vs Na plot is made (Fig 4), which shows marked linearity for station PM, indicating that SO₄, Cl and Na leach uniformly into the river from a common source, typical of anthropogenic inputs. In the rest of the samples, correlation is not very significant, indicating that SO₄ originates from chemical weathering.

3.3 Spatial variations in major ions

Station PM contributes an average of 37 times more Cl and 18 times more Na+K to the Godavari river than the rest of the samples throughout the year. Further, Ca is 7 times as high, and SO₄ 4.6 times higher than the rest of the samples. This is an indication that these compounds used for paper manufacturing has not been treated to the expected levels (Fig. 5 and 6). However, these signals are drastically reduced to the baseline in the station DS and station PG, approximately 2 km and 5 km downstream respectively, from station PM due to dilution along the course of the river, precipitation of Na and K

compounds, and uptake by the biota. At station VIP, Na+K, Cl+SO₄ and Mg show large variations in concentration at different periods. This station is polluted by the use of abundant detergents bearing Mg, SO₄ compounds for cleansing the clothes and body in the banks of the river. Further, the Andhra Pradesh Tourism Development Corporation has set up water sports near this station, which are frequented with tourists who are contributing to the pollution in the river. Rest of the stations (US, DS and PG) does not show significant spatial variations in major ions.

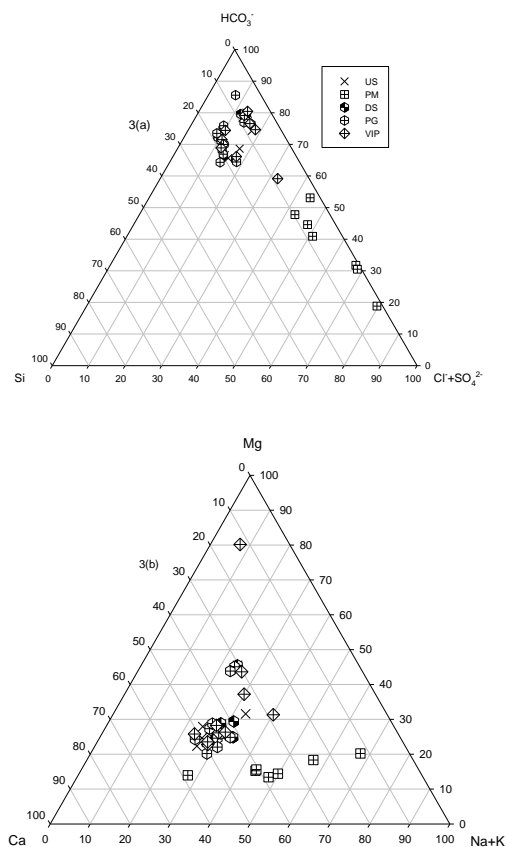


Figure 3: Ternary plot of anions (3(a)) and cations (3(b)) in the river Godavari at Rajahmundry

3.4 Dissolved metals in the Godavari river at Rajahmundry:

The average of dissolved metals (As, Zn, Cd, Co, Cr, Pb, and Ni) concentrations at five different sample stations are tabulated in the Table 1. The station PM shows higher concentration of heavy metals in all the sampling periods. The higher concentration of metals in this sample

Table 1: Major ion and dissolved heavy metal data of river Godavari at Rajahmundry

	T	pH	EC	DO	Na	K	Ca	Mg	HCO ₃	Cl	NO ₃	SO ₄	Si	TDS	As	Zn	Co	Ni	Cu	Pb	Cd	Cr
Upstream of Paper Mills	°C		µS/cm						mg/l													
Mean	29	8	150	8	10	2	31	13	92	7	0	8	8	144	288	2776	64	449	1288	139	11	327
Median	31	8	142	8	9	2	32	12	85	7	0	7	9	136	282	2192	32	232	1232	67	9	221
Std. Dev.	3	0	49	1	3	1	10	5	22	2	0	3	3	31	58	1827	69	419	459	146	13	324
Min	25	7	104	6	8	1	18	8	67	4	0	5	4	107	215	945	24	146	636	0	3	105
Max	32	8	277	9	17	3	48	21	128	10	1	14	11	201	412	6049	222	1329	1880	444	47	1073
Paper Mills																						
Mean	31	8	1233	8	204	10	211	70	242	261	0	35	9	881	1771	3169	400	1509	2119	191	18	219
Median	31	8	824	8	69	6	125	35	195	107	0	25	8	565	1021	1845	269	919	1864	191	14	146
Std. Dev.	4	1	1011	1	192	7	158	63	126	221	0	30	4	622	1844	2968	445	1327	949	184	11	100
Min	26	7	182	7	48	4	64	16	122	65	0	14	5	318	543	695	65	333	1174	31	8	130
Max	39	9	2860	9	504	22	454	177	458	559	1	102	14	1879	5650	8560	1383	4114	4065	561	35	336
Downstream of Paper Mills																						
Mean	30	8	132	8	9	2	26	12	84	6	0	7	8	131	268	1548	56	295	1032	87	13	254
Median	31	8	132	8	9	2	25	12	79	5	0	6	9	128	252	1340	29	202	935	68	5	186
Std. Dev.	2	1	22	1	1	1	6	5	16	2	0	1	3	21	37	714	64	187	333	85	23	199
Min	26	7	102	6	7	1	18	7	67	4	0	5	4	105	228	744	24	168	715	0	1	106
Max	32	8	163	9	11	3	36	21	116	9	1	9	11	174	347	2695	210	703	1672	284	69	706
Pushkar Ghats																						
Mean	30	8	152	8	10	2	32	13	92	6	0	8	7	143	288	2141	68	345	1091	118	5	326
Median	31	8	154	9	10	2	28	10	92	6	0	7	9	146	273	1541	33	221	978	97	4	220
Std. Dev.	3	1	48	1	2	0	10	5	23	2	0	3	3	30	50	1779	63	214	323	83	3	261
Min	27	7	101	6	8	2	22	6	55	3	0	5	4	94	238	124	24	179	743	18	2	116
Max	34	9	279	9	15	2	52	23	122	9	1	13	11	195	392	5038	202	815	1657	297	12	827
VIP Ghat																						
Mean	30	8	168	9	13	2	33	27	96	10	0	9	7	162	406	1158	95	361	1242	96	12	236
Median	31	8	159	9	10	2	33	16	92	7	0	8	8	154	300	1124	62	314	1250	78	7	196
Std. Dev.	2	1	59	2	7	1	11	37	21	9	0	3	3	44	199	878	80	177	377	88	19	185
Min	27	7	100	6	6	1	22	6	67	5	0	5	4	105	258	152	25	170	728	0	2	82
Max	34	9	268	13	29	3	59	129	122	34	0	13	11	233	852	3115	258	701	1813	307	65	684

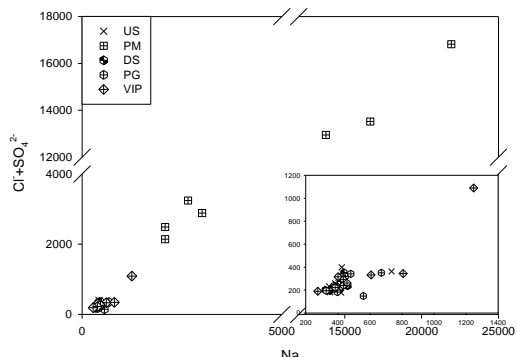


Figure 4: Na vs $\text{Cl}+\text{SO}_4$ ($\mu\text{eq/l}$) plot of river Godavari at Rajahmundry

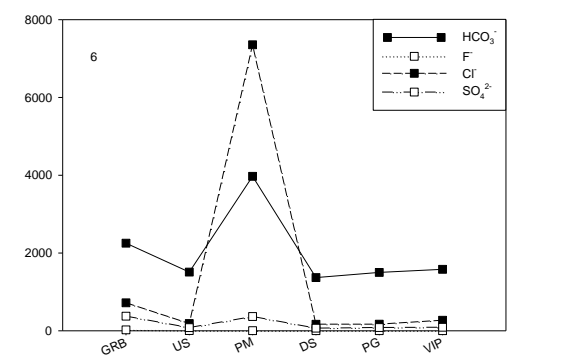
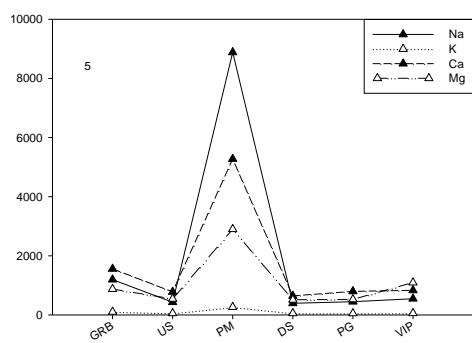


Figure 5 and 6: Variation of major cations (5) and anions (6) among the samples at Rajahmundry, Godavari river

station could be attributed to discharge of effluent water to the river water (Fig 7). Although magnified concentrations of heavy metals is observed at this station, the metal concentration was diluted one kilometer downstream of the paper mills (station DS). It could be explained by biogeochemical conditions prevailing in the catchment. The conditions include redox reactions between the bed sediment or adsorption/desorption reactions mediated by other biogeochemical conditions in the aquatic

environment. Again the concentrations of metals are getting slightly increased at station VIP, four kms downstream of paper mills. This could be due to discharge of domestic and sewage effluents in to the river water. Further studies on the sediment metal chemistry is needed to explain the variability of these metals in the river catchment.

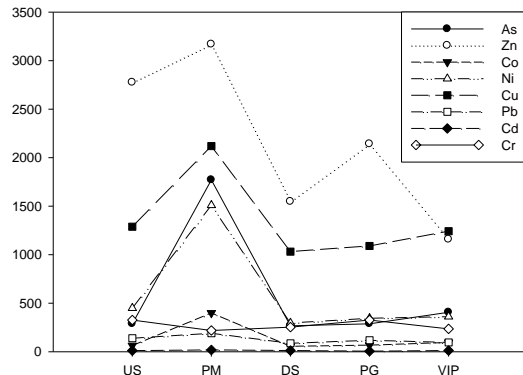


Figure 7 Variation of metals among the samples at Rajahmundry, Godavari river

4. Conclusions

The major ion chemistry of the Godavari river is mainly controlled by chemical weathering of rocks as indicated by the alkaline nature of the river, dominant presence of Ca, Mg and HCO_3^- ions and an average TDS of 145 mg/l characteristic of a rock source. The proportions of silica, $\text{Na}+\text{K}$, Ca and Mg points its source to a mixture of lithological assemblages of basalt, granite-granodiorite, limestones, and other sedimentary rocks that are spread out in its huge catchment area. Spatial variations pointed out two sampling stations PM and VIP that showed major ion concentrations and trace metals higher than the rest of the samples. The station PM receives treated effluents from the paper mill with concentrations 4.6 (SO_4^{2-}) to 37 times (Cl^-) higher than that of the river. However, their levels reach the average of the rest of the samples a couple of kilometers downstream. Studies on sediment geochemistry are needed for better understanding of the particle-water interactions of major ions and trace metals.

Acknowledgements

The Department of Science and Technology (DST) is thanked for the financial support extended to KB under DST Young Scientist Research Project (SR/FTP/ESA-14/2002) at NITK Surathkal. Mr.SubrahmanyBhat, CMFRI, Mangalore is thanked for help in the silica analysis. Thanks to Ms SharmilaSuvarna, Ms. V J Deepa and Mr.IttaArun for help in the field trip and processing of samples. NITK's TIFAC-CORE is thanked for providing laboratory facilities.

References:

- [1] Balakrishna K and Probst, J. L (2005). Organic carbon transport and C/N ratio variations in a large tropical river: Godavari as a case study, India. *Biogeochemistry*.73, 457-473.
- [2] Balakrishna K (2006).Natural and anthropogenic factors controlling the dissolved organic carbon concentrations and fluxes in a large tropical river, India.*Env.Monit.and Assess.*,v.122, pp.355-364
- [3]Berner E K and Berner R A(1996). Global Environment: Water, Air and Geochemical cycles. Prentice Hall, New Jersey.
- [4] Biksham, G., Subramanian, V., 1988. Nature of solute transport in the Godavari Basin,India. *Journal of Hydrology* 103, 375-392.
- [5] Chakrapani GJ and Subramanian V (1990). Rates of erosion and sedimentation in the Mahanadi River Basin, India.*Chemical Geology*, 81, 241-253.
- [6] Dalai T K et al(2002). Major ion chemistry in the headwaters of the Yamuna river system: Chemical Weathering, its temperature dependence and CO₂ consumption rates. *Geochim.Cosmochim.Acta* 66, 3397-3416.
- [7] Dara S S 1998. A text book of environmental chemistry and pollution control, pp.242. S Chand & Co, New Delhi.
- [8] Das A et al(2005). Chemical weathering in the Krishna Basin and Western Ghats of the Deccan Traps, India: Rates of basalt weathering and their controls. *Geochim.Cosmochim.Acta* 69, 2067-2084.
- [9] Drever J I (1997). The geochemistry of natural waters: Surface and groundwater environments, Prentice Hall, New Jersey.
- [10] Flintrop Cet al (1996). Anatomy of pollution: rivers of North Rhine, Westphalia, Germany.
- [11] Gaillardet J et al (1999). Global silicate weathering and CO₂ consumption rates deduced from the chemistry of large rivers. *Chem. Geol.* 159, 3-30.
- [12] Gupta L P et al (1997). Biogeochemistry of particulate organic matter transported by the Godavari river, India. *Biogeochemistry*. 38, 103-128.
- [13] Jha P K (2009).Chemical weathering and associated CO₂ consumption in the Godavari river basin, India, *Chemical Geology*, 264, 364-374.
- [14] Krishnaswami S et al (1999). Silicate weathering in the Himalaya: Role in contributing to major ions and radiogenic Sr to the Bay of Bengal. In: Somayajulu, B.L.K. (Ed.), *Ocean Science: Trends and Future Directions*, pp. 23-51. Indian National Science Academy and Akademia International, New Delhi.
- [15] Meybeck M et al (1992). Rivers In Water Quality Assessments: A Guide to use of biota, sediments and water in environmental monitoring (ed. Chapman, D), pp. 239-316. Chapman and Hall, Cambridge, UK.UNESCO/WHO/UNEP.
- [16] Parashar DC et al (1996). Chemical composition of precipitation in India and Nepal: A preliminary report on Indo-Swedish project on atmospheric chemistry. Report CM-90. Department of Meteorology, Stockholm University.
- [17] Pekka L et al (2004).Geochemistry of the Kola River, northwesternRussia.*Applied Geochemistry*. 19, 1975-1995.
- [18] Ramam PK and Murthy V N(1997). Geology of Andhra Pradesh.pp. 245, Geological Society of India, Bangalore.
- [19] Sarin MM et al (1989). Major ion chemistry of the Ganga-Brahmaputra river system: Weathering processes and fluxes to the Bay of Bengal. *Geochim.Cosmochim.Acta* 53, 997-1009.
- [20] Sarin MM et al (1992). Major ion chemistry of the Ganga source waters: Weathering in the high altitude Himalaya. *Proc. Ind. Acad. Sci. Earth Planet. Sci.* 101, 89-98.
- [21] Sarin M M (2002). Significance of riverine carbon transport: A case study of a large tropical river, Godavari, India, *Science in China (Series C)*. 45, 97-108.
- [22] Singh SK et al (2005). Chemical erosion in the eastern Himalaya: Major ion composition of the Brahmaputra and δ¹³C of dissolved inorganic carbon. *Geochim.Cosmochim.Acta* 69, 3573-3588.
- [23] Yang C K et al (1996). Chemical dynamics of the 'St Lawrence' riverine system: δD_{H2O}, δ¹³C_{DIC}, δ³⁴S_{sulphate} and dissolved ⁸⁷Sr/⁸⁶Sr. *Geochim.Cosmochim.Acta* 60, 851-866.

COMMUNITY RESPONSE TO TRANSPORTATION NOISES IN VIETNAM

THU LAN NGUYEN¹, QUANG NGUYEN HUY¹, TAKASHI YANO¹, TSUYOSHI NISHIMURA², TETSUMI SATO³ and TAKASHI MORIHARA⁴

- 1 *Graduate School of Science and Technology, Kumamoto University, 2-39-1 Kurokami, 860-8555 Kumamoto, Japan; Tel: +81 96 342 3560; e-mail: linh2lan@gmail.com, nhuyquang@yahoo.com and yano@gpo.kumamoto-u.ac.jp.*
 - 2 *Graduate School of Engineering, Sojo University, 4-22-1 Ikeda, 860-0082 Kumamoto, Japan; Tel: +81 96 326 3605; e-mail: nisimura@cis.sojo-u.ac.jp*
 - 3 *Faculty of Engineering, Hokkai Gakuen University, Minami 26-Jo, Chuo-ku, 064-0926 Sapporo, Japan; Tel: +81 11 841 1161; e-mail: sato@arc.hokkai-s-u.ac.jp*
 - 4 *Ishikawa national College of Technology, Kita Nakajo Ta-1, Tsubata, Kahoku, Ishikawa Prefecture, 929-0392; Tel:+81-76-288-8185; email: mail:morihara@ishikawa-nct.ac.jp*
-

Abstract: To formulate Vietnamese and global noise policies, community response to transportation noise has been investigated in Vietnam. Two large-scale socio-acoustic surveys on community response to road traffic noise were conducted first and then two other surveys on the impact of aircraft noise. In total, 3033 and 2900 responses were obtained in Ho Chi Minh City and Hanoi, respectively. The dose-response curve for road traffic noise almost coincided in the position of the EU's data curve, while the curve for aircraft noise was slightly higher than EU's. For the same noise exposure, the noise annoyance in Hanoi was higher than that in Ho Chi Minh City because of the lower background noise level in Hanoi.

Keywords: *community response, road traffic noise, aircraft noise, dose-response relationship*

Introduction

Noise effects in developing countries are continuing to grow because of rapid urbanization in addition to bad planning and poor social infrastructure. However, environmental noise in these countries is insufficiently controlled because of the unavailability of adequate data. The data are insufficient to propose dose-response relationships and this therefore leads to the establishment of inappropriate criteria. Therefore, there is an urgent need to accumulate a reliable dataset to establish the relationship between noise and community annoyance in developing countries for both national and global noise management.

Vietnam is the second most populous country in Southeast Asia with 31.7 million people living in urban areas accounting for

37 percent of the national population. The impact of market-based economic transformation and its pace have severely affected Vietnam's transportation condition, resulting in an increasing volume and abundant noise emitting from transportation vehicles. To formulate Vietnamese and global noise policies, community response to transportation noise has been investigated in Vietnam since 2004. The two cities chosen for the surveys are the busiest major metropolitan areas in Vietnam with a concentration of more than a third of the urban population in Vietnam. Hanoi is the capital city with estimated population of 6.5 million, and Ho Chi Minh City is a major metropolitan area of Southern Vietnam with population of 7.1 million inhabitants (as Census of 2009). Two large-scale socio-acoustic surveys on community response to road traffic noise were conducted first and then two other

surveys on the impact of aircraft noise in 2005, 2007, 2008 and 2009, respectively. Because the two abovementioned cities targeted in this study have different features, the results of this study are expected to provide a broader knowledge of noise annoyance in Vietnam of regions with particular social conditions and habituations.

The objectives of this study were (i) to propose representative dose-response relationships for road traffic and aircraft noise annoyance in Vietnam and (ii) to assess the acoustic and non-acoustic factors moderating the difference in response to noise between the two cities.

Road traffic noise surveys

Survey sites

Eight sites were selected in Hanoi and Ho Chi Minh City. The site selection was intended to reflect not only the road traffic noise covering various traffic volumes but also the characteristics of streets such as road width or the residential identify and so on. All selected sites were streets having residential houses located densely along the road with busy commercial activities.

Social surveys

In September 2005, a large-scaled social survey on community response to road traffic noise was conducted in Hanoi. The survey was principally conducted in weekends when family members were at home. The sample size was 1,503 people in which 1,135 were from row house residents and 368 were from apartments. In August and September 2007, another large-scaled social survey on community response to road traffic noise was carried out in Ho Chi Minh City. 1471 people with 1337 people from row houses and 134 people from apartments participated. Outlines of the social surveys on road traffic noise annoyance in Hanoi and Ho Chi Minh City are presented in Table 1.

Both surveys were carried out in form of face-to-face interviews. The same questionnaires were used in Hanoi Survey and Ho Chi Minh Survey. The content of a questionnaire was shown in Table 2.

In the questionnaire, two scales—5-point verbal and 11-point numeric—constructed

according to the ICBEN (International Commission on Biological Effects of Noise) method were used to evaluate the respondents' noise annoyance [2].

Table 1 Outline of surveys

Road traffic noise	
Area	Hanoi
Housing type	Row houses and apartments
Survey site	Eight sites along streets in Hanoi
Method	Face-to-face interview
Survey term	Sep 2005
Measurement term	24h, Sep 2005, Sep 2006
Sample size	1503
Response rate (%)	50
L_{den} (dB)	75-83
Aircraft noise	
Area	Ho Chi Minh City
Housing type	Row houses and apartments
Survey site	Eight sites along streets in Ho Chi Minh City
Method	Face-to-face interview
Survey term	Aug 2007
Measurement term	24h, Sep 2007
Sample size	1471
Response rate (%)	61
L_{den} (dB)	78-83
Aircraft noise	
Area	Ho Chi Minh City
Housing type	Detached and row houses
Survey site	Ten sites around Tan Son Nhat Airport
Method	Face-to-face interview
Survey term	Aug-Sep 2008
Measurement term	1 week, Sep 22-29, 2008
Sample size	1562
Response rate (%)	87
L_{den} (dB)	53-71
Aircraft noise	
Area	Hanoi
Housing type	Detached and row houses
Survey site	Nine sites around Noi Bai Airport
Method	Face-to-face interview
Survey term	Aug-Sep 2009
Measurement term	1 week, Sep 10-17, 2009
Sample size	1397
Response rate (%)	54
L_{den} (dB)	48-61

Noise measurements

In Hanoi, the first noise measurement for row houses was conducted in September 2005. The 24-hour noise measurement was performed at reference points. Short-term noise measurement was also carried out at the reference points and other

Table 2 Questionnaire items of the surveys

<i>Questions answered by respondents</i>		
Q1 - Q6	Housing factors	
Q7, Q8	Residential environment	
Q9 - Q17	Annoyance	
Q18	Interferences of daily activities	
Q19 - Q27	Sensitivities, attitudes, etc.	
Q28 - Q33	Socio-demographic variables	
<i>Questions answered by interviewers according to the respondents' facts</i>		
Q34	Gender of respondents	
Q35 - Q41	Structural details of the house	

several points simultaneously.

Distance reduction equations were formulated based on the short-term measurement. Noise exposure to each house was estimated by the 24-hour noise measurement values and the distance reduction equations. Additional vertical noise reduction measurement for apartments was conducted at four sites in September 2006. Mainly four and five-storied apartment blocks available at each site were chosen to be the reference points. Short-term vertical noise reduction measurement was performed on each floor of the apartment blocks simultaneously. Twenty-four hour noise exposure to apartment houses was estimated by noise exposure to row houses and the additional measures.

In Ho Chi Minh City, noise measurement was conducted in September 2007, including the 24-hour noise measurement, short-term horizontal and vertical reduction measurements. The same method as previously used in Hanoi was applied.

Aircraft and combined noise surveys

The existence of many residential areas in the vicinity of almost all airports in Vietnam has made aircraft noise, together with road traffic, a main noise source that is causing adverse effects on the quality of Vietnamese life. The impact of aircraft noise in this study is investigated not only as a single source but also as a combined source together with road traffic noise. The data collected in these surveys can also be used to provide more insight to the situation of road traffic noise, especially in the mixed noise environment.

Survey sites

Tan Son Nhat Airport in Ho Chi Minh City and Noi Bai Airport in Hanoi are two largest international airports in Vietnam. Tan Son Nhat Airport is located inside a crowded residential area of Ho Chi Minh City with busy commercial streets, while Noi Bai Airport lies among rural and scattered-populated areas far from downtown Hanoi but right in the hub of many national arterial roads and industrial zones. Ten residential areas were selected around Tan Son Nhat Airport including eight sites under the landing and takeoff paths of aircraft and two other sites laying to the north and south of the runway. Nine sites were selected around Noi Bai airport including seven sites under the landing and takeoff paths of aircraft and two sites to the south of the runway. The site selection was intended to reflect the aircraft noise exposure covering locations at various distances from and directions relative to the airport. At each site, the houses facing the roads were selected for combined noise survey and those apart from the road were for single aircraft noise survey.

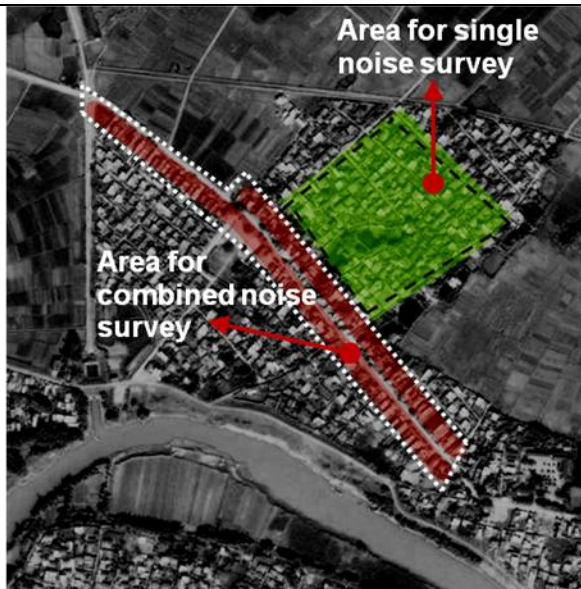


Fig.1 Illustration image of areas for the surveys on single and combined noise (Source: Google Earth)

Social surveys

Social surveys on community response to aircraft noise and combined noise from aircraft and road traffic were carried out in Ho Chi Minh City from August to September 2008 and in Hanoi from August to September 2009. In total, 1562 and 1397 responses were obtained in Ho Chi Minh City and Hanoi, respectively.

Community responses were obtained through an interview questionnaire presented as a social survey of the living environment. The responses to combined noise source were collected from residents of the houses facing the roads that were considered to be exposed to both aircraft and road traffic noise. Fig.1 illustrates the areas for single noise and combined noise surveys.

Two scales—5-point verbal and 11-point numeric—constructed according to the ICBEN method were used. In combined noise surveys, the respondents were asked to evaluate their annoyance successively to all three types of noise sources. They are aircraft, road traffic and combined noise of both.

Noise measurements

Noise measurements were performed in Ho Chi Minh City from September 22 to 29, 2008, and in Hanoi from September 10 to 17, 2009, by applying the same method in both cities. The combined noise of aircraft

and road traffic was measured every 1 s for 24 h on the road shoulder. Aircraft noise exposure was measured every 1 s for seven successive days by using sound level meters (RION NL-21 and NL-22) at the same site but for the areas rather separate from the road which is supposed to be exposed to only aircraft noise. Aircraft and combined noise exposures ranged from 53 to 71 dB and 73 to 83 dB L_{den} in Ho Chi Minh City and from 48 to 61 dB and 70 to 82 dB L_{den} in Hanoi, respectively. Road traffic noise metrics were calculated by energy subtraction of aircraft from combined noise metrics.

Results

Dose-response relationships

Community noise-control policies and guidelines on mitigating noise have been laid down in many developed countries, especially in Europe. In Europe, noise impact is quantified based on the exposure-response relationships between noise and annoyance [3-5]. In 1999, to facilitate global coverage and applicability, the Guidelines for Community Noise (WHO) were prepared as the requirement for improved guidance at the national and regional levels [6]. However, it has been pointed out in many studies that community response to noise was affected by non-acoustical factors such as culture, climate, lifestyle, and house type [7-9]. Hence, a question arises as to whether the findings of previous studies, which were obtained mainly for developed countries, are applicable to the rest of the world, especially developing countries. This part aims to draw dose-response curves for Hanoi and Ho Chi Minh data, and to attend the process in providing fundamental data for the establishment of Vietnamese noise policy.

A logistic regression function was applied to plot the dose-response curves for aircraft and road traffic noise annoyance. This was evaluated by the percentage of people highly annoyed; the day-evening-night average sound level (L_{den}) was chosen as the independent variable. Following the European Union (EU) position paper [4], in which the cut-off point for the highly annoyed was defined

as the top 28%, the authors defined the top three categories of the 11-point numeric scale (top 27%) as highly annoyed.

The dose-response curves for road traffic and aircraft annoyance in Ho Chi Minh City and Hanoi were plotted based on the data from the single and combined noise surveys and are shown in Fig. 2.

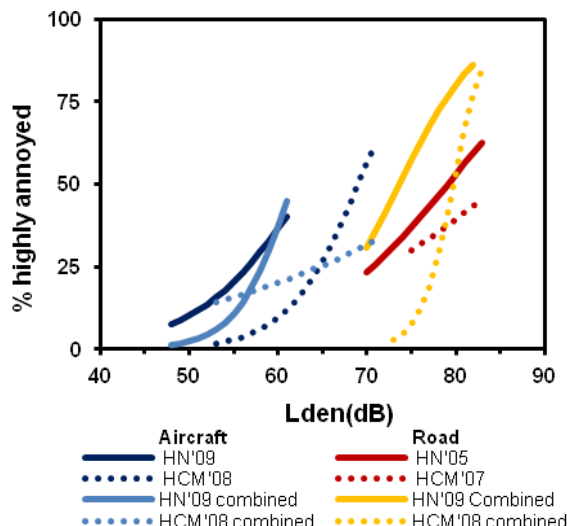


Fig. 2 Comparison of dose-response relationships for road traffic and aircraft noise annoyance in single and combined noise surveys in Hanoi and Ho Chi Minh City

The solid lines were presented for Hanoi's data while the dotted lines were for Ho Chi Minh City's. The dark and light blue lines were for the aircraft noise annoyance in single and combined noise areas, respectively. The dark and light orange lines were for the road traffic noise annoyance in single and combined noise areas, respectively. Hanoi's curves are appeared to be higher than Ho Chi Minh City's in both term of road traffic and aircraft noise no matter whether in single or mixed noise environment. In other words, respondents in Hanoi were more annoyed by aircraft noise than those in Ho Chi Minh City at the same noise level.

Particularly, comparisons were made to the impact of the same noise but in two different environments that are single and combined noise environment. In Hanoi, the curve of road traffic noise annoyance in combined noise survey is higher than that in single noise survey. It means that, at the same noise level, the respondents in combined noise areas seem to be more

annoyed by road traffic than those in single noise areas. It means that the noise emitted from aircraft events made road traffic noise more annoying than when only road traffic noise exists alone. This result could be well-interpreted by the level difference of 11 dB between the average background noise levels of the surveys in Hanoi 2005 and 2009 as shown in Table 3. In other words, the higher background noise level in single noise surveys reduced the nuisance of road traffic noise.

However, contrast situation was found for the case of aircraft noise in Hanoi. The curve of aircraft noise annoyance in combined noise survey is lower than that in single noise survey at the noise level below around 60 dB. In particular, the aircraft noise appeared in mixed noise environment seemed to be less annoying than in a single noise areas. This result is logically reasonable because a noise event at rather low level can easily be masked in environments of continuous noise, here namely, road traffic noise.

For relationships of road traffic noise in Ho Chi Minh City, clearly different trends and the intersection between the curves can be observed. The curve of road traffic noise annoyance in combined noise survey was steeper and crossed that in single noise survey at around 78 dB.

The opposite trend was obtained with curves of aircraft noise annoyance with the intersection point at about 65 dB. The difficulty to explain in consistency for the mechanism of the relationships obtained in Ho Chi Minh City was speculated to be caused by the complex environment is at surveyed sites in Ho Chi Minh City, where the responses were affected by various factors including acoustical and non-acoustical ones. Further studies should be conducted to explain such a complex circumstance.

Fig. 3 shows the relationships for aircraft and road traffic annoyance in Ho Chi Minh City and Hanoi using synthesized data from the single and combined noise surveys. Consistent to the above analysis, Hanoi's curves are higher than Ho Chi Minh City's in both term of aircraft and road traffic noise. In addition to the results of general annoyance, this finding yields a

question as to why the respondents in Hanoi were more annoyed or disturbed than those in Ho Chi Minh City at the same noise exposure.

Finally, the synthesized curves of Hanoi and Ho Chi Minh City were superimposed and fitted on to the EU data curves (Fig. 4). The dose-response curve for road traffic noise almost coincided in the position of the EU's data curve. This could be considered as a supplement to the serial data of the EU for the noise level above 75 dB. Meanwhile, the curve for aircraft noise was slightly higher than EU's. It could be argued that, at the same noise exposure level, despite having the same degree of annoyance to road noise, Vietnamese were more disturbed by aircraft noise than European people. The aviation industry of Vietnam is still relatively new and growing. The aircraft is not the means used regularly for Vietnamese. This might yield a higher aircraft annoyance to Vietnamese than Europeans.

However, this result shows the correctness and the applicability accompanied by the amendment given by a thorough study of European standards with Vietnam in particular and other developing countries in general.

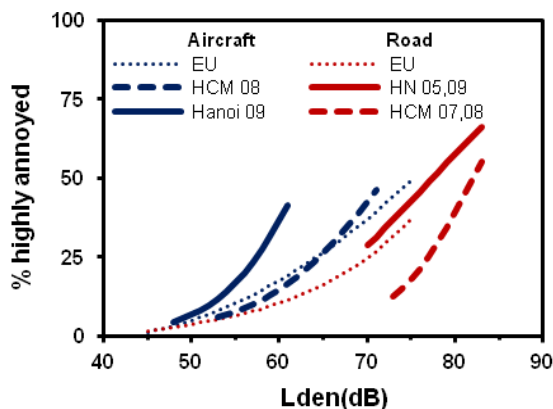


Fig. 3 Dose-response relationships for road traffic and aircraft noise annoyance using synthesized data from surveys in Hanoi and Ho Chi Minh City

Difference in response between cities

Comparing the annoyance response between the two cities, Hanoi respondents seemed to be more annoyed by noise than those in Ho Chi Minh City, even at the

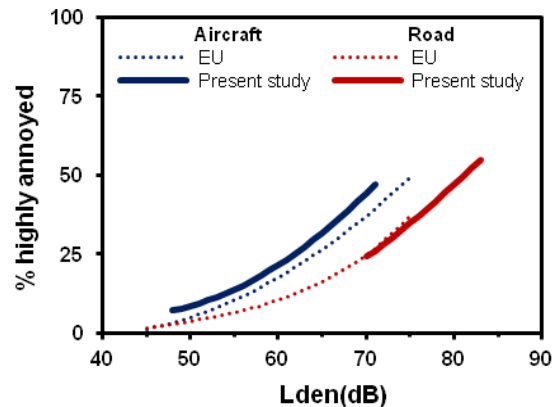


Fig. 4 The synthesized curve of road traffic and aircraft noise surveys in comparison with the EU's curve

same noise level. The results of previous studies indicated that individuals tended to judge the annoyance of an unwanted sound in terms of its relationship to background noise [10]. The background noise level, in this study, is defined as the 95th percentile (L_{95}), as shown in Tables 3. It can be easily observed that the background noise levels at almost all sites of Ho Chi Minh City are higher than at those of Hanoi. The outstandingly larger traffic volume in Ho Chi Minh City might yield the higher background noise level there.

Correlation coefficients were calculated to measure the relationship between aircraft annoyance and background noise levels. The results showed that L_{95} was statistically significantly correlated at the 0.01 level with individual annoyance score evaluated by the respondents of all surveys in both Hanoi and Ho Chi Minh City. It can be speculated that the road traffic and aircraft noise in Hanoi might be generally more noticeable since the background noise levels are lower than in Ho Chi Minh City.

This finding emphasized the role of background noise level on the annoyance of respondents in Ho Chi Minh City and Hanoi.

Conclusions

The results from four large-scale socio-acoustic surveys on community response to road traffic noise and aircraft noise conducted in Hanoi and Ho Chi Minh City

International Engineering Symposium, March 3-5, 2011 Kumamoto Univ., Japan

provided a broader knowledge on exposure situations as well as annoyance of transportation noise in Vietnam. The first dose-response relationship between L_{den} and % highly annoyed was established for road traffic and aircraft noise in Vietnam and fitted onto the curve for the EU. It has been found that the dose-response curve for road traffic noise almost coincided in the position of the EU's data curve and the curve for aircraft noise was 2 to 3 dB lower than that for the EU at the same percentage of high annoyance. Finally, for the same noise exposure, the noise annoyance in Hanoi was higher than that in Ho Chi Minh City because of the lower background noise level in Hanoi.

The data on community response to railway noise in Hanoi is being in process of analysis, with which we can propose soon the dose-response curve with all three type of transportation noises corresponding with EU's works. Further investigations are planned to be conducted in urban areas that have smaller scale to contribute for more comprehensive study on transportation noise in Vietnam. More surveys also intended to be conducted in Hanoi and Ho Chi Minh City to provide additional research on step change on community response in Vietnam.

Acknowledgements

The authors appreciate the support of Ms. T.B.N. Nguyen from Ho Chi Minh City University of Architecture for the social surveys and noise measurements in Ho Chi

Minh City and Professor D.N. Pham and Dr. T.H. Nguyen from Hanoi University of Civil Engineering for their vital help in conducting the surveys in Hanoi. We also appreciate the enthusiastic assistance of the students from both universities, who supported interviews and noise measurements.

References

- [1] Vietnam Chamber of Commerce and Industry, New Vision for Urban Development in Vietnam, VCCI(2009)
- [2] T. Yano and H. Ma, Standardized noise annoyance scales in Chinese, Korean and Vietnamese, Journal of Sound and Vibration, Vol 277 (3), pp.583-588, (2004).
- [3] European Parliament and Council, European Noise Directive 2002/49/EC of the European Parliament and of the Council, 25 June 2002, relating to the assessment and management of environmental noise, END (2002).
- [4] European Communities, Position paper on dose-response relationships between transportation noise and annoyance. EU's future noise policy, WG-Dose/Effect, (2002).
- [5] Report on meeting, WHO noise technical meeting on exposure-response relationships of noise on health, Bonn, Germany (2002).
- [6] World Health Organization, Guidelines for Community Noise (1999).
- [7] T. Yano, T. Sato, M. Bjorkman and R. Rylander, Comparison of community response to road traffic noise in Japan and Sweden, Journal of Sound and Vibration, Vol 250 (1), pp.161-167, (2002).
- [8] E. Pedersen et al., Response to noise from modern wind farms in The Netherlands, J. Acoust. Soc. Am., 126(2), August 2009.
- [9] J.M. Field, Effect of personal and situational variables on noise annoyance in residential areas, J. Acoust. Soc. Am., 93(5), May 1993.
- [10] J.M. Field, Reaction to environmental noise in an ambient noise context in residential areas, J. Acoust. Soc. Am., 93(5), (May 1993).

Table 2 Background noise levels L_{95} (95 percentile noise level) at all surveyed sites

	Site1	Site2	Site3	Site4	Site5	Site6	Site7	Site8	Site9	Average
<i>Hanoi 2005</i>										
L_{95}	57	51	52	54	51	52	65	61		55
<i>HCM City 2007</i>										
L_{95}	53	56	63	60	61	64	65	68		61
<i>HCM City 2008</i>										
Single survey, L_{95}	44	49	47	41	42	45	46	44		45
Combined survey, L_{95}	41	65	44	49	57	53	46	54		51
<i>Hanoi 2009</i>										
Single survey, L_{95}	40	45	48	39	42		41	43	44	43
Combined survey, L_{95}	36	48	48	46	41		41	51	42	44

RAIN WATER HARVESTING

-Conservation and Rescue

DITIMONI BARUAH

*Faculty of Architecture, MIT, Manipal University, Manipal-576104, Karnataka, India.
e-mail:moni.diti@gmail.com*

Abstract: Demand for water is growing in most cities as every urban citizen requires more amount of water than a rural citizen. Moreover, every village and small town is rapidly urbanizing. Not long ago, most of our cities were self-sufficient in meeting their water demand from the extensive urban water bodies. Today these water bodies have completely disappeared. Municipalities have been stretched to their limits to find water for the growing urban populations. Ground water, which is only 30% of available fresh water supply, is being extracted by the government as well as the private parties to its maximum.¹ Rain water is on the other hand, an available fresh water source whose harvesting is being done since long time. It could be a possible solution for water crisis in urban areas. With the help of a case study the working and the benefits of this simple age old traditional methodology has been enhanced. Here in this paper, rainwater harvesting is dealt as a rescuer for today's world.

Keywords: *urbanization, rainwater harvesting, rescuer, water scarcity.*

Introduction

In today's world of rapid urbanization there is an alarm in the demand for water. With cities growing denser, the natural water bodies are drying up and are being replaced by the high rise structures. On one side we see cities being flooded with water but irony is that the same city does not have a drop of potable water.

The very reason of such a pity state is our negligence of what nature has given. Since time immemorial, civilizations have flourished and have vanished because of the natural water bodies.

If we respect them they make us prosper, if we do not then we bear its wrath. In the present scenario, advancement in technology also means reviving the lost customs. It has to be through the implementation of new technical methods to achieve more benefits and to remove the flaws if any.

Water scarcity: What the future is?

If we see the water stress and water scarcity in the global aspect, there is

hardly any country left which are not marked under them, except the ice covered countries. 63% of world's population are unserved by water. The majority is in Asia.¹

In the urban scenario, reasons of water scarcity can be attributed to:

- Distant location of water source
- Growing population
- Increase in the number of industries
- Pollution of water
- Negligence of nature

These are known to us and the solutions for them are there, but the cost benefit factor constrains the implementation of certain innovative methodology.

Here in this paper we will be dealing mainly on the urban scenario where the water crisis is rising every day. The rural people are yet to address this crisis mainly because they never neglected the natural resources. This is the very reason why

these villages are still surviving in spite of global warming.

Few ways that can be implemented to retain water:

- A proper demand management
- Use of water efficient devices
- Reuse and recycling of water
- Innovative design-dry toilets
- Rainwater harvesting

The demand management for water has to be done judiciously with the supply-demand analysis whether at the household level or city level. With the use of efficient devices like the dry toilets, water can be retained upto certain amount. At an individual level we need to act consciously.

Apart from being just conscious and cautious, which can reduce wastage of water, we also need to generate or get hold of new source of water supply to overcome the scarcity. Finding a new source of water is possible if only nature permits. Instead more judicious would be to use what nature has already been providing. Rainwater is one of the means of natural resources which acts as a rescuer for us.

Water harvesting: the only solution?

Majority of Indian cities receives rainfall for most part of the year, but ironically these very cities strive to meet growing water demand. The natural water body are drying up as we see the increasing spread of the urban fabric. The only saviour hence that comes is rainwater. But it is only helpful for places which receives adequate amount of rainfall. When it falls just catch it and store. The rooftops, the ground surfaces wherever it falls, not a single drop can be allowed to go wasted. The whole city itself acts as the catchment. The entire earth surface is getting this privilege. It thus is the one which solves the crisis. This simple technique of collection and storage of water from rooftops or land surfaces is easy to implement. At an individual

household level it gives respite when the whole city is trying to fetch water.

Traditional methods in India

India is one such country which has deserts as well as the glaciers making it a unique land. The traditional methods of rain water harvesting systems have existed here since centuries, but with rapid urbanisation we have lost these assets. The Bikaner houses used to boast of the *tankas* where water was being collected during rains. Now very few houses are still clinging to them. Even *ahar pynes* of southern Bihar used to collect rainwater where the slope was towards the villages from the collection and storage point. In fact the traditional *inundation canals* of West Bengal used to be one of the major reasons for the eradication of malaria from the region during the British rule. The *bhandaras* of Maharashtra are still used to divert water from rivers so that the water level of the river increases. The colder regions are still retaining their own water collection system from the glaciers called the *zings* in Ladakh which are used to collect the melted glacial water.²

These are only few of the innumerable traditional methods of water harvesting in India. The villages are still continuing with these age old techniques but the cities have lost it due to growing population and global warming.

Water harvesting: the methodology

The basic methodology for water harvesting is catchment, conveyance and storage. We just need to catch water, whether it is the rooftop or the paved surface. Let us know the importance of this traditional methodology through one of the successful case studies.

The versatility of rainwater is expressed through this study.

Case study: San Soucci

One of the exemplary implementation of rain water harvesting is San Soucci, the residence of Architect Chitra Vishwanath in Bangalore, Karnataka, India. The average

annual rainfall in Bangalore urban area is 978mm.

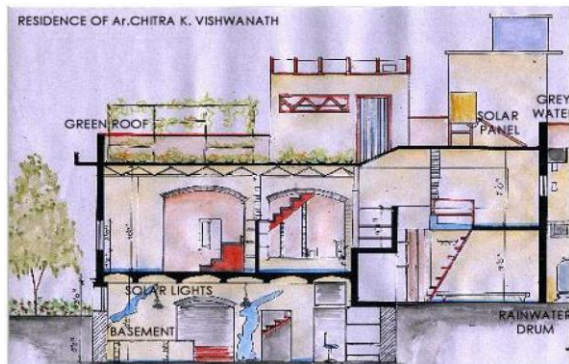


Figure 1: San Soucci

This house boasts of the water it harvests and the owners are proud of this fact. Not only this, they have even channelized system of recharging the water level of the neighbourhood through the recharge well.

At an individual level, this house is not only reviving the old tradition but also highlights that rainwater harvesting is the only available source in the urban scenario (Fig.1). This harvested water suffices the need of the owners.

As the water falls into the terrace, it gets collected into the filter consisting of a consecutive layer of sand, gravel and charcoal each. This filtered water is being carried into the underground sump located in front of the house (Fig.2).

The location of the sump is done in such a way that no amount of the site is being wasted and the vehicle parking is on top of it.

The residence has a roof area 963 sq.ft. The water from the rooftop slopes towards the filtering unit. This water then goes into an underground sump of 6000 ltr capacity.

Thus, San Souci not only looks into conserving resources but also into maximum utilization of available space.

The basic components of rooftop rainwater harvesting system in brief

1. Gutter
2. First rain separator

3. Filters

4. Down pipe

5. Storage tank

1. Gutter

The water from the rooftop gets collected in the gutter pipe of 4"-6" diameter. This is of PVC (Fig.2).

2. First rain separator

The initial rain water which collects through the gutter is allowed to flow away into the first rain separator as this may contain the debris of dry leaves etc. accumulated from the rooftop.

3. Filters

Water from the gutter overflows the first rain separator and goes into the filter. The filters are the crucial elements since the amount of potability of rain water depends on the level of filtration. This filter is made of layers of sand, charcoal and pebbles which is a traditional method of filtering water (Fig.2).

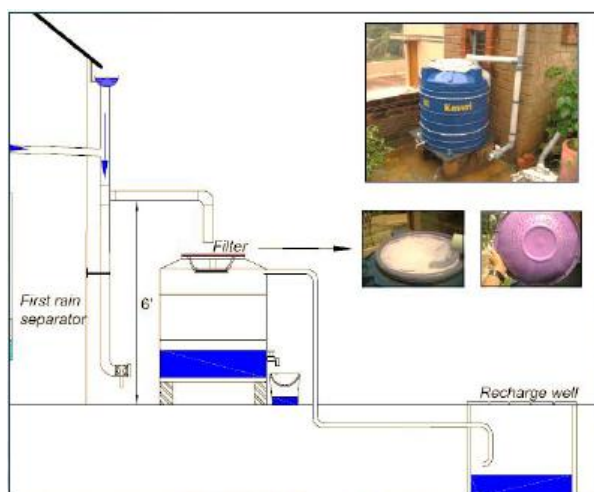


Figure 2: Rooftop rainwater harvesting system

4. Down take pipe

The down take pipes convey the filtered water into the storage tanks. In San Souci, the downtake pipes are of PVC and they drain the filtered water into the underground sump. Instead of pipes,

chains can also be used by making them a part of the landscape (Fig.3).



Figure 3: Downtake chains

5. Storage tank

The sump is made of concrete and is used for storage. An opening has been placed on top of it so that cleaning can be done on a regular interval to prevent the breeding of mosquitoes.

The water from the sump is pumped into the overhead tank from where it gets distributed into the entire household.

The storage of filtered water has to be done in such a way that no contamination occurs.

If stored properly than this water can be used for 8-10 months for drinking. Chitra and her family use this water for drinking purpose.

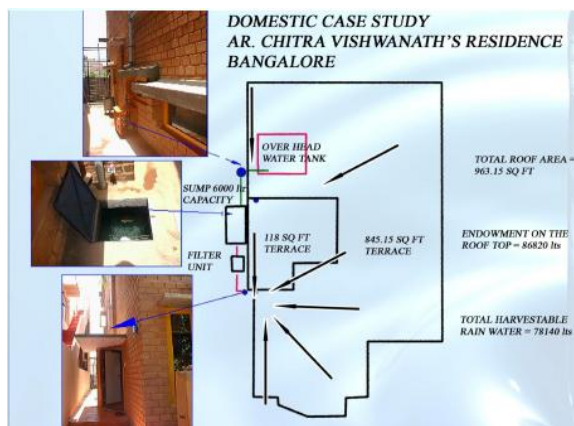


Figure 4: Area of terrace

Harvesting at a community level

The house has been designed in such a way that the whole site is sloped towards the road. The surface water drainage goes into the recharge well adjacent to the road in front of the house. This well is 3 feet in diameter and goes upto a depth of 20 feet (Fig.5).

A perforated cylindrical galvanized iron ring is placed in the well which allows the seepage of water into the ground. This keeps the water level of that area at a level higher than the rest of the city.

The storm water drain collects the water after filtration through which the silt is removed at certain intervals. This water then goes into the revitalization well. It acts as a rescuer for the entire locality.

In this way, San Soucci not only does rain water harvesting for its own occupants but also for the whole neighborhood. As they say "Love thy neighbor!" This house had never and not in future will have scarcity of water due to the awareness of the owner.

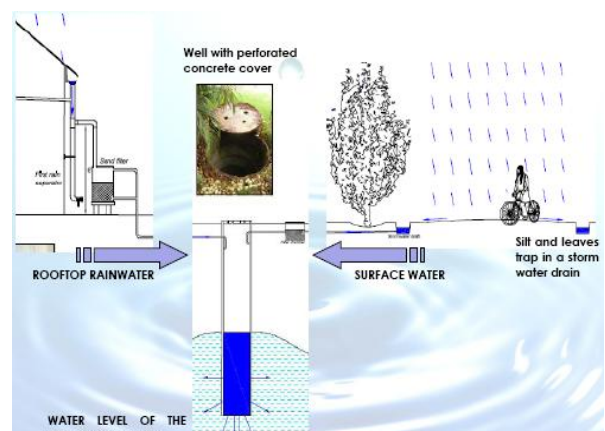


Figure 5: Recharge well

San Soucci has been aptly named by the owner Chitra. In French it means "without worries" and it truly is without any worry. This case study can be taken as one of the success stories where the neighbours of Chitra enjoy plenty of water during the monsoon thanks to her individual initiative. Thus, rain is the rescuer from every aspect

which is proved by this exemplary case study.

Advantages and disadvantages

The method of rainwater harvesting is simple to install and operate where the local people can be trained easily. There is no need of any technical expertise. It is cost effective and the capacity of harvestable water can be increased or decreased within the catchment area. There is no negative environmental impact compared to other methods of water supply systems.

The only major disadvantage is that there is a limited supply and uncertainty of rainfall. If the NGO's and the government take proper initiative then this age old tradition can be revived.

Recent measures

Building byelaws have made it mandatory in major cities of India to include rainwater harvesting in buildings. People should themselves take the initiative of implementing this simple technique in their household. The conservation of water has become one of the most urgent matters of concern.

Conclusion

Rain can no longer be allowed to go wasted. The design of the building should be done consciously. Wherever there is scope, rainwater should be caught and stored for future use.

As a young child it was fun for me when I walked through knee depth water from school to back home. I never realized that it was due to an improper planning of the drainage system of my city, Guwahati, Assam (India). I never knew the drawbacks which lead us to buy water for my home when the streets were full of water! Now I realize the need for such a judicious step where we can not only plan rainwater harvesting system for a single household but as well as for the whole city.

The need of the time has to be meted with urgency until it is too late. As concerned citizens it is our duty towards the society

as well as NATURE who gave us so much and has underwent changes in order to let mankind prosper. We should respect what nature has provided.

Societal responsibility is one of the major solutions which can benefit people in a major way. Only thing is that we need to bring awareness about the future we are heading for. We need to awaken our consciousness now or never.

There is the need to put together everything in place in order to arrive at a complete solution for all.

The only hope termed as the rescuer is rain water. With the case study, it can be derived that rain water harvesting is the only rescuer for the people. With global warming and the increase in water demand, rainwater harvesting is truely seen as the only rescuer. The future can only be saved by the philosophy of

Reduce

Reuse

Recycle

Acknowledgement

I would like to thank Ar. Chitra Vishwanath for allowing me to take her house as case study.

References

1. www.unep.org
2. Agarwal, Anil and Sunita Narain(1997), *Dying Wisdom: Rise, Fall and Potential of India's Traditional Water Harvesting Systems*, Thomas Press (India) Ltd., Faridabad.

Traffic Management proposals for Udupi city.

Raviraj H. Mulangi¹ A.U.Ravi Shankar² and Varghese George³

¹ Department of Civil Engineering, National Institute of Technology Karnataka, Surathkal, Mangalore 575025, India. email: ravirajmh@rediffmail.com

² Department of Civil Engineering, National Institute of Technology Karnataka, Surathkal, Mangalore 575025, India. email: aurshankar@yahoo.com

³ Department of Civil Engineering, National Institute of Technology Karnataka, Surathkal, Mangalore 575025, India. email: varghese-g@lycos.com

Abstract: Udupi is amongst the most prominent places of pilgrimage in the Country and is famous for its Lord Krishna and many other deities. It is having population of 1.476 lacks, with floating population 100000 to 200000 per day. In view of growing importance of the Udupi city in the region of CBD, this is an urgent need for a comprehensive approach to tackle the short range and long-range traffic and transportation problems. To study the existing traffic and transportation system and prepare traffic management plan various traffic surveys have been carried out, and alternate proposal have been made. The proposals have been analysed for Level of Service (LOS) along the urban roads and LOS of turning traffic at junctions for next ten years. In present study an attempt is made to provide traffic management for CBD area.

Keywords: Level of Service (LOS), Traffic Management, CBD

Introduction

Udupi City is situated in Karnataka. Udupi is the district and Taluk headquarters for udupi district and Udupi Taluk respectively. Udupi is amongst the most prominent places of pilgrimage in the Country and is famous for its Lord Krishna and many other deities. It is having population of 1.476 lacks, with floating population 100000 to 200000 per day.

In view of growing importance of the Udupi city in the region of CBD, this is an urgent need for a comprehensive approach to tackle the short range and long-range traffic and transportation problems. To study the existing traffic and transportation system and prepare traffic management plan to provide solution to the present problems and to optimise the use of infrastructure in the city. At present the commercial activities in the city are haphazardly situated in CBD and hence the distributions of the shopping trips is not uniform and are concentrated towards one or more shopping regions and that is the main path for devotees of Lord Krishna Temple. Since these locations are not planned in a scientific manner so the management skill are to be applied, in

present study an attempt is made to provide traffic management for CBD area.

The problems in the CBD area of the Udupi are

- The turning radii are not available at all junctions.
- There are no channelisations to turning traffic at junctions.
- At the junctions the vehicles are experiencing delays.
- There are no provisions of pedestrian facilities.
- The traffic volume flowing towards temple legs are more.
- The flow of buses is more on main roads of CBD.
- The widths of roads are insufficient to cater the traffic flow.

Objectives

This study attempts to develop a traffic management for CBD area, to ensure better traffic circulation in terms of reduced delays, and to provide safety to devotees of Lord Krishna Temple. The objectives of the study are enlisted below.

- To Regularise Traffic and Speeds
- To reduce the traffic congestion on major roads
- To provide necessary junction improvements
- To provide pedestrian facilities at junctions
- To identify parking requirements

Literature review

In review the past studies made on traffic management are studied, with a view to boost up the present study with past studies. The literature review includes.

- Traffic management plan for the central area of Trivandrum,
- Traffic and Transportation Improvement Priorities for Road Corridors of Bangalore.
- Traffic management Plan for Mysore City.
- Comprehensive Traffic and Transportation Plan for Nagpur.

From the above studies it is seen that the traffic movement problems are more at central zone (CBD) compare to other zones, so it is decided to take up CBD area along with temple routes of Udupi city for present study.

Delineation of the Study Area

After collecting the land use, population and Socio-Economic data. It is necessary to define the area for which the traffic management studies are to be carried out. At present commercial activities, Bus Stands and Temple are situated very near in an unplanned manner, in the CBD area. The schematic representation of CBD area is shown in Fig 1.

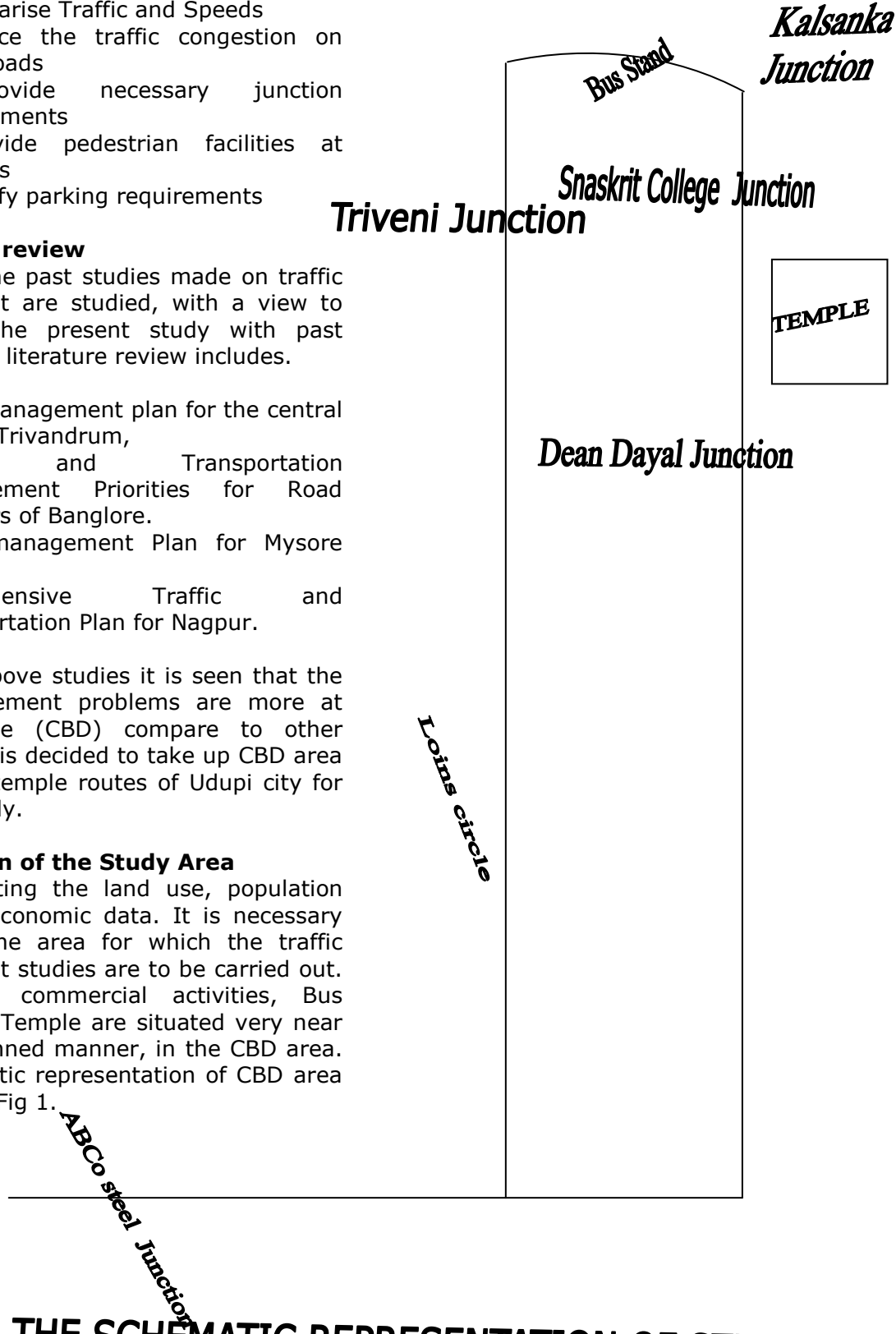


FIG 1: THE SCHEMATIC REPRESENTATION OF STUDY AREA

Field Studies

To solve the above problems and achieve the objectives, various traffic surveys have been Carried out. Relevant data have also been collected from traffic police department and various other government departments

Data collection

The following traffic surveys have been conducted

- Identification of junctions needing improvements
- Turning volume counts at junctions
- Speed and Delay study
- Pedestrian volume counts
- Parking demand survey

Secondary data

The following secondary data have also been collected

- Inception report
- Land use data
- Accident data

Identification of junctions needing improvements

The study area is first surveyed to find the junctions having more traffic flow, more pedestrian conflicts for existing island features. By preliminary survey the following 4 junctions are selected for improvements.

- Diana junction
- Triveni junction
- Sanskrit college junction
- Kalsanka junction

Results and discussions

The various data collected from field are analysed to solve the traffic manoeuvre problems of CBD and to achieve the objectives. The analysis of field data is done in following order

- Turning volume counts.
- Speed and Delay study.
- Pedestrian volume counts.
- Improvement of junctions
- LOS for existing traffic scenario.

Depending on the analysis three Traffic management proposals have been made, the different proposals made are as follows.
Traffic Management Measures

- Shifting of Bus Stand near ABCo steel junction
- Shifting of Bus Stand near ABCo steel junction along with traffic management measures.

The above proposals are carefully studied and finally best proposal is selected, the analyses of different proposals are made as below

Traffic Management Measures

Following traffic management measures are suggested to have streamline flow of traffic and to improve the LOS of road network.

The K.M.Road from Diana Junction to Bus Stand, and Sanskrit College Road from Bus Stand to Road connecting Kalpana Residency road are to be made one way. There should be restriction of the buses flowing from Udupi leg and Kundapur leg at morning and evening peak at Kalsanka Junction.

The vehicles coming from the Manipal leg at Kalsanka junction are diverted to temple through the road connecting the temple and mud road.

At Kalsanka Junction vehicles moving to temple are diverted on mud road to avoid congestion and parking problem at temple. The vehicles moving to temple through Sri Ram Residency leg are diverted to temple through the Deen Dayal junction.

Shifting of Bus Stand near ABCo steel junction

It is observed that the buses moving are moving through ABCo steel junction to Bus Stand from Kundapur and Manglore and returning to the Kundapur and Manglore on the same route. So it is proposed to shift the Bus Stand from CBD area to near ABCo steel junction. Further the buses entering the CBD area junctions through the ABCo steel junction are listed as below

From traffic volume counts in peak hour it is seen that at

Diana junction the buses moving are 41.23% on Municipal office leg and 40.27% on National Highway leg.

Triveni junction the buses moving are 49.12% on Bus Stand leg, 53.45% on Temple leg and 40.09% on Diana leg.

Kalsanka junction the buses moving are 18.25% on Udupi leg, 28.15% on Kundapur leg.

Sanskrit College junction the buses moving are 24.05% on Sri Ram Residency leg, 20.91% on Auto emporium leg, and 3.26% on Gokul leg.

Shifting of Bus Stand near ABCo steel junction along with traffic management measures.

Observing to above V/C ratio of roads, it is thought to implement both the proposals together to maximum streamline flow. The possible V/C ratio after implementing traffic Management Measures and shifting of Bus Stand near ABCo steel junction Proposed road widening

The above proposals have been analysed for LOS along the urban roads and LOS of turning traffic at junctions. And it is found that the third alternative." Shifting of Bus Stand near ABCo steel junction along with traffic management measures" provides good LOS and the number of roads which are not providing $LOS \leq C$ are four only compare to the other two proposals with provision of pedestrian facilities proposed and To provide streamlined traffic flow (Los C) the following roads are proposed for widening.

The road from Bus Stand to Kalpana Residency is proposed to be made 4 lane divided.

The Manipal leg road from Kalsanka junction is to be widened to 9.0M up to 1Km from Kalsanka junction and the Udupi leg is to be widened to 9.0M up to Janta hotel.

Conclusions and Recommendations

Traffic Management for CBD of Udupi city has been intended to include traffic and transportation problems of the city. Proposed Traffic Management Measures and proposals are to be implemented in short and long-term.

The following conclusions and recommendations may be made.

- It is proposed to shift Bus Stands near ABCo steel junction and the K.M.Road

from city Bus Stand Up to Diana Junction and Sanskrit College road from city Bus Stand Up to Kalpana Residency Road is to be made one way, so that the congestion of CBD area will be reduced.

- There should be restriction of the buses flowing from Udupi leg and Kundapur leg at morning and evening peak at Kalsanka Junction. It is proposed to divert them on by pass road.
- The vehicles moving to temple through Kalsanka junction are to be diverted to temple through the road connecting the temple and mud road.
- The vehicles moving to temple from Manipal are to be diverted on mud road (1Km) before reaching at Kalsanka junction to avoid congestion and parking problems at temple leg.
- The vehicles moving to temple through Sri Ram Residency leg at Sanskrit college are diverted to temple through the Deen Dayal junction.
- The details pertaining to the pedestrians path, modification to circle/junctions traffic control devices etc, have been worked out and these should be implemented in Short and Long terms. Speed and Delay studies reveal that the Journey speed is 23.28Km/h, which is less than the posted speed (30Km/h). The traffic management measures listed above (1-6) will certainly increase the journey speed.
- The road from Bus Stand to Kalpana Residency is proposed to be made 4 lane divided.
- The Manipal leg road from Kalsanka junction is to be widened to 9.0M up to 1Km from Kalsanka junction and the Udupi leg is to be widened to 9.0M up to Janta hotel.
- Restrictions like one-way on K.M. road, Sanskrit college road, and restriction on flow of buses on Kundapur leg and Udupi leg at morning and evening peak at Kalsanka Junction are to be implemented gradually and at the earliest with strict enforcement. The turning movements are controlled by police person at the junctions

International Engineering Symposium, March 3-5, 2011 Kumamoto Univ., Japan

References

- [1] CRRI New Delhi, Transport operations planning and informatics centre, Bangalore, and, centre for Transportation engineering Bangalore university (1999): "Traffic and Transportation Improvement Priorities for Road Corridors of Bangalore", final report of Karnataka Urban Infrastructure Development and Finance Corporation Bangalore.
- [2] CRRI New Delhi (1992): "Development of Transport network for Madras metropolitan area".
- [3] CRRI New Delhi (1995): "Traffic Management Studies for Tuticorin town (pearl city)".
- [4] CRRI New Delhi, (1996): "Comprehensive Traffic and Transportation Plan for Nagpur".
- [5] Dalal Consultants and Engineers Ltd (2002): "Traffic management Plan for Mysore City", final report of Karnataka Urban Infrastructure Development and Finance Corporation Bangalore.
- [6] "Guide to traffic counting in state road authorities", by National Association of Australian State Road authorities.
- [7] Highway Capacity Manual.
- [8] IRC: 35 (1970), "Code of practice for road markings", published by Indian Road Congress.
- [9] IRC: 65 (1977), "Space standards for roads in urban areas", published by Indian Road Congress.
- [10]IRC: 79 (1981), "Recommended Practice for pedestrian facilities", published by Indian Road Congress.
- [11]IRC: 103 (1980), "Guidelines for capacity of urban roads in plain areas ", published by Indian Road Congress.
- [12]IRC: SP 41(1994), "Guidelines for the design of at-grade intersections in rural and urban areas", published by Indian Road Congress.
- [13]IRC: SP 43 (1994), "Guidelines for low cost traffic management techniques for urban areas", published by Indian Road Congress.
- [14]Kadiyali L.R, "Traffic engineering and Transportation planning", published by Khanna publishers Delhi.
- [15]Khanna S.K, Gupta A.K and Popat J.L, "Traffic studies and analysis at road intersections-An assimilation", published by Indian Highway journal.
- [16]Khanna S.K and Justo C.E.G, " Highway Engineering", published by Nem Chand and Bros Roorke.
- [17]Karnataka Urban Development and Coastal Environmental Management Project (KUDCEMP) draft final report
- [18]Karnataka Urban Development and Coastal Environmental Management Project (KUDCEMP) inception report (1998) for Udupi.
- [19]Udupi Development Authority, "Land use proposal".
- [20]Papacostas C.S (1990): "Fundamentals of Transportation Engineering", published by Prentice-Hall of India Private Limited, cannought circle New Delhi.
- [21]Srinivas N.S and Herur Arun (1982), "Traffic management plan for the central area of Trivendrum", published by Indian Road Congress.
- [22]William R, McShane, Roger P. Roess and Elena S Prassa, " Traffic Engineering", published by Khanna publishers Delhi.

Development of Concrete Armoured Protected Breakwater Structure

MANU¹

SUBBA RAO²

and

KIRAN G. SHIRLAL³

1. Department of Applied Mechanics and Hydraulics, National Institute of Technology Karnataka, Surathkal, Srinivasnagar 575025, INDIA. Email: gr_manu@yahoo.com
 2. Department of Applied Mechanics and Hydraulics, National Institute of Technology Karnataka, Surathkal, Srinivasnagar 575025, INDIA. Email: surakrec@yahoo.com
 3. Department of Applied Mechanics and Hydraulics, National Institute of Technology Karnataka, Surathkal, Srinivasnagar 575025, INDIA. Email: kshirlal@gmail.com
-

Abstract: The present work involves the physical model study of stability of conventional single breakwater and the reef protected breakwater, constructed with concrete cube as an artificial armour unit. Regular waves of wide ranging heights and periods are used. The tests are carried out for different spacings between the two structures ($X/d = 2.5 - 13.33$) and for different relative heights ($h/d = 0.625 - 0.833$) and relative widths ($B/d = 0.25 - 1.33$) of the reef. It is observed that a reef of width (B/d) of 1.0 - 1.33 constructed at a seaward distance (X/d) of 6.25 - 8.33 exhibits a transmission coefficient (K_t) of 0.38-0.708, wave dissipates energy and protect the breakwater optimally.

Keywords: Reef, Regular waves, Wave breaking, Breakwater, Stability

Introduction

Breakwaters are absolutely necessary for building ports and harbours and its structural stability and economy in construction are the need of the hour. This calls for an innovative design of the structure. But the stark reality is that, however safe the breakwater designs are, there are internal as well as external uncertainties which may become the prime reason for extensive damage to the structure which may have catastrophic consequences for the port. Hence, it is decided that some kind of protection to the breakwaters could ward off significant damage or reduce its magnitude. It is proved that a submerged reef can protect the breakwater (Gadre et al. 1985, Cox and Clark 1992, Shirlal et al. 2006). Also, the submerged reef breakwater serves to reflect and dissipate energy and attenuate waves, thereby reducing the intensity of wave action on the main conventional breakwater. Hence they can then be designed with lighter armour units and may prove economical. The conventional breakwater using natural stone armour can not always be realised due to non-availability of stones in the vicinity (Neelamani and Sunderavadivelu 2003)

and one may have to think about artificial armour units. Under these circumstances, it is natural but to investigate the economical solutions. The present work involves the study of stability of conventional single breakwater and the reef protected breakwater, constructed with concrete cube as an artificial armour unit.

The paper presents the results of the physical model study on stability of reef protected breakwater for different crest widths of submerged reef and distance between the structures and it compares the results with those of conventional single breakwater.

Literature Review

Construction of a rubble mound in front of a structure reduces wave reflection and thereby increases bottom stability. The important parameters that influence the performance are the crest width and the depth of reef submergence. Dattatri (1978) found that the optimum crest width as $B/L = 0.2$ to 0.3 . Gadre et al. (1985) designed a submerged bund to break higher waves and dissipate energy while

protecting the revetment constructed at 100m shoreward to retain land behind it at Chennai port. Thus the required armour stone weight of 15 tons for a conventional reclamation structure in a depth of 8m was downsized to a stone weight of 2 to 3 tons. Gadre et al. (1989) designed a submerged breakwater at 80m seaward to protect a damaged breakwater head of west breakwater at Veraval port in Gujarat, India. This submerged structure broke the storm waves protecting the damaged breakwater which was repaired later. Cornett et al. (1993) after conducting experimental investigation concludes that there may be an optimum location for submerged reef of relative height $h/d > 0.6$ which protects the inner main breakwater. Ahrens (1989) and Pilarzyk & Zeilder (1996) have presented equations and graphs to calculate the armour weight of submerged reef breakwater. Cox and Clark (1992) who coined the term tandem breakwater system examined the effect of wave breaking, overtopping and transmission on stability of the breakwater with the slope of 1V: 1.5H. Shirlal et al. (2006) conducted study of stability of a 1:30 scaled model of breakwater defenced by a seaward submerged reef for varying characteristics of regular waves. They arrived at the optimum armour stone weight (30 gms), spacing ($X/d=6.25-8.33$) and crest width ($B/d=0.6-0.7$, $B/L_o=0.035-0.045$) of reef to protect the main breakwater.

Objectives

The objective of the present experimental investigation is to study the influence of geometry of a submerged reef located at varying seaward distances on wave transmission and stability of the conventional breakwater for a range of wave characteristic.

Methodology

The 1:30 scale model of conventional single breakwater and a reef protected breakwater are tested in a wave flume for stability. The conventional breakwaters are

constructed with concrete cubes while the reef is made of natural stones.

Experimental setup

Wave Flume

The physical models are tested for regular waves in a two dimensional wave flume of Marine Structure laboratory of Department of Applied Mechanics and Hydraulics, National Institute of Technology Karnataka, Surathkal. Fig. 1 gives a schematic diagram of experimental setup. The wave flume is 50m long, 0.71m wide and 1.1m deep. It has a 41.5m long smooth concrete bed. About 15m length of the flume is provided with glass panels on one side. It has a 6.3m long, 1.5m wide and 1.4m deep chamber at one end where the bottom hinged flap generates waves. The flap is controlled by an induction motor of 11Kw power at 1450rpm. This motor is regulated by an inverter drive (0 – 50Hz) rotating with a speed in the range of 0–155rpm. By changing the frequency through inverter, one can generate the desired wave period. A fly-wheel and bar-chain link the motor with the flap. By changing the eccentricity of the bar chain on the fly-wheel, one can vary the wave height for a particular wave period.

Instrumentation

Four capacitance type wave probes are used where, first three probes measures incident wave height (H_i) and wave reflection at about 1m seaward of reef toe and the last probe measures transmitted wave height (H_t) after breaking over the reef (Refer Fig.1). The same probe is moved to measure wave height approaching the breakwater toe. The water surface elevation on seaward and shoreward side of the reef is converted into electrical signals. These are then being stored as digital signals by software controlled 12-bit A/D converter with 16 digital input/output. During the experiment, every time after five waves pass the reef, transmitted waveform for 10sec duration is acquired using software.

Model construction

Conventional breakwater model

The 1:30 scale breakwater model with a uniform slope of 1V:2H is constructed, at

about 32m from wave generator, on the flat bed of the flume with concrete cubes as primary armour. The unit weight (W_{50}) of 79.56gm for primary armour cube is determined using Hudson's formula,

$$W_{50} = \frac{\gamma_r H^3}{K_D (S_r - 1)^3 \cot \alpha} \quad \text{-----(1)}$$

for a design wave height (H) of 0.1m and K_D value (Pilarczyk and Zeilder, 1996) of 5.5. Then using Van der Meer (1988) equation of

$$D_{n50} = \left\{ \frac{W_{50}}{\gamma_r} \right\}^{1/3} \quad \text{----- (2)}$$

the mean armour size (D_{n50}) of 0.0325m is derived. The placement technique used for armour is random placement. The secondary armour and the core were also designed as for a conventional breakwater (US Army Corps of Engineers, Shore Protection manual, 1984).

Protected breakwater Model

The model consists of a conventional breakwater of slope 1V:2H protected by a stable trapezoidal submerged reef having a slope of 1V:2H. The submerged reef is constructed with a height (h) of 0.25m and varying crest width (B) from 0.1 to 0.4m (i.e. $B/d=0.25 - 1.33$), with homogeneous pile of stones of 30gms optimum weight (i.e. nominal diameter, D_{n50} of 0.0221m, Shirlal et al. 2006). The reef is located at varying seaward distances (X) of 1, 2.5 and 4.0m (i.e. $X/d = 2.5 - 13.33$) from the main conventional breakwater as shown in Fig.1.

Model testing

In the first phase, conventional single breakwater model is tested for its armour stability in a varying wave climate and in the second phase protected breakwater is tested for similar wave climate. The test conditions are given in Table 1.

Test procedure

Initially the newly constructed breakwater slope is surveyed with the profiler, which is, the reference survey for comparison of subsequent surveys. The waves are sent in short burst of five waves during the test so that the generator would be shut off just before the wave energy reflected from

breakwater slope could reach the wave flap. The model is subjected to a series of smaller wave heights starting from 0.1m and then gradually wave height is increased by 20% each time till it reached the highest value of 0.16m for different periods of 1.5, 2.0 and 2.5sec and water depths of 0.3, 0.35 and 0.4m.

Waves are run in bursts in the model until it appeared that no armour cubes would be moved further by waves of this height or 3000 waves which is equivalent to an actual storm of 6 to 11hours duration, for each trial or the failure of the structure whichever occurred earlier i.e. number of waves generated (N) could be 3000 or less. This is because more than 90% of the total damage would have already been inflicted by that time and equilibrium would have been established (Hegde and Samaga, 1996 and Van der Meer and Pilarczyk, 1984). The data such as incident and transmitted wave heights and damage profile of conventional single breakwater are collected. Then transmission coefficient (K_t) and Damage level (S) are computed. Damage level is calculated as the ratio of area of erosion (A_e) to square of nominal diameter D_{n50} of breakwater armour (Van der Meer, 1988). The damage criteria for a breakwater with armour slope of 1V: 2H is as follows (Van der Meer, 1988).

$S = 2$ to 3 (No damage)

$S = 5$ to 6 (Intermediate damage)

$S \geq 8$ (Failure)

The failure in these tests is defined as the displacement of primary armour cubes so that filter layer is exposed to wave action. The damage quantification adopted in both the cases is same. Finally the relationship between deep water wave steepness parameter (H_0/gT^2), coefficient of transmission (K_t) and damage level (S) are analysed through the non-dimensional graphs.

Results and discussions

The variation of transmission coefficient (K_t) with deep water wave steepness (H_0/gT^2) and damage level (S) with deep water wave steepness are shown only for typical cases of seaward spacing (X) of 1m, 2.5m and 4m here.

A. Conventional single breakwater

Variation of S with H_o/gT^2

The trends of damage level (S) with varying wave steepness parameter (H_o/gT^2) for increasing depths of water of 0.3m, 0.35m and 0.4m i.e. increasing ranges of depth parameter (d/gT^2) are shown in Fig. 2. The damage increases with an increase in steepness for a particular range of d/gT^2 . This is because steeper waves have higher energy and inflict increased damage on the breakwater. Also impact of wave period also can be seen. The damage due to shorter period waves of 1.5secs (i. e. higher values of H_o/gT^2) is seen on right hand side of the figure whereas, damage of longer period waves of 2.5sec (i. e. zero damage for smaller values of H_o/gT^2) are seen on the left hand side and damages for period of 2sec are in the middle of the figure.

It is also seen that influence of depths of water on damage decreases with an increase in wave period. Figure also shows large damage for waves of period 2sec when compared with the wave period of 1.5sec and no damage occur for wave period of 2.5 sec. Ranges of damage level (S) decreases with an increase in period.

B. Protected breakwater system

(i) Submerged reef of crest width 0.1m (i.e. $B/d=0.25-0.33$) placed at a seaward distance of 1m (i.e. $X/d=2.5-3.33$).

Variation of K_t with H_o/gT^2

Fig. 3 shows the best fit lines for variation of transmission coefficient K_t with the deep water wave steepness parameter (H_o/gT^2) for varying relative reef height (h/d). K_t decreases with an increase in H_o/gT^2 and (h/d). This is because submerged reef is efficient in breaking the steeper waves and efficiency in breaking the waves increases with the increase in reef height.

The influence of H_o/gT^2 on wave breaking is minimal for h/d of 0.833 and 0.625 (i.e. the depths of 0.3m and 0.4m). K_t drops from 0.95 to 0.82 (13.68%), 0.95 to 0.87 (8.42%) and 1.0 to 0.95 (5.0%) for depths of 0.3m, 0.35m and 0.4m respectively. The average trend shows K_t values higher than 0.8 whereas, actual K_t varies between 0.82 and 1.0.

Variation of S with H_o/gT^2

The trends of damage level (S) with varying wave steepness parameter (H_o/gT^2) for increasing depths of water of 0.3m, 0.35m and 0.4m i.e. increasing ranges of depth parameter (d/gT^2) are shown in Fig 4. The damage due to waves of period 2.0sec is seen as sand ditched between that for wave periods of 2.5sec and 1.5sec on left and right side respectively and there is no damage for period of 2.5sec.

More damage is observed for a wave period of 2sec because of resonance of armour units resulting in increase in rocking and displacement. Ranges of damage level S lies between 1.2 to 10.6 and 1.13 to 14 for wave periods of 1.5 sec, and 2.0sec respectively. And comparing with the conventional breakwater for the wave period of 1.5sec, the maximum damage level decreases from 4% to 19%, and it decreases from 5% to 19% for the wave period of 2.0sec and no damage is found for wave period of 2.5sec. However, the increase in reef crest width did not reduce the damage level significantly.

(ii) Submerged reef of crest width 0.4m (i.e. $B/d=1-1.33$) placed at a seaward distance of 2.5m (i.e. $X/d=6.25-8.33$).

When the crest width (B) was 0.1, 0.2 and 0.3m, K_t varied between 0.4 – 0.887 and the damage level of inner breakwater was reduced by 5-26%, 8-62% and 65-100% respectively while comparing with conventional single breakwater. Since the breakwater was not completely protected, it was decided to experiment with a reef of crest width 0.4m and the results of same are presented below.

Variation of K_t with H_o/gT^2

Fig. 5 illustrates the variation of transmission coefficient K_t with the deep water wave steepness parameter (H_o/gT^2) through the best fit lines for varying relative reef height (h/d). K_t decreases with an increase in H_o/gT^2 and (h/d). K_t decreases from 0.55 to 0.38 (30.9%), 0.64 to 0.53 (17.19%), and 0.708 to 0.55 (22.32%), for h/d of 0.833, 0.714 and 0.625 i.e. for depths of water of 0.3m, 0.35m and 0.4m respectively while $1.45 \times 10^{-3} < H_o/gT^2 < 7.85 \times 10^{-3}$.

The wave height attenuation achieved is 29.2% to 62%. The average trends show a decrease in K_t from 0.45 to 0.4, 0.64 to 0.52 and 0.67 to 0.62 for the same depths. It can be observed that with an increase in relative reef height (h/d), wave damping increases and the influence of wave steepness on K_t is relatively more for a depth of 0.35m.

Variation of S with H_o/gT^2

From Fig. 6 it is seen that the reef of crest width 0.4m located 2.5m seaward of breakwater dissipated the wave energy and completely protects the inner main breakwater without allowing the waves to inflict any damage to it.

(iii) Submerged reef of crest width 0.3m (i.e. $B/d=0.75-1$) placed at a seaward distance of 4m (i.e. $X/d=10-13.33$).

For the reef of crest width (B) 0.1 and 0.2m, K_t varied between 0.37 – 0.72 and the damage level of inner breakwater was reduced by 8-28% and 4-39% respectively while comparing with conventional single breakwater. Since, in this case too the breakwater was not completely protected, it was decided to repeat the experiment with a reef of crest width 0.3m and the results of same are presented below.

Variation of K_t with H_o/gT^2

The variation of transmission coefficient K_t with the deep water wave steepness parameter (H_o/gT^2) for varying relative reef height (h/d) is as shown in Fig 7. From the figure it is observed that K_t decreases with an increase in wave steepness parameter. As water depth increases, there is an increase in value of K_t indicating lesser attenuation and varies in the ranges of 0.56 to 0.66, 0.64 to 0.73 and 0.64 to 0.81 for depths of water of 0.3m, 0.35m and 0.4m respectively.

Also more attenuation is observed at depth 0.3m and period of 1.5 sec compared to 2.0 sec and 2.5 sec. This is due to an increased relative reef height, attenuating the steeper waves effectively at the crest of reef.

Variation of S with H_o/gT^2

The trends of damage level (S) with varying wave steepness parameter

(H_o/gT^2) for increasing depths of water of 0.3m, 0.35m and 0.4m i.e. increasing ranges of depth parameter (d/gT^2) are shown in Fig 8.

The damage due to shorter period waves of 1.5sec (i. e. higher values of H_o/gT^2) is seen on right hand side of the figure whereas, damage of longer period waves of 2.5 sec (i. e. smaller values of H_o/gT^2) are seen on the left hand side and there is no damage for period of 2.5sec. More damage is observed for a wave period of 2sec because of resonance of armour units resulting in increase in rocking and displacement. For shallower depth (i.e. $0.004 \leq d/gT^2 \leq 0.013$) the damage progresses slowly as wave steepness increases. On the contrary, for relatively higher depths (i.e. $0.005 \leq d/gT^2 \leq 0.015$ and $0.006 \leq d/gT^2 \leq 0.018$) the damage level increases sharply with the increasing of wave steepness. This behaviour is commonly found for wave period of 1.5sec and 2 sec. Ranges of damage level S lies between 3.71 to 6.92 and 4.97 to 10.60 for wave periods of 1.5 sec, and 2.0sec respectively.

When comparing with the conventional breakwater for the wave period of 1.5sec, the maximum damage level decreases from 35% to 41%, and it decreases from 34% to 50% for the wave period of 2.0sec and no damage is found for wave period of 2.5sec. But while comparing with the reef of crest width 0.3m placed at a seaward distance of 2.5m (i.e. X/d 6.25 – 8.33), maximum damage level is from 100% to 264% and 82% to 211% more for the wave period of 1.5 sec and 2 sec respectively.

Conclusions

The following conclusions are deduced from the present experimental results:

- For conventional single breakwater, as the depth of water increases from 0.3 to 0.4 m (i.e. 33.3%), for the wave period of 1.5 and 2sec, the maximum damage level increases from 5.82 to 11.54 (i.e. by 98.28%), and 9.98 to 16 (i.e. by 60.32%) respectively. While there is no damage for the waves of period of 2.5sec.
- For the protected breakwater with the submerged reef of crest width 0.1m constructed at a seaward distance of 1m,

- K_t varied between 0.82 – 1.0 and the damage level is reduced by 4% to 19% when compared with that of conventional single breakwater.
- Submerged reef of crest width 0.4m ($B/d = 1 - 1.33$) located at 2.5m ($X/d = 6.25 - 8.33$) seaward distance decreased the K_t from 0.708 to 0.38 and completely safeguarded the main breakwater.
 - In case of reef constructed at a seaward distance of 4m with crest width of 0.3m, the K_t varied between 0.56 – 0.81 and damage level reduced by 34-50%.

Acknowledgements

Department of Applied Mechanics and Hydraulics, National Institute of Technology Karnataka, Surathkal, India provided the facility to carry out this research in Marine Structure laboratory.

References

- [1] Ahrens, J. P. (1989), Stability of reef breakwater, J. of Waterw. Port, Coastal and Ocean Engg., 115(2), 221 – 234.
- [2] Cox, J. C., and Clark, G. R. (1992), Design, development of a tandem breakwater system for Hammond, Indiana, Coastal Structures and Breakwaters, Thomas Telford Ltd., London, 111 – 121.
- [3] Cornett, A., Mansard, E., Funke, E.(1993), Wave transformation and load reduction using a small tandem reef breakwater-Physical model tests, Proc., Int. Conf. on Waves-93, New Orleans, USA, 1008-1023.
- [4] Dattatri, J. (1978), Analysis of regular and irregular waves and performance characteristics of submerged breakwaters, Ph.D Thesis Dept. of Civil Engg. IIT Madras, Chennai, India.
- [5] Gadre, M. R., Somayaji, N., and Kale, A. G. (1985), Stones in breakwaters and seawalls, Proc., 1st Nat. Conf.on Dock and Harbour Engg., IIT Bombay, Dec., 1, B-107 – B-112.
- [6] Gadre, M. R., Somayaji, N., Poonawala, I. Z., and Kudale, M. D. (1989), Use of sand filled rubberized coir bags in coastal protection works, Proc., Conf. on Coastal and Port Engg. In Developing Countries, Indonesia, 1, 166 – 180.
- Pacific Regional Division of the Int. Assn for Hydr.Res., Langkawi, Malaysia, 1, 287 – 294.
- [8] Neelamani, S and Sunderavadivelu, R. (2003), Plans to win back a sandy beach in pondicherry, South-East coast of India, Proceedings of the 3rd International Surfing Reef Symposium, June, Raglan, New Zealand, pp 375 – 377.
- [9] Pilarczyk, K. W., and Zeidler, R. B. (1996), Offshore breakwater and shore evolution control, A.A. Balkema Rotterdam, The Netherlands, pp 334.
- [10] Shirlal Kiran G., Subba Rao, venkata Ganesh and Manu (2006), Stability of Breakwater Defended by a Seaward Submerged Reef, Ocean Engineering, An International Journal of research and development, Pergamon, Elsevier Science Ltd. New York, N.Y., U.S.A. Vol. 33 pp 829 -846.
- [11] U. S. Army Corporation of Engineers (1984), "Shore Protection Manual (SPM)", Coastal Engg. Research Centre, U.S. Govt. Printing Office, Washington, D.C.
- [12] Van der Meer, J. W. (1988), Stability of breakwaters – Delft hydraulics developments, Proc., 3rd Nat. Conf .on Dock and Harbour Engg. Dec., K.R.E.C Surathkal, 889-899.
- [13] Van der Meer, J. W., and Pilarczyk K. W. (1984), Stability of rubble mound slopes under random wave attack, Proc., Coasta l Engg. Conf., 2620 – 2634.

Table 1 Test conditions

Water depth (d)	0.3m, 0.35m & 0.4m
Wave height (H _i)	0.1m, 0.12m, 0.14m & 0.16m
Wave periods (T)	1.5sec, 2.0sec & 2.5sec
Wave flume type	Two dimensional
Nature of waves	Regular
Storm duration (N)	3000 waves
Angle of wave attack	90°

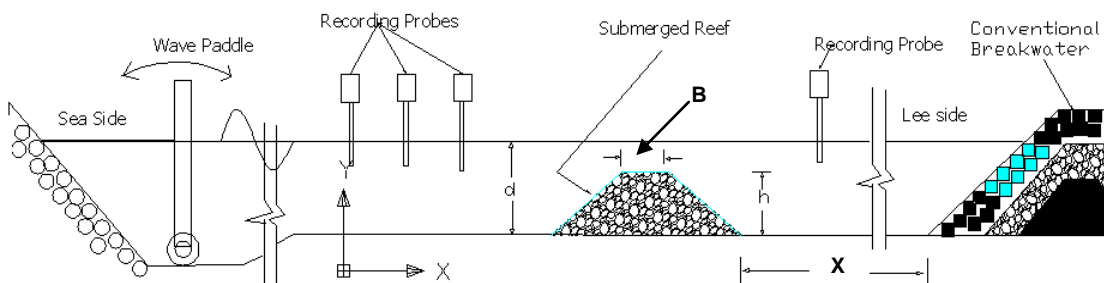


Fig. 1 Experimental set up

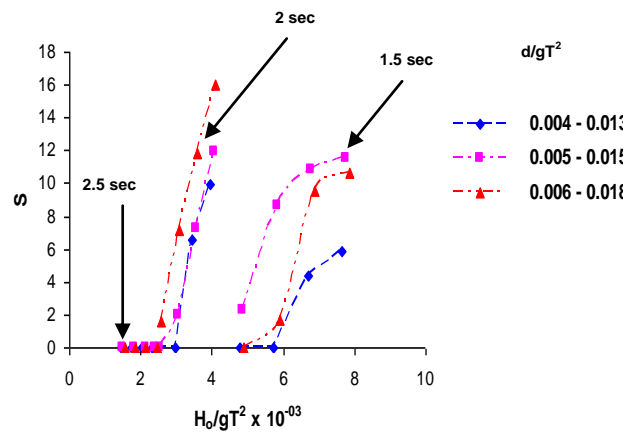


Fig. 2 Variation of S with H_o/gT^2

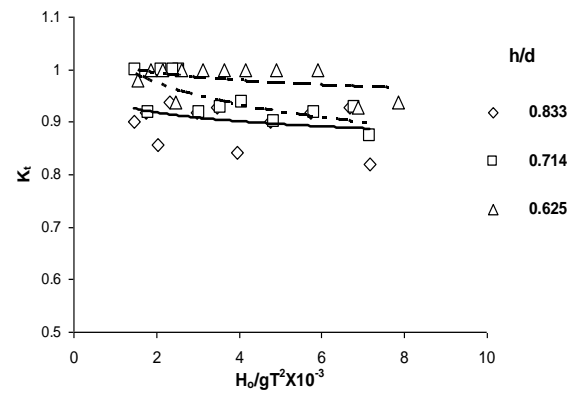


Fig. 3 Variation of K_t with H_o/gT^2

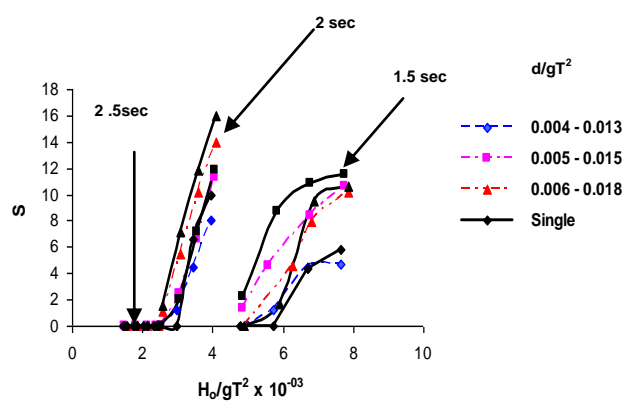


Fig. 4 Variation of S with H_o/gT^2

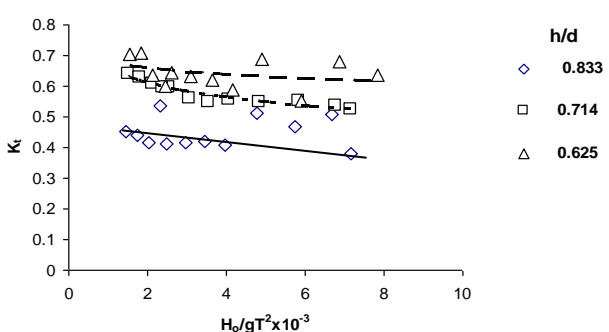


Fig. 5 Variation of K_t with H_o/gT^2

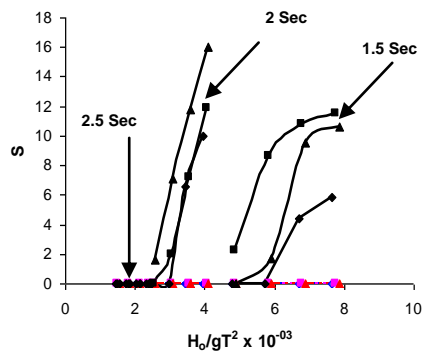


Fig. 6 Variation of S with H_0/gT^2

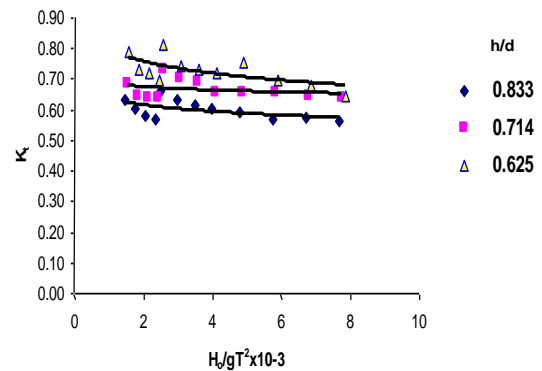


Fig. 7 Variation of K_t with H_0/gT^2

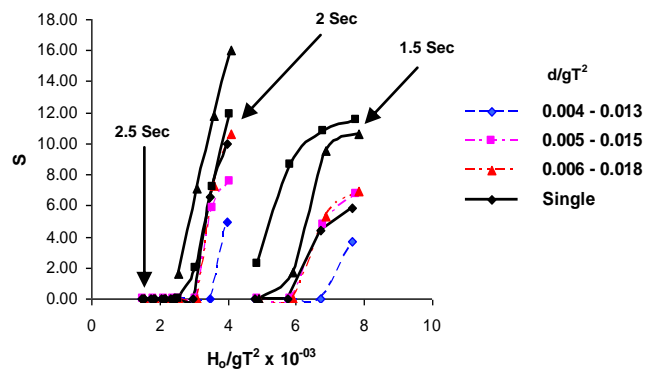


Fig. 8 Variation of S with H_0/gT^2

Comprehensive Physical Model Study on Wave transmission at Plate Structure

KIRAN G. SHIRLAL¹

SUBBA RAO² and **ROOBIN V. VERGHESE³**

1 Department of Applied Mechanics and Hydraulics, National Institute of Technology Karnataka, Surathkal, Mangalore 575025, India. e-mail: kshirlal@gmail.com

2 Department of Applied Mechanics and Hydraulics, National Institute of Technology Karnataka, Surathkal, Mangalore 575025, India. e-mail: surakrec@gmail.com

3 Department of Applied Mechanics and Hydraulics, National Institute of Technology Karnataka, Surathkal, Mangalore 575025, India. e-mail: roobin99@gmail.com

Abstract: Investigators are increasingly concentrating their focus of research on coastal protection which is shifting from the hard measures to eco-friendly solutions with optimal usage of construction materials. A structure located near the water surface is known to be effective in bringing down the wave activity behind it, since; the energy of the waves is concentrated in the region close to the surface. This paper explains the comprehensive experimental study to evaluate the transmission coefficients (K_t) of various configurations of submerged plate structures. K_t for various plate configurations such as single plate, twin plate and combined plate are obtained. It is found that a single plate inclined at 60° to the horizontal is generally effective i. e. $K_t \leq 0.6$ to a large extent. However, the twin and combined plate structures improved the performance.

Keywords: coastal protection, eco-friendly solution, experimental study, single plate structure, combined plate structure, transmission coefficient

Introduction

Investigators are increasingly concentrating their focus of research on coastal protection which is shifting from the hard measures to ecologically acceptable solutions with optimal usage of construction materials. Floating structures, pile breakwaters and horizontal plate breakwaters are being investigated by various researchers with renewed interest. Coastal tourist locations, recreational and water sporting areas etc., need to maintain wave activity in a preset level throughout the year. A structure located near the water surface is known to be effective in bringing down the wave activity behind it, since; the energy of the waves is concentrated in the region close to the surface.

Investigations have shown that a horizontal plate fixed at the surface or slightly below the surface can cause

considerable wave attenuation due to frictional resistance and wave breaking. Inclined plate is found to be more effective

than the horizontal one, since; it penetrates through the layers of water with dissimilar particle velocities and promotes their interaction. (Nallayarasu et al, 1994, Subba Rao et al, 2007, 2009).

The steep waves acting in a region are known to be one of the primary reasons behind the severe coastal erosion at some locations. Dattatri et al. (1978) reported that a plate breakwater can induce breaking of the steep waves. The optimum value of relative depth of submergence (ds/d , where ds is the depth of the top of breakwater from still water level and d is the water depth) may vary from 0 to 0.2. A general solution for the problem of wave scattering on a fixed horizontal plate was attempted by Patarapanich (1984) using finite element method.

Cheong and Patarapanich (1992) conducted a theoretical analysis of double plate system and derived transmission coefficients. It was observed that the lowest wave transmission occurs when ds/d is about 0.10 to 0.20 and the

corresponding transmission coefficient (K_t) is in between 0.3 to 0.5.

Neelamani and Reddy (1992) conducted an experimental study and found that the horizontal plate at the surface provides the least values of K_t .

Nallayarasu et al. (1994) analysed a fully submerged inclined plate using linear diffraction theory using FEM.

Wang and Shen (1999) conducted mathematical model analyses of multiple plate breakwaters and reported a minimum value of $K_t = 0.78$ when $B/L = 0.32$ (where, B is the length of the plate and L is the wave length) and $ds/d = 0.25$. Neelamani and Vedagiri (2002) carried out physical model studies on twin vertical barrier and found that the transmission decreases with the depth of immersion and wave steepness.

A twin plate breakwater system consisting of a pair of identical horizontal plates with one plate at the surface and other just below it was investigated analytically using the linear potential wave theory (Usha and Gayatri, 2005). The K_t values reduced with increase in relative submergence (d/L) for all values of spacing (s) between the plates. The optimum relative spacing of $s/d=0.23$ and the relative width of plate ranged between 0.37 and 0.39 were optimum which resulted in K_t values ranging from 0.2 to 0.4. The performance of the twin plate system was better than that of the single surface plate breakwater and single submerged plate breakwater.

Physical model studies on a single surface plate breakwater and twin plate breakwater with regular and random waves have shown that the wave transmission decreased corresponding to the increase in B/L ratio (Neelamani and Gayathri, 2006). The values of K_t varied between 0.1 and 0.7 for variations of B/L from 0.18 to 0.84 and s/d from 0.5 to 0.40. Multiple-layered breakwater consisting of several horizontal plates was tested using physical models under a regular wave environment (Wang et al. 2006). The transmission coefficient decreased with increase in the relative plate width (B/L). It was below 0.5 for $B/L > 0.25$ which indicated that the multiple layer plate breakwater can dissipate the wave energy significantly. K_t was found to decrease with an increase in wave steepness (H/L).

After going through the available literature, a need was felt to physically model the different configurations of plate structure, to study the performance, as the available results of the numerical studies were far from convincing.

This paper explains the comprehensive experimental study to evaluate the transmission coefficients of different configurations of submerged plate structures.

Objectives

The objectives of the present study are to experimentally investigate the wave transmission coefficient (K_t) and reflection coefficient (K_r) of different submerged plate structure configurations under varying wave characteristics and water depths.

Experimentation

Fig.1 shows the wave flume and the test model. The experiments on the submerged plate structures were carried out in a 50m long, 0.71m wide and 1.1m deep wave flume. The flume has a smooth concrete floor and the side walls are made of glass for about 20m of its length. The flume is provided with a bottom-hinged flap-type wave generator operated by an 11kW, 1450 rpm induction motor which is regulated by an inverter drive (0–50 Hz) so as to rotate at variable speed of 0 to 155 rpm. The system can generate monochromatic waves with a wave height ranging from 0.02 to 0.24m and periods ranging from 0.8 to 4s while water depth can be varied up to 0.5 m. The waves pass through a filter made up of thin parallel vertical plates to produce smooth waves by reducing turbulence.

Model plate structures were constructed using smooth steel plates of 0.003m thickness. The experiments were carried out with depth of submergence (ds) varying from 0 to 0.15m and angle of inclination ranging from 0 to 90° with respect to horizontal. Four numbers of capacitance-type wave probes along with amplification units were used for data acquisition, three for acquiring incident wave (H_i) and reflected wave height (H_r) and one for transmitted wave height (H_t) as shown in Fig.1. Load cells were used to measure the wave forces on the plate structures. The wave flume was filled with

ordinary water to the required depth (d) of 0.3m, 0.4m and 0.5m. The models were tested for regular wave heights (H_i) of 0.05, 0.1 and 0.15m with varying periods (T) of 1.0 to 2.2s. During the experiment, the signals from wave probes were verified online and recorded by the computer through the data acquisition system. The transmission and reflection coefficients are calculated as follows:

$$K_t = \left(\frac{H_t}{H_i} \right) \quad (1)$$

and

$$K_r = \left(\frac{H_r}{H_i} \right) \quad (2)$$

The normalized wave forces $\{F_x\}$ and $\{F_y\}$ are computed as under:

$$\{F_x\} = \left(\frac{F_x}{pgab} \right) \quad (3)$$

and

$$\{F_y\} = \left(\frac{F_y}{pgab} \right) \quad (4)$$

where, F_x and F_y are the absolute values of maximum horizontal and vertical wave forces measured respectively, B is the length of the plate, a is the wave amplitude and 'p' is the specific gravity of water.

The philosophy

The philosophy of the plate structure is that, each plate configuration obstructs the waves propagating in the flume, interferes in the wave field in a unique way and disturbs the wave field. The waves break causing turbulence. Whereas, the gap between the twin and combined plates is expected to act as energy damping zone where the wave energy transmitted over the front plate may get partially dissipated due to turbulence. It is also expected that higher turbulence will be produced in this region as the inclined plate directs the wave to move upward and interact with the upper layers of the water column. The friction, turbulence and wave breaking result in loss of energy.

Results

The data acquired by the probes was analysed using the software to obtain the incident, reflected and transmitted wave characteristics. K_t , K_r , $\{F_x\}$ and $\{F_y\}$ and non-dimensional parameters such as H_0/gT^2 , ds/d , B/d and db/d were calculated and the required graphs were plotted. Only typical graphs, regarding the performance of different plate configurations with B/d of 0.8, are shown to highlight their efficiency in reducing K_t , K_r , $\{F_x\}$ and $\{F_y\}$ for varying relative depth of submergence (ds/d) while varying the wave steepness parameter (H_0/gT^2) and plate angle θ .

a) Single inclined plate structure

Fig. 2 and 3 illustrate K_t and K_r varying with plate angle θ and H_0/gT^2 while Fig. 3 and 4 show the variation of wave forces on the plate. It is generally observed that for a 60° inclined plate, K_t decreases and K_r increases with increase in plate angle respectively for any given H_0/gT^2 . The maximum values of K_t and K_r for ds/d of 0.0 are about 0.75 and 0.5 while the same for ds/d of 0.1 are 0.75 and 0.4 respectively. For a 60° inclined plate, Fig. 4 and 5 indicate moderate normalized wave forces $\{F_x\}$ and $\{F_y\}$ between 0.2 and 0.3 for $ds/d=0.0$ and around 0.2 while ds/d is kept at 0.1.

The plate with 60° inclination is found to have a potential to reduce K_t below 0.6 if its configuration is modified suitably. So this plate is selected for further study.

b) 60° inclined twin plate structure

Two plates with angle of inclination of 60° with varying spacing (s/B) and length B/d are selected as shown in Fig. 6. The length of the plate (B) is 0.24, 0.32 and 0.40m for water depth (d) of 0.30, 0.40 and 0.50m respectively so that B/d , ds/d and db/d are maintained at 0.80, 0.10 and 0.21 respectively for all water depths. The horizontal spacing (s) between the plates is varied such that relative spacing s/B values ranging from 0.125 to 1.375 were obtained.

The results of a typical 60° twin plate structure for a water depth of 0.5m with $B/d = 0.80$ are presented in Fig. 7 and Fig. 8 and are compared with those for a single plate structure.

K_t reduces with increase of s/B and its range of variation is from 0.24 to 0.75 while it varies between 0.5 and 0.75 for single plate. Except in the case of very gentle waves of $H_0/gT^2 < 5 \times 10^{-3}$, for all other waves $K_t < 0.6$ as shown in Fig. 7. In Fig. 8, K_r of the twin plate system is observed to vary from 0.36 to 0.45, while that of a single plate at SWL, it varies from 0.34 to 0.50. Since, even for a twin plate structure, K_t is not smaller than 0.6 for the complete range of test parameters, it is decided to experiment on combined plate structure to determine whether the performance can be further improved.

c) Combined plate structure

A horizontal plate of length B' ($B'/d = 1.0$) is used to improve the performance of a 60° inclined plate of length B by placing it on the leeside of the inclined plate at different spacing (s) shown in Fig. 9.

The plate with angle of inclination of 60° with $B/d=0.80$, $ds/d=0.1$, $db/d = 0.21$ at a relative spacing s/B varying from 0.0 to 0.4 is selected for the study and the results are briefly presented below.

K_t is found to vary from 0.23 to 0.64, when ds/d is 0.0, for different spacing (s/B) as shown in Fig. 10. The trend lines are parallel to each other when plotted against H_0/gT^2 . But for $ds/d=0.1$ $K_t \leq 0.6$ for complete range of test parameters. The smallest K_t is found with $s/B=0.2$. The K_r lies around 0.4 as shown in Fig. 11.

Conclusions

The following conclusions are deduced from the experimental results:

- Among the different single plate configurations tested, the plate with 60° inclination with $ds/d=0.1$ exhibited K_t around 0.6 for steeper waves only and showed the potential for improvement in performance.
- Except in the case of very gentle waves of $H_0/gT^2 < 5 \times 10^{-3}$, $K_t < 0.6$ is observed for the 60° inclined twin plate structure.
- The combined plate structure with a 60° inclined plate and horizontal plate on the leeside with $ds/d=0.1$ and $db/d=0.21$, is found effective with $K_t \leq 0.6$ for complete range of test parameters for which K_r is around 0.4.

Acknowledgements

Authors gratefully acknowledge the support of the Department of Applied Mechanics and Hydraulics, National Institute of Technology Karnataka, Surathkal to carry out this research.

References

- [1] Cheong, H. F., and Patarapanich M., (1992), Reflection and transmission of random waves by a horizontal double-plate breakwater, Coastal Engineering Journal, Vol. 18, pp. 63–82.
- [2] Dattatri, J et al (1978), Performance characteristics of submerged breakwater, Proceedings of 16th International Conference on Coastal Engineering, Hamburg, ASCE, pp. 2153–2171.
- [3] Nallayarasu S et al (1994), Wave induced pressures and forces on a fixed submerged inclined plate. Journal of Finite Elements in Analysis and Design, Vol. 18, pp. 289–299.
- [4] Neelamani S., and Gayathri T., (2006), Wave interaction with twin plate wave barrier. Journal of Ocean Engineering, Vol. 33, pp. 495–516.
- [5] Neelamani, S., and Reddy, M.S., (1992), Wave transmission and reflection characteristics of a rigid surface and submerged horizontal plate. Journal of Ocean Eng., Vol. 19, No. 4, pp. 327–341.
- [6] Neelamani, S., and Vedagiri, M., (2002), Wave interaction with partially immersed twin vertical barrier. Journal of Ocean Eng., Vol. 29, pp. 215–238.
- [7] Patarapanich, M., (1984), Maximum and zero reflection from submerged plate. ASCE Journal of Waterway, Port, Coastal Ocean Eng., Vol. 110, pp. 171 – 181.
- [8] Subba Rao et al (2007), Plate breakwater as a concept of innovative alternative to submerged breakwater, Proceedings of Indian National Conference on Harbour and Ocean Engineering, (INCHOE-2007), NITK, Surathkal, India, December, pp. 361–367.
- [9] Subba Rao et al (2009), Wave forces and performance of submerged plate breakwater through physical model study. Proceedings of International Conference in Ocean Engineering, (ICOE-2009), IIT Madras, Chennai, India, February, pp. 109–110.
- [10] Usha, R., and Gayathri, T., (2005). Wave motion over a twin-plate breakwater. Journal of Ocean Eng., vol. 32. pp. 1054–1072.
- [11] Wang, K.H., and Shen, Q., (1999), Wave motion over a group of submerged horizontal plates. International Journal of Engineering Science, Vol. 37. pp. 703–715.
- [12] Wang, Y et al (2006). Experimental study on the performance of the multiple-layer breakwater. Coastal Engineering Journal, Vol. 33, pp. 1829–1839.

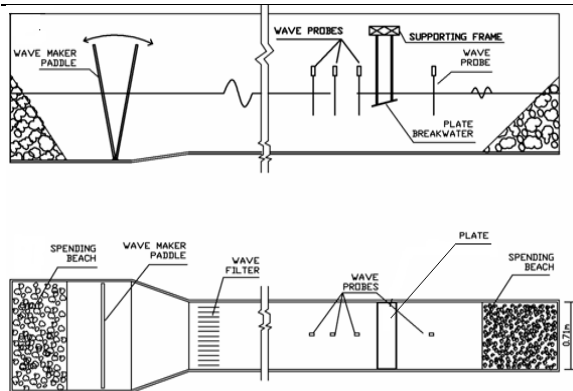


Fig. 1 Side view and plan of the wave flume with plate structure

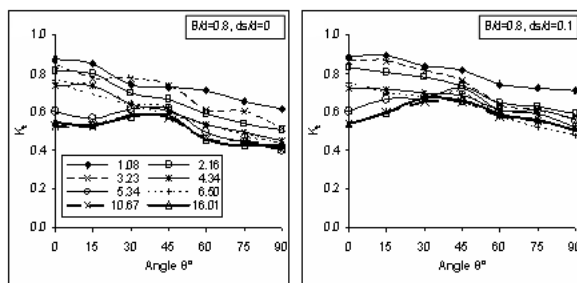


Fig. 2 K_t vs. plate inclination (θ) with $H_0/gT^2 \times 10^{-3}$

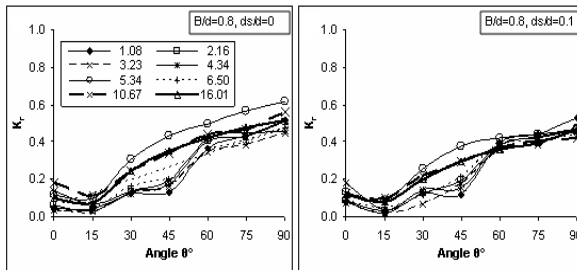


Fig. 3 K_r vs. plate inclination (θ) with $H_0/gT^2 \times 10^{-3}$

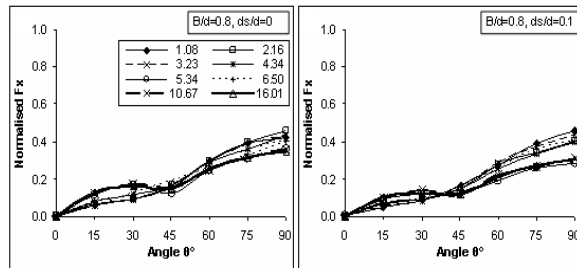


Fig. 4 $\{F_x\}$ vs. plate inclination (θ) with $H_0/gT^2 \times 10^{-3}$

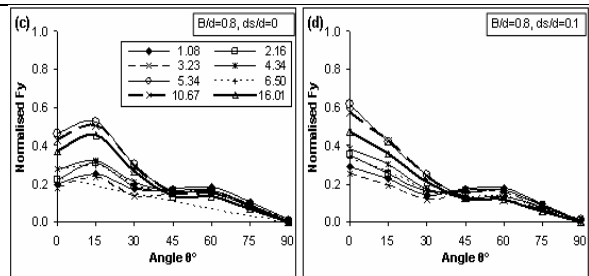


Fig. 5 $\{F_y\}$ vs. plate inclination (θ) with $H_0/gT^2 \times 10^{-3}$

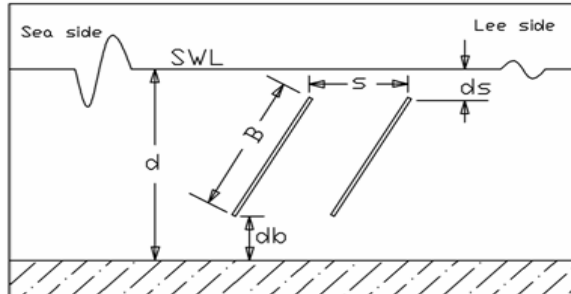


Fig. 6 Definition sketch of twin inclined plate structure

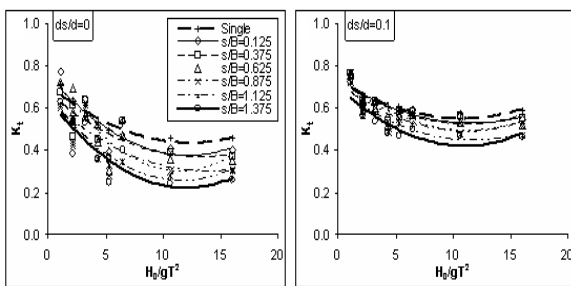


Fig. 7 K_t vs. $H_0/gT^2 \times 10^{-3}$

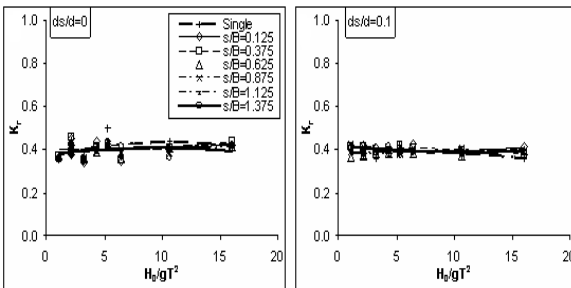


Fig. 8 K_r vs. $H_0/gT^2 \times 10^{-3}$

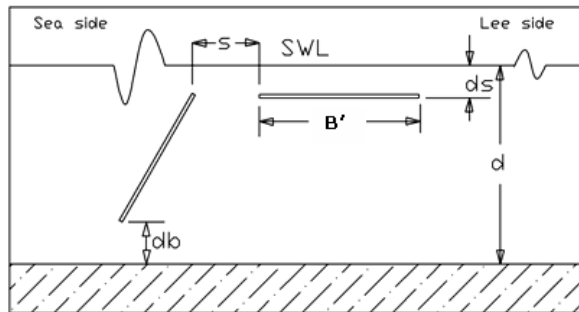


Fig. 9 Definition sketch of combined plate structure

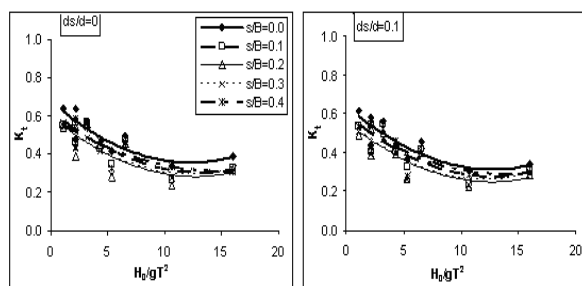


Fig. 10 K_t vs. $H_0/gT^2 \times 10^{-3}$

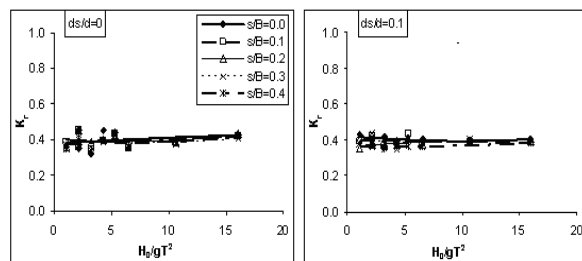


Fig. 11 K_t vs. $H_0/gT^2 \times 10^{-3}$

MICROFABRIC AND MINERALOGICAL STUDIES USING SEM AND XRD ON THE LITHOMARGIC CLAY STABILIZED WITH CEMENT AND QUARRY DUST

PURUSHOTHAM G. SARVADE¹ SITARAM NAYAK²

- ¹ Department of Civil Engineering, Manipal Institute of Technology,
Manipal University, Manipal 576104, Karnataka, India. e-mail:pgsarvade@gmail.com
² Department of Civil Engineering, National Institute of Technology Karnataka,
Surathkal, Mangalore 575025, India. email:snayak65@yahoo.co.in
-

Abstract: The infrastructural development activities due to rapid urbanization, low lying agricultural and marshy lands in and around Mangalore (India) are being converted into estates with locally available lithomargic clay. These filled up areas pose problems of low bearing capacity as well as excessive settlements. As long as this soil is confined and dry, there is a very little or no problem, when it comes in contact with water, it loses its strength. The engineering properties of this soil are enhanced by the addition of additives (cement, quarry dust and quarry dust +cement). In the present study the microfabric and mineralogical aspects of the stabilized lithomargic clay is studied using Scanning Electron Microscope (SEM) and X-ray diffractometer (XRD). The XRD analysis of lithomargic clay stabilized with cement, revealed the formation ettringite, CSH and CAH. The SEM analysis revealed change in the soil structure due to the addition of cement and quarry dust.

Keywords: *lithomargic clay, stabilized, Scanning Electron Microscope, X-ray diffractometer, CSH, CAH*

1. Introduction

The design and construction of the structures on the problematic soil is a challenging task for a geotechnical engineer. For the safe design and construction, the soils should have adequate strength, should be incompressible and have proper permeability. Many soils can prove problematic because they expand, disperse collapse, undergo excessive settlement, lack in strength etc. The soft clays are highly compressible and have a very low bearing capacity. The silty soils possess better strength in dry state and lose considerable strength at saturation. The loose sand is highly compressible and has low bearing capacities, whereas the dense sands cause problems in deep foundation techniques. Such characteristics may be due to their structure, mineralogy, nature of their pore water etc. In such cases, the

properties of the soil have to be improved by suitable means. With the increase in construction activities both in onshore and offshore, it has become imperative to solve the geotechnical problems concerned with soft and compressible soils.

The lithomargic clay is the locally available whitish, pinkish or yellowish silty sand. This type of soil is abundantly available at a depth of 1-3 meters below the top lateritic outcrop in the western coastal belt of Southern India, starting from Cochin to Goa. These soils are the product of tropical or subtropical weathering. Their strength is high in dry conditions, whereas significant reduction of strength takes place when there is an increase in moisture content. These types of dispersive soils are highly susceptible to erosion (Ramesh et al., 2007). Leaching of this soil takes place primarily due to heavy rainfall but other tropical conditions also play their part. Field engineers have to be

extremely careful in handling these types of soil. The construction works in this type of soil is challenging. As long as this soil is confined and dry, there is a very little or no problem, but on the exposure in a cutting or when it comes in contact with water, it loses its strength drastically (Fig. 1). Slope failures, landslides etc., are quite common in this type of soils (Ravishankar et al., 2006).

The infrastructural development activities due to rapid urbanization and fast growing industries in Dakshina Kannada, Udupi and adjacent districts of Karnataka state are forcing the civil engineers to put to the best use of even the poorest sites available which are discarded by our ancestors. These poor sites are characterized by low bearing capacities and large settlements. Low lying agricultural and marshy lands are being converted into estates with locally available lithomargic clay. Large hills are cut for these purposes. These filled up areas pose problems of low bearing capacity as well as excessive settlements because of improper compaction and poor drainage. The best way to improve this soil is to blend it with artificial and natural materials.

The most common additive used for the soil stabilization is Ordinary Portland Cement (OPC). Cement has been found to be effective in stabilizing a wide variety of soils. A cement particle is a heterogeneous substance, containing tricalcium silicate (C_3S), dicalcium silicate (C_2S), tricalcium aluminate (C_3A), and a solid solution tetracalcium alumino-ferrite (C_4A). These four main constituents are the major strength producing compounds. When the pore water of the soil encounters with the cement, the hydration of the cement occurs rapidly and the following major hydration (primary cementitious) products are formed: hydrated calcium silicates, hydrated calcium aluminates, and hydrated lime. The first two hydration products are the main cementitious products formed and the hydrated lime is deposited as a separate crystalline solid phase. The cement particles bind the adjacent cement grains together during hardening and form a hardened skeleton matrix which encloses unaltered soil

particles. In addition, the hydration of cement leads to a rise of pH value of the pore water, and is caused by the dissociation of hydrated lime. The strong bases dissolve the soil silica and alumina (which are inherently acidic) from both the clay minerals and amorphous materials on the clay particle surfaces, in a manner similar to the reaction between a weak acid and a strong base. The hydrous silica and alumina will then gradually react with the calcium ions liberated from the hydrolysis of cement to form insoluble compounds (secondary cementitious products) which harden when cured to stabilize the soil. This secondary reaction is known as the pozzolanic reaction. The primary products harden into high strength additives and differ from the normal cement hydrated in concrete. The secondary processes increase the strength and durability of the soil cement by producing an additional cementing substance to further enhance the bond strength between the particles (Bergado, 1996). The cement stabilization method has gained a wider acceptance in different countries of the world because of the proven versatility of cement as an admixture for stabilization. Hence in the present study cement is used as an admixture to stabilize lithomargic clay.

Due to the high demand for rubble and aggregates for construction purposes, rubble quarries and aggregate crushers are very common. Out of the different quarry wastes, quarry dust is one which is produced in abundance. About 20-25% of the total production in each crusher unit is left out as the waste material. Normally this quarry dust is left in huge heaps in the neighbourhood of the quarry as a waste causing serious health hazards. In this background, any attempt to utilize this waste in developmental activities is relevant. This quarry dust can be used to improve the properties of weak soil. The problems associated with the construction of highways over clayey subgrade can be reduced significantly by mixing with quarry dust (Soosan et al., 2005). Hence quarry dust is also used as an admixture to stabilize lithomargic clay. The stabilization is done in order to increase the strength, reduce deformability, reduce erodability, and provide volume stability.

2. Experimental investigations

For the experimental investigation, lithomargic clay was collected from Kavoor near Mangalore (India) and was studied for geotechnical properties. Ordinary Portland Cement (OPC) was used for stabilizing lithomargic clay and was being carried out by adding various percentages of cement such as 0, 2.5, 5, 7.5 and 10% by weight of dry soil. These soils mixed with cement were tested to get various geotechnical and chemical properties. The samples for strength properties were prepared at maximum dry density and optimum moisture content with the curing period of 7 days. Summary of the results for basic geotechnical characterization is presented in Table 1.

The quarry dust was collected from a nearby quarry and was added to lithomargic clay with various percentages such as 10, 20, 30, 40 and 50% by weight of dry soil. Also the lithomargic clay was stabilized with a combination of quarry dust + cement with various percentages such as 10% quarry dust+2.5% cement, 10% quarry dust+5% cement, 30% quarry dust+2.5% cement, 30% quarry dust+5% cement, 50% quarry dust+2.5% cement and 50% quarry dust+5% cement. These soils mixed with quarry dust and quarry dust+cement were tested to get various geotechnical properties. The samples for strength properties were prepared at maximum dry density and optimum moisture content with the curing period of 7 days. The summary of the results for basic geotechnical characterization for lithomargic clay stabilized with quarry dust is presented in Table 2.

3. Microfabric studies using Scanning Electron Microscope (SEM)

The term "fabric" refers to the arrangement of the particle, particle group, and pore spaces in a soil (Mitchell, 1976). The Scanning Electron Microscope (SEM) is one of the best tools available for the study of the fabric of soils because of its higher resolution capacity together with the large depth of focus. The SEM uses a focused beam of high-energy electrons to generate a variety of signals at the surface of the solid specimens. The signals that

derive from the electron-sample interactions reveal information about the sample including external morphology (texture), chemical composition, and crystalline structure and orientation of materials making up the sample.

In the present study, the scanning electron microscope used is of the type JEOL JSM - 6380 LA and is operated at 5kV and 10kV (Fig.2). The secondary electron imaging (SEI) is used as a mode of imaging. In this case, the secondary electrons are reflected only from the surface of the sample. Thus, the SEM can identify the microfabric of only topmost surface of the sample. First, the entire surface is scanned under low magnification and then, the chosen areas are magnified to get the clear picture of the microfabric arrangement. Seven days cured samples have been taken for this study so that there is reasonable time for the development of the cementitious bonds. The sample preparation included mounting samples on carbon double-stick tape on aluminium stubs. The samples were coated with gold sputter coater.

SEM analysis of lithomargic clay stabilized with cement focuses on understanding the microstructure development with cement content for particular water content (OMC). SEM analysis was carried out on soil samples stabilized with 0%, 2.5%, 5%, 7.5% and 10% cement. Figs. 3a to 3c show some of the typical SEM images of the lithomargic clay, lithomargic clay mixed with 5% of cement and lithomargic clay mixed with 10% of cement respectively.

SEM analysis of lithomargic clay stabilized with various percentages of quarry dust (10%, 20%, 30%, 40% and 50%) was carried out to understand the microstructure development. A typical image of the SEM image of the lithomargic clay stabilized with 50% of quarry dust is shown in Fig. 4.

SEM analysis of lithomargic clay stabilized with quarry dust+cement focuses on understanding the microstructure development with the addition of cement on quarry dust stabilized soil. The analysis is carried out on lithomargic clay stabilized with 10% of

quarry dust + 2.5% cement, lithomargic clay stabilized with 10% of quarry dust + 5% cement, lithomargic clay stabilized with 30% of quarry dust + 2.5% cement, lithomargic clay stabilized with 30% of quarry dust + 5% cement and lithomargic clay stabilized with 50% of quarry dust +2.5% cement and lithomargic clay stabilized with 50% of quarry dust +5% cement. A typical SEM image of lithomargic clay stabilized with 30% quarry dust and 2.5% cement is shown in Fig.5.

4. Mineralogical studies using X Ray Diffraction (XRD)

The X-Ray diffraction method is the most widely used technique for identification, and detection of the clay and non-clay minerals which are present in the soil. All clay minerals have essentially the same general scheme of structure, and their diffraction patterns are similar. But the most characteristic differences are provided by their d -value (d spacing). The X-ray diffractometer used in the present study is of type JEOL- Model DX-GE-2P (Fig.6). In this analysis, the material is exposed to a filtered X-ray beam. The X-ray passes into the material and causes the electrons in the atoms of the minerals to vibrate and reflect the beam through the successive planes. The method involves increasing of incidence angle and monitoring the intensity of the diffracted X-radiation until a maximum value of the diffracted intensity is achieved. Qualitative study by using XRD is carried out to investigate the reaction products of the stabilized soil during the stabilization process. The stabilized soil samples after seven days curing have been used in this investigation.

The XRD analysis is carried out on lithomargic clay stabilized with 0%, 2.5%, 5%, 7.5% and 10% cement. Typical XRD patterns of untreated lithomargic clay and lithomargic clay stabilized with 5% cement are shown in Figs. 7 & 8. The XRD analysis of the lithomargic clay stabilized with 10%, 30% and 50% quarry dust is carried out and a typical pattern of lithomargic clay stabilized with 50% quarry dust is shown in Fig. 9. The XRD analysis is also carried on the lithomargic clay stabilized with 10% quarry dust + 2.5% cement, 30% quarry

dust + 2.5% cement and 50% quarry dust + 2.5% cement and a typical pattern of lithomargic clay stabilized with 50% quarry dust and 2.5% cement is shown in Fig. 10.

5. Results and discussions

The Table 1 and 2 shows the improvement in the geotechnical properties of lithomargic clay stabilized with cement and quarry dust. The SEM image of the lithomargic clay stabilized with 2.5% cement is almost similar to that of the unstabilized sample because the addition of cement is insignificant compared to the soil mass. When the soil is stabilized with 5% (Fig. 3b) and 7.5%, cement hydration products are clearly seen surrounding the soil particles. As the cement content increased, hydration products are clearly seen in the pores and the cementitious products also significantly increased. The cementitious products not only enhance the inter-cluster bonding strength but also fill the pore space. The volume of pores is significantly reduced with cement, thus, the reduction in total pore volume. As a result, the strength significantly increases with cement. In Fig. 3c, when the lithomargic clay is stabilized with 10% cement, inter cluster bonding with cementitious products are clearly visible. The micro structure of the lithomargic clay stabilized with quarry dust differs from that of unstabilized lithomargic clay. When the soil is stabilized with 10%, 30% and 50% quarry dust, there is no cementation between the particles but the structure of the soil becomes denser. And the denseness increases as the percentage of quarry dust increases. Hence a higher densification of soil mass is achieved eliminating all the voids. This increases the strength of the soil (Fig.4). The cementation which is absent in the lithomargic clay blended with only quarry dust is seen when the lithomargic clay is stabilized with selected percentage of quarry dust and cement. As the cement content increased, hydration products are clearly seen in the pores (Fig. 5) and the cementitious products significantly increased.

The XRD pattern of the untreated soil, as shown in Fig. 7, indicated that the soil is composed of silica in the form of

quartz, calcite and kaolinite as dominant minerals. The identification revealed that the untreated soil initially contained no cementing materials. After the stabilization with cement, the formation of CSH and CAH was observed (Fig.8). Ettringite was also found in all the stabilized samples. Ettringite is a calcium aluminum sulfate hydrate (CASH) type mineral which is responsible for the early strength gain [Khoury et al., (2004)]. Ettringite is formed as a result of the reaction of calcium aluminate with calcium sulphate. The XRD pattern of the lithomargic clay stabilized with 10%, 30% and 50% of quarry dust revealed the existence of the following minerals - Quartz, Kaolinite, Magnetite, Zircon and Garnet (Fig.9). The XRD pattern of the lithomargic clay stabilized with quarry dust + cement revealed the existence of the following minerals - Quartz, kaolinite, Calcite, Magnetite, Zircon and Garnet. The formation of hydration product (CSH) is also observed (Fig.10).

6. Conclusions

In the present study SEM and XRD studies are carried out in order to study how the soil properties have been improved. The microfabric (geometric arrangement of platelets) and mineralogical aspects of the lithomargic clay treated with cement and quarry dust have been studied using Scanning Electron Microscope and X-ray diffractometer. The main objective of the investigation is to find out the reason for the strength development of the stabilized lithomargic clay.

The following main conclusions are drawn from the above investigations:

1. The SEM analysis revealed change in the soil structure due to the addition of cement and the quarry dust.
2. The XRD analysis of the shedi soil stabilized with cement resulted in the formation of a new mineral namely, ettringite which is responsible for early strength gain.
3. Due to hydration of cement, it is found from the XRD analysis that there is formation of Calcium Silicate Hydrate (CSH) and Calcium Aluminate Hydrate (CAH) which are responsible for strength development.

References

- [1] Bergado, D. T., Anderson, L. R., Miura, N. and Balasubraminiam, A. S. (1996), Soft ground improvement in low land and other environments, ASCE press, Newyork, pp 234-243.
- [2] Khoury, N. N., Zaman, M. and Laguros, J. G. (2004), Use of XRD patterns to evaluate compressive strength of stabilized aggregates, International center for diffraction data 2004, *Advances in X-ray analysis*, 47, pp 379-384.
- [3] Mitchell, J.K.(1976), Fundamentals of soil behaviour, John Wiley & Sons, Inc. Pp 135.
- [4] Ramesh, H.N. and Nanda, H.S. (2007). "Strength behavior of shedi soil treated with fly ash."13th ARC, Kolkata , pp 893-896.
- [5] Ravishankar, A.U., Suresh, S.N. and Phanikumar, M.V.S.(2006), Strength behavior of shedi soil-lime-pondash mixes-an experimental study, *Highway Research Bulletin*, Indian Roads Congress, pp 1-7.
- [6] Soosan,T.G., Sridharan, A., Jose, B.T. and Abraham, B.M. (2005), Utilization of Quarry Dust to Improve the Geotechnical Properties of Soils in Highway Construction, *Geotechnical Testing Journal*, 28(4), pp 1-10.

Table 1 Geotechnical properties of lithomargic clay stabilized with cement

Parameter	Percentage of cement added				
	0 %	2.5%	5 %	7.5%	10 %
Specific gravity	2.58	2.60	2.62	2.63	2.65
Liquid limit (%)	62	55	52.8	51.8	48
Plastic limit (%)	38.8	39.7	40.3	41.2	43.8
Shrinkage limit (%)	31.8	40.1	41.2	45.4	46.1
Plasticity Index (%)	23.2	15.3	12.5	10.6	4.2
Maximum dry density immediately after cement addition (γ_d) _{max} (kN/m ³)	15.7	15.7	15.7	15.7	15.9
Optimum moisture content immediately after cement addition (%)	22.5	21	20.5	22	22
Maximum dry density after curing period (γ_d) _{max} (kN/m ³)	15.7	15.2	15.4	14.9	14.7
Optimum moisture content after curing period (%)	22.5	22	22.9	25	25
Angle of Internal friction, ϕ	21	31	33	40	45
cohesion value, c (kPa)	29.4	58.8	73.5	88.3	93.2
UCC Strength (kPa)	152	248	397	496	676
Soaked CBR	3.9	28.4	82.5	117.1	138
Coefficient of permeability, k (m/day)	0.00321	0.00172	0.00022	0.00017	0.00010
Compression Index, Cc	5-100 kPa	0.02	0.008	0.007	0.005
	100-800 kPa	0.11	0.1001	0.086	0.063
					0.018

Table 2 Geotechnical properties of lithomargic clay stabilized with quarry dust

Parameter	Percentage of quarry dust added				
	10 %	20%	30 %	40%	50 %
Specific Gravity	2.58	2.60	2.60	2.61	2.62
Liquid limit (%)	54.3	45.5	42.3	40.3	30.7
Plastic limit (%)	36.5	30	29.1	31.1	25.0
Shrinkage limit (%)	30.4	28.5	27.3	26.1	23.6
Plasticity Index (%)	17.8	15.5	13.2	9.2	5.7
Maximum dry density (γ_d) _{max} (kN/m ³)	16.0	16.5	17.0	17.4	18.4
Optimum moisture content (%)	22.0	20.0	17.6	16.6	15.4
UU: Angle of Internal friction, ϕ	25°	26°	28°	29°	30°
UU: cohesion value, c (kPa)	32.36	29.42	22.56	20.59	19.61
UCC Strength (kPa)	354	598	353	141	103
Soaked CBR	4	5	6	8	10
Coefficient of permeability, k (m/day)	0.01313	0.02432	0.0355	0.0467	0.05789
Compression Index, Cc	5-50 kPa	0.0008	0.0004	0.0003	0.0006
	50-400 kPa	0.0016	0.0021	0.0020	0.0018
					0.0004



Fig. 1 Failure of lithomargic clay



Fig. 2 Analytical Scanning Electron Microscope - JEOL JSM – 6380LA

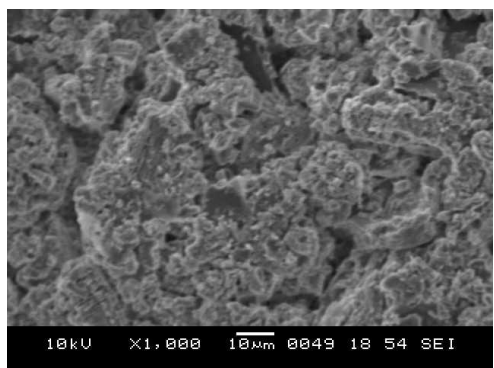


Fig. 3a SEM image of untreated lithomargic clay

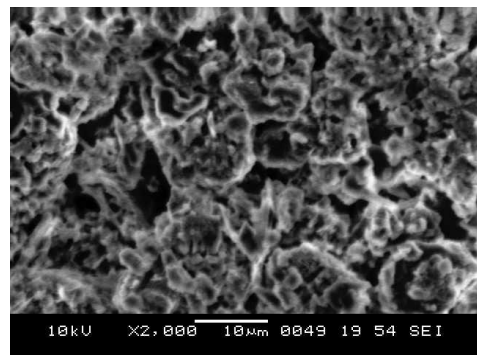


Fig. 3b SEM image of Lithomargic clay+5% cement

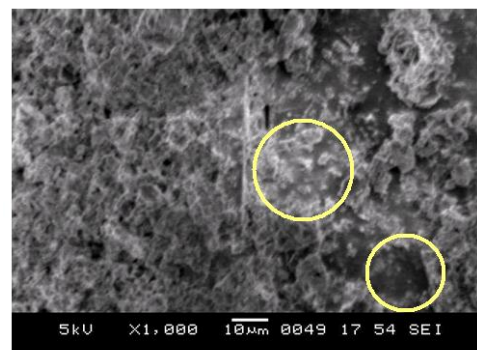


Fig. 3c SEM image of Lithomargic clay+10% cement

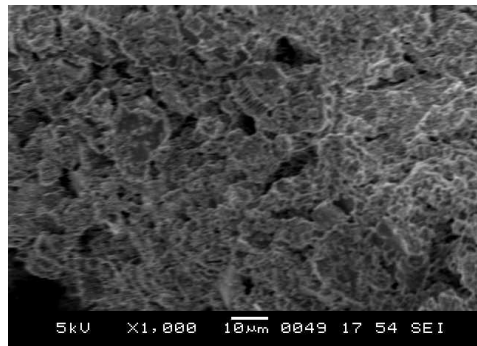


Fig. 4 SEM image of Lithomargic clay+30% quarry dust

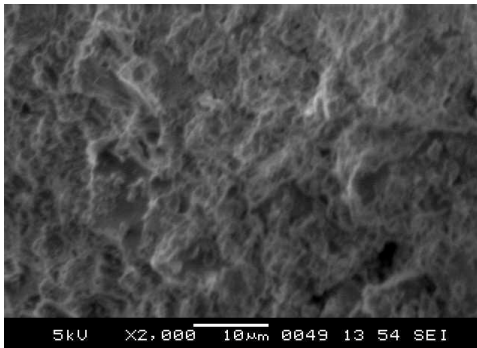


Fig. 5 SEM image of lithomargic clay+30% quarry dust +2.5% cement

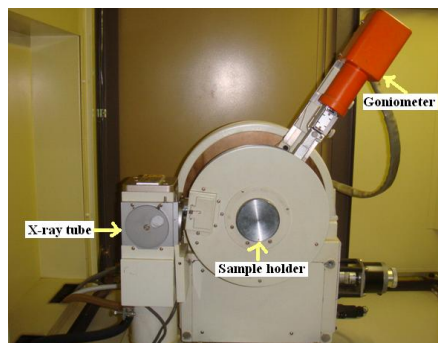


Fig. 6 X-ray Diffractometer-JEOL- Model DX-GE-2P

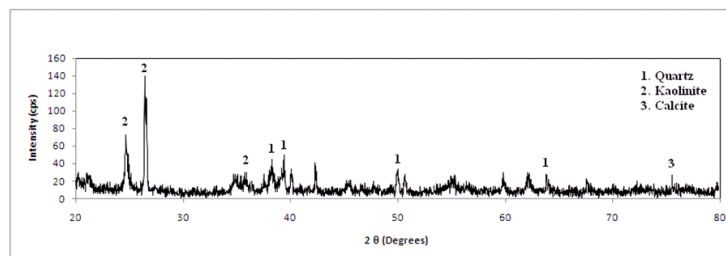


Fig. 7 XRD pattern of untreated lithomargic clay

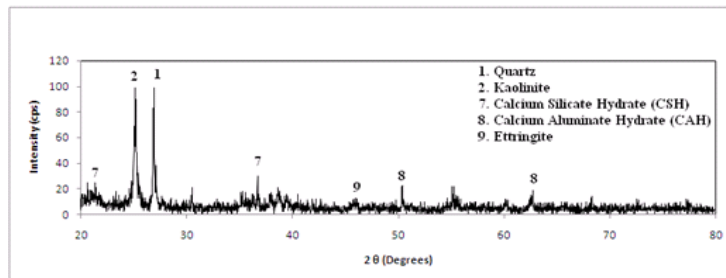


Fig. 8 XRD pattern of lithomargic clay+5% cement

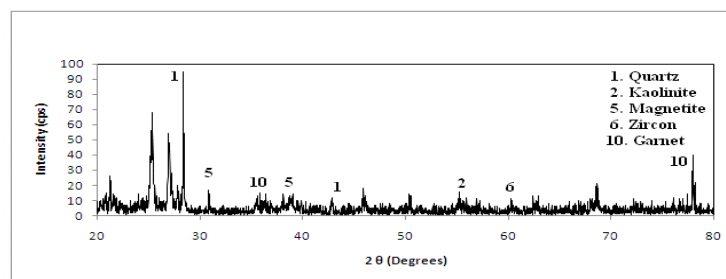


Fig. 9 XRD pattern of lithomargic clay+50% quarry dust

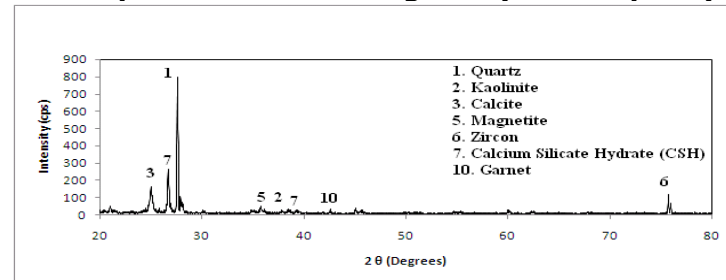


Fig. 10 XRD pattern of lithomargic clay+50% quarry dust+2.5% cement

ANALYSIS OF LONGITUDINAL AND TRANSVERSE PROFILES IN SEETHA-SWARNA AND GANGOLLI RIVERS OF COASTAL KARNATAKA, INDIA

Udaya Shankara H. N.

Department of Civil Engineering, Manipal Institute of Technology, Manipal
(Under Manipal University), India. E-mail: udaya.shankar@manipal.edu

Abstract: The longitudinal profile of a stream is the continuous fall in elevation from origin to mouth. Many stream characteristics like Channel slope, Stream Length, Drainage area, and Bed load can be related to longitudinal and transverse profiles. A range of geological and hydrological factors combine to render most longitudinal profiles to be irregular. These factors are evaluated in this study by considering rivers in the two major watersheds i.e., Seetha-Swarna and Gangolli Composite River Systems of the newly formed Udupi district. Remote Sensing approach is adopted for the purpose. SOI toposheets and updated lineament maps by using the satellite imageries (Indian Remote Sensing satellites, IRS-1C/IRS-1D) of the study area are used for the purpose. Various image processing techniques are adopted for the purpose. The stream is divided into three reaches for the purpose of analysis i.e., upper reach, middle reach and lower reach. The gradient indices which reflect the slope characteristics for these three reaches are calculated for all these rivers and the results are analysed. Many rivers and tributaries in the upper and mid-upper reaches show break in slopes in their longitudinal profiles. This indicates that the streams on the upper reach are structurally controlled. Transverse sections are steep at the origin (V shape) and widen below the Western Ghats and are flat at the alluvium region and river mouth.

Key Words: Longitudinal profile, Transverse profile, Gradient index, Lineament map, structurally controlled, Remote sensing.

Introduction

Longitudinal and transverse characteristics of watersheds are fundamental to describe watershed topography. The longitudinal profile of a valley is the gradient throughout its length. The longitudinal profile of a stream thus is the continuous fall in elevation with respect to horizontal distance from origin to mouth (Ruhe, (1975)). Valleys formed by river action typically have a concave upward profile, steep in the headwaters and gentle in the lower reaches. The lower end of such a profile is adjusted to an effective lower limit of erosion defined by the base level. Transverse profiles are drawn by taking sections perpendicular to the flow directions. The channel shapes are analyzed at different stretches of streams by drawing transverse profiles. Channel slope, Stream Length, Drainage area, and Bed load characteristics are related to longitudinal and transverse profiles (Hack, (1957)). A range of geological and hydrological factors combine to render

most longitudinal profiles to be irregular. A hard resistant rock may cause a waterfall while the presence of a lake may cause a temporary flattening of the profile (Nag, S.K., and Chakraborty, S. (2003)). Tectonic processes causing continents to be uplifted, combined with eustatic (sea level) changes mean that rivers are constantly re-adjusting their longitudinal profiles.

The analysis of the longitudinal profile provides sufficient tectonic information and which can be used to understand the tectonic geomorphology. These profiles contain tectonic information in the form of knick points and their Strahler order as well (Strahler, A. N., (1964)). In any profile the knick points migrate upstream or downstream as the channel responds to the tectonic changes or the change of the lithology along the path of the stream (Shahzad et al (2009)). The sharpness of the knick points gives relative information that how the more recent tectonics or river capture events had occurred. . In general,

the sharper the knick points, the more recently it developed (Wobus et al (2006)). Lineaments are significant lines of landscape caused by joints and faults, revealing the architecture of the rock basement (Hobbs (1904)). According to O Leary et al, (1976), a lineament is a mappable, simple or composite linear feature of a surface, whose parts are aligned in a rectilinear or slightly curvilinear relationship which differs distinctly from the pattern of adjacent features and presumably reflects a subsurface phenomenon. They are the linear features, developed by the tectonic activity, reflecting a general surface manifestation of underground fractures, with inherent characteristics of porosity and permeability of the underlying materials. Structural and tectonic characteristics of an area can be understood better by mapping lineaments. Various image processing techniques adopted on remotely sensed imageries are useful in lineament studies. Data obtained in different spectral bands can be processed which will be used for interpreting lineaments. Dykes and ridges also appear as linear features but they have positive relief. Roads, Railway lines etc which appear as linear structures, have to be distinguished in conjunction with the SOI toposheets.

Methodology

Longitudinal profiles are drawn by considering the stream length along the X-axis and elevation along the Y-axis. The gradient index (Hack, 1981), which is the measure of the slope is calculated by dividing the stream into three reaches i.e., upper reach, middle reach and lower reach. The mid point of the total length of the stream is located on the profile for this purpose and two to four kilometers on either side from this mid point designates middle reach. Upper reach is the segment upstream to this while the segment downstream to this middle reach is the lower reach. The gradient index is computed as follows for individual rivers.

$$\text{Gradient Index(GI)} = \frac{H_1 - H_2}{\log_e L_2 - \log_e L_1} \quad (1)$$

Where H_1 and H_2 are the altitudes of each of a given reach and L_1 and L_2 are the distances from each end of the reach to

the source of the stream measured along the course of the river or tributary. Longitudinal profiles are drawn for the major rivers in both the basins and also for the tributaries (Fig.1 and Fig.2).

Transverse sections are also plotted for the major rivers by considering a length of about one to two kilometres on either side transverse to the main river axis and measuring the distances of the intersecting contours on either side. The contour number gives the elevation at a particular distance from the central axis of the river. Detailed lineament maps of the study area are prepared at the basin level based on digital map of drainage basins, processed satellite imageries and SOI topographical maps. Image processing techniques like non-directional filtering, edge enhancement techniques, band separation etc were adopted for the purpose. Subsequent ground surveys were carried out to confirm these lineaments in the fields. These lineaments represent faults, fractures, joint sets, shear zones, fold limbs etc (Fig.3 and Fig.4).

Results and Discussions

Seetha, Swarna and Madisal rivers are the major rivers in Seetha-Swarna basin. Golihole, Nemar Hole, Markal Hole, Kudluthirtha Hole, Magadde Hole and Kollangar Hole join the Seetha River at the upper reach while Hanakal Halla and Balkattu Hole join at the middle reach and Achladi Hole joins at the lower reach. Machitte Hole, Hekkunje Hole and Happanadka Hole join the Swarna River in Swarna sub-watershed in the upper reach and Durga Hole, Andar Hole and Kada Hole join in the middle reach of Swarna. Similarly, in Madisal sub-watershed, Mathebettu Hole, Kelekila Hole and Jaravattu Hole are the tributaries of Madisal Hole all of which join in the upper reach. There is no major tributary joining in these two rivers in the lower reach.

In Gangolli basin, the main rivers are Kollur, Chakra and Varahi. In Kollur sub watershed, Sowparnika River, Mavinakaru Hole, Belakallu Thirtha Hole and Samse River join the Kollur River at the upper reach. In the middle reach, the major tributary joining this river is Halliberu Hole. In Chakra sub watershed, Savehaklu Hole and Kabbekin Hole join the Chakra River in the upper reach and Idur Halla and Nagodi

Hole combine with Chakra River in the middle reach. No major tributaries exist in the lower reach for these two tributaries. In Varahi or Haladi sub-watershed, Narasipura Hole, Hulikal Hole, Amgudde Hole and Kalu Hole combine with the Varahi River in the upper reach; Dasanakatte River, Sanna Hole and Tombattu Hole join in the middle reach. In the lower reach, Kubja Hole joins with this river. Longitudinal profiles are plotted for all these rivers are plotted (Fig.1 and Fig 2.). The gradient indices computed for different reaches of different rivers are tabulated in tables 1 and table 2.

Sloping pattern observed is similar in all the major rivers. The rivers slope considerably within first 10km length. Drop in elevation of about 900m in case of Seetha and Swarna Rivers and 600m in case of Madisal River is observed. Then onwards, these rivers are moderately sloping. Break in slope is observed in case of Varahi and Chakra rivers. This indicates that the river morphology is structurally controlled.

Gradient index is very high in the first reach of Seetha River with a sudden drop in the middle reach. However, it increases gradually in the lower reach. Similar trend is observed in case of other two main rivers, Swarna and Madisal. The high value of GI is mainly due to the steep topography in the scarp faces of Western Ghats. The variation of the gradient indices follows the similar trend as that of Seetha-Swarna basin. The upper reaches of the major rivers have very high gradient index varying from 200 to 350 and above. (Kollur River – 355.42, Chakra River – 290.44 and Halady River – 215.17). Kollur and Chakra Rivers are having higher values of GI (Gradient Index)

The presence of boulders, cobbles and pebbles as bed materials partially too accounts for a high gradient value. The profiles in this sector are notably steep and the presence of waterfalls and rapids are the prominent features in this reach. The valleys of the streams are typically 'V' shaped.

The middle reach is characterized by moderate slope of Peninsular Gneissic terrain, lack of boulders and presence of coarse sand and intersecting joints which provide a free access to flow and due to these characteristics, the GI reduces. The

third reach experiences a gradual increase in GI value and this can be attributed to discharge of bed materials from numerous tributaries which originate in the central part and merge with these major rivers in the middle or lower middle reach.

The variation of GI values in different reaches also implies that the middle reach assumes a graded phase. The initial reaches of Seetha and Swarna rivers are dominated by Metasediments and Metavolcanics of the younger greenstone clan and middle reach is predominant with Granitic Gneisses with Peninsular Gneissic complex. The initial reach thus flows on relatively less resistant rock terrain instead of a belt of resistant rock. The high gradient of Western Ghat scarps also adds to the high gradient index (Bhat, Gangadhar, H. (1992), Chadaga Mohandas (2009), Raghavan., B. R.,(1989), Sadatipour, S.M.T.(1986), Udayashankar, H.N.(1995)).

Tributaries like Golihole, Kollangar, Megadde, Koodluthirtha, Nemar and Markal join the Seetha river on the upper scarp face and hence exhibit higher values of GI in almost all reaches due to high relief also. GI reduces sharply in case of Hanakal Halla, Balkattu Hole and Achladi hole which join the Seetha river in the middle or lower middle reach. Similar trend can be observed in case of Swarna river and Madisal river. Machitte, Hekkunje Halla and Happanadka Hole are the headwater tributaries of Swarna which show a high value of gradient indices in their upper and middle reaches. Low value of the indices in their lower reaches is due to small length of flow in the lower reaches which flows on less sloped areas while joining the main river.

In case of tributaries in Gangolli basin, Kabbekkin Hole which is the tributary of Chakra river, GI is extremely high (2518). Similar trend can be observed in case of Halliberu River where GI is 1036.69. This is because of the very high slope these tributaries are encountering within a very short length. Total length of flow is within 10km but the fall in the elevation is more than 700m. All the reaches flow within the upper reaches or the upper parts of the middle reaches of the main rivers. Some of the tributaries join Kollur and Chakra rivers in the middle reaches where they again encounter the break in slope of

these two rivers. Therefore, the tributaries in this region also exhibit higher values of GI. In this basin also, many tributaries in the upper and mid-upper reaches show break in slopes in their longitudinal profiles.

Many tributaries in the upper and mid-upper reaches show break in slopes in their longitudinal profiles. (Golihole, Kollangar Hole, Koodluthirtha Hole, Megadde Hole, Markal Hole, Happanadka Hole and Mathebettu Hole). This indicates that majority of the streams on the upper reach are structurally controlled.

Transverse sections are steep at the origin (V shape) and widen below the Western Ghat and are flat at the alluvium region (Fig.3 and Fig.4) and river mouth.

Lineaments are present in large numbers in the study area extending in length from less than 1 km to more than 3 km (Fig.5 and Fig.6). In the central and eastern part of the study area prominent lineaments are very well identified based on the satellite imageries. Majority of the lineaments show NNW-SSE to NW-SE and NNE-SSW to NE-SW trend. The lineaments are prominent in NS and NE-SW directions also. Some lineaments cut across each other and some are parallel to each other. Lineaments which are fairly straight and do not change with stream courses, are considered as faults. Coastlines are sharp and straight and represent a major lineament. These coastlines belong to NNW-NW trending fault and are responsible for the development of Western Ghat scarps. The lineaments near the coast and coast parallel indicate fractures and progradation of sea with prominent beach ridges. The major rivers Kollur, Haladi, Chakra, Madisal and Swarna follow the prominent lineaments. Brahmavara and Manipal mesas are separated by fault plane passing through river Swarna. There are several basic dykes in the form of lineaments trending NNW. Some of the basic dykes passing through Hiriyadka, Perdoor, Herga and Brahmavara trend in E-W direction which indicate that these are fractures perpendicular to west coast faulting. Lineaments in the north-eastern region are represented by linear hill ranges trending NW-SE. The Paduvare mesa is bound by a major fault trending on the northern side and borders other mesas like

Mudugalpare, Kamalashile, Guppipare and Hulimishepare(Udayashankar,H.N.(1995)).

Conclusion

From all these discussions, it can be concluded that in the study area river morphology controlled mainly by lithology in the western part, slope and vegetation in the hilly tract and lithology, structure and slope in the central part.

The rivers of this region are having steep slope for a very short length in the initial stage which is exhibited by longitudinal profiles. In Seetha-Swarna basin, Seetha river is having a fall in the elevation from 1000m to 100m (900m) in a length of 10km (90m/km). The average slope is 12m/km. The average slope in case of Madisal river is 12.2m/km, and Swarna river 12.37m/km. Among the three rivers, the Swarna river has the steepest slope. In Gangolli composite river system basin, the Kollur River experiences a fall in the elevation from 1110m to 120m (990m) in a length of 6.04km with a slope of 1 in 6.1. The average slope in case of Kollur, Chakra and Halady rivers are 15.83m/km, 12.23m/km 9.18m/km respectively. Among the three rivers, the Kollur River has the steepest slope with an average slope of 1 in 62.

Chakra and Halady rivers are exhibiting a slightly different sloping pattern. The Chakra River slopes steeply from origin to 2.62 km and then slopes gently upto 15.2 km with a fall of 120m. But again within a short distance of 5km there is a fall of 240m. For the Varahi river stretch of Halady, similar sloping pattern is observable which indicates the structural control (lineaments) of river beds. Many tributaries in the upper reaches and upper parts of the middle reaches are also structurally controlled.

Transverse profiles are in typical V shaped valleys at the upper reach and tend to flatten towards the middle and lower reaches. Longitudinal steep slopes and steep 'V' shaped transverse profiles at the upper reaches represent the youthfulness of the rivers in the upper reaches and hence severe channel erosion exists especially during the monsoon seasons near the origin and foothills.

Lineament density is high at many places in upper reaches and river courses at many places follow the lineaments. This is

again a proof for the structural control of these rivers.

Acknowledgements

The author is also acknowledging Manipal University for providing financial support to carry out this research. He is also grateful to NRSC, Hyderabad (Under ISRO, Government of India) for providing the Satellite imageries at subsidized prices.

References

- [1] Bhat, Gangadhar, H. (1992), Geology, Geomorphology and Littoral Processes of a part of Dakshina Kannada coast through Remote Sensing – a study. Ph.D. THESIS submitted to Mangalore University.
- [2] Chadaga Mohandas (2009), River Basin Studies of Seetha-Swarna and Gangolli Composite River Systems of Coastal Karnataka, West Coast of India Using Remote Sensing and Geographic Information System (GIS), Ph.D. THESIS submitted to Manipal University.
- [3] Chadaga Mohandas et al (2007), "Hydrogeological Characterization of the Gangolli Composite River systems of Coastal Karnataka", International Conference on Groundwater-2007, Rajasthan University, Jaipur, Rajasthan.
- [4] Nag, S.K., and Chakraborty, S. (2003), Influence of Rock types and Structures in the development of drainage network in Hard Rock Area. JOURNAL OF THE INDIAN SOCIETY OF REMOTE SENSING, V. 31, No.1, pp. 25-35.
- [5] O'LEARY, D.W., DRIEDMAN, J.D. and POHN, H.A., (1976). Lineaments, linear, lineation: Some proposed new standards for old terms. GEO. SOC. AM.BULL., v.87.
- [6] Raghavan., B. R.(1989), Geomorphology and Evolution of the Sita and Swarna river Basin, Karnataka, India. Ph. D. THESIS submitted to Mangalore University.
- [7] Ruhe, R.V. (1975): "Geomorphology: geomorphic processes and surficial geology". HOUTON MIFFLIN. Boston.
- [8] Sadatipour,S.M.T.(1986), Geomorphology and Groundwater studies of Gangolli Basin, Karnataka, India. Ph. D. THESIS submitted to Mangalore University.
- [9] Schumm,S.A.(1956), Evolution of drainage systems and slopes in Badlands at Perth Amby, New Jersey. GEOL. SOC. AMERICA BULL., V. 67, pp. 597-646.
- [10] Strahler, A. N., (1964), Quantitative geomorphology of drainage basins and channel networks. In: V. T. Chow (ed), Handbook of Applied Hydrology. McGRAW HILL BOOK COMPANY, New York, Section 4-II.
- [11] Udayashankar, H.N., (1995), Landform Analysis of Coastland and Hinterland - a part of Dakshina Kannada District by using Remote Sensing techniques. Ph.D. THESIS submitted to Mangalore University.
- [12] Wobus, C., et al (2006). Tectonics from Topography: Procedures, Promise and Pitfalls, in S. D. Willett, N. Hovius, M. T. Brandon, and D. M. Fisher (eds.), TECTONICS, CLIMATE AND LANDSCAPE EVOLUTION, GSA SPECIAL PAPER V. 398, pp. 55-70

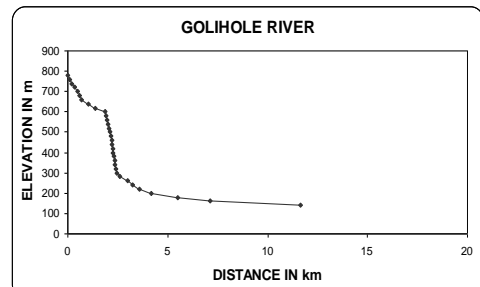
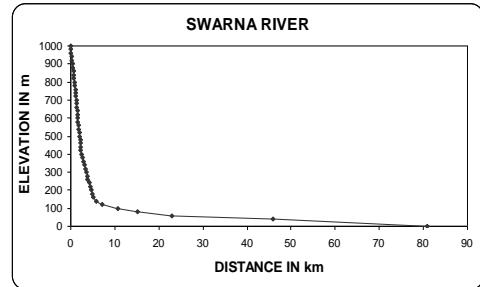
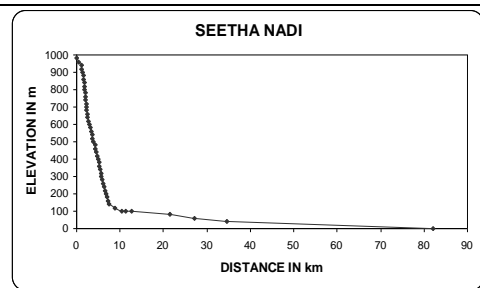
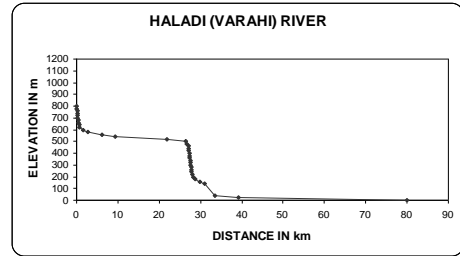
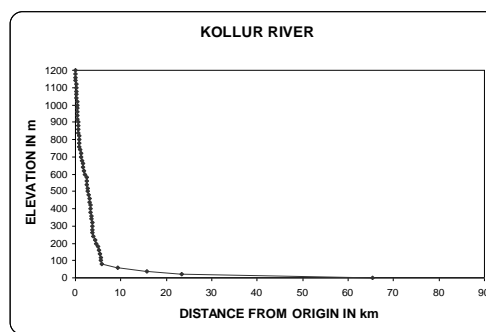


Fig. 1 Few longitudinal profiles of rivers in Seetha-Swarna basin



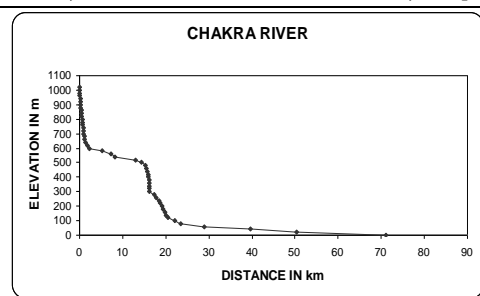
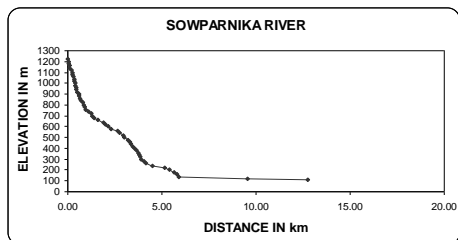


Fig. 2 Few longitudinal profiles of rivers in Gangolli basin

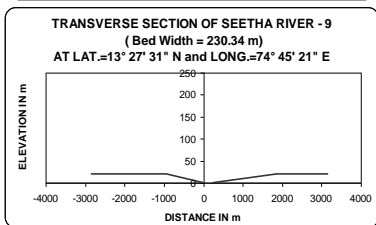
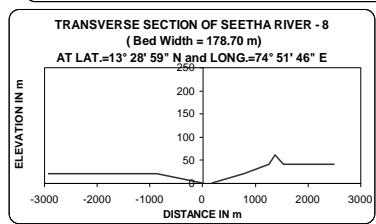
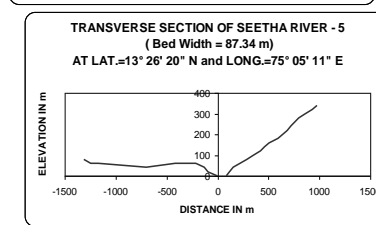
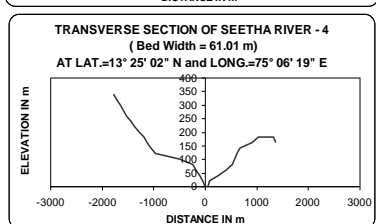
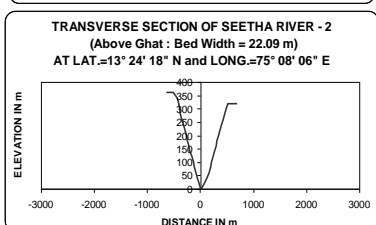
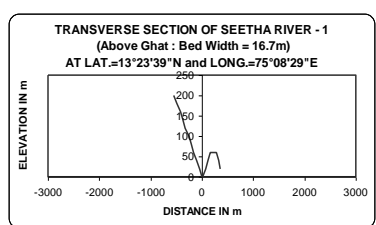
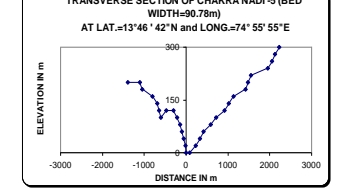
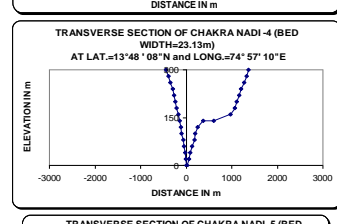
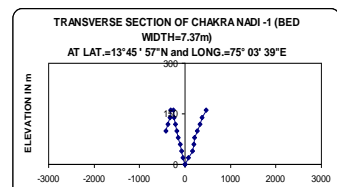


Fig. 3 Transverse sections of Seetha River



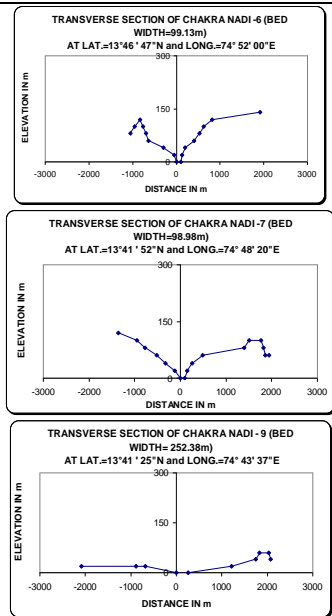


Fig. 4 Transverse sections of Chakra River

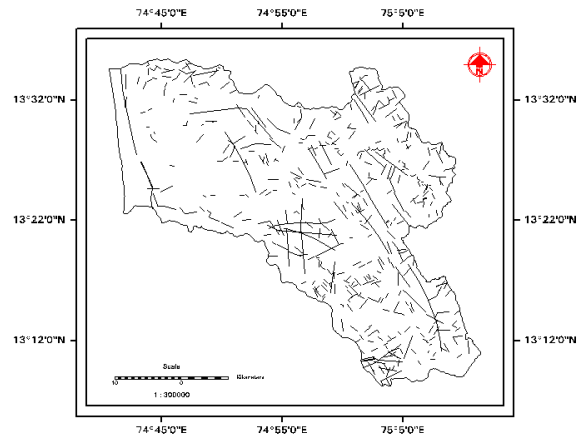


Fig. 5 Lineament map of Seetha-Swarna basin

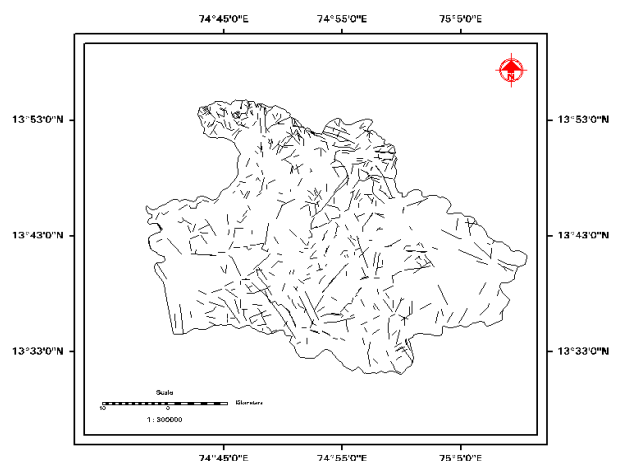


Fig. 6 Lineament map of Gangolli basin

Table 1. Gradient index (GI) for upper, middle and lower reaches of various rivers in Seetha-Swarna basin

River	River reaches		
	Upper reach	Middle reach	Lower reach
Seetha Nadi	262.67	34.35	52.45
Swarna Nadi	266.52	35.07	70.19
Madisal	216.17	24.19	45.23
Golihole	422.40	76.78	42.41
Kollangar	687.51	289.60	114.16
Megadde	424.06	510.13	238.15
Koodluthirtha	310.18	353.46	764.55
Nemar	363.21	411.47	574.33
Markal	206.14	527.99	338.15
Honakal Halla	43.57	24.28	51.04
Balkattu	2.88	38.95	31.91
Machitte	572.93	428.08	18.12
Hekkunje Halla	667.76	313.35	8.25
Happanadka Hole	642.20	37.08	45.12
Durga Hole	100.82	32.23	49.05
Kada Hole	425.76	53.74	26.97
Andar Hole	416.89	6.67	10.80
Mathebettu	336.39	162.41	70.48
Kelekila	305.65	19.29	14.34
Jaravattu	277.68	63.12	40.28

Table 2. Gradient index (GI) for upper, middle and lower reaches of various rivers of Gangolli composite river system basin

River	River reaches		
	Upper reach	Middle reach	Lower reach
Kollur	355.42	15.49	24
Chakra	290.44	23.42	36.05
Haladi	215.17	70.95	29.84
Sowparnika	658.19	185.24	30.09
Mavinakaru	408.41	388.09	44.79
Belakallu Thirtha	443.28	46.58	55.71
Samse Hole	666.62	75.67	57.62
Halliberu	1036.69	97.40	50.40
Savehaklu	127.38	87.55	433.35
Kebbakkin Hole	2518.00	216.96	83.67
Nagodi Hole	179.60	4.56	9.33
Idur Hole	48.41	7.42	12.28
Narasipura	507.42	37.57	16.20
Hulikal Hole	117.52	112.83	1332.85
Amgudde Hole	155.33	72.10	99.98
Kalu Hole	113.76	58.06	66.47
Tombattu Hole	696.01	136.64	35.96
Sanna Hole	45.69	27.97	71.52
Dasanakatte Hole	286.33	59.70	54

HYDROGEOLOGICAL CHARACTERIZATION OF SWARNA WATERSHED OF COASTAL KARNATAKA, INDIA USING GIS APPROACH

PRAKASH RAO B¹ AND MOHANDAS CHADAGA²

- 1 *Department of Civil Engineering, Manipal Institute of Technology, Manipal University, Manipal-576104, Karnataka, India. e-mail: bpkarant@yahoo.co.in*
- 2 *Department of Civil Engineering, Manipal Institute of Technology, Manipal University, Manipal-576104, Karnataka, India. e-mail: mdchadaga@yahoo.com*
-

Abstract: Swarna watershed is one of the important watersheds of Udupi district situated in Coastal Karnataka, India. In the present study, the morphometric parameters like mean stream length, basin elongation ratio, bifurcation ratio etc. have been evaluated using conventional, remote sensing and geographic information system techniques. The results are tabulated and are discussed in detail. It has been found that majority of the sub-watersheds and Swarna basin as a whole, is vulnerable for erosion. The hydrogeological parameters discussed in the paper will play an important role in the selection and location of the water harvesting structures which are site specific.

KeyWords: *Remote Sensing, Geographic Information System, Hydrogeological parameters, Morphometric parameters, Water harvesting structures.*

Introduction

The river Swarna originates in the foothills of Western Ghats. Due to the steep gradient and narrow region of the watershed, heavy rainfall results in large quantity of surface runoff. This paper attempts to evaluate the hydrogeological characteristics of the watershed and to analyse their influence on the various hydrological processes. LISS-III imageries of IRS-1C/1D series and Survey Of India (SOI) topographical maps are used for this purpose. In the present study, some morphometric analysis of the river systems like river order, drainage density, bifurcation ratio etc., are evaluated at the sub watershed levels with an effort to generate correlations between these parameters and the runoff, or other hydrological processes. Six sub-watersheds are considered for this purpose. Many areas in this region are highly sloping with elevation rising to 1300m or more within short distances. Majority of the sub-watersheds and Swarna basin are elongated and time of concentration is more. Hence surface runoff is more and the basin is vulnerable for erosion. These

observations shall be given importance in all model studies for the quantification of various hydrological processes necessary for sustainable development and management of water resources of the watershed which includes selection and location of site specific water harvesting structures.

River Morphology: Morphometry is the measurement and mathematical analysis of shape and dimension of landform of a watershed. The process involves the preparation of drainage basin maps, ordering of streams, measuring the catchment area and perimeter etc., which help to understand the nature of drainage basins. Geographic Information Technique (GIS-Techniques) can be effectively adopted for evaluating various morphometric and topographical parameters like linear, spatial and relief features which are required for further analysis. The advantage with the GIS techniques is that it is a powerful tool for feature identification and extraction, and analysis and manipulation.

Morphometric Parameters: Stream Order is the hierarchic ranking of the streams in the basin. Horton (1945) stated that the total length of the stream segments is maximum for the first order streams and decreases as the stream order increases. Basin Length is the distance from the point of measurement to the most remote point in the basin. Drainage Density serves as an index of the aerial channel development of the basin (Horton(1932)). A high value indicates a well-developed network and torrential runoff, which indicates intense floods. Langbein (1947) suggested a drainage density varying between 0.55 km/km^2 and 2.09 km/km^2 . Drainage Texture represents the relative spacing of drainage lines. Horton(1945) recognized infiltration capacity as the single important factor that influences the drainage texture and correlated drainage texture to drainage density and stream density. Smith (1950) classified drainage density into five different textures viz., less than 2 indicates very coarse drainage texture, between 2 and 4 represents coarse, between 4 and 6 is moderate, between 6 and 8 is fine and more than 8 represents very fine drainage texture. Horton (1945) considered the bifurcation ratio as an index for relief and dissection. The bifurcation ratio shows a small range of variation for different regions or different environment where strong geological control dominates (Strahler (1957)). The values of elongation ratio(Re) vary generally from 0.6 to 1 over a wide climatic changes and geologic types (Singh and Singh(1997)). The values of Elongation ratio can be grouped into four categories such as Circular (Re greater than 0.9), Oval (Re - 0.9 to 0.8), Less elongated (Re - 0.8 to 0.7) and Elongated (Re - less than 0.7). A higher elongation ratio induces lesser erosion. Miller(1953) defined circulatory ratio as the ratio of the area of the basin to the area of a circle having the same circumference as the perimeter of the basin. Circulatory ratio is dependent on length and density of streams, geologic structures, land use/land cover, climate, relief and slope of the basin. A higher circulatory ratio induces lesser erosion. Length of Overland Flow is the length of water flow over the ground

before it gets concentrated into definite stream channels (Horton (1945)). The compactness coefficient is independent of the size of the catchment and is dependent only on the shape. A fan shaped catchment produces greater flood intensity since all the tributaries are nearly of the same length and hence the time of concentration is nearly same and is less, whereas in the fern-shaped catchments, the time of concentration is more and the discharge is distributed over a long time period. These factors have to be considered in the future analysis while evolving decision rules (Akram Javed et al.(2009)) for selecting and locating the water harvesting structures which are site specific.

Study area

The Swarna basin(Fig.1) consists of Machitte Hole, Hekkunje Hole, Happanadka Hole, Durga Hole, Andar Hole and Kada Hole. The basin is bounded by longitudes $74^{\circ}41'42"E$ to $75^{\circ}11'20"E$ and latitudes $13^{\circ}25'59"N$ to $13^{\circ}11'04"N$. The area of the basin is approximately 603.13 km^2 and perimeter is about 168.07 km. Length of the Basin is about 53.6 km and the main stream length is about 77.18km. The basin circulatory ratio is 0.27 and basin elongation ratio is 0.52. It is surrounded by Arabian Sea on the west, Western Ghat on the east, Sita river basin on the north and Netravati-Gurpura system on the south. The net annual rainfall in the region is about 3500-4000mm. Major soil types observed in the region are laterite and alluvial.

Methodology

Base map of the study area on 1:50000 scales were prepared by using Survey of India (SOI) toposheets. IRS-1D, LISS-III images with a spatial resolution of 23.5m cloud free data, covering on January-24, 2003 procured from NRSA was used for the purpose. The satellite image is georeferenced by using the image processing software ERDAS IMAGINE (Version 8.5). The GIS softwares like ArcInfo and MapInfo were used for the digitization and computational purposes. The methodology adopted for the computation of morphometric parameters is given in Table1 as defined by

Srinivasa Vittala et al.(2004); Rajiv Chopra et al.(2005).

Results and discussions

For the analysis of the results, Swarna basin is split into the six sub basins namely, Happanadka river, Machitte river, Hekkunje halla, Andar hole, Durga hole and Kada hole. Morphometric parameters are computed for the Swarna basin (whole) and six sub - water sheds. Various features that are necessary for the study and computation of morphometric variables are extracted by using image processing and GIS soft wares mentioned earlier and the results are tabulated in Tables 2,3,4, and 5.

Stream order: Streams up to V order (Table 3) exist in Happanadka river, Machitte river and Andar hole sub- water sheds, whereas streams up to IV order exist in the sub- watersheds of Hekkunje halla, Durga hole and Kadahole and up to VI order exist in the Swarna basin (whole). Graphs of number of rivers vs. river order (Fig.2) and mean stream length vs. river order (Fig.3) are plotted for all the sub-watersheds. It is found that number of river decreases as the river order increases. However mean stream lengths increase with the increase in river order. These two observations are in accordance with Horton's law.

Mean stream length(L_{sm}): According to Strahler(1964), mean stream length ratio is characteristic property of drainage network components and its associated basin surfaces. It is observed from Table 3 that L_{sm} values vary from 0.54-6.61 for Happanadka river, 0.58-6.05 for Machitte river, 0.47-7.85 for Hekkunje halla, 0.52-7.34 for Andar hole, 0.61-20.21 for Durga hole, 0.53-14.85 for Kada hole and 0.57-51.58 for Swarna basin(whole).

Bifurcation Ratio (R_b): Horton(1945) considered R_b as an index of reliefs and dissections. Strahler(1957) demonstrated that R_b shows only a small variation for different regions with different environments except where powerful geological control dominates. Lower R_b values are the characteristics of structurally less disturbed watersheds without any distortion in drainage pattern

(Nag(1998)). The mean R_b values (Table 4) vary between 3.5 and 5.83 for the six sub-watersheds and is 4.35 for Swarna basin (whole). These values indicate less structural control on the drainage development. However, irregular R_b values do not subscribe to Horton's law of stream numbers which probably represent local variations in the drainage development.

Drainage density(D_d): It is defined as the total length of all the drainage channels divided by the area of the basin. In general, low values of D_d are the characteristics of regions underlain by highly permeable material with vegetative cover and low relief. High values of D_d indicate regions of weak and impermeable subsurface material, sparse vegetation and mountainous relief (Nantiyal(1994)). The D_d values (Table 5) vary between a minimum of 1.54 to a maximum of 3.17 for the six sub water sheds and is 1.89 for the Swarna basin (whole). These values indicate that the entire Swarna basin is underlain by highly permeable material and represents low relief. Drainage density values indicate a well-developed drainage network in the basin. Hence, the surface runoff is more and more is the erosion. The scope for water harvesting is better in the sub water sheds of Happanadkariver, Machitteriver, Hekkunjehalla, Andar hole and Kada hole than in Durga hole as the D_d values are relatively high.

Stream Frequency(F): Horton(1932) defines the stream frequency as the total number of stream segments of all orders per unit area. Stream frequency higher in one area than the other means the growth of new channels or lengthening of the existing streams. F values (Table 5) suggest positive correlation with the drainage density of all the sub water sheds.

Basin circulatory ratio (R_c): This is the ratio of the area of a basin to the area of a circle having the same circumference as the perimeter of the basin (Miller (1953)). R_c values (Table 2) of sub-watersheds range between 0.35 to 0.69 indicating elongated shape of the watersheds. Swarna basin(whole) has a R_c 0.27 indicating more erosion. R_c parameter is helpful in assessing flood hazard. Higher

the R_c value, higher is the flood hazard at a peak time at the outlet point.

Basin elongation ratio (R_e): The values of R_e generally depend upon the variety of climate and geology and can be grouped into three categories i.e, circular (> 0.90), oval ($0.90 - 0.80$), less elongated ($0.80 - 0.70$) and elongated(< 0.70). R_e values (Table 2) range between 0.53 to 0.82.These values indicate that Machitte river with a value of 0.82 represent oval shape whereas Swarna basin (whole) fall in the elongated category.

Gradient(G): This is defined as the ratio of total fall of the stream to the length of the main stream(L_m). The values of G (Table 5) range between a minimum of 9.69 to a maximum of 102.14.This indicates that Hekkunje halla has a very steep slope and Durga hole is comparatively flat. Steeper the slope/gradient, velocity is more and hence the erosion and sedimentation. These are the guiding factors for selection and locating the site specific water harvesting structures.

Form Factor(F_f):

Horton(1932) defined form factor as the ratio of basin area to the square of the basin length. The value of form factor would always be less than 0.7854 (perfectly for a circular basin).For lower values of F_f , the basin will be more elongated. The values of F_f (Table 5) indicate that all the six sub watersheds including the Swarna basin (whole) are elongated.

Conclusion

Morphology analysis gives insight into the watershed characteristics on quantitative basis. The geology, landforms, morphometry and river flow characters of the Swarna basin of coastal Karnataka are highly varying. The basin consists of large number of tributaries and rivulets with a thick drainage network especially in Western Ghats region. Majority of the sub-watersheds and Swarna basin(whole) are elongated, time of concentration is more and hence more is the surface runoff and the basin is vulnerable for erosion. Stream network decreases towards hinterland.

Drainage texture is moderately coarse in Swarna basin. Hence, Swarna basin contributes more towards total surface runoff. The rivers of this region are having steep slope for a very short length in the initial stage. In hilly reaches, channels are steep and flows are swift and rapid. From the above observations, it is evident that the severe channel erosion exists especially during the monsoon seasons near the origin and foothills. These factors have to be considered in the future analysis while evolving decision rules for selecting and locating the water harvesting structures which are site specific. This study demonstrates the usefulness of Remote sensing and GIS techniques in analyzing the hydrological characteristics of water sheds. Further analysis have to be carried out by studying land use/land cover, geology, soil and slope characteristics. Thematic maps will have to be developed based on these analysis.

References

- [1] AkramJaved et al.(2009), Prioritization of Sub-watersheds based on Morphometric and Land Use Analysis using Remote Sensing Techniques, Journal of Indian Society of Remote Sensing, V.37,No.2,pp261-274.
- [2] Horton R.E.(1932),Drainage basin Characteristics,Trans.Am.Geophysc.Union,V.13,pp350-361
- [3] Horton R.E.(1945),Erosional Development of Streams and their Drainage basins; Hydrological Approach to Quantitative Morphology, Geol. Soc.Am.Bull,V.56,pp275-370.
- [4] Langbein, W.B. (1947).Topographic characteristics of drainage basins.U.S. Geol. Surv. Water-Supply Paper,986(C),pp 157-159.
- [5] Miller V.C.(1953), A Quantitative Geomorphic Study of Drainage basin Characteristics on the Clinch Mountain area, Virginia and Tennessee,Proj.NR389-402,Tech Rep3,Columbia University,Department of Geology,ONR,New York.
- [6] Nag S.K.(1998), Morphometric Analysis using Remote Sensing Techniques in the Chaka sub-basin, Purulia District, West Bengal, Journal of Indian Society of Remote Sensing, V.26 No.1&2,No.2,pp69-76.
- [7] Nantiyal, M.D. (1994). Morphometric analysis of a drainage basin, district Dehradun, Uttar Pradesh.J. Indian Soc. Remote SensingV.22(4): 251-261.
- [8] Rajiv Chopra et. al., (2005). Morphometric Analysis of sub-watershed in Gurdaspur District, Punjab using remote Sensing and GIS techniques. Journal of Indian Society of Remote Sensing, V.33, No.4,pp 531 -539.
- [9] Singh, S. and Singh, M.C. (1997). Morphometric analysis of Kanhar river basin.National Geographical J. of India,V.43,No.1,pp 31-43.
- [10]Smith, K.G. (1950).Standards for grading textures of erosional topography.Am. Jour. sci.,248,pp 655-668.

International Engineering Symposium, March 3-5, 2011 Kumamoto Univ., Japan

- [11]Srinivasa Vittala,S., Govindaiah, S., and Honne gowda. H.,(2004). Morphometric analysis of sub-watershedsin the Pavagada area of Tumkur district, South India using Remote Sensing and GIS techniques. Journal of the Indian Society of Remote Sensing, V.32,No.4,pp 351-362.
- [12]Strahler A.N.(1957), Quantitative Analysis of Watershed Geomorphology,Trans.Am.Geophys.Union, V.38,pp913-920.
- [13]Strahler, A. N. (1964).Quantitative geomorphology of drainage basins and channel networks. In: V. T. Chow (ed), Handbook of Applied Hydrology. McGraw Hill Book Company, New York, section 4-II.

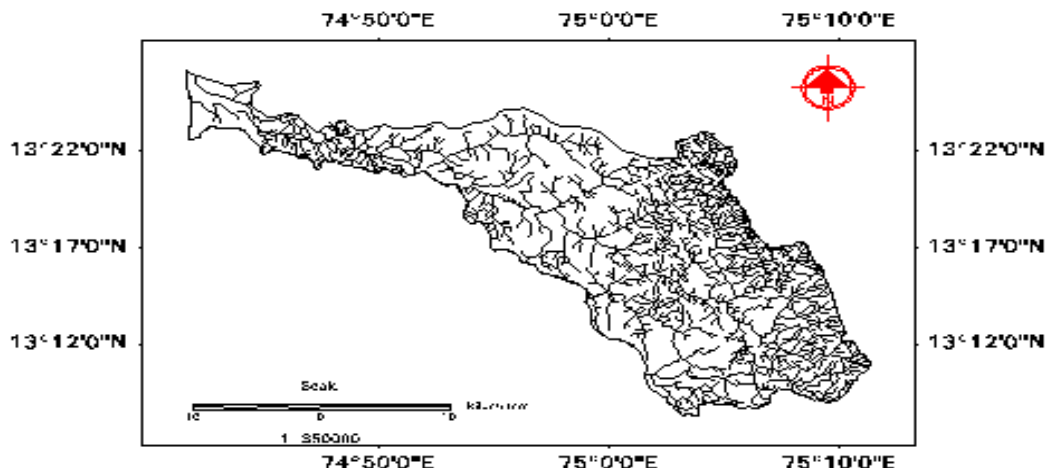


Fig.1Swarna Basin

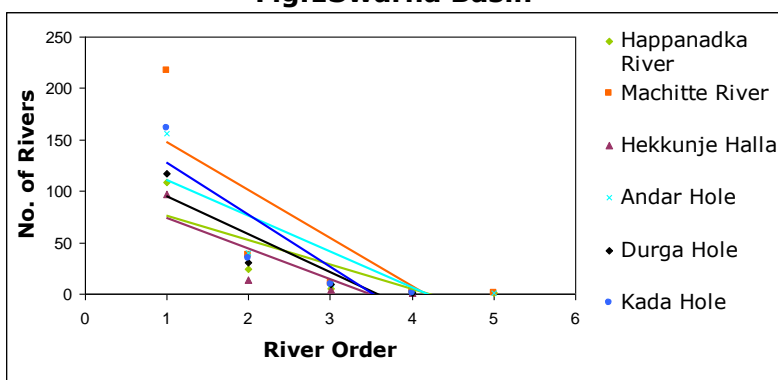


Fig. 2 Plot of Number of Rivers versus River Order

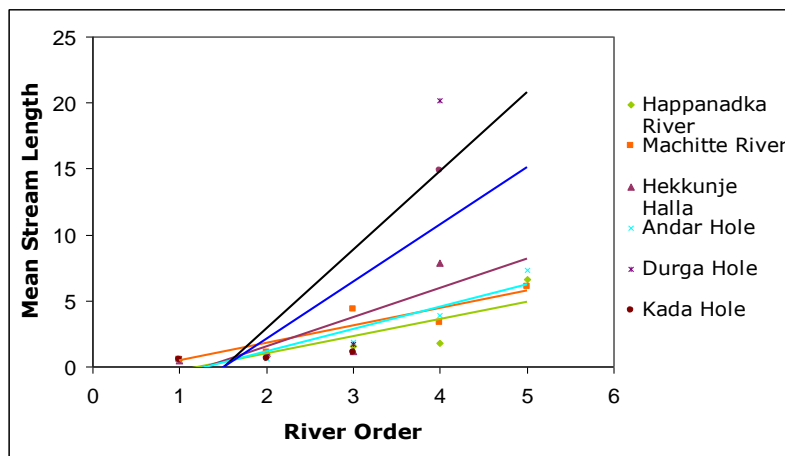


Fig. 3 Plot of Mean Stream Length versus River Order

Table 1 Morphometric Variables

No.	Variable	Symbol	Units	Reference
A. DRAINAGE NETWORK:				
1.	Stream Order	U	Enumerative	Strahler (1964)
2.	Number of streams of order 'u'	Nu	Enumerative	-----
3.	Total length of streams of order 'u'	Lu	Km	Horton (1945)
4.	Mean length of streams of order 'u'	$L_{sm} = \frac{Lu}{Nu}$	Km	Strahler (1964)
5.	Stream Length Ratio	$RL = \frac{Lu}{Lu - 1}$	Km	Horton (1945)
6.	Bifurcation Ratio	$R_b = \frac{Nu}{Nu + 1}$	Enumerative	Schumn (1956)
B. BASIN GEOMETRY				
1.	Area of the basin	A	Km^2	---
2.	Length of the basin	Lb	Km	---
3.	Main stream length	Lm	Km	---
4.	Basin Perimeter	P	Km	---
5.	Basin Circularity (Circulatory ratio)	$R_c = \frac{4 \times \pi \times A}{P^2}$	-----	Miller (1953)
6.	Basin Elongation (Elongation Ratio)	$R_e = \frac{2\sqrt{\frac{A}{\pi}}}{L_b}$	-----	Schumn (1956)
7.	Form factor (F_f)	$F_f = \frac{A}{L_b^2}$	Km	Horton (1932)
8.	Compactness Factor (Cc)	$C_c = \frac{P}{2\sqrt{\pi}A}$	-----	-----
C. MEASURE OF INTENSITY OF DISSECTION				
1.	Drainage Density(D_d)	$D = \frac{L}{A}$ L=total stream length	Km/Km^2	Horton (1932)
2.	Length of Overland Flow(Lg)	$L_g = \frac{1}{2 \times D}$	Km	Horton (1945)
3.	Constant of Channel Maintenance(c)	$C = \frac{1}{D}$	Km^2/Km	Schumn (1956)
4.	Stream Frequency(F)	$F = \frac{N}{A}$	Number/ Km^2	Horton (1932)
5.	Drainage Texture (T)	$T = F \times D$	Number/Km	Horton (1945)
6.	Texture Ratio(Tr)	$T_r = \frac{N}{P}$		
D. MEASURES INVOLVING HEIGHTS				
1.	Height of Highest Point in the watershed	Z	Meters	-----
2.	Height of Lowest Point in the watershed	Z	Meters	-----
3.	Height where the main stream originates	Ho	Meters	-----
4.	Height of basin mouth	He	Meters	-----
5.	Relative Relief(RR)	RR=(H-He)	Meters	-----
6.	Relief ratio(Rh)	$Rh = \frac{RR}{Lb}$		Schumn (1956)
7.	Gradient(G)	$G = \frac{(Ho - He)}{Lm}$	Meter/Km	---
8.	Dissection Index(Di)	$Di = \frac{RR}{Z}$	Meter	-----
9.	Ruggedness Number(Rn)	$Rn = \frac{(D \times RR)}{1000}$	Km	-----
10.	Average Stream Slope (S)	$S = \frac{\text{Total fall}}{\text{Length of stream}}$	-----	-----

Table 2 Basin Geometry

Basin/ Subwatershed	Area, A (Km ²)	Perimeter, P (Km)	Basin Length, L _b (Km)	Length Of Main Stream, L _m (Km)	Basin Circulatory Ratio (R _c)	Basin Elongation , (R _e)
Swarna Basin(whole)	603.13	168.07	53.6	77.18	0.27	0.52
Happanadka River	37.01	27.85	8.87	11.67	0.60	0.77
Machitte River	94.29	41.30	13.41	19.13	0.69	0.82
HekkunjeHalla	22.89	23.91	8.43	10.28	0.50	0.64
Andar Hole	52.66	34.31	11.57	16.8	0.56	0.71
Durga Hole	86.41	47.28	18.36	27.87	0.49	0.57
Kada Hole	57.16	45.42	16.21	16.71	0.35	0.53

Table 3 No. of Streams (Nu), Stream Lengths (Lu) and Mean Stream Length(Lsm)

Basin/ sub watershed	Stream Order (U)	I	II	III	IV	V	VI	Total
Swarna Basin (whole)	Number (Nu)	1191	255	51	10	2	1	1510
	Length (Lu) (km)	681.6	208.39	124.12	55.7	20.21	51.58	1141.59 (L)
	Mean stream Length(Lsm) (km)	0.57	0.82	2.43	5.57	10.11	51.58	-----
Happanadka River	Number (Nu)	109	24	5	3	1	-----	142
	Length (Lu) (km)	59.36	23.04	7.74	5.32	6.61	-----	102.07 (L)
	Mean stream Length(Lsm)(km)	0.54	0.96	1.55	1.77	6.61	-----	-----
Machitte River	Number (Nu)	217	38	11	3	1	-----	270
	Length (Lu)(km)	126.25	40.9	48.4	10.07	6.05	-----	231.67 (L)
	Mean stream Length(Lsm)	0.58	1.08	4.40	3.36	6.05	-----	---
HekkunjeHal la	Number (Nu)	97	14	4	1	-----	-----	116
	Length (Lu)(km)	45.77	14.31	4.56	7.85	-----	-----	72.49 (L)
	Mean stream Length(Lsm)(km)	0.47	1.02	1.14	7.85	-----	-----	---
Andar Hole	Number (Nu)	156	40	9	2	1	-----	208
	Length (Lu)(km)	81.3	26.06	16.64	7.75	7.34	-----	139.09 (L)
	Mean stream Length(Lsm)(km)	0.52	0.65	1.85	3.88	7.34	-----	---
Durga Hole	Number (Nu)	117	31	9	1	-----	-----	158
	Length (Lu)(km)	71.07	26.24	15.69	20.21	-----	-----	133.21 (L)
	Mean stream Length(Lsm) (km)	0.61	0.85	1.74	20.21	-----	-----	-----
Kada Hole	Number (Nu)	161	35	9	1	-----	-----	206
	Length (Lu)(km)	85.42	23.04	10.1	14.85	-----	-----	133.41 (L)
	Mean stream Length(Lsm) (km)	0.53	0.66	1.12	14.85	-----	-----	-----

Table 4 Stream Length Ratio and Bifurcation Ratio

Stream Length Ratio	II/I	III/II	IV/III	V/IV	VI/V	
Swarna Basin(whole)	0.31	0.60	0.45	0.36	2.55	-----
Happanadka River	0.39	0.34	0.69	1.24	-----	-----
Machitte River	0.32	1.18	0.21	0.60	-----	-----
HekkunjeHalla	0.31	0.32	1.72	-----	-----	-----
Andar Hole	0.32	0.64	0.47	0.95	-----	-----
Durga Hole	0.37	0.60	1.29	-----	-----	-----
Kada Hole	0.27	0.44	1.47	-----		
Bifurcation Ratio	I/II	II/III	III/IV	IV/V	V/VI	Mean(Rbm)
Swarna Basin(whole)	4.67	5	5.1	5	2	4.35
Happanadka River	4.54	4.8	1.67	3	-----	3.5
Machitte River	5.71	3.45	3.67	3	-----	3.96
HekkunjeHalla	6.93	3.5	4	-----	-----	4.81
Andar Hole	3.9	4.44	4.5	2	3.71	3.71
Durga Hole	3.77	3.44	9	-----	5.4	5.4
Kada Hole	4.6	3.89	9	-----	5.83	5.83

Table 5 Relief Properties and Parameters involving heights

Basin/Sub watershed	Swarna Basin (Whole)	Happanadka River	Machitte River	Hekkunje Halla	Andar Hole	Durga Hole	Kada Hole
Height of Highest point In the basin (Z)	1180m	840m	1160m	1110m	860m	340m	900m
Height of Lowest Point inthe watershed (z)	0.0m	40m	60m	50m	34m	30m	30m
Height where the main stream originates (Ho)	1100m	780m	1100m	1100m	800m	300m	820m
Height of basin mouth (He)	0.0m	40m	60m	50m	30m	30m	40m
Relative Relief (RR)	1100m	740m	1040m	1050m	770m	270m	780m
Relief ratio (Rh)	14.25 m/km	83.42 m/Km	77.55 m/Km	124.56 m/Km	66.55 m/Km	14.71 m/Km	48.12 m/Km
Gradient (G)	14.25 m/km	63.41 m/Km	54.36 m/Km	102.14 m/Km	45.83 m/Km	9.69 m/Km	46.68 m/Km
Dissection Index (Di)	0.93	0.88	0.90	0.95	0.90	0.79	0.87
Ruggedness Number (Rn)	2.08	2.04	2.56	3.33	2.03	0.42	1.82
Average Stream Slope (S)	15.29 m/km	63.41 m/Km	54.36 m/Km	102.14 m/Km	45.83 m/Km	9.69m/ km	46.68 m/km
Form factor (Ff)	0.21	0.47	0.52	0.32	0.39	0.26	0.22
Compactness Factor (Cc)	1.93	1.29	1.20	1.41	1.33	1.43	1.69
Drainage Density (Dd) km/km ²	1.89	2.76	2.46	3.17	2.64	1.54	2.33
Length of Overland Flow (Lg)	0.26	0.18	0..20	0.16	0.19	0.32	0.21
Constant of Channel Maintenance (C)	0.53	0.36	0.40	0.32	0.38	0.64	0.42
Stream Frequency (F)	2.5	3.84	2.86	5.07	3.95	1.83	3.60
Drainage Texture (T)	4.73	10.60	7.04	16.07	10.43	2.82	8.39
Texture Ratio (Tr)	8.98	5.10	6.54	4.85	6.06	3.34	4.54

EVALUATION OF MORPHOMETRIC CHARACTERISTICS BY USING GIS IN KOLLUR WATERSHED OF COASTAL KARNATAKA, INDIA

**MOHANDAS CHADAGA¹, UDAYASHANKAR H. N.², RAO PRAKASH B.³ and BHAT
GANGADHAR H.⁴**

1. Department of Civil Engineering, Manipal Institute of Technology, Manipal (Under Manipal University), India, e-mail:mdchadaga@yahoo.com

2. Department of Civil Engineering, Manipal Institute of Technology, Manipal (Under Manipal University), India, e-mail:udaya.shankar@manipal.edu

3. Department of Civil Engineering, Manipal Institute of Technology, Manipal (Under Manipal University), India, e-mail: bpkarant@yahoo.co.in

4. Department of Marine Geology, Mangalore University, Mangalore, India, e-mail: gangadharab@yahoo.com

Abstract: Analysis of different Morphometric and Geomorphic characteristics will help us to understand the different hydrologic processes taking place in a watershed. In this study, some of these watershed characteristics are evaluated by using the RS and GIS techniques and approaches. Kollur watershed of Coastal Karnataka, India is considered for this purpose. LISS-III imageries of IRS-1C/1D series and Survey Of India (SOI) topographical maps (Toposheets) are used for the purpose. Lineament map of the study area, updated with IRS imagery is used in this analysis. Longitudinal profiles are plotted and analysed for some of the rivers. It has been observed that many rivers in the Kollur basin are structurally controlled which is evident from the break-in-slope of their longitudinal sections. The cross sections of the rivers are typically 'V' shaped valleys. Many areas in region are highly sloping with elevation of more than 1200m. Longitudinal sections plotted and slope maps derived from the DEM exhibit steep sloping characteristics in initial regions i.e., near the foothills. The computed values of the morphometric parameters and map derived geomorphic features of the study area indicate that characteristics like slope, soil type and land use patterns are the main influencing parameters towards runoff process.

Key Words: *Remote Sensing, Geographic Information System, Morphometric and Geomorphic characteristics.*

Introduction

There are many west flowing rivers originating at Western Ghats and joining Arabian Sea in coastal Karnataka, India, Hence, various water resources serving domestic and agricultural water development and management aspects like requirements of this region. Kollur River is one among them which forms the part of planning and implementing of various Gangolli Composite river systems. The water harvesting and conservation entire watershed has three distinctive structures etc are gaining importance in topographical regions viz., highly sloping this region and watershed as well. As a Ghat (hilly) regions in the east, middle hinterland with moderate slope and coastal plains on the west with varying topography, carried out at sub watershed and micro geology, geomorphology and landuse patterns. These factors expose many challenges to water resources development and management even though it belongs to the class of small watersheds. The region experiences average annual rainfall of about 3500-4000mm but still there is scarcity of water during summer months. The water shed level using remote Sensing and GIS approaches and the results are discussed in this paper.

Study area

The Kollur River originates on the slopes of Western Ghats at an altitude of 1100m near Kodachadri, Kollur in Western Ghats (Fig.1). It flows westwards and has a highly meandering course before joining Chakra River about five kilometers north of Kundapura. The watershed is having a total area of 313.50 km² and perimeter of 115.29 km. Length of the river is about 69.50km. The water shed is located between the longitudes 74°38'25" E and 74°55'50" E and latitudes 13°54'47" N and 13°41'15" N. The River has the major tributaries like Mavinakaru River, Belakallu Thirtha River, Sowparnika River etc.

Morphometric and Geomorphic Parameters

Circulatory ratio, Elongation ratio, Bifurcation ratio, Drainage density and frequency, Longitudinal and Transverse profiles and Lineaments are some of the morphometric and geomorphic parameters and features considered in this study.

Circulatory ratio is the ratio of the area of the basin to the area of a circle having the same circumference as the perimeter of the basin (Miller, (1953)). It is dependent on length and density of streams, geologic structures, land use/land cover, climate, relief and slope of the basin. A higher circulatory ratio indicates less erosion.

Values of elongation ratio vary generally from 0.6 to 1 over a wide climatic changes and geologic types (Singh et al, (1997)). and can be grouped into four categories; Circular (Re greater than 0.9), Oval (Re - 0.9 to 0.8), Less elongated (Re - 0.8 to 0.7) and Elongated (Re less than 0.7). A higher value of elongation ratio means lesser will be the erosion.

Horton (1945) considered bifurcation ratio as an index for relief and dissection. It shows a small range of variation for different regions or environment where strong geological control dominates (Strahler (1957)).

Drainage Density serves as an index of the aerial channel development in a basin (Horton, (1932)). A high value indicates a well-developed network and torrential runoff, which indicates intense floods.

Longitudinal profile of a stream is the continuous fall in elevation with respect to horizontal distance from origin to mouth.

Longitudinal profiles provide sufficient tectonic information to understand the tectonic geomorphology. These profiles contain tectonic information in the form of knick points and their Strahler order as well (Strahler, A. N., (1964)). Transverse profiles are used to analyze the stream shapes at different cross points. Channel slope, Stream Length, Drainage area, and Bed load characteristics are related to longitudinal and transverse profiles (Raghavan., B. R., (1989)).

Significant lines of landscape caused by geologic structures, revealing the architecture of the rock basement are known as lineaments. They represent faults, fractures, joint sets, shear zones, folds etc. Existence of groundwater sources, tectonic influences on geomorphic events etc. can be revealed by studying lineaments (Wobus, C. et al (2006)).

Methodology

Geocorrected satellite image IRS-1D, LISS-III (24m spatial resolution) with the help of Survey Of India (SOI) toposheets on 1:50000 scale is used as a base map. Some of the image processing techniques are adopted on this image by using Image processing software ERDAS IMAGINE (Version 8.5). Analysis of morphometric parameters is done by using the GIS software ArcInfo/ArcGIS. Some of the parameters used in this study are listed in Table1 with their definitions.

To draw the longitudinal profiles, stream length is considered along the X-axis and the elevation along the Y-axis. Gradient index which is the measure of the slope is calculated as follows (Raghavan., B. R., (1989)).

$$\text{Gradient Index (GI)} = \frac{H_1 - H_2}{\log_e L_2 - \log_e L_1} \quad (1)$$

where H1 and H2 are the altitudes of each of a given reach and L1 and L2 are the distances from each end of the reach to the source of the stream measured along the course of the river or tributary. The stream is divided into three reaches i.e., upper reach, middle reach and lower reach.

Length of about one to two kilometres on either side transverse to the main river axis is considered and the distances of the intersecting contours on either side is measured to draw the transverse profiles.

Lineament map of the study area is prepared by using Drainage basin map in

digital form, processed satellite imageries and SOI topographical maps. Various image processing techniques like non-directional filtering, edge enhancement techniques, band separation etc were adopted for the purpose. Ground truth survey is also carried out along with as a part of validation (Lillesand, Thomas M., and Ralph W. Keifer, (2000)).

Results and Discussions

The existence of a thick drainage density can be observed in the eastern and north eastern regions of Kollur basin (Fig.1). In Mavinakaru subwatershed, rivers upto V order and in Salkodu, rivers upto III order exists. All other subwatersheds comprise rivers upto IV order. Regression analysis of stream number versus stream order and stream length versus stream order is done. Stream number decreases as the stream order increases whereas mean stream length increases with the increasing stream order (Table 3, Fig.3 and Fig.4). The trend followed is same for all the subwatersheds. The basin circulatory ratio is in the range of 0.37 to 0.73. The lower value indicates more erosion which takes place in the Belakallu Thirtha and Samse sub watersheds. Elongation ratio varies from 0.59 to 0.81, indicating that the subwatersheds belong to the categories of less elongated and elongated (Table 2). Drainage density is in the range of 2.71 to 3.56 (Table 5). This indicates a very well developed drainage network in the basin. Hence, the surface runoff is more and more is the erosion. Similar trend is observed in the case drainage frequency (Srinivasa Vittala, et al (2004), Rajiv Chopra et al, (2005)).

Rivers slope almost in similar manner. Considerable slope is observed within 5 to 10 km length from the origin. Elevation drops by about 900m or more as indicated by the longitudinal profiles (Fig.5). Then onwards, these rivers are moderately sloping. In some of the tributaries, break in slope is also seen signifying the structural influence on river morphology. Except the Savehaklu, in all other sub watersheds, Gradient index (GI) is very high in the upper reach and decreases towards middle and lower reach (Table 6). In the upper reaches, it varies from 355.42 to 1036.69 and in the middle reaches the value is from 15.49 to 388.09. However, in the lower

reaches, the value ranges from 24 to 433.35. In savehaklu, however, a reverse trend can be seen wherein the value is low in upper reach and highest in the lower reach. The longitudinal profiles in the upper reach are notably steep. The high value of GI thus can be attributed to the steep topography in the scarp faces of Western Ghats. Presence of boulders, cobbles and pebbles as bed materials is also responsible for a high gradient value. The middle and lower reaches are characterized by moderate slope with lack of boulders and presence of coarse sand. These are the influencing factors for a moderate to low value of GI. (Bhat, Gangadhar, H., (1992), Chadaga Mohandas et al (2007), Chadaga Mohandas, (2009), Raghavan., B. R., (1989), Sadatipour, S.M.T., (1986), Udayashankar, H.N., (1995)).

Transverse profiles are steep and 'V' shaped near the origin which widen below the Western Ghat. They are flat at the lower reaches and alluvium plains (Fig.6).

Many prominent lineaments present in eastern and north-eastern parts of the study which can even be identified very well identified in the processed satellite imageries. The length varies from less than 1 km to more than 3 km (Fig.2). Majority of the lineaments show NNW-SSE to NW-SE and NNE-SSW to NE-SW trend and many are prominent in NS and NE-SW directions also. Some lineaments cut across each other while some are parallel. Lineaments which are fairly straight and do not change with stream courses, are considered as faults. Coastlines are sharp and straight and represent a major lineament. They belong to NNW-NW trending fault and are responsible for the development of Western Ghat scarps. The Kollur River follows the prominent coastal lineament near coastline.

Conclusion

The Kollur watershed thus is a typical hillslope small watershed having a varying topography. Some of the conclusions are as follows.

- Analysis of Morphometric characteristics reveal that eastern part of this watershed is subjected to high surface runoff and sedimentation processes. Basin circulatory values justify this.
- A high density of stream network exists in this region. Sub waterheds in this region

International Engineering Symposium, March 3-5, 2011 Kumamoto Univ., Japan

- exhibit high values of stream density and frequency.
- Scarp faces of the western parts of the Western Ghat region are highly sloping for a very short length which is seen by their longitudinal profiles. The GI values of tributaries are varying considerably within three reaches of many tributaries.
 - Transverse profiles are typically 'V' shaped and are steep and gorgeous. This indicates that the rivers are in youthful stage and carry boulders rocks as bed materials.
 - Many of the tributaries are structurally controlled with a tectonic influence especially in the eastern and north eastern regions. This is justified by the break in slope in longitudinal profiles and also by the presence of numerous small and big lineaments in these regions as seen from the lineament maps.
- Thus region specific water resources planning, conservation and management practices should be given importance in hillslope Kollur watershed due to the variations in topographic, geomorphic and morphometric controls. The designing and implementing such programs should also take into account of the influences of these controlling factors on various hydrogeologic processes.
- ### **Acknowledgements**
- The authors express their acknowledgment to Manipal University for providing financial support to carry out this research. They are also grateful to NRSC, Hyderabad (Under ISRO, Government of India) for providing the satellite imageries at concession rates.
- ### **References**
- [1] Bhat, Gangadhar, H. (1992), Geology, Geomorphology and Littoral Processes of a part of Dakshina Kannada coast through Remote Sensing – a study, Ph.D. THESIS submitted to Mangalore University.
- [2] Chadaga Mohandas (2009), River Basin Studies of Seetha-Swarna and Gangolli Composite River Systems of Coastal Karnataka, West Coast of India Using Remote Sensing and Geographic Information System (GIS), Ph.D. THESIS submitted to Manipal University.
- [3] Chadaga Mohandas et al (2007), Hydrogeological Characterization of the Gangolli Composite River systems of Coastal Karnataka, Proceedings of the INTERNATIONAL CONFERENCE ON GROUNDWATER-2007, Rajasthan University, Jaipur, Rajasthan, India.
- [4] Horton, R. E. (1932), Drainage basin characteristics, TRANS. AMER. GEOPHYS. UNION, V. 13, pp. 1081-1086.
- [5] Horton, R. E. (1945), Erosional development of streams and their drainage basins, BUL. GEOL. SOC. AM., V. 56, No. 1, pp. 275-330.
- [6] Lillesand, Thomas M., and Ralph W. Keifer, (2000), Remote Sensing and Image Interpretation, John Wiley and Sons, Inc. NY, USA.
- [7] Miller, V.C. (1953), Relation of Quantitative Geomorphic study of drainage basin characteristics in the Clinch Mountain area, Virginia and Tennessee, TECHNICAL REPORT 3, OFFICE OF THE NAVAL RESEARCH, DEPT. GEOLOGY, Columbia Univ., N. York.
- [8] Raghavan., B. R. (1989), Geomorphology and Evolution of the Sita and Swarna river Basin, Karnataka, India, Ph. D. THESIS submitted to Mangalore University.
- [9] Rajiv Chopra et al., (2005), Morphometric Analysis of subwatersheds in Gurdaspur District, Punjab using remote Sensing and GIS techniques, JOURNAL OF THE INDIAN SOCIETY OF REMOTE SENSING, V. 33, No.4, pp. 531 -539.
- [10] Sadatipour,S.M.T.(1986), Geomorphology and Groundwater studies of Gangolli Basin, Karnataka, India, Ph. D. THESIS submitted to Mangalore University.
- [11] Schumm,S.A.(1956), Evolution of drainage systems and slopes in badlands at Perth Amby, New Jersey. GEOL. SOC. AMERICA BULL., V. 67, pp. 597-646.
- [12] Singh, S. and Singh, M.C. (1997), Morphometric analysis of Kanhar river basin, NATIONAL GEOGRAPHICAL JOURNAL OF INDIA, V.43, No.1, pp. 31-43.
- [13] Smith, K.G. (1950), Standards for grading textures of erosional topography. AM. JOUR. SCI., V. 248, pp. 655-668.
- [14] Strahler, A.N., (1957), Quantitative analysis of watershed geomorphology. TRANS. AM. GEOPHYS. UNION, V. 38, pp. 913-920.
- [15] Strahler, A. N., (1964), Quantitative geomorphology of drainage basins and channel networks, V. T. Chow (ed), Handbook of Applied Hydrology. McGRAW HILL BOOK COMPANY, New York, Section 4-II.
- [16] Srinivasa Vittala, et al (2004), Morphometric analysis of sub-watersheds in the Pavagada area of Tumkur district, South India using Remote Sensing and GIS techniques, JOURNAL OF THE INDIAN SOCIETY OF REMOTE SENSING. V. 32, No. 4, pp. 351-362.
- [17] Udayashankar, H.N. (1995), Landform Analysis of Coastland and Hinterland - a part of Dakshina Kannada District by using Remote Sensing techniques. Ph.D. THESIS submitted to Mangalore University.
- [18] Wobus, C., et al (2006), Tectonics from Topography: Procedures, Promise and Pitfalls, in S. D. Willett, N. Hovius, M. T. Brandon, and D. M. Fisher (eds.), TECTONICS, CLIMATE AND LANDSCAPE EVOLUTION, GSA Special Paper 398, p. 55-70.

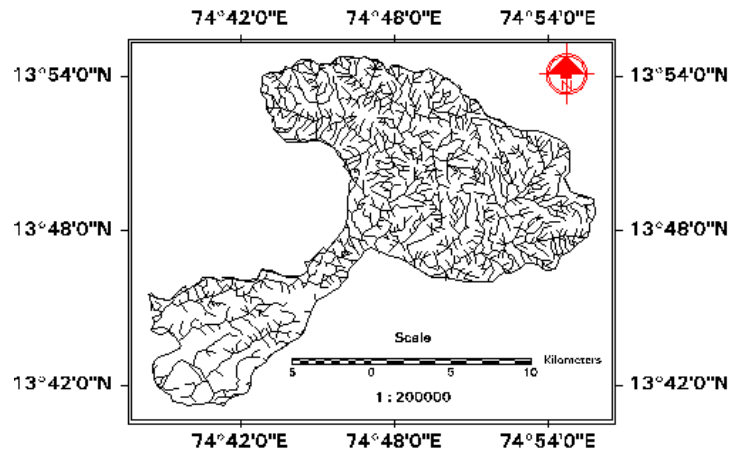


Fig. 1 Kollur Watershed (Drainage System)

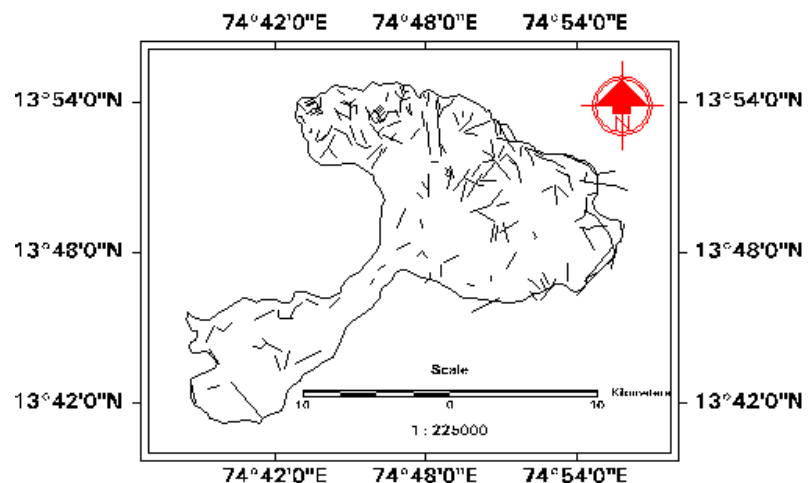


Fig. 2 Lineament Map

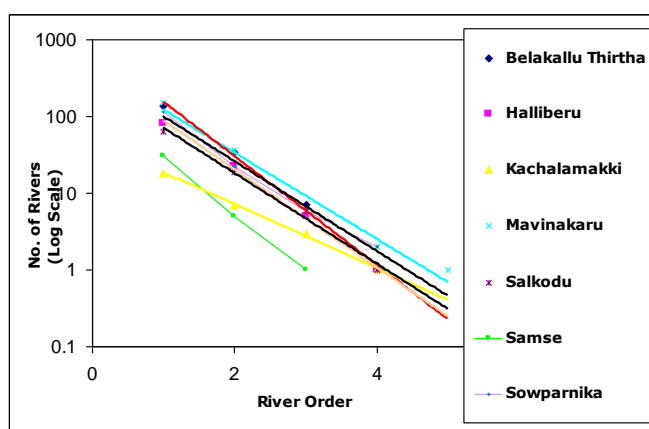


Fig. 3 Graph of Number of rivers (Log scale) versus River order

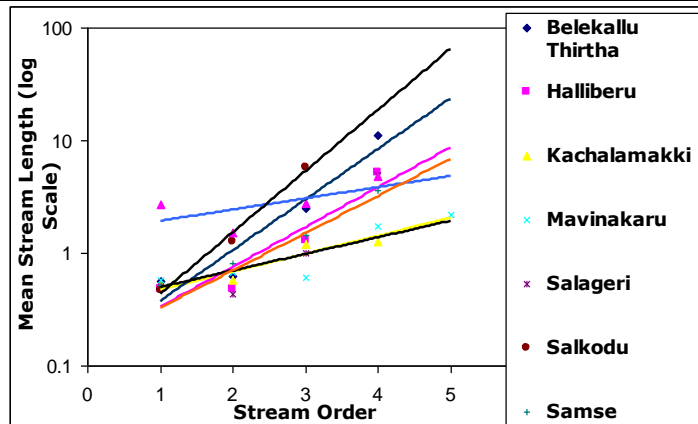


Fig. 4 Graph of Mean Stream Length (Log scale) versus River order

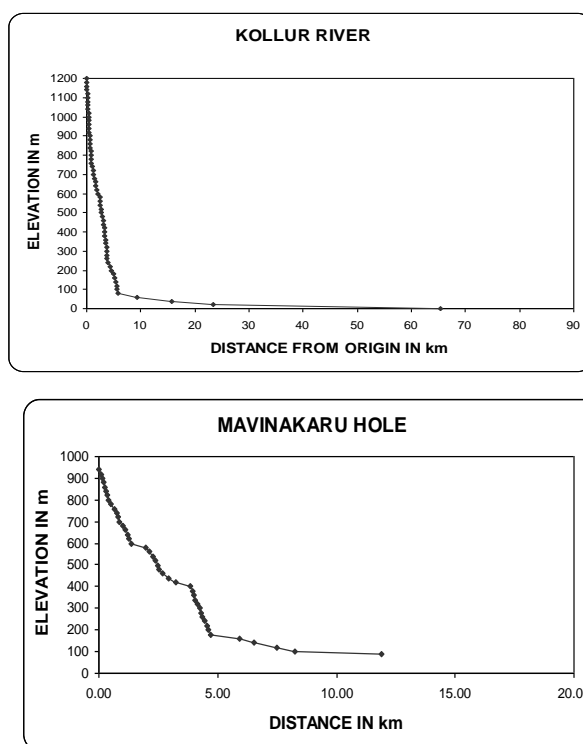


Fig. 5 Longitudinal profiles of some of the rivers in Kollur watershed

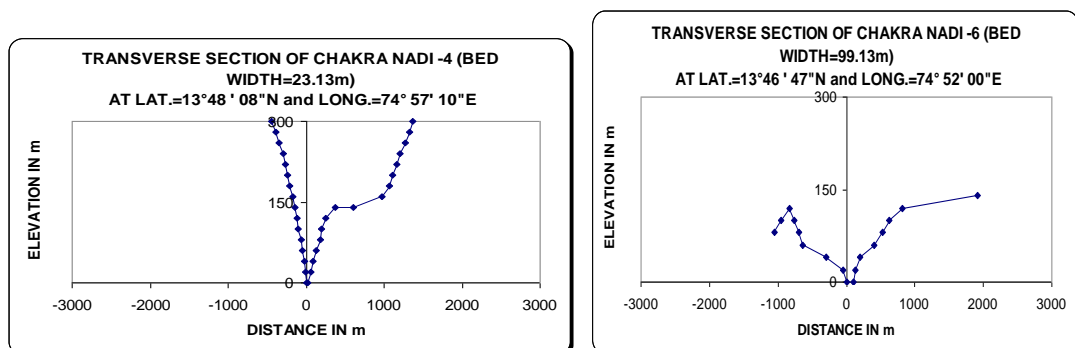


Fig. 6 Transverse profiles

Table 1 Some of the morphometric variables with their definitions

Sl. No.	Variable	Symbol	Units	Reference
A. DRAINAGE NETWORK:				
1.	Area of the basin	A	Km ²	---
2.	Basin Perimeter	P	Km	---
3.	Length of the basin	L _b	Km	---
4.	Main stream length	L _m	Km	---
5.	Basin Circularity (Circulatory ratio)	$R_c = \frac{4 \times \pi \times A}{P^2}$	-----	Miller (1953)
6.	Basin Elongation (Elongation Ratio)	$R_e = \frac{2\sqrt{\frac{A}{\pi}}}{L_b}$	-----	Schumm (1956)
7.	Stream Order	u	Enumerative	Strahler (1964)
8.	Number of streams of order 'u'	N _u	Enumerative	-----
9.	Total length of streams of order 'u'	L _u	Km	Horton (1945)
10.	Mean length of streams of order 'u'	$L_{sm} = \frac{L_u}{N_u}$	Km	Strahler (1964)
12.	Bifurcation Ratio	$R_b = \frac{N_u}{N_u + 1}$	Enumerative	Schumm (1956)
13.	Drainage Density	$D = \frac{L}{A}$ L=total stream length	Km/Km ²	Horton (1932)
14.	Stream Frequency	$F = \frac{N}{A}$	Number/Km ²	Horton (1932)

Table 2 Basin Geometry

Subwatershed	Area, A (Km ²)	Perimeter, P (Km)	Basin Length, L _b (Km)	Length Of Main Stream, L _m (Km)	Basin Circulatory Ratio (R _c)	Basin Elongation, (R _e)
Belakallu Thirtha River	39.50	36.90	11.6	11.89	0.37	0.61
Halliberu River	17.40	18.18	6.77	8.16	0.66	0.70
Mavinakaru RIver	38.90	27.60	9.89	13.07	0.64	0.71
Salageri River	15.40	16.24	5.49	6.54	0.73	0.81
Samse River	29.40	28.00	8.77	8.32	0.47	0.70

Table 3 No. of Streams (Nu), Stream Length (Lu) & Mean Stream Length (Lsm)

Sub watershed	Stream Order (U)	I	II	III	IV	V	Total
Belakallu Thirtha River	Number (Nu)	135	34	7	1	--	177
	Length (Lu)	75.77	21.23	17.35	11.11	--	125.46 Km(L)

International Engineering Symposium, March 3-5, 2011 Kumamoto Univ., Japan

	Mean stream Length(Lsm)	0.56	0.62	2.48	11.11		-----
Halliberu River	Number (Nu)	82	22	5	1	--	110
	Length (Lu)	39.60	10.66	6.51	5.23	--	62.00 Km(L)
	Mean stream Length(Lsm)	0.48	0.48	1.30	5.23	--	---
Mavinakaru River	Number (Nu)	151	36	6	2	1	196
	Length (Lu)	85.72	24.16	3.66	3.49	2.21	119.24 Km(L)
	Mean stream Length(Lsm)	0.57	0.67	0.61	1.75	2.21	---
Salageri River	Number (Nu)	63	19	6	1	-----	89
	Length (Lu)	32.27	8.23	5.91	4.88	-----	51.29 Km(L)
	Mean stream Length(Lsm)	0.51	0.43	0.99	4.88	-----	-----
Samse River	Number (Nu)	115	22	6	2	-----	145
	Length (Lu)	59.53	18	8.64	7.3	-----	93.47 Km(L)
	Mean stream Length(Lsm)	0.52	0.82	1.44	3.65	-----	---

Table 4 Bifurcation Ratio

Bifurcation Ratio	I/II	II/III	III/IV	IV/V	Mean Rbm
Belakallu Thirtha River	3.97	4.86	7.00		5.23
Halliberu River	3.73	4.40	5.00		4.38
Mavinakaru River	4.19	6.00	3.00	2.00	3.80
Salageri River	3.32	3.12	6.00		4.15
Samse River	5.23	3.67	3.00		3.97

Table 5 Drainage Density and Stream frequency

Sub watershed	Drainage Density	Stream Frequency
Belakallu Thirtha River	3.18	4.48
Halliberu River	3.56	6.32
Mavinakaru River	3.07	5.04
Salageri River	3.33	5.78
Samse River	3.18	4.93

Table 6 Gradient index (GI) for upper, middle and lower reaches

River	Upper reach	Middle reach	Lower reach
Mavinakaru	408.41	388.09	44.79
Belakallu Thirtha	443.28	46.58	55.71
Samse Hole	666.62	75.67	57.62
Halliberu	1036.69	97.40	50.40
Savehaklu	127.38	87.55	433.35

PRELIMINARY LIQUEFACTION POTENTIAL ANALYSIS OF VIJAYAWADA REGION

K.RAJESH CHANDRA¹ AKHILA MANNE² AND NEELIMA SATYAM D³

1. *Earthquake Engineering Research Centre, International Institute of Information Technology Hyderabad, India.*
 2. *Earthquake Engineering Research Centre, International Institute of Information Technology, India*
 3. *Earthquake Engineering Research Centre, International Institute of Information Technology Hyderabad, India. Email: neelima.satyam@iiit.ac.in*
-

Abstract: Experience from past earthquakes has demonstrated the vulnerability of structures to seismically induced ground deformation. During earthquake, soil can fail due to liquefaction with devastating effect such as landslides, lateral spreading, or large ground settlement. The phenomenon of liquefaction of soil had been observed for many years, but was brought to the attention of engineers after Niigata (1964) Alaska earthquakes (1964). Liquefaction is a phenomenon in which the strength and stiffness of a soil is reduced by earthquake shaking or other rapid loading. Liquefaction and related phenomena have been responsible for tremendous amounts of damage in historical earthquakes around the world (Borcherdt R.D 1991; Dobry R, 1981). During the Bhuj earthquake, India on 26th January 2001 ($M=7.7$) lot of damages had been occurred due to liquefaction and other ground failures (Rao and Mohanty, 2001). In this paper, a preliminary liquefaction hazard assessment was carried out using the available SPT data. From these investigations it was observed that a vast majority of liquefaction occurrences were associated with sandy soils and silty clays of low plasticity.

Keywords: *Liquefaction potential, seismic hazard assessment*

Introduction

The city Vijayawada occupies an area of 119.8 square kilometers. The population of the whole city (along with Vijayawada Sub-Urban and Vijayawada Rural) is more than 2.5 Million. Vijayawada is bounded by the Indrakiladri Hills on the east and west and the Budameru River on the north. The Northern, North-Western, and South-Western parts of the city are covered by a low range of hills, while the Central, South-Western and North-Western parts are covered by rich and fertile agriculture lands with three major irrigation canals. The topography of Vijayawada is flat. A large number of investigations have been carried out for understanding the phenomenon of soil liquefaction in the last four decades. From these investigations it

was observed that a vast majority of liquefaction occurrences were associated with sandy soils and silty sands of low plasticity.

Mechanism

Liquefaction of soil is a process by which sediments below water table temporarily lose shear strength and behave more as a viscous liquid than as a solid. The water in the soil voids exerts pressure upon the soil particles. If the pressure is low enough, the soil stays stable. However, once the water pressure exceeds a certain level, it forces the soil particles to move relative to each other, thus causing the strength of the soil to decrease and failure of the soil follows. During earthquake when the shear wave passes through saturated soil layers, it causes the granular soil structure to

deform and the weak part of the soil begins to collapse.

The collapsed soil fills the lower layer and forces the pore water pressure in this layer to increase. If increased water pressure cannot be released, it will continue to build up and after a certain limit effective stress of the soil becomes zero. If this situation occurs then the soil layer losses its shear strength and it cannot sustain the total weight of the soil layer above, thus the upper layer soils are ready to move down and behave as a viscous liquid.

Methodology

Ground response analysis is an important factor that is to be taken into consideration for evaluation and remediation of geotechnical as well as structural seismic hazards. For site specific ground response analysis three basic input parameters that are essential are, (i) Input ground motion (ii) Shear wave velocity profile and (iii) Dynamic soil characteristics (e.g., strain dependent modulus reduction and damping behaviour and cyclic strength curves).

Linear analysis using DEEPSOIL (Youssef M.A.H, 2009) in frequency domain was used to compute free field response, which is very popular with practitioners.

Analyses were carried out for the stochastically simulated acceleration time histories from local sources using in-situ measured shear wave velocities. Shear wave velocity (V_s) is one of the most important input parameter to represent the stiffness of the soil layers. It is preferable to measure V_s by in situ wave propagation tests, however it is often not economically feasible to perform the tests at all locations. Hence, a reliable correlation between V_s and standard penetration test blow counts (SPT) would be a considerable advantage. Shear wave velocity was measured using an attenuation relation developed for Delhi region (Neelima Satyam D, 2006)

$$V_s = 61 \times N^{0.5} \quad (1)$$

Where, N = corrected SPT value.

In the current study, Chamba earthquake from long distance of magnitude 4.9 was

considered (Fig.1). Fast Fourier transform was applied. Analysis is performed for 5% damping. Thickness (m), unit weight (kN/m^3) and shear velocity (m/sec) for each layer are given as input as shown in Table 1. Borehole data including corrected SPT values were considered in the analysis. Figure 3 shows the soil profiles of boreholes of 10m deep along with SPT value. After obtaining the Surface PGA from DEEPSOIL as shown in Fig. 3, Matlab is used to generate the liquefaction factor of safety at the locations.

Two methods have been adopted for accuracy. They are Seed and Idriss method and Seed and Peacock method

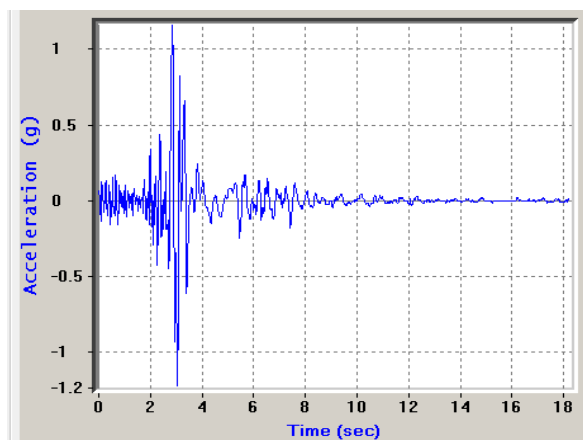


Fig 1. Acceleration time history of 1995 Chamba Earthquake

Table 1. Details of soil profiles given in Deepsoil

Layer no	Thickness (m)	Unit Weight (kN/m^3)	V_s (m/s)	Damping Ratio (%)
1	1.5	14.8	86.26	5
2	6.55	15.3	158.13	5
3	0.95	15.4	192.89	5
4	1	15.5	192.89	5



to be primarily due to the vertical propagation of shear waves in the deposit. This leads to a simplified procedure developed by Seed and Idriss (1971) for evaluating the induced shear stress. The

simplified procedure was evolved initially based on extensive laboratory studies of the behaviour of soils subjected to cyclic loading and later confirmed and supplemented with field case histories. This procedure is based on the relationship between the SPT N' value and the intensity of cyclic loading, expressed as magnitude weighted equivalent uniform cyclic stress ratio. Figure explains the steps involved in the analysis procedure in the simplified Seed and Idriss (1971) method.

In Seed and Peacock (1971) method the induced average cyclic shear stress (τ_{av}) due to a given earthquake can be computed. Using corrected SPT 'N' value the resistance for the soil liquefaction was estimated for the boreholes.

Results

Profiles for each borehole data has been drawn based on the IS Classification of soils and indicating the water table level at each borehole. Chamba earthquake data with a maximum PGA Of 0.118g and magnitude of 4.9 is given as input. The results obtained from the DEEPSOIL as shown in Table 2 by assuming the engineering bedrock at a depth of 200m from ground surface. And the inputs given were Thickness of layers, Unit weight, Shear wave velocity as described earlier. Shear wave velocity for the engineering bed rock was considered as 760m/s and unit weight as 18.5 kN/m³ with a damping of 5%. The water table at each borehole data which has a significant effect on the liquefaction potential at a point is also considered. Rock Property is considered as Rigid Half Space. Number iterations used for fast Fourier transform is 15. Complex shear modulus is taken as Frequency independent. Using the matlab, a code has been developed for calculating the factor of safety using the two methods mentioned are carried out. Peak Ground Acceleration (PGA) obtained above, unit weights of layers, thickness, shear wave velocity and water table level are given as inputs.

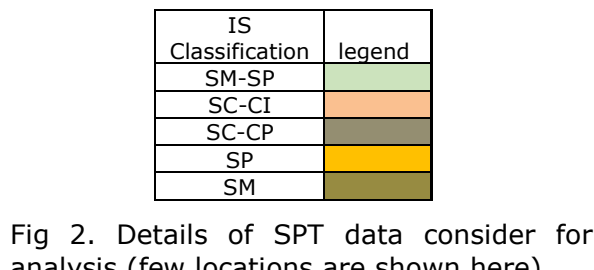


Fig 2. Details of SPT data consider for analysis (few locations are shown here)

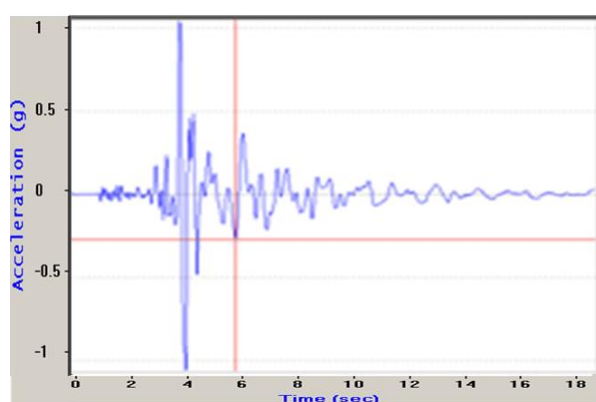


Fig 3. Acceleration time history at the surface

The shear stress developed at any point in a soil strata during an earthquake appear

Conclusions

- Borehole data at 10 locations have been considered based on the existence of important buildings like hospitals, colleges and important buildings in the locality, Population etc. and Preliminary liquefaction potential assessment has been carried out at the study areas.
- The preliminary Liquefaction potential analysis at all these locations has been carried out and estimated the liquefaction potential.
- By Seed and Idriss (1971) Method, at the locations like patamata, Autonagar and kanuru liquefaction can occur.
- In Seed and Peacock (1971) Method, at the locations like Autonagar and kanuru liquefaction is likely to occur.
- Required precautions have to be taken into consideration. As the Preliminary assessment shows the possibility of occurrence, so a detailed liquefaction potential analysis of the area has to be carried out.

References

- [1] Borcherdt R.D. (1994), Estimates of Site Dependent Response Spectra for Design (Methodology and Justification) *Earthquake Spectra*, (10) 4, 617-653.
- [2] Dobry R. (1981), Liquefaction Susceptibility from S Wave Velocity, Insitu Testing to Evaluate Liquefaction Susceptibility, *J. Geotechnical Engg.*, ASCE.
- [3] D.Neelima Satyam, (2006), Seismic Microzonation of Delhi Region, Ph.D Thesis, IIT Delhi
- [4] Rao K.S. and Mohanthy W.K. (2001), The Bhuj Earthquake and Lessons for the Damages, IGS Newsletter, 33, 3-10.
- [5] Steven L. Kramer (1996), Geotechnical Earthquake Engineering, Third Edition.
- [6] Seed H.B and Idriss I.M. (1971) Simplified Procedure for Evaluating Soil Liquefaction Potential, *J. Soil Mechanics and Foundations, ASCE*, (97) SM9, 1249-1273.
- [7] Seed H.B. and Peacock W.H. (1971) Test Procedures for Measuring Soil Liquefaction Characteristics, *J. Soil Mechanics and Foundations Div., ASCE*, 152-167.
- [8] Youssef M.A.H (2009), DEEPSOIL, <http://www.geoengineer.org/software/applications-deepsol.htm>

Table 2 Estimated surface PGA from DEEPSOIL

Location	Latitude	Longitude	Water table(m)	Max. PGA (g)
Auto Nagar	16° 20' 31.31"	80 41'38.01"	9.5	0.2
Benz Circle	16° 49' 65"	80°65'89.00"	4.0	0.13
GovernerPet	16° 51' 42"	80°63'11.00"	5.0	0.12
Kanuru	16° 28' 16.72"	80 43'12.67"	2.4	0.11
Labbipet	16° 50' 29"	80°63'60.00"	9.7	0.13
Moghalrajpuram	16° 50' 87"	80°64'54.00"	9.5	0.14
Patamata	16° 49' 50"	80°66'70.00"	8.6	0.14
Stella College	16° 50' 80"	80°66'06.00"	5.5	0.09
Sub collector Office(bunder road)	16° 50' 65"	80°63'29.00"	6.0	0.13
Surya raopet	16° 49' 16"	80°66'95.00"	7.4	0.11

HYDROGEOCHEMICAL STUDIES OF GROUNDWATER ALONG COASTAL REGION OF MULKI-UDUPI, KARNATAKA STATE, INDIA

RADHAKRISHNAN K.¹, SHENOY K NARAYANA² and LOKESH K.N.³

1 Department of Civil Engineering, NMAMIT., NITTE-574 110, India
E-mail: georadha2000@yahoo.co.in

2 Department of Civil Engineering, M.I.T., Manipal University Manipal- 576 104, India
E-mail: kn.shenoy@manipal.edu

3 Department of Civil Engineering, NITK., Surathkal-575 025, India
E-mail: lokeshkannur@yahoo.com

Abstract: Hydrogeochemical studies of groundwater along the coastal region of Mulki-Udupi, Karnataka state of India have been carried out. Assessment of aquifer contamination has been carried out based on distribution of various chemical constituents in groundwater and factors controlling its chemistry. The impact of human activities on groundwater quality of the area has been discussed. From the spatial variation maps of different water quality parameters prepared, the vulnerable area has been mapped. To understand the relation between the hydro geochemical quality of ground water and spatial distribution of the salinity into groundwater regime along the stretch of coastal region, delineation of groundwater salinity zone has been carried out at selected places by using Electrical resistivity method

Key words: groundwater, aquifer contamination, human activities, spatial distribution, salinity, electrical resistivity.

Introduction

Quality of groundwater is controlled by several factors viz., local climate, geology, topography of the area, saline water ingressoin/intrusion and anthropogenic activities on the ground. In recent years anthropogenic activities such as urbanization and industrialization have become major controlling factors of groundwater chemistry, especially along the coastal regions. Impact of urbanization and industrialization on local environment, particularly on groundwater regime is a major cause of concern. Field observations revealed that deterioration of quality of groundwater along the coastal region of Mulki-Udupi was caused by industrial waste, sewage of urban or semi-urban sanitary effluents, intrusion of salt water due to over exploitation of coastal aquifers, and sea water ingestion through streams during high tidal times (Lokesh

and Shenoy, 1996, 1997a, 1997b, Radhakrishnan and Lokes 2010).

The study area comprises Mulki River Basin (North latitudes $13^{\circ} 02' 28''$ and $13^{\circ} 12' 12''$ and East longitudes $74^{\circ} 46' 14''$ and $75^{\circ} 02' 47''$) and rural and urban areas of Udupi taluk (area lies between $74^{\circ} 41'$ N and $74^{\circ} 57'$ E longitude and $13^{\circ} 5'$ N and $13^{\circ} 31'$ N latitude) along the coastal region of Karnataka state, India. Topographically the area has a lot of lateritic mesas of different elevations with granitic/gneissic inselbergs projections in between and the alluvial plains other than ridges and mounts of gabbros and dolerites.

Geologically the study area comprised the rocks like granite and granitic gneisses with occasional lateritic capping and unconsolidated river and marine sediments. Basic intrusives like dolerite and gabbros,

and acidic intrusives like pegmatites and quartz veins are also found in the study area. Groundwater occurs in the region mainly in various geological formations like alluvium, coastal sediments, laterites and in weathered and fractured granitic gneisses under phreatic and semi-confined to confined conditions. Shallow aquifers occur in highly porous laterites and alluvial plains exploited by dug wells and ponds; whereas the fractured granites and granitic gneisses are the deeper aquifers which are tapped through bore wells. Diversified hydrogeological set up of the region has given rise to widely varying groundwater conditions. Agriculture is the main occupation of the people along the midland and fishing is at the coastal region.

Though the study area is bestowed with heavy rainfall, water cannot be fully utilized or stored. Reservoirs, if constructed in flat terrain near the coastal region, submerge large cultivable lands and inhabited areas. Hence, construction of reservoirs is not feasible in this region. Since most of the rivers are tidal and non-perennial, ingressions of salt water during high tidal periods occurs rendering not only the river water unsuitable for any use but also making the groundwater saline. Due to increase in population, intensive agricultural practices, rapid industrialization and government plans to supply safe drinking water to rural and urban masses, an increase in the tempo of groundwater development has been observed along the fragile coastal regions of Udupi taluk. The study area will be buzzing with industrial activities in near future. The 2000 MW thermal power station is already commissioned at Nandikur besides a Wind farm equipments manufacturing industry at Padubidri situated in the locality. Both of these have an impact on socio-economic status of local people in general and local environment in particular in this region. To meet the ever growing demand for fresh water, a large number of wells have been sunk for domestic, irrigation as well as industrial purposes. Almost every household has an open well. A large number of borewells have been drilled haphazardly in the villages and in urban areas to meet the growing water demand. This has resulted in over exploitation of fragile coastal

aquifer and deterioration of groundwater quality.

In the planning and development of water resources management, quality of the water is as important as its quantity. For the suitability of the resources for the domestic, industrial and agricultural purposes the water quality and its distribution should be known. By keeping these views in background, this work has been taken up to evaluate the present status of groundwater quality in the coastal region from Mulki to Udupi.

Methodology

The groundwater samples were collected from different geological set up viz., Mulki river basin, rural as well as urban areas of Udupi taluk and along the coastal stretch. The samplings have been carried out following the standard procedures (NEERI, 1988).

The various physico-chemical parameters of groundwater such as pH, Temperature, Electrical Conductivity (EC), Total dissolved solids (TDS), Total Hardness (TH), Calcium (Ca^{++}), Magnesium (Mg^{++}), Potassium (K^+), Iron (Fe^{++}), Bicarbonate (HCO_3^-), Sulphates (SO_4^{--}), Chlorides (Cl^-), Nitrate (NO_3^-), etc., were determined by using the standard analytical methods (APHA, 1995) and the results were analyzed using various statistical methods (Table 1) in order to understand the geochemistry of groundwater.

In order to understand the spatial variation of the different hydro chemical parameters in Mulki river basin, the geographical coordinates of the sampling stations in the study area were located by Garmin hand held GPS. The sampling stations have been transferred into the map of the river basin using ERDAS imagine 9.1 version software. Thematic maps of variations in important water quality parameters were prepared transferring the analytical values of chemical constituents using ArcGIS 9 to understand the temporal variation. Then data were merged and interpolated using weighted average method to obtain the variation maps of different parameters. Using ArcGIS Ground water quality vulnerability map of the area has been

prepared overlaying the thematic maps of the above parameters.

Vertical electrical soundings have been carried out at a few places by using Schlumberger electrode configuration to understand the relation between the spatial distribution of the saline water contamination and the hydro chemical quality of ground water along the coastal region. Resistivity logs also have been prepared to verify the litho units and the layer parameters which will give ideas about the saline water ingressions.

Results and Discussion

The study (Radhakrishnan and Lokesh, 2010) shows that majority of the ground water samples in the Mulki River basin fall in the fields of Ca_Mg Bicarbonate and Sulphate fields where alkaline earths ($\text{Ca}+\text{Mg}=89\%$) exceeds alkalies ($\text{Na}+\text{K}$) and Strong acids ($\text{SO}_4+\text{Cl}+\text{F}=53\%$) exceed weak acids (CO_3+HCO_3) along with exceeding secondary alkalinity and secondary salinity. About one fifth of the samples also fall in mixed zones indicating balance on anion-cation pair. In the groundwater chemistry, the order of cations abundance is $\text{Mg}>\text{Ca}>\text{Na}>\text{K}$ and anionic chemistry the order is $\text{HCO}_3>\text{Cl}>\text{SO}_4>\text{NO}_3>\text{F}$. The total hydrochemistry is dominated by alkaline earth and strong acids with primary and secondary salinity and secondary alkalinity influenced by the weathered granitic gneiss and leached laterite. Relative abundance of Na and Cl in groundwater may be related to saline origin. The sources of Sodium are from incongruent dissolution of plagioclase feldspar or from saline water. Since chloride is a predominant anion in sea water and occur only as a minor or trace element in groundwater from crystalline terrain (Freeze and Cherry, 1979), Na and Cl ions might be added to the groundwater due to salt water intrusion and/or from salt water ingressions. Even though 67% of the samples from the Mulki river basin were found to be within the permissible limit of drinking water standards (Radhakrishnan and Lokesh, 2010) based on total dissolved solids, most of the open wells and pond samples from the coastal stretch of the study area were found to be beyond

the permissible limit of drinking water and irrigation water standards.

Similar studies in other parts of the districts (Lokesh and Shenoy, 1997a) show that hydro chemical properties of groundwater from bore wells in rural areas of Udupi taluk are dominated by alkaline earth and weak acids. Amongst the cations, the $\text{Na}+\text{K}$ and Ca predominate and combination of CO_3+HCO_3 ions predominate among anions. Chemistry of groundwater is controlled by the rock types of the area and chemistry of open well water is influenced by precipitation. The chemical properties of groundwater of Udupi city area (Lokesh and Shenoy, 1997c) are dominated by alkalies and strong acids. Amongst the cations the $\text{Na}+\text{K}$ predominates and combination of $\text{SO}_4+\text{Cl}+\text{NO}_3$ ions predominates among anions. The chemistry of the groundwater is mainly controlled by the rock type of the region during pre-monsoon period. However, during post-monsoon period the chemistry of groundwater is influenced by rainfall that occurs during South-west monsoon period. Along the coastal areas of Udupi taluk groundwater is dominated by alkaline earth and weak acids (mainly bicarbonate type of water) and by alkalis and strong acids with more affinity towards chloride (Shenoy, 2000). Areas of saline water contamination has been delineated (Shenoy and Lokesh, 1997b) on the basis of hydro chemical parameters such as Cl/HCO_3 (Revelle, 1941) and Ca/Mg (Mandel and Shiften, 1981) ratios. Fresh water and least contaminated groundwater are expected to have a ratio less than 1, while increase in ratio in excess of 1 is an indication of contamination from saline waters (Narayan and Natarajan, 1993). The Ca/Mg ratio of average sea water is 0.296 (Handa, 1990). In the present study, a number of wells along the coastal region of Udupi taluk show Ca/Mg ratio more than 0.296 (Lokesh and Shenoy, 1997b).

The groundwater vulnerable map of Mulki river basin (Fig. 1) shows that the coastal area is more vulnerable to water quality deterioration in respect of various quality parameters such as pH, Calcium, Chloride, TDS and Total Hardness and it extends up to 7km from the coast especially along the

alluvial plain indicating the influence of rapid urbanization and industrialization in this region.

Delineation of groundwater salinity zone has also been carried out at two selected places viz., Mattu and Padubidri to Padumarnad stretch of Mulki by using Electrical resistivity method. Mattu is located about 3km from Katpadi, near west coast. Geo-electric section of a small agricultural land measuring about 1430 sq.m has been prepared to depict subsurface lithology. The sounding curves are of KQH, KH, QH, H types. It shows five distinct types of litho units in the region viz., sandy soil, sand, saturated alluvium, salinity zones and gneiss (Fig. 2). The resistivity ranges of various litho-units in Mattu region are given in Table 2. Presence of salinity on the region is also found by chemical analysis of groundwater samples which indicates varying values of Electrical conductivity and other chemical parameters (Table 3).

Six stations were selected along the coastal stretch in the alluvial plain of Mulki river basin from Padubidri to Padumarnad area. Resistivity and thickness of different layers, as interpreted from field curves are shown in figure 3. Layer parameters show that there are two distinct types of field curves viz., 3-layered at Avral, Hejamadi Kodi, Bappanadu temple and Kolnada and 5-layered at Bappanadu (VES No. 121). The top most layer is the soil. The resistivity of this layer ranging from 2.11 to 785 ohm-m and thickness varies from 0.54 m to 4.32m. This may be due to the variation in soil moisture and the chemical composition. The resistivity of second layer at Avral is 1236 ohm-m with thickness of 40.8m corresponds laterite. At Hejamadi Kodi (VES 108 & 122), the resistivity of second layer is 39.6 ohm-m with a thickness of about 29.5m. This layer is saturated alluvium. The resistivity of second layer at Bappanadu and Kolnada region is very low and ranges between 0.398 to 4.69 with thickness range from 1.82m to 8.11m corresponds to alluvial beds with saline water in the aquifer. The third layer of 3-layerd type and fifth layer of 5-layered type represent the hard granitic gneiss. This clearly depicts the presence of saline water in the region.

Conclusions

The present study shows that -

- The groundwater of the study area has been influenced by both geology and anthropogenic activities.
- Groundwater vulnerability map of the study area and electrical resistivity survey show that the water quality deterioration is more vulnerable in coastal area with respect to salinity hazard and it extends up to 7km from the coast especially along the alluvial plain.
- This is due to the intensive agricultural practices, influence of rapid urbanization and industrialization.

Acknowledgements

Authors are grateful to the authorities of NMAM Institute of Technology, Nitte & President of Nitte Education Trust; authorities of Manipal Institute of Technology & Manipal University, Manipal and the Directors of National Institute of Technology_Karnataka, Surathkal for their continued support and encouragement

References

- (1) APHA, AWWA,WEF (1995) "Standard methods for the examination of water and waste water", 19th edition, American Public health Association, Washington D.C.
- (2) Freeze, R. Allan and Cherry, A. John (Editors) (1979). Groundwater, Prentice-Hall, Inc., Englewood Cliffs, New Jersey.
- (3) Handa B.K (1990) Norms for identifying saline water intrusions in groundwater. Journal of Applied Hydrology, Vol.III, No.1, pp.27-48.
- (4) Lokesh K.N. and Shenoy, Narayana K. (1996), Quality of groundwater in southern part of Udupi taluk (D.K.) Karnataka state, KREC Research Bulletin, Vol. 5, No.1, 1996, pp10-14.
- (5) Lokesh K.N. and Shenoy, Narayana K. (1997a), Groundwater quality assessment in Hard rock areas of Udupi (D.K.), Karnataka, In Proceedings of National seminar on Hydrogeology of Precambrian terrains and hard rock areas, 3rd and 4th February 1997, Karnataka University, Dharwad, India, pp96-106.
- (6) Lokesh K.N. and Shenoy, Narayana K. (1997b), Quality of Groundwater in coastal region of Udupi taluk- Problems and some mitigative measures, M.I.T., Technical Review Vol. No.6, May 1997, pp.93-100.
- (7) Lokesh K.N. and Shenoy, Narayana K. (1997c) A study on the impact of urbanisation and human activities on quality of groundwater in Udupi municipal area(D.K.), Karnataka. In Proc.symp. Earth Sciences in Environmental Assessment and

International Engineering Symposium, March 3-5, 2011 Kumamoto Univ., Japan

- Management, Lucknow, 9-11, April 1996. Geol.Surv.Ind.spl. Pub, 48(1), 1997, pp.185-196
 (8) Mandel S. and Shiften Z.L (1981) Groundwater resources investigation and development. Academic Press, Inc., NewYork.
 (9) Narayan, S.M and Natarajan K (1993). Seawater-freshwater interface studies in coastal areas with special reference to Tamilnadu. In: Proceedings volume on workshop on artificial recharge of groundwater in coastal aquifers, C.G.W.B, 27-28th March, Bhudaneswara.
 (10) NEERI (1988) "Manual on water and wastewater analysis, NEERI, National Environmental Research Institute, Nagpur, 331p
 (11) Piper A.M.(1953) A graphical procedure in the geological interpretation of water analysis., USGS Groundwater Note, no.12, 63p
- (12) Radhakrishnan K. and Lokesh, K.N. (2010) Integrated Approach for Hydrogeochemical studies of Mulki River Basin, Coastal Dakshina Kannada Districts of Karnataka, Proceedings of SWaRM-2010, NITK Surathkal, pdf.37
 (13) Revelle R (1941) Critiria for recognition of sea water in groundwater. Trans. Amer. Geophys. Union, Vol. 22, pp.593-597
 (14) Shenoy, Narayana K. (2000) Hydrogeological studies in Udupi taluk of coastal Karnataka, India. Unpublished ph.D thesis submitted to the Mangalore University for the award of the Degree of Doctor of Philosophy in Geology.

Table 1: Statistical details of hydrogeochemical parameters in ground water samples of the study area

Chemical Parameters	Mulki river basin (Pre-monsoon)		Rural Udupi				Coastal Udupi				Urban Udupi			
	Max.	Min.	Maximum		Minimum		Maximum		Minimum		Maximum		Minimum	
			Pre-mon.	Post-mon.	Pre-mon.	Post-mon.	Pre-mon.	Post-mon.	Pre-mon.	Post-mon.	Pre-mon	Post-mon	Pre-mon	Post-mon
pH	9.75	4.79	8.21	7.89	6.1	6.98	8.29	8.03	5.41	3.09	8.16	7.87	5.39	4.57
Tot. Hard. (ppm)	9200	9.2	192	164	7	16	912	910	10	10	204	225	10	10
TDS (ppm)	2825.55	24.84	314.4	340.8	20.8	33.2	3852	3928	48.8	36.6	NA	NA	NA	NA
Calcium (ppm)	107.83	1.25	34	50.8	1.6	2.8	100	176	2.4	2	26.87	36.85	2	2
Magnesium (ppm)	972	0.29	27.94	13.6	0	0.49	160.9	127.6	0	0.49	38.64	41.55	0.73	0.73
Sodium (ppm)	155.3	0.48	39.1	52.9	2.76	0	598	1177.	0	1.84	95.45	79.12	6.67	6.67
Potassium (ppm)	76.98	0.03	5.89	6.44	0.59	0.51	40.95	62.4	0.27	0.08	20.09	7.06	0.74	0.16
Iron(ppm)	5.22	ND	1.35	2.575	0	0	NA	NA	NA	NA	NA	NA-	NA	NA
Bicarbonates (ppm)	260	6	181.3	213	27	7.77	263.6	260	4.49	0	98.04	170.3	5.15	1.82
Chlorides (ppm)	4975	1.45	17.8	28.8	2.12	2.63	1206.	1862	4.54	4.35	130.0	77.41	8.1	8.8
Sulphates (ppm)	98	ND	26	22	0	0	440	560	0	2.6	176	88	0	0
Nitrates (ppm)	16.13	ND	28.03	18.25	1.06	0.44	52.92	20.48	3.52	2.44	37	67.84	2.03	1.92
EC ($\mu\text{S}/\text{cm}$)	4880	40	366	507	22	48.5	4620	6350	52	66.8	1440	586	113	46.8

Table 2: Resistivity ranges of various litho-units in Mattu region

Litho-units	Resistivity range in Ohm-m
Sandy soil	14-900
Sand	3800
Saturated alluvium	39-160
Salinity zone	3-9.5
Gneiss	∞

Table 3: Chemical analysis results of groundwater samples from Mattu region

Well Nos.	EC micromhos/cm	TH as CaCO ₃	Cl mg/L	Ca mg/L	Mg mg/L
1	6290	860	1580	168	106.92
2	3820	650	840	172	53.46
3	22800	2900	6550	256	549.18

Table 4: Resistivities and thicknesses of different layers as interpreted from field curves from Mulki River Basin from Padubidri to Padumarnad area

VES No.	Type of curve	No. of layers	Resistivity of layers in ohm-m						Thickness of layers in meters				
			1	2	3	4	5	6	1	2	3	4	5
106	K	3	785	1236	205				4.32	40.8			
108	H	3	531	39.6	a				3.43	29.5			
109	H	3	18.1	0.39	10.7				1.28	1.97			
121	QHKH	5	62.2	4.69	1.21	30.5	1.2	a	0.54	1.82	4.13	5.6	12.6
122	H	3	531	39.6	a				3.43	29.6			
123	H	3	2.11	1.22	a				0.92	8.11			

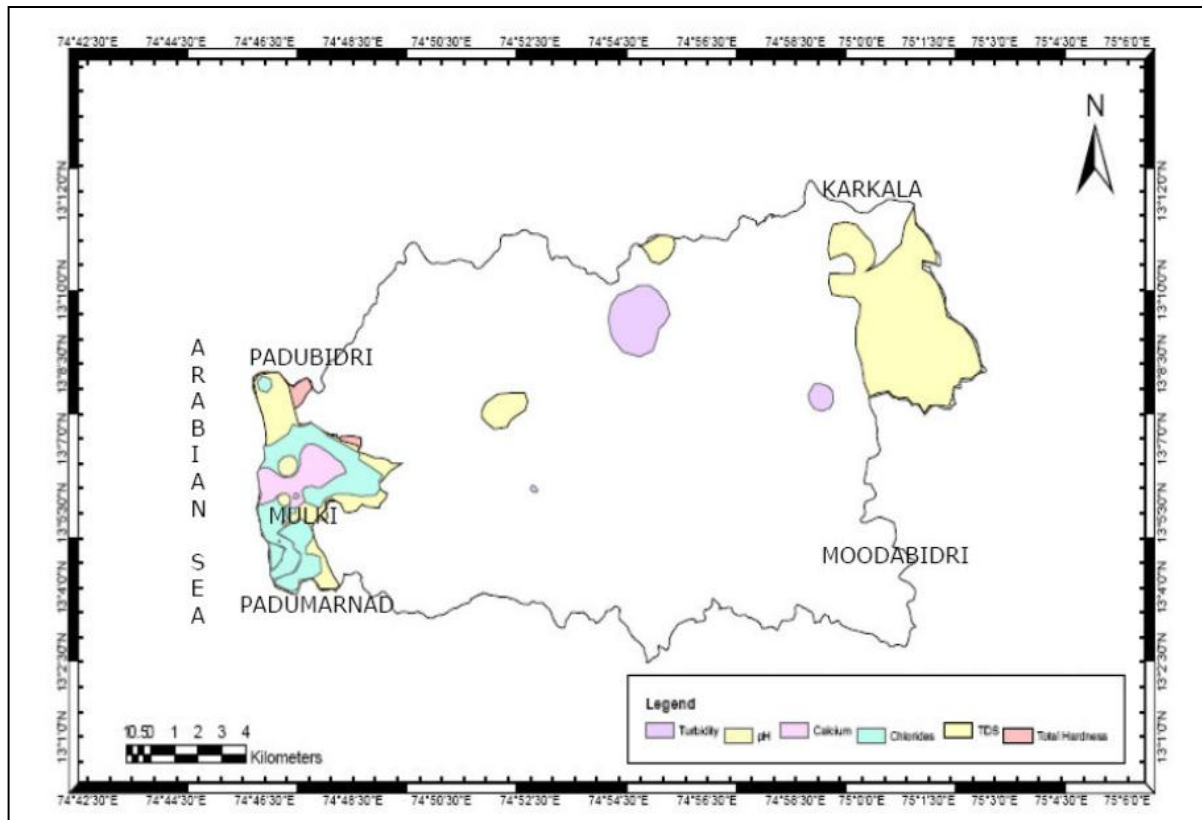


Fig.1 Spatial variation of Water Quality Vulnerability in Mulki River Basin

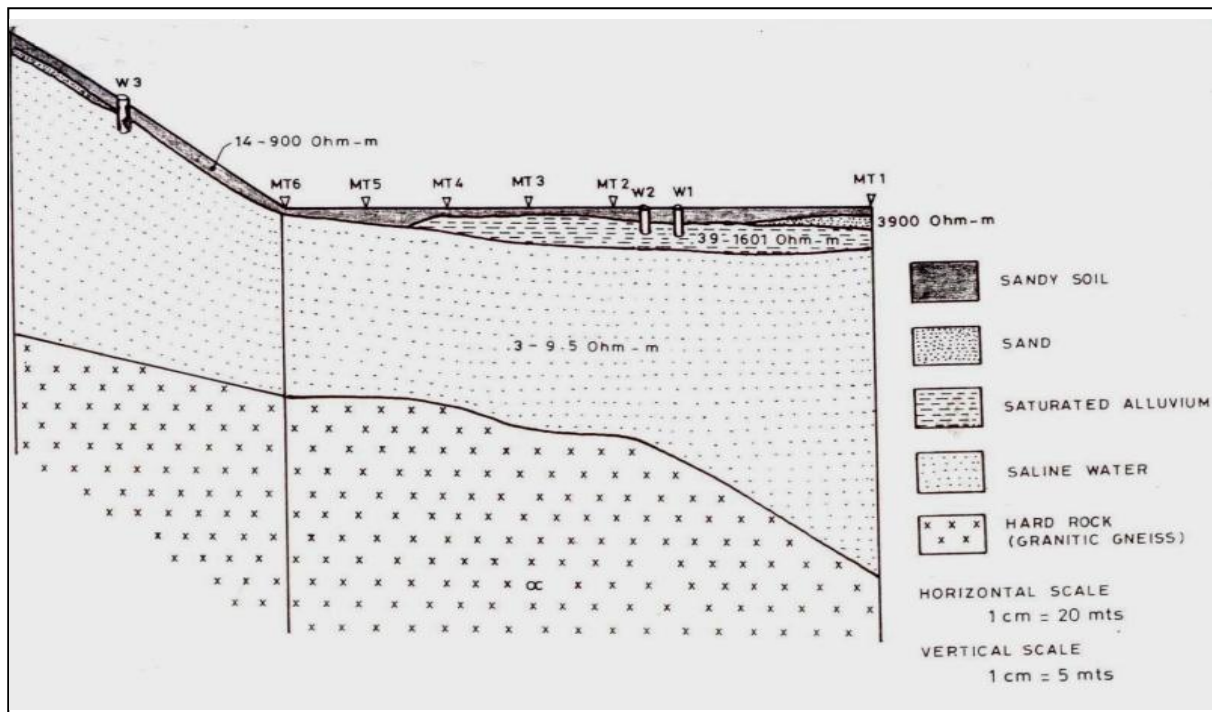


Fig.2. Geo-electric cross section showing various sub-surface litho-units at Mattu region

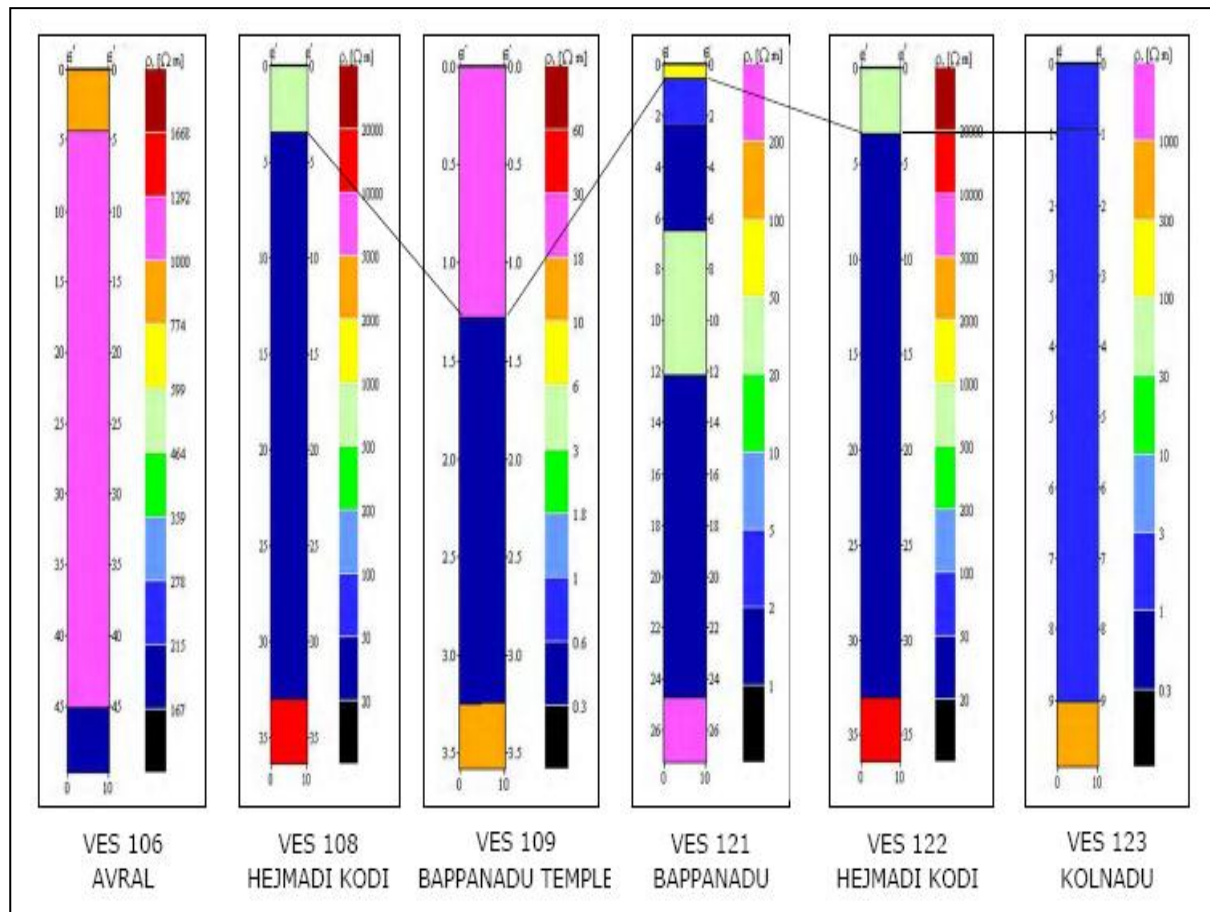


Fig.3: Showing the salinity intrusion in the resistivity cross sections along the Padubidri- Padumarnad coastal stretch of Mulki River basin

Evaluation of reference evapotranspiration methods at a sub-humid location in Karnataka state, India

Boregowda S B¹ **Lakshman Nandagiri²** and **Gicy M Kovoov³**

- 1 *Department of Civil Engineering, P E S College of Engineering, Mandya 571401, Karnataka, India. e-mail:gowdanitk@gmail.com*
 - 2 *Department of Applied Mechanics and Hydraulics, National Institute of Technology Karnataka, Surathkal, Mangalore 575025, India. email:Inand@rocketmail.com*
 - 3 *Department of Civil Engineering, Manipal Institute of Technology, Manipal 576104, Karnataka, India. e-mail:gicykovoov@yahoo.com*
-

Abstract: Reference evapotranspiration (ET_0) is a crucial variable necessary for computing crop water requirements and in irrigation planning. The Food and Agriculture Organization of the United Nations (FAO) has proposed the use of FAO-56 Penman-Monteith equation as the standard for estimating reference evapotranspiration (ET_0). The main obstacle to the widespread use of the FAO-56 Penman-Monteith (PM) equation is that the required climate data may not be available at most stations. In such circumstances, one may have to choose from a variety of other ET_0 estimation equations with simpler data requirements. The present study was taken up with an objective of evaluating the performances of several ET_0 equations relative to the PM equation at a sub-humid location in India. Among the ET_0 methods evaluated, the temperature-based FAO-24 Blaney-Criddle method provided the most comparable results to the more complex FAO-56 Penman-Monteith method.

Keywords: *Reference evapotranspiration, Penman-Monteith, Blaney-Criddle, Hargreaves, Performances, India*

Introduction

Reference Evapotranspiration (ET_0) is an important hydrological variable whose knowledge is essential for irrigation scheduling, developing efficient water management practices and water conservation. Since, direct measurement of ET_0 is costly, tedious and time consuming, the most common procedure is to estimate ET_0 from climate variables such as air temperature, solar radiation, relative humidity and wind speed. Numerous scientists and researchers worldwide have developed a large number of methods for estimating ET_0 using different climatic variables. These approaches may be classified as temperature based methods, radiation based methods, combination methods and pan evaporation methods. These methods have been subject to rigorous local calibrations by various researchers

and proved to have limited global validity. Efforts have been made by the United Nations Food and Agriculture Organization (FAO) to standardize ET_0 estimation procedures using global datasets. In the first report by Doorenbos and Pruitt (1977), four methods were proposed. But, in a subsequent report by Allen et al. (1988), the FAO-56 Penman-Monteith combination method was proposed as the sole approach for all climatic regimes. The FAO-56 Penman-Monteith method has two important advantages over many other methods. 1) It is primarily a physically based approach incorporating the effects of physiological and aerodynamic characteristics of the reference surface and 2) The method is well documented and has been tested using a variety of lysimeters. Numerous studies across the globe have proved the dominance of the FAO-56 Penman-Monteith method across a wide range of climatic conditions. Kashyap and

Panda (2001) carried out study at a sub-humid location in India and found that ET_0 estimates by FAO-56 Penman-Monteith method compared favourably with ET_0 values measured in a grass lysimeter and yielded average root mean square error (RMSE) of 0.08 mm/day, whereas the popular FAO-24 Penman method yielded an average RMSE of 0.76 mm/day.

However, the FAO-56 Penman-Monteith method requires data pertaining to air temperature, solar radiation, relative humidity and wind speed to compute ET_0 , which may not always available at a given location. The temperature and humidity data are routinely measured and solar radiation can be estimated to sufficient accuracy. But, wind speed data are rarely available, and there are no widely accepted and reliable method existing to predict the wind speed with sufficient accuracy. In such cases, simpler or empirical temperature or radiation based methods which require less input parameters are to be used to estimate ET_0 . Since, these simpler or empirical temperature based or radiation based do not incorporate some major weather parameters such as wind speed, solar radiation etc., which effects ET_0 to a greater extent, the performances of these methods need to be investigated to help the practicing engineers, researchers and decision makers to select a better alternate method for a particular climate in order to make more reliable and accurate estimates of ET_0 .

In this regard, several studies were taken up worldwide by the researchers to find best alternate method which would give results almost similar to FAO-56 Penman-Monteith method for a particular climatic condition. Hussein M. A. (2000) made a comparison of five different ET_0 methods for four regions of Saudi Arabia and found that FAO-24 Penman method yielded better estimates for Riyadh and Najran area, while Blaney-Criddle method yielded better estimates for Asir and Jizan areas. Irmak et al. (2003) have taken up such a work at Florida and evaluated 21 methods and compared the values of ET_0 estimates obtained from these methods with standard FAO-56 Penman-Monteith method, and found that the estimates

obtained from these methods were far from that obtained from FAO-56 Penman-Monteith method. Study taken up by Igbadun et al. (2006), revealed that the temperature based Hargreaves and Jensen-Haise methods, yields better estimates from September to November but, not so, for the other months of the year.

Studies carried out in India have identified the FAO-24 Penman combination method to be the most accurate one (Subramaniam and Rao (1985); Mall and Gupta (2002)). On the basis of comparisons with FAO-24 Penman ET_0 estimates, Mohan (1991) recommends the use of the FAO-24 radiation method in perhumid climates, the Hargreaves method for humid climates and the Blaney-Criddle method in semiarid and dry sub-humid climates of Tamil Nadu state, India. Kashyap and Panda (2001) have concluded that FAO-24 Penman, Turc, Blaney-Criddle, and Priestly Taylor methods yield better estimates of ET_0 in order for Kharagpur, a sub-humid region of India. Nandagiri and Kovoor (2006) have evaluated the performances of seven methods on four different climatic regions of India. Their study revealed that Hargreaves method estimated better for arid, semi arid and sub-humid region like Jodhpur, Hyderabad and Bangalore respectively, while for a humid region like Pattambi, Turc method works best.

The present study was taken with an objective to evaluate the performances of six ET_0 methods listed in Table 1 relative to the FAO-56 Penman-Monteith method for a sub-humid region, Mandya of Southern Karnataka, India and also to identify the better alternative method that yield results closest to the FAO-56 Penman-Monteith method for this climate. Further, we hope that, this study would provide relevant information to the irrigation engineers, hydrologists, agricultural scientists and the local authorities involved in water management, irrigation scheduling, water conservation, etc.

STUDY AREA AND METHODOLOGY

Mandya district of Southern Karnataka, India, is a sub humid region located

approximately 100km from capital city, Bangalore of Karnataka state. The temperature of this area varies from 16°C during winter to 34°C during summer months. Average annual rainfall is 691.2mm and is mostly confined to the period from April to November. Total area of the district is 4961 sq. km, out of which 3.11 lakh hectares are cultivated land, 0.24 lakh hectares are covered by forest area and remaining 1.63 lakh hectares are barren and uncultivable. The major crops grown in the area are rice and sugar cane. Historical daily measured data for 10 year period from 1993 to 2002 was obtained from weather station at Vishweshwaraiah Canal Farm, a branch of University of Agricultural Sciences (UAS), Bangalore, Karnataka, India and is used in the present study. The data set used in this study comprised daily values of maximum air temperature (T_{\max}), minimum air temperature (T_{\min}), maximum relative humidity (RH_{\max}), minimum relative humidity (RH_{\min}), actual hours of sunshine (n) and 24 h wind speed (u_z) measured z m above ground level. Site details required in ET_0 calculations are: altitude (z) above mean sea level, height (z_w) at which wind speed is measured and latitude (Φ) of the station.

Standard Error of Estimate (SEE) criterion, a measure of the accuracy of predictions was used to quantify the differences between ET_0 estimates by the FAO-56 Penman-Monteith method and each of the other six methods. The Standard Deviations of the estimates (STDEV) which measures the spread of the data about the mean value and coefficient of determination (R^2) the percent of the variation that can be explained by the regression equation were also computed. Statistical comparisons were made separately for daily and monthly time steps. Out of the six methods, a method which has smallest SEE, the smallest STDEV, and the highest R^2 was considered to be the best alternative to FAO-56 Penman-Monteith method.

RESULTS AND DISCUSSIONS

The mean daily ET_0 estimates for the station under consideration are shown in Table 2. The comparison of ET_0 values

estimated from FAO-56 Penman Monteith-method with those estimates obtained from other methods, show that there is an overestimation of ET_0 values by FAO-24 Penman and FAO-24 Radiation methods, while the estimates obtained from the temperature based FAO-56 Hargreaves and FAO-24 Blaney-Criddle methods respectively show a close comparison with FAO-56 Penman-Monteith estimates. A recent study carried out by Nandagiri and Kovo (2006) for a sub humid climate (Bangalore) had shown same kind of comparison. But, the performances of the other methods relative to the FAO-56 Penman-Monteith method appear to vary widely. The seasonal variability in the performances of the ET_0 methods relative to the FAO-56 Penman-Monteith estimates is clearly shown in Fig. 1. The ET_0 estimates from all the methods show same kind of variation in the respective months. ET_0 estimates are maximum during the summer months and are minimum during monsoon and winter months.

Comparisons of ET_0 estimates for individual daily records for all the methods considered for analysis are shown in Table 3. Comparison between daily ET_0 estimated by FAO-56 Penman-Monteith method and each of the other methods is made in terms of various performance statistics mentioned earlier. Based on the values of SEE, STDEV and R^2 , each of method is given with a rank. It is known that each Statistic used for the comparison emphasize a different feature of model performance. Hence, an overall rank number is calculated which is nothing but the average of rank numbers of the three statistics. This overall rank was used to identify the better alternative method. From the statistical results shown in Table 3 (figures shown in the parenthesis indicate the rank numbers of ET_0 methods for that particular performance statistic), the most popular FAO-24 Penman method yielded the highest overall rank followed by the temperature-based FAO-24 Blaney-Criddle and FAO-56 Hargreaves methods in second and third place, respectively. When the comparison is made only by considering ranking based on SEE, FAO-24 Penman method yielded the highest rank followed by the FAO-24 Blaney-Criddle and FAO-56 Hargreaves method. Even on

the basis of R^2 , FAO-24 Penman method yielded the highest rank followed by the FAO-24 Blaney-Criddle method. But, based on the STDEV statistic, the best method relative to FAO-56 Penman-Monteith values is the FAO-56 Hargreaves method. The performances of daily ET_0 estimates by FAO-24 Penman method and FAO-24 Blaney-Criddle which yielded the highest rank are graphically shown in Fig 2.

A comparison of Monthly ET_0 estimates obtained by all six methods with the estimates obtained from FAO-56 Penman-Monteith is shown in Table 4. The statistical results of monthly ET_0 estimates obtained by all six methods show same kind of performance as that of daily ET_0 statistics with FAO-24 Penman method at the first place followed by the FAO-24 Blaney-Criddle method. The performances of monthly ET_0 estimates by FAO-24 Penman method and FAO-24 Blaney-Criddle which yielded the highest rank are graphically shown in Fig. 3

CONCLUSIONS

Performances of six ET_0 methods listed in Table 1 were evaluated with respect to FAO-56 Penman-Monteith method for Mandya district of Southern Karnataka, India. Daily and monthly ET_0 values (mm/day) estimated by all the six methods were statistically compared with the standard FAO-56 Penman-Monteith method. From the results, it is clear that the FAO-24 Penman method and temperature-based FAO-24 Blaney-Criddle methods yielded ET_0 estimates comparable to FAO-56 Penman-Monteith estimates. For daily comparisons, the associated minimum SEE is 0.43 mm/d and 0.47 mm/d for FAO-24 Penman method and FAO-24 Blaney-Criddle methods respectively. For monthly comparisons, the associated minimum SEE is 0.27 mm/d and 0.36 mm/d for the well performed FAO-24 Penman method and FAO-24 Blaney-Criddle methods respectively. Since, the input data required for FAO-56 Penman-Monteith and FAO-24 Penman methods are almost similar, the study suggests that the temperature-based FAO-24 Blaney-Criddle method may be used as a better alternative to the well recommended FAO-56 Penman-Monteith

method for the estimation of ET_0 in this region.

Notation

a_b	= adjustment factor used in FAO-24 Blaney-Criddle method which depends on minimum relative humidity (RH_{min}) and ratio of actual to possible sunshine hours (n/N);
b_b	= adjustment factor used in FAO-24 Blaney-Criddle method which depends on minimum relative humidity (RH_{min}), ratio of actual to possible sunshine hours (n/N) and daytime windspeed (u_d);
b_r	= adjustment factor used in FAO-24 radiation method which depends on mean relative humidity (RH_{mean}) and day time windspeed (u_d);
C	= adjustment factor used in FAO-24 Penman equation to incorporate differences between day and night weather conditions;
ET_{bc}	= ET_0 (mm/day) by FAO-24 Blaney-Criddle method;
ET_h	= ET_0 (mm/day) by FAO-56 Hargreaves method;
ET_p	= ET_0 (mm/day) by FAO-24 Penman method;
ET_{pt}	= ET_0 (mm/day) by Priestley-Taylor method;
ET_r	= ET_0 (mm/day) by FAO-24 radiation method;
ET_t	= ET_0 (mm/day) by Turc method;
$f(u)$	= Wind function used in FAO-24 Penman method;
e_a	= actual vapor pressure (kPa);
e_s	= saturation vapor pressure (kPa);
G	= soil heat flux density [MJ/ (m ² day)];
P	= ratio of actual daily day time hours to annual mean daily day time hours (%);
R'_a	= extraterrestrial radiation at top of atmosphere (mm/day);
R_n	= net radiation at crop surface [MJ/ (m ² day)];
R'_n	= net radiation at crop surface (mm/day);
R_s	= incoming solar radiation [MJ/ (m ² day)];
RH_{mean}	= mean relative humidity (%);
\bar{T}	= mean air temperature at 2 m height (°C);
U_2	= 24 h windspeed at 2 m height (m/s);
γ	= psychrometric constant (kPa/ °C);
γ'	= psychrometric constant (mbar/ °C);
Δ	= slope of vapor pressure versus temperature curve at mean temperature (kPa/ °C);
Δ'	= slope of vapor pressure versus temperature curve at mean temperature (mbar/ °C).

REFERENCES

- [1] Allen, R. G., Pereira, L. S., Raes, D., and Smith, M. Crop evapotranspiration: Guidelines for computing crop water requirements, Irrigation and Drainage Paper No. 56, Food and Agricultural Organization of the United Nations, Rome, 1988.

International Engineering Symposium, March 3-5, 2011 Kumamoto Univ., Japan

- [2] Doorenbos, J., and Pruitt, W. O. Guidelines for predicting crop water requirements, Irrigation and Drainage Paper No. 24, Food and Agricultural Organization, Rome, 1977.
- [3] Hussein M. Al-Gobari. (2000), "Estimation of reference evapotranspiration for southern region of Saudi Arabia" Irrigation Science, 19:81-86.
- [4] Igbadun, H. E., Mahoo, H.F., Tarimo, A.K.P.R and Salim, B.A. (2006), "Performance of Two Temperature-Based Reference Evapotranspiration Models in the Mkoji Sub-Catchment in Tanzania", Agricultural Engineering International:the CIGR Ejournal, Manuscript, vol.VIII.
- [5] Irmak, S., Allen, R. G., and Whitty, E. B. (2003), "Daily grass and alfalfa-reference evapotranspiration estimates and alfalfa-to-grass evapotranspiration ratios in Florida", J. Irrig. Drain. Eng., 129(5), 360-370.
- [6] Kashyap, P. S., and Panda, R. K. (2001), "Evaluation of evapotranspiration estimation methods and development of crop-coefficients for potato crop
- in sub-humid region", Agricultural Water Management, 50, 9-25.
- [7] Mall, R. K., and Gupta, B. R. D. (2002), "Comparison of evapotranspiration models", Mausam, 53(2), 119-126.
- [8] Mohan, S. (1991), "Intercomparison of evapotranspiration estimates", Hydrological Sciences Journal, 36(5), 447-460.
- [9] Nandagiri, L., and Kovoor, G. M. (2006), "Performance Evaluation of Reference Evapotranspiration Equations across a Range of Indian Climates", Journal of Irrigation and Drainage Engineering, 132(3), 238-249.
- [10] Shuttleworth, W. J. Evaporation. Handbook of hydrology, D. R. Maidment, ed., McGraw-Hill, New York, 4.1-4.53, 1992.
- [11] Subramaniam, A. R., and Rao, A. S. (1985), "Prediction of ET of some crops under semi-arid and dry sub-humid climates of Maharashtra", Mausam, 36(1), 67-70.

Table 1 Details of ET_0 methods used in the study

Method	Basic Equation	Reference
FAO-56 Penman -Monteith (PM)	$ET_o = \frac{0.408\Delta(R_n - G) + \gamma \frac{900}{T} u_2(e_s - e_a)}{\Delta + \gamma(1 + 0.34u_2)}$	Allen et al. (1988)
FAO-24 Penman (PEN)	$ET_P = C \left[\frac{\Delta'}{\Delta' + \gamma'} \right] R'_n + \frac{\gamma'}{\Delta} f(u)(e_s - e_a)$	Doorenbos and Pruitt (1977)
FAO-24 Radiation (RAD)	$ET_r = b_r \left(\frac{\Delta'}{\Delta' + \gamma'} \right) - 0.3$	Doorenbos and Pruitt (1977)
Priestly-Taylor (PT)	$ET_{pt} = \alpha \frac{\Delta}{\Delta + \gamma} (R_n)$	Shuttleworth W. J. (1992)
Turc (TURC)	$ET_t = 0.31 \left(\frac{\bar{T}}{\bar{T} + 15} \right) (R_s + 2.09) \left(1 + \frac{50 - RH_{mean}}{70} \right)$ $ET_t = 0.31 \left(\frac{\bar{T}}{\bar{T} + 15} \right) (R_s + 2.09) \quad \text{for } RH > 50$	Shuttleworth W. J. (1992)
FAO-24 Blaney-Criddle (BC)	$ET_{bc} = a_b + b_b [p(0.46\bar{T} + 8.13)]$	Doorenbos and Pruitt (1977)
FAO-56 Hargreaves (HG)	$ET_h = 0.0023(\bar{T} + 17.8)(T_{max} - T_{min})^{0.5} * R'_a$	Allen et al. 1988)

Table 2 Mean Daily ET₀ Estimates

Station	Mean Daily ET ₀ values (mm/d)						
	Combination methods		Radiation-based methods			Temperature - based methods	
	PM	PEN	RAD	PT	TURC	BC	HG
V C Farm	4.83	5.70	5.04	4.27	4.02	4.64	4.72

Table 3 Comparison of Daily ET₀ estimates

Method	SEE	σ	R^2	Overall Rank
PEN	0.43 (1)	1.65 (6)	0.930 (1)	2.67
RAD	0.84 (6)	1.48 (5)	0.680 (3)	4.67
PT	0.67 (5)	0.97 (3)	0.520 (4)	4.00
TURC	0.66 (4)	0.90 (2)	0.469 (5)	3.66
BC	0.47 (2)	1.33 (4)	0.880 (2)	2.67
HAR	0.56 (3)	0.76 (1)	0.467 (6)	3.33

Table 4 Comparison of Monthly ET₀ estimates

Method	SEE	σ	R^2	Overall Rank
PEN	0.270 (1)	1.29 (6)	0.96 (1)	2.67
RAD	0.580 (6)	1.08 (5)	0.72 (3)	4.67
PT	0.443 (4)	0.72 (3)	0.63 (5)	4.00
TURC	0.444 (5)	0.63 (1)	0.51 (6)	4.00
BC	0.360 (2)	1.01 (4)	0.88 (2)	2.67
HAR	0.370 (3)	0.64 (2)	0.66 (4)	3.00

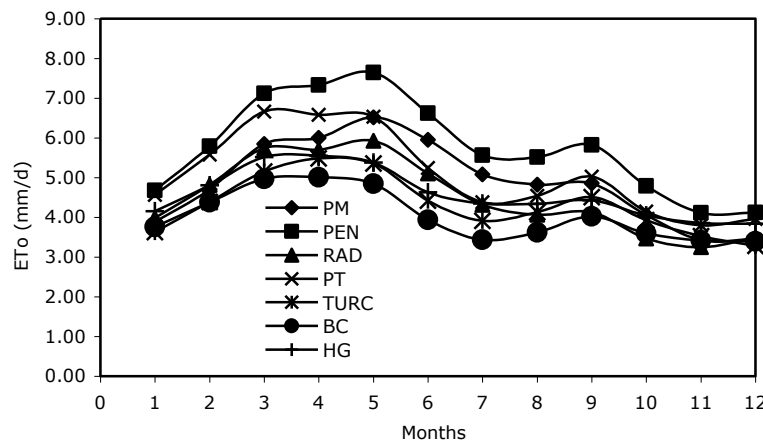


Fig. 1 Seasonal variability of ET₀

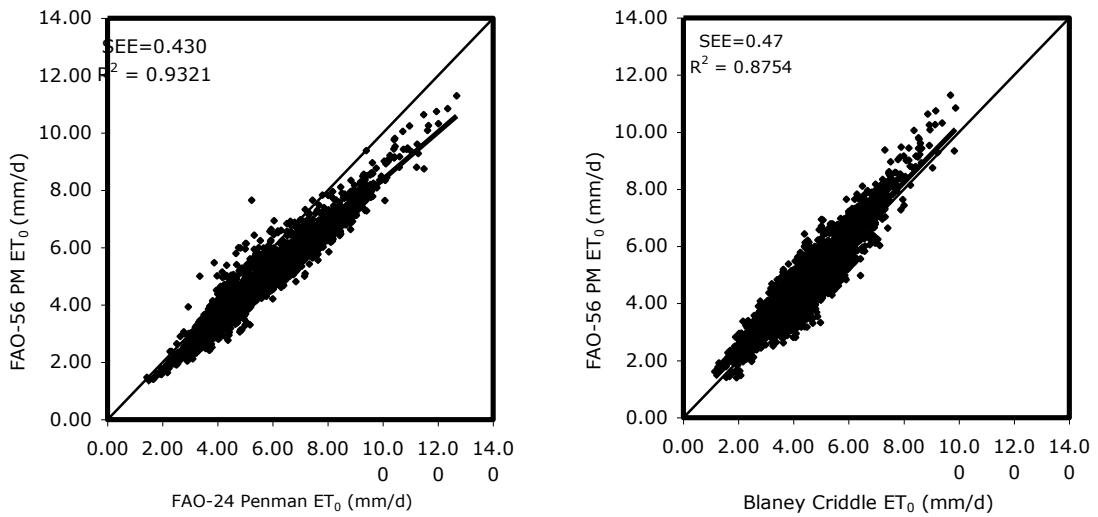


Fig. 2 Performances of Daily ET₀ estimates

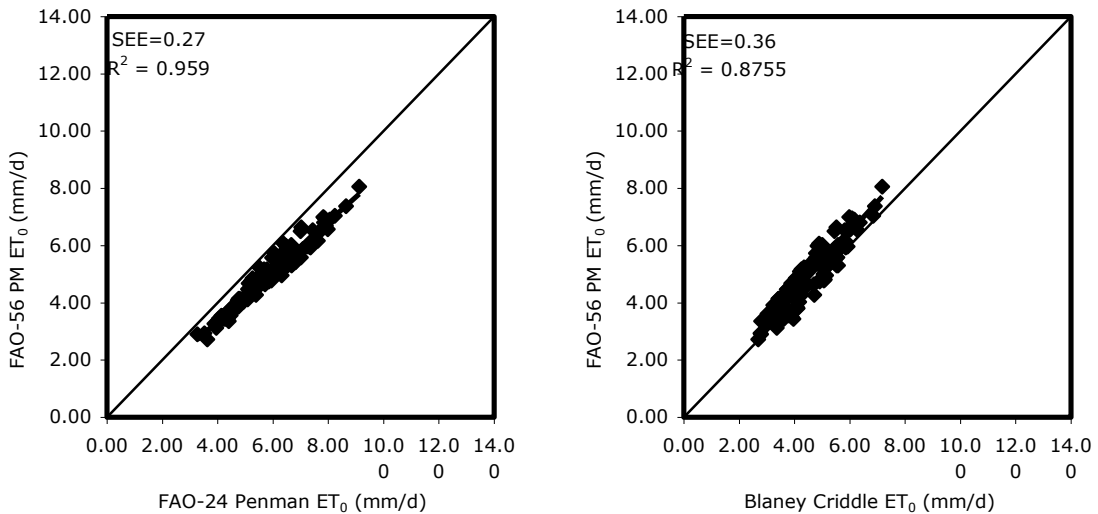


Fig. 3 Performances of Monthly ET₀ estimates

Development of digital terrain modelling using CARTOSAT-1 satellite imagery (A case study of Manipal City of Udupi District, Karnataka State)

K. N. LOKESH¹, B.NAVEENCHANDRA ², USHA³ and H.GANGADHARA BHAT⁴

¹ Department of Civil Engineering, National Institute of Technology Karnataka, Surathkal, Mangalore 575025, India. e-mail: lokesh@nitk.ac.in

² Department of Civil Engineering, National Institute of Technology Karnataka, Surathkal, Mangalore 575025, India. e-mail:naveensde@gmail.com

³ Govt.P.U.College for Girls, Udupi, Karnataka, India, e-mail:unchandra@yahoo.co.in

⁴Department of Marine Geology, Mangalore University, Karnataka, India
e-mail : gangadharab@yahoo.com

Abstract: The maps are the most important aspects of geospatial distribution of Earth's surface features both natural and man-made. Remote sensing data provides accurate maps when used in GIS environment and provides excellent tool for the planner. Today's commercial high-resolution satellite imagery (HRSI) offers the potential to extract useful and accurate spatial information for a wide variety of mapping and GIS applications. CARTOSAT-1 is among the first dedicated satellite mission for acquiring high-resolution stereo images with a capability for global coverage. CARTOSAT-1 provides the along track stereoscopic coverage at 2.5 m resolution globally. One of the most significant applications of CARTOSAT-1 is to generate digital terrain model (DTM). The study area is located in and around Manipal, Udupi District of Karnataka state. The area is 70 km away from Mangalore and lies in between $74^{\circ} 15'$ and $74^{\circ} 30'$ Eastern longitudes and $13^{\circ} 30'$ and $13^{\circ} 45'$ Northern latitudes. The use of 3D cartographic data has become very important for many applications related to urban areas like telecommunication, urban planning, estate agencies, transport, tourism, hydrology, flooding risk, etc. There is an increasing need for accurate, realistic and affordable 3D digital data over cities. In particular, the availability of urban DTM and DSM (Digital Surface Models) is a major concern for most users.

Keywords: Geographical Information System (GIS), DTM (Digital Terrain Model), Digital Surface Model (DSM), High-Resolution Satellite Imagery (HRSI).

Introduction

Geoinformatics encompasses a broad range of disciplines including Surveying, Remote sensing, Geographic Information System, Photogrammetry and the Global Positioning System. Remote sensing and GIS considered extremely important technologies for addressing various issues related to the earth's environment. For mapping, the geometric potential and the information content in the satellite images are important. The demand for accurate and up-to-date spatial information is increasing and its availability is becoming more important for a variety of tasks. Remotely sensed satellite data has

advantages of providing synoptic view, repetitivity and capability to study large & inaccessible areas on a regional scale. Thus it forms a vital tool in natural resources mapping and monitoring and helps to hasten the decision making process at several stages of study. GIS involves the collection, integration and storage of diversified and complete information of a region in a computer system. GPS on the other hand allows us to locate our self on the ground by means of earth's longitude-latitude system. The altitude at any point with respect to mean sea level (MSL) measured accurately with the help of GPS. The future success of economic growth policies depends upon

the infrastructure development. It is universally accepted fact that remote sensing and GIS tools play a major role in different types of infrastructure development. Most of the decision taken at various levels by different development agencies is dependant on the spatial analysis involving many other parameters. The maps are the most important aspects of spatial analysis. Remote sensing data provides accurate maps when used in GIS environment and provides excellent tool for the planner. Collective utilization of these techniques provides a complete solution for most of the natural resources management, infrastructure management and development.

A digital elevation model (DEM) is a digital representation of ground surface topography or terrain. It is also widely known as a digital terrain model (DTM). DTM and DEM describe the continuum of a surface as a finite amount of three dimensional points (x , y , z -values) in a space. A DEM can be represented as a raster (a grid of squares, also known as a height map when representing elevation) or as a triangular irregular network. These irregular spaced points are normally converted in a regular spaced grid (square grid, same spacing in x - and y -direction) by using different interpolation techniques (e.g. kriging). One xyz-triple in the DTM/DEM is therefore representing an area of the square of the grid spacing of the grid thus called grid cell. DEMs are commonly built using remote sensing techniques, but they may also be built from land surveying. Digital Surface Model (DSM) represents the MSL elevations of the reflective surfaces of trees, buildings, mobile sites and other features elevated above the "Bare Earth". A Digital Terrain Model (DTM) is the elevation model of the landscape that does not include above ground objects. On the other hand, a Digital Surface Model (DSM) includes the objects with their heights above the ground as well as the topography. Digital Elevation Model (DEM) derived from stereo images is an important component of geo-spatial data that has wide applications in urban planning, telecom mobile network design, agriculture, defense, etc. The extraction of metric information from images is possible due to suitable sensor orientation models,

which describe the relationship between two-dimensional image coordinates and three dimensional object points. ISRO remote sensing program provides a constellation of polar satellites at various resolutions to map the globe. CARTOSAT-1 provides the along track stereoscopic coverage at 2.5 m resolution globally. One of the most significant applications of CARTOSAT-1 is to generate digital elevation models. In the field of terrain and topographic mapping, the availability of 2.5 m pan stereo data from CARTOSAT-1 will help in preparation of large-scale (1:10,000) base map/topographic maps for planning purposes at micro level to cater to the vast and varied needs of remote sensing scientific community. In stereo imaging, the scene observed from different perspectives or view angles. Height information derived from the parallax between the conjugate pairs. From a LEO platform, stereo imaging achieved in two ways is as below, the scene viewed from adjacent orbits at different view angles (across-track stereo). In across-track stereo, multiple views of the scene obtained by tilting the FOV of the camera in the cross-track direction. Conjugate stereo pairs also generated when swaths of a nadir-looking camera from adjacent orbits overlap. Almost all space-borne scanners on-board LEO platforms have overlapping swath to ensure complete global coverage swath to ensure complete global coverage. However, overlap increases with latitude. Stereo pairs are available for larger areas at higher latitude. In across-track stereo, images usually obtained within a span of few days and any changes in the scene, atmospheric or illumination condition, could affect the accuracy of derived height information. The scene viewed from two positions in a single orbit (Along track stereo) the stereo multiples are obtained either by using different camera heads titled in the along-track direction or by steering the FOV of a single camera (Doyle, 1979).

Two high-resolution panchromatic cameras acquire along-track stereo images of the scene. On-board tape recorders allows it to acquire data from anywhere on the globe. The mission has a revisit capability of 5 days. The highly agile but stable platform

International Engineering Symposium, March 3-5, 2011, Kumamoto Univ., Japan

of CARTOSAT-1 allows it to operate in many modes, obtaining stereo pairs of different B/H ratio, corrected for Earth rotation effect. The stereo imaging payload of CARTOSAT-1 mission consists of two identical cameras; PAN-Fore and PAN-Aft. PAN-Fore is tilted in the along-track direction by +26deg whereas Aft camera is titled by 5 deg. Nominal resolution of cameras is 2.5m and swath coverage is 30km. Both cameras operate in a single panchromatic band (0.5-0.75μm.) covering a dynamic range of 100% at 10-bit radiometric resolution. The video data generated at a rate of about 338 Mbps/camera which is compressed, encrypted; RS encoded and sent to ground stations through two X-bands QPSK carriers. CARTOSAT-1 is among the first dedicated satellite mission for acquiring high-resolution stereo images with a capability for global coverage.

Objectives of the study

- 1) To develop the base map generation, Digital elevation model, ortho imagery of the study area using stereo satellite imagery using Geo-Information technology.
- 2) To prepare the large-scale (1:10,000) thematic maps for planning purposes at micro level to cater to the vast and varied needs of remote sensing scientific community.

The Study Area

The area is 70km away from Mangalore and lies in between $74^{\circ} 15'$ and $74^{\circ} 30'$ Eastern longitudes and $13^{\circ} 30'$ and $13^{\circ} 45'$ Northern latitudes. Manipal is a university town situated in the state of Karnataka in India was chosen for study area (Fig.1). It is a suburb within Udupi city and is administered by Udupi City Municipality. It is located in the rocky hinterland of the Malabar Coast of southwest India, about 8km from the Arabian Sea. From its location on a plateau, it commands a view of the Arabian Sea to the west and the Western Ghats range to the east. It is situated 3 kilometres from the temple city of Udupi, and is 65km north of Mangalore. Manipal was previously under Shivalli village panchayat. It is a center of academic learning, healthcare, industry and finance. Between June and August, it is heavy

monsoon season, with precipitation ranging from 50-80cm. March to May, the temperature peaks at 35°C. At other times, the weather is tropical, approximating 27°C

Materials used

High-resolution panchromatic data (PAN) of the Indian Remote Sensing satellite CARTOSAT-1 was used for this study. CARTOSAT-1 provides the along track stereoscopic coverage at 2.5m resolution globally. One of the most significant applications of CARTOSAT-1 is to generate digital elevation model (DEM). The PAN sensor was primarily chosen for its stereo capability. The stereo pair data of Udupi-Manipal of 24th November 2008 was acquired and selected due to good overlap and a fairly good base to height ratio of 0.68. The data was used to generate the 3D base map and DEM of the study area. RFCs of each image were supplied by NRSA. The GCPs (ground control points) were surveyed using Trimble R3 DGPS during November 2008 as shown in Table1&2.

The research work for DEM generation and stereo processing is created in Lieca Photogrammetry Suite (LPS) S/W where the CARTOSAT-1 stereo images were imported. The interior orientation has been computed for both fore and aft camera images (Band A & Band F) using RPC 8 GCPs have been identified on both the images for Exterior orientation computation of 5 sq.km area of Manipal city as shown in Fig.2. The GIS analysis and manipulations was carried out using SuperGIS desktop and its extensions like spatial and 3D analyst.

Results and Discussions

Remote sensing (RS) data is being extensively used for natural resources mapping, management, monitoring and developmental planning. The geometric accuracy of the satellite output plays a major role in generating precise thematic maps. Conventionally, the satellite data is geo-referenced using ground control points acquired from topographical maps. The administrative boundaries and the base map information also captured from topographical maps. With the present-day availability of high-resolution satellite data,

the corresponding large-scale reference maps are not available for geo-referencing of the satellite data and capturing collateral information. Apart from this, the recent changes in the infrastructure etc., on the land not reflected in the topographical maps. In addition to this, the 'map restriction' policy limits the utilization of spatial information generated on Everest datum using the present-day advanced technological tools. This has necessitated search for alternate ways for base map generation. The satellite data, available with high spatial resolution, possess high geometric fidelity and form the basic source for extracting relevant basic features in stand-alone mode. However, the locational accuracy of this satellite information needs of mapping. The global Positioning System (GPS) provides the well-equipped user accurate coordinates, on WGS-84 datum, at any point on the earth surface, at any time, in any weather conditions. The GPS data, processed in differential mode, can be used for enhancing the locational accuracy of the satellite data. The product thus generated effectively utilized for cartographic mapping and thematic mapping. The Generation of base map using stereo images and its applications are mentioned parawise below.

DGPS Survey

The image coordinates of the GCP points measured manually (Table 1) as shown in CARTOSAT-1 imagery map of the study area (Fig.2). Ground coordinates of the measured points calculated using the RFCs supplied with the data. After registering both sets of ground coordinates within the same reference system, WGS 84, Zone 43 N, differences between the RFC-derived coordinates of the control points and their GPS surveyed coordinates were calculated in UTM format (Table 2). Characteristics of the different control points, where well-designed GPS measurements has been taken and the dimension of the point should be compatible with the resolution of the satellite data used and the precision of the GPS receivers. As the GPS will provide sub-meter accuracy in differential mode, the definition of the point on the ground as well as on the satellite image should be in tune with the GPS accuracy. The primary

characteristics of the GCP are precise boundary, good contrast on the image, identifiable by road, durability of the point etc. In view of these characteristics, the intersection of roads, railway crossings etc. selected as GCP's in the working area. DGPS survey has been conducted at various locations of study area and its field photo taken as shown in Fig.3 and Fig.4. The base point is chosen at syndicate circle of Manipal city as it is having highest measured elevation point. Single-frequency geodetic GPS receivers used for acquiring geographic coordinates. Three receivers operated at the master Reference Stations. The second receiver used as reference station, established for densifying the network at local area. The third receiver used for acquiring the GPS observations at the Ground Control Point. At Master Reference Station and at reference Station, continuous observations carried out from 6 AM to 6 PM. At each GCP, approximately 2 to 3 hours of observations acquired. The specifications that adopted for the GPS observations are:
Mode of operation: Differential GPS
Method adopted: Static
Observation interval: 15 seconds
Observation duration: 2-3 hours
Cut-off angle: 15 deg.
Health condition: Auto
Sampling mode: Compacted

Total 9 numbers of GCPs identified on both the images for Exterior orientation computation.

DEM and Base map generation

Manual stereo mode interpretation and on-screen 3D vector digitization for each earth features and methodologies developed for 3D feature capture from high-resolution images. For example, all the buildings captured in building layer and all the roads captured in road layer. All the image processing, GIS and CAD software packages provide the functions required for feature capturing from monocular images. Captured data layers properly checked for node, line and polygon errors like dangle nodes, undershoot, overshoot and unclosed polygons. The final feature captured data in Autocad-3D vector format imported to GIS 3D-Analyst environment for further analysis. The basic features like road network, drainage network,

settlement area, building sites, water bodies, and Mobile tower sites and forest area are extracted from the satellite data and GIS vector map generated as shown in Fig.5 in 1:10000 scale. Image matching performed between the fore and aft images. A total number of 6326 match points called as Tie points generated at more than 0.80 correlation coefficients. Triangulation performed with RPC at second order polynomial refinement. Creation of DEM from stereo data requires 3D points along profiles, break line and spot height. The regular DEM generated at 5m grid interval. Fig.6 shows the DEM created in free space, thematic map on elevation and wire frame methods respectively.

Building extraction from remote sensing images has been an important research topic for the last decades. In this study, a method developed for automatic building and mobile site extraction from high-resolution space images using the spectral reflectance values, DEM generated from stereo images, and the feature extraction techniques. It appears that the use of aerial/space images or a DEM alone may not be sufficient for automatic extraction of the buildings. First, the spectral information and the DEM generated from stereo images used to discriminate the buildings from other objects. Then, the boundaries of the buildings are delineated using building extraction techniques. The approach consists mainly of three steps for extracting the buildings from high-resolution satellite images, pre-processing, building detection, and building delineation. Manual stereo mode interpretation and on-screen 3D feature digitization methodologies developed for 3D feature capture from high-resolution images.

The DEM provides a so-called bare-earth model, devoid of landscape features. While a DSM may be useful for landscape modeling, city modeling and visualization applications, a DEM is often required for flood or drainage modeling, land-use studies, geological applications, and much more. Topography is an important land-surface characteristic that affects most aspects of the water balance in a catchment, including the generation of surface and sub-surface runoff; the flow paths followed by water as it moves down

and through hill slopes and the rate of water movement. All of the spatially explicit fully distributed hydraulic and hydrological models use topography (represented by the DEM of the area modelled) to derive bathymetry. DEM is also used to derive some other key information critical in fully distributed hydraulic and hydrological models.

In Geographic Information System environment, viewshed analysis is the result of a function that determines, given a terrain model, which areas on a map can be seen from a given point(s), line or area. In the communications industry, this function has been used to model radio wave coverage and to site transceiver towers for cellular phones (Naveenchandra et al, 2010).

For wireless telecommunications providers, a GIS viewshed analysis has great potential to help plan network extensions by siting transmitter towers. A viewshed is the result of a function that determines which areas of a map can be seen from a given point, line, or area. Wireless telecoms provide telecommunications access by using portions of the radio spectrum to transmit data. If the wavelength used is a Line-Of-Sight frequency, then a viewshed should show the regions that can receive a signal from a potential tower site. So, given the LOS properties of the wavelength, a viewshed would show the zones able to receive data, called a communications viewshed or 'commshed'. From that information, further viewshed analyses would aid in creating a chain of towers to cover a desired region. Next, building height data was recorded for the whole study area and about 3200 building sites are extracted from satellite data as shown in Fig.7. Out of these data only sample of 40 building heights are shown (Table 3). The building heights were added as a new column in the building layer of the GIS.

Horizontal accuracy of raw image as supplied by NRSA is 500m. After georectification, using DGPS control points an accuracy of 5m has achieved. The vertical accuracy of the rectified image is 4m. The projection, Spheroid and Datum defined for the base map as Transverse Mercator, EGM 96 (Global) and World Geodetic 84, Zone 43 N respectively. The

International Engineering Symposium, March 3-5, 2011, Kumamoto Univ., Japan

earth features extracted in 3D base map generated verified with Google server (Fig.8). The thematic 3D-base map generated (Fig.9) showing GIS vector layers like road network. Mobile sites, buildings with different elevations, drainage, railway line, vegetation etc extracted in level as per NRSA specification prepared for geospatial analysis.

Conclusions

CARTOSAT-1 provides the along track stereoscopic coverage at 2.5 m resolution globally. One of the most significant applications of CARTOSAT-1 is to generate digital elevation models. In the field of terrain and topographic mapping, the availability of 2.5 m pan stereo data from CARTOSAT-1 will help in preparation of large-scale (1:10,000) base map/topographic maps for planning purposes at micro level to cater to the vast and varied needs of remote sensing scientific community. Digital Terrain Modelling derived from stereo images is an important component of geo-spatial data that has wide applications in urban planning, Telecom mobile network design, agriculture, defense, etc.

Acknowledgements

The authors thank Mr. Super Wang, CEO, Mr. Jason, Intl marketing Manager of SuperGeo Technologies Inc. Taiwan; Chandrahasa Shetty, Managing Trustee of Bhoomi Foundation of Geoinformatics and Natural resources Management, for their valuable support for this work.

References

- [1] Alharthy, A. and Bethel, J. (2002). "Heuristic filtering and 3d feature extraction from LIDAR data." *ISPRS, The International Achieves of the Photogrammetry, Remote Sensing and Spatial Information Sciences*, Vol. XXXIV, 25-36.
- [2] Doyle, F. (1979). "A Large format camera for Shuttle." *Photogrammetric Engineering and Remote Sensing*, 45, 73-78.
- [3] Forshaw, M.R.B., Haskell, A Miller, P.F., Stanley, D.J., and Townshend J.R.G. (1983). "Spatial Resolution of Satellite Imagery." A Review paper, *International Journal of Remote Sensing*, 497-520.
- [4] Fraser, C., Baltsavias, E., and Grün, A. (2002). "Processing of Ikonos imagery for submetre 3D positioning and building extraction." *ISPRS, J. Photogr. Remote Sens*, 56(3), 177-194.
- [5] Huertas, A. and Nevatia, R. (1988). "Detecting buildings in aerial images. Computer Vision, Graphics, and Image Processing." Vol.41, 131-152.
- [6] Jin, X. and Davis, C. H., (2005). "Automated building extraction from high resolution satellite imagery in urban areas using structural, contextual, and spectral information". *EURASIP, Journal on Applied Signal Processing*, 14, 2196-2206.
- [7] Kalyanaraman, K. (2005). "Large scale mapping using high resolution satellite images." *ISG news letter*, Spl.Vol Kiran Kumar A.S. and Kurian
- [8] Krishna, G., Kannan, B., Iyer, V. and Srivatsav, P.K. (2000). "Generation of DEM and Terrain Corrected Products for IRS-1C/1D Data". *In Proceedings of the Tenth User Interaction Workshop*, Hyderabad, India, (Balanagar, India: NRSA), 22-27
- [9] Lee, S., Shan, J. and Bethel, J. S. (2003). "Class-guided building extraction from IKONOS imagery." *Photogrammetric Engineering & Remote Sensing*, Vol. 69, No.2, 143-150.
- [10] Lin, C. and Nevatia, R. 1998. "Building detection and description from a single intensity image." *Computer Vision and Image Understanding*, Vol.72, No.2, 101-121.
- [11] Mathew, (2005). "CARTOSAT-1: A new dimension to Satellite Remote. 11, No. 2 & 3, 12-17. sensing." *ISG news letter* Spl.Vol. 11, No. 2 & 3, 12-17.
- [12] Naveenchandra.B, K.N.Lokesh, Usha, and H. Gangadhara Bhat, (2009). "Integration of stereo products and spatial data for telecom planning in and around Udupi, Karnataka." *Proceedings of 13th International conference on Geospatial Information Technology and applications*, Map India, 2010. 69-79p.
- [13] Niederost, M. (2000). "Reliable reconstruction of buildings for digital map revision." *IAPRS*, Vol. XXXIII, Amsterdam, 66-76
- [14] Shan, J. and Lee, S. (2002). "Generalization of building polygons extracted from IKONOS imagery. Symposium on Geospatial Theory, Processing and Applications." Working Group IV/3, Ottowa. 136p.
- [15] Shan, J. and Lee, S. (2005). "Quality of building extraction from IKONOS imagery." *Journal of Surveying Engineering*, Vol.131, No.1, 27-32.

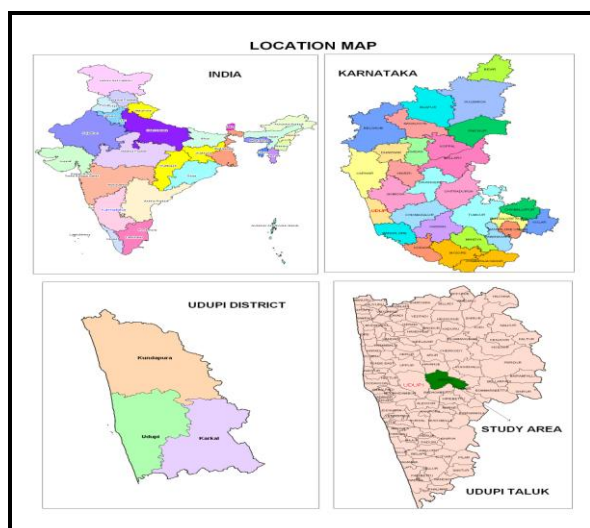


Fig.1 Location Map of Study Area

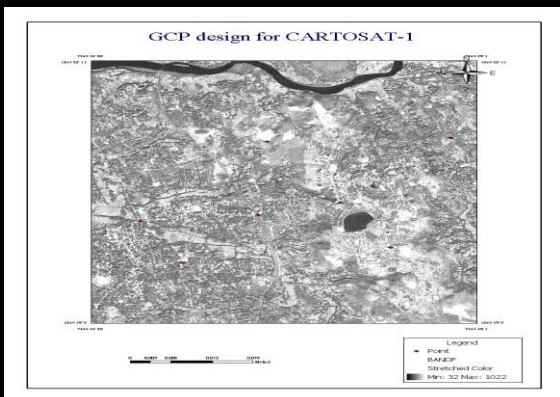


Fig.2 GCP design using imagery of study area

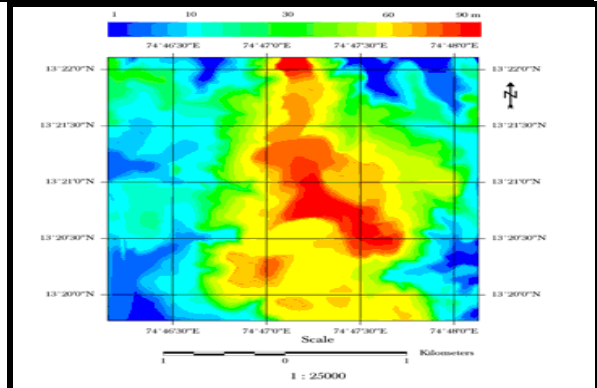


Fig.6 DEM of Manipal City



Fig.3 GCP No:1 at Kalsanka junction Base-Point

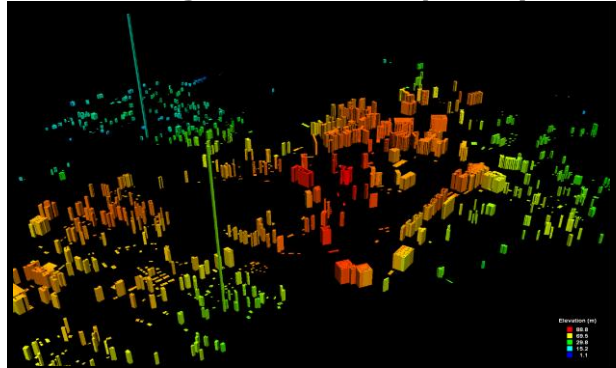


Fig.7 Digital Terrain Modelling of Manipal city as per height factor



Fig.4 GCP No:9 at Kalsanka junction Base-Point



Fig.8 shows buildings sites overlaid with Google server with 1m contours

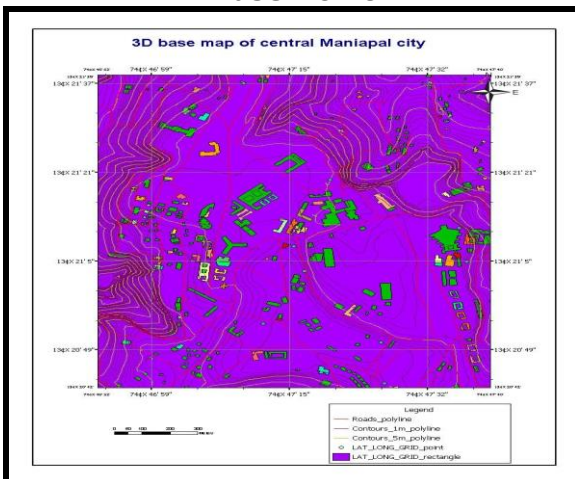


Fig.5 showing GIS vector layers

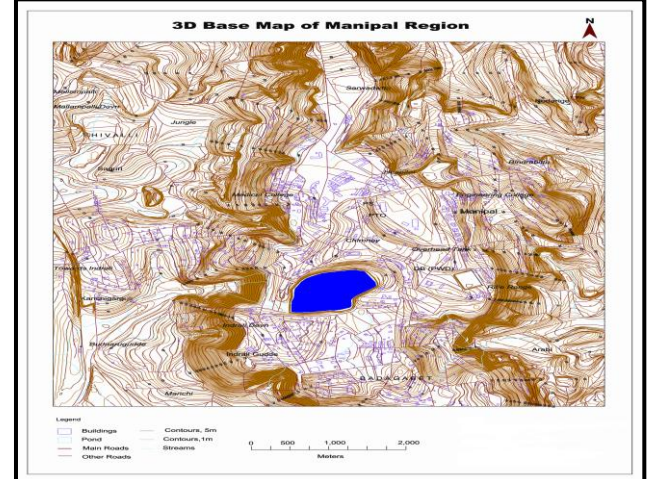


Fig.9 Shows 3D base map of Manipal city with 1m, 5m and buildings etc

Table 1 Selected GCP's in lat/long

Point name	Location Land Mark	Latitude (GCS WGS 84)	Longitude (GCS WGS 84)	Height
GCP_1	Kalsanka Bridge Udupi	13.34556967	74.75179261	2
GCP_2	Ambagilu Junction	13.36912768	74.74736528	20.741
GCP_3	Badagabettu Junction	13.34667689	74.8109981	42.193
GCP_4	Chitpady junction	13.3349548	74.75638947	15.766
GCP_5	Sagri Junction	13.362894	74.77559811	24.604
GCP_6	RajeevaNagar Junction	13.33581761	74.78957011	79.014
GCP_7	Saralabettu Junction	13.36095538	74.79229576	41.565
GCP_8	Syndicate Circle(BasePoint)	13.34750285	74.78428075	79.075
GCP_9	Indrali Railway Track	13.34548998	74.77044982	23.546

Table 2 Measured GCP's in UTM

Point name	DGPS Ground _UTM	DGPS Ground_Y_UTM	DGPS Height_Z_UTM
GCP_1	473121.35754763	1475367.05020427	1.8990377
GCP_2	472645.44186783	1477971.29611901	21.04293799
GCP_3	479532.58785335	1475482.41692165	42.40454937
GCP_4	473618.27120884	1474188.42224773	16.13770151
GCP_5	475700.24673431	1477276.99141723	25.30774263
GCP_6	477212.38731194	1474281.61880960	77.69170056
GCP_7	477509.26252421	1477061.57211140	42.25634313
GCP_8	476638.73710527	1475576.49126227	77.79872634
GCP_9	475141.48369333	1475355.01427576	24.57779708

Table 3 showing the building heights generated using CARTOSAT-1 stereo Imagery

Name of Building	Height in meter	Name of Building	Height in meter
MANIPAL PRESS	21.27	MANDOVI PARADISE	23.92
MIT	9.75	MANDOVI PEARL CITY	15.09
MIC	13.4	KEERTHI SAMRAT	17.18
UDAYAVANI OFFICE	20.7	VALLEY VIEW	16.36
MESCOM	14.56	KMC	11.92
BSNL EXCHANGE	15.47	BIG BOSS HOTEL	15.7
MAHE UNIVERSITY	4.3	HOSTEL BLOCK-1	11.9
SHARADA HOSTEL	15.89	MIT HOSTEL	11.61
INDIRA HOSTEL	18.91	POLICE QUARTERS	19.91
PLANETORIUM	11.57	VENUGOPAL TEMPLE	33.59
SYNIMATE BANK H.O.	14.86	HOTEL BALIGA	11.27
TMA PAI FOUNDATION	13.72	TAPMI OLD BLDG	20.41
VALLEY FLAT	13.4	FOOD COURT	4.09
BLUE DART	13.79	NEHRU HOSTEL	4.09
HOTEL DASHARATH	5.59	LIBRARY	4.09
LAKE VIEW	25.82	POST OFFICE	12.42
SIBM	23.9	POLICE STATION	18.78
MANIPAL MEDIA	14.85	SHAMBHAVI EMPIRE	37.39

Computing of Udyavara fluvial systems-a river of Western Ghats, India: A pragmatic inference of runoff to hydrological cycle

B S Maddodi¹, H N Udaya Shankara¹ and B R Raghavan²

1 Dept. of Civil Engineering, Manipal Institute of Technology, Manipal University, India. *bs.maddodi@manipal.edu, udaya.shankar@manipal.edu*

2 Geoinformatics, Dept. of Marine Geology, Mangalore University, Mangalagangotri, Mangalore, India. *ragvon@yahoo.com*

Abstract: Surface runoff is the water flow which occurs when soil is infiltrated to full capability; it is also the excess water, from rain, snowmelt, or other sources which contribute for the runoff. It is an essential constituent of the Hydrological Cycle. In peninsular India, Western Ghats is a major geomorphologic feature which divides the water between west and east flowing rivers. The Udyavara Drainage is the river which originates on the footstep of Western Ghats and flows down the steep scarp on the west and discharges water and sediment into the Arabian Sea. In this investigation secondary data of four major riverstreams (see Table 1 for data and Source of data) have been used for empirical quantifications of runoff. The paper focuses on the computing of Udyavara drainage basin, which is a realistic estimation of runoff contribution to the hydrological cycle of Udupi Dist, South west Coast of India. The runoff has been quantified using Lacey's formula (Reghuhath, 1996). The factor such as average rainfall, monsoon duration factor, catchment characteristic factor and temperature are used to enumerate the runoff. Studies have shown anomalously high **Gradient Index** value of Western Ghats. ($GI=1188.00$) by Raghavan and Sreedhar Murthy (1991). In case of Udyavara River the stream is typical of a low coastal plain stream with Low GI Value which has a direct impact on Ground Water and Hydrological Cycle of Udupi District Southwest Coast India

Keywords: Surface Runoff, Hydrological Cycle, Rainfall, Catchment, Drainage Basin

Introduction: The Udyavara river basin is located in Udupi District of Karnataka State India (Fig. 1). It is a tropical coastal river basin with Arabian Sea to the west, Western Ghats to the east and couple of Inselbergs to the central and east. The location of the basin is unique because of its diverse physiography of flat coastal plain, intervening Inselbergs, lateritic plateaus and mounds with river system originating from footstep of Western Ghats. The variations in landscapes were explained mainly on the basis of structure, process & stage and the role of climate was recorded less prominence. An emphasis was on 'Normalcy on particular climate' an expression of environmental passivism (Gardiner 1974). Later when

different branches of geomorphology like fluvial, glacial, tropical etc., developed, climate was discerned as an important variable in the genesis and evolution of landforms.

Position and coverage of the Basin: The area investigated is accounted for in the survey of India Maps, 48 K/11, 12, 15, 16, 48 0/4. The basin spans an area of four hundred and twenty two sq. km. The perimeter of the basin is defined by the Tunga Basin, (Mysore Plateau) to the east, Arabian Sea to the West, Sita-Swarna basin to the North and the Mulki Hole to the South. The area is accessible by the National Highway No. 17 (Mumbai-Cochin) from Mangalore and also accessible to the Konkan railway. Fig-1.

Geology of the area: As the work concerns dynamics of a riverine environment with special emphasis only on the geomorphic relations, geology of the study area has been emphasised with secondary data. The Udyavara Basin constitutes as part of the peninsular India shield. Its geological make up typifies that of the migmatised ancient gneissic complex and the south Kanara granitic suite form the basement to the greenstone belts on the western seaboard of Karnataka, (Balasubrahmanyam, 1978) forms a part of the Western Ghats Belt (Ramakrishna and HarinadhaBabu, 1981). It depicts a similarity to the southern part of the Shimoga basin (Radhakrishna, 1983) and finds itself within the geologic and tectonic framework of the western-sub-block of the Precambrian shield of southern India (Drury et.al.,). The most distinguishing characteristic of the study area is the presence of the Kanara Batholiths in the central and eastern parts of the basin. The age of the gneissic complex was suggested to have a minimum K-Ar age of 3200 Ma (Balasubrahmanyam, 1978). The laterites are of Tertiary age (Raghavan, 1988) and the modern beach and Riverine sediments accounts for the recent deposits. (Fig-2)

Physiography of the Basin: The hinterland is located in the eastern part of Udyavara river basin tract. The laterites with varying thickness form a part of the Manipal Plateau. The area also is found of Mounds, Ridges, Valleys and Inselbergs. The granitoids which occur in abundance in this tract form low mounds and ridges standing above the laterites of the coastal tracts. The terrain is moderately dissociated as indicated by entrenched valleys. The Udyavara Basin lies between N20° and S20° latitudinal zone and thus enjoys a tropical wet-dry climate. The basin is marked by heavy rainfall, high humidity and small variation in temperature. In contrast the Mysore Plateau is characterised by less rainfall, less humidity and marked variation in temperature at different seasons. The Physiography of the basin from coast and beyond to the Western Ghats profoundly influences the climate particularly the distribution of rainfall. The Western Ghats scarp and ridges further east act as a

climate divide between the coastal tract in the west and plateau region above the Ghats in the east.

Methodology & Data Interpretation:

Temperature: Panambur and Bajpe are selected to record Temperature, Humidity, Wind and Evaporation. The Bajpe station is located about 8 km away from the shore. There are few rain gauge stations in and around Udyavara basin. The basic data have been obtained from the District Statistical Office, Mangalore. The temperature record of eight years (Table-1) collected from Panambur and Bajpe stations show that the basin experiences comparatively low variations in temperature. March, April and May are the hottest month of the year with an average temperature ranging from 32.73OC to 23.56OC. The day temperature is recorded around 30°C. The day temperature will be around 20°C during the month of July, August and September. December and January are almost Low night Temperature months. The temperature of the study area decreases with the onset of the south west monsoon. The annual mean maximum temperature is around 30°C. Table-1: Mean Temperature (°C) (1975-1982)

Humidity: The weather is highly Humid throughout the basin. The Humidity data available for six years (Table-2) were collected from Ullal Station. The relative humidity is very high in the month of June, July, August and September because of heavy precipitation, low temperature and less evaporation. The relative humidity is maximum in the month of July(90.15%). The relative humidity is less in the month of January. The available evaporation data for a period of 6 years (1978-83) are collected from Ullal meteorological station (Table-2).

Evaporation: The evaporation rate varies from 0.182cm (July) to 0.350cm (April). The rate of evaporation is very low (0.182 to 0.185 cm) during the peak of monsoon (July and August) and steadily increases from the month of October (0.195 cm) to May (0.350 cm). The fluctuation of evaporation rate in monsoon month (June to September) is because of pulsatory nature of monsoon.

Precipitation: Precipitation occurs chiefly as rainfall. Six Rain gauge stations are found around the basin which possesses the best available recorded rainfall data. The rainfall data for a period of 23 years (1972 – 1995) are collected and the mean annual data for each station are furnished in Table-3. Rainfall is the most important exogenic process in shaping the landforms. The alignment of the hills, ridges and scarps with respect to prevailing winds and their elevation profoundly influences the distribution of rainfall along the west coast. On the western margin of India, heavy rainfall occurs along the scarp of the Western Ghats. On the windward side of the Ghats, the annual rainfall is as high as 600 to 700 cm, but within about 80 km to the leeward's side profoundly decreases to about 59 to 60 cm. The continuous steep face of the Western Ghats between Mangalore and Mumbai is more effective in causing precipitation than the high plateaus of the south. The coastal tract of Karnataka has a good network of rain gauge stations. The rainfall data for 50 year (1900 – 1950) suggest an average of 123 rainy days per year and an average annual rainfall of 340 to 440 cm. About 80% of the annual rainfall is recorded during the south-west monsoon season (June to Mid-September). Mean 23 years annual Rainfall is recorded and analysed (Table-3).

Runoff Calculation: It is also noted that precipitation (Rainfall) in the winter was primarily stable and of low concentration, hence lower proportion of run-off is normal, whereas during the monsoon period the intense storm is a reason for higher proportion of run-off. For this reason the monsoon period was the first to be studied, as soon as the data for river flow and rainfall in two monsoon seasons had not been collected. However the runoff calculation of Udyavara basin is from secondary data obtained from different seasonal runoff calculations done by Chandrashekappa K. N. (1989); Raghavan,(1988), Govinda Rao, (1993); Chellasamy R. (1996); Chittaranjan (1997);Davithuraj,(2003)

Considering the starting point of the runoff factors derived by Mr. Barlow (later modified by Mr. Gerald Lacey) for

monsoon precipitation on catchments for Udyavara River Basin South Coast of India was derived. Lacey's thus took account of the rainfall intensity with his composite factor S/f , and of the nature of the ground with the soil factor S.

Lacey's formula- According to Lacey's formula, the width of Udyavara basin flow is proportional to the root of the discharge. It is a very simple formula that has been established by many authors and which, until now, has had no physical explanation. It appears that Lacey's equation is unruffled of physical and measurable parameters which agree with field observations.

$R = P/(1+(304.8f/PS))$ where
R = Runoff in cm, P = Rainfall in cm,
f = Monsoon duration factor:
0.50 – very short; 1.00 – standard length;
1.50 – very long,

S = A value dependent on catchment class characteristic:

0.25– flat, cultivated B.C. soil;
0.60– flat, partly cultivated soils;
1.00– average;
1.70– hills and plains, little cultivated;
3.45– very hilly and steep with hardly any cultivation.

Table-4: Runoff assessment in cm of the rivers flowing from Western Ghats

Result: It could be observed that using Lacey's formula, the runoff in case of Udyavara Drainage Basin is 331.01 cm. For the Sita-Swarna river basin it is as high as 434.78cm. This empirical data is indeed and useful for various other determinations in the absence of instrumental data. The rainfall over the basin is uneven, but the variation of the rainfall from year to year is not significant. The maximum rainfall is received during the south west monsoon (June to September). The north east monsoon (October to December) has a low order impact over hydrological regime of the basin. The numerical data of Udyavara Drainage Basin through which the riverine sample was collected show a changeable rainfall and variable Runoff throughout. The width of the channel varies from two to four meters. Different altitudes are

recorded both in Karkalla and Manipal plateau. Among the altitude Indralli Gudda at an altitude of 92 m, Manipal highland at an altitude of 99 m, Northern eastern part of the basin record the altitude of 80 m, to the south west of Karkalla an altitude of 121 m is recorded.

Conclusion: In case of Udyavara plain the stream is typical of low land coastal plain streams with low Gradient Index values. Because of the low land coastal plain streams and low Gradient Index values it has a direct impact on Ground Water and Hydrological Cycle of Udupi District Southwest Coast India. Understanding hydrologic processes and managing water resources, the hydrologic cycle needs to be viewed at a wide assortment of scales and as having an enormous deal of unpredictability in time and space. Precipitation, which is the source of practical, all freshwater in the hydrologic cycle, falls nearly everywhere, but its distribution, is vastly inconsistent as observed from the mean rainfall data and runoff calculation of Udyavara river basin. As a result, much of the precipitation reaches the oceans as surface and subsurface runoff more over a less contribute is observed for the hydrological cycle of Udyavara river basin.

References

- [1] Baker V R., (1988) Geological fluvial geomorphology Geol. Soc. A.,Bull., v 100, pp 1157-1167.
- [2] Balasubrahmanyam M. N. *1978). Geochronology and Geochemistry of Archaeans tonalitic gneisses and granites of South Kanara District, in B. F. Windley and S. M Naqui(Editors) Archaeans Geochemistry, Elsevier, Amst. Pp. 59-78.
- [3] Balasubramanya, N., Shankar, B.S. (2009) The slow accumulation of sediments in the southern parts of the western continental shelf.
- [4] Chandrashekappa K. N. (1989) *Morphometric analysis of Nethravarthi river basin, Karnataka, India*, Ph.D., thesis, Mangalore Univ.,4-6.
- [5] Chellasamy R. (1996) *Hydro geological studies in the Vaigai River Basin, Tamil Nadu*, Ph. D., Thesis, V.O., Chidambaram College, 5-37.
- [6] Chittaranjan (1997) *Inorganic Geochemistry of bottom sediments of Bahuda estuary east coast of India*. Ph. D., thesis, Berhampur Univ., 3-22.
- [7] Davithuraj J. (2003) *Hydro geological studies of upper Bennihalla Basin, Dharawad and Haveri districts, Karnataka*, Ph. D., thesis Karnataka Univ., 40-90.
- [8] Dhir, R. D., Ahuja, P. D., and Singh, H.,(1955) *Hydrological data-its Necessity and Method of Computation*, Central Water and Power Commission, New Delhi, pp7-15.
- [9] Drury, S. A., Harris N. B. W., Holt, R.W., Reeves-Smith, G. J. and Wightman, R. T. (1984). Precambrian Tectonics and Crustal Evolution in South India, Jour. Geol., v. 92, pp. 3-20.
- [10] Gangadhara Bhat, H (1995). Long-term shorelines changes of Mulki Pavane and Nethravathi-Gurupur Estuaries, Karnataka, Photo nirvana chak Jour, Indian Soc. Rem. Sen., v.23, pp-147-153
- [11] Govinda Rao, P. ,1993 Climatic changes and trends over a major river basin in India.
- [12] Radhakrishna, B. P. (1983). Archaean Granite-Greenstone terrain of South Indian Shield. Geol. Soc. India, Mem. 4, pp. 1-47.
- [13] Raghavan, B. R. (1988) *Geomorphology and Evolution of the Sita and Swarna River Basin*, Karnataka, India .Ph.D. thesis, Mangalore University, Mangalore, 54-61.
- [14] Raghavan, B. R., (1988) Geomorphology and Evolution of the Sita and Swarna river basin, Karnataka India, Ph.D Thesis (Unpubl), Mangalore University., Mangalagangotri, 134 p.,
- [15] Raghavan, B. R., and Sreedhar Murthy, T. R. (1991). Coastal-Upland river profile: Analysis around 13° latitude, west coast, India, Indian Geogr. Jour., v. 66, pp 77-82
- [16] Raghunath, H. M., (1996) *Hydrology: Principles, Analysis and Design*. New Age Intl., Publ. New Delhi.1-29
- [17] Ramakrishna and HarinadhaBabu, P. (1981) Western Ghats Belt. In: J. Swami Nath and M. Ramakrishna (Eds.), Early Precambrian Supra crustal of Southern Karnataka. Geol. Surv. India Mem., v.112, pp.147-162.
- [18] Udayashankara, H, N (1994). Landforms analysis of Coastal and Linter land: A part of Dakshina Kannada Using Remote Sensing Techniques, PhD, Thesis Mangalore Univ., 170 p.

Table 1:

Mean Temperature (°C) (1975-1982)

Month	Panambur Temperature		Bajpe Temperature	
	Max	Min	Max	Min
Jan	31.86	18.13	32.42	20.77
Feb	31.83	21.81	32.66	21.97
Mar	32.36	23.68	33.41	24.33
April	32.96	25.07	33.86	25.02
May	32.85	21.95	33.37	24.92
June	29.23	20.27	29.40	23.35
July	28.33	19.96	28.02	22.68
Aug	28.03	19.90	27.68	22.95
Sept	28.77	20.38	29.42	23.07
Oct	30.83	21.23	31.57	23.18
Nov	30.82	20.03	32.06	22.56
Dec	32.46	18.71	33.27	22.11

Source: Meteorological Stations of Panambur & Bajpe

Table 2:

Relative Humidity (%) and Evaporation (Inch, cm) (1978-1983)

Month	Relative Humidity	Evaporation (inch, cm)	
Jan	62.84	0.088	0.224
Feb	81.70	0.100	0.255
Mar	69.22	0.111	0.218
April	73.23	0.138	0.350
May	74.13	0.121	0.307
June	84.43	0.090	0.229
July	90.15	0.072	0.182
Aug	89.77	0.073	0.185
Sept	88.08	0.086	0.219
Oct	78.03	0.077	0.195
Nov	73.63	0.085	0.215
Dec	67.39	0.087	0.221

Source: Agricultural Research Station (Ullal, Mangalore)

Table 3:

Mean 23 years annual Rainfall (1972-95)

Station	Precipitation (in mm)
Ajaker	4811.1
Brahmavar	4878.2
Kapu	39990
Mulki	4750.4
Udupi	4011.9
Karkala	4808.6

Source: District Statistical Dept. Govt. Of Karnataka

Table 4:

Runoff assessment in cm of the rivers flowing from Western Ghats

	p	f	s	t	r
Sita-Swarna	511.31	0.50	1.70	91.70	434.780
Nethravarthi	434.74	0.50	1.70	93.74	360.418
Udyavara	404.17	0.50	1.70	89.24	331.010
Kali Nadi	201.0	0.50	3.45	85.1	166.110

p- Avg. Rain fall (p) in cm

f - Monsoon duration factor (f)

s - Catchment characteristic factor (s)

t - Temp (t) in °f

r – Run off (r) (lacey's formula) in cm

Source:Chandrashekappa K. N. (1989); Chellasamy R. (1996); Chittaranjan, (1997);Davithuraj,(2003);GovindaRao, (1993); Raghavan,(1988)

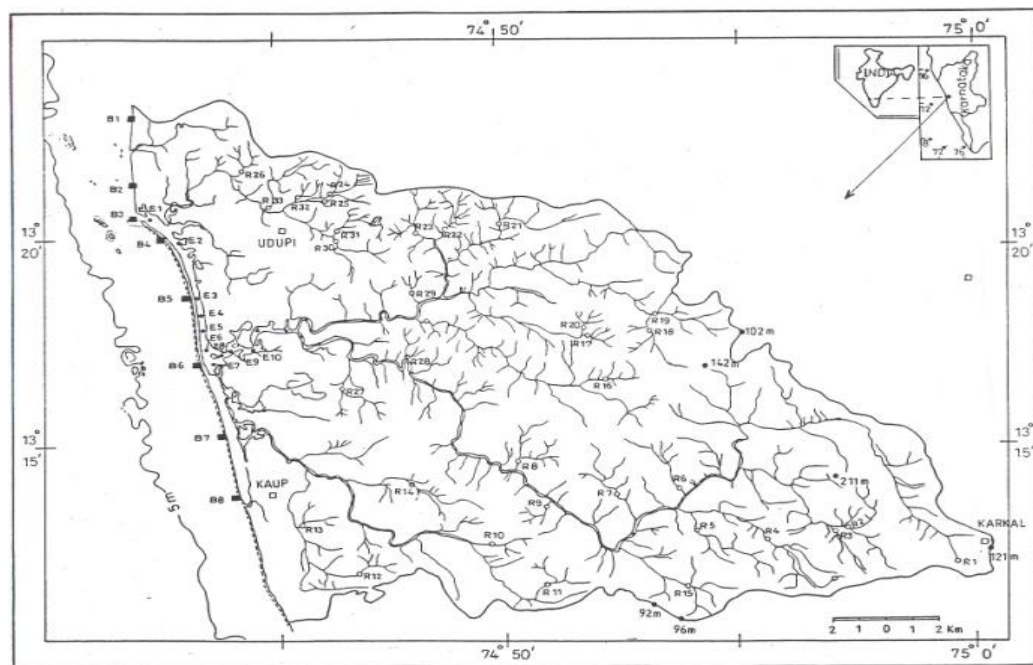


FIG. 1. LOCATION MAP OF UDYAVARA BASIN. DEPICTING SAMPLE AND STATION DISTRIBUTION.

Fig. 1 Location Map of Udyavara Basin (Study Area) depicting sample and station distribution

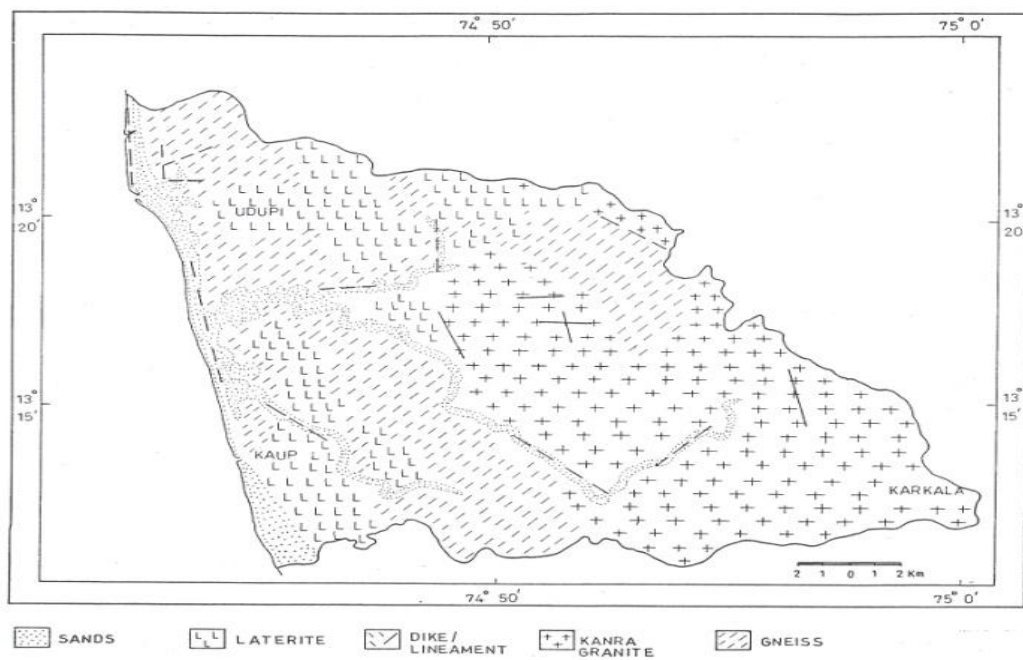


FIG. 2. GEOLOGY MAP OF UDYAVARA BASIN
MODIFIED AFTER BALASUBRAMANYAN, 1978; RAMAKRISHNAN AND HARINADHABABU, 1981; UDAYASHANKAR, 1994.

Fig. 2 Geology map of Udyavara Basin -

Modified after Balasubramanyan, 1978; Ramakrishnan and Harinadababu, 1981; Udaya Shankar 1994

Rain Water Harvesting - a handy tool to preserve water

RAJENDRA KALBAVI RAO¹, SATHYARANJAN RAO², RAVIPRASAD UPADHYAYA ³

- 1 *D. K. Nirmithi Kendra, NITK, Surathkal, Karnataka, India. Pin 575025. Email: dknirmithi@yahoo.co.*
 - 2 *Rachana consultants. Consulting Engineers and Architects, 1st floor, Venkataramana Arcade, Bhavanthi Street, Mangalore, Karnataka, India 575001. Email: rachana.sathyam@gmail.com.*
 - 3 *Premier Associates, Samaj Mandir Complex, Moodabidri, Karnataka, India. Pin 574227. E-mail: urupadhyaya@yahoo.com*
-

Abstract: When there is no water available or less water to utilize, the naturally occurring rain is the best source. Rainwater harvesting is the process of collecting and storing of rainwater when available and use the same during the scarce period. This paper explains the methods of rain water harvesting and its processes involves in construction of rainwater harvesting structures. It also discusses the intricacies involved during implementation. The quantity of rain water harvested depends on the average rain fall in the region and the catchment area from which one has decided to harvest rain water.

Keywords: Harvesting, collecting, storing, filter, quantity, structure.

Introduction

Water, Water everywhere, not a drop to drink.....said the great Columbus. When there is no water available or less water to utilize, the naturally occurring rain is the best source. It is available at free of cost. Rain is the first form of water that we know in the hydrological cycle, hence is a primary source of water for us. Rivers, lakes and groundwater are all secondary sources of water. In present times, we depend entirely on such secondary sources of water. In the process, it is forgotten that rain is the ultimate source that feeds all these secondary sources and remain ignorant of its value. Water harvesting means to understand the value of rain, and to make optimum use of the rainwater at the place where it falls. This is usually found in Asia and Africa during ancient civilizations, still serve as a major source of drinking water. Rainwater harvesting is the process of collecting and storing of rainwater when available and use the same during scarcity. Rainwater systems are simple to construct with inexpensive local materials and are easy to maintain.

Harvesting Rainwater:

Rainwater harvesting is a system by which, the rainwater that falls on the roofs top and the area around the buildings is directed into open wells through a filter tank or into a percolation chamber, built specifically for this purpose. Rainwater can be collected directly in a constructed tank or recharged into the ground to improve ground water storage. Water that is not extracted from ground during rainy days is the water saved. There are a number of types of systems to harvest rainwater ranging from very simple to the complex industrial systems. The rate at which water can be collected from either system is dependent on the plan area of the system, its efficiency, and the intensity of rainfall. Commonly used systems are constructed of four principal components;

- The catchment area
- The conveyance system.
- The filtering system
- The collection device

Need For Rainwater Harvesting:

Major parts of our country have been facing continuous failure of monsoon and deficit of rainfall over the last few years in

those areas. Also, due to ever increasing population of India, the use of ground water has increased drastically leading to constant depletion of ground water level causing the wells and tube wells to dry up. In some places, excessive heat waves during summer create a situation similar to drought. Out of 8760 hours in a year, most of the rain in India falls in just 100 hours. (Fig. 1) It is imperative to take adequate measures to meet the drinking water needs of the people in the country besides irrigation and domestic needs. It reminds a very famous saying 'if at all third world war is fought, the reason for the war would be water alone'. So, Care should be taken in using and preserving rainwater.

Benefits of Rainwater Harvesting:

Harvesting rainwater will not only benefit an individual but the community at large, especially when recharged into the ground to improve ground water storage.

Few of the benefits are:

- RWH is an ideal solution for water requirements in areas having inadequate water resources
- Environment friendly and easy approach for water requirements.
- Increases ground water level.
- Improves ground water quality.
- Mitigates the effects of drought.
- Reduces the runoff, which otherwise flood storm water drains.
- Reduces flooding of roads and low-lying areas.
- Reduces soil erosion.
- Cost effective and easy to maintain.
- Reduces water and electricity bills.

How much water to collect:

The rate at which water can be collected is dependent on the plan area of the system, its efficiency, and the intensity of rainfall.

Quantity of Water harvested (Q) = Average Rainfall of the region (mm) (AR) x Catchment area (A) x collection efficiency (EF)

It is evident that all the rainwater falling over an area cannot be effectively harvested, because of evaporation, spillage etc. Factors like runoff coefficient and the first-flush wastage are taken into

account in arriving at a constant called collection efficiency EF.

The following is an illustrative theoretical calculation that highlights the enormous potential for water harvesting. The same procedure can be applied to get the potential for any plot of land or rooftop area, using rainfall data for that area.

Consider your own building with a flat terrace area of 100 sq m. Assume the average annual rainfall in your area is approximately 500 mm .In simple terms, this means that if the terrace floor is assumed to be impermeable, and all the rain that falls on it is retained without evaporation, then, in one year, there will be rainwater on the terrace floor to a height of 500 mm.

Area of catchment = 100 sq. m.

Height of the rainfall = 500 mm

Assuming that only 60 per cent of the total rainfall is effectively harvested

Quantity of water harvested = $100 \times 500 \times 0.60 = 30,000$ litres

This volume will easily satisfy drinking water requirement of a 5-member family. The average daily requirement per person is 10 litres.

Methods of Rain Water Harvesting:

Rainwater can be harvested in a variety of ways as shown in Fig. 2. In simple terms it can be bifurcated as follows.

- Collection of rain water and preserving for future self use
- Allowing the rain water to recharge the under ground water source

There are basically two models associated with Rainwater harvesting:

- Urban model
- Rural model

Urban model:

This method generally consists of directly harvesting water from roof top. In domestic Rooftop Rainwater Harvesting Systems rainwater from the house roof is collected in a storage vessel or tank for use during the periods of scarcity. Usually these systems are designed to support the drinking and cooking needs of the family at the doorstep. Refer fig. 3.

This system comprises these following elements.

- catchment area or the roof top
- gutter system

- down take pipes
- first flush
- filter unit
- storage tank
- percolation pit

Roof Catchment:

The roof of the house is used as the catchment for collecting the rainwater. Roofs made of corrugated iron sheet, asbestos sheet, tiles or concrete can be utilized for harvesting the rainwater. But thatched roofs are not suitable as it gives some colour and odour to the collected water.

Gutters:

Gutters are channels fixed to the edges of roof all around to collect and transport the rainwater from the roof to the storage tank. Gutters can be prepared in semi-circular and rectangular shapes. Locally available material such as plain galvanized iron sheet can be easily folded to required shapes to prepare semi-circular and rectangular gutters. Semi-circular gutters of PVC material can be readily prepared by cutting the PVC pipes into two equal semi-circular channels. Bamboo poles can also be used in the similar.

Downpipe:

Down pipe is the pipe, which carries the rainwater from the gutters to the storage tank. Down pipe is joined with the gutters at one end, and the other end is connected to the first flush or the filter unit of the storage tank. PVC or GI pipes of diameter 50 mm to 75 mm (2 inch to 3 inch) are commonly used for this purpose.

First Flush Pipe:

The catchment area needs to be clean always. However Debris, dirt and dust collect on the roofs during non-rainy periods. When the first rains arrive, this unwanted material will be washed into the storage tank. This causes contamination of water collected in the storage tank thereby rendering it unfit for drinking and cooking purposes. Therefore, a first flush system is incorporated to dispose off the water from 'first rain' so that it does not enter the tank. It can be a valve or opening given in the down take pipes before the filter as shown in figure 4.

Filter Unit:

The filter unit is used to remove the debris and dirt from water that enters the tank. Varieties of filters can be used depending

on the purpose of the end use of the harvested water. They can be listed as follows

- ❖ cloth filter
- ❖ mesh filter
- ❖ sand bed filter
- ❖ designed filters

Cloth filter: A simple way of filtering the debris and dust particles that came from the roof along with rainwater. It is to use a fine cloth as filter media. The cloth, in 2 or 3 layers, can be tied to the end of the down take pipe or top of a bucket or vessel before collecting the water. Such water can only be used for non-cooking and drinking purposes. These cloths need to be cleaned regularly in-between the rains or during excessive clogging.

Mesh filter: Mesh filters are used in a similar way as cloth filters. Variety of meshes made out of metal, galvanized iron, steel, plastic etc., are available in the market. Any mesh having openings between 4.75mm to .075mm can be effectively used. These filters have longer life compared to cloth filters. The water shall be used for non drinking purposes.

Sand bed filters: A container or chamber filled coarse sand, charcoal, pebbles and gravels to desired depth is a sand bed filter. These filters can be employed for treatment of water to effectively remove turbidity (suspended particles like silt and clay), colour and micro organisms. This can be constructed domestically; the top layer comprises coarse sand of 5-10 mm layer followed by 50 to 150mm thick layer of aggregate followed by another layer of 150-250 mm thick layer of pebbles and boulders as explained in figure 5. An additional layer of mosquito net mesh can also be used as additional security between sand and aggregate. The container is provided with a perforated bottom to allow the passage of water. This filter unit is placed over the storage tank (Fig. 6). Commonly used filters are of two types. One is a Ferro-cement filter unit, which is comparatively heavy and the other is made of either aluminum or plastic bucket. The latter is readily available in market and has the advantage of ease in removing, cleaning and re placing.

Designed filters: Research organizations in different parts of the country and world wide have come out with various models of filters to suit the requirements of the

people. DEWAS of Rajasthan, VARUN of Bangalore, Pop-up of KSCST, Bangalore, (Fig. 7), WISY of Germany etc., are available in the market commercially and can be used according to the individual requirement.

Storage Tank:

Storage tank is used to store the water that is collected during rainwater harvesting. Common vessels used for small scale water storage are plastic bowls, buckets, jerry cans, clay or ceramic jars, cement jars, old oil drums etc. For storing larger quantities of water the system will usually require a bigger tank with sufficient strength and durability. There are unlimited number of options for the construction of these tanks with respect to the shape (cylindrical, rectangular and square), the size (Capacity from 1,000 lt. to 15,000 lt. or even higher) and the material of construction (brickwork, stonework, cement bricks, Ferro cement, plain cement concrete and reinforced cement concrete). For domestic water needs, taking the economy and durability of tanks into consideration, Ferro cement tanks of cylindrical shape in capacities ranging between 4,000 lt. and 15,000 lt. are most suitable and acceptable. Brick, stone, cement brick may be used for capacities ranging between 15,000 lt. to 50,000 lt. Reinforced cement concrete are used for tank capacities usually more than 50,000 lt. The Ferro cement tanks are usually constructed above ground level because of the following advantages:

- Ease in finding structural problems/leaks
- Easy to maintain and clean
- Easy to draw water.

Water from under ground tanks cannot be drawn by gravity. Some kind of manual or power lifting devices need to be used for drawing the water. Further, in coastal areas, under ground tanks are prone to water contamination due to fluctuation in groundwater table and leakage of stored water. The storage tank is provided with a manhole cover on the top to avoid the contamination of water. Pipe fixtures are provided at appropriate places to draw the water, to clean the tank and to dispose of the excess water. They are named as tap or outlet, drainpipe and over flow pipe respectively.

Percolation Pits:

A recharge/soak pits or percolation pits are the easiest and most effective means of harvesting rainwater. Excess water after collection and usage can be let into these pits. The sizes vary from 0.60m to 3m wide and 0.60m to 3m deep designed on the basis of expected runoff. The excavated pit is lined with a brick/stone wall with openings (weep-holes) at regular intervals and filled with pebbles, brick, aggregates and river sand.

Rural model:

In rural areas the people are more concerned of large quantities of water especially for agricultural purposes. The domestic requirement is quite similar to urban model. In rural areas, check dams or vented dams, large ponds, stepped farming etc., are done to store and harvest rainwater. These models vary depending on the terrain, geological conditions, the under ground water source and the volume of water required.

Ground water Recharge structures:

Rainwater may be charged into the groundwater aquifers through any suitable structures like dug wells, bore wells, recharge trenches and recharge pits. Various recharge structures are possible. These promote the percolation of water through soil strata at shallower depth (e.g., recharge trenches, permeable pavements) whereas others conduct water to greater depths from where it joins the groundwater (e.g. recharge wells). At many locations, existing structures like wells, pits and tanks can be modified as recharge structures, eliminating the need to construct any structures afresh as illustrated in Fig. 8.

Maintenance

Rainwater harvesting models, as any other structures needs regular maintenance. In the domestic structure, it is generally limited to the annual cleaning of the tank and regular inspection of the gutters, down-pipes and filters. Maintenance typically consists of the removal of dirt, leaves and other accumulated materials. Such cleaning should take place annually before the start of the rainfall season. However, cracks in the storage tanks can

International Engineering Symposium, March 3-5, 2011 Kumamoto Univ., Japan

create major problems and should be repaired immediately. In the case of ground and rock catchments, additional care is required to avoid damage and contamination by people and animals.

EXPECTED BENEFITS

Rain water harvesting is environmental friendly technique and hence has large interlinked benefits (Fig. 9) to a single user or the society at large. Few of them listed as follows:

1. Prevents water wastage by arresting run off.
2. Prevents soil erosion and mitigates flood.
3. Sustains and safeguards existing water table through recharge.
4. Increases water availability and improves water quality.
5. Arrests sea-water intrusion and prevents salination of ground water.

Conclusion:

Rainwater harvesting technologies are simple to install and operate. Local people can be easily trained to implement such technologies, and construction materials are also readily available. Rainwater harvesting is convenient in the sense that it provides water at the point of consumption, and family members have full control of their own systems, which greatly reduces operation and maintenance problems. Running costs, also, are almost negligible. Water collected from roof catchments usually is of acceptable quality for domestic purposes. As it is collected using existing structures not specially constructed for the purpose. Rainwater harvesting has few negative environmental impacts compared to other water supply project and technologies. Although regional or other local factors can modify the local climatic conditions, rainwater can be a continuous source of water supply for both domestic and commercial purposes.

References:

- [1] Amruthavarshni, Published by Karnataka state council for science and technologies, Bangalore, May 2005.
- [2] Kenneth N. Brooks, Peter F. Ffollitt, Hans M. Grgersen, Leonard F. DeBano, Hydrology and the management of watersheds, Panima Publishing Corporation 1998. P 387-399.
- [3] Anubha Kaushik and C.P. Kaushik, Perspective in environmental studies. 2007. New age international (p) limited New Delhi. P167-171.

[4] M. Anji Reddy, Environmental Science and Technology. BS. Publications, Hyderabad. 2008 p 207-210.

Journal References:

- [1] B. Helmreich, H. Horn. Opportunities in rainwater harvesting. Desalination 248 (2009) p 118-124.
- [2] Fayed A. Abdulla, A.W. Al-Shareef Roof rainwater harvesting systems for household water supply in Jordan. Desalination 243 (2009) p 195-207.
- [3] Jaemin Songa, Mooyoung Han, Tschung-il Kim, Jee-eun Song Rainwater harvesting as a sustainable water supply option in Banda Aceh Desalination 248 (2009) p 233-240.
- [4] N. Hatibu, K. Mutabazi, E.M. Senkondo, A.S.K. Msangi Economics of rainwater harvesting for crop enterprises in semi-arid areas of East Africa Agricultural Water Management 80 (2006) p 74-86.
- [5] Zhe Li, Fergal Boyle, Anthony Reynolds Rainwater harvesting and greywater treatment systems for domestic application in Ireland. Desalination 260 (2010) p 1-8.
- [6] CGWB, UNESCO (2000) Rainwater harvesting and artificial recharge to groundwater, A guide to follow. CGWB, New Delhi. P 1-22.
- [7] Chadha. (2000) Foreword on artificial recharge to groundwater. CGWB guide on artificial recharge, CGWB, New Delhi.
- [8] Radhakrishna, B. P. (2003) Linking of major rivers of India, editorial comment. Jour. Of Geol. Soc. India, Vol 61, no 3, p251 – 256.
- [9] Thangarajan, M. (2002) Editorial comment. Intl. Groundwater conference Sustainable development and management of groundwater resources, Dindigal.
- [10] Venkat Reddy, D. (2002) Hydro geological techniques in groundwater recharge and rainwater harvesting in lateritic terrains in D. K. district, Karnataka. Intl. Groundwater conference Sustainable development and management of groundwater resources, Dindigal, p30 -32.
- [11] M.A.Farooqui and K.R.Sooryanarayana, Rainwater Harvesting for Groundwater Resources Augmentation in Bangalore Metropolitan Area – A case study.

Internet References:

1. www.ccsindia.org/policy/enviro/studies/wp0076.pdf
2. www.gdrc.org/uem/water/rainwater/rainwaterguide.pdf
3. www.self-sufficiency-guide.com
4. www.rainwaterconference.org
5. www.ias.ac.in/currsci/nov102008/1130.pdf
6. www.afhd.org/issues/catalyst-issue5.pdf
7. www.rainwaterclub.org/docs/Domestic_Rainwater_Harvesting.pdf

Acknowledgements:

The authors deeply acknowledge the support and effort done by (RDPR) Rural development and Panchayathraj department. Govt. of Karnataka and Karnataka state council for Science and Technology, Bangalore. All the employees of D.K.Nirmithi Kendra NITK surathkal, for implementing these techniques. Timely support received from Mr. H. Rajanna, Dilip Kumar and Kenet D'souza is also remembered gracefully.

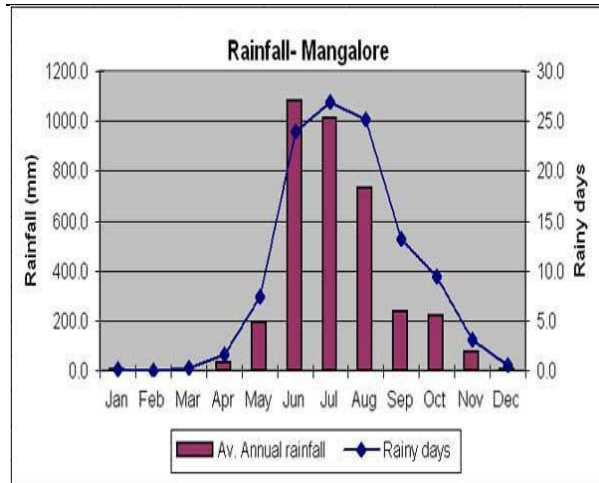


Fig.1. Frequency of rainfall for coastal city, Mangalore.



Fig.4. First flush arrangement with a ball valve.

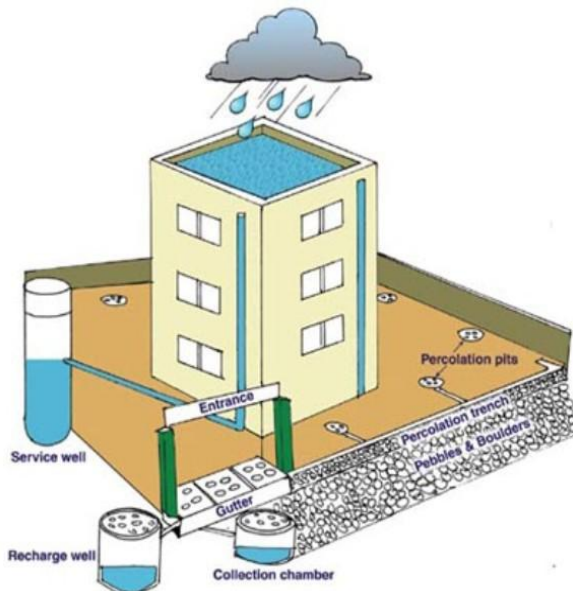


Fig. 2. Schematic representation of various rainwater harvesting techniques

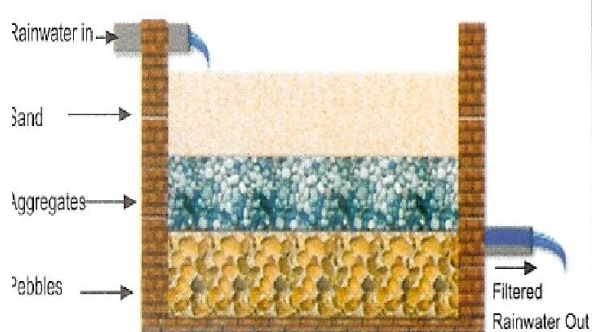


Fig. 5 Typical cross section of a sand bed filter



Fig. 3 A typical set up of rainwater harvesting structure



Fig. 6 A sand bed filter in a masonry enclosure on a tank top.



Fig 7. Installation of Pop-Up filter at residential building.

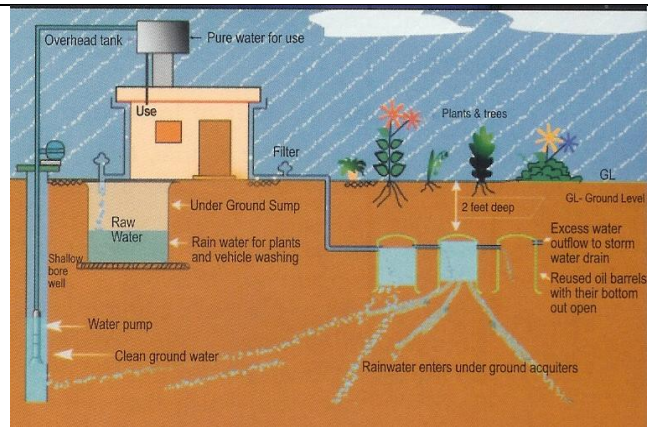


Fig. 9 Sectional view of rainwater harvesting with ground water recharge.



Fig. 8 Installation of open well ground water recharge at authors residence.

Flexure, Shear and Torsion Interaction: Design Aids for Optimization

BABU NARAYAN K.S¹, PRITHIVI HEGDE² and SADANAND SHETTY³

*1 Civil Engineering Department, National Institute of Technology
Karnataka, Surathkal, Mangalore 575025, India, e-mail: shrilalisuta@gmail.com*
2 & 3 Crystal Industrial Syndicate Pvt. Ltd., Navi Mumbai -400614, India

Abstract: Analysis and design of RC sections for flexure, shear and torsion interaction is an exercise that involves tremendous complexities and computational efforts. The behavior of sections is a function of the magnitudes of bending moment, shear force, torsional moment, shape and dimensions of the section and grades of concrete and steel. The complexities associated make this problem an eminently suitable candidate for optimization. This paper presents the problem formulation, solution technique for optimization of RC sections for flexure, shear and torsion interaction. The results are of great help to structural engineers in satisfying the stringent codal requirements optimally.

Keywords: *Torsion, Interaction, Twist, Constraints, Penalty*

Introduction

Torsion combined with shear and moment has always been an interesting aspect of structural behavior. Torsion Shear and moment rarely occur individually. Flexural and shear stresses often combine with torsional stresses in a complicated manner. Axial loads, flexure, shear and torsion are basic loading situations for which independent theories are developed and more complicated interactive loading situations have been dealt with as combination of their basic effects. It need hardly be spelt out that, without an adequate design, the sudden nature of collapse of a member subjected to such loading could cause calamities. Moreover, with the advent of refinements in structural analysis, probabilistic concepts for factor of safety and other pertinent developments in construction technology the need for the due cognizance in design procedures of the effect of such loadings is accentuated.

In the case of reinforced concrete structural systems torsion has been considered secondary in importance, but the modern structural configurations do require the study of torsional behavior.

Marginal beams of concrete framing systems are frequently subjected to combined bending shear and torsion. In addition, as the ability of the structural concrete to assume unusual configurations is more widely utilized, beams having combined loading with variety of ratios between bending shear and torsion are becoming common. The slabs which are built monolithic with floor beams resist lateral loads partially due to torsion at four corners. Ring beams at the bottom of the circular water tanks, particularly Intz type are subjected to tension or compression, flexure, shear and torsion depending upon on the number of intermittent column supports .The beams supporting cantilevered canopy slabs are always subjected to significant torsional loading. Edge beams of concrete shell roofs are also subjected to torsional loading along with flexure and shear. Finally, the helicoidal staircases are to be designed for torsional resistance. Hence it is evident that the torsion along with flexure and shear plays a significant role in resisting loads on structural systems.

Torsion has been assigned greater importance in recent times as structures with difficult geometries and loading cases

are being conceived, analysed, designed, detailed and executed. Satisfaction of stringent codal requirements has forced the designers to seek means, modes and methods of accomplishing optimal solutions.

Flexure, Shear and Torsion Interaction

Few of the very interesting analytical and experimental investigations to understand the phenomena of flexure, shear, torsion interaction better and to propose more meaningful methods of analysis and design have been presented.

Victor and Ferguson (1968) conducted tests on 21 T-beams subjected to eccentric distributed loading. The loading was applied in increments, causing simultaneous proportionate increase in moments. The main variable was torque to shear ratio, also referred to as eccentricity. From the test results, they recommended that if the permissible ultimate flexural shear stress is reduced by about 10 percent for design, a torsional shear stress of about 40 percent of the pure torsion value may be permitted without further special provisions for torsion.

Tests have been carried out by Pandit (1968) for the ultimate strength on fourteen rectangular beams carrying both longitudinal and transverse reinforcement subjected to various combinations of flexure and torsion. He has presented interaction diagrams for ultimate strength in combined bending and torsion. From the test results, he has concluded that the effect of flexural moment on ultimate torsional strength depends upon the magnitude of flexural moment and geometry of beam cross section.

Paul et al. (1969) presented tentative recommendations for the design of reinforced concrete members to resist torsion.

The space truss analogy was originally proposed by Morsch and latter improved by Lampert. Lampert and Collins (1972) have suggested that determination of the strength of a member in combined torsion and bending requires the knowledge of

pure flexural and pure torsional strengths, and also their interaction behavior.

Iyengar and Ram Prakash (1974) published recommendations for design of members subjected to pure torsion, combined torsion, bending and shear. They apply to beams of solid rectangular section or to hollow rectangular section with a wall thickness of at least one sixth the lesser overall dimension of the beam cross section.

Hsu (1985) noticed that plain concrete members under torsion failed by bending on a skew plane at 45 degrees to axis of torsion.

A detailed study on softening of concrete in torsional members due to diagonal cracking was made by Hsu and Mo (1985). Using a new stress strain curve for softened concrete they presented a new theory, which predicted the torsional behavior of 108 test beams available from literature. This theory can predict not only the torsional strength but also the angles of twist, the steel strains and the concrete strains throughout the loading history.

Codes of practice have been immensely helped by these investigations as the propositions, suggestions and modifications by these works form part of recommendations.

Torsional design - optimization problem formulation

The complexities of RC section design to resist torsional loads has been presented in detail in the preceding sections. The computational efforts and rigour required makes this problem eminently suitable for computerization and optimization.

The problem formulation has been explained in the sections that follow.

Design Variables

The breadth and the depth of the section are the two variables, which control the design as well as the total cost. Therefore, in the present problem of optimal design,

the breadth and the depth of the section are selected as design variables.

Objective Function

The objective function, to be minimized is taken as the total cost. The total cost includes cost of materials, cost of formwork and labour. In terms of design variables, the total cost can be written as,

$$C = C_c (b \times D) + C_s \gamma_{st} [(A_{st} + A_{sc}) + A_{sv} (b_1 + D_1) \times 2 / (S_v \times n)] + C_f (b + 2D) + C_l (b \times D)$$

Where

C_c -Unit rate of concrete (per unit volume)

C_s - Unit rate of steel (per unit weight)

C_f -Unit rate of form work (per square meter)

C_l - Unit rate of labor (per unit volume)

In the present work the prevailing unit rates of concrete, steel, formwork and labor have been taken as 3600,45,200 and 300 Rs. respectively.

The Constraints

Following are the different constraints to be satisfied.

1 The breadth of the beam should be non-negative i.e. $b > 0$

2 The depth of the beam should be non-negative i.e. $d > 0$

3. As per clause 41.3.1 of IS: 456-2000, the equivalent shear stress should not exceed the permissible value of shear stress (given in Table 20 of IS: 456-2000)
 $\tau_{ve}/\tau_{cmax} - 1.0 < 0$

Where τ_{ve} - Equivalent shear stress calculated as per clause 41.3.1 of IS: 456-2000

τ_{cmax} - Maximum permissible shear stresses.

The Solution Technique

The solution for the present optimization problem is sought by using Interior Penalty function method. In this method, a new function (ϕ - function) is constructed by

augmenting a penalty term to the objective function .The penalty term chosen is such that its value will be small at points away from the constraint boundaries and will tend to infinity as the constraint boundaries are approached.

The ϕ - function is constructed as follows:

$$\phi(x, rk) = f(x) + rk \sum_{i=1,2,\dots,m} 1/G_i(x)$$

$f(x)$ - Objective function

$G_i(x)$ - is constraint

rk is the penalty parameter

m is the number of constraints

If the unconstrained minimization of ϕ - function is repeated for a sequence of values of penalty parameter rk ($k=1,2,\dots$), the solution is brought to coverage to that of the original problem. This is the reason why the penalty function methods are also known as Sequential Unconstrained minimization Techniques. Since the initial point as well as each of the subsequent points generated in this method lies inside the acceptable region of the design space, the method is classified as 'Interior Penalty Function' formulation.

Results and Discussions

The optimization-programming problem formulated has been run and results obtained have been presented in Table 1 and Figures 1 and 2.

The results obtained indicate that when Bending moments are high and torsional moments are low deep and narrow beams are optimum. Whereas for sections where flexure is associated with high torsional moments wider and shallower beams are preferable. From Graphs for Optimum width and depth v/s Torsional moment/ Bending Moment, it can be seen that as T_u/M_u increases width increases and depth decreases making the section more squarish than oblong. It is prudent here to mention that circular sections are best to handle twisting and when high torsion is to be catered, square RCC sections are to be employed.

Graphs of the kind presented may be generated and utilized as ready reckoners in design office for judicious member sizing.

Conclusions

Structural optimization is an interesting and ever growing area of research. To get the best out of a give situation utilizing the least of the resources, mathematical programming techniques can be used as a decision making tool .The Complex problem of designing RC sections for flexure, shear and torsion interaction can be formulated as an optimization programming problem and solution can be sought by the most popular and versatile SUMT.

The approach suggested could be used to generate design curves for sizing of RC sections, which lead to considerable construction economy.

References

- [1] Dayaratnam P (1988), Design of Reinforced Concrete Structures, Oxford and IBH Publishing Company, Pvt. Ltd.
- [2] Hsu. T.T.C and Y L Mo (1985), Softening of concrete in Torsional members – Theory and Tests, ACI Journal, Vol.82, May –June. pp 290-302
- [3] Iyengar K.T.S and N.Ram Prakash (1974), Recommendations for the design of reinforced concrete beams for torsion, bending and shear, Bridge and Structural Engineer, New Delhi , Vol.4, No.1, March, pp 25 -37
- [4] Lampert, P. and M.P. Collins (1972), Torsion, Bending and Confusion –An attempt to establish the facts, ACI Journal, Vol.69, No.8, August, pp 500-504
- [5] Pandit, G.S.(1968), Combined bending and Torsion of concrete beams, Indian concrete Journal, Vol.42, No.9, September, pp 353-360
- [6] Paul, Zia. and Alan.H.Mattock (1969), Tentative Recommendations for the design of Reinforced Concrete Members to resist Torsion, ACI Journal, Vol.66, January,pp 1-7.
- [7] Victor, D.J and M.Ferguson(1968), Beams under distributed load creating moment, shear and torsion, ACI Journal, Vol.65, April, pp 295 –307.

Table 1 Results of optimization of beams subjected to Torsion

T _u (kNm)	M _u (kNm)	V _u (kN)	Width (mm)	Depth (mm)	Cost /m (Rs)	D/b	T _u /M _u
25	500	150	155.21	1071.35	2172.71	6.90	0.05
50	500	150	201.11	1000.49	2567.01	4.97	0.1
75	500	150	246.06	944.91	2884.1	3.84	0.15
100	500	150	284.08	911.07	3160.21	3.21	0.2
150	500	150	346.17	874.83	3642.67	2.53	0.3
200	500	150	397.99	861.42	4068.91	2.16	0.4
250	500	150	441.88	854.31	4459.6	1.93	0.5
300	500	150	481.19	850.26	4824.93	1.77	0.6
350	500	150	516.14	850.25	5170.91	1.65	0.7
400	500	150	547.90	849.90	5501.47	1.55	0.8
450	500	150	577.12	853.78	5819.14	1.48	0.9

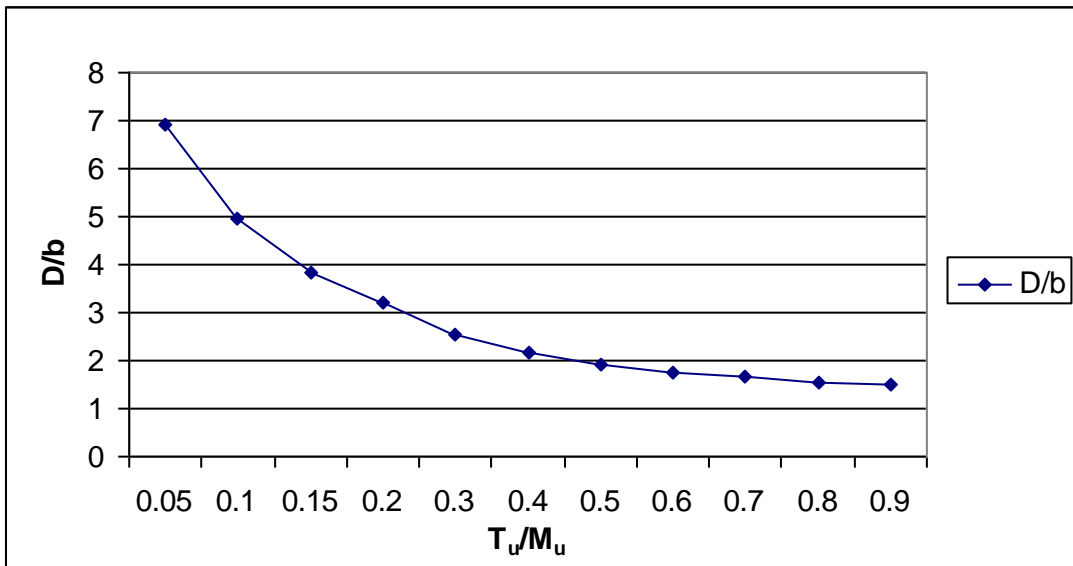


Fig. 1 Variation of Optimum D/b with T_u/M_u

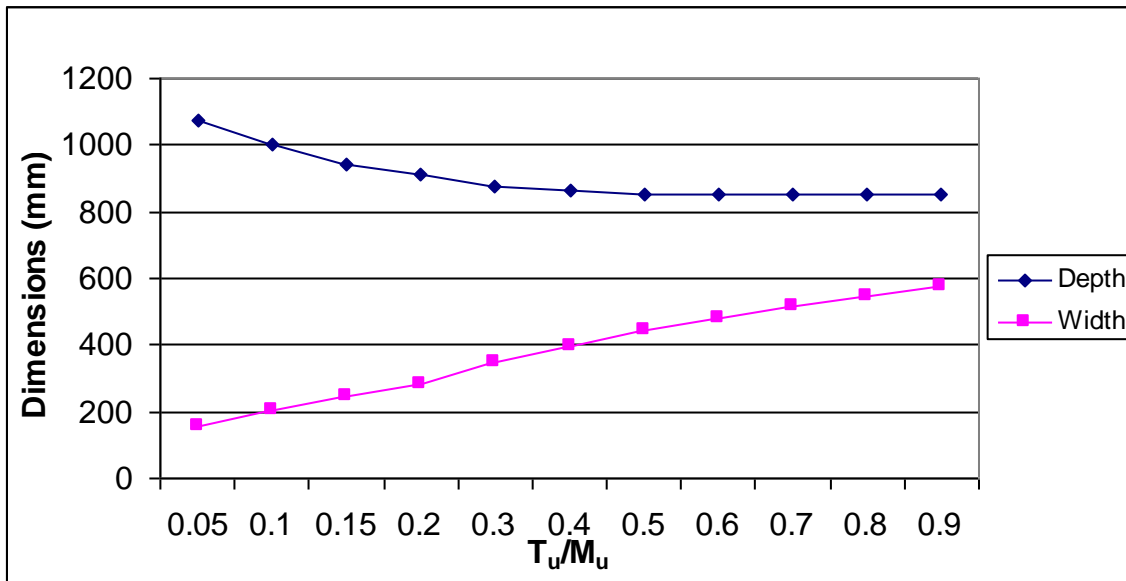


Fig. 2 Variation of Depth and Width with T_u/M_u

SIMPLIFIED SOLUTIONS FOR SHAPE SEARCHING

BABU NARAYAN K.S¹, SHAMIR R.² and SATISH B.³

¹ Civil Engineering Department, National Institute of Technology Karnataka, Surathkal, Mangalore 575025, India, e-mail: shrilalisuta@gmail.com

² Premier Builders, Udupi 576 101, Karnataka, India

³ Tharaka Engineers, Mangalore, 575 003, Karnataka, India

Abstract: The exercise of arriving at the final geometry of a structure through which the most efficient load flow is accomplished represents the highest level of structural engineering. Geometry as a variable is very rarely considered in design. In many situations the configuration dictates the efficiency. The exercise of form finding offers tremendous scope for computerization and optimization. This paper envisages to discuss the need and scope for shape optimization by presenting details of attempts made thus far, and by giving illustrative example of form finding of holding tanks.

Keywords: Optimization, Constraints, Shape, Variable, Programming

Introduction

Structures are built with an intended end use for a specified utility period. The functional requirement is to serve the purpose and the structural requirement constitutes stability, strength, safety, serviceability and durability. Satisfaction of these requirements at affordable costs is the goal of structural optimization. Economy is wise spending and cost effectiveness is "maximum effect with minimum efforts".

Realization of cost effective structures heavily relies on factors like progress made in material sciences, knowledge of behaviour of materials and structural systems, analytical tools for assessment of strength, safety and serviceability, construction practices and construction economy. True innovation is proper synthesis of these factors.

The mode of transmission of force is a function of configuration. The technical success of optimization depends on how efficiently the load flow is accomplished. Decision-making that leads to final geometry represents the highest level of Structural Engineering.

Planning, analysis, design, detailing, execution, operation and maintenance of

engineering systems involve decision making at several stages. The decision making process should lead to utilization of least resources and realization of maximum benefits. Operations Research is the branch of mathematics that deals with the application of scientific methods in decision-making process. Available literature on application of optimization techniques for shape optimization of structures has been gathered and presented in this paper and shape optimization of holding tanks by classical method of calculus has been illustrated.

Literature review

Tzonis and Lefaire (1975) credit Galileo Galilei as the initiator of shape optimization, for it was Galileo who made the famous proposition that "it would be a fine thing if one could discover the proper shape to give to an object in order to make it equally resistant at every point". Much work has been done on optimal structures since then and the search is still on, as there is no single way to address the wide and varied range of problems encountered in Structural Engineering.

The fact that there exists a unique geometry for the structure of absolute minimum weight under a specific loading

arrangement was first suggested by Michell (1904). He demonstrated that optimal structures are built up of orthogonal nets of pin-jointed members shaped like slip-lines.

Richards and Chan (1966) have reviewed and confirmed Michell's theory. Though Michell's gives an inverse design method, it cannot include many design considerations and hence finds little application. Nevertheless Michell's work is regarded as the beginning of shape optimization because it was recognized for the first time that shape should be a fundamental variable in designing an efficient structure.

A method of design that finds best shape without investigating all possible shapes was first attempted by Dorn et al (1964) employing linear programming technique. The results were in the range from the interesting to the unexpected. As objective functions and constraints in structural optimization generally are non-linear, it was accepted that clumsy linearization to include them in linear programming was of no much help.

Application of Dynamic Programming, a method of non-linear programming technique was suggested by Bellman (1957) and applied to pin-jointed frameworks by Porter-Golf (1968). Failure to adequately include design considerations makes this technique generate solutions that are not always optimal. Palmer (1971) has used dynamic programming for limit design of beams, to include asymmetry, alternative loading conditions and use of real members instead of artificial and has demonstrated the benefit of shape optimization over usage of conventional standard geometry.

Geometric programming as a mathematical aid in engineering design was proposed by Zener (1961) and Templeman (1970) showed its utility in Structural Engineering problems. Though the technique depends on the form of objective function and constraints and degree of difficulty, it can be of use coupled with other methods to find either complete solutions or approximate ones.

An approach called Reanalysis with Sub-optimization has been attempted by Tomlassen (1993) for shape optimization of large three-dimensional frameworks. The method assumes that large frame works are assemblages of small groups of limited number of members and only one active constraint for one member of the group that is critical considered for sub-optimization. Sequential Quadratic Programming Technique is employed for sub-optimization. Though there is no sound theoretical basis for the assumptions, experience with the technique has indicated that it is robust and consistent, offering optimum solutions at low computational costs.

Zimmerman et al (1993) have suggested application of stochastic optimization models for identification of geometry and failure modes for structures where loads and resistances are to be treated as random variables. An attempt to address axial-force moment interaction as a function of geometry, integrating rigid plastic model with mathematical programming has been made.

Calatrava (1981) presents detached explanation of the subject of shape optimization by defining Profiling-as selection of geometry contour and Differentiating-as dividing the structure to several separate members each performing different functions using materials best suiting members assigned function. He has demonstrated by mathematical programming that three dimensional space frames can be folded first to two dimensions and then into one. Calling this program a super 3D compass, he tries to explain generation of best geometry by movement of the joints in space.

Genetic Algorithms (GAs) are efficient and broadly applicable global search procedures based on a stochastic approach which rely on the survival of the fittest strategy. In recent years GAs have been used in structural optimization by many researchers (Goldberg and Samtani, 1986; Rajeev and Krishnamoorthy 1992; Rajan 1995; Rajeev and Krishnamoorthy 1997).

All these studies have demonstrated that GAs can be utilized as a powerful decision making tool for optimization. Since GAs do not need gradient information they offer a very general search approach. GAs do not require explicit relationship between the objective function and the constraints. The value of the objective function for a set of design variables is adjusted to reflect any violation of the constraints by using penalty function approach.

Critical review of the available literature shows the complexity of the problem of the shape optimization of structures. It also reveals the need and scope for the same. The availability of the state-of-art computational gadgetry can offer tremendous thrust to this potentially wide and interesting area of research in Structural Engineering. A very general case of shape optimization of holding tanks by the classical method of calculus has been discussed here.

Illustrative examples

Holding Tanks

Households, communities and mega industries need holding tanks for a wide and varied range of use. For instance water and liquid storage tanks, pressure vessel, containment domes of nuclear reactors and containment barriers for hazardous waste management. More often than not a geometrical shape is imposed on a structural form without due consideration to the most optimum shape. Most generally the material consumption of these structures is dictated by requirements other than strength alone leading to satisfaction of the absolute minimum requirements as specified by the standards. In such instances the geometry alone decides the cost. Hence search for a meaningful geometry that leads to the minimum cost is essential as well as logical.

If it assumed that the material costs, fabrication and erection costs are the same irrespective of the shape of the holding tank than we arrive at the inescapable conclusion that the shape, which has least

surface area, is the most optimum. The following sections present the approach to arrive at the best shape. If 'V' is the volume of the tank the most optimum shape is the one for which surface area is the least. Most common geometrical shapes in popular use have been considered here to highlight the need for shape optimization.

(i) Cuboids

For a cuboid of length 'l', breadth 'b' and height 'h'

$$V=lbh$$

$$\text{Let } b=k_1 l \quad h=k_2 l$$

$$\text{Hence, } V= k_1 k_2 l^3$$

$$\begin{aligned} \text{Surface area, } S &= 2 lb + 2 bh + 2 hl \\ &= 2 l^2 (k_1 + k_1 k_2 + k_2) \end{aligned}$$

$$\text{As } V= k_1 k_2 l^3$$

$$l = \sqrt[3]{\frac{V}{k_1 k_2}}$$

$$S = 2 V^{2/3} = \left(\frac{k_1 + k_1 k_2 + k_2}{k_1^{2/3} k_2^{2/3}} \right)$$

For minimum surface area,

$$\frac{\partial S}{\partial k_1} = 0 \quad \frac{\partial S}{\partial k_2} = 0$$

From

$$\frac{\partial S}{\partial k_1} = 0$$

We get

$$k_1 + k_1 k_2 - 2k_2 = 0 \quad \dots\dots\dots(1)$$

$$\text{Similarly from } \frac{\partial S}{\partial k_2} = 0$$

We get

$$k_2 + k_1 k_2 - 2k_1 = 0 \quad \dots\dots\dots(2)$$

Solving equations (1) and (2)
we obtain $k_1 = k_2 = 1$.

This suggests the most optimum cuboid is a cube.

Hence for the cuboids, $S = 6 l^2$ and $V = l^3$
Therefore $S = 6 V^{2/3}$

(ii) Cylinder

For a cylinder of radius 'r' and height 'h'

$$\text{Volume } V = \pi r^2 h$$

$$\begin{aligned} \text{Surface area, } S &= 2 \pi r^2 + 2 \pi r h \\ &= 2 \pi r^2 + 2 V/r \end{aligned}$$

For surface area to be minimum $\frac{dS}{dr} = 0$

Differentiating equation for S above and equating to zero

We get the condition for minimum surface area

$$\frac{dS}{dr} = 4\pi r - \frac{2V}{r^2} = 0$$

And hence,

$$2\pi r^3 = V$$

Since,

$$V = \pi r^2 h$$

$$h = V/\pi r^2 = 2\pi r^3/\pi r^2 = 2r$$

This suggests the most optimum cylinder is the one for which height to the radius ratio is 2

$$\text{Hence } S = 6\pi r^2$$

$$\text{Since, } r = \sqrt[3]{\frac{V}{2\pi}}$$

$$S = \frac{6\pi V^{2/3}}{(2\pi)^{2/3}} = 5.53581 V^{2/3}$$

(iii) Cone

For a cone of radius 'r', height 'h' and slant height 'l'

$$\text{Volume, } V = \frac{1}{3}\pi r^2 h$$

Therefore

$$h = \frac{3V}{\pi r^2}$$

$$\text{And slant height } l = \sqrt{h^2 + r^2}$$

Surface area,

$$\begin{aligned} S &= \pi r^2 + \pi r l \\ &= \pi r^2 + \pi r \sqrt{(h^2 + r^2)} \\ S &= \pi r^2 + \pi r^2 \sqrt{1 + \frac{9V^2}{\pi^2 r^6}} \end{aligned}$$

For minimum surface area

$$\frac{dS}{dr} = 0$$

Differentiating and simplifying the equation for 'S' we obtain

$$\sqrt{1 + \frac{9V^2}{\pi^2 r^6}} - \frac{9V^2}{2\pi^2 r^6} + 1 = 0$$

Putting

$$\frac{9V^2}{\pi^2 r^6} = X$$

We get

$$\sqrt{(1+X)} - \frac{X}{2} + 1 = 0$$

Solving X=8

Hence,

$$\frac{9V^2}{\pi^2 r^6} = 8$$

From which

$$V^2 = \frac{8\pi^2 r^6}{9}$$

Since

$$V = \frac{1}{3}\pi r^2 h \quad V^2 = \frac{1}{9}\pi^2 r^4 h^2$$

Equating we get

$$h = \sqrt{8r^2} = 2.8284 r$$

Most optimum cone has height to radius ratio 2.8284

As ,

$$\begin{aligned} S &= \pi r^2 + \pi r \sqrt{(r^2 + h^2)} \quad \text{and } h^2 = 8r^2 \\ S &= 4\pi r^2 \end{aligned}$$

Substituting radius in terms of volume we get

$$S = 6.093 V^{2/3}$$

(iv) Sphere

For a sphere of radius 'r'

$$\text{Volume, } V = \frac{4}{3}\pi r^3, r = \left(\frac{3V}{4\pi}\right)^{1/3}$$

$$\text{Surface area } S = 4\pi r^2 = 4.836 V^{2/3}$$

Hence the surface areas of most optimum sphere, cylinder, cube and cone for the same holding capacity compare as follows,

$$\begin{array}{l} \text{Sphere : Cylinder : Cube : Cone} \\ 4.836 V^{2/3} : 5.5381 V^{2/3} : 6 V^{2/3} : 6.093 V^{2/3} \end{array}$$

$$1 : 1.145 : 1.24 : 1.26$$

International Engineering Symposium, March 3-5, 2011 Kumamoto Univ., Japan

Cylinder, cube and cone having the same holding capacity as that of a sphere have 15 %, 24 % and 26 % more surface area. Hence shapes should be judiciously selected.

Summary and Conclusions

More often than not an architectural form is imposed on and structural form, it is very essential to recognize the fact the geometry also is a design variable which many times can dictate the cost. Hence the best configuration of the structure through which the most efficient load flow is accomplished needs to be searched and adopted. Shape optimization is an interesting exercise and should rather be the first step in structural optimization.

References

- [1] Bellman R. (1957), "Dynamic Programming", Princeton university Press.
- [2] Dorn W. S et al.(1964), " Automatic Design of Optimal structures", Journal of Mechanics, Vol. 3, pp. 25-52.
- [3] Goldberg, D. E. and Samtani, M. P., (1986). "Engineering Optimization via Genetic Algorithms", Proc. of 9th Conf. on Electronic Computation, ASCE, New York, N. Y., pp. 471-482.
- [4] Michell A.G.M (1904), "The Limits of Economy of Materials in frame structures", Phil. Mag, S6, 8(November), No. 47, Pp. 589-597.
- [5] Palmer A.C (1968), "Optimum Structure Design by Dynamic Programming", Journal of Structural engineering, ASCE, pp. 1887-1907.
- [6] Porter-Goff R.F.D (1968), " Shape as a Structural Design Parameter", PhD thesis, Leicester University.
- [7] Rajan, S. D., (1995). "Sizing, shape and topology design optimization of trusses using genetic algorithms", J. of Struct. Engrg. ASCE, 121 (10), pp. 1480-1487.
- [8] Rajeev, S. and Krishnamoorthy, C. S., (1992). "Descrete Optimization of structures using genetic algorithms", J. of Computing in Civil Engrg., ASCE, 118 (5), pp. 1233-1250.
- [9] Rajeev, S. and Krishnamoorthy, C. S., (1997). "Genetic algorithms-based methodologies for design optimization of trusses", J. of Struct. Engrg., ASCE, 123 (3), pp. 350-358.
- [10] Rao S.S (1991), " Optimization Theory and Applications", Wiley Eastern.
- [11] Richards D.M & Chan H.S.Y (1966), "Developments in Theory of Michell Optimum Structures", AGARD report 543.
- [12] Santiago Calatrava Valls (1981), " Zur faltbarkeit Von Fachwerken", PhD Dissertation, Zurich: TCH.
- [13] Templeman A.B (1970), "Structure Design for Minimum Cost Using the Method of Geometric Programming", Proc. of Institution of Civil Engineers, London, Vol. 46, pp. 459-472.
- [14] Tom Lassen (1993), " Optimum Design of Three Dimensional Frame Work Structures", Journal of Structural Engineering, ASCE, Vol.119, No.3, pp. 713-727.
- [15] Tzonis and Lefaiure (1975), " The Mechanical v/s Divine Body: The Rise of Modern Design Theory", Journal of the Society of Architectural Historians, Vol. 3.
- [16] Zener C (1961), " A Mathematical Aid in Optimizing Engineering Designs", Proc. of National Academy of Sciences, USA, Vol. 47, No.4.
- [17] Zimmerman et al (1993), " Stochastic Optimization Models for Structural Reliability Analysis", Journal of Structural Engineering, ASCE, Vol.119, No.1, pp. 223-239.

Strength Retention Studies on Normal Concrete and Self Compacting Concrete Subjected to Elevated Temperatures

**K S BABU NARAYAN, VINAY KUMAR G, SUBHASH C YARAGAL
and KATTA VENKATARAMANA**

*Civil Engineering Department, National Institute of Technology Karnataka, Surathkal,
Mangalore 575025, India. e-mail: subhashyaragal@yahoo.com*

Abstract: Concrete has been widely used as a construction material in buildings and other industrial structures for a long time. The possibility of its exposure to elevated temperatures is high due to natural hazards, accidents and sabotages. Trial mix designs were attempted to produce M30 normal strength concrete and also self compacting concrete of the same grade. This study reports the strength retention characteristics of normal strength and self compacting concretes at elevated temperatures. Concrete cubes of 100 mm size are tested after subjecting them to elevated temperatures of 200°C, 400°C, 600°C and 800°C with a retention period of 2 hours. Compressive strength and split tensile strength retention of normal strength concrete and self compacting concretes have been presented and discussed.

Keywords: *Elevated Temperatures, Residual Strength, Normal strength Concrete, Self Compacting Concrete, Cubes.*

Introduction

Concrete is most widely used material and will continue to be so in the next millennium. As a construction material concrete has been important in the past, presently indispensable and may be even more useful in future. It is considered as one of the most versatile building material because of its many advantages like high resistance to fire, wind and water and lends itself to almost any type of decorative or architectural application.

The greatest challenge in the next millennium will be to build a durable concrete (durable to fire, elevated temperature, coastal and marine environment, industrial and chemical plants) in as short a time as possible to meet the high infrastructural demands in the developing countries.

The use of self compacting concrete (SCC) was considerably developed during the last years and a growing attention to study of

its mechanical properties at hardened state. The mechanical properties of SCC may vary from normal strength concrete (NSC). The behaviour of SCC compared to NSC subjected to high temperature has in particular to be evaluated.

Studies have identified several mechanisms that have led to deterioration of concrete properties: destruction of gel structure, decomposition of calcium hydroxide compounds into lime and water, expansion of lime in re-hydration, phase transformation in aggregates, development of micro cracks. The behavior of concrete subjected to high temperatures is a result of many factors, such as heating rate, peak temperatures and thermal incompatibility between aggregate and cement paste, type of aggregate, specimen shape and size, moisture content, content of admixture, specimen curing condition, mix proportioning method and etc. Generally, for mature concrete an increase in exposure temperatures causes concrete to gradually lose its mechanical strength.

Mechanical strength

Many researchers have reported strength deterioration with the increase in exposure temperature. The strength degradation is not same under high temperature. It depends on type of aggregates used, the heating and cooling regime, the presence of pozolanas, fibers etc.

Mechanical properties are impaired by the temperature rise. Compared to the reduction in compressive strength the losses in tensile strength and modulus of elasticity is marked.

Y. Xu et al. (2003) has reported loss of tensile strength after exposure to 250°C, this could be largely attributed to the emergence of minor cracks in concrete. Higher temperature exposures induced more damage to the tensile strength of concrete than to the compressive strength.

Albert Noumowe et al. (2006), have reported that the residual mechanical properties in reference to initial mechanical properties of self compacting high strength concretes were similar to that of conventional high-strength concrete. The risk of spalling for self compacting high-strength concrete was greater than that of conventional high strength concrete.

Kosmas K. Sideris (2007), has reported that residual strength of both SCC and conventional concrete was reduced almost similar up to the maximum temperature tested. Explosive spalling occurred in both SCC and CC of the highest strength category at temperatures greater than 380°C. The residual compressive strength of SCC mixtures was higher than the one of CC mixtures for the same strength class. The tentative spalling behaviour of SCC and CC was the same and depended only on the strength category.

Omer Arioz (2007) observed a gradual reduction in residual strength up to 600°C (residual strength 90% for carbonate aggregates and 50% for river gravel) and sharp reduction in relative strength beyond that point.

Hanaa Fares et al. (2009) has reported that between 20°C and 150°C, a small loss of strength was observed and 150°C and 300°C, an increase in compressive strength for the SCC was observed. Nevertheless, the other mechanical properties (flexural strength and modulus of elasticity) continued to decrease in a similar way to the observed evolutions between 20°C and 150°C, due to the departure of bound water, corresponding to a large mass loss. The increase in strength could be attributed to a modification of the bonding properties of the cement paste hydrates (rehydration of the paste due to the migration of water in the pores).

This paper reports the behavior of NSC and SCC when subjected to elevated temperatures ranging from 200°C, 400°C, 600°C and 800°C, 200°C with a focus on loss of strength and to establish relationship between residual compressive strength and residual split tensile strength of specimen exposed to elevated temperatures, for both NSC and SCC.

Mix Proportion

After concrete mix design trials, 100 mm concrete cubes were cast for normal strength concrete and the other for self compacting concrete. Proportions are as listed in Table 1.

Test Procedure

The effects of elevated temperatures on NSC and SCC are attempted in this investigation. The foregoing research makes use of M30 normal strength concrete and self compacting concrete as designed, through trial mixes. Cube specimen of size 100x100x100mm were cast and 28 days water cured. For NSC and SCC totally 96 number specimen were cast. These were divided in to 8 sets, each set consisting of 6(3No.s for compressive strength and 3No.s for split tensile strength) specimen. Within these 8 sets, 1 set was tested under destructive testing before exposure, 4 sets for actual exposure testing, and the remaining 3 sets were cast as reserve.

The specimen were subjected to four different temperature cycles in an electric

furnace up to 200°C, 400°C, 600°C and 800°C, in each case retention period was 2 hours. It is observed that the temperature build up to 400°C is at faster rate of around 20°C /min compared to temperature build up above 400°C. Temperature build up is gradual above 400°C at the rate of 7°C/min. After exposure to elevated temperatures, specimen were allowed to cool within the furnace until reaches room or ambient temperature. After cooling of specimen, weight loss of each specimen was taken, and finally destructive test (direct compressive strength and split tensile strength) was also carried out for strength retention assessment.

Results and discussion

The observations were made on physical properties of specimen, percentage loss in moisture and percentage loss in compressive strength and split tensile strength are tabulated and discussed

Loss of weight before and after exposure to elevated temperatures

From Figure 1, it is observed that the percentage weight loss for SCC is more up to 400°C when compared to conventional concrete and above 400°C NSC shown higher percentage loss of weight compared to SCC and remains almost parallel and same for increment of temperature.

The percentage weight loss of conventional concrete (NSC) is slightly more than the self compacting concrete (SCC) with respective to every incremental temperature. This is because the use of superplasticizer mainly reduces the water cement ratio of concrete keeping the workability to the required degree. Hence percentage of water content will be high in conventional concrete rather than self compacting concrete (SCC). Therefore at elevated temperature percentage weight loss of conventional concrete is more compared to self compacting concrete due to departure of free water contained in the capillary pores.

Residual compressive strength

From Table 2 and Figure 2 it is observed that the residual coefficient of compressive strength of cubes exposed to 200°C is higher by about 26% than that of cubes tested at normal room temperature. This is mainly because, at early elevated temperature the moisture content in the cubes creates vapour pressure, which contributed to the additional compressive strength than that of normal strength as observed by the investigators. Several hypotheses have been proposed in the literature to explain this increase. Dias et al. (2005) attribute it to a rehydration of cement paste due to migration of water in the pores. In another study, Khoury (1992) assumes that the silanol groups lose a part of their bonds with water which induces the creation of shorter and stronger siloxane elements (Si-O-Si) with probably larger surface energies that contribute to the increase in strength. Hanna Fares et al. (2009) reported about 25% increase in compressive strength between 150°C to 300°C due to anhydrous cement.

On further increase of temperature there is loss in compressive strength gradually, as compared to strength at room temperature due to loss of moisture content and disintegration of hydrated cement paste. At 400°C the residual coefficient of compressive strength for SCC is 0.81, and drops gradually to 0.64 and 0.35 at elevated temperatures of 600°C and 800°C respectively.

Residual split tensile strength

From Table 3 and Figure 3 it is observed that the residual coefficient of split tensile strength of cubes exposed to elevated temperature decreases than that of cubes tested at normal room temperature. This is mainly because due to loss of moisture content and disintegration of hydrated cement paste. Hanna Fares et al. (2009) investigated that many micro and macro cracks were produced in the specimen due to the thermal incompatibility between aggregates and cement paste between the transition zone.

It is also observed in this study that there is a disintegration of aggregates from cement paste in the core of specimen, in other words the aggregates not broken

International Engineering Symposium, March 3-5, 2011 Kumamoto Univ., Japan

during conducting split tensile strength test. In case of SCC at 200°C the residual coefficient of split tensile strength is 0.83, and drops gradually to 0.67, 0.42 and 0.31 at elevated temperatures of 400°C, 600°C and 800°C respectively.

- [2] Albert Noumowe, Carre.H, Daoud. A and Toutanji.H (2006) "High-Strength self compacting concrete exposed to fire test", Journal of Materials in Civil Engineering Vol. 18, No. 6, pp. 754-758.

[3]Kosmas K. Sideris (2007), "Mechanical characteristics of self-consolidating concretes exposed to elevated temperatures", Journal of Materials in Civil Engineering Vol. 19, No. 8, PP. 648-654.

[4]Omer Arioz (2007), "Effects of elevated temperatures on properties of concrete", Fire Safety Journal Vol.42, PP. 516-522.

Relation between residual split tensile strength V/s residual compressive strength of NSC and SCC

From Figures 4 and 5 a graph has been plotted between residual split tensile strength to residual compressive strength of concrete for NSC and SCC respectively. From the plot a best fit power line is obtained as given below having regression value of 0.962 and 0.981 respectively.

For NSC
 $f_t = 0.1468(f_{ck})^{0.825}$ (1)

$$f_t = 0.1816(f_{ck})^{0.7671} \dots \dots \dots (2)$$

Conclusions

- As the exposed temperature increases, the percentage of loss in weight of specimen increases. The observed minimum residual compressive strength is 39% and 35% for NSC and SCC respectively at 800°C .
 - In general there is substantial loss (60%) in compressive strength from 200°C to 800°C for NSC and SCC.
 - For NSC and SCC the split tensile strength is decreased continuously with increase in exposure temperature.
 - The minimum residual split tensile strength is 36% and 34% for NSC and SCC respectively at 800°C .
 - For exposure temperature of 600°C to 800°C , during the split tensile strength majority numbers of specimen are failed due to disintegration of cement paste and aggregates at transition zone.
 - The crack density is more when exposure temperature between 600°C to 800°C was observed.

**Table 1 Mix proportion of concrete
(NSC and SCC)**

Designation	Proportion
M30(NSC)	w/c :C :FA :CA 0.45:1:1.198: 2.923
M30 (SCC)	w/c :C :F :FA :CA 0.48:1:0.54:2.035:2.114

Table 2 Comparison of residual compressive strength (Factor/Co-efficient) of NSC and SCC subjected to elevated temperatures

Temperature exposure to (°C)	Residual Compressive Strength of NSC (Factor/ Co-eff.)	Residual Compressive Strength of SCC (Factor/ Co-eff.)
Room temperature	1.00	1.00
200	1.06	1.26
400	0.95	0.81
600	0.51	0.64
800	0.39	0.35

References

- [1] Y. Xu, Y.L. Wong, C.S. Poon, M. Anson (2003), "Influence of PFA on cracking of concrete and cement paste after exposure to high temperatures", Cement and Concrete Research 33, pp 2009 – 2016

Table 3 Comparison of residual split tensile strengths (Factor/Co-efficient) of NSC and SCC subjected to elevated temperatures

Temperature exposure to (°C)	Residual split tensile strength of NSC (Factor/ Co-eff.)	Residual split tensile strength of SCC (Factor/ Co-eff.)
Room temperature	1.00	1.00
200	0.88	0.89
400	0.67	0.62
600	0.44	0.47
800	0.36	0.34

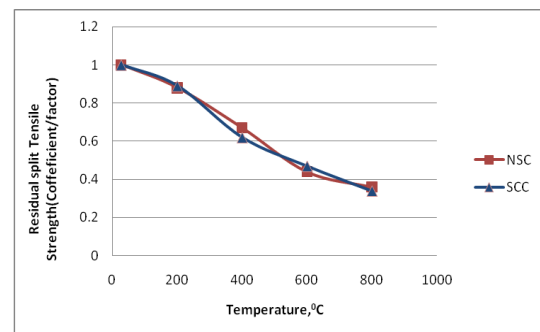


Fig 3 Comparison of residual coefficient of split tensile strength results of M-30 grade NSC and SCC subjected to elevated temperatures

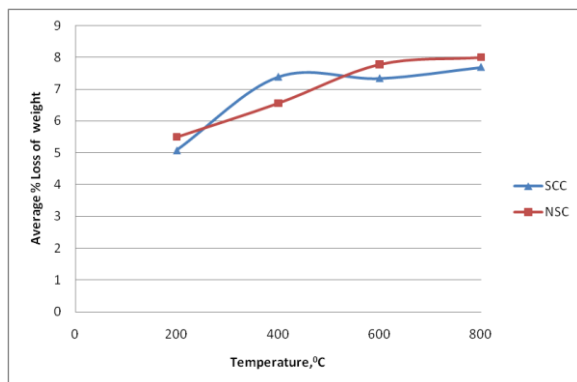


Fig. 1 Variation of % percentage loss of weight V/s temperature for NSC and SCC

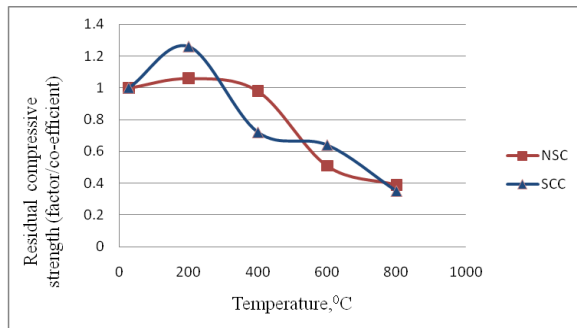


Fig 2 Comparison of residual coefficient of compressive strength of NSC and SCC

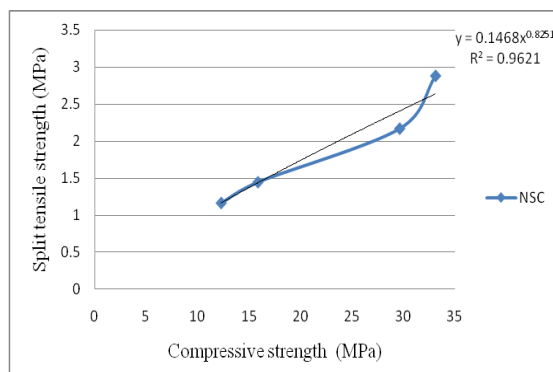


Fig. 4 Relation between residual split tensile strength V/s residual compressive strength of NSC

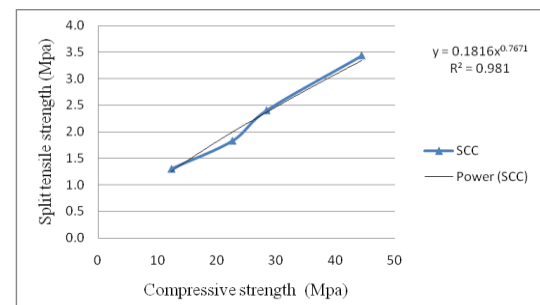


Fig 5 Relation between residual split tensile strength V/s residual compressive strength of SCC

ARCHITECTURE

A field study on the moderating effect of sound absorption on the noisy sound environment in nursery school classrooms

MUNEHIDE SAITO¹

KAZUAKI SAKODA² and

KEIJI KAWAI³

¹ Graduate school of Science and Technology, Kumamoto University, Kurokami, 2-39-1, Kumamoto 860-8555, Japan. e-mail: 105d8911@st.kumamoto-u.ac.jp

² Department of Architecture, Kumamoto University, Japan

³ Graduate school of Science and Technology, Kumamoto University, Japan

Abstract: This study investigated the effect of sound absorption on the comfortable acoustic environment of nursery classrooms. Sound absorbing boards were installed on the ceilings of three classrooms of a nursery school. The different cover ratio of the boards to the ceiling area was assigned for the three rooms in former two weeks, and then same cover ratio for all of the rooms in latter two weeks. The noise levels were compared in the three time periods of lunch, reading and napping. The lunch time noise levels of 0, 40, 80 % cover ratio were, around 75, 70, 68 dB, respectively, and those in the latter period with 40 % cover ratio in each rooms were around 72 dB, respectively. The change of the noise levels were coincided with the changing cover ratio and the level difference were smaller in the latter two weeks. These results suggest that the absorber reduced the noise levels in classrooms.

Keywords: Sound absorption, Acoustic environment, Pre-school, Classroom

Introduction

Acoustic environment in nursery schools have been less discussed than those in elementary schools or junior high schools, and, in Japan, there are no standards or guidelines at present for acoustic planning of preschool classrooms. There are several studies, however, indicate that the acoustic environment in nursery schools can be harmful to physical and mental health of children and teachers. K.P. Waye (2010) reported that the average individual exposure level of children was 84 dB (L_{Aeq}) during the active time period in the play hall or kitchen. L. Grebennikov (2007) pointed out that teachers' exposure level were over up to 85 dB (L_{Aeq}) during the six-hour workday. Furthermore, for children, a study by M. Vallet et al (2002) indicated that the acoustic environment of educational buildings affected their mental development and learning of language and reading. In order to moderate the noisy situation of the indoor acoustic environment, sound absorption is

considered to be a possible solution and this study aims to examine this effect. For this purpose, a field experiments was carried out in which sound absorbing boards were installed in the classrooms of an actual nursery school.

Experiment

The field experiment was carried out for four weeks in a nursery school in Kumamoto city. There are three classrooms each of which contains a mix-age class of about 20 children of from three to five years old. Sound absorbing boards, made of polyester, were hung on the ceilings of the classrooms using nylon strings (Fig. 1). Different conditions of absorbing area, namely about 0, 40 and 80 % of the ceiling area, were assigned for each of the three rooms in former two weeks (period 1). After that, all the rooms were set to the same ratio of 40 % in latter two weeks (period 2) (Table 1). The original surface materials of the classrooms were not apparently sound absorptive with wooden flooring (floor),

wooden or gypsum boards (partition wall), glass windows with wooden or aluminium sashes, and gypsum boards (ceiling).

To obtain the acoustical characteristics of the three rooms, impulse responses were measured for each of the rooms using the maximum length sequence (MLS) signals. MLS signals were produced by an omnidirectional speaker, received at four points per room, and processed into impulse responses.

Indoor sound was recorded in the three rooms to measure the noise levels. Since the sound levels could be affected by the distance between a microphone and sound sources (children), two microphones, both hung 30 cm bellow the ceiling with several meters distance each other, were used for recording the sound simultaneously (Fig. 2). In order to minimize the effect of the distance-dependent energy of direct sounds from the children, simultaneous sound pressure levels were calculated every 100 millisecond of the two recorded sound sequences and the lower value at every moment was chosen. These lower values can be regarded as the sound levels of far from the sound sources and thus can be regarded as the levels that represent the energy of diffused sounds rather than that of direct sounds. Recordings were done for eight hours (9:00-17:00) in three days in both of the periods 1 and 2: a day in the beginning and two days in the end of the period.

It is important to select the representative time periods for the analysis since the levels in classrooms widely changed depending on the children's activity. Thus, three time period were selected: lunch time that was one of the periods in a day when children's voice was loudest, reading time in which the teacher reads a book to the children, and napping time as background noises.



Fig.1 Installation of sound absorbing boards

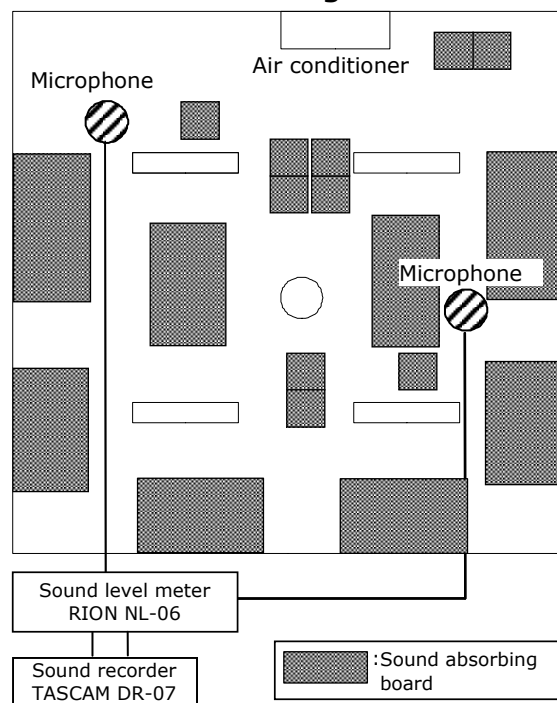


Fig.2 Arrangement of measuring instruments

Table.1 Dimension of classrooms

Classrooms	Number of children	W×D×H (m)	Volume (m ³)	Surface (m ²)	Absorber area (m ²)	
					Period 1	Period 2
A	22	6.0×7.5×3.0	137	173	none	17.1
B	20	6.2×7.5×3.0	141	176	33.4	16.8
C	21	6.6×6.6×2.4	102	102	15.3	15.3

Results and discussion

Acoustic characteristics

Fig. 3 shows the frequency characteristics of children's and teacher's voices in the recorded sound. The children's voices in playing time had its main power in 1 kHz–2 kHz frequency band, and the sound pressure level was much higher than teacher's voice. On the other hand, the frequency range of teacher's voice, with its power mainly in 250 Hz–1 kHz band, was lower than that of the children.

Fig. 4 shows reverberation time (RT) of the rooms with each absorber conditions. The RT of 1 kHz band without sound absorption was 0.75 and 0.72 s in room A and B, respectively, and 0.65 s in room C, which has a lower ceiling than the others. These RTs are considered to be too long compared to the recommended value (0.6 s) of WHO (1999) environmental noise guideline for the speech intelligibility in classrooms of elementary school and kindergarten. After the installation of the absorbing boards at 40 % cover ratio, the RT became 0.41, 0.42 and 0.37 s, respectively for rooms A, B and C. In room B, the RT at 80 % cover ratio was 0.38 second. RASTI (Rapid Speech Transmission Index) values, which were calculated from the impulse responses of the classrooms, were around 0.72 (good) and 0.84 (excellent) before and after the installation, respectively.

Next, average absorption coefficient was estimated from the RT using Eyring's formula. The average absorption coefficient of the rooms at 0, 40, and 80 % cover ratio was around 0.16, 0.26, and

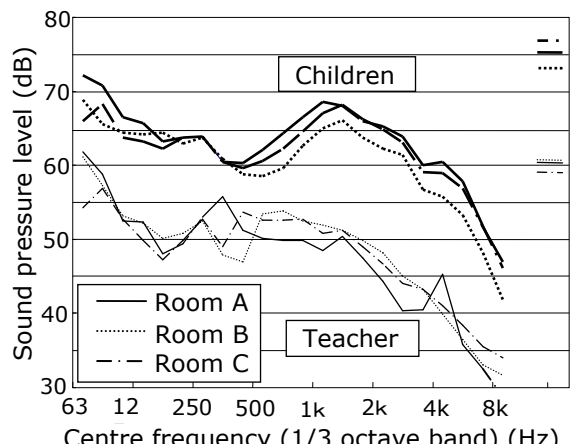


Fig 3 Frequency characteristics of children's and teacher's voices

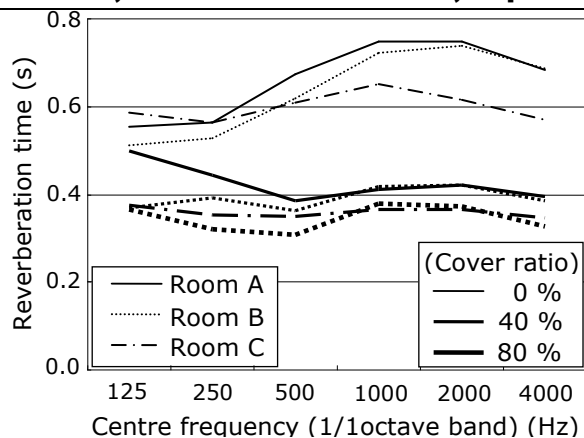


Fig.4 Reverberation time of the rooms

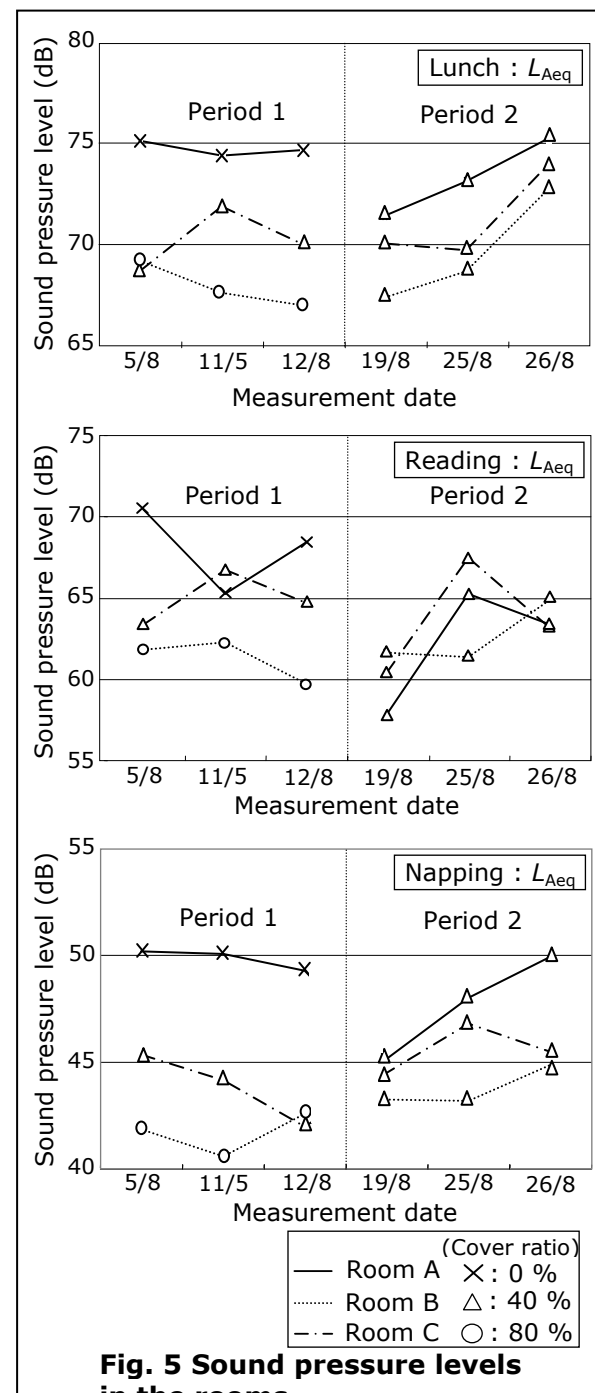


Fig. 5 Sound pressure levels in the rooms

0.28 s respectively for rooms A, B and C in 1 kHz band.

Sound pressure level measurement

The sound pressure levels (SPL) measured in the three time periods are shown in Fig. 5. In period 1, average SPL (L_{Aeq}) of lunch time in the room without sound absorption (room A) were around 75 dB and 6-8 dB higher than those in the rooms with sound absorption (rooms B and C), which were 67-69 and 69-72 dB, respectively. In period 2, in which all the rooms were set at 40% cover ratio, the lunch time L_{Aeq} were 71-75, 67-73, and 70-74 dB in rooms A, B and C, respectively and the level difference between rooms decreased to around 3 dB. This trend also appeared in the napping time L_{Aeq} . The reading time L_{Aeq} fluctuated possibly due to the types of books read but still showed the change in accordance with the condition of the sound absorption. These results suggest that the sound absorption has an effect to induce a decrease in the SPL of classrooms.

Conclusions

In this study, the effect of sound absorption on moderation of the noisy acoustic environment of nursery school classrooms was examined through a field study. The major results are summarized as follows:

- The reverberation time of classrooms without sound absorbing boards was about 0.72 s and became 0.42 s when the boards installed.
- The sound pressure level (L_{Aeq}) of the room without sound absorbing boards was around 75 dB and 6-8 dB higher than those in the rooms with boards.
- The level difference between the rooms became smaller when the condition of sound absorption was set to the same in all the rooms.

These results supported the existence of moderating effect of sound absorption on noisy acoustic environment in nursery school classrooms. The experiment was carried out in rather a short time period of four weeks and the level difference between the days of measurement was observed as well as the effect of sound absorption. A long-term measurement could elicit the effect more clearly from the daily fluctuation of the noises in

classrooms and this is a subject for further studies.

Acknowledgements

The authors would like to thank *Sakuranbo Hoikuen* ("Cherry nursery school" in English) in Kumamoto city for the cooperation and assistance to carry out this research.

References

- [1] K.P. Waye et.al, (2010), "Being in a pre-school sound environment – annoyance subjective symptoms among personnel and children", Proceedings of Inter-noise 2010, DVD-ROM.
- [2] L. Grebennikov, (2007), "Preschool teachers' exposure to classroom noise", Intl. J. Early Years Education 14(1), 35-44.
- [3] M. Vallet et al, (2002), "Some European policies regarding acoustical comfort in educational buildings", Noise Control Engineering Journal 50(2), 58-62.
- [4] WHO, (1999), Guideline for Community Noise. Website:<http://whqlibdoc.who.int/hq/1999/a68672.pdf>

STUDY ON SOUNDPROOFING WINDOWS

**QUANG NGUYEN HUY¹, YUYA NISHIMURA², TAKASHIMA YUSUKE³
and TAKASHI YANO¹**

- 1 *Graduate School of Science and Technology, Kumamoto University, 2-39-1 Kurokami, 860-8555 Kumamoto, Japan; Tel: +81 96 342 3560; e-mail: nhuyquang@yahoo.com and yano@gpo.kumamoto-u.ac.jp.*
 - 2 *Kumamoto National College of Technology*
 - 3 *Graduate School of Engineering, Sojo University, 4-22-1 Ikeda, 860-0082 Kumamoto, Japan; Tel: +81 96 326 3605; e-mail: nisimura@cis.sojo-u.ac.jp*
-

Abstract: A model for manufacturing doors and windows which are capable of natural ventilating, reducing traffic noise and so on for the developing tropical countries is presented. These windows and doors combine two basic components which are ventilation unit and lighting unit. Due to the fact that the ventilation unit must have a large volume to attenuate low frequency noise, many resonance of higher-order mode wave will be generated inside the unit. In this work, a method to predict the insertion-loss of rectangular ventilation unit with input and output openings at various positions is proposed by solving the wave equation, considering the resonance frequencies of higher-order mode. The results of the analysis have been confirmed by experiments.

Keywords: Soundproofing, resonance frequency, casement windows

Introduction

Numerous studies on assessing the acoustic performance of vented facades to inner rooms have been published. However, there are still limited researches on the particular case of housing in tropical and developing country, where the noise propagation needs to be prevented, the natural ventilation is demanded, but technique and economic condition are limited. Attending that demand, a concept for manufacturing windows which are capable of ventilating, regulating sunlight and reducing traffic noise for the developing tropical countries, especially low-cost to produce have been presented [1]-[2]. These windows combine two basic components which are ventilation unit and lighting unit. The former also serves as an import function in reducing noise.

Due to the fact that the ventilation unit must have a large volume to attenuate low-frequency noise, many resonance of higher-order mode wave will be generated inside the unit [3]-[6]. Consequently, it is

necessary to take into consideration the selection of size and placement of input and output openings in such a way that would minimize the effects of higher-order mode in order to have a great soundproofing effect. In previous papers, the characteristic of sound propagation in the rectangular ventilation having an input and output located in various positions has been presented by solving the wave equation, considering the higher-order mode effects [7]. Based on the obtained results, the cause and mechanism of resonance frequencies had been discussed in detail. To prove the theory, experiments with various positions were carried out and excellent agreement is obtained. The formulas derived from the present study enable the account of the insertion loss of the ventilation in practical applications. A method to predict the insertion loss of rectangular cavity with input and output openings at various positions was proposed [8]. However, the optimum location where an insertion loss effect is

effectively achieved is still needs to be further studied.

This paper therefore looks at literature on the subject of soundproofing windows developed by previous studies as well as publishing additional results on calculating the insertion loss of rectangular cavity with input and output openings at various positions. The paper concludes with a comparison between theoretical and laboratory measurements on different openings combinations. In summary, this paper provides a useful insight into the acoustic performance of soundproofing windows in both theory and field measurement.

Design of soundproofing windows/doors and the ventilations unit

Based on the previous reported, our proposed casement's door combines two basic components: ventilation and lighting. The lighting unit can be constructed using one or two glass layers which are mounted between two ventilation components with input and output openings. The ventilation unit can consist of square, rectangular or more complicated shapes depending on decorative considerations. Needless to say, the unit requires a simple internal structure and large input and output to maximize ventilation as well as preventing outside noise from entering the home. Actually, an input and output can be located in various positions on the cavity according to the door or window's design. Therefore, these combinations are considered as follows:

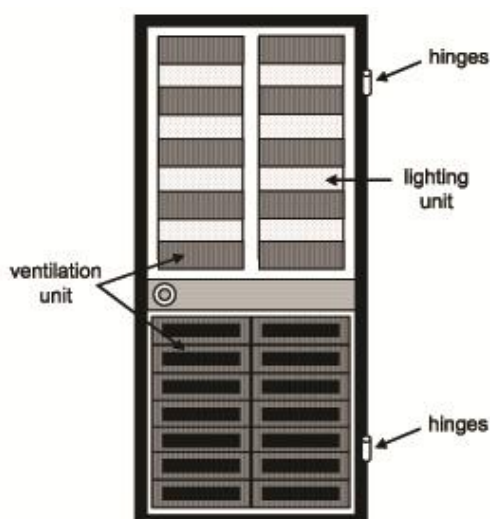


Fig. 1. The proposed casement door

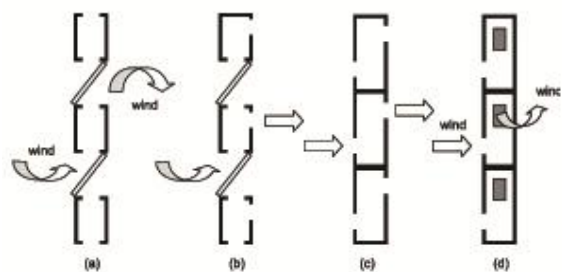


Fig. 2. Design of the proposed casement windows.

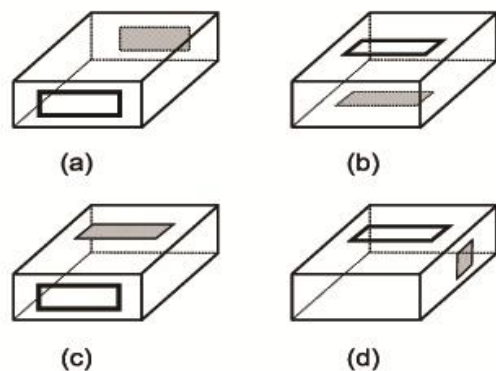


Fig. 3. Combinations of input and output positions

Combinations of input and output positions are shown in Fig. 3 in which (a) and (b) are the cases where they are in opposite faces while (c) and (d) are in faces which crossed right angles. Difference between (a) and (b) is whether they are located in big or small cavity area, however it is quite similar in the theoretical analysis. Hereafter, we name (a) and (b) as Model-1. Similarly, difference between (c) and (d) is whether they are located in big or small side area which crossed right angles. In this analysis, once we can find the acoustic characteristic when the input and output are located in arbitrary face, it is easily computable for other faces by exchanging of coordinates. We name (c) and (d) as Model-2. The sound propagation in (a) is the same as (c) and that in (b) is the same as (d).

Method of analysis

Insertion Loss

Acoustic characteristics of an acoustic element can be described by the four-pole parameters A, B, C and D as [5]

$$\begin{bmatrix} P_1 \\ U_1 \end{bmatrix} = \begin{bmatrix} A & B \\ C & D \end{bmatrix} \begin{bmatrix} P_2 \\ U_2 \end{bmatrix} = \begin{bmatrix} \cos kl & jZ \sin kl \\ j\frac{1}{Z} \sin kl & \cos kl \end{bmatrix} \begin{bmatrix} P_2 \\ U_2 \end{bmatrix} \quad (1)$$

where P_1 and U_1 are the sound pressure and velocity at the input, P_2 and U_2 are those at the output, Z is characteristic impedance, k is wave number and l is length. When this element is connected to the source, their performance can be expressed through the use of insertion loss IL defined by [6]

$$IL = 10 \log \frac{W_r}{W_0} = 10 \log \left| \frac{U_1}{U_2} \right|^2 \quad (2)$$

Here, W_r and W_0 are the radiated power at one point in space with or without the acoustic element inserted between that point and the source. The ratio of U_1/U_2 is equal to the D parameter of Eq. (1), as far as constant velocity source is concerned.

When the acoustic element is connected in series, as the sectional area of element 1 and 3 becomes significantly small as compared to the sectional area of element 2 the D parameter of whole system can be described by the following approximated equation

$$D = (\cos kl_1) (C_w) (jZ_3 \sin kl_3) \quad (3)$$

where C_w denoted the C parameter of element 2. As shown in Eq. (2) and Eq. (3), in order to obtain a reliable IL effect, D parameter must be high enough. In other words, the design of element-2 to have a high enough parameter C_w is demanded.

Computation of C_w

First of all, let we find the sound pressure on the input and output of the Model-1. The input and output have a sectional area of $S_i = 2\alpha_i \times 2\beta_i$ and $S_0 = 2\alpha_0 \times 2\beta_0$ which its

center is located at point $I(x_i, y_i, 0)$ and $O(x_0, y_0, L)$, respectively.

The complete of the wave-equation in terms of the velocity potential ϕ when expressed in rectangular coordinates is given by [1]

$$\phi = (A e^{\mu z} + B e^{-\mu z}) (C \sin \alpha x + D \cos \alpha x) \\ (E \sin \sqrt{s^2 - \alpha^2} y + F \cos \sqrt{s^2 - \alpha^2} y) \quad (4)$$

Finally, C_w can be derived as

$$C_w = \frac{U_i}{\bar{P}_0} \quad (5)$$

Result and discussion

C_w is defined by Eq.(5) including the average output sound pressure \bar{P}_0 at its denominator. In order to obtain an IL effectively C_w must be at great, in other words, low level of \bar{P}_0 is preferable. Generally, at the frequency range where the traverse waves are generated, the sound pressure \bar{P}_0 will increase and when the resonance frequencies of other modes co-occur, C_w will be small and the IL can not be expected to be as great.

Next, in order to examine the accuracy of our predicted result, the measurement in some positions on the cavity was carried out by using the previous measurement method. The measured and theoretical results of Model-2 at point A ($a/2, b, L/2$) located on the top of the cavity and point C ($a, b/2, L/2$) that locates in right side of the cavity have been obtained. The effectiveness of our calculation method has been proven. The theoretical and measured results of Model-1 at point A ($a/2, b, L/2$) which locates on the top of the cavity when the input located in opposite face has also been found. In this case, the first resonances frequencies of $f_{m,n}$ that occur sequentially are shown. Because the input was located on the big cavity area, resonance frequencies of higher-order mode generally appear in low frequency range.

Conclusions

The characteristic of sound propagation in the rectangular ventilation having an input and output located in various positions has been presented by solving the wave equation, considering the higher-order mode effects.

Based on the obtained results, the cause and mechanism of resonance frequencies of parameter C are discussed in detail. To prove the theory, experiments with various positions were carried out and excellent agreement is obtained.

The formulas derived from the present study enable the account of the insertion loss of the ventilation in practical applications. Also, it will be suitable for further study on the determination of optimized positions of input and output.

References

1. Hansen, Terri, "Copenhagen brings indigenous climate change issues to world stage | Indian Country Today | UN Declaration". Indian Country Today. Retrieved 2009-12-19.
2. Paul Gut , Dieter Ackernacht, Appropriate Building Construction in Tropical and Subtropical Regions, SKAT 1993
3. J. G. Ih The reactive attenuation of rectangular plenum chambers Journal of Sound and Vibration 1992; 157 (1); pp. 93-122.
4. Eriksson, L.J Higher order mode effects in circular ducts and expansion chambers. J.Acoust. Soc. Am. 1980; 68(2): pp.545-550.
5. Zander, Hansen Active control of higher order acoustic modes in ducts. J. Acoust. Soc. Am. 1992; 92(1): pp.244-257.
6. Yin, Y., Horoshenkov The attenuation of the higher-order cross-section modes in a duct with a thin porous layer Journal of the Acoustical Society of America 2005; 117 (2); pp. 528-535.
7. Y. Nishimura, S. Nishimura, T. Nishimura, T. Yano Sound propagation in soundproofing casement windows. Journal of Applied Acoustics 2009; 70(2009); pp. 1160-1167.
- 8.Y. Nishimura, Q. Nguyen Huy, S. Nishimura, T. Nishimura, T. Yano The acoustic design of soundproofing doors and windows. The Open Acoustics Journal, 2010, 3 (2010); pp.30-37.

ADVANCED CONSTRUCTION SYSTEMS FOR URBAN HOUSING

N. K. Garg

*Faculty of Architecture, MIT, Manipal University, Manipal – 576 104, India
e-mail: nkgcbri@rediffmail.com nk.garg@manipal.edu*

Abstract: There is fast growing demand for housing in urban areas. Speed of construction, quality of houses and affordability of the house owner are important issues to be addressed for urban housing. The paper is intended to share the research work sponsored by Department of Science and Technology (DST), Govt. of India for development of industrialized building systems with architects, planners, developers, engineers, industries, entrepreneurs, policy makers and others interested in housing. Two advanced industrialized building systems, one for 4 to 5 storey walk up apartments and the other for 10 to 12 storey housing proposed to achieve speed, quality and economy through mass construction are discussed in detail including the details of joints and connections with sketches and drawings.

Keywords: *industrialized construction, urban housing*

Introduction

Economic liberalization and industrialization is facilitating urbanization. Nearly 50% of India is likely to be urban by the year 2050. Increased buying capacity of the people and consumerism given rise to newer type of space requirements such as multi-functional dwelling spaces, spaces for fast developing home appliances, integration of cooking with lining space, flexible spaces to address changing living patterns, more and more durable and maintenance free internal / external finishes. Speed of construction, quality of construction and economy are the core issues of urban housing. Industrialized housing has the potential to address these issues. One can achieve speed of construction as well as quality of construction by prefabricating building components as an industrial product. Large volume of production of building components and their assembly at site is likely to reduce costs and result in affordable housing options. People are used to borrowing money from financial institutions and pay it back in easy installments. Some enhancement in the

value / number of installments is acceptable for quickly available quality housing.

With this preamble, Department of Science and Technology (DST), Government of India sponsored an inter-institutional research program on development of Industrialized Building System for Affordable Quality Housing at the Central Building Research Institute (CBRI), Roorkee with the author of the paper as Principal Investigator of the program. School of Planning and Architecture (SPA), New Delhi; Indian Institute of Technology (IIT), New Delhi and Structural Engineering Research Centre (SERC), Chennai being the participating institutions. Two advanced construction technologies (building systems) of construction developed under this program are as follows.

Building System 1

It is intended for 4 – 5 storey walk up apartments. It consists of columns and

beams of hollow cold rolled steel sections (approximately 200mm X 200mm in size) manufactured by the industry in standardized sizes. These are assembled on site with pre-fabricated steel joints. Floors consist of light weight folded steel sheets with insulation on either side and a composite board pasted on top. Walls consist of matrix of light weight rectangular steel tubes with composite panels for interior / exterior applications. All the steel members are coated with intumescent paints. Constructability of the system through various stages is described in following paragraphs.

STAGE 1.

Columns are located at desired points as per a dimensionally coordinated plan (Fig. 1).

STAGE 2.

Typical factory produced joints are fixed on top of columns as per location of beams (Fig. 2).

STAGE 3.

Beams, the industry produced & dimensionally coordinated hollow hallow sections having a cut in the bottom flange are placed on flange of the factory produced joints and welded in position (Fig. 3, 4).

STAGE 4.

Columns for the next storey fixed on the top of male joints already in position (Fig.5).

STAGE 5.

Floor panels manufactured in standardized sizes are placed in position (Fig. 6). The floor panels consist of folded steel sheets with EPS insulation on either side (Fig.7). These panels are screwed to the top of the beams and amongst themselves. A light weight board such as jute coir board is pasted on and desired floor finish such as PVC / ceramic tiles is provided to complete the floor (Fig. 8). False ceiling may also be provided.

STAGE 6.

Columns for the next floor already in position on top of the columns at lower floor (Fig. 9).

STAGE 7.

Wall panels manufactured in standard sizes are placed in position (Fig. 10). The wall panels consist of an assembly of light weight slotted steel tubes with EPS insulation panels and have wire mesh on either side. Spacers are provided in the mesh to hold the insulation panels in position (Fig. 11). This panel is screwed to the column beam frame at specified points (Fig. 12). The walls are completed by appropriate lining such as composite panels on interior / exterior side (Fig. 13, 14).

STAGE 8.

The process is repeated for upper floors by locating the columns on the male joints.

Building System 2

This construction system is intended for 10 - 12 storey housing in urban areas. It consists of hollow light gauge steel sections for columns & beams and folded steel sheet for floors. The columns and beams have sections of the order of 300 mm X 300 mm & 200 mm X 200 mm respectively. The surfaces are embossed for improved bond with concrete (Fig. 15). All components, factory produced in standardized sizes & profiles are assembled at site, necessary reinforcement is placed and concrete is poured to give a monolithic structure. Walls consisting of an arrangement of light weight rectangular tubes with insulation panels and welded wire mesh on either side are attached to the structural frame. Concrete is sprayed on either side to complete the shell of the building. The sequence of construction through various stages is described in following paragraphs.

STAGE 1.

Reinforcement of columns is erected at desired locations as per the plan of the housing block (Fig. 16).

STAGE 2.

Form work of the columns is placed around the reinforcement of columns that is already in position (Fig. 17).

STAGE 3.

Columns are clamped & braced suitably to check their bulging / alignment. Concrete is poured in (Fig. 18).

STAGE 4.

Form work of beams is aligned in position, screwed to the flanges of the columns and appropriately clamped & braced. Flanges of different beams on a column are also screwed (Fig. 19 & 20).

STAGE 5.

Floor panels in standardized sizes and profiles (Fig. 21) are placed in position & screwed to the flanges of beams (Fig. 22).

STAGE 6.

Necessary reinforcement is placed for beams (Fig. 23).

STAGE 7.

Desired reinforcement is also placed for floor slabs (Fig. 24).

STAGE 8.

Concrete is placed to complete the floors slabs (Fig. 25).

STAGE 9.

Reinforcement for next level of columns is erected. (Fig. 26).

STAGE 10.

Column formwork is positioned around the column reinforcement (Fig. 27).

STAGE 11.

As before, higher levels are added (Fig. 28).

STAGE 12.

Factory produced, dimensionally coordinated wall panels consisting of an arrangement of light weight rectangular tubes with insulation panels and welded mesh on either side are screwed to the

structural frame at specified points (Fig. 29). Finally concrete is sprayed on either side of wall panels to complete the shell of the building (Fig. 30).

Conclusions

The paper describes advanced technologies addressing the issues of speed, quality and affordability for urban housing. Industrialization – sufficient work done at the factory under controlled conditions is expected to bring speed in construction & improve the quality of construction. Large scale repetitive construction is expected to reduce the cost of construction for affordability. It covers detailed description of the above mentioned advanced construction technologies including the sequence of construction, details of joints & connections with the help of sketches and drawings. It is expected that attempts to adopt these advanced technologies will result in significant speed in construction, desired quality of construction as well as economy in construction. The paper is intended to share the work with architects, planners, developers, engineers, industries, entrepreneurs, policy makers and others interested in housing with a view to promote advanced construction technologies

Acknowledgements

The author is thankful to Director, CBRI, to all the team members of the participating institutions as well as CBRI for their cooperation in conducting the project. He is grateful to the DST for sponsoring this research. The paper is based on references from number of unpublished interim reports submitted to DST.

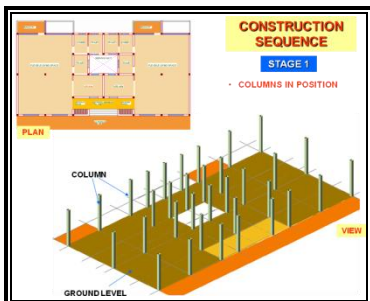


Figure 1. Columns are located.

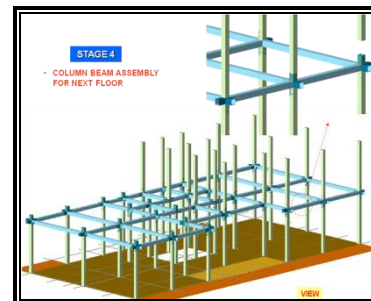


Figure 5. Columns for next storey.

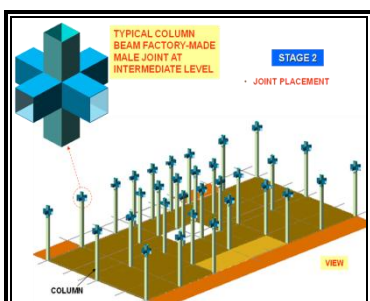


Figure 2. Joints are fixed.

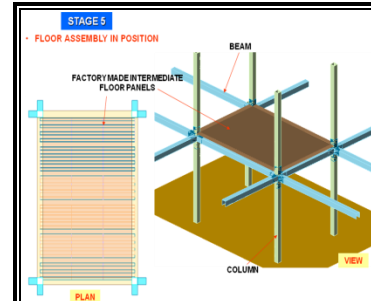


Figure 6. Floor panels in position.

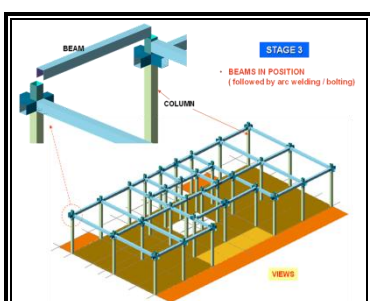


Figure 3. Beams in position.

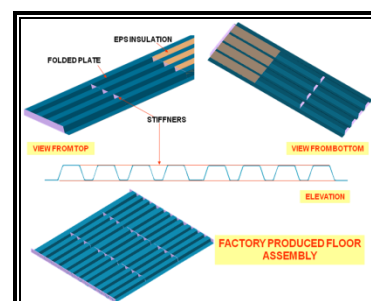


Figure 7. Floor panel details.

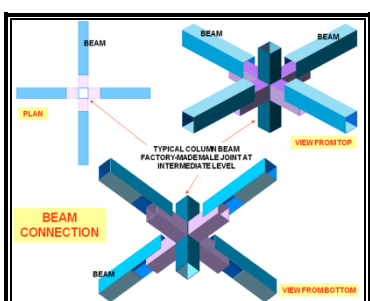


Figure 4. Detail of joints & beam.

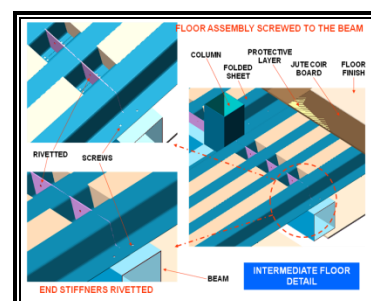


Figure 8. Fixing of floor panels.

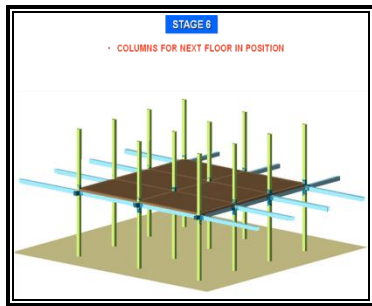


Figure 9. Ready for next floor.

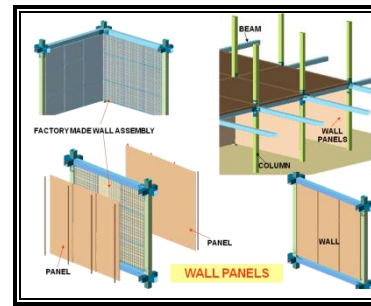


Figure 13. Lining of composite panels.

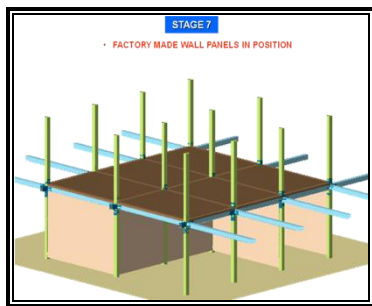


Figure 10. Wall panels for lower floor.

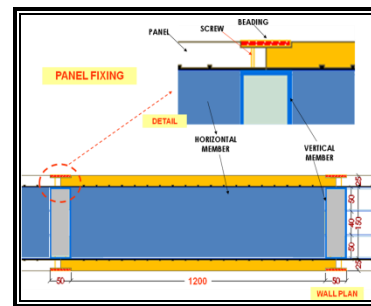


Figure 14. Fixing of composite panels.

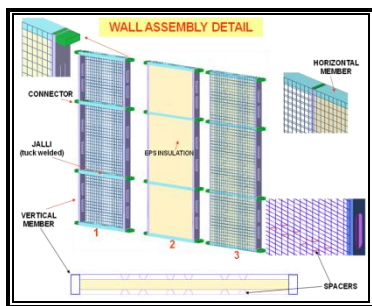


Figure 11. Detail of wall panels.

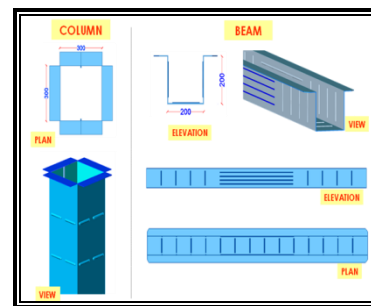


Figure 15. Column & beam profiles.

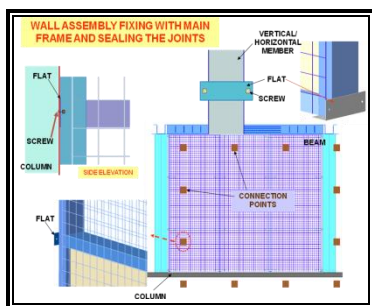


Figure 12. Fixing of wall panels.

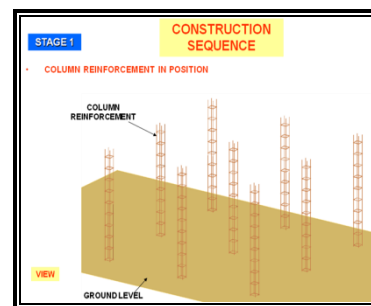


Figure 16. Column reinforcement.

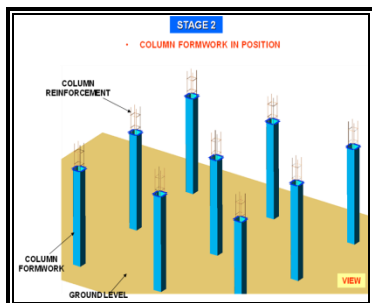


Figure 17. Column form work.

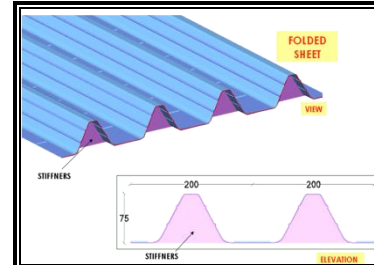


Figure 21. Floor panels.

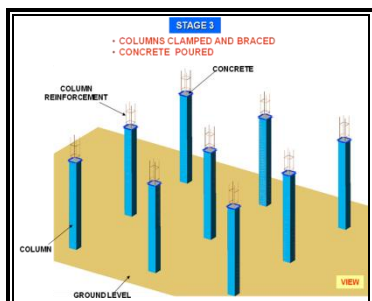


Figure 18. Columns clamped & braced.

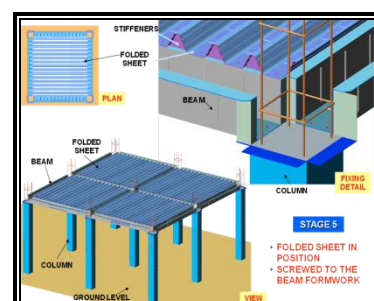


Figure 22. Fixing of floor panels.

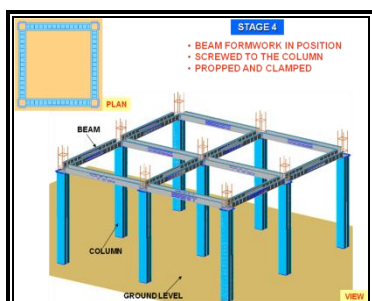


Figure 19. Beam profiles in position.

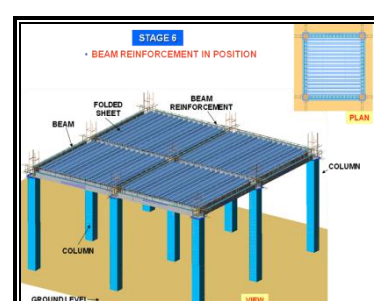


Figure 23. Beam reinforcement placed.

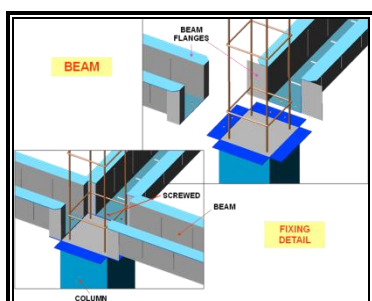


Figure 20. Fixing of beam profiles.

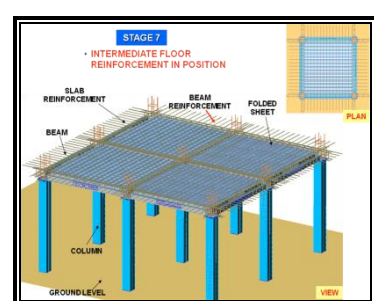


Figure 24. Slab reinforcement placed.

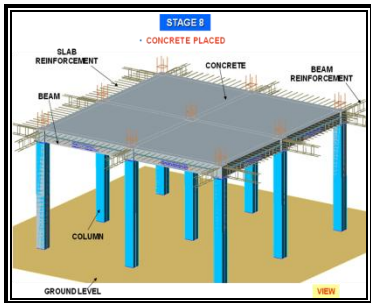


Figure 25. Concrete is placed.

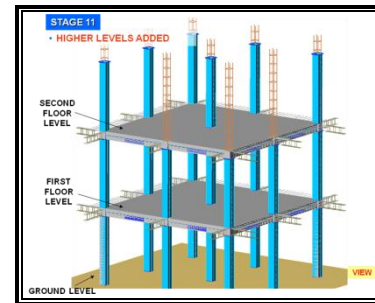


Figure 28. Higher levels added.

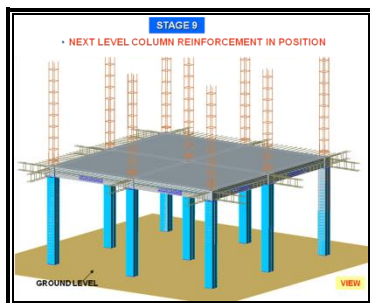


Figure 26. Column reinforcement for next floor in position.

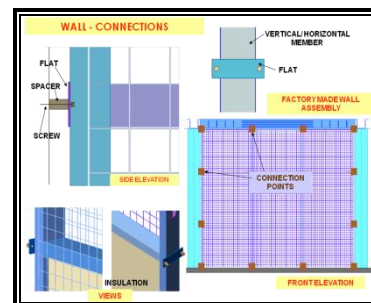


Figure 29. Wall panels fixed.

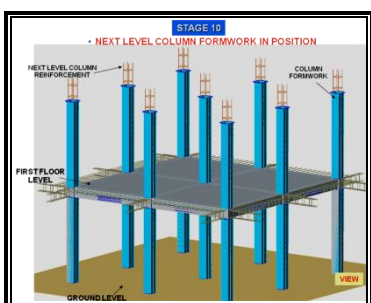


Figure 27. Column profiles.

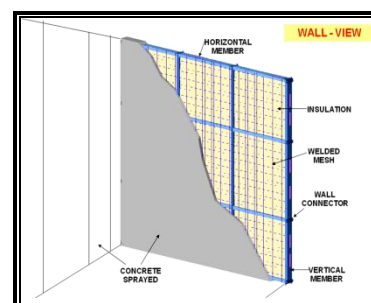


Figure 30. Concrete sprayed

Living the Common Styles---Tracing Common Paradigms between Indo-Japanese Architecture.

NISHA SOARES¹ AJAI CHANDRAN C K²

1. Faculty of Architecture, Manipal School of Architecture and Planning, Manipal – Karnataka, arch.soares@gmail.com
 2. Faculty of Architecture, Manipal School of Architecture and Planning, Manipal-Karnataka, ajaichandran@yahoo.com
-

Abstract: This article focuses on the *similarities of the Domestic and Religious culture* which is reflected in the Architecture of these geographies namely India and Japan. We need to study the rich Traditional Architecture of these identified regions. In this interesting search, the amazing facts regarding *similarities between Kerala's (South Indian State) traditional Nalukettu houses and traditional Japanese Buddhist temples* need to be highlighted. It is believed that the Nalukettu houses were influenced by the Japanese, history of how they were influenced however remains ambiguous. The *Nalukettu* is the traditional style of architecture of Kerala (called as God's Own Country) where in an agrarian setting a house has a quadrangle in the centre. Originally the abode of the wealthy Brahmin and Nair families, this style of architecture has today become a status symbol among the well-to-do in Kerala. Nalukettu is evident in the traditional homes of the upper class homestead where customs and rituals were a part of life. Temples are the places of worship in Japanese Buddhism, where these 4 religions are also strong namely Confucianism, Taoism, Emperor Worship and Shinto. Virtually every Japanese municipality has at least one temple, while large cultural centers like Kyoto and Nara have several thousands. The pagoda, a structure that has evolved from the Indian stupa, usually comes with three (sanju no to) or five (goju no to) stories.

Keywords: *Nalukettu houses, Japanese Temple Shrines, Pagoda, Stupa,*

Introduction

Architecture over the ages has been an expression of social values. This has been reflected in the domestic and religious architecture of Kerala (India's southern state) and Japan (the far-east of the globe) respectively. Although ever-changing, a distinct regional character has evolved in Kerala, decided by the local materials, climate, aesthetic values, geographical and historical factors. The same would also apply for Japanese traditional architecture. Architecture is one of the most inspired manifestations of Japanese civilizations, a pillar of both traditional society and the modern state¹.

KERALA ARCHITECTURE –NALUKETTU HOUSES

Architecture of Kerala may be classified under two broad heads, namely Domestic and Religious Architecture. The traditional

houses and the '*Nalukettu*' belong to the domestic architecture. These are timber walled houses of the Malabar Coast in different settings such as beaches, lagoons and undulating terrains. The materials used for building the houses were biodegradable in some cases. The following stages of design have been analysed as follows:-

THE ENVIRONMENT / SITE

Typically a Nalukettu is a detached, independent house in a large parcel of land surrounded by field and live stock. The position and sizes of various buildings, including the location of trees and paths earmarked the boundary which were to be decided from the analysis of the site according to the prescriptions in the classic texts.

THE SCALE

The architecture of this region has been of a humble scale, merging with nature.

ARCHITECTURAL DESIGN CONSIDERATIONS

Nalukettu is typically a rectangular structure where four halls are joined together with a central court-yard open to the sky. The four halls on the sides are named :

Vadakkini (northern block),

Padinjattini (western block),

Kizhakkini (eastern block)

and **Thekkini** (southern block).

The outer verandahs along the four sides of the *Nalukettu* are enclosed differently. While both the western and eastern verandahs are left open, the northern and southern verandahs are enclosed or semi-enclosed².

DESIGNATED FUNCTIONS

The designated functions of the four halls are as follows- *Kizhakkini* is for prayer and *pooja*, *Thekkini* for keeping wealth and for human dwelling, *Padinjattini* for storage (crops and grains in the olden days) and *Vadakkini* for Kitchen.

Thachushasthram, or the Techniques of Carpentry and Traditional *Vaastu* (Simply means instructions laid down for building a structure), is the governing science in the architectural form of *Nalukettu*. This branch of knowledge was well developed in the traditional architecture of Kerala and has its own branch of literature under the titles-Tantrasamuchaya, Vastuvidya, Manushyalaya-Chandrika, and Silparatna².

THE COURTYARD-INTERACTION ZONE.

In the *Nalukettu* design, all the rooms are open to a common court-yard which helps the family to interact more often. The open courtyard provides natural ventilation as well as adequate lighting for the household, offering a healthier environment. Abundant sunlight falling inside the house through the open central courtyard acts as a natural disinfectant and limits the presence of bacteria and fungus inside the house. The rainwater would collect in open vessels placed in the courtyard thereby enabling Rain water harvesting. The inside open verandah with open court yard provides ample space for children for their activities. The central courtyard is an outdoor living space which may house some object of cult worship such as raised

bed for Tulsi. (Sacred Plant) as seen in FIG-1

ETTUKETTU AND PATHINARUKETTU

For larger homes and wealthier families, there are more elaborate forms of the *Nalukettu*, called the *Ettukettu* (eight halled with two central courtyards) or *Pathinarukettu* (sixteen halled with four central courtyards) as in FIG-2

PLANNING AND LAYOUT

Basically the domestic Architecture of Kerala follows the style of detached building. The rectangular plan is usually divided into two or three activity rooms with access from a front passage. The projecting eaves cover a verandah all around as in FIG-3

A Kerala court yard house is a compact structure in a large compound, next to a *kullam*, bathing tank. In its most developed form the typical Kerala house is a courtyard type---*Nallukettu*. The *Nallukettu* is the principal structure of a garden compound. The setting of the building in the open garden plot was again necessitated by the requirement of wind for giving comfort in the humid climate. The garden may contain cattle sheds, bathing tanks, wells , farm buildings, grain stores (silos) , etc., as ancillary structures, the whole being protected with a compound wall or fence³.

JAPANESE ARCHITECTURE –TEMPLE SHRINES.

HISTORY

Japanese culture and tradition always followed certain principles and doctrines such as personal salvation can be attained by freeing oneself of materialistic desires and to serve public in order to achieve "Nirvana"---The state of void or nothingness whereby all mental, physical and emotional forces are in perfect equilibrium. These are the principles of Buddhism founded in India during the 6th Century BCE (Before Common Era). Nirvana could be achieved through acts such as personal meditation, invocation of Buddha's saving grace, rhythmic magical chants. And the focal point for such congregational activities was the Buddhist Temple Complex

ARCHITECTURAL DESIGN

The salient features of Tang Era Temple Architecture (without referring to the others) were the degree of visual elegance and natural balance harnessed from the environment. The Japanese believed in harnessing natural forces such as that of "Ying Yang"(a belief that there exist two complementary forces in the universe. One is Yang which represents everything positive or masculine and the other is Yin which is characterized as negative or feminine, and "Feng Shui" (is an ancient Chinese system of aesthetics believed to use the laws of both Heaven (astronomy) and Earth (geography) to help one improve life).

The Temple Complexes were located in scenic settings such as mountain tops, hill curvatures, near waterfalls and rivers. The temples were constructed according to strict principles of symmetry and axis alignment.

Symmetry referred to the placement of worship halls and pagodas in visual balance to each other. *Axis alignment* referred to the line of sight, construction of the entry gate, walking path, and worship hall, mostly on the North- South axis and to a lesser degree the East-West axis. In both cases, it was the conscious actions of mankind in partitioning sacred landscape to replicate cosmic order, and thus prepared the spiritual pilgrimage of the person entering Buddha's realm. (FIG-4) With these concepts at hand, a *grid pattern* was superimposed upon the entire temple compound to identify the building locations, main pilgrimage paths, and auxiliary walking paths⁵.

Another particular Japanese feature was the construction of temples on *raised platforms*. Due to the hot and humid climate conditions, these stilts provided the necessary ventilation along the foundation base to *prevent moisture from compromising structural integrity*⁵.

The Torii represented the *spiritual gateway* whereby the pilgrims would commence their spiritual purification tasks. Between the 7th and 19th century, Shinto and Buddhist temples were interwoven as combined worship centers. Therefore,

some Buddhist temples had the Torii gateway, while other installed the regular TANG era gateways. A good surviving example is the Japanese Buddhist-Shinto multiplex at Nashi⁵. (FIG-5)

MATERIALS

In contrast to her Asian mainland neighbours which used a combination of configurations, of wood materials for temple configurations, Japan almost exclusively used wood in such endeavours. The nation was blessed (as still is today) with abundant forests throughout all the home islands, and was thus complemented with a skilled class of woodworking artisans like their counterparts in Kerala. Wood also represented life, hence to envelope one's creation with wood was to celebrate the existence of life itself. Stone, despite its strength and time resiliency, was time-consuming to carve and incurred high transportation cost. Not to mention, the Samurai warrior class who monopolized most of the stone quarries for walled fortifications and castle escarpments⁵.

Common Paradigms between the 2 styles and their features.

(To be read along with the Matrix at the end-FIG-6)

SITE PLANNING:-

Both the layouts are detached, independent in a large parcel of land with certain waterbodies enhancing the landscape

ENTRANCE GATEWAYS:-

Both the contexts have got Bold Entrance Gateways emphasizing entrance into an abode. In Kerala the entrance structure is (*padippura*) constructed like the Gopuram of a temple. In the Japanese context this gateway has a higher scale called *torana* of Buddhist Architecture. It usually consists of two tiered roof with ornamental finials.

COURTYARD/ PRAYER HALL

In the context of Kerala, the Courtyard acts as a space for rituals besides acting as a comfort provider. One usually sees a

International Engineering Symposium, March 3-5, 2011 Kumamoto Univ., Japan

Tulsi plant in the middle of the courtyard. In the case of Japan it is the Prayer /Worship Hall which is the main focus, in some cases it houses the statue of Buddha.

ROOF FORMS

Keralan roofs are pitched at steep 45 degrees, with a curved ridge from which rafters radiate at either end and gables projecting over a hipped section suggest Japanese forms. In style and technique there are remarkable similarities between these two contexts.

In Japan, in order to maintain geometric balance with the natural surroundings, a parametric (gently angled) roof, with decorative eaves (projecting overhang at the lower portions of a roof) was conceived. A steep-angle of descent began at the top of the roof, but tapered off to a more gradual incline upon reaching the eaves. This easy-flowing rhythm blended well into the background scenery of hills, forest, mountains. The eaves were carved in a style similar to modern day French curves (FIG-7).

BRACKET & RAFTERS

Overshadowed by the immense stimuli of the temple exterior, this interlacing framework was actually the prime innovation behind the spacious interior worship hall and supported the wide parametric roof. The original challenge was to optimally enhance the "Customer Experience" of the pilgrims, by manipulating the spatial acuity of the worship hall as they directed their prayers to the Buddhist statue. Constructing a traditional high-angled narrow roof, would not have been able to cover the entire hall. Constructing a low-angled wide roof, required extensive interior support columns, which would have obstructed the spacious interior view. The solution was to stack interdependent purlins and rafters onto a limited set of columns. Purlins were horizontal wooden beams braced to the rafters. Rafters were sloping wooden beams that supported the pitched roof. Special grooves were cut into these components for a custom fit. Multiple wooden brackets were installed in a step-wise fashion at major connection points

where the purlins, rafters, and column all met. Thus, forming the critical framework underneath the roof. This was even applicable to the roofs of domestic Kerala Architecture. They arrived at *innovative joints and connection details in wood for the roof system*⁵.

ELEVATIONAL TREATMENT

The elevation is simple with clean lines rising to support the roof above which appears projecting the flow of a smooth circular arc onto its eaves.

PLANNING

In its Layout the Nallukettu house has rooms surrounding a central courtyard. In Japanese temple forms the spatial organisation starts with a bold entrance into the worship hall. The courtyard acts as a place of worship for the dwellers, whereas it is the Worship hall in the Japanese context.

COLUMNS

Depending upon the stress being channeled, three types of columns were used. The first type, "*Intercolumnar*", was the most important since it held the bracket assembly, which consisted of the leverage arm, connection block, the block itself, and the extension arm. They were strategically installed throughout the temple interior since they carried more weight than regular non-bracketed columns. The second type, "*Columnar*", was deployed near the temple perimeter and supported the nested purlins and bracket sets. The last type, "*Corner*", upheld the heavy external eaves along the corners of the temple. An intriguing characteristic is the Japanese purlin bottom attached to column's hardwood's geo-resonance quality within the column framework. It has been documented that during low-intensity earthquakes, the interlaced bracketed columns are able to convert kinetic energy from the ground tremors, into thermal energy via moderate friction among the wooden components. No doubt ancient man would have viewed this quality to be divinely inspired⁵.

MATERIALS

Timber/ Wood is the prime structural material abundantly available in many varieties in Kerala and Japan ---from bamboo to teak. The skilful choice of timber, accurate joinery, artful assembly and delicate carving of wood work for columns walls and roof frames are the unique characteristics of Traditional Kerala and Japanese Temple architecture. In Japan one views simple ceramic roof tiles, with its reflective and rhythmic qualities. In the case of Kerala, Mangalore tiles (baked mud-clay) have been used as roofing material. The resin of cashewnut seed is applied to the timber because of its availability, economy and power of preservation.

Conclusions:-

Since time immemorial, Traditional Domestic Architecture of Kerala and the Religious Architecture of Japanese Temple Shrines have had some similarities which have been reflected in their Design and Roof forms. The Design has further been influenced by climatic, geographical and historical factors. A study of this sort has enabled me as a researcher to understand the similarities in a very meticulous way.

Acknowledgements

I would like to acknowledge my Co-Author for introducing me to the Symposium to be held at Japan which enabled me to write a Research Paper for the same.

References

- [1]William H Coardrake, 2002, Architecture and Authority in Japan,
- [2]http://www.kerala-travel-tours.com/kerala_architecture/nalukettu.html
- [3]<http://keralaarchitect.blogspot.com/2009/12/design-of-kerala-nalukettu.html>
- [4]<http://knol.google.com/k/kerala-architecture>
- [5]<http://www.lehrmarch.com/japantemplearchitecture.htm>



FIG-1: These Courtyards act as ventilator. The roof drains into the sunken central area and from there out of the house. Rooms are placed around the courtyard.

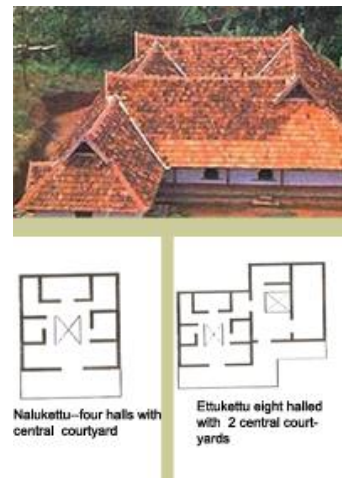


FIG-2: Nalukettu Houses and Ettukettu houses

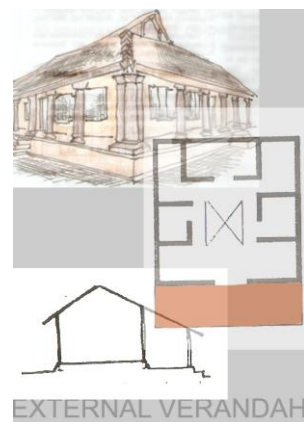


FIG-3 : Verandahs ---A transition from the outside to the inside

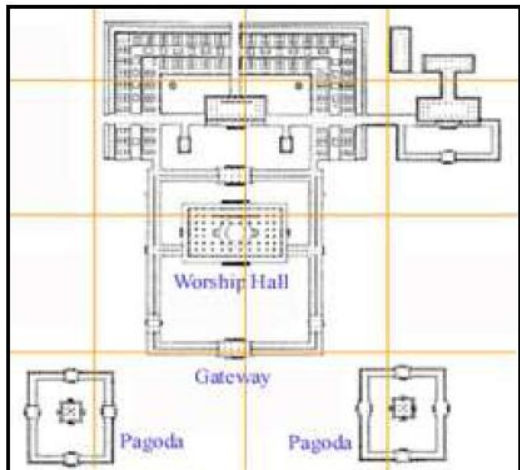


FIG-4: Symmetrical layout of the temple, pagodas, pathways. Monk residences in upper right corner is not part of this overall symmetry, but is symmetrical within its own design.



FIG-5 : Traditional Japanese TORII spiritual gateway.

FEATURES /STYLE	KERALA NALLUKETTU HOUSES	JAPAN TEMPLE SHRINES
A) SITE PLANNING		
B) ENTRANCE / GATEWAY		
C) COURTYARD PUBLIC SPACE		
D) ROOF FORMS		
E) BRACKETS & RAFTERS		
F) ELEVATION TREATMENT		
G) PLANS		

FEATURES /STYLE	KERALA NALLUKETTU HOUSES	JAPAN TEMPLE SHRINES
SJ COLUMNS		
KJ MATERIALS		

FIG-6: Comparative Matrix with Illustrations

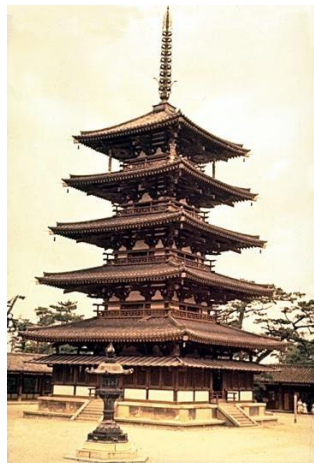


FIG-7 : Roof Forms

Beyond Activism

Ajai Chandran.C.K¹

Priti Pai²

1 Manipal School of Architecture and Planning (MSAP), Manipal University, Manipal-576104, India. email : ajai.chandran@manipal.edu

2 Manipal School of Architecture and Planning (MSAP), Manipal University, Manipal - 576104, India. email : pmpai88@gmail.com (Intern from University of Florida USA)

Abstract: What we, as a society, build is shaped by what we know and feel. The built environment carries not only historical and socio-economical implications, but speaks of our priorities as a community. Hence, a need for a more relevant planning, architecture catering towards today's environmental and humanitarian crisis is being felt; one that planners and architects are actively responding to. Studies by the United Nations Human Settlements Program (UN-HABITAT) declare that "about 40% of the world's population by 2030 will need to have housing and basic infrastructure services." Like-minded organizations, including Leadership in Environmental Design (LEED) Network and the Social, Economic, and Environmental Design (SEED) Network, provide architects an opportunity to look beyond aesthetics and tackle these problems in our communities. Opportunities are rising for planners, architects to take action, to implement environmentally and socially sound practices, but a shift is required in our thinking: from the needs of an individual or specific group to the collective.

Keywords: *built environment, UN-HABITAT, communities, environmentally and socially sound practices*

The Built Environment

Most of us exhibit a one-dimensional understanding of our surroundings; we walk, drive, or cycle through our communities daily, internalizing and accepting what we see around us- but not consciously relating to it. Most of us consider the environment as an autonomous figure in our life, something that just exists in parallel and can be meddled with to our liking. What most people fail to gather, however, is that our built environment is merely a physical extension of our psyche as a culture, as a society. Our surroundings tell our stories, expressing our collective ideas, beliefs, and priorities; a city's dominate skyline may speak of humanity's need to conquer the environment, while a secluded cottage in the forest may speak of an individual's more intimate desire to experience nature. What we, as a society, build is shaped in a plural manner: by many hands and minds, expressing what we think and how we feel. We are intrinsically tied to our surroundings: historically, socially,

economically, and politically. The transformative nature of the buildings around us narrates a time-line of events, of beliefs. We can analyze and understand the different eras and social factors of a building's façade or a city plan.

Architects act as a bridge between society and physical expression, framing the community's priorities into the built environment. A need for a more relevant architecture catering towards new, rising issues is being felt worldwide. The call for an architect is usually reserved for the privileged or elite; often used by big corporations to make their authority and money visible. What does this say about our priorities as a society when the most important buildings of our time are monuments to wealth and consumption? By expanding both our minds regarding the built environment, and the groups served by architects, the profession can move beyond aesthetics and become something more meaningful.

Complexities of the Urban Fabric

"Proceeding through the space in the city we move within a network of overlapping perspectives in motion. As the body advances, vistas open and close- distant, middle, and near views palpitate. The shifting movement between near and far objects, walls, and buildings makes an always-changing, visually tectonic landscape called 'parallax.' The promenade elicits a host of spontaneous intertwined experiences within urban space. In the complex spaces of the modern city, buildings are not so much objects as partial visions forming a perspectival continuum" -Steven Holl, *Intertwining*

Perhaps the most pressing issue involving the built environment of our lifetime is the nature of the city. The city serves society as a conglomeration of events, bodies, situations: a series of spontaneous events unfolding before our eyes while simultaneously folding our identities into them. These hubs of activity, energy, and people speak of a culture of production and consumption, but also hold a deeper meaning: acting as a beacon of hope, of opportunity in an otherwise relentless landscape.

Today more than ever, urban landscapes are growing at unprecedented rates. Mike Davis quotes United Nations research in *Planet of Slums*, stating that in 1950; only 86 cities existed with a population of more than one million, whereas today there are 400 cities, with a projected 550 cities by 2015 (5). The UN states that cities are now home to half of humankind. This phenomenon is taking place globally, but the process can be closely observed in the Asian continent, where the majority of the world's *mega-cities*, cities defined as having 10 million or more occupants, exist. Between the years 1990 and 2010 alone, population growth in urban sections of Asia equaled the combined populations of the USA and the European Union; no other continent has experienced an increase of this size and in such a brief time (8). Furthermore, these massive pockets of occupation are fusing with other major populated areas, forming colossal urban corridors and regions.

Issues of technology, ideology, and population growth have especially accelerated the new urbanized era, illustrating a global cultural shift towards urbanism. It is clear that cities act as centers of production and consumption, generating opportunity and wealth; but they also carry inherent issues such as disease, crime, pollution, poverty and social divide. In many cities, especially in developing countries, slum dwellers make up more than 50 per cent of the population, having little or no access to shelter, water, and sanitation, education or health services. The UN Human Settlements Program (UN-HABITAT) estimates that 600 million urban residents and 1 billion rural dwellers in developing countries live in 'overcrowded housing with poor water quality, lack of sanitation, and no garbage collection.' In extreme situations, people live in old buses or shipping containers, among other forms of inadequate housing (6).

The issue of creating adequate housing is one that UN-HABITAT emphasizing and documenting; explaining that "about 40% of the world's population by 2030 will need to have housing and basic infrastructure services (2)." This is especially exaggerated in developing countries, as thousands desperately flock to the new opportunities the urban landscape offers. The housing crisis is multi-dimensional—caused by such factors as rapid urbanization, economic restructuring, natural disasters, and displacement from political events such as regime changes and wars. China's rapid urbanization puts the situation in perspective, as its quickly growing economy will create a need for more than 200 million new housing units in the next few decades; that is almost twice the amount of existing housing units in the United States (2).

The issue of natural disasters causes communities to shift between urban and rural landscapes, and usually results in devastation and displacements of thousands of people. The recent devastating floods in Pakistan submerged one-fifth of the country and have left more than 1.89 million homes destroyed, with even more people displaced. Estimations

International Engineering Symposium, March 3-5, 2011 Kumamoto Univ., Japan

show that by 2050, as many as 200 million people will experience displacement by climate change and natural disasters (3). These studies show that catastrophic natural disasters may become an ongoing story and cannot be ignored.

Major political issues can also force whole communities to migrate towards already-crowded cities; one example of this is Porto Romano, Albania. Porto Romano hosts a community of an estimated 6,000-10,000 people: half of which live in a rundown factory formerly used to make pesticide lindane and chromium-6 for tanning leather. (These chemicals are extremely toxic and have been linked with health problems such as breast cancer, ulcers, and seizures.) Most of the occupants settled in the factory in 1991, after the collapse of communism in Albania which caused thousands to migrate into the city. Eight years later, the 1999 war in neighboring Kosovo moved even more refugees into Albania, an estimated 450,000. The 750-acre site was an inviting home for the poor and displaced because of its available building materials and supply of water and electricity (2). Declared a disaster area in 2001 by the UN Environment program because of the enormous amounts of exposed toxic chemicals, the authorities were urged to close the factory and relocate those living within it. Unfortunately, the country's new, shaky government has failed to take much action on the matter. This situation in Albania is just one of many examples describing how major political events are capable of displacing thousands of people, leaving them with inadequate resources and shelter.

The benefits of a city cannot be ignored, but we, as a society, must re-organize our priorities and tackle these pressing issues of our times. Over the past two decades, Asian governments have realized that urban expansion is a major factor in economic development, but investment in infrastructure, including housing, has failed to match increasing demographic pressures. The previously mentioned organization, UN-HABITAT, is one example of an organization actively seeking to solve these problems. It is a human settlements agency mandated by the UN General

Assembly to promote socially and environmentally sustainable towns and cities, with the goal of providing adequate shelter for all. UN-HABITAT's work is directly related to the United Nations Millennium Declaration, particularly the vow to improve the lives of at least 100 million slum dwellers by the year 2020 (7).

The role of the Planner, Architect, Urban Designer

Groups like UN-Habitat are setting a standard for humanitarian development to be pursued in the situations previously described, and many other organizations and architects are following their lead. If we are to broaden the work of an architect, to expand the clients we serve, than this movement can progress beyond activism, and become a reality.

World renowned Japanese architect, Shigeru Ban, provides an excellent example of an architect using innovative technologies to better human lives. Ban has worked on projects of various scales and purposes, from museums to houses, but his most interesting works are his disaster-relief projects: including work in Sri Lanka after the 2004 tsunami, Turkey after a 1999 earthquake, and most currently in Haiti. After the 1995 earthquake in Kobe, Japan, Ban responded with ingenious designs for temporary houses and a community center, all with cardboard tubes. The foundation of the houses consisted of donated beer crates loaded with sandbags, with walls made of 4mm thick paper tubes, and tenting material for the roof. A waterproof sponge tape is sandwiched between the paper tubes of the walls, providing insulation. The units are easy to dismantle, and the materials easily disposed or recycled. Ban's design proves to be well-thought out, innovative, and cost-effective. Similarly, After the Gujarat Earthquake struck India in 2001, Shigeru Ban ventured to the city of Bhuj and provided designs for temporary housing units, again from paper tubes. This time, rubble from the destroyed building was used as a foundation and was coated with the traditional mud floor. The roof uses a split bamboo rib vault system, and a whole bamboo for ridge beams. Two locally

International Engineering Symposium, March 3-5, 2011 Kumamoto Univ., Japan

woven cane mat were placed over the ribs, with a clear plastic tarpaulin sandwiched between, providing protection from rain. Ban provided natural ventilation through the gables, where small holes in the mat encouraged air to circulate: allowing cooking to be done inside, as well as repelling mosquitoes (4). Using local materials and taking cultural aspects into consideration, Ban's disaster-relief work serves as a remarkable example for others pursuing humanitarian design. His use of paper isn't designated for disaster-relief projects either: Ban has used them to construct simple refugee tents, but also for a luxurious weekend retreat and a soaring exhibition pavilion. In an interview with *Architectural Record*, Ban explains that the most important part of this kind of work "is to go there immediately and meet the right people. Architects tend to be very bureaucratic. So there are lots of discussions but nothing happens. From experience, I know I just have to go there, even without any connections, to find out who needs what. Then one thing leads to another."

Shigeru Ban is leading the way for many up and coming architects, and organizations like Social, Economic, and Environmental Design (SEED) Network provide architects that may otherwise have trouble seeking these projects, a place to gather and collect ideas. SEED® is a "principle-based network of individuals and organizations dedicated to building and supporting a culture of civic responsibility and engagement in the built environment and the public realm (1)." Its purpose is to share practices and ideas, creating a 'pool of knowledge' for interested professionals and public "based on a set of shared principles (1)." The organization works to connect people from all planning disciplines: engineers, architects, urban planners, etc.

The SEED network was formed subsequent to the Leadership in Environmental Design (LEED) Network, a network provided for architects to understand the environmental footprint of their construction and building. The group is an internationally recognized green building certification system whose goals include: "defining 'green building' by establishing a common standard of

measurement" and "promoting integrated, whole-building design practices," among many. The rating system addresses eight major systems, including 'location and planning, sustainable sites, water efficiency, energy and atmosphere, materials and resources, indoor environmental quality, innovation and design process, and regional priority.' This organization has become a basic standard of construction, and many people have begun using the terms LEED certified buildings and "sustainable design" simultaneously. Though LEED provides architects a means of measuring a building's environmental consequence, there are still many gaps in the system, including a misguided definition of 'sustainable' building.

For one, a LEED certified building just checks that a building has been constructed efficiently- it does not undertake the building's economical footprint in the long-term. But more importantly, we must look into the term 'sustainable' and attempt to grasp its full, complete meaning. This term has completely turned the building industry upside-down, but many seem to lack an in-depth understanding of what it means. In the United Nations report, *Our Common Future*, sustainability is quoted as follows, "Humanity has the ability to make development sustainable to ensure that it meets the needs of the present without compromising the ability of future generations to meet their needs (9)." This asks the present generation "to make every decision on behalf of the seventh generation to come" to design thoughtfully and with foresight. Basically, an organization like LEED does well to touch on the idea of sustainability, but cannot be thought to encompass the entire idea. Quoted from *Our Common Future*, "Sustainable development requires meeting the basic needs of all and extending to all the opportunity to fulfil their aspirations for a better life. A world in which poverty is endemic will always be prone to ecological and other catastrophes." It seems that the very idea of sustainability stems from the idea of thinking collectively, thinking of others, and recognizing poverty as a major issue.

International Engineering Symposium, March 3-5, 2011 Kumamoto Univ., Japan

The idea of affordable housing, itself, holds a negative connotation in today's society, often bringing to mind a bad design reserved for the poorest inhabitants. Unfortunately, those who can afford to build expensively and inefficiently often do. English-born Indian architect Laurie Baker, spent his career in India, especially in the southern state of Kerala, delving into the practice of affordable design. He states,

"Cost-effective houses are not just for the poor, they are for everyone. The equation that a cost-effective house is a house for the poor, implying a bad looking house, can definitely be proved wrong. Isn't it the responsibility of the upper and middle classes to stop indulging in extravagance and make better looking houses instead? This entire classification is wrong."

The sheer diversity and volume of Baker's architectural wonders, as well as his innovative concepts, makes his work very significant in architectural studies. His work varies greatly: from building a dance village and fishermen's huts to designing chapels and churches. Though the scale and purpose varied, his work held a common thread of purpose: building what was necessary, and excluding all that was unnecessary.

Baker, an English-born Indian, lived and worked in India for over 50 years. He later set up an organization in Kerala, called COSTFORD (Centre of Science and Technology for Rural Development), for spreading awareness for low cost housing. He used traditional, time-tested methods to deal with the unique climate and factors of the region. His designs questioned all that we take for granted: from cutting unnecessary door frames to re-designing the nature of a window, Baker sought to find the most efficient solution. His houses often exhibited the brick *jali* design, using a perforated brick screen both to naturally ventilate the spaces and to create intricate patterns of light and shadow on the floor. With his expert use of local materials, from the masonry construction of the walls to the traditional sloping terracotta-tile roofs, Baker fused locality and efficiency to create intimate and smart spaces.

The organization, Habitat for Humanity, is a religiously affiliated group that focuses

on affordable design all over the world. In Mongolia, the organization has partnered with JCS International to build homes using a combination of traditional Mongolian techniques and Western methods and materials. After communism collapsed in Mongolia a decade ago, thousands of nomads and rural dwellers flocked to Ulaanbaatar, the capital of Mongolia that now serves the home for a third of the country's population. These new crowds arriving have resulted in the rise of get districts circling the developed city center (a get, also known as a yurt, is a round felt tent used by nomadic herders in Mongolia). These rising districts have no access to drinkable water or sewage, and poor indoor air quality of the housing structures causes over-exposure to smoke, resulting in many respiratory problems for the inhabitants.

The JCS International/Habitat project aims at improving indoor air quality by maintaining consistent indoor temperatures as well as improving upon the traditional get stove by reducing its pollution factor. This project serves as an example of an organization seeking to both protect a community's traditional practices while developing sustainable means of living (2).

Conclusions

Opportunities are rising for planners, architects, development related professionals to take action, to implement environmentally and socially sound practices, but a shift is required in our thinking: from the needs of an individual or a particular user group to the collective.

Acknowledgements

The Manipal University, India had given all the environment and support for the networking which enabled for this joint venture paper.

References

- [1] Abendroth, Lisa & Field, Eric. "SEED Pledge" (2011) Website:
<http://www.seed-network.org/join/pledge.php>.
- [2] Brown, Valerie. (2003) "Give me shelter: the global housing crisis". Website:
http://findarticles.com/p/articles/mi_m0CYP/is_2_111/ai_99185877/

International Engineering Symposium, March 3-5, 2011 Kumamoto Univ., Japan

[3]Refugees International: Executive Summary, "Confronting Climate Displacement: Learning from Pakistan's Floods" (2010). Website: <http://www.refugeesinternational.org/policy/in-depth-report/confronting-climate-displacement>

[4] Shigeru Ban Architects, "Works- Paper Tube Structures". Website: http://www.shigerubanarchitects.com/SBA_WORKS/SBA_PAPER/SBA_PAPER_6/SBA_paper_6.html

[5] UN Department of Economic and Social Affairs, Population Division, World Urbanization Prospects, the 2001 Revision, New York 2002.

[6] United Nations Report, 2005. "Financing Urban Shelter: Global Report on Human Settlements 2005"

[7] United Nations declaration in Target 11, Millennium Development Goal No. 7 and Target 10

[8] UN-HABITAT Report: The State of Asian Cities 2010/2011.

[9] Wilson, Barbara. "The Architectural Bat-Signal: Exploring the Relationship between Justice and Design" in Design as Activism. New York: Metropolis Books. 2008.

**ELECTRICAL, ELECTRONICS,
COMPUTER ENGINEERING
&
RELATED FIELDS**

Bandwidth Enhancement of Circularly Polarized Square Slot Antenna with Separated L- Probes

RONALD JOSEPH SHUHEI NAKAO and TAKESHI FUKUSAKO

Department of Computer Science and Electrical Engineering, Kumamoto University, Kurokami, 2-39-1, Kumamoto 860-8555, Japan. e-mail: ronald@st.cs.kumamoto-u.co.jp, nakao@st.cs.kumamoto-u.co.jp, fukusako@cs.kumamoto-u.co.jp,

Abstract: A novel circularly polarized square slot antenna with separated L-probes to enhance circular polarization bandwidth is presented in this paper. Placing Stubs in the slot by studying the electric field could enhance the axial ratio (AR) bandwidth of the antenna by around 10%. Also creating an L-shaped slot on the ground plane, where the electric field rotates in the desired clockwise direction, can further enhance the bandwidth by 7%. A <-10 dB S_{11} bandwidth of 46.15% from 2.5 to 4 GHz and a < 3 dB axial ratio bandwidth of 50.35% from 2.6 to 4.35 GHz could be achieved with the present design. The antenna also shows a cross polarization discrimination of more than 15 dB on a wide azimuth range and achieves a maximum gain of 5.45 dBic. The measured results well comply with the simulated results.

Keywords: *circular polarization, L-probes, broadband characteristics*

Introduction

Circularly polarized antennas have been extensively studied recently and received much attention because of their alluring applications in satellites, RADARs, GPS and mobile communications, Chen et al. (2009) and Fukusako et al. (2003). The two orthogonal linearly polarized modes of equal amplitude and quadrature phase difference to obtain circular polarization are typically generated by the use of a feeding structure as mentioned in Wong and Lin (1998). Circular polarization can also be achieved by adding two orthogonal strips or by inserting a pair of slits as in Row (2004). Single feed circularly polarized antennas are more advantageous since they have simple design but the downside is their considerably narrow bandwidth. Thicker substrate with low dielectric constant is the most commonly used method to enhance the bandwidth. The large inductance that ensues is the drawback of such antennas because it not only causes high cross polarization but also limits the bandwidth to less than 10% of the resonant frequency. In order to overcome this problem, the use of an L-shaped probe or an L-shaped ground plane with air as the dielectric is recommended

in Chang et al. (2003). A printed slot antenna design is a desirable solution if the antenna bandwidth has to be improved without increasing the antenna size and thickness. An attracting feature of slot antenna is the ability to provide greater bandwidth when wide slot is used as the radiating element. Also, it provides bidirectional radiation, simultaneous RHCP and LHCP, along with greater manufacturing tolerances compared to normal microstrip patch antennas. Since the polarization sense changes from RHCP to LHCP and vice versa when reflected, an antenna which could receive both senses is significant, when the antenna need to receive the reflected signal if the direct signal is obstructed.

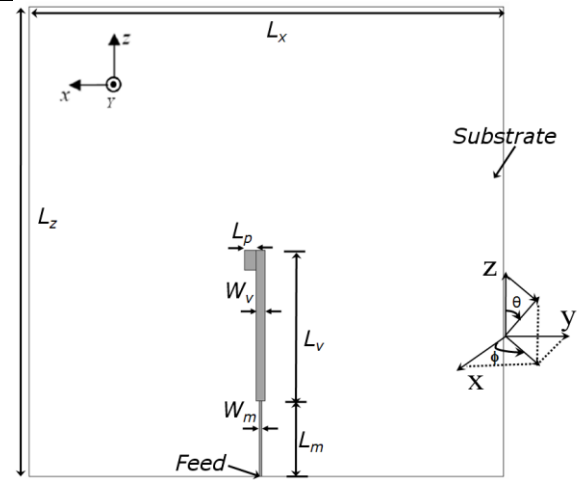
The CP bandwidth achieved by a coplanar wave guide (CPW) fed square slot antenna in Chen et al. (2003) is 17% and only 12.9% of CP bandwidth is achieved by the microstrip line fed cross- patch-loaded square slot antenna in Chou et al. (2007). The planar circular slot antenna in Tseng and Han (2008) claimed to have impedance and CP bandwidth of 38% and 44% respectively but the antenna has a size of 100×100 mm and shows high cross polarization except in the bore sight direction.

This paper presents a wideband planar square slotted antenna with horizontal and vertical components of the L-shaped probe separated and fabricated on the front and back side of the substrate. The effect of placing stubs in the slot, which could control the undesired electric field rotations in the slot, is proposed to improve the AR bandwidth to 43.75%. Having an additional L-shaped slot on the right side top corner of the ground plane could further improve the CP bandwidth to 50.35%. The simulated input and far field characteristics are compared with the experimental results and are in good agreement.

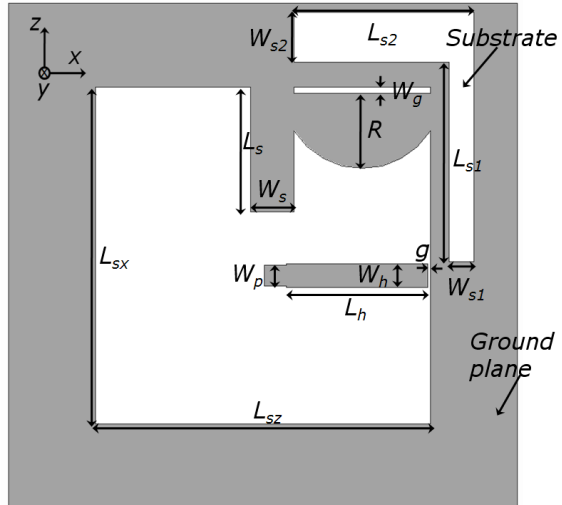
Structure and Design

The structure of the antenna is shown in Fig. 1. The antenna is designed at a centre frequency of 3 GHz and uses a 0.8 mm thick Arlon Diclad 522 substrate with a permittivity (ϵ_r) of 2.5 and a dielectric loss ($\tan \delta$) of 0.001. The substrate dimension is fixed as $L_x = 82$ mm and $L_z = 81$ mm which is at $0.82 \lambda_0$ and $0.81 \lambda_0$ respectively, where λ_0 is the wavelength at the centre frequency of 3 GHz. The square slot has a dimension of $L_{sx} = L_{sz} = 54$ mm and is designed to be around $\lambda_0/2$ of the centre frequency. The L-probe is fed through a 118Ω inductive microstrip feed line which has a width (W_m) of 0.4 mm and length (L_m) of 13.5 mm. This is to cancel off the capacitive impedance at the edge of the slot of the antenna and to match with the impedance of the 50Ω feeding coaxial cable. CP is generated when the two orthogonal linear components, E_θ and E_ϕ , have the same amplitude and 90° of phase difference. The vertical (L_v) and horizontal (L_h) components of the L-shaped probe respectively generate the E_θ and E_ϕ constituents of the CP. The vertical probe that succeeds the microstrip feed line, designed at around $\lambda_0/4$ of the centre frequency, is 26 mm long (L_v) and 1 mm wide (W_v). The phase condition of CP prominently depends on this parameter.

The horizontal and vertical components of the L-shaped probe are separated and placed on the front and backside of the substrate to enhance the capacitance in the antenna. By incorporating capacitance in the antenna, the phase difference can be set to 90° , which yields to broadband CP.



(a) Front View



(b) Back View

Fig. 1 Antenna structure

A 2-mm long patch (L_p) of 3.4-mm width is attached at the end of the vertical probe, also to enhance the capacitance. The horizontal component of the L-probe has uneven widths. The region (W_p) of the horizontal probe equals the width of patch L_p placed at the front side of the substrate. The remaining portion of the horizontal probe has a width (W_h) of 3.8 mm and a 0.1 mm gap (g) is made between the horizontal probe and the ground plane, so as to enhance the capacitance.

Different parametric studies are conducted on the antenna using Ansoft HFSS 10.1 simulation software, which utilizes 3D full wave finite element method (FEM).

The antenna is initially analyzed with a square slot, without having any stubs in the slot and additional L-slot at the top right corner of the ground plane. The CP bandwidth was only 33.84% even after optimizing different parameters of the antenna. In order to enhance the bandwidth, the electric field vector behaviour in the slot of the antenna for one complete cycle is studied at 3 GHz. The polarization phase of the electric field vector at 0° , 120° and 240° is shown in Fig. 2.

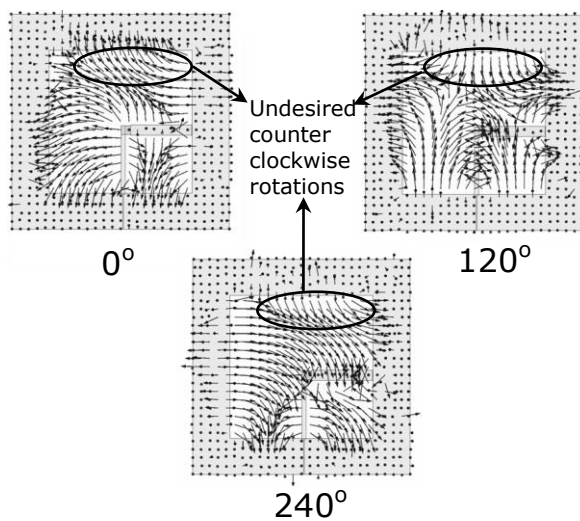


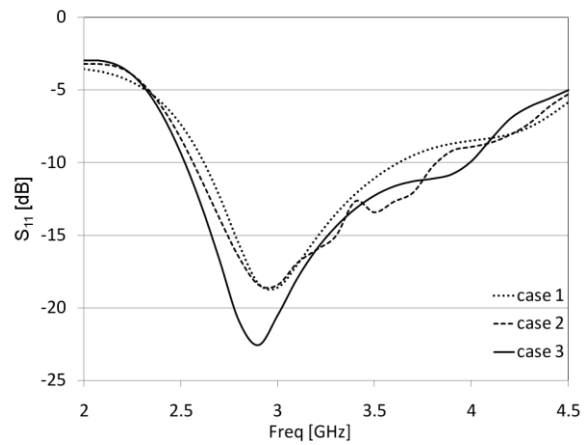
Fig. 2 Electric field vector behaviour in the slot at 3 GHz

A complete clockwise rotation of the electric field vector in the entire slot is required to have a pure wideband CP. But at the marked regions in the slot, the electric field vector shows undesired counter clockwise rotations. So, a rectangular stub of width $W_s = 7$ mm and length $L_s = 20$ mm, and a semi-circular stub with a radius $R = 12$ mm, are placed in the slot so as to eliminate the counter clockwise rotation. The semi-circular stub in the slot is placed in such a way that, it creates a 22-mm long rectangular slot of width $W_g = 1$ mm. These parameters are optimized through parametric studies. Placing stubs in the slot can enhance the AR bandwidth to 43.75%, which is approximately 10% more than the antenna without stubs in the slot.

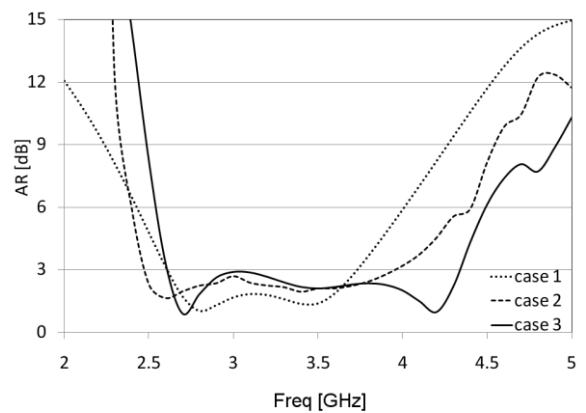
In order to further enhance the bandwidth, an L-shaped slot is created at the top right corner of the ground plane. Different parametric studies are conducted

to optimize the position and the parameters of this slot. The electric field vector in this slot also rotates in the clockwise direction, which leads to the enhancement of the CP bandwidth to 50.35%. The optimized slot dimensions are $L_{s1} = 32$ mm, $W_{s1} = 4$ mm, $L_{s2} = 29$ mm and $W_{s2} = 8$ mm.

For comparison, the S_{11} and axial ratio (at $\phi = \theta = 90^\circ$, i.e., in the +y direction) characteristics of the antennas, without stubs and L-slot (case 1), with stubs without L-slot (case 2) and with stubs and L-slot (case 3) are shown in Fig. 3.



(a) S_{11} characteristics



(b) AR characteristics (+ y direction)

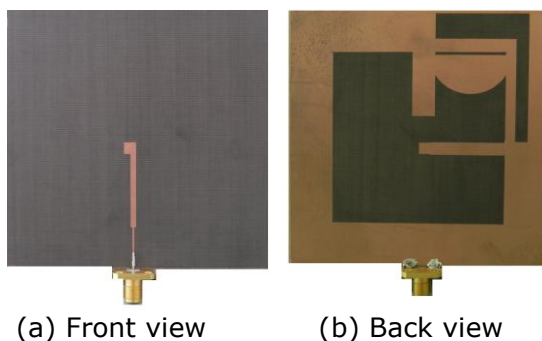
Fig. 3 Comparison between antenna characteristics

The bandwidth is enhanced even in S_{11} characteristics from case 1 to case 3 because the antenna becomes more capacitive with the addition of stubs and L-slot. The resonance frequency of the antenna remains unchanged but the < -10

dB S_{11} bandwidth is improved from 37.5% to 41.8% to 46.15% from case 1 to case 3.

Experimental Results

The antenna with stubs in the slot and additional L-slot (case 3) is fabricated on an Arlon Diclad 522 substrate with thickness of 0.8 mm. The photograph of the fabricated antenna is shown in Fig. 4. The measured results are compared with the simulated results and explained in this section.



(a) Front view

(b) Back view

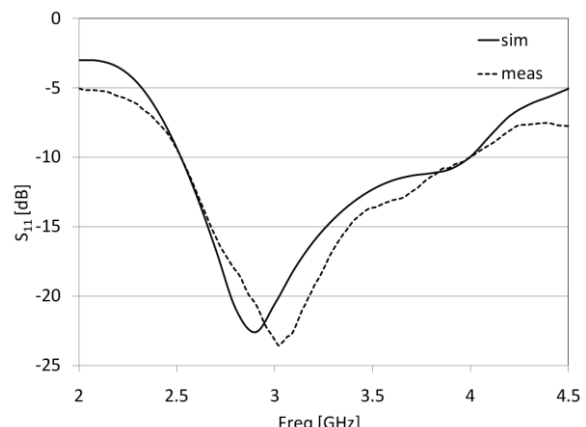
Fig. 4 Fabricated antenna

The simulated and measured S_{11} characteristics of the antenna are shown in Fig. 5 (a). The antenna resonates at around 3 GHz and the measured characteristics are well matched with the simulated results. A < -10 dB bandwidth of 46.15% from 2.5 GHz to 4 GHz is obtained in simulation as well as in measurement.

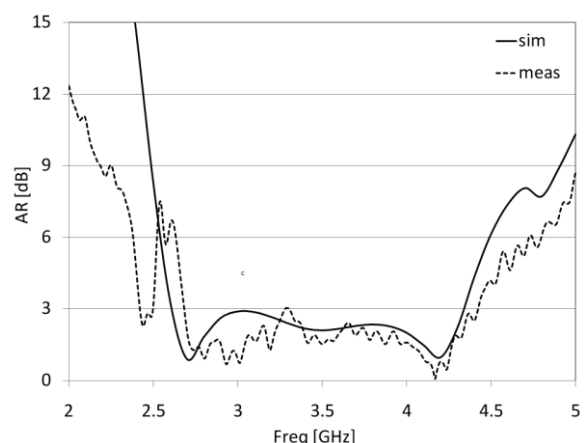
The simulated AR characteristics in Fig. 5 (b) show broadband characteristics of 50.35% from 2.6 GHz to 4.35 GHz. The measured characteristics are well complied with the simulated results and show a bandwidth of 50.14% from 2.66 GHz to 4.44 GHz.

The far field radiation pattern characteristics of the antenna in x-y and y-z plane at 3 GHz, 3.5 GHz and 4 GHz are simulated and measured. The results are shown in Fig. 6. The antenna shows bidirectional radiation patterns since it is a slot antenna.

The radiation pattern in the x-y plane at 3 GHz shows a cross polarization discrimination (XPD) of more than 15 dB in a wide azimuth range from 80° to 130° . Also a front to back (FB) ratio of around 18 dB is obtained. At 3.5 GHz, a XPD of more than 15 dB from 70° to 130° is obtained along with a FB ratio of 18 dB.



(a) S_{11} characteristics



(b) AR characteristics (+ y direction)

Fig. 5 S_{11} and AR characteristics

The antenna has a XPD of more than 15 dB from 50° to 100° and a FB ratio of 15 dB at 4 GHz. The measured and simulated characteristics are also in good agreement with each other.

The simulated and measured radiation pattern characteristics in the y-z plane, presented in Fig. 6 (b), also are well matched. A XPD of 15 dB from 70° to 100° at 3 GHz and 3.5 GHz and 12dB from 80° to 110° at 4 GHz are obtained. The FB ratio is more than 15 dB in all the cases.

The simulated and measured gain characteristics of the antenna in the + y direction ($\phi = \theta = 90^\circ$) are shown in Fig. 7. The two characteristics agree each other very well. A maximum gain of 5.45 dBic is obtained in simulation as well as in measurement at 4 GHz.

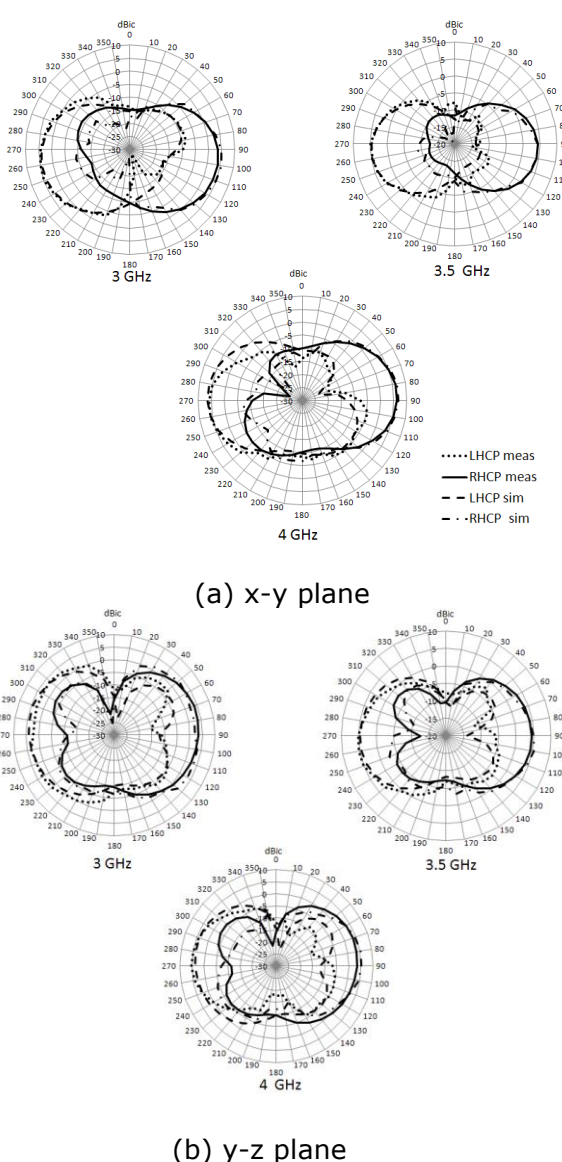


Fig. 6 Radiation pattern

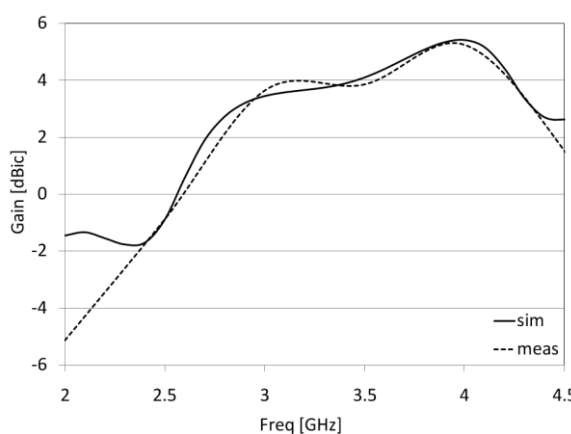


Fig. 7 Gain characteristics

Conclusions

A novel technique of bandwidth enhancement for planar circularly polarized slot antenna is presented in this paper. Changing the slot aperture by placing appropriate stubs in the slot by observing the electric field behaviour is proposed to eliminate the undesired electric field rotations and enhance the AR bandwidth by around 10%. In order to further improve the bandwidth, creating an additional L-slot on the ground plane of the antenna is also presented. The proposed antenna could attain an S_{11} bandwidth of 46.15% and CP bandwidth of 50.35%. A cross polarization discrimination of more than 15 dB on a wide azimuth range along with a maximum gain of 5.45 dBic is also obtained. The proposed planar antenna is a promising candidate for short distance pulse RADARs, WLAN and RFID reader applications.

References

- [1] Chang, F.S et al (2003), Low-cost broadband circularly polarized patch antenna, IEEE Trans. on Antennas Propag., vol.51, pp.3006-3009.
- [2] Chen, H.M et al (2009), Microstrip fed circularly polarized square ring patch antenna for GPS application, IEEE Trans. Antennas Propag., vol.57, No.4, pp.1264-1267.
- [3] Chen, Y.B et al (2006), CPW-fed broadband circularly polarized square slot antenna, Electron. Lett., vol. 42, pp 1074-1075.
- [4] Chou, C. C et al (2007), Broadband circularly polarized cross-patch-loaded square slot antenna, Electron. Lett., vol.43, pp. 485-486.
- [5] Fukusako, T et al (2003), Generation of circular polarization using rectangular waveguide with L-type Probe., IEICE Trans. Commun., vol.e86-B, 7.
- [6] Row, J. S. (2004), Dual-frequency circularly polarized annular-ring microstrip antenna, Electron. Lett., vol. 40, no. 3, pp.154– 154.
- [7] Tseng, L.Y., and Han, T.Y. (2008), Microstrip fed circular slot antenna for circular polarization, Microw. Opt. Technol. Lett., vol. 50, No.4, pp. 1056-1058.
- [8] Wong K. L., and Lin, Y. F. (1998), Circularly polarized microstrip antenna with a tuning stub, Electron. Lett., vol. 34, pp.831- 832.

Confirmed Message Delivery to Mobile Agents: A Theoretical Model

KUMKUM GARG¹ RAMA SUSHIL²

1 Director, MIT, Manipal University, India. email:kgargfec@gmail.com

2 Department of Computer applications, SGRRITS, Dehradun, India
Email: ramasushil@yahoo.co.in.

Abstract: A Mobile Agent (MA) is a running program that can move from host to host in a network when and where it chooses. Because of the extremely dynamic nature of MAs, mobile agent platforms should not only feature mobility but also have a technique to discover their position at any time for message delivery. This technique is called the Location Management Technique (LMT). This paper presents a theoretical model for confirmed message delivery with location management of MAs. This model discusses the issues, essential functions, and performance metrics of a LMT. Query propagation technique is used for confirmed message delivery. Orphan detection and termination is identified an important function of a LMT. It makes the network free from orphan agents and avoiding network congestion. Two novel static and dynamic approaches for orphan detection and termination are also presented as part of the theoretical model.

Keywords: Mobile Agent, Location Management Technique, Orphan agents, LMT issues, LMT functions, Performance Metrics.

1. Introduction

Wireless networks and mobile devices are becoming popular by the day. Wireless mobile computing breaks the stationary barrier and allows users to compute and access information anywhere-anytime. However, this new freedom of movement does not come without new challenges. The mobile computing environment is constrained in many ways. Mobile devices are resource poor and unreliable. Their network connectivity is often achieved through low bandwidth wireless links. Furthermore, connectivity is frequently lost for varying periods of time, because of change in the availability of both communication and computational resources. This severely complicates the development of certain types of applications like compute-intensive, collaborative issues over long distances and massive databases. Mobile agents offer a potential solution to network problems associated with hand held devices and support disconnected operation [Karenos et al. (2004)].

A Mobile Agent (MA) is a program, like an active and autonomous object, which may be dispatched from a client computer and

transported to a remote server for execution [Milojicic et al. (1998)], assisting users and acting on their behalf. Mobile agents have been used for load balancing, network management [Onifade et al. (2009)], workflow management, E-commerce, distributed information retrieval [Zhao et al. (2009)] and management, etc. [Outtagarts (2009), Zafoune et al. (2009)]. Locating a MA is a major requirement [Pitoura et al. (2001)] as the user may need to contact the agent to know the status of its allocated task, to stop it or to give it some additional task. Also, mobile agents may need to contact each other for current status collaboration through message passing. Two fundamental issues in message passing are tracking the migration of the agent and delivering messages to it. Tracking and communicating messages requires the location management of mobile agents. A theoretical model is presented in this paper, to aid the development of a LMT, by identifying the issues, functions and parameters for measuring efficiency of a LMT,

2. Existing Work

There are two extremes in the space of existing algorithms for locating MAs for location independent message delivery to migrating agents [Hac and Liu (1998), Tao and Lui (2000), Pitoura and Fudos (2001), Wojciechowski (2001), Murphy and Picco (2001), Stefano and Santoro (2002), Cao et al. (2002)], Cao and Feng et al. (2002), Samaras and Spyrou et al. (2002), Kastidou et al (2003), Choi et al. (2004), Yeh and Wang (2005), Patel and Martorakis (2005), Wang and Keh et al. (2005), Shinsuke K. et al. (2005), Yeh and Wang (2009), Wang and Yeh (2010), Yaragal et al. (2009)]. One extreme is the no-information approach. This approach does not assume any location update by the agent at migration. The other extreme is the full-information approach. This requires every site in the network to maintain this current location information of every agent. The "No Information" approach suffers from high cost of search. While the "Full Information" strategy suffers from high cost of update.

We have noted the following limitations in existing techniques. It is observed that there is no consideration given to orphan agents in these LMT. There is no available theoretical model to aid an understanding and development of LMT. Orphan agents unnecessarily move around the network, increase the network load and occupy space in the database. Message complexity calculation is not considered for LMT. Some existing techniques do not ensure confirmed message delivery; some cannot handle concurrent interaction and migration phases, some exhibit high associated update cost and some use longer locating times.

In this paper we present a theoretical model to aid an understanding and development of LMT. This model presents two novel algorithms for detection and termination of orphan MAs and Query propagation technique for confirmed message delivery with other issues, functions and performance metrics of LMT.

3. Theoretical Model

3.1 Issues in Location Management

The issues like location of the database [Pitoura and Fudos (2001)], agent naming schemes [Stefano and Santoro (2002)], update and search schemes [Li and Zhang

(2002)] are central for efficient and complete design of a LMT and are shown pictorially in Fig. 1. Database distribution and placement in the network can be centralized, distributed or hierarchical [Wang and Keh et al. (2005)] or a combination of these. Database placement depends on the size of the network, the migration frequency of agents and the number of agents in the network. Location database placement in a network affects its operations like insertion, deletion, search and update.

A centralized location database is a good choice for small sized networks with a limited number of agents and their migrations. However, in a distributed environment, a centralized location database is not reliable, efficient or scalable. In such a wide network the location database should be centralized region wise and distributed in the whole network. This arrangement reduces the frequency of the database bottleneck. A hierarchical arrangement of the location database maintains location information at all levels of the hierarchy. This arrangement results in cost-effective lookups.

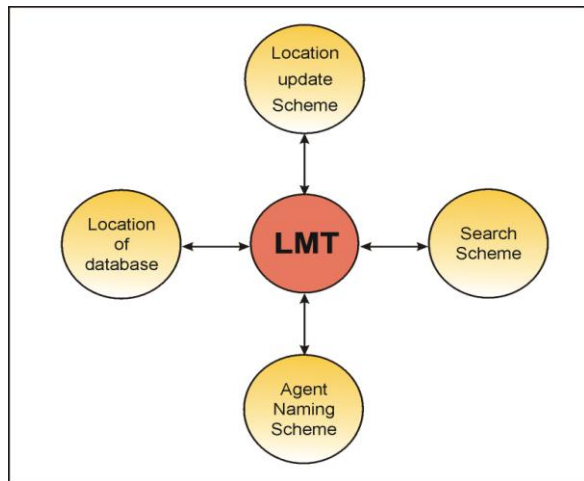


Fig. 1 Issues in LMT

Design of a good naming scheme is closely related with the design of a good location protocol. The location protocol should encode information to be used as a starting point in the location finding process. In designing a naming scheme, the main questions to address are; "What should the agent name represent ?" and "How should it be chosen and used ?" A good way to select the agent name is to make it reflect the service offered by it. A well-designed

naming scheme should have all the properties of Transparency, Agent Location Independence and Selectability.

The cost of a LMT mainly depends on the cost of location search and update. In order to save update cost, mobile agents should not update their location every time they change the host [Sushil et al. (2008)]. It is obvious that in a single region environment, only intraregional migrations are applicable while interregional migrations are also applicable for multiregional environments. MAs can update their location using time based or movement based update schemes. In movement based update schemes, the update operation can be performed either after every migration, or after counting an optimal number of migrations, or after crossing from the birth region, or after crossing from Immediate Neighbor Nodes (INN).

In single region environments an agent can update its location by three methods; leaves its proxy at the source host, specialized site to keep the location information, the agent updates its location at the source site after d hops, where d is a positive integer [Li and Zhang (2002)]. In multi-region environments further procedure is required for location update in interregional migrations. This is implemented by providing interaction between region servers, as implemented in SPC and MBLM [Stefano and Santoro (2002), Bavandla (2004)], BSPC [Sushil et al. (2007) and MCMB [Sushil (2010)].

Different search schemes depend on the structure of the location database, the number of agents and their mobility in the network [Tanenbaum (2003)]. Linear search is efficient for small number of agents with low and non-deterministic migrations. Binary search is efficient for large number of agents with highly mobile and deterministic itineraries.

3.2 Functions of Location Management

The essential functions that an efficient LMT server should provide are: management of a Current Location DataBase (CLDB) viz. insertion, search and deletion operations, detection and termination of orphan agents, message delivery confirmation [Cao and Zang et al (2004), Choi et al (2010)] and locating mobile agents [Ming (2008), Patel and Martorakis (2005), Pitoura, E. and

Samaras, G. (2001)]. These functions are shown pictorially in Fig. 2.

An application may launch one or more agents in the network to perform some task. However, at times, the application itself terminates before getting the results of the tasks given to the agents. Such agents are called orphan agents. Termination of the parent application means that the agent will not be used in future.

In such a case, agents unnecessarily roam in the network, increasing the network load and consuming resources. Normally no MAS have provision to detect and terminate such agents. However, we have identified this as important to LMT as garbage collection is to Distributed Systems and memory management is to Operating Systems. Detection of orphan agents and their termination obviously improves network performance by reducing network load and avoiding CLDB bottleneck. It also controls network congestion and optimizes resource usage. This process should also be followed by the deletion of the location information of terminated agents from the CLDB. It is implemented in Mole [Baumann (1998, 1999)] using the shadow concept. We have not used this concept, as the shadow is also application dependent. We directly use the process identity of the parent application of the agent to check if the agent is an orphan. A register called Agent Life Register (ALR) is maintained at the time of creation of an agent by an application.

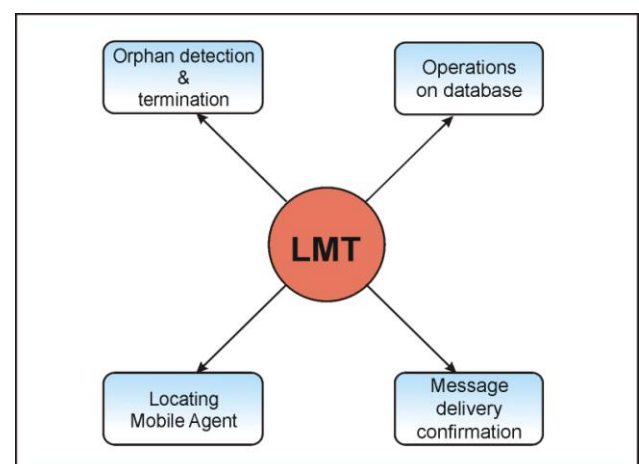


Fig. 2 Functions of LMT

The ALR contains the following information for orphan detection and termination.

1. Unique identity of the agent.
2. Process identity of the agent's

- parent application.
- 3. Time To Live (TTL), the life time given to an agent.
- 4. Locating Query Time (LQT), the time at which a query is made for locating an agent.

A static algorithm is developed for detecting orphan agents, when the agent's life time and roaming is not taken into consideration. However, it should not be executed very frequently. This is because, during the process of orphan detection and termination, the CLDB get locked and LMT cannot be used for locating or updating location information of migrating agents. In the dynamic mechanism for orphan detection and termination, an agent is checked for its orphan status periodically, once in every TTL. These two algorithms are based on page replacement algorithms in memory management [Tanenbaum (2008)]. These are given next.

Static Algorithm

1. Start
- /* Mark the agents which have not been located for the longest period of time, by checking LQT maintained in ALR */
2. Mark tuples of CLDB by checking LQT in ALR.
3. Check status of parent application of marked agents.
4. If (status = terminated)
 - a. Locate agent and terminate
 - b. Delete location tuple from location database
- }
5. While (marked tuple) go to step 3
6. Stop

Dynamic Algorithm

1. Start
2. If (TTL= nil) for running agent A
 - { Check the status of parent application of A
 - If (status = terminated)
 - { Locate the A and terminate.
 - Delete location tuple for A
 - from
 - CLDB.
 - }
 - }
 - else
3. Update TTL for next life cycle of A
4. Stop.

It can be seen that the dynamic algorithm checks the status of the agent every time its TTL expires. This is not efficient. We need a mechanism to reduce the frequency of this check. We suggest that an agent can be checked for being an orphan at some multiple of TTL. This value can be decided by noting the average life time of agents in an application. For example, if the average life time of an agent is one hour and TTL is half an hour, the agent status can be checked after 2*TTL.

It is important to note that the MA location process should not stop when the agent location is found in CLDB. Rather it should stop after the message is delivered to the agent. It is possible that, once the current location of an agent is found, it may leave that place before the location finder send message. In this case, it becomes necessary to repeat the entire process of locating and performing communication. If an agent moves rapidly, several retries may be required for message delivery.

If the agent migrates at the moment it is located, it is a situation when a single interaction overlaps with a single migration. When more than one interaction is concurrent with a single migration, there must be a mechanism to serialize them. A single interaction may also overlap with several migrations. This happens when a location search and catch phase is long enough to include two or more migrations of the agent. This is a race condition between interaction and migration and leads to a situation when termination of the locating phase cannot be guaranteed and confirmed message delivery [Patel and Garg (2002)], is not possible.

In order to provide confirmed message delivery, the LMT should have a mechanism to overcome the loss caused by asynchronous operations of agent migration and message forwarding. This can be resolved by tracking the migration of the target agent and terminating the locating phase when the message is delivered. To guarantee the termination of the locating phase, the following condition should be satisfied:

$$t_c < (t_m + t_u + t_t) \quad (1)$$

where t_c is the time it takes for message delivery to the agent after retrieval of location information from CLDB. t_c is the sum of migration time (t_m) of the agent,

update operation duration (t_u) and task completion time (t_b).

Since migration and locating speeds are comparable, to satisfy the condition given in eqn. (1), a “query propagation technique” is used. In this technique, when location is queried from LMT server, the server accesses the location register for location of the agent. If the server does not get the exact location, it queries the next register and this goes on till the agent’s exact location is found. For exact location, the server itself replies to the query maker and locks the agent at that location.

The agent is locked till the message reaches the agent and is delivered to it. The message is delivered using some communication protocol [Cao and Zhang et al. (2004), Choi et al. (2010)]. To avoid message loss, two message-forwarding approaches, namely push and pull are explored to design adaptive and reliable message delivery protocols [Patel and Garg (2002), Wojciechowski (2001)].

3.3 Performance Metrics of a LMT

Database location and the four operations of insert, delete, search and update on the database, if not designed properly, may degrade the performance of multi-agent applications. The performance of a LMT is governed by the following metrics [Sushil et al. (2008)], which is shown pictorially in Fig. 3. **Availability** is the ability of a functional component to be in a state to perform a required function, at some instant of time, within a given time interval. It refers to failure-free operation at a given instant of time and defined as the percentage of time the system works.

For LMT we consider location update and interaction availability as defined below.

Location Update Availability is the extent to which a LMT is available for migration of an agent with some permissible fault rate due to errors [Stefano and Santoro (2002)].

Interaction Availability is the extent to which a LMT is available for interaction with an agent with some permissible fault rate due to errors.

A system is scalable, if it can be changed in size or configuration to suit changing conditions [Gray et al (2001), Weinstock and Goodenough (2006)]. Here, for **LMT scalability**, we measure the overall system response, when the number of agents and their migrations increase. These

parameters affect the network and site usage. We calculate global system usage as the sum of network usage and site usage, suitably weighted. In determining an expression for network usage [Stefano and Santoro (2002)], the topology of the global network should be considered, which leads to evaluation of various specialized sites.

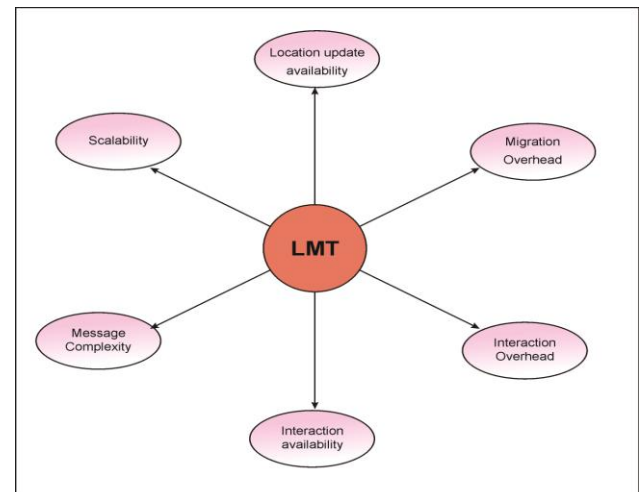


Fig. 3 Performance Metrics of LMT

Migration Overhead is the percentage of time spent by the execution of a location update operation, during agent migration. It is given as in eqn. (3):

$$M = TU/(TM+TU) \quad (3)$$

where TU is the time spent in executing the location update operation and TM is the duration of the agent migration process. It is evaluated by measuring the additional delay introduced by the location update operation, in the total agent execution time during migration. This delay includes the time taken by the location update operation locally or remotely.

Interaction Overhead is the percentage of time spent in searching the location from the database and message delivery duration. It is given as in eqn. (4):

$$I = TC/(TC+TI) \quad (4)$$

where TC is the duration of the location finding and agent catching phase, and TI is the duration of the interaction (i.e., message delivery time).

Message complexity is defined as the total number of messages needed to locate an agent in a network [Sushil et al. (2008)]. It is proportional to network usage by a LMT. Therefore, a LMT with lesser message complexity is preferable.

Any well-designed LMT should aim to achieve the best values for the parameters

mentioned above. Achieving the best value simultaneously for all of them can be hard to guarantee. The LMTs proposed in this thesis aim to obtain optimal values of the parameters mentioned above.

The complete theoretical framework for a LMT can now be given as shown in Fig. 4. It combines the central issues, functions and metrics needed to be considered for

efficient design of a LMT. As shown in Fig. 4, the performance metrics are dependent either on some issue or on some function of LMT, e.g., scalability is shown to be dependent on the orphan detection and termination function. Similarly message complexity is dictated by the location of database.

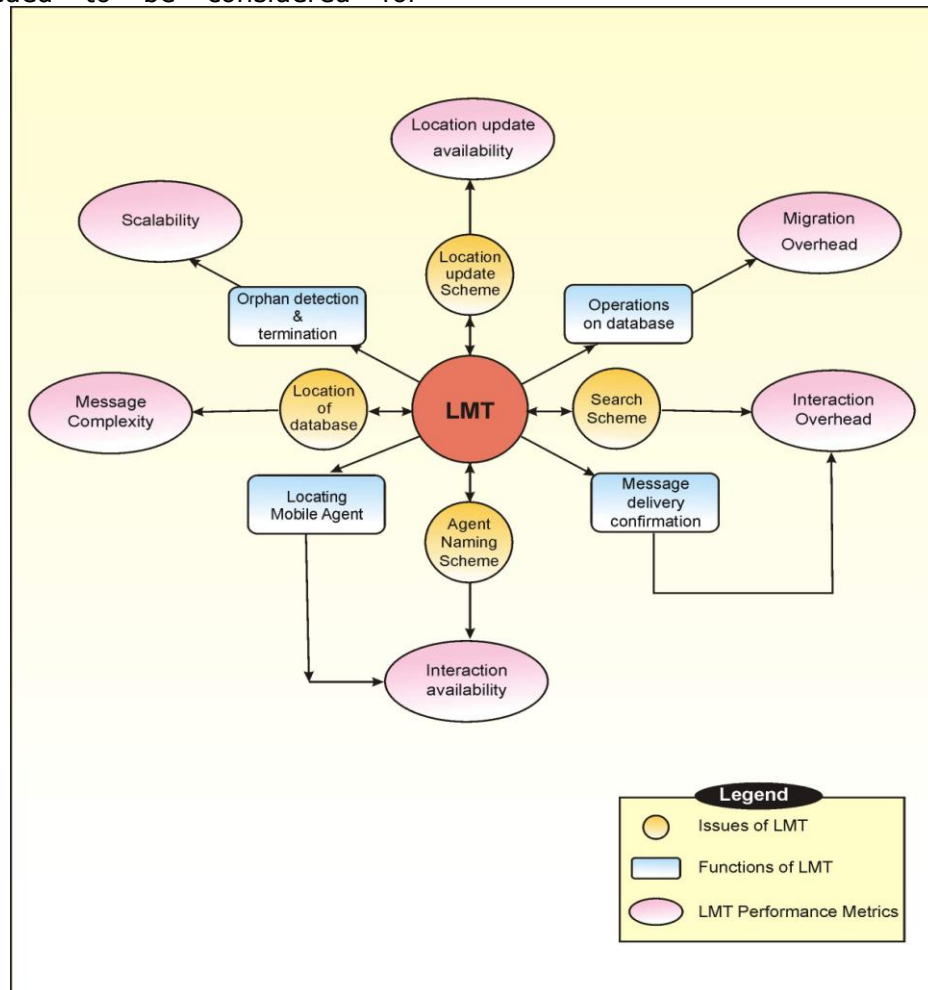


Fig. 4 LMT Model

4. Conclusion

Query propagation technique confirms message delivery to the mobile agent. Orphan detection and termination makes the network free from orphan agents, consequently reducing network load and optimally utilizing the database. The metrics identified for performance comparison of various LMT include location update and interaction availability, scalability, migration and interaction overhead and message complexity. To balance the cost of location search and update, the location management

problem can be solved by a good combination of MASIF's "Logging", "Agent Registration", with "Broadcasting" and "Multicasting". A mobile agent can update its location at any one or more of the following times: at every hop, after d (optimal number) hops, where d is fixed, after d hops, where d is decided dynamically, periodically, on crossing its birth region, on crossing Immediate Neighbor Nodes. The proposed model can be used for the development of an efficient LMT according to the agent mobility frequency and itinerary in an application.

References

- [1] Baumann, J. (1999), A comparison of mechanisms for locating mobile agents, Technical Report, 1999/11, Univ. Of Stuttgart, faculty of computer science, pp. 1-25, Website:<http://elib.unistuttgart.de/opus/volltexte/1999/515/>.
- [2] Baumann, J. and Rothermal, K. (1998), Shadow approach: an orphan detection protocol for mobile agents, 2nd workshop on Mobile Agents (MA'98), LNCS 1477, pp. 2-13.
- [3] Bavandla, M. (2004), Improving the performance of location management protocols in a multiregion environment, Master thesis IIT Roorkee, India.
- [4] Cao, J., Feng, X., Lu, J. and Das, S. K. (2002), Mailbox-based scheme for mobile agent communications, IEEE Computer, pp. 5-60.
- [5] Cao, J., Leung, P., and Chan, A. T. (2002), A Scalable and Reliable Multicast Communication Service in Java, Proc. of the 16th international Parallel and Distributed Processing Symposium, 15-19April 2002, IEEE Computer Society, Washington, DC., pp. 43-48.
- [6] Cao, J., Zhang, L. et al (2004), A Reliable Mobile Agent Communication Protocol, Proceedings of 24th IEEE Int. Conf. on Distributed Computing Systems (Icdcs'04), Washington DC., 24-26March 2004, pp. 468-477.
- [7] Choi, S., Baik M., Hwang, C. (2004), Location Management & Message Delivery Protocol in Multi-region Mobile Agent Computing Environment, Proceedings of the 24th IEEE Int. Conf. on Distributed Computing Systems (ICDCS'04), pp. 476-483.
- [8] Choi, S., Baik, M., Kim, H. et al (2010), A Reliable Communication Protocol for Multiregion Mobile Agent Environments, IEEE Transactions on Parallel and Distributed Systems, vol. 21, no. 1, pp. 72-85.
- [9] Gray, R. S., Kotz, D. et al (2001), Mobile-Agent versus client/server performance: Scalability in an information-retrieval task, LNCS 2240, pp. 229-243.
- [10] Hac, A. and Liu, B. (1998), Database and location management schemes for mobile communication, IEEE/ ACM Transactions on networking, vol. 6, no. 6, pp. 851-865.
- [11] Karenos, K., Samaras, G. et al (2004), Mobile agent-based services for view materialization, Mobile Computing and Communications Review, vol. 8, no. 3, pp. 32-43.
- [12] Kastidou, G., Pitoura, E. and Samaras, G. (2003), A scalable hash-based mobile agent location mechanism, Proceedings of the 23rd IEEE Int. conf. on distributed computing systems workshops (ICDCSW'03), pp. 472-477.
- [13] Li, T. Y. and Zhang, J. F. (2002), An Optimal Location Update and Searching Algorithm for Tracking Mobile Agent, proceedings of AAMAS'02, Bologna, Italy.
- [14] Milojicic, D., Breugst, M. et al (1998), MASIF-The OMG Mobile Agent System Interoperability Facility, Personal Technologies, Springer Verlag, pp. 117-129.
- [15] Ming, X. (2008), Locating mobile agents through distributed mechanisms, Ph.D. Thesis, Univ. of Ottawa, , NR48664, 58 pp.
- [16] Murphy, A. L., Picco, G. P. (2001), Reliable communication for highly mobile agents, Kluwer Academic Publishers, printed in Netherlands.
- [17] Onifade, O. F. W. et al (2009), Mobile Agent Technology Enabled Recharge Systems for Efficient Bandwidth Utilization on Mobile Networks, Int. J. of Soft Computing Applications, Issue 4, pp. 5-12.
- [18] Outtagarts, A. (2009), Mobile Agent-based Applications: a Survey, Int. J. of Computer Science and Network Security, vol. 9, no. 11, pp. 331-339.
- [19] Patel, R. B. and Garg, K. (2002), Communication Mechanisms for mobile agents, proceedings of 1st Int. ICSC Congress on Autonomous Intelligent Systems, Deakin University Waterfront Campus, Geelong, Australia, 12-15 Feb2002.
- [20] Patel, R. B. and Martorakis, N. (2005), Locating mobile agents in a wide distributed system: a dynamic approach, Proceedings of 7th WSEAS Int. Conf. on Mathematical Methods and Computational Techniques, Sofia, Bulgaria, pp. 96-109.
- [21] Pitoura, E. and Fudos, I. (2001), Distributed location databases for tracking highly mobile objects, The Computer Journal, Vol. 44, pp. 75-91.
- [22] Pitoura, E. and Samaras, G. (2001), Locating objects in mobile computing, IEEE Transaction on Knowledge and Data Engineering, vol. 13, no. 4, pp. 571-592.
- [23] Samaras, G. And Spyrou, C. et al (2002), Tracker: A Universal Location Management System for Mobile Agents, European Wireless Conf. on Next Generation Wireless Networks: Technologies, Protocols, Services and Applications, Florence, Italy, 25-28February 2002.
- [24] Shinsuke, K. et al (2005), Location Management of Mobile Agents Based on Their Behavior, Transactions of Information Processing Society of Japan, vol. 46, no.2, pp. 506-516.
- [25] Stefano, D. and Santoro, C. (2002), Locating mobile agents in wide distributed environment, IEEE Trans. Parallel Distrib. Syst., vol. 13, no. 8, pp. 844-864.
- [26] Sushil, R. (2010), Design and validation of location management techniques for mobile agents, PhD thesis, IIT Roorkee, India.
- [27] Sushil, R., Bhargava, R., Garg, K. (2008), Location update schemes for mobile agents, INFOCOMP Journal of Computer Science, Int. Scientific Journal, vol. 7, no. 2, pp. 37-43.
- [28] Sushil, R., Bhargava, R., Garg, K., 2007, Reduced Cost location update scheme: a reactive approach for mobile agents, Proceedings of Int. Conf. on High Performance Computing, ISRST, HPCNCS07, 9-12 July2007, Orlando, Florida, USA pp. 128-135.
- [29] Sushil, R., Garg, K. and Bhargava, R. (2008), Comparison of location management techniques for mobile agents, Proceedings of 16th IEEE Int. Conf. on Networks (ICON 2008), New Delhi, India 12-14 Dec 2008,.
- [30] Tanenbaum, A. S. (2003), Computer Networks, 4th Edition, Publisher: Prentice Hall, 912 pp.

- [31] Tanenbaum, A. S. (2008), Modern Operating Systems, 3rd edition, Prantice- Hall, Inc, 013-6006639.
- [32] Tao, X. and Lul, J. (2000), Communication Mechanism in Mogent System (2000), Journal of Software, vol. 11, no. 8, pp. 1060-1065.
- [33] Wang, T. I., Yeh, T. Y. (2010), Development of Low Cost Message Delivery Path for Mobile Agent Communication, Journal of Convergence Information Technology, vol. 5, no. 2, April 2010, pp. 163-173.
- [34] Wang, Y. H., Keh, H. et al (2005), A hierarchical dynamic monitoring mechanism for mobile agent location, Proceedings of 19th IEEE Int. Conf. on Advanced Information networking and Applications (AINA'05), pp. 351-356.,
- [35] Weinstock, B. and Goodenough, J. B. (2006), System Scalability, Technical Note, CMU/SEI-2006-TN-012.
- [36] Wojciechowski, P. T. (2001), Algorithms for Location-Independent Communication between Mobile Agents, Technical Report 2001/13, Communication Systems Dept., EPFL.
- [37] Yeh, T. Y. and Wang, T. I. (2005), A mechanism for tracking mobile agents in a cluster topology, Proceedings of 11th Int. Cong, Parallel and distributed systems, 20- 22 July 2005, vol. 1, pp. 320-327.
- [38] Yeh, T. Y. and Wang, T. I. (2009), A Ratio-Based Update Scheme for Mobile Agent Location Management, vol. 5559, LNCS, pp. 100-109.
- [39] Zafoune, Y., Mokhtar, A. and Kanawati, R. (2009), Mobile-Agent Approach for Mobile Code Localization in Ad hoc Networks, proceedings of 33rd Annual IEEE Intl. Conf. On Computer Software and Applications, USA, pp. 36-39.
- [40] Zhao, J., Zhang, J. and Fang, H. (2009), A study of a mobile agent based information searching system, Proc. Intl. Workshop on Information Security and Application, China, 21-22 November 2009, pp. 209-213.

Design and Implementation of Genetic Algorithm as the PID Controller Parameter Optimization Method for Networked Control System

ADITYA TEJO WIDAGDO¹, KATJUK ASTROWULAN¹, and IMAM ARIFIN¹

- ¹ Department of Electrical Engineering, Faculty of Industrial Technology, Sepuluh Nopember Institute of Technology (ITS); Gedung B dan C Kampus ITS Sukolilo, Surabaya, East Java, Indonesia - 50111.
e-mail: a_tejo_w@elect-eng.its.ac.id; katjuk_as@ee.its.ac.id; arifin_iii@ee.its.ac.id
-

Abstract: Delay time which is occurred in Networked Control System (NCS) could interfere with the system performances. This disadvantage could impact on the stability of the system. In network control concept, this disadvantage could not be eliminated. However, compensation could be given for maintaining the system performance. In this undergraduate thesis book, a proportional plus integral plus derivative (PID) controller was designed for controlling a plant over communication network. PID parameters searching process was performed through the implementation of Genetic Algorithm (GA). GA which was built was using Model Reference Adaptive Control (MRAC) in updating the parameters of the system to be controlled. GA was used to search the optimal parameter values of PID controller with respect to the current condition of the system. This study was tested on the Pressure Process Rig 38-714 and DC Servo Motor as the plant by providing different treatments for each disadvantage to be compensated. By using GA in optimizing the parameters of PID controller, the performance of NCS was remained intact even if it was affected by various plant and communication network disturbances.

Keywords: NCS, PID Controller, GA

1. Introduction

An NCS is a closed loop control system of which the control and feedback signals are exchanged through a real-time network. NCS is consisted of four main elements, that is, sensor, controller, actuator, and the communication network. [Yang and Fang, (2009)].

As one of the remote control method, there are several problems relating with the NCS communication and transmission media. The common occurred problem is the delay time that can cause instability on the system performance. [García-Rivera, (2007)]

One of the most widely-used controllers is the PID controller. Its calculation algorithm involves three separated parameters. The P value determines the control action based on the comparison of the error signal. The value I provide proportional control action based on the amount of time when error is occurred.

The value of D determines the control action which is proportional to the changes of error. [Pohjola, (2006)]

The concept of adaptive control involves the ability of controller that is able to adjust parameter that tends to have values which are uncertain and time-varying behaviour. One of the adaptive control schemes is the Model Reference Adaptive Control (MRAC). MRAC is a controller parameter adjustment scheme based on the defined model reference system that has been previously. [Astrom and Wittenmark, (1994)]

One of the methods that can be used in tuning the PID controller parameters is GA. It is part of the concept of smart control and evolutionary computation. This technique inspired by natural selection mechanism, namely the biological process with the concept that individuals are more strongly inclined to be a winner in a competitive environment [Kim, (2008)]. GA uses a direct analogy of natural

evolution to perform global optimization in the context of solving a very complex problem [Goldberg, (1989)]. GA working principle based on the assumption that a potential solution to the problem is individual and can be represented by a set of parameters. These parameters are considered as genes from the chromosome and can be structured with a series of values which is defined by a coding scheme. Variables can be represented by binary, real numbers, or other forms depending on the application data.

As one of the search method that uses the concept of artificial intelligence-based numerical computation, Genetic Algorithm (GA) can be used to find the optimum value of the PID controller parameters in line with the characteristic changes that occur at the NCS. By applying the GA in PID controller, it is expected an output of a controller is able to maintain performance despite NCS is affected by the delay.

The main background of the experiment was shown in this section. The existence of delay time and its effect on NCS performance were explained in Section 2. Section 3 presented the building architecture of NCS and GA-based PID controller. The result of experiments was described and analysed in Section 4. Section 5 provides the conclusions and future recommendations of this research.

2. Delay Time Effect on NCS

The installation of communication networks in the feedback loop makes the design and analysis of NCS becomes more complex. This is happened due to the utilization of a communication network which is affected by delay time. NCS which is operated on a network will cause the data transmission delayed. This is occurred because the control and feedback signals require time to be exchanged over a communication network. Most of the NCS is using a discrete time formulation. Fig.1 shows the delay in the loop with r is the reference signal, u is the control signal, y is the output signal, k is time index, and T is the sampling period.

Delay time in NCS can be categorized into two forms: the delay time caused by the transmission of signals from the sensor to the controller (denoted by τ^{sc}) and the delay time from controller to actuator

(denoted by τ^{ca}). Thus, the delay can be calculated as follows:

$$\tau^{sc} = t^{cs} - t^{se} \quad (1)$$

$$\tau^{ca} = t^{rs} - t^{ce} \quad (2)$$

with t^{se} is the time needed by the plant-loop to convert the measured output signal into data packets that are ready to be sent, t^{cs} is the time required by the controller to begin the process of receiving and processing data in packets, t^{ce} is the time required by the controller to change the control signals into packets data which is ready to send, and t^{rs} is the time needed by the plant-control loop to process a given signal. In fact, the delay time in the NCS configuration can be larger or smaller than the time since it is purely random process.

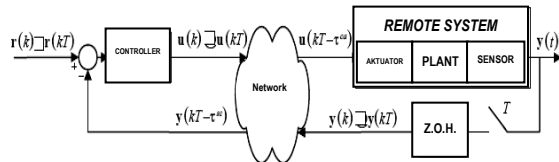


Fig.1 General Configuration NCS and Delay Time for Formulation [Yang and Fang, (2009)]

The time required by the controller in processing the signal (τ^c) and delay time on the network can be used as a single unit of total delay time (τ). Although the controller processing time is still exists, but this delay can be ignored because it is generally smaller compared with the delay time network. In addition, there is the possibility of sampling time difference between the plant-controller loop for several different cases.

Delay time is consisted of three parts.

- 1) Waiting delay time (τ^w) is a delay time on the controller or plant-loop due to the queues and the availability of the network before the controller sends the data packet.
- 2) Frame delay time (τ^f) is the time required for the conversion of control signals into data packets before it is ready to be transmitted over the network.
- 3) Propagation delay (τ^p) is the time taken by data packets for transmission through media. The amount of this

delay depends on the speed of transmission media as well as the distance between source and destination.

In general, there are three fundamental part of the delay time which occurs within a Local Area Network (LAN): delay time of control signals and sensor measurements due to the queuing process at both the data packet switches, routers and hubs. Delay time also depends on other factors such as maximum bandwidth specs on the protocol used and the size of data packets. These three sections are represented by Fig.2.

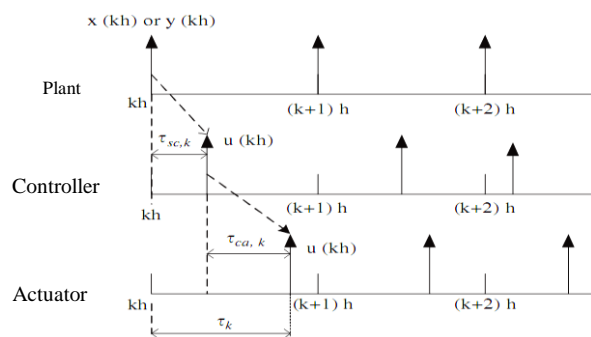


Fig.2 Delay time of NCS [Yang and Fang, (2009)]

3. NCS Architecture and Controller Design

a. System Requirements

The architecture of NCS was built using five main parts. Computer takes a role as a digital controller and error detector. Ethernet cable and embedded system supports the communication network. In this experiment, two plants are used: Pressure Process Rig 38-714 as a pressure control system and DC Servo Motor MS150 as a speed control system.

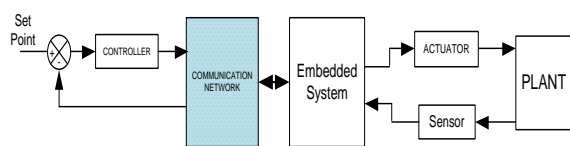


Fig.3 Block Diagram of Single-Plant NCS Configuration

b. Plant Description

Feedback® Pressure Process Rig 38-714 is one of the control modules for pressure

and flow [Anonym, (2001)]. This module uses the air pressure which is low to medium scale process. This module also provides pressure and flow measuring devices. In addition, there is also a differential pressure sensor, gauge pressure sensors and air valves which are pneumatically controlled. The process selected from the module to be regulated through the NCS is the pressure. The front panel plant is shown in Fig.4.

Feedback® DC Modular MS150 is a product of in form of modular servo system is presented in Fig.5 [Anonym, (2001)]. This set is an electronic circuit block which is used for setting the speed and position of DC servomotor. Modular Servo System MS 150 consists of a power supply, servo amplifier, two units of DC motors, tachogenerators , and multiple transducers and modules.

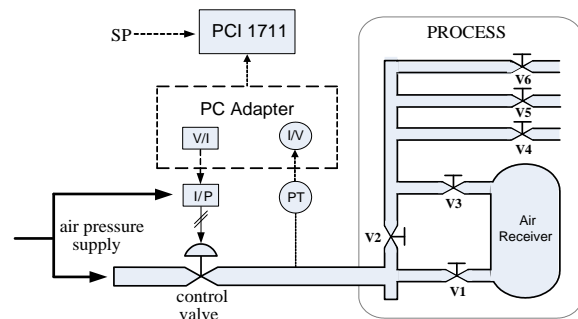


Fig.4 Scheme Block of Pressure Control System



Fig.5 A Set of DC Modular Servo System

c. System Identification and Modeling

Static identification of the plant was done by providing a constant set point value in a time range. The built configuration is an open loop system

without controller. The response given can be used as a reference in plant modeling. Static identification of Pressure Process Rig 38-714 was done with the technical specifications as follows.

- Input voltage : 2.5 volts, DC
- Number of iterations : 1000
- Nominal condition :
 - Valve open : V2, V4, and V5
 - Valve closed : V1, V3, V6, and V7
 - Air Receiver : not used

DC servo motor is statically identified by the following criteria.

- Voltage input : 1 volt, DC
- Number of iterations : 1000
- Nominal conditions : no magnetic load

The process of identifying the static modeling consists of three stages [Ogata, (1997)].

1) Calculation of overall gain:

$$K = \frac{Y_{ss}}{X_{ss}} \quad (3)$$

Y_{ss} is a response by the system at steady-state conditions and X_{ss} is the input system in steady-state conditions.

- 2) Calculation of time-constant (τ) of the graph by finding the value of t when the system response reaches 63.2% of the steady-state.
- 3) Provided with a system transfer function equation:

$$G(s) = \frac{K}{\tau s + 1} \quad (4)$$

for example first-order system.

After static identification, the obtained transfer function of Pressure Process Rig 38-714 is:

$$\frac{C(s)}{R(s)} = \frac{0.7202}{0.2147s + 1} \quad (5)$$

And the obtained transfer function of DC servo motor is:

$$\frac{C(s)}{R(s)} = \frac{3.5553}{0.004s + 1} \quad (6)$$

Dynamic plant identification was done by giving the set point varies with time. The given set point is a Pseudo-Random Binary Sequence (PRBS) signal which is consisted of ten-bit binary number [Dotanziv, (2003)]. The built configuration

is an open loop system without controller. The response given can be used as a reference in plant modeling. Dynamic identification of Pressure Process Rig 38-714 was done with the technical specifications as follows.

- Input voltage :
 - upper bound : 3.5 volts, DC
 - lower bound : 1.5 volts, DC
- PRBS Signals : 1101 0010 11₂
- Number of iterations : 1000
- The nominal condition:
 - Valve open : V2, V4, and V5
 - Valve closed : V1, V3, V6, and V7
 - Air Receiver : not used

DC servo motor is dynamically identified by the following criteria.

- Input voltage :
 - upper bound : 1.5 volts, DC
 - lower bound : 0.5 volts, DC
- PRBS Signals : 1110 1001 10₂
- Number of iterations : 1000
- Condition nominal : no magnetic load

The process of identifying the dynamic model consists of three stages [Anonym, (2010)].

- 1) Calculation of ARX model parameters according to the following equations:

$$A(q) = 1 + a_1q^{-1} + \dots + a_{n_a}q^{-n_a} \quad (7)$$

$$B(q) = b_1 + b_2q^{-1} + \dots + b_{n_b}q^{-n_b+1} \quad (8)$$

with the standard least square method.

- 2) Z-transform of the ARX model, with sampling time of 0.01 seconds and zero order hold.
- 3) Perform transformation on the result in point (2) into the S-domain to obtain the system transfer function.

After static identification, the obtained transfer function of Pressure Process Rig 38-714 is:

$$\frac{C(s)}{R(s)} = \frac{0.8966}{4.4944s + 1} \quad (9)$$

And the obtained transfer function of DC servo motor is:

$$\frac{C(s)}{R(s)} = \frac{3.6597}{0.121s + 1} \quad (10)$$

The obtained plant models were validated using error function. It is obtained that dynamic system identification provided less error than static

one. Therefore, eqn.9 was chosen to represent the mathematic model of Pressure Process Rig 38-714 and eqn.10 was chosen to represent the mathematic model of DC servo motor.

d. Controller Design

At this stage, a PID controller was designed with K_p , K_i , and K_d as variables that will be optimized by the GA. The design of this controller can be divided into three main processes: the design of PID parameter tuning scheme, the determination of GA parameters, and design diagrams in the form of system simulation.

PID controller parameter tuning process begins with the initialization of the system reference model. This reference model represents some characteristic that is expected to be achieved after tuning process such as e_{ss} and offset. This reference model associated with the GA as an adaptive mechanism. GA plays a role in reading the current state of the system and make comparisons with the reference model. GA produces the outputs which are PID controller parameters that will be applied to the system [Griffin, (2003)] [Ibrahim, (2005)]. This tuning process can only be run once or repeatedly according to certain conditions. Scheme tuning in is presented in Fig.6.

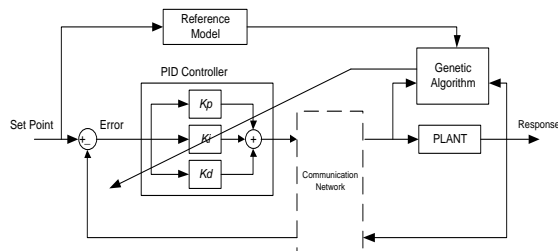


Fig.6 Schematic MRAC Tuning PID Parameters

GA has several parameters that can be varied. The variation of each parameter will determine the performance of the object to be optimized [9], in this case is the PID controller. In this test, there are nine parameters to be varied: the number of variables, variable bounds, the number of chromosomes bits, the size of population, the type of objective function, the mechanism of selection, crossover

probability, mutation probability, and the termination condition of iteration.

The determination of GA parameters was shown in Table 1. In this experiment, three variables were used: K_p , K_i , K_d . These are used to manipulate the PID control action in the control system in order to obtain a response and a good performance. The boundary of variables were varied between Pressure Process Rig 38-714 and DC servo motor due to differences in the characteristics of systems that require adjustments to the model controller. A binary number coding scheme with 30 chromosomes was used, with ten chromosomes for each variable.

Table 1 GA Parameters

Parameter	Value
Number of Variables	3
Variable Bounds	Not exact
Number of Chromosome Bit	10
Population Size	25
Objective Function	RMSE
Selection Mechanism	Roulette Wheel
Probability of Crossover	0.95
Probability of Mutation	0.05
Terminating Conditions	$E_{ss} < 5\%$

A 25 population size was determined for both Pressure Process Rig 38-714 and DC servo motor. RMSE is the appropriate objective function which didn't burden the system and controller performance during the iteration process. The equation of RMSE is shown below:

$$RMSE = \sqrt{\frac{1}{n} \sum_{i=1}^n (y(t) - x(t))^2}, \quad (11)$$

$$i = 1, 2, 3, \dots, n$$

Roulette wheel selection method has pretty good selection ability and doesn't require a long execution time. The probability of occurrence of crossovers should be of high value [Suyanto, (2005)]. This experiment used the 95 percent of crossover probability value. The probability of occurrence of mutations has the opposite characteristic of crossovers; it has to be very small [Suyanto, (2005)]. In this experiment, the 0.5 percent mutation probability value was used. The execution

of the program will stop after the steady state error reached under 5 percent.

4. Experiments and Analysis

In this paper, experiments were done under simulation. Eqn.9 was used as a transfer function of pressure control system, while eqn.10 was used as a transfer function of DC motor speed control system. By using the built NCS architecture in Fig.3, the system performances were compared between network utilization and without network utilization.

The first simulation was a pressure control system without utilizing a network. The result was shown in Fig.7. From Fig.7, it is obtained that the system approached first order system response. The system has no overshoot and it has 3 percent of steady state errors. The change of set point was well-responded by the system and it was stable.

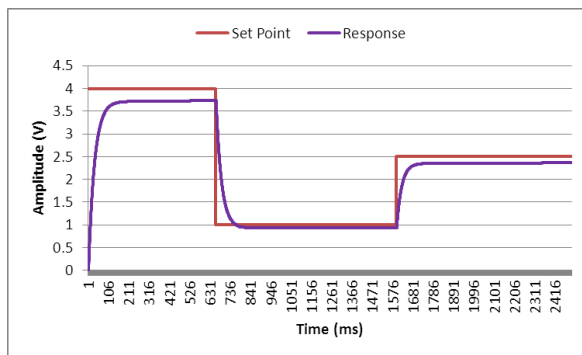


Fig.7 Response of Pressure Control System without Network

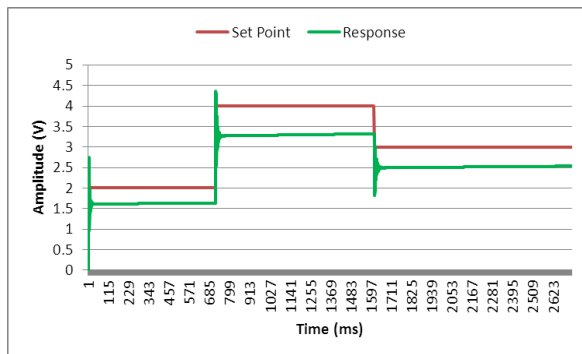


Fig.8 Response of Pressure Control System through Network

The second simulation was a pressure control system by utilizing a network. The

result was shown in Fig.8. From Fig.8, it is obtained that the system approached second order system response. The system has 8 percent of steady state errors and 25 percent of maximum overshoot. Although its overshoot is high, the system was stable and followed the change of set point.

The third simulation was a DC motor speed control system without utilizing a network. The result was shown in Fig.9. From Fig.9, it is obtained that the system approached second order system response. The system has 5 percent of steady state errors and 35 percent of maximum overshoot. This overshoot is extremely high and it could be dangerous if it is implemented in the real plant. The change of set point was well-responded by the system and it was stable.

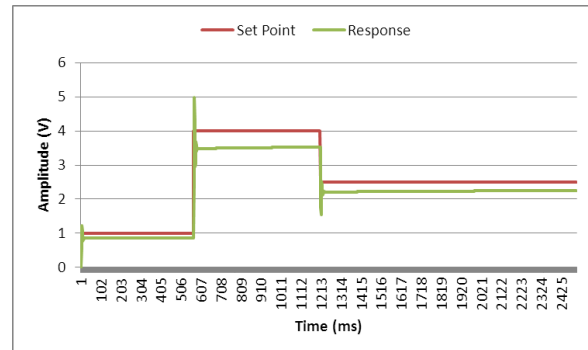


Fig.9 Response of DC Motor Speed Control System without Network

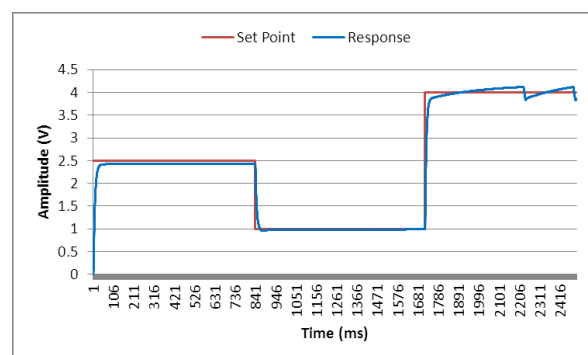


Fig.10 Response of DC Motor Speed Control System through Network

The fourth simulation was a DC motor speed control system by utilizing a network. The result was shown in Fig.10. From Fig.10, it is obtained that the system approached first order system response.

The system has no overshoot and it has 3 percent of steady state errors. Although in the beginning the system responded well into the change of set point, but system tend to be unstable when it approached a high set point. It was seen in the Fig 10 that a small oscillation was occurred.

By comparing the four results above, it can be clearly seen that the effect of delay time caused the NCS to be unstable. These instabilities were seen as the high of maximum overshoot and the occurrence of oscillation. However, the implemented GA-optimized PID controller could make a well compensation for the system so that its response could approached the desired set point.

5. Conclusion and Recommendation

Based on the results of experiments and analysis, some conclusions can be obtained as follows.

- 1) The existence of delay time can cause the NCS to be unstable.
- 2) Delay time in the NCS could not be eliminated, but it could be compensated by doing modification on the control method.
- 3) GA can be used as an adaptive mechanism to perform tuning of PID controller parameters.
- 4) PID controller that had been tuned by the GA could compensate the delay time occurred in NCS.

Besides the conclusion of experiments, several recommendations for future research can be formulated as follows.

- 1) Experiments could be conducted on a variety of plant types, both for sequential and process control.
- 2) The number of plant and controller which are working in parallel could be added to allow deeper analysis on the effect of the delay time due to the increasing of communication network utility.
- 3) Instead of MRAC, it can used directly some other adaptive mechanisms in controller parameter tuning.

Acknowledgements

The acknowledgements were given to the Department of Electrical Engineering, Faculty of Industrial Technology, Sepuluh Nopember Institute of Technology (ITS) for issuing the permission of submitting this paper and Control Engineering Laboratory which providing the necessary experiments facilities.

References

- [1] Anonym. ARX: Estimate parameters of ARX or AR Model Using Least Squares. Matlab Help Menu: The Mathworks Incorporation. 2010.
- [2] -----. Modular Servo System MS150: DC, Synchro & AC Basic Assignments, Versi Manual: 150-1 EdG 0193. England: Feedback Instruments Limited. 2001.
- [3] -----. Pressure Control Trainer Instruction Manual: 38-714. Versi Manual: 38-series, Ed04-012003. England: Feedback Instruments Limited. 2001.
- [4] Astrom, K.J. and Wittenmark, Bjorn. *Adaptive Control: Second Edition*. United Kingdom: Pearson Education. 1994.
- [5] Dotanziv. PRBS Generation: Signature Addition. Hebrew University of Jerusalem: Department of Computer Science and Engineering. 2003.
- [6] García-Rivera, Matías and Antonio Barreiro. *Analysis of Networked Control Systems with Drops and Variable Delays*. Elsevier Automatica 43 (2007). Page 2054 – 2059. 2007.
- [7] Goldberg, D. E., *Genetic Algorithms in Search, Optimization, and Machine Learning*. Addison-Wesley Publishing Co., Inc., 1989
- [8] Griffin, Ian. *On-line PID Controller Tuning using Genetic Algorithms*. Dublin City University. 2003
- [9] Ibrahim, Saifudin Bin Mohamed. *The PID Controller Design Using Genetic Algorithm*. University of Southern Queensland: Faculty of Engineering and Surveying. 2005.
- [10] Kim, Jing-Sun, et al. 2008. *Auto Tuning PID Controller based on Improved Genetic Algorithm for Reverse Osmosis Plant*. World Academy of Science, Engineering, and Technology 47 (2008). Page 384-389. 2008.
- [11] Ogata, Katsuhiko. *Modern Control Engineering 3rd Edition*. New Jersey: Prentice Hall. 1997
- [12] Pohjola, Mikael. *PID Controller Design in Networked Control Systems*. Helsinki University of Technology: Department of Automation and Systems Technology. 2006.
- [13] Suyanto. *Algoritma Genetika dalam MATLAB*. Yogyakarta: Andi Publisher. 2005.
- [14] Yang, Fang and Huajing Fang. *Control Structure Design of Networked Control Systems Based on Maximum Allowable Delay Bounds*. Elsevier Journal of the Franklin Institute 346 (2009). Page 626–635. 2009.

Improving Modern Port Competitiveness by using Data Mining to obtain Strategic Decision

DHANIKA BUDHI A.¹ MAHENDRAWATHI E.R.² and RULLY SOELAIMAN³

- 1 *Graduate School of Management of Information Technology, Department of Magister Management of Technology, Institute Technology of Sepuluh Nopember (ITS), Surabaya, Indonesia. email: dhanika09@mhs.mmt.its.ac.id , dhanika.budhi@yahoo.com*
 - 2 *Department of Information System, Faculty of Information Technology, Institute Technology of Sepuluh Nopember (ITS), Surabaya, Indonesia. email: mahendra_w@is.its.ac.id*
 - 3 *Department of Informatics, Faculty of Information Technology, Institute Technology of Sepuluh Nopember (ITS), Surabaya, Indonesia. email: rully@is.its.ac.id*
-

Abstract: Modern port management nowadays is a demand in the global era. Port services are consist of various kind, among them, there are many customers that need to be understand. It is important to define customer attribute and behavior to drive port's profitability. In this study, RFM (Recency, Frequency, Monetary) is one kind of data mining technique used to analyse customers based on their buying behavior. With this method, high-to-low response customers can be identified. The result of this study is expected can help the management in a decision making process in order to improve services development, customer service customization and competitiveness of the company.

Keywords: *Decision Support System, Data Mining, RFM, Customer Relationship*

Introduction

Modern port management nowadays, the speed and accuracy of goods delivery in fact being a bet in order to succeed the development of an archipelago country like Indonesia. There are many kinds of port services, such as shipping services, cargo handling, and container services. Each of them consist of many customers that have each of their own behavior.

It is important to understand their behavior. Better services such as customer service customization, targeting customer, and services development improvement can be build if the company understand it well.

RFM (Recency, Frequency, Monetary) analysis can be used to characterize customers behavior. By understanding it, management of the port company can obtain better strategic decisions to treat their customer than before and improve their competitiveness level to a new high.

There is no doubt that if a company wants to keep its advantage, it needs not only to attract new customers, but also to keep and maintain old valuable ones [5].

Data used in this study presented on anonymous. Further explanation of RFM is presented in section 2. Meanwhile, implementation of RFM to make customer profilings will be discussed on section 3. On the section 4, the result of RFM analysis is described. Conclusion of this study will be stated on section 5. SPSS 17 is used as a tool to help the RFM calculation process.

RFM analysis

RFM is a method of segmenting customers on their buying behaivor. Its use is primarily for improving the efficiency of marketing efforts to existing customers. It is a very powerful tool that involves little more than creating segments from the three groups. [4]

RFM analysis is a three-dimensional way of classifying or ranking customers to determine the top 20% or it can be said as best customers. It is based on the 80/20 principle that 20% of customers bring in 80% of revenue [1]. RFM analysis uses information about customer past behavior that is easily tracked and readily available. [3]

Recency is the number of months since the last purchase occurred. It is typically the most powerful of the three characteristics for predicting response. It is said that if people recently purchased something from a company, they are more likely to make another purchase than someone who did not recently make a purchase [4].

Frequency is how many purchases the customer has made within a specified time period. Meanwhile, monetary is total money spent by the customer, again, in a specified time period. [3]. These three characteristics can be used alone or in combination with other characteristics to assist in CRM (customer relationship management) efforts [4].

In order to group customers and perform analysis, a customer model known as pyramid model is used. The pyramid model groups customers by the revenue they generate into categories as shown in Fig. 1. The advantages of this approach is that it focuses the analytical process on categories and terminology that can be meaningful for business, such as decision making, prediction concerning of customer's position alteration in the pyramid, knowing the inactive customers, and so on.[1].

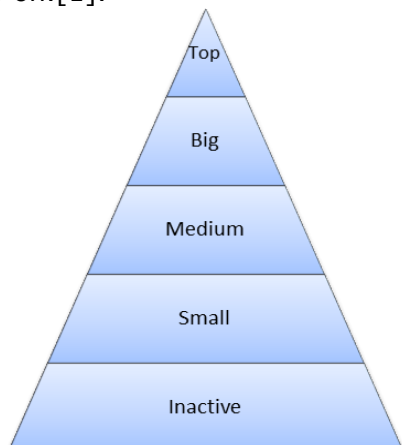


Fig.1: Pyramid Model

The pyramid model splits customers into five segments. If RFM combined with pyramid model, there would be five segments on each of recency, frequency, and monetary factors.

Customer Profiling by using RFM Analysis

RFM can be used not only on catalog or merchandise company but also on services company. This study will take place on a modern port company. This company moves on port services business, domestic and international purposes. There are various kinds of port services. It includes ships services, cargo services, and container services [2]. This study just takes definition of customers in general meaning, it is not specific on the deep definition kind of customers like people who used the ships as passengers, or how many containers that filled the ship. It can be said that customers are ships departed and make transactions on the port.

Definition of recency on the case study is the number of months in the last 18 months since the last transaction occurred by the ship. Frequency is how many times the ship has visited. It is limited from 5 to 50 visits in the last 18 months. Monetary value is the total amount of money spent by the ship while making transactions on the port.

Data used for test purpose retrieved from random data of company's database. By selecting random sample of customers, it is hoped that all types of customers would be presented, both recent and not so-recent customers, frequent and less-frequent customers, also range of customers that spent their money to get the port services.

Objective of this study is to use the results of test to identify which groups of customers are more likely to respond.

Customer segmentation begins with finding a distribution of customers in general pattern. Table-1 shows about category of customer (ship) based on their recency of visiting the port.

Table-2 tells about how frequent the ship visits the port. Monetary factor range are spread from 250 million rupiah.

Table 1: Recency of Visits

type	last transaction	category
5	0-1 months	top
4	2-3 months	big
3	4-7 months	medium
2	8-12 months	small
1	13-18 months	inactive

Table 2: Frequency of Visits

type	frequency of transaction	category
5	46-50	top
4	31-45	big
3	16-30	medium
2	11-15	small
1	5-10	inactive

After split customers into several category like on pyramid model, next steps is use SPSS 17 to calculate the RFM score. In this version of SPSS, it has a feature to make the analysis process become easier. There are two kind of RFM analysis on SPSS 17. It is based on transaction datas or customer datas. This study using the second option, using customer datas.

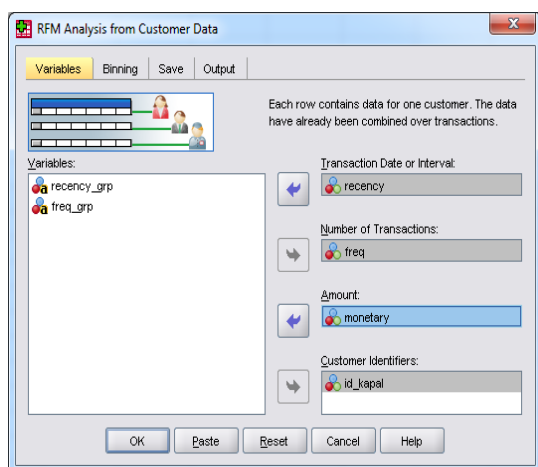


Fig.2: RFM Analysis using SPSS 17

Fig. 2 above shows what data need to be filled in order to do the process. By completing the pre-requisite datas, RFM analysis can be done.

Experimental Result

RFM Analysis tools of SPSS 17 will have several results, such as:

- Recency_score
- Frequency_score
- Monetary_score
- RFM_Score

From the 100 datas used in this test, the results are categorized in pyramid model, presented in Fig.3 for Recency score chart, Fig.4 tells about frequency score chart, Fig.5 shows about the monetary score.

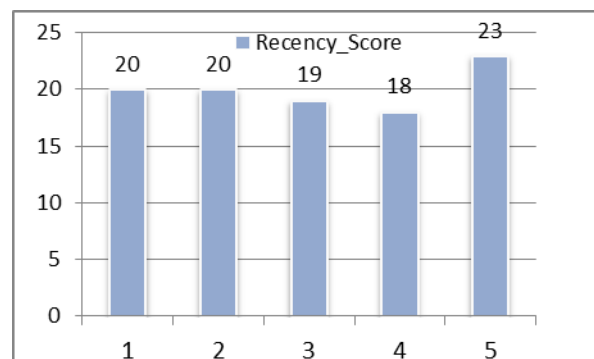


Fig.3: Recency Score

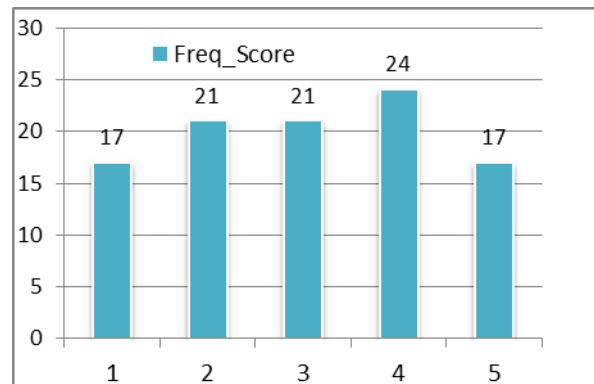


Fig.4: Frequency Score

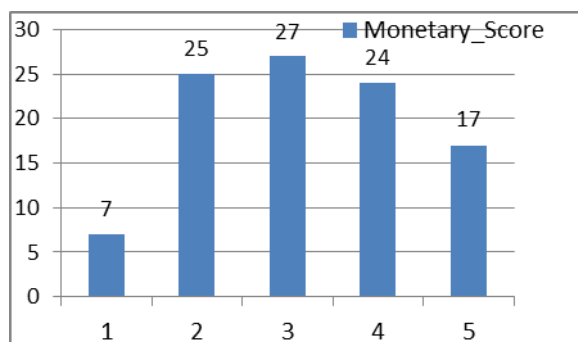


Fig.5: Monetary Score

Besides of three of these reviews, there is a combination of three of them, it called RFM score or RFM index. This index can be easily collected on append each of R,F,M score for each of customer. For example, if R=1, F=3, and M=4 then RFM score=134.

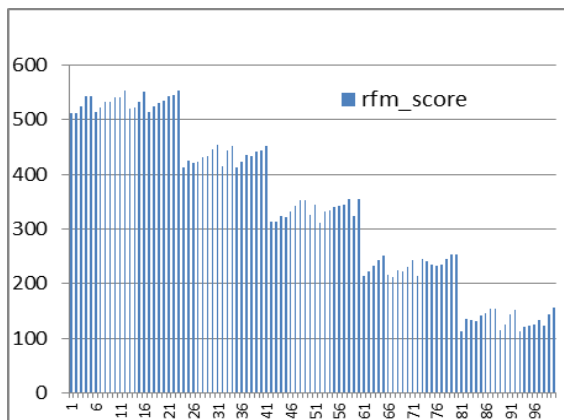


Fig.6: RFM Score Result

Fig.6 above shows that there are 5 major categories formed from the combination of RFM factors. Furthermore, Fig.7 shows the summarize of RFM score in categorical. category=1 identical with 'inactive' on pyramid model and category=5 is the same as 'top' on pyramid model.

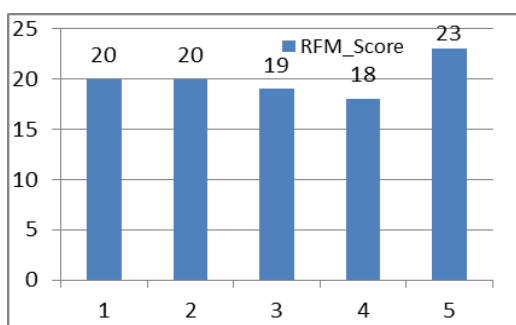


Fig.7: RFM score Summarized

Conclusion

The following conclusions are deducted from the experimental results:

- Customer behavior can be identified by using RFM to find their characteristic from their habit of visiting the port.
- RFM was shown to be effective approach for predicting responses.
- RFM can be used to support the customer relationship program as part of strategic planning of the company

- By using RFM analysis, segments of customer can be identified. It said that from 100 of customers, the company has about 41% of loyal customer and moderate customer about 19% and small potential customer is about 40%. Almost half of them. It means that company do not need to waste their energy to keep these unpotential customers.
- By understanding behavior and characteristics of customers, the company can plan a special service to keep the loyal customers and better services to retain moderate customers.

Future Research

As in any research, our study has its limitation. Further study is needed to see if the result of RFM can be combined with other methods, or make a deeper RFM analysis for each kind of port services and comparation from one another.

Acknowledgement

The acknowledgements were given to the Department Magister Management of technology, Graduate School of Institute Technology of Sepuluh Nopember (ITS) (ITS) for issuing the permission of submitting this paper and which providing the necessary facilities.

References

- [1] Aggelis, Vasilis et al (2005). Customer Clustering using RFM Analysis, ICCOMP'05 Proceedings of the 9th WSEAS International Conference on Computers. ISBN:960-8457-29-7.
- [2] Budyanto, Eko Hariyadi et al (2007). Manajemen Bisnis Pelabuhan, PT. Andhika Prasetya Ekawahana, Surabaya, Indonesia.
- [3] Mason, Charlotte (2003). Recency, Frequency and Monetary (RFM) Analysis. Kenan-Flagler Business School, University of North Carolina
- [4] Rud, Oliviar Parr. (2001), Data Mining CookBook, Willey & Sons, Canada.
- [5] Wang Hei-Chia et al (2006). A Web Service for Evaluating an e-Commerce Site: Mining On-Line Customers' Preferences. IJCSNS International Journal of Computer Science and Network Security, Vol.6 No.7B, July 2006.

INTELLIGENT CLUSTERING OF SPATIAL DATA FOR SPATIAL CLASSIFICATION USING DATA MINING

AHAMED SHAFEEQ B M¹ GOVARDHAN HEGDE²

- 1 *Department of Computer Science & Engineering, Manipal Institute Of Technology, Manipal University, Manipal -576104, India email : ahamed.shafeeq@manipal.edu*
- 2 *Department of Computer Science & Engineering, Manipal Institute Of Technology, Manipal University, Manipal -576104, India email : govardhan.hegde@manipal.edu*
-

Abstract: Clustering large spatial databases is an important problem which tries to find the densely populated regions in the feature space to be used in data mining. The aim of this paper is to study the regional economic difference with the spatial data mining theories and classify the regions intelligently for the sustainable development of the province. This information can be used by the administrative department for launching the various plans for the development of the province. In this paper, we take the per capita GDP as index variable, and take the state administration as basic analysis unit and clustering the states based on per capita GDP. Based on the ESDA methods(global and local spatial autocorrelation) of spatial data mining theory, including Moran I index, Moran scatter plot and LISA, we research and analyze the economy of spatial distribution of India in 2009 from the spatial interactive angle. The results show that economy of Indian states has a strong spatial correlation and there also exist spatial heterogeneity problems between states. Clustering is an important task in spatial data mining and spatial analysis. A family of bio-inspired algorithms, well-known as Swarm Intelligence (SI) has recently emerged that meets these requirements and has successfully been applied to a number of real world clustering problems. A very important analysis on state's economy data would be clustering to identify state groups with the attributes of interest which have similar properties so that the central administration can plan for the sustainable development of the province. In contrast to the prevalent research efforts of developing new algorithms, there has been a lack of effort to re-use existing algorithms for varying domain and tasks. One such intelligent clustering algorithm is the Automatic Clustering with Particle Swarm Optimization (MEPSO) algorithm which was recently proposed as a very good candidate to solve such problems.

Keywords: *Spatial data mining, Spatial autocorrelation, ESDA, Clustering*

1. Introduction

Spatial data mining is the process of discovering interesting and previously unknown, but potentially useful patterns from large spatial datasets and other character hidden in the database. Extracting interesting and useful patterns from spatial datasets is more difficult than extracting the corresponding patterns from traditional numeric and categorical data due to the complexity of spatial data types, spatial relationships, and spatial autocorrelation [10]. Spatial auto correlation is a powerful technique for the

analysis of spatial pattern in variant values which has been successfully applied in location geography [6, 10]. In the recent years, the techniques of spatial data mining have been becoming a research hotspot of space information fields, and great results have been achieved. The disparity of regional economy has always been the hot topic in the regional economic fields [13]. The large differences in observed levels of per capita real income across the major states of India are arising from differences in the steady state levels, rather than from differences in the position of states along

their similar transitional growth paths[12]. Most of the traditional methods that have been used identical to investigate the disparity of regional economy [8, 16], but the research indicates that it's a universal problem that there exists spatial disparity in regional economic development, particularly spatial autocorrelation and spatial heterogeneity must be taken into account when analyzing convergence process of regional scale [6].

Exploratory spatial data analysis method (ESDA) of spatial data mining is a set of techniques aimed at describing and visualizing spatial distributions, at identifying atypical localizations or spatial outliers, at detecting patterns of spatial association, clusters or hot spots, and at suggesting spatial regimes or other forms of spatial heterogeneity. Through analysis of spatial autocorrelation, we can use the exploratory spatial data analysis method to reveal spatial dependency and spatial heterogeneity, and with further research, we can get a deep understanding of regional economic problems [2]. In this paper, we take the states of India as an example, and take the per capita GDP scale as research unit. With the correlation analysis of ESDA in spatial data mining, we describe and visualize the spatial patterns and characteristics economy in Indian states.

2. Exploratory spatial data analysis (ESDA)

In this paper, with exploratory spatial data analysis(ESDA) of spatial data mining, from the angle of spatial interaction, we get the spatial dependency and spatial heterogeneity through spatial autocorrelation analysis [5], and on this basis we investigate the characteristics of regional economic disparity in the states of India .

ESDA is essentially the "data-driven" analysis method, with the spatial correlation measures as its core. The spatial autocorrelation is an important index to test the coincidence of value similarity with location similarity [6]. We carry out the global statistics and the local statistics by computing spatial autocorrelation index [17]. In this paper, we investigate the spatial autocorrelation with the software GeoDa designed by

Anselin(GeoDA Center for Geospatial Analysis and computation, Arizona state University) to get spatial weight matrix, on this basis finally we measure global or local spatial autocorrelation using Moran's I or Local Moran I (LISA) index.

A. Spatial Weights Matrix

Spatial weights matrix W is the precondition of exploratory spatial data analysis. The appropriate choice of the spatial weight matrix is one of the most difficult and controversial methodological issues in exploratory spatial data analysis and spatial econometrics [3].

The matrix W is defined as follows:

$$\left(\begin{array}{cccc} W_{11} & W_{12} & \dots & W_{1n} \\ W_{21} & W_{22} & \dots & W_{2n} \\ \dots & \dots & \dots & \dots \\ W_{n1} & W_{n2} & \dots & W_{nn} \end{array} \right)$$

Where n is the region numbers. If regions i and j is neighbour relationship, $W_{ij}=1$; else $W_{ij}=0$. Generally, we hold that a region has no neighbour relationship with itself, that is $W_{ii}=0$.

B. Global Spatial Autocorrelation Indexes

When the same attribute of different observe objects in space present some regularity, but not random distribution, we can believe that there exists some spatial autocorrelation between observed objects. The measurement of global spatial autocorrelation is usually based on Moran's I statistic, this statistic is written in the following form: [6]

$$I = \frac{N \sum_i \sum_j w_{ij} (x_i - \bar{x})(x_j - \bar{x})}{(\sum_i \sum_j w_{ij}) \sum (x_i - \bar{x})^2}$$

Where N is the observe regions; w_{ij} is spatial weights matrix; x_i is the value of region i ; \bar{x} is the mean value of all observation values. Moran's I varies between -1 and 1. On a given significant level, a value near 1 indicates that similar attributes are clustered, and a value near -1 indicates that dissimilar attributes are clustered. If a Moran's I is close to 0, it indicates a random pattern or absence of spatial autocorrelation.

C. Local Spatial Autocorrelation Indexes

The way to detect local spatial clusters but also to analyze local instability in the form of atypical localizations, spatial outliers, and spatial regimes is to use Moran scatter plots in conjunction with LISA as suggested by Anselin (1995). In the presence of global positive autocorrelation, Moran's I statistic may indeed mask regions that deviate from this global pattern [11].

Anselin (1995) proposed a local Moran index or local indicator of spatial association (LISA) to capture the instability or local clusters. The local Moran index for a region i measure the association between a value at i and values of its nearby areas, defined as: [4]

$$I_i = \frac{(x_i - \bar{x})}{(S_x)^2} \sum_j w_{ij} (x_j - \bar{x}) \quad (2)$$

A positive I_i means either a high value surrounded by high values (high - high) or a low value surrounded by low values (low - low). A negative I_i means either a low value surrounded by high values (low - high) or a high value surrounded by low values (high - low).

3. ESDA on rural regional economy

In this paper, we take the agricultural total output value per capita as index variable, and take the state administration as the basic analysis unit to research the regional economy spatial distribution of India.

A. Global spatial autocorrelation

Firstly, the normal transformation was applied to research variable of the agricultural total output value per capita to fulfil the demand of global spatial autocorrelation test. With the formula 1, we continue to calculate the research variable's spatial correlation coefficient and the corresponding standardized statistics (Ref: table 1)

Table 1 display the Moran's I statistic of the per capita GDP of 2009 for the 32 states of India. In the future our plan is to focus on 626 district administrations of India. Inference is based on the permutation approach with 1000 permutations. It appears that per capita

GDP is positively spatially autocorrelated since the statistic is significant with $p=0.001$. This result suggests that the distribution of per capita GDP total output value is by nature clustered.

B. Local spatial autocorrelation

1) Moran Scatter Plot.

In this paper, we adopted the GeoDa software designed by Anselin to calculate the Moran scatter plot of per capita GDP of Indian states of 2009 (as Figure 1).

Figure 1 displays the Moran scatter plot for our sample: 28 States of India and 4 union territories. It can be seen that most Indian states are characterized by positive spatial association. In 2009, 56.3% of Indian states exhibited association of similar values (18.7% in quadrant HH and 37.5% in quadrant LL). Furthermore, the Moran scatter plot can help to identify atypical regions. In 2009, 9 states of India displayed association of dissimilar values (4 in quadrant HL and 5 in quadrant LH). Most of the north eastern states shown LL type association. Only few LH regions are detected.

2) Local Spatial Autocorrelation and LISA
LISA is a local spatial correlation index to measure the similar or dissimilar degree between research region and its neighbours. With GeoDa, we calculated local Moran I of per capita GDP total output value of every states of India, and plotted the LISA distribution diagram on the basis of z-test ($p \leq 0.05$). (Figure 2).

With the global spatial autocorrelation statistic, we can measure the spatial correlation degree, and then to capture the spatial correlation structure from the whole view. Since global spatial autocorrelation statistic yields a single result for the entire data set, it cannot discriminate between a spatial clustering of high values and a spatial clustering of low values in the case of a global positive spatial autocorrelation [4], and the global statistic may indeed mask regions that deviate from this global pattern. So we need to analyze the regional per capita GDP of India from local scale. From the Moran scatter plot and LISA diagram, we conclude that:

For the research variable of per capita GDP total output value, such clusters are detected. For instance, the core regions

and some eastern regions of India are LL state. It means that the per capita GDP total output values of these regions are all lower than others, at the same time, these regions cluster together. From the calculated data, we know that 18.7% of Indian states are HH, and 37.5% are LL, that is there are more than 50% of Indian states are correlated in the distribution status. In addition, more insight into the scatter plot and LISA diagram, we can find that there exists spatial heterogeneity (HL or LH). We have done the preliminary study of disparity of per capita GDP in Indian states. In continuation with this work we plan to cluster 626 districts of India using intelligent clustering algorithm with the various attributes. The output will be useful for the local administration to focus on the sustainable development of the province.

4. Clustering

Clustering is an important task in spatial data mining and spatial analysis. Cluster analysis, one of the data mining techniques, provides the capability to investigate the spatial variation of data. Clustering aims at representing large data sets by a fewer number of prototypes or clusters. The clustering algorithm which employs the PSO model automatically determines the number of clusters in a previously unhandled dataset [15]. PSO-based clustering algorithm was first introduced by Omran et.al showed that the method outperformed K-means, FCM and a few other state-of-the-art clustering algorithms. Our proposed method is depicted in the figure.(Ref: Figure 3).

We have considered 32 states and few attributes for our experiment with WEKA software using simple k-means algorithm (refer figure-4). But for the natural clustering we need intelligent clustering so that the administrative department can plan in a better way. The following Intelligent Clustering Algorithm will be implemented in MATLAB to check its effectiveness in our application. The statistics(1,15) shows the method outperformed K-means, FCM and a few other state-of-the-art clustering algorithms.

4.1 Automatic clustering Algorithm based on using PSO

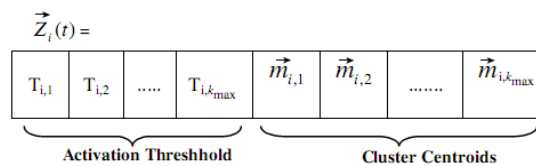
PSO-based clustering algorithm was introduced by Omran et al.The results of

Omran et al.[16]showed that PSO based method outperformed K-means, FCM and a few other state-of-the-art clustering algorithms.

The process of knowledge discovery from databases necessitates fast and automatic clustering of very large datasets with several attributes of different types[14]. Tremendous research effort has gone in the past few years to evolve the clusters. However, little work has been taken up to determine the optimal number of clusters at the same time. Most of the existing clustering techniques, based on evolutionary algorithms, accept the number of classes K as an input instead of determining the same on the run.

4.1.1 Particle representation

In the proposed method, for n data points, each p-dimensional, and for a user-specified maximum number of clusters k_{max} ,a particle is a vector of real numbers of dimension $k_{max} + k_{max} \times p$.The first k_{max} entries are positive floating-point numbers in(0,1),each of which determines whether the corresponding cluster is to be activated (i.e.to be really used for classifying the data) or not. The remaining entries are reserved for k_{max} cluster centres, each p-dimensional. A single particle can be shown as[15]



Algorithm: The MEPSO Algorithm

1. for $t = 1$ to t_{max} do
2. if $t < t_{max}$ then
3. for $j = 1$ to N do {swarm size is N }
4. If the fitness value of the particle_j in t -th time-step > that of particle_j in $(t-1)$ th time-step then
5. $\beta_j = \beta_j + 1$
6. end if
7. Update Local best_j
8. If the fitness of Local best_j > that of Global best now then

9. Choose Local best_j put into candidate area.
10. end if
11. end for
12. Calculate β of every candidate, and record the candidate of β_{max} .
13. Update the Global best to become the candidate of β_{max} .
14. else
15. Update the Global best to become the particle of highest fitness value.
16. end if.
- 17 end for.

When the fitness value of a particle at the t^{th} iteration is higher than that of a particle at the $(t+1)^{th}$ iteration, the β will be increased. After the local best of all particles are decided in each generation, the local best is moved, which has higher fitness value than the global best into the candidate area. Then the global best will be replaced by the local best with the highest growth rate β .

Conclusions

The study of the spatial distribution of regional per capita GDP value in Indian states of 2009 using exploratory spatial data analysis (ESDA) method of spatial data mining highlights the importance of spatial interactions and geographical including spatial weights matrix, Moran I index, Moran scatter plot and LISA is proved to be a powerful tool to reveal the characteristics of regional economy of each states in relation to those of its geographical environment. ESDA reveals significant positive global spatial autocorrelation and very strong spatial cluster characteristics to regional rural economy of India and the analysis of Moran scatters plot and LISA diagram reveals that there exists spatial autocorrelation and spatial heterogeneity of per capita GDP between Indian states. The GeoDa software is useful only for the preliminary study of spatial correlation. The k-means clustering will be useful for the known, small dataset. The intelligent Clustering mechanism will resolve the

major drawback of k-means algorithm is to determine the parameter k to represent natural cluster. In contrast to the prevalent research efforts of developing new algorithms, there has been a lack of effort to re-use existing algorithms for varying domain and task. We have used 32 states data for the experiment. In continuation with this work we plan to cluster 626 districts of India using intelligent clustering algorithm with the various attributes which affects the development of the province. By using intelligent clustering our plan is to provide useful information for the local administration to focus on the sustainable development of the province. The clustering algorithm will be used to examine i) how growth has varied across India's states (ii) the income gap between rich and poor states (iii) reduction of poverty in rich and faster-growing states (iv) Employment rate (v) the main features affecting the economic growth in poor and rich states.

References

- [1] Ajith Abraham, Swagatam Das, and Sandip Roy, "Swarm Intelligence Algorithms for Data Clustering", soft computing for knowledge discovery and data mining, spinger verlog, Germany ISBN 978-0-387-69934-9 pp 27-313, 2007
- [2] Anselin L., "Interactive techniques and exploratory spatial data analysis in Geographical Information Systems, Principles, Technical Issues, Management Issues and Applications", John Wiley & Sons, Inc, 1999. pp. 253-266.
- [3] Anselin L, "Spatial econometrics: methods and models", Kluwer Academic Publishers, Dordrecht, 1998.
- [4] Anselin L, "Local indicators of spatial association-LISA", Geographical Analysis, 1995, pp. 93-115
- [5] Cliff A D, Ord J K, "Spatial Auto-correlation", Pion, London, 1973.
- [6] Cliff A D, Ord J K. "Spatial Processes: Models and Applications", Pion, London, 1981.
- [7] Goodchild M, Anselin L, Applebaum R, "Towards a spatial integrated social Science", International Regional Science Review, 2000, pp. 139-159.
- [8] Guo Qingwang, Jia Junxue, "The Factors Contribution to Regional Economic Convergence and Disparity in China", Finance & Trade Economics, 2006, pp. 11-17.
- [9] Haggett P, A.D.Cliff, A.Frey, "Location Analysis in Human Geography2: Locational Methods", John Wiley, New York, 1977.
- [10] Han J., Kamber M., Tung A.K.H.: "Spatial Clustering Methods in Data Mining: A Survey. In: Geographic Data Mining and Knowledge Discovery", pp. 1-29. Taylor & Francis, Abington (2001).

International Engineering Symposium, March 3-5, 2011 Kumamoto Univ., Japan

- [11]Julie Le Gallo, Cem Ertur, "Exploratory spatial data analysis of the distribution of regional per capita GDP in Europe, 1980-1995", Regional Science, 2003, pp. 175-201
- [12]Kshamanidhi Adabar," Economic Growth and Convergence in India", Journal in growth and development, Indian Statistical Institute, 2003.
- [13] Li Xiaojian, Qiao Jiajun, "County Level Economic Disparities of China in the 1990s", ACTA GEOGRAPHICA SINICA, 2001, pp.136-145.
- [14]Mitra S, Pal S K and Mitra P,(2002),Data mining in soft computing framework: A survey, IEEE Transactions on Neural Networks,Vol.13,pp.3-14.
- [15]Omran M,Salman A and Engelbrecht A P,(2002),"Image Classification using Particle Swarm Optimization". In Conference on Simulated Evolution and Learning, volume1, pp.370 - 374.
- [16] Paul Cashin, Rathna Sahay," Regional Economic Growth and Convergence in India", Finance & Development ,March 1996
- [17] Wang Yuanfei, He Honglin, Spatial Data Analysis Method, Science Press, Beijing, 2007.

Table 1

Moran's I Statistics for Research Variable

Variable	Moran's I	Standard Deviation
per capita GDP	0.2344	0.1267

Note: The expected value for Moran's I statistic is constant: $E(I) = -0.0323$
All statistics are significant at $p = 0.001$

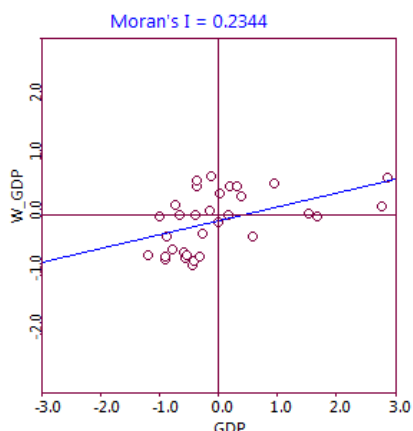


Figure 1 Moran scatter plot

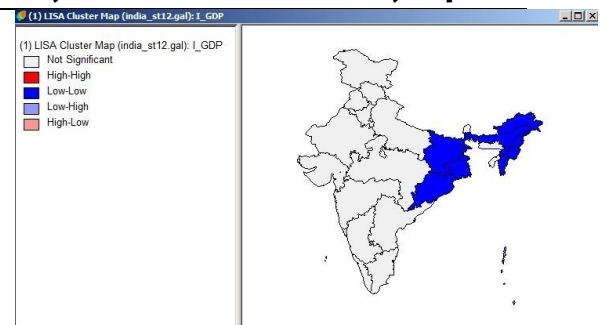


Figure 2: LISA cluster map

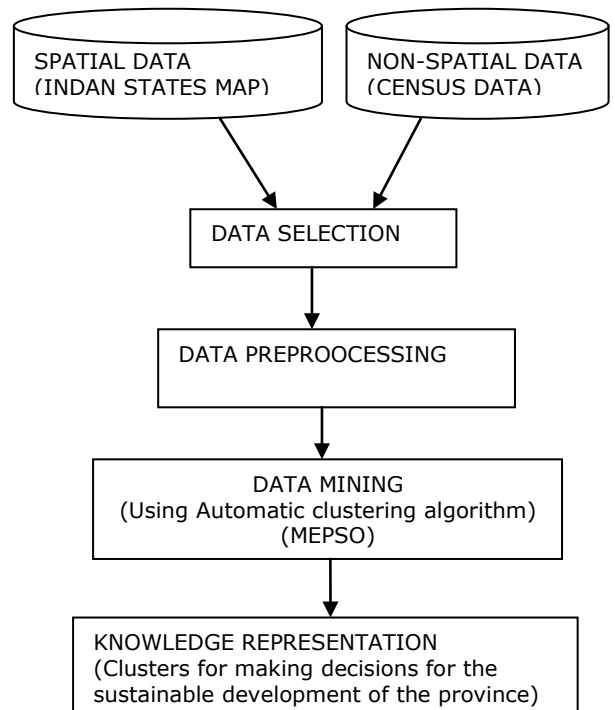


Figure 3 Proposed approach –Intelligent Clustering

Attribute	Full Data (32)	Cluster#				
		0 (6)	1 (3)	2 (6)	3 (4)	4 (13)
GDP	44427.9688	25614.8333	43923.6667	25916.5	102313	43960.3077
Literacyrate	69.9641	63.465	89.1033	56.1417	83.8675	70.6485
TaxRevenues	267799.5	163479.6667	162788.6667	299960.1667	570031.25	232342.6154

Clustered Instances						
0	6 (19%)					
1	3 (9%)					
2	6 (19%)					
3	4 (13%)					
4	13 (41%)					

Figure 4 Clustering using k-means (WEKA)

Reliability of fault tolerant routing algorithm for torus embedded hypercube interconnection network

N. GOPALAKRISHNA KINI¹ M. SATHISH KUMAR² and MRUTHYUNJAYA H.S³

- 1 *Department of Computer Science and Engineering, Manipal Institute of Technology, Manipal University, Manipal, India. Email : ng.kini@manipal.edu*
 - 2 *Department of Electronics and Communication Engineering, Manipal Institute of Technology, Manipal University, Manipal, India. Email : mskuin@yahoo.com*
 - 3 *Department of Electronics and Communication Engineering, Manipal Institute of Technology, Manipal University, Manipal, India. Email : mruthyu.hs@manipal.edu*
-

Abstract: Reliability and availability are two common measures normally used to evaluate the fault-tolerance of a system. We present a reliability and availability analysis of fault tolerant routing algorithm for a newly proposed Torus embedded hypercube interconnection network for parallel computers. Algorithm has been designed such that an optimum routing path will be selected if there are selectable paths between two nodes to provide an efficient fault tolerant mechanism. Reliability and availability analysis has been done on such proposed network. According to the analysis it is observed that the reliability of the torus embedded hypercube interconnection network improves with respect to the scalability of the network. It is also observed that the availability of a system can be high even if individual components have low reliability.

Keywords: *Torus network, Hypercube network, embedded network, Data routing path, Fault tolerance, Reliability, Availability.*

Introduction

The significant advantages of hypercube and torus networks as in Hennessy and Patterson (2005), Hwang and Briggs (1990) can be combined by embedding them to give rise to a torus embedded hypercube network as suggested in Kini et al. (2009a). Such a combination results in a system which can be implemented with small node degree, which implies a reduction in hardware cost per node Louri and Sung (1994), Kini et al. (2009a). Also, a constant node degree results in a system that is scalable without having to modify the individual nodes as suggested in Louri and Sung (1994), Kini et al. (2009b), Kini et al. (2009c).

Fault tolerance in highly parallel computers is important for achieving reliable and high performance computing as given in Hennessy and Patterson (2005), Kini et al. (2009f). It is worth to note that, in our proposed torus embedded hypercube

interconnection network, when one or more nodes fail, a large number of available links enable the fault free nodes to continue communicating with other nodes as shown in Kini et al. (2009e), Kini et al. (2009f).

An efficient fault tolerant data routing algorithm is presented for torus embedded hypercube interconnection network Kini et al. (2009f). Our algorithm gives the optimum path even in the presence of single/multiple faulty nodes in the interconnection network. In this paper, we present a reliability and availability analysis on fault tolerant data routing algorithm for our proposed network.

Theoretical Consideration

A brief discussion on embedding of the torus and the hypercube networks to obtain the torus embedded hypercube network is presented here. More details on this can be found in Kini et al. (2009a), Kini et al. (2009c).

Several concurrent torus networks are used in the architecture while combining the torus and the hypercube network. Let $l \times m$ be the size of concurrent torus network and N be the number of nodes connected in the hypercube, then the torus embedded hypercube interconnection network will be of size (l, m, N) . Nodes with identical positions in the torus networks will form a group of N number of nodes. These nodes will be connected in the hypercube configuration. Such nodes can be addressed with three components; row number i and column number j of torus appended with the address of node k of hypercube. Hence, a (l, m, N) -torus embedded hypercube network will have $l \times m \times N$ number of nodes and a node will be addressed as (i, j, k) where $0 \leq i < l$, $0 \leq j < m$ and $0 \leq k < N$. More details on combining the data routing functions of independent torus and hypercube along with routing algorithm can be found in Kini et al. (2009c), Kini et al. (2009e).

For a $(4, 4, 8)$ -torus embedded hypercube interconnection network, a node with a seven bit address has its left most two bits representing row number, the very next two bits representing column number and the remaining least significant bits representing the address of the hypercube as shown in Fig. 1. Note that end to end connections of concurrent torus are not shown for simplicity in the diagram.

Reliability on Fault Tolerance

Initially the algorithm developed was applied to the network assuming that there will never be any faulty nodes present in it. Once the algorithm has given promising result such as tracing the optimal path between any sources to any destination the work was enhanced by introducing faulty nodes in the network. More details on this is explained in Kini et al. (2009d), Kini et al. (2009f). This algorithm developed formally proves that even with multiple faulty nodes, the proposed torus embedded hypercube interconnection network can still establish optimal routing path successfully. Optimum routing path will be selected if there are selectable paths between two nodes to provide an efficient fault tolerant mechanism.

The torus embedded hypercube interconnection network is highly scalable. More details about the scalability of a network can be obtained from Kini et al. (2009a), Kini et al. (2009b). Reliability analysis has been done on such proposed network. To define the Reliability of a network that addresses the probability that a given source-destination pair has at least one fault-free path between them as in Nidhi Sharma (2008), Vicente Chirivella et al. (2001). In the reliability analysis the probability of node/link failure in a scaled up network is considered. An analytical methodology is used in predicting the reliability and availability of interconnection network. This methodology takes into account the network topology, network size and the routing algorithm used. The reliability analysis presented here is with respect to the failure of the neighboring nodes/links along a routing path. The reliability aspects are examined and presented for simulated interconnection network.

Availability of network

Availability is the probability that the system is operational. It is the fraction of time that the system is performing as intended over a period of time. Availability is different from reliability for a repairable system because it covers the operation of a system over sequences of failure-free periods and repair periods. As failures occur, the network state changes into the degraded states and ultimately to the failed State as in Vicente Chirivella et al. (2001).

The network remains operational as long as at least one of the neighbouring nodes/link remains operational such that a node will never get isolated. Assuming that link/node fails independently, the availability of the network is measured. This methodology considers that the degrading of the network occurs for some duration in a day. Using the network failure rate λ , repair rate μ , mean time between failure MTBF and mean time to repair MTTR as in Nidhi Sharma (2008), network availability is obtained.

Result

Table 1 gives the reliability analysis for the torus embedded hypercube

interconnection network. Possibility of number of neighboring node/link failure along a routing path is taken into account considering the scalability of torus embedded hypercube interconnection network.

As the scalability of the network is done a study on the reliability is made. For a defined network configuration, each and every node possesses equal link complexity. The graphical reliability analysis of scaled up torus embedded hypercube interconnection network is presented in Fig. 2.

Table 2 shows the comparison of availability for the network shown in Fig. 1, when the neighboring node/link failure is observed for 1 hour, 2 hours and 3 hours a day, which includes repair time after failure. It is assumed that the network works normally for the remaining period of the day.

Conclusion

Fault tolerance in interconnection networks determines the worst possible combination of faulty components that causes its failure. But, the probability of the worst possible combination is usually low, and the routing algorithm is able to find a route between the source and destination nodes.

We have analysed the reliability on proposed torus embedded hypercube interconnection network. The results show that the reliability of the torus embedded hypercube interconnection network improves with respect to the scalability of the network. Larger the network better the reliability. Fall in the reliability also gets minimized as the network is scaled up.

Analysis of availability shows that when the network has a lower failure rate, it spends most of the time in the initial degraded states. This is due to the long time to network failure and a high repair rate. If the network is repaired immediately, it will usually be back to the normal functioning state, and it will move away from this normal functioning state as time taken to repair increases. It is observed that the availability of a system can be high even if individual components have low reliability. It is also noted that for

any assumed time duration of the network failure, the availability remains constant and availability of the network reduces as the failure time duration increases.

References

- [1] J. L. Hennessy and D. A. Patterson, Computer Architecture: A Quantitative Approach, 3rd ed., Morgan Kaufmann, 2005, 702 pp.
- [2] K. Hwang and A. Briggs, Computer Architecture and Parallel Processing, 1st ed., McGraw-Hill, Inc. New York, 1990, 334 pp.
- [3] Louri and H. Sung (1994), An Optical Multi-Mesh Hypercube: A Scalable Optical Interconnection Network for Massively Parallel Computing, IEEE Journal of Lightwave Technology, V. 12, pp. 704-716.
- [4] Kini N. G. et al (2009a), Analysis and Comparison of Torus Embedded Hypercube Scalable Interconnection Network for Parallel Architecture, International journal of Computer Science and Network Security, V. 9, No.1, pp. 242-247.
- [5] Kini N. G. et al (2009b), Design and Comparison of Torus Embedded Hypercube with Mesh Embedded Hypercube Interconnection Network, International journal of Information Technology and Knowledge Management, V. 2, No.1, pp. 87-90.
- [6] Kini N. G. et al (2009c), A Torus Embedded Hypercube Scalable Interconnection Network for Parallel Architecture, IEEE Explore Conference Publications, pp. 858-861.
- [7] Kini N. G. et al (2009d), An Optimal Data Routing Scheme for Mesh Embedded Hypercube Interconnection Network with Multiple Faulty Nodes, International journal of Computer and Information Science and Engineering, World Academy of Science, Engineering and Technology WASET, V.3, No.1, pp. 26-30.
- [8] Kini N. G. et al (2009e), Performance Metrics Analysis of Torus Embedded Hypercube Interconnection Network, International journal on Computer Science and Engineering, V.1, No.2, pp. 78-80.
- [9] Kini N. G. et al (2009f), A case study of Fault Tolerant Routing Mechanism for Torus Embedded Hypercube Interconnection Network, International journal of Information Technology and Knowledge Management, V. 2, No.2, pp. 361-364.
- [10] Nidhi Sharma (2008), "Reliability Analysis of Multistage Optical Interconnect Networks for High Speed Parallel Computing", Proceedings of the International Conference on Parallel and Distributed Techniques and Applications (PDPA 2008), Las Vegas, Nevada, USA, July 14-17, pp. 352-358.
- [11] Vicente Chirivella et al (2001), "Accurate Reliability and Availability Models for Direct Interconnection Networks", IEEE International Conference on Parallel Processing, Sept 3-7, pp. 517-524.

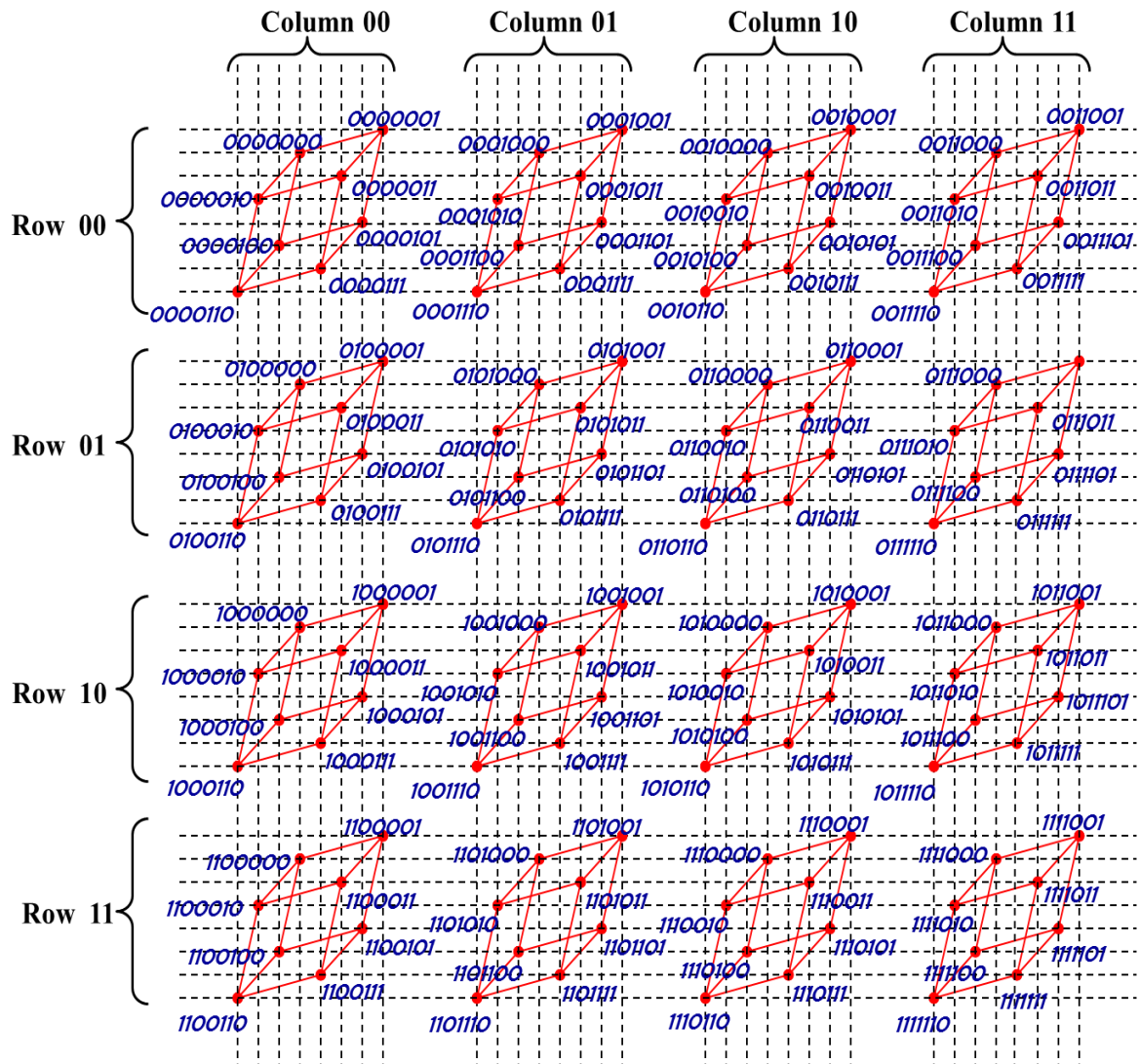


Fig. 1 A (4, 4, 8)-Torus Embedded Hypercube Interconnection Network

Table 1 Reliability analysis for torus embedded hypercube interconnection network

No. of links/nodes Failure predicted	Reliability of network in percentage			
	(4,4,8)	(4,4,16)	(4,4,32)	(4,4,64)
1	85.7	87.5	88.9	90
2	71.4	75	77.8	80
3	57.1	62.5	66.7	70
4	42.9	50	55.6	60
5	28.6	37.5	44.4	50
6	14.3	25	33.3	40
7	00	12.5	22.2	30
8	-	00	11.1	20
9	-	-	00	10

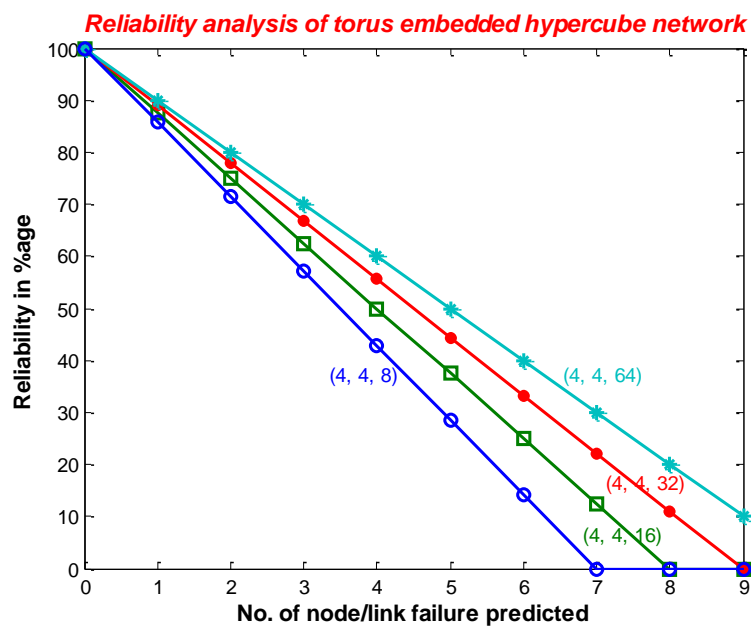


Fig. 2 Graphical reliability analysis for torus embedded hypercube interconnection network

Table 2 Comparison of Availability analysis for torus embedded hypercube interconnection network

Number of nodes / links failure	1 hour			2 hours			3 hours		
	Failure rate	Repair rate	Availability in percentage	Failure rate	Repair rate	Availability in percentage	Failure rate	Repair rate	Availability in percentage
1	0.044	1	95.83	0.045	0.5	91.67	0.048	0.33	87.5
2	0.087	2	95.83	0.09	1	91.67	0.095	0.667	87.5
3	0.131	3	95.83	0.136	1.5	91.67	0.143	1	87.5
4	0.174	4	95.83	0.182	2	91.67	0.190	1.333	87.5
5	0.217	5	95.83	0.227	2.5	91.67	0.238	1.667	87.5
6	0.260	6	95.83	0.272	3	91.67	0.286	2	87.5

An intelligent cashew kernels classification using color features

NARENDRA V G¹ and **HAREESHA K S²**

Dept. of Computer Science and Engineering,

Manipal Institute of Technology, Karnataka, India-576 104

E-mail: narendra.vg@manipal.edu¹ and hareesh.ks@manipal.edu²

Abstract: Cashew is a commercial commodity that plays a major role in earning foreign revenue among export commodities in India. The purpose of this research work is to explore image processing techniques and approaches on Indian cashew variety identification based on their kernels. Color is an important quality factor for grading, marketing, and end users. Our primary objective is to develop a cost-effective intelligent model to identify the cashew kernels.

Color features in the RGB (red-green-blue) color space are extracted and computed. A feed-forward neural network is trained to classify sample cashew kernels. An intelligent classification system based on computer vision system can be developed for automated grading and sorting to speed up the classification of cashew kernels. This will solve the major problems of many of the cashew export industries also, gives justice to the cashew growing farmers in accurate grading. The classification system is evaluated on cashew kernels of 6 different grades. The results of our study shows that, the system gives about 80% classification rate.

Keywords: *Image Processing, color features, cashew kernel, grading, Neural Network.*

Introduction

Cashews are most widely grown crop of India especially in coastal areas. In the recent years, Cashew is a commercial commodity that plays a major role in earning foreign currency among export commodities in India. The Assessment of cashew quality is the function of government agency entrusted to perform cashew kernel grading and it is important for the cashew export industry.

The grading operation is important, as it is the last opportunity for quality control on the kernels. With the exception of a few grading aids, all grading is being done by manually. In the present international market scenario, it is very much essential to keep our products well graded automatically to compete in the market place. For large operations looking towards export markets, it is necessary to grade the kernels to an international level. India, the largest exporter & distributor of Cashew Nuts in the world, cashew nut are of the highest quality and has helped in

gaining repute amongst all in the international market.

Grading of cashew kernels is based on inspection of physical quality attributes such as color, shape, and size. By using these physical attributes, a trained person determines the cashew kernel of which class (i.e.white wholes). The Table 1 illustrates the Grade designations and definitions of quality of cashew kernels (i.e.white wholes). Reference color slides are available to assist with the assessment of cashew kernel color. Despite the training of grading personnel and the availability of reference slides, the current methods for cashew kernel quality evaluation is time consuming, tedious, and inherently inconsistent. An objective and cost-effective computer vision system is needed to segregate cashew kernels. Such a system would not only facilitate cashew grading but also serve as a quality control tool for processing facilities such as elevators, seed cleaning plants, and oil mills.

There have been successful applications of computer vision in agricultural product inspection, but most efforts are still in the research and development stage. Research endeavors have grown rapidly in the past 10 years. Extracting various morphological, tonal, textural, and color features for classification of grains by variety, grades, and damage has been the focus of the reported research and only a few researchers have reported work on soybean[5].

The objective of this study was to determine the usefulness of color features of cashew kernel images in classifying them into white wholes categories. The research entailed the development of an algorithm to segment images of cashew kernels of different shades and colors. The proposed work emphasizes on development of Artificial Neural Networks (ANN) based method for automatic classification of cashew kernel samples instead of using color histograms. Color histograms have several inherent limitations for the task of image indexing and retrieval. The images of the cashew kernel were scanned using Compaq S200 scanner with a resolution of 300 dpi. The seed images were then segmented, isolating the region of interest from the background and 15 color parameters were extracted. The 15 distinguishable features are mentioned in Table 2. The parameters obtained were used to train a neural network created. Once trained, the network was tested with other cashew kernel for the desired results. All these programs were developed using MATLAB 7.8 version.

Proposed system

The system acquires images of the cashew kernel and this forms an input to the image-processing unit that extracts the necessary features of the cashew kernel in Fig. 1. The features obtained were the inputs to the neural network, the network is trained using supervised learning to recognize cashew kernel of category White Wholes. To test the network, 6 sets consisting of all white wholes category of each 10 cashew kernels were used.

Materials and Methods

Experiment Samples

Cashew kernel samples were obtained from the Karnataka Cashew Board, Mangalore District, Karnataka State. The samples included cashew kernels of white wholes class. Cashew inspectors manually classify the kernels. Examples of cashew kernels are shown in Fig. 2.

Collection of sample Images

A high-resolution (5-megapixel) Sony digital color camera (Model DSCV3) was utilized. The captured images were obtained as JPEG image files.

The cashew kernel samples were photographed at a particular position at specific lighting conditions. The images are likely to have a high resolution since it yields a better image processing result. An example of a sample jpeg image of a Cashew kernel is shown in Fig 2.

Image Segmentation

Image segmentation refers to the process of delineating the regions or objects of interest in an image. For this work, the cashew kernel must be isolated from the background before they could be characterized. The first step in image analysis is to find objects. For this, object color must be different from colored foreground, based on a given color threshold set by the user. Thresholding is an important part of image segmentation. The threshold value is generated according to the results of the histogram analysis and was constant for the same environment conditions. This results in a black and white (binary) image from the color image, where background pixels are painted black and objects painted white. The image must retain the color information of the cashew kernel when segmentation was processed. All the pixels with intensity value greater than 35 were assigned the value 255, and all pixels with intensity value less than or equal to 35 were not processed in any operation [2]. For the technology to be practically useful, the segmentation algorithm needs to be fast and capable of handling variations in cashew kernels.

The input data will be an image consisting of multiple nuts, so the first step is to segment this image in order to view and extract features from each individual nut

separately. The problem is simplified by considering only the grey-scale image Fig. 3 rather than a 3-dimensional color image.

Due to the nature of the contrast between background and foreground, a thresholding technique has been applied in order to create a binary image: i.e. all nut pixels are represented as '1' and all background pixels are represented a '0' (Fig. 3(c)). The value of a suitable threshold has been determined empirically. In this form it becomes straight forward to identify each region by examining groups of connected pixels, and labelling the region appropriately (as shown in Fig. 3(c)). A labelled region can be segmented by ignoring all the other labelled regions (Fig. 3(d)).

Once segmentation process is over, the image data for each individual nut is stored in a structure array with the following fields:

CASHEWS.color- N-by-M-by-3 colour image of nut
 CASHEWS.grey- N-by-M grey-scale intensity image of nut
 CASHEWS.bw - N-by-M binary mask
 CASHEWS.label- string containing the class label

Feature Extraction

Image features of the cashew kernels were extracted to characterize the physical quality attributes of cashews. A number of color features were computed and tested. They included the means and standard deviations of R, G, and B(red, green, and blue); the means of H, S, and I (hue, saturation, and intensity); excess red ($2R-G-B$), excess green ($2G-R-B$), and excess blue ($2B-R-G$). The excess colors correspond more closely to the way humans perceive colors than the RGB representation [4]. Also the other feature has been investigated as morphological characteristics of cashew kernel.

However, the main focus so far has been morphological features as these are the most appropriate for discriminating between different grades of 'White Wholes' due to fact these grades are indeed assigned according to the number of nuts found in a given weight. The function `cashew_morph()` performs the appropriate analysis and returns a

quantitative value for each of the following features to the data structure of each nut.

- Area
- Perimeter Length
- Major Axis Length
- Minor Axis Length
- Convex Area
- Boundary Pixels

Using the binary representation of each nut, an algorithm that counts the pixels in the nut image is used to calculate an area description. The boundary of each nut is also traced, which is used to measure the perimeter. The major axis length is also indicated in the Fig. 3(e).

Feature vectors can be formed easily by extracting the values out of the data structure as follows

`areas = [cashews.Area];`

Algorithms were developed in Windows environment using Matlab 7.8 programming tools to extract color features of individual cashew kernel. From the red (R), green (G), and blue (B) color bands of an image, hue (H), saturation (S), and intensity (I) were calculated using the following equations[5]:

$$I = \frac{1}{3}(R + G + B)$$

$$S = 1 - \frac{3}{(R + G + B)}[\min(R, G, B)]$$

$$H = \arccos \left\{ \frac{[(R - G) + (R - B)/2]}{(R - G)^2 + (R - B)(G - B)^{1/2}} \right\}$$

Neural Network Classifier

Jayas et al. (2000) have indicated that back propagation neural network (BPNN) suits the best in these applications [1] [3]. A feed-forward neural network was trained for classification of the cashew kernel samples into W-180,W-210,W-240,W-320,W-450 and W-500 classes. Inputs to the network were image features computed, and six outputs formed a three-bit binary number representing the category of classification (000 to black, 001 to W-180, 010 to W-210, 011 to W-240, 100 to W-320, 101 to W-450, 110 to W-500 and 111 to white). Levenberg-Marquardt Back Propagation algorithm was used for training. Using an

approximation to Newton's method is called "Levenberg-Marquardt approximation". This is an improved back propagation method. Levenberg-Marquardt algorithm has the best convergence speeds for small and medium size networks. Tan sigmoid function was used in the hidden layers. Log-sigmoid transfer function was selected because its output (0 to 1) was fit for classification. The network was trained to output a 1 in the correct variety of the output vector and to fill the rest of the output vector with 0. Different numbers of layers and nodes were tested for the network structure. Hidden layers are required, as the patterns belonging to various classes (colors) are linearly non-separable. The mean squared error (MSE) of prediction for the validation data set was used to select an appropriate network structure without over-fitting. Four steps were followed in the training process:

- 1) Assemble the training data.
- 2) Create the network.
- 3) Train the network.
- 4) Test and validate network response to new inputs.

The function `cashew_classify()` performs this task. Below is a summary of the results obtained when each cashew kernel is input to the system.

Result and Discussion

Image Segmentation

A typical segmented image of cashew kernel from the image background is shown in Fig. 2. The cashew kernels were of different colors but the background color was fixed. Fig.3 shows the segmented images along with the mask. The results show that the segmentation algorithm could consistently segment the images. The ability to segment images of cashew kernels of different colors in the same background is important for practical implementation of this technology.

Under laboratory conditions, different background colors may be used for different classes of cashew kernel. Practically, however, cashew kernel of different classes and colors are present in the same sample, and thus they must be imaged with the same background.

Network Structure

The number of neurons in the first layer is 'n' which is equal to the number of input pattern vectors. The number of neurons in the output layer is one which is equal to the number of pattern classes that the neural network has been trained to recognize. The network recognizes a pattern vector P as belonging to class O_i if the i^{th} output of the network is "high" while all other outputs are "low". Trial and error approach was used to find a suitable number of the hidden layer that provided good classification accuracy based on the data input to the neural network. The mean squared errors for the validation data set were compared among different neural network structures.

Classifier Performance

A test sample set, which was not part of either the training or validation samples, was used to test the neural network classifier trained. The test set included 100 randomly selected cashew kernels. The test results of classification are summarized in Table 3. Almost all (80%) of the cashew kernels were correctly classified.

As can be seen, using the current features the first 4 grades can be discriminated with no errors. However work still has to be carried out to discriminate between grades '450' and '500'.

Conclusions

The results of this study show that color features and a properly trained neural network can effectively classify cashew kernels. A computer vision-based system could be developed for automated grading and sorting.

The classification accuracy was acquired under laboratory setting, so it had some limits. In future work, a large quantity of cashew kernels will be investigated.

Acknowledgement

The author would like to thank the Zonal Agricultural Research Station, Brahmavar, Udupi Taluka, Udupi District and Balaji Exports Jarkal Karkal Taluka, Udupi District, Karnataka State, India for providing the cashew kernels samples and relevant information.

References

- [1] Jayas, D.S., Paliwal, J. And Visen, N.S. (2000), "Multi-layer neural networks for image analysis of agricultural products", Journal of Agricultural Engng. Research, vol. 7(2), pp. 119-128.
- [2] Liu et al.(2005), J Zhejiang Univ SCI, 6B(11), pp.1095-1100.
- [3] Rumelhart D. E., G. E. Hinton, and R. J. Williams, (1986). Learning representations by back-propagating errors. Nature 323:533-536.
- [4] Shatalal P, J. Tan.(2003), "Identifying damaged soybeans by color image analysis", Applied Engineering in agriculture, Vol. 19(1),pp.65-69.
- [5] Sujata Kotabagi, B.L.Desai, K. Linganagouda, V.C.Patil, Shashidhar, Sudhir Gupta, Smitha Patil, Asha Kulkarni and Zoheb Hukkeri(2006), "Classification of Soybean Seeds Using Color Image Analysis", Proceedings of (AFITA 2006) 5th conference of Asian federation for information technology in agriculture.

Table 01: Cashew Kernels (White Wholes)

Grade	Count per 454 gms size description	General Characteristic
W-180	170-180	Cashew kernels shall have been obtained through shelling and peeling cashew nuts. Shall have the characteristic shape; shall be white, pale ivory or light ash in color reasonably dry and free from insect damage, damaged kernels and black or brown spots. The kernels shall be completely free from testa.
W-210	200-210	
W-240	220-240	
W-320	300-320	
W-450	400-450	
W-500	450-500	

Table 2: Extracted Features

SN	Features	S N	Features
1	Red mean	9	Saturation mean
2	Red standard deviation	10	Saturation standard deviation
3	Green mean	11	Intensity mean
4	Green standard deviation	12	Intensity standard deviation
5	Blue mean	13	Excess red mean
6	Blue standard deviation	14	Excess green mean
7	Hue mean	15	Excess blue mean
8	Hue standard deviation		

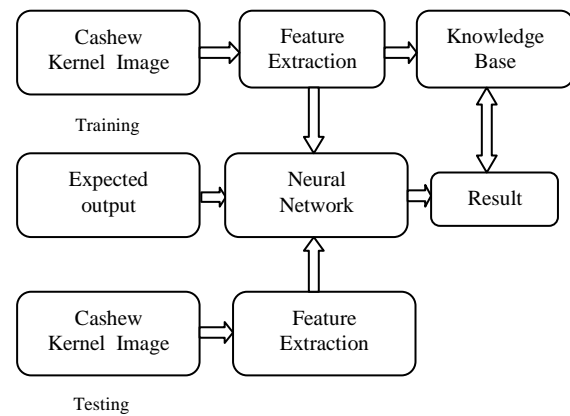


Fig. 1 Block diagram of the system for classification of cashew kernels.

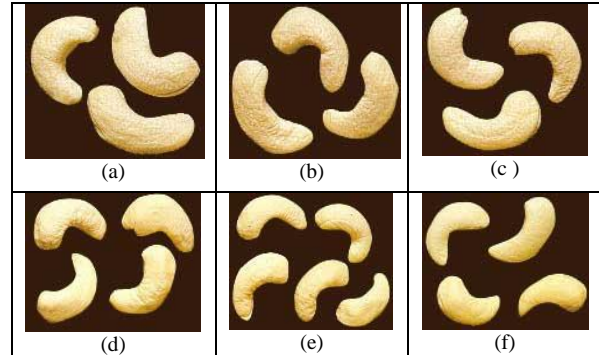


Fig. 2 Images of cashew kernels (a) White wholes-180 (b) White wholes-210 (c) White wholes-240 (d) White wholes-320 (e) White wholes-450 (f) White wholes-500

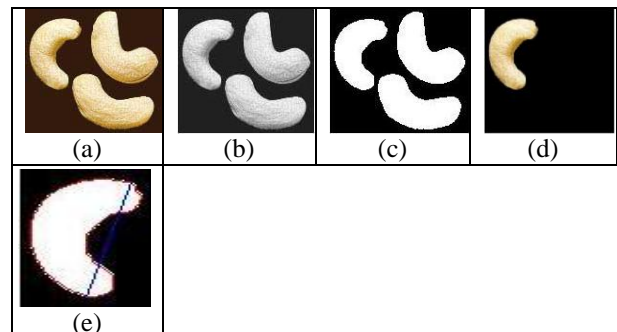
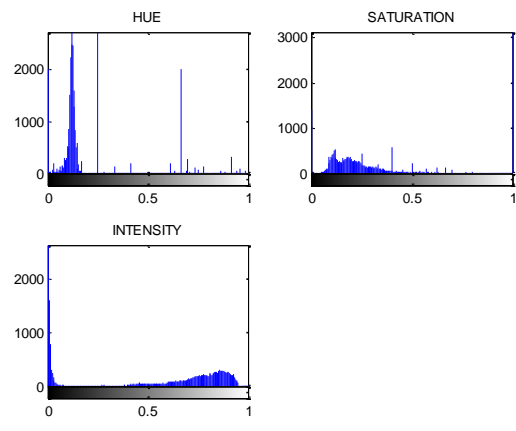
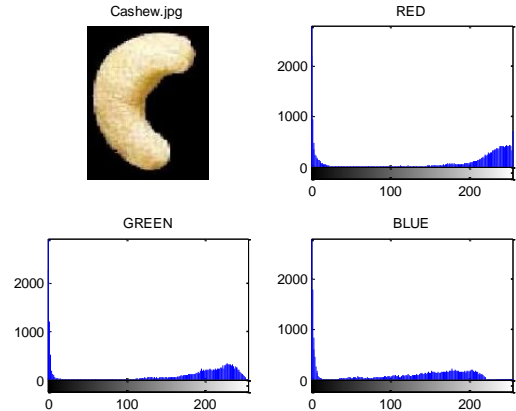


Fig. 3 (a) Cashew Kernel (b) Gray-scale image (c) Mask (d) Individual Cashew kernel (e) Individual Mask



(a)



(b)

Fig. 4 Histograms of (a)RGB and (b)HIS components of Cashew kernel

Table 3: Classification Results for 'White Wholes'

SI No	Grade	No.of samples tested	No. of samples classified correctly	% of classification obtained
01	180	20	19	95.00
02	210	22	20	90.90
03	240	20	17	85.00
04	320	20	18	90.00
05	450	10	08	80.00
06	500	10	04	40.00

Enterprise Knowledge Grid Provisioning for Resource Sharing

PRAVEEN DESAI¹

U. DINESH ACHARYA²

¹ Department of Computer Science& Engineering, Manipal Institute of Technology Manipal, 576 104, India. e-mail:praveen.desai@manipal.edu

² Department of Computer Science& Engineering, Manipal Institute of Technology, Manipal, 576 104, India. e-mail:dinesh.acharya@manipal.edu

Abstract: In today's knowledge based economy, most organizations increased individuals and collective knowledge as the factor for economical performance. Innovation is built on collective knowledge sharing activities of, especially tacit knowledge. The partnership between humans and machines has automated machine control yielding faster performance and improved outcomes with reduced human effort through cognitive capabilities.

This paper considers peering arrangements pre-established. The model needs resource providers being able to provide information in a grid. The mapping of work flow and knowledge flow modelled as direct acyclic graph and investigates heuristics that allow scheduling nodes for optimized resource sharing in cooperative teams and thus provide a new way to model and manage team work processes.

Keywords: Knowledge, Team Work, Work Flow. Knowledge Grid, Scheduling

1. Introduction

Information Technology has amplified our intellectual and physical abilities more than anything. Most organizations collect enormous amounts of historical data about their business operations, transactions, employees etc. This includes not only the structured data (e.g. Database) but also document repositories (e.g. report, proposals, notes, emails et al.). Historical repositories can be analyzed to improve the operational efficiency-reduce operating, production and support cost, improve employee productivity, improve resource utilization, design better products and services, reduce time-to-market etc- if the wisdom hidden in them can be extracted and used to transform operations. However because of distributed and diverse nature of these data sources and the sheer volume of data, a holistic end-to-end analysis of "Knowledge" is often required.

Internal knowledge of the firm refers to product and process specifications and capabilities, technology capabilities, inter-operability, reconfigurations,

organizational culture, employee skill sets and leadership. The external knowledge refers to the knowledge of markets, competitors, technological trends, changing consumer preferences and others.

The performance of team work is not only dependent on the knowledge and capabilities of the individual members but also on how they collaborate [7]. Web based Information Communities (WebIC's) are work systems facilitated by internet infrastructure and composed of voluntary actors that attempt to produce a product or a service.

A typical corporate employees today are mobile all the time; they work in the office but also work from home; they often on the road attending meetings, their project team is distributed geographically across several time-zones. From their blog, intranet tags, wiki entries and e-profiles, people contact them from the other divisions within the company as well as from outside the company, including professionals in their field in different countries and see them

as an expert which empowers and engage them in his work.

In the following sections, we discuss about related work, Knowledge Grid and its features, Knowledge Life cycle, work flow process and algorithms for multi criteria resource selection and time based constraints and finally conclude the paper in section V.

2. Related Work

Web enables us to communicate with the geographically dispersed team. However, HTML based web can't reflect the machine understandable resources. Hence semantic web provides the across platform media basis to exchange knowledge between distributed team members. Resource Description Framework [RDF], Ontology Inference Language [OIL] and DARPA Agent Markup Language [DAML] are XML based semantic web.

Workflow establishes the logical independence order relationship between team member's activities which is pre designed; however it can not cooperate with knowledge assimilation.

So the current technologies such as the Internet, Web, Grid, peer-to-peer networking, data/text mining, information retrieval, question answering, and AI are helpful references but not enough to realize the Knowledge Grid environment. The audacious challenge is to understand how to use Web2.0 to augment social cognition to increase group of users' capacity; speed to acquire-produce-communicate and assimilate knowledge.

3. Knowledge Grid

The Knowledge Grid methodology [5] is a multi disciplinary systems methodology for establishing and maintaining a knowledge world that obeys the principles and laws of economic, nature, society, culture, psychology and Information Technology. Hence it is a sustainable human-machine interconnection environment that enables people or agents to effectively generate, capture, publish, share, manage and promote knowledge, to

process any type of resource through machine, and to transform resources from one form to another. The Knowledge Grid consists of requirements, roles, resources and regulations. It provides appropriate on-demand service to support innovation, team work, simulation, problem solving and decision making by using sharable knowledge. The Knowledge Grid domain is shown in Fig.1. Knowledge Grid exhibits following features.

A. Semantic Networking

The Knowledge Grid needs an open semantic system to establish the understanding between machines as well as between machine and human.

B. Virtual Cyberspace

With machine-understandable semantics, a resource can actively and dynamically gather relevant resources and fuse them to provide appropriate on-demand services for applications by understanding requirements and functions and relating them to each other. A resource can intelligently cooperate with others to accomplish complex tasks and to solve problems by virtual flow dynamics.

C. Economic and Adaptive System

The Knowledge Grid adapts the behaviour of different participants namely producers, consumers and market mechanism. Adopting economical and ecological principles to balance the interests of knowledge producers and knowledge consumers can adapt to appropriate evolution and expansion of resources.

D. Social Grid System

The Knowledge Grid is a virtual social grid, where people enjoy and provide services through versatile flow cycles like control flows, material flows, energy flows, information flows and knowledge flows. People can communicate and gain knowledge from each other through mutually understandable semantics.

3a. Knowledge Flow networks

A Knowledge flow[2] is the passing of knowledge between nodes according to

certain rules and principles. A knowledge node is a team member or role. A knowledge flow starts and ends at a node. A node can generate, learn, process, understand, synthesize and deliver knowledge. A knowledge flow has direction, content and carrier as attributes and sequential, join, split and broadcast as type of flows. Each node is assigned with 'rank/reputation' based on cognitive and creative ability relative to other nodes in the network. The effectiveness of team work requires the reputation differences between the nodes. The rank of a node may change through learning and the more nodes it passes knowledge to, the greater its rank.

Knowledge spirals are formed when knowledge flows in the networks. An effective knowledge spiral maintains the energy differences between nodes and ensures only necessary knowledge is passed between nodes. The knowledge spiral process model is shown in Fig.2A

A node can deliver knowledge to its successors either by forwarding or by passing its own knowledge. Each node has fields such as knowledge area dimension [A] and knowledge Level [L] as

KS₁ (Li,Aj)-> KS₂ (Li,Aj)->.....-> KS_n (Li,Aj)

Above flow structure represents sequential flow chain between Knowledge Spaces[KS].

Knowledge Energy[KE] of node 'i' at time 't' in knowledge space 's' can be represented as KE(s, i ,t) which is a distinguishing factor of a node.

3b. Knowledge Flow pattern

Knowledge gained by composing the team should complete the tasks. A basic knowledge flow pattern[3] is the abstraction of organizational structure and defined as authority [star topology], peer-to-peer [ring topology], hybrid and resource mediated patterns.

In resource mediated pattern[3] there is no direct link between the nodes. So black boards, repositories, portals etc. act as a resource. Knowledge Flow is controlled by imposing constraints such as topic relevancy, cooperation and access privileges.

The cooperation among team members is based on trust between them. So a special matrix 'Trust' records the need for and level of trust between members. Each element in Trust is a function of time $trust_{ij}(t)$ i.e. member 'i' trusts member 'j' at time 't'. The elements can be initialized by team leader and then adjusted based on cooperation score during work.

4. Work flow networks

A workflow can be modeled as a Directed Acyclic Graph [DAG]. We consider that a DAG starts with a single entry node and has a single exit node. Each node connects to other node with edges based on node dependencies.

In workflow graph, a task which doesn't have any parent task is an *entry task* and a task which doesn't have any child task is an *exit task*. If there are multiple entry tasks and exit tasks in a workflow, we can connect them to a zero-cost pseudo entry or exit task. Each task is only assigned for execution on one service and the set of services S_i capable of executing task T_i.

Cost based Scheduling Heuristics

Work flow scheduling focuses on mapping and managing the execution of inter dependent tasks. The heuristics follow the divide -and-conquer technique and the methodology is listed as follow.

1. identify available resource and predict execution time for every task
2. distribute deadline for each task
3. Investigate available time durations, generate schedule and reserve resource based on local optimal solution of every task partition.

The *Heterogeneous Earliest Finish Time* [HEFT] algorithm is a list scheduling algorithm which attempts to schedule

DAG tasks at minimum execution time on a heterogeneous environment.

The *Greedy Cost* [GC] approach is to minimize workflow execution cost by assigning tasks to services of lowest cost.

Suppose C_{\min} and C_{\max} be the total cost by GC and HEFT respectively, and T_{\max} and T_{\min} be their corresponding total execution time then

Deadline D is defined as

$$D = T_{\min} + k(T_{\max} - T_{\min}) \quad \dots [1]$$

Budget B is defined by

$$D = C_{\min} + k(C_{\max} - C_{\min}) \quad \dots [2]$$

The value of k varies from 0 to 10 from tight constraint to relaxed constraint.

A reference model for integrating knowledge flow and workflow can be defined for three levels as shown in Fig5. The role level reflects the organization architecture which maps knowledge flow level, work flow level and team members.

4a. Deadline Constrained Scheduling

The algorithm maps every task T_i onto a suitable service to minimize the execution cost of the workflow and completes it before deadline D. Workflow tasks grouped into task partitions and assigns sub-deadlines to each task based on their workload and dependencies. At runtime, a task is scheduled on a service, which is able to complete it within its assigned sub deadline at the lowest cost.

In workflow task partitioning, workflow tasks are first categorized as either *synchronization tasks* or *simple tasks*. A synchronization task is defined as a task which has more than one parent or child task. In Figure 3, T_1 , T_{10} and T_{14} are synchronization tasks. Other tasks which have only one parent task and child task are simple tasks.

After workflow task partitioning, the overall deadline is distributed over each partition V_i in partition graph ' Ω '. The deadline assigned to any V_i is called a *sub-deadline* of the overall deadline D. The details of Greedy Cost time constrained algorithm is shown below.

Algorithm: Greedy Cost-Time constrained Heuristic

Input: A workflow graph $\Omega(\mathcal{F}, \Pi)$, deadline D
Output: A schedule for all workflow tasks

- 1 Request processing time and cost from available services for $T \in \mathcal{F}$
- 2 Convert Ω into task partition graph $\Omega(\mathcal{F}, \Pi)$,
- 3 Distribute deadline D over $V_i \in \mathcal{F}$ and assign a sub-deadline to each task
- 4 Put the entry task into ready task queue Q
- 5 **while** Q not empty **do**
- 6 Sort all tasks in Q
- 7 T_i = the first task from Q
- 8 Compute ready time of T_i
- 9 Query available time during ready time and sub-deadline
- 10 S = a service which meets Equation 1
- 11 **if** $S=0$ **then**
- 12 $S = S_i^j$ where $j = \min [t_i]^j ; 1 \leq j \leq S_i$
- 13 **end if**
- 14 Make advance reservations of T_i on S
- 15 Put ready child tasks into Q whose parent tasks have been scheduled
- 16 **end while**

$$\text{Minimize Cost } (T_i) = \min C_i^j ; 1 \leq j \leq S_i \quad (4)$$

4b. Budget Constrained Scheduling

If B be the cost constraint [budget] and D be the time constraint [deadline] for work flow execution, then map every T_i on to a suitable request to minimize the execution time of the workflow and complete it with total cost less than B for Budget Constrained scheduling.

Cost distribution attempts to allocate the fastest service to each task among the assigned budget. If Time[T_i] is the completion time of T_i , then scheduling of T_i is given as

$$\text{Minimize Time } (T_i) = \min [t_i]^j ; 1 \leq j \leq S_i \quad (5)$$

4c. Provisioning techniques

A resource sharing creates a large volume of unnecessary traffic [9] in the flow network since a node may receive same queries multiple times through different nodes. The provisioning techniques will help users to obtain the resource availability information from neighbour nodes. Following techniques help in resource identification in knowledge transfer belt.

Least Loaded resource: Knowledge Grid submits a request to the least loaded node based on the information $KE(s, i, t)$

sent by the resource providers for every timeslot.

Feedback based algorithm: This algorithm identifies edges on which redundant information are produced and during execution phase, decides whether to forward information over an edge or not.

During initial phase, a feedback message KS (L_i, A_j) is returned to the upstream node for each duplicate message. Each node in a network forms a group of other nodes, and a different count is kept on each one of node's incident edges for duplicate messages originating from nodes of each different group. Grouping of nodes[11] is based on following criteria.

Hops creation: each node keeps a different count on each of its incident edges for duplicates originating k hops away. Thus, messages originating from close by nodes are most probably not duplicates and each message stores the number of hops traversed so far as shown in Fig4.

Horizon criterion: node is in the horizon of some node if its distance in hops is less than the horizon value [integer] while other nodes are outside its horizon.

As shown in Fig6, generalized knowledge flow discovery architecture is illustrated. A directory service called Knowledge Grid Directory [KGD] supports publishing and discovery of knowledge. Each resource will be registered in KGD and users can access knowledge to meet their requirements. A suitable knowledge is queried as per work flow engine updates.

5. Performance Evaluation

In this section evaluation scenario, performance metrics and observation summary are discussed.

5a. Evaluation Scenario

The evaluation of the strategies is performed using Knowledge Grid Operation Language.[KGOL]. The simulation helps in repeating experiments and thus minimizes cost

incurred. To store the information about resources available in Knowledge Grid, the scheduler uses non-slotted time data structure, allowing for a finer time granularity for the requests accepted as the period allocated minimizing iteration of slots which would be time consuming.

5b. Performance Matrix

The matrices related to request response times include Average Waited Response Time [AWRT]. The AWRT measures how long a user waits to have their requests completed. A minimum AWRT indicates that response is quicker and defined as follows.

Equation3:

$$AWRT = \frac{\sum p_j m_j (c t_j - s t_j)}{\sum p_j m_j}$$

where m_j number of requests ,
 p_j request execution time
 $c t_j$ request time completion
 $s t_j$ submission time
 $(p_j m_j)$ resource consumption of each request
 j weight assigned to each request

In order to compute the benefits of using one strategy over another, compute the cost ratio between AWRT and the amount spent in running request on grid.

DAGs considered here contains about 10 nodes with different schedulers and [1] and [2] holds good for HEFT.

In order to compare the quality of the schedules by algorithms for DAG, Average Normalised Difference Matrix [AND] can be used .

5c. Result Summary

The algorithm proposed in this paper is able to find affordable assignments with better make span when HEFT approach is applied and in budget constrained approach the cheapest assignment is used to build a schedule; this may have the worst make span. The optimization in the performance can be achieved

when the available budget is close to the cheapest budget as obtained.

Regarding running time, HEFT approach takes more time as we move towards a budget close to the cost of the cheapest assignment.

6. Conclusions

The paper began by introducing a Knowledge Grid and characterizing several aspects of the Grid system including knowledge flow, workflow using DAG, resource identification, scheduling and data movement. Taxonomy for each of these areas have been mentioned. This study not only enhances the design and methodologies adopted in current enterprise systems, but also provides a reference to identify areas that need further research.

The workflow model discussed is based on the facts that task dependencies are well defined and work flow doesn't contain any loop and conditional branch. Also looping conditions can be incorporated for domains like medical.

The constraints such as budget and time used in this paper are based on the generalization of heterogeneous model and its usage. However other parameters such as security levels and fidelity could be considered for specific domain.

Acknowledgements

The authors would like to acknowledge the guidance provided by the parent Institution as well as the anonymous reviewers for their constructive comments and suggestions during IES2011.

References

- [1] Adamic, L.A. and Huberman, B.A. Power-Law distribution of the World Wide Web. *Science*, 287, 24 (2000), 2115.
- [2] Berners-Lee, T., Hendler, J., and Lassila, O. Semantic Web. *Scientific American* 284, 5 (2001) 34-[3] Foster, I. Internet computing and the emerging grid. *Nature* 408, 6815 (2000).
- [4] Nonaka, A dynamic theory of organizational knowledge creation, *Organization Science* 5 (1) (1994) 14- 37
- [5] Zhuge H, China's e-science Knowledge Grid environment, *IEEE Intelligent Systems* 19 (1) (2004) 13-17.
- [6] Zhuge, H., 2004b. China's e-Science knowledge grid environment. *IEEE Intelligent Systems* 19 (1), 13-17.
- [7] Zhuge, "The Future Interconnection Environment", *IEEE Computer*, vol.38, no.4, 2005, pp. 27
- [8] Zhuge, H., 2006. Discovery of knowledge flow in science. *Communications of the ACM* 49 (5), 101-107.
- [9] Zhuge, H., Guo, W., Li, X., 2006. The potential energy of knowledge flow. *Concurrency and Computation: Practice and Experience*,
- [10] Zhuge, X. Chen, X. P. Sun and E. L. Yao, "HRing: a Structured P2P Overlay Based on Harmonic Series", *IEEE Transactions on Parallel and Distributed Systems*, vol.19, no.2, 2008, pp.145-158.
- [11] Zhuge, J.Zang, "Topological Centrality and applications", 2009

Table 1 Feedback based approach

Hops creation		Horizon Creation	
Hops	Groups formed by node A	Node in A' horizon	Groups formed by node A
1	B	B	B
2	C	C	C
3	D,J	D	D,E,F,G,H,I
4	E,K	J	J,K
5	F		
6	G,H		
7	I		

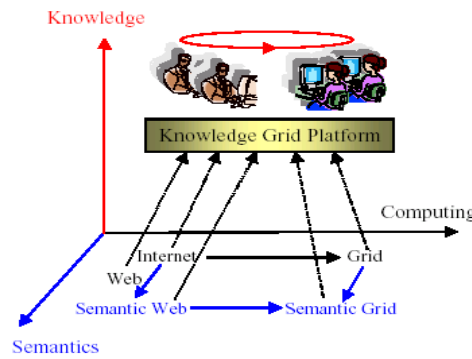


Fig.1 Knowledge Grid domain

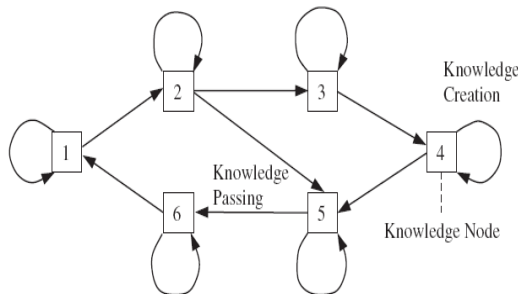
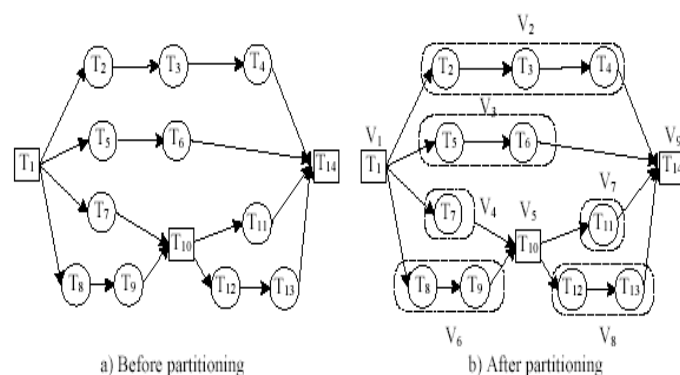


Fig.2 Knowledge spiral process

○ Simple task □ Branch

□ Synchronization task



Simple task



Synchronised task
Branch

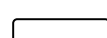


Fig.3 Workflow task partition

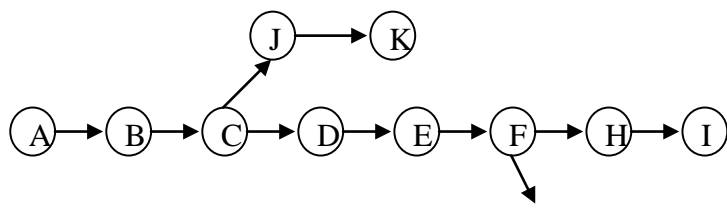


Fig.4 Illustration of feedback based algorithm

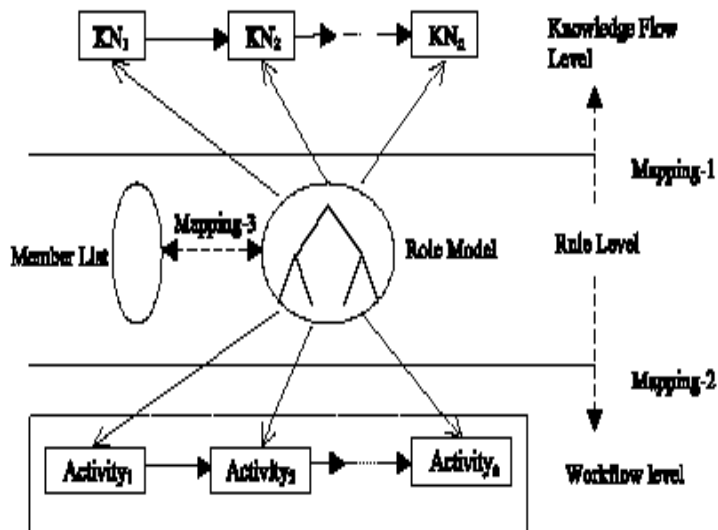


Fig.5 A reference model for integrating Work and Knowledge Flow

Activity1 Register
 Activity2 Update
 Activity3 Publish
 Activity4 Create
 Activity5 Notify
 Activity6 Subscribe

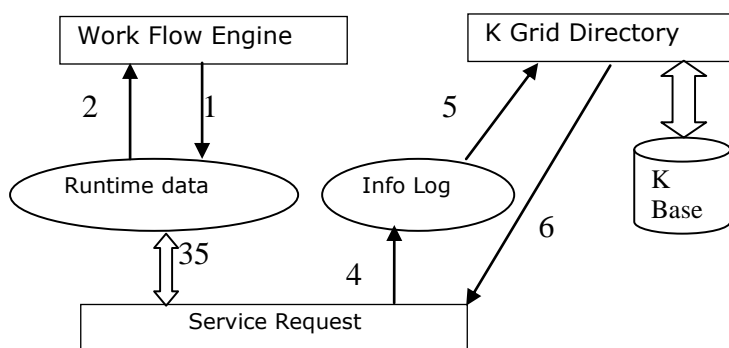


Fig.6 Knowledge Flow Discovery architecture

**BIOLOGY, CHEMISTRY
&
CHEMICAL ENGINEERING**

Tissue Culture Studies on Different Explants of Rice (*Oryza sativa L.*) Varieties Cultivated By Ethnic Communities of Jharkhand State, India

H.P.SHARMA¹, KANAK² and MEENA MISRA³

1,2 University Department of Botany, Ranchi University, Ranchi-834008, Jharkhand, India
e-mail: hanumanpdsharma@yahoo.co.in

3 Department of Biosciences & Biotechnology, School of Biotechnology, Fakir Mohan University, Nuapadhi Campus, Balasore-756020, Odisha State, India.
e-mail:meenamisra@yahoo.com

Abstract: Six local rice varieties were taken for tissue culture studies. Explants of cv. Badshah Bhog showed highest callus induction and regeneration frequencies. Callusing response from young panicle, shoot apex and seed were 100, 90 and 85% in MS + 2,4-D (2.5mg/L). The respective regeneration frequencies were 100, 85 and 79 % in MS+ IAA (2mg/L) + KN(4mg/L).

Keywords: Rice, Callus, Regeneration, Genotype, Physiological status

Introduction

Rice (*Oryza sativa L.*) is a very important food crop because it ensures nutritional security. Rice improvement through conventional method of plant breeding is inadequate as it fails to give desired results. Tissue cultures, on the other hand, holds much promise, therefore, can be utilized as an effective tool of biotechnology for fruitful results.

Jharkhand is a tribal dominated region where different ethnic communities still lead a very simple and primitive life. Because of ethnic diversities, tribes cultivate large number of rice cultivars, their wild relatives/ land races. Although rice tissue culture has been successfully established but still there are huge numbers which needs to be explored for morphogenic studies as cultural response vary greatly with genotypes, organs of the plants and developmental stages of the organs. However, culture medium is also of no less significance. Moreover, role of tissue culture in artificial induction of genetical variables in the rice and other cereal improvement programme has been fairly proved over the decades (Green, 1977; Vasil, 1986 Cantrell and Hettel, 2004; Ozgen et al.,

1996; Bajaj and Mohanty, 2005; Rashid et al., 2003; Carsono and Yoshida, 2006). Therefore, before any meaningful work, it is imperative to establish profuse callus induction and regeneration of rice varieties (Pandey et al 1994; Rashid et al., 1999; Yang et al., 1999; Suprasanna et al., 2000; Islam et al., 2004; Saharan et al., 2004; Al-Forkan et al., 2004; Kumar et al., 2005; Niroula et al., 2005; Afolabi et al. 2008).

Material and Method

The experiments were performed with six local varieties of rice (*Oryza sativa L.*); Badshah Bhog, kanak, Sathi, Sita, Sugapankhi and Tulsi. These cultivars are either upland (Tulsi), medium land (kanak) or Lowland (Badshah Bhog, Sita and Sugapankhi). Seeds and plant materials were obtained from local farmers and Birsa Agriculture University, Kanke, Ranchi. Different explants; seeds, shoot apices and panicles were screened for their morphogenic potentials. Seeds were dehusked manually, steeped in 70% ethanol for 1 min followed by treatment of 0.01% mercuric chloride solution for 15 to 20 min and finally rinsed three times with sterile distilled water.

In order to obtain spikelet the main stem were cut 5-10 cm from base, washed under tap water, scrubbed with 75% alcohol and dipped in alcohol for 10 min. Finally, washed 3-5 times with autoclaved distilled water and stripped of inner leaves under Laminar Air Flow cabinet to dissect out shoot apices and panicles of different length/developmental stages. The young panicles were divided into five developmental stages; P-1 (0.5cm), P-2 (1.5 cm), P-3(3.0 cm), P-4 (4 .0 cm) and P-5 (5.0 cm).

The sterile materials were inoculated in MS (Murashige and Skoog, 1962) medium supplemented with 2.5 mg/L 2,4-D. The pH of the media was adjusted to 5.8 with acid (0.1N HCl) or alkali (0.1N NaOH). The rice seeds, 2-3 in numbers were inoculated into culture tubes under a laminar airflow cabinet.

Regeneration efficacy was observed with MS medium supplemented with 2 mg/L IAA + 4 mg/L KN. All the cultures were incubated at $25 \pm 3^{\circ}\text{C}$ with 16 h light and 8 h dark at 2000 lux light intensity with 60% relative humidity. For callus induction the culture were initially place under dark condition for 10-15 days. Weekly visual observation of cultures was made and frequency of culture proliferation and regenerations were recorded.

Results and Discussion

Callus induction was induced in seeds, shoot apices and panicles (different developmental stages). Hypertrophy of tissues was observed in 4-6 days and full growth of callus was obtained within 4-6 weeks. The callus induction in seeds was generally seen from scutellar end (Fig. 1A) or together with emergence of coleoptile(Fig. 1 B). The nature of callus (compact or friable), rate of growth and colours (cream or white) were dependent on the genotype up to certain stage only, thereafter marked differences were completely lost from 3-4 week onwards. Rhizogenesis and necrotic regions were seen sometimes on callus tissues (Fig.1C). Out of the six varieties of rice; seeds and shoot apex of Badshah Bhog revealed best callus induction frequency (85% and 90%,

respectively) and young panicles of 1 and 3 cm long showed profuse callus (Fig.1G), highest callus percentage (100%) and earliest to reach at maturity. Other varieties, namely, Sugapankhi, Sathi, Tulsi, Kanak and Sita had their maximum callusing of 75, 65, 61, 50 and 45%, respectively from seed explant. Shoot apices also responded good. Mature panicles which were about to emerge from the boot leaves were least responsive in all the undertaken varieties (Table-1). In the present investigation percentage of callus formation was genotype dependent. This observation is in conformity with works of earlier workers (Pandey *et al.*, 1994; Rashid *et al.*, 2003; Niroula, 2005; Wang *et al.*, 2005; Narsircilar *et al.*, 2006; Alina *et al.*, 2008; Shah *et al.*, 2009).

Calli derived from different explants when transferred to differentiating medium, MS+ IAA (2mg/L) + KN (4mg/L), regeneration of complete plants were noticed (Table-2). Differentiation was initiated within a week with notably enlargement of the callus followed by the appearance of green spots which later turned into shoots (Fig. 1D, E, F). Root initiated later, thus complete plantlets were regenerated within 6-8 weeks. In addition to whole plants other responses were also noticed, such as shoots only (Fig.1 I), roots only (Fig.1H), unresponsive or necrotic callus. The whole plant was regenerated within 4-6 weeks. The regeneration depends upon the nature of callus; the embryogenic callus. In the present investigation dry, compact and nodular callus soon changes into embryoids, thus establishing embryogenesis as the main pathway of regeneration in all the five cultivars. These observations are in agreement with the findings of other workers (Nabors *et al.*, 1983; Rueb *et al.*, 1994; Jaminez and Bangerth, 2001; Quiroz- Figueira *et al.*, 2006). Variety Badshah Bhog show and Sugapankhi showed 100% regeneration from panicle of 1.5 and 3.0 cm length, respectively. On the other hand, Sathi, Tulsi, Kanak and Sita had the best response of 95, 83,80 and 78% respectively. Culture

responses of experimental plant materials determine its tissue culture application as genotypes and types of explants were the major factors on culture response. In this experiment, there was significant difference among different genotypes of the same explant and among different explants of the same genotype. The variance of different genotypes resulted from the different physiological characteristics and developmental stages, which led to the different concentrations and ratios of endogenous hormones (Gu *et al.*, 1999). Different explants and their morphogenic response *in vitro* have been attributed to the age and physiological status of explant by different workers, while working with different plants (Ozgen *et al.*, 1996; Diah and Bhalla, 2000). In the present study young explants which are in active phase of growth are considered to be more potential than older ones where growth has ceased. In addition to growth phase of the explants the genotypes also have great bearing on morphogenic response. It accorded with the result of earlier workers (Gao *et al.*, 1999; Wang *et al.*, 2005; Niroula *et al.*, 2005; Afolabi *et al.* 2008).

Conclusion

In the present investigation genotype, nature of the explants and physiological status (age) of the rice varieties has great bearing on callus induction and regeneration potentials of rice varieties. Out of the six local varieties, Badshah Bhog proved to be the best cultivar as its different explants responded better than other varieties. Therefore, this variety will be adopted in future improvement programme.

Acknowledgement

I am grateful to Dr. H.B. Sahu, Head, University Department of Botany for providing research facilities.

References

- [1] Afolabi, A.S., Oyebanj, O., Odusanya, O., Abo, M. E., Misra, M., and Ogbadu, G. H. (2008) Regeneration of Plants from Rice Caryopsis derived Callus Culture of Nigerian Local cv. Suakoko 8 and a NERICA cv. FARO 55. African J. Plant Sci. V.2, No.9, pp. 109-112.
- [2] Al-Forkan, M., Power, J.B., Anthony, P., Lowe, K.C. and Davey, M.R. (2004) Agrobacterium Mediated Transformation of Bangladeshi Indica Rices. Cellu. Mole. Biol. Lett. V. 9, No.2, pp. 287-300.
- [3] Alina, W., Ismanizan, I., Che, R., Md. Jain and Rusian, A. (2008), Improvement of Plant Regeneration From Embryogenic Suspension Cell Culture of Japonica Rice. J. Biol. Sci., V.10 pp. 570-576.
- [4] Bajaj, S. and Mohanty, A. (2005), Recent Advances In Rice Biotechnology Towards Genetically Superior Transgenic Rice. J. Plant Biotechnol. V. 3, pp. 275-307.
- [5] Cantrell, R.P. and Hettel, G.P. (2004), New Challenges and Technological Opportunities for Rice-Based Production Systems For Food Security and Poverty Alleviation in Asia and The Pacific. Paper presented at the FAO Rice conference, FAO, Rome, Italy, February 12-13, 2004.
- [6] Carsono, N. and Yoshida, T. (2006), Plant Regeneration Capacity Of Calluses Derived From Mature Seeds of Five Indonesian Rice Genotypes. Plant Prod. Sci., V.9, No.1, pp. 71-77.
- [7] Diah, A. and Bhalla, P.L. (2000), Plant Regeneration from Mature Embryo-Derived Callus of Australian Rice (*Oryza Sativa L.*) Varieties. Aust. J. Agric. Res., V. 51, No.2, pp. 305-312.
- [8] Gao Z Y, Huang D N. (1999), Some Factors Influencing the Callus Formation and Plant Regeneration in Indica Rice Varieties. *Plant Physiol Comm*, V.35, No.2, pp. 113-115. (in Chinese with English abstract)
- [9] Green ,C. E. (1977), Prospects for Crop Improvement in The Field Of Cell Culture. Hort. Science, V. 12, pp. 131-134.
- [10] Gu R S, Jiang X N, Guo Z C. (1999), Advances In the Studies on The Mechanism of Plant Organogenesis *In Vitro*. Chinese Bull Bot, V. 16, No.3, pp. 238-244. (in Chinese with English abstract).
- [11] Islam,M. M., Wahed, S.A. and Khan, S. A. K. U.(2004), Studies on Callus Induction and Regeneration from Dehusked Rice (*Oryza sativa L.*) seeds. Plant Tissue Cult.V. 14, No.2, pp. 155-160,
- [12] Jaminez, V.M. and Bangerth, F. (2001), Endogenous Hormone Levels in Explants and Embryogenic and Non-Embryogenic Cultures of Carrot. Physiol. Plant., V. 111, No.3, pp. 389-385.
- [13] Kumar, K.K., Maruthasalam, S., Loganathan, M., Sudhakar, D. and Balasubramaniam, P. (2005), An Improved Agrobacterium – Mediated Transformation Protocol For Recalcitrant Elite Indica Rice Cultivars. Plant Mol. Biol. Rep. V, 23, pp. : 67-73
- [14] Murashige, T. and Skoog, F. 1962. A Revise Medium for Rapid Growth and Bio-Assay With Tobacco Tissue Culture. Plant Physiol. V. 1, pp. 473-497.
- [15] Nabors, M.W., Heyser, J.W., Dykes, T.A. and Demott, K.J. (1983), Long Duration, High Frequency Plant Regeneration from Cereal Tissue Culture. Planta, V.157, No.5, pp. 385-391.
- [16] Nasircilar, A. G., Turgut, K. and Fiskin, K. (2006), Callus Induction and Plant Regeneration from Mature Embryos of Different Wheat Genotypes. Pak. J. Bot., V. 38, No. 2, pp. 637-645.
- [17] Niroula, R.K., Sah B.P., Bimp, H.P. and Nayak, S. (2005), Effect of Genotype and Culture Media on Callus Induction and Plant Regeneration from Mature Rice Grain Culture. J. Inst. Agric. Anim. Sci., V.26, pp. 21-26.
- [18] Ozgen, M., M. Turet, S. Ozcan and C. Sancak. (1996), Callus Induction and Plant Regeneration

from Immature and Mature Embryos of Winter Wheat Genotypes. Plant Breeding, V. 115, pp. 455-458.

[19] Pandey, S.K., Ramesh, B. and Gupta, P.K. (1994), Study Of The Effect Of Genotype And Culture Medium on Callus Formation and Plant Regeneration in Rice (*Oryza Sativa L.*). Theor. Appl. Genet. V. 77, pp.205-211.

[20] Quiroz- Figueroa, F.R., Rojas-Herrera, R.M., Galaz-Avalos, R.M. and Loyola -Vargas, V.M. (2006), Embryo Production Through Somatic Embryogenesis Can Be Used to Study Cell Differentiation in Plants. Plant Cell issue Organ Cult., V. 86, No. 3, pp. 285-301.

[21] Rashid, H., Mohammad, A. and quraisi, A. (2003), Plant Regeneration from Seed Derived Callus of Three Varieties of Rice. Plant Tissue Cult., V. 13, No. 1, pp. 75-79.

[22] Rashid, H., Yokoi, S., Toriyama, K and Hinata, K. (1999), Transgenic Plant Production Mediated by *Agrobacterium* in Indica Rice (*Oryza sativa L.*)Plant Cell Rep., V. 15, pp. 727-730.

[23] Rueb, S., Leneman, M., Schilperoort, R.A. and Hensgen, L.A.M.(1994), Efficient Plant Regeneration Through Somatic Embryogenesis from Callus Induced on Mature Rice Embryos (*Oryza Sativa L.*). Tissue Organ Cult., V.36, No.2, pp. 259-264.

- [24] Saharan, V., Yadav, R.C., Yadav, N.K. and Chagpain, B.P. (2004), High Frequency Regeneration from Dessicated Calli of Indica Rice (*Oryza sativa L.*) Afr. J. Biotechnol., V.3, pp. 256-259.
- [25] Shah, M.M., Khalid, Q., Khan, U.W., Shah S.A.H., Shah, S.H. Hassan, A. and Pervez, A. (2009), Variation in Genotypic Responses and Biochemical Analysis of Callus Induction in Cultivated Wheat. Genet. Mol. Res. V. 8, No. 3, pp. 783-793.
- [26] Suprasanna,S., Ganapathi, T.R. and Rao, P.A. (2000), High frequency plant regeneration from somatic embryos of indica rice. Rice Genetics Newsletter V.1, pp. 183.
- [27] Vasil, I.K and Vasil, V. (1986). Regeneration in Cereal and Other Grass Species. In: Cell Culture and Somatic Cell Genetics of Plants. Volume 3.
- [28] Wang, X. H., Shi, X.Y. and Wu, Y. J. (2005), Tissue Culture Response from Different Explants of Rice. Rice Sci., V. 3, pp. 229-23.
- [29] Yang, Y.S., Zheng, Y.D., Chen, Y.L. and Jian, Y.Y. (1999), Improvement of Plant Regeneration from Long-Term Cultured Calluses of Taipei 309, or Model Rice Variety in *In Vitro* Studies. Plant Cell Tissue Org. Cult., V. 57, pp. 199 – 206.

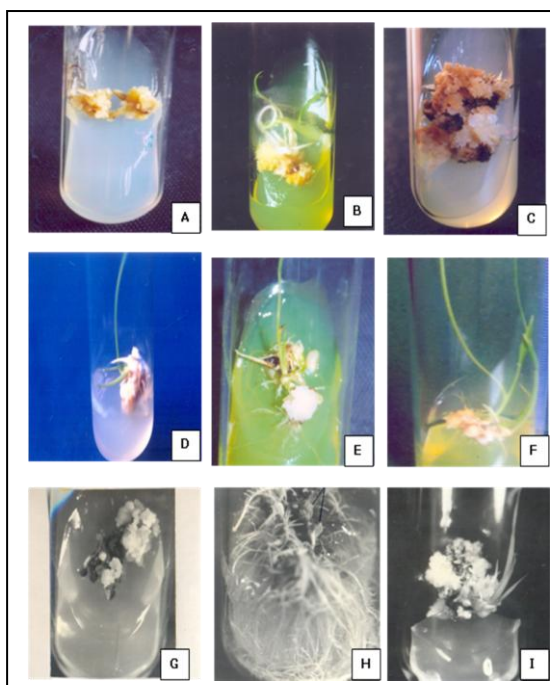


Fig. 1 Morphogenic response of different varieties of rice.

(A) Callus arising from scutellar end, (B) Callus with roots and emergence of coleoptile, (C) Callus showing roots and necrotic regions, (D-F) Seed-derived callus showing regeneration of plantlets.

(G) Panicle showing callus, (H) profuse rooting of callus, (I) shoot organogenesis in callus.

Callus inducing medium: MS+ 2,4-D (2mg/L);Regeneration medium: MS+ IAA (2mg/L)+ KN (4mg/L).

Cultivars: Badshah Bhog (C,F), Sugapankhi (A,D), Sathi (B,E). and Tulsi (G,H,I)

Table 1: Rice varieties showing percentage callus induction from different explants in MS + 2,4-D (2.5 mg/L)

Variety	Seed	Shoot Apex	Length of Panicle(cm)					
			0.5	1.5	3.0	4.0	5.0	Mature
Badshah Bhog	85	90	80	100	100	90	50	15
Kanak	50	55	70	80	78	79	43	08
Sathi	65	68	75	90	90	84	56	07
Sita	45	50	53	74	75	40	37	05
Sugapankhi	75	70	80	92	95	86	60	10
Tulsi	61	65	72	86	80	80	54	09

Table 2: Rice varieties showing percentage regeneration into plantlets from callus, derived from different explants in MS + IAA(2mg/L)+ KN (4mg/L)

Variety	Seed	Shoot Apex	Length of Panicle(cm)						Mature
			0.5	1.5	3.0	4.0	5.0		
Badshah Bhog	79	85	80	100	95	92	60	20	
Kanak	55	65	73	80	83	75	48	05	
Sathi	70	80	78	95	95	88	57	18	
Sita	52	63	70	78	80	71	43	07	
Sugapankhi	75	83	85	95	100	85	55	15	
Tulsi	60	70	75	83	90	78	50	12	

Evaluation of feeding strategies for enhanced Cell-associated tannase production by *Serratia ficaria* DTC

PRASANNA D.BELUR¹ and DINESH C.GOUNDAR²

1 Department of Chemical Engineering, National Institute of Technology Karnataka, Surathkal, Mangalore, India-575 025. e-mail : prsnbhat@gmail.com

2 Department of Chemical Engineering, National Institute of Technology Karnataka, Surathkal, Mangalore, India-575 025. e-mail : dineshgouder@gmail.com

Abstract:

Batch studies on Cell-associated tannase production showed 2.6 U/L activity in the declining phase of growth in the bioreactor. It was observed that Cell-associated tannase production under declining phase was depending upon the bacterial biomass produced under exponential phase and gallic acid level. The peak production of enzyme was always accompanied by a sharp rise in dissolved oxygen concentration. Based on these observations, fed batch fermentation by feeding a mixture of nutrients (glucose and tryptose) and Dissolved oxygen (DO) based feeding strategy of gallic acid were designed. Nutrient feeding strategy showed 10 U/L of enzyme activity at 14th h of fermentation. DO based feeding strategy of gallic acid resulted in the production of 14.4 U/L enzyme activity in the 12th h of fermentation. The enzyme production rate of 1.2 U/L.h achieved in this mode was 4.6-fold greater than the values observed in batch process and 1.68 fold greater than the productivity achieved by feeding nutrients. Hence, DO based feeding strategy of gallic acid was proved to be an effective strategy for enhanced cell-associated tannase production by *Serratia ficaria* DTC.

Keywords: Cell-associated tannase, Fed-batch process, *Serratia ficaria*

Introduction

Tannin acyl hydrolase (E.C. 3.1.1.20), commonly known as "Tannase" catalyses the hydrolysis of ester and depside bonds in hydrolysable tannins. Hydrolysis of gallotannins (Tannic acid) results in the release of gallic acid and glucose. Tannase finds use in the production of gallic acid, which is used for the manufacture of an antimalarial drug, Trimethoprim and an antioxidant, propyl gallate. Tannase is being used for the production of instant tea preparations, wines, juices of fruits and refreshing drink with coffee flavor (Belmares et al. 2004). Tannase has potential uses in the treatment of tannery effluents and pre-treatment of tannin containing animal feed (Lekha and Lonsane 1997). Many molds, yeasts and bacteria have the ability to produce tannase. Majority of the reports are

pertaining to extracellular tannase production from bacteria and fungi (Aguilar et al. 2007). For the first time, Belur et al. (2010) had reported cell-associated tannase (CAT) activity in several bacterial isolates. CAT provides a unique naturally immobilized form of tannase. Such naturally immobilized tannases have many advantages as they avoid expensive and laborious operation of isolation, purification and immobilization. Furthermore, natural immobilization has higher recovery and yield compared with chemical or physical immobilization. Naturally immobilized enzymes invariably shows very high stability against adverse pH and temperature compared to the free enzyme (Kopecny and John Wallace 1982, Sinsuwan et al. 2008).

Culture strategy greatly affects the effectiveness of a process. All the available literature on tannase production made use

of batch processes. It has inherent disadvantages such as substrate limitation, catabolite repression and feedback inhibition. Fed-batch culture mode emerges consequently as an attractive choice in numerous biotechnological processes due to its operational simplicity, reliability and flexibility for the implementation in multipurpose facilities (Gordillo et al. 1998)

In the present paper, two different fed-batch strategies, Dissolved Oxygen (DO) based feeding strategy of gallic acid and nutrient feeding strategy were evaluated for enhanced tannase production.

Materials and Methods

Microorganism and Culture conditions

Serratia ficaria DTC (MTCC 8930) capable of producing CAT, isolated previously in our laboratory was used for the current study (Belur et al. 2010). The culture was maintained on nutrient agar slants at 4°C.

Analytical Methods

Tannase activity was measured by determining the amount of gallic acid released by hydrolysis of tannic acid. Since tannase produced by *Serratia ficaria* DTC is cell associated, bacterial biomass obtained by centrifugation at 5500 × g for 15 min was washed with buffer and used as source of enzyme. Tannase activity was determined as per the method described by Van de Lagemaat and Pyle (2001). One unit of tannase activity is defined as the amount of enzyme required to release 1 μmole of gallic acid per minute under standard reaction conditions.

Glucose content of fermentation broth was determined by 3,5 dinitro salicylic acid method (DNS method) using D-glucose as standard. Gallic acid content of fermentation broth was determined using gallic acid as standard as per the method described by Van de Lagemaat and Pyle (2001). Growth was monitored by measuring dry cell weight (DCW). DCW was determined by centrifuging the fermentation broth at 5500 × g, 15 min, and sediments were dried at 95°C for 36 hours. All the estimations were made in triplicate and mean values were considered for the analysis.

Bioreactor Studies

Batch fermentations were carried out in 3 L stirred tank bioreactor (Scigenics India) containing 1.7 L medium. Medium used for bioreactor studies had glucose 20 g/L, tryptose broth (Himedia India) 30 g/L. Gallic acid (4 g/L) was used as the inducer in the place of tannic acid. Poly propylene glycol 0.2 %(v/v) was used as the antifoam. 12 h old culture, cultivated in 250 ml Erlenmeyer flask containing 100 ml of nutrient broth (13 g/L) was used as the inoculum. 5% v/v of inoculum was used. The reactor was maintained at an aeration of 5 LPM, agitation of 800 rpm at 30°C. Sterilizable DO and pH probes (Mettler Toledo) were used for monitoring. pH of the process was maintained at 5 through out, by adding appropriate amount of 1 M NaOH and HCl.

Fed-batch experiments were conducted in the same bioreactor with the same operating conditions as mentioned above. The process was started with medium consisting of glucose (20 g/L), tryptose broth (30 g/L) and gallic acid (4 g/L). Glucose and tryptose mixture was fed in the form of pulses at 7th hr and 7.5th hr which incidentally corresponds to the declining phase of growth. Each pulse of 10 ml had the composition of glucose 2.125 g, tryptose 1.175 g which was based on substrate utilization rate under batch conditions. DO based fed-batch experiment was started with medium consisting of only glucose (20 g/L) and tryptose broth (30 g/L). Sharp rise in DO due to decreased growth rate during the transition of exponential phase to stationary phase was used as an indicator to give gallic acid pulse. 20 ml of solution containing 6.8 g gallic acid neutralized with 1 M NaOH was used as gallic acid pulse. Batch and fed-batch trials were conducted in duplicate and mean values were taken for analysis. pH of the process was maintained at 5 by adding appropriate amount of 1 M NaOH and HCl during the fermentation.

Results and discussion

Batch cultivation in Bioreactor

Most of the reports pertaining to the microbial production of tannase have reported tannic acid as an inducer for tannase production. Gallic acid was proved

to be an alternative inducer to tannic acid by same authors earlier (unpublished). Hence gallic acid 4 g/L was used as an inducer in present studies. Fig 1 shows the profiles of DCW, DO (% saturation) and CAT activity of *Serratia ficaria* DTC under batch cultivation. Exponential phase terminated approximately at 6 h and was followed by declining phase from 6 to 12 h (transition phase between exponential and stationary phase) and subsequently culture entered stationary phase. Enzyme production was minimal under exponential phase and reached 2.6 U/L under declining phase (10 h) indicating non-growth associated characteristics of tannase production. Reduced growth rate during declining phase was accompanied by steady rise in DO (% saturation) and onset of stationary phase was indicated by sharp rise in DO from 45 to 65 %. Growth parameters of batch cultivation are given in Table 1. Analysis of residual glucose concentration strengthens the logic that reduction in growth rate was due to nutrient depletion. Simultaneous consumption of glucose and gallic acid as carbon sources was also noticed. Perhaps, depletion of gallic acid in the broth by the time declining phase was reached could be the reason for low tannase activity. It was evident from results that CAT production under declining phase was directly proportional to the bacterial biomass produced under exponential phase and gallic acid levels during declining phase. Based on these conclusions following two strategies were evaluated for enhanced CAT production.

1. Fed batch fermentation using mixture of glucose and tryptose.
2. DO based feeding strategy of gallic acid.

Fed-batch fermentation with nutrient feeding.

Nutrient mixture consists of glucose and tryptose was fed in the form of pulses which prolongs exponential phase and thereby increases biomass concentration. It was based on logic that enhanced bacterial biomass under declining phase in the presence of gallic acid expresses higher CAT.

Fig. 2 shows the profile of DO (% saturation), cell concentration (DCW), CAT activity, residual glucose and gallic acid level under fed-batch cultivation. Glucose

and tryptose mixture was fed in the form of pulses at 7th hr and 7.5th hr in order to prolong the exponential phase which terminated at 6th hr in batch process with similar medium and conditions. Each pulse of 10 ml had the composition of glucose 2.125 g, tryptose 1.175 g based on substrate utilization rate under batch conditions. Addition of glucose and tryptose mixture prolonged exponential phase by 4hrs and shifted maximum tannase production by 4hrs. Specific growth rate and biomass concentration at maximum tannase activity was increased to 0.465 h⁻¹, 12 g/L (14th hr) in fed-batch strategy compared to 0.303 h⁻¹, 11.52 g/L (10th hr) in batch process respectively. Fed-batch fermentation using mixture of glucose and tryptose produced CAT activity of 10 U/L at 14th hr. Fed-batch production of CAT by *Serratia ficaria* DTC enhanced tannase production by 3.8-fold, compared to batch production conducted with the same medium and conditions. Reasons for enhanced production of cell-associated tannase in fed-batch fermentation using mixture of glucose and tryptose are higher biomass level during maximum tannase production phase (declining phase) and higher level of gallic acid under declining phase when bacteria is under stress, looking for alternative carbon sources. Sharp rise in DO from 40 to 65% at 13th h indicating onset of stationary phase was in agreement with limitation of glucose in fermentation broth.

DO based feeding strategy of gallic acid.

Fig. 3 shows the profile of DO (% saturation), cell concentration (DCW) and residual glucose level under fed-batch cultivation. Sharp rise in DO level from 25 % to 51% at 10th h was used as an indicator of onset of stationary phase to feed gallic acid pulse of 20 ml. Sharp rise in DO was in agreement with limitation of glucose in fermentation broth. Gallic acid pulse addition induced maximum CAT activity of 14.4 U/L at 12th h and consequently reduced due to reduction in cell concentration. Fed-batch process enhanced tannase production by 5.5-fold, compared to batch production conducted with the same medium and conditions. Growth parameters and tannase

production in batch and fed-batch fermentation are compared in Table 1. Fed-batch process is a very promising culture mode for the production of secreted proteins with regard to the maximization of volumetric productivity. Numerous reports are available on utilizing fed-batch strategy for maximizing production. But most of the applications involve the evasion of feedback inhibition / feedback repression or catabolite repression by feeding the carbon or nitrogen sources (Singh et al. 2004; Turki et al. 2010). Some reports are available where fed-batch strategy was used to maintain DO level at a favorable range so as to achieve the desired productivity (Barberis and Sagovia 1997; Kole et al. 1998). But reports on using fed-batch strategy for inducing the enzyme synthesis by feeding the inducer are scarce. Hofer et al. (2002) had successfully demonstrated the use of this strategy to induce Acetopyruvate hydrolase production by *Pseudomonas putida*, by feeding the inducer Orcinol.

Effective and robust fed-batch control strategies are required for the success of fed-batch process. Development of these strategies requires model-based control and on-line monitoring of process variables closely related to cell metabolism. However, these strategies normally involve relatively complicated control models requiring online estimation of cell density, specific growth rate and cellular yields. Monitoring the control variables other than pH and DO is often difficult and requires specialized sensors and analytical instruments (Nor et al. 2001). Reports on DO based feeding strategies in fed-batch process are in plenty. However, reports on DO based induction strategy are few in number. Use of DO based induction strategy for tannase production does not require any real time data regarding specific growth rate, substrate utilization rate or complex control system. Simple DO Probe which gives real time data regarding DO (% saturation) of fermentation broth under constant aeration and agitation could be used effectively to enhance tannase production.

Conclusion

- ❖ The experimental work thus reiterates that fed-batch fermentation is superior to batch fermentation in case of enzyme production.
- ❖ DO based feeding of gallic acid was found to be more productive compared to nutrient feeding strategy.
- ❖ Probably this is the first report of feeding the inducer making use of novel and simple DO based feeding strategy, producing an inducible enzyme.

References

1. Belmares R et al. (2004) Microbial production of tannase: an enzyme with potential use in food industry. *Lebenson Wiss Technol*, 37: 857-864.
2. Aguilar CN et al. (2007) Microbial Tannases: advances and perspectives. *Appl Microbiol Biotechnol* 76: 47-59.
3. Belur PD et al. (2010) Production of novel cell-associated tannase from newly isolated *Serratia ficaria* DTC. *J Microbiol Biotechnol* 20(4): 722-726.
4. Kopecny J and John Wallace R (1982) Cellular location and some properties of proteolytic enzymes of rumen bacteria. *Appl Microbiol Biotechnol* 43: 1026-1033.
5. Sinsuwan S et al. (2008) Characterization of Ca^{2+} - activated cell-bound proteinase from *Virgibacillus sp.* SK37 isolated from fish sauce fermentation. *LWT-Food Sci. Technol.* 41: 2166-2174.
6. Lekha PK and Lonsane BK (1997). Production and application of tannin acyl hydrolase: state of the art. *Adv. Appl. Microbiol.* 44: 215-260.
7. Van de Lagemaat J, Pyle DL (2001) Solid state fermentation and bioremediation: Development of continuous process for the production of fungal tannase. *Chem Eng J* 84: 115-123.
8. Singh J et al. (2004). Enhanced production of alkaline protease by *Bacillus sphaericus* using fed-batch culture. *Process Biochem* 39: 1093-1101
9. Turki S et al. (2010). An enhanced process for the production of a highly purified extracellular lipase in the Non-conventional yeast *Yarrowia lipolytica*. *Appl Biochem Biotechnol* 160: 1371-1385.
10. Barberis SE and Segovia RF (1997) Dissolved oxygen concentration-controlled feeding of substrate into *Kluyveromyces fragilis* culture. *Biotechnol Techniques* 11: 797-799.
11. Kole MM et al. (1998). Protease production by *Bacillus subtilis* in oxygen-controlled, glucose fed-batch fermentations. *Appl Microbiol Biotechnol* 28: 404-408.
12. Hofer H et al. (2002) Acetopyruvate hydrolase production by *Pseudomonas Putida* 01-Optimization of batch and fed-batch fermentations. *Appl Microbiol Biotechnol* 60: 293-299.
13. Nor ZM et al. (2001) Improvement of intracellular β -galactosidase production in fed-batch culture of *Kluyveromyces fragilis*. *Biotechnol. Lett.* 23: 845-849

Table 1: Characteristics of cell-associated tannase production from *Serratia ficaria* DTC in batch and fed-batch fermentation.

Parameters	Batch process	DO based Fed-batch process	Fed-batch with nutrient feed
Maximum apparent growth rate μ (h^{-1})	0.303	0.37	0.465
Maximum biomass production (g/L)	17	8.77	12.2
Maximum biomass productivity (g/L.h)	0.684	0.49	0.76
Total glucose utilization (g/L)	18	8	14.82
Average glucose utilization (g/L.h)	1.125	0.5	0.988
Maximum tannase production (U/L)	2.6	14.4	10
Average tannase productivity (U/L.h)	0.26	1.2	0.714
$Y_{p/\text{glucose}}$ (U/g)	0.144	1.8	0.674

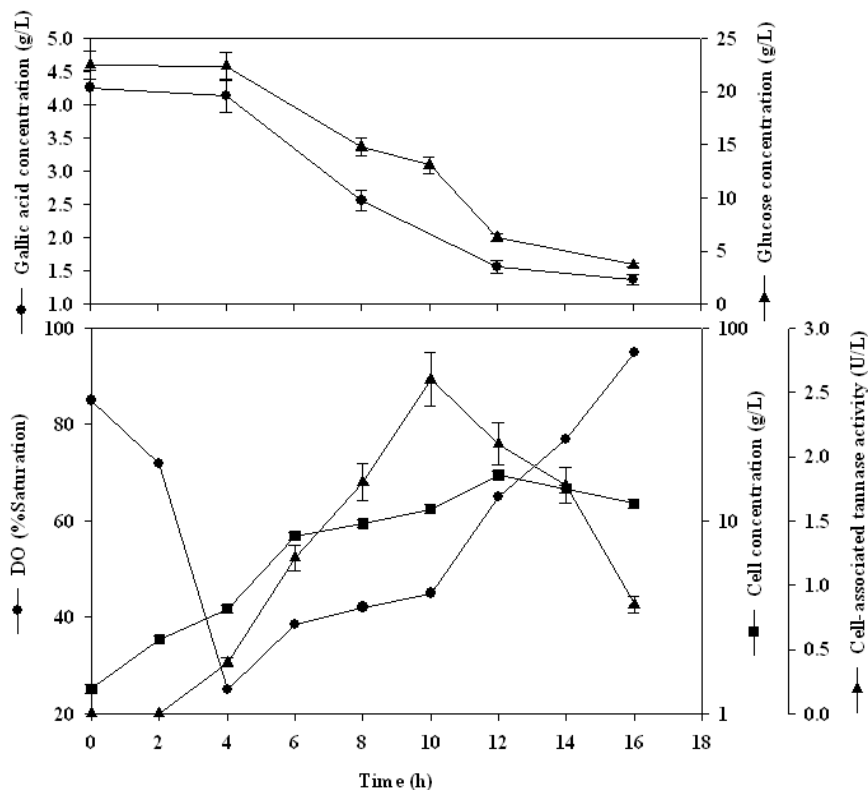


Fig. 1: Batch cultivation of *Serratia ficaria* DTC in medium having Glucose (20 g/L), tryptose broth (30 g/L) and gallic acid (4 g/L) in stirred tank bioreactor at process pH 5.0. (a) Profile of glucose concentration and gallic acid concentration (b) Profile of DO (% saturation), Cell concentration (DCW) and Cell-associated tannase activity.

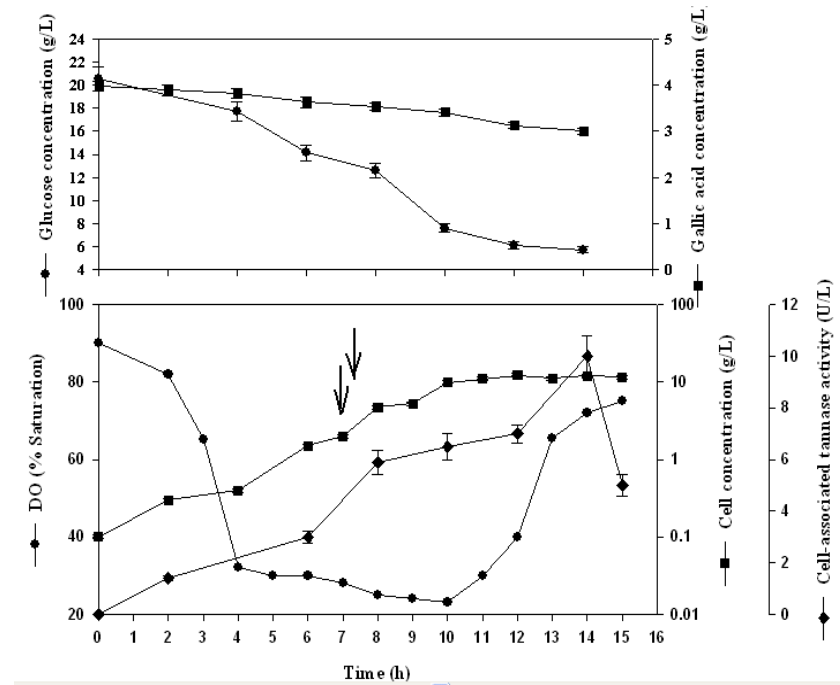


Fig. 2: Profile of Cell concentration (DCW), DO (% saturation), Glucose concentration and Cell-associated tannase activity during fed-batch cultivation of *Serratia ficaria* DTC. Medium consists of Glucose (20 g/L) and tryptose broth (30 g/L) and gallic acid (4g/L). 10 ml nutrient (glucose 2.125 g and tryptose 1.175 g mixture) was fed at 7th and 7.5th h.

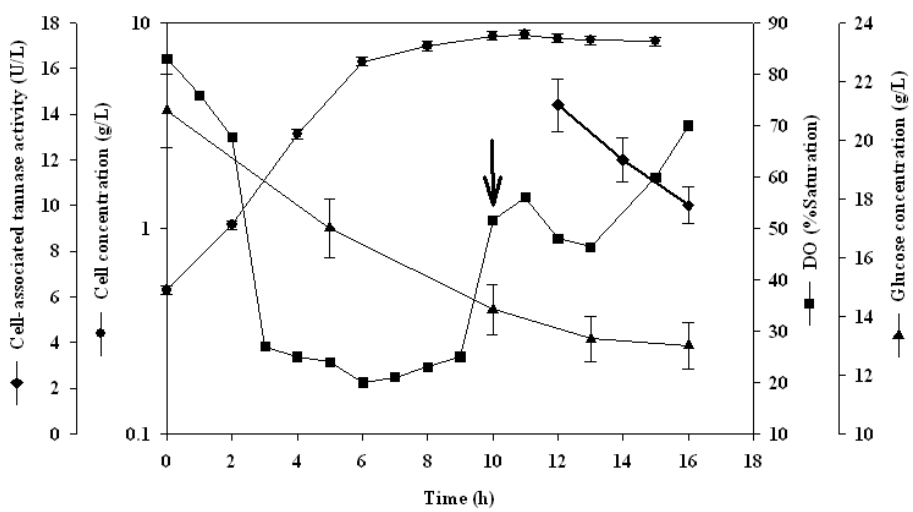


Fig. 3: Profile of Cell concentration (DCW), DO (% saturation), Glucose concentration and Cell-associated tannase activity during fed-batch cultivation of *Serratia ficaria* DTC. Medium consists of Glucose (20 g/L) and tryptose broth (30 g/L). 20 ml Gallic acid solution (34 % w/v) was fed as a pulse at the 10th h when DO was sharply increasing.

Studies on chitosan incorporated nanocomposite polymer membranes

K. KARUPPASAMY¹ C.VIJIL VANI² S. BALAKUMAR³ and X. SAHAYA SHAJAN⁴

School of Basic Engineering and Sciences, PSN College of Engineering and Technology, Melathediyoor, Tirunelveli 627152, India.

¹ email :kannanvhns@yahoo.com

² email :vijilvani@gmail.com

³ email :prof_balakumar@rediffmail.com

⁴ email :shajan89@gmail.com

Abstract: Chitin and chitosan, the most abundant biopolymers are less toxic, biodegradable and antibacterial. They occur as ordered crystalline micro fibrils and are useful in applications that require reinforcement and strength. Nanochitosan was prepared by standard method. Nanocomposite polymer electrolytes with polyethylene oxide (PEO) and salt for different proportions of nanochitosan were prepared by membrane hot press method. The prepared membranes were subjected to electrochemical studies, TGA-DTA, DSC and FTIR spectral analysis. It is observed that the ionic conductivity was found to increase on the addition of nanochitosan.

Keywords: *nanocompostie polymer electrolytes, electrochemical studies, nanochitin*

Introduction

Advances in solid polymer electrolyte research are significant in the recent years. Safety issues such as possibility of leakage, internal shorting and flammability existing in liquid electrolyte battery system can be considerably offset by the use of solid polymer electrolytes. Flexible geometry, good process ability, and light weight, miniaturizing the battery are the added merits of solid polymer electrolytes, Manuel Stephan et al., (2006), Manuel Stephan et al., (2006). On the other hand, the ionic conductivity of solid polymer electrolyte has not reached a reasonable value to be used in ambient temperature. Poor mechanical strength of polymer hinders the usage of free standing electrolytes.

A considerable amount of work has been done in this aspect and lot of methods was evolved to improve the conductivity and mechanical strength at room temperature. One such widely accepted method is to incorporate nanofillers in the polymer matrix so that the fillers can suppress the crystalline nature of polymer as well as can act as good binders and thereby

improve its mechanical strength, Chang et al., (2007), Cha et al., (2006).

Chitin is the most abundant biopolymer next to cellulose and its deacetylated product chitosan has been used in a wide range of applications like membrane separation, prevention of water pollution, medicine, food processing, biotechnology etc. It is non-toxic, biodegradable and anti-bacterial, Kuo-Shien et al., (2009). Chitosan is a cationic polysaccharide with several polar groups (OH and NH₂), which can act as electron donors and interact with inorganic salts. Though chitin and chitosan have been explored in various fields only a little work has been done in the area of polymer electrolyte, Manuel Stephan et al. (2009), Ravikumar et al., (2000)

Polyethylene oxide (PEO) remains the most explored and suitable candidate in the research of polymer electrolytes and lithium batteries from the very beginning. Its ability to solvate lithium salt by the formation of stable complexes with lithium and helping the hoping mechanism of lithium through ether oxygen has favored

the polymer to be used in solid polymer electrolyte system.

In this present study, PEO based polymer electrolytes were prepared by incorporating nanochitosan and lithium perchlorate (LiClO_4). Nanochitosan was used as filler. The details are presented.

Experimental

Synthesis of nanochitosan

Three grams of chitosan were dissolved in 100 ml of 0.1M HCl and stirred for one hour. To this, 5% H_2O_2 was added. The resulting mixture was heated and stirred around 50 °C for four hours and then vacuum filtered. The upper residue was neutralized with distilled water, baked, and weighed. Ethanol was added to the filtrate, which was left for one day to precipitate, after which it was filtered, dried and weighed. After H_2O_2 treatment, the molecular weight of the chitosan decreased and continued to decrease as more H_2O_2 was added. This was due to degradation of biopolymer chain by H_2O_2 . The precipitate obtained was dissolved in 1L acetic acid and stirred for one hour. This solution was added to sodium tripolyphosphate and stirred for 2 h at ambient temperature and then centrifuged at 2000 rpm/s. The isolated nanochitosan was rinsed with distilled water, freeze dried and weighed. The resulting nanochitosan was kept in a refrigerator with sodium azoture as a protectant against micro organisms, Hui-Chia Yang et al., (2010).

Preparation of Nanocomposite Polymer membranes

PEO(Aldrich) and lithium perchlorate, LiClO_4 (Merck), were dried under vacuum for 2 days at 60°C and 100°C, respectively. Nanochitosan was also dried under vacuum at 50°C for five days before use. Nanocomposite polymer electrolytes were prepared by dispersing appropriate amounts of chitosan in PEO- LiClO_4 matrix and made into films by using a hot

membrane press. This procedure gave mechanically strong homogeneous

membranes, which were dried under vacuum at 50°C for 2 days for further characterization, Kalaprasad et al., (2003).

The lithium/polymer electrolyte interface was analysed using Fourier Transform Infrared Spectroscopy (JASCO, Japan) by single internal reflection mode. The infrared spectra were obtained at ambient temperature with an 8 cm^{-1} resolution.

The morphology of the films was examined with a scanning electron microscope (JSM-6390) with accelerating voltage and magnification of 10kV and 10000 respectively.

The thermal stability of the films was examined by TG/DTA measurement with temperature range from 20 to 300°C.

Electrochemical Characterisation

The ionic conductivity of the membranes sandwiched between two stainless steel blocking electrodes (1cm² diameter)was measured using an electrochemical impedance analyser (IM6 Zahner, Germany) in the 50mHz to 100KHz frequency range at various temperatures (25,30,35,40,45,50,55,60,65 and 70°C).

Results and Discussion

1) Determination of Molecular weight (M_w):

The viscosity of chitosan was measured using an Ostwald's capillary viscometer and the intrinsic viscosity was determined, the solvent was 5% acetic acid and 0.1M KCl. The obtained intrinsic viscosity was used to calculate the molecular weight of the prepared nanochitosan samples from the Mark-Houwink-Sakurada equation.

$$\eta = KM^a \quad (1)$$

Where K and a are constants and their values are available in the literature, Yong-Woo Cho et al., (1999).

0.5g of nanochitosan was dissolved in 25ml of 0.1M standard HCl aqueous solution. Then the solution was made up to 100ml with distilled water. The calculated amount of KCl was added to adjust the ionic strength to 0.1. The titrant was a

solution of 0.05M NaOH. pH meter was used for pH measurements under continuous stirring. The titrant was added until the pH value reached 2, the standard NaOH was added stepwise until the pH values of the solution were recorded and the curve with two inflection points was obtained. The difference of NaOH solution volumes between these points corresponds to the acid consumed for salification of the amine groups of chitosan and allows the determination of DDA% of the chitosan, Entsar et al., (2008).

The DA was calculated from the relation

$$\text{DDA\%} = [1-161Q/1+42Q] \quad (2)$$

where $Q = N\Delta V/m$, ΔV is the volume of NaOH solution between the two inflection points in litres, N is concentration of NaOH (in mol/l) and m is the dry weight of chitosan (0.5g).

The molecular weight of nanochitosan prepared in the present study was calculated to be 2.3×10^5 using equation (1) and DDA% was determined to be 74.29 ± 0.42 using equation (2).

2) FT-IR analysis

Being sensitive to molecular and structural changes in the polymer electrolyte systems FTIR has been identified as the powerful tool to study the complexation between salts and polymers. FTIR traces in figures 1(a) to 1(d) show the spectra of PEO, nanochitosan, PEO+LiClO₄, PEO+nano-chitosan+LiClO₄ respectively. The band in figure 1 that appears at 2886 cm⁻¹ can be assigned to C-H stretching mode, and the peak at 1967 cm⁻¹ is due to an asymmetric stretching mode. The peaks at 1466, 1103, 956 and 841 cm⁻¹ are assigned to -CH₂-scissoring, -C-O-C- stretching, -CH₂-twisting and -CH₂- wagging modes respectively. Also, PEO exhibits -C-H-stretching (between 2800 and 2935 cm⁻¹), asymmetric stretching (1950 – 1970 cm⁻¹), asymmetric bending (1450 cm⁻¹), CH₂ scissoring (1465-1485 cm⁻¹), -CH₂-twisting (991 cm⁻¹) and -CH₂- wagging (842 cm⁻¹). Several IR spectra studies have been made on the infrared spectra of chitosan. Because of the high crystalline nature of PEO, it displaces a series of very

sharp absorption bands. For example the peak at 1560 cm⁻¹ is characteristic of a -NH-bending. Upon incorporation of LiClO₄ in the polymer host, the peak at 956 cm⁻¹ shifts to 961 cm⁻¹. In a similar manner, the characteristic frequencies of LiClO₄ at 1300 cm⁻¹ and 920 cm⁻¹ are shifted, respectively to 1350 and 940 cm⁻¹. With incorporation of chitosan in the polymer matrix, the intensity of the peak was reduced and it was little shifted to 1557 cm⁻¹, which indicates the formation of complex in system.

3) Morphology of polymer membranes:

An examination of cryo fractured surface of chitosan/polymer composites was carried out using SEM. Panels (a)-(d) of figure 2 show the SEM of various ratios of chitosan-incorporated polymer membranes which were prepared from solvent casting evaporation method. According to Chang et al., the morphology of electrolyte surface can be tailored by incorporation of both ionic salts and fillers, Vikash et al., (2010). The SEM images of nanochitosan-incorporated membranes show surfaces, which indicate sufficiently good miscibility of nanochitosan with PEO and lithium salt. The smooth morphology was attributed to reduction in crystalline nature of PEO due to cross linking with cations of both lithium ions and nanochitosan. The smooth surface was due to the fact that the chitosan particles were uniformly distributed through out the matrix of the polymer and were attributed to the formation of rigid filler-filler network. The surface of high filler content membranes showed a hard rough surface morphology.

4) Ionic conductivity

The temperature dependence of ionic conductivity of nanocomposite polymer electrolytes (Arrhenius plot) and variation of ionic conductivity as a function of nanochitosan concentration are shown in Figures 3(a) and (b) respectively. It is quite obvious from the figure that the ionic conductivity of the composite polymer electrolyte increases with the increase of temperature and also with the increase of salt content. The ionic conductivity also increases with the increase of filler content up to 10 wt.-% and then decreases with

further increase of filler content. The ionic conductivity of the polymer membrane has been increased to one order magnitude upon addition of filler in the polymer matrix. These results are in accordance with those reported earlier in which Al_2O_3 was used as filler in the PEO-based electrolytes. A similar trend has been observed for the polymer electrolytes with LiClO_4 as salt in the present study also (Figure 3 (a) and (b)).

As commonly observed in composite materials the conductivity is not a linear function of filler concentration. At low concentration, the dilution effect which tends to depress the ionic conductivity is effectively contrasted by the specific interactions of the ceramic surfaces, which promotes faster ion transport. Hence an apparent enhancement in conductivity is seen in both cases. On the other hand at higher filler concentration the dilution effect predominates and the conductivity gets lowered. Thus the maximum conductivity is achieved only in the concentration region of 5-10wt.-%. These results are in accordance with those reported on PEO-based polymer electrolytes with lithium imide anions, Stephan et al., (2006).

The Lewis base reactions between the filler surface and the PEO segments may induce structural modifications in the polymer matrix. The Lewis acid character of the added ceramics would compete with the Lewis acid character of the lithium cations for the formation of complexes with the PEO chains. In the present study, chitosan may act as cross-linking centers for the PEO segments, which lowers the polymer chain reorganization tendency, and promoting an overall stiffness to the structure. However, the resulting structure provides Li^+ -conducting pathways at the filler surface and enhances ionic transport.

5) Thermal analysis:

TG/DTA analysis is sensitive enough to record the thermal events such as melting, decomposition and corresponding weight loss of the electrolyte sample Rajendran et al., (2002). The result of thermo gravimetric and differential thermal

analysis of PEO- LiClO_4 -nanochitosan complex is discussed from TG/DTA curve (not shown here). An endothermic peak observed around 60°C indicates a eutectic decomposition of the composite membrane accompanied by weight loss. The next thermal peak observed beyond 172°C beyond that temperature, a rapid decrease in weight of the film has been observed. It was inferred from the thermo gram that the prepared membrane was thermally stable up to 172°C.

Conclusion

Further the film possessed uniform surface morphology which suggested that chitosan is dispersed throughout the membrane and the thermal stability of the film was limited to 172 °C. The ionic conductivity behavior of chitosan incorporated polymer containing lithium salt had been studied. The conductivity of the films increases up to filler concentration of 10% and beyond that limit it decreased gradually.

Acknowledgements

Authors (XSS) and (SB) acknowledge the financial support received from Department of Science and Technology (DST), Govt. of India for carrying out project (Sanction No. SR/S1/PC54/2009 dated 17.6.2010).

References

- [1] Angulakshmi, N,Premkumar, T,Sabu Thomas, Manuel Stephan, A (2010), Ionic conductivity and interfacial properties of nanochitin-incorporated polyethylene oxide- LiBETI polymer electrolytes, *Electrochimica Acta*, V. 55, No. 4, pp.1401-1406.
- [2] Cha, E.H et al., (2006), Ionic conductance of PDMAEMA/PEO polymeric electrolyte containing lithium salt mixed with plasticizer, *Journal of Power Sources*, V.163, No. 1, pp. 269-273.
- [3] Entsar Abdou, S, Khaled Nagy, S.A, Maher Elsabeem, Z (2008), Extraction and characterization of chitin and chitosan from local sources, *Bioresource Technology*, V. 99, No. 5, pp.1359-1367.
- [4] Feng-Chih Chang, et al., (2007) Complicated phase behavior and ionic conductivities of PVP-co-PMMA-based polymer electrolytes, *Polymer*, V.48, No. 5, pp.1329-1342.
- [5] Hui-Chia Yang,Wen-Hong Wang, Kuo-Shien Huang, Min-Hsiung Hon (2010), Preparation and application of nanochitosan to finishing treatment

International Engineering Symposium, March 3-5, 2010 Kumamoto Univ., Japan

with anti-microbial and anti-shrinking properties, *Carbohydrate Polymers*, V.79, No. 1, pp.176-179.

[6] Kalaprasad Gopalan Nair and Alain Dufresne (2003), Crab shell chitin whisker reinforced natural

rubber nanocomposites 2. Mechanical behavior, *Biomacromolecules*, V.4, No.1, pp.666-674.

[7] Kuo-Shien Haung, Yea-Ru Sheu and In-Chum Chao (2009), Preparation and properties of nanochitosan, *Polymer Plastics Technology and Engineering*, V.48, No.12, pp.1239-1243.

[8] Ravikumar, M. N.V. (2000), A review of chitin and chitosan applications, *Reactive & Functional Polymers*, V.46, No.1, pp. 1-27.

[9] Manuel Stephen, K.S.Nahm (2006), Review on composite polymer electrolytes for lithium batteries, *Polymer*, V. 47, No.16, pp.5952.

[10] Manuel Stephen, Nahm K.S, Premkumar T, Anbu Kulandainathan M, Ravi G, Wilson J (2006), Nanofiller incorporated (PVdF-HFP) composite electrolytes for lithium batteries, *Journal of Power Sources*, V.159 , No.2, pp.1316-1321.

[11] Manuel Stephen, Premkumar T, Anbu Kulandainathan M and Angulakshmi N (2009), Chitin incorporated polyethylene oxide based nanocomposite electrolytes for lithium batteries, *J.Phys.Chem.B*, V.113, No.2, pp.1963-1971.

[12] Rajendran S, Mahendran O, Kannan R (2002), Lithium ion conduction in plasticized PMMA-PVdF polymer blend electrolytes, *Materials Chemistry and Physics*, V.74, No.1, pp.52-57.

[13] Vikash P.M, Sabu Thomas (2010), Preparation of bionanomaterials and their polymer nanocomposites from waste and biomass, *Waste and Biomass Valorization*, V. 1, No.1, pp.121-134.

[14] Yong-Woo cho et al., (1999), Water soluble chitin as wound healing accelerator, *Biomaterials*, V.20, No. 22, pp.2139-2145.

Table 1: Composition of polymer, nanochitosan and lithium salt

Sample	Polymer (in wt%)	Filler (in wt%)	Li-salt (in wt%)
S1	95	0	5
S2	90	5	5
S3	85	10	5
S4	80	15	5
S5	75	20	5

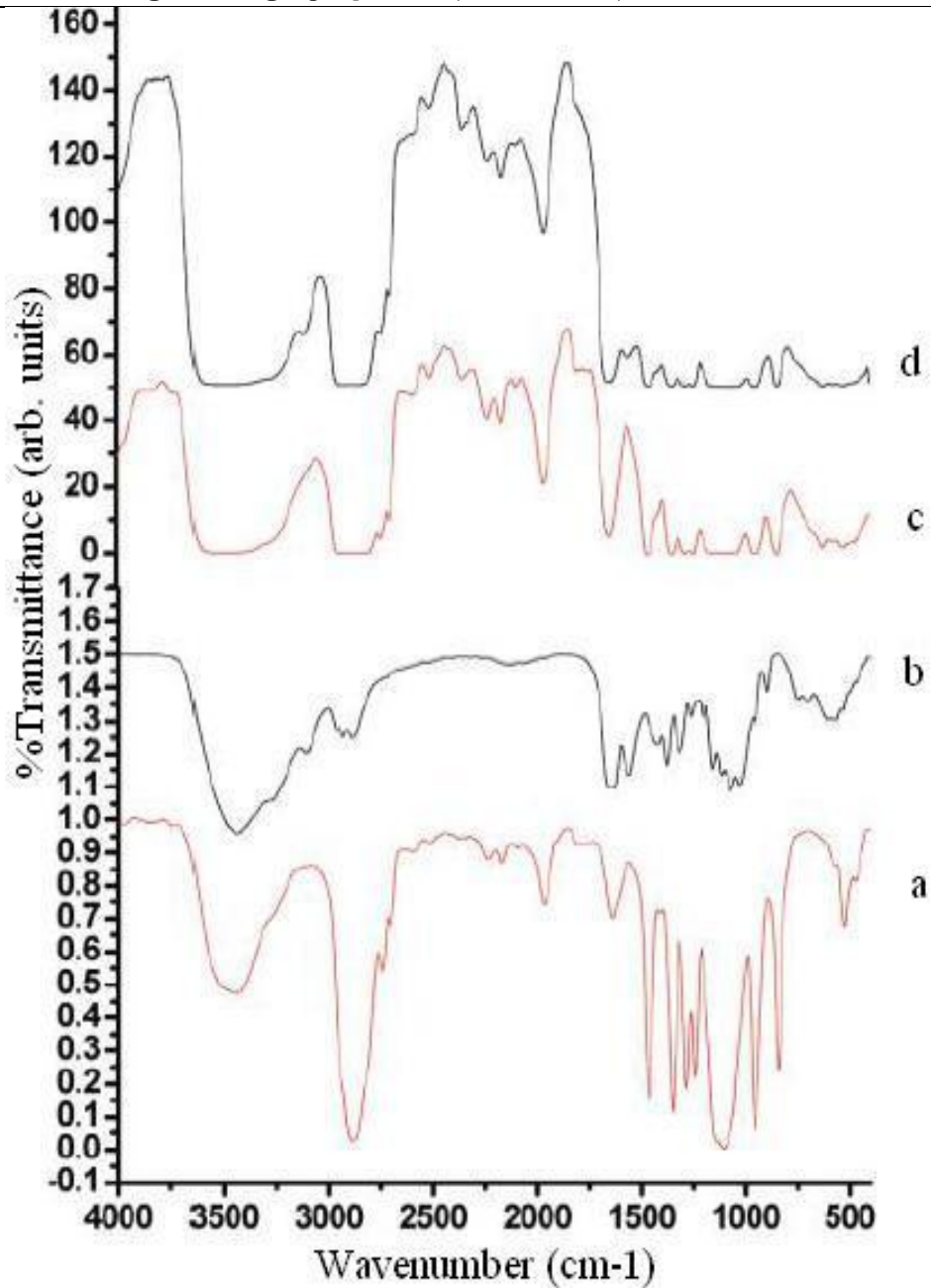


Figure 1 FT-IR spectra of (a) PEO b) nanochitosan (c) PEO+LiClO₄
(d) PEO+LiClO₄+ nanochitosan (85%+5%+10%)

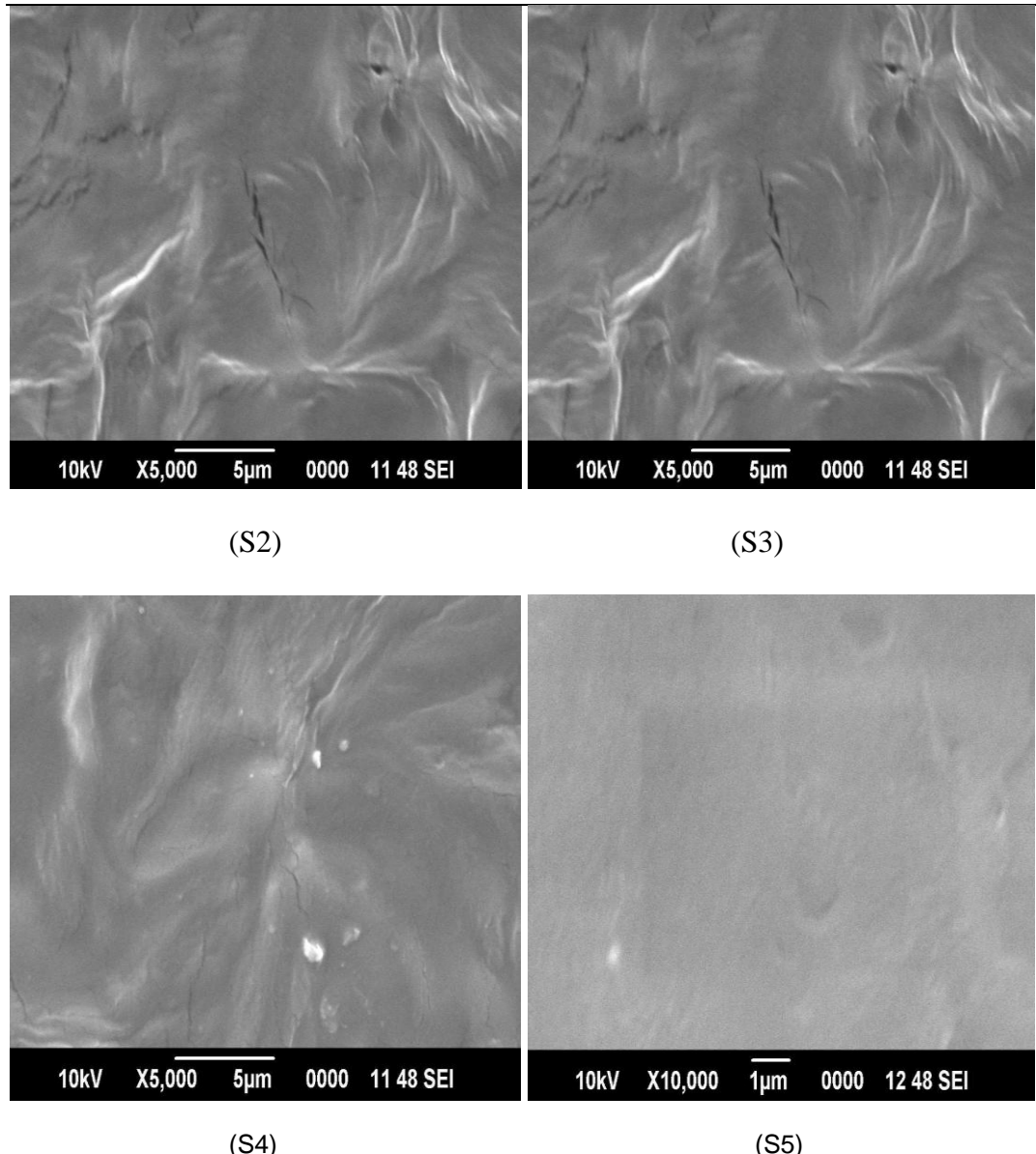


Figure 2 SEM images of the prepared nanocomposite polymer membranes

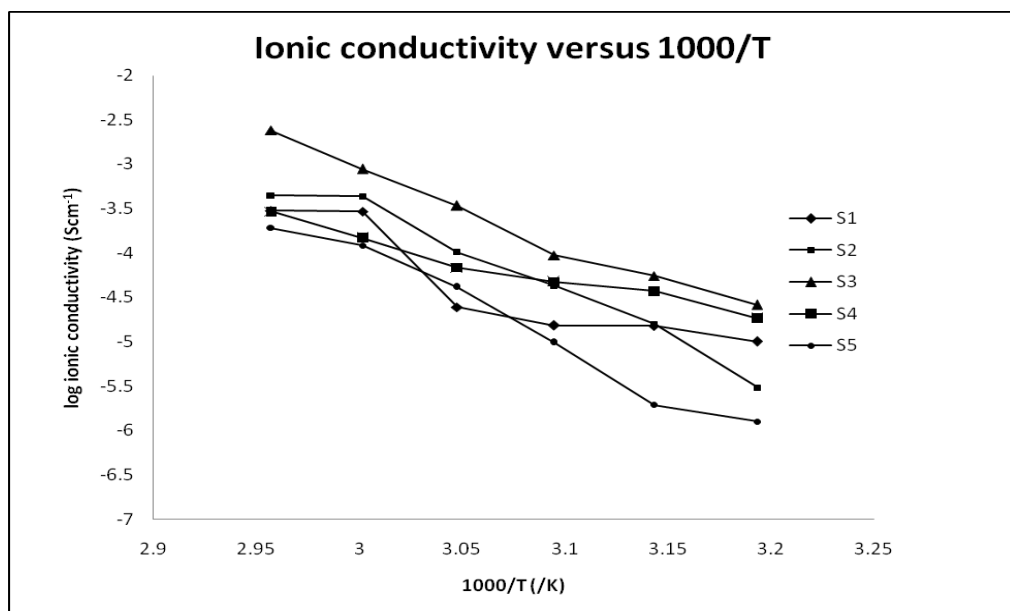


Figure 3(a) Arrhenius plot of log ionic conductivity vs 1000/T for PEO+LiClO₄+nanochitosan

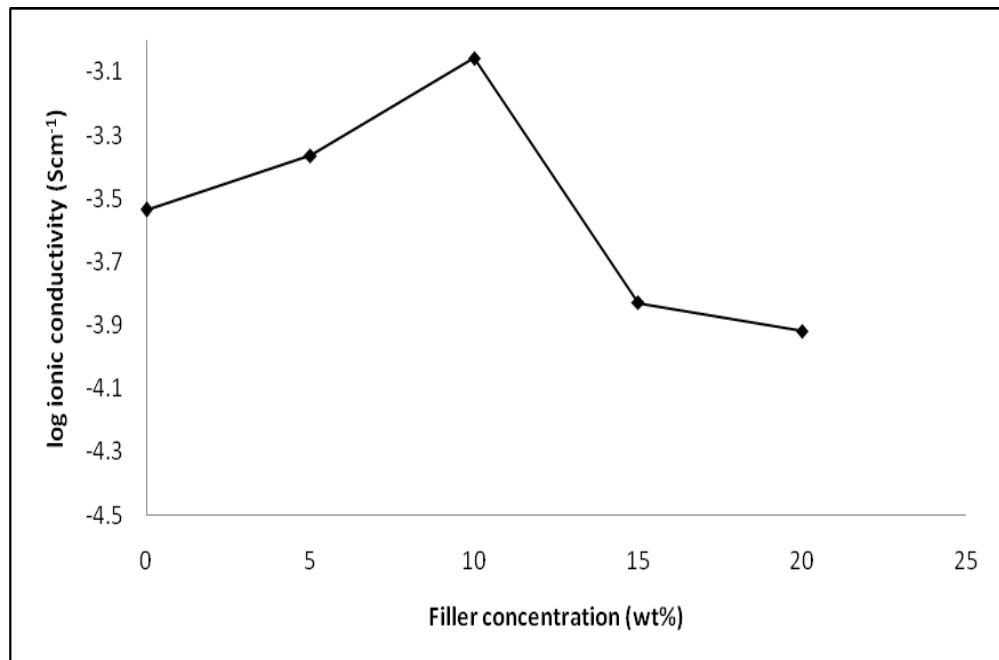


Figure 3 (b) Variation of ionic conductivity of polymer electrolytes for filler concentration

Alumina supported nanoruthenium efficient catalyzed N-Oxidation of tertiary amines by using H₂O₂

P.Veerakumar¹, S.Balakumar² and S.Rajagopal^{1*}

¹Department of Physical Chemistry, School of Chemistry, Madurai Kamaraj University, Madurai, 625 021, India.

²Department of Chemistry, PSN college of Engineering and Technology, Tirunelveli, 627 152, India.

Abstract: Several aromatic heterocyclic N-oxides have been synthesized in very high yields using nanoruthenium (Ru (PVP)/ γ -Al₂O₃, catalyst I,) in the presence of 30% H₂O₂ as an oxidant. The catalyst I has shown good activity in N-oxidation reactions. The catalyst I displayed consistency for several cycles without loss of activity.

Keywords: N-Oxides, Tertiary amines, CH₃CN, Catalyst I, Ru colloids.

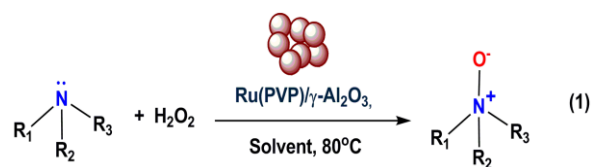
Introduction

In recent years, nanoparticles particularly supported nanocatalysts, have proven to be efficient and selective oxidation catalysts for a variety of organic reactions. Oxidation is one of the most fundamental reactions in organic synthesis. The oxidation of organo nitrogen compounds opens up an access to a multitude of versatile building blocks for organic synthesis as well as good oxidants. The chemistry and applications of N-oxides have recently received much attention due to their usefulness as synthetic intermediates and their biological importance. Heterocyclic N-oxides are also useful as protecting groups, auxiliary agents, oxidants, ligands in metal complexes and catalysts. Very recently, several reports concerning the preparation and catalytic activity of the metal nanoparticles on oxide supports such as TiO₂, SiO₂, MgO and SBA-15 have been published. The synthesis of the γ -Al₂O₃ supported Ru catalysts from the Ru colloid and its catalytic activity have been reported. Silica supported vanadium, titanium molecular sieves [TiMCM-41 and TiZSM-5(30)], Mg-Al-OtBu hydrotalcite (HT-OtBu), tungstate-exchanged layered double hydroxide (LDH-WO₄), titanium silicalite(TS-1),vanadium-silicate molecular sieve materials were used as catalysts for the oxidation of heterocyclic nitrogen compounds into their N-oxides by using

H₂O₂ as an oxidant. Some oxides of metals Cu, Re, Fe, Co(II) Schiff base complexes and heteropolyacids Preyssler's anion [NaP₅W₃₀O₁₁₀]¹⁴⁻ and Mg₁₀Al₂(OH)₂₄CO₃, were used as catalyst for oxidation of tertiary amines.(Jain et al., 2003)

More powerful oxygen transfer agents m-CPBA, KHSO₅, oxaziridines or dioxiranes, H₂SO₅ (Caro's acid), ozone, peroxymonocarbonate ion, HCO₄⁻, Urea-hydrogen peroxide (UHP), HOCH₃CN, aqueous chlorine, carbon-based solid acid, and flavin (Bergstad et al., 1998) were also acting as oxygen transfer catalysts in the formation of N-oxides. Most of these reagents are not only expensive, but also generate large amounts of effluent during the reaction process and demand a laborious work-up procedure. Aqueous H₂O₂ is an ideal oxidant in view of its high effective oxygen content, and greener reagent producing only water as the by-product, safety in storage and operation, and low cost of production and transportation. It is a clean process and the catalyst I is recyclable without loss of activity in ruthenium catalyzed oxidation of tertiary nitrogen compounds to N-oxides with molecular oxygen as the sole oxidant. The catalyst I has been applied for the oxidation of tertiary amines to the corresponding N-oxides with 30% H₂O₂ in high yields (equation 1). To the best of our knowledge, there is no literature report on the oxidation of tertiary nitrogen

compounds to N-oxides using ruthenium nanoparticles (RuNPs).



2. Experimental

2.1. Materials

Pyridine, *N,N*-dimethyl aniline (DMA), *para*-substituted *N,N*-dimethyl anilines (*p*-methyl, *p*-cyano, *p*-bromo and *p*-carboxy), quinoline, phenazine, quinoxaline, pyrazine, morpholine, 2,2'-bipyridine (2,2'-bipy), 4,4'-bipyridine (4,4'-bipy), 1,10-phenanthroline (phen) and triphenylphosphine (PPh₃) were purchased from Aldrich and used as such. Dichloromethane (Merck), HPLC grade acetonitrile and 30% H₂O₂ were used as received.

2.2. General procedure for the oxidation of amines using H₂O₂

A typical procedure for the oxidation of tertiary nitrogen compounds to its N-oxide is as follows: Catalyst I (1wt%, 0.5-2.0 mmol) and amine (2.0 mmol) were dissolved in CH₃CN (3 ml) at 298K. To this mixture, 30% H₂O₂ (2.0 mmol) was added dropwise slowly, then the temperature is raised to 70-80°C and continued the reaction. The progress of the reaction was monitored by TLC (SiO₂). At the end of reaction, the catalyst was removed by filtration and dried over MgSO₄ to afford the product and the reaction mixture thus obtained was purified by passing through a column of silica gel using CHCl₂/MeOH (95:5) as eluent. To the filtrate a small amount of triphenylphosphine was added to decompose the unreacted H₂O₂. Removal of the solvent and usual workup gave N-oxide. Similarly other N-oxides were prepared and the reaction times required and yields obtained are shown in Table 1. The products were identified by comparing their physical and spectral data given in the supporting information.

3. Results and discussion

Fig.1. (a) HRTEM image of catalyst I, (b) single particle with EDX (c) adsorption-desorption isotherm and (d) hydrogen

chemisorption isotherm of catalyst I. The bars represent (a) 50 nm and (b) 20nm.

The catalyst I was prepared as detailed in the experimental section and it is well characterized by XRD, HRTEM, BET, H₂ chemisorption, SEM-EDX, AFM, FT-IR, and UV-vis spectral techniques. The HRTEM, BET and H₂ chemisorption of catalyst I were given in the Figure 1.

3.1. Oxidation of tertiary amines

A wide variety of tertiary nitrogen compounds were oxidized to their corresponding N-oxides in near quantitative yields and results are summarized in Table 1. In our studies it is observed that pyridines having electron donating substituents such as -CH₃ is oxidized rapidly in a single step to yield the corresponding N-oxides as the exclusive oxidation product when the substrate is treated with 30% of H₂O₂. Lower activity was observed with pyridine unless aromatic substitution changes markedly the electronic properties of the heteroatom (Table 1, entries 1 and 2) due to their intrinsic lower basicity and nucleophilicity. The catalyst I is used as catalyst for the oxidation of pyridine, DMA, substituted DMA and quinoline (Table 1, entries 1-5) and these tertiary amines required 3mmol of H₂O₂ for the oxidation. On the other hand the oxidation of pyrazine, phenazine, quinoxaline, 2,2'-bipy, and 4,4'-bipy (Table 1, entries 6-10) required 6mmol of H₂O₂ for the oxidation and their products are obtained in quantitative yields.

DMA containing the presence of electron donating substituent reacts faster and required lower reaction time when compared to electron withdrawing substituents. The oxidation process was repeated for three consecutive cycles with little loss of activity (Table 1, entry 8).

3.2. Product analysis

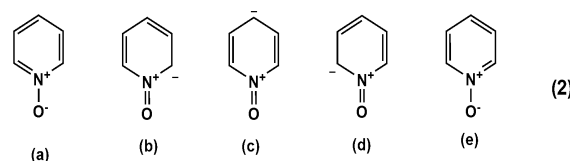
The N-oxides play significant role as an important target in anticancer chemotherapy, DNA cleavage, anti-cancer activity. Similarly PDO and their derivatives have major applications in the field of antitumor effect and selective hypoxic cytotoxins (Lavaggi et al., 2010). FT-IR and NMR techniques have been used for the analysis of the products obtained during the course of the reaction. The FT-IR spectral analysis of orange-red crystals phenazine-5,10- dioxide (PDO) shows a

strong absorption band at N-O at 1348cm^{-1} corresponding to the formation of N-oxide. The product analysis demonstrates that N-oxide is the only product formed under the present reaction conditions.(Nansathit et al., 2009)

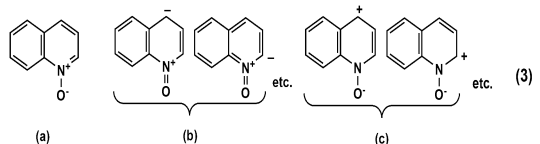
The ^1H NMR data also confirmed the structure of the PDO. Peaks between 7.82 - 8.76 ppm are consistent with the presence of signals for aromatic protons. The ^{13}C -NMR spectra showed the peaks between 120.16 - 136.02 ppm indicating the presence of aromatic carbons. The PDO absorption maxima at 277, 392, 435 and 462 nm in CH_2Cl_2 also supported the formation of PDO.

3.3 Resonance structure

The five resonating forms of pyridine N-oxides may be represented as in Eq. (2). The (N-O) bond will not be purely dative-covalent but will possess some double bond character. In pyridine N-oxide (a) there will be contributions from the forms (b), (c), (d) and (e) represented in Eq. (2) where the negative charge on the oxygen atom is being partially distributed to carbon atoms.



In the resonance system of quinoline 1-oxide (a), just as in that of pyridine 1-oxide, the contribution of mesomeric structure like (b) is expected to be great, as well as that of the ionic structure like (c) represented as in Eq. (3).



Consequently, the N-O bond in quinoline 1-oxide may be expected to have a considerable double bond character, and many chemical and physical studies indicate that the N-O bond in quinoline 1-oxide has essentially the same properties as that in pyridine 1-oxide. Therefore, the N-O stretching frequencies of quinoline 1-oxides can be expected to absorb strongly also in the region of 1176 and 1330 cm^{-1} .

3.4 Influence of different solvents on the reaction

The effect of varying the solvent is also studied for this reaction and the results are presented in Table 2. We first investigated the oxidation reaction with phenazine as model substrate by using 30% H_2O_2 (4.0 mmol) as an oxidant(Pan et al., 2001). Without any solvent the reaction required long time and trace amount of product was observed.

The data collected in Table 2 show that the reaction is sensitive to the change of solvent. Generally tertiary amines are insoluble in water, but when a mixed solvent ($\text{H}_2\text{O}:\text{CH}_3\text{CN}$) 1:1 (v/v) is used for the oxidation the yield is 70%. As far as the oxidation of phenazine is concerned CH_3CN is the best solvent. On the other hand, acetic acid seems to be the better solvent for the oxidation of pyridine and it provides the highest yield (98%). The data collected in Table 2 show that of all the solvents, the yield is best in CH_3CN but lower in the mixed solvent $\text{H}_2\text{O}:\text{CH}_3\text{CN}$ (1:1) because the substrates are poorly soluble in water specifically(Gomez et al., 2003).

3.5 Influence of reaction time

The effect of varying the reaction temperature and time for the oxidation of phenazine is studied and the results are presented in Table 3. Initially the oxidation reaction is slow till 30 min but the reaction is completed in 60 min

The progress of the oxidation reaction is monitored from RT to 100°C . The yield was 50% in 30 min but the maximum yield is obtained in 60 min (99%). But during the increase in the time from 60 to 100 min there is no significant changes in the yield compared with the results obtained in 30 min (Table 3, entry 2 vs. entry 4). Acetonitrile is the suitable solvent for N-oxidation reactions at 80°C to give the optimum yield of the product.

3.6 Mechanism for the oxidation of amines to N-oxides

Generally, amines ($-\text{NH}_2$) interact strongly with transition metal nanoparticles. Among these nanoparticles Ru also binds fairly well with amines (Jansat et al, Favier et al., 2006). A possible reaction mechanism for the H_2O_2 oxidation of amines to N-oxides using catalyst I is proposed in Scheme 1.

In step I, the nitrogen atom of the substrate is likely to attach with the surface of the ruthenium nanoparticles. It is proposed that the interaction between

the metal and nitrogen is due to metal-to-nitrogen charge transfer resulting in nitrogen–metal bonds at the surface of the particles (step II) (Leger et al 2008., Rucareanu et al., 2006). A stronger and favorable interaction between the amines and RuNPs is proposed in Scheme 2.

Previous studies show that 4-dimethylaminopyridine (DMAP), 2,2'-bipyridine (2,2'-bipy) stabilized Au, Pd and Rh NPs. It has been proposed that ligands bind to the surface of these nanoparticles in a perpendicular orientation via the lone pair of electrons on the endocyclic nitrogen atom.(Flanagan et al.,2007,Gandubert et al., 2005) It is believed that electron delocalization places a formal negative charge on the endocyclic nitrogen atom, which is highly favorable for bonding to the metal nanoparticles while concomitantly placing a formal positive charge on the exocyclic nitrogen atom. A similar weak noncovalent interaction may be expected for the DMAP with RuNPs reported here (see Scheme 1). In this mechanism step III involves the addition of aqueous H₂O₂ which is also bound on the Ru surface. Finally, nitrogen atom of amine is oxidized by H₂O₂ in a heterotypic process involving the nucleophilic attack of the nitrogen atom on the oxygen in the step IV. Therefore, the importance of H₂O₂ as a “green” oxidizing agent has grown considerably. The progress of the reaction is monitored using TLC and products analyzed by using NMR, FTIR techniques. Also, the catalyst I is reused up to three times (entry 8 in Table 1) and the catalytic activity decreased only slightly.

4. Conclusions

In this work, we have reported a new and highly efficient methodology for the oxidation of tertiary amines to N-oxides with aqueous hydrogen peroxide in the presence of catalyst I. The simplicity of the system, easy separation of the catalyst I, simple workup and excellent yields make this method an attractive, environmentally acceptable synthetic tool for the oxidation of tertiary nitrogen compounds to their corresponding N-oxides. The cheapness and the availability of the reagents, easy and clean work-up, and good to high yields make this method attractive for large-scale operations.

Acknowledgements

The authors thank UGC for a JRF position under Meritorious Fellowship Scheme and DST, India for the financial support.

References

- [1] Favier I, Massou S, Teuma E, Philippot K, Chaudret B , Gomez M (2008) ,A new and specific mode of stabilisation of metallic nano particles, *Chem. Commun.* No. 28, pp.3296-3298.
- [2] Flanagan K.A, Sullivan J.A, Müller-Bunz H (2007),Preparation and characterization of 4-Dimethylaminopyridine-stabilised palladium nanoparticles, *Langmuir*. V.23, No.25,pp.12508-12520.
- [3] Gandubert V.J, Lennox R.B(2005),Assessment of 4-(Dimethylaminopyridine-stabilised palladium nanoparticles, *Langmuir* V.21, No.14,pp.6532-6539.
- [4] Gomez M, Philippot K, Colliere V, Lecante P, Muller G, Chaudret B (2003), Novel super structures resulting from the co ordination of oxazolines on platinum nanoparticles, *New J. Chem.*V.27, No.1,pp. 114-120
- [5] Jain S.L, Sain B (2003), An unconventional cobalt catalysed aerobic oxidation of tertiary nitrogen compounds to N- oxides, *Angew. Chem. Int. Ed.*, V. 42, No.11, pp.1265-1267.
- [6] Jansat S, Picurelli D, Pelzer K, Philippot K, Gomez M, Muller G, Lecante P, Chaudret B(2006), Synthesis characterization and catalytic reactivity of ruthenium nanoparticles stabilized by chiral N-donor ligands,*New J. Chem.* V.30, No.1,pp.115-122.
- [7] Lavaggi M.L, Nieves M, Cabrera M, Olea-Azar C, Ceráin A. L , Monge A, Cerecetto H, González M(2010), Structural modifications on the phenazine N,N' -dioxide – scaffold looking for new selective hypoxic cyclotoxins, *Eur. J. Med. Chem.* V.45, No. 11,pp.5362-5369.
- [8] Leger B,Denicourt-Nowicki A, Olivier-Bourbigou H, Roucoux A (2008), Rhodium nanocatalysts stabilised by various bipyridine ligands in non aqueous ionic liquids ,*Inorg. Chem.*V.48, No. 19,pp.9090-9096.
- [9] Nansathit A, Apipattarakul S, Phaosiri C, Pongdontri P, Chanhai S, Ruangviriyachai C, Walailak (2009),Synthesis,isolation of phenazine derivatives and their antimicrobial activities,*J Sci & Tech* V.6,No.1,pp.79-91.
- [10] Pan C, Pelzer K, Philippot K, Chaudret B, Dassenoy F, Lecante P, Casanove M.J (2001),Ligand stabilized ruthenium nanoparticles: Synthesis,organization and dynamics, *J. Am. Chem. Soc.* V 123, No 31,pp.7584-7593.
- [11] Rucareanu S, Gandubert V.J,Lennox R.B (2006),4-(N-N-Dimethylamino)pyridine protected Au nanoparticles: *Chem. Mater.*, V.18, No.19,pp.4674-4680.

International Engineering Symposium, March 3-5, 2011 Kumamoto Univ., Japan

Table 1 Oxidation of tertiary amines to N-oxides with H₂O₂ catalyzed by catalyst I^a.

Entry	Substrate	Product	Time/h	Yield (%) ^{b,c}
1			3	95
2			2	98
3			1	>99
4			3	94, 96, 96, 95, 85
(R = H, CH ₃ , Br, CN, COOH)	(R = H, CH ₃ , Br, CN, COOH)			
5			2.5	90
6			3	95 ^d
7			3	97 ^d
8			3	^d 98, 95 ^e , 90 ^f , 87 ^g
9			3	95 ^d
10			3	98 ^d
11			3	96 ^d

^a Experimental conditions: [amine] = 2.0 mmol, [30%H₂O₂] = 3.0 mmol, catalyst I (1 wt%, 0.5-2 mmol), acetonitrile (CH₃CN, 3.0 mL) were stirred at 80°C.

^b Yield of isolated product.

^c Determined by ¹H NMR using an internal standard technique on the crude reaction mixture; Yield = No. of moles of N-oxide/No. of moles of amine.

^d 6 mmol of 30%H₂O₂ used.

^{e,f,g} The catalyst is reused repeatedly

Table 2 Oxidation of phenazine by H₂O₂ in the presence of catalyst **I**^a.

Entry	Solvent	Reaction time/h	Conversion (%) ^b	Yield (%) ^{b,c}
1	-	42	40	trace
2	H ₂ O	12	60	50
3	MeOH	3	80	70
4	EtOH	3	85	65
5	H ₂ O:CH ₃ CN	12	75	70
6	CH ₃ CN	1	98	99
7	CHCl ₃	4	80	75
8	CH ₂ Cl ₂	3	85	80
9	1,4-Dioxane	10	60	50
10	Acetic acid	8	92	98 ^d

^a Reaction conditions: 3 mL of solvent; 2.0 mmol of phenazine; 6 mmol H₂O₂; 0.5 mmol (catalyst **I**) were stirred at 80°C.

^b Determined by TLC and NMR method.

^c Yield = No. of moles of N-oxide/No. of moles of amine.

^d The substrate used was pyridine

Table 3 Oxidation of phenazine NMA: variation of reaction temperature^a

Entry	Temp (°C)	Time (min)	Conversion (%) ^b	Yield (%) ^{b,c}
1	RT	15	30	trace
2	40	30	60	50
3	60	45	90	85
4	80	60	98	99
5	80	100	98	99

^a Reaction conditions: 3 mL of solvent; 2.0 mmol of phenazine; 6 mmol, H₂O₂; 0.5 mmol (catalyst **I**).

^b Determined by TLC and NMR method.

^c Yield = No. of moles of N-oxide/No. of moles of amine.

RT= Room temperature.

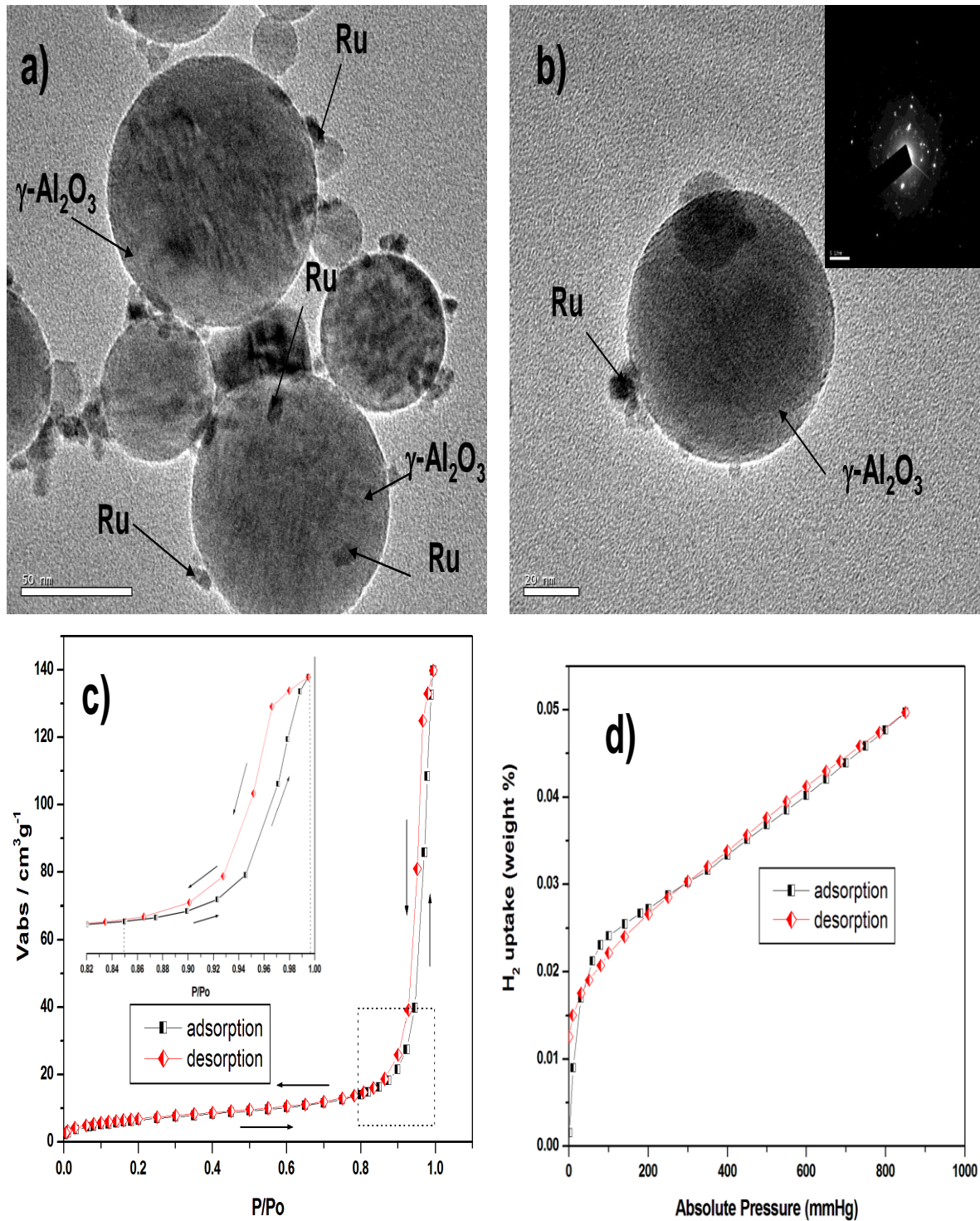
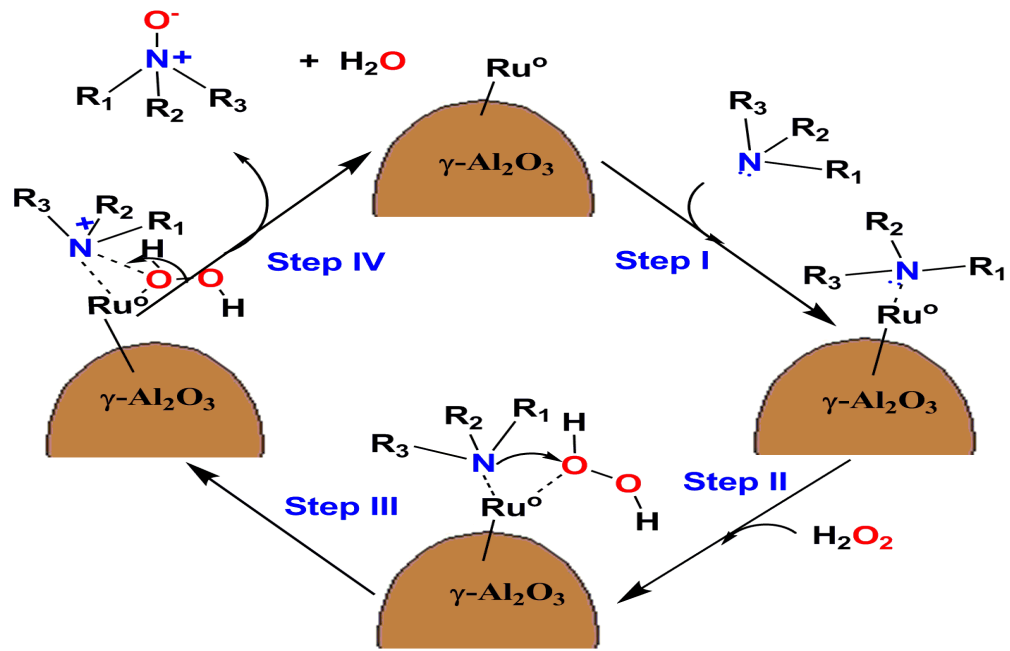


Figure 1

- (a) HRTEM image of catalyst **I**,
 - (b) single particle with EDX
 - (c) adsorption-desorption isotherm and (d) hydrogen chemisorption isotherm of catalyst **I**.
- The bars represent (a) 50 nm and (b) 20nm.

Scheme 1 Mechanism for the oxidation of tertiary amines using catalyst I in CH₃CN.



Scheme 2 Representation of binding orientations of amines (a) 4-picoline, (b) 4-dimethylaminopyridine, (c) 2,2-bipyridine and (d) 1,10-phenanthroline onto surface of RuNPs.

